frontiers | Research Topics

Community series in combining chemo/radio therapy and immunotherapy for cancers—perfect mix of old and new, volume II

Edited by
Jian Zhang, Linlang Guo, Feng-Ming (Spring) Kong and Clare Y. Slaney

Published in
Frontiers in Immunology
Frontiers in Oncology

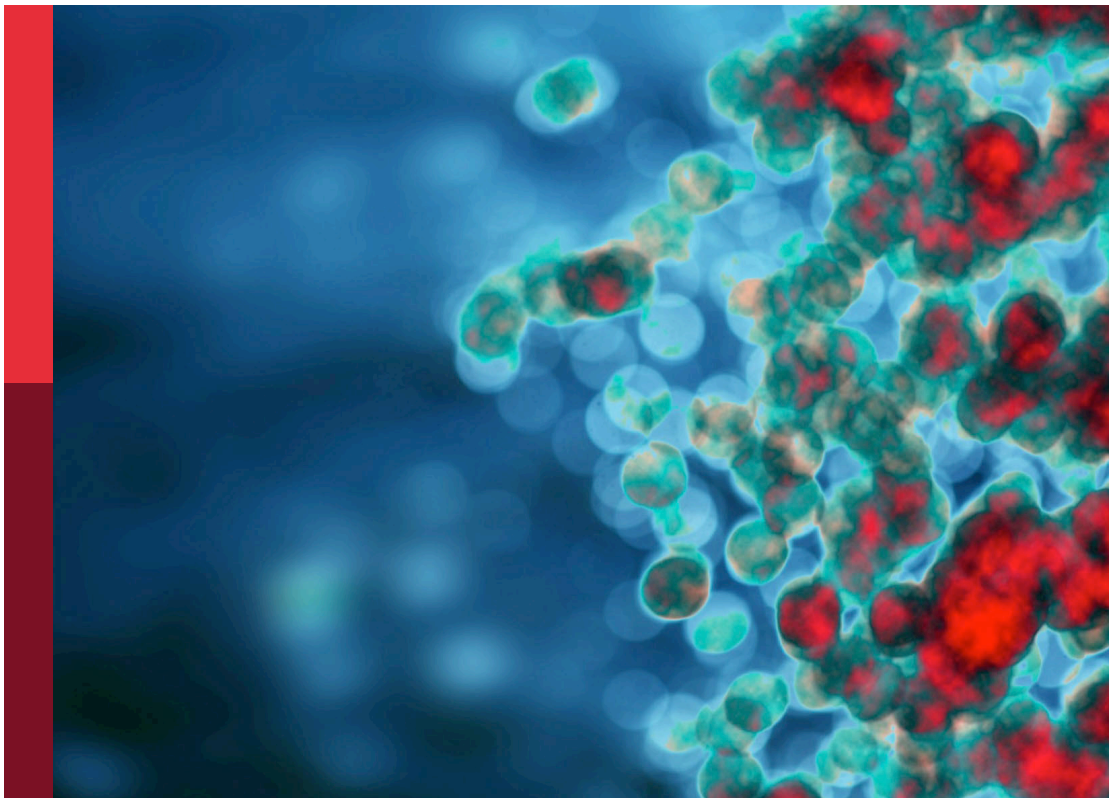

FRONTIERS EBOOK COPYRIGHT STATEMENT

The copyright in the text of individual articles in this ebook is the property of their respective authors or their respective institutions or funders. The copyright in graphics and images within each article may be subject to copyright of other parties. In both cases this is subject to a license granted to Frontiers.

The compilation of articles constituting this ebook is the property of Frontiers.

Each article within this ebook, and the ebook itself, are published under the most recent version of the Creative Commons CC-BY licence. The version current at the date of publication of this ebook is CC-BY 4.0. If the CC-BY licence is updated, the licence granted by Frontiers is automatically updated to the new version.

When exercising any right under the CC-BY licence, Frontiers must be attributed as the original publisher of the article or ebook, as applicable.

Authors have the responsibility of ensuring that any graphics or other materials which are the property of others may be included in the CC-BY licence, but this should be checked before relying on the CC-BY licence to reproduce those materials. Any copyright notices relating to those materials must be complied with.

Copyright and source acknowledgement notices may not be removed and must be displayed in any copy, derivative work or partial copy which includes the elements in question.

All copyright, and all rights therein, are protected by national and international copyright laws. The above represents a summary only. For further information please read Frontiers' Conditions for Website Use and Copyright Statement, and the applicable CC-BY licence.

ISSN 1664-8714
ISBN 978-2-8325-3227-0
DOI 10.3389/978-2-8325-3227-0

About Frontiers

Frontiers is more than just an open access publisher of scholarly articles: it is a pioneering approach to the world of academia, radically improving the way scholarly research is managed. The grand vision of Frontiers is a world where all people have an equal opportunity to seek, share and generate knowledge. Frontiers provides immediate and permanent online open access to all its publications, but this alone is not enough to realize our grand goals.

Frontiers journal series

The Frontiers journal series is a multi-tier and interdisciplinary set of open-access, online journals, promising a paradigm shift from the current review, selection and dissemination processes in academic publishing. All Frontiers journals are driven by researchers for researchers; therefore, they constitute a service to the scholarly community. At the same time, the *Frontiers journal series* operates on a revolutionary invention, the tiered publishing system, initially addressing specific communities of scholars, and gradually climbing up to broader public understanding, thus serving the interests of the lay society, too.

Dedication to quality

Each Frontiers article is a landmark of the highest quality, thanks to genuinely collaborative interactions between authors and review editors, who include some of the world's best academicians. Research must be certified by peers before entering a stream of knowledge that may eventually reach the public - and shape society; therefore, Frontiers only applies the most rigorous and unbiased reviews. Frontiers revolutionizes research publishing by freely delivering the most outstanding research, evaluated with no bias from both the academic and social point of view. By applying the most advanced information technologies, Frontiers is catapulting scholarly publishing into a new generation.

What are Frontiers Research Topics?

Frontiers Research Topics are very popular trademarks of the *Frontiers journals series*: they are collections of at least ten articles, all centered on a particular subject. With their unique mix of varied contributions from Original Research to Review Articles, Frontiers Research Topics unify the most influential researchers, the latest key findings and historical advances in a hot research area.

Find out more on how to host your own Frontiers Research Topic or contribute to one as an author by contacting the Frontiers editorial office: frontiersin.org/about/contact

Community series in combining chemo/radio therapy and immunotherapy for cancers—perfect mix of old and new - volume II

Topic editors

Jian Zhang — Southern Medical University, China

Linlang Guo — Zhujiang hospital, China

Feng-Ming (Spring) Kong — The University of Hong Kong, Hong Kong, SAR China

Clare Y. Slaney — Peter MacCallum Cancer Centre, Australia

Citation

Zhang, J., Guo, L., Kong, F.-M., Slaney, C. Y., eds. (2023). *Community series in combining chemo/radio therapy and immunotherapy for cancers—perfect mix of old and new - volume II*. Lausanne: Frontiers Media SA.

doi: 10.3389/978-2-8325-3227-0

Table of contents

07 Crosstalk of RNA Adenosine Modification-Related Subtypes, Establishment of a Prognostic Model, and Immune Infiltration Characteristics in Ovarian Cancer
Xiaoge Ni, Can Chen, Guoliang Cui, Wei Ding and Jinhui Liu

26 CD8+ T cell trajectory subtypes decode tumor heterogeneity and provide treatment recommendations for hepatocellular carcinoma
Long Liu, Zaoqu Liu, Jie Gao, Xudong Liu, Siyuan Weng, Chunguang Guo, Bowen Hu, Zhihui Wang, Jiakai Zhang, Jihua Shi, Wenzhi Guo and Shuijun Zhang

43 Identification of a novel cuproptosis-related gene signature and integrative analyses in patients with lower-grade gliomas
Jia-hao Bao, Wei-cheng Lu, Hao Duan, Ya-qi Ye, Jiang-bo Li, Wen-ting Liao, Yong-chun Li and Yang-peng Sun

69 Integrated driver mutations profile of chinese gastrointestinal-natural killer/T-cell lymphoma
Shanshan Li, Tingzhi Liu, Hailing Liu, Xiaohui Zhai, Taiyuan Cao, Hongen Yu, Wanjia Hong, Xiaoru Lin, Ming Li, Yan Huang and Jian Xiao

81 An open, observational, three-arm clinical study of 2–3 cycles of treatment as neoadjuvant therapy in operable locally advanced non-small cell lung cancer: An interim analysis
Linping Gu, Xue Wang, Yile Sun, Yunhua Xu, Xiaomin Niu, Ruiying Zhao, Yaxian Yao, Hong Jian, Yuchen Han, Jinwang Wei, Zhiwei Chen and Shun Lu

92 Robust pyroptosis risk score guides the treatment options and predicts the prognosis of bladder carcinoma
Dingshan Deng, Fenglian Liu, Zhi Liu, Zuowei Wu, Yunbo He, ChunYu Zhang, Xiongbin Zu, Zhenyu Ou and Yongjie Wang

111 Definition of a new blood cell count score for early survival prediction for non-small cell lung cancer patients treated with atezolizumab: Integrated analysis of four multicenter clinical trials
Jian-Guo Zhou, Ada Hang-Heng Wong, Haitao Wang, Su-Han Jin, Fangya Tan, Yu-Zhong Chen, Si-Si He, Gang Shen, Benjamin Frey, Rainer Fietkau, Markus Hecht, Shamus R. Carr, Ruihong Wang, Bo Shen, David S. Schrump, Hu Ma and Udo S. Gaipl

122 Integrated genomic, transcriptomic, and epigenetic analyses identify a leukotriene synthesis-related M2 macrophage gene signature that predicts prognosis and treatment vulnerability in gliomas
Hang Ji, Zhihui Liu, Nan Wang, Jiaqi Jin, Jiheng Zhang, Jiawei Dong, Fang Wang, Xiuwei Yan, Qin Gong, Hongtao Zhao, Haogeng Sun, Yongzhe Li, Shaoshan Hu and Chao You

139 Novel macrophage-related gene prognostic index for glioblastoma associated with M2 macrophages and T cell dysfunction
Hang Ji, Zhihui Liu, Fang Wang, Haogeng Sun, Nan Wang, Yi Liu, Shaoshan Hu and Chao You

155 Combining autophagy and immune characterizations to predict prognosis and therapeutic response in lung adenocarcinoma
Qiaxuan Li, Daipeng Xie, Lintong Yao, Hongrui Qiu, Peimeng You, Jialong Deng, Congsen Li, Weijie Zhan, Maotao Weng, Shaowei Wu, Fasheng Li, Yubo Zhou, Fanjun Zeng, Yong Zheng and Haiyu Zhou

174 Radiotherapy improves the outcomes of immunotherapy with Sintilimab in non-small-cell lung cancer: A real-world analysis
Shuling Li, Kuifei Chen, Meiwen Yang, Swe Swe Hlaing, Meng Chen, Pinjun Gu, Yinnan Meng and Haihua Yang

186 Identification of four immune subtypes in locally advanced rectal cancer treated with neoadjuvant chemotherapy for predicting the efficacy of subsequent immune checkpoint blockade
Le He, Min Jin, Dan Jian, Bo Yang, Nan Dai, Yan Feng, He Xiao and Dong Wang

198 A novel medication decision gene signature predicts response to individualized therapy and prognosis outcomes in hepatocellular carcinoma patients
Jingsheng Yuan, Zijian Liu, Zhenru Wu, Lvnan Yan, Jiayin Yang and Yujun Shi

216 A prognostic signature consisting of metabolism-related genes and SLC17A4 serves as a potential biomarker of immunotherapeutic prediction in prostate cancer
He Li, Jie Gu, Yuqiu Tian, Shuyu Li, Hao Zhang, Ziyu Dai, Zeyu Wang, Nan Zhang and Renjun Peng

235 Low-dose immunogenic chemotherapeutics promotes immune checkpoint blockade in microsatellite stability colon cancer
Yuhang Fang, Haoyu Sun, Xinghui Xiao, Maoxing Tang, Zhigang Tian, Haiming Wei, Rui Sun and Xiaodong Zheng

248 Toxicity profile of combined immune checkpoint inhibitors and thoracic radiotherapy in esophageal cancer: A meta-analysis and systematic review
Tongzhen Xu, Yunsong Liu, Xiaotong Lu and Jun Liang

260 Photodynamic therapy improves the clinical efficacy of advanced colorectal cancer and recruits immune cells into the tumor immune microenvironment
Baohong Gu, Bofang Wang, Xuemei Li, Zedong Feng, Chenhui Ma, Lei Gao, Yang Yu, Jing Zhang, Peng Zheng, Yunpeng Wang, Haiyuan Li, Tao Zhang and Hao Chen

275 Identification of fatty acid metabolism–related molecular subtype biomarkers and their correlation with immune checkpoints in cutaneous melanoma
Yujian Xu, Youbai Chen, Weiqian Jiang, Xiangye Yin, Dongsheng Chen, Yuan Chi, Yuting Wang, Julei Zhang, Qixu Zhang and Yan Han

292 Crosstalk of angiogenesis-related subtypes, establishment of a prognostic signature and immune infiltration characteristics in colorectal adenocarcinoma
Guoliang Cui, Jinhui Liu, Manli Wang, Kinyu Shon, Can Wang, Fei Wei and Zhiguang Sun

309 MYCBP2 expression correlated with inflammatory cell infiltration and prognosis immunotherapy in thyroid cancer patients
Guilin Wang, Chen Miao, Lijun Mo, Ulf D. Kahlert, Jinfeng Wu, Minglin Ou, Renxiang Huang, Ruifa Feng, Weiyi Pang and Wenjie Shi

321 IP-score correlated to endogenous tumour antigen peptide processing: A candidate clinical response score algorithm of immune checkpoint inhibitors therapy in multiple cohorts
Yutao Wang, Kexin Yan, Ye Guo, Yi Lu, Hao Su and Hongjun Li

338 The application basis of immuno-checkpoint inhibitors combined with chemotherapy in cancer treatment
Ming-Yan Shi, Han-Ge Liu, Xiao-Hong Chen, Ye Tian, Zhi-Nan Chen and Ke Wang

347 Effects of chemotherapy and immunotherapy on microbial diversity in TME and engineered bacterial-mediated tumor therapy
Heng Zheng, Xianxian Chen, Qiyang Li, Yuqi Liu and Jinzhong Cai

356 Predictive value of ^{18}F-FDG PET/CT for evaluating the response to hypofractionated radiotherapy combined with PD-1 blockade in non-small cell lung cancer
Shan Tang, Yan Zhang, Yunfei Li, Yan Zhang, Yuke Xu, Haoyuan Ding, Yue Chen, Peirong Ren, Hua Ye, Shaozhi Fu and Sheng Lin

368 Pre-immunotherapy radiotherapy enhanced the efficacy of multi-line sintilimab in unresectable advanced esophageal squamous cell carcinoma
Shuhui Xu, Xianxing Xu and Hui Zhu

376 Combining chemotherapy with CAR-T cell therapy in treating solid tumors
Arthur Xuan Wang, Xiao Jing Ong, Criselle D'Souza, Paul J. Neeson and Joe Jiang Zhu

387 Tumor immune microenvironment changes are associated with response to neoadjuvant chemotherapy and long-term survival benefits in advanced epithelial ovarian cancer: A pilot study
Guangming Cao, Dingchao Hua, Jinfeng Li, Xuefang Zhang, Zhiqiang Zhang, Bei Zhang, Ting Bei, Lina Cui, Shiqing Chen, Shuzhen Wang and Lei Zhu

397 Total neoadjuvant treatment and PD-1/PD-L1 checkpoint inhibitor in locally advanced rectal cancer
Weiwei Xiao, Huilong Luo, Ye Yao, Yaqin Wang, Shuang Liu, Rui Sun and Gong Chen

408 Efficacy and safety of combined immunotherapy and stereotactic radiosurgery in NSCLCBM patients and a novel prognostic nomogram: A real-world study
Shoaib Bashir, Lei Wen, Ping Zhang, Minting Ye, Yin Li, Weiping Hong, Junjie Zhen, Mingyao Lai, Hui Wang, Yanying Yang, Xingrui Chen, Rishun Luo, Guoxia Jia, Yao Guo, Linbo Cai and Meng Xu

426 Demethylating therapy increases cytotoxicity of CD44v6 CAR-T cells against acute myeloid leukemia
Ling Tang, Yingjie Kong, Haobing Wang, Ping Zou, Ting Sun, Ying Liu, Juan Zhang, Na Jin, Hanwen Mao, Xiaojian Zhu, Jue Wang, Fankai Meng and Yong You

441 Spatial distribution of tumor-infiltrating T cells indicated immune response status under chemoradiotherapy plus PD-1 blockade in esophageal cancer
Cihui Yan, Hui Huang, Zhunhao Zheng, Xiaoxue Ma, Gang Zhao, Tian Zhang, Xi Chen, Fuliang Cao, Hui Wei, Jie Dong, Peng Tang, Hongjing Jiang, Meng Wang, Ping Wang, Qingsong Pang and Wencheng Zhang

frontiers | Frontiers in Immunology

ORIGINAL RESEARCH
published: 28 June 2022
doi: 10.3389/fimmu.2022.932876

Crosstalk of RNA Adenosine Modification-Related Subtypes, Establishment of a Prognostic Model, and Immune Infiltration Characteristics in Ovarian Cancer

Xiaoge Ni[1†], *Can Chen*[2†], *Guoliang Cui*[3†], *Wei Ding*[4†] *and Jinhui Liu*[5*]

[1] Department of Obstetrics and Gynecology, Affiliated People's Hospital of Jiangsu University, Zhenjiang, China, [2] Department of Laboratory Medicine, The First Affiliated Hospital of Nanjing Medical University, Nanjing, China, [3] Department of Gastroenterology, The Second Affiliated Hospital of Nanjing University of Chinese Medicine, Nanjing, China, [4] Department of Nuclear Medicine, The First Affiliated Hospital of Nanjing Medical University, Nanjing, China, [5] Department of Gynecology, The First Affiliated Hospital of Nanjing Medical University, Nanjing, China

OPEN ACCESS

Edited by:
Clare Y. Slaney,
Peter MacCallum Cancer Centre, Australia

Reviewed by:
Feng Jiang,
Fudan University, China
Xinyuan Zhao,
Nantong University, China

***Correspondence:**
Jinhui Liu
jinhuiliu@njmu.edu.cn

[†]These authors have contributed equally to this work

Specialty section:
This article was submitted to Cancer Immunity and Immunotherapy, a section of the journal Frontiers in Immunology

Received: 30 April 2022
Accepted: 30 May 2022
Published: 28 June 2022

Citation:
Ni X, Chen C, Cui G, Ding W and Liu J (2022) Crosstalk of RNA Adenosine Modification-Related Subtypes, Establishment of a Prognostic Model, and Immune Infiltration Characteristics in Ovarian Cancer. Front. Immunol. 13:932876. doi: 10.3389/fimmu.2022.932876

Background: Four RNA adenosine modifications, including m6A, m1A, alternative polyadenylation, and adenosine-to-inosine RNA editing, have been identified as potentially valuable in influencing colorectal carcinogenesis, immune infiltration, and response to drug therapy. However, the regulatory mechanisms and clinical significance of these four RNA modifications in ovarian cancer (OC) remain unknown.

Methods: We comprehensively described the transcriptional and genetic modifications of 26 RNA modification "writers" in OC and assessed the expression patterns. We identified two RNA modification subtypes using an unsupervised clustering approach. Subsequently, using differentially expressed genes (DEGs) in both subtypes, we calculated RNA modification "writer" scores (RMW scores) to characterize the RNA modifications of single OC patients. RMW score-related gene expression was investigated by qRT-PCR. We explored the correlation between RMW score and clinical features, immune infiltration, and drug sensitivity. We drew a nomogram to more intuitively and accurately describe the application value of the RMW score.

Results: We found that molecular alterations in "writers" are strongly related to prognostic and immune-infiltrating features in OC patients. We identified two different clusters of RNA modifications. According to the immune infiltration characteristics in the two RNA modification isoforms, cluster A and cluster B can correspond to "hot" and "cold" tumors, respectively. With the median RMW score, we classified the patients into high- and low-score subgroups. A low RMW score was associated with good patient prognosis and lower immune infiltration. In addition, a low RMW score equated with a higher cancer stem cell index and a lower tumor mutation burden, which to some extent affected the sensitivity of patients to therapeutic drugs. Seven RMW score-related gene expressions

were investigated by qRT-PCR in three OC cell lines. Compared to previously known models, our established RMW score has higher accuracy in predicting patient survival.

Conclusion: A comprehensive analysis of four RNA modification patterns in OC reveals their potential value in OC prognosis, immune microenvironment, and drug sensitivity. These results could deepen our knowledge of RNA modification and yield fresh insights for new personalized therapeutic strategies.

Keywords: RNA modification "writers", ovarian cancer, immune infiltration, RMW score, drug sensitivity

INTRODUCTION

Ovarian cancer (OC) is a malignant tumor that grows on the ovaries, 90%–95% of which are primary (1). Because the ovary is located in the pelvis, the onset is insidious, and there is no perfect early diagnosis and identification method. Once symptoms appear, it is often a late-stage disease (2). Of newly diagnosed OC patients, 70%~80% can achieve a certain curative effect, but because OC easily spreads and metastasizes in the abdominal cavity, most advanced OC patients will still face tumor recurrence (3). OC has the highest mortality rate among gynecological malignancies and has become the most threatening to women's life and health among all gynecological tumors (4).

Like epigenetic DNA and histone modifications, RNA modifications have become important modulators of gene expression throughout eukaryotic development. So far, several kinds of RNA modifications have been recognized, including N6-methyladenosine (m6A) and N1-methyladenosine (m1A) (5). These modifications can be installed, removed, and decoded in a reversible manner *via* their specific cellular compositions and perform critical functions in multiple biotic processes (6). All RNA nucleotides, including adenine nucleotides, guanine nucleotides, cytosine nucleotides, and uracil nucleotides, are chemically modified (7). Among them, the modification of adenine nucleotide (A) is the most common, such as m1A, m6A, alterative polyadenylation (APA), and adenosine-to-inosine RNA editing (A-to-I). The RNA epigenetic modifications on these A bases are very different in catalytic principle and occurrence position (8–11) and generally do not compete to occur at the same A base position. However, some studies have elucidated the negative regulation of m6A modification on A-to-I editing and its mechanism (12). Considering the interaction between different RNA modifications and the fact that these modifications are mainly regulated by methyltransferases (writers) (13), we set out to study the regulatory network among the RNA "writers" with the above four modifications.

m6A is a methylation modification on the 6th nitrogen atom of adenine (14). m6A methylation is currently the most important chemical modification found in eukaryotic cells and plays an important role in various cellular processes, especially tumor development (15–17). During transcription m6A deposition occurs in nascent pre-mRNAs by methyltransferase complexes in the nucleus. Complexes include METTL3, METTL14, RBM15, WTAP, and KIAA1429, among others (18).

m1A is a methylation modification that occurs on the first nitrogen atom of adenine. A high abundance of m1A modifications is present on tRNA and rRNA (19, 20). Furthermore, m1A modifications also occur on mRNA (21). m1A plays a key role in regulating mRNA translation initiation and elongation, mRNA stability, and related developmental processes (22). The m1A "writers" that have been found so far mainly include TRMT10C, TRMT6, TRMT61A, and TRMT61B (21, 23).

APA is a widespread gene post-transcriptional regulation process in eukaryotes. Most APAs occur in the 3′UTR region (24). Through the selection of different polyadenylations in the 3′-UTR region, APA can affect important processes such as mRNA stability, translation efficiency, and cellular localization (25). The factors that regulate the formation of APA mainly include CFI, NUDT21, CPSF, PABPN1 family (CPSF1-4), and CTSF family (CSTF1-3) protein complexes (11, 24).

A-to-I type RNA editing is a fundamental biological phenomenon that is widespread in mammals and is considered a post-transcriptional modification mechanism capable of generating molecular diversity (26). It regulates protein translation by recoding, greatly enriching genetic information. A-to-I type RNA editing not only has an important impact on the regulation of gene expression but also is intimately linked to the pathogenesis of many diseases (27, 28). ADAR, ADARB1, and ADARB2 are the catalytic enzymes that exercise this important type of RNA modification (29).

The tumor immune microenvironment (TME) refers to the immediate ecological niche surrounding a tumor, consisting of various types of cells in the metabolic environment. TME contains a complex immune cellular environment that includes cells engaged in the innate immune response, such as natural killer (NK) cells and dendritic cells, and cells engaged in the adaptive immune response, such as T and B cells (30, 31). Some studies have classified tumors into "cold tumors" and "hot tumors" according to the presence or absence of tumor-infiltrating lymphocytes (TILs) in the TME. "Hot" tumors are tumors with infiltrating lymphocytes, whereas "cold" tumors are the opposite. In general, hot tumors are more immunogenic than "cold" tumors (32, 33). Recent findings suggest that RNA modifications are an essential epigenetic regime affecting tumor immune response and tumorigenesis (34). METTL3 deletion disrupts T-cell homeostasis and differentiation. METTL3-deficient T cells fail to perform homeostatic

proliferation and maintain naïve (35). Four types of RNA modification "writers" have been shown to form a complex regulatory network in colorectal cancer to influence immune regulation and immunotherapy in the TME (36). However, whether this regulatory network plays an effect on OC TME is still unknown and needs to be further explored.

In this study, we assessed expression levels and genomic alterations in 26 "writers" in OC specimens from The Cancer Genome Atlas (TCGA) and Gene Expression Omnibus (GEO) databases, and we compared expression levels with normal ovarian samples from the GTEx database. By comprehensively evaluating the two RNA modification patterns of OC samples, we revealed that RNA modification modes are related to not only tumor immune infiltration, which can correspond to different immune typing, but also cell proliferation and oncogenic mechanisms. Patients were then categorized into distinct gene clusters according to the expression profiles of differentially expressed genes (DEGs) in two RNA modification clusters. Considering individual differences in RNA modification, we calculated the RNA modification score to accurately quantitate RNA modification patterns in a single OC patient and proved that this score can correctly predict patient outcomes, immune characteristics, and treatment efficacy.

MATERIALS AND METHODS

Data Collection and Processing

The process of this research is illustrated in **Figure S1A**. Gene expression data and full clinical descriptions for OC were retrieved and obtained from GEO and TCGA databases. Somatic mutation and copy number variation (CNV) datasets were obtained from TCGA database. This study used three cohorts, TCGA-OV, GSE9891, and GSE26193, for subsequent analysis. Only tumor samples were retained for this study. Duplicate samples from the same patient were removed. Samples with no follow-up information and incomplete clinical information were also deleted. For TCGA-OV cohort, after converting the genes' fragments per kilobase (FPKM) values to transcripts per kilobase (TPM), the "normalizeBetweenArrays" function of the R package "Limma" were applied to perform data normalization. For the GEO dataset, probe IDs were converted to gene symbols according to the platform annotation file. Normalized expression values were log-transformed and scaled before being used for model validation. The mean value of genes with multiple probes was used as their expression value (37). Normalization and removal of batch effects between TCGA-OV and two GEO datasets were performed using the "ComBat" algorithm from the "sva" package (38).

Unsupervised Cluster Analysis of RNA Modification "Writers"

A total of 26 RNA modification "writers" were identified based on previous research (36). **Table S1** shows the details of these genes. According to these gene expression profiles, the "ConsensusClusterPlus" package was used to perform an unsupervised cluster analysis of the patients and divided the samples into two distinct subtypes. For the major parameters in the "ConsensusClusterPlus" function, the following was set: the max cluste number (maxK) = 9, proportion of items to sample (pItem) = 0.8, proportion of features to sample (pFeature) = 1, cluster algorithm (clusterAlg) = hc/hierarchical, and distance = spearman. The above process is repeated 1,000 times to ensure the consistency of the classification (39).

Gene Set Variation Analysis

To explore the biological functions between different RNA modification patterns, based on the "c2.cp.kegg.v6.2.symbols.gmts" gene set in the MsigDB database, with two RNA modification isoforms as phenotypic features, the Gene Set Variation Analysis ("GSVA") package was used to determine biological process differences between different RNA modification (40).

Assessment of Immune Infiltration

The Single-Sample Gene Set Enrichment Analysis (ssGSEA) algorithm was applied to estimate the immune infiltration of each OC sample, and an enrichment score was used to indicate the degree of enrichment of each immune cell (41). The CIBERSORT algorithm assesses the composition and relative proportions of tumor-infiltrating immune cells in OC samples (42). CIBERSORT results are available online (https://gdc.cancer.gov/about-data/publications/panimmune) (43). ESTIMATE algorithm was used to compute immune and stromal scores between subgroups to deduce tumor purity (44).

Correlation Between RNA Modifications and Other Biological Processes

Rosenberg et al. built a set of gene sets associated with biological processes, including epithelial–mesenchymal transition (EMT) markers, DNA damage repair, nucleotide excision repair, and CD8 T-effector signature (45–47). A correlation analysis of these biological pathways with RNA modification isoforms and RMW scores was performed to reveal the potential biological effects of RNA modifications.

Identification of Differentially Expressed Genes Between RNA Modification Isoforms and Functional Annotation

Empirical Bayesian methods in the "limma" package were used for identifying DEGs of different RNA-modifying isoforms (48). A total of 1,641 DEGs were screened using adjusted p-value < 0.05 as criteria. "clusterProfiler" was used to perform Gene Ontology (GO) and Kyoto Encyclopedia of Genes and Genomes (KEGG) functional enrichment analysis to explore the potential biological functions of these DEGs (49).

Construction of RNA Modification Gene Signature

All OC patients were equally randomized into training and test groups, and then RNA modification-related RMW scores were constructed using the training group. First, in the training set, a univariate Cox regression analysis of 1,641 DEGs identified 10

RNA modification "writers"-related genes significantly linked to prognosis ($p < 0.001$). The model fit was then minimized using the least absolute shrinkage and selection operator (LASSO) regression analysis (50). Finally, by obtaining the seven central DEGs and their correlation coefficients through a multivariate Cox regression model, an RNA modification gene signature, called the RMW score, was constructed. RMW score = Σ(Expi * coefi), where Coefi and Expi represent the correlation coefficient and expression of each gene, respectively. The sample was categorized into the high and low groups by median score. The "survminer" package was applied to perform survival analysis between the two groups and plot the receiver operating characteristic (ROC) curve to evaluate the model's precision.

RNA Extraction and qRT-PCR

TRIZOL reagent (Thermo Fisher Scientific, Waltham, MA, USA) was used to isolate total RNA from cell lines, and Revert Aid First Strand cDNA Synthesis kit (Thermo Fisher Scientific, USA) was used to synthesize cDNA. GAPDH was chosen as the internal reference. The relative expression of the target gene was estimated using the $2^{-\Delta\Delta CT}$ method. The primer sequences are listed in **Table S2**.

Cell Culture

The OC cell lines (SKOV3, HO8910, and OVCAR3) were purchased from China Center for Type Culture Collection (CCTCC) and CRC/PUMC (Cell Resource Center, IBMS, and CAMS/PUMC). The normal ovarian cell line (IOSE) was obtained from Shanghai Yaji Biotechnology Co., Ltd. All cells were maintained in Dulbecco's modified Eagle medium (DMEM) (Gibco; Thermo Fisher Scientific, Inc.) containing 10% fetal bovine serum (FBS) (Gibco; Thermo Fisher Scientific, Inc.) in a humidified incubator at 37°C and 5% CO_2.

Creation and Validation of Nomogram

The "rms" package was used to integrate clinical characteristics and risk scores and draw a nomogram to visualize the relationship between variables in the prediction model (51). The calibration curve is used to verify the predictive ability of the prediction model. The closer the curve is to the diagonal, the better the prediction effect. Decision curve analysis (DCA) assessed the clinical application of the model by calculating the net benefit rate.

Phenotypes of DNA and RNA Differentiation

Cancer stem cell scores, including mRNA expression-based RNAs and DNA methylation-based DNAs, were designed to gauge cancer stem cell association (52). Scores range from 0 to 1. The closer the score is to 1, the stronger the degree of stemness and the lower the degree of differentiation. Both RNA and DNA scores were obtained from the xena browser (https://xenabrowser.net/datapages/).

Drug Sensitivity Prediction

The CellMiner database is based on the 60 types of cancer cells (NCI-60) listed by the National Cancer Institute's Center for Cancer Research (NCI) (53). The NCI-60 cell line is the most widely used cancer cell sample population for anticancer drug testing. The CellMiner database was queried for 22,379 identified gene expression data and drug sensitivity data (IC50) for 20,503 analyzed compounds in NCI-60 cell lines to analyze the sensitivity between genes and drugs. Tumor Immune Dysfunction and Exclusion (TIDE) score is based on the analysis of T-cell dysfunction under a high level of cytotoxic T-cell infiltration and T-cell rejection characteristic genes in immunosuppression, which can effectively predict the effect of immune checkpoint inhibitor (ICI) therapy. The TIDE score is composed of two components: dysfunction score and exclusion score. The higher the TIDE score, the worse the efficacy of ICIs and the shorter the survival of patients (54). The Genomics of Drug Sensitivity in Cancer (GDSC) database contains information on molecular markers of drug sensitivity in cancer cells, which is important for discovering potential targets for tumor therapy. The GDSC database can be used to examine the sensitivity between RMW scores and cancer drugs (55).

Statistical Analysis

Spearman's and distance correlation analyses were performed to estimate correlation coefficients between the expression of RNA modification "writers" and immune infiltrating cells. Wilcoxon's test was performed to analyze the variation between the two groups. Survival curves were drawn using the Kaplan–Meier (K-M) method, and a log-rank test was performed to determine the significance of the differences. ROC curve was performed to verify the validity of the model. $p < 0.05$ was considered statistically significant. All data were processed using R 4.0.1 software.

RESULTS

Genetic and Transcriptional Alterations in RNA Modification "Writers" in Ovarian Cancer

Altogether, 26 RNA modification "writers" were included in this study (**Table S1**) (15, 21, 24, 28, 36). First, we comprehensively analyzed the somatic mutation status of these "writers" in TCGA-OC cohort. Overall, 26 "writers" had low mutation rates in OC. Only 31 of 436 OC patients had RNA-modifying mutations (7.11%), and only ADAR and ZC3H13 mutations were present (**Figure 1A**). Next, we analyzed the CNVs and revealed that CNVs were ubiquitous in all "writers." Among them, the vast majority of "writers", such as CSAF and ADAR, showed copy number gain, while WTAP and others showed copy number loss (**Figure 1B**). **Figure 1C** shows the chromosomal locations of CNV variants in 26 "writers".

To reveal whether genetic variation in these "writers" in OC interferes with gene expression, we compared these "writers" expressions in normal and OC tissues. Compared with normal tissues, the number of "writers" with increased, decreased expression was approximately equal in OC samples, and the difference in expression of these genes in both tissues was

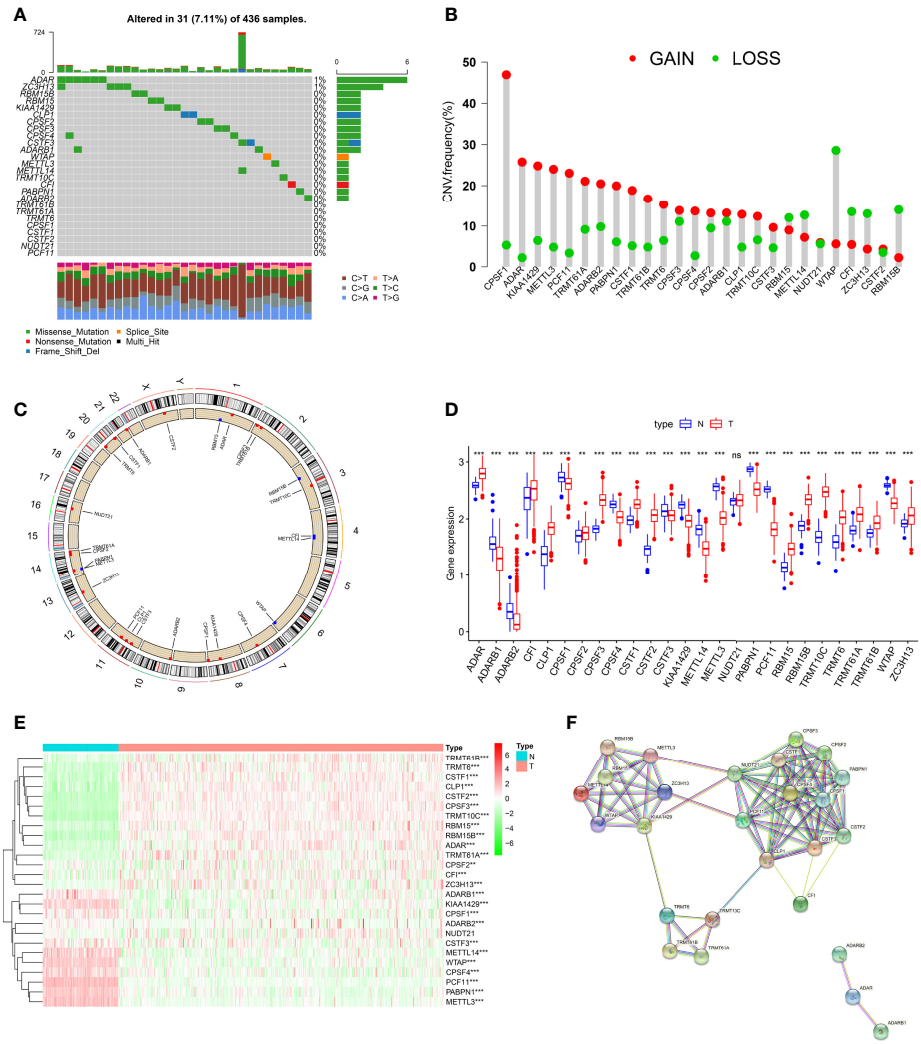

FIGURE 1 | Genetic and transcriptional alterations of RNA modification "writers" in ovarian cancer (OC). **(A)** The mutation frequency of 26 RNA modification "writers" in 436 OC patients from The Cancer Genome Atlas (TCGA) cohort. **(B)** Frequencies of copy number variation (CNV) gain, loss, and non-CNV among RNA modification "writers." **(C)** Locations of CNV alterations in RNA modification "writers" on 23 chromosomes. **(D)** Expression distributions of 26 RNA modification "writers" between normal and colorectal cancer (CRC) tissues. **(E)** Heatmap showing expression profiles of 26 RNA modification "writers" in OC and normal tissues. **(F)** The protein–protein interaction (PPI) network of RNA modification "writers". Adjusted p-values were shown as ns, not significant; $^{**}p<0.01$; $^{***}p<0.001$.

essentially statistically significant (**Figures 1D, E**). Previous studies have shown a coordination or inhibitory relationship between the four RNA modifications (12). These grooming functions are not completely independent, and the protein–protein interaction (PPI) network diagram shows the interrelationships that exist between these "writers" (**Figure 1F**). Subsequently, after further analysis, we found that there is a certain correlation between CNV changes and the expression of "writers." CNV increases in genes such as CPSF1, KIAA1429, METTL3, and PCF11 were often accompanied by decreased expression levels, whereas ADAR, TRMT61A, and CSTF1, among others, showed the opposite. Likewise, "writers" with CNV loss also showed increased or decreased expression levels (**Figures 1B, D**). These results suggest that expression levels of RNA modification "writers" are affected by CNV, but CNV is not the only factor affecting gene expression (56); other factors, including multiple epigenetic modifications, also largely regulate gene expression (57).

The above analysis shows that the expression and genetic changes of RNA modification "writers" in normal and OC are highly heterogeneous, implying that RNA modification "writers" play a certain role in the occurrence and pathogenesis of OC.

Determination of RNA Modification "Writers" Patterns in Ovarian Cancer

To better characterize RNA modifications in the development of OC, we integrated samples from TCGA-OC and GSE9891

cohorts and used them for further analysis. The Kaplan–Meier analysis revealed that 14 "writers" expression levels correlate with OC survival ($p < 0.05$, **Figure S1B**). Subsequently, we analyzed the relevance of expressions between "writers" and discovered a general agreement between positive and negative relationships (**Figure 2A**). The expression of "writers" was significantly correlated not only within the same category but also across different categories. Interestingly, the negative correlations between the expression of PCF11, PABPN1, METTL3, and other "writers" were relatively strong. The opposite is true for TRMT10C, CPSF3, and RBM15B. Likewise, the synthesis of "writers" interactions and prognostic value were demonstrated in the RNA modification network (**Figure 2B**). Therefore, the crosstalk among "writers" may largely influence RNA modification patterns in OC.

Subsequently, according to 26 "writers" mRNA expression profiles, we employed a consensus clustering algorithm to classify OC samples and divided the entire cohort into two clusters, including cluster A (n = 321) and cluster B (n = 340) (**Figures 2C**, **S2A, B**). Principal component analysis (PCA) showed that cluster A and cluster B could be well distinguished based on this classification (**Figure 2D**). The heatmap illustrates the possible relevance of the expression of RNA modification "writers" to some clinical traits (**Figure S2C**). Moreover, the K-M analysis revealed a more significant survival advantage for cluster B ($p = 0.032$, **Figure 2E**).

Immune Signatures of Distinct RNA Modification Clusters

To gain insight into the potential biological meaning of two clusters, we conducted GSVA on two clusters. As can be seen from **Figure 3A**, some immune activation-related pathways are abundantly enriched in cluster A, including NK cell-mediated cytotoxicity and NOD-like and Toll-like receptor signaling

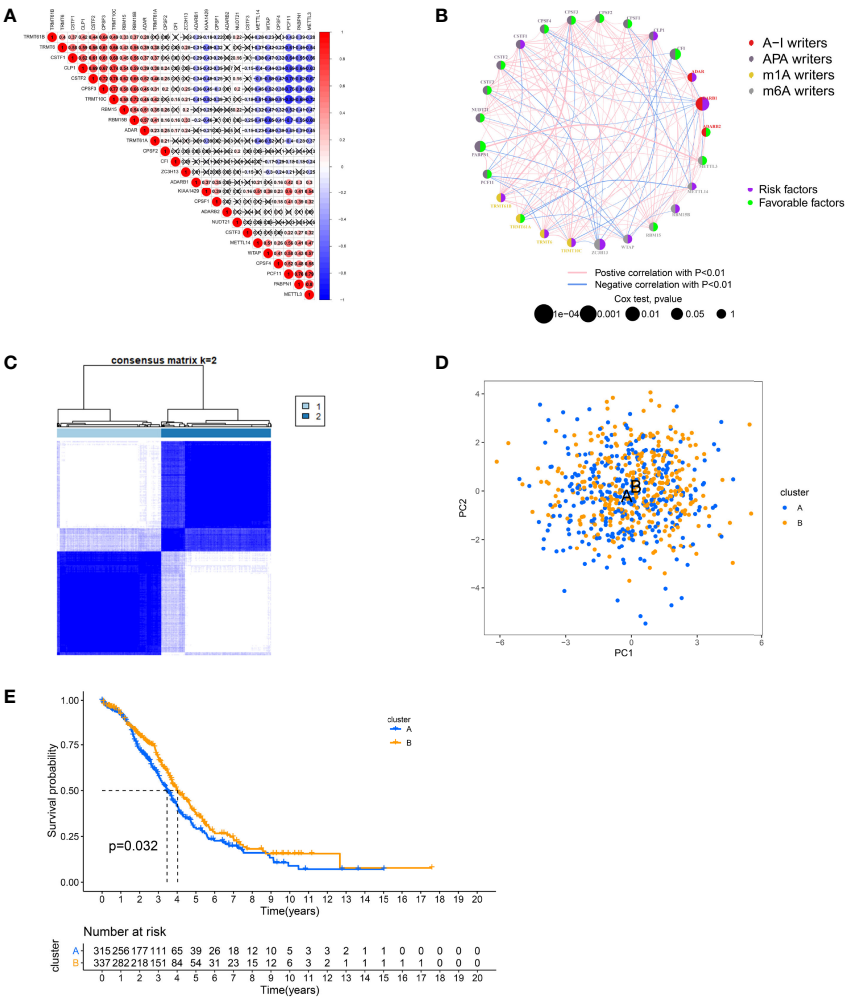

FIGURE 2 | Patterns of RNA modification and clinical characteristics divided by consistent clustering. **(A)** Heatmap shows positive (red) and negative (blue) correlations among RNA modification "writers" in ovarian cancer (OC). **(B)** Interactions among RNA modification "writers" in OC. **(C)** Unsupervised clustering of RNA modification "writers" and Consensus matrix heatmaps for k = 2. **(D)** Principal component analysis (PCA) showing a remarkable difference in transcriptomes between different modification patterns. **(E)** Kaplan–Meier curves for the two RNA modification patterns of OC patients.

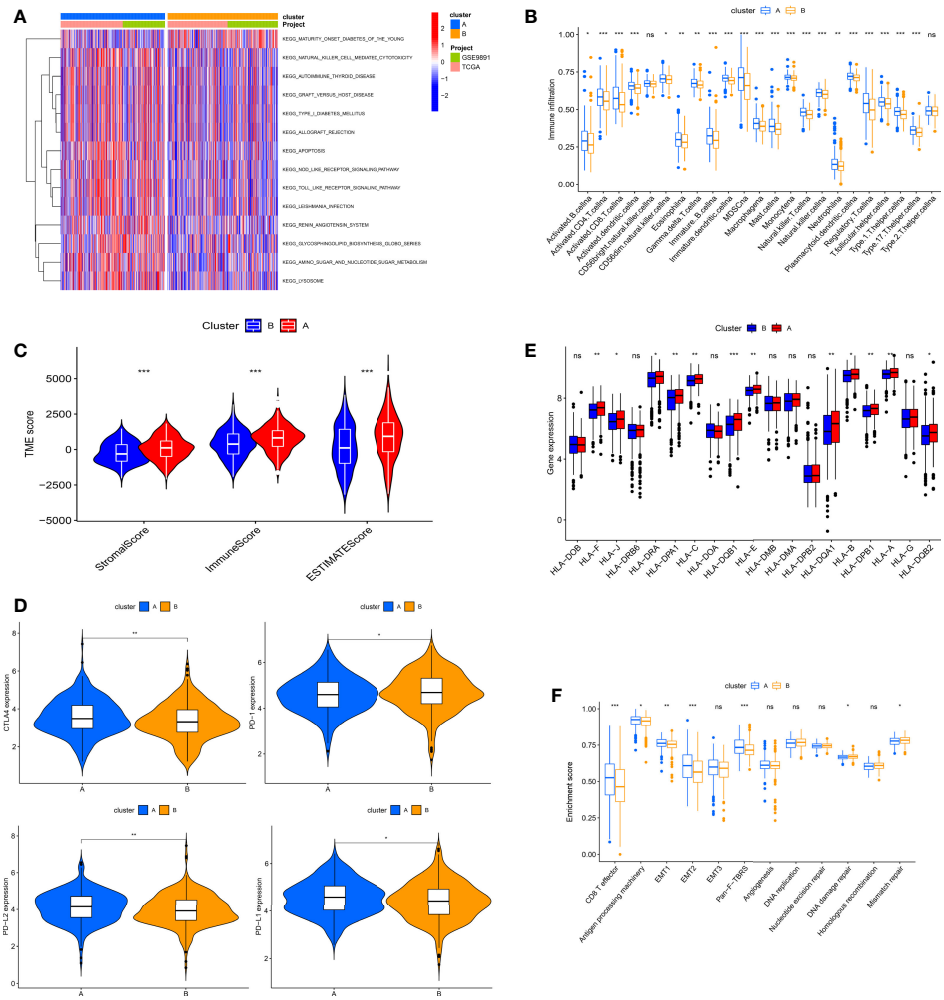

FIGURE 3 | Biological characteristics and tumor immune microenvironment (TME) cell infiltration in two RNA modification patterns of ovarian cancer (OC). **(A)** Gene Set Variation Analysis (GSVA) analyzed the biological pathways between two modification patterns. **(B)** 23 TME cells' infiltration abundance of two RNA modification patterns. **(C)** Correlations between two RNA modification patterns and TME score. **(D)** The RNA expression levels of HLA genes in samples from two patterns. **(E)** Expression levels of CTLA4, PD-1, PD-L2, and PD-L1 in two modification patterns. **(F)** Differences in interstitial activation pathways of two RNA modification patterns. Adjusted p-values were shown as ns, not significant; *$p < 0.05$; **$p < 0.01$; ***$p < 0.001$.

pathways, indicating that these "writers" may be linked to immune activation. Therefore, we next explored the role of "writers" in OC TME. First, we performed ssGSEA in OC to assess immune infiltration in these clusters according to immune cell-specific marker gene expression levels. We found that cluster A was very rich in immune infiltration, with a significantly higher degree of infiltration than cluster B. Innate and adaptive immune cells including T and B cells, macrophages, and NK cells were significantly enriched in cluster A (**Figure 3B**). We then evaluated the correlation among the two RNA modification isoforms and 22 immune cell subpopulations with the CIBERSORT algorithm. Surprisingly, we found no difference between the two subtypes in most immune cell infiltrations (**Figure S2D**). This may be due to different algorithms. Furthermore, we employed the ESTIMATE algorithm to infer the proportions of immune cells and stromal cells in both subtypes and calculate tumor purity. The results showed that stromal cells and immune cells were significantly more abundant in cluster A, which also indicated that the tumor purity of cluster A was relatively low (**Figure 3C**). Based on these analyses, we found that the two RNA modification patterns have completely different immune infiltration characteristics. Among them, cluster A roughly corresponds to "hot" tumors, characterized by more activated immune cell infiltration and better response to immunotherapy, while cluster B corresponds to "cold" tumors, characterized by few infiltrating immune cells and a weak response to immunotherapy. However, cluster A with this immune signature did not have a matching survival advantage (**Figure 2E**).

To explore the expression characteristics of immune-related genes, we next analyzed the link between the immune checkpoint and HLA genes in both clusters. Immune checkpoint analysis

revealed that, with the exception of PD-1, the remaining single genes, including PD-L1, CTLA-4, and PD-L2, were more highly expressed in cluster A (**Figure 3D**). Notably, all differentially expressed HLA genes were the highest in cluster A (**Figure 3E**). In addition, we further analyzed the correlation of known biological processes with the two isoforms in order to better characterize RNA modification patterns. The results showed that most biological processes were more prominent in cluster A, but pathways related to mismatch repair, including DNA replication, DNA damage repair, nucleotide excision repair, and mismatch repair, were significantly enriched in cluster B (**Figure 3F**).

Construction of RNA Modification "Writer" Gene Clusters

We used the "limma" package to screen out 1,641 DEGs (**Figure S3A**) and performed GO and KEGG functional analysis on DEGs. Gene enrichment analysis demonstrated that these DEGs were dramatically abundant in cell activation, proliferation, and immune-related pathways, including T-cell activation, lymphocyte proliferation, and neutrophil-mediated immunity (**Figures 4A, B**). This also indirectly indicates that RNA modification "writers" are essential in OC immune regulation. Subsequently, to determine the prognostic worth of these DEGs, we performed a univariate Cox analysis on these DEGs and screened out 10 genes associated with overall survival (OS) ($p < 0.001$, **Table S3**). Based on these 10 survival-related DEGs, we also used a consensus clustering algorithm to categorize OC simples into two gene clusters, namely, gene clusters A and B (**Figures S3B–D**). The expression of RNA modification "writers" differed between the two groups, with "writers" having relatively high expression in cluster B (**Figure 4C**). Consistent with the RNA modification cluster, the two gene clusters also each had different clinical and prognostic characteristics (**Figure S3E**), among which the K-M curve displayed a more pronounced survival advantage for patients in cluster B ($p < 0.001$, **Figure 4D**).

Subsequently, we further investigated immunological behavior in the two gene clusters. The ssGSEA results indicated that the vast majority of immune cells had higher levels of infiltration in cluster A (**Figure 4E**). The CIBERSORT algorithm results showed that gene cluster A was mainly infiltrated by adaptive immune cells (T and B cells), while gene

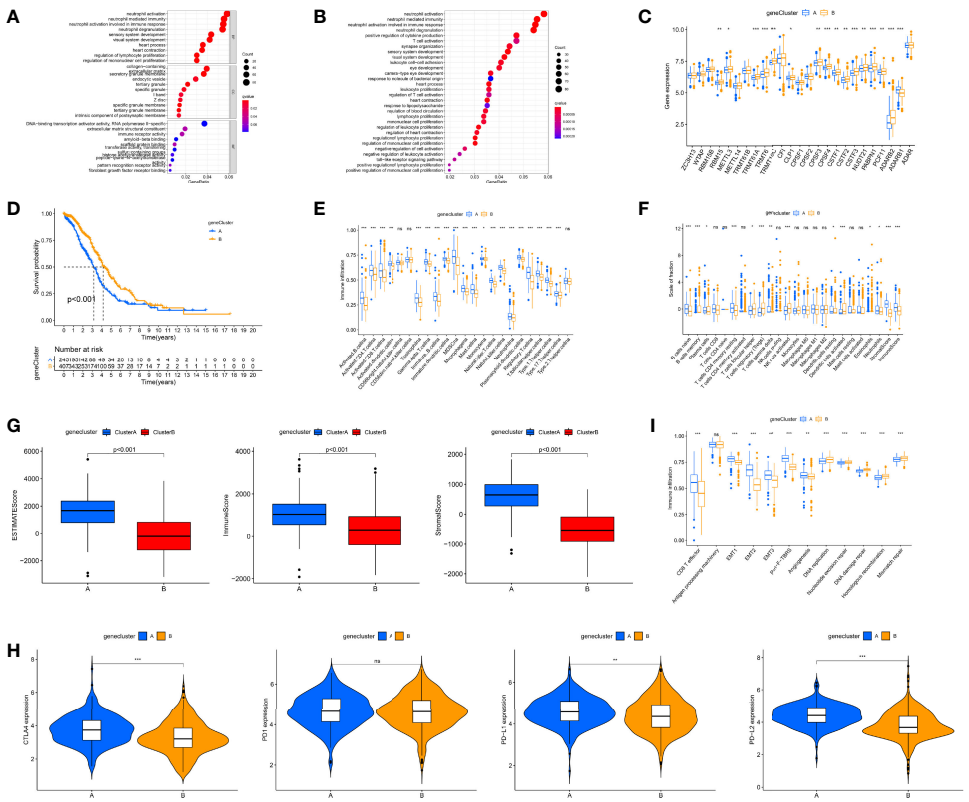

FIGURE 4 | Identification of gene clusters based on differentially expressed genes (DEGs) and tumor immune microenvironment (TME) cell infiltration characteristics and transcriptome traits in distinct gene clusters. **(A)** Gene Ontology (GO) enrichment analyses of DEGs among two gene clusters. **(B)** Kyoto Encyclopedia of Genes and Genomes (KEGG) enrichment analyses of DEGs among two gene clusters. **(C)** Differences in the expression of 26 RNA modification "writers" among the two gene clusters. **(D)** Kaplan–Meier curves for the two gene clusters of ovarian cancer (OC) patients. **(E)** 23 TME cells' infiltration abundance of two gene clusters. **(F)** The proportion of each immune cell in two gene clusters. **(G)** Correlations between two gene clusters and TME score. **(H)** Expression levels of CTLA4, PD-1, PD-L1, and PD-L2 in two gene clusters. **(I)** Differences in interstitial activation pathways of two gene clusters. Adjusted p-values were shown as ns, not significant; $*p < 0.05$; $**p < 0.01$; $***p < 0.001$.

cluster B was mainly infiltrated by innate immune cells, including NK cells and monocytes (**Figure 4F**). The results of tumor purity analysis showed that gene cluster A tumor tissues had a high content of immune and stromal cells, which also represented low tumor purity ($p < 0.001$, **Figure 4G**). Consistent with RNA modification typing, except for PD-1, the expression of other immune checkpoints in gene cluster A was also significantly higher (**Figure 4H**). In addition, classical biological pathways, including CD8 T effector, EMT1-3, Pan-F-TBRS, and Angiogenesis, were more prominent in gene cluster A, while pathways related to mismatch repair were significantly enriched in gene cluster B (**Figure 4I**). Again, based on these immune signatures, we believe that gene cluster A roughly corresponds to "hot" tumors, while gene cluster B corresponds to "cold" tumors.

Construction and Validation of RMW Score

Considering the complexity of RNA modification and individual differences, based on these DEGs, we created a scoring system to measure RNA modification patterns in single OC patients, called the RMW score. **Figure 5A** visually illustrates the distribution of sufferers across RNA modification clusters, genotypes, and RMW score groups. First, the expression profile data of the samples were merged with the survival information, and we selected 652 samples for subsequent analysis. These samples were averaged at random into a training group (n = 326) and a test group (n = 326) with the "caret" package. Based on previous genetic screening results, LASSO and multivariate Cox analyses were conducted on 10 prognostic-related DEGs in the training set to facilitate the selection of the best prognostic features. Nine OS-related DEGs were still screened by LASSO regression (**Figures S4A, B**). Subsequently, we applied multivariate Cox analysis to these 9 genes, and finally we obtained 7 genes for further analysis, including three low-risk genes (PLCH1, ZNF429, and MYCNOS) and four high-risk genes (ZFHX4, DYRK1B, GFPT2, and ADNP) (**Figure S4C**). Based on the correlation coefficient calculated by multivariate Cox regression, we established the calculation formula of RMW score: RMW score/risk score = (−0.1671 * PLCH1 expression) + (−0.6230 * ZNF429 expression) + (−0.2306*MYCNOS expression) + (0.1385 * ZFHX4 expression) + (0.5187 * DYRK1B expression) + (0.1590 * GFPT2 expression) + (1.0575 * ADNP expression).

Clearly, we observed significant differences in the distribution of RMW scores across different RNA modification clusters and gene clusters (**Figures 5B, C**). Among them, the RMW scores of cluster A and gene cluster A were relatively high, indicating that the high RMW score may be related to the immune infiltration and activation of patients. To estimate the clinically relevant nature of the RMW score, we categorized patients into high- and low-score (risk) groups by median RMW score. We observed significant expression variations in 7 genes between the two groups, with high-risk genes having higher expression in the high-score group, while low-risk genes showed the opposite (**Figure 5D**). **Figures 5E, F** show the distribution of RMW scores. It can be seen that the higher the RMW score, the shorter the patient's survival time and the higher the mortality rate. The K-M survival curves highlight greater survival benefits for the high-score group ($p < 0.001$, **Figure 5G**). In addition, ROC curves illustrated the sensitivity and specificity of RMW score in predicting 1-, 3-, and 5-year survival, with area under the curve (AUC) values of 0.761, 0.661, and 0.662, respectively (**Figure 5H**).

To further investigate the predictive behavior of the RMW score, we calculated the RMW score for the test and all sets (TCGA-OV+GSE9891) and the external validation group (GSE26193) according to the formula and categorized the patients into two score groups (**Figures S5-S9**). The heatmap illustrated the variation in RMW score-related gene expression among two groups (**Figures S5-9A**). **Figure S5-9B, C** show the change trend of RMW score and patient survival status in the two groups, respectively. Survival curves showed that the low-score group exhibited a significant survival benefit ($p < 0.001$; **Figures S5-9D**). ROC curves showed relatively high AUC values of RMW score in predicting 1-, 3-, and 5-year outcomes (**Figures3S5-9E**). These results suggest that the RMW score could mirror RNA modification patterns and forecast outcomes in OC.

We further validated the expression of 7 RMW score-related genes in OC cell HO8910, SKOV3, and OVCAR3 by qRT-PCR. As shown in **Figure S10**, the expressions of ADNP, PLCH1, ZFHX4, and ZNF429 were significantly lower in OC cell lines compared to those in IOSE cells. Meanwhile, DYRK1B and GFPT2 expressions were significantly upregulated in OC cell lines. However, there was no significantly different in MYCNOS expression in OC cell lines.

Clinical Correlation Analysis and Stratified Analysis of RMW Score

We discussed the relevance of RMW scores to various clinical features, including survival status, age, and stage. We noticed that a greater proportion of patients over 60 years of age, with advanced disease and death, were in the high group (**Figures S11A–C**), and these patients had higher RMW scores (**Figures S11D–F**). In addition, stratified analysis assessed whether the RMW score could predict survival in different clinical subgroups, including age (≤60 and >60 years), grade (stages 1–2 and 3–4), stage (stages I–II and stages III–IV), BRCA1 (mutant and wild type), and chemotherapy (accepted and non-accepted). **Figures S11G–N** show that the low RMW score group has a more favorable prognostic outlook among patients stratified by various clinical traits. These results suggest that the RMW score can be employed to estimate several clinical characteristics, including age, stage, grade, and survival status.

RMW Score Is Associated With Tumor Immune Microenvironment Immune Infiltration

First, we performed GSEA to identify the underlying biological properties of different scoring groups. As expected, significant enrichment of immune pathways, including T- and B-cell receptor pathways, chemokine signaling pathway, and cytokine–cytokine receptor interaction, was detected in high-risk patients compared with low-score patients (**Figure 6A**).

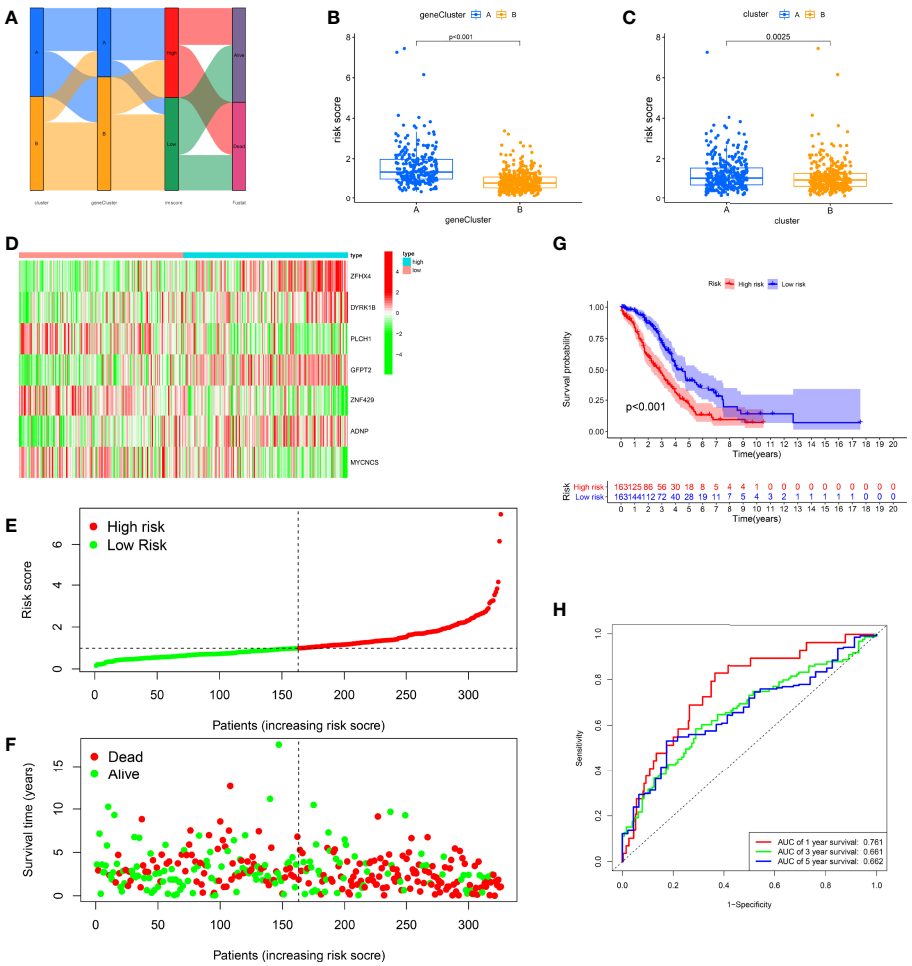

FIGURE 5 | Construction of the RMW score in the training set. **(A)** Alluvial diagram of subtype distributions in groups with different RMW scores and survival outcomes. **(B)** Differences in RMW score between gene clusters. **(C)** Differences in RMW score between RNA modification patterns. **(D)** Heatmap shows the distribution of core genes in models between normal and ovarian cancer (OC) tissues. **(E)** Ranked dot showing the RMW score distribution and patient survival status. **(F)** Scatter plots showing the RMW score distribution and patient survival status. **(G)** Kaplan–Meier analysis of the overall survival (OS) between the two groups. **(H)** Receiver operating characteristic (ROC) curves to predict the sensitivity and specificity of 1-, 3-, and 5-year survival according to the RMW score.

Further studies showed that pan-F-TBRS and TME stroma were markedly activated in the high group, which, to some extent, mediated tumor immune tolerance (**Figure 6B**). Subsequently, we applied ssGSEA to assess immune infiltration in both groups. As depicted in **Figure 6C**, the level of immune cell infiltration was generally higher in the high group. To better illustrate the effect of the RMW score on TME immune infiltration, we also tested the correlation between different immune cells and the RMW score (**Figure S12A**). The CIBERSORT algorithm revealed that the RMW score was negatively linked to regulatory T cells, memory B cells, activated dendritic cells, and activated NK cells, while naive B cells, eosinophil, M0 macrophages, activated mast cells, plasma cells, and γδ T cells were positively correlated (**Figure S12B**). **Figure S12C** indicates the ratio of each immune cell in two groups. ESTIMATE results confirmed a positive relationship between RMW scores and both immune and stromal scores, indicating lower tumor purity in the high group (**Figures 6D, E**). Moreover, we assessed the relationship between seven RMW score-related genes and immune cell abundance and observed that the majority of immune cells were markedly linked to seven genes (**Figure 6F**).

Furthermore, we surveyed the connection between immune checkpoints and our risk model. **Table S4** lists 47 immune checkpoint-related genes. **Figure 6G** depicts 23 immune checkpoints with differential expression in both groups, including HAVCR2, IDO1, PDCD1LG2, and CTLA4, and most immune checkpoints were overexpressed in the high group. To better illustrate the characteristics between immune checkpoints and RMW scores, we also tested the correlation between some drug target genes and RMW scores (**Figures 6H**, **S12D**). In addition to IDO1, three other genes, including PDCD1LG2, HAVCR2, and CTLA4, were positively correlated with the RMW score.

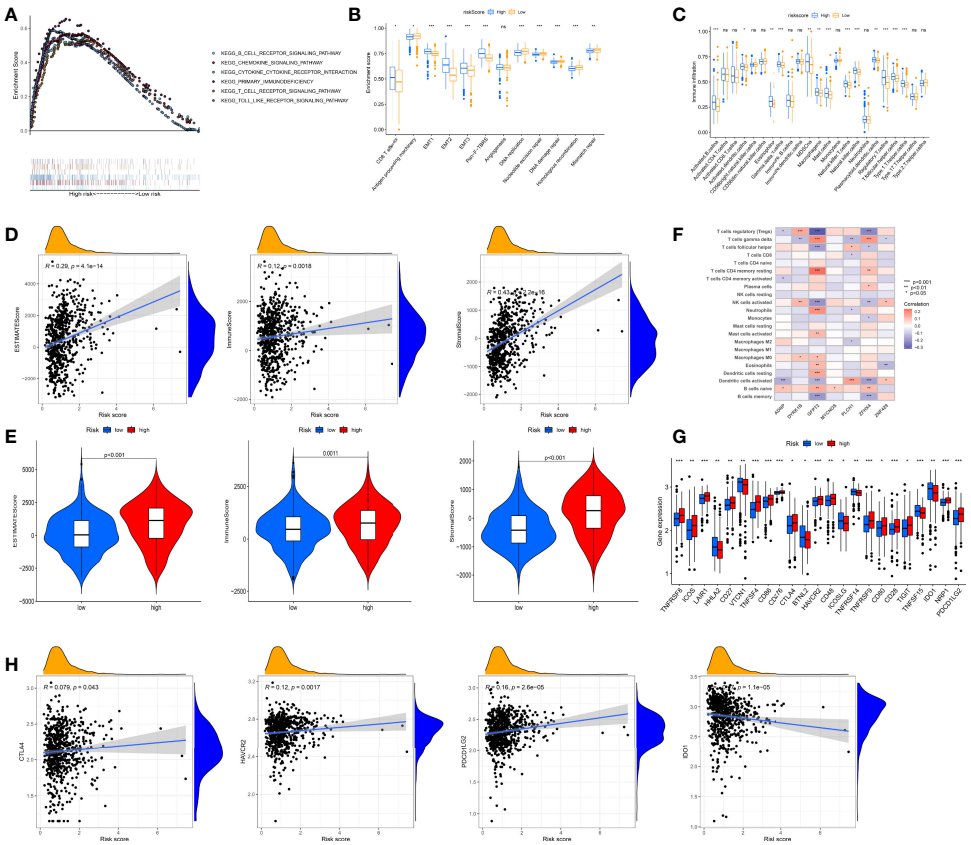

FIGURE 6 | Evaluation of the tumor immune microenvironment (TME) and checkpoints between the two groups. **(A)** Enrichment plots showing B-cell receptor signaling pathway, chemokine signaling pathway, cytokine–cytokine receptor interaction, T-cell receptor signaling pathway, primary immunodeficiency, and Toll-like receptor signaling pathway were enriched in the high RMW score subgroup. **(B)** Differences in interstitial activation pathways of two groups. **(C)** 23 TME cells' infiltration abundance of two RMW score subgroups. **(D, E)** Correlations between two groups and TME score. **(F)** Correlations between the abundance of immune cells and seven genes in model. **(G)** Expression of 23 immune-related genes in two groups. **(H)** Expression levels of CTLA4, HAVCR2, PDCD1LG2, and IDO1 in two groups. Adjusted p-values were shown as ns, not significant; *p < 0.05; **p < 0.01; ***p < 0.001.

Correlation Between RMW Score and Tumor Stem Cells and Tumor Mutation Burden

Recently, studies have found that cancer stem cells interact with immune cells in the TME and can promote the progression of various cancers (58, 59). We analyzed the regulatory role of the RMW score in OC stem cells by analyzing mRNA expression (RNAs) and DNA methylation patterns (DNAs). It is evident from **Figures S13A, B** that the RMW score was clearly negatively dependent on both RNAs and DNAs, although these correlations were not statistically significant. These results suggest that a high RMW score is associated with reduced tumor cell stemness.

Growing evidence suggests that the higher the tumor mutation burden (TMB), the greater the number of neoantigens in the tumor, and the better the patient's susceptibility to immunotherapy (60). Therefore, we next comprehensively evaluated the distribution of TMB in the two groups. **Figure S13C** highlights the higher TMB for the high group (p = 0.0072). Subsequently, the somatic mutation distribution results revealed a high mutation frequency in both groups, with the highest mutation frequency being in TP53, which can be as high as 88% and 80%. High score patients had a markedly higher frequency of mutations (**Figures S13D,E**).

RMW Score Can Predict Drug Sensitivity in Ovarian Cancer Patients

To explore whether the RMW score can predict the immunotherapy response to ICIs, we used the TIDE score to model the two main mechanisms of tumor immune evasion and provide predictive outcomes for immunotherapy. We found that TIDE scores in the high-score group were much higher, suggesting that the low RMW score patients were more likely to respond to immunotherapy (**Figures 7A–C**). Microsatellite instability (MSI) refers to the difference in the number of repeat units of the same microsatellite locus between different individuals or between normal tissues and some abnormal tissues of the same individual. Growing evidence indicates that patients with higher MSI are better able to respond to and

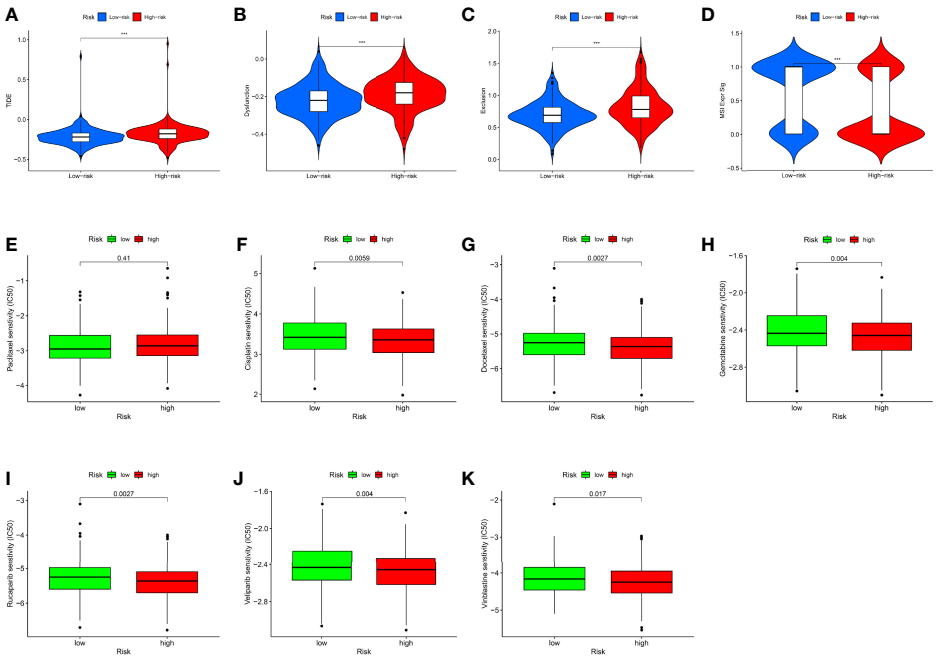

FIGURE 7 | The role of RMW score in ovarian cancer (OC) treatment drug sensitivity. **(A–C)** The correlation between the RMW score and Tumor Immune Dysfunction and Exclusion (TIDE) Score. **(D)** Relationships between RMW score and microsatellite instability (MSI). **(E–K)** Relationships between RMW score and chemotherapeutic sensitivity. Adjusted p-values were shown as ***p < 0.001.

gain from immunotherapy (61). From **Figure 7D**, we can see that the MSI was higher in the low RMW score group. This also proves that low-score patients with high MSI can benefit from immunotherapy.

We next selected chemotherapeutic agents available for OC to assess the sensitivity of the two groups to these agents. Interestingly, we found that with the exception of paclitaxel, the IC50 values of the rest of the drugs, including rucaparib, veliparib, vinblastine, cisplatin, docetaxel, and gemcitabine, were significantly elevated in the low RMW score group (**Figures 7E–K**). **Figure S14** shows the correlation between RMW score-related genes and different drugs. These results suggested that RNA modification "writers" are associated with drug sensitivity, including immunotherapy and chemotherapeutics, where a lower RMW score suggests better treatment outcomes for patients.

Plot a Nomogram to Predict Survival

Considering the inconvenient clinical application of RMW scores in predicting the prognosis of OC patients, we combined RMW scores with independent prognostic clinical traits, including age and stage, to draw a nomogram to more intuitively demonstrate the validity of these factors, especially RMW scores, in predicting 1-, 3-, and 5-year survival (**Figure 8A**). In addition, the conjoint univariate and multivariate analyses confirmed that the signature of the RMW score was an independent prognostic factor in five sets (**Table 1**). Considering the effect of sample number on the results, we used the samples from the ALL sets (TCGA-OV +GSE9891) to plot the nomogram and carry out the next step of the analysis. ROC results showed that the accuracy of OS at 1 year was higher than that at 3 and 5 years (**Figures 8B–D**). DCA showed that the net benefit of our RMW score-based prognostic model was high compared to clinical factors if the patient or physician threshold probability was greater than 50%, particularly when predicting 1-year survival. Within this range, the RMW score outperformed the predictions of individual predictors (**Figures 8E–G**). Subsequently, we plotted ROC curves to analyze the accuracy of combining the three predictors for a common prediction. Clearly, combining clinical factors with the RMW score predicted larger AUC values with higher accuracy (**Figures 8H–J**). The calibration curves showed that the proposed nomogram was the best at predicting 1-year survival, followed by 3 years, compared to the ideal model (**Figures 8K–M**).

RNA Modification "Writers" Models as Ovarian Cancer Novel Predictors

To compare the predictive performance of our RNA modification "writers" signature with other models, we selected four risk models, including 5-gene (62), 7-gene (63), 8-gene (64), and 11-gene (65) features. To make them comparable, according to the expression of corresponding genes in these four models, we also applied multivariate Cox regression analysis to calculate the risk value and prognostic evaluation for each dataset. Samples were divided into high and low groups according to the median value. Survival curves indicated that the high-risk

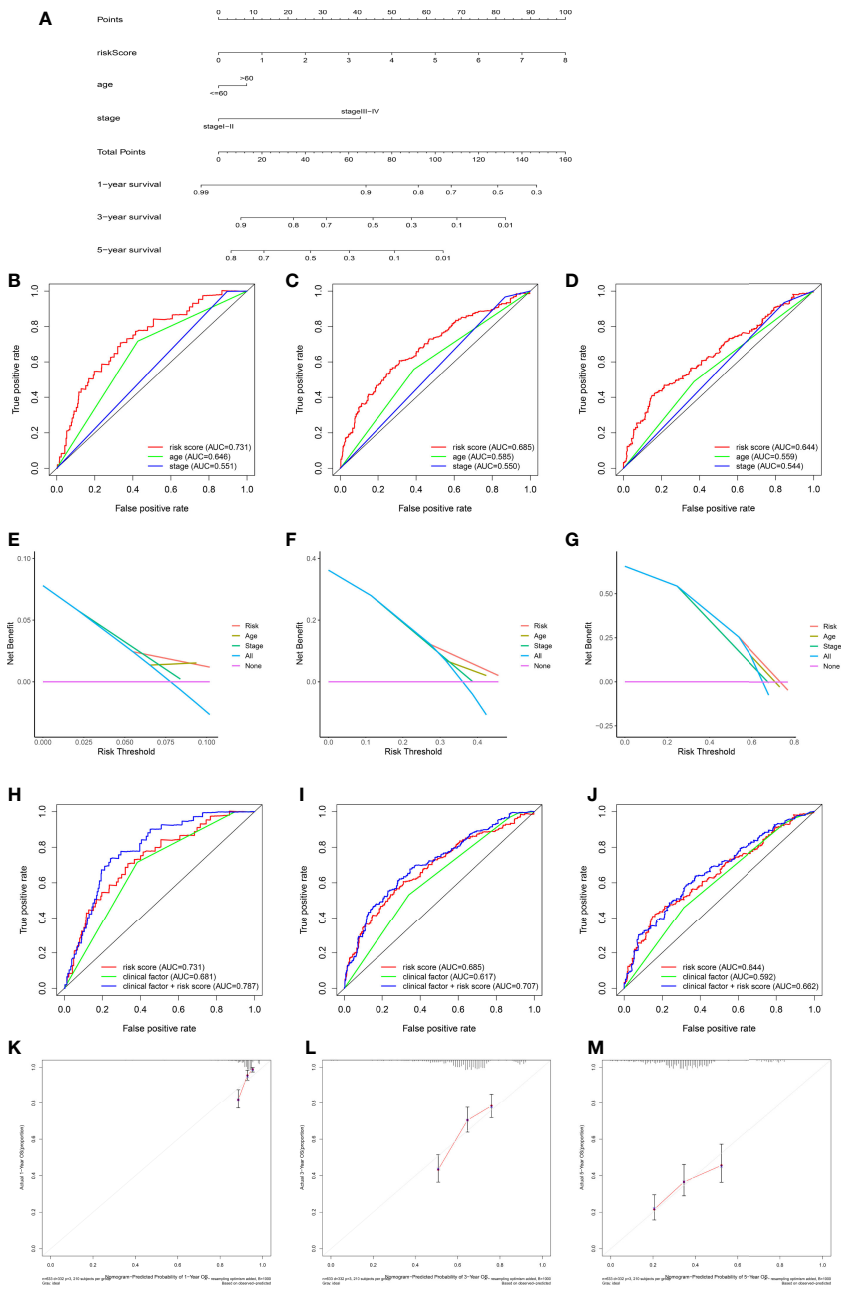

FIGURE 8 | Construction and validation of nomograms. **(A)** Nomogram for predicting the 1-, 3-, and 5-year overall survival (OS) of ovarian cancer (OC) patients in the training set. **(B–D)** Receiver operating characteristic (ROC) curve showing the area under the curve (AUC) values of risk, nomogram, age, and stage in predicting survival in OC patients. **(E–G)** Decision curve analysis of the risk, age, and stage at 1-, 3-, and 5-year OS. The x-axis shows the threshold probability, and the y-axis measures the net benefit. **(H–J)** Receiver operating characteristic (ROC) curve showing the AUC values of risk score, clinical factors, and both sides in predicting survival in OC patients. **(K–M)** Calibration curves of the nomogram for predicting 1-, 3-, and 5-year OS.

group had a greatly worse prognosis in the four models (**Figure 9A**). ROC curves illustrated that the AUC values were lower in all four models (**Figure 9B**). Therefore, we believe that they are inferior in predicting prognosis compared with our model. The restricted mean survival (RMS) package was employed to calculate the C-index for all prognostic features. Clearly, our model has the highest C-index at 0.67 (**Figure 9C**). With the use of RMS time, the predictive effect of gene signatures at different time points can be evaluated. Therefore, our genetic signatures perform best over time periods of about 5 years. This indicated that our model was the best predictor of 5-year survival in patients as compared with other models (**Figure 9D**).

TABLE 1 | Univariate and multivariate Cox regression analysis of RMW score and clinical characteristics in five cohorts.

	Univariate analysis				Multivariate analysis			
Training set								
Parameters	HR	HR.95L	HR.95H	pvalue	HR	HR.95L	HR.95H	pvalue
age	1.5809	1.1791	2.1196	0.0022	1.4109	1.0464	1.9022	0.0240
grade	1.1540	0.8078	1.6484	0.4312				
stage	4.3236	1.7715	10.5524	0.0013	3.6604	1.4979	8.9453	0.0044
RMW score	1.7699	1.5458	2.0264	0.0000	1.6933	1.4729	1.9466	0.0000
Testing set								
Parameters	HR	HR.95L	HR.95H	pvalue	HR	HR.95L	HR.95H	pvalue
age	1.3427	0.9763	1.8467	0.0699				
grade	1.3518	0.8890	2.0556	0.1586				
stage	3.9164	1.2448	12.3219	0.0196	3.5110	1.1138	11.0670	0.0320
RMW score	1.4056	1.2321	1.6035	0.0000	1.3829	1.2102	1.5802	0.0000
TCGA set								
Parameters	HR	HR.95L	HR.95H	pvalue	HR	HR.95L	HR.95H	pvalue
age	1.4054	1.0784	1.8317	0.0118	1.2402	0.9479	1.6225	0.1164
grade	1.1815	0.7885	1.7705	0.4189				
stage	2.4177	0.9945	5.8771	0.0514				
RMW score	1.8450	1.5814	2.1527	0.0000	1.8076	1.5451	2.1146	0.0000
GSE9891 set								
Parameters	HR	HR.95L	HR.95H	pvalue	HR	HR.95L	HR.95H	pvalue
age	1.5628	1.0743	2.2734	0.0196	1.3806	0.9383	2.0314	0.1017
grade	1.3024	0.8817	1.9236	0.1843				
stage	7.0056	2.2210	22.0977	0.0009	6.0557	1.9127	19.1730	0.0022
RMW score	1.4180	1.2441	1.6162	0.0000	1.3218	1.1481	1.5218	0.0001
ALL set								
Parameters	HR	HR.95L	HR.95H	pvalue	HR	HR.95L	HR.95H	pvalue
age	1.4563	1.1740	1.8066	0.0006	1.2840	1.0293	1.6019	0.0267
grade	1.2264	0.9353	1.6080	0.1399				
stage	4.0521	2.0069	8.1812	0.0001	3.5366	1.7494	7.1498	0.0004
RMW score	1.5346	1.4041	1.6773	0.0000	1.4718	1.3412	1.6150	0.0000

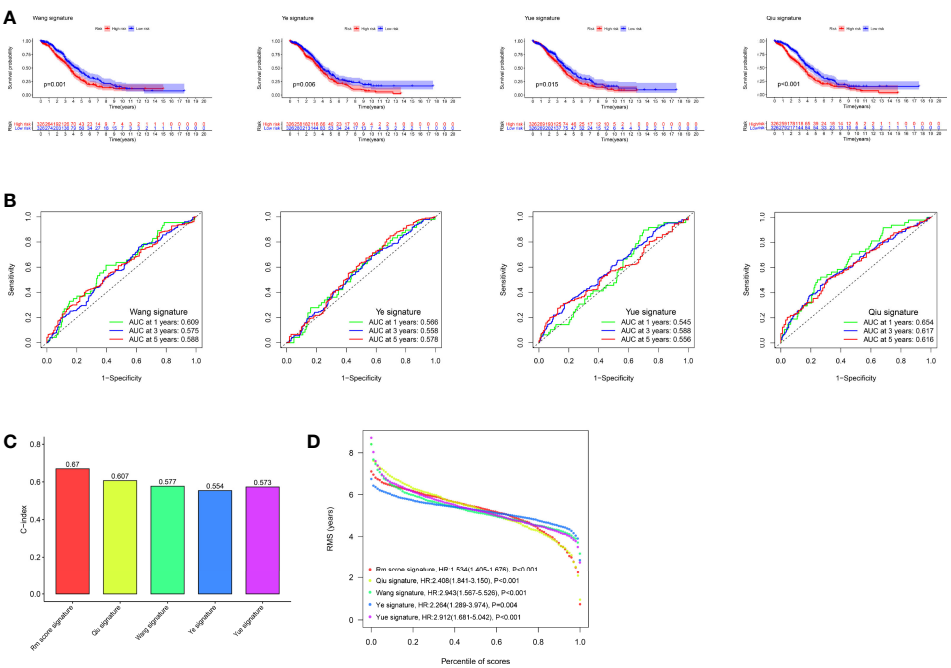

FIGURE 9 | Comparison of our risk model with other established models. **(A)** Kaplan–Meier (K-M) curves of four other published gene signatures. **(B)** Receiver operating characteristic (ROC) curves of four other published gene signatures. **(C)** Concordance index (C-index) of the five prognostic risk models. **(D)** Restricted mean survival (RMS) time curve of all five prognostic risk models.

DISCUSSION

To date, most studies have pointed to RNA modification as a key mechanism in the epigenetic regulation of immune responses and tumorigenesis. The dysregulation of m6A, m1A, APA, and A-to-I, four common RNA adenosine modifications mediated by "writers" enzymes, has been implicated in the pathogenesis of human diseases. However, most studies have focused on a single type of RNA modification "writers". Thus, corporate effects and TME infiltration traits mediated by the combined action of multiple "writers" in OC have not been fully elucidated. In this study, we reveal the overall alterations and interactions of RNA modification "writers" at transcriptional and genetic levels in OC. Based on the expression levels of the 26 "writers", we identified two distinct RNA modification clusters. Compared with cluster A patients, cluster B patients had milder clinicopathological features and a better prognostic outlook. There were significant differences in immune cell abundance in the TME between the two RNA modification subtypes. Among them, cluster A was characterized by abundant immune infiltration and significant immune activation, which contained a large number of T and B lymphocytes and was associated with immune-activated pathways, such as T- and B-cell receptor signaling pathways and NOD-like and Toll-like receptor signaling pathways. Moreover, transcriptome differences between RNA modification isoforms were markedly associated with cell proliferation and immune-related biological pathways. We identified two sets of gene clusters according to DEGs between two RNA-modification clusters. We believe that RNA modification "writers" may act as a major factor influencing the clinical outcome of OC and immune infiltration of the TME. We select "writers" that can robustly and effectively predict OC survival to calculate the RMW score. We demonstrate the RMW score's predictive value and explore the expression of RMW score-related genes in OC tissues. RNA modification patterns characterized by high immune infiltration and immune activation showed higher RMW scores. Patients in the two groups exhibited significantly different clinicopathological features, prognosis, mutations, TME, immune checkpoints, CSC index, and drug sensitivity. Finally, by integrating age, stage, and RMW score, we built a nomogram to more intuitively display the performance of these factors and improve the applicability of the RMW score. This prognostic model might be employed for the prognostic stratification of OC patients, which helps to better understand the molecular mechanism of RNA methylation in OC and provides new ideas for personalized treatment.

Recently, immunotherapy has gradually achieved some advances in gynecological cancer. However, OC does not respond well to many immunotherapy drugs, and the immune characteristics of OC itself limit the response to immunotherapy and disease progression to a large extent (66). Previous studies have shown that the TME changes during malignant progression, mainly in non-malignant cells, cytokine networks, and the extracellular matrix. The heterogeneity of the TME may be one of the main reasons for the unsuccessful immunotherapy of OC (67). In this study, RNA modification patterns characterized by high immune infiltration and immune activation were associated with higher RMW scores. We found considerable variations in TME characteristics and relative abundance of immune cells between the two patterns, genotypes and different RMW score subgroups. This highlights an essential contribution of RNA modification "writers" in regulating the OC TME and progression.

Studies have proved that the presence of TILs is directly associated with a higher prognosis in OC patients (68). Among them, CD8+ T cells infiltrate tumors as a symbol of immune recognition and destroy tumor cells by secreting granzyme B, TNF, and IFNγ, indicating better survival in OC patients (69). B cells can also inhibit OC migration and metastasis through antitumor immunity to a certain extent, and some B cells differentiate into plasma cells to produce tumor-specific antibodies (70). Myeloid-derived suppressor cells (MDSCs) are a subset of immunoregulatory immature myeloid cells that proliferate throughout cancer progression and perform immunosuppressive functions by modulating the escape of antitumor T-cell immunity (71). In OC, MDSCs enhance cancer cell stemness and accelerate metastasis and tumor formation by triggering microRNA expression and inhibiting the co-suppressor gene C-terminal binding protein-2 (72). The high expression of immunosuppressive molecules, including vascular endothelial growth factor and interleukin 10 in OC TME, causes abnormal dendritic cell function, which not only fails to activate cytotoxic T lymphocytes but also induces regulatory differentiation of effector T lymphocytes, further suppressing the immune response of effector T lymphocytes to tumors (73). In addition, the extracellular matrix protein transforming growth factor beta (TGFBI), an essential component of the OC TME, is significantly upregulated in ovarian lesions and serous OC, which may contribute to immunosuppression and disease progression (74). We observed that subtype A had more immune cell infiltration, including antitumor cells such as T and B and tumor-promoting cells such as MDSCs and Treg. Likewise, we observed a similar phenomenon in the high RMW score group. However, subtypes with such high immune infiltration did not show a matching survival advantage. This indicates that in the immune microenvironment of OC, cells such as Treg and MDSCs may be primarily involved in suppressing the anticancer immune response. This is consistent with our finding of low immune infiltration and favorable prognosis in patients with subtype B and high RMW scores. T-cell exhaustion is characterized by loss of T-cell effector function, increased and persistent inhibitory receptor (IRS) expression, altered epigenetic and transcriptional profiles, and altered metabolic patterns (75). T-cell exhaustion is one of the major factors in immune dysfunction in cancer patients, including OC (76). Therefore, we speculate that the increased infiltration of T cells in the poor-prognosis cohort may be dominated by exhausted T cells, which indirectly suggests why high T-cell infiltration in the tumor worsens the prognosis. Exhausted T cells may have new targets for OC immunotherapy and represent a potent weapon to fight tumors.

With the deepening of tumor immunology and molecular biology research, immunotherapy and targeted therapy have

become new directions of clinical research. Our findings suggest that RNA modification patterns may be considered appropriate "predictors" for assessing clinical outcomes of chemotherapy or targeted therapy. The correlation between RMW score and cancer stem cells can be used to predict patient responsiveness to immunotherapy. By identifying RNA modification signatures of individual tumors, our findings provide new possibilities for improving OC therapy and enabling personalized cancer treatment outcomes. However, the article still has shortcomings. First, all conclusions are derived from processing and retrospective analysis of data from public databases, lacking clinical data and experimental studies to validate the results. Furthermore, due to data limitations, our analysis lacked a large-scale clinical cohort to validate the correlation between RNA modifications and tumor immune infiltration and the prognostic value of the RMW score in OC. A large number of prospective clinical analyses are required for further validation in the future.

CONCLUSION

Our comprehensive analysis of the four types of RNA modification "writers" uncovered broad regulatory mechanisms that influence TME infiltration characteristics and prognosis and identified their therapeutic utility in targeted therapy and immunotherapy. These findings emphasize the important clinical relevance of RNA modification "writers" and point to novel approaches for directing personalized treatment strategies for OC patients.

DATA AVAILABILITY STATEMENT

The datasets presented in this study can be found in online repositories. The names of the repository/repositories and accession number(s) can be found in the article/supplementary material.

AUTHOR CONTRIBUTIONS

JL and XN conceived the study and participated in the study design, performance, and manuscript writing. CC, GC, and WD conducted the bioinformatics analysis. All authors read and approved the final manuscript.

ACKNOWLEDGMENTS

We would like to thank the researchers and study participants for their contributions.

SUPPLEMENTARY MATERIAL

The Supplementary Material for this article can be found online at: https://www.frontiersin.org/articles/10.3389/fimmu.2022.932876/full#supplementary-material

Supplementary Figure 1 | Overview of study design and prognostic characteristics of RNA modification writers. **(A)** Overview of this work. **(B)** Kaplan-Meier survival analysis of different RNA modification "writers" in OC.

Supplementary Figure 2 | Clinical and immune infiltration characteristics in two modification patterns. **(A)** Cumulative distribution function curves for unsupervised clustering of 26 RNA modification "writers", k = 2-9. **(B)** Relative change in area under the CDF curve for unsupervised clustering of 26 RNA modification "writers", k = 2-9. C Heatmap showing differences in clinicopathologic features and expression levels of RNA modification "writers" between the two modification patterns. **(D)** The proportion of each immune cell in two modification patterns.

Supplementary Figure 3 | Clinical and immune infiltration characteristics in two gene clusters. **(A)**, 1641 RNA modification patterns-related DEGs shown in venn diagram. **(B)** Heat map of the consensus matrix for the OC sample at k = 2. C Cumulative distribution function curves for unsupervised clustering of DEGs, k = 2-9. **(D)** Relative change in area under the CDF curve for unsupervised clustering of DEGs, k = 2-9. **(E)** Heatmap showing differences in clinicopathologic features and expression levels of RNA modification "writers" between gene clusters.

Supplementary Figure 4 | Identifying representative candidate prognostic genes. **(A-B)** The LASSO regression analysis and partial likelihood deviance on the prognostic genes. **(C)** Forest plot of multivariate cox regression analysis for prognostic genes.

Supplementary Figure 5 | Validation of RMW score in testing set. **(A)** Heatmap shows the distribution of core genes in models between normal and OC tissues. **(B)** Ranked dot showing the RMW score distribution and patient survival status. **(C)** Scatter plots showing the RMW score distribution and patient survival status. **(D)** Kaplan–Meier analysis of the OS between the two groups. **(E)** ROC curves to predict the sensitivity and specificity of 1-, 3-, and 5-year survival according to the RMW score.

Supplementary Figure 6 | Validation of RMW score in TCGA-OC set. **(A)** Heatmap shows the distribution of core genes in models between normal and OC tissues. **(B)** Ranked dot showing the RMW score distribution and patient survival status. **(C)** Scatter plots showing the RMW score distribution and patient survival status. **(D)** Kaplan–Meier analysis of the OS between the two groups. **(E)** ROC curves to predict the sensitivity and specificity of 1-, 3-, and 5-year survival according to the RMW score.

Supplementary Figure 7 | Validation of RMW score in GSE9891 set. **(A)** Heatmap shows the distribution of core genes in models between normal and OC tissues. **(B)** Ranked dot showing the RMW score distribution and patient survival status. **(C)** Scatter plots showing the RMW score distribution and patient survival status. **(D)** Kaplan–Meier analysis of the OS between the two groups. **(E)** ROC curves to predict the sensitivity and specificity of 1-, 3-, and 5-year survival according to the RMW score.

Supplementary Figure 8 | Validation of RMW score in whole set. **(A)** Heatmap shows the distribution of core genes in models between normal and OC tissues. **(B)** Ranked dot showing the RMW score distribution and patient survival status. **(C)** Scatter plots showing the RMW score distribution and patient survival status. **(D)** Kaplan–Meier analysis of the OS between the two groups. **(E)** ROC curves to predict the sensitivity and specificity of 1-, 3-, and 5-year survival according to the RMW score.

Supplementary Figure 9 | Validation of RMW score in GSE26193 set. **(A)** Heatmap shows the distribution of core genes in models between normal and OC tissues. **(B)** Ranked dot showing the RMW score distribution and patient

survival status. **(C)** Scatter plots showing the RMW score distribution and patient survival status. **(D)** Kaplan–Meier analysis of the OS between the two groups. **(E)** ROC curves to predict the sensitivity and specificity of 1-, 3-, and 5-year survival according to the RMW score.

Supplementary Figure 10 | The expression level of 7 RMW score-related gens. **(A–G)** The expression level of ADNP, DYRK1B, GFPT2, MYCNOS, PLCH1, ZFHX4 and ZNF429 in OC cell lines.

Supplementary Figure 11 | Stratification analysis of the RMW score in OC. **(A–C)** The proportion of patient age, stage and survival status in high- and low-RMW score groups. **(D–F)** Boxplots for RMW score between different characteristics OC patients, including patient age, stage and survival status. **(G–N)** Kaplan-Meier curves depicted the survival difference between low and high RMW score in the stratified analysis of OC patients.

Supplementary Figure 12 | Immune infiltration characteristics between the two RMW score subgroups. **(A)** Heatmap showing the association between RMW score and immune cells. **(B)** The proportion of each immune cell in two RMW score subgroups. **(C)** Correlations between RMW score and immune cell types. **(D)** Heatmap shows a positive and negative correlation between drug targeted genes and RMW score in OC.

Supplementary Figure 13 | The Correlation between the RMW score and genetic variations. **(A)** Relationships between RMW score and CSC index (RNAss). **(B)** Relationships between RMW score and CSC index (DNAss). **(C)** TMB in different RMW score groups. **(D)** The waterfall plot of somatic mutation features in high RMW score. **E** The waterfall plot of somatic mutation features in low RMW score.

Supplementary Figure 14 | Scatter plots to show the association between different "writers" expression and drug sensitivity.

REFERENCES

1. Lheureux S, Gourley C, Vergote I, Oza AM. Epithelial Ovarian Cancer. *Lancet* (2019) 393:1240–53. doi: 10.1016/S0140-6736(18)32552-2
2. Matulonis UA, Sood AK, Fallowfield L, Howitt BE, Sehouli J, Karlan BY. Ovarian Cancer. *Nat Rev Dis Primers* (2016) 2:16061. doi: 10.1038/nrdp.2016.61
3. Torre LA, Trabert B, DeSantis CE, Miller KD, Samimi G, Runowicz CD, et al. Ovarian Cancer Statistics, 2018. *CA Cancer J Clin* (2018) 68:284–96. doi: 10.3322/caac.21456
4. Siegel RL, Miller KD, Fuchs HE, Jemal A. Cancer Statistics, 2021. *CA Cancer J Clin* (2021) 71:7–33. doi: 10.3322/caac.21654
5. Motorin Y, Helm M. RNA Nucleotide Methylation. *Wiley Interdiscip Rev RNA* (2011) 2:611–31. doi: 10.1002/wrna.79
6. Zhao BS, Roundtree IA, He C. Post-Transcriptional Gene Regulation by mRNA Modifications. *Nat Rev Mol Cell Biol* (2017) 18:31–42. doi: 10.1038/nrm.2016.132
7. Cantara WA, Crain PF, Rozenski J, McCloskey JA, Harris KA, Zhang X, et al. The RNA Modification Database, RNAMDB: 2011 Update. *Nucleic Acids Res* (2011) 39:D195–201. doi: 10.1093/nar/gkq1028
8. Nishikura K. Functions and Regulation of RNA Editing by ADAR Deaminases. *Annu Rev Biochem* (2010) 79:321–49. doi: 10.1146/annurev-biochem-060208-105251
9. Meyer KD, Saletore Y, Zumbo P, Elemento O, Mason CE, Jaffrey SR. Comprehensive Analysis of mRNA Methylation Reveals Enrichment in 3' UTRs and Near Stop Codons. *Cell* (2012) 149:1635–46. doi: 10.1016/j.cell.2012.05.003
10. Safra M, Sas-Chen A, Nir R, Winkler R, Nachshon A, Bar-Yaacov D, et al. The M1a Landscape on Cytosolic and Mitochondrial mRNA at Single-Base Resolution. *Nature* (2017) 551:251–5. doi: 10.1038/nature24456
11. Tian B, Manley JL. Alternative Polyadenylation of mRNA Precursors. *Nat Rev Mol Cell Biol* (2017) 18:18–30. doi: 10.1038/nrm.2016.116
12. Xiang JF, Yang Q, Liu CX, Wu M, Chen LL, Yang L. N(6)-Methyladenosines Modulate A-To-I RNA Editing. *Mol Cell* (2018) 69:126–135.e126. doi: 10.1016/j.molcel.2017.12.006
13. Shi H, Wei J, He C. Where, When, and How: Context-Dependent Functions of RNA Methylation Writers, Readers, and Erasers. *Mol Cell* (2019) 74:640–50. doi: 10.1016/j.molcel.2019.04.025
14. Dominissini D, Moshitch-Moshkovitz S, Schwartz S, Salmon-Divon M, Ungar L, Osenberg S, et al. Topology of the Human and Mouse M6a RNA Methylomes Revealed by M6a-Seq. *Nature* (2012) 485:201–6. doi: 10.1038/nature11112
15. Chen XY, Zhang J, Zhu JS. The Role of M(6)A RNA Methylation in Human Cancer. *Mol Cancer* (2019) 18:103. doi: 10.1186/s12943-019-1033-z
16. He L, Li H, Wu A, Peng Y, Shu G, Yin G. Functions of N6-Methyladenosine and its Role in Cancer. *Mol Cancer* (2019) 18:176. doi: 10.1186/s12943-019-1109-9
17. Wang T, Kong S, Tao M, Ju S. The Potential Role of RNA N6-Methyladenosine in Cancer Progression. *Mol Cancer* (2020) 19:88. doi: 10.1186/s12943-020-01204-7
18. Zaccara S, Ries RJ, Jaffrey SR. Reading, Writing and Erasing mRNA Methylation. *Nat Rev Mol Cell Biol* (2019) 20:608–24. doi: 10.1038/s41580-019-0168-5
19. El Yacoubi B, Bailly M, de Crécy-Lagard V. Biosynthesis and Function of Posttranscriptional Modifications of Transfer RNAs. *Annu Rev Genet* (2012) 46:69–95. doi: 10.1146/annurev-genet-110711-155641
20. Sharma S, Watzinger P, Kötter P, Entian KD. Identification of a Novel Methyltransferase, Bmt2, Responsible for the N-1-Methyl-Adenosine Base Modification of 25S rRNA in Saccharomyces Cerevisiae. *Nucleic Acids Res* (2013) 41:5428–43. doi: 10.1093/nar/gkt195
21. Dominissini D, Nachtergaele S, Moshitch-Moshkovitz S, Peer E, Kol N, Ben-Haim MS, et al. The Dynamic N(1)-Methyladenosine Methylome in Eukaryotic Messenger RNA. *Nature* (2016) 530:441–6. doi: 10.1038/nature16998
22. Liu F, Clark W, Luo G, Wang X, Fu Y, Wei J, et al. ALKBH1-Mediated tRNA Demethylation Regulates Translation. *Cell* (2016) 167:816–828.e816.
23. Li X, Xiong X, Wang K, Wang L, Shu X, Ma S, et al. Transcriptome-Wide Mapping Reveals Reversible and Dynamic N(1)-Methyladenosine Methylome. *Nat Chem Biol* (2016) 12:311–6. doi: 10.1038/nchembio.2040
24. Di Giammartino DC, Nishida K, Manley JL. Mechanisms and Consequences of Alternative Polyadenylation. *Mol Cell* (2011) 43:853–66. doi: 10.1016/j.molcel.2011.08.017
25. Elkon R, Ugalde AP, Agami R. Alternative Cleavage and Polyadenylation: Extent, Regulation and Function. *Nat Rev Genet* (2013) 14:496–506. doi: 10.1038/nrg3482
26. Baysal BE, Sharma S, Hashemikhabir S, Janga SC. RNA Editing in Pathogenesis of Cancer. *Cancer Res* (2017) 77:3733–9. doi: 10.1158/0008-5472.CAN-17-0520
27. Han SW, Kim HP, Shin JY, Jeong EG, Lee WC, Kim KY, et al. RNA Editing in RHOQ Promotes Invasion Potential in Colorectal Cancer. *J Exp Med* (2014) 211:613–21. doi: 10.1084/jem.20132209
28. Huang H, Tan BZ, Shen Y, Tao J, Jiang F, Sung YY, et al. RNA Editing of the IQ Domain in Ca(v)1. *3 Channels Modulates Ca^{2+}-dependent Inactivation Neuron* (2012) 73:304–16.
29. Nishikura K. A-To-I Editing of Coding and non-Coding RNAs by ADARs. *Nat Rev Mol Cell Biol* (2016) 17:83–96. doi: 10.1038/nrm.2015.4
30. Gajewski TF, Schreiber H, Fu YX. Innate and Adaptive Immune Cells in the Tumor Microenvironment. *Nat Immunol* (2013) 14:1014–22. doi: 10.1038/ni.2703
31. Egeblad M, Nakasone ES, Werb Z. Tumors as Organs: Complex Tissues That Interface With the Entire Organism. *Dev Cell* (2010) 18:884–901. doi: 10.1016/j.devcel.2010.05.012
32. Galon J, Bruni D. Approaches to Treat Immune Hot, Altered and Cold Tumours With Combination Immunotherapies. *Nat Rev Drug Discov* (2019) 18:197–218. doi: 10.1038/s41573-018-0007-y
33. Nagarsheth N, Wicha MS, Zou W. Chemokines in the Cancer Microenvironment and Their Relevance in Cancer Immunotherapy. *Nat Rev Immunol* (2017) 17:559–72. doi: 10.1038/nri.2017.49
34. Zhang B, Wu Q, Li B, Wang D, Wang L, Zhou YL. M(6)A Regulator-Mediated Methylation Modification Patterns and Tumor Microenvironment Infiltration Characterization in Gastric Cancer. *Mol Cancer* (2020) 19:53. doi: 10.1186/s12943-020-01170-0
35. Li HB, Tong J, Zhu S, Batista PJ, Duffy EE, Zhao J, et al. M(6)A mRNA Methylation Controls T Cell Homeostasis by Targeting the IL-7/STAT5/SOCS Pathways. *Nature* (2017) 548:338–42. doi: 10.1038/nature23450

36. Chen H, Yao J, Bao R, Dong Y, Zhang T, Du Y, et al. Cross-Talk of Four Types of RNA Modification Writers Defines Tumor Microenvironment and Pharmacogenomic Landscape in Colorectal Cancer. *Mol Cancer* (2021) 20:29. doi: 10.1186/s12943-021-01322-w
37. Conesa A, Madrigal P, Tarazona S, Gomez-Cabrero D, Cervera A, McPherson A, et al. A Survey of Best Practices for RNA-Seq Data Analysis. *Genome Biol* (2016) 17:13. doi: 10.1186/s13059-016-0881-8
38. Leek JT, Johnson WE, Parker HS, Jaffe AE, Storey JD. The Sva Package for Removing Batch Effects and Other Unwanted Variation in High-Throughput Experiments. *Bioinformatics* (2012) 28:882–3. doi: 10.1093/bioinformatics/bts034
39. Wilkerson MD, Hayes DN. ConsensusClusterPlus: A Class Discovery Tool With Confidence Assessments and Item Tracking. *Bioinformatics* (2010) 26:1572–3. doi: 10.1093/bioinformatics/btq170
40. Hänzelmann S, Castelo R, Guinney J. GSVA: Gene Set Variation Analysis for Microarray and RNA-Seq Data. *BMC Bioinf* (2013) 14:7. doi: 10.1186/1471-2105-14-7
41. Barbie DA, Tamayo P, Boehm JS, Kim SY, Moody SE, Dunn IF, et al. Systematic RNA Interference Reveals That Oncogenic KRAS-Driven Cancers Require TBK1. *Nature* (2009) 462:108–12. doi: 10.1038/nature08460
42. Newman AM, Liu CL, Green MR, Gentles AJ, Feng W, Xu Y, et al. Robust Enumeration of Cell Subsets From Tissue Expression Profiles. *Nat Methods* (2015) 12:453–7. doi: 10.1038/nmeth.3337
43. Thorsson V, Gibbs DL, Brown SD, Wolf D, Bortone DS, Ou Yang TH, et al. The Immune Landscape of Cancer. *Immunity* (2018) 48:812–830.e814. doi: 10.1016/j.immuni.2018.03.023
44. Yoshihara K, Shahmoradgoli M, Martínez E, Vegesna R, Kim H, Torres-Garcia W, et al. Inferring Tumour Purity and Stromal and Immune Cell Admixture From Expression Data. *Nat Commun* (2013) 4:2612. doi: 10.1038/ncomms3612
45. Rosenberg JE, Hoffman-Censits J, Powles T, van der Heijden MS, Balar AV, Necchi A, et al. Atezolizumab in Patients With Locally Advanced and Metastatic Urothelial Carcinoma Who Have Progressed Following Treatment With Platinum-Based Chemotherapy: A Single-Arm, Multicentre, Phase 2 Trial. *Lancet* (2016) 387:1909–20. doi: 10.1016/S0140-6736(16)00561-4
46. Mariathasan S, Turley SJ, Nickles D, Castiglioni A, Yuen K, Wang Y, et al. III, Et al. *TGFβ Attenuates Tumour Response PD-L1 Blockade Contributing Exclusion T Cells Nat* (2018) 554:544–8.
47. Şenbabaoğlu Y, Gejman RS, Winer AG, Liu M, Van Allen EM, de Velasco G, et al. Tumor Immune Microenvironment Characterization in Clear Cell Renal Cell Carcinoma Identifies Prognostic and Immunotherapeutically Relevant Messenger RNA Signatures. *Genome Biol* (2016) 17:231. doi: 10.1186/s13059-016-1092-z
48. Ritchie ME, Phipson B, Wu D, Hu Y, Law CW, Shi W, et al. Limma Powers Differential Expression Analyses for RNA-Sequencing and Microarray Studies. *Nucleic Acids Res* (2015) 43:e47. doi: 10.1093/nar/gkv007
49. Yu G, Wang LG, Han Y, He QY. Clusterprofiler: An R Package for Comparing Biological Themes Among Gene Clusters. *Omics* (2012) 16:284–7. doi: 10.1089/omi.2011.0118
50. Gao J, Kwan PW, Shi D. Sparse Kernel Learning With LASSO and Bayesian Inference Algorithm. *Neural Netw* (2010) 23:257–64. doi: 10.1016/j.neunet.2009.07.001
51. Iasonos A, Schrag D, Raj GV, Panageas KS. How to Build and Interpret a Nomogram for Cancer Prognosis. *J Clin Oncol* (2008) 26:1364–70. doi: 10.1200/JCO.2007.12.9791
52. Malta TM, Sokolov A, Gentles AJ, Burzykowski T, Poisson L, Weinstein JN, et al. Machine Learning Identifies Stemness Features Associated With Oncogenic Dedifferentiation. *Cell* (2018) 173:338–354.e315. doi: 10.1016/j.cell.2018.03.034
53. Reinhold WC, Sunshine M, Liu H, Varma S, Kohn KW, Morris J, et al. CellMiner: A Web-Based Suite of Genomic and Pharmacologic Tools to Explore Transcript and Drug Patterns in the NCI-60 Cell Line Set. *Cancer Res* (2012) 72:3499–511. doi: 10.1158/0008-5472.CAN-12-1370
54. Jiang P, Gu S, Pan D, Fu J, Sahu A, Hu X, et al. Signatures of T Cell Dysfunction and Exclusion Predict Cancer Immunotherapy Response. *Nat Med* (2018) 24:1550–8. doi: 10.1038/s41591-018-0136-1
55. Yang W, Soares J, Greninger P, Edelman EJ, Lightfoot H, Forbes S, et al. Genomics of Drug Sensitivity in Cancer (GDSC): A Resource for Therapeutic Biomarker Discovery in Cancer Cells. *Nucleic Acids Res* (2013) 41:D955–961.
56. Sebestyén E, Singh B, Miñana B, Pagès A, Mateo F, Pujana MA, et al. Large-Scale Analysis of Genome and Transcriptome Alterations in Multiple Tumors Unveils Novel Cancer-Relevant Splicing Networks. *Genome Res* (2016) 26:732–44. doi: 10.1101/gr.199935.115
57. Dawson MA, Kouzarides T. Cancer Epigenetics: From Mechanism to Therapy. *Cell* (2012) 150:12–27. doi: 10.1016/j.cell.2012.06.013
58. Ohm JE, McGarvey KM, Yu X, Cheng L, Schuebel KE, Cope L, et al. A Stem Cell-Like Chromatin Pattern may Predispose Tumor Suppressor Genes to DNA Hypermethylation and Heritable Silencing. *Nat Genet* (2007) 39:237–42. doi: 10.1038/ng1972
59. Jones PA, Baylin SB. The Epigenomics of Cancer. *Cell* (2007) 128:683–92. doi: 10.1016/j.cell.2007.01.029
60. McGranahan N, Furness AJ, Rosenthal R, Ramskov S, Lyngaa R, Saini SK, et al. Clonal Neoantigens Elicit T Cell Immunoreactivity and Sensitivity to Immune Checkpoint Blockade. *Science* (2016) 351:1463–9. doi: 10.1126/science.aaf1490
61. Ganesh K, Stadler ZK, Cercek A, Mendelsohn RB, Shia J, Segal NH, et al. Immunotherapy in Colorectal Cancer: Rationale, Challenges and Potential. *Nat Rev Gastroenterol Hepatol* (2019) 16:361–75. doi: 10.1038/s41575-019-0126-x
62. Wang R, Ye XH, Zhao XL, Liu JL, Zhang CY. Development of a Five-Gene Signature as a Novel Prognostic Marker in Ovarian Cancer. *Neoplasma* (2019) 66:343–9. doi: 10.4149/neo_2018_180705N447
63. Ye Y, Dai Q, Qi H. A Novel Defined Pyroptosis-Related Gene Signature for Predicting the Prognosis of Ovarian Cancer. *Cell Death Discovery* (2021) 7:71. doi: 10.1038/s41420-021-00451-x
64. Yue H, Wang J, Chen R, Hou X, Li J, Lu X. Gene Signature Characteristic of Elevated Stromal Infiltration and Activation Is Associated With Increased Risk of Hematogenous and Lymphatic Metastasis in Serous Ovarian Cancer. *BMC Cancer* (2019) 19:1266. doi: 10.1186/s12885-019-6470-y
65. Qiu Y, Pan M. Chen X. >A Liquid-Liquid Phase Separation-Related Gene Signature Progn biomark Epithelial Ovarian Cancer. *Front Oncol* (2021) 11:671892. doi: 10.3389/fonc.2021.671892
66. Odunsi K. Immunotherapy in Ovarian Cancer. *Ann Oncol* (2017) 28:viii1–7. doi: 10.1093/annonc/mdx444
67. Jiménez-Sánchez A, Cybulska P, Mager KL, Koplev S, Cast O, Couturier DL, et al. Unraveling Tumor-Immune Heterogeneity in Advanced Ovarian Cancer Uncovers Immunogenic Effect of Chemotherapy. *Nat Genet* (2020) 52:582–93. doi: 10.1038/s41588-020-0630-5
68. Duraiswamy J, Turrini R, Minasyan A, Barras D, Crespo I, Grimm AJ, et al. Myeloid Antigen-Presenting Cell Niches Sustain Antitumor T Cells and License PD-1 Blockade *via* CD28 Costimulation. *Cancer Cell* (2021) 39:1623–1642.e1620. doi: 10.1016/j.ccell.2021.10.008
69. Scheper W, Kelderman S, Fanchi LF, Linnemann C, Bendle G, de Rooij MAJ, et al. Low and Variable Tumor Reactivity of the Intratumoral TCR Repertoire in Human Cancers. *Nat Med* (2019) 25:89–94. doi: 10.1038/s41591-018-0266-5
70. Montfort A, Pearce O, Maniati E, Vincent BG, Bixby L, Böhm S, et al. A Strong B-Cell Response Is Part of the Immune Landscape in Human High-Grade Serous Ovarian Metastases. *Clin Cancer Res* (2017) 23:250–62. doi: 10.1158/1078-0432.CCR-16-0081
71. Marvel D, Gabrilovich DI. Myeloid-Derived Suppressor Cells in the Tumor Microenvironment: Expect the Unexpected. *J Clin Invest* (2015) 125:3356–64. doi: 10.1172/JCI80005
72. Cui TX, Kryczek I, Zhao L, Zhao E, Kuick R, Roh MH, et al. Myeloid-Derived Suppressor Cells Enhance Stemness of Cancer Cells by Inducing Microrna101 and Suppressing the Corepressor Ctbp2. *Immunity* (2013) 39:611–21. doi: 10.1016/j.immuni.2013.08.025
73. Motz GT, Santoro SP, Wang LP, Garrabrant T, Lastra RR, Hagemann IS, et al. Tumor Endothelium FasL Establishes a Selective Immune Barrier Promoting Tolerance in Tumors. *Nat Med* (2014) 20:607–15. doi: 10.1038/nm.3541
74. Lecker LSM, Berlato C, Maniati E, Delaine-Smith R, Pearce OMT, Heath O, et al. TGFBI Production by Macrophages Contributes to an Immunosuppressive Microenvironment in Ovarian Cancer. *Cancer Res* (2021) 81:5706–19. doi: 10.1158/0008-5472.CAN-21-0536
75. Wherry EJ. T Cell Exhaustion. *Nat Immunol* (2011) 12:492–9. doi: 10.1038/ni.2035

76. Anderson KG, Stromnes IM, Greenberg PD. Obstacles Posed by the Tumor Microenvironment to T Cell Activity: A Case for Synergistic Therapies. *Cancer Cell* (2017) 31:311–25. doi: 10.1016/j.ccell.2017.02.008

Conflict of Interest: The authors declare that the research was conducted in the absence of any commercial or financial relationships that could be construed as a potential conflict of interest.

Publisher's Note: All claims expressed in this article are solely those of the authors and do not necessarily represent those of their affiliated organizations, or those of the publisher, the editors and the reviewers. Any product that may be evaluated in this article, or claim that may be made by its manufacturer, is not guaranteed or endorsed by the publisher.

Copyright © 2022 Ni, Chen, Cui, Ding and Liu. This is an open-access article distributed under the terms of the Creative Commons Attribution License (CC BY). The use, distribution or reproduction in other forums is permitted, provided the original author(s) and the copyright owner(s) are credited and that the original publication in this journal is cited, in accordance with accepted academic practice. No use, distribution or reproduction is permitted which does not comply with these terms.

frontiers | Frontiers in Immunology

TYPE Original Research
PUBLISHED 27 July 2022
DOI 10.3389/fimmu.2022.964190

Check for updates

OPEN ACCESS

EDITED BY
Linlang Guo,
Zhujiang Hospital, China

REVIEWED BY
Xiaosong Li,
Chongqing Medical University, China
Antonella Argentiero,
National Cancer Institute Foundation (IRCCS), Italy
Weimin Lin,
Sichuan University, China

*CORRESPONDENCE
Shuijun Zhang
Zhangshuijun@zzu.edu.cn

†These authors have contributed equally to this work

SPECIALTY SECTION
This article was submitted to Cancer Immunity and Immunotherapy, a section of the journal Frontiers in Immunology

RECEIVED 08 June 2022
ACCEPTED 04 July 2022
PUBLISHED 27 July 2022

CITATION
Liu L, Liu Z, Gao J, Liu X, Weng S, Guo C, Hu B, Wang Z, Zhang J, Shi J, Guo W and Zhang S (2022) CD8+ T cell trajectory subtypes decode tumor heterogeneity and provide treatment recommendations for hepatocellular carcinoma. *Front. Immunol.* 13:964190. doi: 10.3389/fimmu.2022.964190

COPYRIGHT
© 2022 Liu, Liu, Gao, Liu, Weng, Guo, Hu, Wang, Zhang, Shi, Guo and Zhang. This is an open-access article distributed under the terms of the Creative Commons Attribution License (CC BY). The use, distribution or reproduction in other forums is permitted, provided the original author(s) and the copyright owner(s) are credited and that the original publication in this journal is cited, in accordance with accepted academic practice. No use, distribution or reproduction is permitted which does not comply with these terms.

CD8+ T cell trajectory subtypes decode tumor heterogeneity and provide treatment recommendations for hepatocellular carcinoma

Long Liu[1,2,3,4†], Zaoqu Liu[5†], Jie Gao[1,2,3,4], Xudong Liu[1,2,3,4], Siyuan Weng[5], Chunguang Guo[6], Bowen Hu[1,2,3,4], Zhihui Wang[1,2,3,4], Jiakai Zhang[1,2,3,4], Jihua Shi[1,2,3,4], Wenzhi Guo[1,2,3,4] and Shuijun Zhang[1,2,3,4*]

[1]Department of Hepatobiliary and Pancreatic Surgery, The First Affiliated Hospital of Zhengzhou University, Zhengzhou, China, [2]Henan Research Centre for Organ Transplantation, The First Affiliated Hospital of Zhengzhou University, Zhengzhou, China, [3]Henan Diagnosis and Treatment League for Hepatopathy, The First Affiliated Hospital of Zhengzhou University, Zhengzhou, China, [4]Henan Engineering and Research Center for Diagnosis and Treatment of Hepatobiliary and Pancreatic Surgical Diseases, The First Affiliated Hospital of Zhengzhou University, Zhengzhou, China, [5]Department of Interventional Radiology, The First Affiliated Hospital of Zhengzhou University, Zhengzhou, China, [6]Department of Endovascular Surgery, The First Affiliated Hospital of Zhengzhou University, Zhengzhou, China

Introduction: Mounting evidence has revealed that the interactions and dynamic alterations among immune cells are critical in shaping the tumor microenvironment and ultimately map onto heterogeneous clinical outcomes. Currently, the underlying clinical significance of immune cell evolutions remains largely unexplored in hepatocellular carcinoma (HCC).

Methods: A total of 3,817 immune cells and 1,750 HCC patients of 15 independent public datasets were retrieved. The Seurat and Monocle algorithms were used to depict T cell evolution, and nonnegative matrix factorization (NMF) was further applied to identify the molecular classification. Subsequently, the prognosis, biological characteristics, genomic variations, and immune landscape among distinct clusters were decoded. The clinical efficacy of multiple treatment approaches was further investigated.

Results: According to trajectory gene expression, three heterogeneous clusters with different clinical outcomes were identified. C2, with a more advanced pathological stage, presented the most dismal prognosis relative to C1 and C3. Eight independent external cohorts validated the robustness and reproducibility of the three clusters. Further explorations elucidated C1 to be characterized as lipid metabolic HCC, and C2 was referred to as cell-proliferative HCC, whereas C3 was defined as immune inflammatory HCC. Moreover, C2 also displayed the most conspicuous genomic instability, and C3 was deemed as "immune-hot", having abundant immune cells and an elevated expression of immune checkpoints. The assessments of therapeutic

intervention suggested that patients in C1 were suitable for transcatheter arterial chemoembolization treatment, and patients in C2 were sensitive to tyrosine kinase inhibitors, while patients in C3 were more responsive to immunotherapy. We also identified numerous underlying therapeutic agents, which might be conducive to clinical transformation in the future.

Conclusions: Our study developed three clusters with distinct characteristics based on immune cell evolutions. For specifically stratified patients, we proposed individualized treatment strategies to improve the clinical outcomes and facilitate the clinical management.

KEYWORDS

hepatocellular carcinoma, single-cell RNA-seq, immunotherapy, heterogeneity, prognosis, clinical treatment

Introduction

Hepatocellular carcinoma (HCC) is a common liver malignant tumor, which ranks sixth in terms of global incidence and second as a cause of global mortality (1). With the knowledge of tumorigenesis that has evolved, HCC is dominantly induced by a series of chronic liver diseases, such as liver cirrhosis, HBV/HCV infection, and fatty liver disease (2). Currently, more curative treatment approaches than ever are proposed for HCC patients, including radical surgery, transcatheter arterial chemoembolization (TACE), molecular targeted agents, and immunotherapy (3). With the advent of many treatments, there are more various options provided for HCC patients to improve the clinical efficacy. However, due to its superior aggressive capacity and high relapse, HCC patients display a dismal prognosis, such that the 5-year survival is only 18% (4). In addition, previous research has elucidated that even patients with the same clinical stage had differences in therapeutic efficacy and display conspicuous heterogeneity in prognosis (5, 6). This is mainly since the widely used clinical classification systems focus on the clinicopathological characteristics, which are limited to stratifying the patients and thus ignoring their molecular features (7, 8). Hence, it is imperative to increase the understanding of genomic heterogeneity. Seeking a novel molecular classification is significant to stratifying patients and making clinical decisions, thus further improving the prognosis.

In recent years, the continued interests on single-cell RNA-seq, an emerging technology, have provided the exploration of tumor heterogeneity and depicted the characteristics of genomic codes (9). The traditional RNA-seq technology actually obtains the average number of gene expressions in tumor tissue or multi-cellular populations, losing the transcriptome heterogeneity at the cell level (10). Intriguingly, single-cell RNA-seq has been proven as an advancement in decoding the genomic codes and widely used to reveal inter-tumor and intra-tumor heterogeneity (11, 12). Previous studies have demonstrated that the immune microenvironment, hypoxia, and ferroptosis all display significant heterogeneity in HCC (13–15). The tumor microenvironment (TME) contained abundant immune cells, stromal cells, and tumor cells as well as plays a key role in tumor heterogeneity and malignant progression (14). Moreover, the interactions and dynamic variations among immune cells are critical to shape the TME and ultimately map onto heterogeneous clinical outcomes (16). Therefore, it is essential to explore the dynamic process of immune cell subpopulations by single-cell RNA-seq and then further propose a new molecular classification, indicating the heterogeneous genomic characteristics and clinical outcomes.

With the enormous advancements in tumor research, individualized comprehensive treatments and precision medicine have gradually become the goal of humans (7). Using a traditional therapy strategy might bring overtreatment or undertreatment as lacking the knowledge of molecular characteristics, while integrated treatments unite novel approaches, such as immunotherapy and targeted therapy, and might produce encouraging efficacy (6, 8). Immunotherapy has made revolutionized impacts on anti-tumor therapy, which performs its capacity by acting on specific molecular markers, including PD1, PD-L1, and CTLA-4. Nevertheless, only a subset of patients displayed a curative response (17). As a common targeted therapy, multi-kinase inhibitors (tyrosine kinase inhibitors, TKIs) perform tumor suppression *via* restraining tumor angiogenesis and cell proliferation. However, a part of the patients present obvious drug resistance (18). Thus, patients with HCC are stratified appropriately, and personalized

therapeutic strategies are implemented, which are conducive to enhancing the clinical efficacy. Additionally, owing to the poor therapeutic efficacy of chemotherapy and high expense (3), developing novel potential agents might bring the dawn for HCC patients.

In this context, according to single-cell RNA-seq data, we depicted the landscape of immune cells and identified the trajectory genes involved in the dynamic evolution of CD8+ T cells. Subsequently, three heterogeneous clusters were developed by The Cancer Genome Atlas (TCGA)-Liver Hepatocellular Carcinoma (LIHC) cohort and validated using eight independently external cohorts. The three clusters had distinct prognosis, biological characteristics, genomic variations, and immune infiltration microenvironment. In addition, the treatment recommendations were proposed for HCC patients using diverse clinical treatment cohorts, including immunotherapy, TACE, and sorafenib therapy. The potential therapeutic agents were also identified among the three clusters. Overall, the patients in the three clusters displayed distinct therapeutic responses, which provide the theoretical basis for developing an individualized treatment strategy.

Materials and methods

Data acquisition and processing

A total of 15 independent public datasets were collected and processed in this study, including single-cell RNA-seq cohort, high-throughput RNA-seq cohorts, microarray cohorts, and clinical treatment cohorts. The single-cell RNA-seq cohort GSE140228 was downloaded from Gene Expression Omnibus (GEO), which deciphered the immune landscape and dynamics of HCC. The TCGA-LIHC cohort (n = 369), International Cancer Genome Consortium (ICGC)-LIRI cohort (n = 232), and GSE14520 cohort (n = 221) included gene expression, and corresponding complete clinical information were retrieved from TCGA, ICGC, and GEO, respectively. In the TCGA-LIHC cohort, somatic mutation data and copy number variation (CNV) information were accessed from the online portal cBioPortal. In addition, the E-TABM-36 cohort (n = 60) was generated from ArrayExpress database. Other microarray cohorts were also collected from the GEO database, encompassing GSE25097 (n = 268), GSE76427 (n = 115), GSE116174 (n = 64), GSE144269 (n = 68), GSE104580 (n = 147), and GSE109211 (n = 67). Among these, GSE104580 and GSE109211 contained TACE treatment and sorafenib therapy information, respectively. Additionally, we enrolled four eligible immunotherapy cohorts with 98 non-responders and 41 responders, including GSE35640 (n = 56), GSE91061 (n = 39), GSE100797 (n = 21), and Nathanon (n = 23) cohorts. The details of all retrieved cohorts are shown in Supplementary Table S1.

The RNA-seq raw count data were converted to transcripts per million format and further log-2 transformed. The expression profiles from GEO and ArrayExpress databases were processed and normalized by *affy* and *lumi* packages based on different platforms. According to the RECIST v1.1 standard, patients with complete response/partial response and patients with stable disease/progressive disease were deemed as responders and non-responders, respectively. Patients who were not evaluable were excluded.

Single-cell RNA-seq data analysis

The *Seurat* (v4.0.6) package was utilized to process data for further dimension reduction and cell clustering analysis (19). Single-cell gene expression profiles were filtered to exclude cells that had either over 10% mitochondria genes or fewer than 200 transcripts/cell. PCA linear dimensional reduction and clustering visualization were performed using RunPCA function and RunTSNE function implemented in *Seurat*. The *SingleR* package was applied to annotate distinct cell clustering, and then unique marker genes were identified *via* the FindAllMarkers function of *Seurat*. The *irGSEA* package with UCell method was used to accomplish single-cell gene set enrichment analysis. The pseudo-time trajectory analysis of single cells was conducted by *Monocle 2* package (20). Cellular trajectory ordered in pseudo-time was presented with multiple branches, and genes along the trajectory were enrolled in a subsequent analysis.

Cluster identification *via* nonnegative matrix factorization

Nonnegative matrix factorization (NMF) algorithm executed in the *NMF* package was performed to identify molecular clustering by factorizing matrix and running iterations (21). Using univariate Cox regression, the trajectory genes were screened, and prognosis-associated candidate genes were generated for a better clinical application. Based on the nonnegative matrix of these genes, consensus clustering was deciphered with the following criteria in the *NMF* package: possible factorization ranks = 2–9, number of iterations = 100, and method = "lee". Cophenetic coefficient was employed to determine optimal rank, and silhouette statistic was used to quantify the robustness of clustering patterns. Usually, when the value of cophenetic correlation coefficient starts decreasing, it is deemed as optimal factorization rank (21). The magnitude of silhouette coefficient was linked with the similarity of a sample to its own cluster, a higher silhouette value, and a better one matched to its own cluster (22).

Weighted gene co-expression network analysis

The weighted gene co-expression network analysis (WGCNA) aims to explore and reveal the correlations

between gene modules and phenotypes (23). The characteristic genes of distinct clusters were identified using the *WGCNA* package. After excluding the outlier samples, gene co-expression network was constructed based on the top 5,000 genes and further transformed into a scale-free network *via* selecting an appropriate soft threshold β. Subsequently, the topological overlap matrix (TOM) describing the overlap of network neighbors and 1-TOM representing gene dissimilarity were generated by the weighted adjacency matrix. Eventually, gene modules with various colors were identified by dynamic tree algorithm. Based on the relationship between the module eigenvalue and phenotypes, three modules with highest correlation were filtered, and the characteristic genes were acquired for subsequent analysis.

Nearest template prediction validation

The nearest template prediction (NTP) is a flexible approach that evaluates class prediction confidence for a single patient (24). To further assess the reliability and stability of clusters, the NTP algorithm implemented in the *CMScaller* package was utilized to validate by multiple cohorts from inconsistent platforms. The signature gene list used in NTP was derived from modules' characteristic genes and differentially expressed genes.

Explorations of the underlying biological characteristics

To explore the specific biological characteristics of distinct clusters, gene set enrichment analysis (GSEA) algorithm was performed, which displayed pathway activities by gene rank information. Differentially expressed genes (DEGs) were identified *via* the *limma* package and then ordered according to descending $\log_2$ fold change value. The *clusterProfiler* package was used to exhibit the GSEA analysis, and Benjamin–Hochberg-corrected adjusted *P*-value <0.05 was regarded as statistically significant. The gene set variation analysis (GSVA) was broadly utilized in pathway activity assessment (13). Based on 50 Hallmark gene sets, the *GSVA* package was applied to further evaluate and elucidate different biological characteristics among clusters.

Somatic mutation and copy number variation analysis

The landscape of genomic variations was depicted by the mutation and CNV data. The *maftools* package was used to display somatic variants among distinct clusters, including single-nucleotide polymorphism (SNP), insertion and deletion (INDEL), tumor mutation burden (TMB), and mutation frequency (25). Generally, frequently mutated genes (FMGs) that had top 20 mutation frequency were considered the main driver genes for malignant tumor (26). We also dissected the CNV among clusters and further exhibited frequently AMP or HOMDEL genes, which possessed the top 10 genes with amplification or deletion.

The assessment of immune cell infiltration and immunotherapy

To decode the landscape of immune cell infiltration, immune gene sets were obtained from a previous study which stored 28 immune cell subgroups (27) (Supplementary Table S2). The single-sample gene set enrichment analysis (ssGSEA) algorithm was used to compute the relative infiltration abundance of 28 immune cells. The expression of 27 immune checkpoints was evaluated to further depict the tumor immune microenvironment, encompassing the B7-CD28 superfamily, TNF superfamily, and other molecules (15) (Supplementary Table S3). The capacity of antigen presentation was estimated based on nine human leukocyte antigen (HLA) molecule expression profiles (16). Two prevalent approaches were employed to assess the immunotherapeutic efficacy among distinct clusters, including T cell inflammatory signature (TIS) and unsupervised subclass mapping (Submap). TIS, which contained 18 inflammatory genes, was scored by ssGSEA algorithm, which gave a higher score to indicate a better response to PD-1 blockade (28). The Submap was utilized to measure the expression profile similarity between HCC patients and immunotherapeutic patients, which was consistent with the similarity of clinical responses (29). Four immunotherapy cohorts were applied to further reveal the immunotherapy significances of different clusters. Receiver operating characteristic curve (ROC) was executed to estimate the accuracy of the immunotherapeutic prediction.

The evaluation of clinical treatment

The *pRRophetic* package encompassing linear ridge regression model was applicable to predict drug response based on gene expression data (30). Using *pRRophetic* package, we calculated the half-maximal inhibitory concentration (IC50) of clinical tissues. Potential therapeutic agents were screened when the IC50 value was lowest among distinct clusters. The Connectivity Map (CMap) was a systematic approach for searching potential therapeutic compounds based on the similarity of gene expression profile (31). We executed CMap database to identify potential therapeutic compounds and target pathways. DEGs were firstly screened by the *limma* package, and the expression similarity was compared with database signatures, and then enrichment score-quantified therapeutic value was generated. Additionally, the TACE and sorafenib

treatment-associated cohorts were also enrolled to assess the clinical efficacy among distinct clusters.

Statistical analysis

The Kaplan–Meier and Cox regression analyses were conducted by the *survival* package. The log-rank test was applied to compare the survival statistics of categorical variables. Multivariate Cox regression analysis was utilized to calculate the hazard ratio and verify the independent significance of multiple traits. Using Pearson's correlation analysis, the correlation between two continuous variables was evaluated. Kruskal–Wallis test was performed to compare the difference among three groups. The *pROC* package was carried out to draw the ROC for predicting binary categorical variables. All data cleaning, statistical analysis, and visualization were conducted in R v4.1 software. All statistical tests were two-sided. P <0.05 was considered statistically significant.

Results

Single-cell analysis reveals cell subtypes

To depict the landscape and dynamics of CD45+ immune cells, single-cell transcriptomes were performed with subcluster analysis and visualized by t-distributed stochastic neighbor embedding (t-SNE) approach. A total of 3,817 immune cells originated from tumor and normal tissue were classified into 17 clusters (Figure 1A). Based on the gene signature of distinct subclusters, these cells were mainly composed of five immune cell clusters, including B cells, dendritic cells, monocyte cells, natural killer cells, and T cells (Figure 1B). To describe the source of immune cells, 2,212 tumor-derived cells and 1,605 non-tumor-derived cells were clustered separately (Figure 1C). Single-cell enrichment analyses exhibited that all cells were involved in immune inflammation pathway, especially dendritic cells, monocyte cells, and T cells (Figure 1D). We further measured the percentage composition and extracted the top 5 markers of each immune cells cluster (Figures 1E, F). In addition, the accuracy of B cell populations was verified by analyzing the expression of specific markers: CD79A, IGHG3, and IGLC2 (Supplementary Figures S1A–F). A concern was that T cells from tumor tissue displayed the most prevalent cell cluster. It was well known that T cells had anti-tumor immunity ability and power in directly killing cells in tumor progression. Thus, T cells were further explored and decoded at single-cell level.

The dynamics of T cells during HCC progression

The tumor-derived T cells were employed to reveal the evolution of T cells using dimensional reduction, unsupervised clustering, and trajectory analysis. All T cells were clustered again and divided into six cell subpopulations (Figure 2A and Supplementary Figure S2A). A previous study has elucidated that CD3D and CD3E were shared gene markers of CD4+ and CD8+ T cells (32). Thus, our study suggested that the T cells retrieved in this study mainly consisted of CD4+ and CD8+ T cells (Figures 2B, C and Supplementary Figures S2B, C). The specific marker gene CD4 was expressed in clusters 1, 2, 3, and 5, which indicated that these clusters represented CD4+ T cells (Figure 2D and Supplementary Figure S2D). We also noticed that cluster 0 and cluster 4 were enriched for CD8+ T cell markers, such as CD8A and CD8B, confirming the identity of CD8+ T cells (Figures 2E, F and Supplementary Figures S2E, F). These specific cell subpopulations were visualized with two-dimensional distributions by the t-SNE method (Figure 2A). As the tumor progressed, the cell status in TME was dynamic rather than immobile, and the dynamic process was depicted by the Monocle algorithm. For CD4+ T cells, there was a gradual evolution process from CD4+ T clusters 3 and 4 to CD4+ T clusters 1 and 2 (Supplementary Figures S2G, H). The immune checkpoints were further investigated in CD8+ T cells (32). Strikingly, most inhibitory checkpoints represented T cell exhaustion, such as HAVCR2 (TIM3), LAG3, TIGIT, PDCD1 (PD-1), and CTLA-4, which were significantly upregulated in CD8+ T cluster 2 (Figure 2G). The pseudo-time and trajectory analysis indicated that CD8+ T cells tended to be exhausted with tumor progression, which might be linked with poor prognosis (Figures 2H, I). A previous study had also demonstrated that T cell exclusion is common in TME and associated with immune privilege (33). Thus, these genes along the trajectory might play an important role in TME and in the clinical outcomes of HCC patients (Supplementary Table S4).

The identification of three molecular clusters

The trajectory genes were employed to extract prognosis-associated candidate genes. Based on the expression of these genes, the NMF approach was utilized to decipher heterogeneous molecular clusters. As illustrated in Figure 3A, the optimal cluster option was three due to the cophenetic coefficient that started to rapidly decline. The consensus matrices also suggested that three clusters had optimal stratification (Figure 3B). The silhouette statistic was used to assess the stability of molecular clusters, and the samples were further detected by silhouette width (34). Therefore, samples with a positive silhouette width were divided into three stable and robust clusters (Figure 3C). To facilitate the clinical application, the prognostic significance of clusters was further explored. C2 exhibited poor overall survival (OS) and recurrence-free survival, whereas C3 presented a favorable prognosis (P <0.05) (Figures 3D, E).

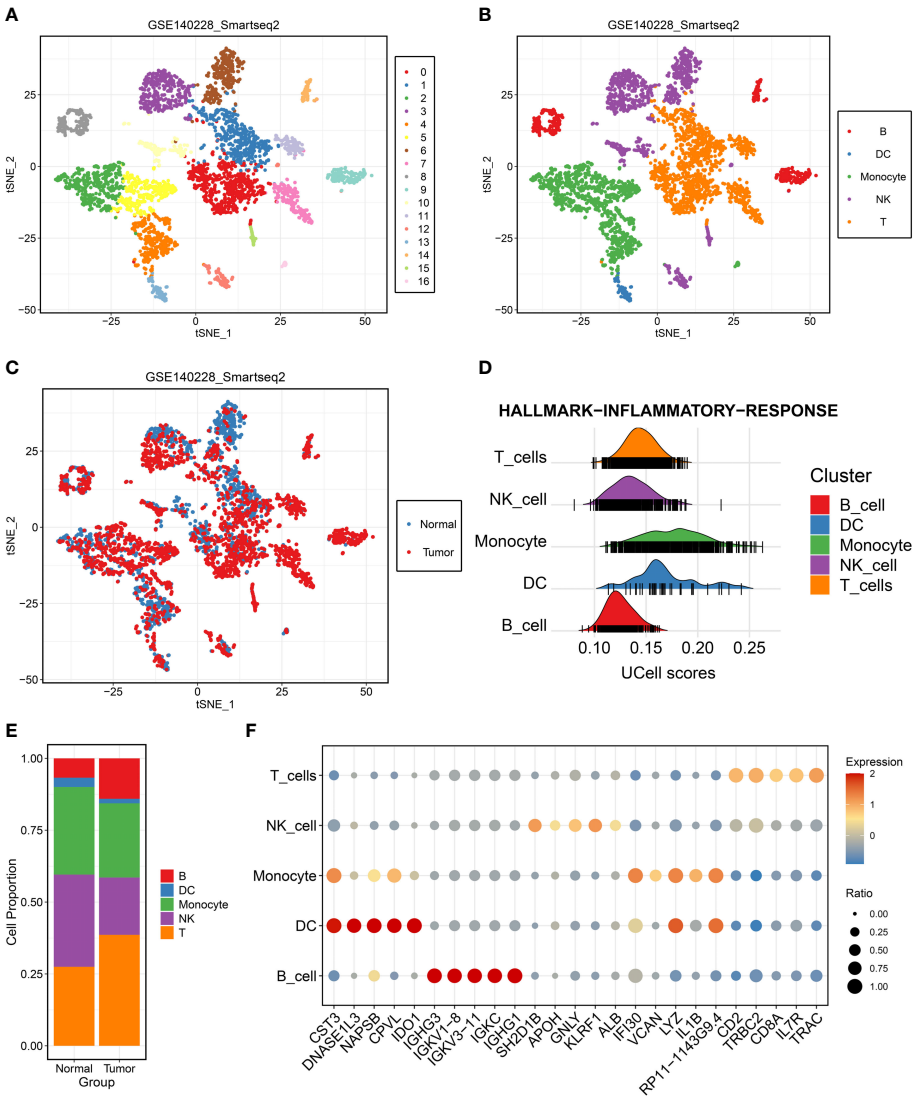

FIGURE 1
Single-cell RNA-seq profiling of different immune cell clusters derived from hepatocellular carcinoma (HCC). **(A–C)** t-distributed stochastic neighbor embedding plot of all the single cells, with each color coded for **(A)** 17 major cell clusters, **(B)** immune cell types, and **(C)** sample origin (normal or tumor) in HCC. **(D)** Single-cell gene set enrichment analysis of inflammatory response activity among distinct immune cell types. **(E)** Proportions of five immune cell types originated from tumor and normal tissue. **(F)** Top five marker genes of five immune cell types identified in this profile.

The characteristic genes and specific pathway of three clusters

The characteristic genes of three clusters were identified using *WGCNA* package. First of all, the outlier samples were removed, and then the remaining samples were clustered (Supplementary Figure S3A). When β was set to 6, the no-scale R^2 was 0.9, developing a scale-free network (Figure 4A). As shown in Supplementary Figure S3B, the TOM network was displayed *via* a heat map. Subsequently, a total of 12 co-expression modules were obtained by dynamic tree cutting, and the eigengene adjacency of various modules was depicted *via* a heat map (Supplementary Figures S3C, D). Furthermore, the module–trait relationships were exhibited to measure the correlations between the modules and the three clusters. The turquoise, blue, and purple module presented the strongest correlation with C1, C2, and C3, respectively (Figure 4B). The correlation values between gene significance and module membership indicated that the construction of the gene modules was robust (Figures 4C–E). The genes in each module were defined as characteristic genes and are shown in Supplementary Table S5. To decode the specific biological characteristics of three clusters, we performed GSEA analysis using gene sets from Gene Ontology and

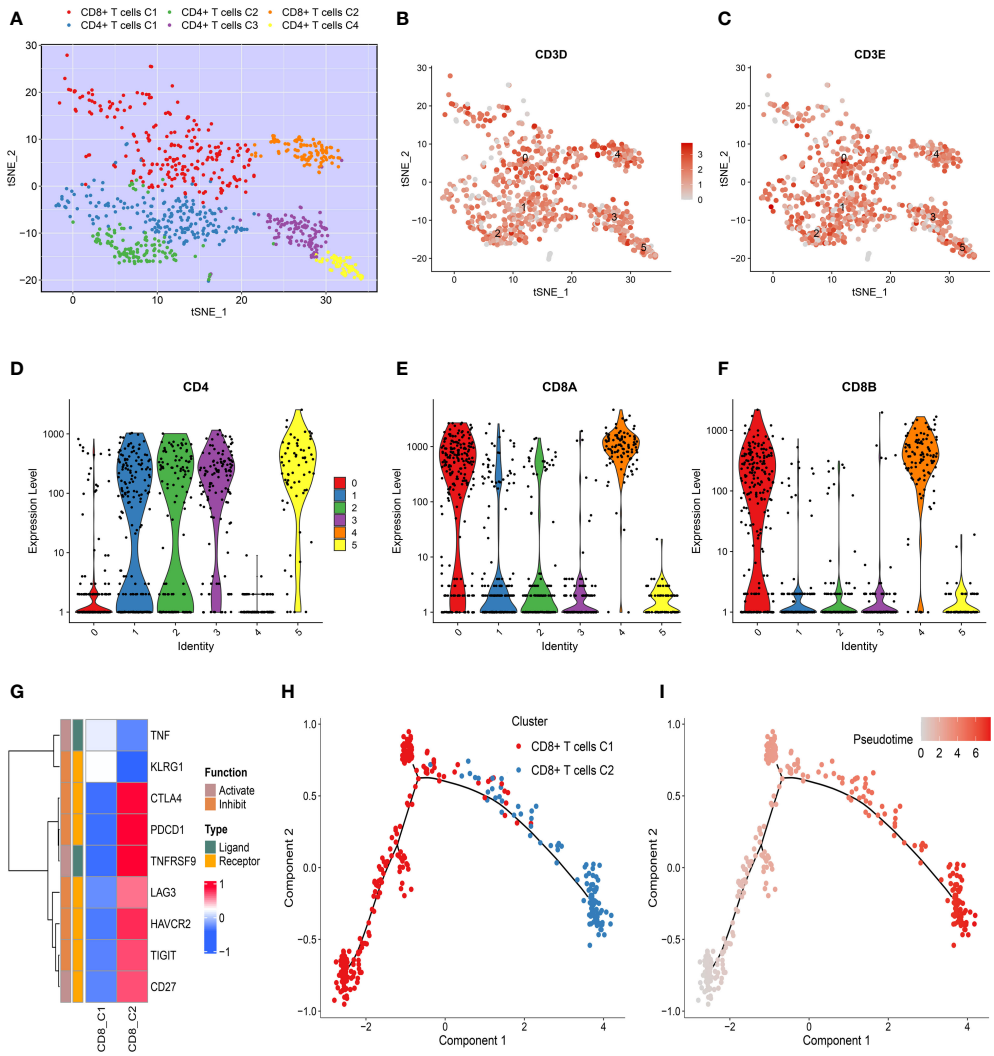

FIGURE 2
Dynamics of T cells during hepatocellular carcinoma (HCC) progression. **(A)** t-SNE plot of only T cells, with each color coded for CD4+ T and CD8+ T cell clusters. **(B, C)** t-SNE plots showing the expression level of specific T cell subset marker genes, **(B)** CD3D, and **(C)** CD3E. **(D–F)** Violin plots demonstrating the identity of CD4+ T cells and CD8+ T cells through analyzing the expression of specific markers **(D)** CD4, **(E)** CD8A, and **(F)** CD8B. **(G)** Heat map of immune checkpoints upregulated or downregulated in CD8+ T cells. A row Z-score was used to represent the expression level. **(H)** Differentiation trajectory of CD8+ T cells in HCC, with a color code for pseudo-time. **(I)** Differentiation trajectory of CD8+ T cells in HCC, with a color code for clusters.

Kyoto Encyclopedia of Genes and Genomes. C1 was mainly associated with metabolism pathways, including fatty acid oxidation and bile secretion. There are tight links between tumor immune microenvironment and metabolism activity such as fatty metabolism and bile acid metabolism in liver. The important source of energy is generated from the elevated lipid metabolism activity, which is the power and key regulator for immune cells and tumor cells. Meanwhile, elevated lipid metabolism activity impacts the inflammatory pathway in the tumor microenvironment, even resulting in immune escape (35). C2 possessed conspicuous enrichment in proliferation pathways such as cell cycle and nuclear division. C3 was obviously enriched in immune pathways encompassing the adaptive immune response and chemokine signaling pathway (Figures 4F, G). Therefore, we characterized C1 as lipid metabolic HCC and C2 as cell proliferative HCC, whereas C3 was defined as immune inflammatory HCC.

Nearest template prediction verifies three heterogeneous clusters

Based on signature gene expression, NTP analysis was performed to assess the reliability and stability of the three clusters. The signature genes were generated from the overlaps

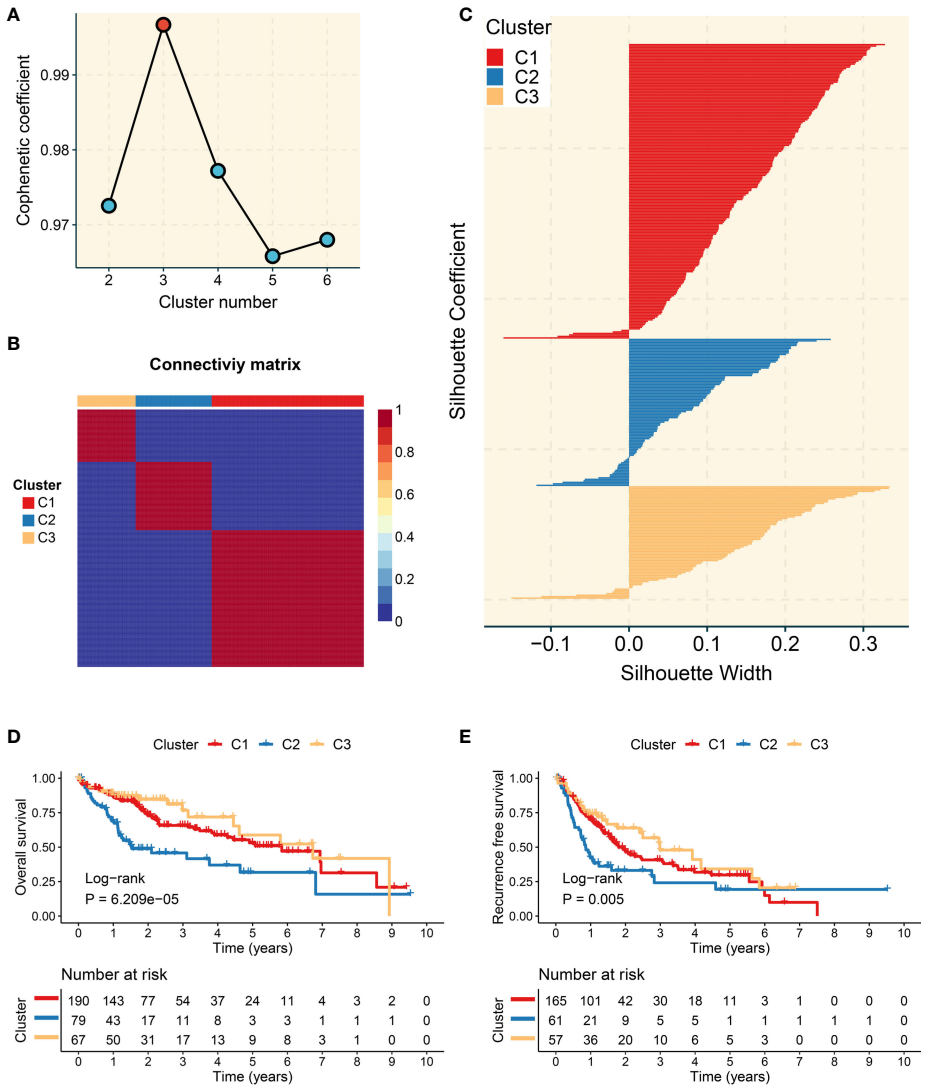

FIGURE 3
Development of three molecular clusters with heterogeneous clinical outcomes by nonnegative matrix factorization (NMF) analysis. **(A)** The optimal rank was 3 as the cophenetic coefficient started firstly decreasing. **(B)** Consensus map of NMF clustering results in The Cancer Genome Atlas-Liver Hepatocellular Carcinoma (TCGA-LIHC) cohort. **(C)** Silhouette statistic of three heterogeneous clusters. **(D)** Kaplan–Meier curves of overall survival according to three clusters in the TCGA-LIHC cohort. **(E)** Kaplan–Meier curves of recurrence-free survival according to three clusters in the TCGA-LIHC cohort.

between characteristic genes and upregulated DEGs (24). Using the NTP method, a total of eight cohorts obtained from distinct platforms were executed to measure and evaluate the prediction confidence for each patient, including GSE14520 (Figure 5A), ICGC-LIRI (Figure 5C), E-TABM-36, GSE76427, GSE25097, GSE104580, GSE116174, and GSE144269 (Supplementary Figures S4A–F). Consistent with a previous study, patients with false discovery rate <0.05 were detected for a subsequent analysis (36). In GSE14520 and ICGC-LIRI cohorts, Kaplan–Meier and multivariate Cox regression analyses were utilized to further elucidate the prognostic implications of the three clusters. The Kaplan–Meier analysis suggested that C2 still possessed the most unfavorable OS, while C3 presented the most favorable OS (P <0.05), which was coincident with previous results (Figures 5B, D). Multivariate Cox regression indicated that C2 was an independent prognostic indicator in the TCGA-LIHC, GSE14520, and ICGC-LIRI cohorts (Figures 5E–G). In addition, the proportions of the three clusters were displayed among distinct cohorts, which showed a high similarity (Figure 5H). Overall, the three clusters had heterogeneous clinical outcomes and were reproducible and robust in HCC.

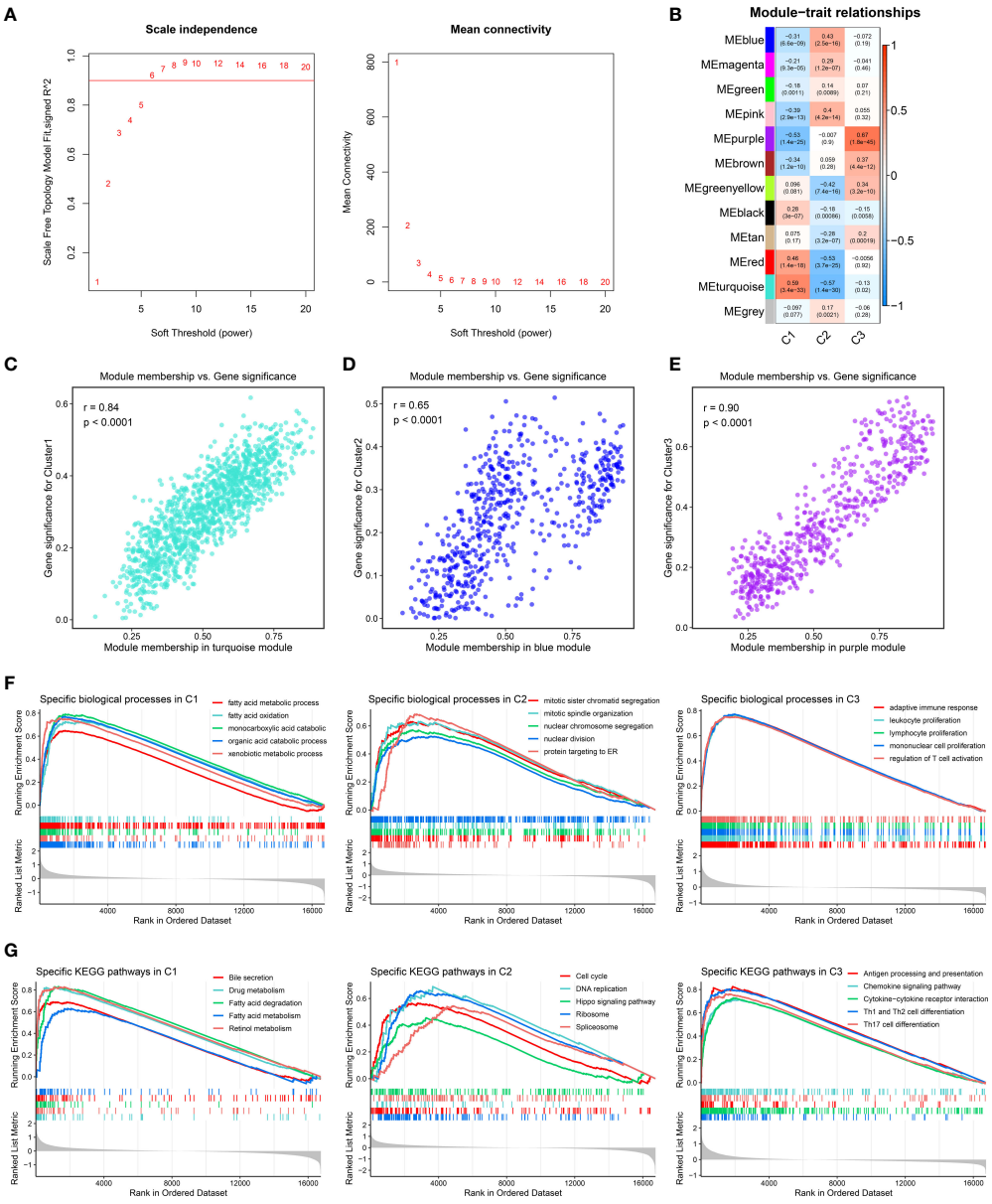

FIGURE 4
Identification of characteristic genes and specific biological pathways. **(A)** Analysis of network topology for different soft-threshold power by weighted gene co-expression network analysis. The left panel shows the impact of soft-threshold power on the scale-free topology fit index; the right panel displays the impact of soft-threshold power on the mean connectivity. **(B)** Correlation analysis between module eigengenes and molecular phenotype. (**C**–**E**) Scatterplot of module membership *vs*. gene significance of the three modules, including **(C)** turquoise, **(D)** blue, and **(E)** purple modules, respectively. **(F, G)**. Enrichment plots depicted by gene set enrichment analysis based on **(F)** Gene Ontology and **(G)** Kyoto Encyclopedia of Genes and Genomes gene sets, respectively.

The landscape of genomic variations

We further depicted the landscape of genomic variations among the three heterogeneous clusters. As illustrated in Figure 6A, the mutation frequency of the top 20 FMGs was exhibited, and the overview of SNP, INDEL, and TMB was also displayed. To increase the understanding of somatic mutation, we compared the mutational differences of 20 FMGs among three clusters (Figure 6B). Strikingly, there were three universal FMGs exhibited in all molecular clusters, encompassing TP53, CTNNB1, and TTN, indicating that these FMGs might play a key role in tumorigenesis or tumor progression (Figure 6B). Among the three FMGs, the CTNNB1 and TTN mutations were pronounced in C1, while the TP53 mutation was dominant in

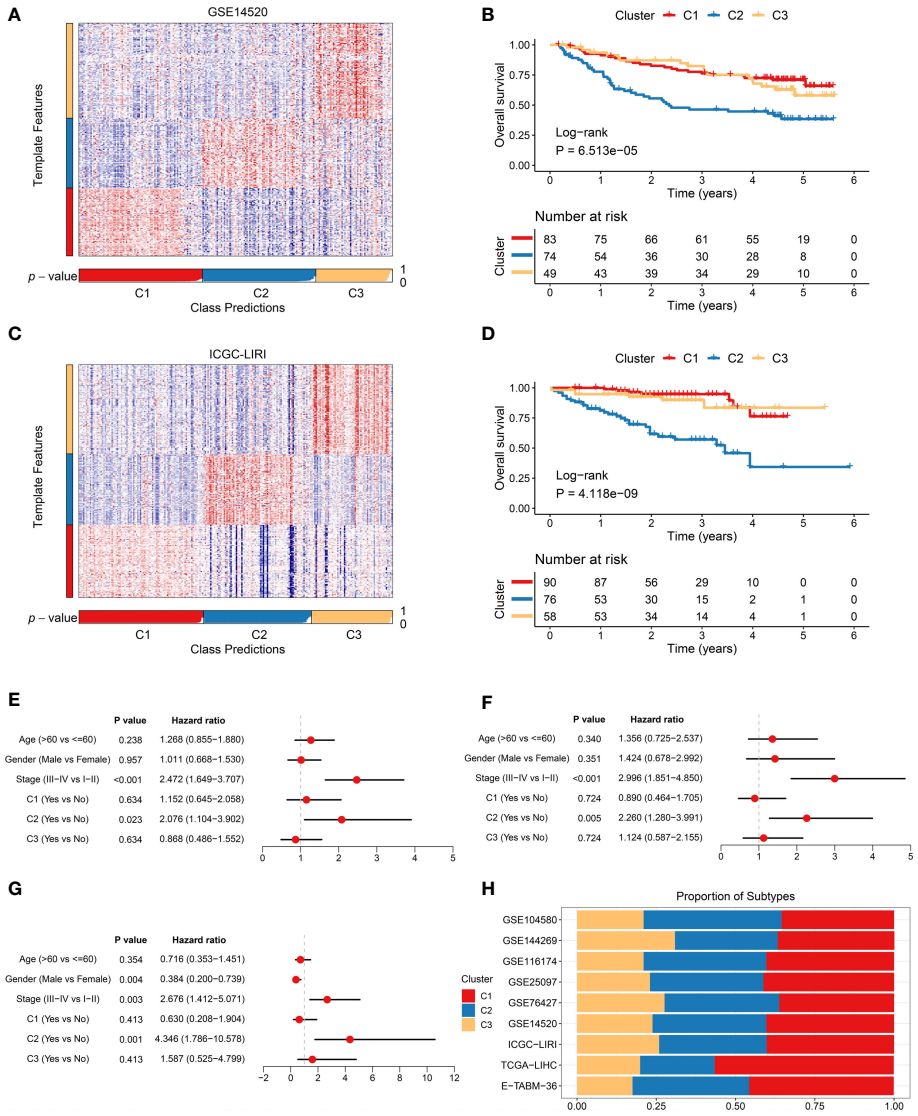

FIGURE 5
Validation and clinical features of three heterogeneous clusters. **(A)** Heat map of the expression level of the template feature between three clusters in the GSE14520 cohort. **(B)** Kaplan–Meier curves of overall survival (OS) according to three clusters in the GSE14520 cohort. **(C)** Heat map of the expression level of the template feature between three clusters in the ICGC-LIRI cohort. **(D)** Kaplan–Meier curves of OS according to three clusters in the ICGC-LIRI cohort. **(E–G)** Multivariate Cox regression of OS in **(E)** TCGA-LIHC, **(F)** GSE14520, and **(G)** ICGC-LIRI cohorts. **(H)** Proportions of three clusters among nine cohorts derived from distinct platforms.

C2. A previous study had elucidated that the gradual accumulation of gene mutations was prone to tumorigenesis (37). C3 possessed the lowest gene mutation relative to others, implying better clinical outcomes. We further explored the summary of CNV and depicted the top 10 frequent AMP and HOMDEL genes among the three clusters (Figure 6C). Interestingly, C2 was characterized by a higher CNV compared to the other clusters, and CSMD1 gene had the most conspicuous CNV loss (Figure 6C). In line with previous research, the loss of a putative tumor suppressor gene, CSMD1, might be the driven event in HCC progression (38, 39). Taken together, patients in C2 conveyed prominent genomic variations, indicating a highly genomic instability.

The assessment of immune infiltration and immunotherapy

The 50 Hallmark gene sets were broadly performed in cancer-related research (14). We further revealed the potential carcinogenic characteristics of the three clusters using GSVA algorithm. Consistent with the above-mentioned results, C1 was

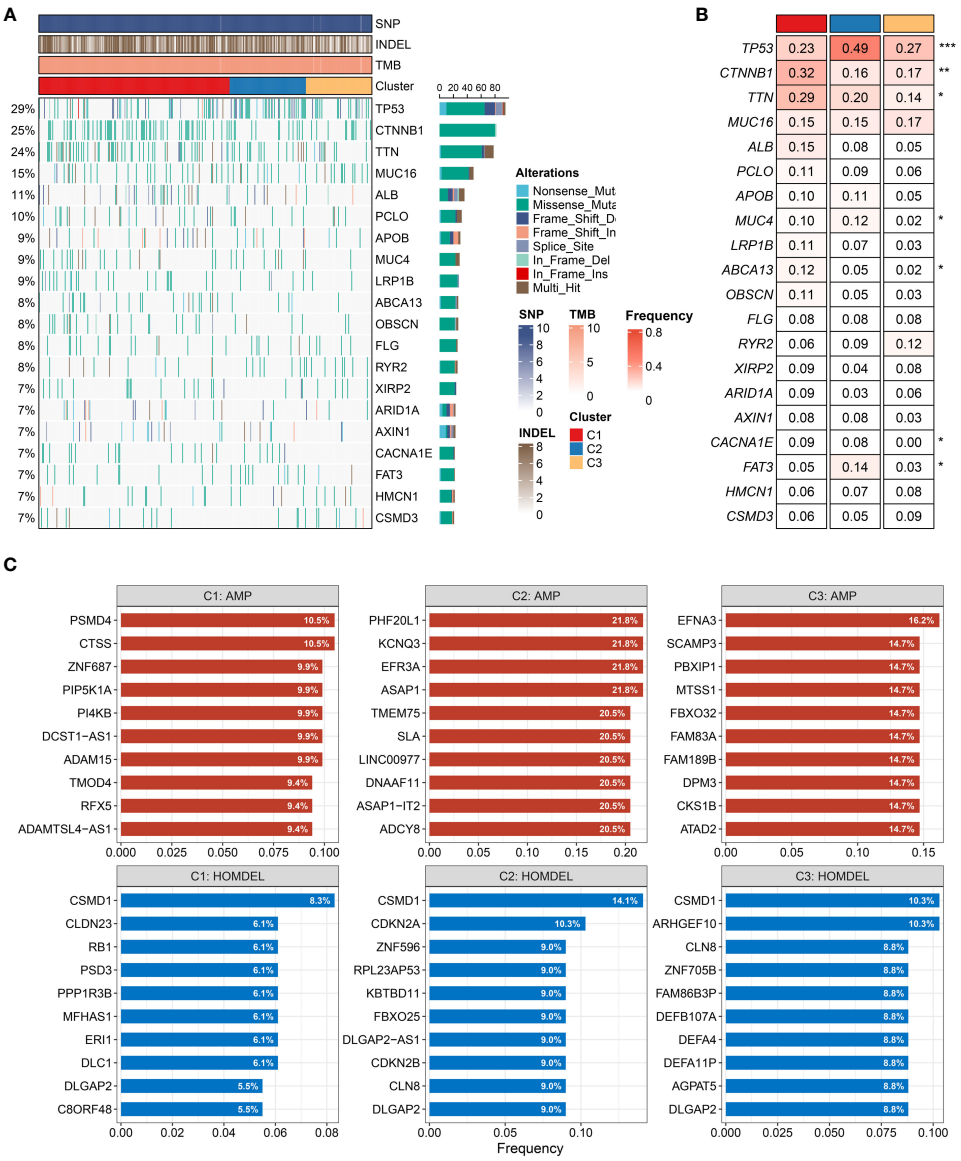

FIGURE 6
Characteristics of genomic variations among three clusters **(A, B)**. **(A)** The waterfall plot depicted the differences in frequently mutated genes (FMGs) of hepatocellular carcinoma among three clusters. The right panel shows the mutation rate, and genes were ordered by their mutation frequencies. **(B)** Mutation frequency of the top 20 FMGs among three clusters. **(C)** Amplified and homozygously deleted genes among the three clusters. *$P < 0.05$, **$P < 0.01$, ***$P < 0.001$, ****$P < 0.0001$.

characterized by lipid metabolic pathways, and C2 was mainly associated with cell proliferative pathways, while C3 was enriched in immune inflammatory pathways (Supplementary Figure S5A). These results indicated that patients in C3 might obtain better immunotherapeutic efficacy. Therefore, the landscape of immune cell infiltration and immune checkpoint expression was delineated to decipher the underlying mechanism. Compared to other clusters, C3 exhibited more infiltration abundance of immune cells (Figure 7A). Patients in C3 tended to be the "immune-hot" subtype, which stored massive immune cells in TME, including CD4+ T cell, CD8+ T cell, activated dendritic cell, nature killer cell, and so on ($P < 0.05$) (Supplementary Figure S6A). Among the three clusters, C3 also displayed the highest expression of immune checkpoints, such as CD274 (PD-L1), CTLA-4, and LAG3, which suggested that C3 might be more sensitive to immune checkpoint inhibitors (ICI) therapy (Figure 7B). Furthermore, the expression of HLA molecules was conspicuously higher in C3, which proved that patients in C3 possessed a strong power of antigen presentation (Figure 7C). Overall, precision immunotherapy might be applicable to patients in C3.

To yield deep insights on immunotherapy, the TIS and Submap methods were applied to assess the clinical efficacy among distinct clusters. As expected, C3 had the highest TIS score, hinting immune activation and elevated response to ICIs (P < 0.0001) (Figure 7D). Based on the Submap algorithm, patients in C3 had a superior similarity of expression patterns with patients responding to PD-L1 inhibitor (Bonferroni corrected P <0.01), indicating more benefits from anti-PD-L1 treatment (Figure 7E). Subsequently, the characteristic genes of C3 were extracted to serve as the measured score, named as cluster-associated immunotherapy score (CAIS). The patients were classified into high and low groups based on the constant ratio (3 *vs.* 7). Four immunotherapy cohorts contained 98 non-responders, and 41 responders were retrieved to evaluate the

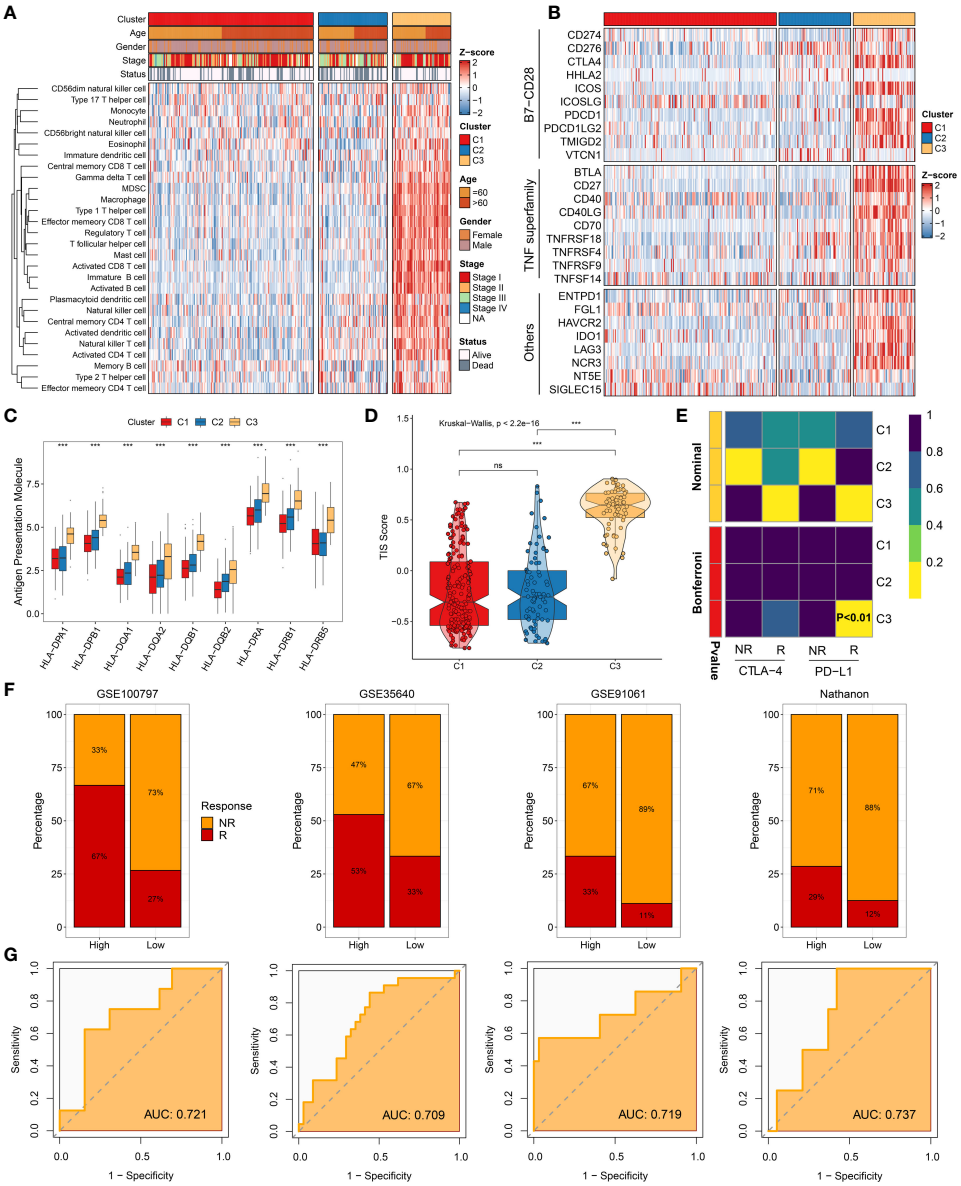

FIGURE 7
Immune landscape and immunotherapy responses. **(A)** Infiltration abundance of 28 immune cell subsets evaluated by single-sample gene set enrichment analysis algorithm. **(B)** Twenty-seven immune checkpoint profiles of three clusters. **(C)** Distribution of nine human leukocyte antigen molecular expressions among three clusters. **(D)** Distribution difference of T cell inflammatory signature prediction scores among three clusters. **(E)** Submap analysis manifesting that C3 could be more sensitive to anti-PD-1 therapy (Bonferroni, P < 0.01). **(F)** Immunotherapy response ratio of cluster-associated immunotherapy score (CAIS) in GSE100797, GSE35640, GSE91061, and Nathanon cohorts. **(G)** Receiver operating characteristic curves of CAIS to predict the benefits of immunotherapy in GSE100797, GSE35640, GSE91061, and Nathanon cohorts. ^{ns}P < 0.05, ***P < 0.001.

clinical applications of CAIS. Notably, patients in the high group exhibited a superior response to immunotherapy in all cohorts (Figure 7F). The area under the curve values of CAIS for predicting the accuracy of immunotherapeutic efficacy were 0.721, 0.709, 0.719, and 0.737 in GSE100797, GSE35640, GSE91061, and Nathanon cohorts, respectively (Figure 7G). Collectively, the above-mentioned data suggested that CAIS was a robust and promising immunotherapy indicator. Patients in C3 were recommended to be taken into consideration in using immunotherapy.

The evaluation of clinical treatment and identification of potential therapeutic drugs

Two other clinical treatment cohorts, GSE140580 and GSE109211, were collected to seek a high-potency treatment strategy and facilitate the clinical benefits for HCC patients. The TACE and sorafenib therapies were widely applied to clinical practice. As displayed in Supplementary Figure S5B, both C1 and C3 were characterized with early AJCC stage, which is predominantly associated with a superior prognosis. According to the updated clinical guideline, the TACE treatment was recommended for patients with primary stage (7). In line with that, our results also demonstrated that patients in C1 and C3 had a desirable efficacy for TACE treatment (Figure 8A). The therapy sensitivity of sorafenib was further estimated among the three clusters, and it was substantiated that patients in C2 could obtain more clinical benefits (Figure 8B). To identify latent therapeutic drugs, the *pRRophetic* package was used to evaluate the sensitivity of numerous agents, which was quantified by half-maximal inhibitory concentration (IC50). In the TCGA-LIHC cohort, patients in C2 also displayed superior response to nilotinib and bosutinib relative to other clusters (Figures 8C, D). Furthermore, patients in C1 might be more sensitive to axitinib for the lower IC50 value (Figure 8E). Obatoclax, docetaxel, and cisplatin were potential therapeutic agents for patients in C3 (Supplementary Figures S6B–D). These drugs might be developed into promising therapeutic agents for distinctly classified HCC patients. The CMap database contained a massive gene expression profile, which could assess the relationships among gene expression, phenotype, and drugs, and was further utilized to identify other potential compounds and shed light on the mode of action. We exhibited 20 compounds that possessed personalized therapeutic potential for three clusters (Figure 8F). The targeted pathways of these compounds were depicted, which could be used to develop numerous drugs (Figure 8G). According to patients in distinct clusters, applying individualized therapy patterns would produce curative clinical efficacy.

Discussion

As we have known, the HCC is characterized by high heterogeneity and inferior prognosis (2). Together with the updated guidelines and deep research, there are various treatment options for HCC patients (3, 7). Nevertheless, the standardized treatment displays heterogeneity even with patients in the same clinical stage, which is mainly owing to ignoring patients with distinct molecular characteristics (40). The heterogeneous clinical outcomes mean that it is necessary to explore genomic characteristics and develop a new molecular classification for HCC patients.

In this study, using the advantage of emerging technology at exploring tumor heterogeneity, we performed single-cell RNA-seq analysis to uncover the immune cell subpopulations and the dynamics of T cells. Previous studies had reported that TME is strongly correlated with tumor heterogeneity and modulates anti-tumor immune responses (14, 41). Among various cell distributions in TME, the T cells play a leading role in immune regulation and exert anti-tumor activity (42). The CD4+ T cells are recognized to portray an accessory role, and CD8+ T cells are defined as cytotoxic T lymphocytes killing tumor cells (43). Moreover, both of them are linked with prognosis and immunotherapy responses (42, 43). The distinct immune cells were depicted, and specific markers were identified based on a single-cell level. We also demonstrated that the immune inflammatory pathway was active among immune cell clusters. The T cells possessed a dynamic process, and CD8+ T cells were likely to be exhausted in the course of tumor progression. In our opinion, genes along the evolutive trajectory of CD8+ T cells were significant to prognosis and heterogeneous clinical efficacy, which are good bases to construct a molecular classification.

Subsequently, the NMF algorithm was utilized to identify heterogeneous molecular clusters, and the WGCNA algorithm was performed to detect characteristic genes. Based on multiple assessment indexes, three robust clusters were identified in the TCGA-LIHC cohort. Further prognostic implications were explored, and the results suggested that C2 presented adverse prognosis and could serve as an independent prognostic indicator. Among the three clusters, the overlap of characteristic genes and differentially upregulated genes was defined as signature genes, and then the NTP algorithm was employed. The results indicated that the three clusters with heterogeneous clinical outcomes were reproducible and robust in eight cohorts obtained from different platforms, encompassing GSE14520, ICGC-LIRI, E-TABM-36, GSE76427, GSE25097, GSE104580, GSE116174, and GSE144269.

Our study also delineated the underlying biological characteristics of the three clusters. Both GSEA and GSVA enrichment analyses elucidated that C1 was dominantly

10.3389/fimmu.2022.964190

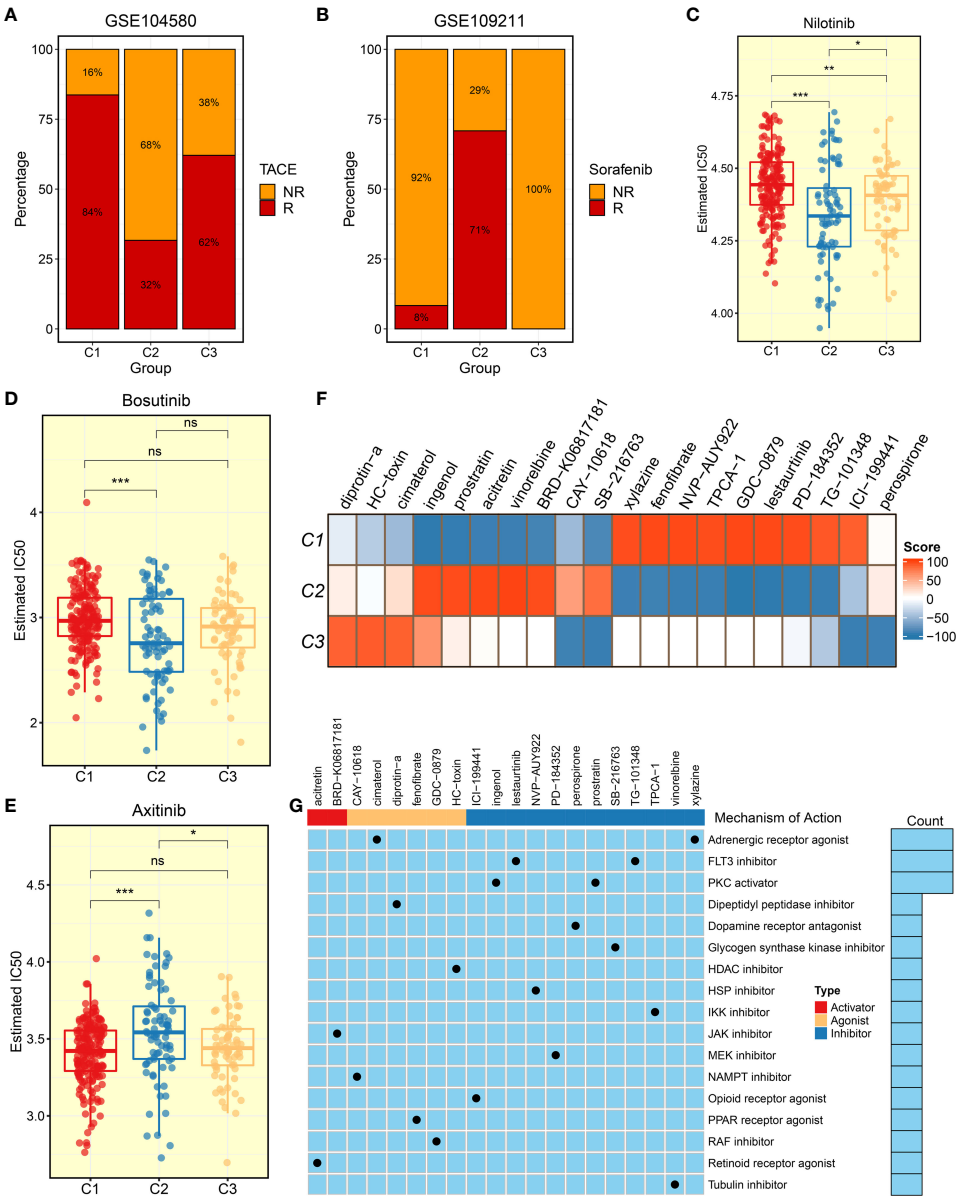

FIGURE 8
Evaluation of treatment efficacy and identification of potential therapeutic agents. **(A)** Treatment response ratio among three clusters of transcatheter arterial chemoembolization (TACE) in GSE104580. **(B)** Treatment response ratio among three clusters of sorafenib in GSE109211. **(C–E)** Distribution of IC50 value among three clusters of **(C)** nilotinib, **(D)** bosutinib, and **(E)** axitinib. **(F)** Heat map of enrichment score generated from potential therapeutic compounds. **(G)** Description of mode of action of compounds targeting corresponding molecular pathways. $^{ns}P < 0.05$, $^{*}P < 0.05$, $^{**}P < 0.01$, $^{***}P < 0.001$.

associated with lipid metabolic pathways, and C2 was significantly enriched in cell proliferative pathways, while C3 was mainly associated with immune inflammatory pathways. In addition, the three clusters displayed diverse genomic characteristics. Both somatic mutation and CNV emphasized that C2 had the most conspicuous genomic instability. Previous research had suggested that patients with TP53 mutation were more likely to encounter immune escape and have a dismal prognosis (44). Consistent with that, our study also proved that C2, with the highest TP53 mutation, presented an inferior prognosis. Patients with Wnt/CTNNB1 mutations are linked with resistance to immunotherapy (45). Correspondingly, C1 had a higher mutation frequency of CTNNB1, implying poor immunotherapy response. Due to the superior immune inflammatory activity, good clinical outcomes, and more stable genomic features, patients in C3 were more prone to exert anti-tumor activity and benefit from immunotherapy.

As is well known, distinct molecular characteristics could map into heterogeneous clinical outcomes and hint at individualized treatment recommendations. Seeking a personalized treatment strategy is essential to tailor a clinical management for HCC patients, thus improving their prognosis and therapeutic efficacy. Among the three clusters, therapeutic efficacy was assessed and compared for distinct clinical treatments. C3 was determined to have an "immune-hot" pattern with abundant immune cells and an elevated expression of immune checkpoints, such as CD4+ T cell, CD8+ T cell, activated dendritic cell, CD274 (PD-L1), CTLA-4, LAG3 molecular, *etc.* The dendritic cell initiates immune responses, and activated CD8 T cells have an anti-tumor effect, thus eliminating tumor cells (42, 46). Moreover, PD-L1 is correlated with immune escape and releases negative regulatory signaling (42). On one hand, the CTLA-4 binding to B7 inhibits T cell activation; on the other hand, CTLA-4 drives immunosuppressive Treg cell activation (47). C3 also indicated a strong ability of antigen presentation. Two prevalent approaches, TIS and Submap analysis, showed that C3 might obtain more benefits from immunotherapy. Overall, patients in C3 should be recommended to take more consideration for immunotherapy. Our study also suggested that patients in C1 were advised to TACE treatment, and patients in C2 were encouraged to apply sorafenib treatment.

As described above, C2 is characterized by elevated proliferative activities, pronounced genomic instability, high malignant phenotype, and poor prognosis; more considerations are needed to facilitate prognosis and therapeutic efficacy for patients. In clinical practice, some patients are sensitive to a specific drug therapy, while some patients are suffering from drug side effects (48). Previous studies suggested that the combination of anti-angiogenic therapy and immunotherapy has a huge potential to improve prognosis and facilitate clinical efficacy (49, 50). To deliver a precise treatment, the potential therapeutic drugs for C2 were identified by pRRophetic algorithm, such as nilotinib and bosutinib. Tyrosine kinases are promising therapeutic targets for HCC, and nilotinib, a TKI, could slow down HCC growth in mice by inhibiting ABL1 gene expression (51). A third-generation TKI, targeting Axl, restrains Slug expression and further decreases tumor invasiveness in HCC cell lines (52). These TKIs brought more effective treatment recommendations to C2 with elevated proliferative activities, thus improving the clinical outcomes. Moreover, patients with HCC display poor sensitivity to chemotherapy and bear the heavy burden of costs (53, 54). The development of novel potential therapeutic agents might bring more therapy application offer hopes to HCC patients. Based on Camp datasets, we depicted representative therapeutic compounds and the underlying mechanism of action, which laid a foundation for drug development.

Our study identified three heterogeneous clusters and proposed individualized treatment strategies. Although it is attractive to improve prognosis and facilitate clinical management, some limitations should be acknowledged. First, all the samples enrolled in this research were retrospective, and a prospective study should be applied to validate the results. Second, a multicenter and large-sample dataset, containing eligible patients with immunotherapy, needs to be further executed to assess the clinical efficacy. Third, the novel potential therapeutic agents should be further investigated and explored by clinical trial research.

In conclusion, we revealed the tumor heterogeneity and proposed three clusters in HCC. Various molecular characteristics were depicted among the three clusters, which had distinct clinical outcomes, biological features, genomic variations, immune landscape, and treatment responses. Patients in C1 were advised to TACE treatment, and patients in C2 were encouraged to TKI treatment, while patients in C3 were recommended to immunotherapy. Taken together, this work afforded a robust classification system and provided individualized treatment strategies, which contributed to improving the clinical outcomes and facilitating the clinical management.

Data availability statement

Public data used in this work can be acquired from The Cancer Genome Atlas portal (TCGA, https://portal.gdc.cancer.gov/), International Cancer Genome Consortium portal (ICGC, https://dcc.icgc.org/), ArrayExpress database (E-TABM-36, https://www.ebi.ac.uk/arrayexpress/experiments/E-TABM-36/) and Gene Expression Omnibus (GEO, http://www.ncbi.nlm.nih.gov/geo/). The 50 Hallmark gene sets could be obtained from Hallmark Molecular Signature Database (MSigDB, https://www.gsea-msigdb.org/gsea/msigdb/). The Connectivity Map analysis could be generated from CMap database (https://clue.io).

Author contributions

LL, ZL, and SZ designed this work. LL, ZL, JG, SW, and CG integrated and analyzed the data. LL, JG, XL, BH, ZW, and JZ wrote this manuscript. LL, JS, WG, and SZ edited and revised the manuscript. All authors contributed to the article and approved the submitted version.

Funding

This study was supported by the Youth Project of National Natural Science Foundation of China (82103282) and the Youth Project of Medical Science and Technology of Henan Province (SBGJ202103061).

Conflict of interest

The authors declare that the research was conducted in the absence of any commercial or financial relationships that could be construed as a potential conflict of interest.

Publisher's note

All claims expressed in this article are solely those of the authors and do not necessarily represent those of their affiliated organizations, or those of the publisher, the editors and the reviewers. Any product that may be evaluated in this article, or claim that may be made by its manufacturer, is not guaranteed or endorsed by the publisher.

Supplementary material

The Supplementary Material for this article can be found online at: https://www.frontiersin.org/articles/10.3389/fimmu.2022.964190/full#supplementary-material.

SUPPLEMENTARY FIGURE 1
Expression of marker genes of B cell populations.

SUPPLEMENTARY FIGURE 2
Identification of CD4+ T cells and CD8+ T cell subpopulations.

SUPPLEMENTARY FIGURE 3
Construction of co-expression modules by weighted gene co-expression network analysis.

SUPPLEMENTARY FIGURE 4
Validation of three heterogeneous clusters based on the nearest template prediction analysis in E-TABM-36, GSE76427, GSE25097, GSE104580, GSE116174, and GSE144269 cohorts.

SUPPLEMENTARY FIGURE 5
Underlying biological features and clinical stage characteristics.

SUPPLEMENTARY FIGURE 6
Landscape of immune cell infiltration and assessment of drug sensitivity.

References

1. Sung H, Ferlay J, Siegel RL, Laversanne M, Soerjomataram I, Jemal A, et al. Global cancer statistics 2020: GLOBOCAN estimates of incidence and mortality worldwide for 36 cancers in 185 countries. *CA Cancer J Clin* (2021) 71(3):209–49. doi: 10.3322/caac.21660

2. Craig AJ, von Felden J, Garcia-Lezana T, Sarcognato S, Villanueva A. Tumour evolution in hepatocellular carcinoma. *Nat Rev Gastroenterol Hepatol* (2020) 17 (3):139–52. doi: 10.1038/s41575-019-0229-4

3. Llovet JM, Kelley RK, Villanueva A, Singal AG, Pikarsky E, Roayaie S, et al. Hepatocellular carcinoma. *Nat Rev Dis Primers*. (2021) 7(1):6. doi: 10.1038/s41572-020-00240-3

4. Zheng R, Qu C, Zhang S, Zeng H, Sun K, Gu X, et al. Liver cancer incidence and mortality in China: Temporal trends and projections to 2030. *Chin J Cancer Res* (2018) 30(6):571–9. doi: 10.21147/j.issn.1000-9604.2018.06.01

5. Beaufrere A, Caruso S, Calderaro J, Pote N, Bijot JC, Couchy G, et al. Gene expression signature as a surrogate marker of microvascular invasion on routine hepatocellular carcinoma biopsies. *J Hepatol* (2022) 76(2):343–52. doi: 10.1016/j.jhep.2021.09.034

6. Zhang EL, Cheng Q, Huang ZY, Dong W. Revisiting surgical strategies for hepatocellular carcinoma with microvascular invasion. *Front Oncol* (2021) 11:691354. doi: 10.3389/fonc.2021.691354

7. Reig M, Forner A, Rimola J, Ferrer-Fabrega J, Burrel M, Garcia-Criado A, et al. BCLC strategy for prognosis prediction and treatment recommendation Barcelona clinic liver cancer (BCLC) staging system. the 2022 update. *J Hepatol* (2021). doi: 10.1016/j.jhep.2021.11.018

8. Rebouissou S, Nault JC. Advances in molecular classification and precision oncology in hepatocellular carcinoma. *J Hepatol* (2020) 72(2):215–29. doi: 10.1016/j.jhep.2019.08.017

9. Shaw R, Tian X, Xu J. Single-cell transcriptome analysis in plants: Advances and challenges. *Mol Plant* (2021) 14(1):115–26. doi: 10.1016/j.molp.2020.10.012

10. Wang Y, Mashock M, Tong Z, Mu X, Chen H, Zhou X, et al. Changing technologies of RNA sequencing and their applications in clinical oncology. *Front Oncol* (2020) 10:447. doi: 10.3389/fonc.2020.00447

11. Hu J, Chen Z, Bao L, Zhou L, Hou Y, Liu L, et al. Single-cell transcriptome analysis reveals intratumoral heterogeneity in ccRCC, which results in different clinical outcomes. *Mol Ther* (2020) 28(7):1658–72. doi: 10.1016/j.ymthe.2020.04.023

12. Davis-Marcisak EF, Sherman TD, Orugunta P, Stein-O'Brien GL, Puram SV, Roussos Torres ET, et al. Differential variation analysis enables detection of tumor heterogeneity using single-cell RNA-sequencing data. *Cancer Res* (2019) 79 (19):5102–12. doi: 10.1158/0008-5472.CAN-18-3882

13. Liu Z, Liu L, Lu T, Wang L, Li Z, Jiao D, et al. Hypoxia molecular characterization in hepatocellular carcinoma identifies one risk signature and two nomograms for clinical management. *J Oncol* (2021) 2021:6664386. doi: 10.1155/2021/6664386

14. Liu Z, Zhang Y, Shi C, Zhou X, Xu K, Jiao D, et al. A novel immune classification reveals distinct immune escape mechanism and genomic alterations: implications for immunotherapy in hepatocellular carcinoma. *J Transl Med* (2021) 19(1):5. doi: 10.1186/s12967-020-02697-y

15. Shi JY, Wang X, Ding GY, Dong Z, Han J, Guan Z, et al. Exploring prognostic indicators in the pathological images of hepatocellular carcinoma based on deep learning. *Gut* (2021) 70(5):951–61. doi: 10.1136/gutjnl-2020-320930

16. Thorsson V, Gibbs DL, Brown SD, Wolf D, Bortone DS, Ou Yang TH, et al. The immune landscape of cancer. *Immunity* (2018) 48(4):812–830.e814. doi: 10.1016/j.immuni.2018.03.023

17. Fang H, Guo Z, Chen J, Lin L, Hu Y, Li Y, et al. Combination of epigenetic regulation with gene therapy-mediated immune checkpoint blockade induces anti-tumour effects and immune response *in vivo*. *Nat Commun* (2021) 12(1):6742. doi: 10.1038/s41467-021-27078-x

18. Ruiz de Galarreta M, Bresnahan E, Molina-Sanchez P, Lindblad KE, Maier B, Sia D, et al. Beta-catenin activation promotes immune escape and resistance to anti-PD-1 therapy in hepatocellular carcinoma. *Cancer Discovery* (2019) 9 (8):1124–41. doi: 10.1158/2159-8290.CD-19-0074

19. Butler A, Hoffman P, Smibert P, Papalexi E, Satija R. Integrating single-cell transcriptomic data across different conditions, technologies, and species. *Nat Biotechnol* (2018) 36(5):411–20. doi: 10.1038/nbt.4096

20. Qiu X, Mao Q, Tang Y, Wang L, Chawla R, Pliner HA, et al. Reversed graph embedding resolves complex single-cell trajectories. *Nat Methods* (2017) 14 (10):979–82. doi: 10.1038/nmeth.4402

21. Brunet JP, Tamayo P, Golub TR, Mesirov JP. Metagenes and molecular pattern discovery using matrix factorization. *Proc Natl Acad Sci U S A*. (2004) 101 (12):4164–9. doi: 10.1073/pnas.0308531101

22. Lovmar L, Ahlford A, Jonsson M, Syvanen AC. Silhouette scores for assessment of SNP genotype clusters. *BMC Genomics* (2005) 6:35. doi: 10.1186/1471-2164-6-35

23. Langfelder P, Horvath S. WGCNA: an r package for weighted correlation network analysis. *BMC Bioinf* (2008) 9:559. doi: 10.1186/1471-2105-9-559

24. Hoshida Y. Nearest template prediction: a single-sample-based flexible class prediction with confidence assessment. *PloS One* (2010) 5(11):e15543. doi: 10.1371/journal.pone.0015543

25. Mayakonda A, Lin DC, Assenov Y, Plass C, Koeffler HP. Maftools: efficient and comprehensive analysis of somatic variants in cancer. *Genome Res* (2018) 28 (11):1747–56. doi: 10.1101/gr.239244.118

26. Liu Z, Wang L, Guo C, Liu L, Jiao D, Sun Z, et al. TTN/OBSCN 'Double-hit' predicts favourable prognosis, 'immune-hot' subtype and potentially better immunotherapeutic efficacy in colorectal cancer. *J Cell Mol Med* (2021) 25 (7):3239–51. doi: 10.1111/jcmm.16393

27. Charoentong P, Finotello F, Angelova M, Mayer C, Efremova M, Rieder D, et al. Pan-cancer immunogenomic analyses reveal genotype-immunophenotype relationships and predictors of response to checkpoint blockade. *Cell Rep* (2017) 18 (1):248–62. doi: 10.1016/j.celrep.2016.12.019

28. Ayers M, Lunceford J, Nebozhyn M, Murphy E, Loboda A, Kaufman DR, et al. IFN-gamma-related mRNA profile predicts clinical response to PD-1 blockade. *J Clin Invest.* (2017) 127(8):2930–40. doi: 10.1172/JCI91190

29. Hoshida Y, Brunet JP, Tamayo P, Golub TR, Mesirov JP. Subclass mapping: identifying common subtypes in independent disease data sets. *PloS One* (2007) 2 (11):e1195. doi: 10.1371/journal.pone.0001195

30. Geeleher P, Cox N, Huang RS. pRRophetic: an r package for prediction of clinical chemotherapeutic response from tumor gene expression levels. *PloS One* (2014) 9(9):e107468. doi: 10.1371/journal.pone.0107468

31. Malta TM, Sokolov A, Gentles AJ, Burzykowski T, Poisson L, Weinstein JN, et al. Machine learning identifies stemness features associated with oncogenic dedifferentiation. *Cell* (2018) 173(2):338–354.e315. doi: 10.1016/j.cell.2018.03.034

32. Huang S, Yang J, Fong S, Zhao Q. Artificial intelligence in cancer diagnosis and prognosis: Opportunities and challenges. *Cancer Lett* (2020) 471:61–71. doi: 10.1016/j.canlet.2019.12.007

33. Joyce JA, Fearon DT. T Cell exclusion, immune privilege, and the tumor microenvironment. *Science* (2015) 348(6230):74–80. doi: 10.1126/science.aaa6204

34. Isella C, Brundu F, Bellomo SE, Galimi F, Zanella E, Porporato R, et al. Selective analysis of cancer-cell intrinsic transcriptional traits defines novel clinically relevant subtypes of colorectal cancer. *Nat Commun* (2017) 8:15107. doi: 10.1038/ncomms15107

35. Li X, Ramadori P, Pfister D, Seehawer M, Zender L, Heikenwalder M. The immunological and metabolic landscape in primary and metastatic liver cancer. *Nat Rev Cancer.* (2021) 21(9):541–57. doi: 10.1038/s41568-021-00383-9

36. Wu X, Jiang D, Liu H, Lu X, Lv D, Liang L. CD8(+) T cell-based molecular classification with heterogeneous immunogenomic landscapes and clinical significance of clear cell renal cell carcinoma. *Front Immunol* (2021) 12:745945. doi: 10.3389/fimmu.2021.745945

37. Saito Y, Koya J, Araki M, Kogure Y, Shingaki S, Tabata M, et al. Landscape and function of multiple mutations within individual oncogenes. *Nature* (2020) 582(7810):95–9. doi: 10.1038/s41586-020-2175-2

38. Midorikawa Y, Yamamoto S, Tsuji S, Kamimura N, Ishikawa S, Igarashi H, et al. Allelic imbalances and homozygous deletion on 8p23.2 for stepwise progression of hepatocarcinogenesis. *Hepatology* (2009) 49(2):513–22. doi: 10.1002/hep.22698

39. Zhu Q, Gong L, Wang J, Tu Q, Yao L, Zhang JR, et al. miR-10b exerts oncogenic activity in human hepatocellular carcinoma cells by targeting expression of CUB and sushi multiple domains 1 (CSMD1). *BMC Cancer.* (2016) 16(1):806. doi: 10.1186/s12885-016-2801-4

40. Llovet JM, De Baere T, Kulik L, Haber PK, Greten TF, Meyer T, et al. Locoregional therapies in the era of molecular and immune treatments for hepatocellular carcinoma. *Nat Rev Gastroenterol Hepatol* (2021) 18(5):293–313. doi: 10.1038/s41575-020-00395-0

41. Fu Y, Liu S, Zeng S, Shen H. From bench to bed: the tumor immune microenvironment and current immunotherapeutic strategies for hepatocellular carcinoma. *J Exp Clin Cancer Res* (2019) 38(1):396. doi: 10.1186/s13046-019-1396-4

42. Mariathasan S, Turley SJ, Nickles D, Castiglioni A, Yuen K, Wang Y, et al. TGFbeta attenuates tumour response to PD-L1 blockade by contributing to exclusion of T cells. *Nature* (2018) 554(7693):544–8. doi: 10.1038/nature25501

43. Kumar BV, Connors TJ, Farber DL. Human T cell development, localization, and function throughout life. *Immunity* (2018) 48(2):202–13. doi: 10.1016/j.immuni.2018.01.007

44. Long J, Wang A, Bai Y, Lin J, Yang X, Wang D, et al. Development and validation of a TP53-associated immune prognostic model for hepatocellularxcarcinoma. *EBioMedicine* (2019) 42:363–74. doi: 10.1016/j.ebiom.2019.03.022

45. Pinyol R, Sia D, Llovet JM. Immune exclusion-Wnt/CTNNB1 class predicts resistance to immunotherapies in HCC. *Clin Cancer Res* (2019) 25(7):2021–3. doi: 10.1158/1078-0432.CCR-18-3778

46. Lee YS, Radford KJ. The role of dendritic cells in cancer. *Int Rev Cell Mol Biol* (2019) 348:123–78. doi: 10.1016/bs.ircmb.2019.07.006

47. Lingel H, Brunner-Weinzierl MC. CTLA-4 (CD152): A versatile receptor for immune-based therapy. *Semin Immunol* (2019) 42:101298. doi: 10.1016/j.smim.2019.101298

48. Rimassa L, Danesi R, Pressiani T, Merle P. Management of adverse events associated with tyrosine kinase inhibitors: Improving outcomes for patients with hepatocellular carcinoma. *Cancer Treat Rev* (2019) 77:20–8. doi: 10.1016/j.ctrv.2019.05.004

49. Solimando AG, Susca N, Argentiero A, Brunetti O, Leone P, De Re V, et al. Second-line treatments for advanced hepatocellular carcinoma: A systematic review and Bayesian network meta-analysis. *Clin Exp Med* (2022) 22(1):65–74. doi: 10.1007/s10238-021-00727-7

50. Esteban-Fabro R, Willoughby CE, Pique-Gili M, Montironi C, Abril-Fornaguera J, Peix J, et al. Cabozantinib enhances anti-PD1 activity and elicits a neutrophil-based immune response in hepatocellular carcinoma. *Clin Cancer Res* (2022) 28(11):2449–60. doi: 10.1158/1078-0432.CCR-21-2517

51. Wang F, Hou W, Chitsike L, Xu Y, Bettler C, Perera A, et al. ABL1, overexpressed in hepatocellular carcinomas, regulates expression of NOTCH1 and promotes development of liver tumors in mice. *Gastroenterology* (2020) 159 (1):289–305.e216. doi: 10.1053/j.gastro.2020.03.013

52. Lee HJ, Jeng YM, Chen YL, Chung L, Yuan RH. Gas6/Axl pathway promotes tumor invasion through the transcriptional activation of slug in hepatocellular carcinoma. *Carcinogenesis* (2014) 35(4):769–75. doi: 10.1093/carcin/bgt372

53. Kim DW, Talati C, Kim R. Hepatocellular carcinoma (HCC): beyond sorafenib-chemotherapy. *J Gastrointest Oncol* (2017) 8(2):256–65. doi: 10.21037/jgo.2016.09.07

54. Llovet JM, Montal R, Sia D, Finn RS. Molecular therapies and precision medicine for hepatocellular carcinoma. *Nat Rev Clin Oncol* (2018) 15(10):599–616. doi: 10.1038/s41571-018-0073-4

frontiers | Frontiers in Immunology

TYPE Original Research
PUBLISHED 15 August 2022
DOI 10.3389/fimmu.2022.933973

Check for updates

OPEN ACCESS

EDITED BY
Jian Zhang,
Southern Medical University, China

REVIEWED BY
Fangfang Duan,
Sun Yat-sen University, China
Ruonan Shao,
Sun Yat-sen University Cancer Center, China
Tong Lu,
The Second Affiliated Hospital of Harbin Medical University, China
Hao Zhang,
Xiangya Hospital Central South University, China
Dingkang Xu,
Chinese Academy of Medical Sciences and Peking Union Medical College, China
Zaixiang Tang,
Soochow University Medical College, China
Rensheng Wan,
Hannover Medical School, Germany

*CORRESPONDENCE
Yang-peng Sun
sunyp6@mail.sysu.edu.cn
Yong-chun Li
liyongch@sysucc.org.cn
Wen-ting Liao
liaowt9@mail.sysu.edu.cn

†These authors have contributed equally to this work and share the first authorship

SPECIALTY SECTION
This article was submitted to Cancer Immunity and Immunotherapy, a section of the journal Frontiers in Immunology

RECEIVED 01 May 2022
ACCEPTED 22 July 2022
PUBLISHED 15 August 2022

CITATION
Bao J, Lu W, Duan H, Ye Y, Li J, Liao W, Li Y and Sun Y (2022) Identification of a novel cuproptosis-related gene signature and integrative analyses in patients with lower-grade gliomas. *Front. Immunol.* 13:933973. doi: 10.3389/fimmu.2022.933973

Identification of a novel cuproptosis-related gene signature and integrative analyses in patients with lower-grade gliomas

Jia-hao Bao[1†], Wei-cheng Lu[2†], Hao Duan[3†], Ya-qi Ye[2], Jiang-bo Li[1], Wen-ting Liao[1*], Yong-chun Li[2*] and Yang-peng Sun[1*]

[1]Hospital of Stomatology, Guanghua School of Stomatology, Sun Yat-sen University, Guangdong Provincial Key Laboratory of Stomatology, Guangzhou, China, [2]State Key Laboratory of Oncology in Southern China, Department of Anesthesiology, Sun Yat-sen University Cancer Center, Collaborative Innovation for Cancer Medicine, Guangzhou, China, [3]Department of Neurosurgery/ Neuro-oncology, Sun Yat-sen University Cancer Center, State Key Laboratory of Oncology in South China, Collaborative Innovation Center for Cancer Medicine, Guangzhou, China

Background: Cuproptosis is a newly discovered unique non-apoptotic programmed cell death distinguished from known death mechanisms like ferroptosis, pyroptosis, and necroptosis. However, the prognostic value of cuproptosis and the correlation between cuproptosis and the tumor microenvironment (TME) in lower-grade gliomas (LGGs) remain unknown.

Methods: In this study, we systematically investigated the genetic and transcriptional variation, prognostic value, and expression patterns of cuproptosis-related genes (CRGs). The CRG score was applied to quantify the cuproptosis subtypes. We then evaluated their values in the TME, prognostic prediction, and therapeutic responses in LGG. Lastly, we collected five paired LGG and matched normal adjacent tissue samples from Sun Yat-sen University Cancer Center (SYSUCC) to verify the expression of signature genes by quantitative real-time PCR (qRT-PCR) and Western blotting (WB).

Results: Two distinct cuproptosis-related clusters were identified using consensus unsupervised clustering analysis. The correlation between multilayer CRG alterations with clinical characteristics, prognosis, and TME cell infiltration were observed. Then, a well-performed cuproptosis-related risk model (CRG score) was developed to predict LGG patients' prognosis, which was evaluated and validated in two external cohorts. We classified patients into high- and low-risk groups according to the CRG score and found that patients in the low-risk group showed significantly higher survival possibilities than those in the high-risk group (P<0.001). A high CRG score implies higher TME scores, more significant TME cell infiltration, and increased mutation burden. Meanwhile, the CRG score was significantly correlated with the cancer stem cell index, chemoradiotherapy sensitivity–related genes and immune

checkpoint genes, and chemotherapeutic sensitivity, indicating the association with CRGs and treatment responses. Univariate and multivariate Cox regression analyses revealed that the CRG score was an independent prognostic predictor for LGG patients. Subsequently, a highly accurate predictive model was established for facilitating the clinical application of the CRG score, showing good predictive ability and calibration. Additionally, crucial CRGs were further validated by qRT-PCR and WB.

Conclusion: Collectively, we demonstrated a comprehensive overview of CRG profiles in LGG and established a novel risk model for LGG patients' therapy status and prognosis. Our findings highlight the potential clinical implications of CRGs, suggesting that cuproptosis may be the potential therapeutic target for patients with LGG.

KEYWORDS

cuproptosis, lower-grade gliomas, molecular subtypes, tumor microenvironment, immune checkpoint inhibitors, chemoradiotherapy

Introduction

Lower-grade gliomas (LGGs; addressed as WHO grades II and III here), consisting of diffuse low-grade gliomas and intermediate-grade gliomas, are usually slow-growing, infiltrative, and intermittently progressive, which accounts for approximately 22% of all brain tumors in adults (1). Most LGGs can be further divided according to their clinical histopathologic features and classic molecular markers, including isocitrate dehydrogenase (*IDH*) mutation and the 1p/19q codeletion status (2). With tremendous progress that has been made in therapy like surgical resection and chemotherapy, LGGs often have better prognoses, while high-grade gliomas (HGG) have worse prognoses due to their malignant aggressivity (3). However, although 5-year overall survival (OS) for patients with LGG is 85%, progression-free survival (PFS) for those with unresectable/residual disease requiring treatment is approximately 40%, making the prognosis grim (4). Meanwhile, it was indicated that progression of LGGs occurs in almost 70% of patients within 10 years, thus worsening the prognosis (5). Hence, there is an urgent need to characterize specific and practical molecular signatures for the accurate diagnosis, individualized treatment, and assessment of the prognosis of LGG.

Cuproptosis, first proposed by Todd R. Golub's lab in 2022, is a unique non-apoptotic programmed cell death distinguished from known death mechanisms like ferroptosis, pyroptosis, and necroptosis (6). It is copper-triggered and mediated by protein lipoylation mainly in mitochondria. Mechanistically, cuproptosis occurs through the direct binding of copper to the lipoylated components of the tricarboxylic acid (TCA) cycle. When respiring, the lipoylated TCA enzymes [particularly the pyruvate dehydrogenase (PDH) complex] increase and result in an abnormal aggregation of lipoacylated proteins and the loss of Fe-S cluster–containing proteins, which leads to inevitably acute proteotoxic stress and ultimately cell death (6). The research provided a further in-depth look at the role of copper and mitochondria homeostasis, demonstrating a potentially critical role of cuproptosis in cell biology (7).

Numerous recent studies have consistently illuminated the functions of copper homeostasis and mitochondria in many diseases, including heart failure, neurodegenerative diseases, metabolic diseases, and genetic disorders (8). Copper serves as a catalytic and structural cofactor for enzymes that regulate mitochondrial respiration, antioxidant defense, redox signaling, kinase signaling, autophagy, and other processes (9–11). It can also function as a signal to enable responses to the enhanced host defenses resulting from immune activation (12). It has been an excellent candidate for cancer treatment since the 1960s. Emerging studies have shown that an elevated level of copper is directly associated with cancer progression. Brady et al. demonstrated that copper is critical in driving lung adenocarcinoma *via* regulating the autophagic kinases *ULK1/2* (13). Mittal and his colleagues found that the depletion of mitochondrial copper significantly suppresses triple-negative breast cancer in mice (14). The inhibition of copper trafficking can attenuate cancer cell proliferation (15). Meanwhile, mitochondria are critical in various cellular functions such as cellular energy metabolism, ion homeostasis regulation, redox signaling, and cell death, and its dysfunction has already been known in glioma initiation, progression, and drug resistance (16–18). Different levels

of mitochondrial aberrations might contribute to disparities in the aggressiveness of patients with glioma. Yang et al. demonstrated that mitochondrial *PKM2* plays a vital role in the ROS adaptation of cancer cells, which implicates the *HSP90-PKM2-Bcl2* axis as a potential target for therapeutic intervention in gliomas (19). The suppression of mitochondrial ROS can also drive the glioma therapeutic resistance due to the dysregulation of glioma stem-like cells (20), while the activation of the mitochondrial-dependent apoptotic pathway potentiates temozolomide sensitivity and thus improves patients' outcomes (21). These discoveries shed light on the tumor copper and mitochondria homeostasis related to cuproptotic plasticity and possibly explain whether and how cuproptosis is associated with the persistence, differentiation, and expansion of cancer cells. It is a conceivable complex interplay that cuproptosis would be a new molecular signature and target for future investigations. The regulations of the cancer cells' susceptibilities to cuproptosis should be a fruitful area in cancer research. However, to our best knowledge, it remains to be elucidated whether cuproptosis plays a critical role in LGG, and the relationships with survival in LGG patients have never been explored.

In this study, we aim to investigate the whole aspects of cuproptosis-related genes (CRGs) and their values in the prognosis, tumor microenvironment (TME) infiltration, and responses to treatments in LGG through integrative bioinformatics analyses. The results were further verified in clinical specimens from Sun Yat-sen University Cancer Center (SYSUCC) through quantitative real-time PCR (qRT-PCR) and Western blotting (WB).

Materials and methods

Data acquisition

The gene expression data and corresponding clinical information of LGG samples were obtained from The Cancer Genome Atlas (TCGA) (https://portal.gdc.cancer.gov/) and Chinese Glioma Genome Atlas (CGGA) (http://cgga.org.cn/) databases. A total of 529 samples with a gene expression profile, copy number variation (CNV), single-nucleotide variant (SNV), and relevant clinicopathological data were downloaded from TCGA-LGG. The fragments per kilobase million values of TCGA-LGG were transformed into transcripts per kilobase million. For all the included RNA-seq data, normalization and log2 transformation were performed. The loss and gain levels of copy-number changes have been identified using segmentation analysis and the GISTIC algorithm. The SNV data were further analyzed by R package "maftools" and visualized by R package "oncoplot". We further downloaded the TPM- normalized GTEx RNAseq data of 1,152 normal human brain samples from the GTEx data portal (https://xenabrowser.net/datapages/). Two CGGA cohorts that contained 182 and 174 LGG samples (CGGA1, mRNAseq_325, RNA-seq; CGGA2, mRNA-array_301, Microarray) were obtained as external validation cohorts.

Unsupervised clustering for cuproptosis-related genes

A total of 13 CRGs were extracted from the previous study (6), and the details of genes were shown in Supplementary Table 1. Based on the expression levels of CRGs, we performed consensus unsupervised clustering analysis to classify patients into distinct cuproptosis-related clusters (CRG clusters) using the R package "ConsensusClusterPlus" (22), with the parameters of reps = 1000 and pItem = 0.8. Principal component analysis was conducted to show the classification of CRG clusters. Then, we compared the OS probability of CRG clusters using the R package "survival" and "jskm". A landmark time of 9 years was chosen. Chemoradiotherapy sensitivity–related genes (CRSGs) and immune checkpoint genes (ICGs) were further retrieved (23–28), and their expression levels between CRG clusters were analyzed.

Estimation of tumor microenvironment cell infiltration between cuproptosis-related gene clusters

R package "ESTIMATE" can calculate TME scores including the stromal score, immune score, and estimate score using gene expression profiles (29). TME scores for LGG patients were evaluated and compared between CRG clusters. A single sample gene-set enrichment analysis (ssGSEA) algorithm was used to quantify the immune infiltration degree of immune cells in the LGG TME.

Gene set variation analysis and gene set enrichment analysis

To investigate the difference of the biological function between CRG clusters, gene set variation analysis (GSVA) was performed with "c2.cp.kegg.v7.5.symbols" and "c5.go.bp.v7.5.symbols" using R package "GSVA". R package "pheatmap" was applied to visualize the results. GSEA was performed by R package "clusterProfiler" to determine whether the prior-defined functional sets of genes differ significantly between CRG clusters with the hallmark gene set ("h.all.v7.2.symbols") from the MSigDB database.

Identification of differentially expressed genes between cuproptosis-related gene clusters and functional annotation

The differentially expressed genes (DEGs) between different CRG clusters were identified using R package "Limma". The

significance criteria for identifying DEGs was set as |log2 (FoldChange)| > 0.5 and adjusted *P*-value< 0.05. To explore the biological functions of CRG cluster-related DEGs, Gene Ontology (GO) and Kyoto Encyclopedia of Genes and Genomes (KEGG) enrichment analyses were conducted by applying the "clusterProfiler" package (30).

Identification of cuproptosis gene clusters in lower-grade glioma

We performed univariate Cox regression analysis for CRG cluster–related DEGs to identify DEGs that were related to OS (OS-related DEGs). According to the expression levels of OS-related DEGs, we performed consensus unsupervised clustering analysis using R package "ConsensusClusterPlus", with the parameters of reps = 1000 and pItem = 0.8. The TCGA-LGG patients were divided into distinct cuproptosis gene clusters, and the OS time was compared through Kaplan–Meier analysis.

Construction of the cuproptosis-related prognostic model

Then, patients in the TCGA-LGG cohort were randomly divided into the training cohort and internal testing cohort at a ratio of 1:1 using R package "caret". Based on OS-related DEGs, the least absolute shrinkage and selection operator (LASSO) Cox regression were performed to reduce the dimension of high-latitude data using R package "glmnet". Ten-fold cross-validation was employed to avoid the overfitting problem and select the penalty parameter (λ) according to the minimum criteria. We conducted a multivariate Cox regression analysis to determine genes from candidate genes and further performed GSEA analyses based on a single gene expression, respectively. Next, we construct the cuproptosis-related predictive model in the training cohort. We calculated the CRG score for each sample using the following formula: $CRG_score = \sum_{i=1}^{n} Coef_i \times Exp_i$, with Coef indicating the coefficient and Exp referring to the expression level of each CRG.

Evaluation and validation of the cuproptosis-related prognostic model

The prognostic scoring system for LGG patients was established, and the median value of the predicted CRG scores was regarded as the cut-off. Then, patients were divided into high-risk (CRG score > median value) and low-risk (CRG score< median value) groups accordingly. R package "survival" and "survminer" was applied to compare the survival probability between the two groups *via* Kaplan–Meier analysis. The R package "timeROC" was employed to perform 1-, 3- and 5- year receiver operating characteristic (ROC) analysis and calculate the value of the area under the curve (AUC). The calibration plots were further conducted to better validate the advantage of the CRG_score. The expression levels of CRGs were analyzed between different CRG score groups. The internal testing cohort and two external cohorts CGGA1 and CGGA2 were employed to verify the cuproptosis-related prognostic model. The CRG score was calculated for LGG patients in each cohort, and samples were divided into different risk groups. Similarly, they were subjected to Kaplan–Meier analysis, ROC analysis, and calibration analysis. In CGGA1 and CGGA2 cohorts, patients were also stratified into four risk-treatment subgroups by the CRG score and treatment with temozolomide (TMZ) or radiotherapy. In addition, survival analyses among risk-treatment subgroups were conducted.

Correlations of cuproptosis-related gene score with immune infiltrates and cancer stem cell index in lower-grade glioma

In order to identify the gene sets of statistical differences between high- and low-risk groups, GSEA was performed. The annotated gene sets "h.all.v7.2.symbols" and "c5.bp.v7.2.symbols" from the MSigDB database were adopted in our analysis. The enrichments of gene sets with an adjusted *P*-value<0.05 were regarded to be significant. We employed R package "ESTIMATE" to evaluate the TME score levels between high- and low-risk groups. Cell-type Identification by Estimating Relative Subsets of RNA Transcripts (CIBERSORT) is a developed algorithm that uses a set of reference gene expression matrices to evaluate 22 immune cell type proportions from bulk tumor sample expression data based on the principle of linear support vector regression (31). We processed the TCGA-LGG RNA-Seq data (TPM normalized) to calculate the relevant abundance of immune cells. We analyzed the Spearman correlation between the abundance of infiltrating immune cells and the CRG score. Furthermore, we downloaded the RNAss file named "StemnessScores_RNAexp_20170127.2.tsv". The tumor stem cell characteristics were extracted from the transcriptome and epigenetics of the samples and then used to evaluate the stem cell-like features of tumors. We performed a correlation analysis the investigate the association between the CRG score and Cancer Stem Cell (CSC) index.

Correlations of cuproptosis-related gene score with tumor mutation burden and immune checkpoint genes in lower-grade glioma

TMB and ICGs were associated with patients' response rate to immunotherapy. We extracted the mutation annotation format (MAF) from the TCGA database with the "maftools" R package to identify the mutational landscape of LGG patients

between different CRG score groups. The TMB score was also calculated for each LGG patient in the entire TCGA cohort. Then, we evaluated the correlations of ICGs with the CRG score and five genes in the cuproptosis-related prognostic model using Spearman's rank correlation coefficient.

Estimation of cuproptosis-related prognostic model in immunotherapy response

The immunotherapy response for LGG patients was estimated through the Tumor Immune Dysfunction and Exclusion (TIDE) algorithm (http://tide.dfci.harvard.edu), which can help doctors select patients who are more suitable for immunotherapy (32). Furthermore, GSE126044, GSE78220, checkmate cohort (33), and IMvigor210 cohort (34) were used to validate the predictive ability of the cuproptosis-related prognostic model in immunotherapy response.

Correlations of cuproptosis-related gene score with cuproptosis-related genes and chemotherapeutic sensitivity in in lower-grade glioma

We compared the expression levels of CRSGs between different risk groups and performed the correlation between CRG scores and gene expression levels. The calcPhenotype function of the "oncoPredict" R package was applied to estimate drug sensitivity scores for common drugs in the LGG therapy regimen including TMZ, procarbazine, teniposide, and vincristine in the TCGA cohort. The lower-imputed drug sensitivity represents more sensitivity to the drug.

Independent prognostic analysis and establishment of a nomogram

We obtained the clinical characteristics including the age, grade, and IDH mutation status of LGG patients in the entire TCGA cohort and two CGGA cohorts. In combination with the CRG score, these variables were analyzed in univariate and multivariable Cox regression analyses.

To individualize the predicted LGG patients' survival probability, we developed a nomogram using clinical characteristics and the CRG score. The R package "rms" and "regplot" were employed. Time-dependent ROC analysis was conducted to assess the predictive accuracy for 1-, 3-, and 5-year survival probability. The calibration plots were applied to compare model-predicted probability with observed outcomes in the TCGA-LGG cohort and two validation cohorts (CGGA1 and CGGA2).

Tissue samples, quantitative real-time PCR, and Western blotting

To further validate the potential roles of signature genes in LGG, five paired LGGs and matched normal adjacent tissue samples were collected from the SYSUCC. Ethical approval was confirmed by the ethical committee of the hospital. Associated clinicopathological features were further confirmed as listed in Supplementary Table 2. Tissue specimens were frozen in liquid nitrogen and stored at −80°C until used.

Total RNA was extracted with a TRIzol Reagent (ThermoFisher: #15596018), and the concentration was calculated by the A260/A280 ratio. The PrimeScript RT reagent kit (EZBioscience: #A0010CGQ) and SYBR-Green PCR reagent (EZBioscience: #A0012-R2-L) were used to perform cDNA synthetization and further conduct RT-qPCR based on the LightCycler ® 480 System (Roche). The housekeeping gene GAPDH was used as an endogenous control. The $2^{-\Delta\Delta CT}$ cycle threshold method was used to calculate the relative expression. Supplementary Table 3 lists the primers used in this study.

The protein expression levels of crucial CRGs were confirmed by Western blotting. Tissues were treated with RIPA lysis buffer (Fdbio: #FD009) containing phosphatase and protease inhibitors. The BCA protein detection kit (ThermoFisher: #23227) was applied to detect the protein concentration. Equivalent protein was then separated by 10% Tris-Tricine SDS-PAGE and transferred onto polyvinylidene fluoride (PVDF) membranes. After blocking with skimmed milk in TBST for 2 h, the membrane was further probed using antibodies against GAPDH (Proteintech: #60004-I-Ig), C21orf62 (Signalway Antibody, SAB: #C08364H), DRAXIN (Proteintech: #26342-1-AP), ITPRID2 (Proteintech: #14157-1-AP), MAP3K1 (Proteintech: # 19970-1-AP), and MOXD1 (Bioss: bs-17733R) overnight at 4°C. The membranes were subsequently washed with Tris-buffered saline containing Tween and then incubated with an HRP-conjugated anti-rabbit antibody at 37°C for 1 h. Finally, the bands on the membranes were observed with a ChemiDoc™ Imaging System.

Statistical analysis

All statistical analyses were performed using R software (Version 4.1.2). Correlation coefficients were evaluated by Spearman analysis. To compare variables between two groups, we employed the independent sample t-tests for normally distributed continuous variables, and Mann–Whitney U tests for non-normally distributed continuous variables. One-way ANOVA and Kruskal–Wallis tests were used to perform the difference comparisons of three or more groups. The survival analysis was conducted *via* the Kaplan–Meier method, and log-rank tests were employed to identify the significance of differences. The statistical significance was defined as $P< 0.05$.

Results

Landscape of genetic and transcriptional variations of cuproptosis-related genes in lower-grade glioma

TThe workflow of the study is outlined in Figure 1. A total of 13CRGs were included in our study The genetic mutation landscape in LGG patients is shown in Figures 2A–D. Of the 506 LGG patients in the TCGA cohort, 488 (96.44%) had genetic mutations and *IDH1* had the highest mutation frequency (77%), followed by *TP53*, *ATRX*, *CIC*, and *TTN*. However, only seven samples had genetic mutations in CRGs (Supplementary Figure 1). We investigated the frequencies of the CNVs of 13 CRGs in LGG. *DLD* exhibited the highest amplification frequency, while *ATP7B* and *DLST* had a widespread frequency of CNV loss (Figure 2E). Figure 2F shows the location of the CNV alterations of 13 CRGs on 23 chromosomes.

We then explored the expression levels, molecular interactions, and prognostic values of 13 CRGs. Twelve CRGs were upregulated in tumor samples including *FDX1*, *LIPT1*, *LIAS*, *DLD*, *DBT1*, *GCSH*, *DLST*, *DLAT*, *PDHA1*, *PDHB*, *SLC31A1*, and *ATP7A* ($P< 0.001$), whereas only *ATP7B* was downregulated ($P< 0.001$) (Figure 2G). Figure 2H exhibits the molecular interactions between CRGs. Nine prognostic CRGs were identified by Kaplan–Meier analysis and univariate Cox regression analysis (Supplementary Figure 2). The result of multivariate Cox regression analysis further revealed that three prognostic CRGs (*FDX1*, *GCSH*, and *ATP7B*) were independent prognostic factors (Table 1).

Identification of cuproptosis-related gene clusters in lower-grade glioma

In order to investigate the expression features and potential biological characteristics of CRGs in LGG, a consensus clustering algorithm was utilized to classify LGG patients in the TCGA cohort. Based on the expression of 13 CRGs, patients were categorized into CRG cluster A (n=219) and CRG cluster B (n=292) (Supplementary Figures 3A–3H). The PCA plot demonstrated an obvious different distribution between CRG clusters (Supplementary Figure 3I).

Correlations of cuproptosis-related gene clusters with clinical features, chemoradiotherapy sensitivity–related genes, immune checkpoint genes and tumor microenvironment

Figure 3A shows the different expressions of CRGs and clinicopathological characteristics between CRG cluster A and B. CRG cluster A was preferentially associated with higher expression levels of CRGs, higher grade (G3), and more death events. As the Kaplan–Meier survival curves crossed, we employed landmark analysis to compare the difference between CRG clusters (Figure 3B). The result of landmark analysis showed a longer OS in LGG patients in CRG cluster B within 9 years ($P = 0.003$). Nevertheless, no significant difference was found in the survival probability beyond 9 years ($P = 0.149$).

Then, we explored the correlation of CRG clusters with ICGs, CRSGs, and the TME. We found that CRG cluster A was associated with a higher expression of ICGs (Figure 3C). In addition, CRSGs, including *AKR1C1*, *EGFR*, *EZH2*, *HOXA9*, *HGMT*, *SOX2*, and *TBX5*, were differentially expressed between two CRG clusters (Figure 3D). To explore the potential function of CRGs in the immune infiltration of LGG, we compared the TME score and the relevant abundance of immune cells between two CRG clusters using "ESTIMATE" and "ssGSEA" algorithms. Patients in CRG cluster B had higher immune scores than those in CRG cluster A (Figure 3E). We observed that the immune infiltration levels of the activated CD4+ T cell, gamma delta T cell, and Type 2 T helper cell were significantly higher in CRG cluster A than those in CRG cluster B, while the CD56 dim natural killer cell and monocyte had significantly lower infiltration levels in CRG cluster A than those in CRG cluster B (Figure 3F).

Identification of differentially expressed genes between cuproptosis-related gene clusters and functional annotation

To further explore the functional annotation between CRG cluster A and B, GSVA and GSEA were performed. The results of the GSVA of the gene ontology biological process (GOBP) showed that CRG cluster A was significantly enriched in transportation-related processes including Golgi vesicle transport, nuclear pore organization, and vesicle targeting (Figure 4A). In addition, the GSVA of KEGG terms showed that CRG cluster A was abundant in metabolism-related pathways (citrate cycle TCA cycle, glycosylphosphatidylinositol GPI anchor biosynthesis), cancer-related pathways (small cell lung cancer, endometrial cancer), cell cycle–related pathways (cell cycle), and genomic stability–related pathways (mismatch repair, nucleotide excision repair) (Figure 4B). GSEA indicated that CRG cluster A was predominantly associated with the cell cycle, tumorigenesis, and metastasis including the G2M checkpoint hallmark, E2F target hallmark, epithelial mesenchymal transition hallmark, and angiogenesis hallmark (Figures 4C–E) (Supplementary Tables 4–5).

A total of 1,966 CRG cluster–related DEGs were identified between CRG clusters using R package "Limma". Consistent with GSVA and GSEA, the result of GO and KEGG showed that these DEGs were associated with the cell cycle, genomic stability, and cancer, which

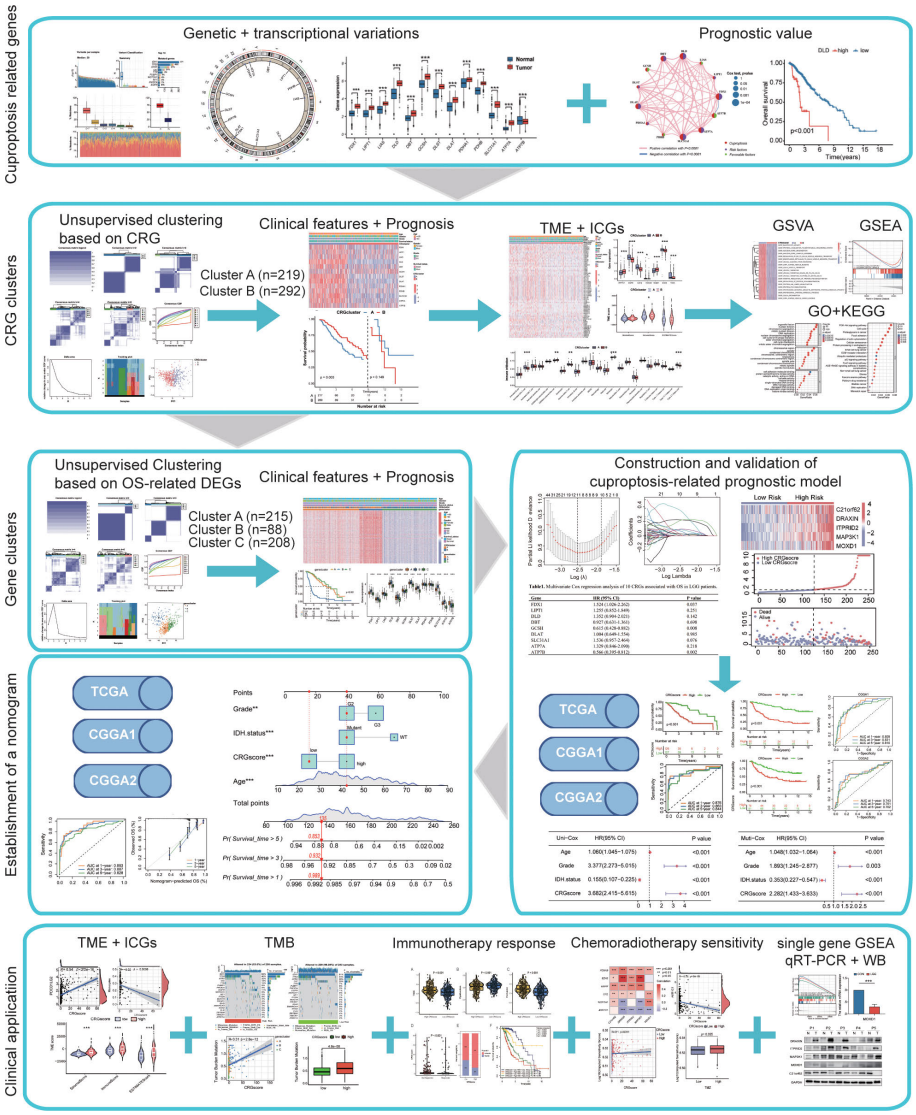

FIGURE 1
Flow chart of this study. *P< 0.05; **P< 0.01; ***P< 0.001

revealed that cuproptosis plays a significant role in tumorigenesis and metastasis (Figures 4F–H) (Supplementary Table 6).

Identification of cuproptosis gene clusters in lower-grade glioma

Subsequently, the prognostic values of the above 1,966 CRG cluster-related DEGs were assessed by univariate Cox regression analysis and a total of 1,424 genes associated with OS (OS-related DEGs) were screened out (*P*< 0.05). Based on the expression levels of OS-related DEGs, a consensus clustering algorithm was employed and LGG patients were classified into three gene clusters, termed gene cluster A (n=215), gene cluster B (n=88), and gene cluster C (n=208) (Supplementary Figures 4A–H). PCA analysis revealed that gene clusters could be identified clearly (Supplementary Figure 4I). The expression profiles and clinical information of OS-DEGs in different gene clusters are shown in Figure 5A. We found that gene cluster B was correlated with high gene expression levels, an advanced grade (G3), and more death events. Patients in gene cluster B were proven to be related to worse prognosis than those in gene cluster A and C by Kaplan–Meier analysis (*P*< 0.001) (Figure 5B). Furthermore, CRGs were differentially expressed among three gene clusters, with the highest expression levels in gene cluster B and the lowest expression levels in gene cluster C. (Figure 5C).

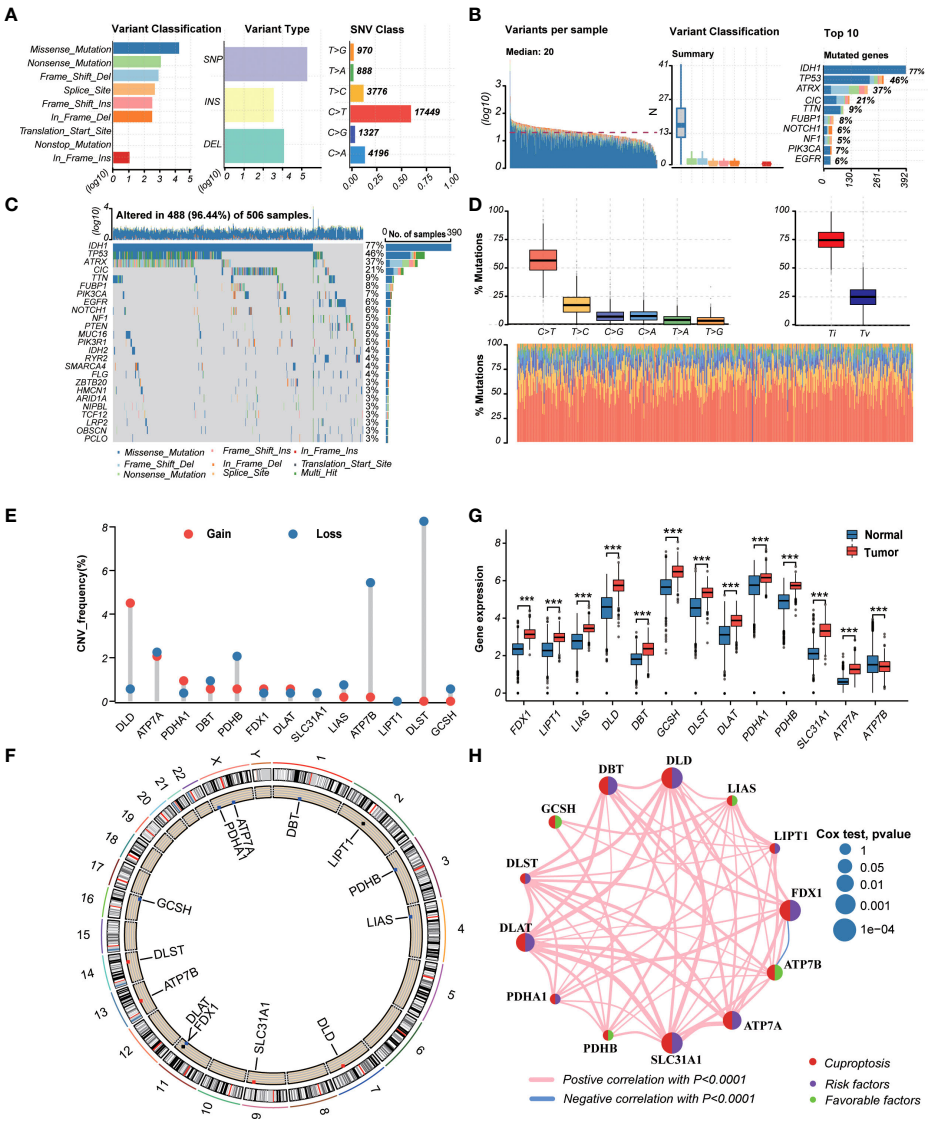

FIGURE 2
Landscape of genetic and transcriptional variations of cuproptosis-related genes (CRGs) in lower-grade glioma (LGG). **(A, B)** Summary of variation across 506 lower-grade glioma (LGG) patients including the variant classification, variant type, single-nucleotide variant (SNV) class, variants per sample, and top 10 mutated genes. **(C, D)** Landscape of genetic variations of 506 LGG patients in The Cancer Genome Atlas (TCGA) cohort. **(E)** Copy number variation (CNV) amplifications and deletions of CRGs in LGG patients. **(F)** The circus plot showed the location of CNV alteration of CRGs on 23 chromosomes. **(G)** Differences in the expression levels of 13 CRGs between tumor and normal samples. (tumor, red; normal, blue) *P*-values were shown as: ***$P < 0.001$. **(H)** The network showed interactions among CRGs in LGG. LGG, lower-grade glioma (WHO II and III); TCGA, the Cancer Genome Atlas; SNV, single-nucleotide variant; CNV, copy number variation; CRGs, cuproptosis-related genes.

Construction and evaluation of the cuproptosis-related prognostic model

We performed LASSO and multivariate Cox regression analysis for 1,424 OS-related DEGs to establish the cuproptosis-related prognostic model. Patients in the TCGA cohort were divided into training and test cohorts at a ratio of 1:1. In the TCGA training cohort, 11 genes were obtained, followed by LASSO Cox regression analysis, and were subjected to multivariate Cox regression analysis (Supplementary Figure 5). Ultimately, five key genes remained, including Chromosome 21 Open Reading Frame 62 (*C21orf62*), Dorsal Inhibitory Axon Guidance Protein (*DRAXIN*), ITPR Interacting Domain Containing 2 (*ITPRID2*), Mitogen-Activated Protein Kinase Kinase Kinase 1 (*MAP3K1*) and Monooxygenase DBH Like 1 (*MOXD1*). Further GSEA analyses based on a single gene expression indicated that B-cell-mediated immunity,

Table 1. Multivariate Cox regression analysis of 10 cuproptosis-related genes associated with overall survival in lower-grade glioma patients.

Gene	HR (95% CI)	P-value
FDX1	1.524 (1.026-2.262)	0.037
LIPT1	1.255 (0.852-1.849)	0.251
DLD	1.352 (0.904-2.021)	0.142
DBT	0.927 (0.631-1.361)	0.698
GCSH	0.615 (0.428-0.882)	0.008
DLAT	1.004 (0.649-1.554)	0.985
SLC31A1	1.536 (0.957-2.464)	0.076
ATP7A	1.329 (0.846-2.090)	0.218
ATP7B	0.566 (0.395-0.812)	0.002

complement cascade, interferon-gamma response, chromosome segregation, mitotic spindle checkpoint, G2M checkpoint, T-cell receptor complex, CD22-mediated BCR regulation, epithelial–mesenchymal transition, cell cycle checkpoints, voltage-gated potassium channels, and other biological processes related to immunity or cancer were significantly enriched (Supplementary Figure 6). Next, we constructed a five-gene cuproptosis-related prognostic model and the associated CRG score can be calculated as follows: CRG_score= 0.164859* *C21orf62* + 0.293187* *DRAXIN* + 0.882099* *ITPRID2* + 0.625577* *MAP3K1* + 0.256801* *MOXD1*. We also explored the relationship between CRG clusters, gene clusters, and CRG scores. We found that CRG scores in CRG cluster A were significantly higher than that in CRG cluster B, and the expression of CRGs were upregulated in the high-risk group, which suggested that a high CRG score and the high expression of CRGs were associated with tumorigenesis and metastasis (Figures 5D, E). Meanwhile, the rank order of the CRG score in gene clusters was B > A > C (Figure 5F). The Sankey diagram showed subgroup distributions in groups with different CRG scores and survival outcomes (Figure 5G).

The heatmap showed the different expressions of *C21orf62*, *DRAXIN*, *ITPRID2*, *MAP3K1*, and *MOXD1* between the high- and low-risk groups in TCGA training and test cohorts (Figure 6A). In addition, the risk plot of the CRG score revealed that patients with a high CRG score were related to more cases of death and shorter survival time (Figures 6B, C). Kaplan–Meier analysis showed that patients in the high-risk group had a worse OS than low-risk patients in both TCGA training and testing cohorts ($P< 0.001$) (Figures 6D, E). The 1-, 3-, and 5-year survival probability of the CRG score was represented by the AUC values of 0.876, 0.863, and 0.844, respectively, in the TCGA training cohort (Figure 6F). In the TCGA testing cohort, AUC values for predicting 1-, 3-, and 5-year OS were 0.852, 0.856, and 0.805. Meanwhile, the calibration curve also manifested a satisfactory agreement between predictive and observational values at the probabilities of 3- and 5-year survival (Supplementary Figures 7A, B).

External validation of the cuproptosis-related prognostic model

To further verify the prognostic performance of the model, we applied two external validation cohorts (CGGA1 and CGGA2) (Supplementary Table 7). Patients were also classified into high- and low-risk groups according to CRG scores. Kaplan–Meier analysis showed a significantly better prognosis in the low-risk group compared to that in the high-risk group (Figures 7A, B). Meanwhile, the model also demonstrated a high AUC value in external validation cohorts (Figure 7C, D), and the calibration curve also exhibited a satisfactory agreement between predictive and observational values at the probabilities of 3- and 5-year survival (Supplementary Figures 7C, D).

Then, patients were stratified into four groups by the CRG score and treatment strategies. Kaplan–Meier analysis showed that patients in low-risk and no-radiotherapy groups had the best prognosis (Figures 7E, F). However, the predictive ability of the model was not impacted by TMZ treatment. Whether patients received TMZ or not, the low-risk group always showed a strong survival advantage (Figures 7G, H).

Correlations of cuproptosis-related gene score with immune infiltration and cancer stem cell index in lower-grade glioma

GSEA was conducted to explore the potential biological functions between high- and low-risk groups (Figures 8A, B) (Supplementary Table 8). We observed that a high CRG score was mainly related to the cell cycle (negative regulation of metaphase–anaphase transition of the cell cycle, G2M checkpoint hallmark, E2F target hallmark), tumor progression (epithelial–mesenchymal transition hallmark, angiogenesis hallmark), and immunity (interferon gamma–mediated signaling pathway, T-cell activation *via* T-cell receptor contact with antigen bound to the MHC molecule on antigen-presenting cell, inflammatory response hallmark). TME scores including the stromal score, immune score, and ESTIMATE score were significantly higher in the high-risk group (Figure 8C). We assessed the correlation of immune infiltration with the five genes cuproptosis-related prognostic model (Figure 8D). Macrophage M0 and Macrophage M1 were positively correlated with the CRG score, while mast cells activated, monocytes, neutrophils, and NK cells activated were negatively correlated with the CRG score (Figures 8E–K).

Cancer stem cells are a group of cells with the features of self-renewing, being multipotent, and tumor-initiating, which can drive the growth and recurrence of tumors and are resistant to many current treatments. The CRG score and CSC index were synthesized to evaluate their relationship. A mild but significant negative correlation (R = -0.24, P = 4.2e-08) was detected (Figure 8L).

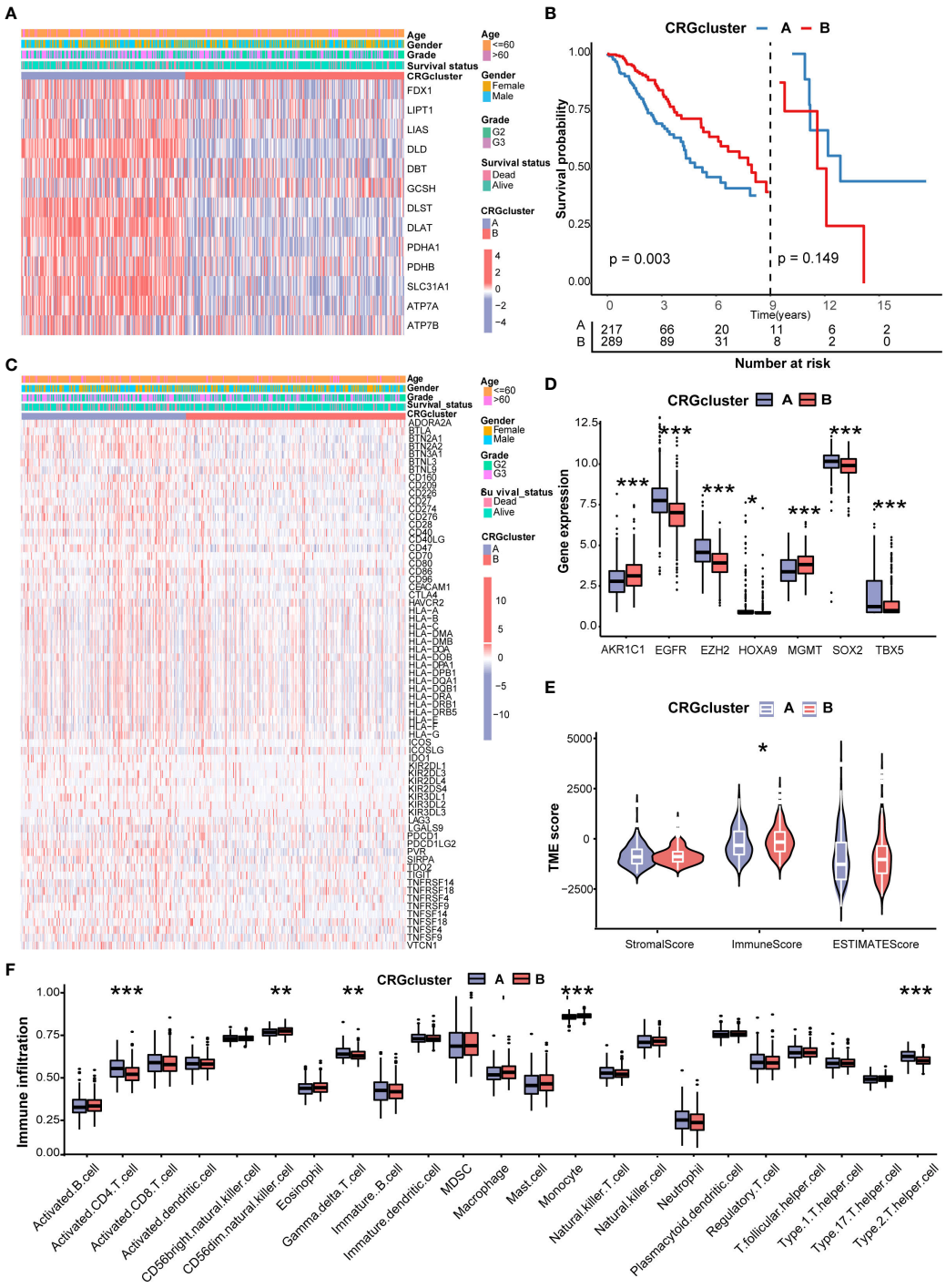

FIGURE 3
Correlations of CRG clusters with clinical features, CRSGs, immune checkpoint genes (ICGs), and tumor microenvironment (TME). **(A)** The heatmap showed the different expressions of CRGs and clinicopathological characteristics between CRG cluster A and **(B)**(B) Landmark survival analysis for two CRG clusters. The overall survival probability of LGG patients in the two CRG clusters was calculated by Kaplan–Meier analysis (log-rank tests). A landmark time of 9 years was set. **(C)** The heatmap showed the different expressions of ICGs and clinicopathological characteristics between CRG cluster A and B **(D)** Differences in the expression levels of seven chemoradiotherapy sensitivity–related genes (CRSGs) between CRG cluster A and B**(E)** Correlations between the two CRG clusters and TME scores. **(F)** Differences in the abundance of infiltrating immune cells between CRG cluster A and B (CRG cluster A, blue; CRG cluster B, red) *P* values were shown as: **P*< 0.05; ***P*< 0.01; ****P*< 0.001. CRGs, cuproptosis-related genes; CRSGs, chemoradiotherapy sensitivity–related genes; ICGs, immune checkpoint genes; TME, tumor microenvironment; LGG, lower-grade glioma (WHO II and III).

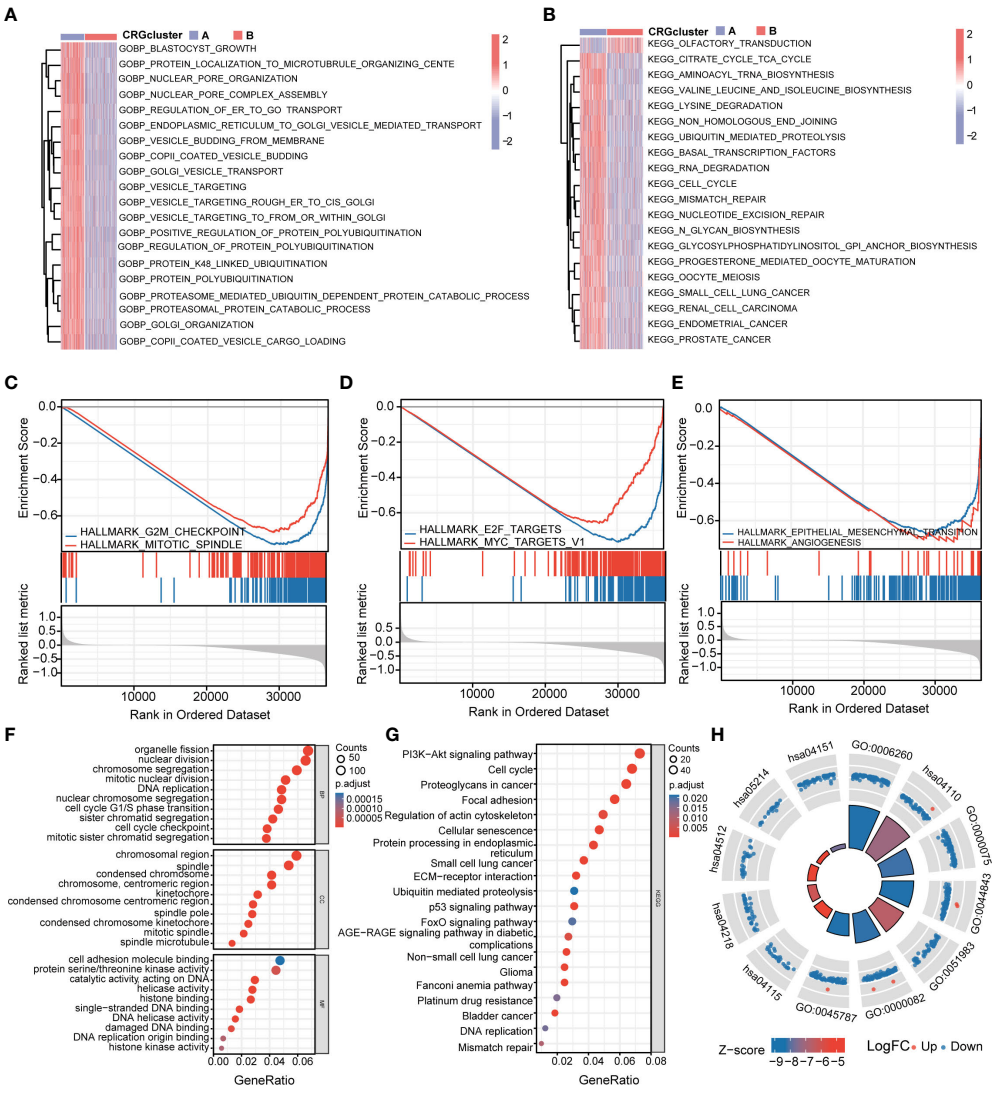

FIGURE 4
Functional enrichment analysis and identification of differentially expressed genes (DEGs) between CRG clusters. **(A)** Gene set variation analysis (GSVA) of gene ontology biological process (GOBP) terms between CRG cluster A and B, in which red and blue represent activated and inhibited, respectively. **(B)** GSVA of Kyoto Encyclopedia of Genes and Genomes (KEGG) terms between CRG cluster A and B, in which red and blue represent activated and inhibited, respectively. **(C-E)** Gene set enrichment analysis (GSEA) of significant HALLMARK enriched in CRG cluster **(A) (F–H)** GO and KEGG enrichment analyses of DEGs between two CRG clusters. DEGs, differentially expressed genes; GSVA, gene set variation analysis; GOBP, gene ontology biological process; GSEA, gene set enrichment analysis; GO, Gene Ontology; KEGG, Kyoto Encyclopedia of Genes and Genomes.

Correlations of cuproptosis-related gene score with tumor mutational burden and immune checkpoint genes in lower grade glioma

Previous studies demonstrated that high TMB scores are associated with increased treatment response to immunotherapy. Here, patients in the high-risk group (64%) had a markedly lower mutation incidence of *IDH1* than those patients in the low-risk group (91%) (Figures 9A, B). The TMB score was significantly higher in the high-risk group (P = 4.8e-0.8), and the CRG score was positively correlated with the TMB score (R = 0.31, P = 2.8e-12) (Figures 9C, D). Considering that the expression levels of ICGs have been reported to correlate with the clinical benefit of checkpoint blockade immunotherapy (35, 36), we further explored the relationship between the CRG score and ICGs. We found that most ICGs were significantly correlated with the five genes in the

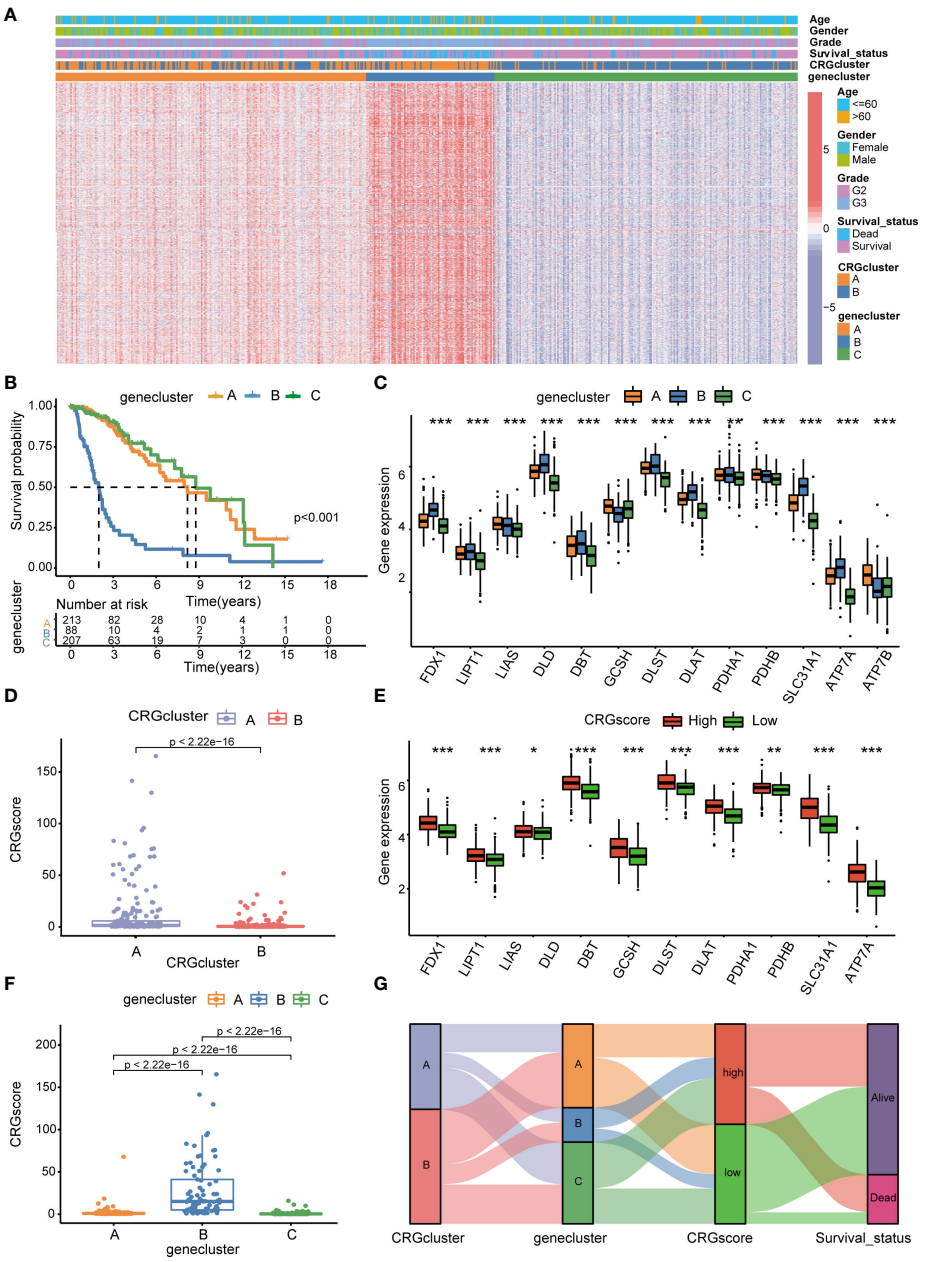

FIGURE 5
Identification of cuproptosis gene clusters and construction of the cuproptosis-related prognostic model in LGG. **(A)** The heatmap showed the different expressions of overall survival (OS)–DEGs and clinicopathological characteristics among gene cluster A to C **(B)** Kaplan–Meier OS curves for patients in the three gene clusters (log-rank test). **(C)** Differences in the expression levels of 13 CRGs among gene cluster A to C. **(D)** Differences in CRG scores between CRG cluster A and B **(E)** Differences in the expression levels of 13 CRGs between high- and low-risk groups. **(F)** Differences in CRG scores among gene cluster A to C, **(G)** Sankey diagram of subtype distributions in groups with different CRG scores and survival outcomes. *P*-values were shown as: *$P< 0.05$; **$P< 0.01$; ***$P< 0.001$. LGG, lower-grade glioma (WHO II and III); OS, overall survival; DEGs, differentially expressed genes; CRGs, cuproptosis-related genes.

model (Figure 9E). The expression levels of 61 ICGs including *CD276*, *BTN2A2*, *PDCD1LG2*, *CD274*, and *CD40LG* increased with the increasing CRG score (Figure 9F). Only *BTNL9* was negatively correlated with the CRG score (R = -0.24, P = 2.6e−08) (Supplementary Table 9). Then, we found that patients with a high CRG score and high expression levels of *CD276*, *CD274*, *BTN2A2*, *PDCD1LG2*, and *CD40LG* were associated with poor OS than others (Supplementary Figure 8).

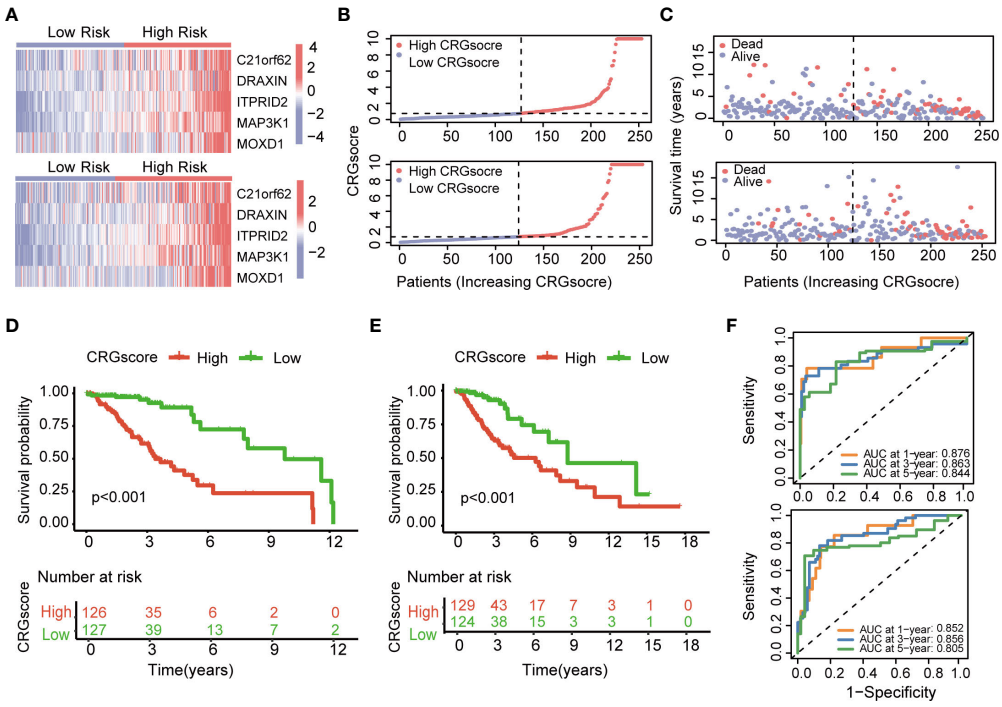

FIGURE 6
Evaluation of the cuproptosis-related prognostic model in the TCGA cohort. **(A)** The heatmap showed the different expressions of genes in the cuproptosis-related prognostic model between the high- and low-risk groups in TCGA training and test cohorts. **(B)** Distribution of the CRG score in TCGA training and testing cohorts. **(C)** The risk point plot showed the patterns of the survival time and survival status between the high- and low-risk groups in TCGA training and test cohorts. **(D)** The Kaplan–Meier OS curves for patients in the high- and low-risk groups in the TCGA training cohort (log-rank test). **(E)** The Kaplan–Meier OS curves for patients in the high- and low-risk groups in the TCGA testing cohort (log-rank test). **(F)** ROC curves showed the prognostic performance of the cuproptosis-related prognostic model in TCGA training and testing cohorts. TCGA, the Cancer Genome Atlas; CRGs, CRGs, cuproptosis-related genes; OS, overall survival.

Estimation of cuproptosis-related prognostic model in immunotherapy response

The TIDE algorithm was applied to estimated immunotherapy response for LGG patients based on the transcriptomic data. The results showed that the TIDE score of the high-risk group was significantly higher than that of the low-risk group, indicating that the patients in the low-risk group could benefit more from immunotherapy (Figure 10A). Patients in the low-risk group were associated with a higher dysfunction score and lower exclusion score (Figures 10B, C). Moreover, patients were classified into no responders and responders by the TIDE algorithm. We found that immunotherapy responders were correlated with a lower CRG score (Figures 10D, E). Patients with a combination of a high CRG score and high TIDE score group showed an association with the worst prognosis (Figure 10F). Then, we validated the predictive value of the cuproptosis-related prognostic model in immunotherapy response. The clinical response to immunotherapy in patients with non-small cell lung cancer or metastatic melanoma in the low-risk group compared to those in the high-risk group were confirmed (Figures 11A, B). However, no differences were identified in renal cell carcinoma patients and urothelial cell carcinoma patients (Figures 11C–E). Figure 11F shows the subtype distributions in groups with different CRG scores and immunotherapy response in the IMvigor210 cohort. Furthermore, in the IMvigor210 cohort, the CRG scores were different among different immune phenotypes, tumor cell (TC) levels, and immune cell (IC) levels (Figures 11G–I).

Correlations of cuproptosis-related gene score with chemoradiotherapy sensitivity–related genes and chemotherapeutic sensitivity in lower-grade glioma

Additionally, we observed a strong correlation between the expression levels of CRSGs and the expression levels of *C21orf62*,

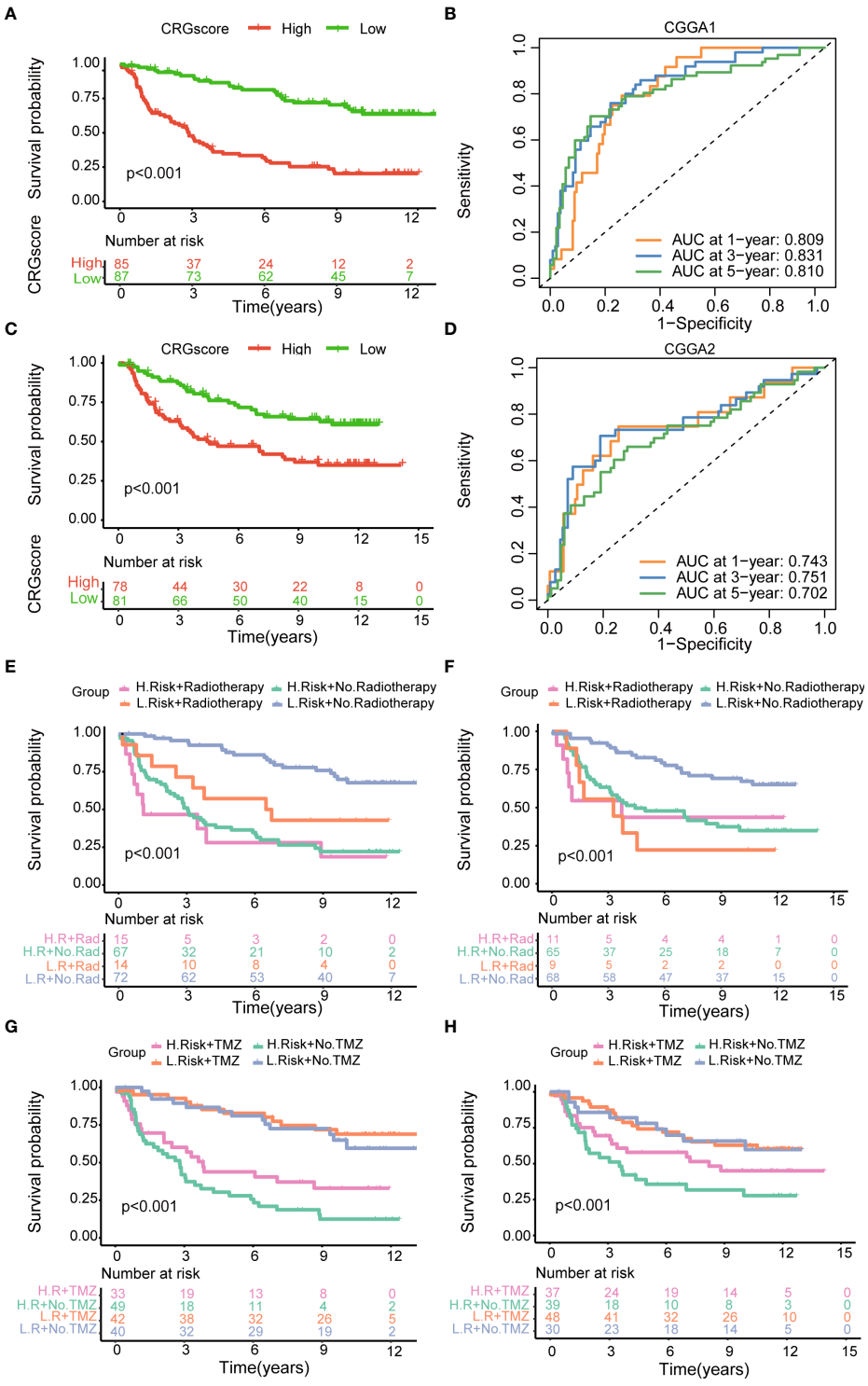

FIGURE 7
Validation of the cuproptosis-related prognostic model in CGGA cohorts. **(A)** The Kaplan–Meier OS curves for patients in the high- and low-risk groups in the CGGA1 cohort. **(B)** The Kaplan–Meier OS curves for patients in the high- and low-risk groups in the CGGA2 cohort. **(C)** ROC curves showed the prognostic performance of the cuproptosis-related prognostic model in the CGGA1 cohort. **(D)** ROC curves showed the prognostic performance of the cuproptosis-related prognostic model in the CGGA2 cohort. **(E–G)** The Kaplan–Meier OS curves among four groups classified by the CRG score and treatment with radiotherapy in CGGA1 and CGGA2 cohorts. **(G–H)** The Kaplan–Meier OS curves among four groups classified by the CRG score and treatment with TMZ in CGGA1 and CGGA2 cohorts. CGGA, Chinese Glioma Genome Atlas; ROC, receiver operating characteristic; OS, overall survival; TMZ, temozolomide; CRGs, cuproptosis-related genes.

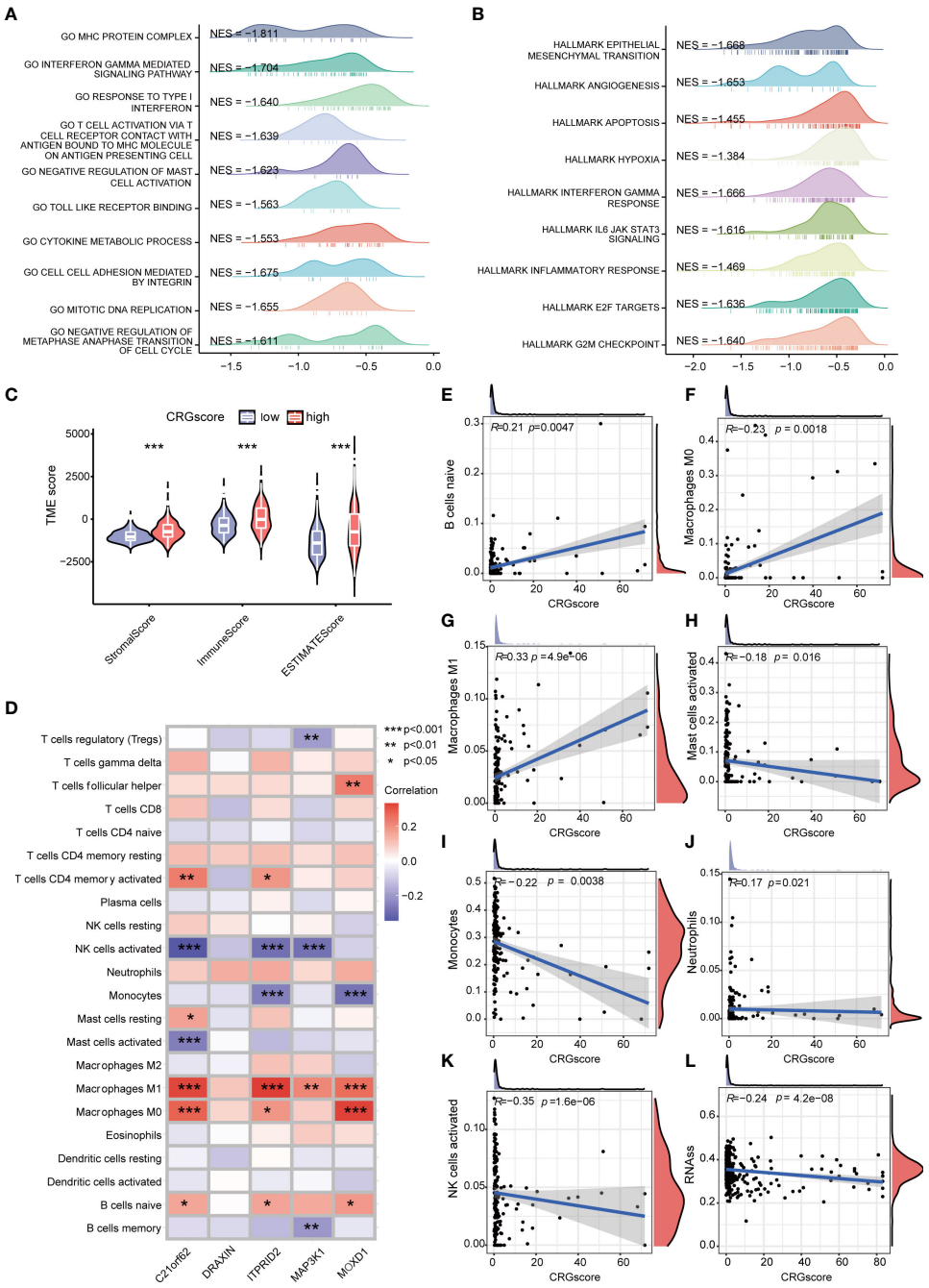

FIGURE 8
Correlations of the CRG score with immune infiltration and the cancer stem cell (CSC) index in LGG. **(A)** GSEA of significant GOBP terms enriched in the high-risk group. **(B)** GSEA of significant HALLMARK terms enriched in the high-risk group. **(C)** Correlations between CRG scores and TME scores. **(D)** Correlations between the abundance of immune cells and five genes in the cuproptosis-related prognostic model. **(E–K)** Correlations between the abundance of immune cells and the CRG score. **(L)** Correlations between the CSC index and the CRG score. *P*-values were shown as: **P*< 0.05; ***P*< 0.01; ****P*< 0.001. CRGs, cuproptosis-related genes; CSC, cancer stem cell; LGG, lower-grade glioma (WHO II and III); GSEA, gene set enrichment analysis; GOBP, gene ontology biological process; TME, tumor microenvironment.

DRAXIN, *ITPRID2*, *MAP3K1*, and *MOXD1* (Figure 12A). As the CRG score increased, the expression levels of *CPZ*, *EGFR*, *EZH2*, and *HOXA9* increased, but the expression levels of *AKR1C1* decreased, which revealed a potential association between the CRG score and chemoradiotherapy (Figures 12B–G). To explore the values of the CRG score as a biomarker to predict the chemotherapeutic response in LGG patients, we performed drug sensitivity analysis using the "oncoPredict" R package. A higher

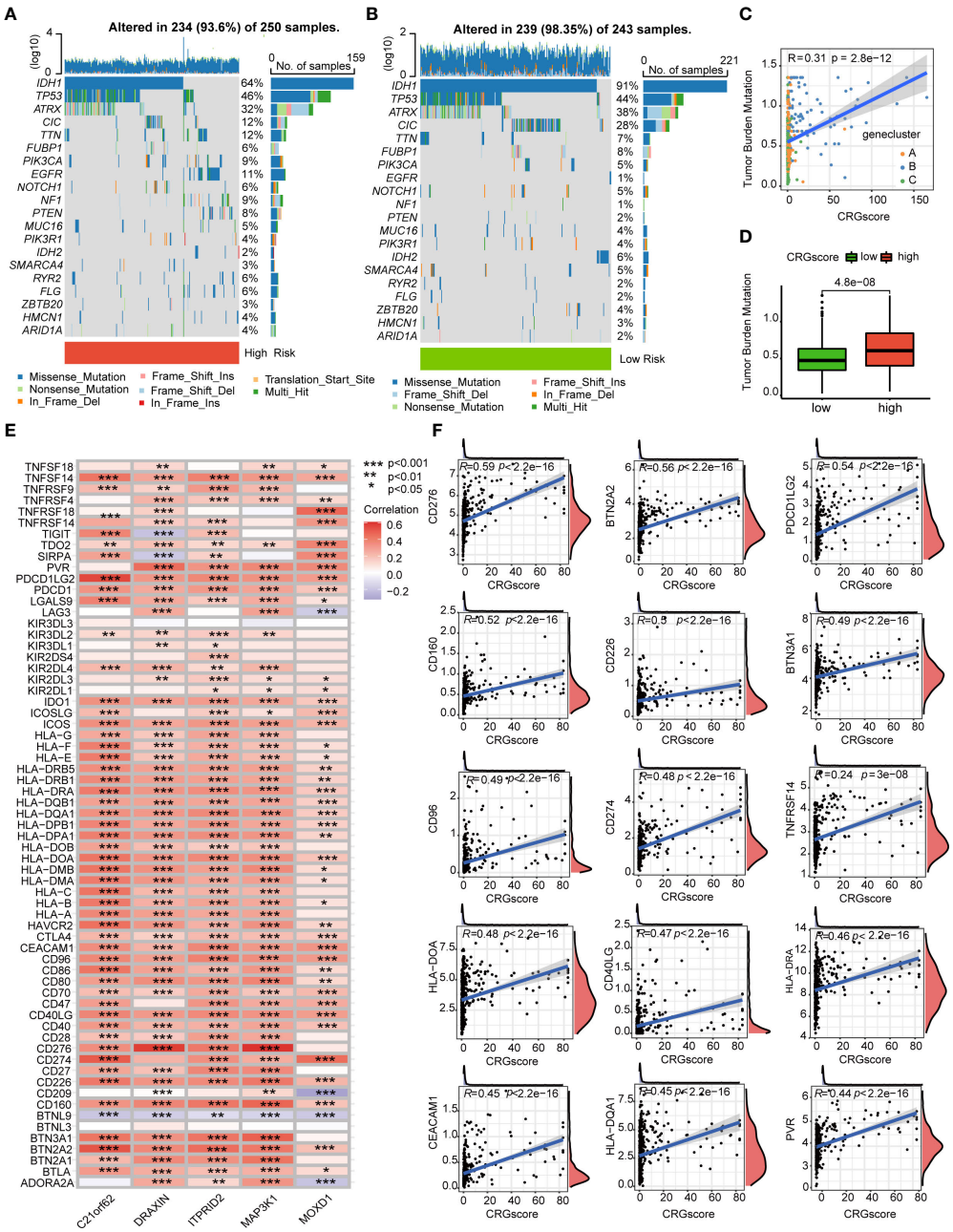

FIGURE 9
Correlations of the CRG score with TMB and ICGs in LGG. **(A, B)** The mutational landscape of LGG patients in high- and low-risk groups. **(C)** Correlations between the TMB and the CRG score in different gene clusters. **(D)** Difference in the TMB scores between high- and low-risk groups. **(E)** Correlations between the expression of ICGs and five genes in the cuproptosis-related prognostic model. **(F)** Correlations between the expression of ICGs and the CRG score. *P*-values were shown as: *$P< 0.05$; **$P< 0.01$; ***$P< 0.001$. CRGs, cuproptosis-related genes; TMB, tumor mutation burden; ICGs, immune checkpoint genes; LGG, lower-grade glioma (WHO II and III).

imputed sensitivity score represented lower sensitivity to the drug. We found patients in the high-risk group had higher imputed sensitivity scores of TMZ and procarbazine, while the imputed sensitivity scores of teniposide and vincristine were lower in patients in the high-risk group (Figures 12H–L).

Independent prognostic analysis and establishment of a nomogram

To determine if the CRG score could be used as an independent prognostic predictor for OS, we combined

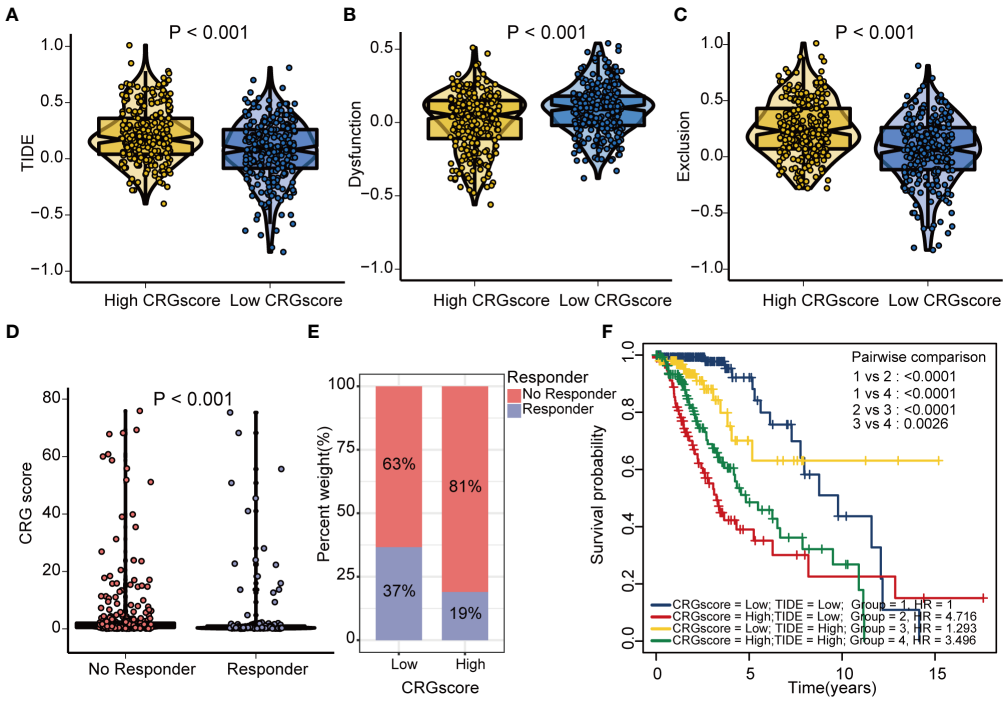

FIGURE 10
Estimation of the cuproptosis-related prognostic model in immunotherapy response in LGG. **(A)** Difference in TIDE scores between high- and low-risk groups. **(B)** Difference in dysfunction scores between high- and low-risk groups. **(C)** Difference in exclusion scores between high- and low-risk groups. **(D)** Difference in CRG scores between responder and no responder groups based on the TIDE algorithm. **(E)** The distribution of immunotherapy response in indicated groups stratified by the CRG scores based on the TIDE algorithm. **(F)** The Kaplan–Meier OS curves among four groups classified by the CRG score and TIDE score. TIDE, tumor immune dysfunction and exclusion; CRG, cuproptosis-related genes; OS, overall survival.

clinical characteristics and the CRG score to conduct univariate and multivariate Cox regression analyses. In the TCGA cohort, age, grade, IDH mutation status, and CRG score demonstrated significant differences (Figures 13A, B). The prognostic value of the CRG score was also verified in external CGGA cohorts, and the results showed that CRG score is an independent prognostic predictor for LGG patients (Supplementary Figure 9).

Then, we combined the CRG score and clinical chrematistics (age, grade, IDH mutation status) to establish a nomogram in the TCGA cohort, which exhibited a quantitative method to generate personalized predictions for LGG patients (Figure 13C). The AUC values of the model were estimated, and calibration analyses were performed to assess the predictive ability and accuracy for prognosis. Figure 13D showed that 1-, 3- and 5-year AUC values of the model in the TCGA cohort were 0.893, 0.887, and 0.828, respectively. The model also had good predictive ability in the CGGA1 cohort (AUC > 0.75) and CGGA2 cohort (AUC > 0.7) (Figures 13F, H). Subsequently, the calibration plots demonstrated good agreement between model-predicted probability and the observed outcomes (Figures 13E, G, I).

Tissue samples, quantitative real-time PCR, and Western blotting

To verify the expression level of signature genes in LGG, we collected five paired cancer- and adjacent normal tissues from SYSUCC. As shown in Figures 14A–D, qRT-PCR showed that the expression of the *DRAXIN*, *ITPRID2*, and *MAP3K1* were significantly upregulated while *MOXD1* was downregulated in tumor samples. Nevertheless, there was no significant difference in the expression of *C21orf62* (Figure 14E). Further investigation indicated heterogeneity in the expression of *C21orf62*. Briefly, it was upregulated in two patients but downregulated in the remaining patients (the relative expression was 5.33, 1.68, 0.36, 0.07, and 0.04, respectively). The results of WB also demonstrated the heterogeneity in *C21orf62*, *MAP3K1*, and *MOXD1* but consistently a significant upregulation in *DRAXIN* and *ITPRID2* at the protein level (Figure 14F).

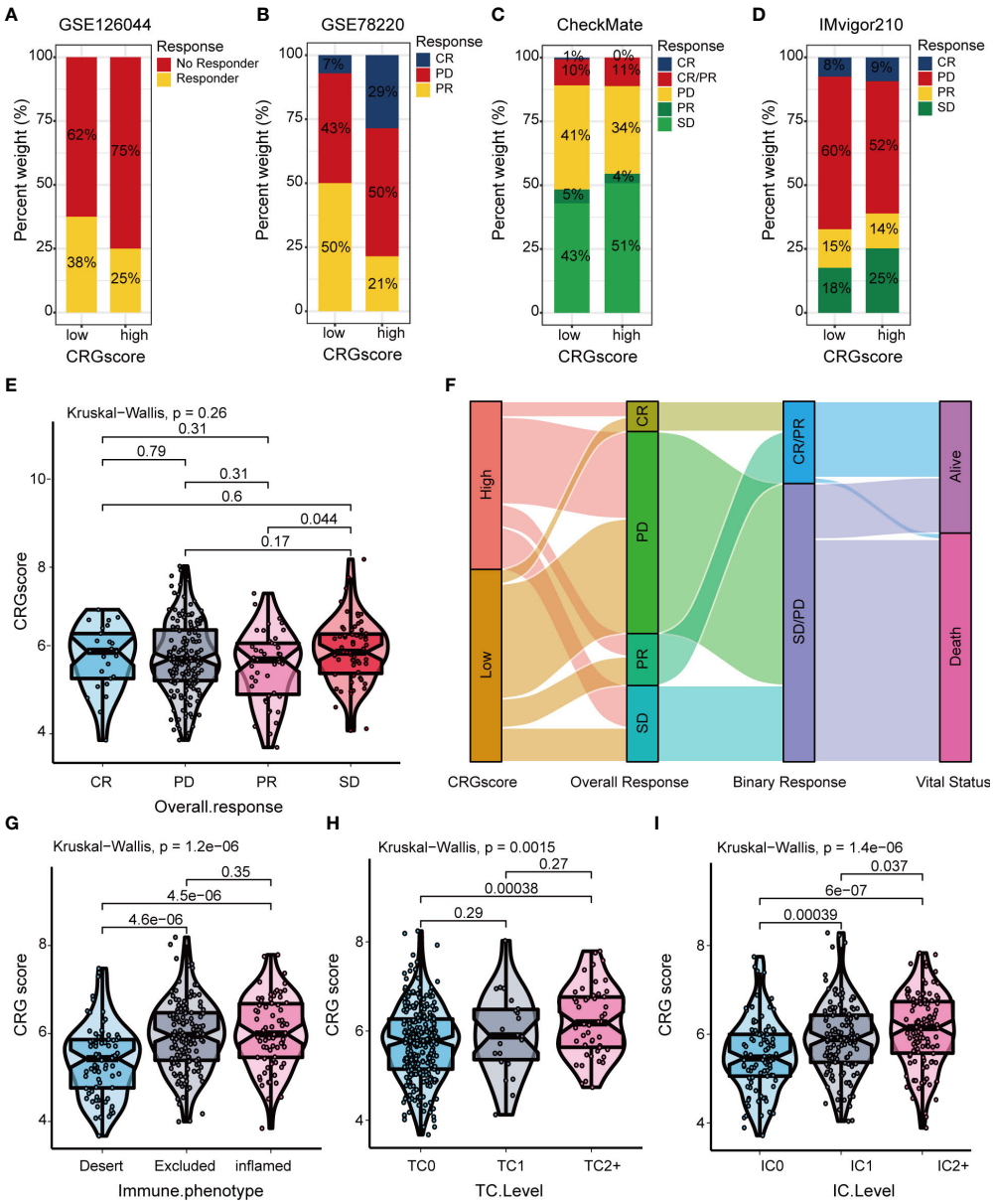

FIGURE 11
Correlation of the CRG score with immunotherapy response in mutiple cohorts. The distribution of immunotherapy response in indicated groups stratified by CRG scores in **(A)** GSE126044, **(B)** GSE78220, **(C)** the CheckMate cohort, and **(D)** the IMvigor210 cohort. **(E)** Difference in CRG scores among four immunotherapy response groups in the IMvigor210 cohort. **(F)** Sankey diagram of subtype distributions in groups with different CRG scores and immunotherapy response in the IMvigor210 cohort. Differences in the CRG score among **(G)** three immune phenotypes, **(H)** three TC levels, and **(I)** three immune cell (IC) levels in the IMvigor210 cohort. CRGs, cuproptosis-related genes; TC, tumor cell; IC, immune cell.

Discussion

Cell death is critical for maintaining organismal homeostasis, developing, and preventing excessively proliferative malignancy (37, 38). As a hallmark of cancer, metabolism plays an indispensable role in cell death (39). Numerous studies have demonstrated a correlation between metabolism and multiple cell deaths in cancer (40). In gliomas, stress-induced cell death signaling usually involves the mitochondria and endoplasmic reticulum, which activates reactive oxygen intermediates and regulates lipid mediators in cell proliferation, migration, and interaction with endothelial and microglial cells (41, 42). Nevertheless, the underlying mechanisms and correlations among metabolism, mitochondria, and cell death in gliomas still remain poorly understood.

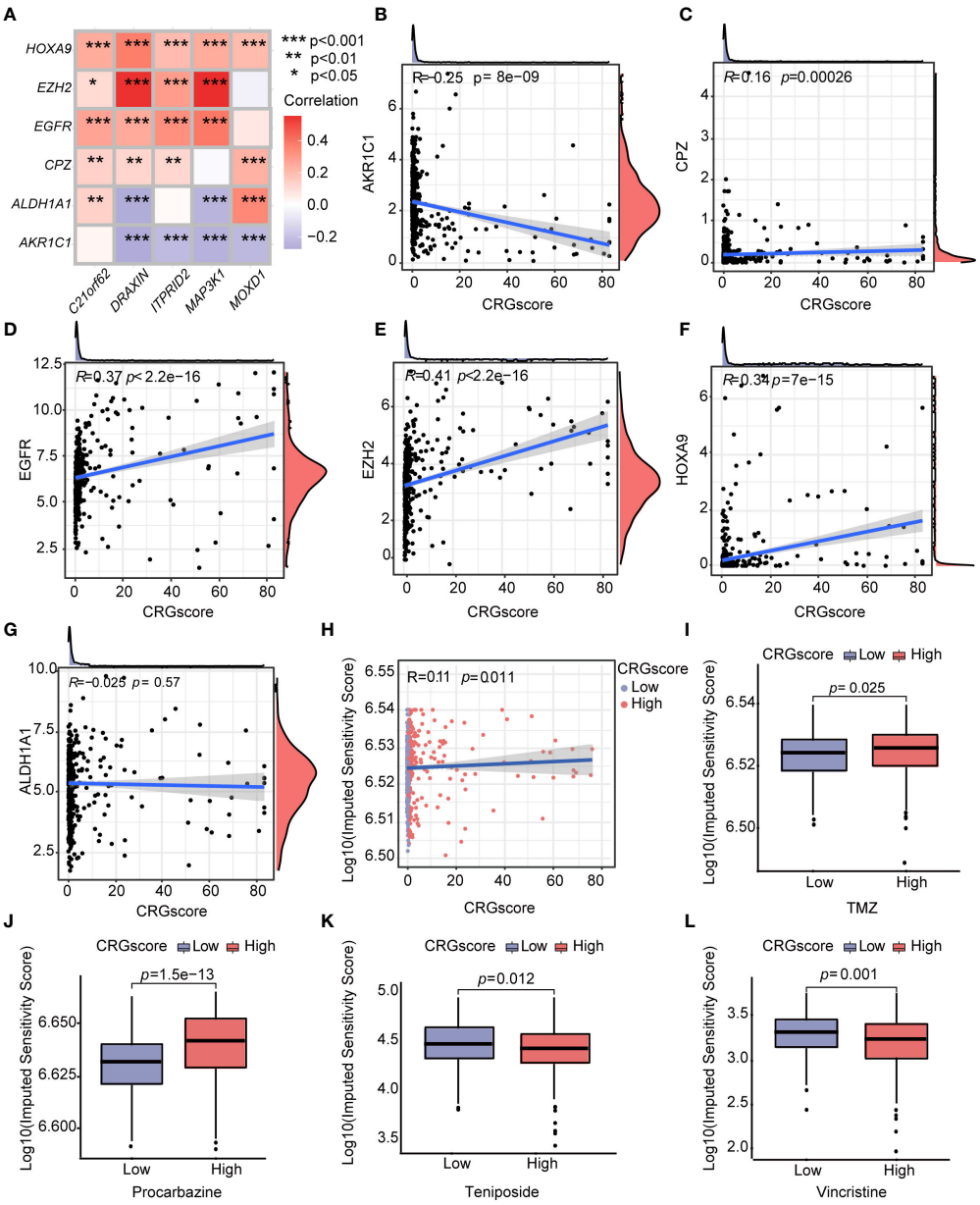

FIGURE 12
Correlations of the CRG score with CRSGs and chemotherapeutic sensitivity in LGG. **(A)** Correlations between the expression of CRSGs and five genes in the cuproptosis-related prognostic model. **(B–G)** Correlations between the expression of CRSGs and the CRG score. **(H)** Correlations between the imputed sensitivity score of TMZ and the CRG score. **(I–L)** Difference in chemotherapeutic sensitivity between high- and low-risk groups. *P*-values were shown as: **P*< 0.05; ***P*< 0.01; ****P*< 0.001. CRSGs, chemoradiotherapy sensitivity–related genes; CRGs, cuproptosis-related genes; TMZ, temozolomide.

Cuproptosis, first named by Todd R. Golub, sheds light on copper metabolism and mitochondrial dysregulation in cell death. Several studies have focused on a single cuproptosis regulator in cancer; however, the overall effect of multiple CRGs has not been fully characterized. The specific role of cuproptosis in LGG remains unclear. Furthermore, although many prognostic signatures have been established based on the patterns of pseudogenes (43), N6-methylandenosine (44), immunity (45), ferroptosis (46), and pyroptosis (47) their predictive ability needs to be further improved, and there is still a lack of a prognostic signature based on the characteristics of cuproptosis. In the present study, we systematically investigated the global alterations in 13 CRGs at genetic and transcriptional levels in LGG, established a scoring system

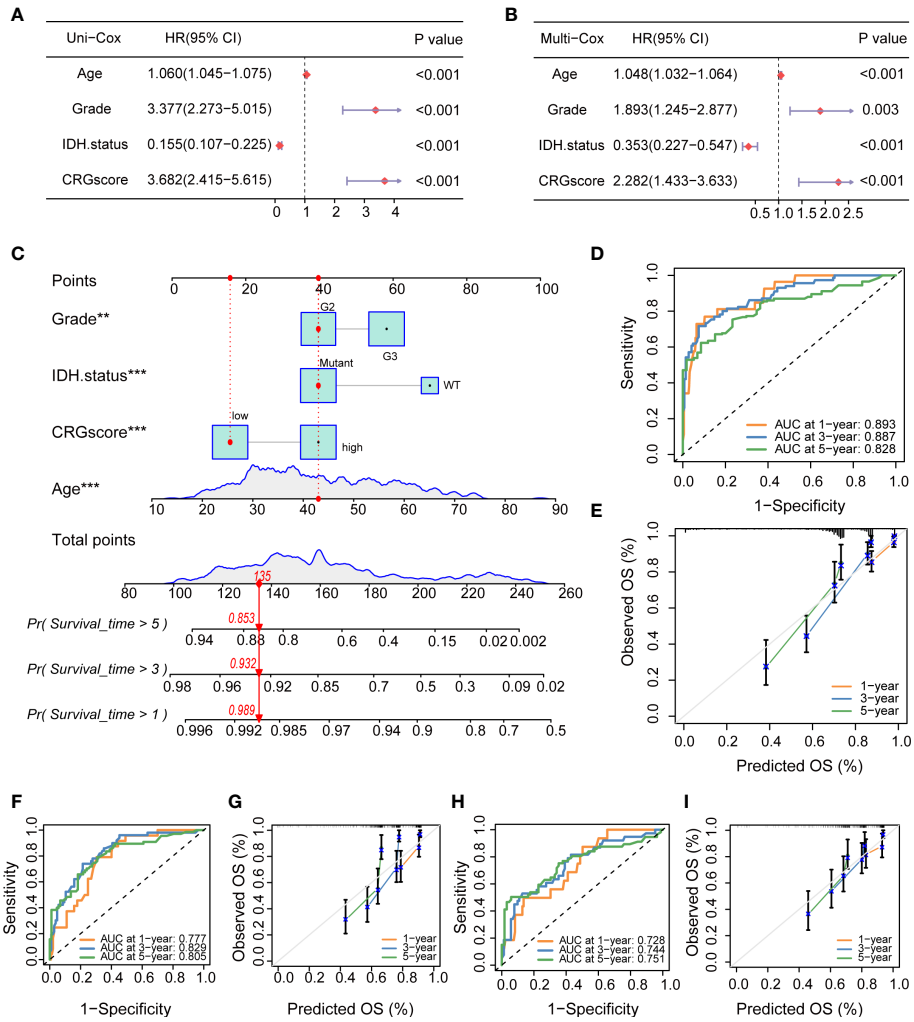

FIGURE 13
Independent prognostic analysis and establishment of a nomogram. **(A)** Univariate Cox regression analysis of the CRG score and clinical characteristics in the TCGA cohort. **(B)** Multivariate Cox regression analysis of the CRG score and clinical characteristics in the TCGA cohort. **(C)** The nomogram was established to predict 1-, 3-, and 5-year overall survival probability of LGG patients in the TCGA cohort. **(D)** ROC curves showed the prognostic performance of the model in the TCGA cohort. **(E)** The calibration curves measured the relationship between the outcomes predicted by the model and the observed outcomes in the TCGA cohort. **(F)** ROC curves showed the prognostic performance of the model in the CGGA1 cohort. **(G)** The calibration curves measured the relationship between the outcomes predicted by the model and the observed outcomes in the CGGA1 cohort. **(H)** ROC curves showed the prognostic performance of the model in the CGGA2 cohort. **(I)** The calibration curves measured the relationship between the outcomes predicted by the model and the observed outcomes in the CGGA2 cohort. CRGs, cuproptosis-related genes; TCGA, the Cancer Genome Atlas; LGG, lower-grade glioma (WHO II and III); ROC, receiver operating characteristic; CGGA, Chinese Glioma Genome Atlas.

consisting of five signature core genes, and eventually constructed a quantitative nomogram by integrating the CRG score and clinicopathological features including grades, IDH status, and age. Compared to other models, our model has better performance overall and has better clinical application value (Supplementary Table 10).

Copper metabolism plays a crucial role in diverse biological processes (48). We first characterized the landscape of genetic and transcriptional variations of CRGs in LGG. Although only seven samples had genetic mutations in CRGs, we were surprised to find that 12 CRGs were upregulated between the LGG and normal tissues, while *ATP7B* was downregulated. We noticed that the expression of most CRGs was significantly correlated with poor prognosis. Based on CRG expression profiles, we further divided LGG patients into two distinct molecular subtypes with the unsupervised clustering approach. Compared to patients with subtype B, patients with subtype A had a worse prognosis within the early 9 years and more advanced clinicopathological features. We speculate that the differences may be partially attributed to different responses to

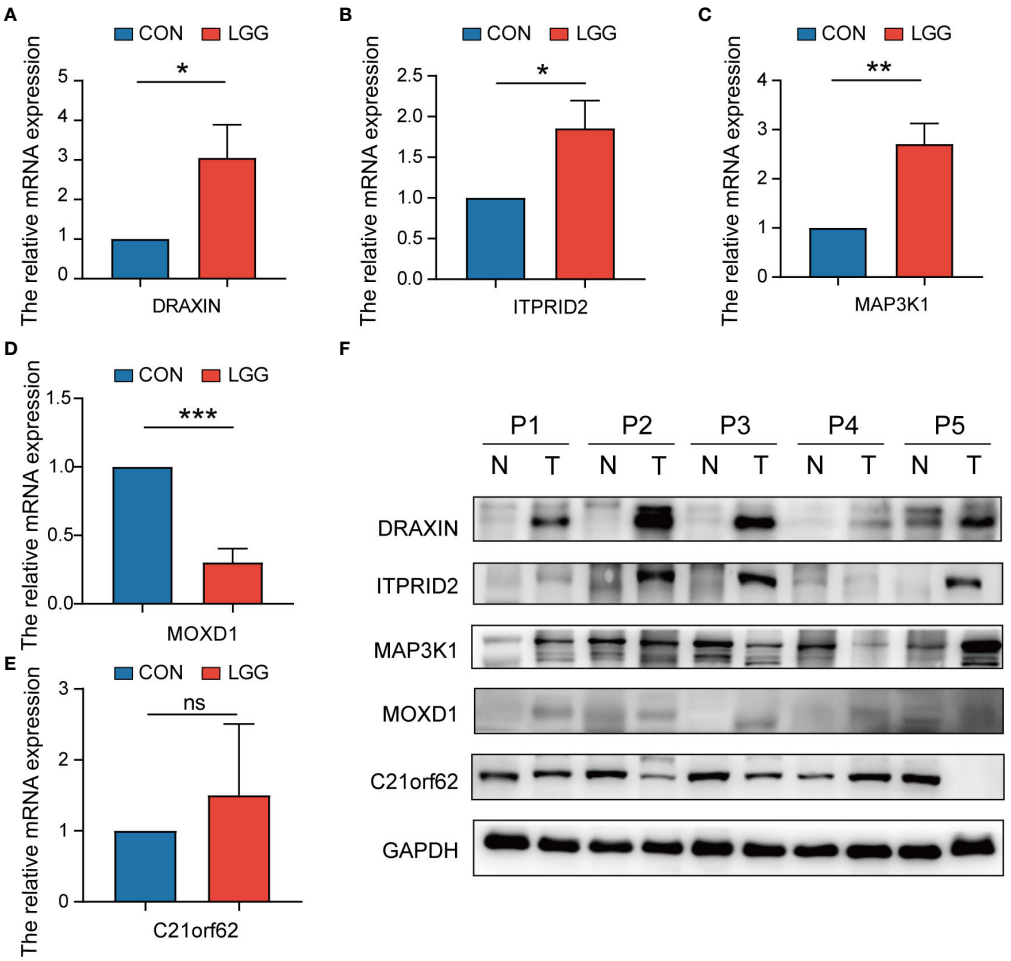

FIGURE 14
The expressions of five signature genes were validated by quantitative real-time PCR (qRT-PCR) and Western blotting (WB). **(A–E)** Expression of genes at the mRNA level by qRT-PCR. **(F)** Expression of genes at the protein level by WB. qRT-PCR, quantitative real-time PCR; WB, Western blotting. *$P< 0.05$; **$P< 0.01$; ***$P< 0.001$. ns, no significance.

treatment. To further validate the speculations, we analyzed the patterns of immune checkpoints and chemoradiotherapy-associated genes. *AKR1C1, EGFR, EZH2, HOX9, HGMT, SOX2*, and *TBX5* have been implicated in chemoradiotherapy resistance due to their roles in DNA damage repairing, signaling, angiogenesis, and TME remodeling (49–51). For example, the overexpression of *AKR1C1* can reduce the production of reactive oxygen species, eliminate free radicals, and inactivate anthracycline anticancer drugs, thereby decreasing DNA damage and inhibiting cell apoptosis, which can finally reduce the sensitivity of chemotherapy (24). High *EGFR* expression was associated with poor response to radiation or chemoradiotherapy, and specifically targeting EGFR and EGFR variant receptors is undergoing clinical evaluation in patients with glioma (52). Consistent with the above assumption, we verified that different subtypes vary significantly in the expression of the therapy-associated genes, including CRSGs and ICGs. In addition, the characteristics of the TME like the stromal score, immune score, and ESTIMATE score also indicated significant differences. Increasing evidence has shown that multiple immune cells play a vital role in the immune defense of LGG (53). The densities of tumor-infiltrating T cells were also proven to be critical for the initial stage and development of LGG, and the γδT cell can effectively recognize and kill tumor cells (54). Here, we observed striking differences in the type of CD4+ T cell, CD56+ T cell, γδT cell, and T helper2 cell between subtypes, which demonstrates a close relevance between cuproptosis and tumor immunity. These results strongly implied the potential roles of cuproptosis in LGG prognosis.

The essence of cuproptosis is a copper-induced cell death mediated by protein lipoylation (6). TCA enzymes (in particular, the PDH complex) are indispensable for initiating lipoylation, which contributes to the induction of HSP70 and is reflective of

acute proteotoxic stress (7). Consistent with the facts, functional enrichment analyses demonstrated that protein alteration like localization to the microtubule organizing center, polyubiquitination, lysine degradation, ubiquitin-mediated proteolysis, and citrate cycle TCA cycle processes showed a significant difference in the subtypes we identified. Moreover, our results revealed that the G2M checkpoint, E2F targets, MYC targets, epithelial–mesenchymal transition, and angiogenesis were also mainly associated with different subtypes based on the CRG expression, which have been known in the progression of malignancies (55–57). In addition, the GO and KEGG results about the differential expression genes between subtypes indicated a close link between cuproptosis and the cell cycle as well as genomic stability, including organelle fission, nuclear division, and chromosome segregation. As many studies have illustrated the role of copper metabolism in cancer, our study added to the evidence that directly or indirectly targeting cuproptosis may bring a satisfactory effect in anti-glioma therapy.

Increasing evidence has illustrated the function of copper in the initial stage and progression of tumors at the transcriptomic level (58). In this study, mRNA transcriptome differences between distinct cuproptosis patterns have also been explored. Through multivariate Cox analyses about DEGs between CRG clusters, 1,424 OS-associated DEGs remained. Similar to the clustering of the CRG phenotypes, three genomic subtypes were identified based on the above DEGs, which demonstrated a close relationship with patients' prognosis, indicating its predictive ability for LGG. To better evaluate the cuproptosis pattern of individual patients with LGG, we further constructed a predictive cuproptosis-related prognostic model and a CRG score system, which consisted of *C21orf62*, *DRAXIN*, *ITPRID2*, *MAP3K1*, and *MOXD1*. As a coding gene for chromosome 21 open reading frame, *C21orf62* has a great impact on the gene structure, thus regulating the biological homeostasis (59). *DRAXIN*, a recently identified axon guidance protein, is crucial for the formation of forebrain commissures and repulsion of netrin-stimulated spinal commissural axons (60, 61). *DRAXIN* also plays a vital role in lung carcinomas (62). However, its role in LGG remains elusive. *ITPRID2*, also known as *SSFA2*, has been reported in the development of many malignancies (63, 64). In LGG, the inhibition of *ITPRID2* can regulate the cell cycle to significantly reduce the proliferation ability and induce the early apoptosis rate (65). As a member of mitogen-activated protein kinases, *MAP3K1* is an important regulator of evolutionarily conserved proteins in various cellular physiologies (66). Numerous studies have confirmed that the activation of MAPKs was positively correlated to the progression and therapy resistance of glioma (67). Based on the public database, Xie and his colleagues identified *MAP3K1* as a novel prognostic biomarker and potential therapeutic target in glioma (68). *MOXD1* has also been predicted to enable copper ion–binding activity (69), and *MOXD1* knockdown significantly suppresses the proliferation and tumor growth of glioblastoma cells *via* ER stress-inducing apoptosis (70). Accumulating evidence seems to indicate the potential roles of signature genes in glioma. In our validation experiments, although there was heterogeneity in their expressions at the protein level, almost all genes were significantly verified at the mRNA level. Further function enrichment analyses based on a single gene also demonstrated a close link between signature genes and immunity as well as malignant processes. Meanwhile, patients with gene cluster B exhibited a higher CRG score and the worst outcomes, and a higher CRG score is usually accompanied by higher expression levels of CRGs in LGG tissues. Correlation analysis among the CRG cluster, gene cluster, CRG score, and survival status further indicated our scoring system's robust and stable prognostic-predictive ability. The distribution plots and K-M plot validated that survival times decreased when the CRG score increased in the TCGA training and validation cohorts. In addition, this prediction ability was further confirmed by two cohorts from CGGA as well. Furthermore, patients with low- and high-risk CRG scores showed significant differences in responses to radiotherapy or chemotherapy. Taken together, we demonstrated an independent and predictive role of CRG score in LGG.

Accumulative in-depth research has suggested some prognosis factors for LGG. Immunobiology has been acknowledged as a dominant factor for malignant processes (71). Additionally, the immune infiltrating cell signature has also been indicated as a prognostic marker in gliomas (72, 73). As copper has been strongly indicated in the regulation of immunity (74), identifying the role of cuproptosis in the TME cell infiltration might enhance our understanding of LGG antitumor therapy response, thus guiding more effective immunotherapy strategies. In this study, GSEA enrichment analysis illustrated the key role of immune processes between high- and low-risk CRG score patients. The patterns characterized by the immune-inflamed phenotype, higher stromal score, and higher ESTIMATE score exhibited a higher CRG score, while the other showed a lower CRG score. Five OS-associated gene signatures were found to be significantly correlated with immune cells. In addition, a higher CRG score was positively associated with the infiltration of B cells naive, macrophages M0 and M1, T cells CD4 memory activated and T cells follicular helper, while it was negatively correlated with mast cells activated, monocytes, and NK cells activated. Evidence has shown the crucial roles of these cells in LGG. Myeloid-derived suppressive cells were reported to promote B-cell-mediated immunosuppression *via* the transfer of PD-L1 in gliomas (75). Infiltrated tumor-associated macrophages have been revealed to be negatively associated with the survival of glioma patients, and its related prognostic model based on MScores demonstrated a high accuracy rate (76). T cells were thought to infiltrate gliomas at an early stage, mediating immunosuppression and resistance to

treatment (77). NK-cell-targeted therapies have also been highlighted in the immune escape of IDHmut gliomas (78). As immune cells participate in various biologies, including tumorigenesis and progression of LGG, targeting these cells may benefit LGG patients with unfavorable prognosis. Meanwhile, combined with the potential correlation between the above signature genes and immune checkpoints, targeting these immune checkpoints may benefit patients more. Furthermore, we noticed that the RNA stemness score increased with increasing CRG score, suggesting the critical role of cuproptosis patterns in LGG tumor maintenance.

Despite great advances in LGG therapy over the past decade, a substantial room for progress remains and improvements are in demand. Even standard-of-care multimodal treatment approaches including surgery, radiation, immunotherapy, and chemotherapy have been proposed (79); LGG patients show heterogeneity in their treatment response and outcomes when considering the pathologic features, especially in terms of mutation and therapy resistance (80). Further studies are required to assess the impact of intratumor heterogeneity and its TMB characteristic on prognosis and response to treatment. Alireza Mansouri and his colleagues reported that the methylation of the *MGMT* promoter provides better outcome prediction when patients receive temozolomide chemotherapy (81). *IDH1/2* mutation, which induced a high concentration of 2-hydroxyglutarate through the upregulation of *HIF-1α* and *VEGF*, could also benefit the patients (82). Similar to previous studies, our data revealed a markable difference in tumor mutation burden between CRG score subgroups. Patients with a low CRG score showed a higher rate of *IDH1* and *IDH2* mutation. In addition, the lower mutation rates of *TP53*, *EGFR*, and *PTEN* were also observed in low-risk patients, which has been demonstrated to correlate with worse clinical outcomes (83). Additionally, it has been reported that *ATRX* and *CIC* can also influence the prognosis. The profiling of gliomas has revealed that the majority (~75%) of low-grade gliomas that carry *IDH1* and *TP53* mutations also harbor *ATRX* mutations, thus underscoring their crucial role in gliomagenesis, which has been indicated in the procession of impairing non-homologous end-joining DNA repair (84, 85). Recent genomic analyses of brain cancers have implicated *CIC* as a critical suppressor gene in diffuse gliomas (86). Here, we discovered the significant mutations of these genes in our cohort, which provides a deeper understanding of LGG. Given the correlation between TMB and enhanced clinical response to immunotherapy, we further explored immunotherapy effectiveness in the subgroups of LGG. In the present study, 33 immune checkpoints were observed to be differentially expressed in the two groups. Five CRG signatures and the total CRG score were respectively associated with *CD276*, *BTN2A2*, and *PDCD1LG2*, which may be a potential treatment response predictor in the clinic.

Furthermore, we explored the role of cuproptosis patterns in the radiation and chemotherapy of LGG. Results showed a correlation between the CRG score and expression profiles of radiotherapy-associated genes. Targeting CRGs might contribute to enhancing therapeutic effects. Moreover, it has been considered reasonable to apply adjuvant temozolomide for patients with gliomas (87). TMZ can act as a radiosensitizer and be given full consideration to be part of standard treatment for newly diagnosed glioblastoma (88, 89). In our study, we discovered that patients with low CRG scores were more susceptive to the TMZ and procarbazine, suggesting a higher response to treatment and better clinical outcomes. Though low-risk patients in CGGA here did not benefit from the addition of TMZ, the complexity of TMZ in LGG is still worth exploring. Finally, to further improve the performance and facilitate the application of the CRG score, we established a quantitative nomogram that can be used for the prognosis stratification of LGG patients. Given the superior performance validated by multiple cohorts, the nomogram enables patients and physicians to create a more individualized surveillance program for LGG, thus improving the prognosis.

Nevertheless, there are still several issues to be addressed. First, the CRG risk signature was conducted based on the data retrospectively obtained from public databases, which was inevitably limited by an inherent case selection bias. More large-scale prospective and multicenter clinical studies are needed to confirm our findings. Second, some critical clinical variables like chemoradiotherapy and surgery were lacking for analysis in some datasets, which may influence the results of treatment response and cuproptosis state analyses. Though we analyzed several immunotherapy datasets in this study, most of them were not based on data from LGGs, which should be further studied. Furthermore, more clinical pathology samples should be included for validating the expression of signature genes, and more functional *in vivo* or *in vitro* experiments are further needed to verify the roles of signature genes in the future.

Conclusion

Briefly, we demonstrated a comprehensive overview of CRG profiles in LGG and established a novel risk model for LGG patients' therapies status and prognosis, which was partially constituted by a 5-CRG signature (*C21orf62*, *DRAXIN*, *ITPRID2*, *MAP3K1* and *MOXD1*). We also determined the roles of these genes in LGG by affecting the tumor-immune-stromal microenvironment, clinical features, therapy strategies, and prognosis. These findings highlight the potential clinical implications of CRGs, suggesting that cuproptosis may be the potential therapeutic target for patients with LGG.

Data availability statement

The analyzed data could be obtained at TGCA (https://portal.gdc.cancer.gov/) and CGGA (www.cgga.org.cn) databases. The code applied in the study is available from the corresponding author on reasonable request. The accession number(s) can be found in the article/Supplementary Material.

Ethics statement

The studies involving human participants were reviewed and approved by The Institutional Ethics Committee for Clinical Research and Animal Trials of the Sun Yat-sen University Cancer Center (B2022-246-01). The patients/participants provided their written informed consent to participate in this study.

Author contributions

JB developed the study concept and design, JB and WC-L performed data acquisition, bioinformatics and statistical data analyses. JB, WC-L and HD drafted the manuscript together. HD collected clinic samples. WC-L and YY performed the validation experiments. JB, WC-L and HD constructed the figures and tables. WT-L, YL and YS were responsible for the integrity of the entire study and manuscript review. All authors contributed to the article and approved the submitted version.

Funding

This study was supported by the National Natural Science Foundation of China (81800996).

Conflict of interest

The authors declare that the research was conducted in the absence of any commercial or financial relationships that could be construed as a potential conflict of interest.

The reviewers RS and FD declared a shared affiliation with the authors to the handling editor at time of review.

Publisher's note

All claims expressed in this article are solely those of the authors and do not necessarily represent those of their affiliated organizations, or those of the publisher, the editors and the reviewers. Any product that may be evaluated in this article, or claim that may be made by its manufacturer, is not guaranteed or endorsed by the publisher.

Supplementary material

The Supplementary Material for this article can be found online at: https://www.frontiersin.org/articles/10.3389/fimmu.2022.933973/full#supplementary-material

References

1. Schiff D, Van den Bent M, Vogelbaum MA, Wick W, Miller CR, Taphoorn M, et al. Recent developments and future directions in adult lower-grade gliomas: Society for neuro-oncology (Sno) and European association of neuro-oncology (Eano) consensus. *Neuro Oncol* (2019) 21(7):837–53. doi: 10.1093/neuonc/noz033

2. Brat DJ, Verhaak RGW, Aldape KD, Yung WKA, Salama SR, Cooper LAD, et al. Comprehensive, integrative genomic analysis of diffuse lower-grade gliomas. *N Engl J Med* (2015) 372(26):2481–98. doi: 10.1056/NEJMoa1402121

3. Weller M, van den Bent M, Tonn JC, Stupp R, Preusser M, Cohen-Jonathan-Moyal E, et al. European Association for neuro-oncology (Eano) guideline on the diagnosis and treatment of adult astrocytic and oligodendroglial gliomas. *Lancet Oncol* (2017) 18(6):e315–e29. doi: 10.1016/S1470-2045(17)30194-8

4. Ater JL, Zhou T, Holmes E, Mazewski CM, Booth TN, Freyer DR, et al. Randomized study of two chemotherapy regimens for treatment of low-grade glioma in young children: A report from the children's oncology group. *J Clin Oncol* (2012) 30(21):2641–7. doi: 10.1200/JCO.2011.36.6054

5. Kiran M, Chatrath A, Tang X, Keenan DM, Dutta A. A prognostic signature for lower grade gliomas based on expression of long non-coding rnas. *Mol Neurobiol* (2019) 56(7):4786–98. doi: 10.1007/s12035-018-1416-y

6. Tsvetkov P, Coy S, Petrova B, Dreishpoon M, Verma A, Abdusamad M, et al. Copper induces cell death by targeting lipoylated tca cycle proteins. *Science* (2022) 375(6586):1254–61. doi: 10.1126/science.abf0529

7. Tang D, Chen X, Kroemer G. Cuproptosis: A copper-triggered modality of mitochondrial cell death. *Cell Res* (2022) 32(5):417–18. doi: 10.1038/s41422-022-00653-7

8. Trammell R, Rajabimoghadam K, Garcia-Bosch IA-O. Copper-promoted functionalization of organic molecules: From biologically relevant Cu/O(2) model systems to organometallic transformations. *Chem Rev* (2019) 119(4):2954–3031. doi: 10.1021/acs.chemrev.8b00368

9. Kim BE, Nevitt T, Thiele DJ. Mechanisms for copper acquisition, distribution and regulation. *Nat Chem Biol* (2008) 4(3):176–85. doi: 10.1038/nchembio.72

10. Rae TD, Schmidt Pj Fau - Pufahl RA, Pufahl Ra Fau - Culotta VC, Culotta Vc Fau - O'Halloran TV, O'Halloran TV. Undetectable intracellular free copper: The requirement of a copper chaperone for superoxide dismutase. *Sci (New York N.Y.)* (1999) 284(5415):805–8. doi: 10.1126/science.284.5415.805

11. Denoyer D, Masaldan S, La Fontaine S, Cater MA. Targeting copper in cancer therapy: 'Copper that cancer'. *Metallomics* (2015) 7(11):1459–76. doi: 10.1039/c5mt00149h

12. Hodgkinson V, Petris MJ. Copper homeostasis at the host-pathogen interface. *J Biol Chem* (2012) 287(17):13549–55. doi: 10.1074/jbc.R111.316406

13. Tsang T, Posimo JM, Gudiel AA, Cicchini M, Feldser DM, Brady DC. Copper is an essential regulator of the autophagic kinases Ulk1/2 to drive lung adenocarcinoma. *Nat Cell Biol* (2020) 22(4):412–24. doi: 10.1038/s41556-020-0481-4

14. Ramchandani D, Berisa M, Tavarez DA, Li Z, Miele M, Bai Y, et al. Copper depletion modulates mitochondrial oxidative phosphorylation to impair triple negative breast cancer metastasis. *Nat Commun* (2021) 12(1):7311. doi: 10.1038/s41467-021-27559-z

15. Wang J, Luo C, Shan C, You Q, Lu J, Elf S, et al. Inhibition of human copper trafficking by a small molecule significantly attenuates cancer cell proliferation. *Nat Chem* (2015) 7(12):968–79. doi: 10.1038/nchem.2381

16. Guntuku L, Naidu VGM, Yerra VG. Mitochondrial dysfunction in gliomas: Pharmacotherapeutic potential of natural compounds. *Curr Neuropharmacol* (2016) 14(6):567–83. doi: 10.2174/1570159X14666160121115641

17. Yuan S, Lu Y, Yang J, Chen G, Kim S, Feng L, et al. Metabolic activation of mitochondria in glioma stem cells promotes cancer development through a reactive oxygen species-mediated mechanism. *Stem Cell Res Ther* (2015) 6:198. doi: 10.1186/s13287-015-0174-2

18. Ordys BB, Launay S, Deighton RF, McCulloch J, Whittle IR. The role of mitochondria in glioma pathophysiology. *Mol Neurobiol* (2010) 42(1):64–75. doi: 10.1007/s12035-010-8133-5

19. Liang J, Cao R, Wang X, Zhang Y, Wang P, Gao H, et al. Mitochondrial Pkm2 regulates oxidative stress-induced apoptosis by stabilizing Bcl2. *Cell Res* (2017) 27(3):329–51. doi: 10.1038/cr.2016.159

20. Huang H, Zhang S, Li Y, Liu Z, Mi L, Cai Y, et al. Suppression of mitochondrial ros by prohibitin drives glioblastoma progression and therapeutic resistance. *Nat Commun* (2021) 12(1):3720. doi: 10.1038/s41467-021-24108-6

21. Yang C, He L, Chen G, Ning Z, Xia Z. Lrrc8a potentiates temozolomide sensitivity in glioma cells *Via* activating mitochondria-dependent apoptotic pathway. *Hum Cell* (2019) 32(1):41–50. doi: 10.1007/s13577-018-0221-2

22. Wilkerson MD, Hayes DN. Consensusclusterplus: A class discovery tool with confidence assessments and item tracking *Bioinformatics* (2010) 26(12):1572–3. doi: 10.1093/bioinformatics/btq170

23. Hu F-F, Liu C-J, Liu L-L, Zhang Q, Guo A-Y. Expression profile of immune checkpoint genes and their roles in predicting immunotherapy response. *Brief Bioinform* (2021) 22(3):bbaa176. doi: 10.1093/bib/bbaa176

24. Zeng C-M, Chang L-L, Ying M-D, Cao J, He Q-J, Zhu H, et al. Aldo-keto reductase Akr1c1-Akr1c4: Functions, regulation, and intervention for anti-cancer therapy. *Front Pharmacol* (2017) 8:119. doi: 10.3389/fphar.2017.00119

25. Schlegel J, Merdes A, Stumm G, Albert FK, Forsting M, Hynes N, et al. Amplification of the epidermal-Growth-Factor-Receptor gene correlates with different growth behaviour in human glioblastoma. *Int J Cancer* (1994) 56(1):72–7. doi: 10.1002/ijc.2910560114

26. Liu H, Sun Q, Sun Y, Zhang J, Yuan H, Pang S, et al. Melk and Ezh2 cooperate to regulate medulloblastoma cancer stem-like cell proliferation and differentiation. *Mol Cancer Res* (2017) 15(9):1275–86. doi: 10.1158/1541-7786.MCR-17-0105

27. Gonçalves C, Xavier-Magalhães A, Martins E, Pinto AA, Pires MM, Pinheiro C, et al. A novel molecular link between Hoxa9 and Wnt6 in glioblastoma identifies a subgroup of patients with particular poor prognosis. *Mol Oncol* (2020) 14(6):1224–41. doi: 10.1002/1878-0261.12633

28. Molinaro AA-O, Taylor JW, Wiencke JK, Wrensch MR. Genetic and molecular epidemiology of adult diffuse glioma. *Nat Rev Neurol* (2019) 15 (7):405–17. doi: 10.1038/s41582-019-0220-2

29. Yoshihara K, Shahmoradgoli M, Martínez E, Vegesna R, Vegesna R, Kim H, et al. Inferring tumour purity and stromal and immune cell admixture from expression data. *Nat Commun* (2013) 4:2612. doi: 10.1038/ncomms3612

30. Yu G, Wang L-G, Han Y, He Q-Y. Clusterprofiler: An r package for comparing biological themes among gene clusters. *OMICS* (2012) 16(5):284–7. doi: 10.1089/omi.2011.0118

31. Newman AM, Liu CL, Green M, Gentles A, Feng W, Xu Y, et al. Robust enumeration of cell subsets from tissue expression profiles. *Nat Methods* (2015) 12 (5):453–7. doi: 10.1038/nmeth.3337

32. Jiang P, Gu S, Pan D, Fu J, Sahu A, Hu X, et al. Signatures of T cell dysfunction and exclusion predict cancer immunotherapy response. *Nat Med* (2018) 24(10):1550–8. doi: 10.1038/s41591-018-0136-1

33. Braun DA, Hou Y, Bakouny Z, Ficial M, Sant' Angelo M, Forman J, et al. Interplay of somatic alterations and immune infiltration modulates response to pd-1 blockade in advanced clear cell renal cell carcinoma. *Nat Med* (2020) 26(6):909–18. doi: 10.1038/s41591-020-0839-y

34. Mariathasan S, Turley SJ, Nickles D, Castiglioni A, Yuen K, Wang Y, et al. Tgfβ attenuates tumour response to pd-L1 blockade by contributing to exclusion of T cells. *Nature* (2018) 554(7693):544–8. doi: 10.1038/nature25501

35. Zhang H, Dai Z, Wu W, Wang Z, Zhang N , Zhang L, et al. Regulatory mechanisms of immune checkpoints pd-L1 and ctla-4 in cancer. *J Exp Clin Cancer Res* (2021) 40(1):184. doi: 10.1186/s13046-021-0198-7

36. Gibney GT, Weiner LM , Atkins MB. Predictive biomarkers for checkpoint inhibitor-based immunotherapy. *Lancet Oncol* (2016) 17(12):e542–e551. doi: 10.1016/S1470-2045(16)30406-5

37. Strasser A, Vaux DL. Cell death in the origin and treatment of cancer. *Mol Cell* (2020) 78(6):1045–54. doi: 10.1016/j.molcel.2020.05.014

38. Bertheloot D, Latz E, Franklin BS. Necroptosis, pyroptosis and apoptosis: An intricate game of cell death. *Cell Mol Immunol* (2021) 18(5):1106–21. doi: 10.1038/s41423-020-00630-3

39. Hanahan D. Hallmarks of cancer: New dimensions. *Cancer Discovery* (2022) 12(1):31–46. doi: 10.1158/2159-8290.CD-21-1059

40. Villa E, Ricci JE. How does metabolism affect cell death in cancer? *FEBS J* (2016) 283(14):2653–60. doi: 10.1111/febs.13570

41. Leaver HA, Rizzo MT, Whittle IR. Glioma cell death: Cell-cell interactions and signalling networks. *Mol Neurobiol* (2010) 42(1):89–96. doi: 10.1007/s12035-010-8135-3

42. Colquhoun A. Lipids, mitochondria and cell death: Implications in neuro-oncology. *Mol Neurobiol* (2010) 42(1):76–88. doi: 10.1007/s12035-010-8134-4

43. Liu B, Liu J, Liu K, Huang H, Li Y, Hu X, et al. A prognostic signature of five pseudogenes for predicting lower-grade gliomas. *BioMed Pharmacother* (2019) 117:109116. doi: 10.1016/j.biopha.2019.109116

44. Bai Z, Wang X, Zhang Z. Establishment and validation of a 5 M6a rna methylation regulatory gene prognostic model in low-grade glioma. *Front Genet* (2022) 13:655169. doi: 10.3389/fgene.2022.655169

45. Tan YQ, Li YT, Yan TF, Xu Y, Liu BH, Yang JA, et al. Six immune associated genes construct prognostic model evaluate low-grade glioma. *Front Immunol* (2020) 11:606164. doi: 10.3389/fimmu.2020.606164

46. Zhao J, Liu Z, Zheng X, Gao H, Li L. Prognostic model and nomogram construction based on a novel ferroptosis-related gene signature in lower-grade glioma. *Front Genet* (2021) 12:753680. doi: 10.3389/fgene.2021.753680

47. Zheng J, Zhou Z, Qiu Y, Wang M, Yu H, Wu Z, et al. A pyroptosis-related gene prognostic index correlated with survival and immune microenvironment in glioma. *J Inflammation Res* (2022) 15:17–32. doi: 10.2147/JIR.S341774

48. Tsang T, Davis CI, Brady DC. Copper biology. *Curr Biol* (2021) 31(9):R421–R427. doi: 10.1016/j.cub.2021.03.054

49. Jin X, Kim LJY, Wu Q, Wallace LC, Prager BC, Sanvoranart T, et al. Targeting glioma stem cells through combined Bmi1 and Ezh2 inhibition. *Nat Med* (2017) 23(11):1352–61. doi: 10.1038/nm.4415

50. Stupp R, Hegi ME, Gilbert MR, Chakravarti A. Chemoradiotherapy in malignant glioma: Standard of care and future directions. *J Clin Oncol* (2007) 25 (26):4127–36. doi: 10.1200/JCO.2007.11.8554

51. Geraldo LHM, Garcia C, da Fonseca ACC, Dubois LGF, de Sampaio E Spohr TCL, Matias D, et al. Glioblastoma therapy in the age of molecular medicine. *Trends Cancer* (2019) 5(1):46–65. doi: 10.1016/j.trecan.2018.11.002

52. Jackson HJ, Rafiq S, Brentjens RJ. Driving car T-cells forward. *Nat Rev Clin Oncol* (2016) 13(6):370–83. doi: 10.1038/nrclinonc.2016.36

53. Gieryng A, Pszczolkowska D, Walentynowicz KA, Rajan WD, Kaminska B. Immune microenvironment of gliomas. *Lab Invest* (2017) 97(5):498–518. doi: 10.1038/labinvest.2017.19

54. Kane JR, Zhao J, Tsujiuchi T, Laffleur BA-O, Arrieta VA, Mahajan A, et al. Cd8(+) T-Cell-Mediated immunoediting influences genomic evolution and immune evasion in murine gliomas. *Clin Cancer Res* (2020) 26(16):4390–401. doi: 10.1158/1078-0432.CCR-19-3104

55. Ramjiawan RR, Griffioen AW, Duda DG. Anti-angiogenesis for cancer revisited: Is there a role for combinations with immunotherapy? *Angiogenesis* (2017) 20(2):185–204. doi: 10.1007/s10456-017-9552-y

56. Dongre A, Weinberg RA. New insights into the mechanisms of epithelial-mesenchymal transition and implications for cancer. *Nat Rev Mol Cell Biol* (2019) 20(2):69–84. doi: 10.1038/s41580-018-0080-4

57. Powles RL, Wali VB, Li X, Barlow WE, Nahleh Z, Thompson AM, et al. Analysis of pre- and posttreatment tissues from the swog S0800 trial reveals an effect of neoadjuvant chemotherapy on the breast cancer genome. *Clin Cancer Res* (2020) 26(8):1977–84. doi: 10.1158/1078-0432.CCR-19-2405

58. Tisato F, Marzano C, Porchia M, Pellei M, Santini C. Copper in diseases and treatments, and copper-based anticancer strategies. *Med Res Rev* (2010) 30(4):708–49. doi: 10.1002/med.20174

59. Gardiner K, Slavov D, Bechtel L, Davisson M. Annotation of human chromosome 21 for relevance to down syndrome: Gene structure and expression analysis. *Genomics* (2002) 79(6):833–43. doi: 10.1006/geno.2002.6782

60. Ahmed G, Shinmyo Y Fau - Ohta K, Ohta K Fau - Islam SM, Islam Sm Fau - Hossain M, Hossain M Fau - Naser IB, Naser Ib Fau - Riyadh MA, et al. Draxin inhibits axonal outgrowth through the netrin receptor DCC. *J Neurosci* (2011) 31 (39):14018–23. doi: 10.1523/JNEUROSCI.0943-11.2011

61. Morcom L, Edwards TJ, Rider E, Jones-Davis D, Lim JW, Chen K-S, et al. Draxin regulates interhemispheric fissure remodelling to influence the extent of corpus callosum formation. *Elife* (2021) 10:e61618. doi: 10.7554/eLife.61618

62. Sato Y, Matsuo A, Kudoh S, Fang L, Hasegawa K, Shinmyo Y, et al. Expression of draxin in lung carcinomas. *Acta Histochem Cytochem* (2018) 51 (1):53–62. doi: 10.1267/ahc.17035

63. Wang W, Yi J, Dong D, Mao W, Wang X, Yan Z. Mirna-877-5p inhibits malignant progression of prostate cancer by directly targeting Ssfa2. *Eur J Histochem* (2021) 65(3):3243. doi: 10.4081/ejh.2021.3243

64. Fujimoto T, Koyanagi M, Baba I, Nakabayashi K, Kato N, Sasazuki T, et al. Analysis of krap expression and localization, and genes regulated by krap in a human colon cancer cell line. *J Hum Genet* (2007) 52(12):978–84. doi: 10.1007/s10038-007-0204-8

65. Zhu A, Li X, Wu H, Miao Z, Yuan F, Zhang F, et al. Molecular mechanism of Ssfa2 deletion inhibiting cell proliferation and promoting cell apoptosis in glioma. *Pathol Res Pract* (2019) 215(3):600–6. doi: 10.1016/j.prp.2018.12.035

66. Uhlik MT, Abell AN, Cuevas BD, Nakamura K, Johnson GL. Wiring diagrams of mapk regulation by Mekk1, 2, and 3. *Biochem Cell Biol* (2004) 82 (6):658–63. doi: 10.1139/o04-114

67. Ma L, Liu J, Zhang X, Qi J, Yu W, Gu Y, et al. P38 mapk-dependent Nrf2 induction enhances the resistance of glioma cells against TMZ. *Med Oncol* (2015) 32(3):69. doi: 10.1007/s12032-015-0517-y

68. Wang J, Zuo J, Wahafu A, M-d W, Li R-C, Xie W-F. Combined elevation of Trib2 and Map3k1 indicates poor prognosis and chemoresistance to temozolomide in glioblastoma. *CNS Neurosci Ther* (2020) 26(3):297–308. doi: 10.1111/cns.13197

69. Xin X, Mains RE, Eipper BA, Monooxygenase X. A member of the copper-dependent monooxygenase family localized to the endoplasmic reticulum. *J Biol Chem* (2004) 279(46):48159–67. doi: 10.1074/jbc.M407486200

70. Shi P, Xu J, Xia F, Wang Y, Ren J, Liang P, et al. Moxd1 knockdown suppresses the proliferation and tumor growth of glioblastoma cells *Via* er stress-inducing apoptosis. *Cell Death Discovery* (2022) 8(1):174. doi: 10.1038/s41420-022-00976-9

71. Dunn GP, Old LJ, Schreiber RD. The immunobiology of cancer immunosurveillance and immunoediting. *Immunity* (2004) 21(2):137–48. doi: 10.1016/j.immuni.2004.07.017

72. Zhang H, Wang Z, Dai Z, Wu W, Cao H, Li S, et al. Novel immune infiltrating cell signature based on cell pair algorithm is a prognostic marker in cancer. *Front Immunol* (2021) 12:694490. doi: 10.3389/fimmu.2021.694490

73. Zhang N, Zhang H, Wang Z, Dai Z, Zhang X, Cheng Q, et al. Immune infiltrating cells-derived risk signature based on Large-scale analysis defines immune landscape and predicts immunotherapy responses in glioma tumor microenvironment. *Front Immunol* (2021) 12:691811. doi: 10.3389/fimmu.2021.691811

74. Culbertson EM, Culotta VC. Copper in infectious disease: Using both sides of the penny. *Semin Cell Dev Biol* (2021) 115:19–26. doi: 10.1016/j.semcdb.2020.12.003

75. Lee-Chang C, Rashidi A, Miska J, Zhang P, Pituch KC, Hou D, et al. Myeloid-derived suppressive cells promote b cell-mediated immunosuppression *Via* transfer of pd-L1 in glioblastoma. *Cancer Immunol Res* (2019) 7(12):1928–43. doi: 10.1158/2326-6066.CIR-19-0240

76. Zhang H, Luo YB, Wu W, Zhang L, Wang Z , Dai Z, et al. The molecular feature of macrophages in tumor immune microenvironment of glioma patients. *Comput Struct Biotechnol J* (2021)19:4603–4618. doi: 10.1016/j.csbj.2021.08.019.

77. Choi BD, Maus MV, June CH, Sampson JH. Immunotherapy for glioblastoma: Adoptive T-cell strategies. *Clin Cancer Res* (2019) 25(7):2042–8. doi: 10.1158/1078-0432.CCR-18-1625

78. Lupo KB, Matosevic S. Cd155 immunoregulation as a target for natural killer cell immunotherapy in glioblastoma. *J Hematol Oncol* (2020) 13(1):76. doi: 10.1186/s13045-020-00913-2

79. Yang K, Wu Z, Zhang H, Zhang N, Wu W , Wang Z, et al. Glioma targeted therapy: Insight into future of molecular approaches. *Mol Cancer* (2022) 21(1):39. doi: 10.1186/s12943-022-01513-z.

80. Vitucci M, Irvin DM, McNeill RS, Schmid RS, Simon JM, Dhruv HD, et al. Genomic profiles of low-grade murine gliomas evolve during progression to glioblastoma. *Neuro Oncol* (2017) 19(9):1237–47. doi: 10.1093/neuonc/nox050

81. Mansouri A, Hachem LD, Mansouri S, Nassiri F, Laperriere NJ, Xia D, et al. Mgmt promoter methylation status testing to guide therapy for glioblastoma: Refining the approach based on emerging evidence and current challenges. *Neuro Oncol* (2019) 21(2):167–78. doi: 10.1093/neuonc/noy132

82. Mirchia K, Richardson TE. Beyond idh-mutation: Emerging molecular diagnostic and prognostic features in adult diffuse gliomas. *Cancers (Basel)* (2020) 12(7):1817. doi: 10.3390/cancers12071817

83. Kristensen BW, Priesterbach-Ackley LP, Petersen JK, Wesseling P. Molecular pathology of tumors of the central nervous system. *Ann Oncol* (2019) 30(8):1265–78. doi: 10.1093/annonc/mdz164

84. Koschmann C, Calinescu A-A, Nunez FJ, Mackay A, Fazal-Salom J, Thomas D, et al. Atrx loss promotes tumor growth and impairs nonhomologous end joining DNA repair in glioma. *Sci Transl Med* (2016) 8(328):328ra28. doi: 10.1126/scitranslmed.aac8228

85. Danussi C, Bose P, Parthasarathy PT, Silberman PC, Van Arnam JS, Vitucci M, et al. Atrx inactivation drives disease-defining phenotypes in glioma cells of origin through global epigenomic remodeling. *Nat Commun* (2018) 9(1):1057. doi: 10.1038/s41467-018-03476-6

86. Bettegowda C, Agrawal N, Jiao Y, Sausen M, Wood LD, Hruban RH, et al. Mutations in cic and Fubp1 contribute to human oligodendroglioma. *Science* (2011) 333(6048):1453–5. doi: 10.1126/science.1210557

87. Agarwala SS, Kirkwood JM. Temozolomide, a novel alkylating agent with activity in the central nervous system, may improve the treatment of advanced metastatic melanoma. *Oncologist* (2000) 5(2):144–51. doi: 10.1634/theoncologist.5-2-144

88. van Rijn J, Heimans JJ, van den Berg J, van der Valk P, Slotman BJ. Survival of human glioma cells treated with various combination of temozolomide and X-rays. *Int J Radiat Oncol Biol Phys* (2000) 47(3):779–84. doi: 10.1016/S0360-3016(99)00539-8

89. Kil WJ, Cerna D, Burgan WE, Beam K, Carter D, Steeg PS, et al. *In vitro* and in vivo radiosensitization induced by the DNA methylating agent temozolomide. *Clin Cancer Res* (2008) 14(3):931–8. doi: 10.1158/1078-0432.CCR-07-1856

COPYRIGHT

© 2022 Bao, Lu, Duan, Ye, Li, Liao, Li and Sun. This is an open-access article distributed under the terms of the Creative Commons Attribution License (CC BY). The use, distribution or reproduction in other forums is permitted, provided the original author(s) and the copyright owner(s) are credited and that the original publication in this journal is cited, in accordance with accepted academic practice. No use, distribution or reproduction is permitted which does not comply with these terms.

frontiers | Frontiers in Oncology

TYPE Original Research
PUBLISHED 18 August 2022
DOI 10.3389/fonc.2022.976762

Check for updates

OPEN ACCESS

EDITED BY
Linlang Guo,
Zhujiang Hospital, China

REVIEWED BY
Liang Wang,
Capital Medical University, China
Zhengang Qiu,
First Affiliated Hospital of Gannan Medical University, China
Xiaohua Li,
Sixth People's Hospital of Chengdu, China

*CORRESPONDENCE
Yan Huang
huangy27@mail.sysu.edu.cn
Jian Xiao
xiaoj26@mail.sysu.edu.cn

†These authors have contributed equally to this work and share first authorship

SPECIALTY SECTION
This article was submitted to Cancer Immunity and Immunotherapy, a section of the journal Frontiers in Oncology

RECEIVED 23 June 2022
ACCEPTED 15 July 2022
PUBLISHED 18 August 2022

CITATION
Li S, Liu T, Liu H, Zhai X, Cao T, Yu H, Hong W, Lin X, Li M, Huang Y and Xiao J (2022) Integrated driver mutations profile of chinese gastrointestinal-natural killer/T-cell lymphoma.
Front. Oncol. 12:976762.
doi: 10.3389/fonc.2022.976762

COPYRIGHT
© 2022 Li, Liu, Liu, Zhai, Cao, Yu, Hong, Lin, Li, Huang and Xiao. This is an open-access article distributed under the terms of the Creative Commons Attribution License (CC BY). The use, distribution or reproduction in other forums is permitted, provided the original author(s) and the copyright owner(s) are credited and that the original publication in this journal is cited, in accordance with accepted academic practice. No use, distribution or reproduction is permitted which does not comply with these terms.

Integrated driver mutations profile of chinese gastrointestinal-natural killer/T-cell lymphoma

Shanshan Li[1,2†], Tingzhi Liu[2,3†], Hailing Liu[2,4†], Xiaohui Zhai[1,2†], Taiyuan Cao[1,2], Hongen Yu[1,2], Wanjia Hong[1,2], Xiaoru Lin[1,2], Ming Li[1,2], Yan Huang[2,4*] and Jian Xiao[1,2*]

[1]Department of Medical Oncology, The Sixth Affiliated Hospital of Sun-Yat Sen University, Guangzhou, China, [2]Guangdong Provincial Key Laboratory of Colorectal and Pelvic Floor Diseases, The Sixth Affiliated Hospital, Sun Yat-sen University, Guangzhou, China, [3]Department of Medical Hematology, The Sixth Affiliated Hospital of Sun Yat-Sen University, Guangzhou, China, [4]Department of Pathology, The Sixth Affiliated Hospital of Sun-Yat Sen University, Guangzhou, China

Background: One of the most common nasal external sites in extranodal Natural Killer/T-cell lymphoma (NKTCL) is in the gastrointestinal (GI) system. Despite this, reports on gastrointestinal-Natural Killer/T-cell lymphoma (GI-NKTCL) are very few. To obtain a better understanding of this manifestation of NKTCL, we conducted a retrospective study on GI-NKTCL to analyze its clinical features, genomic changes and immune infiltration.

Methods: We retrospectively collected patients diagnosed with GI-NKTCL in the Sixth Affiliated Hospital of Sun Yat-sen University from 2010 to 2020. From this cohort we obtained mutation data *via* whole exome sequencing.

Results: Genomic analysis from 15 patients with GI-NKTCL showed that the most common driving mutations were ARID1B(14%, 2/15), ERBB3(14%, 2/15), POT1(14%, 2/15), and TP53(14%, 2/15). In addition, we found the most common gene mutation in patients with GI-NKTCL to be RETSAT(29%, 4/15) and SNRNP70(21%, 3/15), and the most common hallmark pathway mutations to be G2M checkpoint pathway (10/15, 66.7%), E2F targets (8/15, 53.3%), estrogen response late (7/15, 46.7%), estrogen response early (7/15, 46.7%), apoptosis (7/15, 46.7%) and TNFA signaling *via* NFKB (7/15, 46.7%). In the ICIs-Miao cohort, SNRNP7-wild-type (WT) melanoma patients had significantly prolonged overall survival (OS) time compared with SNRNP7 mutant type (MT) melanoma patients. In the TCGA-UCEC cohort, the patients with RETSAT-MT or SNRNP7-MT had significantly increased expression of immune checkpoint molecules and upregulation of inflammatory immune cells.

Conclusions: In this study, we explored GI-NKTCL by means of genomic analysis, and identified the most common mutant genes (RETSAT and SNRNP70), pathway mutations (G2M checkpoint and E2F targets) in GI-NKTCL patients. Also, we explored the association between the common

mutant genes and immune infiltration. Our aim is that our exploration of these genomic changes will aid in the discovery of new biomarkers and therapeutic targets for those with GI-NKTCL, and finally provide a theoretical basis for improving the treatment and prognosis of patients with GI-NKTCL.

KEYWORDS

driver gene, mutation, gastrointestinal-natural killer/T-cell lymphoma (GI-NKTCL), immune infiltration, genomic analysis

Introduction

Extranodal natural killer/T-cell lymphoma (ENKTCL) is a rare type of Non-Hodgkin's Lymphoma (NHL) (1–3). It is characterized by extranodal involvement, with tumor cells predominantly from peripheral mature NK cells, and less from cytotoxic T cells. One site of extranodal involvement is the gastrointestinal system (GI-NKTCL); however, reports of patients with primary GI-NKTCL are rare (4, 5). Currently, the treatment of NKTCL is still based on radiotherapy, or a combination of radiotherapy and chemotherapy, and stage I/II NKTCL patients showed locoregional control rates of >90% and five-year overall survival (OS) rates of approximately 70–90% (6). Stage III/IV NKTCL patients were treated with combination chemotherapy that includes menadione enzymes (7–9). The SMILE protocol (dexamethasone, methotrexate, ifosfamide, l-asparaginase, and etoposide) can be the standard of care for stage III/IV NKTCL patients, with one-year OS rates of >50%.

Whole exome sequencing (WES), also known as targeted exon capture, is a new technology which explores disease-related genes by studying only the coding regions of the human genome (10–13). It is comparable to whole genome sequencing (WGS), which samples the entire human genome. WES, however, only samples 1%, while still allowing for analysis of single nucleotide variants (SNV), insertion-deletions (indel), and structural variations (SV) of pathogenic genes (14, 15). Applying this new generation sequencing technology to ENKTCL further confirmed the complexity of gene changes present, including the deletion of chromosome 6q, and PRDM1, ATG5, AIM1, FOXO3, HACE1 as common deletion segments on chromosome 6q (16). Additionally, tumor-related genes with known mutations include some tumor suppressor genes (such as TP53, DDX3X, and MGA), JAK/STAT pathway genes (such as JAK3, STAT3, and STAT5), and some epigenetic modified genes (such as KMT2D, BCOR, ARID1A, and EP300) (4, 17–20). The proteins encoded by these mutant genes show a loss of normal original functions, with some increase of invasive functions. Additionally, the tumor immune microenvironment (TIME) plays important role in the tumor development and progression. Although some genetic studies on ENKTCL have been conducted, genomic changes and immune infiltration in GI-NKTCL have not been fully explored due to the low number of reported cases.

In this study, we carried out WES on patients diagnosed with GI-NKTCL in China, explored the genomic-level changes of these patients, and analyzed the mutational profiles and common pathway mutation landscapes. Also, we analyzed the relationship between the top mutated genes and the prognosis of the immune checkpoint inhibitors (ICIs) treatment, and TIME. We hope that by deeply studying the molecular mechanism of the pathogenesis of GI-NKTCL, looking specifically for potential molecular targets and exploring new treatment methods, we can improve the prognosis of patients with GI-NKTCL.

Methods

Sample collection and raw data sequencing of NK/T cell lymphoma

We retrospectively collected 15 samples of NKTCL from patients diagnosed with GI-NKTCL at the Sixth Affiliated Hospital of Sun Yat-sen University from 2010 to 2020. The pathological diagnosis of GI-NKTCL was based on the revised European and American lymphoma (REAL) classification, and the classification standard of the World Health Organization (WHO). The study was approved by the Research Ethics Committee of the Sixth Affiliated Hospital of Sun Yat-sen University. The details of the raw data sequencing are listed in the Supplementary Methods. Additionally, we downloaded the WES data from the NKTCL cohort reported by Li et al. (21).

Pan-cancer datasets and ICIs datasets collection

Data sets for the following 33 cancer types were downloaded from The Cancer Genome Atlas (TCGA) database: adrenocortical carcinoma (ACC), bladder urothelial carcinoma (BLCA), breast

invasive carcinoma (BRCA), cervical squamous cell carcinoma and endocervical adenocarcinoma (CESC), cholangiocarcinoma (CHOL), colon adenocarcinoma (COAD), colorectal cancer (CRC), lymphoid neoplasm diffuse large B-cell lymphoma (DLBC), esophageal carcinoma (ESCA), glioblastoma multiforme (GBM), head and neck squamous cell carcinoma (HNSC), kidney chromophobe (KICH), kidney renal clear cell carcinoma (KIRC), kidney renal papillary cell carcinoma (KIRP), acute myeloid leukemia (LAML), brain lower grade glioma (LGG), liver hepatocellular carcinoma (LIHC), lung adenocarcinoma (LUAD), lung squamous cell carcinoma (LUSC), mesothelioma (MESO), non-small cell lung cancer (NSCLC), ovarian serous cystadenocarcinoma (OV), pancreatic adenocarcinoma (PAAD), pheochromocytoma and paraganglioma (PCPG), prostate adenocarcinoma (PRAD), rectum adenocarcinoma (READ), sarcoma (SARC), skin cutaneous melanoma (SKCM), stomach adenocarcinoma (STAD), testicular germ cell tumors (TGCT), thyroid carcinoma (THCA), thymoma (THYM), uterine corpus endometrial carcinoma (UCEC), uterine carcinosarcoma (UCS), and uveal melanoma (UVM) (22). Also, we downloaded a pan-cancer data set published by Zehir et al. from the cBioPortal web tool (https://www.cbioportal.org/) (23). We downloaded the ICIs-cohorts reported by the Miao et al. (24). and Allen et al. (25). to explore the association between the top mutated genes and ICIs-related prognosis.

Genome analysis

The somatic mutation data of our cohort was subjected to preprocessing and any synonymous mutations were deleted. Based on the non-synonymous mutation data, we identified the types and frequency of gene mutations in GI-NKTCL that had a mutation frequency greater than or equal to 2. In addition, we downloaded the Hallmark pathway gene set (h.all.v7.1.symbols.gmt) from the MsigDB database (http://www.gsea-msigdb.org/gsea/downloads.jsp) and used this to count the number of gene mutations in different Hallmark pathways in each patient. We calculated the number of gene mutations in different Hallmark pathways for each cancer type in both the TCGA-Pancancer and Zehir-Pancancer cohort and, using the MutationMapper function in the cBioPortal web tool (https://www.cbioportal.org/mutation_mapper), visualized the mutation sites of the two genes with the highest frequency of mutation in GI-NKTCL. Additionally, we counted the proportion of six single base substitution types in our GI-NKTCL cohort.

Immune infiltration

The gene lists of the immune checkpoint molecules were downloaded from the previous study (25). The proportion of the immune cells was estimated by CIBERSORT (25).

Statistical analysis

Fisher's exact test was used to analyze the mutual exclusion and co-occurrence of gene mutations. Heatmaps were visualized using the ComplexHeatmap (26) and pheatmap (27) R packages, and histograms were visualized using the ggplot2 (28) R package. The Maftools (29) R package was used for mutual exclusion and co-occurrence between gene mutations. All analyses in this study were carried out using R software (Version 3.8.1). A P value of less than 0.05 was regarded as statistically significant, and the P value was bilateral.

Results

Overview of the mutational spectrum and pattern of GI-NKTCL

In this study, we collected data from 12 male and 3 female patients with GI-NKTCL, with an average age of 49.6 years old (comparable to the general characteristics reported by ENKTL) (30). The basic clinical features of our cohort are shown in Table 1. Of the primary tumor sites, six cases were colonic (40.0%), four cases were ileocecal (26.7%), and five cases were small intestinal (33.3%). Five cases were treated with surgery (33.3%), and ten cases were treated with combined surgery and chemotherapy (66.7%). One patient survived (6.7%), and the remaining 11 patients died (93.3%). Supplementary Figure 1 shows the overall survival (OS) time of GI-NKTCL. Also, We calculated and counted the proportion of six single base substitution types for the SNV detection results of all samples, and found that C>T/G>A accounted for the most single base substitution types in each patient (Figure 1A), which was analogous to the somatic SNV spectrum in other cancers (including B-cell acute lymphoblastic leukemia and NKTCL) (31, 32). On the other hand, T>A/A>T had the least proportion of single base substitution types in each patient. Clustering the samples according to the distribution of mutation types resulted in the cluster heat map seen in Figure 1B, representing the mutation spectrum in the cohort. A variety of mutation processes, such as mismatching in the process of DNA replication, induction of endogenous or exogenous mutagens, and defects of DNA repair mechanism, were responsible for producing somatic mutations. These processes give rise to specific combinations of mutation types, which can be seen as mutation patterns. Point mutations can be divided into 96 types by considering the base types at the 1bp positions upstream and downstream of the point mutation site. The mutation pattern of the 96 mutation types in all samples is presented in Figure 1C. Based on cosine similarity, we clustered the mutation pattern with 30 known mutation features in the COSMIC website (https://cancer.sanger.ac.uk/signatures/signatures_v2/). We

TABLE 1 Clinical features of GI-NKTCL cases (N = 15).

Characteristics	N
Age	
≤60	10
>60	5
Sex	
Female	3
Male	12
Primary Site	
Rectum	5
Colon	6
Small intestine	4
LDH Status	
Increase	6
Normal	9
CD56	
(+)	7
(-)	7
Missing	1
Surgery	
YES	15
NO	0
Treatment	
Surgery	10
Surgery+Chemotherapy	5
Survival status	
Dead	14
Alive	1

found the mutation pattern of GI-NKTCL was highly correlated with COSMIC signature 1 (cosine similarity score: 0.91) (Figure 1D). COSMIC signature 1 was the result of an endogenous mutational process initiated by spontaneous deamination of 5-methylcytosine and associated the age of cancer diagnosis (33).

Panoramic overview of mutations in GI-NKTCL

We analyzed and visualized the data of non-synonymous somatic mutations from patients diagnosed with GI-NKTCL. The genes with the highest mutation frequency in these patients were identified as RETSAT (29%, 4/15); SNRNP70 (21%, 3/15); and ADGRL3, AHNAK2, ARID1B, C8orf44, CAMSAP1, DNAH5, DNM3, DSCAML1, ERBB3, FLG, HELZ2, IDUA, LRRIQ1, MUC17, NOP9, NT5C1B, PDE3A, POT1, PTPN22, SLC35G5, SOX11, TNXB, TP53, UBE3C, and USP34 (each being 14%, 2/15) (Figure 2A). Additionally, the main type of gene mutation was found to be missense, followed by inframe ins/del, splice site, and finally frameshift mutation. Following this, we analyzed the mutual exclusion and co-occurrence of the gene mutations with the highest mutation frequency. As can be seen in Figure 2B: mutations in MUC17 gene and POT1 gene often occur together ($P < 0.05$); mutations in NT5C1B gene and NOP9 gene usually occur together ($P < 0.05$); and mutations in PTPN22 gene and ARID1B gene will occur at the same time ($P < 0.05$). The protein structural mutation points in the two genes with the highest mutation frequency (RETSAT and SNRNP70) in patients with GI-NKTCL were visualized in the form of lollipop plots. In the GI-NKTCL cohort, we found the protein mutation site of RETSAT to be mainly p.Ala533Val (Figure 3A), while in the TCGA-Pancancer cohort, it is mainly p.Arg125Leu/His (Figure 3B). In the GI-NKTCL cohort, we found the protein structural mutation site of SNRNP70 to be mainly p.Asp236_Arg237del (Figure 3C), and in TCGA-Pancancer cohort, it is mainly p.Arg155Gln/Pro, occurring predominantly in the RRM_1 domain (Figure 3D). The genes with the highest mutation frequencies in NKTCL (Li-cohort) are shown in Supplementary Figure 2. The genes with the highest mutation frequency in these patients were identified as FSIP2 (22%), GNAQ (22%), USP8 (22%), IGFN1 (19%), KMT2D (19%), LOC401052 (19%), MUC21 (19%) and TTN (19%) (Supplementary Figure 2).

Overview of abrupt change of Hallmark pathway signaling in GI-NKTCL

Hallmark pathways are landmark gene sets which can represent biological processes and states and may also play a vital role in tumor development. Therefore, we explored the mutations of each GI-NKTCL patient in a variety of hallmark pathways (Figure 4A). We found mutations in the G2M checkpoint pathway 66.7% of patients (10/15). The next most common mutated pathways were E2F targets (8/15, 53.3%), estrogen response late (7/15, 46.7%), estrogen response early (7/15, 46.7%), apoptosis (7/15, 46.7%), and TNFA signaling *via* NFKB (7/15, 46.7%). The mutation of various cancer types in different hallmark pathways in the TCGA-Pancancer and Zehir-Pancancer cohorts are shown in Figures 4B, C respectively. Found in all samples (41/41, 100%) were mutations in apoptosis, E2F targets, mitotic spindle, myogenesis, p53 pathway, PI3K-AKT-mTOR signaling, TGF beta signaling, UV response DN, UV response UP, and WNT beta catenin signaling.

Association between most frequently mutated genes (RETSAT and SNRNP70) and immune infiltration

We explored the effect of the most frequently mutated genes (RETSAT and SNRNP70) on the prognosis of the two ICI-treated cohorts (Allen-Melanoma and Miao-Melanoma). We

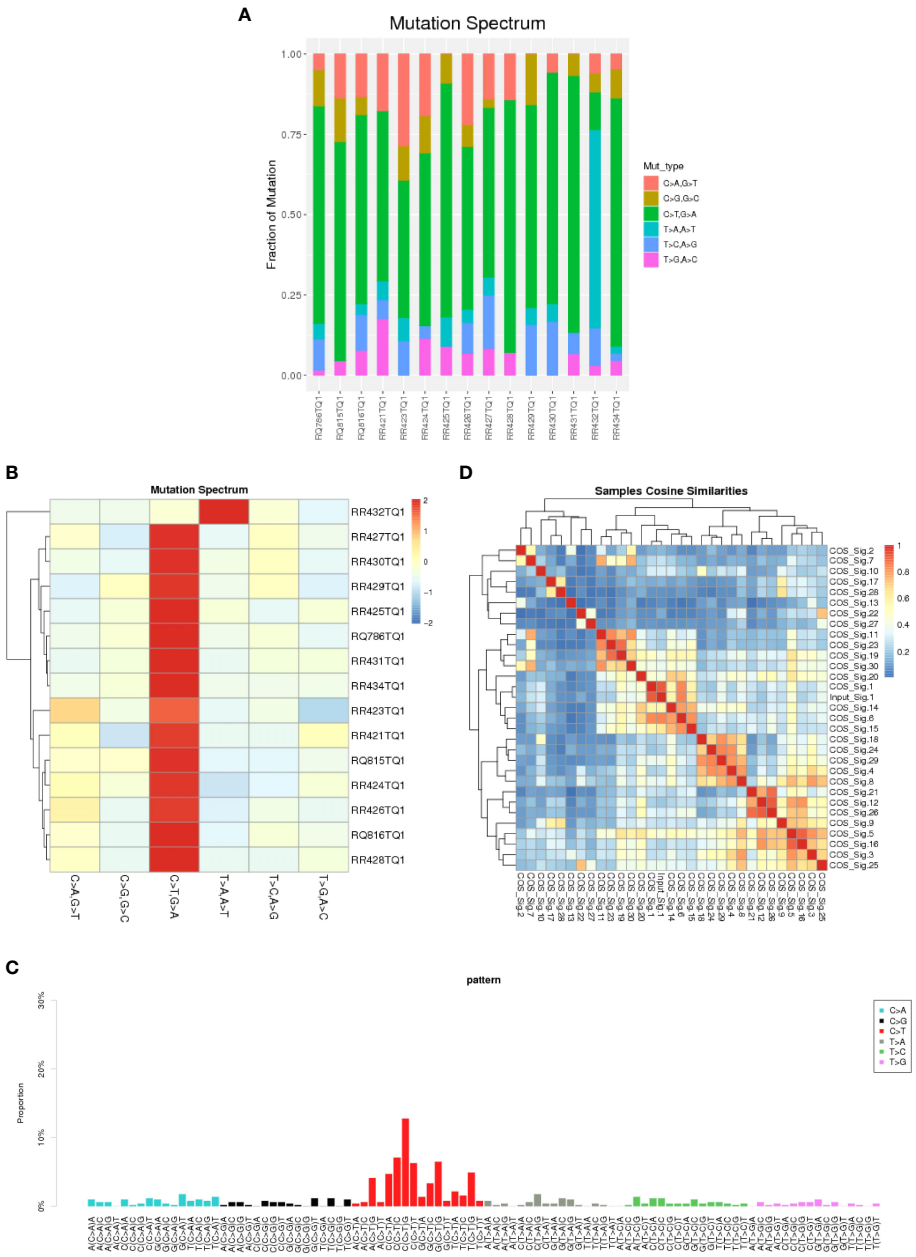

FIGURE 1
A barplot **(A)** and heatmap **(B)** depicting the mutation spectrum of the GI-NKTCL cohort. **(C)** The mutation pattern of the GI-NKTCL cohort obtained *via* Nonnegative Matrix Factorization (NMF). **(D)** Heatmap showing the correlation between the COSMIC signatures.

found that SNRNP70-MT melanoma had a significantly decreased OS time compared to SNRNP70-WT melanoma (Figure 5A). In the TCGA cohort, we found that RETSAT was the most frequently mutated gene in the UCEC (5.9%,31/525), DLBC (5.6%,2/36), CHOL (3.9%,2/51), STAD (3.7%,16/435), COAD (3.0%,12/395), and SKCM (3.0%,14/465) subtypes (Figure 5B). Figure 5C shows that SNRNP70 was the most frequently mutated gene in the UCEC (6.3%,33/525), ESCA (2.9%,5/173), CHOL (2.0%,1/51), COAD (1.5%,6/395), and READ (1.5%,2/134). In the TCGA-UCEC cohort, RETSAT-MT was associated with higher expression of immune checkpoint molecules (including PD-L1, HAVCR2, LAG3, CTLA4, TIGIT, PD-1, and PDCD1LG2; Figure 5D) and immune cell enrichment (including CD8+ T cells, activated memory CD4+ T cells, and M1-macrophages; Figure 5E). Similarly, we found that SNRNP70-MT cases in the TCGA-

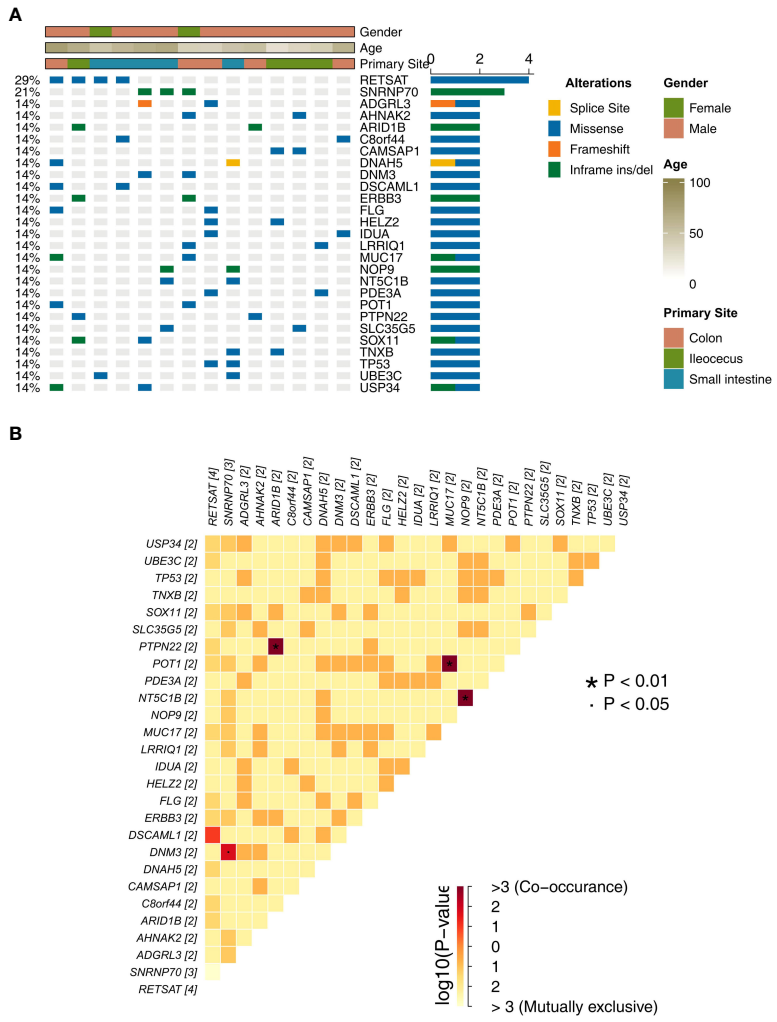

FIGURE 2
(A) The top 27 mutations of the GI-NKTCL cohort. The clinical feature of each patient is annotated in the top panel. **(B)** The co-occurrence and mutually exclusivity of the top 27 mutations (shown in Panel **A**).

UCEC cohort had increased expression of immune checkpoint-related genes (Figure 5F). Compared with SNRNP70-WT, SNRNP70-MT UCEC patients had significant enrichment of CD8+ T cells, activated memory CD4+ T cells, follicular helper T cells, and M1-macrophages (Figure 5G).

Discussion

The prevalence of ENKTCL is highest in Asian and Latin American countries. Primary GI-NKTCL is extremely rare (1–3), with a limited number of reported cases and very few studies specifically focused on this subtype of NKTCL (34–37). Due to the rarity of the disease, the clinical, genomic and immune characteristics have not yet been clarified. Thus, we carried out this study to explore the genomic changes, mutation panorama, and common pathway mutations present, utilizing WES data from 15 Chinese GI-NKTCL patients. We have provided a comprehensive description of the genomic features of GI-NKTCL through bioinformatics, such as gene mutation patterns (base pair alterations, COSMIC signature), high-frequency mutations, and common pathology-related pathways with high-frequency mutations. Additionally, we explored the relationship between the high-frequency mutations and ICIs-related prognosis, and immune infiltration (including immune checkpoint inhibitors and immune cells). The discovery of commonly mutated genes and signaling pathways can offer salient theoretical guidance for the prevention and treatment of future cancer patients (10, 38). We hope that by deeply studying the molecular mechanism of the pathogenesis of GI-NKTCL,

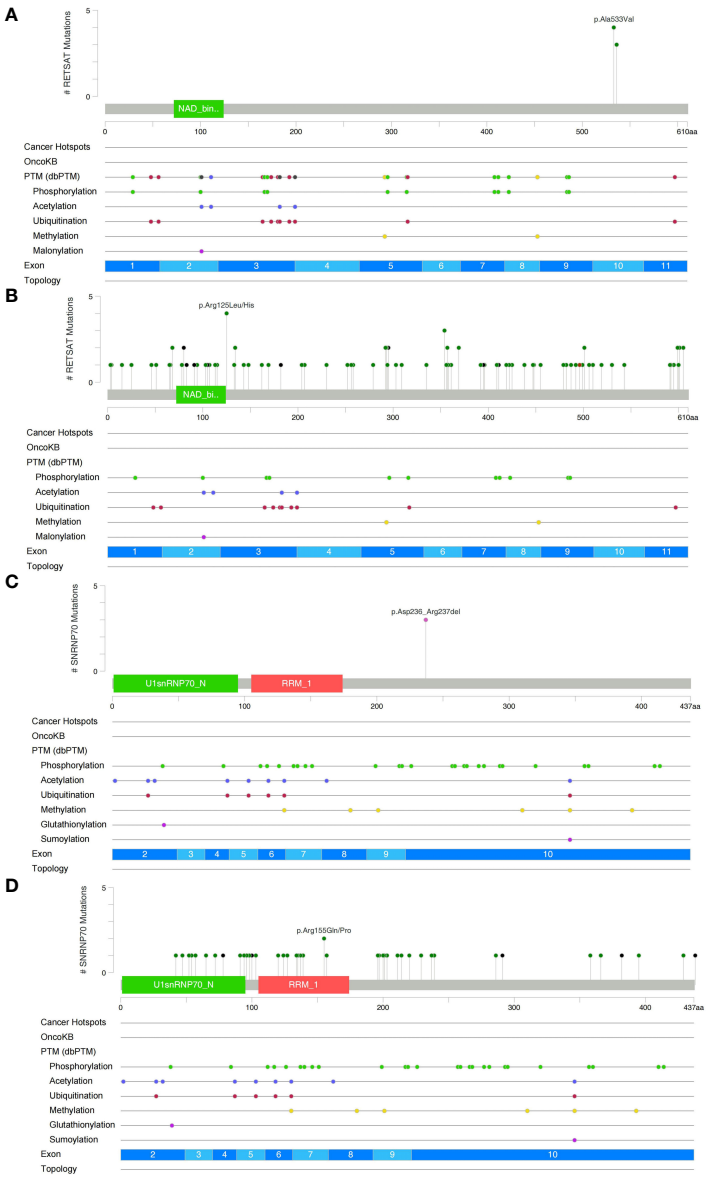

FIGURE 3
Lollipop plot illustrating RETSAT mutations in the GI-NKTCL **(A)** and TCGA-Pancancer **(B)** cohorts. Lollipop plot illustrating SNRNP70 mutations in the GI-NKTCL **(C)** and TCGA-Pancancer **(D)** cohorts.

looking for potential molecular targets and exploring new treatment methods, we can improve the prognosis of patients with GI-NKTCL.

Gene and pathway mutations may be related to the occurrence and development of GI-NKTCL, and as such, may also be indicative of potential targets for treatment. In this study, we found common driving mutations in the tumor suppressor gene TP53 (mainly in exons 5–8) (39), and oncogenes ARID1B, ERBB3, and POT1. TP53 acts as a tumor suppressor by inducing G1 cell cycle arrest in DNA damaged cells. Other functions of TP53 include the regulation of DNA repair, apoptosis, aging, and metabolism (4). In NKTCL, the mutation rate of TP53 is 20–60% (18), and is one of the potential reasons for the low survival rate of NKTCL patients (40). ErbB3 belongs to the ErbB family of receptor tyrosine kinases, and regulates the proliferation and survival of epithelial cells (41). It is highly expressed in common tumors such as breast cancer, melanoma, and pancreatic cancer (42–44), and when activated, can cause resistance to a range of anticancer drugs (45). One example is through the activation of PI3K/AKT and JAK/STAT signaling pathways, which has been shown to produce drug resistance in colon and non-small cell lung cancer patients (46–48). POT1 is an important gene that

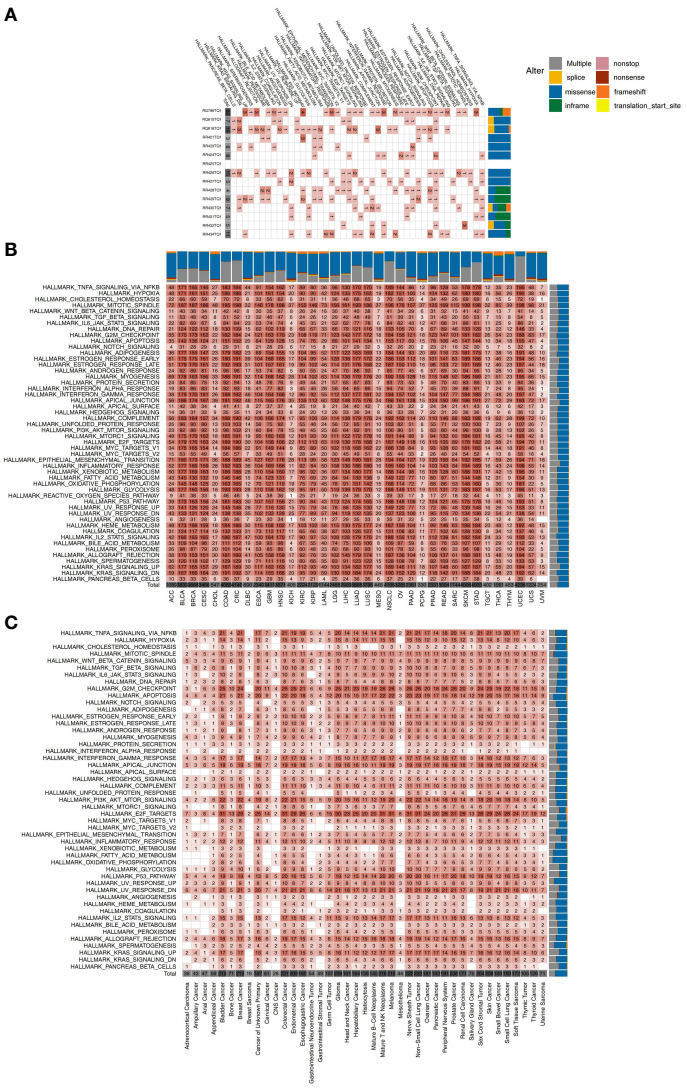

FIGURE 4
(A) The mutation counts of hallmark signaling pathways for each patient in the GI-NKTCL cohort. The mutation counts of hallmark signaling pathways for each cancer type in the TCGA-Pancancer **(B)** and Zehir-Pancancer **(C)** cohorts.

protects telomeres by inhibiting DNA damage and regulates telomere length *via* telomerase activity (49). Studies have shown that mutations in POT1 are often found in patients with B-cell lymphoma (50), and that POT1 gene mutation can lead to the occurrence of various tumors, such as lymphomas (51). Apart from these driving mutations, the gene with the highest mutation frequency in patients with GI-NKTCL was found to be the RETSAT gene(4/15, 29%). Research has indicated that this gene is important for promoting adipogenesis and normal adipocyte differentiation, and it follows that mutation of this gene may affect adipogenesis and differentiation of adipocytes (52). Many studies suggest that lipid metabolism plays a role in the occurrence and development of tumors, regulates cell proliferation (53) and invasion (54, 55), and influences the development of drug resistance (56, 57). Regarding pathway mutations in our study cohort, we found mutations in the G2M checkpoint pathway in 66.7% (10/15) of patients. The results from Song et al. are consistent with this, showing that the application of histone deacetylase (HDAC) inhibitor chidamide, and DNA damage agent etoposide to NKTCL cells not only played a synergistic role in anti-proliferation and enhanced apoptosis, but also made the cell cycle stop at the G2/M phase (58). Also of note, we found changes in TNFA signaling due to mutation in the NFKB pathway in 46.7% (7/15) of GI-NKTCL patients. This is consistent with the results of Zhong et al., who found that a relationship exists between an

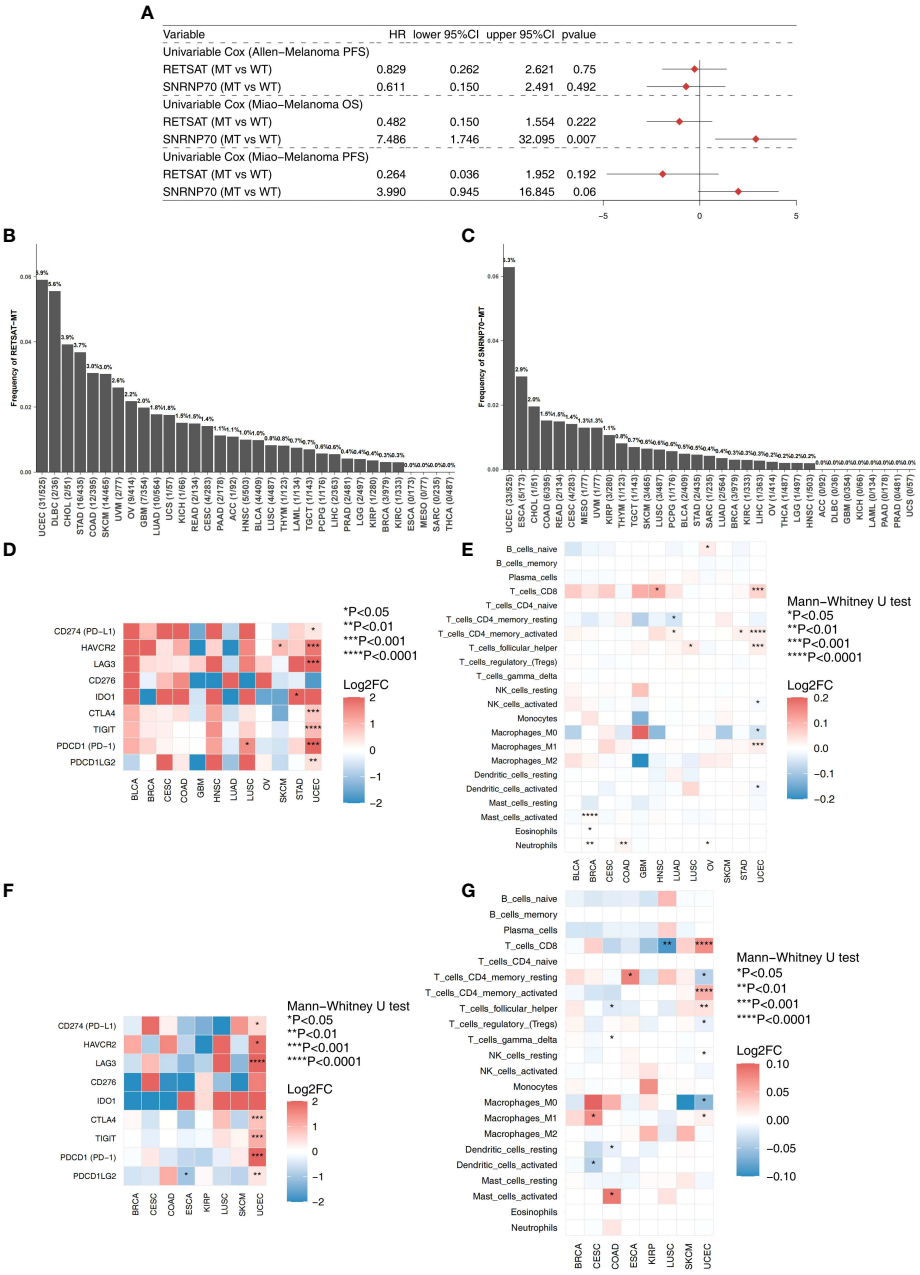

FIGURE 5
(A) The univariable cox regression model of the top mutated genes (RETSAT and SNRNP70) in the two ICIs-treated cohorts (Allen-Melanoma and Miao-Melanoma). **(B)** The mutation frequencies of the RETSAT in the 33 cancer types of TCGA database. **(C)** The mutation frequencies of the SNRNP70 in the 33 cancer types of TCGA database. **(D)** Heatmap depicted the logFC of the expression levels of the immune checkpoint molecules between the RETSAT-MT and RETSAT-WT among multiple cancer types (TCGA database). **(E)** Heatmap depicted the logFC of the immune cells scores estimated by the CIBERSORT method between the RETSAT-MT and RETSAT-WT among multiple cancer types (TCGA database). **(F)** Heatmap depicted the logFC of the expression levels of the immune checkpoint molecules between the SNRNP70-MT and SNRNP70-WT among multiple cancer types (TCGA database). **(G)** Heatmap depicted the logFC of the immune cells scores estimated by the CIBERSORT method between the SNRNP70-MT and SNRNP70-WT among multiple cancer types (TCGA database).

imbalance of TNFA receptor signal and the poor clinical characteristics of patients with diffuse large B-cell lymphoma (59).

There were some limitations in this study: 1) The number of GI-NKTCL samples included in this study was limited to 15 cases; and 2) No follow-up functional analysis of high-frequency gene mutations and signaling pathway mutations in GI-NKTCL was conducted in this study. 3) We were unable to validate the relationship between RETSAT and SNRNP70 and the prognosis of immunotherapy in patients in the GI-NKTCL cohort due to the lack of survival data for immunotherapy in the GI-NKTCL cohort. Furthermore, the relationship between RETSAT and SNRNP70 and the prognosis of immunotherapy in patients with different cancers may be different due to tumor heterogeneity among different cancer types. In the future, we hope to further validate this by collecting data from patients with multiple cancer types receiving immunotherapy.

Conclusions

In this study, we discovered the most common mutant genes and pathway mutations in a cohort of GI-NKTCL patients by analyzing genome level data obtained *via* WES. The most common mutated genes in GI-NKTCL patients are RETSAT and SNRNP70. Additionally, in G2M checkpoint and E2F targets are the most commonly mutated signaling pathways. In-depth exploration of the genomic changes of GI-NKTCL is helpful in understanding the pathogenesis of this disease, and we hope that the results of this study can be beneficial for providing a theoretical basis for finding new biomarkers and therapeutic targets.

Data availability statement

The original contributions presented in the study are included in the article/Supplementary Materials. Further inquiries can be directed to the corresponding authors.

Ethics statement

The studies involving human participants were reviewed and approved by the Sixth Affiliated Hospital of Sun Yat-Sen University. The patients/participants provided their written informed consent to participate in this study.

Author contributions

Conceptualization, YH and JX. Formal analysis, SL, TL, HL, and XZ. Visualization, SL, TL, HL, and XZ. Writing–original draft, TC, HY, WH, XL, and ML. Writing–review & editing, SL, TL, HL, XZ, TC, HY, WH, XL, ML, YH and JX. All authors read and approved the final manuscript.

Funding

This work was supported by Guangzhou General Planned Project of Science and Technology (grant number 202102080283) and Key Project of Rural Science and Technology Commissioner of Guangdong Province (grant number KPT20190263).

Acknowledgments

We thank the Genetron Health (Beijing) Co. Ltd.

Conflict of interest

The authors declare that the research was conducted in the absence of any commercial or financial relationships that could be construed as a potential conflict of interest.

Publisher's note

All claims expressed in this article are solely those of the authors and do not necessarily represent those of their affiliated organizations, or those of the publisher, the editors and the reviewers. Any product that may be evaluated in this article, or claim that may be made by its manufacturer, is not guaranteed or endorsed by the publisher.

Supplementary material

The Supplementary Material for this article can be found online at: https://www.frontiersin.org/articles/10.3389/fonc.2022.976762/full#supplementary-material

SUPPLEMENTARY FIGURE 1
Kaplan-Meier(KM) curve of GI-NKTCL patients.

SUPPLEMENTARY FIGURE 2
The mutation landscape of Li-NKTCL patients (top mutated genes frequencies ≥ 4).

References

1. Kim SJ, Yoon DH, Jaccard A, Chng WJ, Lim ST, Hong H, et al. A prognostic index for natural killer cell lymphoma after non-anthracycline-based treatment: a multicentre, retrospective analysis. *Lancet Oncol* (2016) 17:389–400. doi: 10.1016/S1470-2045(15)00533-1

2. Wu J, Qiu YJ, Xu AG, Xing LH, Zhang QX. Clinical characteristics of lung NK/T cell lymphoma misdiagnosed as pneumonia. *Zhonghua Yi Xue Za Zhi* (2019) 99:2696–700. doi: 10.3760/cma.j.issn.0376-2491.2019.34.012

3. Yamaguchi M, Suzuki R, Oguchi M, Asano N, Amaki J, Akiba T, et al. Treatments and outcomes of patients with extranodal natural killer/T-cell lymphoma diagnosed between 2000 and 2013: a cooperative study in Japan. *J Clin Oncol* (2017) 35:32–9. doi: 10.1200/JCO.2016.68.1619

4. Jiang L, Gu Z-H, Yan Z-X, Zhao X, Xie Y-Y, Zhang Z-G, et al. Exome sequencing identifies somatic mutations of DDX3X in natural killer/T-cell lymphoma. *Nat Genet* (2015) 47:1061–6. doi: 10.1038/ng.3358

5. Kim SJ, Jung HA, Chuang S-S, Hong H, Guo C-C, Cao J, et al. Extranodal natural killer/T-cell lymphoma involving the gastrointestinal tract: analysis of clinical features and outcomes from the Asia lymphoma study group. *J Hematol Oncol* (2013) 6:86. doi: 10.1186/1756-8722-6-86

6. Yang Y, Zhu Y, Cao J-Z, Zhang Y-J, Xu L-M, Yuan Z-Y, et al. Risk-adapted therapy for early-stage extranodal nasal-type NK/T-cell lymphoma: analysis from a multicenter study. *Blood* (2015) 126:1424–32. doi: 10.1182/blood-2015-04-639336

7. Yamaguchi M, Kwong Y-L, Kim WS, Maeda Y, Hashimoto C, Suh C, et al. Phase II study of SMILE chemotherapy for newly diagnosed stage IV, relapsed, or refractory extranodal natural killer (NK)/T-cell lymphoma, nasal type: the NK-cell tumor study group study. *J Clin Oncol Off J Am Soc Clin Oncol* (2011) 29:4410–6. doi: 10.1200/JCO.2011.35.6287

8. Li X, Cui Y, Sun Z, Zhang L, Li L, Wang X, et al. DDGP versus SMILE in newly diagnosed advanced natural Killer/T-cell lymphoma: A randomized controlled, multicenter, open-label study in China. *Clin Cancer Res an Off J Am Assoc Cancer Res* (2016) 22:5223–8. doi: 10.1158/1078-0432.CCR-16-0153

9. Kim M, Kim TM, Kim KH, Keam B, Lee S-H, Kim D-W, et al. Ifosfamide, methotrexate, etoposide, and prednisolone (IMEP) plus l-asparaginase as a first-line therapy improves outcomes in stage III/IV NK/T cell-lymphoma, nasal type (NTCL). *Ann Hematol* (2015) 94:437–44. doi: 10.1007/s00277-014-2228-4

10. de Mel S, Hue SS-S, Jeyasekharan AD, Chng W-J, Ng S-B. Molecular pathogenic pathways in extranodal NK/T cell lymphoma. *J Hematol Oncol* (2019) 12:33. doi: 10.1186/s13045-019-0716-7

11. Ye Q, Chen H, Wen Z, Guo W, Huang Y, Mo X. Abnormal expression of p-ATM/CHK2 in nasal extranodal NK/T cell lymphoma, nasal type, is correlated with poor prognosis. *J Clin Pathol* (2021) 74:223–7. doi: 10.1136/jclinpath-2020-206476

12. Xiong J, Zhao W-L. Advances in multiple omics of natural-killer/T cell lymphoma. *J Hematol Oncol* (2018) 11:134. doi: 10.1186/s13045-018-0678-1

13. de Mel S, Soon GS-T, Mok Y, Chung T-H, Jeyasekharan AD, Chng W-J, et al. The genomics and molecular biology of natural Killer/T-cell lymphoma: Opportunities for translation. *Int J Mol Sci* (2018) 19(7):1931. doi: 10.3390/ijms19071931

14. Zhang J, Chiodini R, Badr A, Zhang G. The impact of next-generation sequencing on genomics. *J Genet Genomics* (2011) 38:95–109. doi: 10.1016/j.jgg.2011.02.003

15. Ng SB, Turner EH, Robertson PD, Flygare SD, Bigham AW, Lee C, et al. Targeted capture and massively parallel sequencing of 12 human exomes. *Nature* (2009) 461:272–6. doi: 10.1038/nature08250

16. Huang Y, de Leval L, Gaulard P. Molecular underpinning of extranodal NK/T-cell lymphoma. *Best Pract Res Clin Haematol* (2013) 26:57–74. doi: 10.1016/j.beha.2013.04.006

17. Sugimoto K, Kawamata N, Sakajiri S, Oshimi K. Molecular analysis of oncogenes, ras family genes (N-ras, K-ras, h-ras), myc family genes (c-myc, n-myc) and mdm2 in natural killer cell neoplasms. *Jpn J Cancer Res* (2002) 93:1270–7. doi: 10.1111/j.1349-7006.2002.tb01234.x

18. Quintanilla-Martinez L, Kremer M, Keller G, Nathrath M, Gamboa-Dominguez A, Meneses A, et al. p53 mutations in nasal natural killer/T-cell lymphoma from Mexico: association with large cell morphology and advanced disease. *Am J Pathol* (2001) 159:2095–105. doi: 10.1016/S0002-9440(10)63061-1

19. Küçük C, Hu X, Jiang B, Klinkebiel D, Geng H, Gong Q, et al. Global promoter methylation analysis reveals novel candidate tumor suppressor genes in natural killer cell lymphoma. *Clin Cancer Res* (2015) 21:1699–711. doi: 10.1158/1078-0432.CCR-14-1216

20. Zhang Y, Li C, Xue W, Zhang M, Li Z. Frequent mutations in natural Killer/T cell lymphoma. *Cell Physiol Biochem Int J Exp Cell Physiol Biochem Pharmacol* (2018) 49:1–16. doi: 10.1159/000492835

21. Li Z, Zhang X, Xue W, Zhang Y, Li C, Song Y, et al. Recurrent GNAQ mutation encoding T96S in natural killer/T cell lymphoma. *Nat Commun* (2019) 10:4209. doi: 10.1038/s41467-019-12032-9

22. Tomczak K, Czerwińska P, Wiznerowicz M. The cancer genome atlas (TCGA): an immeasurable source of knowledge. *Contemp Oncol (Poznan Poland)* (2015) 19:A68–77. doi: 10.5114/wo.2014.47136

23. Zehir A, Benayed R, Shah RH, Syed A, Middha S, Kim HR, et al. Mutational landscape of metastatic cancer revealed from prospective clinical sequencing of 10,000 patients. *Nat Med* (2017) 23:703–13. doi: 10.1038/nm.4333

24. Miao D, Margolis CA, Vokes NI, Liu D, Taylor-Weiner A, Wankowicz SM, et al. Genomic correlates of response to immune checkpoint blockade in microsatellite-stable solid tumors. *Nat Genet* (2018) 50:1271–81. doi: 10.1038/s41588-018-0200-2

25. Van Allen EM, Miao D, Schilling B, Shukla SA, Blank C, Zimmer L, et al. Genomic correlates of response to CTLA-4 blockade in metastatic melanoma. *Science* (2015) 350:207–11. doi: 10.1126/science.aad0095

26. Gu Z, Eils R, Schlesner M. Complex heatmaps reveal patterns and correlations in multidimensional genomic data. *Bioinformatics* (2016) 32:2847–9. doi: 10.1093/bioinformatics/btw313

27. Quan J, Wu Z, Ye Y, Peng L, Wu J, Ruan D, et al. Metagenomic characterization of intestinal regions in pigs with contrasting feed efficiency. *Frontiers in microbiology* (2020) 11:32.

28. Zhou G, Zhang S, Jin M, Hu S. Comprehensive analysis reveals COPB2 and RYK associated with tumor stages of larynx squamous cell carcinoma. *BMC cancer* (2022) 22(1):1–5.

29. Mayakonda A, Lin D-C, Assenov Y, Plass C, Koeffler HP. Maftools: efficient and comprehensive analysis of somatic variants in cancer. *Genome Res* (2018) 28:1747–56. doi: 10.1101/gr.239244.118

30. Huh J. Epidemiologic overview of malignant lymphoma. *Korean J Hematol* (2012) 47:92–104. doi: 10.5045/kjh.2012.47.2.92

31. Xiong J, Cui B-W, Wang N, Dai Y-T, Zhang H, Wang C-F, et al. Genomic and transcriptomic characterization of natural killer T cell lymphoma. *Cancer Cell* (2020) 37:403–419.e6. doi: 10.1016/j.ccell.2020.02.005

32. Liu Y-F, Wang B-Y, Zhang W-N, Huang J-Y, Li B-S, Zhang M, et al. Genomic profiling of adult and pediatric b-cell acute lymphoblastic leukemia. *EBioMedicine* (2016) 8:173–83. doi: 10.1016/j.ebiom.2016.04.038

33. Jones CL, Degasperi A, Grandi V, Amarante TD, Mitchell TJ, Nik-Zainal S, et al. Spectrum of mutational signatures in T-cell lymphoma reveals a key role for UV radiation in cutaneous T-cell lymphoma. *Sci Rep* (2021) 11:3962. doi: 10.1038/s41598-021-83352-4

34. Zhang L, Zhang P, Wen J, Chen X, Zhang H. Primary gastric natural killer/T-cell lymphoma with diffuse CD30 expression and without CD56 expression: A case report. *Oncol Lett* (2016) 11:969–72. doi: 10.3892/ol.2015.4015

35. Ogawa S, Imai Y, Inokuma T. Mimicking gastric natural Killer/T-cell lymphoma. *Gastroenterology* (2017) 153:e22–3. doi: 10.1053/j.gastro.2016.11.055

36. Huang Y-H, Huang C-T, Tan SY, Chuang S-S. Primary gastric extranodal natural killer/T-cell lymphoma, nasal type, with acquisition of CD20 expression in the subcutaneous relapse: report of a case with literature review. *J Clin Pathol* (2015) 68:943–5. doi: 10.1136/jclinpath-2015-203188

37. Yang H, Wu M, Yin W, Sun W, Zhang G. Diagnosis and treatment of a patient with primary gastric extranodal natural killer/T-cell lymphoma, nasal type. *Leuk Lymphoma* (2010) 51:2137–40. doi: 10.3109/10428194.2010.512964

38. Selvarajan V, Osato M, Nah GSS, Yan J, Chung T-H, Voon DC-C, et al. RUNX3 is oncogenic in natural killer/T-cell lymphoma and is transcriptionally regulated by MYC. *Leukemia* (2017) 31:2219–27. doi: 10.1038/leu.2017.40

39. Sandal T. Molecular aspects of the mammalian cell cycle and cancer. *Oncologist* (2002) 7:73–81. doi: 10.1634/theoncologist.7-1-73

40. Morin RD, Mendez-Lago M, Mungall AJ, Goya R, Mungall KL, Corbett RD, et al. Frequent mutation of histone-modifying genes in non-Hodgkin lymphoma. *Nature* (2011) 476:298–303. doi: 10.1038/nature10351

41. Bindels EMJ, van der Kwast TH, Izadifar V, Chopin DK, de Boer WI. Functions of epidermal growth factor-like growth factors during human urothelial reepithelialization *in vitro* and the role of erbB2. *Urol Res* (2002) 30:240–7. doi: 10.1007/s00240-002-0260-7

42. Liles JS, Arnoletti JP, Tzeng C-WD, Howard JH, Kossenkov AV, Kulesza P, et al. ErbB3 expression promotes tumorigenesis in pancreatic adenocarcinoma. *Cancer Biol Ther* (2010) 10:555–63. doi: 10.4161/cbt.10.6.12532

43. Morrison MM, Williams MM, Vaught DB, Hicks D, Lim J, McKernan C, et al. Decreased LRIG1 in fulvestrant-treated luminal breast cancer cells permits ErbB3 upregulation and increased growth. *Oncogene* (2016) 35:1206. doi: 10.1038/onc.2015.418

44. Capparelli C, Rosenbaum S, Berger AC, Aplin AE. Fibroblast-derived neuregulin 1 promotes compensatory ErbB3 receptor signaling in mutant BRAF melanoma. *J Biol Chem* (2015) 290:24267–77. doi: 10.1074/jbc.M115.657270

45. Amin DN, Campbell MR, Moasser MM. The role of HER3, the unpretentious member of the HER family, in cancer biology and cancer therapeutics. *Semin Cell Dev Biol* (2010) 21:944–50. doi: 10.1016/j.semcdb.2010.08.007

46. Tanizaki J, Okamoto I, Okabe T, Sakai K, Tanaka K, Hayashi H, et al. Activation of HER family signaling as a mechanism of acquired resistance to ALK inhibitors in EML4-ALK-positive non-small cell lung cancer. *Clin Cancer Res* (2012) 18:6219–26. doi: 10.1158/1078-0432.CCR-12-0392

47. Lee H, Lee H, Chin H, Kim K, Lee D. ERBB3 knockdown induces cell cycle arrest and activation of bak and bax-dependent apoptosis in colon cancer cells. *Oncotarget* (2014) 5:5138–52. doi: 10.18632/oncotarget.2094

48. Zupa A, Improta G, Silvestri A, Pin E, Deng J, Aieta M, et al. A pilot characterization of human lung NSCLC by protein pathway activation mapping. *J Thorac Oncol Off Publ Int Assoc Study Lung Cancer* (2012) 7:1755–66. doi: 10.1097/JTO.0b013e3182725fc7

49. Baumann P, Cech TR. Pot1, the putative telomere end-binding protein in fission yeast and humans. *Science* (2001) 292:1171–5. doi: 10.1126/science.1060036

50. Smith PAD, Waugh EM, Crichton C, Jarrett RF, Morris JS. The prevalence and characterisation of TRAF3 and POT1 mutations in canine b-cell lymphoma. *Vet J* (2020) 266:105575. doi: 10.1016/j.tvjl.2020.105575

51. Lazzerini-Denchi E, Sfeir A. Stop pulling my strings - what telomeres taught us about the DNA damage response. *Nat Rev Mol Cell Biol* (2016) 17:364–78. doi: 10.1038/nrm.2016.43

52. Chan JYK, Poon PHY, Zhang Y, Ng CWK, Piao WY, Ma M, et al. Case report: Exome sequencing reveals recurrent RETSAT mutations and a loss-of-function POLDIP2 mutation in a rare undifferentiated tongue sarcoma. *F1000Research* (2018) 7:499. doi: 10.12688/f1000research.14383.1

53. Liu M, Du K, Jiang B, Wu X. High expression of PhospholipaseD2 induced by hypoxia promotes proliferation of colon cancer cells through activating NF- κ Bp65 signaling pathway. *Pathol Oncol Res* (2020) 26:281–90. doi: 10.1007/s12253-018-0429-1

54. Sánchez-Martínez R, Cruz-Gil S, Gómez de Cedrón M, Álvarez-Fernández M, Vargas T, Molina S, et al. A link between lipid metabolism and epithelial-mesenchymal transition provides a target for colon cancer therapy. *Oncotarget* (2015) 6:38719–36. doi: 10.18632/oncotarget.5340

55. Nath A, Chan C. Genetic alterations in fatty acid transport and metabolism genes are associated with metastatic progression and poor prognosis of human cancers. *Sci Rep* (2016) 6:18669. doi: 10.1038/srep18669

56. Fiucci G, Czarny M, Lavie Y, Zhao D, Berse B, Blusztajn JK, et al. Changes in phospholipase d isoform activity and expression in multidrug-resistant human cancer cells. *Int J Cancer* (2000) 85:882–8. doi: 10.1002/(sici)1097-0215(20000315)85:6<882::aid-ijc24>3.0.co;2-e

57. Cotte AK, Aires V, Fredon M, Limagne E, Derangère V, Thibaudin M, et al. Lysophosphatidylcholine acyltransferase 2-mediated lipid droplet production supports colorectal cancer chemoresistance. *Nat Commun* (2018) 9:322. doi: 10.1038/s41467-017-02732-5

58. Song W, Chen Z, Shi C, Gao Y, Feng X, Li H, et al. Synergistic anticancer effect of a combination of chidamide and etoposide against NK/T cell lymphoma. *Hematol Oncol* (2021). doi: 10.1002/hon.2954

59. Zhong H, Chen J, Cheng S, Chen S, Shen R, Shi Q, et al. Prognostic nomogram incorporating inflammatory cytokines for overall survival in patients with aggressive non-hodgkin's lymphoma. *EBioMedicine* (2019) 41:167–74. doi: 10.1016/j.ebiom.2019.02.048

frontiers | Frontiers in Immunology

TYPE Clinical Trial
PUBLISHED 19 August 2022
DOI 10.3389/fimmu.2022.938269

Check for updates

OPEN ACCESS

EDITED BY
Jian Zhang,
Southern Medical University, China

REVIEWED BY
Ze-Rui Zhao,
Sun Yat-sen University Cancer Center (SYSUCC), China
Bakulesh Mafatlal Khamar,
Cadila Pharmaceuticals Limited, India

*CORRESPONDENCE
Zhiwei Chen
czw75shchest@163.com
Shun Lu
shunlu@sjtu.edu.cn

†These authors have contributed equally to this work

SPECIALTY SECTION
This article was submitted to Cancer Immunity and Immunotherapy, a section of the journal Frontiers in Immunology

RECEIVED 07 May 2022
ACCEPTED 29 July 2022
PUBLISHED 19 August 2022

CITATION
Gu L, Wang X, Sun Y, Xu Y, Niu X, Zhao R, Yao Y, Jian H, Han Y, Wei J, Chen Z and Lu S (2022) An open, observational, three-arm clinical study of 2–3 cycles of treatment as neoadjuvant therapy in operable locally advanced non-small cell lung cancer: An interim analysis. *Front. Immunol.* 13:938269. doi: 10.3389/fimmu.2022.938269

COPYRIGHT
© 2022 Gu, Wang, Sun, Xu, Niu, Zhao, Yao, Jian, Han, Wei, Chen and Lu. This is an open-access article distributed under the terms of the Creative Commons Attribution License (CC BY). The use, distribution or reproduction in other forums is permitted, provided the original author(s) and the copyright owner(s) are credited and that the original publication in this journal is cited, in accordance with accepted academic practice. No use, distribution or reproduction is permitted which does not comply with these terms.

An open, observational, three-arm clinical study of 2–3 cycles of treatment as neoadjuvant therapy in operable locally advanced non-small cell lung cancer: An interim analysis

Linping Gu[1†], Xue Wang[1†], Yile Sun[1†], Yunhua Xu[1], Xiaomin Niu[1], Ruiying Zhao[2], Yaxian Yao[1], Hong Jian[1], Yuchen Han[2], Jinwang Wei[3], Zhiwei Chen[1*] and Shun Lu[1*]

[1]Department of Shanghai Lung Cancer Center, Shanghai Chest Hospital, Shanghai Jiao Tong University, Shanghai, China, [2]Department of Pathology, Shanghai Chest Hospital, Shanghai Jiao Tong University, Shanghai, China, [3]Department of Data Science, Genomicare Biotechnology (Shanghai) Co., Ltd., Shanghai, China

Background: An open, observational, three-arm clinical study aimed at investigating the efficacy of different neoadjuvant therapies (neoadjuvant immunotherapy with(out) chemotherapy, neoadjuvant chemotherapy, and neoadjuvant targeted therapy) in operable locally advanced non-small cell lung cancer (NSCLC) was conducted (NCT04197076). We report an interim analysis of 49 of 53 evaluable patients.

Methods: This study was conducted at Shanghai Chest Hospital and included eligible NSCLC patients who were 18 years old and had clinical stage IIB–IIIB disease. All 49 patients had surgical resection within 4–6 weeks after 2–3 cycles of neoadjuvant treatment consisting of immunotherapy (24 patients), chemotherapy (16 patients), and a targeted therapy (9 patients) regimen starting on the first day of each 21-day cycle. Pathologic complete response (pCR) was evaluated as the primary endpoint. Major pathological response (MPR) and tumor regression rate (TRR) were also evaluated.

Results: An improved pathologic complete response was achieved in the neoadjuvant immunotherapy arm compared with the neoadjuvant chemotherapy arm and neoadjuvant targeted therapy arm [20.8% (5/24) vs. 6.3% (1/16) vs. 0.0% (0/9); P = 0.089, 95% CI 0.138–0.151]. More importantly, we found that the curative effect of the neoadjuvant immunotherapy arm in pCR+MPR was better than that of the neoadjuvant chemotherapy arm and neoadjuvant targeted therapy arm [45.8% (11/24) vs. 18.8% (3/16) vs. 0.0% (0/9); P = 0.006, 95% confidence interval, 0.008–0.012]. Different neoadjuvant therapies had a statistically significant effect on postoperative pathological tumor downstaging (*P* = 0.017).

Conclusions: Neoadjuvant immunotherapy was associated with a trend toward better pCR than the neoadjuvant chemotherapy arm and neoadjuvant targeted therapy. Curative effect (pCR + MPR) was significantly better with neoadjuvant immunotherapy (P = 0.006, 95% confidence interval, 0.008–0.012).

Clinical Trial Registration: https://clinicaltrials.gov/ct2/show/NCT04197076?recrs=a&cond=NCT04197076&draw=2&rank=1.

KEYWORDS

operable locally advanced NSCLC, neoadjuvant therapy, major pathological response, tumor regression rate, clinical trial

Introduction

Lung cancer is still the leading cause of cancer death in 2020 worldwide. Of lung cancer cases, approximately 80% are classified as non-small cell lung cancer (NSCLC), and approximately one-third of NSCLC cases are diagnosed at a locally advanced stage (1, 2). For locally advanced NSCLC, the standard treatment is multidisciplinary therapy, including neoadjuvant therapy, complete surgical resection, and adjuvant treatment (3, 4). Although neoadjuvant chemotherapy represents a promising treatment strategy that significantly improves the survival rate in operable locally advanced NSCLC, the 5-year survival rate remains less than 50% in these patients (5, 6). Based on this unsatisfactory benefit, researchers have focused on exploring various neoadjuvant therapies in operable locally advanced NSCLC.

The emergence of immune checkpoint inhibitors (ICIs), including programmed cell death 1 (PD-1) or programmed cell death ligand 1 (PD-L1) antibodies and cytotoxic T-lymphocyte-associated protein 4 (CTLA-4) antibodies, has completely revolutionized the situation of neoadjuvant chemotherapy for operable locally advanced NSCLC. Checkmate 159 was the first clinical trial to report neoadjuvant immunotherapy before surgery in 21 limited-stage NSCLC patients who received 2 cycles of nivolumab (7). Then, the NADIM trial (neoadjuvant chemotherapy plus nivolumab) and NEOSTAR trial (neoadjuvant nivolumab or nivolumab plus ipilimumab) also demonstrated the potential value of neoadjuvant immunotherapy in operable NSCLC (8, 9). In addition to neoadjuvant immunotherapy, the EMERGING-CTONG 1103 trial (erlotinib vs. gemcitabine plus cisplatin (GC chemotherapy) as neoadjuvant therapy) also achieved better results in patients with locally advanced epidermal growth factor receptor (EGFR) mutation-positive NSCLC (10). We designed this clinical trial aiming to investigate the efficacy of different neoadjuvant therapies (neoadjuvant immunotherapy with(out) chemotherapy, neoadjuvant chemotherapy, and neoadjuvant targeted therapy) in operable locally advanced NSCLC. Hence, neoadjuvant immunotherapy or neoadjuvant targeted treatment seems to be a promising treatment for operable locally advanced NSCLC. The CheckMate 816 trial showed a significantly longer event-free survival and a higher percentage of patients with a pathological complete response (pCR) than chemotherapy alone in patients with resectable NSCLC (11). In view of the outcome of CheckMate 816, we carried out an interim analysis of the study to evaluate the efficacy of neoadjuvant therapy on pCR, MPR, and TRR before surgery. Overall survival (OS) and progression-free survival (PFS) directly represent patient survival and have been considered the gold standard for evaluating efficacy in many large clinical trials. Pathological complete response (pCR) and major response (MPR) are considered surrogate for PFS and OS (6, 12). Therefore, some clinical trials use pathologic evaluation after neoadjuvant therapy as the endpoint. At present, many studies have shown that a 10% residual viable tumor after surgery in locally advanced NSCLC patients indicates a major pathological response (MPR), and it is ideal for predicting the improvement of long-term prognosis (6, 7, 13, 14). In this context, we report the first clinical results of an interim analysis of the pCR, MPR after surgery, and tumor regression rate (TRR) before surgery in this study after 53 patients were enrolled of which 49 had surgery and are included in analysis for pCR and MPR.

Methods

Study design and participants

This open, observational, three-arm clinical study of 2–3 cycles of neoadjuvant targeted therapy, chemotherapy, and immunotherapy with(out) chemotherapy for operable locally advanced NSCLC was conducted at Shanghai Chest Hospital. Biopsy samples of adenocarcinoma were obtained and assessed

for EGFR mutation, anaplastic lymphoma kinase (ALK) translocation, and robot operating system (ROS-1) fusion. Patients diagnosed with adenocarcinoma with EGFR mutation, ALK translocation, or ROS-1 rearrangement were offered an appropriate tyrosine kinase inhibitor. The other patients for whom these three mutant genes were not detected were assigned to the immunotherapy ± chemotherapy arm or chemotherapy-alone arm as per discretion of the treating physician. Assessment of PD-L1 expression (22C3 pharmDx kit) was optional.

Eligible patients had Eastern Cooperative Oncology Group performance status 0 or 1, were aged 18 years or older, had cytology or histology documented, had tumor samples available for gene detection (EGFR/ALK/ROS-1), and did not receive antitumor treatment for NSCLC stages IIB–IIIB (American Joint Committee on Cancer 8th edition criteria) that was considered to be surgically operable within 4–6 weeks as assessed by multiple disciplinary teams after 2–3 cycles of neoadjuvant therapy. Patients were excluded from enrollment if they had a history of autoimmune disease, had a malignancy within the past 5 years, or were receiving ongoing treatment with systemic immunosuppressive medications. This study was registered at ClinicalTrials.gov [NCT04197076]. Full inclusion and exclusion criteria are included in the trial protocol. The trial protocol was approved by the institutional review board, and the trial was performed according to the International Conference on Harmonization Good Clinical Practice guidelines. All patients signed informed consent to participate according to the Declaration of Helsinki.

Procedures

The targeted drugs used against the EGFR 19del/21L858R mutation included afatinib, erlotinib, or gefitinib. Crizotinib was used for EML4-ALK translocation or ROS-1 rearrangement. Different chemotherapy regimens were adopted according to the clinical characteristics following National Comprehensive Cancer Network (NCCN) guidelines and Chinese Society of Clinical Oncology (CSCO) guidelines. Patients in the Immunotherapy group received immunotherapy ± chemotherapy or dual checkpoint inhibitors. Immunotherapy was selected from nivolumab, pembrolizumab, sintilimab, and ipilimumab.

All patients were reviewed for response to therapy at the end of 2–3 cycles (approximately 42 days) according to response evaluation criteria in solid tumors (RECIST) 1.1, and the operation was performed within 4–6 weeks. Necessary radiotherapy, chemotherapy, immunotherapy, or targeted therapy were administered according to NCCN and CSCO guidelines after the operation, and adverse events were evaluated according to common terminology criteria for adverse events (CTCAE) v4.0. The primary endpoint was pCR, which was defined as the lack of all signs of cancer in tissue samples removed during surgery after treatment. The other prespecified outcome was MPR, defined as <10% residual viable tumor, and TRR after neoadjuvant therapy. Patients had the right to withdraw from the trial for any reason at any time. Researchers had the right to withdraw patients from the study due to intolerant toxicity, violation of protocol violation, or other reasons.

After completion of the treatment, patients are being followed up every 3 months for the first 2–3 years, every 4–6 months for an additional 2 years, and annually thereafter. The follow-up evaluations consisted of a physical examination, complete blood count, blood biochemistry, tumor marker, thoracic computed tomography (CT) scan, abdomen B-ultrasound examination, and enhanced CT or magnetic resonance imaging examination of suspected lesions.

Statistical analysis

The full analysis set, which included all the patients, was used for demographic summaries and efficacy analyses. Continuous variables are expressed as the mean ± standard deviation. Treatment-related adverse events (TRAEs) were defined as adverse events (AEs) with possible or likely attribution to study drugs. All statistical analyses were performed using SPSS (IBM SPSS Statistics 25) and R V.4.1.1, and a two-sided *P* value of less than 0.05 indicated a statistically significant difference.

Results

Patient characteristics

From September 2018 to May 2021, 53 operable locally advanced NSCLC patients were enrolled and received 2–3 cycles of neoadjuvant therapy. Twenty-five patients received neoadjuvant immunotherapy (21 patients received immunotherapy + chemotherapy [one patient was from CheckMate-816], one patient received pembrolizumab alone, one patient received sintilimab alone, and two patients received nivolumab + ipilimumab from CheckMate-816), nine patients received neoadjuvant targeted therapy (six patients had EGFR 19del/21L858R mutations, two patients had EML4-ALK translocations, and one patient had ROS-1 rearrangements), and 16 patients received neoadjuvant chemotherapy (one patient was from CheckMate-816). Table 1 presents the characteristics of all patients at baseline.

TRR after 2–3 cycles of neoadjuvant therapy

After 2–3 cycles of neoadjuvant therapy, 13 patients (52.0%) achieved PR in the neoadjuvant immunotherapy arm, nine

10.3389/fimmu.2022.938269

TABLE 1 Baseline characteristics of all patients (N = 53).

Characteristics	Chemotherapy N = 19 (%)	Immunotherapy N = 25 (%)	Targeted therapy N = 9 (%)
Age, (years)			
Median (range)	64 (54-77)	60 (43-72)	47 (35-64)
BMI (kg/m2)			
Median (range)	24.2 (19.8-27.0)	25.0 (18.0-27.7)	22.7 (20.8-26.0)
Gender			
Male	16 (84.2)	23 (92.0)	0 (0.0)
Female	3 (15.8)	2 (8.0)	9 (100)
ECOG			
0	2 (10.5)	1 (4.0)	1 (11.1)
1	17 (89.5)	24 (96.0)	8 (88.9)
Smoke			
Never	4 (21.1)	9 (36.0)	9 (100)
Yes/ever	15 (78.9)	16 (64.0)	0 (0.0)
Pathology			
ADC	6 (31.6)	5 (20.0)	8 (88.9)
SCC	12 (63.2)	18 (72.0)	1 (11.1)
Not specified	1 (5.3)	2 (8.0)	0 (0.0)
cT-TNM8			
T1b	1 (5.3)	0 (0.0)	0 (0.0)
T1c	1 (5.3)	1 (4.0)	0 (0.0)
T2a	3 (15.8)	6 (24.0)	7 (77.8)
T2b	5 (26.3)	3 (12.0)	0 (0.0)
T3	4 (21.1)	10 (40.0)	2 (22.2)
T4	5 (26.3)	5 (20.0)	0 (0.0)
cN-TNM8			
N0	3 (15.8)	1 (4.0)	0 (0.0)
N1	3 (15.8)	8 (32.0)	1 (11.1)
N2	13 (68.4)	16 (64.0)	8 (88.9)
TNM8			
IIB	2 (10.5)	3 (12.0)	0 (0.0)
IIIA	10 (52.6)	14 (56.0)	8 (88.9)
IIIB	7 (36.8)	8 (32.0)	1 (11.1)
Gene status			
Wild-type	14 (73.7)	19 (76.0)	0 (0.0)
EGFR mutation	1 (5.3)	0 (0.0)	6 (66.7)
ALK translocation	1 (5.3)	0 (0.0)	2 (22.2)
ROS-1 rearrangement	0 (0.0)	0 (0.0)	1 (11.1)
Unknown	3 (15.8)	6 (24.0)	0 (0.0)
PD-L1 expression			
<1%	2 (10.5)	8 (32.0)	0 (0.0)
1%–50%	3 (15.8)	6 (24.0)	1 (11.1)
>50%	2 (10.5)	7 (28.0)	0 (0.0)
Unknown	12 (63.2)	4 (16.0)	8 (88.9)

BMI, body mass index; ECOG, Eastern Cooperative Oncology Group; ADC, adenocarcinoma; SCC, squamous cell carcinoma; SD, standard deviation; PD, progressive disease; cT-TNM8, clinical T stage according TNM eighth edition; cN-TNM8, clinical N stage according TNM eighth edition; TNM8, stage according TNM eighth edition. TRR, tumor regression rate.

patients (47.4%) achieved PR in the neoadjuvant chemotherapy arm, and four patients (44.4%) achieved PR in the neoadjuvant targeted therapy arm. The TRRs of all patients are shown in Figure 1A. No significant differences among the arms were noted (P = 0.59) (Table 2, Figure 2).

Surgery

Forty-nine patients were scheduled to successfully undergo surgery within 4–6 weeks after 2–3 cycles of neoadjuvant therapy. In the neoadjuvant immunotherapy arm, 23 patients (23/24, 95.8%) achieved complete tumor resection (R0), including eight patients (8/9, 88.9%) in the neoadjuvant targeted therapy arm and 15 patients (15/16, 93.8%) in the neoadjuvant chemotherapy arm. Table 3 shows all the characteristics of the surgical outcomes. Nineteen patients (79.2%) achieved pathological tumor downstaging in the neoadjuvant targeted therapy arm compared with four patients (44.4%) in the neoadjuvant targeted therapy arm and six patients (37.5%) in the neoadjuvant chemotherapy arm. Additionally, a significant difference in pathological tumor downstaging was noted among the different neoadjuvant therapy arms (P = 0.017).

Pathological response rate

The characteristics of 49 patients in different percentage viable tumor groups are shown in Figure 3. Five patients (20.8%) presented pCR in the neoadjuvant immunotherapy arm, and one patient (6.3%) achieved pCR in the neoadjuvant chemotherapy arm. However, no patients presented pCR in the target arm. Moreover, eight patients presented with MPR, including six patients (25%) in the neoadjuvant immunotherapy arm and two patients (12.5%) in the neoadjuvant chemotherapy arm. pCR+MPR significantly differed among the different neoadjuvant therapy arms (P = 0.006; 95% confidence interval [CI], 0.008–0.012) (Table 4).

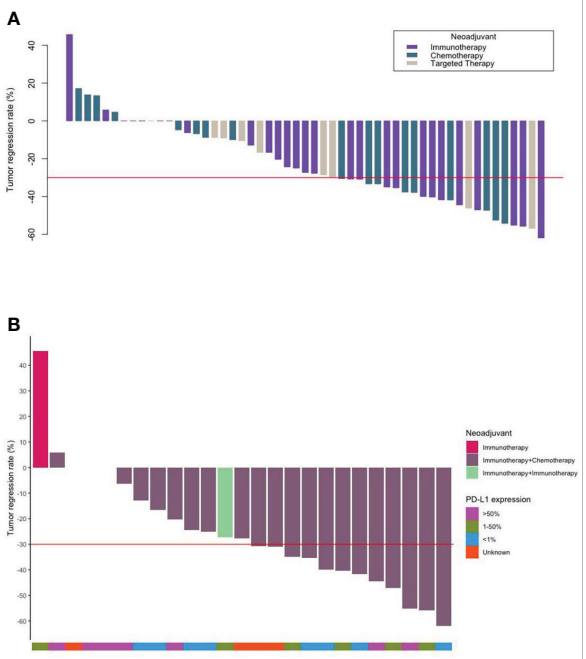

FIGURE 1
Waterfall plots. **(A)** The tumor regression and number of each type of all patients who underwent neoadjuvant therapy (N = 53). **(B)** The tumor regression of the patients who underwent neoadjuvant immunotherapy and their PD-L1 expression (N = 25).

Adverse events and long-term follow-up

The toxicity of the neoadjuvant immunotherapy arm was manageable overall, and no new safety concerns, including operative mortality, were noted. By 4 November 2021, 16 patients (five patients in the neoadjuvant chemotherapy arm, eight patients in the neoadjuvant immunotherapy arm, and three patients in the neoadjuvant targeted arm) had progressive disease, and five of these patients (four patients in the neoadjuvant chemotherapy arm and one patient in the neoadjuvant immunotherapy arm) died (Figure 3).

TABLE 2 Response and TRR of operable locally advanced NSCLC patients in different neoadjuvant therapy groups after neoadjuvant therapy.

Characteristics.	Chemotherapy N = 19 (%)	Immunotherapy N = 25 (%)	Targeted therapy N = 9 (%)
RECIST 1.1			
PR	9 (47.4)	13 (52.0)	4 (44.4)
SD	9 (47.4)	11 (44.0)	5 (55.6)
PD	1 (5.3)	1 (4.0)	0 (0.0)
TRR (%)			
Mean ± SD	18.42 ± 23.78	25.10 ± 23.73	22.97 ± 18.99
(range)	(-17.14-54.26)	(-45.65-61.90)	(0.00-56.92)

(N = 53).

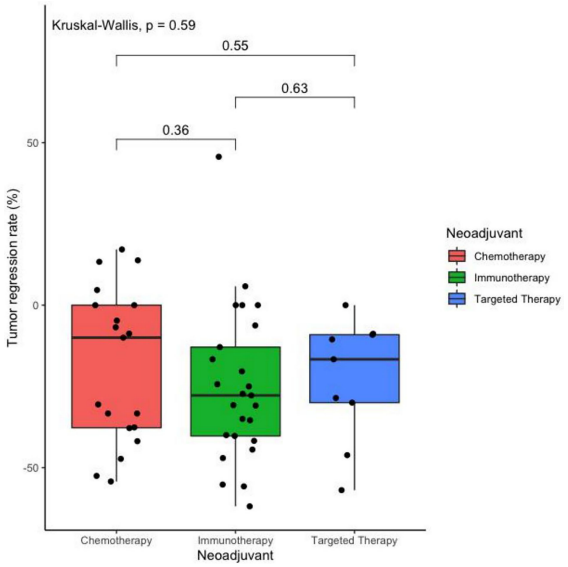

FIGURE 2
Boxplot of the tumor regression rate after two cycles of different treatments as neoadjuvant therapy in operatable locally advanced NSCLC. (N = 53).

Subgroup analysis

In the subgroup analysis, TRR and pCR+MPR were observed regardless of PD-L1 expression (P = 0.859, 0.053), and PD-L1 expression did not seem to predict the benefit of neoadjuvant benefit (Figure 1B, Table 5). Neoadjuvant immunotherapy was better than neoadjuvant chemotherapy in terms of TRR (30.76 ± 18.13 vs. 23.57 ± 22.16) and pCR+MPR (47.6% vs. 18.8%), but the difference was not significant (P = 0.399, 0.063) (Table 5).

Discussion

Although the efficacy of available treatment methods for operable locally advanced NSCLC has continuously improved in recent years, most of the relevant clinical trials employ OS and PFS as the primary endpoints, which not only leads to the high cost of time-consuming clinical trials but also hinders research on and the development of newly marketed drugs (12). It seems that the pathologic response could represent an interim surrogate analysis endpoint for OS because pathological assessment, which includes pCR and MPR, can be available using primary lesions resected during surgery in patients undergoing neoadjuvant therapy based on some previous studies (6, 9, 13, 15, 16). Neoadjuvant immunotherapy has a better clinical effect than neoadjuvant chemotherapy and neoadjuvant-targeted therapy based on pCR, MPR, TRR, or pathological T downstaging. The toxicity of neoadjuvant immunotherapy was generally controllable, and no new safety problems, including the operation mortality rate, were noted. The efficacy of neoadjuvant immunotherapy was not related to PD-L1 expression in subgroup analysis.

A previous review reported that the median rate of pCR from 15 clinical trials of neoadjuvant chemotherapy was 4% (range 0%–16%) (6). Mouillet et al. also retrospectively analyzed 492 patients with stage IB or II NSCLC who received 2 cycles of neoadjuvant chemotherapy. In total, 41 patients (8.3%) achieved pCR, and it was a favorable prognostic factor for OS in multivariate analysis (RR = 0.34; 95% CI = 0.18–0.64) (17). Compared with previous studies, only one patient (1/16, 6.3%) in the neoadjuvant chemotherapy arm achieved pCR in this study. Pataer et al. found that the percentage of viable tumor cells was significantly associated with OS (P = 0.005; HR = 1.01; 95% CI = 1.00–1.02), and 19% of patients (39/192) achieved MPR after neoadjuvant chemotherapy in a retrospective study (18). Weissferdt et al. also reported that MPR is related to OS (P < 0.01; HR = 2.68) after reevaluating the postoperative pathological specimens of 151 patients with operable NSCLC who received neoadjuvant chemotherapy, and 22% of patients (33/151) achieved MPR (19). Similar to previous studies, three patients (3/16, 18.8%) reached MPR after neoadjuvant chemotherapy in the present study.

For patients with driver gene-positive NSCLC, several studies have reported some positive results regarding neoadjuvant treatment. EMERGING-CTONG 1103 was a multicenter (17 centers in China), open-label, phase II, randomized controlled trial of erlotinib vs. GC chemotherapy as neoadjuvant/adjuvant therapy in patients with stage IIIA-N2 non-small cell lung cancer with EGFR mutations in exon 19 or 21 (10). In the erlotinib group, three patients (3/31, 9.7%) achieved MPR compared to only one patient (1/24, 4.2%) who achieved MPR in the GC chemotherapy group. Another single-arm, phase II trial that aimed to investigate the efficacy and safety of preoperative gefitinib in 35 patients with stage II–IIIA operable NSCLC reported that the rate of MPR was 24.2% (20). Zhang et al. also described 11 ALK receptor tyrosine kinase gene (ALK)-positive patients with pathologically confirmed N2 NSCLC who were treated with neoadjuvant crizotinib and suggested that neoadjuvant crizotinib might be feasible and well tolerated in locally advanced diseases for complete resection (21). However, in the current study, no patients reached pCR or MPR in the neoadjuvant-targeted therapy arm. The most important limitation of this study could be that only nine patients were included in the neoadjuvant-targeted therapy arm, which was far less than the number of patients in the neoadjuvant chemotherapy arm and neoadjuvant immunotherapy arm. However, the effect of TRR and pathological tumor downstaging in the neoadjuvant-targeted therapy arm was better than that noted for neoadjuvant

chemotherapy. Hence, more prospective clinical trial data are needed to further support the application of pCR/MPR in neoadjuvant-targeted therapy.

The remarkable effect of immunotherapy in advanced NSCLC brings the dawn for operable NSCLC and prompts researchers to conduct a large number of clinical trials in operable locally advanced NSCLC. Moreover, PD-1/L1 inhibitors combined with platinum-based chemotherapy are widely used in early neoadjuvant clinical trials because neoadjuvant chemotherapy has been demonstrated to enhance PD-L1 expression and promote the infiltration of immune cells in tumors (22). NADIM was the first phase II trial to explore 3 cycles of neoadjuvant immunotherapy + chemotherapy (nivolumab plus paclitaxel–carboplatin regimen) in patients with operable clinical stage IIIA NSCLC, and 41 patients (41/46, 89%) successfully underwent R0 resection (8). Moreover, the rates of MPR and pCR were 83% (34/41) and 63% (26/41), respectively. Another clinical trial of neoadjuvant atezolizumab and paclitaxel–carboplatin in resectable stage IB-IIIA NSCLC also showed that 26 (26/30, 87%) patients underwent successful

TABLE 3 Tumor location, surgical approach, and surgical outcomes of operable locally advanced NSCLC patients in different neoadjuvant therapy groups.

Characteristics.	Chemotherapy N = 16 (%)	Immunotherapy N = 24 (%)	Targeted therapy N = 9 (%)	P
Tumor location				0.866[a]
LUL	4 (25.0)	7 (29.2)	2 (22.2)	
LLL	1 (6.3)	3 (12.5)	1 (11.1)	
RUL	6 (37.5)	10 (41.7)	2 (22.2)	
RML	2 (12.5)	1 (4.2)	2 (22.2)	
RLL	3 (18.8)	3 (12.5)	2 (22.2)	
Approach				0.065[a]
VATS	4 (25.0)	6 (25.0)	6 (66.7)	
Thoracotomy	12 (75.0)	18 (75.0)	3 (33.3)	
Surgical margin				0.780[a]
R0	15 (93.8)	23 (95.8)	8 (88.9)	
R1	1 (6.1)	1 (4.2)	1 (11.1)	
ypT-TNM8				0.022[a]
T0	1 (6.3)	5 (20.8)	0 (0.0)	
T1b	0 (0.0)	1 (4.2)	2 (22.2)	
T1c	1 (6.3)	8 (33.3)	1 (11.1)	
T2a	6 (37.5)	4 (16.7)	4 (44.4)	
T2b	0 (0.0)	2 (8.3)	0 (0.0)	
T3	6 (37.5)	2 (8.3)	2 (22.2)	
T4	2 (12.5)	2 (8.3)	0 (0.0)	
ypN-TNM8				0.405[a]
N0	6 (37.5)	11 (45.8)	4 (44.4)	
N1	3 (18.8)	5 (20.8)	0 (0.0)	
N2	7 (43.8)	7 (29.2)	5 (55.6)	
N3	0 (0.0)	1 (4.2) [b]	0 (0.0)	
yp-TNM8				0.147[a]
Stage 0	1 (6.3)	5 (20.8)	0 (0.0)	
IA	0 (0.0)	3 (12.5)	1 (11.1)	
IB	2 (12.5)	2 (8.3)	1 (11.1)	
IIB	2 (12.5)	6 (25.0)	2 (22.2)	
IIIA	9 (56.3)	4 (16.7)	5 (55.6)	
IIIB	2 (12.5)	3 (12.5)	0 (0.0)	
IVA	0 (0.0)	1 (4.2)	0 (0.0)	
Pathological downstaging				
T stage				0.017[a]
Yes	6 (37.5)	19 (79.2)	4 (44.4)	

(Continued)

TABLE 3 Continued

Characteristics.	Chemotherapy N = 16 (%)	Immunotherapy N = 24 (%)	Targeted therapy N = 9 (%)	P
No	10 (62.5)	5 (20.8)	5 (55.6)	
N stage				0.956[a]
Yes	8 (50.0)	12 (50.0)	4 (44.4)	
No	8 (50.0)	12 (50.0)	5 (55.6)	
TNM stage				0.986[a]
Yes	9 (56.3)	14 (58.3)	5 (55.6)	
No	7 (43.8)	10 (41.7)	4 (44.4)	

(N = 49)*.

LUL, left upper lobe; LLL, left lower lobe; RUL, right upper lobe; RML, right middle lobe; RLL, right lower lobe; VATS, video-assisted thoracic surgery; ypT-TNM8, ypT stage according TNM eighth edition; ypN-TNM8, ypN stage according TNM eighth edition;

[a]likelihood ratio.

[b]this patient was pathologically evaluated as N3 after surgical treatment due to the lymph nodes of the contralateral 4R group and 10R group were obtained, and the pathological diagnosis was positive.

*, 49 patients (49/53, 92.5%) had underwent surgical resection with curative intent. Four patients did not undergo surgery after neoadjuvant therapy. Three patients were in the chemotherapy arm, and one patient with squamous cell carcinoma was in the immunotherapy arm. In the chemotherapy arm, one patient with adenocarcinoma had refused surgical resection after neoadjuvant chemotherapy. Although the efficacies of two patients with squamous cell carcinoma in the chemotherapy arm were evaluated as SD after neoadjuvant chemotherapy, the lesions were enlarged, and the investigators evaluated that those two patients did not have the possibility of complete surgical resection, so they did not receive surgical resection. Later, these two patients received local radiotherapy. One patient in the immunotherapy group did not receive surgical treatment because of the failure of neoadjuvant therapy for disease progression.

R0 resection, and the rates of MPR and pCR were 57% and 33%, respectively (13). CheckMate 816 was the first phase III trial to confirm the benefit of nivolumab plus platinum-doublet chemotherapy as neoadjuvant treatment for resectable NSCLC. Neoadjuvant nivolumab and platinum-doublet chemotherapy significantly improved the pCR, MPR, and R0 resection rates compared with neoadjuvant chemotherapy (24% vs. 2.2%; 36.9% vs. 8.9%; 83% vs. 78%), and patients who underwent neoadjuvant nivolumab and platinum-doublet chemotherapy all experienced benefits regardless of disease stage, histology, and PD-L1 expression levels (11, 23). Our interim analysis showed that the patients in the neoadjuvant immunotherapy arm had the best benefits, including MPR (25% vs. 12.5% vs. 0.0%) or pCR (20.8% vs. 6.3% vs. 0.0%), compared with the neoadjuvant chemotherapy arm or neoadjuvant-targeted therapy arm. This finding also verified the value of

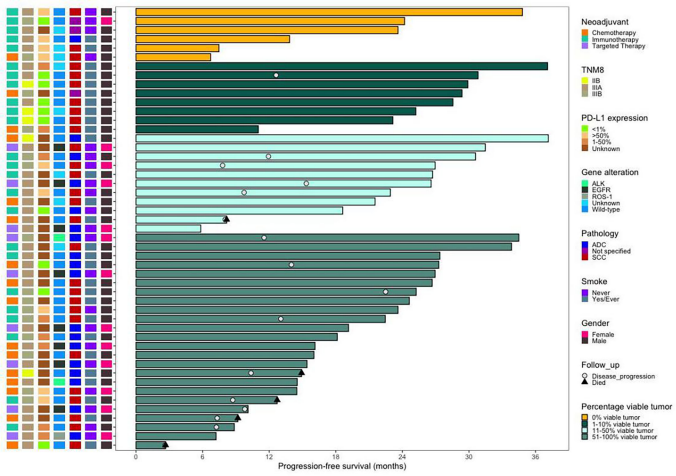

FIGURE 3
Swimming plot of progression-free survival in the patients who underwent surgery. (N = 49). Each bar represents one patient. The left column shows clinical characterestics. Date cutoff was Nov. 4, 2021, sixteen (32.7%) patients who underwent surgery had disease progression, five (10.2%) of whom died. Of the 14 patients with pCR or MPR, one patient who received neoadjuvant immunotheraphy had disease progression. Of the 16 (one patient has died), 5 patient received neoadjuvant immunotheraphy (four patients have died), and 3 patients received neojuvant targeted chemotheraphy.

TABLE 4 Pathological response rates of operable locally advanced NSCLC patients in different neoadjuvant therapy groups after surgery.

Percentage viable tumor	Total N = 49 (%)	Chemotherapy N = 16 (%)	Immunotherapy N = 24 (%)	Targeted therapy N = 9 (%)	P
pCR +MPR	14 (28.6)	3 (18.8)	11 (45.8)	0 (0.0)	0.006(0.008-0.012)
pCR(0% viable tumor)[a]	6 (12.2)	1 (6.3)	5 (20.8)	0 (0.0)	0.089(0.138-0.151)
MPR(1%–10% viable tumor)[b]	8 (16.3)	2 (12.5)	6 (25.0)	0 (0.0)	
11%–50% viable tumor	11 (22.4)	3 (18.8)	5 (20.8)	3 (33.3)	
51%–100% viable tumor	24 (49.0)	10 (62.5)	8 (33.3)	6 (66.7)	

(N = 49).

neoadjuvant immunotherapy in pathological tumor downstaging (79.2% vs. 37.5% vs. 44.4%) and successful R0 resection (95.8% vs. 93.8% vs. 88.9%). Although, in our study, the incidence of pCR was not significantly different in the three groups, we suggest that the small sample size explains why the results did not achieve statistical significance. Similar to our results, another phase II study of 2–4 cycles of neoadjuvant immune chemotherapy for resectable stage IIIA NSCLC reported MPR and pCR values of 43.3% and 20%, respectively (24). One reason could be that for operable NSCLC patients, the use of ICIs as neoadjuvant treatment is beneficial to reactivate the activity of antitumor immune T cells and improve the ability to remove potential micrometastases in the body (25). Another reason could be the presence of more gene mutations in tumor cells that produce new epitopes after chemotherapy, which can enhance the immunogenicity of the tumor and improve the efficacy of immunotherapy (26, 27). Although the results of many studies have suggested a correlation between PD-L1 expression and immunotherapy efficacy, even patients with a negative expression of PD-L1 can still benefit from neoadjuvant immunotherapy in subgroup analysis.

In our study, six patients (12.2%, 6/49) achieved pCR, including four stage IIIA NSCLC patients and two stage IIIB NSCLC patients (Figure 3). When evaluating the efficacy of neoadjuvant immunotherapy before the operation, special attention should be given to pseudoprogression and hyperprogression. Surgical treatment after neoadjuvant immunotherapy was well tolerated with no significant delays to surgery or unexpected surgical complications.

Several limitations to this study should be noted. First, this was an interim analysis, and we hope to observe the OS and PFS of this study in the future. Second, we did not analyze the mechanism of different neoadjuvant arms, especially in the neoadjuvant immunotherapy and neoadjuvant-targeted therapy arms. Third, this was a single-center study with a small sample, which limited its applicability to some extent. In the future, we should focus on studying the mechanism of different neoadjuvant therapies and screening the best neoadjuvant therapy mode to prolong the survival rate of operable NSCLC. Whether this pathological response results in prolonged survival requires further analysis in a larger patient cohort.

Conclusion

In conclusion, neoadjuvant immunotherapy appears to be safe and feasible and does not increase perioperative morbidity following surgery. The existing data suggest that neoadjuvant immunotherapy is promising in terms of pCR, MPR, and TRR among patients with operable locally advanced NSCLC compared with neoadjuvant-targeted therapy and neoadjuvant

TABLE 5 The results in different groups of PD-L1 expression and treatments.

	Expression of PD-L1[a]			Chemotherapy	Immunotherapy + chemotherapy	
Characteristic	<1%, N = 8 (%)	≥1%, N = 10 (%)	P	N = 16 (%)	N = 21 (%)	P
TRR (%)			0.859[b]			0.399[b]
Mean ± SD(range)	32.25 ± 15.91(12.90-61.90)	31.12 ± 21.89(-5.80-55.77)		23.57 ± 22.16(-17.14-54.26)	30.76 ± 18.13(-5.80-61.90)	
Percentage viable tumor			0.053[c]			0.063[c]
pCR+MPR	6 (75.0)	3 (30.0)		3 (18.8)	10 (47.6)	
Non-pCR/MPR	2 (25.0)	7 (70.0)		13 (81.3)	11 (52.4)	

[a]all patients who were detected PD-L1 in neoadjuvant immunotherapy + chemotherapy. (N=18).
[b]Mann–Whitney U test.
[c]likelihood ratio.

chemotherapy. Neoadjuvant immunotherapy could therefore represent a potential therapeutic strategy for operable locally advanced NSCLC patients.

Data availability statement

The original contributions presented in the study are included in the article/supplementary material. Further inquiries can be directed to the corresponding authors.

Ethics statement

The studies involving human participants were reviewed and approved by the IRB of Shanghai Chest Hospital (No. KS1971). All patients had provided consent for the use of the medical information contained in this trial for research and publication. The patients/participants provided their written informed consent to participate in this study.

Author contributions

Conceptualization: ZC, XN, and LG; data curation: LG, XW, and YS; formal analysis: LG, XW, and YS; funding acquisition: ZC and XN; investigation: YX, XN, RZ, YH, YY, and HJ; methodology: LG, XW, YS, and ZC; project administration: LG, ZC, and SL; resources: LG; software: LG, XW, and JW; supervision: YX, XN, YH, YY, and HJ; Validation: LG, XW, YS, YX, XN, YH, YY, HJ, and ZC; visualization: XW. All authors read and approved the final manuscript.

Funding

The Technology Transfer Project of Shanghai Jiao Tong University School of Medicine (No. ZT202010); the National Natural Science Foundation of China (No. 81972187); Projects of the Committee of Shanghai Science and Technology (Nos. 19ZR1449800 and 20Y11913700); Projects of Shanghai Municipal Public Health Bureau (Nos. 201840122 and 2019SY048); Doctoral Innovation Fund of Shanghai Jiao Tong University School of Medicine (No. BXJ201952); Interdisciplinary Program of Shanghai Jiao Tong University (No. YG2017MS80); Project of Shanghai Talent Development Fund (No. 2019074); National Natural Science Foundation of China (82030045); National Multi-disciplinary Treatment Project for Major Diseases (2020NMDTP); Technology Innovation Program of Shanghai (19411950500); and the National Key R&D Program of China (2016YFC1303300).

Acknowledgments

The authors thank GenomiCare Biotechnology (Shanghai) for their effort in Gene analysis in the neoadjuvant-targeted therapy arm.

Conflict of interest

Author JW is employed by GenomiCare Biotechnology (Shanghai) Co, Ltd.

The remaining authors declare that the research was conducted in the absence of any commercial or financial relationships that could be construed as a potential conflict of interest.

Publisher's note

All claims expressed in this article are solely those of the authors and do not necessarily represent those of their affiliated organizations, or those of the publisher, the editors and the reviewers. Any product that may be evaluated in this article, or claim that may be made by its manufacturer, is not guaranteed or endorsed by the publisher.

References

1. Sung H, Ferlay J, Siegel RL, Laversanne M, Soerjomataram I, Jemal A, et al. Global cancer statistics 2020: GLOBOCAN estimates of incidence and mortality worldwide for 36 cancers in 185 countries. *CA Cancer J Clin* (2021) 71:209–49. doi: 10.3322/caac.21660

2. Bagcchi S. Lung cancer survival only increases by a small amount despite recent treatment advances. *Lancet Respir Med* (2017) 5:169. doi: 10.1016/S2213-2600(17)30041-3

3. Herbst RS, Morgensztern D, Boshof C. The biology and management of non-small cell lung cancer. *Nature* (2018) 553:446–54. doi: 10.1038/nature25183

4. Chaft JE, Shyr Y, Sepesi B, Forde PM. Preoperative and postoperative systemic therapy for operable non-Small-Cell lung cancer. *J Clin Oncol* (2022) 40 (6):546–55. doi: 10.1200/JCO.21.01589

5. Group NMC. Preoperative chemotherapy for non-small-cell lung cancer: a systematic review and meta-analysis of individual participant data. *Lancet* (2014) 383:1561–71. doi: 10.1016/S0140-6736(13)62159-5

6. Hellmann MD, Chaft JE, William WN, Rusch V, Pisters KMW, Kalhor N, et al. Pathological response after neoadjuvant chemotherapy in resectable non-small-cell lung cancers: proposal for the use of major pathological response as a

surrogate endpoint. *Lancet Oncol* (2014) 15:e42–50. doi: 10.1016/S1470-2045(13)70334-6

7. Forde PM, Chaft JE, Smith KN, Anagnostou V, Cottrell TR, Hellmann MD, et al. Neoadjuvant PD-1 blockade in resectable lung cancer. *N Engl J Med* (2018) 378(21):1976–86. doi: 10.1056/NEJMoa1716078

8. Provencio M, Nadal E, Insa A, García-Campelo MR, Casal-Rubio J, Dómine M, et al. Neoadjuvant chemotherapy and nivolumab in resectable non-small-cell lung cancer (NADIM): an open-label, multicentre, single-arm, phase 2 trial. *Lancet Oncol* (2020) 21(11):1413–22. doi: 10.1016/S1470-2045(20)30453-8

9. Cascone T, William WNJr, Weissferdt A, Leung CH, Lin HY, Pataer A, et al. Neoadjuvant nivolumab or nivolumab plus ipilimumab in operable non-small cell lung cancer: the phase 2 randomized NEOSTAR trial. *Nat Med* (2021) 27(3):504–14. doi: 10.1038/s41591-020-01224-2

10. Zhong WZ, Chen KN, Chen C, Gu CD, Wang J, Yang XN, et al. Erlotinib versus gemcitabine plus cisplatin as neoadjuvant treatment of stage IIIA-N2 EGFR-mutant non-Small-Cell lung cancer (EMERGING-CTONG 1103): A randomized phase II study. *J Clin Oncol* (2019) 37(25):2235–45. doi: 10.1200/JCO.19.00075

11. Forde PM, Spicer J, Lu S, Provencio M, Mitsudomi T, Awad MM, et al. Neoadjuvant nivolumab plus chemotherapy in resectable lung cancer. *N Engl J Med* (2022) 386(21):1973–85. doi: 10.1056/NEJMoa2202170

12. Kilickap S, Demirci U, Karadurmus N, Dogan M, Akinci B, Sendur MAN. Endpoints in oncology clinical trials. *J BUON* (2018) 23(7):1–6.

13. Shu CA, Gainor JF, Awad MM, Chiuzan C, Grigg CM, Pabani A, et al. Neoadjuvant atezolizumab and chemotherapy in patients with resectable non-small-cell lung cancer: an open-label, multicentre, single-arm, phase 2 trial. *Lancet Oncol* (2020) 21(6):786–95. doi: 10.1016/S1470-2045(20)30140-6

14. Qu Y, Emoto K, Eguchi T, Aly RG, Zheng H, Chaft JE, et al. Pathologic assessment after neoadjuvant chemotherapy for NSCLC: importance and implications of distinguishing adenocarcinoma from squamous cell carcinoma. *J Thorac Oncol* (2019) 14:482–93. doi: 10.1016/j.jtho.2018.11.017

15. Liu X, Sun W, Wu J, Feng Y, Mao L, Chen M, et al. Major pathologic response assessment and clinical significance of metastatic lymph nodes after neoadjuvant therapy for non-small cell lung cancer. *Mod Pathol* (2021) 34(11):1990–8. doi: 10.1038/s41379-021-00871-1

16. Duan H, Wang T, Luo Z, Tong L, Dong X, Zhang Y, et al. Neoadjuvant programmed cell death protein 1 inhibitors combined with chemotherapy in resectable non-small cell lung cancer: an open-label, multicenter, single-arm study. *Transl Lung Cancer Res* (2021) 10(2):1020–8. doi: 10.21037/tlcr-21-130

17. Mouillet G, Monnet E, Milleron B, Puyraveau M, Quoix E, David P, et al. Pathologic complete response to preoperative chemotherapy predicts cure in early-stage non-small-cell lung cancer: combined analysis of two IFCT randomized trials. *J Thorac Oncol* (2012) 7(5):841–9. doi: 10.1097/JTO.0b013e31824c7d92

18. Pataer A, Kalhor N, Correa AM, Raso MG, Erasmus JJ, Kim ES, et al. Histopathologic response criteria predict survival of patients with resected lung cancer after neoadjuvant chemotherapy. *J Thorac Oncol* (2012) 7(5):825–32. doi: 10.1097/JTO.0b013e318247504a

19. Weissferdt A, Pataer A, Vaporciyan AA, Correa AM, Sepesi B, Moran CA, et al. Agreement on major pathological response in NSCLC patients receiving neoadjuvant chemotherapy. *Clin Lung Cancer* (2020) 21(4):341–8. doi: 10.1016/j.cllc.2019.11.003

20. Zhang Y, Fu F, Hu H, Wang S, Li Y, Hu H, et al. Gefitinib as neoadjuvant therapy for resectable stage II-IIIA non-small cell lung cancer: A phase II study. *J Thorac Cardiovasc Surg* (2021) 161(2):434–442.e2. doi: 10.1016/j.jtcvs.2020.02.131

21. Zhang C, Li SL, Nie Q, Dong S, Shao Y, Yang XN, et al. Neoadjuvant crizotinib in resectable locally advanced non-small cell lung cancer with ALK rearrangement. *J Thorac Oncol* (2019) 14(4):726–31. doi: 10.1016/j.jtho.2018.10.161

22. Parra ER, Villalobos P, Behrens C, Jiang M, Pataer A, Swisher SG, et al. Effect of neoadjuvant chemotherapy on the immune microenvironment in non-small cell lung carcinomas as determined by multiplex immunofluorescence and image analysis approaches. *J Immunother Cancer* (2018) 6(1):48. doi: 10.1186/s40425-018-0368-0

23. Spicer J, Wang C, Tanaka F, Saylors GB, Chen K, Liberman M, et al. Surgical outcomes from the phase 3 CheckMate 816 trial: nivolumab (NIVO) + platinum-doublet chemotherapy(chemo) vs chemo alone as neoadjuvant treatment for patients with resectable non-small cell lung cancer (NSCLC). *J Clin Oncol* (2021) 39(suppl 15):8503. doi: 10.1200/JCO.2021.39.15_suppl.8503

24. Zhang P, Dai J, Sun F, Xia H, He W, Duan L, et al. Neoadjuvant sintilimab and chemotherapy for resectable stage IIIA non-small-cell lung cancer. *Ann Thorac Surg* (2022) S0003-4975(22)00191-6. doi: 10.1016/j.athoracsur.2022.01.039

25. Hurkmans DP, Kuipers ME, Smit J, Van Marion R, Mathijssen RHJ, Postmus PE, et al. Tumor mutational load, CD8+ T cells, expression of PD-L1 and HLA class I to guide immunotherapy decisions in NSCLC patients. *Cancer Immunol Immunother* (2020) 69(5):771–7. doi: 10.1007/s00262-020-02506-x

26. Brown JS, Sundar R, Lopez J. Combining DNA damaging therapeutics with immunotherapy: more haste, less speed. *Br J Cancer* (2018) 118(3):312–24. doi: 10.1038/bjc.2017.376

27. Hato SV, Khong A, de Vries IJ, Lesterhuis WJ. Molecular pathways: the immunogenic effects of platinum-based chemotherapeutics. *Clin Cancer Res* (2014) 20(11):2831–7. doi: 10.1158/1078-0432.CCR-13-3141

frontiers | Frontiers in Immunology

TYPE Original Research
PUBLISHED 24 August 2022
DOI 10.3389/fimmu.2022.965469

Check for updates

OPEN ACCESS

EDITED BY
Linlang Guo,
Zhujiang Hospital, China

REVIEWED BY
Enchong Zhang,
ShengJing Hospital of China Medical University, China
Xu-Sheng Liu,
Hubei University of Medicine, China
Rui Cao,
Capital Medical University, China

*CORRESPONDENCE
Yongjie Wang
ujee921@163.com

†These authors have contributed equally to this work

SPECIALTY SECTION
This article was submitted to Cancer Immunity and Immunotherapy, a section of the journal Frontiers in Immunology

RECEIVED 09 June 2022
ACCEPTED 29 July 2022
PUBLISHED 24 August 2022

CITATION
Deng D, Liu F, Liu Z, Wu Z, He Y, Zhang C, Zu X, Ou Z and Wang Y (2022) Robust Pyroptosis Risk Score Guides the Treatment Options and Predicts the Prognosis of Bladder Carcinoma. *Front. Immunol.* 13:965469. doi: 10.3389/fimmu.2022.965469

COPYRIGHT
© 2022 Deng, Liu, Liu, Wu, He, Zhang, Zu, Ou and Wang. This is an open-access article distributed under the terms of the Creative Commons Attribution License (CC BY). The use, distribution or reproduction in other forums is permitted, provided the original author(s) and the copyright owner(s) are credited and that the original publication in this journal is cited, in accordance with accepted academic practice. No use, distribution or reproduction is permitted which does not comply with these terms.

Robust pyroptosis risk score guides the treatment options and predicts the prognosis of bladder carcinoma

Dingshan Deng[1,2†], Fenglian Liu[3†], Zhi Liu[1,2], Zuowei Wu[4], Yunbo He[1,2], ChunYu Zhang[1,2], Xiongbin Zu[1,2], Zhenyu Ou[1,2] and Yongjie Wang[2,5*]

[1]Departments of Urology, Xiangya Hospital, Central South University, Changsha, China, [2]National Clinical Research Center for Geriatric Disorders, Xiangya Hospital, Changsha, China, [3]Departments of Laboratory Medicine, The Second Affiliated Hospital, Guizhou Medical University, Kaili, China, [4]Department of Interventional Radiology, Third Xiangya Hospital, Central South University, Changsha, China, [5]Department of Burns and Plastic Surgery, Xiangya Hospital, Central South University, Changsha, China

Background: Bladder carcinoma (BLCA) is a heterogeneous disease that makes it difficult to achieve proper individual treatment and predict prognosis. This study aimed to develop a risk score from a new perspective of pyroptosis and guide accurate treatment and prognosis prediction for BLCA.

Methods: The TCGA-BLCA cohort data were downloaded from The Cancer Genome Atlas database. Two external validation cohorts were collected from the Gene Expression Omnibus. Another independent validation cohort (the Xiangya cohort) was recruited from our hospital. The least absolute shrinkage and selector operation (LASSO) algorithm and Cox regression models were used to establish the pyroptosis risk score. Thereafter, we correlated the pyroptosis risk score with prognosis, tumor microenvironment (TME) immune hallmarks, and multiple treatments, including anticancer immunotherapy, chemotherapy, radiotherapy, and targeted therapy.

Results: The pyroptosis risk score was an independent prognostic predictor of BLCA. We found that the activities of multiple steps of the anticancer immune response cycle, such as the release of cancer cell antigens, CD8 T cell recruitment, and NK cell recruitment, were significantly higher in the high-risk score group than in the low-risk score group. In addition, the infiltration levels of the corresponding tumor-infiltrating immune cells (TIICs), such as CD8 T cells and NK cells, were positively correlated with the pyroptosis risk score. Thus, BLCA with a high-risk score may be associated with inflamed phenotypes. Simultaneously, the expression of multiple immune checkpoints (such as PD-L1, CTLA-4, and PD-1) and enrichment scores of gene signatures positively correlated with immunotherapy response were positively correlated with the pyroptosis risk score. Therefore, patients with a high pyroptosis risk score may be more sensitive to immunotherapy. In addition, patients with high

pyroptosis risk scores may be more sensitive to chemotherapeutic drugs, such as cisplatin, docetaxel, and paclitaxel. In addition, the pyroptosis risk score accurately predicted the molecular subtypes of BLCA, which were cross-validated in several independent systems.

Conclusions: This study developed and validated a robust pyroptosis risk score that can predict the clinical outcomes and TME immune phenotypes of BLCA. In summary, the pyroptosis risk score helps drive precision therapy in patients with BLCA.

KEYWORDS

bladder cancer, pyroptosis, risk score, tumor immune microenvironment, immunotherapy, chemotherapy, radiotherapy

Introduction

Bladder cancer is one of the most common urinary tumors with an increasing incidence. Approximately 150,000 people worldwide die of this disease every year (1). Non-muscle invasive bladder cancer (NMIBC) can be treated with surgical resection and intravesical perfusion therapy; however, most patients still experience recurrence (2). In muscle invasive bladder cancer (MIBC), the main treatments include surgery, radiotherapy, targeted therapy, and anticancer immunotherapy (2, 3). However, these treatment options are insufficient to cure BLCA. Only a minority of patients are sensitive to these regimens, which are caused by many primary or acquired resistance mechanisms such as pyroptosis (4). The inherent genetic heterogeneity of tumor cells and metabolism-related factors cause tumor cells to acquire drug resistance to treatments (4). Bladder cancer is a heterogeneous tumor with many molecular subtypes, making it difficult to achieve accurate treatment (2). Therefore, it is important to develop effective tools to reveal the heterogeneity of BLCA and predict its prognosis and efficacy.

Pyroptosis is a programmed inflammatory cell death usually accompanied by the activation of inflammatory bodies and maturation of proinflammatory cytokines IL-1 β (IL-1 β) and interleukin-18 (IL-18) (4, 5). In recent years, researchers have conducted several studies on tumor cell pyroptosis. Pyroptosis inhibits tumor growth in colorectal, liver, skin, and other cancers (6). The role of pyroptosis in bladder tumors requires further investigation. Some studies have shown that GSDME, a member of the gasdermin superfamily, can trigger pyroptosis by cleaving GSDMD by activating caspase-3 during chemotherapy (7). Caspase 8 is considered a molecular switch that regulates pyroptosis (8). Pyroptosis affects tumor proliferation, invasion, and metastasis, reshapes the tumor microenvironment, and stimulates anti-tumor immune responses. Some molecules related to pyroptosis have been identified in some tumors and can be used to predict prognosis and therapeutic response (5, 9). Current immunotherapy, including anti-CTLA-4, anti-PD-1/PD-L1, and chimeric antigen receptor (CAR) T-cell therapy, has significantly improved the survival outcomes of patients with cancers (10–12). However, the relationship between pyroptosis and the tumor immune microenvironment in BLCA needs to be further explored.

This study integrated several independent BLCA datasets and developed a novel pyrolysis risk score. We correlated the pyrolysis risk score with clinical prognosis, the tumor microenvironment (TME) phenotypes, and response to multiple treatment regimens.

Materials and methods

Data sets collection

External public cohorts

The mRNA expression matrix (FPKM) of 414 BLCA tumor samples and 19 normal tissues were downloaded from the TCGA Cancer Genome Atlas (https://portal.gdc.cancer.gov/). Thereafter, the FPKM values were converted to TPM values. Two externally validated GSE cohorts with detailed survival data, GSE32894 and GSE48075 were collected from the Gene Expression Omnibus (GEO). GSE32894 (platform: GPL6947) contained 224 BLCA samples and GSE48075 (platform: GPL6947) contained 73 BLCA samples with survival information.

Xiangya cohort: According to our previous study, the Xiangya cohort (GSE188715) comprised 57 BLCA samples sequenced on the BGISEQ-500 platform (BGI-Shenzhen, China) (13–15). Determination of pyroptosis gene sets: The keyword “pyroptosis” was searched in the GSEA public database (http://www.gsea-

msigdb.org/gsea/msigdb/genesets.jsp). Two gene sets, "GO BP_PYROPTOSIS" and "REACTOME_PYROPTOSIS, " were obtained. Forty pyroptosis-related genes were also identified. In addition, we extracted 33 pyroptosis-related genes from previous studies (16–19). Finally, 57 pyroptosis-related genes were obtained (Supplementary Table 1).

The detailed information of these cohorts was provided in Supplementary Table 1.

Single cell RNA sequencing (scRNA-seq)

Three muscle-invasive bladder cancer (MIBCs) samples were obtained from the Department of Urology, Xiangya Hospital, and scRNA-seq was performed at OE Biotech Co, Ltd (Shanghai, China), named as the Xiangya scRNA cohort. There are studies reporting that the detailed preparation of single-cell suspensions is based on droplet processing of raw data and single-cell sequencing (20, 21). After processing through cell ranger, the Seurat R package (version 4.1.0) was used to convert the count matrix to a Seurat object. Low-quality cells were cells with a unique molecular identifier (UMI) number of less than 1000, a gene number of less than 200, a log10GenesPerUMI number of less than 0.70, and a mitochondrial-derived UMI number of more than 20%, and these cells were discarded. The count matrixs were then normalized and the effects of mitochondrial proportion were regressed. The functions SelectIntegrationFeatures, findinintegrationanchors and IntegrateData integrate these three samples based on the first 3000 variable features. Afterwards, principal component analysis (PCA) was used to display the cell clusters through the tSNE plot and use the FindClusters function to screen the main cell clusters (res=0.4). To identify malignant bladder cancer cells, CNVs in epithelial cells were screened by the InferCNV package.

Identification of differentially expressed pyroptotic genes (pyroptotic DEGs) and functional analysis

The empirical Bayesian method of the limma R package was used to identify differentially expressed pyroptotic DEGs between bladder cancer and normal tissues. The screening criteria for pyroptotic DEGs were as follows: |log(fold change)|>1 and adjusted P-value< 0.05 (22). The Kyoto Encyclopedia of Genes and Genomes (KEGG) and Gene Ontology (GO) analyses were performed using the aforementioned pyroptotic DEGs (23).

Development and validation of pyroptosis risk score

First, pyroptotic DEGs from cancerous and paracancerous tissues were screened in the TCGA-BLCA cohort. Thereafter, we screened the prognostic pyroptotic genes in the TCGA-BLCA cohort using univariate Cox analysis. Furthermore, least absolute shrinkage and selection operator (LASSO) regression was performed to identify the pyroptotic DEGs with the best prognosis. Finally, based on the best prognostic pyroptotic DEGs, the risk score for pyroptosis was calculated using the LASSO coefficient: Risk score = $\sum \beta i * RNAi$, where βi is the coefficient of the i-th.

Patients were divided into high- and low-scoring groups according to the median pyroptosis risk score. Kaplan-Meier survival analysis was used to obtain the survival curves. The predictive prognostic accuracy of pyroptosis risk score was determined using the tROC R package. The prognostic accuracy of the pyroptosis risk score was validated in the GSE32894, GSE48075, and an internal cohort (Xiangya cohorts). In addition, the pyroptosis risk score was correlated with the grade and stage of tumors. Univariate and multivariate Cox analyses were used to analyze the independent prognostic role of sex, age, stage, and the pyroptosis risk score in the TCGA-BLCA cohort. Finally, a nomogram was plotted based on these factors with an independent prognostic predictive value. The nomogram was validated using clinical decision curves.

Description of BLCA molecular subtypes and TME characteristics

In our previous study, seven independent molecular subtype systems were analyzed, including the UNC, Baylor, TCGA, MDA, CIT, and consensus systems (15). Relevant molecular subtype-specific signatures were collected and correlated with pyroptosis risk scores. In our previous study, the related immunological characteristics and algorithms in the TME were described in detail (13–15, 20, 24). The steps of the cancer-immune cycle include cancer antigen presentation, release, immune cell trafficking, recognition, and killing. Thereafter, various independent algorithms, such as TIP, CiberSort-ABS, and TIMER, were used to obtain the infiltration degree of tumor-infiltrating immune cells (TIIC) (13–15, 20, 24).

Gene set variation analysis (GSVA) and response prediction of several treatment options

GSVA is often used to estimate the activity differences of pathways or biological processes in expression dataset samples and is a nonparametric unsupervised method (25). To study the differences of 50 correlation pathways among the pyroptosis risk score groups, the corresponding paths from MSigDB and analyzed GSVA enrichment were collected using "GSVA" R software package (26). Individualized chemotherapy response

was estimated using the pRRophetic software package based on data from the Genomics of Cancer Drug Sensitivity (GDSC) (https://www.ancerrxgene.org/) (27). We calculated the IC50 values of cisplatin, docetaxel, paclitaxel, bleomycin, camptothecin, and vinblastine. In addition, we summarized some effective indicators for predicting the efficacy of ICB, including the pan-cancer T cell inflammation score (TIS) and 20 inhibitory immune checkpoints (15). Finally, the enrichment fraction of the signature related to clinical response to targeted therapy and radiotherapy was calculated using the ssGSEA algorithm.

Statistical analysis

Statistical analysis of all relevant data was performed using the R software. Pearson or Spearman coefficients were used to analyze the correlations between variables. The t-test or Mann-Whitney U test was used to compare differences in continuous variables between the groups. Survival curves were plotted using the Kaplan-Meier method. We used receiver operating characteristic (ROC) curves to calculate the accuracy of pyroptosis risk scores for predicting survival and molecular subtypes. Statistical tests were two-sided, and the level of significance was set at $P< 0.05$.

Results

Identifying differentially expressed genes between bladder cancer and normal tissues

Among the 57 pyroptosis-related genes, 14 were differentially expressed between BLCA and adjacent normal tissues (Figure 1A), including CASP9, CHMP3, CHMP7, BAX, CHMP4B, HMGB1, CASP3, CHMP4C, CASP8, ELANE, IL6, TREM2, BAK1, and PYCARD. Meanwhile, we further analyzed the expression patterns of these DEGs in the BLCA microenvironment from the single cell level. First, it was found that seven genes, BAK1, CASP3, CASP8, CASP9, CHMP7, ELANE, and IL6, were not specifically expressed in each cell line (Supplementary Figure 1). In contrast, the genes HMGB1, PYCARD and BAX were expressed in all cell lines without specificity (Supplementary Figure 4). Second, two genes, CHMP4B and CHMP3, were not expressed in immune cells (T/NK and B cells) (Supplementary Figure 2). Third, the CHMP4C was specifically expressed in bladder cancer epithelial cells (Supplementary Figure 3). Last, the gene TREM2 was found to be specifically expressed in myeloid cell lines (Supplementary Figure 5).

Figure 1B shows the correlation network diagram of the 14 pyroptotic DEGs, and the results show that most of the genes were related to each other. To observe the genetic variation in pyroptotic molecules in bladder cancer, we displayed the somatic mutation frequencies of 14 differentially expressed pyroptotic molecules in the TCGA-BLCA cohort using waterfall plots. Among the 412 BLCA samples, pyroptotic mutations were found in 37 cases with a mutation frequency of 8.98%. We found that CASP8 had the highest mutation frequency (2%), of which missense mutations were the most common. In summary, the mutation frequencies of these pyroptosis-related genes were low (Figure 1C). Therefore, we performed a functional enrichment analysis based on these 14 pyroptosis DEGs. GO analysis showed that these differentially expressed pyroptotic genes were enriched in multiple biological pathways, including multi-organism processes, ESCRT III complex, and membrane proteins (Figure 1D). KEGG analysis showed that these pyroptosis genes were enriched in Necroptosis, Apoptosis and Influenza A (Figure 1E). Furthermore, we performed pan-cancer analysis based on the 14 differentially expressed pyroptosis genes. The results suggested that 14 pyroptosis genes were closely related to nine important tumor-related pathways in pan-cancer (Figure 1F). We found that most pyroptosis genes were related to activation of the apoptosis pathway. For example, BAK1, BAX, and IL6 are associated with the activation of apoptosis in 50%, 32%, and 29% of tumors, respectively. In contrast, only ELANE was associated with apoptosis inhibition in 15% of tumors. Several other obvious pathways have been described in the manner of apoptosis: cell cycle, EMT, hormone AR, hormone ER, and RTK.

Pan-cancer multi-omics analysis of pyroptotic DEGs

We further analyzed the multi-omics features of the 14 pyroptotic DEGs in pan-cancer. The results suggested that these genes had high mutation frequencies in UCEC, HNSC, STAD, COAD, and BLCA. Among them, the mutation frequency of the CASP8 gene was the highest at 55% in UCEC (Supplementary Figure 6A). In addition, we found that TREM2, CASP3, BAX, CASP8, PYCARD, CHMP4C, and BAK1 were highly expressed in most tumors compared to paracancerous tissues. Conversely, IL6 and ELANE were downregulated in most tumors compared to adjacent tissues (Supplementary Figure 6B). The main types of copy number variations of pyroptosis genes in pan-cancer were heterozygous amplifications and deletions, among which the CNVs of CHMP4B, CHMP4C, and IL6 in most tumors were heterozygous amplifications. In contrast, CASP3, CASP9, and CHMP7 had CNV-type loss-of-heterozygosity in most tumors (Supplementary Figure 6C). We found that an important factor affecting the expression of pyroptotic molecules was gene copy number variation, as CNV and mRNA expression levels were positively correlated in most tumor types (Supplementary

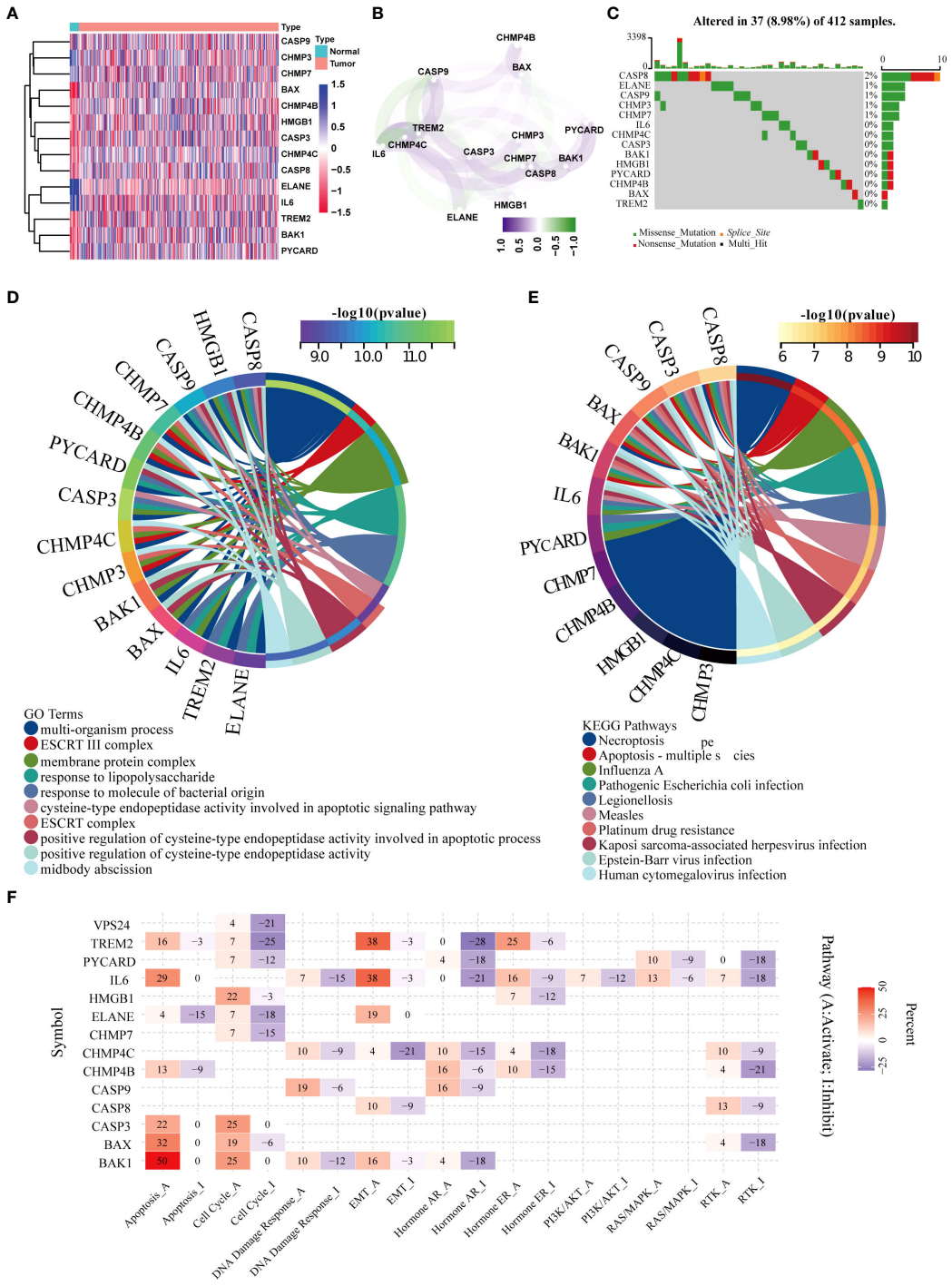

FIGURE 1
Screening of differentially expressed pyroptotic genes and functional analysis. **(A)** Fourteen pyroptotic genes differentially expressed in BLCA and normal tissues. **(B)** protein–protein interaction (PPI) network of the differentially expressed pyroptotic genes. **(C)** Landscape of mutation profiles in 412 patients with bladder cancer from the TCGA-BLCA cohort. Each waterfall plot represents the mutation information of each pyroptosis-related regulator. Corresponding colors have annotations at the bottom, indicating different mutation types. The barplot shows mutation burden. The right numbers represent mutation frequency individually. **(D)** GO analysis of the differentially expressed pyroptotic genes. The corresponding colors have annotations at the bottom, indicating different biological pathways. **(E)** KEGG analysis of the differentially expressed pyroptotic genes. The corresponding colors have annotations at the bottom, indicating different pathways. **(F)** Heatmap showing correlations between 14 pyroptotic genes and their expression levels in important cancer signaling pathways. Red represents the activated pathway, whereas blue represents the inhibitory pathway.

Figure 6E). In particular, for CHMP7, there was a significant positive correlation between CNV and mRNA expression in most tumors (Supplementary Figure 6E). Furthermore, in most cancers, the methylation levels of the aforementioned pyroptotic genes were negatively correlated with the mRNA expression levels (Supplementary Figure 6D).

Development and validation of a pyroptosis risk score in the TCGA-BLCA cohort

First, we performed a univariate Cox regression analysis based on 14 pyroptotic DEGs in the TCGA-BLCA cohort. Univariate Cox regression analysis revealed that CASP9, CHMP4C, and CASP8 were associated with prognosis. Furthermore, we identified three optimal candidates for constructing a pyroptosis risk score using the LASSO algorithm (Figures 2A–C). In the TCGA training cohort, we divided the patients into low-and high-risk score groups based on the median risk score. The results showed that the overall survival time of patients in the low-score group was significantly longer than that in the high-score group (Figure 2D). The AUC of the pyroptosis risk score for predicting the OS of bladder cancer OS was 0.650, 0.636, and 0.658 at 1, 3, and 5 years, respectively (Figure 2E). In the independent external validation cohort GSE32894, patients in the low-score group also had a significantly longer overall survival than those in the high-score group (Figure 2F). The AUC of the pyroptosis risk score for predicting bladder cancer OS were 0.802, 0.824, and 0.804 at one, three, and five years, respectively (Figure 2G). We found consistent results in the Xiangya internal validation cohort. The patients in the low-scoring group had a better overall prognosis (Figure 2H). The AUC of the pyroptosis risk score for predicting the OS of bladder cancer OS was 0.596, 0.642, and 0.816 at 1, 3, and 5 years, respectively (Figure 2I).

Relationship between pyroptosis risk score and clinicopathological features

As shown in Figures 3A, B, patients with higher grades and stages had higher risk scores, which was consistent with the prognostic correlation of pyroptosis risk scores. Muscle invasive status, metastasis and histological type also had the same relationship with pyroptosis risk score (Supplementary Figure 7).Furthermore, univariate Cox analysis suggested that age, stage, and the pyroptosis risk score were significant prognostic predictors (Figure 3C). Further multivariate Cox analysis confirmed that the pyroptosis risk score was an independent prognostic risk factor (Figure 3D). However, staging no longer has an independent prognostic predictive value. These results demonstrate that the pyroptosis risk score is an effective indicator for predicting the prognosis of patients with BLCA. To improve the predictive value of the pyroptosis risk score for the prognosis of bladder cancer, we established a comprehensive line chart by combining the pyroptosis risk score with several factors that had prognostic value in the univariate Cox regression analysis, such as age and tumor stage. Figure (Figure 3E). We further used the ROC and calibration curves to verify the accuracy of the line chart in predicting the prognosis of bladder cancer. In the TCGA-BLCA cohort, the prediction accuracies of the line charts for 1-, 3-, and 5-year OS were 0.714, 0.711, and 0.737, respectively (Figure 4A). As shown in the calibration curve (Figure 4B), the OS predicted by the line chart was highly consistent with the actual OS, highlighting the clinical significance and accuracy of this comprehensive line chart. More importantly, the line chart showed a higher prognosis prediction accuracy in the two verification sets, GSE32894 and Xiangya cohorts. (Figures 4C–F).

Pyroptosis risk score were related to TME immune characteristics and ICB clinical response

Immunotherapy has become the first-line treatment for advanced bladder cancer. Therefore, it is crucial to explore the correlation between the pyroptosis risk score and the immune microenvironment of bladder cancer. The fate of cancer cells and the efficacy of immunotherapy depend on the state of the tumor immune microenvironment. The whole cancer immune cycle consists of a series of continuous steps (28), the seven main steps were: release of cancer cell antigens, cancer antigen presentation, priming and activation, trafficking of immune cells to tumors, infiltration of immune cells into tumors, recognition of cancer cells by T cells, and killing of cancer cells (15). We analyzed the correlation between risk score and activities of several anticancer immune steps. The results suggested that the activities of release of cancer cell antigens, T cell recruitment, CD8 T cell recruitment, Th1 cell recruitment, NK cell recruitment, and other steps were significantly higher in the high-score group than in the low-score group (Figure 5A). Consistently, the infiltration levels of the corresponding TIICs, such as CD8 T cells, NK cells, Th1 cells, and dendritic cells, were positively correlated with the pyroptosis risk score. These results were highly consistent across the six independent algorithms (Figure 5B). These results suggest that patients in the high-risk score group may have an inflammatory phenotype that is more sensitive to ICB. Therefore, we correlated the risk score with several predictors of ICB efficacy. We found a significant positive correlation between the risk scores and TIS (Figure 5C). In addition, the expression of many immune checkpoints (such as CD274, CTLA4, and PDCD1) and the enrichment score of immunotherapy-related gene signatures were positively correlated with the risk score (Figures 5D, E).

In summary, high-risk score tumors are inflamed phenotypes that are more sensitive to ICB.

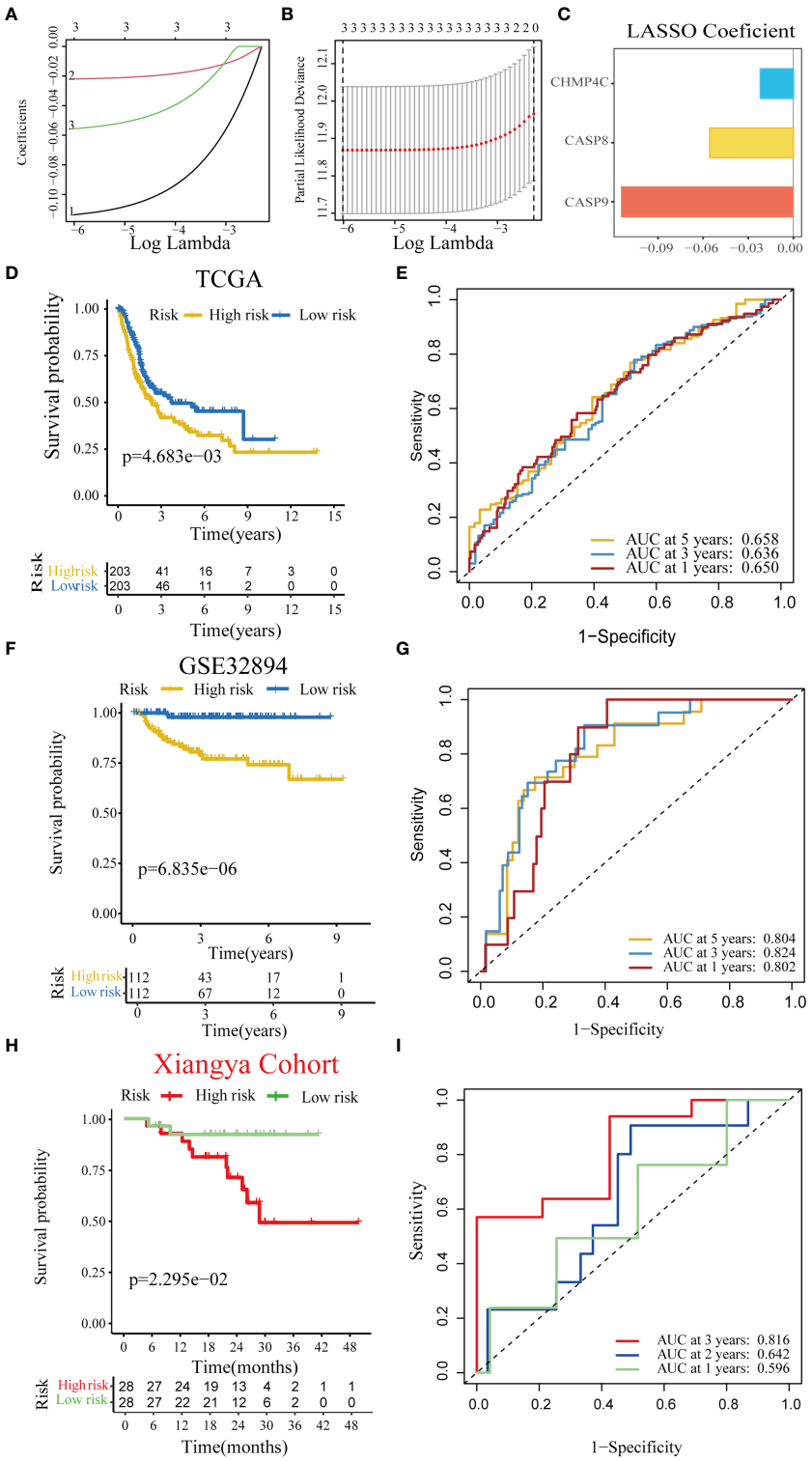

FIGURE 2
Construction and validation of a pyroptosis risk score in the multiple BLCA cohorts. **(A)** Lasso coefficients of 14 predicted pyroptotic genes in the TCGA-BLCA cohort. **(B)** Cross-validation for turning parameter selection *via* minimum criteria in the LASSO regression model. **(C)** Three best candidates were screened by LASSO algorithm to further determine the generation of the pyroptosis risk score. **(D)** Kaplan–Meier analysis of OS for the pyroptosis risk score in the TCG-BLCA cohort. **(E)** ROC curves of the pyroptosis risk score for predicting OS in the TCG-BLCA cohort. **(F, G)** Validation of the pyroptosis risk score in GSE32894. **(H, I)** Validation of the pyroptosis risk score in the Xiangya cohort.

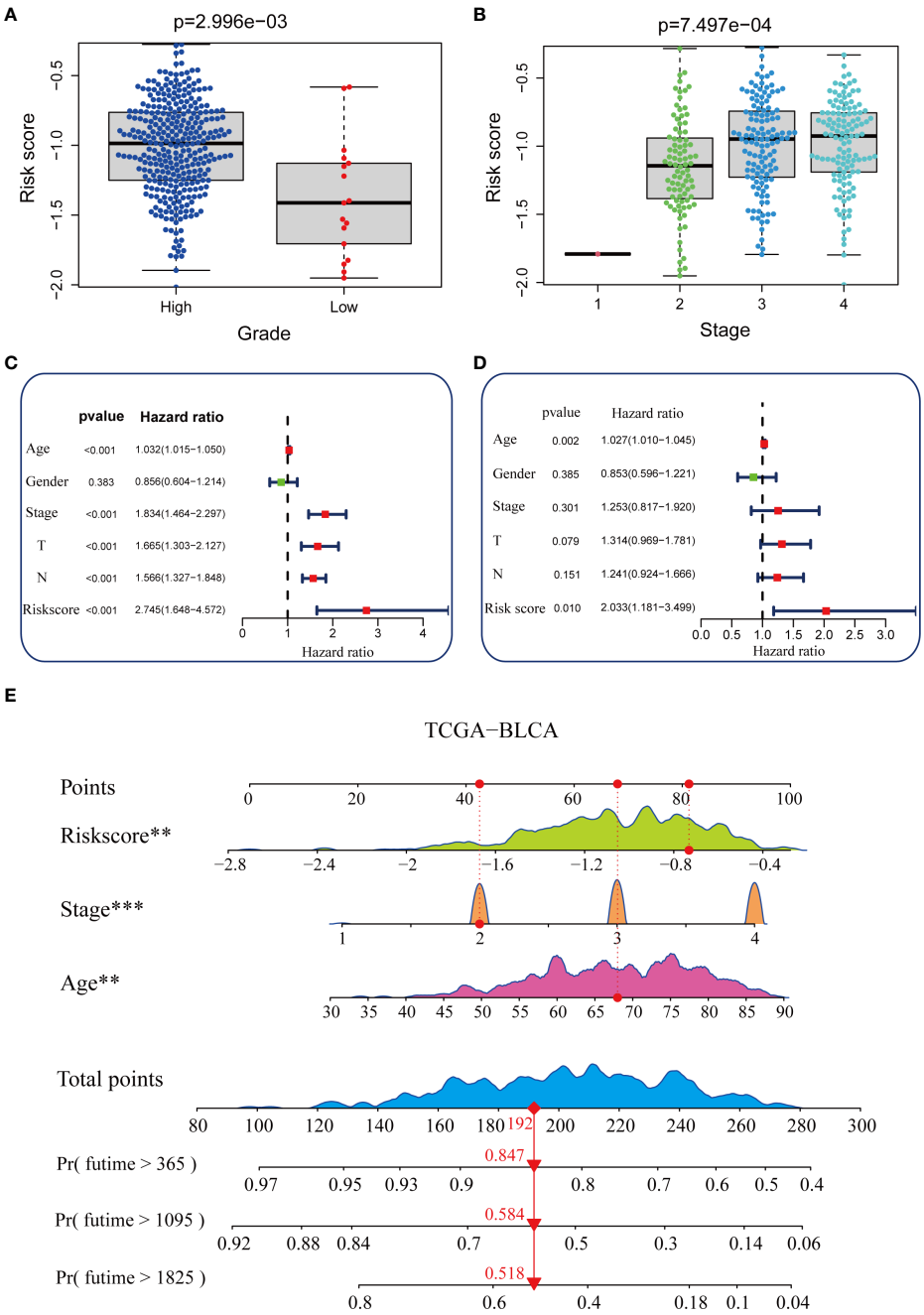

FIGURE 3
Construction of a nomogram in the TCGA-BLCA cohort. **(A, B)** Relationship between the pyroptosis risk score and tumor grade and stage in the TCGA-BLCA cohort. **(C, D)** Results of univariate and multivariate Cox analyses. **(E)** Nomogram developed based on stage, age, and the pyroptosis risk score to predict overall survival at 1, 3, and 6 years. **P value < 0.01, ***P value < 0.001.

Pyroptosis risk score accurately predicts molecular subtypes and promotes precision medicine for BLCA

Bladder cancer comprises a variety of molecular subtypes with significantly different biological functions. Therefore, we first compared the differences in the enrichment activities of the 50 hallmark signaling pathways between the high- and low-risk groups. We found significantly different biological functions between the high- and low-pyroptosis score groups (Figure 6A). EPITHELIAL MESENCHYMAL TRANSITION and INFLAMMATORY RESPONSE were the most abundant

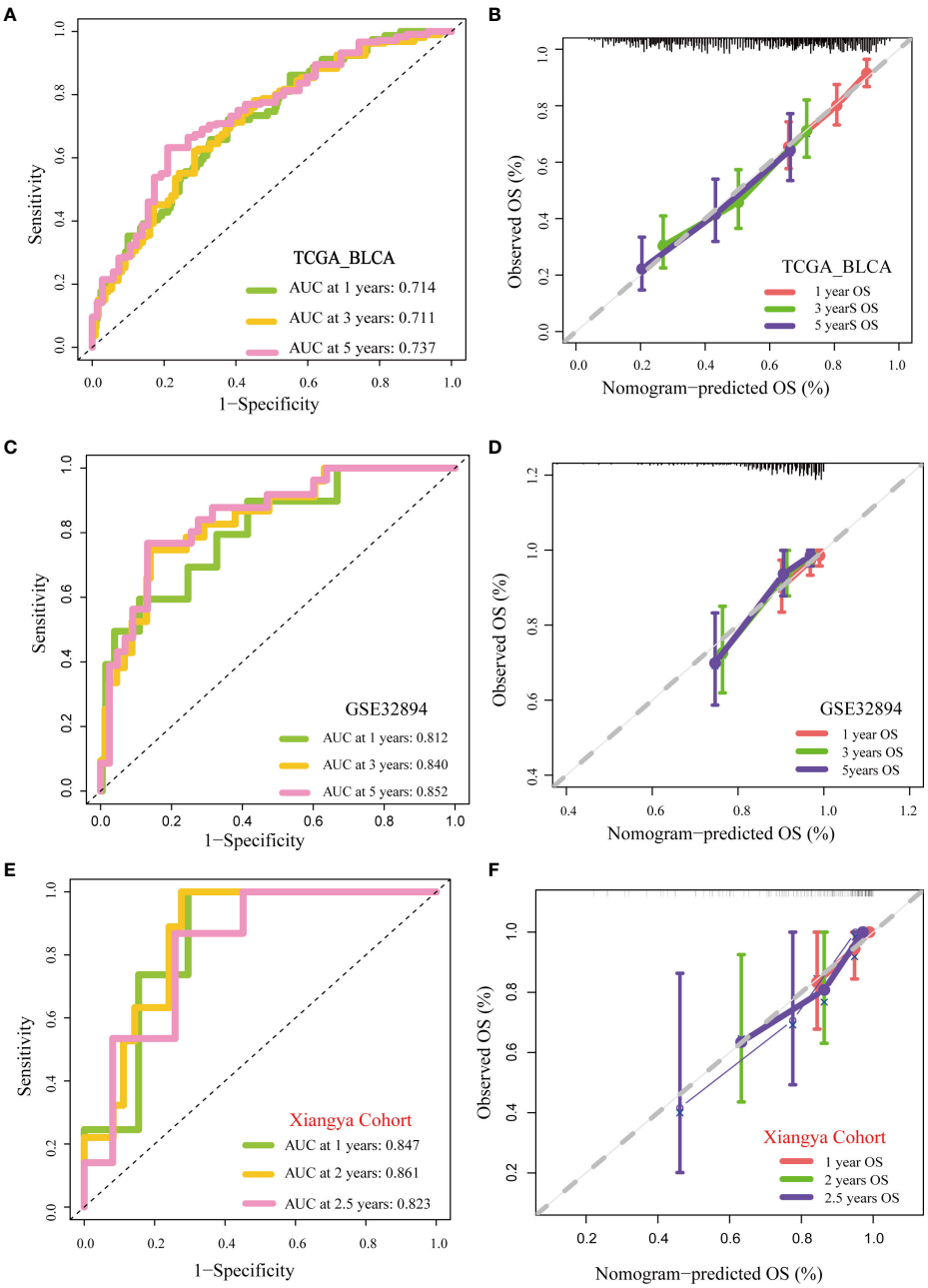

FIGURE 4
Validation of multiple cohorts of the pyroptosis risk score **(A)** ROC curves of the nomogram. **(B)** Calibration curves of the nomogram measured using the Hosmer–Lemeshow test. **(C, D)** Validity of pyroptosis risk score in GSE32894. **(E, F)** Validity of the pyroptosis risk score in the Xiangya cohort.

signals in the high-risk group, whereas PEROXISOME and ESTROGEN RESPONSE_EARLY were the most abundant signals in the low-score group. These results suggest that pyroptosis genes may affect the progression of BLCA by regulating hallmark signaling pathways. Thereafter, we analyzed the correlation between risk score and molecular typing of bladder cancer. The results showed that the high-scoring group was mostly the basal subtype characterized by basal differentiation, EMT differentiation, immune differentiation, myofibroblasts, and interferon response, whereas the low-scoring group was mainly the luminal subtype characterized by the Ta pathway and luminal differentiation (Figure 6B). Figure 6C shows that the risk score of pyroptosis could accurately predict molecular subtypes, and

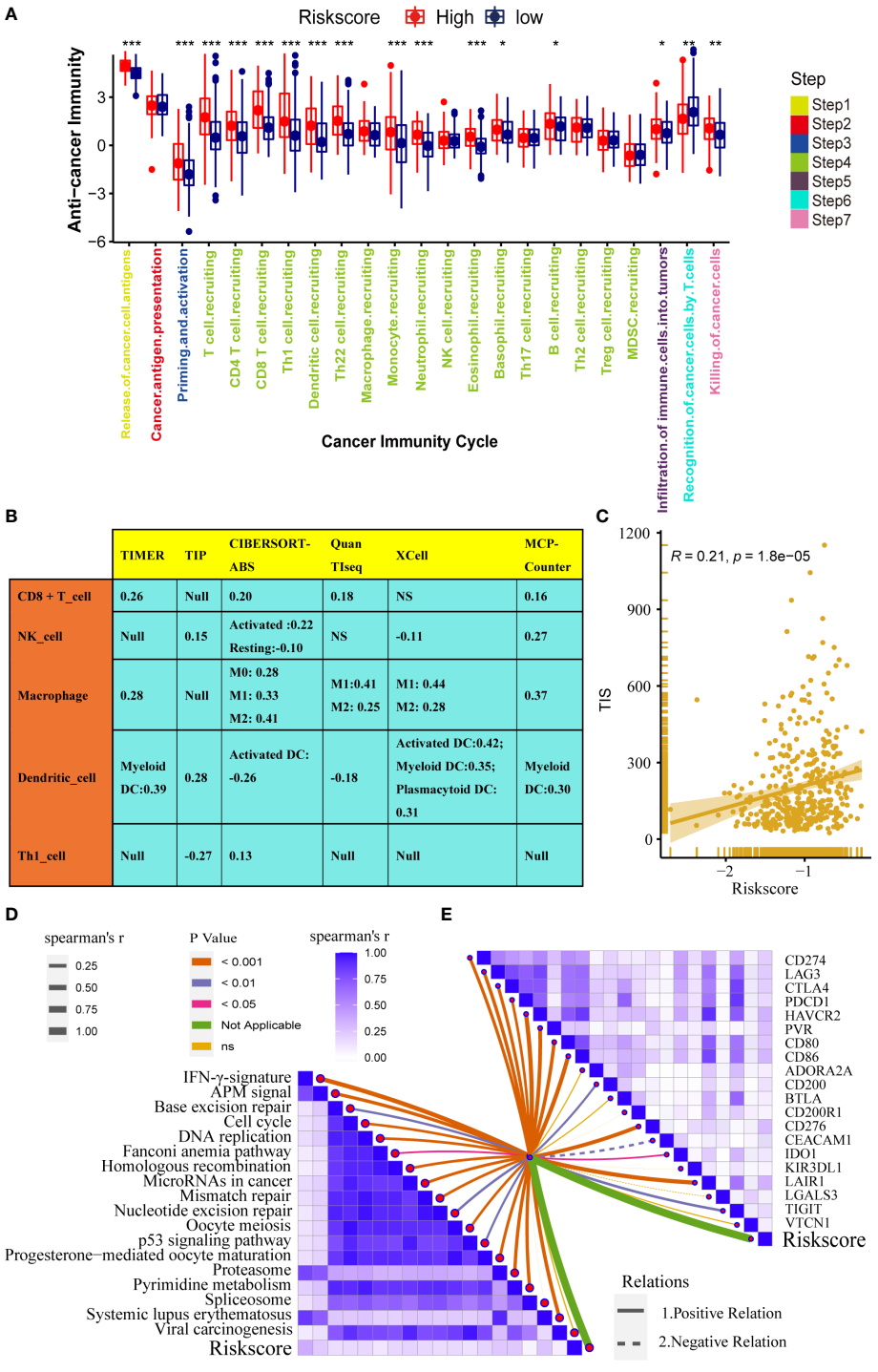

	TIMER	TIP	CIBERSORT-ABS	Quan TIseq	XCell	MCP-Counter
CD8 + T_cell	0.26	Null	0.20	0.18	NS	0.16
NK_cell	Null	0.15	Activated :0.22 Resting:-0.10	NS	-0.11	0.27
Macrophage	0.28	Null	M0: 0.28 M1: 0.33 M2: 0.41	M1:0.41 M2: 0.25	M1: 0.44 M2: 0.28	0.37
Dendritic_cell	Myeloid DC:0.39	0.28	Activated DC: -0.26	-0.18	Activated DC:0.42; Myeloid DC:0.35; Plasmacytoid DC: 0.31	Myeloid DC:0.30
Th1_cell	Null	-0.27	0.13	Null	Null	Null

FIGURE 5
Pyroptosis risk score correlated with the tumor immune microenvironment characteristics. **(A)** Differences in cancer immune cycling activity between high- and low-risk groups. **(B)** Relationships between the pyroptosis risk score and several immune cells (CD8+T cells, NK cells, macrophages, Th1 cells, and DCs) in six independent algorithms. **(C)** Relationships between the pyroptosis risk score and T cell inflamed score (TIS). **(D)** Correlation between the pyroptosis risk score and enrichment of ICB response-related pathways. **(E)** Relationship between pyroptosis risk scores and immune checkpoints (*P < 0.05; **P < 0.01; ***P < 0.001). NS, P value > 0.05, no significant difference;

10.3389/fimmu.2022.965469

the AUC for predicting molecular subtypes in UNC, TCGA, MDA, Lund, CIT, consensus, and Baylor were 0.78,0.78,0.79,0.89,0.82,0.76, and 0.65, respectively. Different molecular types have different sensitivities to different treatments, including radiotherapy, chemotherapy, and targeted therapies. Therefore, we further analyzed the sensitivity of the pyroptosis risk score in predicting the most frequently used chemotherapeutic drugs among the six BLCA. Patients with high scores were more sensitive to chemotherapy drugs including cisplatin, camptothecin, paclitaxel, bleomycin, docetaxel, and vinblastine (Figure 6D). Finally, we found that the enrichment activity of gene signatures related to the efficacy of

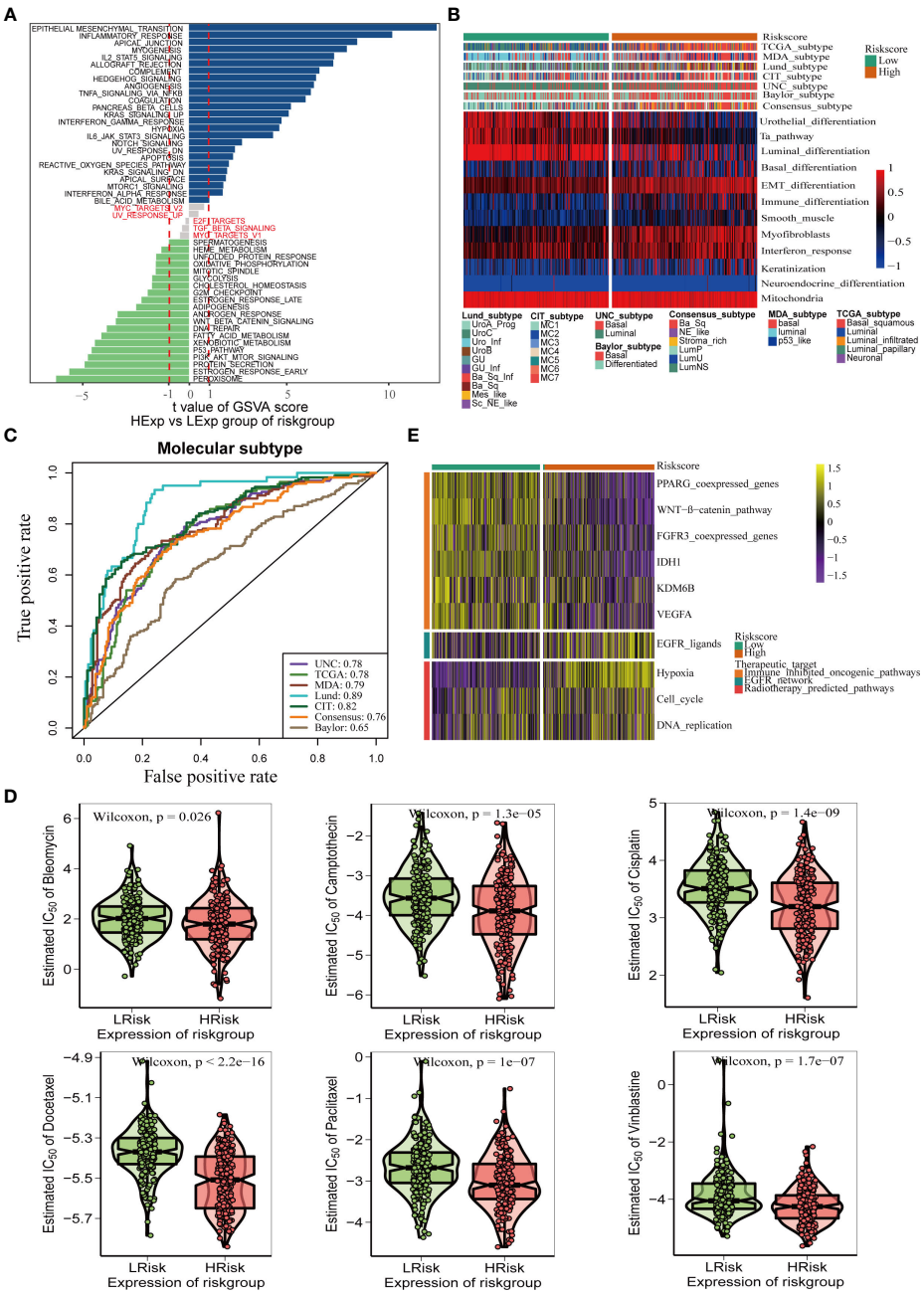

FIGURE 6
Pyroptosis risk score effectively predicts molecular subtypes and guides precise treatment of BLCA. **(A)** Differences in biological function between pyroptosis risk groups. **(B)** Relationships between pyroptosis risk score and seven classical molecular subtypes. **(C)** Predictive accuracy of pyroptosis risk score for molecular subtypes in multiple different algorithms. **(D)** Difference on the effects of six chemotherapy drugs. **(E)** Relationships between the pyroptosis risk score and enrichment scores of multiple therapeutic signatures.

EGER-targeted therapy and radiotherapy was higher in the high-score group, indicating that patients in the high-score group were sensitive to EGER-targeted therapy and radiotherapy (Figure 6E).

To verify the role of pyroptosis risk score in Xiangya cohort, GSE32894, and GSE48075

The role of the pyroptosis risk score in predicting immune-related phenotypes, molecular subtypes, and treatment regimen efficacy was further validated in the Xiangya cohort. The pyroptosis risk score was positively correlated with the enrichment scores for most steps of the anticancer immune cycle (Figure 7A). Consistently, the pyroptosis risk score was positively correlated with the corresponding degree of TIIC infiltration by CD8 + T cells, NK cells, and dendritic cells (Figure 7E). Enrichment scores for signaling pathways positively correlated with immune checkpoint, TIS, and ICB responses were also positively correlated with the pyroptosis risk scores (Figures 7B–D). Therefore, in the Xiangya cohort, tumors with high-risk scores also belonged to the inflammatory phenotype. In addition, in the Xiangya cohort, the pyroptosis risk score was accurate for the molecular subtypes (Figure 7F). In these seven independent systems, the AUC ranged from 0.83 to 0.97 (Figure 7G). As expected, in the Xiangya cohort, the pyroptosis risk score could also accurately predict the effects of radiotherapy and several targeted therapies, and patients in the high score group were more sensitive to EGFR-targeted therapy and radiotherapy; targeted therapy such as blockade of the FGFR3 network, WNT-b-catenin network, and PPRAG network were more sensitive to low-score patients (Figure 7H). All the above results were effectively validated in GSE32894 and GSE48075 (Figures 8A–F and 9A–F). Finally, we correlated the 14 pyroptotic DEGs with the sensitivity to many different drugs, and found that HMGB1, CASP3, CHMP7, and most drugs were negatively correlated, whereas IL-6, CHMP4C, CHMP4B, and large drug sensitivities were positively correlated (Figures 10A, B).

Discussion

An increasing number of studies have shown that pyroptosis plays an important regulatory role in tumors; however, current research on the role of pyroptosis in bladder cancer remains unclear. This study screened 14 pyroptotic DEGs from cancerous and paracancerous tissues of BLCA. We found that imbalances in the expression of pyroptotic molecules might be related to the regulation of genomic variation. To develop new ideas and effective treatment targets for BLCA, it is necessary to formulate an efficient predictive model. At present, the pyroptosis risk scores have been developed to predict the prognosis and TME characteristics of cancer (2, 29). However, there is still a lack of research to systematically explore the correlation between pyroptosis-related features, TME features, and the molecular types of BLCA. This study developed and validated a novel pyroptosis risk score by using a combination of multiple independent BLCA datasets and the Xiangya cohort. The pyroptosis risk score can predict clinical outcomes, molecular subtypes, and TME characteristics and the therapeutic effect of chemotherapy, radiotherapy, ICB, and targeted therapy in BLCA.

Pyroptosis affects tumor proliferation, invasion, and metastasis (30). Some studies have found that high expression of GSDME in esophageal cancer causes cells to undergo pyroptosis (31). The pyroptosis risk score reflects the actual pyroptosis in the TME from different aspects. First, the pyroptosis risk score can be used to predict the prognostic and clinical features of BLCA. The higher the score, the worse the OS and the higher the tumor grade and stage. Second, we analyzed the differences in the enrichment scores of 50 landmark signaling pathways between the pyroptosis risk score groups and found that EPITHELIAL MESENCHYMAL TRANSITION and INFLAMMATORY RESPONSE were most abundant in the high-risk group, whereas PEROXISOME and ESTROGEN RESPONSE_EARLY were the most abundant signals in the low-risk groups. Chemotherapy is an important treatment option for metastatic bladder cancer (MBC). There is an urgent need to develop accurate chemotherapy predictors that can provide patients with precise treatment options. Our study found that the six most commonly used chemotherapeutic drugs in BLCA were the most sensitive in the high-risk group, indicating that patients with high-risk scores were more effectively treated with chemotherapeutic drugs.

Chen et al. found 28 genes related to cell death in BLCA (32). They found that patients in the high PyroScore group had better prognosis. Conversely, our study found that patients in the high-risk score group had worse prognosis. However, we consistently found that patients in the high scoring group were more sensitive to chemotherapy. However, our study and that of Chen et al. have several different focuses. First, the sets of pyroptotic genes selected were different between the two studies. Chen et al. summarized 28 genes related to pyroptosis in previous studies (33–35). In our study, we developed a pyroptosis risk score based on hallmark pyroptosis signatures with more robust enrichment analysis results than other published pyroptosis genomes. Second, Chen et al. A scoring system was constructed using the orthogonal rotation (PCA) method and named PyroScore (32). Therefore, we generated a pyroptosis risk score by integrating differential expression analysis, Cox analysis, and the LASSO algorithm. Third, Chen et al. did not analyze the relationship between the pyroptosis risk score and clinical outcomes, radiotherapy, or immune markers without systematic analysis. However, in our study, our system

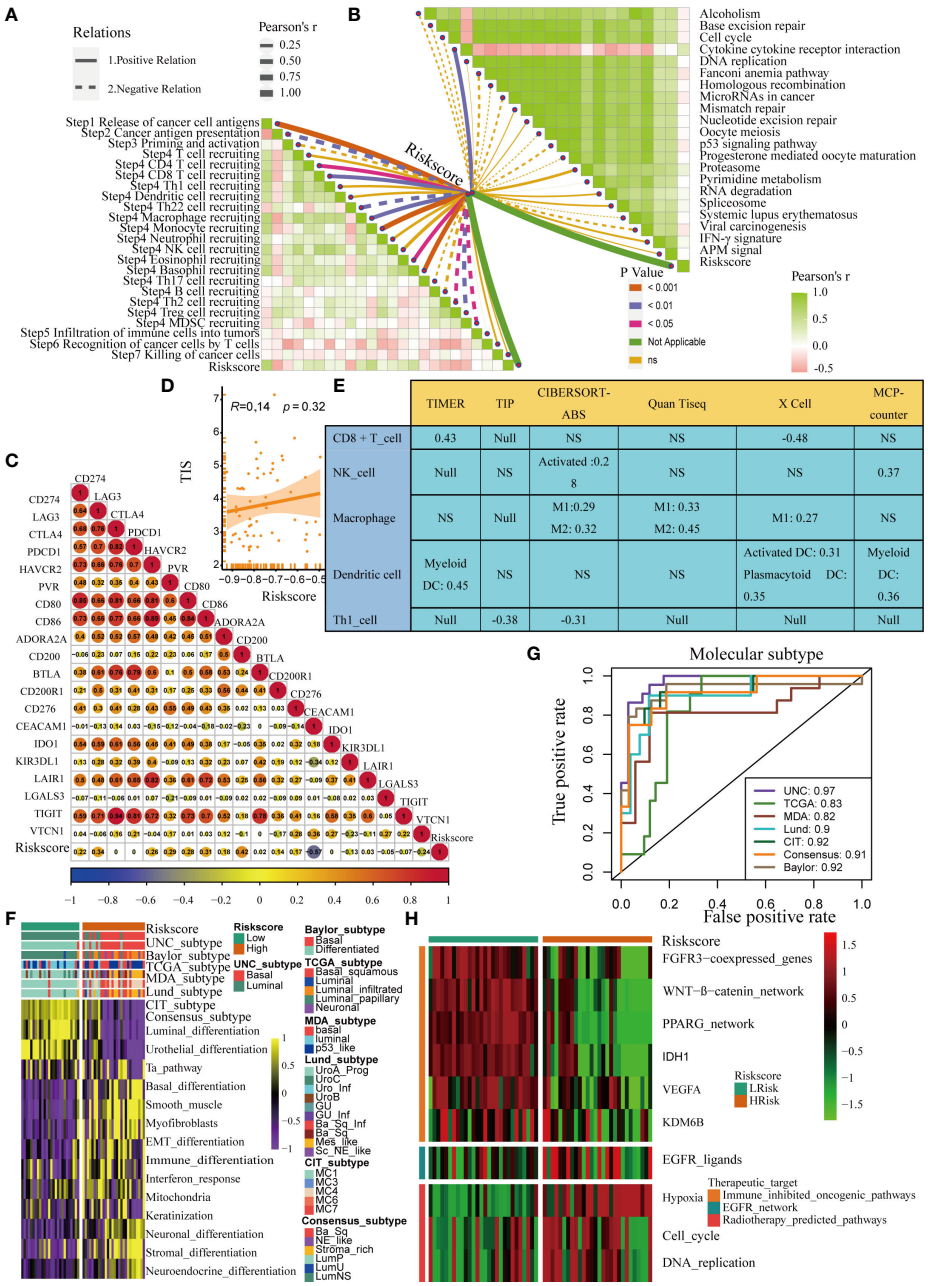

	TIMER	TIP	CIBERSORT-ABS	Quan Tiseq	X Cell	MCP-counter
CD8 + T_cell	0.43	Null	NS	NS	-0.48	NS
NK_cell	Null	NS	Activated :0.28	NS	NS	0.37
Macrophage	NS	Null	M1:0.29 M2: 0.32	M1: 0.33 M2: 0.45	M1: 0.27	NS
Dendritic cell	Myeloid DC: 0.45	NS	NS	NS	Activated DC: 0.31 Plasmacytoid DC: 0.35	Myeloid DC: 0.36
Th1_cell	Null	-0.38	-0.31	Null	Null	Null

FIGURE 7
Validation of the pyroptosis risk score in the Xiangya cohort. **(A)** Relationships between the pyroptosis risk score and activities of the cancer immunity cycles. **(B)** Relationships between the pyroptosis risk score and immunotherapy-predicted pathways. **(C)** Correlations between the pyroptosis risk score and several immune checkpoints. **(D)** Relationships between the pyroptosis risk score and T cell inflammation score (TIS). **(E)** Relationship between the pyroptosis risk score and infiltration levels of five tumor-infiltrating immune cells. **(F)** The pyroptosis risk score accurately stratified the molecular subtypes in seven different algorithms. **(G)** Accuracy of the pyroptosis risk score in predicting molecular subtypes in seven different algorithms. **(H)** Relationships between the pyroptosis risk score and the enrichment scores of several therapeutic signatures. NS, P value > 0.05, no significant difference.

correlated the pyroptosis risk score with several TME immune signatures, such as TIICs, immune checkpoints, and TIS.

An increasing number of studies have focused on the tumor immune microenvironment (36, 37). Pyroptosis regulates the tumor immune microenvironment through various mechanisms. Pyroptosis regulates the expression of several immune-enhancing molecules, thereby forming the immune-promoting TME. For example, studies have found that GZM-B

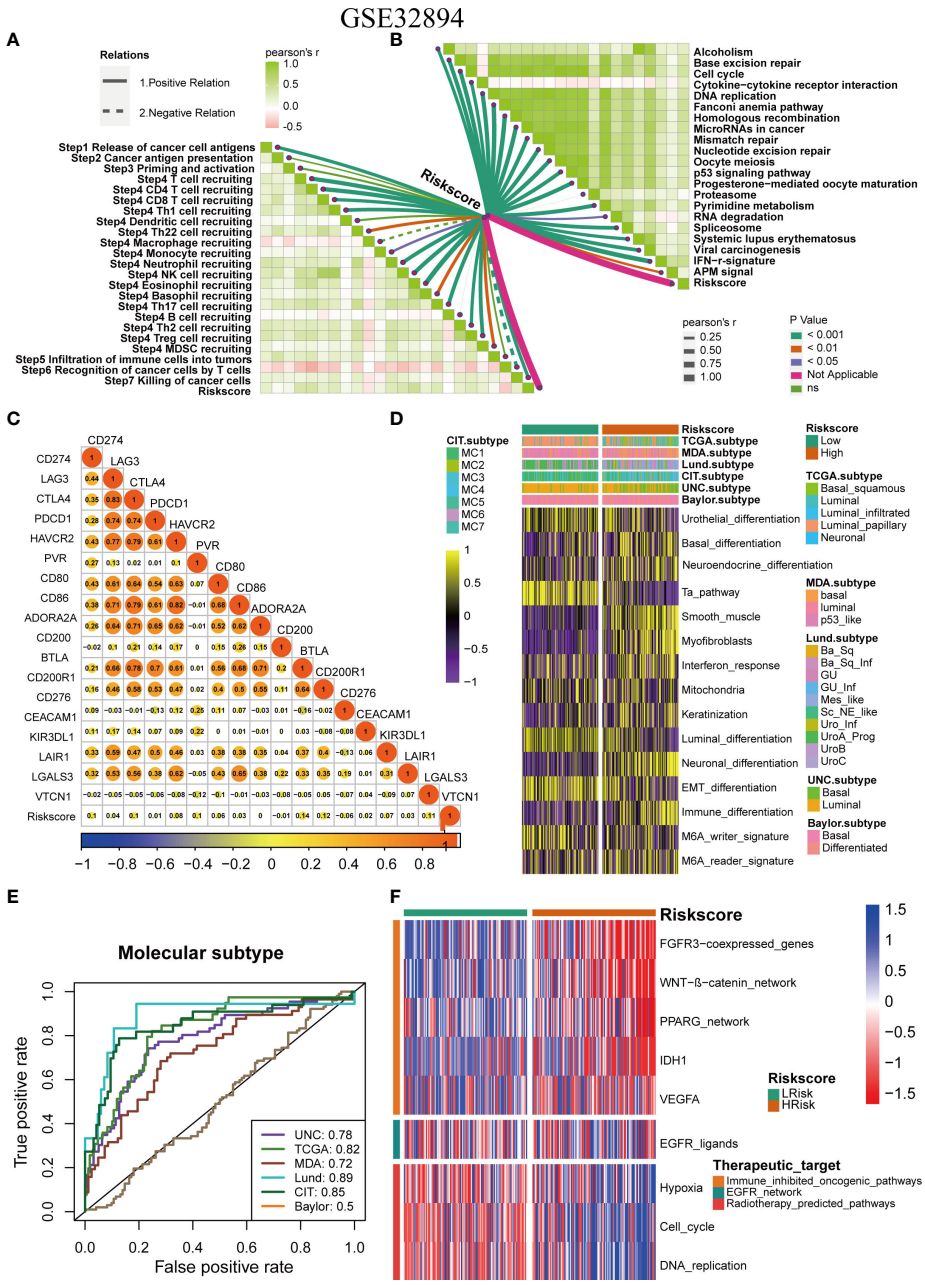

FIGURE 8
Validation of the pyroptosis risk score in the GSE32894 cohort. **(A)** Relationships between pyroptosis risk score and the activities of the cancer immunity cycles. **(B)** Relationships between the pyroptosis risk score and immunotherapy-predicted pathways. **(C)** Correlations between the pyroptosis risk score and several immune checkpoints. **(D)** The pyroptosis risk score accurately stratified the molecular subtypes in seven different algorithms. **(E)** Accuracy of the pyroptosis risk score in predicting molecular subtypes in seven different algorithms. **(F)** Relationships between the pyroptosis risk score and enrichment scores of several therapeutic signatures.

can also increase the number of macrophages, NK cells, and CD8+ T lymphocytes by cleaving GSDME, thereby activating antitumor immunity, activating caspase-3 in target cells, and inducing pyroptosis (38, 39). Two recent studies found that granzymes released by CD8+ T cells and NK cells can cleave GSDMB/E, thereby triggering tumor cell pyroptosis, and pyroptosis may be an important effector in anti-tumor immunity (38, 40). The study found that PD-L1 converts tumor necrosis factor α-induced apoptosis of cancer cells into pyroptosis, resulting in tumor necrosis (41). Studies have shown

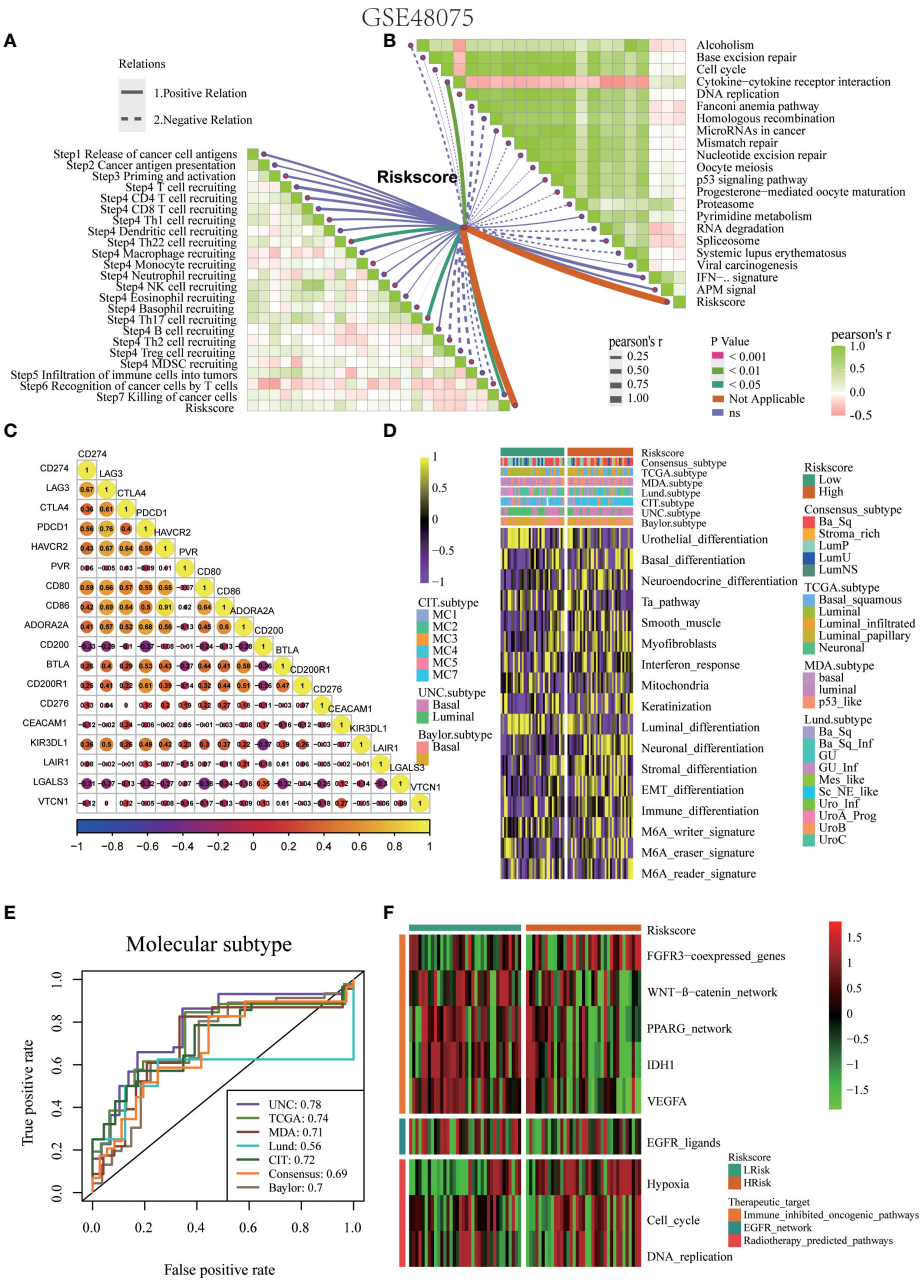

FIGURE 9
Validation of the pyroptosis risk score in the GSE48075 cohort. **(A)** Relationships between the pyroptosis risk score and activities of the cancer immunity cycles. **(B)** Relationships between the pyroptosis risk score and immunotherapy-predicted pathways. **(C)** Correlations between the pyroptosis risk score and several immune checkpoints. **(D)** The pyroptosis risk score accurately stratified the molecular subtypes in seven different algorithms. **(E)** Accuracy of the pyroptosis risk score in predicting molecular subtypes in seven different algorithms. **(F)** Relationships between the pyroptosis risk score and enrichment scores of several therapeutic signatures.

that pyroptotic cell death of cancer cells promotes dendritic cell activation and T cell infiltration and enhances anti-tumor immune responses by releasing high mobility group protein B1 (42). Further studies have shown that overexpression of GSDME results in enhanced drug sensitivity *in vivo* and *in vitro* (43). All the above data are helpful for exploring the role of the pyroptosis risk score in predicting TME immune characteristics.

This study found that the pyroptosis risk score correlated with immune checkpoints (such as CD274, CTLA4, and PDCD1), TIS score, and anticancer immune cycle enrichment score (such as release of cancer cell antigens, T cell recruitment,

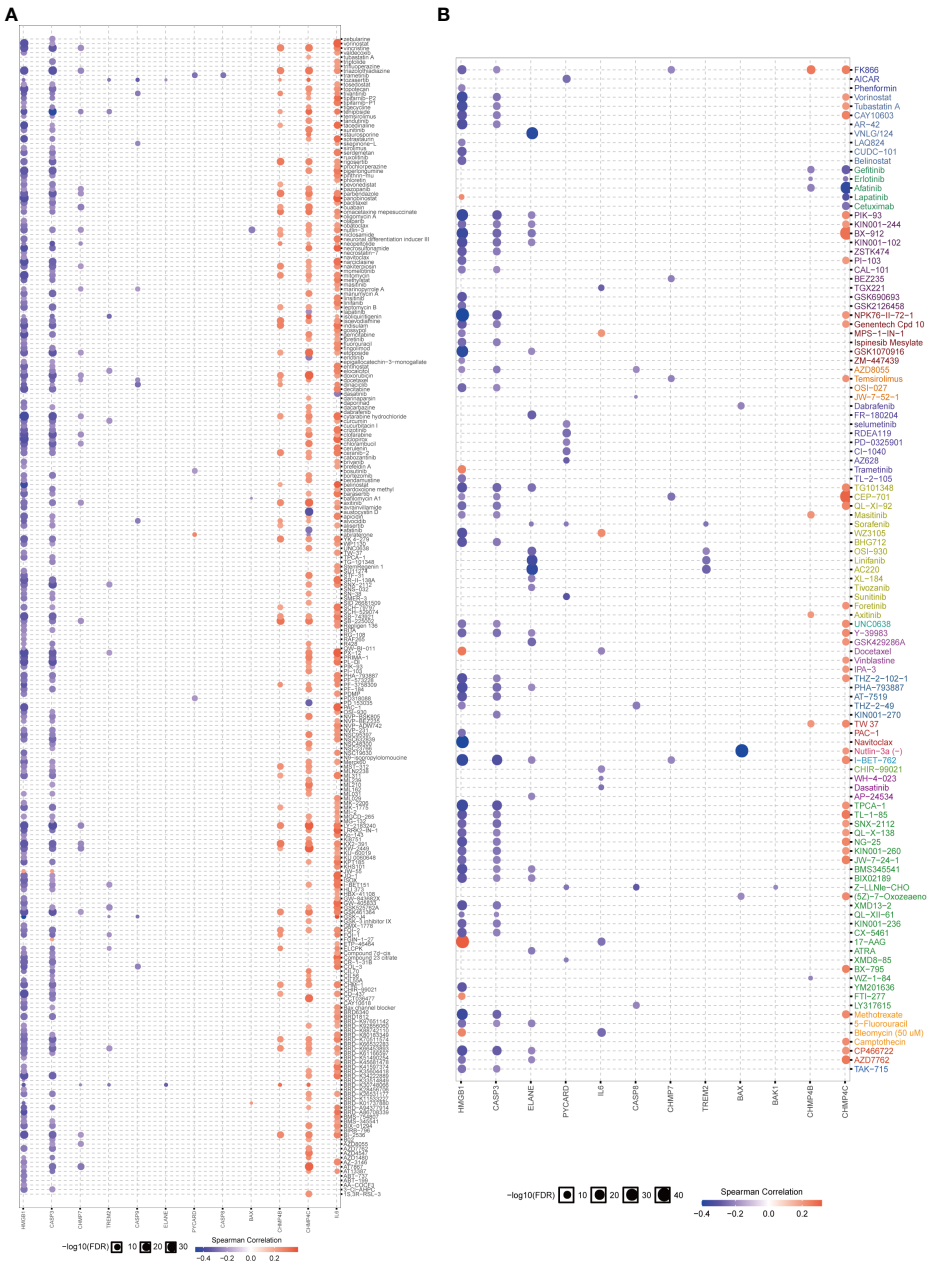

FIGURE 10
Correlation analysis between pyroptosis-related genes and drug sensitivity. **(A, B)** Bubble chart shows the correlation analysis between these pyroptotic genes and drug susceptibility. Red indicates positive correlation and blue indicates negative correlation. The darker the color, the higher the correlation index. Bubble size indicates the FDR.

CD8 T cell recruiting, Th1 cell recruiting, NK cell recruiting), and TIICs (such as CD8 T cells, NK cells, Th1 cells, and dendritic cells) were positively correlated, suggesting that there is higher anticancer immunity in the TME of patients in the high-risk score group. However, some tumor tissues have large numbers of immune cells (endothelial cells, mast cells, M2 macrophages, and quiescent T4 memory cells), which cannot penetrate the tumor and are forced to stay in the surrounding stroma. Anticancer immunity in the tumor microenvironment is considered an immunosuppressive state (44). This was because the pyroptosis risk score positively correlated with M2 macrophages (Figure 5B), which suppressed anticancer immunity, and the degree of infiltration was positively regulated by pyroptosis. It is well known that immune

checkpoint inhibitors (ICIS) have achieved good results in tumor immunotherapy (10–12). Our study found that the pyroptosis risk score was positively correlated with the expression of many immune checkpoints such as CD274, CTLA4, and PDCD1. Therefore, anticancer immunotherapy such as ICB is more effective in patients with high-risk scores. In contrast, patients in the low-risk score group had significantly fewer TIS and immune checkpoints, which were negatively correlated, indicating that the TME had fewer immunotherapeutic targets. Therefore, the effect of ICB in patients in the low-risk score group was unsatisfactory.

This study had certain limitations. First, this study was conducted using a bioinformatics analysis. Although we have repeatedly validated these results in several public cohorts, we need to perform studies on the relevant mechanisms of pyroptosis *in vivo* or *in vitro*. Second, the clinical value of our pyroptosis risk score requires further validation through prospective clinical trials. Third, we did not determine the optimal cut-off value for the pyroptosis risk score.

In conclusion, we developed and validated a novel pyroptosis risk score that can effectively predict clinical outcomes and TME characteristics in BLCA. Pyroptosis risk score may contribute to the choice of BLCA treatment and enable patients to receive precise treatment. For patients in the high-risk score group, they may respond better to immunotherapy, chemotherapy, radiotherapy, and EGFR-targeted therapy. In contrast, patients in the low-risk score group may benefit from several targeted treatments, such as blockade of the PPARG, WNT-b-catenin, and FGFR3 networks.

Data availability statement

The datasets presented in this study can be found in online repositories. The names of the repository/repositories and accession number(s) can be found in the article/Supplementary Material.

Authors contributions

Conception and design: DD, FL, YW, ZO, and XZ. Provision of study materials or patients: ZW, YH, and CZ. Collection and assembly of data: YW, ZO, and ZL. Data analysis and interpretation: DD, YW, ZO, and FL. Manuscript writing: All authors. Final approval of manuscript: All authors.

Funding

This work was supported by the grants from the Hunan Provincial Natural Scientific Foundation [2020JJ5916], the National Natural Science Foundation of China [82070785, 81873626, 81902592], and the Science and Technology fund project of Health and Family Planning Commission of Guizhou province (No.gzwjkj2022-100).

Acknowledgments

We sincerely thank all participants in the study.

Conflict of interest

The authors declare that the research was conducted in the absence of any commercial or financial relationships that could be construed as a potential conflict of interest.

Publisher's note

All claims expressed in this article are solely those of the authors and do not necessarily represent those of their affiliated organizations, or those of the publisher, the editors and the reviewers. Any product that may be evaluated in this article, or claim that may be made by its manufacturer, is not guaranteed or endorsed by the publisher.

Supplementary material

The Supplementary Material for this article can be found online at: https://www.frontiersin.org/articles/10.3389/fimmu.2022.965469/full#supplementary-material

SUPPLEMENTARY FIGURE 1
Expression patterns of these DEGs in the BLCA microenvironment from the single cell level.

SUPPLEMENTARY FIGURE 2
Expression patterns of these DEGs in the BLCA microenvironment from the single cell level.

SUPPLEMENTARY FIGURE 3
Expression patterns of these DEGs in the BLCA microenvironment from the single cell level.

SUPPLEMENTARY FIGURE 4
Expression patterns of these DEGs in the BLCA microenvironment from the single cell level.

SUPPLEMENTARY FIGURE 5
Expression patterns of these DEGs in the BLCA microenvironment from the single cell level.

SUPPLEMENTARY FIGURE 6
Expression variation of pyroptotic genes. **(A)** Fourteen pyroptosis genes had high mutation frequencies in UCEC, HNSC, STAD, COAD, and BLCA. Among them, the mutation frequency of the CASP8 gene was the highest, reaching 55%, particularly in UCEC. The darker the color, the higher is the mutation frequency, and vice versa. **(B)** Bubble chart shows the differential expression of these pyroptotic genes in the cancerous and paracancerous tissues of various tumors. Red indicates a positive correlation, and blue indicates a negative

correlation. The darker the color, the higher is the correlation index. Bubble size indicates FDR. **(C)** Copy number variation pie chart distribution shows the types of copy number variation for these genes. Corresponding colors have annotations at the bottom, which indicate different types of copy number variation. **(D)** Bubble chart shows the correlation between the methylation of pyroptosis-related molecules and mRNA expression, with blue representing negative correlations and red representing positive correlations. Darker colors indicate a larger correlation index. The bubble size indicates the FDR. **(E)** Bubble chart showing the correlation between CNV and mRNA expression levels. Red indicates a positive correlation and blue indicates a negative correlation. The darker the color, the higher is the correlation index. The bubble size indicates the FDR.

SUPPLEMENTARY FIGURE 7

Correlation analysis of pyroptosis risk score with muscle invasive status and metastasis. **(A-C)** Relationship between the pyroptosis risk score and muscle invasive status in the TCGA-BLCA 、GSE32894 and Xiangya cohort. **(D-E)** Relationship between the pyroptosis risk score and metastasis in the TCGA-BLCA and Xiangya cohort. **(F)** Relationship between the pyroptosis risk score and histological type in the TCGA-BLCA.

SUPPLEMENTARY TABLE 1

Pyroptosis-related genes and detailed clinical information of four BLCA cohorts applied in our analysis.

References

1. Barani M, Hosseinikhah SM, Rahdar A, Farhoudi L, Arshad R, Cucchiarini M, et al. Nanotechnology in bladder cancer: diagnosis and treatment. *Cancers (Basel)* (2021) 13(9):2214. doi: 10.3390/cancers13092214

2. Alifrangis C, McGovern U, Freeman A, Powles T, Linch M. Molecular and histopathology directed therapy for advanced bladder cancer. *Nat Rev Urol* (2019) 16(8):465–83. doi: 10.1038/s41585-019-0208-0

3. Witjes JA, Bruins HM, Cathomas R, Compérat EM, Cowan NC, Gakis G, et al. European Association of urology guidelines on muscle-invasive and metastatic bladder cancer: summary of the 2020 guidelines. *Eur Urol* (2021) 79 (1):82–104. doi: 10.1016/j.eururo.2020.03.055

4. Tan Y, Chen Q, Li X, Zeng Z, Xiong W, Li G, et al. Pyroptosis: a new paradigm of cell death for fighting against cancer. *J Exp Clin Cancer Res* (2021) 40 (1):153. doi: 10.1186/s13046-021-01959-x

5. Yu J, Li S, Qi J, Chen Z, Wu Y, Guo J, et al. Cleavage of GSDME by caspase-3 determines lobaplatin-induced pyroptosis in colon cancer cells. *Cell Death Dis* (2019) 10(3):193. doi: 10.1038/s41419-019-1441-4

6. Zaki MH, Vogel P, Body-Malapel M, Lamkanfi M, Kanneganti TD. IL-18 production downstream of the Nlrp3 inflammasome confers protection against colorectal tumor formation. *J Immunol* (2010) 185(8):4912–20. doi: 10.4049/jimmunol.1002046

7. Wang Y, Gao W, Shi X, Ding J, Liu W, He H, et al. Chemotherapy drugs induce pyroptosis through caspase-3 cleavage of a gasdermin. *Nature* (2017) 547 (7661):99–103. doi: 10.1038/nature22393

8. Fritsch M, Günther SD, Schwarzer R, Albert MC, Schorn F, Werthenbach JP, et al. Caspase-8 is the molecular switch for apoptosis, necroptosis and pyroptosis. *Nature* (2019) 575(7784):683–7. doi: 10.1038/s41586-019-1770-6

9. Jiang M, Qi L, Li L, Li Y. The caspase-3/GSDME signal pathway as a switch between apoptosis and pyroptosis in cancer. *Cell Death Discovery* (2020) 6:112. doi: 10.1038/s41420-020-00349-0

10. Sharma P, Allison JP. The future of immune checkpoint therapy. *Science* (2015) 348(6230):56–61. doi: 10.1126/science.aaa8172

11. Kalos M, Levine BL, Porter DL, Katz S, Grupp SA, Bagg A, et al. T Cells with chimeric antigen receptors have potent antitumor effects and can establish memory in patients with advanced leukemia. *Sci Transl Med* (2011) 3(95):95ra73. doi: 10.1126/scitranslmed.3002842

12. Hahn AW, Gill DM, SK P, Agarwal N. The future of immune checkpoint cancer therapy after PD-1 and CTLA-4. *Immunotherapy* (2017) 9(8):681–92. doi: 10.2217/imt-2017-0024

13. Liu Z, Tang Q, Qi T, Othmane B, Yang Z, Chen J, et al. A robust hypoxia risk score predicts the clinical outcomes and tumor microenvironment immune characters in bladder cancer. *Front Immunol* (2021) 12:725223. doi: 10.3389/fimmu.2021.725223

14. Liu Z, Qi T, Li X, Yao Y, Othmane B, Chen J, et al. A novel tgf-β risk score predicts the clinical outcomes and tumour microenvironment phenotypes in bladder cancer. *Front Immunol* (2021) 12:791924. doi: 10.3389/fimmu.2021.791924

15. Hu J, Yu A, Othmane B, Qiu D, Li H, Li C, et al. Siglec15 shapes a non-inflamed tumor microenvironment and predicts the molecular subtype in bladder cancer. *Theranostics* (2021) 11(7):3089–108. doi: 10.7150/thno.53649

16. Xia X, Wang X, Cheng Z, Qin W, Lei L, Jiang J, et al. The role of pyroptosis in cancer: pro-cancer or pro-"host"? *Cell Death Dis* (2019) 10(9):650. doi: 10.1038/s41419-019-1883-8

17. Wang B, Yin Q. AIM2 inflammasome activation and regulation: A structural perspective. *J Struct Biol* (2017) 200(3):279–82. doi: 10.1016/j.jsb.2017.08.001

18. Man SM, Kanneganti TD. Regulation of inflammasome activation. *Immunol Rev* (2015) 265(1):6–21. doi: 10.1111/imr.12296

19. Karki R, Kanneganti TD. Diverging inflammasome signals in tumorigenesis and potential targeting. *Nat Rev Cancer.* (2019) 19(4):197–214. doi: 10.1038/s41568-019-0123-y

20. Hu J, Othmane B, Yu A, Li H, Cai Z, Chen X, et al. 5mC regulator-mediated molecular subtypes depict the hallmarks of the tumor microenvironment and guide precision medicine in bladder cancer. *BMC Med* (2021) 19(1):289. doi: 10.1186/s12916-021-02163-6

21. Chen Z, Zhou L, Liu L, Hou Y, Xiong M, Yang Y, et al. Single-cell RNA sequencing highlights the role of inflammatory cancer-associated fibroblasts in bladder urothelial carcinoma. *Nat Commun* (2020) 11(1):5077. doi: 10.1038/s41467-020-18916-5

22. Ritchie ME, Phipson B, Wu D, Hu Y, CW L, Shi W, et al. Limma powers differential expression analyses for RNA-sequencing and microarray studies. *Nucleic Acids Res* (2015) 43(7):e47. doi: 10.1093/nar/gkv007

23. Yu G, Wang LG, Han Y, He QY. clusterProfiler: an r package for comparing biological themes among gene clusters. *Omics* (2012) 16(5):284–7. doi: 10.1089/omi.2011.0118

24. Li H, Hu J, Yu A, Othmane B, Guo T, Liu J, et al. RNA Modification of n6-methyladenosine predicts immune phenotypes and therapeutic opportunities in kidney renal clear cell carcinoma. *Front Oncol* (2021) 11:642159. doi: 10.3389/fonc.2021.642159

25. Hänzelmann S, Castelo R, Guinney J. GSVA: gene set variation analysis for microarray and RNA-seq data. *BMC Bioinf* (2013) 14:7. doi: 10.1186/1471-2105-14-7

26. Liberzon A, Birger C, Thorvaldsdóttir H, Ghandi M, JP M, Tamayo P. The molecular signatures database (msigdb) hallmark gene set collection. *Cell Syst* (2015) 1(6):417–25. doi: 10.1016/j.cels.2015.12.004

27. Geeleher P, Cox N, Huang RS. pRRophetic: an r package for prediction of clinical chemotherapeutic response from tumor gene expression levels. *PLoS One* (2014) 9(9):e107468. doi: 10.1371/journal.pone.0107468

28. Chen DS, Mellman I. Oncology meets immunology: the cancer-immunity cycle. *Immunity* (2013) 39(1):1–10. doi: 10.1016/j.immuni.2013.07.012

29. Shao W, Yang Z, Fu Y, Zheng L, Liu F, Chai L, et al. The pyroptosis-related signature predicts prognosis and indicates immune microenvironment infiltration in gastric cancer. *Front Cell Dev Biol* (2021) 9:676485. doi: 10.3389/fcell.2021.676485

30. Fang Y, Tian S, Pan Y, Li W, Wang Q, Tang Y, et al. Pyroptosis: A new frontier in cancer. *BioMed Pharmacother* (2020) 121:109595. doi: 10.1016/j.biopha.2019.109595

31. Wu M, Wang Y, Yang D, Gong Y, Rao F, Liu R, et al. A PLK1 kinase inhibitor enhances the chemosensitivity of cisplatin by inducing pyroptosis in oesophageal squamous cell carcinoma. *EBioMedicine* (2019) 41:244–55. doi: 10.1016/j.ebiom.2019.02.012

32. Chen X, Chen H, Yao H, Zhao K, Zhang Y, He D, et al. Turning up the heat on non-immunoreactive tumors: pyroptosis influences the tumor immune microenvironment in bladder cancer. *Oncogene* (2021) 40(45):6381–93. doi: 10.1038/s41388-021-02024-9

33. Van Opdenbosch N, Lamkanfi M. Caspases in cell death, inflammation, and disease. *Immunity* (2019) 50(6):1352–64. doi: 10.1016/j.immuni.2019.05.020

34. Broz P, Pelegrín P, Shao F. The gasdermins, a protein family executing cell death and inflammation. *Nat Rev Immunol* (2020) 20(3):143–57. doi: 10.1038/s41577-019-0228-2

35. Bergsbaken T, SL F, Cookson BT. Pyroptosis: host cell death and inflammation. *Nat Rev Microbiol* (2009) 7(2):99–109. doi: 10.1038/nrmicro2070

36. Liu XS, Kui XY, Gao Y, Chen XQ, Zeng J, Liu XY, et al. Comprehensive analysis of ythdf1 immune infiltrates and cerna in human esophageal carcinoma. *Front Genet* (2022) 13:835265. doi: 10.3389/fgene.2022.835265

37. Liu XS, Gao Y, Wu LB, Wan HB, Yan P, Jin Y, et al. Comprehensive analysis of glut1 immune infiltrates and cerna network in human esophageal carcinoma. *Front Oncol* (2021) 11:665388. doi: 10.3389/fonc.2021.665388

38. Zhou Z, He H, Wang K, Shi X, Wang Y, Su Y, et al. Granzyme a from cytotoxic lymphocytes cleaves GSDMB to trigger pyroptosis in target cells. *Science* (2020) 368(6494):eaaz7548. doi: 10.1126/science.aaz7548

39. Bollino D, Colunga A, Li B, Aurelian L. ΔPK oncolytic activity includes modulation of the tumour cell milieu. *J Gen Virol* (2016) 97(2):496–508. doi: 10.1099/jgv.0.000353

40. Zhang Z, Zhang Y, Xia S, Kong Q, Li S, Liu X, et al. Gasdermin e suppresses tumour growth by activating anti-tumour immunity. *Nature* (2020) 579 (7799):415–20. doi: 10.1038/s41586-020-2071-9

41. Hou J, Zhao R, Xia W, CW C, You Y, JM H, et al. PD-L1-mediated gasdermin c expression switches apoptosis to pyroptosis in cancer cells and facilitates tumour necrosis. *Nat Cell Biol* (2020) 22(10):1264–75. doi: 10.1038/s41556-020-0575-z

42. Erkes DA, Cai W, Sanchez IM, Purwin TJ, Rogers C, Field CO, et al. Mutant BRAF and MEK inhibitors regulate the tumor immune microenvironment *via* pyroptosis. *Cancer Discovery* (2020) 10(2):254–69. doi: 10.1158/2159-8290.CD-19-0672

43. Lu H, Zhang S, Wu J, Chen M, MC C, Fu Y, et al. Molecular targeted therapies elicit concurrent apoptotic and gsdme-dependent pyroptotic tumor cell death. *Clin Cancer Res* (2018) 24(23):6066–77. doi: 10.1158/1078-0432.CCR-18-1478

44. Chen DS, Mellman I. Elements of cancer immunity and the cancer-immune set point. *Nature* (2017) 541(7637):321–30. doi: 10.1038/nature21349

frontiers | Frontiers in Immunology

TYPE Original Research
PUBLISHED 02 September 2022
DOI 10.3389/fimmu.2022.961926

Check for updates

OPEN ACCESS

EDITED BY
Jian Zhang,
Southern Medical University, China

REVIEWED BY
Quan Cheng,
Central South University, China
Fan Zhang,
University of New South Wales, Australia
Dapeng Hao,
Harbin Medical University, China

*CORRESPONDENCE
Udo S. Gaipl
udo.gaipl@uk-erlangen.de
Hu Ma
mahuab@163.com
David S. Schrump
David_Schrump@nih.gov

†These authors have contributed equally to this work and share first authorship

‡These authors have contributed equally to this work and share senior authorship

SPECIALTY SECTION
This article was submitted to Cancer Immunity and Immunotherapy, a section of the journal Frontiers in Immunology

RECEIVED 05 June 2022
ACCEPTED 15 August 2022
PUBLISHED 02 September 2022

CITATION
Zhou J-G, Wong AH-H, Wang H, Jin S-H, Tan F, Chen Y-Z, He S-S, Shen G, Frey B, Fietkau R, Hecht M, Carr SR, Wang R, Shen B, Schrump DS, Ma H and Gaipl US (2022) Definition of a new blood cell count score for early survival prediction for non-small cell lung cancer patients treated with atezolizumab: Integrated analysis of four multicenter clinical trials. *Front. Immunol.* 13:961926. doi: 10.3389/fimmu.2022.961926

Definition of a new blood cell count score for early survival prediction for non-small cell lung cancer patients treated with atezolizumab: Integrated analysis of four multicenter clinical trials

Jian-Guo Zhou[1,2,3,4†], Ada Hang-Heng Wong[5†], Haitao Wang[6†], Su-Han Jin[7], Fangya Tan[8], Yu-Zhong Chen[9], Si-Si He[1], Gang Shen[1], Benjamin Frey[2,3,4], Rainer Fietkau[3,4], Markus Hecht[3,4], Shamus R. Carr[6], Ruihong Wang[6], Bo Shen[9], David S. Schrump[6*‡], Hu Ma[1*‡] and Udo S. Gaipl[2,3,4*‡]

[1]Department of Oncology, The Second Affiliated Hospital of Zunyi Medical University, Zunyi, China, [2]Department of Radiation Oncology, Translational Radiobiology, Universitätsklinikum Erlangen, Erlangen, Germany, [3]Department of Radiation Oncology, Universitätsklinikum Erlangen, Erlangen, Germany, [4]Comprehensive Cancer Center Erlangen-EMN, Erlangen, Germany, [5]AW Medical Co. Ltd., Macau, Macao SAR, China, [6]Thoracic Epigenetics Section, Thoracic Surgery Branch, Center for Cancer Research National Cancer Institute, National Institutes of Health, Bethesda, Maryland, United States, [7]Special Key Laboratory of Oral Diseases Research, Stomatological Hospital Affiliated to Zunyi Medical University, Zunyi, China, [8]Department of Analytics, Harrisburg University of Science and Technology, Harrisburg, PA, United States, [9]The Affiliated Cancer Hospital of Nanjing Medical University, Jiangsu Cancer Hospital and Jiangsu Institute of Cancer Research, Nanjing, China

Importance: Blood cell count test (BCT) is a robust method that provides direct quantification of various types of immune cells to reveal the immune landscape to predict atezolizumab treatment outcomes for clinicians to decide the next phase of treatment.

Objective: This study aims to define a new BCTscore model to predict atezolizumab treatment benefits in non-small lung cell cancer (NSCLC) patients.

Design, Setting, and Participants: This study analyzed four international, multicenter clinical trials (OAK, BIRCH, POPLAR, and FIR trials) to conduct *post-hoc* analyses of NSCLC patients undergoing atezolizumab (anti–PD-L1) single-agent treatment (n = 1,479) or docetaxel single-agent treatment (n = 707). BCT was conducted at three time points: pre-treatment (T1), the first day of treatment cycle 3 (T2), and first day of treatment cycle 5 (T3). Univariate and multivariate Cox regression analyses were conducted to identify early BCT biomarkers to predict atezolizumab treatment outcomes in NSCLC patients.

10.3389/fimmu.2022.961926

Main Outcomes and Measures: Overall survival (OS) was used as the primary end point, whereas progression-free survival (PFS) according to Response Evaluation Criteria in Solid Tumors (RECIST), clinical benefit (CB), and objective response rate (ORR) were used as secondary end points.

Results: The BCT biomarkers of neutrophil-to-lymphocyte ratio (NLR) and platelet-to-lymphocyte ratio (PLR) at time point T3 and neutrophil-to-monocyte ratio (NMR) at time point T2 with absolute cutoff values of NLR_T3 = 5, PLR_T3 = 180, and NMR_T2 = 6 were identified as strong predictive biomarkers for atezolizumab (Ate)–treated NSCLC patients in comparison with docetaxel (Dtx)–treated patients regarding OS (BCTscore low risk: $HR_{Ate\ vs.\ Dtx}$ = 1.54 (95% CI: 1.04–2.27), P = 0.031; high risk: $HR_{Ate\ vs.\ Dtx}$ = 0.84 (95% CI: 0.62–1.12), P = 0.235). The identified BCTscore model showed better OS AUC in the OAK ($AUC_{12month}$ = 0.696), BIRCH ($AUC_{12month}$ = 0.672) and POPLAR+FIR studies ($AUC_{12month}$ = 0.727) than that of each of the three single BCT biomarkers.

Conclusion and Relevance: The BCTscore model is a valid predictive and prognostic biomarker for early survival prediction in atezolizumab-treated NSCLC patients.

KEYWORDS

NSCLC, atezolizumab, biomarker, blood cell count, clinical trial

Background

Non-small cell lung cancer (NSCLC) accounts for 84% of all lung cancer incidence, roughly accounting for 235,170 new cases in the United States in 2021 (1). Therapy for advanced NSCLC can include chemotherapy, radiotherapy, or tyrosine kinase inhibitors (TKIs) as first-line therapy for patients carrying genetic mutations in the genes of *EGFR*, *ALK*, *ROS1*, and *NTRK* (2). However, for patients without TKI-targeted mutations, safe and effective therapeutic options were limited. With the development of immune checkpoint inhibitors (ICIs), this has changed. ICIs were developed against programmed cell death ligand 1 (PD-L1) on cancer cells, such as atezolizumab, and the immune suppressive receptors programmed cell death 1 (PD-1), such as nivolumab and pembrolizumab, and cytotoxic T lymphocyte-associated antigen 4 (CTLA-4), such as ipilimumab, being present on cytotoxic T cells (2).

These therapies have improved NSCLC treatment outcomes in patients with advanced disease (3–5). However, without the implementation of patient selection by predictive or prognostic biomarkers, no significant PFS or OS improvement by ICI therapy, as compared with chemotherapy, is observed (6). PD-L1 expression and tumor mutational burden (TMB) are often recommended for patient selection before treatment, but contrasting results are seen in clinical trials involving atezolizumab (3, 4, 7) and nivolumab (6). Other biomarkers such as chromosome instability, tumor microsatellite instability, and T-cell surface markers such as PD-1[1], CD38 and CD39[2], or tumor-infiltrating PD-1^{hi} $CD8^{+}$ T cells (8) might serve as prognostic and predictive biomarkers for ICI therapy (9, 10). However, genetic biomarkers require tumor biopsy samples, which are invasive and limit longitudinal analysis for continuous disease monitoring. Hence, liquid biopsy-based biomarkers are attracting more recent attention (11–15).

Blood cell count test (BCT) is a routine, regularly performed blood test conducted before and during treatment. The less invasiveness of BCT makes it potentially useful for longitudinal disease monitoring, especially at the end of each treatment cycle to decide if the treatment plan needs to be altered. BCT provides a direct overview of the immune landscape based on the counts of various types of immune cells. For instance, high pre-treatment neutrophil-to-lymphocyte ratio (NLR) and platelet-to-lymphocyte ratio (PLR) correlated with poor survival outcomes in NSCLC patients treated with ICIs, regardless of TMB (16–18). However, a limitation of most of the published studies is either small cohorts or analysis of multiple ICI therapies in diverse clinical settings, which may compromise the validity of findings. Consequently, this study focuses on survival data obtained from four international, multicenter clinical trials to conduct *post-hoc* analysis of NSCLC

1 PD-1, programmed cell death protein 1

2 CD38 and CD39, clusters of differentiation 38 and 39

patients undergoing atezolizumab (Ate) single-agent treatment, whereas docetaxel (Dtx) single-agent treatment, the standard protocol for second-line NSCLC treatment at the time of clinical trial, served as control. BCT was conducted at three time points: baseline (T1), 6 weeks on-treatment (T2), and 12 weeks on-treatment (T3). The overarching goal was to identify a BCTscore as a biomarker that may predict overall survival in NSCLC patients treated with atezolizumab.

Methods

Study cohort

Pseudonymized individual participant data from the single-arm phase II studies FIR (NCT01846416) (19) and BIRCH (NCT02031458) (20) and the two-arm randomized controlled trials (RCTs) POPLAR phase II study (NCT01903993) (3) and OAK phase III study (NCT02008227) (4) were provided by Genentech Inc. and accessed through the secure Vivli online platform. Docetaxel was used in the POPLAR and OAK studies as chemotherapy control to the anti–PD-L1 immunotherapy atezolizumab. Raw data were extracted and compared with the available published data to ensure accuracy. Secondary analysis of the trial data was deemed to be of negligible risk and was approved by the Institutional Review Board of the Second Affiliated Hospital, Zunyi Medical University (No. YXLL(KY-R)-2021-010). Deidentified data were accessed according to Roche's policy and process for Vivli. Data analyses were conducted from 2 March 2021 to 30 June 2021.

A total of 2,316 patients were included from the four clinical trials, and after the exclusion of untreated patients and patients without pre-treatment BCT, 1,479 and 707 advanced NSCLC patients undergoing atezolizumab and docetaxel treatment, respectively, were included in this study (Figure 1). Of note, atezolizumab was administered either as first-line or second-line therapy after failure of prior chemotherapy in the four trials used in this study. Atezolizumab and docetaxel were both administered every 3 weeks in the two-arm RCTs POPLAR and OAK. BCT was obtained at three time points: pre-treatment baseline (T1), 6 weeks on-treatment (T2), and 12 weeks on-treatment (T3). Baseline was defined as within 28 days prior to the start of treatment. Time points T2 and T3 corresponded to the first day of treatment cycles 3 and 5, respectively.

Predictor and treatment outcome definitions

The definitions of OS, PFS, clinical benefit (CB), and objective response rate (ORR) were detailed in each trial (3, 4, 19, 20). In this study, OS was used as the primary end point, whereas PFS, according to Response Evaluation Criteria in Solid Tumors (RECIST version 1.1), CB, and ORR was used as secondary end points.

All biomarkers acquired from BCT, such as absolute cell counts of red blood cells, white blood cells, platelets, as well as the ratios of immune cell subgroups were subjected to the biomarker screening. The BCT biomarkers of NLR, PLR, NMR, and lymphocyte-to-monocyte ratio (LMR) were calculated by dividing absolute cell counts of corresponding immune cells acquired from BCT. The identified biomarkers were named with the abbreviation of the immune cell ratios followed by the indication of the time points T1, T2, and T3, respectively.

Statistical analysis

Associations between BCT biomarkers and OS or PFS were calculated by the Cox proportional hazards regression model and reported as the mean of hazard ratio (HR) with two-sided 95% confidence interval (CI) and *p*-value as calculated by the Wald test. The Kaplan–Meier method was used to estimate median OS and PFS between risk groups with a stratified log-rank test at the two-sided significance level. Survival analysis was performed by the *survival* (V.3.2-11) and *survminer* (V.0.4.9) packages. To analyze the degree of discrimination of biomarkers, we performed time-dependent receiver-operating characteristic (ROC) analysis and calculated the area under curve (AUC) for the indicated survival outcomes by the *timeROC* (V.0.3) and *pROC* (V.1.17.0.1) packages. Comparisons of CB, ORR, or clinical factors between the specified groups were calculated by the generalized linear model (GLM) to report relative risk (RR) with 95% CI and *p*-value as calculated by the Pearson's $\chi 2$-test or Fisher's exact test. Comparisons of BCT biomarkers between the treatment groups or different time points of the same treatment group were performed using Wilcoxon signed-rank test. All statistical analyses were carried out in R V.3.6.1 (R Foundation for Statistical Computing). $P \leq 0.050$ was considered to be statistically significant. All analyses were univariate except for the multivariate Cox analyses. In multivariate analysis, the BCT biomarker(s) and the clinical factors of sex (male/female), age, race (white/Asian/other), Eastern Cooperative Oncology Group performance status (ECOG PS), metastasis, and pre-treatment PD-L1 (high ≥ 1%/low < 1%; except for the BIRCH study, high ≥ 5%/low < 5%) were included; however, the additional biomarkers of body mass index (BMI) and smoker (never/previous/current) were insignificant as assessed by univariate Cox analysis and were, hence, removed from the analyses.

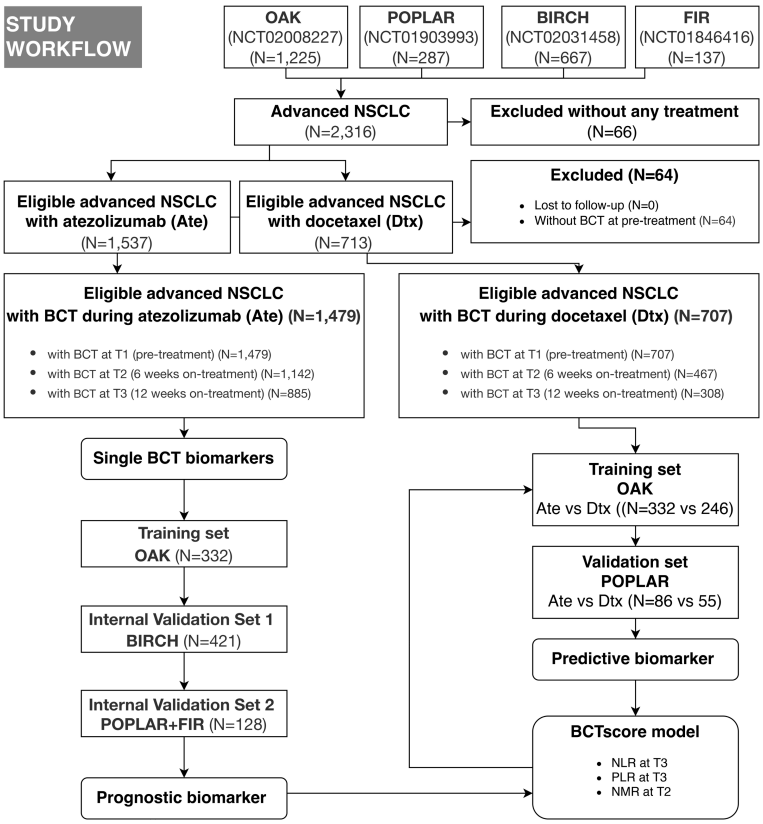

FIGURE 1
Flow chart demonstrating the patient cohorts of the indicated trials and the approach for the development of a blood cell count test (BCT)–based score (BCTscore). The internal cohorts are from four international, multicenter studies (OAK, POPLAR, BIRCH, and FIR). Ate, atezelizumab; Dtx, docetaxel.

Results

Identification of BCT biomarkers related to treatment outcomes of patients treated with atezolizumab but not of those treated with docetaxel

Initially, the datasets of the four international, multicenter studies containing 1,479 atezolizumab-treated patients' survival data (the baseline characteristics of these patients are summarized in Supplementary Table S1) were combined to identify 80 common BCT biomarkers that demonstrated correlations to PFS and OS in advanced NSCLC based on HR calculation. Next, we removed the 62 BCT biomarkers that we identified from analyses of the survival data of 707 advanced NSCLC patients who underwent docetaxel treatment. Moreover, all biomarkers containing absolute cell counts were eliminated to avoid sampling-based systemic errors. Hence, 11 BCT biomarkers unique to the atezolizumab-treated patient group remained. Consequently, based on existing knowledge of immune biomarkers, we selected the cell ratios of NLR, PLR, and LMR at 12 weeks on-treatment (NLR_T3, PLR_T3, and LMR_T3), and NMR at 6 and 12 weeks on-treatment (NMR_T2 and NMR_T3), for further analysis. Frequency distribution analysis of these four BCT biomarkers at pre-treatment (T1), followed by Wilcoxon signed-rank test of the absolute difference between the mean values of the two patient groups showed no significant difference between the atezolizumab and docetaxel treatment groups in OAK and POPLAR studies (Supplementary Figure S1). This suggested that baseline levels of these biomarkers were comparable between the two treatment groups. Hence, we deduced that changes in subsequent time points at T2 and T3 likely occurred after treatment started (Supplementary Figure S2).

Next, we performed univariate Cox analysis by decile patient fractions [Ref: Valero] at 10% intervals from 10% to 90% or by the quadrant percentiles of 25% and 75% for all five biomarkers in the combined datasets of atezolizumab-treated patients to calculate HRs for OS and PFS (Figure 2), respectively. NLR_T3 showed significant HR for all patient cutoffs examined in the atezolizumab-treated group and for both OS and PFS. PLR_T3 showed significant PFS HR for the > 10% patient fractions and

significant OS HR for all defined patient fractions. LMR_T3 showed significant but inconsistent PFS HR between the 25% and 80% patient fractions and significant OS HR for the > 10% patient fraction. NMR_T2 showed significant PFS HR at the > 20% patient fractions and significant OS HR at the > 10% patient fractions. NMR_T3 showed significant PFS HR at the > 10% patient fractions and significant OS HR for all patient fractions.

On multivariate analysis, we initially screened for clinical factors that might confer to PFS and OS in atezolizumab-treated NSCLC patients (Supplementary Table S2). Similar to univariate analysis, we performed multivariate Cox analysis using the same patient fractions in the combined datasets for PFS and OS (Figure 2), respectively. NLR_T3, PLR_T3, NMR_T2, and NMR_T3 all depicted identical trends to univariate analysis. Alternatively, LMR_T3 showed significant PFS HR from 10% to 80% patient fractions and significant OS HR from 10% to 50% patient fractions. In contrast, all five BCT biomarkers showed non-significant HRs for both OS and PFS in the docetaxel-treated group (Figure 2). Collectively, these results suggested that LMR_T3 exhibited significant but inconsistent HRs as compared with the rest of the selected biomarkers. Furthermore, as deduced from its definition, LMR_T3 displayed HR < 1, whereas the other four biomarkers displayed HR > 1.

After that, we applied the univariate and multivariate Cox analysis with decile patient fractions to the cohort of atezolizumab-treated NSCLC patients in the four individual trials, respectively (Supplementary Figure S3). In concordance to the joint analyses, all of the five biomarkers showed no significant HRs for both PFS and OS in the docetaxel treatment group. In contrast, positive results, consistent to the combined cohort, were obtained for all biomarkers in the BIRCH and OAK cohorts for both PFS and OS. This was also true of the POPLAR cohort, except for LMR_T3. However, in the FIR cohort none of the biomarkers demonstrated significant HRs for either PFS or OS, but this is most likely because of the small sample size (21). Consequently, absolute integer cutoff values were set for the combined cohort using the patient fractions of 25–50% for all five biomarkers to establish a BCTscore model. The application of these variables to univariate and multivariate Cox analysis of each trial's cohort succeeded in narrowing the range of each biomarker's integer cutoff values to uncover the significant range (Supplementary Figure S4). NLR_T3, PLR_T3, and NMR_T2 confirmed consistently significant PFS and OS HRs in the cohorts of BIRCH, OAK, and POPLAR. In contrast, all cutoff values of LMR_T3 did not. Because LMR_T3 showed consistently poor

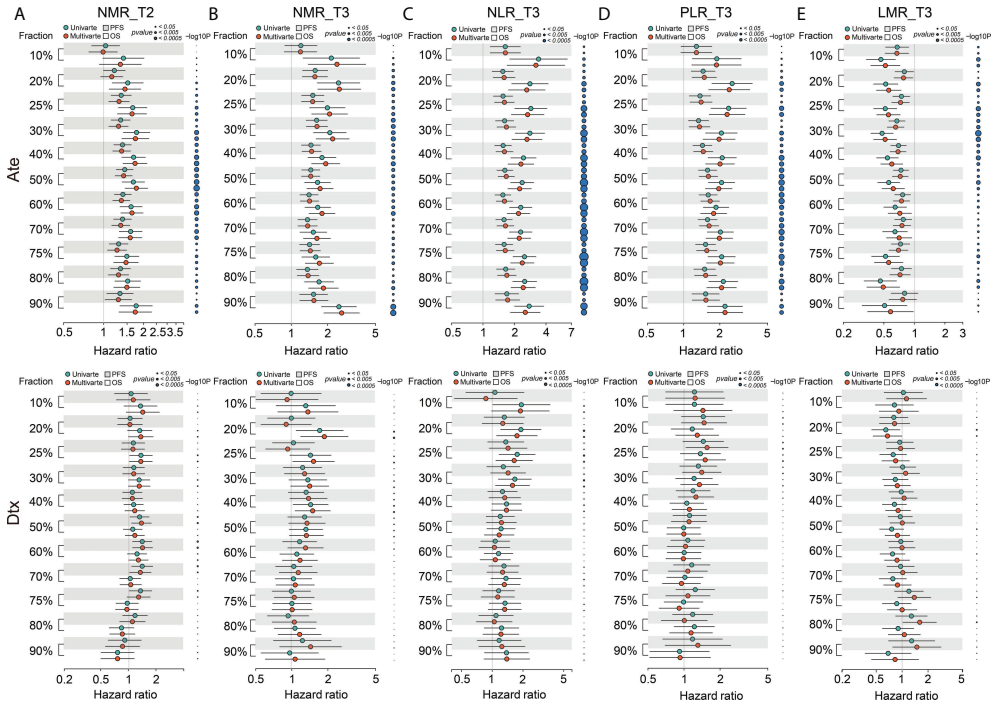

FIGURE 2
Forest plot of hazard ratio (HR) for overall survival (OS) and progression-free survival (PFS) of the BCT biomarkers **(A)** NMR_T2, **(B)** NMR_T3, **(C)** NLR_T3, **(D)** PLR_T3, and **(E)** LMR_T3 in decile patient fractions in the atezolizumab (Ate) or docetaxel (Dtx) treatment groups of the combined internal cohorts. Mean HRs for OS (white shade) or PFS (gray shade) under univariate (green) or multivariate (red) Cox analysis is indicated by the dots, the range of HR is indicated by the error bar of the forest plot; $-\log_{10}$ *p*-value of each calculated HR is indicated by the size of the blue dots adjacent to the forest plot.

prognostic power in all of the above outlined analyses, it was removed from the biomarker selection for the BCTscore.

Hence, all combinations of the three selected BCT biomarkers, namely, NLR_T3, PLR_T3, and NMR_T2, formed the 16 BCTscore candidates subjected to further optimization for clinical application (Supplementary Table S3).

Optimization of BCT biomarker combinations to establish the BCTscore model

To establish the BCTscore model, the OAK study was used as our training cohort. Next, the BIRCH study was used as internal validation cohort 1, and the POPLAR combined with the FIR study as internal validation cohort 2. Univariate and multivariate Cox analysis demonstrated that all of the 16 BCTscore candidates demonstrated significant HRs in both OS and PFS, as well as RR for CB and ORR (Supplementary Figure S5). To further narrow down the BCTscore candidates, we performed ROC analysis for OS, PFS, CB, and ORR. The BCTscore candidate 2 (BCTscore #2) was the only candidate that had good AUC for OS, PFS, CB, and ORR in all of the three internal cohorts (Supplementary Table S4). Hence, BCTscore candidate 2, composing of the BCT biomarkers of NLR and PLR at 12 weeks on-treatment (T3) and NMR at 6 weeks on-treatment (T2) with absolute cutoff values of NLR_T3 = 5, PLR_T3 = 180, and NMR_T2 = 6, respectively, was selected as the BCTscore model for NSCLC.

This BCTscore model displayed significant OS and PFS HRs in both univariate and multivariate Cox analysis in all of the three cohorts (Supplementary Figure S5A). The OAK cohort's RR for CB (univariate = 0.60 [95% CI: 0.39–0.93], P = 0.024; multivariate = 0.56 [95% CI: 0.35–0.88], P = 0.014) (Supplementary Figure S5B) and ORR (univariate = 0.53 [95% CI: 0.31–0.91], P = 0.22; multivariate = 0.58 [95% CI: 0.37–0.88], P = 0.013) with BCTscore stratification (Supplementary Figure S5B) were good. The rate of CB (high risk = 38%, low risk = 51%) and ORR (high risk = 17%, low risk = 28%) of the low-risk atezolizumab-treated patients in the OAK cohort after BCTscore stratification (Supplementary Table S5) were also higher than the 48% CB and 14% ORR reported in the original study (4). Furthermore, survival analysis also showed that our newly identified BCTscore model presented significant difference in both OS and PFS between high- and low-risk patients in the atezolizumab-treated group (Figure 3). ROC analysis resulted in a BCTscore model that consistently exhibited better OS AUC in the OAK ($AUC_{12month}$ = 0.696), BIRCH ($AUC_{12month}$ = 0.672), and POPLAR+FIR studies ($AUC_{12month}$ = 0.727) than that of each of the three single BCT biomarkers in these studies (Figure 4). However, the AUCs of the BCTscore model were lower than those of NLR_T3 for PFS (Supplementary Figure S6), CB (Supplementary Figure S7), and ORR (Supplementary Figure S7) in the OAK cohort, whereas the BCTscore model depicted better AUCs than the standalone BCT biomarkers for these survival indicators in the BIRCH and POPLAR+FIR cohorts.

Investigation of the BCTscore model as a predictive biomarker

Last, in order to test whether the newly identified BCTscore model could serve as a predictive biomarker, we performed survival analysis on the OAK and POPLAR RCTs. The Ate *versus* Dtx HRs of each BCT biomarker's absolute cutoff value or decile fractionated BCTscore candidates above and below the cutoff were also calculated to determine whether each BCTscore candidate was a predictive biomarker (22). Results showed that NLR_T3 presented significant PFS prognosis in the OAK study and may be prognostic of OS in the POPLAR study, whereas PLR_T3 and NMR_T2 achieved no significant results in both RCTs (Supplementary Table S6). On the other hand, all the 16 BCTscore candidates had some predictive power in > 75% fractions in the OAK and the POPLAR RCTs (Supplementary Table S7).

In this regard, our newly developed BCTscore model is a strong predictive model specific to atezolizumab-treated NSCLC patients in comparison to docetaxel-treated patients for OS in the cohorts of OAK (BCTscore low risk: $HR_{Ate\ vs.\ Dtx}$ = 1.54 [95% CI: 1.04–2.27], P = 0.031; high risk: $HR_{Ate\ vs.\ Dtx}$ = 0.84 [95% CI: 0.62–1.12], P = 0.235) (Figure 5) and POPLAR (BCTscore low risk: $HR_{Ate\ vs.\ Dtx}$ = 2.93 [95% CI: 1.21–7.10], P = 0.013; high risk: $HR_{Ate\ vs.\ Dtx}$ = 0.56 (95% CI: 0.29-1.07), P = 0.074) (Supplementary Figure S8).

In contrast, no significant difference was observed in PFS between the atezolizumab and docetaxel treatment groups in both the OAK (BCTscore low risk: $HR_{Ate\ vs.\ Dtx}$ = 1.22 [95% CI: 0.85–1.75], P = 0.267; high risk: $HR_{Ate\ vs.\ Dtx}$ = 0.79 [95% CI: 0.60–1.04], P = 0.092) (Supplementary Figure S9) and POPLAR studies (BCTscore low risk: $HR_{Ate\ vs.\ Dtx}$ = 1.06 [95% CI: 0.50–2.24], P = 0.877; high risk: $HR_{Ate\ vs.\ Dtx}$ = 0.87 (95% CI: 0.47–1.59), P = 0.652) (Supplementary Figure S10), in consistence to the findings of the two studies (3, 4). Similarly, analysis of the relative response rate suggested that our BCTscore model did not distinguish between the atezolizumab- and docetaxel-treated patients in both CB (OAK high risk: Ate *versus* Dtx = 1.25, low risk: Ate *versus* Dtx = 0.85; POPLAR high risk: Ate *versus* Dtx = 0.67, low risk: Ate *versus* Dtx = 0.95) and ORR (OAK high risk: Ate *versus* Dtx = 0.96, low risk: Ate *versus* Dtx = 0.95; POPLAR high risk: Ate *versus* Dtx = 0.79, low risk: Ate *versus* Dtx = 0.78) (Supplementary Table S8), reinforcing the fact that our newly defined BCTscore model is a predictive and prognostic biomarker particularly for OS.

Taken together, these results indicate that our BCTscore model can predict the overall survival of NSCLC patients treated with anti–PD-L1 atezolizumab therapy at 12 weeks on-treatment to decide whether treatment can be terminated or alternative treatment plans should be devised.

10.3389/fimmu.2022.961926

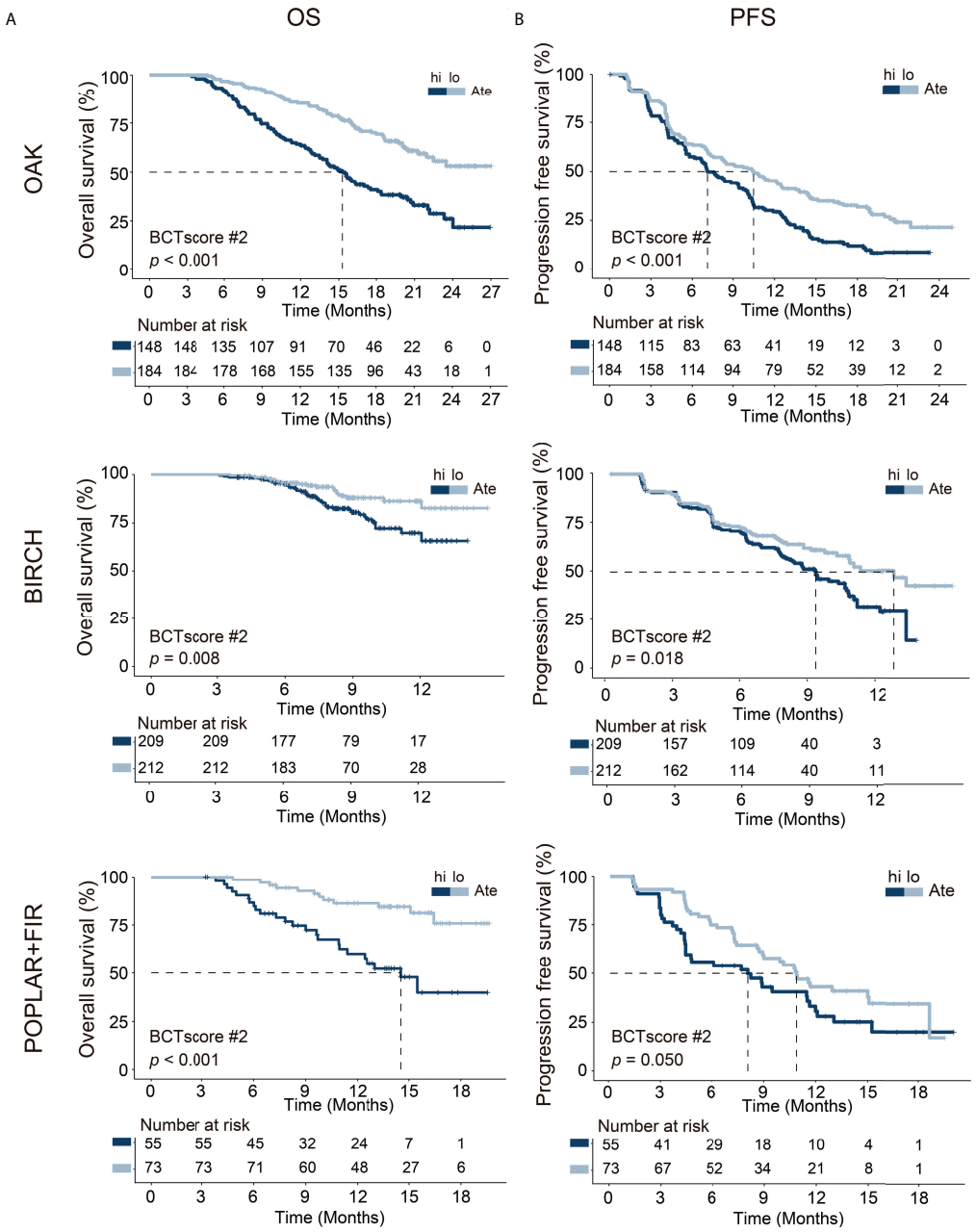

FIGURE 3
Kaplan–Meier analysis of **(A)** overall survival (OS) and **(B)** progression-free survival (PFS) between high-risk (hi) and low-risk (lo) patients, as defined with the identified BCTscore candidate 2 (BCTscore #2), treated with atezolizumab (Ate) of the training cohort (OAK) and the internal validation cohorts (BIRCH and POPLAR + FIR). The percentage of survival of high-risk (dark blue) and low-risk (light blue) patients is plotted against the time in months.

Discussion

In spite of the success of ICI therapy in NSCLC treatment, robust prediction of treatment response remains one of the biggest challenges (23). BCT, which is a routine clinical procedure, provides an unbiased overview of the immune landscape for patient stratification and longitudinal ICI efficacy assessment without the need for specialized analysis. This study showed that the BCTscore model serves as both a strong prognostic and predictive biomarkers of ICI efficacy, especially the prediction of overall survival beyond the date of the BCT test. The strengths of this study are manyfold. First, the

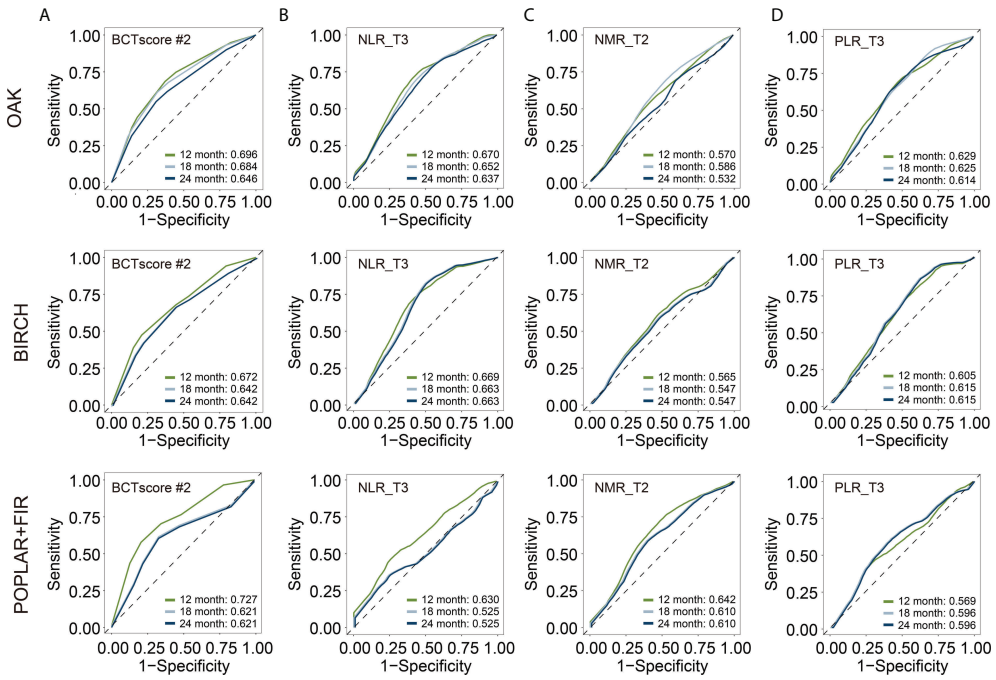

FIGURE 4
Time-dependent receiver-operating characteristic (ROC) analysis for overall survival (OS) to obtain the area under curve (AUC) of **(A)** BCTscore candidate 2 (BCTscore #2) and the BCT biomarkers **(B)** NLR_T3, **(C)** NMR_T2, and **(D)** PLR_T3 of the atezolizumab-treated patients of the training cohort (OAK) and the internal validation cohorts (BIRCH and POPLAR + FIR). Sensitivity is plotted against specificity.

OS AUCs of our newly identified BCTscore model surpassed that of PD-L1 (24) and TMB (25, 26), both of which can only be applied by more invasive tissue biopsy procedures. Hence, our BCTscore model complements PD-L1 and TMB at later stages to predict survival beyond the initial treatment cycle. Next, an important feature of our analyses is easily obtainable longitudinal data. We presume that the immune landscape alters during treatment, so each time point signifies a discrete event (27). Simultaneously, we removed any BCT biomarker at any time point that is correlated to patient survival after docetaxel treatment during initial biomarker screening, thus selecting atezolizumab-specific BCT biomarkers. Our assumption is that BCT biomarkers typical to cancer prognosis regardless of biological mechanism will show significant HR in the docetaxel patient group and, hence, should be removed from subsequent analyses. Hence, prognostic biomarkers were ruled out using our approach.

Furthermore, delays in immune response have been frequently observed during ICI therapy (28, 29). That is why later time points are hypothesized to have better indicative power as compared with earlier time points. Nevertheless, the biological nature of the BCT biomarker still holds the key to a successful predictive biomarker. For example, both NMR_T2 and NMR_T3 depicted significant HRs in our preliminary analysis. However, NMR_T2 showed better results in the survival analysis of the OAK and POPLAR studies than NMR_T3, whereas NLR_T3 and PLR_T3 displayed good results in the same analysis. This result demonstrated that after the number of neutrophils increased at 6 weeks on-treatment (T2), subsequent increase had little impact on disease prognosis and prediction; instead, the reduction of lymphocytes and increase in platelet numbers at 12 weeks on-treatment (T3) come into play. No prior studies have examined this, to our understanding, in the context of ICI, and the biological mechanism on the temporal changes of the immune landscape during ICI treatment remains elusive.

Additionally, we picked immune cell ratios over absolute cell numbers to avoid systemic errors during blood sampling and sample analysis performed in different medical centers. The cell ratios used for our analysis were selected based on cell lineage and published data. For example, NMR and NLR were picked to distinguish changes in the neutrophil population against the immune cell lineages of monocytes and lymphocytes. It is known that lymphocytes are directly involved in tumor killing, whereas monocytes have more diverse biological roles. Indeed, the fact that NLR outperforms all other cell ratios as a single BCT biomarker reinforces previous observations that increasing neutrophil numbers and decreasing lymphocyte numbers result in poor cancer prognosis (30, 31). Alternatively, the poor correlation between LMR and survival supports the

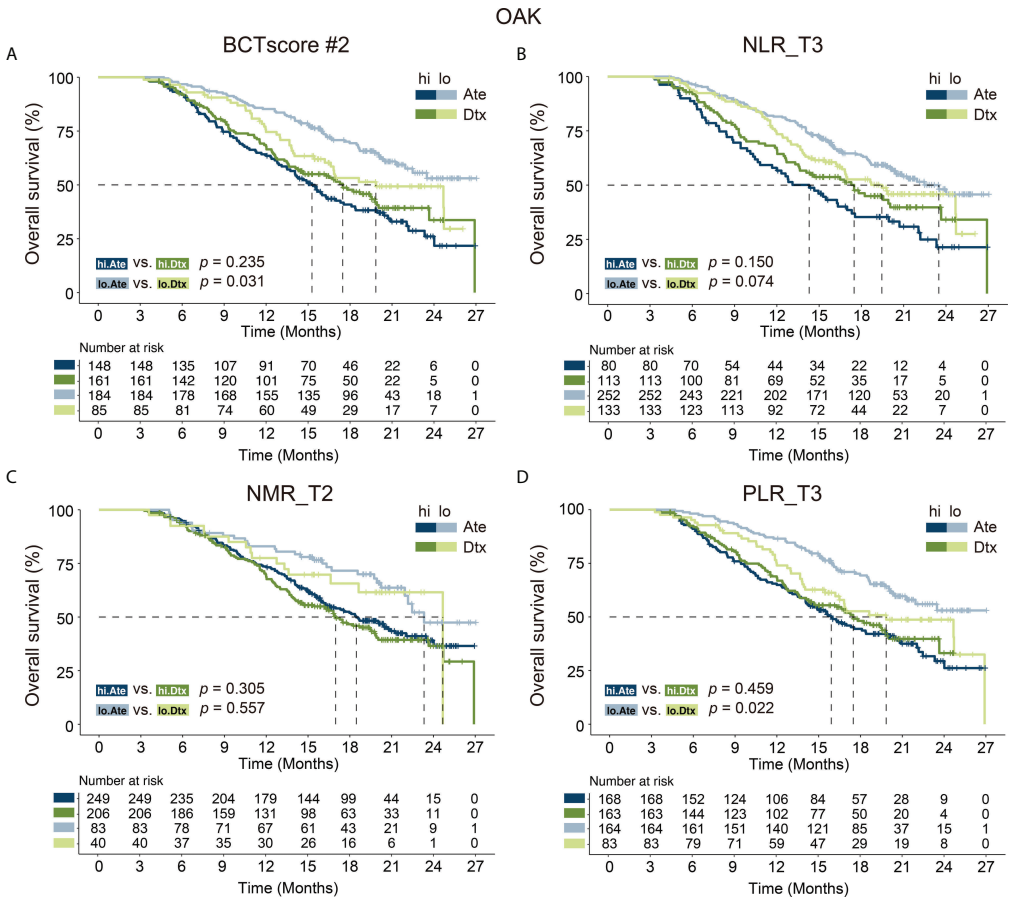

FIGURE 5
Kaplan–Meier analysis of overall survival (OS) for **(A)** BCTscore candidate 2 (BCTscore #2) and the BCT biomarkers **(B)** NLR_T3, **(C)** NMR_T2, and **(D)** PLR_T3 comparing atezolizumab (Ate)–treated patients (dark blue) against docetaxel (Dtx)–treated patients (dark green) in the high-risk (hi) group, and comparing between Ate-treated patients (light blue) against Dtx-treated patients (light green) in the low-risk (lo) group of the training cohort (OAK).

hypothesis that neutrophils, but not the entire monocyte population, contribute to cancer prognosis. Next, the improvement in prognostic ability by combining multiple immune cell ratios suggests that many factors play a role in ICI treatment; for instance, neutrophils were shown to promote tumor metastases (32, 33); platelets present antigens to trigger immune evasion (34). We deduce that future immunological studies will deepen our knowledge of the correlation between the immune landscape and ICI treatment success to unravel more effective and accurate biomarkers (35).

Finally, analysis of the four international, multicenter clinical trials consisting of 1,479 NSCLC patients treated with atezolizumab provides strong statistical evidence to support our findings. We observed statistically significant associations for OS, PFS, ORR, and CB with powerful diagnostic abilities, suggesting that the newly defined BCTscore has prognostic and predictive value in the context of anti–PD-L1 atezolizumab therapy. Nevertheless, because the mechanistic role of atezolizumab is restricted to tumor recognition by T cells, the application of our model to other ICI therapies, such as anti–PD-1 and anti–CTLA-4 therapies, remains to be tested.

A limitation of our study is the lack of TMB measurements in our dataset that would enable direct comparison between the predictive power of our newly defined BCTscore model and TMB. We were restricted in the validation of our results because of the shortage of patients treated by atezolizumab alone. Future studies will focus on the optimization of the absolute cutoff values of each BCT biomarker for different ICI therapies as well as combination therapies.

In summary, we demonstrated, for the first time, *via* a *post-hoc* analysis of four clinical trials, the predictive value of longitudinal blood cell count ratio for NSCLC patients treated with atezolizumab. Together, this study proved that the BCTscore combination of NLR at 12 weeks, PLR at 12 weeks, and NMR at 6 weeks provides prognostic and predictive information without the need to re-biopsy patients undergoing

anti–PD-L1 atezolizumab monotherapy. Future studies utilizing our BCTscore model may demonstrate its broader versatility as a prognostic and predictive biomarker in all lung cancer patients undergoing atezolizumab treatment.

Data availability statement

Data are available upon reasonable request from lead investigator: J-GZ, jianguo.zhou@yahoo.com.

Ethics statement

The studies involving human participants were reviewed and approved by Zunyi Medical University. Written informed consent for participation was not required for this study in accordance with the national legislation and the institutional requirements. Written informed consent was not obtained from the individual(s) for the publication of any potentially identifiable images or data included in this article.

Author contributions

Conceptualization, J-GZ, AHW, HM, UG, S-HJ, and DS. Methodology, J-GZ, AHW, and FT. Validation, Y-ZC, BS, RF, MH, HM, UG, and J-GZ. Data curation, J-GZ, AHW, GS, S-SH, HM, SC, and UG. Writing—original draft preparation, AHW, HW, J-GZ, and HW. Writing—review and editing, UG, HM, BF, SC, DS, and MH. Visualization, J-GZ and HW. Supervision, HM, UG, J-GZ, and DS. Project administration, J-GZ, HM, UG, and RW. Funding acquisition, J-GZ, S-HJ, and AHW. All authors contributed to the article and approved the submitted version.

Funding

This research was funded by the National Natural Science Foundation of China (Grant No. 82060475), the National Natural Science Foundation of Guizhou Province (Grant Nos. [2020]1Z062, ZK2021-YB435, and ZK2022-YB632), Lian Yun Gang Shi Hui Lan Public Foundation (Grant No. HL-HS2020-92). AW Medical Company Limited received startup funding from the University Development Fund of University of Macau.

Acknowledgments

We would like to thank all of the patients, investigators, and staff involved in the FIR, BIRCH, POPLAR, and OAK studies who released and shared their data. This publication is based on research using data from data contributors, Roche, that has been made available through Vivli, Inc. (Data Request ID: 5935; Lead Investigator: J-GZ). Vivli has not contributed to or approved, and is not in any way responsible for, the contents of this publication. The present work was performed by J-GZ in partial fulfillment of the requirements for containing the degree "Dr. rer. biol. hum."

Conflict of interest

MH and UG reports collaborations with Merck Serono (advisory role, speakers' bureau, honoraria, travel expenses, and research funding), MSD (advisory role, speakers' bureau, honoraria, travel expenses, and research funding), AstraZeneca (research funding), Novartis (research funding), BMS (advisory role, honoraria, speakers' bureau), Teva (travel expenses). AHW is a founder and shareholder of AW Medical Co. Ltd.

The remaining authors declare that the research was conducted in the absence of any commercial or financial relationships that could be construed as a potential conflict of interest.

Publisher's Note

All claims expressed in this article are solely those of the authors and do not necessarily represent those of their affiliated organizations, or those of the publisher, the editors and the reviewers. Any product that may be evaluated in this article, or claim that may be made by its manufacturer, is not guaranteed or endorsed by the publisher.

Supplementary material

The Supplementary Material for this article can be found online at: https://www.frontiersin.org/articles/10.3389/fimmu.2022.961926/full#supplementary-material

References

1. Siegel RL, Miller KD, Fuchs HE, Jemal A. Cancer statistics, 2021. *CA: A Cancer J Clin* (2021) 71:7–33. doi: 10.3322/caac.21654

2. Duma N, Santana-Davila R, Molina JR. Non-small cell lung cancer: Epidemiology, screening, diagnosis, and treatment. *Mayo Clinic Proc* (2019) 94:1623–40. doi: 10.1016/j.mayocp.2019.01.013

3. Fehrenbacher L, Spira A, Ballinger M, Kowanetz M, Vansteenkiste J, Mazieres J, et al. Atezolizumab versus docetaxel for patients with previously treated non-small-cell lung cancer (POPLAR): a multicentre, open-label, phase 2 randomised controlled trial. *Lancet* (2016) 387:1837–46. doi: 10.1016/S0140-6736(16)00587-0

4. Rittmeyer A, Barlesi F, Waterkamp D, Park K, Ciardiello F, von Pawel J, et al. Atezolizumab versus docetaxel in patients with previously treated non-small-cell lung cancer (OAK): a phase 3, open-label, multicentre randomised controlled trial. *Lancet* (2017) 389:255–65. doi: 10.1016/S0140-6736(16)32517-X

5. Reck M, Rodríguez-Abreu D, Robinson AG, Hui R, Csőszi T, Fülöp A, et al. Pembrolizumab versus chemotherapy for PD-L1-Positive non-Small-Cell lung cancer. *New Engl J Med* (2016) 375:1823–33. doi: 10.1056/NEJMoa1606774

6. Carbone DP, Reck M, Paz-Ares L, Creelan B, Horn L, Steins M, et al. First-line nivolumab in stage IV or recurrent non-Small-Cell lung cancer. *N Engl J Med* (2017) 376:2415–26. doi: 10.1056/NEJMoa1613493

7. Brahmer J, Reckamp KL, Baas P, Crinò L, Eberhardt WE, Poddubskaya E, et al. Nivolumab versus docetaxel in advanced squamous-cell non-Small-Cell lung cancer. *N Engl J Med* (2015) 373:123–35. doi: 10.1056/NEJMoa1504627

8. Hecht M, Gostian AO, Eckstein M, Rutzner S, von der Grün J, Illmer T, et al. Safety and efficacy of single cycle induction treatment with cisplatin/docetaxel/durvalumab/tremelimumab in locally advanced HNSCC: first results of CheckRad-CD8. *J Immunother Cancer* (2020) 8(2):e001378. doi: 10.1136/jitc-2020-001378

9. Jamal-Hanjani M, Wilson GA, McGranahan N, Birkbak NJ, Watkins TBK, Veeriah S, et al. Tracking the evolution of non-Small-Cell lung cancer. *N Engl J Med* (2017) 376:2109–21. doi: 10.1056/NEJMoa1616288

10. Peters S, Reck M, Smit EF, Mok T, Hellmann MD. How to make the best use of immunotherapy as first-line treatment of advanced/metastatic non-small-cell lung cancer. *Ann Oncol Off J Eur Soc Med Oncol* (2019) 30:884–96. doi: 10.1093/annonc/mdz109

11. Bonaventura A, Grossi F, Carbone F, Vecchié A, Minetti S, Bardi N, et al. Serum PCSK9 levels at the second nivolumab cycle predict overall survival in elderly patients with NSCLC: a pilot study. *Cancer Immunology Immunotherapy CII* (2019) 68:1351–8. doi: 10.1007/s00262-019-02367-z

12. Anagnostou V, Forde PM, White JR, Niknafs N, Hruban C, Naidoo J, et al. Dynamics of tumor and immune responses during immune checkpoint blockade in non-small cell lung cancer. *Cancer Res* (2019) 79:1214–25. doi: 10.1158/0008-5472.CAN-18-1127

13. Thommen DS, Koelzer VH, Herzig P, Roller A, Trefny M, Dimeloe S, et al. A transcriptionally and functionally distinct PD-1(+) CD8(+) T cell pool with predictive potential in non-small-cell lung cancer treated with PD-1 blockade. *Nat Med* (2018) 24:994–1004. doi: 10.1038/s41591-018-0057-z

14. Yu H, Guan Z, Cuk K, Zhang Y, Brenner H. Circulating MicroRNA biomarkers for lung cancer detection in East Asian populations. *Cancers* (2019) 11(3):415. doi: 10.3390/cancers11030415

15. Zhou JG, Donaubauer AJ, Frey B, Becker I, Rutzner S, Eckstein M, et al. Prospective development and validation of a liquid immune profile-based signature (LIPS) to predict response of patients with recurrent/metastatic cancer to immune checkpoint inhibitors. *J Immunother Cancer* (2021) 9(2):e001845. doi: 10.1136/jitc-2020-001845

16. Valero C, Lee M, Hoen D, Weiss K, Kelly DW, Adusumilli PS, et al. Pretreatment neutrophil-to-lymphocyte ratio and mutational burden as biomarkers of tumor response to immune checkpoint inhibitors. *Nat Commun* (2021) 12:729. doi: 10.1038/s41467-021-20935-9

17. Diem S, Schmid S, Krapf M, Flatz L, Born D, Jochum W, et al. Neutrophil-to-Lymphocyte ratio (NLR) and platelet-to-Lymphocyte ratio (PLR) as prognostic markers in patients with non-small cell lung cancer (NSCLC) treated with nivolumab. *Lung Cancer (Amsterdam Netherlands)* (2017) 111:176–81. doi: 10.1016/j.lungcan.2017.07.024

18. Russo A, Russano M, Franchina T, Migliorino MR, Aprile G, Mansueto G, et al. Neutrophil-to-Lymphocyte ratio (NLR), platelet-to-Lymphocyte ratio (PLR), and outcomes with nivolumab in pretreated non-small cell lung cancer (NSCLC): A Large retrospective multicenter study. *Adv Ther* (2020) 37:1145–55. doi: 10.1007/s12325-020-01229-w

19. Spigel DR, Chaft JE, Gettinger S, Chao BH, Dirix L, Schmid P, et al. FIR: Efficacy, safety, and biomarker analysis of a phase II open-label study of atezolizumab in PD-L1–selected patients with NSCLC. *J Thorac Oncol* (2018) 13:1733–42. doi: 10.1016/j.jtho.2018.05.004

20. Peters S, Gettinger S, Johnson ML, Jänne PA, Garassino MC, Christoph D, et al. Phase II trial of atezolizumab as first-line or subsequent therapy for patients with programmed death-ligand 1–selected advanced non–Small-Cell lung cancer (BIRCH). *J Clin Oncol* (2017) 35:2781–9. doi: 10.1200/JCO.2016.71.9476

21. Button KS, Ioannidis JPA, Mokrysz C, Nosek BA, Flint J, Robinson ESJ, et al. Power failure: why small sample size undermines the reliability of neuroscience. *Nat Rev Neurosci* (2013) 14:365–76. doi: 10.1038/nrn3475

22. Polley MY, Freidlin B, Korn EL, Conley BA, Abrams JS, McShane LM. Statistical and practical considerations for clinical evaluation of predictive biomarkers. *J Natl Cancer Institute* (2013) 105:1677–83. doi: 10.1093/jnci/djt282

23. Hegde PS, Chen DS. Top 10 challenges in cancer immunotherapy. *Immunity* (2020) 52:17–35. doi: 10.1016/j.immuni.2019.12.011

24. Ugurel S, Schadendorf D, Horny K, Sucker A, Schramm S, Utikal J, et al. Elevated baseline serum PD-1 or PD-L1 predicts poor outcome of PD-1 inhibition therapy in metastatic melanoma. *Ann Oncol* (2020) 31:144–52. doi: 10.1016/j.annonc.2019.09.005

25. Alborelli I, Leonards K, Rothschild SI, Leuenberger LP, Savic Prince S, Mertz KD, et al. Tumor mutational burden assessed by targeted NGS predicts clinical benefit from immune checkpoint inhibitors in non-small cell lung cancer. *J Pathol* (2020) 250:19–29. doi: 10.1002/path.5344

26. Yu Y, Zeng D, Ou Q, Liu S, Li A, Chen Y, et al. Association of survival and immune-related biomarkers with immunotherapy in patients with non–small cell lung cancer: A meta-analysis and individual patient–level analysis. *JAMA Network Open* (2019) 2:e196879–e196879. doi: 10.1001/jamanetworkopen.2019.6879

27. Hiam-Galvez KJ, Allen BM, Spitzer MH. Systemic immunity in cancer. *Nat Rev Cancer* (2021) 21:345–59. doi: 10.1038/s41568-021-00347-z

28. Owen CN, Bai X, Quah T, Lo SN, Allayous C, Callaghan S, et al. Delayed immune-related adverse events with anti-PD-1-based immunotherapy in melanoma. *Ann Oncol* (2021) 32:917–25. doi: 10.1016/j.annonc.2021.03.204

29. Couey MA, Bell RB, Patel AA, Romba MC, Crittenden MR, Curti BD, et al. Delayed immune-related events (DIRE) after discontinuation of immunotherapy: diagnostic hazard of autoimmunity at a distance. *J ImmunoTherapy Cancer* (2019) 7:165. doi: 10.1186/s40425-019-0645-6

30. Grecian R, Whyte MKB, Walmsley SR. The role of neutrophils in cancer. *Br Med Bull* (2018) 128:5–14. doi: 10.1093/bmb/ldy029

31. Shaul ME, Fridlender ZG. Tumour-associated neutrophils in patients with cancer. *Nat Rev Clin Oncol* (2019) 16:601–20. doi: 10.1038/s41571-019-0222-4

32. Park J, Wysocki RW, Amoozgar Z, Maiorino L, Fein MR, Jorns J, et al. Cancer cells induce metastasis-supporting neutrophil extracellular DNA traps. *Sci Trans Med* (2016) 8:361ra138. doi: 10.1126/scitranslmed.aag1711

33. Wu M, Ma M, Tan Z, Zheng H, Liu X. Neutrophil: A new player in metastatic cancers. *Front Immunol* (2020) 11:2198. doi: 10.3389/fimmu.2020.565165

34. Menter DG, Tucker SC, Kopetz S, Sood AK, Crissman JD, Honn KV. Platelets and cancer: a casual or causal relationship: revisited. *Cancer Metastasis Rev* (2014) 33:231–69. doi: 10.1007/s10555-014-9498-0

35. Havel JJ, Chowell D, Chan TA. The evolving landscape of biomarkers for checkpoint inhibitor immunotherapy. *Nat Rev Cancer* (2019) 19:133–50. doi: 10.1038/s41568-019-0116-x

COPYRIGHT

© 2022 Zhou, Wong, Wang, Jin, Tan, Chen, He, Shen, Frey, Fietkau, Hecht, Carr, Wang, Shen, Schrump, Ma and Gaipl. This is an open-access article distributed under the terms of the Creative Commons Attribution License (CC BY). The use, distribution or reproduction in other forums is permitted, provided the original author(s) and the copyright owner(s) are credited and that the original publication in this journal is cited, in accordance with accepted academic practice. No use, distribution or reproduction is permitted which does not comply with these terms.

frontiers | Frontiers in Immunology

TYPE Original Research
PUBLISHED 08 September 2022
DOI 10.3389/fimmu.2022.970702

Check for updates

OPEN ACCESS

EDITED BY
Clare Y. Slaney,
Peter MacCallum Cancer Centre, Australia

REVIEWED BY
Sabita Pokhrel,
University of Akron, United States
Julien Faget,
INSERM U1194 Institut de Recherche en Cancérologie de Montpellier (IRCM), France

*CORRESPONDENCE
Chao You
YouChao_westchina@163.com
Shaoshan Hu
Shaoshanhu421@163.com
Yongzhe Li
liyongzhe18@163.com

SPECIALTY SECTION
This article was submitted to Cancer Immunity and Immunotherapy, a section of the journal Frontiers in Immunology

RECEIVED 16 June 2022
ACCEPTED 16 August 2022
PUBLISHED 08 September 2022

CITATION
Ji H, Liu Z, Wang N, Jin J, Zhang J, Dong J, Wang F, Yan X, Gong Q, Zhao H, Sun H, Li Y, Hu S and You C (2022) Integrated genomic, transcriptomic, and epigenetic analyses identify a leukotriene synthesis-related M2 macrophage gene signature that predicts prognosis and treatment vulnerability in gliomas. *Front. Immunol.* 13:970702. doi: 10.3389/fimmu.2022.970702

COPYRIGHT
© 2022 Ji, Liu, Wang, Jin, Zhang, Dong, Wang, Yan, Gong, Zhao, Sun, Li, Hu and You. This is an open-access article distributed under the terms of the Creative Commons Attribution License (CC BY). The use, distribution or reproduction in other forums is permitted, provided the original author(s) and the copyright owner(s) are credited and that the original publication in this journal is cited, in accordance with accepted academic practice. No use, distribution or reproduction is permitted which does not comply with these terms.

Integrated genomic, transcriptomic, and epigenetic analyses identify a leukotriene synthesis-related M2 macrophage gene signature that predicts prognosis and treatment vulnerability in gliomas

Hang Ji[1,2,3], Zhihui Liu[2,3], Nan Wang[2,3], Jiaqi Jin[2,3], Jiheng Zhang[2,3], Jiawei Dong[2,3], Fang Wang[2,3], Xiuwei Yan[2,3], Qin Gong[4], Hongtao Zhao[2,3], Haogeng Sun[1], Yongzhe Li[3]*, Shaoshan Hu[2,3]* and Chao You[1]*

[1]Department of Neurosurgery, West China Hospital, Sichuan University, Chengdu, China, [2]Cancer Center, Department of Neurosurgery, Zhejiang Provincial People's Hospital, Affiliated People's Hospital, Hangzhou Medical College, Hangzhou, China, [3]Department of Neurosurgery, Second Affiliated Hospital of Harbin Medical University, Harbin, China, [4]School of Life Sciences, Nanjing University, Nanjing, China

The pathological implications of tumor-associated macrophages in the glioma microenvironment have been highlighted, while there lacks a gene signature to characterize the functional status and clinical implications of these cells. Comprehensive bioinformatics approaches were employed to develop an M2 macrophage-associated gene signature at bulk-tumor and single-cell levels and explore immunological and metabolic features. Consequently, the PI3K pathway and fatty acid metabolism were correlated with the M2 fraction. Further distilling the pathway members resulted in a leukotriene synthesis-related gene signature (Macro index), including PIK3R5, PIK3R6, ALOX5, ALOX5AP, and ALOX15B, that was primarily expressed by monocytes/macrophages. Increased Macro index predicted IL13-induced macrophages, and was associated with T-cell dysfunction at both transcriptional and epigenetic levels and predicted an unfavorable outcome. Besides, the Macro index was proportional with PAI1 at the protein level, with high levels of the latter suggesting a decreased progression-free interval of glioblastoma. Notably, the monocytes/macrophages in the glioma environment contribute to the expression of immune checkpoints and the Macro index predicts glioma responsiveness to anti-PD1 treatment. Together, our study proposed a leukotriene synthesis-related M2 macrophage gene signature, which may

provide insights into the role of these cells in the glioma microenvironment and facilitate individually tailored therapeutic strategies for the disease.

KEYWORDS

lower-grade glioma, glioblastoma, PI3K/Akt signaling pathway, leukotrienes, M2 macrophage, tumor microenvironment

Introduction

Gliomas represent the most common types of brain malignancy that are characterized by high morbidity and mortality. This group of heterogeneous tumors accounts for approximately 80% of primary brain malignancies (1–3), and includes lower-grade glioma (LGG) that comprising WHO II and III diffuse low grade glioma and intermediate grade glioma and WHO IV GBM with some differences in aetiology, histology, and molecular underpinnings (1, 4, 5). Research achievements in gliomas culminate in the proposal of classification schemes and molecular biomarkers with prognostic and therapeutic implications. Histologically, gliomas are classified as astrocytomas, oligodendrogliomas, and mixed oligodendrogliomas based on the morphological characteristics of the tumor cells (1). The addition of anaplasia features (mitotic activity, microvascular proliferation, and necrosis) led to the WHO tumor grade for glioma which is indicative of malignant degrees (6). At the molecular pathogenesis level, the status of isocitrate dehydrogenase (IDH) gene mutation and chromosome arm 1p19q deletion defines three types of invasive gliomas: IDH-mutant with 1p19q co-deleted, IDH mutant with 1p19q non-co-deleted, and IDH wild-type glioma, greatly advancing our knowledge of the etiology (1, 7, 8). In addition, transcriptome subtyping of IDH wild-type glioblastoma (GBM), including proneuronal, mesenchymal and classical, delineated an insightful theoretical basis for the evolution of GBM subtypes and provided vital evidence that NF1expressing macrophage/macroglia facilitates the transformation of GBM subtype towards worse (9, 10). Nevertheless, glioma, especially malignant glioma, remains treatment-resistance (11). The mainstay of treatments, including invasive surgery combined with radiotherapy and alkylating agents, as well as newly thriving tumor treating fields (TTF), are far from achieving satisfactory improvements for patients with malignant glioma. Immune checkpoint blockade (ICB) therapy, which is a landmark in several types of tumors, is still dismally effective in the treatment of GBM (12–14). Therefore, there remains an urgent need to explore key molecular mechanisms in the pathological process of glioma and to develop new molecular biomarkers for individually tailored strategies.

The tumor microenvironment (TME) instigated by tumor cells is a complex, active ecosystem in which tumor-associated macrophages (TAMs) have content and functional superiority over other non-tumor cells (15, 16). TAMs in glioma TME indicate two types of cells of different origins: intrinsic microglia and blood-derived monocytes/macrophages, with functional consistency when interacting with glioma cells (17–19). The TAMs in TME are dogmatically defined as pro-tumoral M2 phenotypes and anti-tumoral M1 phenotypes, and this dichotomy is overly simplistic and a much broader repertoire of the polarization of macrophages lays the foundation of difficulties in designing therapies targeting M2 macrophages (20, 21). Transcriptome-based studies further defined the M2 phenotype at the gene expression level and identified the expression and functional characteristics of macrophage polarization mediated by various stimulators (22, 23). However, due to the immunological specificity of the central nervous system, the phenotype of TAMs in glioma TME remains loosely defined. Overall, TAMs play a paramount role in promoting angiogenesis, tumor invasion, and impeding antitumor immunity, the latter being closely related to the local chronic inflammation mediated by eicosanoid derivatives (15, 24, 25). TAMs derived and differentiated from blood precursor cells have theoretically a complete set of eicosanoid-metabolizing enzymes, and previous studies have emphasized the role of prostaglandins such as PGE_2 in remodeling the TME, while the LOX pathway and leukotrienes are overlooked. Moreover, the role of the oncogenic PI3K/Akt signaling pathway, one of the hallmarks of GBM, in the regulation and integration of tumor metabolism, and thus in promoting tumor development, is gaining increasing attention (26, 27). In addition to glycolysis, the interaction of PI3K/Akt signaling with eicosanoid metabolism in TAMs is less understood, and exploring its pathological and clinical significance and association with TAMs phenotype may lead to novel therapeutic targets.

In this study, we explored the signaling pathways and gene expression associated with the fraction and phenotype of TAMs in glioma TME through correlation and network analysis based on multi-omics data from multiple glioma cohorts. We identified a gene signature linking to TAMs (Macro index) and validated their association with the functional status of TAMs, immune function, prognosis, and immunotherapy

efficacy at the bulk-tumor and single-cell levels. These results may open attractive avenues for designing novel glioma therapy since leukotriene synthesis plays a vital role in glioma TME, and provide an effective mRNA metric for characterizing alternatively activated TAMs for glioma.

Materials and methods

Sample collection

Multiple glioma datasets from WHO grade II to IV were included in this study. Of these, the integrated mRNA expression profile (n = 702), single nucleotide polymorphisms (SNP) (n = 825), copy number variation (CNV) (n = 1122), and methylation (n = 685) profiles were retrieved from the UCSC Xena portal, and clinical phenotypes, including transcriptome subtype, were summarized by Ceccarelli et al. (28). Other glioma expression profiles with corresponding demographics, including CGGA693, CGGA325, CGGA301, Ducray, Gravendeel, Joo, Nutt, and Kamoun were retrieved from the CGGA and the GlioVis data portal (29–32). Bulk-tumor mRNA sequencing data were TPM normalized for further analysis. The single-cell transcriptome profile was retrieved from the TISCH database (Glioma GSE131928 10X) (33, 34).

Consensus clustering and sample selection

Three *in silico* algorithms were performed to infer the immune infiltration, including CIBERSORT, QUANTISEQ, and XCELL (35–38). The CIBERSORT-derived immune infiltration fraction was used for consensus clustering. Samples with a p-value > 0.05 and cells with a fraction of 0 in over half of the samples were excluded. Consensus clustering was employed to stratify the immune infiltration fraction matrix (39). The maximum number of clusters was set to 6, the clustering algorithm was 'PAM', and the distance was set to 'Pearson'. The optimal number of clusters was determined by the proportion of ambiguous clusters (PAC) method. Identification of core members of each cluster was based on the R packages 'cluster' and 'vegan'. Samples with silhouette width ranked top 75% were included.

Identifying signaling pathways and gene signature associated with M2 fractions

Gene sets of the HALLMARK (n = 50), BIOCARTA (n = 292), and PID (n = 196) were retrieved from the MSigDB database (v7.5.1), and the GSEA software (v4.2.3) and ssGSEA algorithms were employed to assess the pathway activity (40–42). The correlation between signaling pathways and gene expression with M2 fraction was evaluated by calculating the regression coefficient using a multivariate regression model. Logistic regression analysis was performed to evaluate the correlation of SNP and somatic copy number alteration (SCNA) with the M2 fraction. The vif value of each independent variable was adjusted to within 5 using the R function 'step' to avoid the potential interactions between independent variables. The differentially expressed genes (DEGs) were calculated using the R packages 'limma' and 'edgeR' (43, 44). Functional enrichment analysis was performed using the web tool Metascape (45, 46). We defined the Macro index as the average log2 transformed TPM value of PIK3R5, PIK3R6, ALOX5, ALOX5AP, and ALOX15B. The ranked gene list for GSEA was sorted according to logFC values or Spearman rho of genes of interest with Macro index.

scRNA-seq data analysis

The expression of immune checkpoints at the single-cell scape in multiple datasets was integrated using the webtool TISCH. The R package 'Seurat' was employed for the management of sample quality control, normalization, data dimensionality reduction, clustering, and re-clustering of the scRNA-seq expression profile (GSE131928 10X) (47). Identification of the cell identity was based on the CellMarker database and signature genes summarized by Neftel et al. (48). The expression profile of the Mono/Macro subcluster was extracted, and Mono/Macro cells were split into Macro index-high and -low groups. DEGs (Macro index-high vs. -low) were calculated using 'Seurat', and transcription factor enrichment analysis was performed using the web tool Metascape based on the TRRUST database (49). Functional enrichment analysis was performed using Cytoscape plugins 'Bingo' and 'EnrichmentMap'. To evaluate the association between the Macro index and function state of TAMs, the top and bottom 150 DEGs of macrophages (Supplementary File 1) under different culture conditions were used as the corresponding gene signatures, including glucocorticoids (GC), IL-10, IL-13, IL-4, and PGE_2 (23).

Evaluating immunological characteristics and potential ICI responsiveness

The anti-tumor immune response was conceptually divided into 7 stepwise events, including step1. Cancer antigen releasing, step2. Cancer antigen presentation, step3. T cell priming and activation, step4. Trafficking of immune cells to tumor, step5. Infiltration of immune cells to tumor, step6. Tumor call recognition, and step7. Tumor cell killing (50). The activity of each stepwise event was assessed using the webtool TIP. Macrophage functional status gene signature was defined as the top 150 up- or down-regulated genes in macrophages

cultured under specific conditions for 72h (Supplementary File 1). T cell dysfunction gene signatures were generated based on the shRNA screen and have been summarized by Jiang et al. (51). Positive hit genes were defined as the upregulated genes and negative hit genes were the downregulated genes. The Spearman rho between Macro index and positive or negative hit genes were used as input of ROC analysis for evaluating the concordance of Macro index with macrophage functional status and T-cell dysfunction. Besides, sample responsiveness to immune checkpoint inhibitors (ICI) was predicted using the TIDE algorithm (51). The Submap algorithm was also employed to classify the sensitivity of glioma samples to ICI treatment, as referenced by a cutaneous melanoma cohort receiving PD-1 and CTLA4 inhibitors (52, 53). Another uroepithelial tumor cohort with a corresponding response to PD-L1 inhibitors was introduced to this study (54). Samples were split into Macro index-high and -low groups following the above methods. The composition of patients with progressive disease (PD), stable disease (SD), partial response (PR), and complete response (CR) included in the two groups was compared.

Statistics

All statistics were performed using R software (v4.1.1). Log-rank tests and the Cox-ph model were used to classify survival differences. Two-tailed Wilcoxon test was employed to compare the difference in the immune infiltration fraction, ssGSEA scores of signaling pathways, and gene expression. The correlation between gene expression, mutation, or SCNA with M2 fraction was assessed using constructing multivariate and logistic regression models or Spearman correlation tests. In the regression analysis, two or more significant regression coefficients with the same positive or negative sign were considered statistically significant. Fisher's exact test was employed to compare the composition ratios. In the absence of a specific statement, a p-value < 0.05 was considered significant.

Results

Combined M2 macrophage fraction and histology defined three groups of gliomas

First, we re-clustered LGG and GBM samples based on M2 fractions estimated by CIBERSORT, and two clusters were identified by the Consensus cluster (Figures 1A, S1A-B). The cluster with significantly increased M2 macrophage fraction was defined as cluster 1, and the other cluster 2. Ranking the silhouette widths of samples in descending order, the top 75% of samples were selected from each cluster (cluster 1, n = 283; cluster 2, n = 171) for further analysis (Figure 1B). Cluster 1 of the TCGA cohort is comprised of 132 GBM and 151 LGG, which differ significantly in pathogenesis. Thereafter, cluster 1 was further divided into two subgroups, namely Macro1 (GBM) and Macro2 (LGG). On this basis, the TCGA glioma samples were split into three subgroups (Macro1, n = 132, GBM; Macro2, n = 151, LGG; and Macro3, n = 171, LGG), with Macro1 and Macro2 containing comparable M2 macrophages, and Macro3 the least (Figures 1C, S1C). Following the same procedure, we identified cluster 1 and cluster 2 in the Rembrandt and CGGA693 cohorts. Thus, the GBM samples in cluster 1, the LGG in cluster 1, and the LGG in cluster 2 were defined as Macro 1, Macro 2, and Macro 3, respectively (Supplementary File 2).

The clinical features between groups were exhibited (Figure 1D and Table 1). The transition of transcriptome subtypes from Classical (CL) and Mesenchymal (ME) dominance of Macro1 to Proneural (PN) and Neural (NE) dominance of Macro3 was found. Although Macro2 and Macro3 were both LGG, Macro2 had an increased proportion of WHO grade III tumors (58.94%, fisher's exact p = 0.00004) (Table 1). As expected, Macro1, Macro2, and Macro3 differed significantly in OS and PFI, where Macro1 had the most unfavorable prognosis (Figures 1E, S1D).

Signaling pathways correlated with M2 fractions

Next, we explored the signaling pathways affecting the M2 fraction. The gene expression profiles were converted into the HALLMARK, BIOCARTA, and PID signaling pathway matrices using the ssGSEA algorithm. Consequently, the FA metabolism, PI3KCI pathway, and integrin2 pathways were significantly correlated with the fraction of M2 macrophage in Macro1 and Macro3 (Figure 2A). Consistently, Macro1 had increased ssGSEA scores of PI3K signaling pathway and FA metabolism than Macro3 (Figure 2B). Besides, samples were also split into high, median, and low groups based on the M2 fraction, and the ssGSEA scores of the PI3K pathway and FA metabolism were increased in the macrophage-high group in Macro1 (Figure S2A), corroborating an association between the PI3K pathway and FA metabolism with the M2 macrophage. To further demonstrated the correlation between the PI3K pathway and M2 macrophage, members of the PI3K pathway were collected by massive literature search (Supplementary File 3). The mutation frequency of PTEN, PIK3R1, PIK3CA, and EGFR differed significantly between groups (Fisher's exact test $p < 0.0001$), and the mutation of PTEN and EGFR was correlated with M2 fraction (Figures S2B, S2C). As expected, the frequency of SCNA in EGFR and PTEN decreased from Macro1 to Macro3 (Figure S2D), in line with the pro-tumoral role of dysregulated PI3K pathway. We systemically screened genes with significant

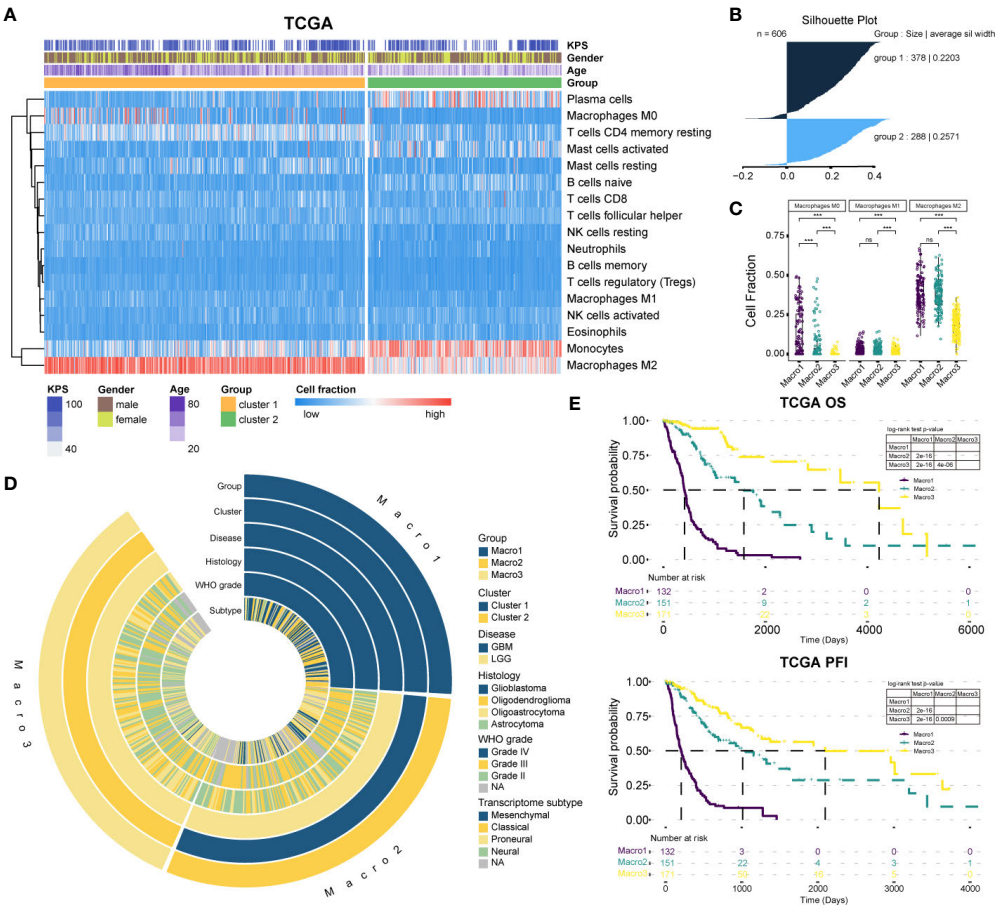

FIGURE 1
The classification of gliomas. **(A)** The abundance of estimated immune infiltration of glioma clusters. Five types of cells including dendritic cells activated, dendritic cells resting, T cells CD4 memory activated, T cells CD4 naïve, and T cells gamma delta were excluded for low content. **(B)** The silhouette width for the selection of core samples of each cluster. **(C)** Comparison of the fraction of macrophages between glioma groups. **(D)** Association of the glioma groups with prevalent clinicopathological biomarkers. **(E)** The survival differences between glioma groups. ***p < 0.001. ns, non significant.

differences in SCNA frequency between groups (Fisher's exact $p < 0.05$) and exhibited the association between SCNA and M2 fraction (Figure S2E). For example, the M2 fraction was positively correlated with copy number gain of EGFR, AKT2, and PIK3CA and copy number loss of PTEN, AKT1, and ERBB2, while negatively associated with copy number loss of AKT2 and MTOR. The association between gene SCNA, expression, and their correlation with M2 fraction was summarized (Figure 2C). We found that copy number gain events that were positively associated with the M2 fraction tended to enrich in Macro1, while copy number loss events negatively associated with M2 tended to enrich in Macro3, indicating differential molecular mechanisms associated with the M2 fraction. In terms of gene expression, PIK3R5 was positively correlated with the M2 fraction across groups and AKT1 was negatively correlated with M2 in Macro1 and Macro3 (Figure 2D). Besides, the association between several genes and M2 was group-specific, such as PIK3R3, PIK3C2A, ERBB2, and PIK3CA.

Rewired FA metabolism also plays a vital role in remodeling the TME, which has been underestimated previously. We collected and exhibited the expression of genes involved in the *de novo* FA synthesis, FA uptake, and eicosanoid metabolism between groups (Supplementary File 3). As a result, Macro1 had significantly downregulated genes involved in the *de novo* FA synthesis, particularly ACACA, FASN, SCD, and SREBF1/2, and upregulated genes involved in FA uptake, such as CD36, SLC27A3, FABP5, and FABP7 (Figures S3A, S3B), while the opposite was true for Macro3, possibly indicating the heterogenous FA sources between glioma groups. Since eicosanoid metabolism as a branch of FA metabolism is involved in the production of many inflammatory mediators,

10.3389/fimmu.2022.970702

TABLE 1 Comparison of clinical features between subtypes.

Term	Macro1	Macro2	Macro3	P value
Cohort		**TCGA**		
Age	59.28 (± 14.02)	45.95 (± 13.47)	40.11 (± 12.57)	< 2.2E-16
Gender				
Male	88 (66.67%)	85 (56.29%)	98 (57.31%)	
Female	44 (33.33%)	66 (43.71%)	73 (42.69%)	0.15
Histology				
Astrocytoma		61 (40.40%)	44 (25.73%)	
Oligoastrocytoma		33 (21.85%)	55 (32.16%)	
Oligodendroglioma		42 (27.81%)	58 (33.92%)	
Glioblastoma	132 (100%)			0.0097[a]
WHO grade				
WHO II		47 (31.13%)	93 (54.39%)	
WHO III		89 (58.94%)	64 (37.43%)	
WHO IV	132 (100%)			3.732E-05[a]
Transcriptome subtype				
Classic	40 (30.30%)	21 (13.91%)	2 (1.17%)	
Neural	6 (4.55%)	12 (7.95%)	58 (33.92%)	
Proneural	16 (12.12%)	49 (32.45%)	70 (40.94%)	
Mesenchymal	57 (43.18%)	20 (13.25%)	2 (1.17%)	< 2.2E-16
Cohort		**Rembrandt**		
Age	55-59	40-44	35-39	
Gender				
Male	62 (54.39%)	36 (59.02%)	41 (50%)	
Female	37 (32.46%)	12 (19.67%)	32 (39.02%)	0.1116
Histology				
Astrocytoma		23 (37.70%)	12 (14.63%)	
Oligodendroglioma		12 (19.67%)	31 (37.80%)	
Mixed		2 (3.28%)	1 (1.22%)	
Glioblastoma	114 (100%)			0.001111[a]
WHO grade				
WHO II		23 (37.70%)	46 (56.10%)	
WHO III		30 (49.18%)	22 (26.83%)	
WHO IV	114 (100%)			0.009657[a]
Cohort		**CGGA693**		
Age	48.39 (± 13.49)	38.26 (± 10.13)	40.11 (± 9.25)	2.2E-16
Gender				
Male	58 (61.70%)	64 (60.38%)	21 (58.33%)	
Female	36 (38.30%)	42 (39.62%)	15 (41.67%)	0.8638
Histology				
Astrocytoma		34 (32.08%)	10 (27.78%)	
Anaplastic astrocytoma		53 (50%)	12 (33.33%)	
Oligodendroglioma		4 (3.77%)	1 (2.78%)	
Anaplastic oligodendroglioma		13 (12.26%)	12 (33.33%)	
Anaplastic oligoastrocytoma		2 (1.87%)	1 (2.78%)	
Glioblastoma	94 (100%)			0.05901[a]
WHO grade				
WHO II		38 (35.85%)	11 (30.56%)	
WHO III		68 (64.15%)	25 (69.44%)	
WHO IV	94 (100%)			0.6858[a]

[a]Comparison between Macro2 and Macro3.

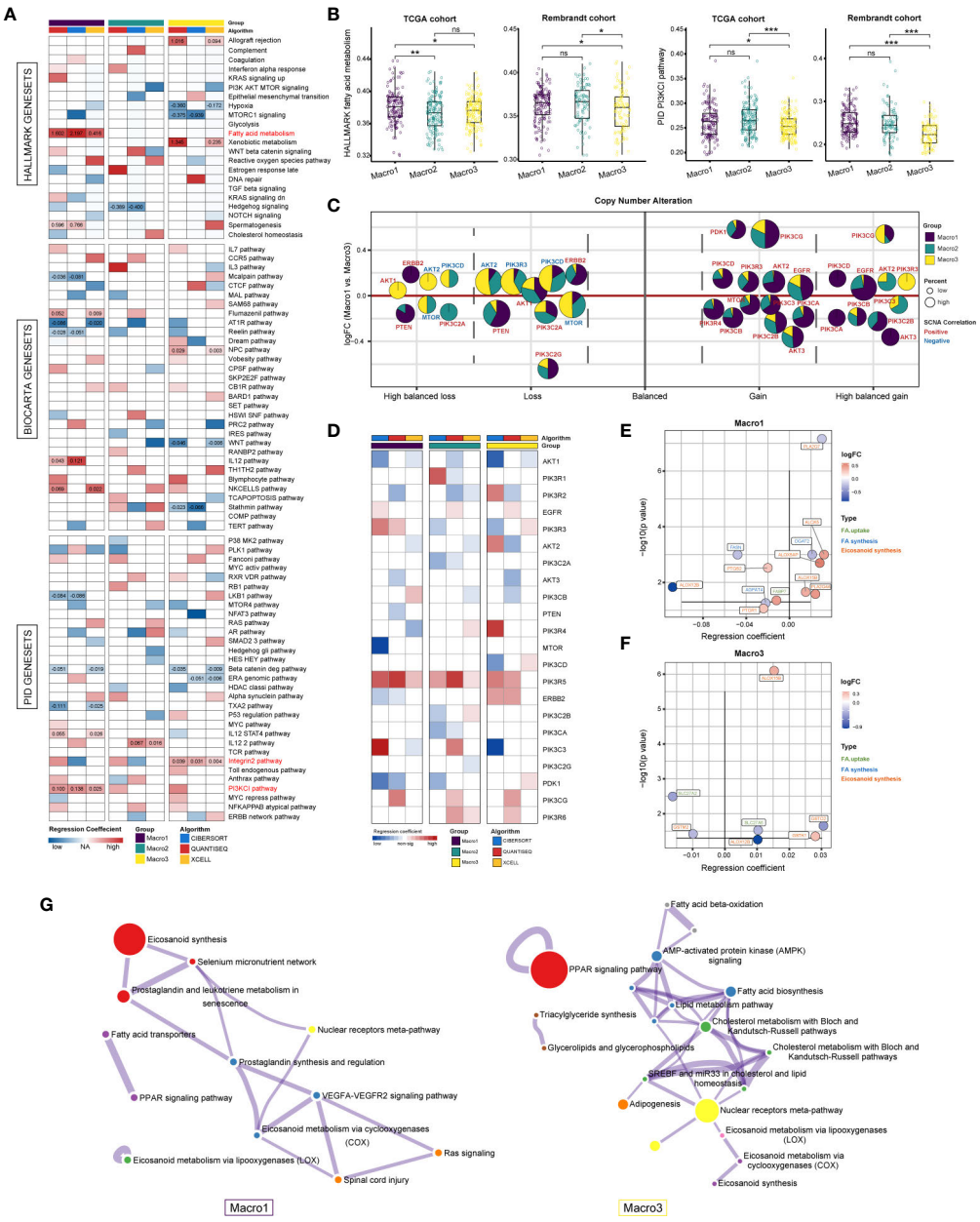

FIGURE 2
Resolving signaling pathways correlated with M2 fraction using multivariate regression analysis. **(A)** Correlation between M2 fractions and the 538 HALLMARK, BIOCARTA, and PID signaling pathways. Regression coefficients that were significant in at least two independent algorithms were marked. **(B)** Comparison of the ssGSEA score of the PID PI3KCI pathway and HALLMARK FA metabolism between groups. **(C)** Evaluation of the correlation between genes with significant copy number variants in the PI3K pathway and M2 fraction based on logistic regression. The colors represent the regression coefficients between a certain type of SCNA of a gene and the M2 fraction, with red being positive and blue being negative. The size of the bubble represents the frequency of SCNA. The area of the sector indicates the distribution of this type of SCNA of a gene in each group. **(D)** Assessing the correlation between the mRNA expression of PI3K pathway members and M2 fraction using multivariate linear regression. We determined results with significant and consistently positive and negative regression coefficients in two or more algorithms were statistically significant. **(E, F)** The correlation between FA metabolism genes and M2 fraction in Macro1 and Macro3. Colors represent the log2FC (Macro1 vs. Macro3). **(G)** Functional enrichment analysis of FA metabolic genes that are significantly associated with the M2 fraction in each group. *p < 0.05, **p < 0.01, ***p < 0.001. ns, non significant.

we also exhibited the differences in eicosanoid metabolic-related gene expression between groups (Figure S3C). The expression of the PLA family, which generates AA through hydrolysis, differs between groups. For example, the expression of PLA2G4A, PLA2G2A, and PLA2G5 was significantly increased in Macro1, while the opposite was true for PLA2G6, PLA2G12A, and PLA2G4C. In terms of FA metabolic genes significantly associated with M2 fractions, a comparable proportion was found in genes involved in eicosanoid metabolism between groups (Macro1 8/12, Macro2 8/11, and Macro3 6/8), higher than that of FA synthesis and uptake (Figure S3D), suggesting that the eicosanoids metabolism was indeed related to the abundance of TAMs. Notably, we exhibited the types of these genes, their expression, and their regression coefficients with the M2 fraction. In Macro1, genes including ALOX5, ALOX5AP, and ALOX15B were upregulated and positively correlated with M2, and ALOX12B seemed to be a negative regulator that has been downregulated (Figure 2E). Interestingly, PTGS2, an inducible COX enzyme, was negatively correlated with the M2 fraction. There were few intersections of genes correlated with M2 in Macro1 and Macro3, except for ALOX15B/12B (Figure 2F), possibly indicating a functional transition of M2 macrophages in different classes of gliomas, with macrophages relying on ALOX15B for leukotriene synthesis in Macro3, which represents the lower grade, and ALOX15B and ALOX5/ALOX5AP in the higher grade. From a holistic perspective, functional enrichment analysis found that FA-metabolism associated genes upregulated in Macro1 were significantly enriched in leukotriene (ALOX5/ALOX15B/DPEP1/PTGR1) and prostaglandin (PLA2G4A/PLA2G5/PTGS1/PTGS2/PTGR1) synthesis, while in Macro3, only PTGDS, PLA2G6, and PNPLA3 were involved in the eicosanoid metabolism (Figure 2G), suggesting that genes involved in leukotriene synthesis were remarkably altered between low- and high-grade glioma.

The intersection of PI3K signaling and FA metabolism defines M2 and leukotriene synthesis-related gene signature

Several studies revealed the interaction between the PI3K signaling and FA metabolism (24, 25), we, therefore, addressed such association in glioma. The correlation of PI3K pathway members with FA metabolism-related genes was calculated using a multivariate linear regression model and genes that were significantly associated with M2 fraction were of particular interest. Genes significantly correlated with M2-related eicosanoid metabolism genes were mainly those encoding different subunits of PI3K ($p < 0.0001$) (Figure 3A). For instance, PIK3R5 was positively correlated with leukotriene metabolic genes like ALOX5, ALOX5AP, and ALOX15B. In addition to leukotriene metabolic genes, PDK1 was also correlated with PTGS2, which was shown to be negatively correlated with the M2 fraction. As Macro2 was a subset of LGG with increased M2 fraction when corrected for WHO grade, histology, and transcriptome subtype, the increased expression of PIK3R6 remained significant (Figures S4A-C). Besides, Spearman analysis showed a sparse association of PTGS2 and ALOX12B with PIK3R5/6, ALOX5/5AP/15B (Figure 3B). Therefore, we proposed that PIK3R5/6, ALOX5/5AP/15B comprised of an M2-related gene network associated with leukotriene metabolism (Figure S5A). In evaluating the association of these genes with FA metabolism pathways, we found that PIK3R6 was correlated with only a few pathways, including AA and glycerol metabolism, in Macro1, but with most FA metabolism pathways in Macro3 (Figures 3C-E), suggesting different levels of involvement of PIK3R6 in FA metabolism between groups. The opposite was seen in the correlation of ALOX15B with FA metabolism and immune pathways (Figures 3C-E, S5B-E). Thereafter, we defined the average expression of PIK3R5/6, ALOX5/5AP/15B as an mRNA metric (Macro index), which was significantly associated with the M2 fraction (Figure S5F). GSEA found that inflammation-related signaling pathways such as inflammatory response, allograft rejection, and TNFA signaling were correlated with Macro index across groups (Figure 3F), while the correlation between signaling pathways such as angiogenesis, TGFB, glycolysis, etc. and Macro index was differentiated. Together, these results proposed an M2 and leukotriene synthesis-associated gene signature, and the differential regulation mechanisms for this network among glioma groups.

Differences in anti-tumor immune responses in glioma groups and the association with Macro index

The anti-tumor immune response is critical in influencing tumor outcome and has been artificially defined as several step-wise events for quantitative assessment. In general, Macro1 scored higher in the recruitment of immune cells but was less active in T-cell activation and tumor cell killing than Macro2 and Macro3 (Figure S6A). We enumerated the expression and methylation of genes involved in T-cell activation (step3), immune cell infiltration into tumors (step5), and tumor cell killing (step7), and found that most of the differences in gene expression converged on their methylation levels (Figure 4A). However, there were exceptions, for example, the methylation levels of EZH2 did not differ significantly between groups and its differential expression may be regulated by factors associated with the Macro index (Figure S6B). The overall expression of genes that play either positive or negative roles in steps 3, 5, and 7 of the anti-tumor immune response were significantly increased in Macro1 (Figure 4B), suggesting that the activated immune response in Macro1 was accompanied by enhanced

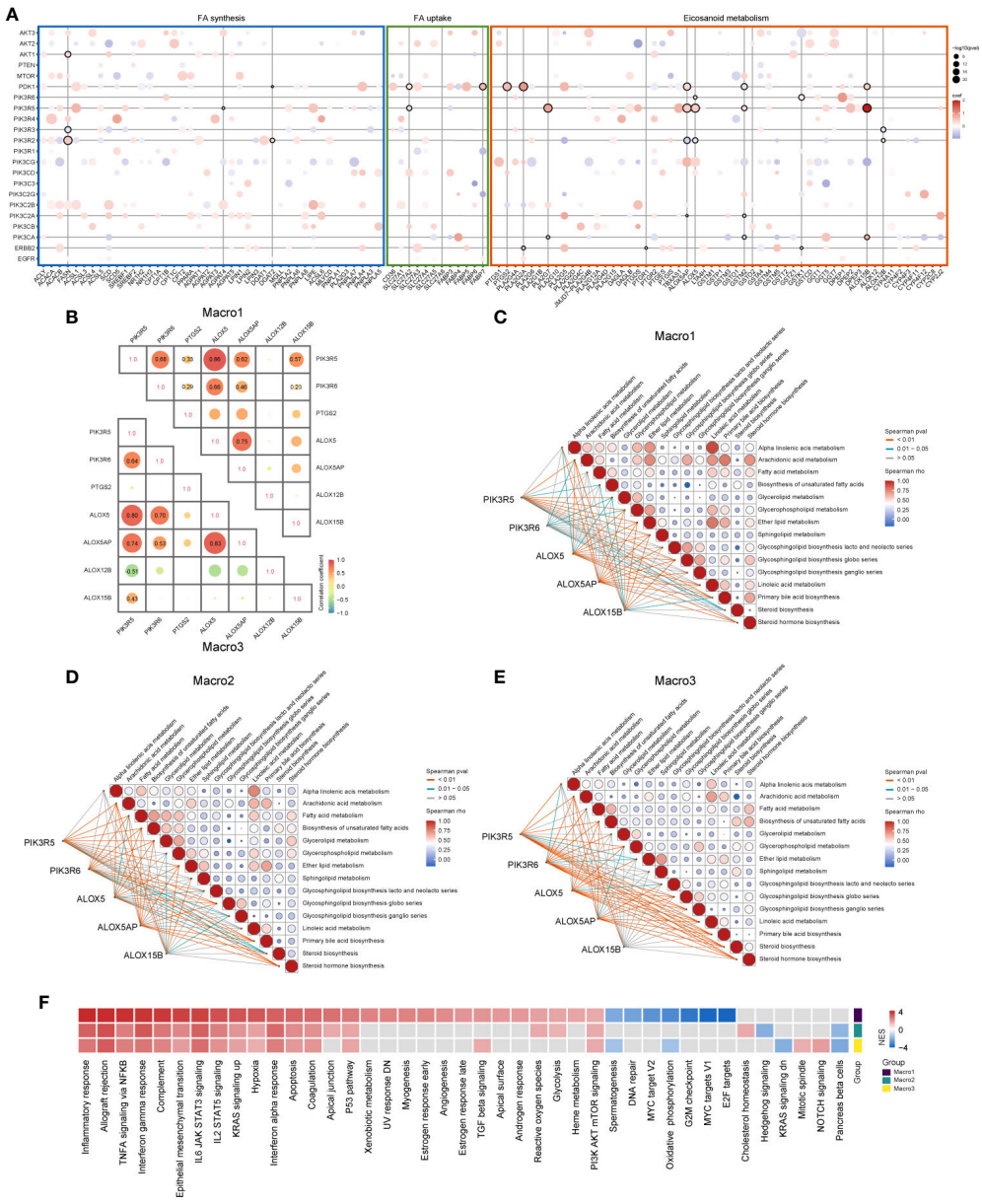

FIGURE 3
Association of PI3K signaling pathway members with FA metabolic genes that significantly correlated with M2 fraction. **(A)** The correlation between PI3K pathway members and FA metabolic genes was evaluated using a multivariate regression model at the significance level of $p < 0.0001$. Bubbles indicate that the regression coefficients of the two are significant, red indicates positive regression coefficients and blue negative. Horizontal or vertical lines mark PI3K members or FA metabolic genes that are significantly correlated with the M2 fraction. **(B)** Spearman correlation analysis of candidate genes that were likely to form a gene network. **(C-E)** Correlation of PIK3R5/6, ALOX5/5AP/15B, and KEGG lipid metabolism-related signaling pathways in each group. **(F)** GSEA analysis determines signaling pathways that affect the M2-related gene network based on the HALLMARK gene sets. The input pre-ranked gene list is a ranked list of genes determined by the Spearman rho of all human genes with the Macro index.

inhibitory mechanisms. The overall methylation level of the genes between groups was opposite to their expression level (Figure 4C), suggesting a role for methylation in regulating the immune response, and the Macro index was significantly negatively correlated with gene methylation level (Figure 4D). Similarities were found between the association of Macro index with immune responses in each group, positively correlating with immune cell recruitment but negatively correlating with T cell activation and tumor cell killing (Figures S6C, D), suggesting an active but 'ineffective' immune response.

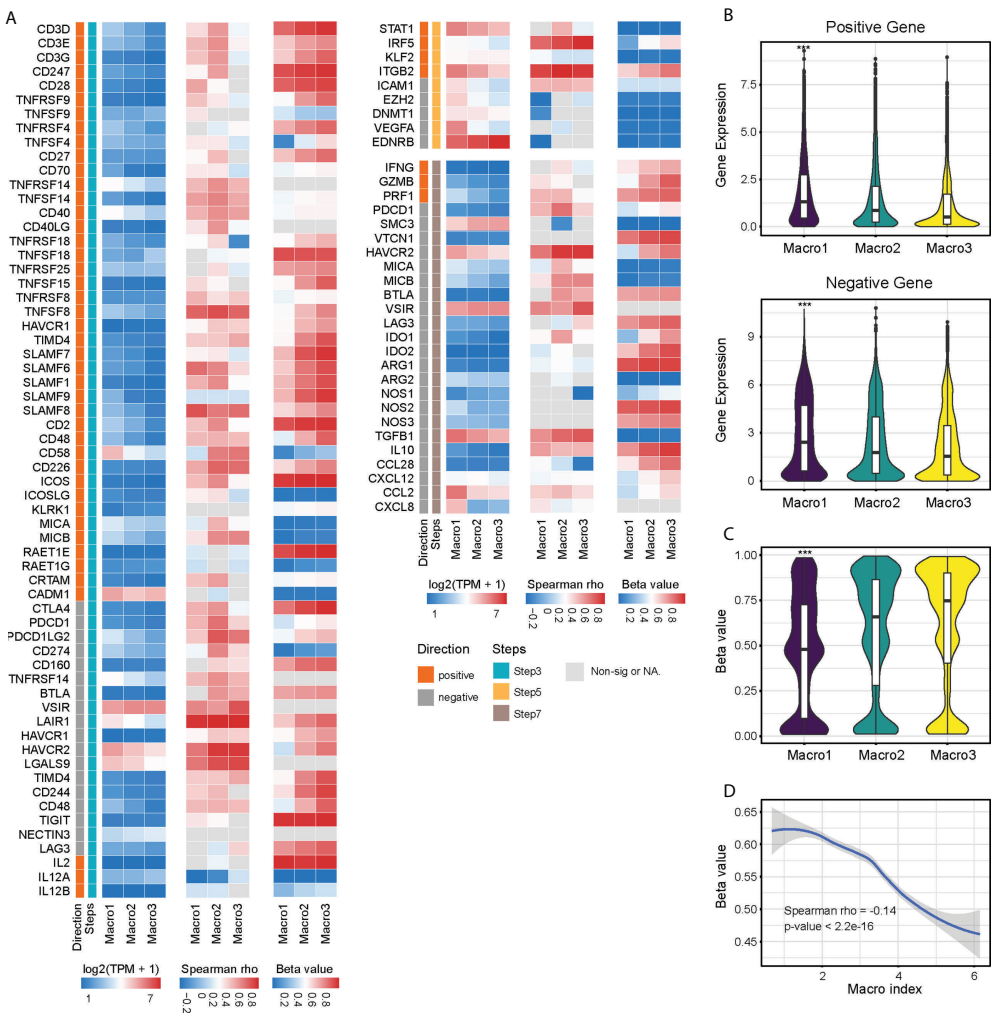

FIGURE 4
Immunological characteristics associated with Macro index-based groups. **(A)** Expression, methylation of immune-related genes and correlation with Macro index. Genes assigned to the TIP step3 (T cell priming and activation), step5 (infiltration of immune cells into cancer), and step7 (cancer cell killing) were included. **(B)** The overall expression of immune-activating and immune-suppressing genes in each group. **(C)** The overall methylation levels of these genes in each group. **(D)** Spearman correlation analysis of the Macro index with the overall gene methylation level. ***p < 0.001.

The association between the Macro index and the functional state of TAMs

Since the Macro index correlated with the M2 fraction, we proceeded to interrogate its association with the functional status of TAMs. TAMs were loosely defined as M1 and M2 phenotypes, and recent studies have shown the complexity of functional states of macrophages induced and activated by different stimulators (23). We defined the positive and negative hit genes as the top and bottom 150 DEGs of macrophages under each condition (Supplementary File 1) and determined whether the Macro index predicted positive or negative hit genes. We found that the macro index performed better in predicting macrophages induced by IL13, IL4, and HDL, with similar efficiency between glioma groups (Figures 5A-D). From a single-cell perspective, genes comprised of the Macro index were mainly expressed by monocytes and macrophages (Mono/Macro) in glioma (Figure S7A). We extracted the expression profile of monocytes/macrophages and grouped the monocytes/macrophages according to the median Macro index. As a result, the Macro index-high group was mainly transcriptionally regulated by NF-KB and STAT3 (Figures S7B, C), corroborating that STAT3 induces the immunosuppressive phenotype of glioma TAMs

10.3389/fimmu.2022.970702

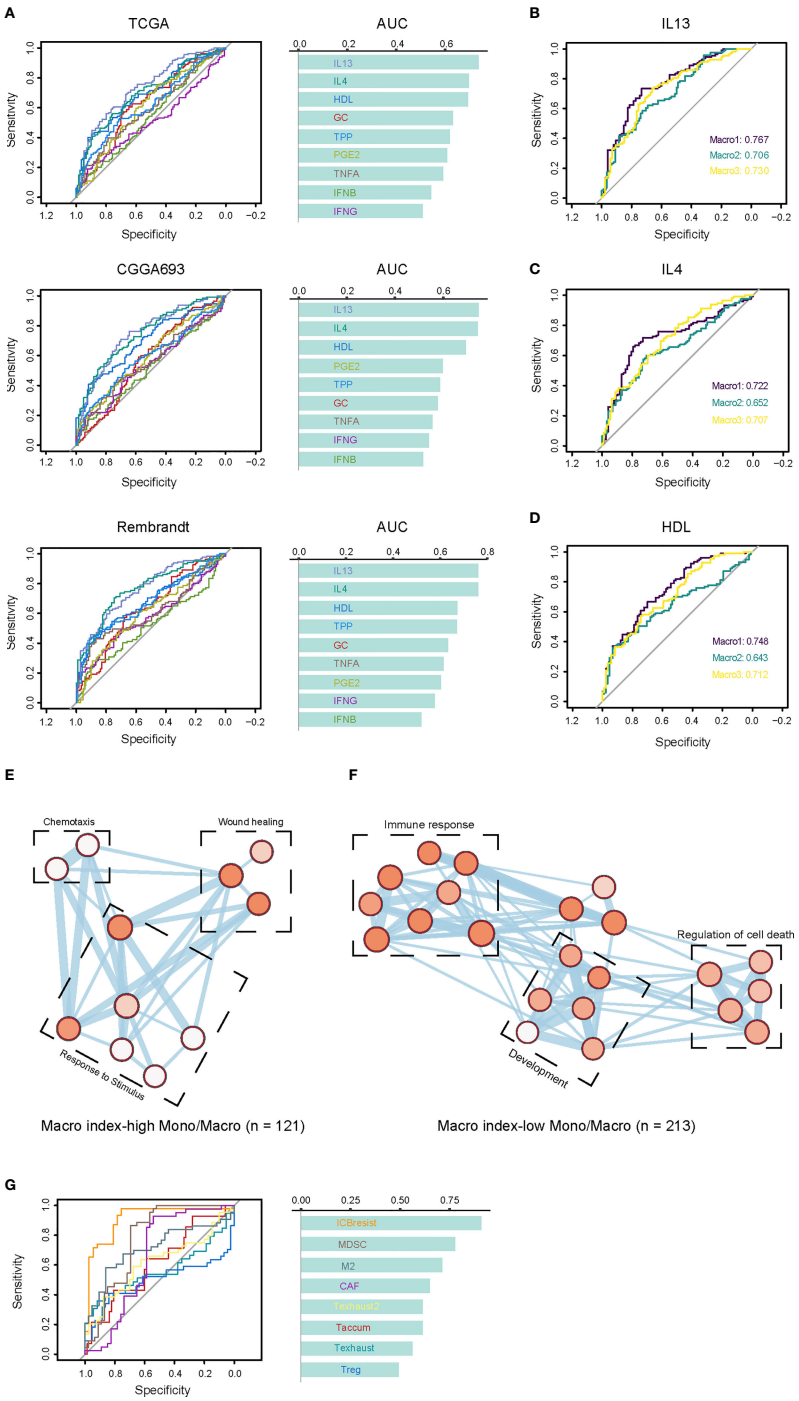

FIGURE 5
Association between the Macro index and the TAM phenotypes. **(A)** The consistency between the Macro index and gene signatures of TAM phenotype. Cells stimulated with GMCSF for 72 hours were M0 macrophages, and positive cells are cells cultured for 72 hours under different conditions after GMCSF-induced differentiation. Genes defined as positive or negative hits were the top 150 up- or down-regulated in the positive vs. M0 group, respectively. The ROC curves measure the performance of the Macro index in the prediction of the positive or negative hit genes based on the significant Spearman rho of the two. **(B-D)** The efficiency Macro index in predicting positive and negative hit genes induced by IL13, IL4, and HDL in each group. **(E, F)** Enrichment analysis of the biological processes of DEGs in Mono/Macro cells of the Macro index-high and Macro index-low groups. The color of the bubbles is inversely proportional to the q value of the enrichment score. **(G)** The prediction of T cell dysfunction-related gene signatures by the Macro index.

(55). Besides, the Macro index-high group had increased expression of CD163, as well as other macrophage alternative activation-related gene signatures (Figure S7D). Functional enrichment analysis found that genes upregulated in the Macro index-high monocytes/macrophages mainly enriched in BPs including wound healing, chemotaxis, and response to stimulus (Figure 5E). Genes upregulated in the Macro index-low group were mainly involved in the inflammatory response (Figure 5F). Moreover, recent studies based on the shRNA screen have identified genes involved in T cell dysfunction. Using ROC curves, we found that the Macro index gave the best performance in predicting ICB resistance (anti-CTLA4), as well as MDSC and M2 (Figure 5G). Therefore, these results highly suggested that the Macro index was associated with an immunosuppressive M2 phenotype of TAMs, and was involved in the T cell dysfunction.

The prognostic significance of the Macro index

Then, we explored the prognostic significance of the Macro index. As a result, K-M analysis showed that an increased Macro index predicted decreased OS and PFI in both Macro2 and

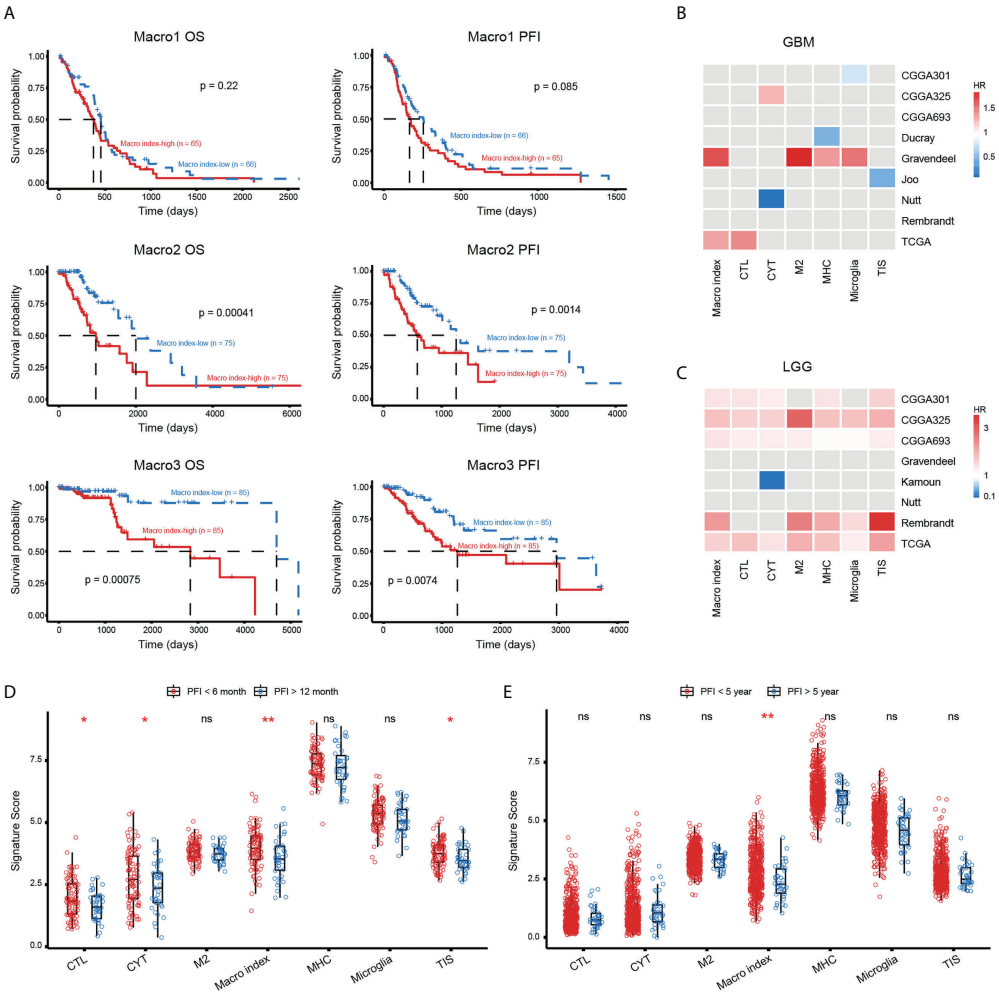

FIGURE 6
The prognostic significance of Macro index-based groups. **(A)** The differences in OS and PFI between the Macro index-high and -low groups based on the TCGA cohort. (**B**, **C**) The prognostic significance of the Macro index as well as other immune-related gene signatures in GBM and LGG of multiple cohorts. The Gray box represents statistically insignificant. CTL, cytolytic T lymphocyte; CYT, cytolytic activity; MHC, major histocompatibility complex; TIS, T cell inflammation signature. **(D)** Comparison of the scores of immune gene signatures in GBM patients that were early relapsed (PFI < 6 months) and late relapsed (PFI > 12 months). **(E)** Comparison of the scores of immune gene signatures in LGG patients that were early relapsed (PFI < 5 years) and late relapsed (PFI > 5 years). *p < 0.05, **p < 0.01, ns, non significant.

Macro3 (Figure 6A), thus an unfavorable outcome in LGG (Figures S8A-C). From a broader perspective, the Macro index was a robust risk prognostic factor for LGG, which performs comparably to other immune-related gene sets, but not for GBM (Figures 6B, C). In addition, the GBM samples were split into early (PFI < 6 months) and late (PFI > 12 months) relapse groups. Macro index, as well as several other immune-related indicators, such as CTL, CYT, and TIS, were significantly decreased in the late relapse group, suggesting an association between Macro index and disease progression (Figure 6D). Notably, the LGG was split into two groups based on the PFI and the Macro index was the only immune-related biomarker that may indicate PFI beyond 5 years in LGG (Figure 6E). Further at the protein level, we found that the Macro index was positively correlated with PAI1 (Spearman rho = 0.286, p = 0.015), and GBM patients with decreased PAI1 had prolonged PFI (Figures S8D, E). Together, these results indicate that the Macro index was a robust prognostic biomarker for LGG, and its clinical implication in GBM needs further exploration.

The Macro index was associated with ICI responsiveness

M2 macrophages are vital in remodeling the TME and frustrating the anti-tumor immune response (56, 57), therefore, we investigated the relationship between the Macro index and the immune checkpoint blockade that aimed at reviving the antitumor immune response by relieving the inhibition of cytolytic T lymphocyte by TME. Integration of multiple glioma single-cell expression profiles revealed that considerable immune checkpoints were expressed by monocytes/macrophages in the glioma TME (Figure 7A), which suggested that TAMs in the glioma TME may impede the anti-tumor immune response through immune checkpoints. TIDE provides a computational framework for assessing tumor immune evasion, i.e., induction of T-cell dysfunction in tumors with high CTL infiltration and prevention of T-cell infiltration in tumors with low CTL infiltration (51). Evidence suggested that gliomas, especially LGG, have little T-cell infiltration and abundant TAMs and are therefore lymphocyte-depleted or immune-quiet tumors (58). In our context, the Macro index was positively correlated with T-cell dysfunction and negatively correlated with T-cell exclusion (Figure S9), indicating that induction of T-cell dysfunction was the predominant mode of immune evasion in samples with an increased Macro index. Consistently, samples with elevated Macro index and TIDE T-cell dysfunction scores scored higher in cytolytic activity (Figure 7B), and the Macro index-high group had decreased TIDE score (Figure 7C), characterizing higher levels of antitumor activity with lower levels of tumor immune evasion. Notably, TIDE predicted that a greater proportion of patients in the Macro index-high group were likely to respond to ICI (fisher's exact p = 0.012) (Figure 7D). Although we have shown that increased Macro index was strongly associated with anti-CTLA4 resistance, unsupervised machine learning algorithms suggested that these samples may still benefit from anti-PD-1 treatment (Figure 7E). As an indirect testimony to the significance of the Macro index in facilitating the application of ICI therapy, a similar approach was employed to stratify the uroepithelial carcinoma cohort that received ICI treatment, and the proportion of patients with stable disease (SD) after anti-PD1 therapy was significantly higher in the Macro index-high group (fisher's exact test p = 0.023) (Figure 7F). Taken together, these results indicated that the Macro index showed promise for facilitating the application of PD-1 antibodies in glioma, which deserves further investigation.

Discussion

The importance of TAMs in the glioma TME cannot be overstated. With the rise of ICI therapy, there has been an increasing interest in the immunological properties of glioma TME (57). TAMs are involved in the failure of the anti-tumor immune response by promoting the formation of an immunosuppressive TME (15, 16), which makes them one of the sizzling therapeutic targets. Our knowledge of glioma TAMs remained at the M2 phenotype, a category that encompasses several functional states, which has hindered the development of TAMs-targeting therapies. Furthermore, recent studies have found that the metabolic and functional states of immune cells are conjugated and that alterations in lipid metabolism have important implications for the TME (24–26, 59). This has inspired the exploration of the association between the lipid metabolism of TAMs and the immunological properties of the glioma TME.

Several studies highlighted the impact of the PI3K/Akt pathway on macrophages. For example, advanced oxidative protein products inhibit autophagy by activating the PI3K/AKT/mTOR pathway, leading to macrophage dysfunction and impaired M1 polarization (60). Also, PM2.5 activates macrophages in a PI3K/Akt signaling-dependent manner. Akt is essential for the IL-4-induced M2 polarization of macrophages and the deficiency of TSC attenuates such a program by regulating mTOR (61). Particularly, TSC-deficient bone marrow-derived macrophages were impaired in the induction of Arg1, Fizz1, and Ym1 by IL-4 (62). Therefore, the PI3K/Akt signaling plays a role in macrophage M2 polarization. The PI3K/Akt signaling pathway also induces increased levels of FA β-oxidation in M2-type macrophages under chronic inflammatory conditions, thereby maintaining sustained energy expenditure (26). However, TAMs in the GBM TME may not have increased mitochondrial β-oxidation compared to LGG, as we found the

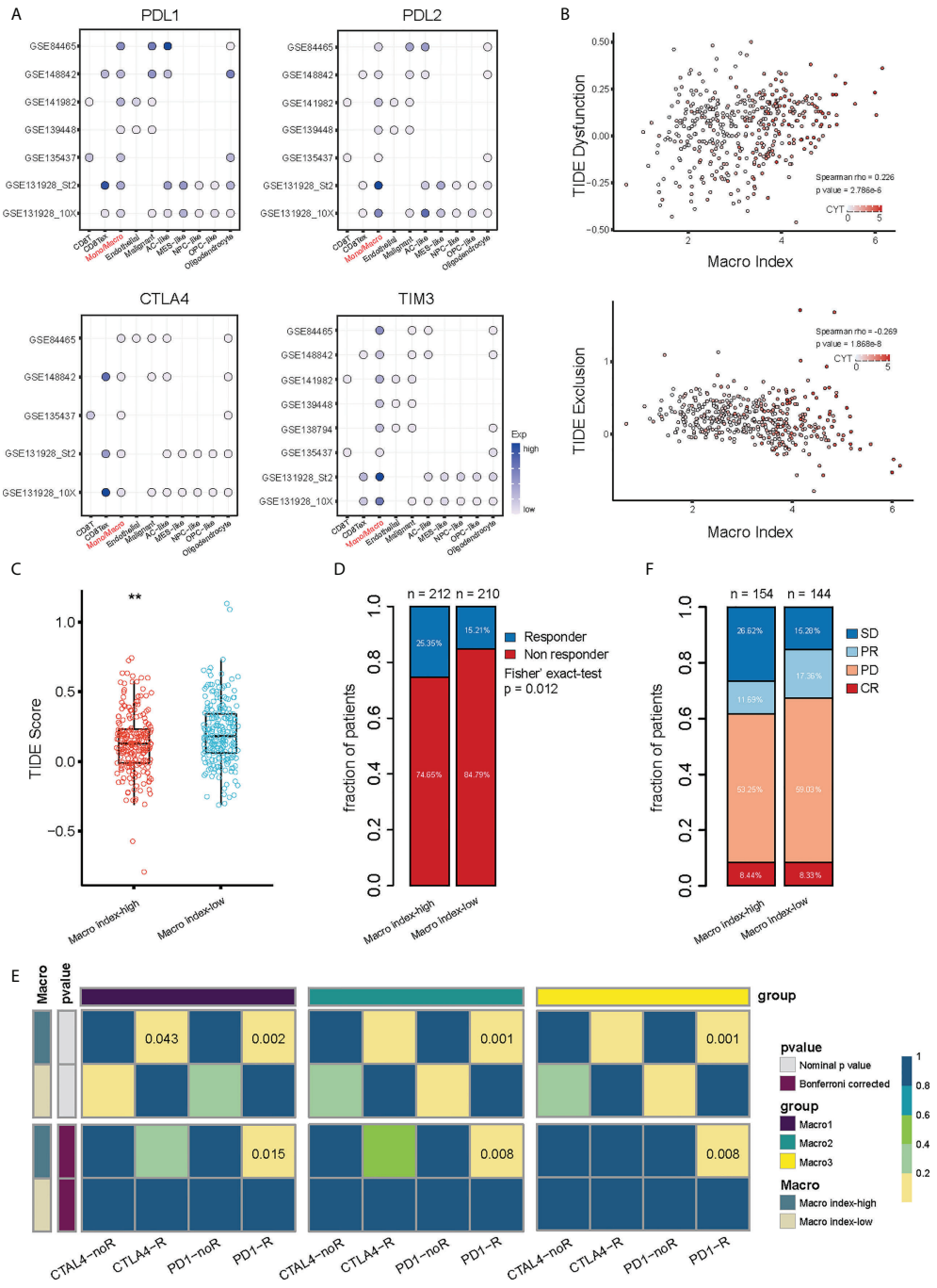

FIGURE 7
Association between the Macro index and ICI responsiveness. **(A)** Expression of immune checkpoints by different types of cells in the glioma TME at the single cell scope. **(B)** Association between the Macro index, TIDE T cell Dysfunction score, TIDE T cell Exclusion score, and CYT. Spearman rho measures the correlation between Macro index with Dysfunction and Exclusion scores. **(C)** TIDE score between Macro index-high and -low groups of TCGA glioma. **(D)** Distribution of predicted ICI responders and non-responders between the Macro index-high and -low groups. **(E)** Sample responsiveness to anti-PD1 or anti-CTLA4 was evaluated using the unsupervised Submap algorithm. **(F)** Macro index-based group in predicting the ICI benefit of the uroepithelial carcinoma sample. SD, stable disease; PR, partial response; PD, progression disease; CR, complete response. **p < 0.01.

expression of CPT1A/B/C was significantly reduced in Macro1. Furthermore, the relatively reduced FA β-oxidation in macrophages of the glioma TME may lead to the greater shunt of FA to phospholipids and then AA, the substrate of eicosanoids, and overexpression of lipid carriers should also allow for a greater influx of exogenous FAs or AA, making macrophages to be vehicles for tumor shaping of TME.

The interaction between PI3K/Akt signaling and eicosanoids is less characterized. Tong WG et al. reported that LTB_4 activates PI3K/Akt signaling and the blockade of the PI3K pathway using wortmannin attenuated LTB_4-mediated tumor cell proliferation (63). Likewise, PGE_2 promotes tumor cell invasion and metastasis in a PI3K/Akt-dependent manner (64). Therefore, it appears that eicosanoid derivatives promote various malignant behaviors of tumor cells *via* the PI3K/Akt signaling pathway. Nevertheless, insufficient evidence is found for direct regulation of LTs production by the PI3K/Akt pathway. Nikos Koundouros et al. demonstrated that mutant PIK3CA facilitates the production of AA and subsequently eicosanoids through activating PI3K/Akt/PLA2 axis (65). Zhou et al. also reported an association between the PI3K/Akt signaling pathway and the expression of ALOX5 in breast cancer (66). Mechanistically, PI3K/Akt signaling regulates the activity of multiple FA synthesis and transport enzymes, thereby funding anabolism (26, 27). PLA_2 is the main enzyme that dissociates AA from phospholipids when cells encounter a stimulus resulting in increased intracellular Ca^{2+} (67). Gimenes et al. reported that γCdcPLI1 inhibits the activity of PLA_2 in a PI3K/Akt dependent manner, possibly by interfering with the expression of Akt1/3 and PI3KR1 (68). Besides, PI3K also funds the activity of Crotoxin B, a catalytically active subunit IIA sPLA (69). These results are not yet sufficient to demonstrate a regulatory relationship between the PI3K signaling pathway and leukotriene production, and we raise the possibility by correlating the PI3K signaling pathway with the alternative activation of TAMs and eicosanoid metabolism.

The Macro index comprised of PIK3R5, PIK3R6, ALOX5, ALOX5AP, and ALOX15B serves as a valid prognostic biomarker for gliomas, especially LGG. Macro index is not a valid prognostic predictor for GBM, although abnormalities in the PI3K signaling pathway are present in over half of GBM (70). This may be related to the consensus that it is mainly the deletion of PTEN or abnormal activation of RTKs that accelerates the development of GBM. Although PIK3R5 and PIK3R6 are involved in the encoding of regulatory subunit of the class I PI3K gamma complex, their weight in the Macro index is diluted by three other genes related to leukotriene synthesis, whose impact on the GBM microenvironment is not yet known. Interestingly, we did not directly screen for genes of prognostic value, thus these results preliminarily confirmed the important role of the PI3K/Akt pathway and leukotrienes in glioma. Notably, we found that the Macro index-high group expressed more immune checkpoints and was characterized by dysfunction of CD8 T cells. Decreased TIDE scores in the Macro index-high group may indicate reduced levels of CD8 T cell dysfunction as well as immune evasion, as we have shown that the Macro index was positively correlated with T cell dysfunction score. Overall, Macro index acts as an inflammatory biomarker of the glioma microenvironment and is associated with the recruitment of multiple immune cells. However, M2-type polarization of macrophages and release of leukotrienes in this type of TME hindered the function of effector T cells, which may be one of the reasons that the Macro index is associated with ICI responsiveness in gliomas. Therefore, leukotriene synthesis and alternative activation of TAMs characterized by the Macro index are essential for the regulation of immunity in glioma TME where various factors intermingle.

Data availability statement

The original contributions presented in the study are included in the article/Supplementary Material. Further inquiries can be directed to the corresponding authors.

Author Contributions

SH, HJ, ZL, and JJ conceived and designed the study. HJ, HZ, XY, and NW were responsible for data collection, curation, quality control, and analysis. ZL and JZ reviewed and repeated the process of data analysis. HJ and ZL wrote the original draft of the manuscript, which was reviewed and revised by QG, JD, and FW. HJ and HS drafted and typeset the figures. CY, SH, and YL supervised the study. All authors contributed to the article and approved the submitted version.

Funding

This work was funded by the National Natural Science Foundation of China (No. 61575058) and Zhejiang Provincial People's Hospital Talent Introduction Project (No. C-2021-QDJJ03-01).

Acknowledgments

The authors gratefully acknowledge databases including TCGA, CGGA, UCSC, GlioVis, TISCH, and many other open access data portals for offering convenient access to datasets and user-friendly online analysis.

Conflict of interest

The authors declare that the research was conducted in the absence of any commercial or financial relationships that could be construed as a potential conflict of interest.

Publisher's note

All claims expressed in this article are solely those of the authors and do not necessarily represent those of their affiliated organizations, or those of the publisher, the editors and the reviewers. Any product that may be evaluated in this article, or claim that may be made by its manufacturer, is not guaranteed or endorsed by the publisher.

Supplementary material

The Supplementary Material for this article can be found online at: https://www.frontiersin.org/articles/10.3389/fimmu.2022.970702/full#supplementary-material

References

1. Weller M, Wick W, Aldape K, Brada M, Berger M, Pfister SM, et al. Glioma. *Nat Rev Dis Primers* (2015) 1:15017. doi: 10.1038/nrdp.2015.17

2. Jiang T, Mao Y, Ma W, Mao Q, You Y, Yang X, et al. CGCG clinical practice guidelines for the management of adult diffuse gliomas. *Cancer Lett* (2016) 375 (2):263–73. doi: 10.1016/j.canlet.2016.01.024

3. Wen PY, Reardon DA. Neuro-oncology in 2015: Progress in glioma diagnosis, classification and treatment. *Nat Rev Neurol* (2016) 12(2):69–70. doi: 10.1038/nrneurol.2015.242

4. Melin BS, Barnholtz-Sloan JS, Wrensch MR, Johansen C, Il'yasova D, Kinnersley B, et al. Genome-wide association study of glioma subtypes identifies specific differences in genetic susceptibility to glioblastoma and non-glioblastoma tumors. *Nat Genet* (2017) 49(5):789–94. doi: 10.1038/ng.3823

5. Cancer Genome Atlas Research N, Brat DJ, Verhaak RG, Aldape KD, Yung WK, Salama SR, et al. Comprehensive, integrative genomic analysis of diffuse lower-grade gliomas. *N Engl J Med* (2015) 372(26):2481–98. doi: 10.1056/NEJMoa1402121

6. Louis DN, Ohgaki H, Wiestler OD, Cavenee WK, Burger PC, Jouvet A, et al. The 2007 WHO classification of tumours of the central nervous system. *Acta Neuropathol* (2007) 114(2):97–109. doi: 10.1007/s00401-007-0243-4

7. Yan H, Parsons DW, Jin G, McLendon R, Rasheed BA, Yuan W, et al. IDH1 and IDH2 mutations in gliomas. *N Engl J Med* (2009) 360(8):765–73. doi: 10.1056/NEJMoa0808710

8. Jenkins RB, Blair H, Ballman KV, Giannini C, Arusell RM, Law M, et al. A t (1;19)(q10;p10) mediates the combined deletions of 1p and 19q and predicts a better prognosis of patients with oligodendroglioma. *Cancer Res* (2006) 66 (20):9852–61. doi: 10.1158/0008-5472.CAN-06-1796

9. Verhaak RG, Hoadley KA, Purdom E, Wang V, Qi Y, Wilkerson MD, et al. Integrated genomic analysis identifies clinically relevant subtypes of glioblastoma characterized by abnormalities in PDGFRA, IDH1, EGFR, and NF1. *Cancer Cell* (2010) 17(1):98–110. doi: 10.1016/j.ccr.2009.12.020

10. Wang Q, Hu B, Hu X, Kim H, Squatrito M, Scarpace L, et al. Tumor evolution of glioma-intrinsic gene expression subtypes associates with immunological changes in the microenvironment. *Cancer Cell* (2018) 33(1):152. doi: 10.1016/j.ccell.2017.12.012

11. Tan AC, Ashley DM, Lopez GY, Malinzak M, Friedman HS, Khasraw M. Management of glioblastoma: State of the art and future directions. *CA Cancer J Clin* (2020) 70(4):299–312. doi: 10.3322/caac.21613

12. AC F, M H, Recurrent glioma clinical trial MD. CheckMate-143: the game is not over yet. *Oncotarget* (2017) 8:91779–94. doi: 10.18632/oncotarget.21586

13. Zhao J, Chen A, Gartrell R, Silverman A, Aparicio L, Chu T, et al. Immune and genomic correlates of response to anti-PD-1 immunotherapy in glioblastoma. *Nat Med* (2019) 25(3)462–9. doi: 10.1038/s41591-019-0349-y

14. Schalper KA, Rodriguez-Ruiz ME, Diez-Valle R, Lopez-Janeiro A, Porciuncula A, Idoate MA, et al. Neoadjuvant nivolumab modifies the tumor immune microenvironment in resectable glioblastoma. *Nat Med* (2019) 25(3):470–6. doi: 10.1038/s41591-018-0339-5

15. Broekman ML, Maas SLN, Abels ER, Mempel TR, Krichevsky AM, Breakefield XO. Multidimensional communication in the microenvirons of glioblastoma. *Nat Rev Neurol* (2018) 14(8):482–95. doi: 10.1038/s41582-018-0025-8

16. Cassetta L, Pollard JW. Targeting macrophages: therapeutic approaches in cancer. *Nat Rev Drug Discovery* (2018) 17(12):887–904. doi: 10.1038/nrd.2018.169

17. Hambardzumyan D, Gutmann DH, Kettenmann H. The role of microglia and macrophages in glioma maintenance and progression. *Nat Neurosci* (2016) 19 (1):20–7. doi: 10.1038/nn.4185

18. Hussain SF, Yang D, Suki D, Aldape K, Grimm E, Heimberger AB. The role of human glioma-infiltrating microglia/macrophages in mediating antitumor immune responses. *Neuro Oncol* (2006) 8(3):261–79. doi: 10.1215/15228517-2006-008

19. Xuan W, Lesniak MS, James CD, Heimberger AB, Chen P. Context-dependent glioblastoma-Macrophage/Microglia symbiosis and associated mechanisms. *Trends Immunol* (2021) 42(4):280–92. doi: 10.1016/j.it.2021.02.004

20. Murray PJ, Allen JE, Biswas SK, Fisher EA, Gilroy DW, Goerdt S, et al. Macrophage activation and polarization: nomenclature and experimental guidelines. *Immunity* (2014) 41(1):14–20. doi: 10.1016/j.immuni.2014.06.008

21. Martinez FO, Helming L, Gordon S. Alternative activation of macrophages: an immunologic functional perspective. *Annu Rev Immunol* (2009) 27:451–83. doi: 10.1146/annurev.immunol.021908.132532

22. Martinez FO, Gordon S, Locati M, Mantovani A. Transcriptional profiling of the human monocyte-to-macrophage differentiation and polarization: new molecules and patterns of gene expression. *J Immunol* (2006) 177(10):7303–11. doi: 10.4049/jimmunol.177.10.7303

23. Xue J, Schmidt SV, Sander J, Draffehn A, Krebs W, Quester I, et al. Transcriptome-based network analysis reveals a spectrum model of human macrophage activation. *Immunity* (2014) 40(2):274–88. doi: 10.1016/j.immuni.2014.01.006

24. Wang D, Dubois RN. Eicosanoids and cancer. *Nat Rev Cancer* (2010) 10 (3):181–93. doi: 10.1038/nrc2809

25. Koundouros N, Poulogiannis G. Reprogramming of fatty acid metabolism in cancer. *Br J Cancer* (2020) 122(1):4–22. doi: 10.1038/s41416-019-0650-z

26. Hoxhaj G, Manning B. The PI3K-AKT network at the interface of oncogenic signalling and cancer metabolism. *Nat Rev Cancer* (2020) 20:74–88. doi: 10.1038/s41568-019-0216-7

27. He Y, Sun MM, Zhang GG, Yang J, Chen KS, Xu WW, et al. Targeting PI3K/Akt signal transduction for cancer therapy. *Signal Transduct Target Ther* (2021) 6 (1):425. doi: 10.1038/s41392-021-00828-5

28. Ceccarelli M, Barthel FP, Malta TM, Sabedot TS, Salama SR, Murray BA, et al. Molecular profiling reveals biologically discrete subsets and pathways of progression in diffuse glioma. *Cell* (2016) 164(3):550–63. doi: 10.1016/j.cell.2015.12.028

29. Bowman RL, Wang Q, Carro A, Verhaak RG, Squatrito M. GlioVis data portal for visualization and analysis of brain tumor expression datasets. *Neuro Oncol* (2017) 19(1):139–41. doi: 10.1093/neuonc/now247

30. Wang Y, Qian T, You G, Peng X, Chen C, You Y, et al. Localizing seizure-susceptible brain regions associated with low-grade gliomas using voxel-based lesion-symptom mapping. *Neuro-Oncology* (2015) 17:282–8. doi: 10.1093/neuonc/nou130

31. Liu X, Li Y, Qian Z, Sun Z, Xu K, Wang K, et al. A radiomic signature as a non-invasive predictor of progression-free survival in patients with lower-grade gliomas. *NeuroImage Clin* (2018) 20:1070–7. doi: 10.1016/j.nicl.2018.10.014

32. Madhavan S, Zenklusen J, Kotliarov Y, Sahni H, Fine H, Buetow K. Rembrandt: helping personalized medicine become a reality through integrative translational research. *Mol Cancer Res* (2009) 7:157–67. doi: 10.1158/1541-7786.MCR-08-0435

33. Sun D, Wang J, Han Y, Dong X, Ge J, Zheng R, et al. TISCH: a comprehensive web resource enabling interactive single-cell transcriptome visualization of tumor microenvironment. *Nucleic Acids Res* (2020) 8;49(D1): D1420–30. doi: 10.1101/2020.08.15.251959

34. Neftel C, Laffy J, Filbin MG, Hara T, Shore ME, Rahme GJ, et al. An integrative model of cellular states, plasticity, and genetics for glioblastoma. *Cell* (2019) 178(4):835–49 e21. doi: 10.1016/j.cell.2019.06.024

35. Aran D, Hu Z, Butte AJ. xCell: digitally portraying the tissue cellular heterogeneity landscape. *Genome Biol* (2017) 18(1):220. doi: 10.1186/s13059-017-1349-1

36. Finotello F, Mayer C, Plattner C, Laschober G, Rieder D, Hackl H, et al. Molecular and pharmacological modulators of the tumor immune contexture revealed by deconvolution of RNA-seq data. *Genome Med* (2019) 11:34. doi: 10.1186/s13073-019-0638-6

37. Newman AM, Liu CL, Green MR, Gentles AJ, Feng W, Xu Y, et al. Robust enumeration of cell subsets from tissue expression profiles. *Nat Methods* (2015) 12 (5):453–7. doi: 10.1038/nmeth.3337

38. Li T, Fu J, Zeng Z, Cohen D, Li J, Chen Q, et al. TIMER2.0 for analysis of tumor-infiltrating immune cells. *Nucleic Acids Res* (2020) 48(W1):W509–W14. doi: 10.1093/nar/gkaa407

39. Wilkerson MD, Hayes DN. ConsensusClusterPlus: a class discovery tool with confidence assessments and item tracking. *Bioinformatics* (2010) 26 (12):1572–3. doi: 10.1093/bioinformatics/btq170

40. Liberzon A, Birger C, Thorvaldsdottir H, Ghandi M, Mesirov JP, Tamayo P. The molecular signatures database (MSigDB) hallmark gene set collection. *Cell Syst* (2015) 1(6):417–25. doi: 10.1016/j.cels.2015.12.004

41. Hanzelmann S, Castelo R, Guinney J. GSVA: gene set variation analysis for microarray and RNA-seq data. *BMC Bioinf* (2013) 14:7. doi: 10.1186/1471-2105-14-7

42. Subramanian A, Tamayo P, Mootha VK, Mukherjee S, Ebert BL, Gillette MA, et al. Gene set enrichment analysis: a knowledge-based approach for interpreting genome-wide expression profiles. *Proc Natl Acad Sci U.S.A.* (2005) 102(43):15545–50. doi: 10.1073/pnas.0506580102

43. Ritchie ME, Phipson B, Wu D, Hu Y, Law CW, Shi W, et al. Limma powers differential expression analyses for RNA-sequencing and microarray studies. *Nucleic Acids Res* (2015) 43(7):e47. doi: 10.1093/nar/gkv007

44. Robinson MD, McCarthy DJ, Smyth GK. edgeR: a bioconductor package for differential expression analysis of digital gene expression data. *Bioinformatics* (2010) 26(1):139–40. doi: 10.1093/bioinformatics/btp616

45. Zhou Y, Zhou B, Pache L, Chang M, Khodabakhshi AH, Tanaseichuk O, et al. Metascape provides a biologist-oriented resource for the analysis of systems-level datasets. *Nat Commun* (2019) 10(1):1523. doi: 10.1038/s41467-019-09234-6

46. Bader GD, Hogue CW. An automated method for finding molecular complexes in large protein interaction networks. *BMC Bioinf* (2003) 4:2. doi: 10.1186/1471-2105-4-2

47. Hao Y, Hao S, Andersen-Nissen E, Mauck WM3rd, Zheng S, Butler A, et al. Integrated analysis of multimodal single-cell data. *Cell* (2021) 184(13):3573–87 e29. doi: 10.1016/j.cell.2021.04.048

48. Zhang X, Lan Y, Xu J, Quan F, Zhao E, Deng C, et al. CellMarker: a manually curated resource of cell markers in human and mouse. *Nucleic Acids Res* (2019) 47 (D1):D721–D8. doi: 10.1093/nar/gky900

49. Han H, Cho JW, Lee S, Yun A, Kim H, Bae D, et al. TRRUST v2: an expanded reference database of human and mouse transcriptional regulatory interactions. *Nucleic Acids Res* (2018) 46(D1):D380–D6. doi: 10.1093/nar/gkx1013

50. Xu L, Deng C, Pang B, Zhang X, Liu W, Liao G, et al. TIP: A web server for resolving tumor immunophenotype profiling. *Cancer Res* (2018) 78(23):6575–80. doi: 10.1158/0008-5472.CAN-18-0689

51. Jiang P, Gu S, Pan D, Fu J, Sahu A, Hu X, et al. Signatures of T cell dysfunction and exclusion predict cancer immunotherapy response. *Nat Med* (2018) 24(10):1550–8. doi: 10.1038/s41591-018-0136-1

52. Hoshida Y, Brunet JP, Tamayo P, Golub TR, Mesirov JP. Subclass mapping: identifying common subtypes in independent disease data sets. *PloS One* (2007) 2 (11):e1195. doi: 10.1371/journal.pone.0001195

53. Roh W, Chen PL, Reuben A, Spencer CN, Prieto PA, Miller JP, et al. Integrated molecular analysis of tumor biopsies on sequential CTLA-4 and PD-1 blockade reveals markers of response and resistance. *Sci Transl Med* (2017) 9(379): eaah3560. doi: 10.1126/scitranslmed.aah3560

54. Mariathasan S, Turley SJ, Nickles D, Castiglioni A, Yuen K, Wang Y, et al. TGFbeta attenuates tumour response to PD-L1 blockade by contributing to exclusion of T cells. *Nature* (2018) 554(7693):544–8. doi: 10.1038/nature25501

55. Ou A, Ott M, Fang D, Heimberger AB. The role and therapeutic targeting of JAK/STAT signaling in glioblastoma. *Cancers (Basel)* (2021) 13(3):437. doi: 10.3390/cancers13030437

56. Berghoff AS, Kiesel B, Widhalm G, Rajky O, Ricken G, Wohrer A, et al. Programmed death ligand 1 expression and tumor-infiltrating lymphocytes in glioblastoma. *Neuro Oncol* (2015) 17(8):1064–75. doi: 10.1093/neuonc/nou307

57. Shu C, Li Q. Current advances in PD-1/PD-L1 axis-related tumour-infiltrating immune cells and therapeutic regimens in glioblastoma. *Crit Rev Oncol Hematol* (2020) 151:102965. doi: 10.1016/j.critrevonc.2020.102965

58. Thorsson V, Gibbs DL, Brown SD, Wolf D, Bortone DS, Ou Yang TH, et al. The immune landscape of cancer. *Immunity* (2018) 48(4):812–30 e14. doi: 10.1016/j.immuni.2018.03.023

59. O'Neill LA, Kishton RJ, Rathmell J. A guide to immunometabolism for immunologists. *Nat Rev Immunol* (2016) 16(9):553–65. doi: 10.1038/nri.2016.70

60. Liao Y, Xu J, Qin B, Shi J, Qin C, Xie F, et al. Advanced oxidation protein products impair autophagic flux in macrophage by inducing lysosomal dysfunction *via* activation of PI3K-Akt-mTOR pathway in crohn's disease. *Free Radic Biol Med* (2021) 172:33–47. doi: 10.1016/j.freeradbiomed.2021.05.018

61. Byles V, Covarrubias AJ, Ben-Sahra I, Lamming DW, Sabatini DM, Manning BD, et al. The TSC-mTOR pathway regulates macrophage polarization. *Nat Commun* (2013) 4:2834. doi: 10.1038/ncomms3834

62. Zhu L, Yang T, Li L, Sun L, Hou Y, Hu X, et al. TSC1 controls macrophage polarization to prevent inflammatory disease. *Nat Commun* (2014) 5:4696. doi: 10.1038/ncomms5696

63. Tong WG, Ding XZ, Talamonti MS, Bell RH, Adrian TE. LTB4 stimulates growth of human pancreatic cancer cells *via* MAPK and PI-3 kinase pathways. *Biochem Biophys Res Commun* (2005) 335(3):949–56. doi: 10.1016/j.bbrc.2005.07.166

64. Finetti F, Solito R, Morbidelli L, Giachetti A, Ziche M, Donnini S. Prostaglandin E2 regulates angiogenesis *via* activation of fibroblast growth factor receptor-1. *J Biol Chem* (2008) 283(4):2139–46. doi: 10.1074/jbc.M703090200

65. Koundouros N, Karali E, Tripp A, Valle A, Inglese P, Perry NJS, et al. Metabolic fingerprinting links oncogenic PIK3CA with enhanced arachidonic acid-derived eicosanoids. *Cell* (2020) 181(7):1596–611 e27. doi: 10.1016/j.cell.2020.05.053

66. Zhou X, Jiang Y, Li Q, Huang Z, Yang H, Wei C. Aberrant ALOX5 activation correlates with HER2 status and mediates breast cancer biological activities through multiple mechanisms. *BioMed Res Int* (2020) 2020:1703531. doi: 10.1155/2020/1703531

67. Haeggstrom JZ, Funk CD. Lipoxygenase and leukotriene pathways: biochemistry, biology, and roles in disease. *Chem Rev* (2011) 111(10):5866–98. doi: 10.1021/cr200246d

68. Gimenes SNC, Lopes DS, Alves PT, Azevedo F, Vecchi L, Goulart LR, et al. Antitumoral effects of gammaCdcPLI, a PLA2 inhibitor from crotalus durissus collilineatus *via* PI3K/Akt pathway on MDA-MB-231 breast cancer cell. *Sci Rep* (2017) 7(1):7077. doi: 10.1038/s41598-017-07082-2

69. Giannotti KC, Leiguez E, Carvalho AEZ, Nascimento NG, Matsubara MH, Fortes-Dias CL, et al. A snake venom group IIA PLA2 with immunomodulatory activity induces formation of lipid droplets containing 15-d-PGJ2 in macrophages. *Sci Rep* (2017) 7(1):4098. doi: 10.1038/s41598-017-04498-8

70. Brennan CW, Verhaak RG, McKenna A, Campos B, Noushmehr H, Salama SR, et al. The somatic genomic landscape of glioblastoma. *Cell* (2013) 155(2):462–77. doi: 10.1016/j.cell.2013.09.034

frontiers | Frontiers in Immunology

TYPE Original Research
PUBLISHED 13 September 2022
DOI 10.3389/fimmu.2022.941556

Check for updates

OPEN ACCESS

EDITED BY
Jian Zhang,
Southern Medical University, China

REVIEWED BY
Guan Xu,
Chinese Academy of Medical Sciences and Peking Union Medical College, China
Chengyu Yang,
The Affiliated Hospital of Qingdao University, China
Yongqiang Zhang,
Center for Biosafety Mega-Science (CAS), China
Zhirui Zeng,
Guizhou Medical University, China
Lai Shi,
Dana–Farber Cancer Institute, United States

*CORRESPONDENCE
Chao You
YouChao_westchina@163.com
Shaoshan Hu
Shaoshanhu421@163.com
Yi Liu
Liuyi@wchscu.cn

SPECIALTY SECTION
This article was submitted to Cancer Immunity and Immunotherapy, a section of the journal Frontiers in Immunology

RECEIVED 11 May 2022
ACCEPTED 22 August 2022
PUBLISHED 13 September 2022

CITATION
Ji H, Liu Z, Wang F, Sun H, Wang N, Liu Y, Hu S and You C (2022) Novel macrophage-related gene prognostic index for glioblastoma associated with M2 macrophages and T cell dysfunction. *Front. Immunol.* 13:941556. doi: 10.3389/fimmu.2022.941556

Novel macrophage-related gene prognostic index for glioblastoma associated with M2 macrophages and T cell dysfunction

Hang Ji[1,2], Zhihui Liu[2], Fang Wang[2], Haogeng Sun[1], Nan Wang[2], Yi Liu[1]*, Shaoshan Hu[2]* and Chao You[1]*

[1]Department of Neurosurgery, West China Hospital, Sichuan University, Chengdu, China, [2]Cancer Center, Department of Neurosurgery, Zhejiang Provincial People's Hospital, Hangzhou Medical College, Hangzhou, China

This study aims to construct a Macrophage-Related Gene Prognostic Index (MRGPI) for glioblastoma (GBM) and explore the underlying molecular, metabolic, and immunological features. Based on the GBM dataset from The Cancer Genome Atlas (n = 156), 13 macrophage-related hub genes were identified by weighted gene co-expression network (WGCNA) analysis. 5 prognostic genes screened by Kaplan-Meire (K-M) analysis and Cox regression model were used to construct the MRGPI, including GPR84, NCF2, HK3, LILRB2, and CCL18. Multivariate Cox regression analysis found that the MRGPI was an independent risk factor (HR = 2.81, CI95: 1.13-6.98, p = 0.026), leading to an unfavorable outcome for the MRGPI-high group, which was further validated by 4 validation GBM cohorts (n = 728). Thereafter, the molecular, metabolic, and immune features and the clinical implications of the MRGPI-based groups were comprehensively characterized. Gene set enrichment analysis (GSEA) found that immune-related pathways, including inflammatory and adaptive immune response, and activated eicosanoid metabolic pathways were enriched in the MRGPI-high group. Besides, genes constituting the MRGPI was primarily expressed by monocytes and macrophages at single-cell scope and was associated with the alternative activation of macrophages. Moreover, correlation analysis and receiver operating characteristic (ROC) curves revealed the relevance between the MRGPI with the expression of immune checkpoints and T cell dysfunction. Thus, the responsiveness of samples in the MRGPI-high group to immune checkpoint inhibitors (ICI) was detected by algorithms, including Tumor Immune Dysfunction and Exclusion (TIDE) and Submap. In contrast, the MRGPI-low group had favorable outcome, was less immune active and insensitive to ICI. Together, we have developed a promising biomarker to classify the prognosis, metabolic and immune features for GBM, and provide references for facilitating the personalized application of ICI in GBM.

KEYWORDS

glioblastoma, tumor microenvironment, tumor-associated macrophage, immune checkpoint inhibition, eicosanoid metabolism

Introduction

Glioblastoma (GBM) is the most common and devastating primary brain tumor that possess a desperate outcome, with median survival remaining around 15 months after standard treatment (1–3). Developing robust biomaerkers for prognosis and therapies remains challenging. Novel tumor therapies including immune checkpoint inhibition (ICI) aim to block immune checkpoint signaling pathways, such as the PD-1/PD-L1 axis and CTLA4, which bring remarkable survival benefits for several malignancies (4–7). Yet, the application of ICI in GBM is limited, which may partially ascribe to the immune-suppressive tumor microenvironment (TME) (8, 9). Tumor-associated macrophages (TAMs) in GBM refer to blood-derived monocytes/macrophages and intrinsic microglia, and the alternatively activated TAMs orchestrate an immunosuppressive TME thus impeding the anti-tumor immune activity (10–12). Interstingly, increasing evidence suggests that TAMs involve in the expression of immune checkpoints in the TME and play a vital role in inducing CD8 T lymphocyte dysfunction (11, 13–15). Given that GBM is a class of TAMs-rich tumors (16), the identification of biomarkers associated with alternative activation of TAMs may provide prognostic convenience for GBM on the one hand, and pave the way for the application of ICI on the other.

Although TAMs can be simply divided into M1 and M2 phenotypes, the molecular features characterizing the functional status of TAMs in the GBM TME remain loosely defined. Unlike the usual dogma, MARCO may be a transcriptomic marker for TAMs in GBM (17). In addition, STAT3 signaling is responsible for the polarization and immunosuppressive functions of macrophages and microglia in the GBM microenvironment instead of STAT6 (11, 18). Therefore, the identification of biomarkers associated with alternative activation of macrophages needs to take into account the specific immune context of the central nervous system. Recently, great advances have been made in the study of the spectrum of the functional state of macrophages based on the transcriptome (19, 20), which resolved the molecular functional networks associated with the different polarization states of alveolar macrophages. Building on these achievements, we have the opportunity to identify the gene signatures associated with the alternative activation of TAMs in GBM and to explore their clinical significance.

From this perspective, we developed a macrophage-related gene prognostic index and explore its molecular underpinnings and clinical implications. We started with the differentially expressed macrophage-related genes in the GBM expression profile and screened out the hub genes of prognostic significance and constructed the MRGPI. Then, we comprehensively explored the molecular, metabolic, and immunological features of MRGPI at bulk tumor, single-cell transcriptome, and protein levels and identified the expression patterns of immune checkpoints and the functional states of TAMs associated with MRGPI. Based on several machine learning algorithms, the association between the MRGPI with ICI responsiveness of GBM samples were also revealed. Overall, our study not only provide a biomarker of clinical implications, but also offer some insights into understanding the cancer biology of GBM.

Materials and methods

Data collection and pre-processing

RNA-seq data of 173 GBM samples and corresponding demographics were retrieved from The Cancer Genome Atlas (TCGA) database (https://portal.gdc.cancer.gov). 156 GBM samples remaining after exclusion of normal and formalin-fixed samples and was difined as the training data set. 4 additional GBM cohorts were collected and used as the validation data sets, including CGGA325 (n = 139), CGGA693 (n = 249), Rembrandt (n = 181), and Gravendeel (n = 159). RNA-seq data of integrated GBM and LGG dataset (n = 702) and corresponding demographics were downloaded from the UCSC Xena data portal (https://xenabrowser.net/). RNA-seq data of 214 normal brain tissue samples (cortex) were retrieved from the UCSC Xena data portal (http://xena.ucsc.edu/). The batch effect was eliminated using the R package 'sva'. Count value was converted to TPM for regression analysis, GSEA, and comparison of gene expression at the bulk-tumor level. The macrophage bona fide gene (BFG) list was summarized by Xue J. et al (19). Single-cell RNA-seq datasets including GSE131928 and GSE70630 were retrieved from the TISCH data portal (http://tisch.comp-genomics.org/) (21). The expression profile of 30 types of TCGA cancers was integrated by Thorsson et al. (16), and corresponding demographics were retrieved from the UCSC Xena data portal. The transcriptome subtype of TCGA GBM samples was summarized by Wang et al. (22).

Identification of macrophage-related hub genes and constriction of MRGPI

Based on the merged TCGA GBM and GTEx normal tissue RNA-seq expression profile, the differentially expressed genes (DEGs) were estimated using the R packages 'limma' and 'edgeR' ($|\log_2 FC| >= 0.5$, adj p-val < 0.05) (23, 24). After intersecting the macrophage BFGs with the DEGs, differentially expressed macrophage-related genes were obtained and annotated using functional enrichment analysis based on the webtool Metascape (http://www.metascape.org/) (25). WGCNA analysis was performed to identify hub genes (26). Briefly, the similarity matrix and adjacency matrix (signed) were constructed sequentially based on the expression profile of differentially expressed macrophage-related genes, and the soft threshold of β was calculated. Then, the adjacency matrix was transformed into the topological matrix and the dynamic pruning tree was built to identify the gene modules with a merging threshold function at 0.25. Genes involved in the module brown and turquoise were candidates for K-M analysis to determine prognostic significance. Further, univariate and multivariate Cox regression analysis was performed to determine the independent prognostic significance of these genes. To reveal the regulatory mechanism of genes of independent prognostic significance, related transcriptional factors (TFs) and miRNA interaction network was constructed using the webtool NetworkAnalyst (https://www.networkanalyst.ca/) (27). The regression coefficients of genes of independent prognostic significance were determined using multivariate Cox regression analysis. The MRGPI was defined as the sum of gene expression multiplied by its multivariate regression coefficient. Samples were then split into MRGPI-high and MRGPI-low groups by the median value. The web tool TISCH was employed to identify the cellular location of selected genes.

Immunohistochemistry for genes comprising MRGPI

All samples were obtained according to the protocol approved by the Ethics Review Committee of Zhejiang Provincial People's Hospital. All subjects were given written informed consent to participate. Formalin-fixed, paraffin-embedded tumor tissues (approximately 0.5cm×0.5cm×0.2cm) were collected during surgical excision and were further divided into core and margins by two senior neurosurgeons. The procedure for immunohistochemical staining has been described before (28). Briefly, after heat-induced antigen retrieval, tumor sections were stained with a 1:500 dilution of the corresponding antibody against CCL18 (22303-1-AP, Proteintech, Wuhan Sanying, China), GPR84 (DF2769, Affinity Biosciences, China), HK3 (13333-1-AP, Proteintech, Wuhan Sanying, China), LILRB2 (DF9604, Affinity Biosciences, China), and NCF2 (15551-1-AP, Proteintech, Wuhan Sanying, China). The staining intensity of the tissue sections was calculated by the IHC profiler plugin of the imageJ software. We selected 4-5 tissue sections from the 3 pairs of tumors and peritumoural tissues for immunohistochemical staining and calculated IHC scores. The score of each section was assigned as the sum of 4 multiplied by the proportion of the strong positive pixels, 3 multiplied by the proportion of the positive pixels, 2 multiplied by the low positive pixels and 1 multiplied by the negative pixels, as described in the original study (29).

Exploring the molecular and immune characteristics and ICB responsiveness of MRGPI

Gene set enrichment analysis (GSEA) software (v4.2.3) was employed to assess enriched signaling pathways based on the Molecular Signature Database (http://www.gsea-msigdb.org/gsea/msigdb/v7.5.1) (FDR-q < 0.1) (30, 31). Then, genes involved in the WP eicosanoid synthesis pathway were candidates for the multivariate regression model to determine their association with MRGPI. The fraction of 22 immune infiltrations was estimated using the CIBERSORT algorithm (32). Samples with p-value < 0.05 and cells with 0 value in over half of the samples were filtered. To address the association between the functional state of macrophages and MRGPI, single-cell RNA-seq datasets GSE131928 and GSE70630 were included and the R package 'Seurat' was employed to dissect these datasets (33–35). Briefly, cells with abnormal gene numbers and ribosome ratios were filtered, and the effect of cell cycle-related genes on clustering was excluded using regression analysis after the identification of highly variable genes. Clustering was performed at a resolution of 0.5. The non-malignant cells were determined using marker genes summarized by the CellMarker database (http://bio-bigdata.hrbmu.edu.cn/CellMarker/) and Neftel et al. (34, 36). For instance, macrophages marker genes include CD14, AIF1, FCER1G, FCGR3A, TYROBP, CSF1R, T cell marker genes include CD2, CD3D, CD3E, CD3G, and marker genes of other cells (mainly oligodendrocytes) include MBP, TF, PLP1, MAG, MOG, CLDN11. The online tool TIDE algorithm was performed to predict sample responsiveness to ICI (http://tide.dfci.harvard.edu/) (37). The TIS score was calculated as an average of log-scale normalized expression of the 18 signature genes associated with interferon-gamma. Besides, the submap algorithm was employed to correct the predicted results with a default parameter (https://cloud.genepattern.org/gp/pages/index.jsf) (38). To evaluate the association between MRGPI and genes related to T cell function, 4 published studies of tumor immune

evasion were employed and the hub genes have been collected and screened by Peng et al. Briefly, we calculated the Spearman rho for each positive and negative hit gene and excluded those with insignificant rho with the MRGPI. When measuring the performance of the MRGPI in predicting the positive and negative hits using ROC, positive hits were marked as 1 and negative hits 0.

Statistics

All statistics were performed using the R software (v4.1.2). Wilcox test was performed to compare continuous variables between groups (t-test for normally distributed variables). K-M survival analysis with the log-rank test was performed to classify survival differences. Univariate and multivariate Cox regression analysis was conducted to determine the independent prognostic value of the variables. The composition ratios were compared using the Chi-square test or Fischer's exact test. ROC and corresponding AUC were employed to evaluate the association between MRGPI and genes related to T cell function. A two-sided p-value < 0.05 was considered significant. In the GSEA analysis, FDR-q < 0.1 was considered significant.

Results

Workflow of the research

This study was divided into 4 parts (Figure 1). We first identified genes that were aberrantly expressed in GBM by differential analysis and then intersected these DEGs with macrophage BFGs to obtain macrophage-associated genes. Macrophage-associated hub genes were further screened by WGCNA and those genes significantly associated with GBM prognosis were identified by K-M analysis as candidates for subsequent Cox analysis. Next, genes that were statistically significant in the univariate Cox analysis were injected into the univariate Cox analysis, and the resulting five genes and their Cox regression coefficients constituted the MRGPI. We then explored the immune features associated with MRGPI. CIBERSORT and GSEA were conducted to identify characteristics of immune infiltration and immune-related signalling pathways and their relevance with MRGPI. Finally, we employed ROC analysis, the TIDE algorithm, a previously well-constructed TIS score, and the Submap algorithm to assess the association between MRGPI and T cell dysfunction as well as the potential of MRGPI to predict ICI responses.

Identification of Macrophage-related hub genes

Differential expression analysis was performed to identify macrophage-related hub genes. A total of 3528 DEGs were identified between the GBM sample (n = 156) and normal controls from the GTEx (n = 214), including 1775 upregulated DEGs and 1753 downregulated DEGs (Supplementary Figure 1A). Intersecting these DEGs with 9498 macrophage BFGs resulted in 537 differentially expressed macrophage-related genes, of which 416 genes were upregulated and 121 were downregulated (Supplementary Figure 1B). Functional enrichment analysis of the 537 genes found that these genes were preferentially enriched in signaling pathways associated with inflammation, cytokine production as well as leukocyte activation (Supplementary Figure 1C).

To identify the macrophage-related hub genes, WGCNA analysis was performed on the 537 candidate genes. Setting the

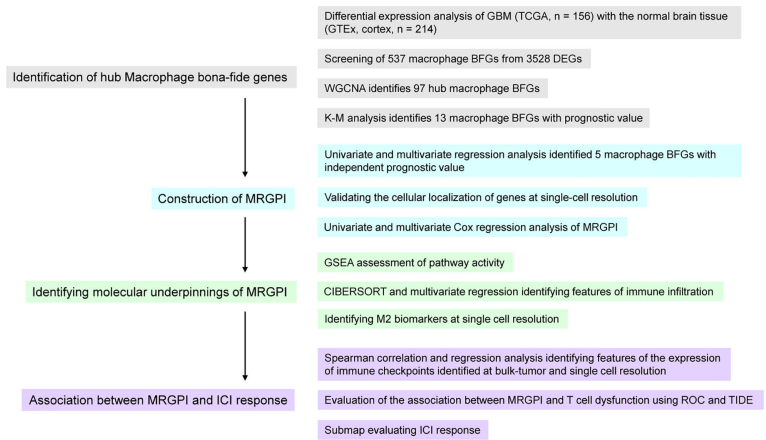

FIGURE 1
Overview of the workflow of this study.

correlation coefficient between the log(k) of a node with connectivity log(P(k)) of that node over 0.9, the estimated optimal soft threshold power for a scale-free network was 16 (Supplementary Figure 2A). Thereafter, 4 modules were identified based on the optimal soft-thresholding power (Supplementary Figure 2B, C). Based on the Pearson correlation coefficient between the module and clinical features, module brown and turquoise were significantly correlated with GBM (cor = 0.8 and 0.69, respectively). A total of 232 genes were included in module brown (n = 54) and turquoise (n = 178). Functional enrichment analysis showed that genes in module brown were mainly enriched in pathways associated with cell proliferation and division, and genes in module turquoise were enriched in pathways related to cell activation and inflammation (Supplementary Figure 3). Setting the adjacency threshold for including edges to 0.2, 97 out of 232 genes were defined as hub genes, and their module membership (MM) values and connectivity (within (Kwithin) and outside (Kout) of a module) were summarized in Supplementary Table 1. K-M analysis found that 13 of them were of prognostic significance in GBM patients (Supplementary Figure 4). Besides, the molecular characteristics of the 13 differentially expressed macrophage-related hub genes were explored. In regulatory network, there were 83 interacting pairs between the hub genes and TFs (Supplementary Figure 5A) and 94 interacting pairs between the hub genes and miRNAs (Supplementary Figure 5B). To validate the cellular expression of these genes at single cell resolution, multiple single-cell expression profiles were integrated. As a result, the 5 genes were significantly upregulated in the Mono/Macro cluster, both in glioma and a pan-cancer scale (Supplementary Figure 6A, B).

Prognostic significance of the MRGPI

Next, we determined the independent prognostic significance of the 13 differentially expressed macrophage-related hub genes using the univariate and multivariate Cox regression analysis. As a result, GPR84, NCF2, HK3, LILRB2, and CCL18 significantly affected the overall survival (OS) of GBM patients (multivatiate Cox $p < 0.05$) (Figure 2A), of which the protein level of GPR84 and NCF2 was significantly increased in the tumor core region (Figure 2E, F, Supplementary Figure 6C). Thereafter, a prognostic index (MRGPI) for GBM samples was constructed based on the regression coefficients derived from multivariate Cox analysis (0.2598, 0.1038, 0.0885, -0.1356, 0.0652 for GPR84, NCF2, HK3, LILRB2, and CCL18), and samples were split into MRGPI-high and -low groups by the median value. The clinical features associated with the MRGPI-based groups were summarized in Table 1. Notably, multivariate Cox regression analysis identified that MRGPI was an independent prognostic risk factor (HR = 2.81, CI95: 1.13-6.98, p = 0.026) in the TCGA cohort after adjusted for covariates, including age, sex, IDH mutation, MGMT promoter methylation, ATRX mutation and TERT promoter mutation (Figure 2B), as well as in validation data sets (Table 2). Nevertheless, ROC curves and corresponding area under curves (AUCs) suggested that the MRGPI provided a mediocre prediction performance (Supplementary Figure 7A). Thus, the MRGPI-high group had decresed OS and progression-free interval (PFI) in the TCGA, and in the CGGA325 and Gravendeel cohorts (Figure 2C, D). Moreover, 30 types of cancers in the TCGA project were included and samples were divided into early relapse (PFI < 6 months) and late relapse (PFI > 12 months) groups. Only in the GBM sample was there a significant difference in MRGPI between the two groups (Figure 2G).

We also explored the prognostic value of MRGPI for LGG. Samples in the TCGA (n = 525), CGGA325 (n = 172), CGGA693 (n = 420), Rembrandt (n = 123), and Gravendeel (n = 116) were included in our study. Consistently, the MRGPI-high group had a significantly decreased OS and PFI (Figure S7B-G), indicating that the MRGPI-high robustly predicted an unfavorable outcome of LGG.

Molecular underpinnings associated with MRGPI-based group

Then, the molecular underpinnings underlying the MRGPI were explored. GSEA analysis revealed an enrichment of the ME subtype in the MRGPI-high group (Figure 3A; Supplementary Table 2), which accounted for approximately 72% of the MRGPI-high group. Besides, the MRGPI-high group had activated immune response and altered fatty acid and glucose metabolism (FDR-q < 0.1). On the other hand, the MRGPI-low group had enriched PN subtype gene signature and significant alterations in cell cycle-related signaling pathways. Dysregulated fatty acid metabolism is associated with the biosynthesis of eicosanoids and derivatives and has profound impacts on the immunological features of the TME (39, 40). In terms of the expression pattern of genes involved in eicosanoid metabolism, ALOX5, ALOX5AP, ALOX15B, PTGS1/2, and TBXAS1 were significantly upregulated in the MRGPI-high group (Figure 3B), implying an association between the immune response and the activated eicosanoid metabolic pathways in the MRGPI-high group. Furthermore, in the multivariate regression analysis, the expression of ALOX5 and ALOX5AP was proportional to the MRGPI, whereas the opposite was true for ALOX15B (Figure 3C). Therefore, these results highlighted that the LOX pathway, especially ALOX and ALOX5AP may play a role in the TME of the MRGPI-high group.

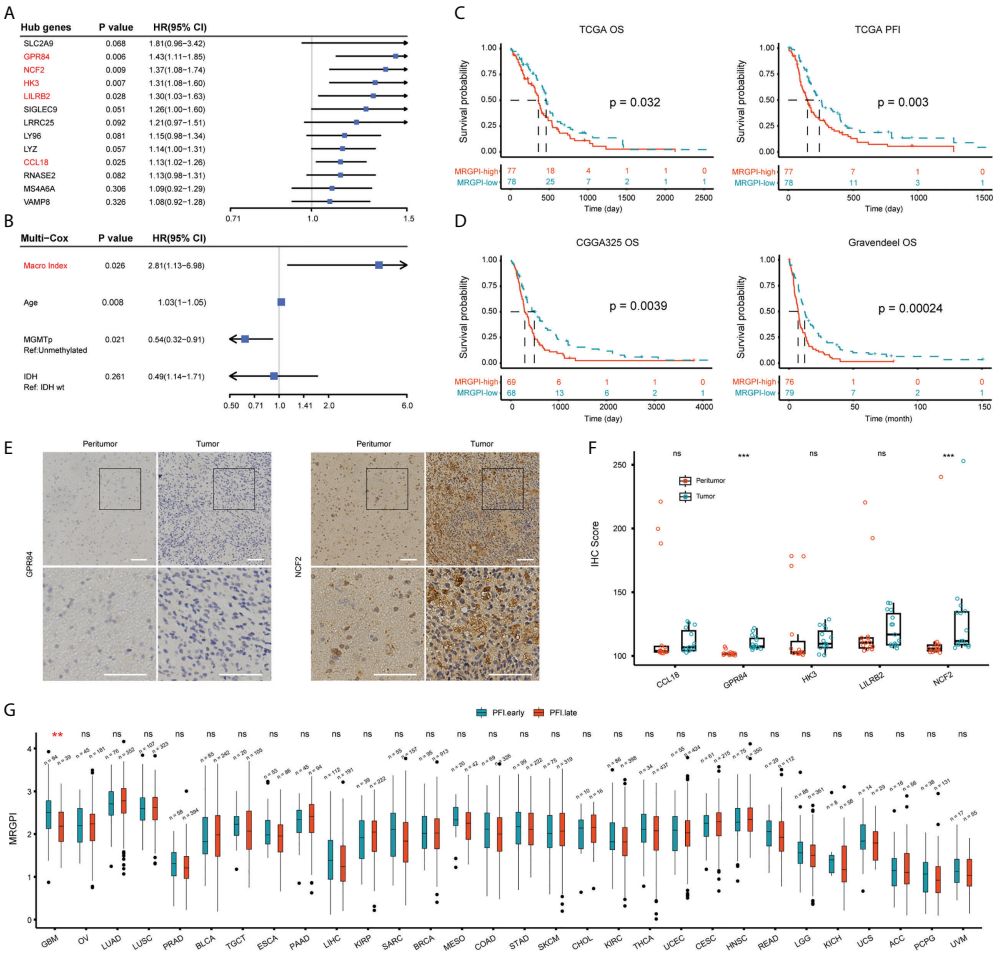

FIGURE 2
Prognostic significance of MRGPI-based groups. **(A)** Multivariate Cox regression analysis of 13 differentially expressed macrophage-related hub genes. **(B)** Cox regression analysis of the MRGPI and clinicopathological parameters based on the TCGA cohort. Covariates including age, gender, IDH mutation, ATRX mutation, MGMT promoter methylation status, TERT promoter mutation, and MRGPI were included in the initial univariate Cox regression. Covariates with p-values less than 0.01 were further included in the multivariate Cox model. **(C, D)** K-M analysis of the survival and tumor progression-free interval differences between MRGPI-based groups based on TCGA, CGGA325, and Gravendeel GBM cohorts. **(E, F)** Immunohistochemical staining of five genes at the protein level. The tissue was divided into core of the tumor (Tumor) and the margin containing infiltrating tumor cells (Peritumor) in three patients with a pathological diagnosis of GBM. The intensity of staining for the proteins encoded by these genes at the tissue level ranged from negative to positive, with E showing genes with significantly higher IHC scores in the tumor core. The IHC scores of the five genes were shown in F (Scale bar, 100μm). **(G)** Pan-cancer-based MRGPI prognostic significance. Samples were split into early (PFI < 6 months) and late (PFI > 12 months) relapse groups based on PFI. OV, Ovarian serous cystadenocarcinoma; LUAD, Lung adenocarcinoma; LUSC, Lung squamous cell carcinoma; PRAD, Prostate adenocarcinoma; BLCA, Bladder urothelial carcinoma; TGCT, Testicular germ cell tumors; ESCA, Esophageal carcinoma; PAAD, Pancreatic adenocarcinoma; LIHC, Liver hepatocellular carcinoma; KIRP, Kidney renal papillary cell carcinoma; SARC, Sarcoma; BRCA, Breast invasive carcinoma; MESO, Mesothelioma; COAD, Colon adenocarcinoma; STAD, Stomach adenocarcinoma; SKCM, Skin cutaneous melanoma; CHOL, Cholangiocarcinoma; KIRC, Kidney renal clear cell carcinoma; THCA, Thyroid carcinoma; UCEC, Uterine corpus endometrial carcinoma; CESC, Cervical squamous cell carcinoma and endocervical adenocarcinoma; HNSC, Head and neck squamous cell carcinoma; READ, Rectum adenocarcinoma; LGG, Lower grade glioma; KICH, Kidney chromophobe; UCS, Uterine carcinosarcoma; ACC, Adrenocortical carcinoma; PCPG, Pheochromocytoma and paraganglioma; UVM, Uveal melanoma. ***p < 0.001. ns, non significant.

Immune characteristics associated with MRGPI

To characterize the TME of GBM, the CIBERSORT algorithm was employed to estimate the fraction of 22 immune infiltrations. 13 types of immune cells were retained after excluding cells with 0 value over half of the samples. As expected, the MRGPI-high group had significantly increased infiltration of monocyte, M2 macrophage, as well as Treg, NK cell (resting), and neutrophil (Figure 4A). Monocytes/macrophages in the TME are functionally pleiotropic and plastic (10). To further explore the association between MRGPI and the functional state of monocytes/macrophages, scRNA-seq

TABLE 1 Clinical features associated with MRGPI.

	MRGPI-high	MRGPI-low	p-value
Age			
>= 60	40 (54.79%)	38 (49.35%)	
< 60	33 (45.21%)	39 (50.65%)	0.518
Gender			
Male	47 (64.38%)	53 (68.83%)	
Female	26 (35.62%)	24 (31.17%)	0.606
IDH status			
Mutation	3 (4.2%)	8 (10.96%)	
Wildtype	69 (95.83%)	65 (89.04%)	0.208
MGMT promoter			
Methylated	17 (32.08%)	30 (46.88%)	
Unmethylated	36 (67.92%)	34 (53.13%)	0.131
Transcriptome subtype			
ME	51 (71.83%)	12 (19.05%)	
PN	3 (4.23%)	15 (23.81%)	
CL	13 (18.31%)	33 (52.38%)	
NE	4 (5.63%)	3 (4.76%)	8.876E-10

ME, mesenchymal; PN, proneural; CL, classical; NE, neural.

dataset GSE131928 was employed in our study. As a result, 4 types of cells including malignant cell, Mono/Macro cell, CD8 T cell, and other unclassified cells were identified (Supplementary Figure 8; Supplementary Table 3). MRGPI was calculated based on the expression profile of the Mono/Macro (n = 3236) subcluster and GSEA analysis found the enrichment of inflammation, immunosuppression, and altered fatty acid and glucose metabolic signaling pathways in the MRGPI-high group of the Mono/Macro cells (FDR-q < 0.1)(Figure 4B, Supplementary Table 2), corroborating the results of the bulk-tumor level. The ribosome-related signaling pathways and cellular response to starvation were top enriched in the MRGPI-low group. In addition, cells in the Mono/Macro subcluster were further divided into high, medium, and low groups by the MRGPI. The expression of CD40, CD163, andMSR1 (CD204) was significantly increased in the MRGPI-high group (Figure 4C), indicating that MRGPI-high was associated with the alternative activation of macrophages. At the bulk-tumor level, multivariate regression analysis found a significant positive correlation between MRGPI and the fraction of M2 macrophages (Figure 4D), validating the association between MRGPI and alternative activation of TAMs in GBM TME.

Expression of immune checkpoints associated with MRGPI

TAMs are known sources of immune checkpoints in TME, which contributes to the dysfunction of tumor-infiltrating CD8

TABLE 2 Cox regression analysis of the MRGPI in validation data sets.

Cohort	Type	Sample size	Covariates	Uni-Cox			Multi-Cox		
				HR	CI95	P value	HR	CI95	P value
TCGA	RNA-seq	n = 156	Age, Gender, IDH mutation, ATRX mutation, TERT promoter mutation, MGMT promoter methylation	2.75	1.40-5.38	0.003	2.81	1.13-6.98	0.026
CGGA325	RNA-seq	n = 139	Age, Gender, IDH mutation, MGMT promoter methylation, Primary/Recurrent,1p19q co-deletion	1.87	1.26-2.78	0.002	2.07	1.36-3.17	0.001
CGGA693	RNA-seq	n = 249	Age, Gender, IDH mutation, MGMT promoter methylation, Primary/Recurrent,1p19q co-deletion	1.20	0.87-1.66	0.275	NA	NA	NA
Gravendeel	Microarray	n = 159	Age, Gender, EGFR amplification, IDH1 mutant	2.48	1.55-3.98	2e-4	2.16	1.05-4.41	0.036
Rembrandt	Microarray	n = 181	Age, Gender, 1p19q co-deletion	1.04	0.43-2.52	0.93	NA	NA	NA

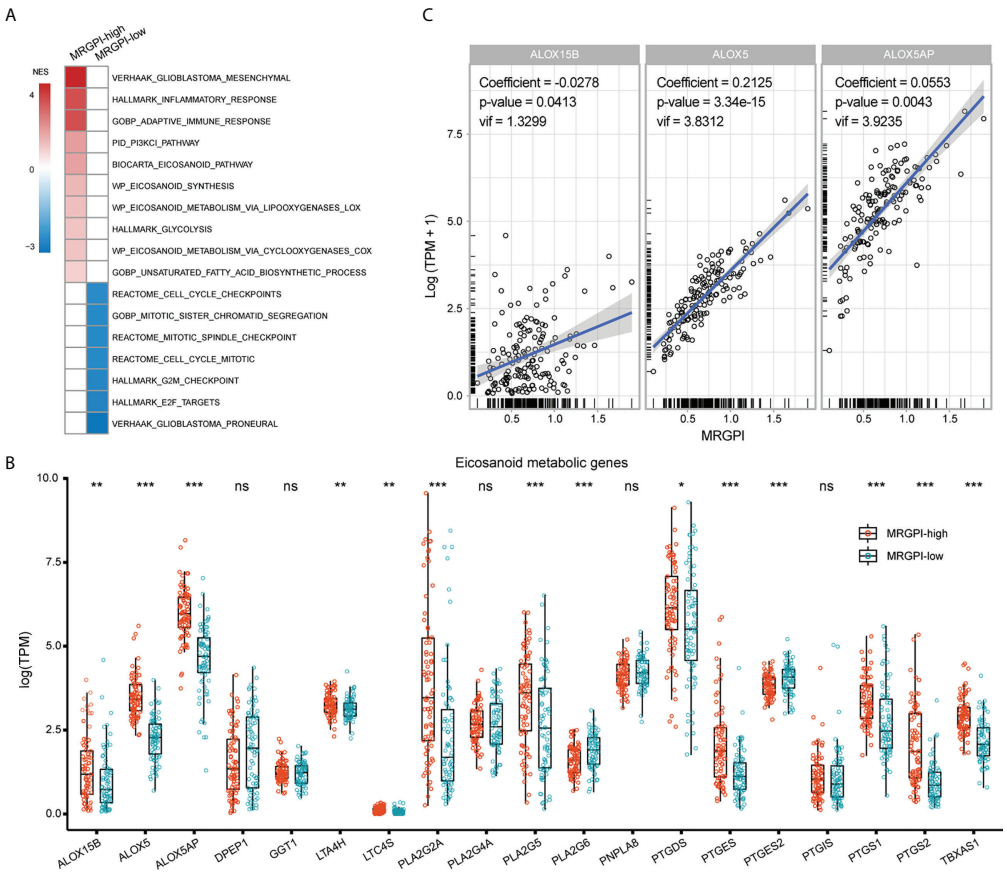

FIGURE 3
Molecular underpinnings associated with the MRGPI-based groups. **(A)** GSEA analysis of signaling pathways enriched in each group. Pathways of interest with FDR-q < 0.1 were exhibited. The color of the box was proportional to the NES. **(B)** The expression pattern of genes involved in the eicosanoid metabolic pathway between groups. **(C)** Multivariate Cox regression analysis of genes involved in the eicosanoid pathway for the estimation of their correlation with the MRGPI. *p < 0.05, **p < 0.01, ***p < 0.001. ns, non significant.

T cells and frustration of anti-tumor immunity (12, 41). We first explored the expression pattern of immune checkpoints between groups. As a result, the expression of PD-L1, PD-L2, TIM3, and CTLA4 was significantly upregulated in the MRGPI-high group (Figure 5A), and the expression of these genes was positively correlated with the faction of M2 macrophages in the multivariate regression model, except for PD-L1 (Figure 5B). On a pan-cancer scale, the MRGPI was positively correlated with the PD-L2 and TIM3, whether in cancers that lack lymphocyte infiltration (ACC and UVM) or that are lymphocyte-rich (LUAD and LUSC) (Figure 5C). To further demonstrate, the scRNA-seq dataset GSE70630 was included and 3 types of cells were identified, including malignant cells, Mono/Macro, and other cells (mainly oligodendrocyte) (Supplementary Figure 9, Supplementary Table 4). At single-cell resolution, the expression of PD-L1, PD-L2, and TIM3 was predominantly located at the Mono/Macro subcluster (Figure 5D). Together, the MRGPI-based group identified a subset of GBM with increased expression of immune checkpoints in the TME, which may be associated with the M2 macrophages.

Prediction of ICI responsiveness by MRGPI

Lastly, we evaluated the association between MRGPI and GBM responsiveness to ICI. There are published studies on tumor evasion and T-cell function, in which key genes have been screened and collated by Peng et al. (Supplementary Table 5) (37, 42–45). Briefly, the positive or negative hits are defined as genes upregulated or downregulated in the shRNA screen. We analyzed the association of the positive and negative hit genes with MRGPI using the spearman correlation test and rho instead of Peng et al. using the Cox-ph model test and d values. As a result, MRGPI had

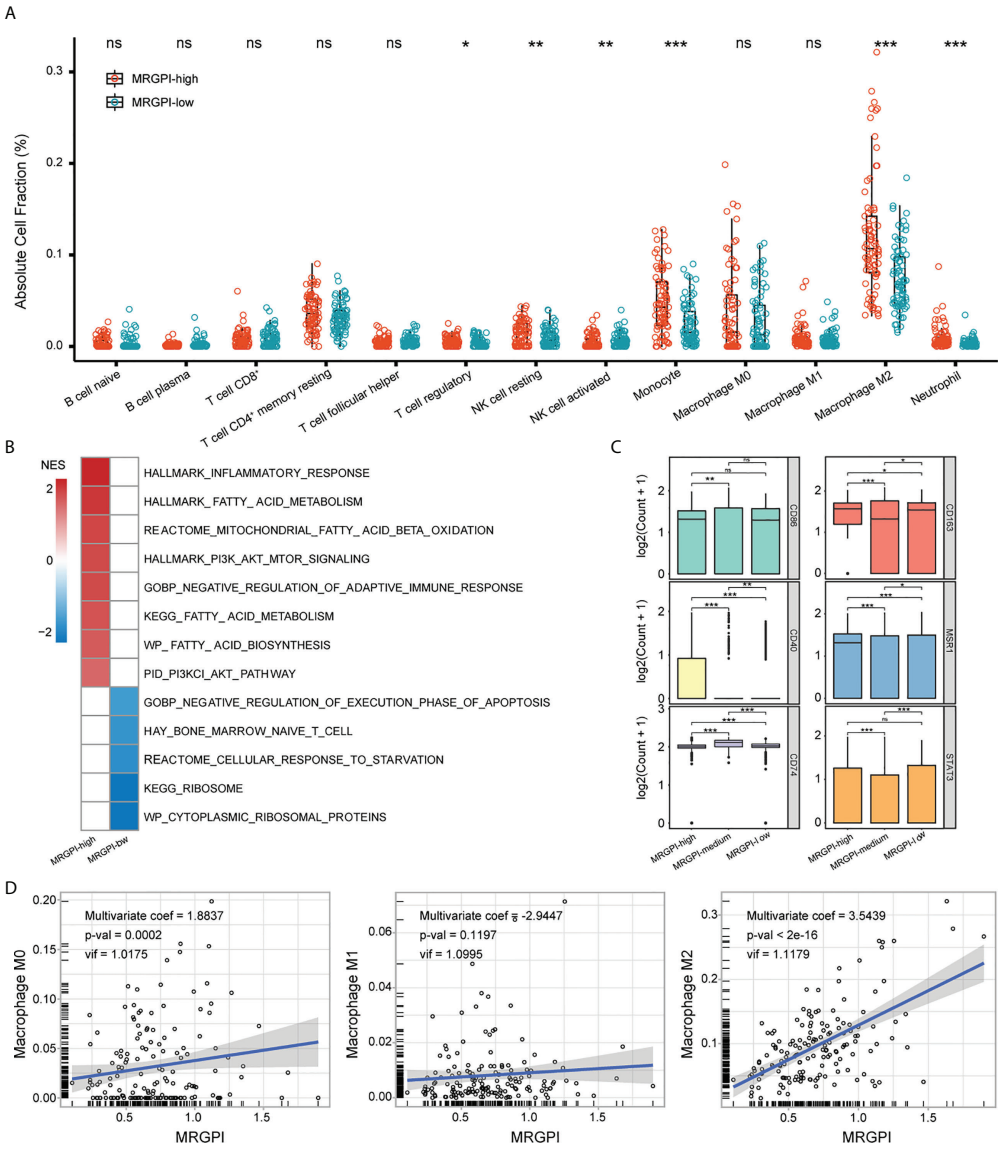

FIGURE 4
Immune characteristics of MRGPI groups. **(A)** The fraction of immune infiltration was estimated by CIBERSORT. **(B)** GSEA analysis of pathways enriched in each group based on the expression profile of the Mono/Macro subcluster. Pathways with FDR-q < 0.1 were exhibited. The color (red or blue) was proportional to the NES of the corresponding pathway in MRGPI-high or -low groups. **(C)** The expression of macrophage biomarkers in MRGPI-based groups. Mono/Macro subcluster was split into -high, -medium, and -low groups by the MRGPI. **(D)** Correlation between the MRGPI and different macrophages at the bulk-tumor level. *p < 0.05, **p < 0.01, ***p < 0.001. ns, non significant.

a significantly increased correlation with genes that are functionally related to T cell exhaustion, T regulatory cell, and ICB resistance (anti-CTLA4) (Figure 6A). The ROC curves indicated that the MRGPI gave the best performance in predicting T regulatory and ICB resistance (anti-CTLA4 treatment) genes (Figure 6B), indicating the association between MRGPI and T cell dysfunction. TIDE dysfunction score is associated with T cell dysfunction for lymphocyte-rich tumors and the prevention of T cell infiltration for lymphocyte-poor tumors at transcriptome level (37). As a result, the MRGPI-high group had a significantly decreased TIDE score (Figure 6C). Given that GBM is a kind of tumor lacking lymphocytic infiltration, a reduced TIDE score may indicate that the MRGPI-high group is less efficient at suppressing local antitumor immune responses by impeding T cell infiltration. Meanwhile, the TIS score was an mRNA metric associated with interferon gamma-mediated PD-1 signaling that was also

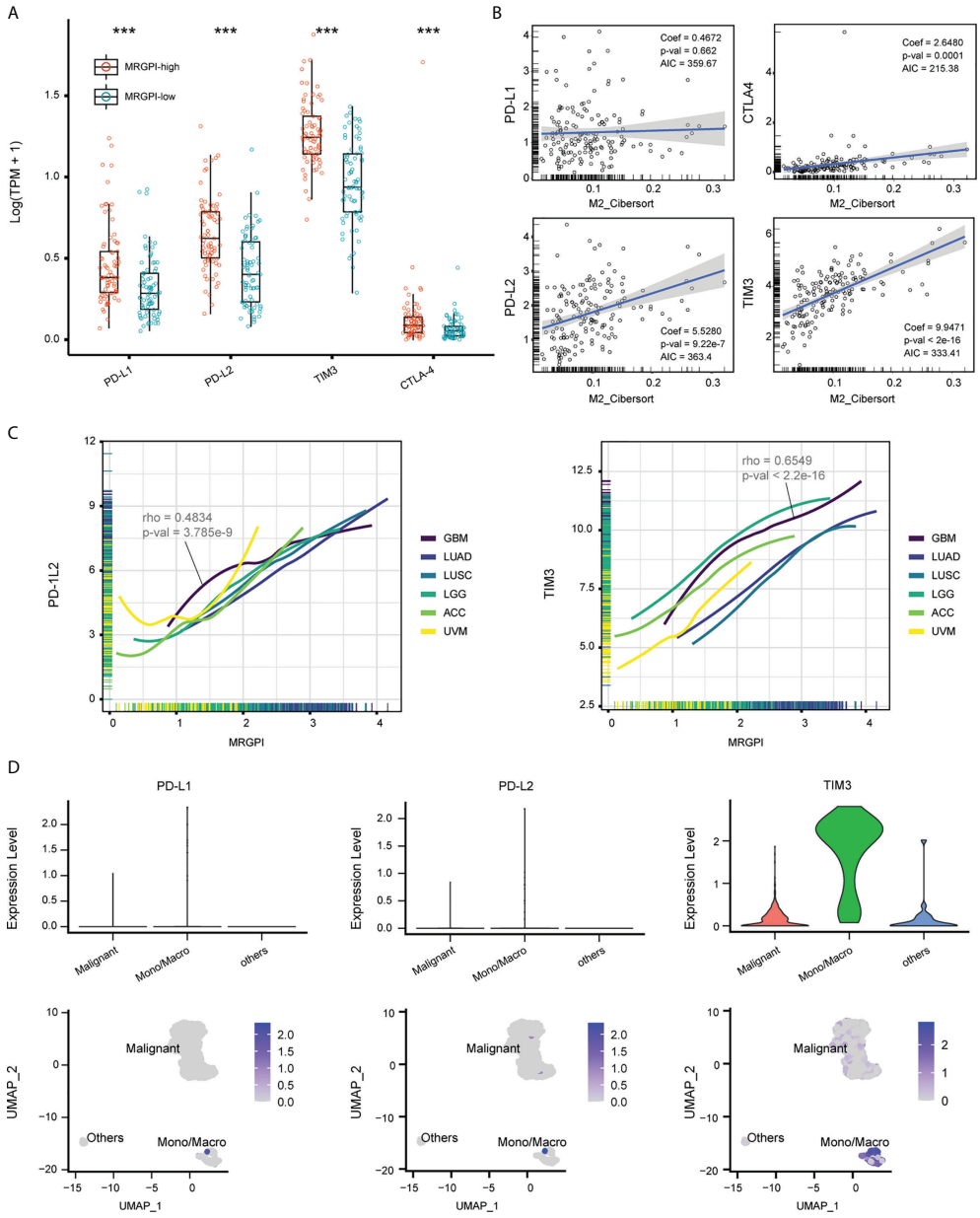

FIGURE 5
Expression of immune checkpoints associated with MRGPI. **(A)** The expression of PD-L1/2, TIM3, and CTLA-4 based on the TCGA cohort. **(B)** Multivariate regression analysis estimating the association between the expression of immune checkpoints and M2 macrophage faction. **(C)** Association between MRGPI and expression of PD-L2 and TIM3 on a pan-cancer scale. ACC and UVM that had sterile lymphocyte infiltration and LUAD and LUSC that had abundant lymphocyte infiltration were used as references. ACC, Adrenocortical carcinoma; UVM, Uveal Melanoma; LUAD, Lung adenocarcinoma; LUSC, Lung squamous cell carcinoma. **(D)** The expression of PD-L1/2 and TIM3 at a single-cell resolution based on GSE70630.

associated with sample response to ICI (46). We found that the MRGPI-high group had significantly increased TIS scores, and a robust correlation was found between the MRGPI and TIS score (univariate regression coef = 0.936) (Figure 6D, E). Then, we employed the submap algorithm to classify sample responsiveness to PD-1 and CTLA4 inhibitors, with reference to a cohort of cutaneous melanomas treated with ICI inhibitors (47). With the 3 GBM cohorts corroborating each other, the MRGPI-high group showed potential responsiveness to anti-PD1 treatment (FDR-q < 0.01) (Figure 6F). Therefore, these results suggested that blocking the PD1/PD-L1 axis may be applicable to the MRGPI-high group.

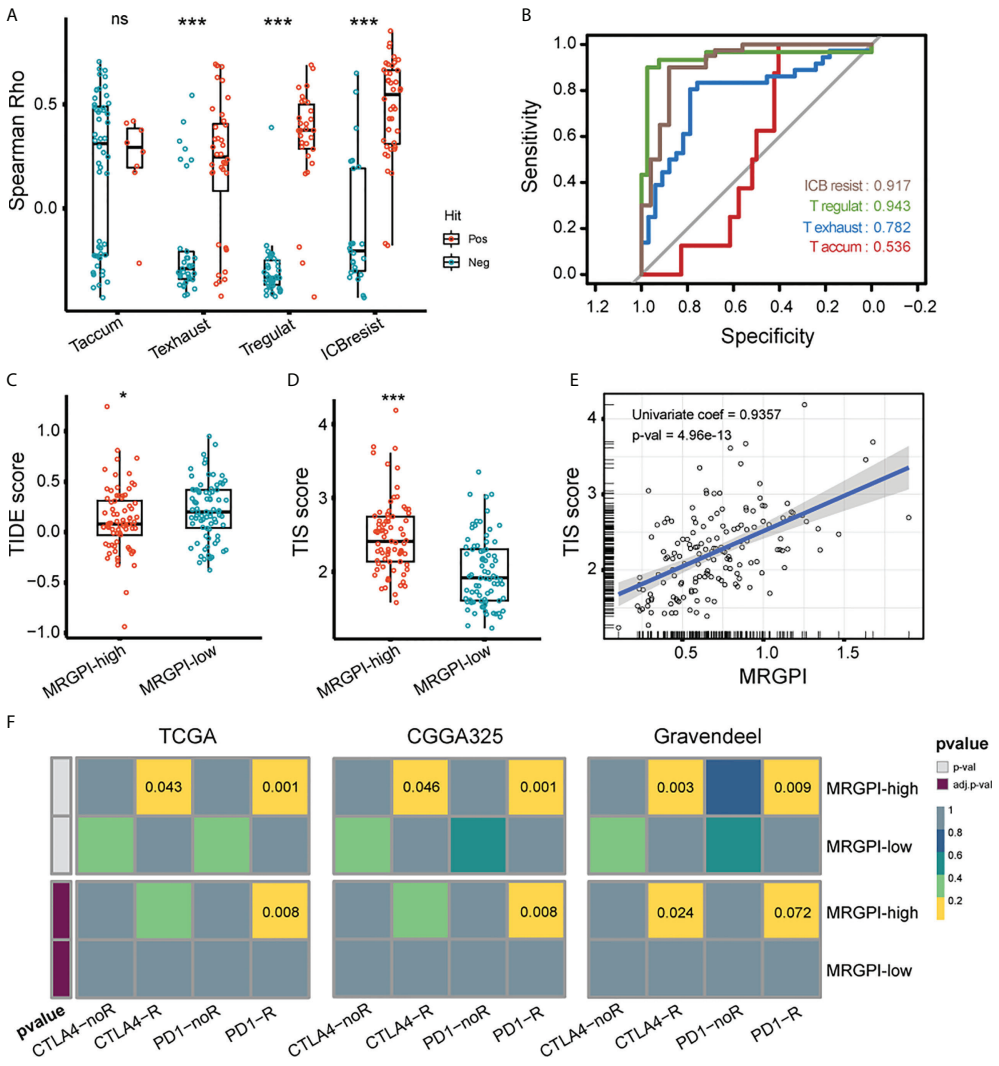

FIGURE 6
Potential of MRGPI in predicting ICB responsiveness. **(A)** Association between MRGPI and T cell dysfunction-related genes. To achieve this, 4 published gene signatures related to T cell dysfunction were collected and screened. The Spearman rho of positive (red) and negative (green) hit genes with MRGPI was exhibited. The difference in rho between positive and negative groups was compared through the two-sided Wilcoxon test. Taccum, T cell accumulation; Texhaust, T cell exhaustion; Tregulat, regulatory T cell; ICBresist, ICB resistance. **(B)** ROC curves evaluating the performance of MRGPI in predicting the positive and negative hit gene associated with T cell function. **(C)** TIDE score between the MRGPI-high and -low groups. **(D)** TIS score between the MRGPI-high and -low groups. **(E)** Correlation between the MRGPI and TIS score. **(F)** Submap algorithm manifested association between MRGPI-based groups and sample responsiveness to PD-1 and CTLA4 inhibitors. ***p < 0.001. ns, non significant.

Discussion

A great deal of research is currently dedicated to improving the treatment of GBM, and the efficacy of ICIs, although remains limited, is still a promising treatment modality. Given that the overall response rate of GBM to ICI remains dismal, it is crucial to determine who will benefit from the therapy. Several studies are devoted to develop biomarkers related to the prognosis and treatment effecacy of GBM from a tumor ontology or TME perspective, but the results are not yet satisfactory (48). Recent transcriptome-based achievements in immunophenotyping of gliomas and transcriptomic characterization of macrophage polarization provide the basis for screening genetic metrics of clinical implication from TAMs.

TAMs are the main immune cells in the GBM microenvironment, accounting for up to 30% or more of the tumor tissue, and are decisive for several endowments of the TME (49). The role of TAMs in remodeling the extracellular matrix through MMPs and in inducing angiogenesis through the production of VEGF/EGF is well-documented (10, 50). With the rise of immunotherapy, the immunological features of the TME have received increasing attention and thus driven the understanding of

how TAMs abet the immunosuppressive TME (11, 51). Previous studies have reported the role of the PI3K-Akt-mTOR signaling pathway in promoting tumor cell proliferation and rewiring tumor metabolism (40). In terms of microglia, mTOR-mediated activation of STAT3 and NK-κB is associated with an immunosuppressive phenotype. Inhibition of mTOR then promoted an inflammatory microenvironment and the proliferation of $CD4^+$ and $CD8^+$ T cells (11). In addition, the PI3K/Akt signaling pathway has been associated with dysregulation of lipid metabolism. The rewired lipid metabolism is associated with the hydrolysis of arachidonic acid from the membrane, and the production of bioactive eicosanoid derivatives such as PGE_2 and LTB_4 (40, 52). TAMs are responsible for the production of such inflammatory response mediators in the TME (39). Notably, TAMs are involved in the dysfunction of CD8 T cells by expressing multiple immune checkpoints and the induction of other cells in the TME in expressing immune checkpoints (13, 15). On this basis, we consider that the construction of gene signatures associated with TAMs may also be useful for immunotherapy. There are two concerns, however. The measurement of immune checkpoints from mRNA expression levels alone may be inadequate, and future studies should take into account the tissue and cellular localization of immune checkpoints. As well, the M1 and M2 typing of TAMs is oversimplistic (53), and identifying subtypes of TAMs that specifically express immune checkpoints would promote precision oncology.

MRGPI is composed of 5 genes, including GPR84, NCF2, HK3, LILRB2, and CCL18. G protein-coupled receptor 84 (GPR84) is a receptor for medium-chain free fatty acids with carbon chain lengths of C9 to C14 (54). It is mainly expressed by monocytes, macrophages, and neutrophils and promotes inflammatory responses by activating ERK and elevating levels of intracellular Ca^{2+} and IP (55). Inflammatory colon tissue from patients who suffered from ulcerative colitis is filled with large numbers of GPR84-positive macrophages, whose involvement in the inflammatory response may depend on the activation of NLRP3 inflammasome (56). Neutrophil cytoplasmic factor 2 (NCF2) encodes a subunit of the multi-protein NADPH oxidase complex, which is involved in the bursting of superoxide in neutrophils. Single nucleotide polymorphisms in NCF2 are associated with diminished NADPH oxidase activity, which in turn is involved in the pathogenesis of systemic lupus erythematosus (57). In addition, Wang et al. identified that NCF2 was associated with poor prognosis in GBM by WGCNA analysis (58). Xu et al. reported that the inhibition of glioma cell growth by miR-524 was achieved by targeting NCF2 (59). Hexokinase 3 (HK3) phosphorylates glucose to produce glucose-6-phosphate, which is then imported into the glucose metabolic pathway. In non-small cell lung cancer, HK3 expression correlates with immune cell infiltration and tumor sensitivity to Pembrolizumab (60). In addition, HK3 overexpression also promotes prostate cancer, acute myeloid lymphoblastic leukemia, and colon tumors (61–63). Leukocyte immunoglobulin-like receptor B2 (LILRB2) is a member of the leukocyte immunoglobulin-like receptor (LIR) family and encodes a protein that belongs to the B subfamily of LIR receptors. One ligand for LILRB2 is HLA-G. The level of serum soluble HLA-G is negatively associated with survival of glioma patients (64). Previous study haa highlighted the function of HLA-G in promoting immune escape from tumors, but the exact mechanism has not been elucidated (65). Our results suggested that HLA-G may regulate the function of TAMs in GBM *via* binding to LILRB2. C-C motif chemokine ligand 18 (CCL18) encodes the cytokine CCL18 which has bactericidal and T lymphocyte chemotactic effects. CCL18 promotes the invasion and epithelial-mesenchymal transition of a variety of tumor cells, including squamous skin cancer, breast cancer and liver cancer, through interaction with its receptor PITPNM3 (66, 67). A recent study indicate that CCL18 derieved from TAMs are vital in promoting glioma progression. GBM releases extracellular vesicles containing CCL18 to allow surrounding tumor cells to acquire resistance to temozolomide (68). Notably, in addition to being expressed at the mRNA level and having functional implications, proteins encoded by these genes showed a tendency to be differentially expressed between tumor core and margin. Through immunohistochemical staining, we found that the proteins encoded by GPR84 and NCF2 were significantly increased in tumor core, further suggesting a pro-tumoral role of these genes. However, more samples were needed in future study. Taken together, MRGPI is a prognostic marker associated with the inflammatory response mediated by TAMs.

TME is a sophisticated multi-cellular collaborative system. In the central nervous system, the GBM microenvironment is unique due to the presence of the brain-blood barrier, the type and number of resident immune cells, the type of extracellular matrix, and the specific immunological properties of brain tissue (49, 69). When exploring the association between the MRGPI-based group and immune infiltration in the GBM microenvironment, we found that the MRGPI-high group contained more immune cells involved in the inflammatory response, including monocytes, M2 type macrophages, and neutrophils, while there was little difference in the content of lymphocytes associated with the adaptive immune response. The type of inflammatory response affects the growth of tumor cells, and it is generally accepted that acute inflammatory responses have an overall inhibitory effect on tumor cells, but chronic inflammatory responses promote malignancies (70, 71). However, the toxic effects of inflammation on neurons would be very similar, i.e. inducing demyelination and death of these cells (49). In addition, as the volume of the cranial cavity is limited, edema and increased intracranial pressure caused by a strong or persistent inflammatory response can be fatal (72, 73). These features of the central nervous system may hinder the application of immunotherapies: the immune response cannot be enhanced indefinitely but should be kept within a tolerable range. Determining such a range should take into account individual factors, including gender, age, the fullness of brain tissue on imaging, and neurological function. This may suggest that, in addition to the development of biomarkers to predict the sensitivity of GBM patients to immunotherapy, markers to

predict the upper limit of patients' tolerance to immune responses are also needed.

In characterizing the molecular mechanisms associated with the MRGPI-based group, we found increased eicosanoid metabolic response activity in the MRGPI-high group, particularly in the leukotriene metabolic pathway. Leukotrienes are derived from the processing of arachidonic acid by lipoxygenases and the end products include LTA_4, LXA_4, LTB_4, and LTC_4 (74). The origin of leukotrienes in inflammation is complex and can be produced by a single cell with an entire enzyme system or by multiple cells working in collaboration (74, 75). Similar to prostaglandins, leukotrienes are undoubtedly potent inflammatory factors involved in the development and progression of asthma, rheumatoid arthritis, and age-related central nervous system disorders (76). However, their role in tumors remains controversial. LTB_4-mediated chronic inflammation contributed to the growth of transplanted melanoma and blocking LTB_4 partially inhibited such effect. Interestingly, it was not the well-known pro-tumoral COX-1/2 that promoted tumor cell proliferation in this model (77). Jung Yeon Lim et al. reported that *in vitro* interference with 5-LO or FLAP expression using MK886 or siRNA induced apoptosis of glioma cells, suggesting a role for leukotrienes in promoting glioma proliferation (78). In TME, a range of 5-LO expressing stromal and immune cells have also been found to promote tumor metastasis, recruit other inflammatory cells, and create a chronic inflammatory response to accelerate tumor progression (79). Therefore, prohibiting leukotrienes, especially LTB_4, may be promising for both targeting GBM cells and TME.

The TIDE score is an integrated metric evaluating T cell dysfunction in tumors with high cytotoxic T lymphocyte infiltration and the inhibitory of T cell infiltration in tumors with low cytotoxic T lymphocyte infiltration and is a valid marker in predicting ICI benefits (37). Samples with increased TIDE scores have a higher potential for immune evasion, indicating that they are less likely to benefit from ICI (37). However, the original study found that GBM lacks genes that interact with the CD8 T cell mRNA metric in the Cox-ph model, which may reduce the effectiveness of TIDE for GBM. Besides, the TIS score consists of 18 genes associated with interferon-gamma. As interferon-gamma upregulates PD-L1 *via* the JAK-STAT pathway, the TIS score is also a highly effective prognostic and predictive marker for ICI benefit in pan-cancer analysis (46, 80). In our study, no significant differences in the level of lymphocyte infiltration emerged between MRGPI groups, but significant differences in the expression of immune checkpoints were found, suggesting that MRGPI may distinguish between GBM samples that avoid immune attack *via* the immune checkpoint pathway. Such a presumption would also fit with the TIS score assuming the presence of an activated but suppressed adaptive immune response in the tumor sample. To further validate these results, we employed a subclass mapping method algorithm to categorize GBM samples according to the expression profile of cutaneous melanoma and the corresponding responsiveness to ICI treatment, and the results again supported the sensitivity of the MRGPI-high group to PD1 blockade treatment. Therefore, although GBM is a 'cold tumor' with low immune cell infiltration and the CNS is compatible with multiple immunosuppressive mechanisms, MRGPI is still a potential marker that identifies a class of GBM characterized by immune checkpoint-mediated immunosuppression.

In conclusion, MRGPI is a promising prognostic biomarker. The MRGPI-based group may help to differentiate immunological features and serve as a potential response indicator for immunotherapy.

Data availability statement

Datasets included in this study can be found on the website described in the material and methods, and they can be acquired from the corresponding authors upon reasonable request.

Ethics statement

The studies involving human participants were reviewed and approved by The Ethics Committee of the Ethics Committee of Zhejiang Provincial People's Hospital. The patients/participants provided their written informed consent to participate in this study.

Author contributions

HJ and ZL conceived and designed the study. HJ collected and analysed the data and generated the figures. HJ drafted the manuscript. ZL and HS revised the manuscript. NW provided analytical support. FW and YL conducted the immunohistochemical staining. CY, SH, and YL supervised the study. All authors contributed to the article and approved the submitted version.

Funding

This work is funded by Zhejiang Provincial People's Hospital Talent Introduction Project (No. C-2021-QDJJ03-01)

Acknowledgments

We thank Miss Zhou Jie and Mr. Zhang Jing for providing additional statistical support.

Conflict of interest

The authors declare that the research was conducted in the absence of any commercial or financial relationships that could be construed as a potential conflict of interest.

Publisher's note

All claims expressed in this article are solely those of the authors and do not necessarily represent those of their affiliated organizations, or those of the publisher, the editors and the reviewers. Any product that may be evaluated in this article, or claim that may be made by its manufacturer, is not guaranteed or endorsed by the publisher.

Supplementary material

The Supplementary Material for this article can be found online at: https://www.frontiersin.org/articles/10.3389/fimmu.2022.941556/full#supplementary-material

References

1. Tan AC, Ashley DM, Lopez GY, Malinzak M, Friedman HS, Khasraw M. Management of glioblastoma: State of the art and future directions. *CA Cancer J Clin* (2020) 70(4):299–312. doi: 10.3322/caac.21613

2. Jiang T, Mao Y, Ma W, Mao Q, You Y, Yang X, et al. CGCG clinical practice guidelines for the management of adult diffuse gliomas. *Cancer Lett* (2016) 375 (2):263–73. doi: 10.1016/j.canlet.2016.01.024

3. P JR, L N, OC CJ, B AA, M J, P C, et al. Short-course radiation plus temozolomide in elderly patients with glioblastoma. *New Engl J Med* (2017) 376:1027–37. doi: 10.1056/NEJMoa1611977

4. Adams S, Loi S, Toppmeyer D, Cescon D, De Laurentiis M, Nanda R, et al. Pembrolizumab monotherapy for previously untreated, PD-L1–positive, metastatic triple-negative breast cancer: Cohort b of the phase 2 KEYNOTE-086 study. *Ann Oncol* (2019) 30:405–11. doi: 10.1093/annonc/mdy518

5. Borghaei H, Paz-Ares L, Horn L, Spigel D, Steins M, Ready N, et al. Nivolumab versus docetaxel in advanced nonsquamous non–Small-Cell lung cancer. *New Engl J Med* (2015) 373:1627–39. doi: 10.1056/NEJMoa1507643

6. Brahmer J, Reckamp K, Baas P, Crinò L, Eberhardt W, Poddubskaya E, et al. Nivolumab versus docetaxel in advanced squamous-cell non–Small-Cell lung cancer. *New Engl J Med* (2015) 373:123–35. doi: 10.1056/NEJMoa1504627

7. Weber JS, D'Angelo SP, Minor D, Hodi FS, Gutzmer R, Neyns B, et al. Nivolumab versus chemotherapy in patients with advanced melanoma who progressed after anti-CTLA-4 treatment (CheckMate 037): a randomised, controlled, open-label, phase 3 trial. *Lancet Oncol* (2015) 16(4):375–84. doi: 10.1016/S1470-2045(15)70076-8

8. Cloughesy TF, Mochizuki AY, Orpilla JR, Hugo W, Lee AH, Davidson TB, et al. Neoadjuvant anti-PD-1 immunotherapy promotes a survival benefit with intratumoral and systemic immune responses in recurrent glioblastoma. *Nat Med* (2019) 25(3):477–86. doi: 10.1038/s41591-018-0337-7

9. F AC, H M, D. M. Recurrent glioma clinical trial, CheckMate-143: the game is not over yet. *Oncotarget* (2017) 8:91779–94. doi: 10.18632/oncotarget.21586

10. Broekman ML, Maas SLN, Abels ER, Mempel TR, Krichevsky AM, Breakefield XO. Multidimensional communication in the microenvirons of glioblastoma. *Nat Rev Neurol* (2018) 14(8):482–95. doi: 10.1038/s41582-018-0025-8

11. Dumas AA, Pomella N, Rosser G, Guglielmi L, Vinel C, Millner TO, et al. Microglia promote glioblastoma *via* mTOR-mediated immunosuppression of the tumour microenvironment. *EMBO J* (2020) 39(15):e103790. doi: 10.15252/embj.2019103790

12. Andersen JK, Miletic H, Hossain JA. Tumor-associated macrophages in gliomas-basic insights and treatment opportunities. *Cancers (Basel)* (2022) 14 (5):1319. doi: 10.3390/cancers14051319

13. Fierro JJr., DiPasquale J, Perez J, Chin B, Chokpapone Y, Tran AM, et al. Dual-sgRNA CRISPR/Cas9 knockout of PD-L1 in human U87 glioblastoma tumor cells inhibits proliferation, invasion, and tumor-associated macrophage polarization. *Sci Rep* (2022) 12(1):2417. doi: 10.1038/s41598-022-06430-1

14. Tu C, Wang Z, Xiang E, Zhang Q, Zhang Y, Wu P, et al. Human umbilical cord mesenchymal stem cells promote macrophage PD-L1 expression and attenuate acute lung injury in mice. *Curr Stem Cell Res Ther* (2022) 17 (6):564–75. doi: 10.2174/1574888X17666220127110332

15. Vitale I, Manic G, Coussens LM, Kroemer G, Galluzzi L. Macrophages and metabolism in the tumor microenvironment. *Cell Metab* (2019) 30(1):36–50. doi: 10.1016/j.cmet.2019.06.001

16. Thorsson V, Gibbs DL, Brown SD, Wolf D, Bortone DS, Ou Yang TH, et al. The immune landscape of cancer. *Immunity* (2018) 48(4):812–30.e14. doi: 10.1016/j.immuni.2018.03.023

17. Sa JK, Chang N, Lee HW, Cho HJ, Ceccarelli M, Cerulo L, et al. Transcriptional regulatory networks of tumor-associated macrophages that drive malignancy in mesenchymal glioblastoma. *Genome Biol* (2020) 21(1):216. doi: 10.1186/s13059-020-02140-x

18. Zhang L, Alizadeh D, Van Handel M, Kortylewski M, Yu H, Badie B. Stat3 inhibition activates tumor macrophages and abrogates glioma growth in mice. *Glia* (2009) 57(13):1458–67. doi: 10.1002/glia.20863

19. Xue J, Schmidt SV, Sander J, Draffehn A, Krebs W, Quester I, et al. Transcriptome-based network analysis reveals a spectrum model of human macrophage activation. *Immunity* (2014) 40(2):274–88. doi: 10.1016/j.immuni.2014.01.006

20. Hume DA, Freeman TC. Transcriptomic analysis of mononuclear phagocyte differentiation and activation. *Immunol Rev* (2014) 262(1):74–84. doi: 10.1111/imr.12211

21. Sun D, Wang J, Han Y, Dong X, Ge J, Zheng R, et al. TISCH: a comprehensive web resource enabling interactive single-cell transcriptome visualization of tumor microenvironment. *Nucleic Acids Res* (2020) 8(49):D1420-30. doi: 10.1101/2020.08.15.251959

22. Wang Q, Hu B, Hu X, Kim H, Squatrito M, Scarpace L, et al. Tumor evolution of glioma-intrinsic gene expression subtypes associates with immunological changes in the microenvironment. *Cancer Cell* (2018) 33(1):152. doi: 10.1016/j.ccell.2017.12.012

23. Ritchie ME, Phipson B, Wu D, Hu Y, Law CW, Shi W, et al. Limma powers differential expression analyses for RNA-sequencing and microarray studies. *Nucleic Acids Res* (2015) 43(7):e47. doi: 10.1093/nar/gkv007

24. Robinson MD, McCarthy DJ, Smyth GK. edgeR: a bioconductor package for differential expression analysis of digital gene expression data. *Bioinformatics* (2010) 26(1):139–40. doi: 10.1093/bioinformatics/btp616

25. Zhou Y, Zhou B, Pache L, Chang M, Khodabakhshi AH, Tanaseichuk O, et al. Metascape provides a biologist-oriented resource for the analysis of systems-level datasets. *Nat Commun* (2019) 10(1):1523. doi: 10.1038/s41467-019-09234-6

26. Langfelder P, Horvath S. WGCNA: an r package for weighted correlation network analysis. *BMC Bioinf* (2008) 9:559. doi: 10.1186/1471-2105-9-559

27. Zhou G, Soufan O, Ewald J, Hancock REW, Basu N, Xia J. NetworkAnalyst 3.0: a visual analytics platform for comprehensive gene expression profiling and meta-analysis. *Nucleic Acids Res* (2019) 47(W1):W234–W41. doi: 10.1093/nar/gkz240

28. Jan CI, Tsai WC, Harn HJ, Shyu WC, Liu MC, Lu HM, et al. Predictors of response to autologous dendritic cell therapy in glioblastoma multiforme. *Front Immunol* (2018) 9:727. doi: 10.3389/fimmu.2018.00727

29. Varghese F, Bukhari AB, Malhotra R, De A. IHC profiler: an open source plugin for the quantitative evaluation and automated scoring of immunohistochemistry images of human tissue samples. *PLoS One* (2014) 9(5): e96801. doi: 10.1371/journal.pone.0096801

30. Subramanian A, Tamayo P, Mootha VK, Mukherjee S, Ebert BL, Gillette MA, et al. Gene set enrichment analysis: a knowledge-based approach for interpreting genome-wide expression profiles. *Proc Natl Acad Sci U.S.A.* (2005) 102(43):15545–50. doi: 10.1073/pnas.0506580102

31. Liberzon A, Birger C, Thorvaldsdottir H, Ghandi M, Mesirov JP, Tamayo P. The molecular signatures database (MSigDB) hallmark gene set collection. *Cell Syst* (2015) 1(6):417–25. doi: 10.1016/j.cels.2015.12.004

32. Steen CB, Liu CL, Alizadeh AA, Newman AM. Profiling cell type abundance and expression in bulk tissues with CIBERSORTx. *Methods Mol Biol* (2020) 2117:135–57. doi: 10.1007/978-1-0716-0301-7_7

33. Hao Y, Hao S, Andersen-Nissen E, Mauck WM3rd, Zheng S, Butler A, et al. Integrated analysis of multimodal single-cell data. *Cell* (2021) 184(13):3573–87.e29. doi: 10.1016/j.cell.2021.04.048

34. Neftel C, Laffy J, Filbin MG, Hara T, Shore ME, Rahme GJ, et al. An integrative model of cellular states, plasticity, and genetics for glioblastoma. *Cell* (2019) 178(4):835–49.e21. doi: 10.1016/j.cell.2019.06.024

35. Tirosh I, Venteicher AS, Hebert C, Escalante LE, Patel AP, Yizhak K, et al. Single-cell RNA-seq supports a developmental hierarchy in human oligodendroglioma. *Nature* (2016) 539(7628):309–13. doi: 10.1038/nature20123

36. Zhang X, Lan Y, Xu J, Quan F, Zhao E, Deng C, et al. CellMarker: a manually curated resource of cell markers in human and mouse. *Nucleic Acids Res* (2019) 47 (D1):D721–D8. doi: 10.1093/nar/gky900

37. Jiang P, Gu S, Pan D, Fu J, Sahu A, Hu X, et al. Signatures of T cell dysfunction and exclusion predict cancer immunotherapy response. *Nat Med* (2018) 24(10):1550–8. doi: 10.1038/s41591-018-0136-1

38. Hoshida Y, Brunet JP, Tamayo P, Golub TR, Mesirov JP. Subclass mapping: identifying common subtypes in independent disease data sets. *PLoS One* (2007) 2 (11):e1195. doi: 10.1371/journal.pone.0001195

39. Wang D, Dubois RN. Eicosanoids and cancer. *Nat Rev Cancer* (2010) 10 (3):181–93. doi: 10.1038/nrc2809

40. He Y, Sun MM, Zhang GG, Yang J, Chen KS, Xu WW, et al. Targeting PI3K/Akt signal transduction for cancer therapy. *Signal Transduct Target Ther* (2021) 6 (1):425. doi: 10.1038/s41392-021-00828-5

41. Malfitano AM, Pisanti S, Napolitano F, Di Somma S, Martinelli R, Portella G. Tumor-associated macrophage status in cancer treatment. *Cancers (Basel)* (2020) 12(7):1987. doi: 10.3390/cancers12071987

42. Zhou P, Shaffer DR, Alvarez Arias DA, Nakazaki Y, Pos W, Torres AJ, et al. *In vivo* discovery of immunotherapy targets in the tumour microenvironment. *Nature* (2014) 506(7486):52–7. doi: 10.1038/nature12988

43. Giordano M, Henin C, Maurizio J, Imbratta C, Bourdely P, Buferne M, et al. Molecular profiling of CD8 T cells in autochthonous melanoma identifies maf as driver of exhaustion. *EMBO J* (2015) 34(15):2042–58. doi: 10.15252/embj.201490786

44. Wakamatsu E, Mathis D, Benoist C. Convergent and divergent effects of costimulatory molecules in conventional and regulatory CD4+ T cells. *Proc Natl Acad Sci U.S.A.* (2013) 110(3):1023–8. doi: 10.1073/pnas.1220688110

45. Twyman-Saint Victor C, Rech AJ, Maity A, Rengan R, Pauken KE, Stelekati E, et al. Radiation and dual checkpoint blockade activate non-redundant immune mechanisms in cancer. *Nature* (2015) 520(7547):373–7. doi: 10.1038/nature14292

46. Ayers M, Lunceford J, Nebozhyn M, Murphy E, Loboda A, Kaufman D, et al. IFN-γ–related mRNA profile predicts clinical response to PD-1 blockade. *J Clin Invest* (2017) 127:2930–40. doi: 10.1172/JCI91190

47. Roh W, Chen PL, Reuben A, Spencer CN, Prieto PA, Miller JP, et al. Integrated molecular analysis of tumor biopsies on sequential CTLA-4 and PD-1 blockade reveals markers of response and resistance. *Sci Transl Med* (2017) 9(379). doi: 10.1126/scitranslmed.aah3560

48. Lim M, Weller M, Idbaih A, Steinbach J, Finocchiaro G, Raval RR, et al. Phase 3 trial of chemoradiotherapy with temozolomide plus nivolumab or placebo for newly diagnosed glioblastoma with methylated MGMT promoter. *Neuro Oncol* (2022) 2:noac116. doi: 10.1093/neuonc/noac116

49. Quail DF, Joyce JA. The microenvironmental landscape of brain tumors. *Cancer Cell* (2017) 31(3):326–41. doi: 10.1016/j.ccell.2017.02.009

50. Gordon S, Martinez FO. Alternative activation of macrophages: mechanism and functions. *Immunity* (2010) 32(5):593–604. doi: 10.1016/j.immuni.2010.05.007

51. Hambardzumyan D, Gutmann DH, Kettenmann H. The role of microglia and macrophages in glioma maintenance and progression. *Nat Neurosci* (2016) 19 (1):20–7. doi: 10.1038/nn.4185

52. Hoxhaj G, Manning B. The PI3K-AKT network at the interface of oncogenic signalling and cancer metabolism. *Nat Rev Cancer* (2020) 20:74–88. doi: 10.1038/s41568-019-0216-7

53. Murray PJ, Allen JE, Biswas SK, Fisher EA, Gilroy DW, Goerdt S, et al. Macrophage activation and polarization: nomenclature and experimental guidelines. *Immunity* (2014) 41(1):14–20. doi: 10.1016/j.immuni.2014.06.008

54. Liu Y, Xu H, Dahir N, Calder A, Lin F, Gilbertson TA. GPR84 is essential for the taste of medium chain saturated fatty acids. *J Neurosci* (2021) 41(24):5219–28. doi: 10.1523/JNEUROSCI.2530-20.2021

55. Peters A, Rabe P, Liebing AD, Krumbholz P, Nordstrom A, Jager E, et al. Hydroxycarboxylic acid receptor 3 and GPR84 - two metabolite-sensing G protein-coupled receptors with opposing functions in innate immune cells. *Pharmacol Res* (2022) 176:106047. doi: 10.1016/j.phrs.2021.106047

56. Zhang Q, Chen LH, Yang H, Fang YC, Wang SW, Wang M, et al. GPR84 signaling promotes intestinal mucosal inflammation via enhancing NLRP3 inflammasome activation in macrophages. *Acta Pharmacol Sin* (2021) 43 (8):2042–54. doi: 10.1038/s41401-021-00825-y

57. Jacob CO, Eisenstein M, Dinauer MC, Ming W, Liu Q, John S, et al. Lupus-associated causal mutation in neutrophil cytosolic factor 2 (NCF2) brings unique insights to the structure and function of NADPH oxidase. *Proc Natl Acad Sci U.S.A.* (2012) 109(2):E59–67. doi: 10.1073/pnas.1113251108

58. Wang D, Liu J, Chen Q, Yang R, Jiang Q. Upregulation of glutaminase 2 and neutrophil cytosolic factor 2 is associated with the poor prognosis of glioblastoma. *biomark Med* (2020) 14(16):1585–97. doi: 10.2217/bmm-2020-0341

59. Xu T, Yu W, Li Q, Li X, Shi Y, Cao B, et al. MicroRNA-524 inhibits the progress of glioma *via* the direct targeting of NCF2. *Am J Transl Res* (2019) 11(3):1605–15.

60. Tuo Z, Zheng X, Zong Y, Li J, Zou C, Lv Y, et al. HK3 is correlated with immune infiltrates and predicts response to immunotherapy in non-small cell lung cancer. *Clin Transl Med* (2020) 10(1):319–30. doi: 10.1002/ctm2.6

61. Pudova EA, Kudryavtseva AV, Fedorova MS, Zaretsky AR, Shcherbo DS, Lukyanova EN, et al. HK3 overexpression associated with epithelial-mesenchymal transition in colorectal cancer. *BMC Genomics* (2018) 19(Suppl 3):113. doi: 10.1186/s12864-018-4477-4

62. Federzoni EA, Humbert M, Torbett BE, Behre G, Fey MF, Tschan MP. CEBPA-dependent HK3 and KLF5 expression in primary AML and during AML differentiation. *Sci Rep* (2014) 4:4261. doi: 10.1038/srep04261

63. Becker C, Noldus J, Diamandis E, Lilja H. The role of molecular forms of prostate-specific antigen (PSA or hK3) and of human glandular kallikrein 2 (hK2) in the diagnosis and monitoring of prostate cancer and in extra-prostatic disease. *Crit Rev Clin Lab Sci* (2001) 38(5):357–99. doi: 10.1080/20014091084236

64. Bucova M, Kluckova K, Kozak J, Rychly B, Suchankova M, Svajdler M, et al. HLA-G 14bp Ins/Del polymorphism, plasma level of soluble HLA-G, and association with IL-6/IL-10 ratio and survival of glioma patients. *Diagn (Basel)* (2022) 12(5):1099. doi: 10.3390/diagnostics12051099

65. Wiendl H, Mitsdoerffer M, Weller M. Hide-and-seek in the brain: a role for HLA-G mediating immune privilege for glioma cells. *Semin Cancer Biol* (2003) 13 (5):343–51. doi: 10.1016/S1044-579X(03)00025-7

66. Aravind A, Palollathil A, Rex DAB, Kumar KMK, Vijayakumar M, Shetty R, et al. A multi-cellular molecular signaling and functional network map of c-c motif chemokine ligand 18 (CCL18): a chemokine with immunosuppressive and pro-tumor functions. *J Cell Commun Signal* (2022) 16(2):293–300. doi: 10.1007/s12079-021-00633-3

67. Long L, Hu Y, Long T, Lu X, Tuo Y, Li Y, et al. Tumor-associated macrophages induced spheroid formation by CCL18-ZEB1-M-CSF feedback loop to promote transcoelomic metastasis of ovarian cancer. *J Immunother Cancer* (2021) 9(12):e003973. doi: 10.1136/jitc-2021-003973

68. Berenguer J, Lagerweij T, Zhao XW, Dusoswa S, van der Stoop P, Westerman B, et al. Glycosylated extracellular vesicles released by glioblastoma cells are decorated by CCL18 allowing for cellular uptake *via* chemokine receptor CCR8. *J Extracell Vesicles* (2018) 7(1):1446660. doi: 10.1080/20013078.2018.1446660

69. Engelhardt B, Vajkoczy P, Weller RO. The movers and shapers in immune privilege of the CNS. *Nat Immunol* (2017) 18(2):123–31. doi: 10.1038/ni.3666

70. Coussens LM, Zitvogel L, Palucka AK. Neutralizing tumor-promoting chronic inflammation: a magic bullet? *Science* (2013) 339(6117):286–91. doi: 10.1126/science.1232227

71. Chen DS, Mellman I. Oncology meets immunology: the cancer-immunity cycle. *Immunity* (2013) 39(1):1–10. doi: 10.1016/j.immuni.2013.07.012

72. Zhang M, Ye F, Su M, Cui M, Chen H, Ma X. The prognostic role of peritumoral edema in patients with newly diagnosed glioblastoma: A retrospective analysis. *J Clin Neurosci* (2021) 89:249–57. doi: 10.1016/j.jocn.2021.04.042

73. Liotta EM. Management of cerebral edema, brain compression, and intracranial pressure. *Continuum (Minneap Minn)* (2021) 27(5):1172–200. doi: 10.1212/CON.0000000000000988

74. Feussner I, Wasternack C. The lipoxygenase pathway. *Annu Rev Plant Biol* (2002) 53:275–97. doi: 10.1146/annurev.arplant.53.100301.135248

75. Haeggstrom JZ, Funk CD. Lipoxygenase and leukotriene pathways: biochemistry, biology, and roles in disease. *Chem Rev* (2011) 111(10):5866–98. doi: 10.1021/cr200246d

76. Yan M, Zhang S, Li C, Liu Y, Zhao J, Wang Y, et al. 5-lipoxygenase as an emerging target against age-related brain disorders. *Ageing Res Rev* (2021) 69:101359. doi: 10.1016/j.arr.2021.101359

77. Bachi AL, Kim FJ, Nonogaki S, Carneiro CR, Lopes JD, Jasiulionis MG, et al. Leukotriene B4 creates a favorable microenvironment for murine melanoma growth. *Mol Cancer Res* (2009) 7(9):1417–24. doi: 10.1158/1541-7786.MCR-09-0038

78. Lim JY, Oh JH, Jung JR, Kim SM, Ryu CH, Kim HT, et al. MK886-induced apoptosis depends on the 5-LO expression level in human malignant glioma cells. *J Neurooncol* (2010) 97(3):339–46. doi: 10.1007/s11060-009-0036-9

79. Tian W, Jiang X, Kim D, Guan T, Nicolls MR, Rockson SG. Leukotrienes in tumor-associated inflammation. *Front Pharmacol* (2020) 11:1289. doi: 10.3389/fphar.2020.01289

80. Danaher P, Warren S, Lu R, Samayoa J, Sullivan A, Pekker I, et al. Pan-cancer adaptive immune resistance as defined by the tumor inflammation signature (TIS): results from the cancer genome atlas (TCGA). *J immunother Cancer* (2018) 6:63. doi: 10.1186/s40425-018-0367-1

COPYRIGHT

© 2022 Ji, Liu, Wang, Sun, Wang, Liu, Hu and You. This is an open-access article distributed under the terms of the Creative Commons Attribution License (CC BY). The use, distribution or reproduction in other forums is permitted, provided the original author(s) and the copyright owner(s) are credited and that the original publication in this journal is cited, in accordance with accepted academic practice. No use, distribution or reproduction is permitted which does not comply with these terms.

frontiers | Frontiers in Immunology

TYPE Original Research
PUBLISHED 13 September 2022
DOI 10.3389/fimmu.2022.944378

Check for updates

OPEN ACCESS

EDITED BY
Jian Zhang,
Southern Medical University, China

REVIEWED BY
Xingxing Huo,
First Affiliated Hospital of Anhui University of Traditional Chinese Medicine, China
Xianghong Zhou,
Sichuan University, China
Chao Ma,
First Affiliated Hospital of Zhengzhou University, China

*CORRESPONDENCE
Haiyu Zhou
zhouhaiyu@gdph.org.cn
Yong Zheng
zheng9998@sina.com
Fanjun Zeng
zengfanjun@gdph.org.cn

†These authors have contributed equally to this work and share first authorship

SPECIALTY SECTION
This article was submitted to Cancer Immunity and Immunotherapy, a section of the journal Frontiers in Immunology

RECEIVED 15 May 2022
ACCEPTED 17 August 2022
PUBLISHED 13 September 2022

CITATION
Li Q, Xie D, Yao L, Qiu H, You P, Deng J, Li C, Zhan W, Weng M, Wu S, Li F, Zhou Y, Zeng F, Zheng Y and Zhou H (2022) Combining autophagy and immune characterizations to predict prognosis and therapeutic response in lung adenocarcinoma. *Front. Immunol.* 13:944378. doi: 10.3389/fimmu.2022.944378

COPYRIGHT
© 2022 Li, Xie, Yao, Qiu, You, Deng, Li, Zhan, Weng, Wu, Li, Zhou, Zeng, Zheng and Zhou. This is an open-access article distributed under the terms of the Creative Commons Attribution License (CC BY). The use, distribution or reproduction in other forums is permitted, provided the original author(s) and the copyright owner(s) are credited and that the original publication in this journal is cited, in accordance with accepted academic practice. No use, distribution or reproduction is permitted which does not comply with these terms.

Combining autophagy and immune characterizations to predict prognosis and therapeutic response in lung adenocarcinoma

Qiaxuan Li[1,2†], Daipeng Xie[1,3†], Lintong Yao[1,2†], Hongrui Qiu[1,4], Peimeng You[5], Jialong Deng[1], Congsen Li[1,2], Weijie Zhan[1,6], Maotao Weng[1,2], Shaowei Wu[1,2], Fasheng Li[7], Yubo Zhou[1], Fanjun Zeng[8*], Yong Zheng[9*] and Haiyu Zhou[1,2,10*]

[1]Department of Thoracic Surgery, Guangdong Provincial People's Hospital, Guangdong Academy of Medical Sciences, Guangzhou, China, [2]Shantou University Medical College, Shantou, China, [3]Guangdong Cardiovascular Institute, Guangzhou, China, [4]Guangzhou University of Chinese Medicine, Guangzhou, China, [5]Department of Thoracic radiology, Cancer Hospital of Nanchang University, Jiangxi Key Laboratory of Translational Cancer Research (Jiangxi Cancer Hospital of Nanchang University), Nanchang, China, [6]The Second School of Clinical Medicine, Southern Medical University, Guangzhou, China, [7]Department of Cardiothoracic Surgery, Affiliated Hospital of Guangdong Medical University, Guangzhou, China, [8]Department of General Practice, Guangdong Provincial Geriatrics Institute, Guangdong Provincial People's Hospital, Guangdong Academy of Medical Sciences, Guangzhou, China, [9]Department of Anesthesiology, Guangdong Provincial People's Hospital, Guangdong Academy of Medical Sciences, Guangzhou, China, [10]Jiangxi Lung Cancer Institute, Nanchang, China

Background: Autophagy, a key regulator of programmed cell death, is critical for maintaining the stability of the intracellular environment. Increasing evidence has revealed the clinical importance of interactions between autophagy and immune status in lung adenocarcinoma. The present study evaluated the potential of autophagy-immune-derived biomarkers to predict prognosis and therapeutic response in patients with lung adenocarcinoma.

Methods: Patients from the GSE72094 dataset were randomized 7:3 to a training set and an internal validation set. Three independent cohorts, TCGA, GSE31210, and GSE37745, were used for external verification. Unsupervised hierarchical clustering based on autophagy- and immune-associated genes was used to identify autophagy- and immune-associated molecular patterns, respectively. Significantly prognostic autophagy-immune genes were identified by LASSO analysis and by univariate and multivariate Cox regression analyses. Differences in tumor immune microenvironments, functional pathways, and potential therapeutic responses were investigated to differentiate high-risk and low-risk groups.

Results: High autophagy status and high immune status were associated with improved overall survival. Autophagy and immune subtypes were merged into a two-dimensional index to characterize the combined prognostic classifier,

with 535 genes defined as autophagy-immune-related differentially expressed genes (DEGs). Four genes (C4BPA, CD300LG, CD96, and S100P) were identified to construct an autophagy-immune-related prognostic risk model. Survival and receiver operating characteristic (ROC) curve analyses showed that this model was significantly prognostic of survival. Patterns of autophagy and immune genes differed in low- and high-risk patients. Enrichment of most immune infiltrating cells was greater, and the expression of crucial immune checkpoint molecules was higher, in the low-risk group. TIDE and immunotherapy clinical cohort analysis predicted that the low-risk group had more potential responders to immunotherapy. GO, KEGG, and GSEA function analysis identified immune- and autophagy-related pathways. Autophagy inducers were observed in patients in the low-risk group, whereas the high-risk group was sensitive to autophagy inhibitors. The expression of the four genes was assessed in clinical specimens and cell lines.

Conclusions: The autophagy-immune-based gene signature represents a promising tool for risk stratification in patients with lung adenocarcinoma, guiding individualized targeted therapy or immunotherapy.

KEYWORDS

microenvironment, autophagy, preclinical models, chemotherapy, immunotherapy

Introduction

Lung cancer is one of the most common cancers worldwide with a high mortality rate and poor prognosis. About 85% of patients with lung cancer have non-small cell lung cancer (NSCLC), with the most prevalent histological form of NSCLC being lung adenocarcinoma (LUAD) (1). The prognosis of LUAD patients is still dismal despite advances in diagnosis and treatment, including the introduction of target therapy and immune checkpoint inhibitors (2). As a complex multi-step process, the formation of LUAD may be intimately linked to the expression of various genes (3). Additional molecular indicators are needed to predict the prognosis of patients with LUAD.

Autophagy, a major regulator of programmed cell death, maintains the stability of the intracellular environment by eliminating damaged organelles, misfolded proteins, and pathogens (4). Autophagy has been found to have a key function in various diseases, including infectious diseases, neurodegenerative diseases, and cancer (5). However, the biological mechanism of autophagy in cancer is dependent on cancer type, stage, and other variables (6). Autophagy can suppress tumors by eliminating harmful substances and maintaining genome stability, especially during early stages of tumor growth (7). However, once a tumor has progressed to an advanced stage, autophagy protects tumor cells by enabling them to adapt to hypoxia and nutrient deprivation (8). The overexpression of Beclin1, an essential autophagy gene, is linked to the progression of various tumor types (9). Moreover, autophagy may act as a promoter, enhancing tumor metastasis and aggressiveness (9). Thus, modulation of autophagy has a significant impact on the tumor microenvironment (TME), promoting or inhibiting tumor growth.

Immune cells that infiltrate tumors have been linked to tumor growth, metastasis, and progression (10). The levels of expression of immune checkpoints, such as PD-L1, PD-1, and CTLA-4, play an important role in cancer prognosis and response to immunotherapy (11). Autophagy has been shown to influence the immunological state of the TME, either directly or indirectly (12). Interplay between autophagy and immunity may affect tumor occurrence and development. Autophagy has been reported to be associated with T-cell survival, activation, and effector function (13), whereas tumor autophagy has been shown to weaken NK-cell-mediated tumor cell lysis in a mouse cancer model (14). Additional studies, however, are needed to better understand the mechanism underlying the interactions between autophagy and immunity.

Interactions between autophagy and immunity may have prognostic relevance in patients with LUAD. The present study was designed to create and validate a comprehensive index of molecules and cells associated with immunological and autophagy status that might be used to better describe the TME and predict prognosis in patients with LUAD. This

autophagy-immune-related prognostic risk model may be a more accurate prognostic and therapeutic indicator in LUAD.

Materials and methods

Data acquisition

All the clinical information and gene expression profiling of patients with LUAD were accessed from The Cancer Genome Atlas (TCGA, https://portal.gdc.cancer.gov/) and Gene Expression Omnibus (GEO, https://www.ncbi.nlm.nih.gov/geo/) databases, including the TCGA-LUAD (n = 500), GSE72094 (n = 398), GSE31210 (n = 226), and GSE37745 (n = 106) datasets. Table 1 shows the clinical baseline characteristics of these datasets in detail. The immunotherapy clinical cohorts included 82 patients with advanced solid tumors (15) and the GSE100797 dataset. Fragments per kilobase per million mapped reads (FPKM) format data were downloaded for the cohorts from the TCGA-LUAD dataset. Autophagy-related genes were obtained from the HADb dataset (http://www.autophagy.lu/), and immune-related genes were obtained from the ImmPort dataset (https://www.immport.org/home). An ethics statement was not required because all of the datasets used in the present investigation were from open-access databases. Genes associated with autophagy, immune signatures, ferroptosis and HLA were included for further analysis in different molecular patterns (Supplementary Table 1).

Identification of autophagy-related and immune-related molecular patterns of LUAD

The k-means machine learning technique was used for unsupervised consensus clustering and to separate samples in the GSE72094 dataset into different molecular patterns based on autophagy- and immune-related genes. Briefly, k-means clustering implemented in the "ConsensusClusterPlus" R package was applied to 1,000 iterations by taking 80% of the samples in each iteration. The optimal number of clusters was determined by the proportional change in the area under the

TABLE 1 Characteristic baseline of patients in clinical cohorts.

Variable	GSE72094 (N = 398)			TCGA (N = 500)	GSE31210 (N = 226)	GSE37745 (N = 106)
	Training cohort(N = 286)	Testing cohort(N = 112)	p-value			
Gender			0.0572			
Male	118 (41.3)	58 (51.8)		230 (46.0)	105 (46.5)	46 (43.4)
Female	168 (58.7)	54 (48.2)		270 (54.0)	121 (53.5)	60 (56.6)
Age, years			0.2509			
≤60 years	52 (18.2)	15 (13.4)		157 (31.4)	108 (47.8)	46 (43.4)
>60 years	234 (81.8)	97 (86.6)		333 (66.6)	118 (52.2)	60 (56.6)
Missing	0 (0.0)	0 (0.0)		10 (2.0)	0 (0.0)	0 (0.0)
Pathological stage			0.4585			
Stage I	186 (65.0)	68 (60.7)		269 (53.8)	168 (74.3)	70 (66.0)
Stage II	43 (15.0)	24 (21.4)		125 (25.0)	58 (25.7)	19 (17.9)
Stage III	42 (14.7)	15 (13.4)		81 (16.2)	0 (0.0)	13 (12.4)
Stage IV	12 (4.2)	3 (2.7)		25 (5.0)	0 (0.0)	4 (3.7)
NA	3 (1.1)	2 (1.8)		0 (0.0)	0 (0.0)	0 (0.0)
KRAS status			0.6595			
Mutation	98 (34.3)	41 (36.7)				
Wild type	188 (65.7)	71 (63.3)				
EGFR status			0.5918			
Mutation	28 (9.8)	13 (11.6)				
Wild type	258 (90.2)	99 (88.4)				
TP53 status			0.8551			
Mutation	69 (24.1)	28 (25.0)				
Wild type	217 (75.9)	84 (75.0)				
Survival status			0.7665			
Alive	206 (72.0)	79 (70.6)		318 (63.6)	188 (83.2)	29 (27.4)
Dead	80 (28.0)	33 (29.4)		182 (36.4)	38 (16.8)	77 (72.6)

cumulative distribution function (CDF) curves, the consensus matrix heatmap, the proportion of ambiguous clustering (PAC), and the NbClust method, with the number of clusters ranging from 2 to 8 (16, 17). Principal component analysis (PCA) was used to separate diverse subtypes of information in two-dimensional space.

Validation of the autophagy-immune-related prognostic risk model

Genes overlapping in the intersections of autophagy-, immune-, and autophagy-immune-related DEGs were chosen for univariate Cox regression analyses. Hub genes were filtered using the "glmnet" R package and an autophagy-immune-related prognostic risk model developed using least absolute shrinkage and selection operator (LASSO) analysis and multivariate Cox ratio hazard regression analysis. The risk score of each sample was calculated as:

$$Risk\ \ score = \sum_{i=1}^{n} Coef_i \times x_i$$

where $Coef_i$ represents the coefficients and x_i represents the expression of each hub gene. Based on their risk scores, patients with LUAD in the TCGA, GSE72094, GSE31210, and GSE37745 cohorts were categorized into high-risk and low-risk subgroups. The sensitivity and specificity of the autophagy-immune-related prognostic risk model were assessed using the "survival" package of R software by applying OS and survival-dependent receiver operating characteristic (ROC) curves.

Immune cell infiltration

Single sample gene set enrichment analysis (ssGSEA) using R software was utilized to determine the levels of infiltration of subtypes of immune cells, including activated B cells, activated CD4 T cells, activated CD8 T cells, and T follicular helper cells. CIBERSORT and xCell algorithms were utilized to compare differences in the infiltration of 22 and 64 types of immune cells, respectively, based on gene expression profiles among different groups. Tumor purity was assessed using the ESTIMATE algorithm, with ESTIMATE score, immune score, and stromal score determined using the "estimate" package of R software.

Functional enrichment analysis of autophagy-immune-related prognostic risk model

To investigate possible biological pathways among distinct subtypes, DEGs in the GSE72094 cohort with |log2 fold change (FC)| > 0.5 and an adjusted p-value of 0.001 were identified using the "Limma" program. Gene ontology (GO) term enrichment analysis and Kyoto Encyclopedia of Genes and Genomes (KEGG) pathway analysis were performed based on DEGs using R software. In addition, gene set enrichment analysis (GSEA) provided by MsigDB was performed using GSEA, version 4.1.0 (http://www.gsea-msigdb.org/gsea) (18).

Prediction of tumor chemosensitivity to drugs and potential responses to immunotherapy

Sensitivities to chemotherapeutic agents in the high- and low-risk groups, based on their IC_{50} values, were evaluated using the GDSC database (https://www.cancerrxgene.org/) and the "pRRophetic" package of R software. Potential chemotherapeutic medicines in the CTRP2.0 and PRISM databases were investigated, based on the area under the dose–response curve (SUC) as a measure of drug sensitivity (19). Lower IC_{50} and AUC values were indicative of greater sensitivity to the chemotherapeutic agent. Prospective responses to immunotherapy in the high- and low-risk groups were subsequently compared using the Tumor Immune Dysfunction and Exclusion (TIDE) algorithm.

Cell culture

A normal lung epithelial cell line (BEAS-2B) and four LUAD cell lines (H1975, HCC827, A549, and PC9) were purchased from the China Center for Type Culture Collection (CCTCC). All cells were maintained in Roswell Park Memorial Institute 1640 (RPMI-1640) medium (Gibco; Thermo Fisher Scientific, Inc.) containing 10% fetal bovine serum (FBS) (Gibco) in a humidified incubator at 37°C and 5% CO_2.

qRT-PCR

Seventeen paired LUAD and adjacent normal tissue samples were obtained from Jiangxi Cancer Hospital after gaining ethical approval from the Human Research Ethics Committee of Jiangxi Cancer Hospital (No. 2022ky013). Total RNA was extracted from cell lines and tissue samples using TransZol Up Plus RNA Kits (Transgen Biotech, Beijing, China). A 1.0 mg aliquot of each total RNA sample was reverse transcribed to cDNA using TransScript II One-Step RT-PCR SuperMix. Gene expression was quantified by real-time fluorescent quantitative PCR using SYBR green mixture (Novoprotein) and specific primers (Supplementary Table 2) on an ABI Step 1 Plus RT-PCR system (Applied Biosystems, USA). The expression of each target gene relative to that of GADPH was estimated using the $2^{-\Delta\Delta CT}$ method.

Statistical methods

The relationships between patient characteristics and overall survival were analyzed by univariate and multivariate Cox regression analyses. The correlations between overall survival and tumor subtypes were calculated using the Kaplan–Meier method with the "survminer" R package. Differences between two groups were compared by two-tailed Student's *t*-tests or Wilcoxon rank sum tests, as appropriate, whereas differences among three or more groups were compared by the Kruskal–Wallis test. Correlations were analyzed using Pearson's or Spearman's correlation methods. R software, version 4.1.0, was used for all analyses, with p-values<0.05 defined as statistically significant.

Results

Autophagy-associated molecular patterns and autophagy-related DEGs in lung adenocarcinomas

The intersection of the TCGA-LUAD, GEO, and HADb datasets yielded a total of 208 autophagy-related genes (ARGs), which were utilized to investigate autophagy-related molecular trends in LUAD. Based on ARG expression levels, the R software program ConensusClusterPlus categorized 398 LUAD patients from the GSE72094 cohort into qualitatively different autophagy-associated molecular patterns. The consensus clustering matrix heatmap and the CDF curve indicated that $k = 2$ was optimal (Figures 1A, B; Supplementary Figure 1A). In addition, the PAC and NbClust algorithms indicated that $k = 2$ was the optimal number for cluster stability (Supplementary Figures 1B, C). Thus, two autophagy-associated molecular subtypes were identified, including 247 samples in subtype A and 151 in subtype B. These subtypes were named AutCluster A and AutCluster B, which differed significantly on principal component analysis (Figure 1C). Kaplan–Meier analysis showed that survival was significantly better in AutCluster A ($p< 0.0001$, Figure 1D). To explore the molecular mechanisms associated with these autophagy-associated subtypes, the expression of ARGs was compared and GSEA enrichment analysis was performed. The levels of most ARGs were significantly higher in AutCluster A than in AutCluster B (Figure 1E). GSEA showed that AutCluster A was enriched in autophagy-related pathways, such as those associated with selective autophagy, autophagosome organization, and regulation of autophagy, whereas AutCluster B was enriched mainly in pathways associated with the cell cycle (Figure 1F, Supplementary Table 3). Overall, patients in AutCluster A and AutCluster B were defined as the autophagy^{high} and autophagy^{low} groups, respectively. In addition, ssGSEA and ESTIMATE analyses showed that the levels of tumor-infiltrating immune cells were higher in the autophagy^{high} than in the autophagy^{low} group (Supplementary Figures 1D–F), with GSEA showing that immune-associated pathways were enriched in the autophagy^{high} group (Supplementary Table 3). Comparisons of the levels of gene expression in autophagy^{high} and autophagy^{low} groups identified a total of 259 autophagy-related DEGs, with 215 genes overexpressed in the autophagy^{high} group and 44 overexpressed in the autophagy^{low} group (Supplementary Figure 1G).

Immune-associated molecular patterns and immune-related DEGs in lung adenocarcinoma

Combining the genes from the TCGA-LUAD, GEO, and ImmPort datasets yielded 988 immune-related genes that were used to implement consensus clustering in the GSE72094 cohort. Based on the CDF curve of the consensus score, the GSE72094 cohort was divided into two immune-associated subtypes, with 263 patients having subtype A and 135 having subtype B (Figures 2A, B; Supplementary Figure 2A). Similar results were obtained following PAC and NbClust analyses (Supplementary Figures 2B, C), with principal component analysis showing that these two subtypes, defined as ImmCluster A and ImmCluster B, respectively, could be clearly distinguished (Figure 2C). Kaplan–Meier analysis showed that patients in ImmCluster A had better survival than those in ImmCluster B (Figure 2D). The potential immune landscape of these two subtypes was assessed using ssGSEA and ESTIMATE analyses to investigate their immunologic characteristics. ssGSEA showed that the levels of tumor-infiltrating immune cells, including activated B cells, activated CD8 T cells, effector memory CD8 T cells, activated CD4 T cells, CD56+ natural killer (NK) cells, and T follicular helper cells, were significantly higher in ImmCluster A than in ImmClusterB (Figure 2E). CIBERSORT and xCell analysis also showed that the level of adaptive immune cell infiltration was higher in ImmCluster A (Supplementary Figures 2D, E). Analysis of the associations between these two immune subtypes and HLA genes showed that the levels of expression of HLA genes were significantly higher in samples from the mmCluster A than the mmCluster B group (Figure 2F). Moreover, the ESTIMATE algorithm showed that immune, stromal, and ESTIMATE scores were higher in ImmCluster A than in ImmCluster B, indicating that immune cell infiltration was significantly higher and tumor purity was significantly lower in the ImmCluster A group ($p< 0.0001$ each, Figure 2G). Based on these findings, the ImmCluster A and ImmCluster B groups were designated the immunity^{high} and immunity^{low} groups, respectively. A comparison of the immunity^{high} and immunity^{low} groups showed that 365 immune-related DEGs were differentially expressed (Supplementary Figure 2F). GSEA

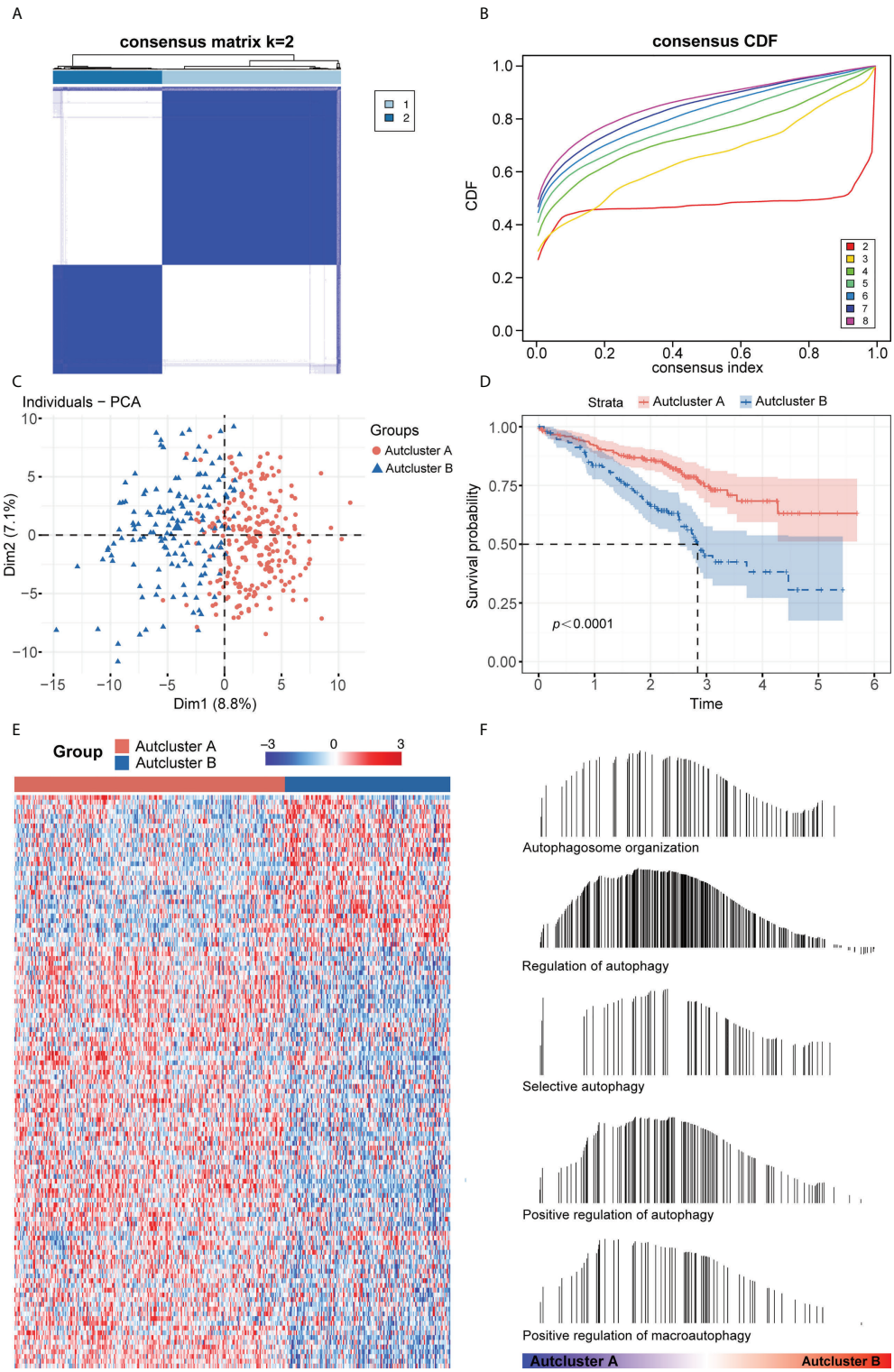

FIGURE 1
(A) Consensus clustering matrix heatmap with autophagy-related molecular pattern in GSE72094 when k = 2. **(B)** The CDF curves with k valued 2 to 8 (indicated by colors). **(C)** Principal component analysis (PCA) was performed to distinguish AutCluster A and AutCluster B. **(D)** Survival analysis showed better survival among AutCluster A in GSE72094. **(E)** Heatmap of autophagy-related genes in AutCluster A and AutCluster B. **(F)** Autophagy-related pathways enriched in AutCluster A by GSEA.

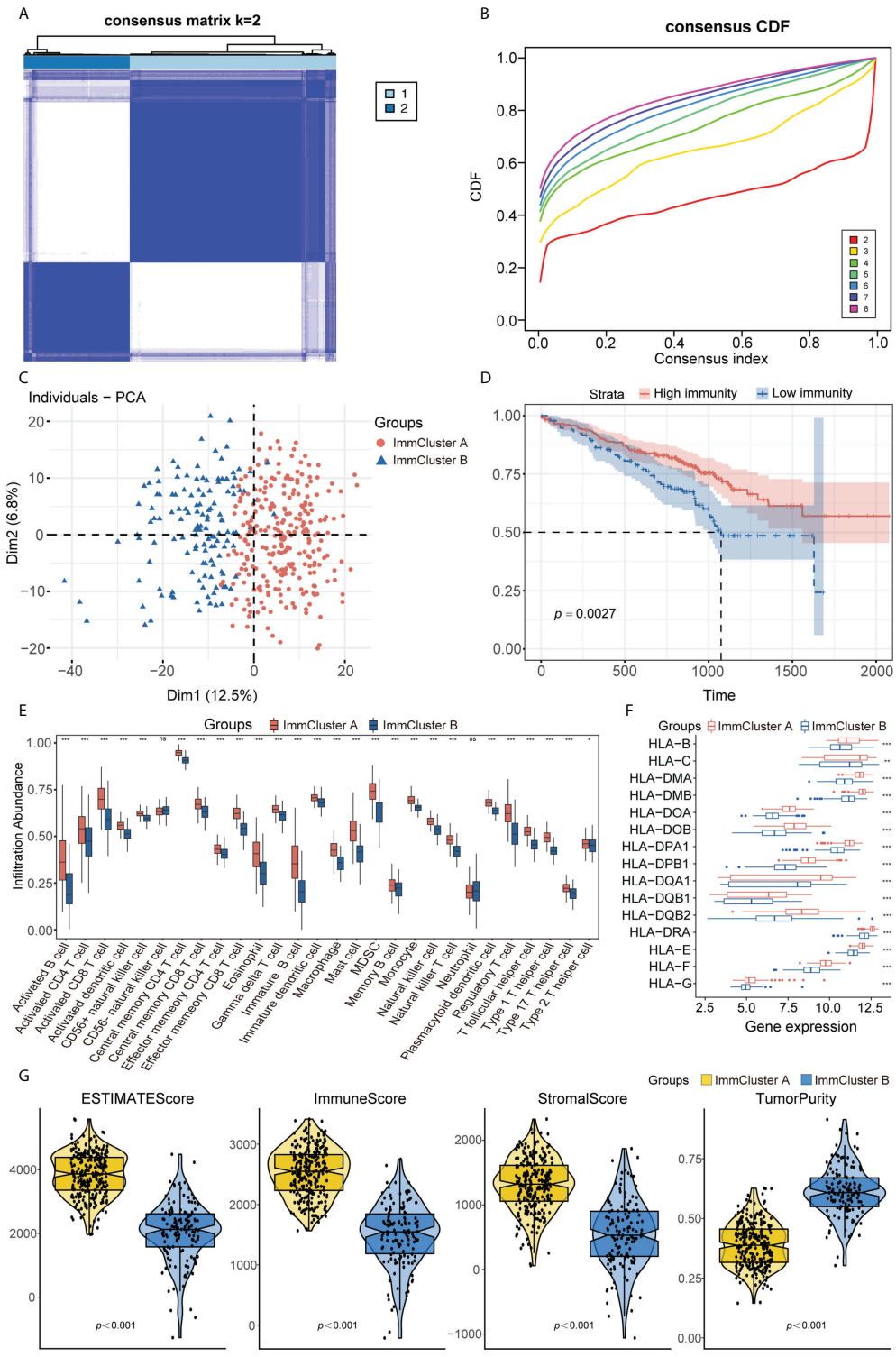

FIGURE 2
(A) Consensus clustering matrix heatmap with immune-related molecular pattern in GSE72094 when k = 2. **(B)** The CDF curves with k valued 2 to 8 (indicated by colors). **(C)** Principal component analysis (PCA) was performed to distinguish ImmCluster A and ImmCluster B. **(D)** Survival analysis showed better survival among ImmCluster A. **(E)** ssGSEA suggested that ImmCluster A has the higher level of tumor-infiltrating immune cells, such as CD8+ T cell and CD4+ T cell. ns for $p > 0.05$, * for $p < 0.05$, ** for $p < 0.01$, *** for $p < 0.001$. **(F)** Gene expression of HLA gene sets between two distinct clusters. **(G)** Higher immune score, stromal score, estimate score, and lower tumor purity are analyzed in ImmCluster A by ESTIMATE algorithm. ssGSEA, Single sample gene set enrichment analysis.

showed that autophagy-related pathways were enriched in the immunity^{high} group (Supplementary Figure 2G; Supplementary Table 4).

Construction and verification of a combined prognostic classifier and autophagy-immune-related prognostic risk model in lung adenocarcinoma

Autophagy and immune subtypes were merged into a two-dimensional matrix to characterize the combined prognostic classifier. Patients were split into three groups: autophagy^{high}-immune^{high}, autophagy^{low}-immune^{low}, and mixed groups (i.e., autophagy^{high}-immune^{low} and autophagy^{low}-immune^{high}). Survival analysis showed that the prognoses were significantly better in the autophagy^{high}-immune^{high} and mixed groups than in the autophagy^{low}-immune^{low} group ($p< 0.0001$ each, Figure 3A). A comparison of gene expression in the autophagy^{high}-immune^{high} and autophagy^{low}-immune^{low} groups identified 535 DEGs, which were defined as autophagy-immune-related DEGs (Supplementary Figure 3A).

The intersection of the autophagy-related, immune-related, and autophagy-immune-related DEGs identified 182 overlapping genes for further investigation (Figure 3B). The GSE72094 cohort of 398 patients was divided in a 7:3 ratio into a training set of 286 patients and a testing set of 112. Univariate Cox regression analysis showed that the levels of 24 autophagy-immune-related genes in the training set correlated significantly with OS. LASSO analysis and multivariate Cox ratio hazard regression analysis identified four genes, C4BPA, CD300LG, CD96, and S100P, that were used to construct an autophagy-immune-related prognostic risk model (Supplementary Figures 3B, C). The equation for the risk model from these four genes was:

Risk score = (−0.08563) * expression of C4BPA + (−0.12297) * expression of CD300LG + (−0.16202) * expression of CD96 + 0.14384 * expression of S100P (Figure 3C).

The relationships of these four genes with tumor-infiltrating immune cells and with essential autophagy-related target genes and the relationships of risk scores with essential autophagy-related target genes and with tumor-infiltrating immune cells were further investigated (Supplementary Figures 3D–G). The training set was divided into high-risk and low-risk groups based on the median cutoff value of the prognostic risk grade. Survival analysis showed that OS was significantly longer in the low-risk than in the high-risk group ($p = 0.00014$), and the areas under the curves (AUCs) for 1-, 3-, and 5-year survival were 0.686, 0.731, and 0.805, respectively (Figure 3D). Patients in the low-risk group also had more favorable prognoses ($p = 0.00015$), with AUCs for 1-, 3-, and 5-year survival of 0.728, 0.775, and 0.779, respectively (Figure 3E). To confirm the reliability of the autophagy-immune-related prognostic risk model, it was used to assess the entire GSE72094 dataset, as well as the TCGA, GSE37745, and GSE31210 cohorts, with similar results observed in all of these cohorts ($p< 0.0001$, Figure 3F; Supplementary Figures 4A–C).

Clinical value of autophagy-immune-related prognostic risk model

The prognostic abilities of the autophagy-immune-related prognostic risk model and of many clinicopathological characteristics were investigated using univariate Cox regression analyses. Factors significantly prognostic for OS in the GSE72094 dataset included risk score based on the four autophagy-immune-related genes, as well as patient gender and tumor TNM stage, KRAS status, and EGFR status. Multivariate analysis showed that risk score, gender, and TNM stage were independently associated with patient prognosis (Table 2). Patients in the GSE72094 dataset were subsequently stratified by the clinicopathologic characteristics differentiating the high-risk and low-risk groups, including gender (male vs. female), age (<60 vs. ≥60 years), tumor stage (I–II vs. III–IV), KRAS status (wild type vs. mutant), and EGFR status (wild type vs. mutant), and OS was compared in these two groups. Because the number of patients with EGFR mutations was relatively small, the difference in prognosis between high- and low-risk groups, as determined by EGFR mutation status, did not achieve statistical significance. Stratification by other characteristics showed that OS was significantly longer in the low-risk than in the high-risk group (Figure 4A; Supplementary Figure 5A).

To explore the effects of the autophagy-immune-related prognostic risk model in autophagy and immune groups, the model was evaluated in the autophagy^{high}, autophagy^{low}, immunity^{high}, and immunity^{low} groups. The risk model separated the patients in these four subtypes into high- and low-risk groups, with the low-risk group having a better prognosis. ROC curve analysis showed that the model had better predictive accuracy in the autophagy^{high} and immunity^{high} groups than in the autophagy^{low} and immunity^{low} groups (Supplementary Figures 5B–E).

Exploration of the tumor microenvironment and responses to immune therapy

To further investigate the TME in each endotype, the expression of individual critical autophagy- and immune

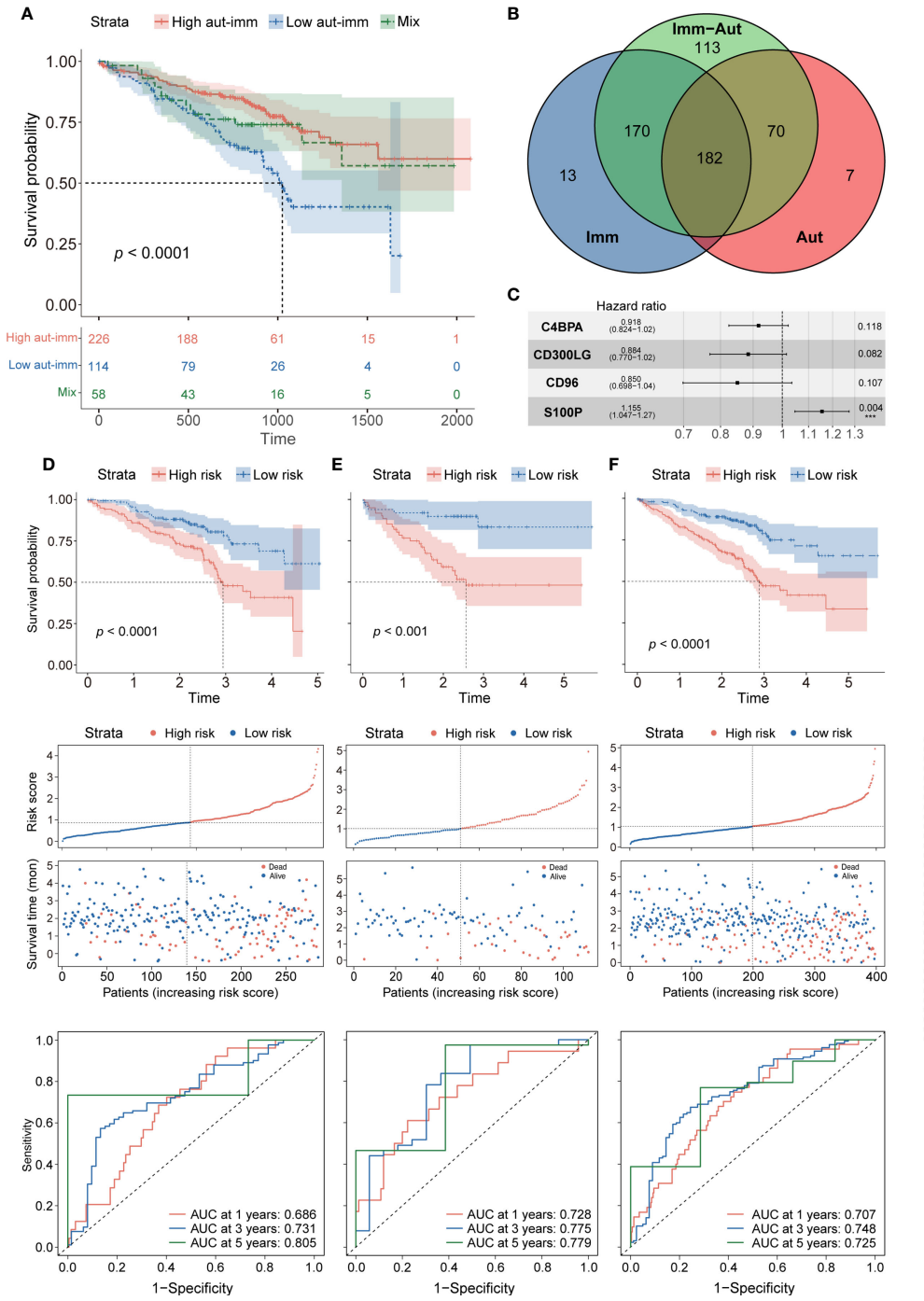

FIGURE 3
(A) Survival analysis between autophagy^{high}-immune^{high}, autophagy^{low}-immune^{low}, and mix groups. **(B)** The intersection of autophagy-immune-related genes between different molecular patterns. **(C)** Forest plot of hazard ratios for four autophagy-immune–related prognostic variables. **(D)** The overall survival analysis of the GSE72094 training dataset; construction of the GSE72094 training dataset; the ROC curves at 1, 3, and 5 years of prognostic value of the prognostic in the GSE72094 training dataset. **(E, F)** The validation sets using the GSE72094 testing dataset and the GSE72094 entire dataset.

TABLE 2 Univariate and multivariate analysis of clinical characteristics in GSE72094.

Variable	Univariate		Multivariate	
	HR (95% CI)	*p*-value	HR (95% CI)	*p*-value
Age (years)	1.395 (0.810–2.403)	0.229		
Gender	1.552 (1.072–2.246)	0.020	1.506 (1.027–2.209)	0.036
Pathological stage				
I	1	–	1	–
II	2.134 (1.324–3.439)	< 0.001	2.335 (1.440–3.786)	< 0.001
III	3.095 (1.927–4.972)	< 0.001	2.685 (1.667–4.326)	< 0.001
IV	3.351 (1.590–7.062)	< 0.001	3.732 (1.754–7.939)	< 0.001
KRAS status	0.6867 (0.472–0.999)	0.049	0.559 (0.265–1.181)	0.127
EGFR status	3.821 (1.408–10.37)	< 0.001	2.553 (0.922–7.072)	0.071
TP53 status	0.8099 (0.964–1.009)	0.239		
Tumor Purity	2.899 (0.8107–10.37)	0.101		
riskScore	2.041 (1.661–2.508)	< 0.001	1.506 (1.027–2.209)	< 0.001

response-related genes was mapped to the low- and high-risk groups. The expression of essential autophagy-related target genes was found to be higher in the low-risk group (Figure 4B). Immune response-related genes also showed a similar pattern of differential expression, including T-cell phenotypic and functional markers, myeloid lineage phenotypic and functional markers, activating immune receptors, immune modulators, and IFNγ signatures (Figure 4C). These results suggested that the levels of autophagy and immune cell infiltration were higher in the low-risk group. In addition, the expression of ferroptosis-driver genes was higher and the expression of ferroptosis-suppressor genes was lower in the low-risk group (Figure 4D), suggesting that ferroptosis is activated in the low-risk group and suppressed in the high-risk group.

To further explore differences in the tumor immune microenvironment of high- and low-risk patients with LUAD, their levels of immune cell infiltration were evaluated using ssGSEA, CIBERSORT, and xCell. ssGEA showed that the low-risk group had higher levels of most types of infiltrating immune cells, including activated B cells, activated CD8 T cells, effector memory CD8 T cells, central memory CD4 T cells, CD56+ natural killer cells, immature B cells, mast cells, and T follicular helper cells (Figures 5A, B). These findings, along with the results of CIBERSORT and xCell analyses (Supplementary Figures 6A, B) showed that the proportion of infiltrating immune cells was higher in the low-risk group than in the high-risk group. Moreover, the ESTIMATE algorithm showed that the low-risk group was positively associated with higher ESTIMTE, immune, and stromal scores, indicating lower tumor purity ($p< 0.001$, Figure 5C). The potential responses to immune therapy in the low- and high-risk groups were assessed by comparing their expression of immune checkpoint genes, such as PD1, PD-L1, LAG3, CTLA4, CD276, TIGIT, and HAVCR2. The levels of CTLA4, HAVCR2, PD-L1, and TIGIT were significantly higher in the low-risk group, while the level of CD274 was higher in the high-risk group (Figure 5D). The score on the TIDE algorithm, which integrates T-cell dysfunction and exclusion signature to evaluate tumor immune escape, was found to be significantly higher ($p< 0.001$, Figure 5E), whereas the predicted proportion of responders was lower (Figure 5F), in the high-risk group. We further used Pender et al.'s cohort (immune checkpoint inhibitors to treat advanced solid tumors) and GSE100797 to analyze whether an autophagy-immune-related risk score can predict immune efficacy. The Kaplan–Meier survival analysis shows that the low-risk group has a better survival prognosis than the high-risk group in Pender et al.'s cohort ($p = 0.013$, Figure 5G). Analyses of biologic pathways showed that autophagy- and immune-related pathways were enriched in the low-risk group (Supplementary Figure 6C). Similar results were observed in the GSE100797 cohort ($p = 0.042$, Figure 5G), with patients in this cohort achieving partial response (PR) or complete response (CR) having significantly lower risk scores than those who achieved stable disease (SD) or progressive disease (PD) ($p = 0.031$, Supplementary Figure 6D).

10.3389/fimmu.2022.944378

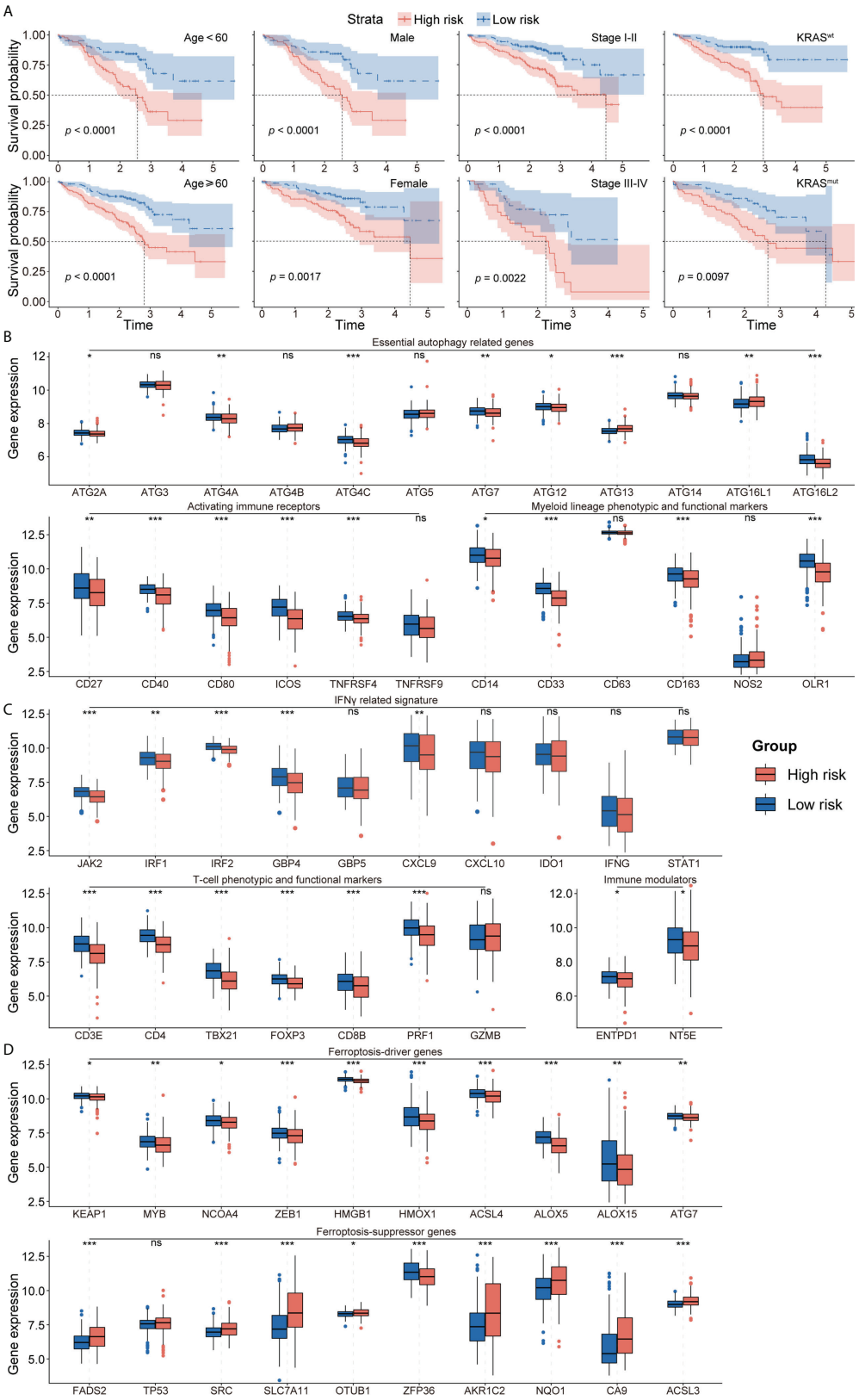

FIGURE 4 (Continued)

FIGURE 4 (Continued)
(A) Survival analysis showed favorable survival for low-risk patients in different age, gender, pathological stage, and KRAS status. **(B)** The expression of essential autophagy-related genes between the low- and high-risk group. **(C)** The expression of immune response-related genes between the low- and high-risk group. **(D)** The expression of ferroptosis-driver and ferroptosis-suppressor genes between the low- and high-risk group. ns for $p > 0.05$, * for $p < 0.05$, ** for $p < 0.01$, *** for $p < 0.001$.

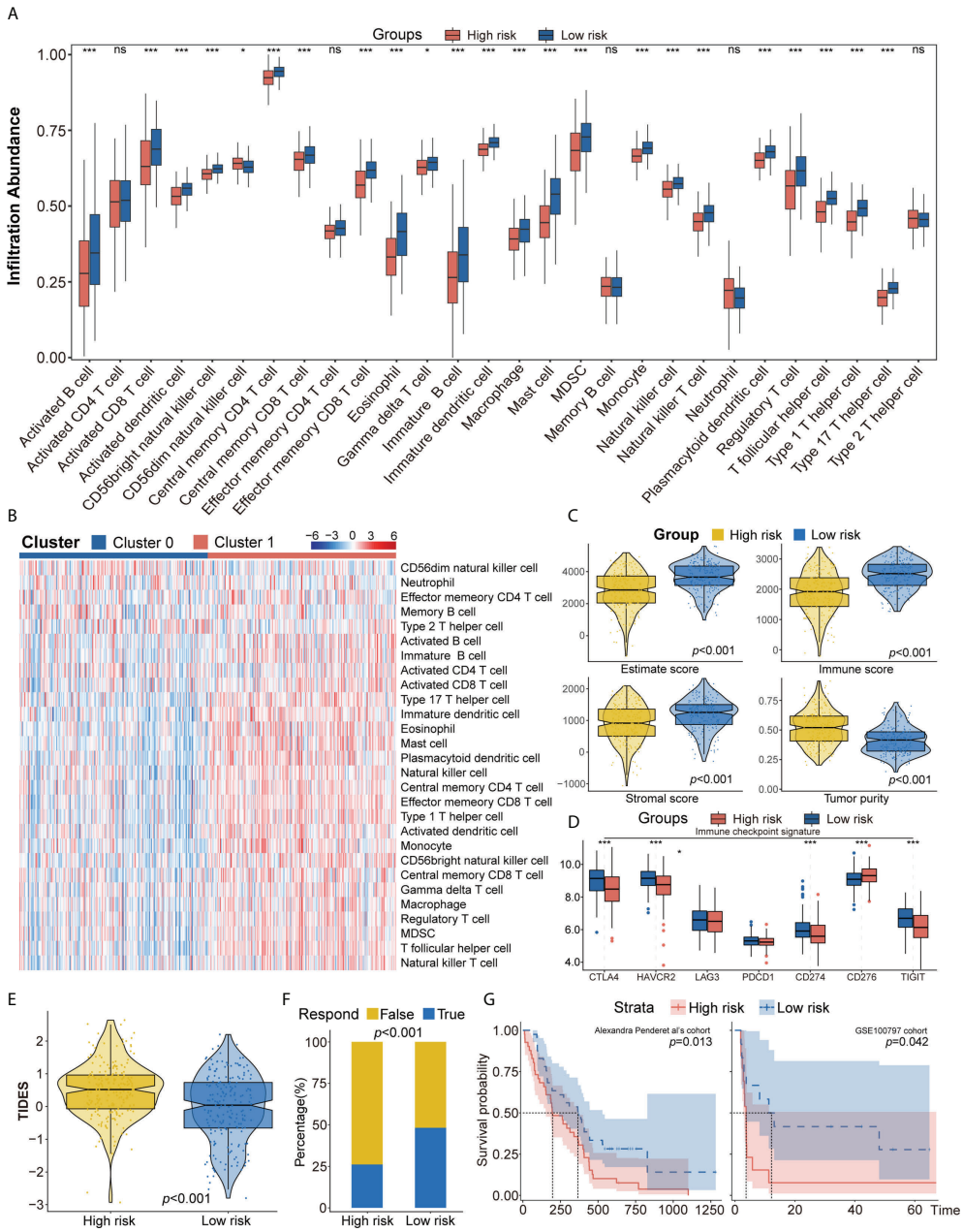

FIGURE 5
(A, B) ssGSEA suggested that the low-risk group has the higher level of tumor-infiltrating immune cells, such as CD8+ T cell and CD4+ T cell. **(C)** Higher immune score, stromal score, estimate score, and lower tumor purity are analyzed in the low-risk group by ESTIMATE algorithm. **(D)** The different expression of common immune checkpoint molecules between the low- and high-risk group, including *PD1*, *PD-L1*, *LAG3*, *CTLA4*, *CD276*, *TIGIT*, and *HAVCR2*. **(E, F)** Estimating T-cell dysfunction and exclusion and predicting response of immunotherapy in the low- and high-risk group by TIDE analysis. **(G)** Describing the model's efficacy in immunotherapy cohorts by Kaplan–Meier survival analysis. ssGSEA, single sample gene set enrichment analysis; TIDE, Tumor Immune Dysfunction and Exclusion. ns for $p > 0.05$, * for $p < 0.05$, ** for $p < 0.01$, *** for $p < 0.001$.

Identification and functional enrichment analysis of autophagy-immune-related prognostic risk model

A comparison of the high- and low-risk groups with the "Limma" package, using the criteria $p< 0.05$ and log (fold change) > 0.5, identified 1,342 DEGs (Supplementary Figure 6E). GO functional enrichment analysis showed significant enrichment of DEGs associated with T-cell activation, immune receptor activity, chromosomal region, and glycosaminoglycan binding (Figure 6A). KEGG pathway analysis indicated that DEGs associated with cell adhesion molecules, cytokine receptor interaction, and T-cell receptor signaling pathways were enriched in the low-risk group, whereas DEGs associated with the cell cycle and metabolic pathways were upregulated in the high-risk group (Figure 6B). GSEA pathway enrichment analysis showed that several autophagy-related pathways, such as selective autophagy, positive regulation of autophagosome, and regulation of autophagy and autophagosome organizational pathways, were enriched in the low-risk group, whereas the mTORC1 signaling pathway was upregulated in the high-risk group (Figure 6C, Supplementary Table 5). These findings indicated that the low-risk group had higher levels of immune cell infiltration and autophagy, as well as higher levels of lysosomes and higher levels of expression of genes associated with Fc epsilon receptor signaling, T-cell receptor signaling, Toll-like receptor signaling pathway, IL6_JAK_STAT3 signaling, apoptosis, interferon-γ responses, and inflammatory responses (Figure 6C, Supplementary Table 5). Pathways upregulated in the high-risk group included those associated with MYC targets, DNA replication, cell cycle, ribosomes, and glycolysis (Figure 6C, Supplementary Table 5).

Predicting the chemosensitivity of high- and low-risk groups to drugs

Because chemotherapy plays an important role in the treatment of LUAD, three separate drug response databases (GDSC, CTRP, and PRISM) were evaluated to identify possible treatment candidates with high drug sensitivity in high- and low-risk LUAD groups. Determination of the IC_{50} values of tumor cells treated with several targeted anticancer agents from the GDSC dataset showed that the estimated IC_{50} levels of cisplatin and docetaxel were significantly lower in the high-risk group, suggesting that this group was more sensitive to these drugs. Patients in the high-risk group were also found to be sensitive to gemcitabine. In addition, several inducers of autophagy, including sorafenib, AKT inhibitor VIII, AZD8055, rapamycin, MK2206, and NVP BEZ235, were identified as potential chemotherapeutic drugs for patients in the high-risk group (Figure 6D). Further assessment of chemotherapy candidates using PRISM and CTRP showed that several inducers of autophagy, such as AZD8055, KU-0063794, and deforolimus, were more suitable for patients in the high-risk group, whereas AZD8330, ixazomib, LY2090314, narasin, YM-155, and TAK-733 were found to be potentially effective in the low-risk group (Figure 6E). Six CTRP-derived compounds, namely, AZD8055, brefeldin A, paclitaxel, vincristine, KX2-391, and BI-2536, showed high sensitivity in the high-risk group, whereas fumonisin B1, an autophagy inhibitor, was identified as a potential chemotherapeutic drug in the low-risk group (Figure 6F). To further validate the synergistic effects of chemoimmunotherapeutic agents, potential drug responses were assessed in immunotherapy cohorts by GDSC. AKT inhibitor VIII, rapamycin, MK2206, and NVP BEZ235 showed greater sensitivity in patients with poorer prognosis for survival (Figure 6G). These findings indicate targeted multichannel combinations of autophagy inducers and immune checkpoint inhibitors may enhance immune responses and increase survival rates.

Expression level of four autophagy-immune-related genes by qRT-PCR

The expression of the four major autophagy-immune genes was assessed by qRT-PCR in 17 paired LUAD and adjacent normal tissue samples. The level of CD300LG mRNA was found to be significantly higher in normal lung than in LUAD tissue samples (Supplementary Figure 7A). Similarly, the levels of expression of CD96 and C4BPA were higher in normal lung, although the differences were not statistically significant (Supplementary Figures 7B, C). In contrast to previous findings, however, the present study found that level of expression of S100P mRNA was significantly higher in tumor samples than in adjacent normal tissue (Supplementary Figure 7D). To further evaluate the role of S100P in lung cancer, its level of expression was compared in the normal lung epithelial cell line (BEAS-2B) and four LUAD cell lines (H1975, HCC827, A549, and PC9). These findings showed that the levels of S100P were higher in all LUAD cell lines than in normal lung epithelium (Supplementary Figure 7E).

Discussion

Autophagy and the immune status of LUAD have been found to affect tumor progression and patient prognosis. Thus, in developing a prognostic strategy, focusing on a single feature may not be sufficient to classify patients with LUAD. The present study explored the potential role of a classifier based on autophagy and immune expression profiles in determining the prognosis of patients with LUAD.

FIGURE 6
(A) GO analysis of differentially expressed genes between the high- and low-risk group. **(B)** KEGG pathways enrichment analysis of differentially expressed genes between the high- and low-risk group; blue represents the high-risk group and red represents the low-risk group. **(C)** GSEA enrichment results of the low-risk group and the high-risk group. **(D)** The results of potential chemotherapy response by the GDSC dataset. **(E)** The results of Spearman's correlation analysis and differential drug response analysis of 12 PRISM-derived compounds. **(F)** The results of Spearman's correlation analysis and differential drug response analysis of 12 CTRP-derived compounds. **(G)** The results of potential autophagy inducers in the immunotherapy cohort by the GDSC dataset. GO, Gene Ontology; KEGG, Kyoto Encyclopedia of Genes and Genomes; GSEA, Gene set enrichment analysis. ns for $p > 0.05$, * for $p < 0.05$, ** for $p < 0.01$, *** for $p < 0.001$.

LASSO and univariate and multivariate Cox regression analyses identified four signature genes that comprised an autophagy-immune-related gene model. Three of these genes, C4BPA, CD96, and CD300LG, were associated with better OS, whereas the fourth, S100P, correlated with poorer prognosis. C4BPA had been identified as a novel serum biomarker for pancreatic ductal adenocarcinoma (PDAC) and breast cancer (20, 21). C4BPA was shown to enhance T cell-mediated antitumor immunity in patients with PDAC by promoting CD8+ cell proliferation (22). Regulation of C4BPA can inhibit the PI3K/Akt/mTOR signaling pathway induced by the overexpression of CADM1, thereby affecting the migration and invasion of ovarian cancer cells (23). C4BPA was also found to regulate NF-κB-dependent apoptosis (24). The present study confirmed that C4BPA was overexpressed in the low-risk group and was associated with a higher proportion of infiltrating immune cells and better prognosis in patients with LUAD, as well as being correlated with apoptosis. The expression of CD96 was shown to be significantly elevated in various cancers and to correlate positively with levels of infiltration of several types of immune cells, including CD8+ T cells, DCs, macrophages, monocytes, NK cells, neutrophils, and Tregs (25). As a novel immune checkpoint, CD96 expression was found to correlate strongly with the levels of expression of several other immune checkpoints, such as PD-1, TIGIT, CTLA-4, and CD266 (26). The TIGIT–CD96–CD266 axis was shown to play an important role in regulating T- and NK-cell functions and potential cancer immunotherapy (27). Blockade of CD96 can enhance PD-1/PD-L1 and anti-TIGIT inhibition, leading to increased tumor regression and greater efficacy of immunotherapy (25). The present study showed that CD96 was highly expressed in the low-risk group and was correlated with greater immune cell infiltration and the expression of other co-inhibitory receptors, such as TIGIT and PD-1. Moreover, the higher expression of CD96 in the low-risk group suggested that this group was more likely to benefit from immunotherapy. The only gene associated with the risk of LUAD in the present study was S100P, which had been identified as associated with the risk of several other types of cancer and in the promotion of metastasis. For example, S100P was found to be significantly associated with early recurrence and poorer clinical outcomes in patients with hepatocellular carcinomas (28). S100P was shown to be highly expressed in pancreatic cancer, adult rhabdomyosarcoma, colorectal cancer, and breast cancer (29–32). S100P was also found to be associated with metastasis and poorer survival in patients with LUAD (33). S100P overexpression was also associated with increased angiogenesis and metastasis in subcutaneous tumor xenograft models (34). In addition, the interaction between Keap1 and Nrf2 was found to suppress LUAD tumor progression by inhibiting the S100P protein (35). Although the present study found that S100P expression was associated with autophagy status, further studies are needed to evaluate the relationship between LUAD progression induced by S100P overexpression and autophagy. The present study also identified several potential anticancer agents for treatment of high-risk and low-risk patients, based on the different levels of expression of the four key genes. Additional studies of the relationships of these four genes with potential chemotherapeutic agents may be useful to guide treatment options for patients with LUAD. Overall, the present results provided valuable information on potential biomarkers to determine molecular mechanisms in LUAD. To our knowledge, this is the first composite signature risk model of immunity and autophagy status in LUAD.

Differences in immune and inflammatory landscapes in the low-risk and high-risk groups were evaluated by analysis of tumor-infiltrating immune cells and by metagene analysis. The low-risk group showed higher proportions of immune invading cells, including activated CD8 T cells, effector memory CD8 T cells, central memory CD4 T cells, M1 macrophages, activated B cells, and T follicular helper cells than the high-risk group. Cytotoxic CD8+ T lymphocytes have been identified as anti-tumor immune cells (36). By directly presenting antigen to T cells, B cells play a critical role in anti-tumor immunological responses (37). ESTIMATE analysis in the present study showed that both immune scores and stromal scores were higher in the low-risk group. These results suggest significant associations between immune landscapes and clinical outcomes in patients with LUAD.

The involvement of autophagy in cancer progression remains unclear, as the expression of autophagy-related genes has been associated with both tumor suppression and tumor enhancement (38). Autophagic death can systemically eliminate pre-malignant cells (39). Defective autophagy can result in the accumulation of damaged organelles and misfolded proteins, which can lead to DNA damage and cancer (40). However, autophagy has the potential to promote tumor growth by facilitating immune evasion and cancer metastasis (41, 42). 5′-AMP-activated protein kinase (AMPK) and mTOR complex 1 (mTORC1) have been identified as key regulatory kinases that affect the autophagy process, with AMPK activating and mTORC1 inhibiting autophagy (13). Based on enrichment of autophagy-related pathways, the low- and high-risk groups in the present study were characterized as having high- and low-autophagy status, respectively. The levels of expression of several core autophagic genes, including ATG3, ATG4A, ATG7, ATG12, ATG16L2, and ULK3, were found to be higher in the low- than in the high-risk group. ATG7, a major component of the CK1α/PTEN/FOXO3a/ATG7 axis, has been shown to be involved in the tumor-suppressive process in early LUAD (43). The expression of other autophagy-related genes, such as ATG13, BECN1, and ULK1, was found to be higher in high-risk groups. ULK1-ATG13 was shown to influence the cell cycle and promote tumor progression (44), with GSEA results in the present study also suggesting that the cell cycle pathway was enriched in the high-risk group. In addition, BECN1 and ULK1

have been shown to promote tumor growth in various cancers (45).

Autophagy occurs in all cellular components of the TME, allowing active interventions in interactions among stromal, immunological, and cancer cells (46). Autophagy was found to be involved in modulating immune cell development and differentiation (12). A greater knowledge of the link between autophagy and the immune system might allow the development of individualized cancer therapy. ssGSEA and ESTIMATE analyses in the present study showed a correlation between autophagy status and immune cell infiltration. GSEA pathway analysis of autophagy-associated DEGs showed enrichment of several immune-related pathways, whereas GSEA of immune-associated DEGs showed enrichment of several autophagy-related pathways. These findings indicated that autophagy status and immune status were associated with each other. Toll-like receptors are important mediators of immune regulation that have been shown to promote the activation of autophagy by upregulating the autophagy receptor p62 (47). In addition, damage-associated molecular patterns (DAMPs) have been found to activate innate immune cells and drive autophagic responses *via* Toll-like receptors (48, 49). The present study found that the Toll-like receptor signaling pathway was more prevalent in the low-risk group with better immunological and autophagy states. Tumor-derived lactate has been shown to suppress FIP200 expression, which is required for autophagosome formation, in tumor-infiltrating T cells, resulting in T-cell apoptosis and attenuation of antitumor immunity (50). PIK3C3, an early key player in autophagy, plays a critical role in regulating T-cell differentiation (51). ATG7 deletion results in autophagy-deficient effector CD4+ T cells, which express low levels of IL-2 and IFN (52). Inhibition of autophagy results in the accumulation of depolarized mitochondria in memory CD8+ T cells, resulting in terminal exhaustion of T-cell functional and epigenetic features (53). In contrast, activation of CD8+ cytotoxic T cells by the major histocompatibility complex (MHC) class I frequently results in an immune response, with intact autophagosomes of dead tumor cells required for MHC class I-mediated cross-presentation to CD8+ T lymphocytes (54). The findings of the present study are in agreement with results showing the roles of autophagy in T-cell survival, differentiation, and function. Moreover, autophagy can influence chemokine expression in tumor cells as well as immune cell migration to the tumor. $Kras^{G12D}$-driven lung cancer cells with defective autophagy exhibit high levels of the proinflammatory chemokine CXCL5 (55).

Ferroptosis has been shown to be an important mechanism by which CD8+ T lymphocytes influence tumor death (56). Autophagy plays an indispensable role in the process of ferroptosis, including in ROS accumulation (57). Thus, activation of autophagy may enhance tumor ferroptosis and increase the effectiveness of tumor immunotherapy. The present study found that the expression of ferroptosis-driver genes was higher in the low-risk group, consistent with results linking increases in autophagy and immunity with increases in ferroptosis. Evaluations of cell metabolism has shown that glycolysis is activated following reduction in autophagy flux, with this being corrected by decreased CD8+ T-cell infiltration (58). The present study found that the glycolysis pathway was more prevalent in the high-risk group, confirming the relationships among glycolysis, autophagy, and immunity. Overall, autophagy appears to change tumor antigen presentation, immune cell survival, and function in the TME.

Because autophagy is required for the modulation of tumor immunity, targeting autophagy in combination with other cancer therapies may enhance patient prognosis. Autophagy is involved in the regulation of immunogenic cell death (ICD), which is important for tumor-specific immunity and anticancer immune responses. In response to ICD inducers, such as oxaliplatin, tumor autophagy can promote the preservation of lysosomal ATP reserves and increase the number of dendritic cells to enhance antitumor immunity (59). Autophagy may induce tumor immunogenicity during radiotherapy (60). In contrast, preclinical studies have found that high autophagic flux may lead to chemotherapy resistance of several cancers, such as NSCLC and bladder cancer (61, 62). A comprehensive understanding of the nature of chemotherapy-induced autophagy will guide the development of future clinical trials.

Because autophagy is involved in tumor-infiltrating immune cell development, inducers of autophagy may enhance the efficacy of immunotherapy. Several preclinical models, however, have shown that the immune system may tolerate a certain level of autophagy suppression (63). The efficacy of autophagy inhibitors in combination with immunotherapy has therefore been evaluated. For example, when combined with ICB therapy, CQ, a traditional inhibitor of autophagy, was found to improve antitumor immune response by preventing autophagy-mediated MHC class I degression (64). In addition, CQ was found to limit the toxicity and enhance the immunotherapeutic efficacy of high-dose IL-2 in a mouse model of metastatic liver cancer (65). Clinical trials testing HCQ in combination with immunotherapy are currently underway in patients with metastatic RCC and pancreatic cancer (13). The present study found that patients in the high-risk group in the GSE72094 dataset, with poorer immunological and autophagy status, were more sensitive to inducers of autophagy, such as AKT inhibitor VIII, AZD8055, rapamycin, MK2206, NVP BEZ235, and KU −0063794, than patients in the low-risk group. Several inducers of autophagy were identified as potential chemotherapeutic drugs for patients in the high-risk group. In contrast, patients in the low-risk group were found to be highly sensitive to fumonisin B1, an inhibitor of ceramide synthesis that interferes with autophagy. These findings suggest the following hypothesis: At lower levels of immune cell infiltration, autophagy plays a protective role in inhibiting tumor growth,

with autophagy-inducing agonists improving the prognosis of patients with LUAD. At higher levels of immune cell infiltration, however, autophagy may impair immune function and promote tumor growth, such that autophagy inhibitors can be used to effectively treat these patients. Evaluation of the tumor immune microenvironment is therefore required to determine the optimal patient treatment strategy, which may consist of combinations of immunotherapeutic agents and either inhibitors or inducers of autophagy. Additional studies are needed to fully determine the various functions of autophagy pathways and their possible interactions in tumor immunity and immunotherapy. Combining autophagy and immunity may not only serve to classify patient prognosis but to guide treatment.

The present study had several limitations. First, all analyses were performed on data obtained from public databases. Prospective, multicenter studies are therefore required to validate the generalizability of this model. Second, because the microenvironmental properties of various tumor regions differ, the autophagy and immunological states at distinct tumor locations may not be distinguishable when the tumor is viewed as a whole. In addition, because of the limitation of the drug dataset, many autophagy core drugs, such as HCQ, CQ, and 3-MA, were included in the present study. Additional preclinical and clinical trials are required to verify the effect of combinations of immunotherapeutic agents with autophagy inducers and inhibitors. Third, the numbers of paired clinical specimens and cell lines used to assess gene expression by qRT-PCR may have been too small. The lack of a sufficient number of samples may explain the disparate qRT-PCR results obtained in clinical specimens and cell lines. Finally, because the regulation of autophagy depends on the phosphorylation and dephosphorylation of autophagy-related proteins, the present findings based on RNA sequences do not provide a complete picture of the role of autophagy in LUAD. Proteomic analyses are needed prior to applying these findings to clinical practice.

Data availability statement

The datasets presented in this study can be found in online repositories. The names of the repository/repositories and accession number(s) can be found in the article/Supplementary Material.

Ethics statement

The studies involving human participants were reviewed and approved by The Human Research Ethics Committee at Jiangxi Cancer Hospital (NO.2022ky013). The patients/participants provided their written informed consent to participate in this study.

Authors contributions

QL, DX, and LY contributed to conceptualization, data curation, formal analysis, data curation, software and project administration, and writing manuscript. HQ contributed to software, visualization, and manuscript editing. PY and JD contributed to experiment and validation. CL, WZ, and MW contributed to the methodology and resources. YBZ, SW, and FL contributed to manuscript review. HZ, YZ, and FZ contributed to project administration and supervision. All authors contributed to the article and approved the submitted version.

Funding

This study was funded by the Natural Science Foundation of Guangdong (Grant Number 2021A1515010838), the Science and Technology Program of Guangzhou (Grant Number 201903010028), and the Guangdong Provincial People's Hospital Intermural Program (Grant Number KJ012019447).

Acknowledgments

We appreciate the data obtained from TCGA and GEO. We sincerely thank all the people involved.

Conflict of interest

The authors declare that the research was conducted in the absence of any commercial or financial relationships that could be construed as a potential conflict of interest.

The handling editor JZ declared a shared parent affiliation with the author WZ at the time of review.

Publisher's note

All claims expressed in this article are solely those of the authors and do not necessarily represent those of their affiliated organizations, or those of the publisher, the editors and the reviewers. Any product that may be evaluated in this article, or claim that may be made by its manufacturer, is not guaranteed or endorsed by the publisher.

Supplementary material

The Supplementary Material for this article can be found online at: https://www.frontiersin.org/articles/10.3389/fimmu.2022.944378/full#supplementary-material

References

1. Siegel RL, Miller KD, Fuchs HE, Jemal A. Cancer statistics, 2022. *CA Cancer J Clin* (2022) 72:7–33. doi: 10.3322/caac.21708

2. Thai AA, Solomon BJ, Sequist LV, Gainor JF, Heist RS. Lung cancer. *Lancet* (2021) 398:535–54. doi: 10.1016/S0140-6736(21)00312-3

3. Pi J, Hu X, Zhang Y, Wang Y, Jiang J, Yi F, et al. Integrated analysis of genetic ancestry and genomic alterations across cancers. *Cancer Cell* (2019) 34:549–60. doi: 10.1016/j.ccell.2018.08.019

4. Agholme L, Agnello M, Agostinis P, Aguirre-ghiso JA, Ahn HJ, Ait-mohamed O, et al. Guidelines for the use and interpretation of assays for monitoring autophagy. *Autophagy* (2012) 8:445–544.

5. Klionsky DJ, Abdel-Aziz AK, Abdelfatah S, Abdellatif M, Abdoli A, Abel S, et al. Guidelines for the use and interpretation of assays for monitoring autophagy (4th edition)(1). *Autophagy* (2021) 17:1–382. doi: 10.1080/15548627.2020.1797280

6. Rybstein MD, Bravo-San Pedro JM, Kroemer G, Galluzzi L. The autophagic network and cancer. *Nat Cell Biol* (2018) 20:243–51. doi: 10.1038/s41556-018-0042-2

7. Guo JY, Chen HY, Mathew R, Fan J, Strohecker AM, Karsli-Uzunbas G, et al. Activated ras requires autophagy to maintain oxidative metabolism and tumorigenesis. *Genes Dev* (2011) 25:460–70. doi: 10.1101/gad.2016311

8. Chen W, Zhang L, Zhang K, Zhou B, Kuo ML, Hu S, et al. Reciprocal regulation of autophagy and dNTP pools in human cancer cells. *Autophagy* (2014) 10:1272–84. doi: 10.4161/auto.28954

9. White E. Deconvoluting the context-dependent role for autophagy in cancer. *Nat Rev Cancer* (2012) 12:401–10. doi: 10.1038/nrc3262

10. Bremnes RM, Busund LT, Kilver TL, Andersen S, Richardsen E, Paulsen EE, et al. The role of tumor-infiltrating lymphocytes in development, progression, and prognosis of non-small cell lung cancer. *J Thorac Oncol* (2016) 11:789–800. doi: 10.1016/j.jtho.2016.01.015

11. He Y, Yu H, Rozeboom L, Rivard CJ, Ellison K, Dziadziuszko R, et al. LAG-3 protein expression in non–small cell lung cancer and its relationship with PD-1/PD-L1 and tumor-infiltrating lymphocytes. *J Thorac Oncol* (2017) 12:814–23. doi: 10.1016/j.jtho.2017.01.019

12. Clarke AJ, Simon AK. Autophagy in the renewal, differentiation and homeostasis of immune cells. *Nat Rev Immunol* (2019) 19:170–83. doi: 10.1038/s41577-018-0095-2

13. Xia H, Green DR, Zou W. Autophagy in tumour immunity and therapy. *Nat Rev Cancer* (2021) 21:281–97. doi: 10.1038/s41568-021-00344-2

14. Baginska J, Viry E, Berchem G, Poli A, Noman MZ, Van Moer K, et al. Granzyme b degradation by autophagy decreases tumor cell susceptibility to natural killer-mediated lysis under hypoxia. *Proc Natl Acad Sci U.S.A.* (2013) 110:17450–5. doi: 10.1073/pnas.1304790110

15. Pender A, Titmuss E, Pleasance ED, Fan KY, Pearson H, Brown SD, et al. Genome and transcriptome biomarkers of response to immune checkpoint inhibitors in advanced solid tumors. *Clin Cancer Res* (2021) 27:202–12. doi: 10.1158/1078-0432.CCR-20-1163

16. Charrad M, Ghazzali N, Boiteau V, Niknafs A. Nbclust: An r package for determining the relevant number of clusters in a data set. *J Stat Softw* (2014) 61:1–36. doi: 10.18637/jss.v061.i06

17. Şenbabaoğlu Y, Michailidis G, Li JZ. Critical limitations of consensus clustering in class discovery. *Sci Rep* (2014) 4:6207. doi: 10.1038/srep06207

18. Subramanian A, Tamayo P, Mootha VK, Mukherjee S, Ebert BL, Gillette MA, et al. Gene set enrichment analysis: a knowledge-based approach for interpreting genome-wide expression profiles. *Proc Natl Acad Sci U.S.A.* (2005) 102:15545–50. doi: 10.1073/pnas.0506580102

19. Yang C, Huang X, Li Y, Chen J, Lv Y, Dai S. Prognosis and personalized treatment prediction in TP53-mutant hepatocellular carcinoma: An in silico strategy towards precision oncology. *Brief Bioinform* (2021) 22:1–13. doi: 10.1093/bib/bbaa164

20. Sogawa K, Takano S, Iida F, Satoh M, Tsuchida S, Kawashima Y, et al. Identification of a novel serum biomarker for pancreatic cancer, C4b-binding protein α-chain (C4BPA) by quantitative proteomic analysis using tandem mass tags. *Br J Cancer* (2016) 115:949–56. doi: 10.1038/bjc.2016.295

21. Suman S, Basak T, Gupta P, Mishra S, Kumar V, Sengupta S, et al. Quantitative proteomics revealed novel proteins associated with molecular subtypes of breast cancer. *J Proteomics* (2016) 148:183–93. doi: 10.1016/j.jprot.2016.07.033

22. Sasaki K, Takano S, Tomizawa S, Miyahara Y, Furukawa K, Takayashiki T, et al. C4b-binding protein α-chain enhances antitumor immunity by facilitating the accumulation of tumor-infiltrating lymphocytes in the tumor microenvironment in pancreatic cancer. *J Exp Clin Cancer Res* (2021) 40:1–16. doi: 10.1186/s13046-021-02019-0

23. Si X, Xu F, Xu F, Wei M, Ge Y, Chenge S. CADM1 inhibits ovarian cancer cell proliferation and migration by potentially regulating the PI3K/Akt/mTOR pathway. *BioMed Pharmacother* (2020) 123:109717. doi: 10.1016/j.biopha.2019.109717

24. Olcina MM, Kim RK, Balanis NG, Li CG, von Eyben R, Graeber TG, et al. Intracellular C4BPA levels regulate NF-κB-Dependent apoptosis. *iScience* (2020) 23:101594. doi: 10.1016/j.isci.2020.101594

25. Mittal D, Lepletier A, Madore J, Aguilera AR, Blake SJ, Whitehall VLJ, et al. CD96 is an immune checkpoint that regulates CD8+ T-cell antitumor function. *Cancer Immunol Res* (2019) 7:559–71. doi: 10.1158/2326-6066.CIR-18-0637

26. Lepletier A, Lutzky VP, Mittal D, Stannard K, Watkins TS, Ratnatunga CN, et al. The immune checkpoint CD96 defines a distinct lymphocyte phenotype and is highly expressed on tumor-infiltrating T cells. *Immunol Cell Biol* (2019) 97:152–64. doi: 10.1111/imcb.12205

27. Jin Hs, Park Y. Hitting the complexity of the TIGIT-CD96-CD112R-CD226 axis for next-generation cancer immunotherapy. *BMB Rep* (2021) 54:2–11. doi: 10.5483/BMBRep.2021.54.1.229

28. Hwang HS, An J, Kang HJ, Oh B, Oh YJ, Oh JH, et al. Prognostic molecular indices of resectable hepatocellular carcinoma: Implications of S100P for early recurrence. *Ann Surg Oncol* (2021) 28:6466–78. doi: 10.1245/s10434-021-09825-y

29. Camara R, Ogbeni D, Gerstmann L, Ostovar M, Hurer E, Scott M, et al. Discovery of novel small molecule inhibitors of S100P with *in vitro* anti-metastatic effects on pancreatic cancer cells. *Eur J Med Chem* (2020) 203:112621. doi: 10.1016/j.ejmech.2020.112621

30. Kikuchi K, McNamara KM, Miki Y, Iwabuchi E, Kanai A, Miyashita M, et al. S100P and ezrin promote trans-endothelial migration of triple negative breast cancer cells. *Cell Oncol* (2019) 42:67–80. doi: 10.1007/s13402-018-0408-2

31. De Vita A, Vanni S, Fausti V, Cocchi C, Recine F, Miserocchi G, et al. Deciphering the genomic landscape and pharmacological profile of uncommon entities of adult rhabdomyosarcomas. *Int J Mol Sci* (2021) 22(21):11564. doi: 10.3390/ijms222111564

32. Lin M, Fang Y, Li Z, Li Y, Feng X, Zhan Y, et al. S100P contributes to promoter demethylation and transcriptional activation of SLC2A5 to promote metastasis in colorectal cancer. *Br J Cancer* (2021) 125:734–47. doi: 10.1038/s41416-021-01306-z

33. Diederichs S, Bulk E, Steffen B, Ji P, Tickenbrock L, Lang K, et al. S100 family members and trypsinogens are predictors of distant metastasis and survival in early-stage non-small cell lung cancer. *Cancer Res* (2004) 64:5564–9. doi: 10.1158/0008-5472.CAN-04-2004

34. Wang T, Du G, Wang D. The S100 protein family in lung cancer. *Clin Chim Acta* (2021) 520:67–70. doi: 10.1016/j.cca.2021.05.028

35. Chien MH, Lee WJ, Hsieh FK, Li CF, Cheng TY, Wang MY, et al. Keap1-Nrf2 interaction suppresses cell motility in lung adenocarcinomas by targeting the S100P protein. *Clin Cancer Res* (2015) 21:4719–32. doi: 10.1158/1078-0432.CCR-14-2880

36. Hu Z, Qu G, Yu X, Jiang H, Teng XL, Ding L, et al. Acylglycerol kinase maintains metabolic state and immune responses of CD8+ T cells. *Cell Metab* (2019) 30:290–302.e5. doi: 10.1016/j.cmet.2019.05.016

37. Sharonov GV, Serebrovskaya EO, Yuzhakova DV, Britanova OV, Chudakov DM. B cells, plasma cells and antibody repertoires in the tumour microenvironment. *Nat Rev Immunol* (2020) 20:294–307. doi: 10.1038/s41577-019-0257-x

38. Li X, He S, Ma B. Autophagy and autophagy-related proteins in cancer. *Mol Cancer* (2020) 19:1–16. doi: 10.1186/s12943-020-1138-4

39. Gonzalez JB, Exposito LG, Hoang SM, Lee M, Roncaioli JL, Ghosh A, et al. RAD51AP1 is an essential mediator of alternative lengthening of telomeres. *Mol Cell* (2020) 76:11–26. doi: 10.1016/j.molcel.2019.06.043

40. Boya P, Reggiori F, Codogno P. Emerging regulation and functions of autophagy. *Nat Cell Biol* (2013) 15:713–20. doi: 10.1038/ncb2788

41. Dower CM, Wills CA, Frisch SM, Wang HG. Mechanisms and context underlying the role of autophagy in cancer metastasis. *Autophagy* (2018) 14:1110–28. doi: 10.1080/15548627.2018.1450020

42. Young TM, Reyes C, Pasnikowski E, Castanaro C, Wong C, Decker CE, et al. Autophagy protects tumors from T cell-mediated cytotoxicity *via* inhibition of TNFα-induced apoptosis. *Sci Immunol* (2020) 5:1–18. doi: 10.1126/sciimmunol.abb9561

43. Cai J, Li R, Xu X, Zhang L, Lian R, Fang L, et al. CK1α suppresses lung tumour growth by stabilizing PTEN and inducing autophagy. *Nat Cell Biol* (2018) 20:465–78. doi: 10.1038/s41556-018-0065-8

44. Li Z, Tian X, Ji X, Wang J, Chen H, Wang D, et al. ULK1-ATG13 and their mitotic phospho-regulation by CDK1 connect autophagy to cell cycle. *PloS Biol* (2020) 18:1–29. doi: 10.1371/journal.pbio.3000288

45. Levy JMM, Towers CG, Thorburn A. Targeting autophagy in cancer. *Nat Rev Cancer* (2017) 17:528–42. doi: 10.1038/nrc.2017.53

46. Yamazaki T, Bravo-San Pedro JM, Galluzzi L, Kroemer G, Pietrocola F. Autophagy in the cancer-immunity dialogue. *Adv Drug Delivery Rev* (2021) 169:40–50. doi: 10.1016/j.addr.2020.12.003

47. Mittmann N, Stout NK, Lee P, Tosteson ANA, Trentham-Dietz A, Alagoz O, et al. NF-κB restricts inflammasome activation *via* elimination of damaged mitochondria. *Cell* (2015) 26:16–25. doi: 10.1016/j.cell.2015.12.057

48. Gong T, Liu L, Jiang W, Zhou R. DAMP-sensing receptors in sterile inflammation and inflammatory diseases. *Nat Rev Immunol* (2020) 20:95–112. doi: 10.1038/s41577-019-0215-7

49. Ma Y, Galluzzi L, Zitvogel L, Kroemer G. Autophagy and cellular immune responses. *Immunity* (2013) 39:211–27. doi: 10.1016/j.immuni.2013.07.017

50. Girirajan S, Campbell C, Eichler E. Suppression of FIP200 and autophagy by tumor-derived lactate promotes naïve T cell apoptosis and affects tumor immunity. *Physiol Behav* (2011) 176:139–48. doi: 10.1126/sciimmunol.aan4631. Suppression

51. Yang G, Song W, Postoak JL, Chen J, Martinez J, Zhang J, et al. Autophagy-related protein PIK3C3/VPS34 controls T cell metabolism and function: PIK3C3/VPS34 in T cell metabolism and function. *Autophagy* (2021) 17:1193–204. doi: 10.1080/15548627.2020.1752979

52. Pauff SM, Miller SC. Macroautophagy regulates energy metabolism during effector T cell activation. *Bone* (2012) 78:711–6. doi: 10.4049/jimmunol.1000576. Macroautophagy

53. Swadling L, Pallett LJ, Diniz MO, Baker JM, Amin OE, Stegmann KA, et al. Human liver memory CD8+ T cells use autophagy for tissue residence. *Cell Rep* (2020) 30:687–698.e6. doi: 10.1016/j.celrep.2019.12.050

54. Pauff SM, Miller SC. Tumor-derived autophagosome vaccine: Mechanism of cross- presentation and therapeutic efficacy. *Bone* (2012) 78:711–6. doi: 10.1158/1078-0432.CCR-11-0951.Tumor-Derived

55. Rao S, Tortola L, Perlot T, Wirnsberger G, Novatchkova M, Nitsch R, et al. A dual role for autophagy in a murine model of lung cancer. *Nat Commun* (2014) 5:3056. doi: 10.1038/ncomms4056

56. Wang W, Green M, Choi JE, Kennedy PD, Johnson JK, Liao P, et al. CD8+ T cells regulate tumor ferroptosis during cancer immunotherapy. *Nature* (2019) 569:270–4. doi: 10.1038/s41586-019-1170-y

57. Hou W, Xie Y, Song X, Sun X, Lotze MT, Zeh HJ, et al. Autophagy promotes ferroptosis by degradation of ferritin. *Autophagy* (2016) 12:1425–8. doi: 10.1080/15548627.2016.1187366

58. Mani DR, Krug K, Zhang B, Satpathy S, Clauser KR, Ding L, et al. Cancer proteogenomics: Current impact and future prospects. *Nat Rev Cancer* (2022) 22 (5):298–313. doi: 10.1038/s41568-022-00446-5

59. Sompolinsky H, Sejnowski T, Zador AM, Lampl I, Merzenich MM, Schreiner CE, et al. Autophagy-dependent anticancer immune responses induced by chemotherapeutic agents in mice. *Science* (2011) 334:1573–8.

60. Ko A, Kanehisa A, Martins I, Senovilla L, Chargari C, Dugue D, et al. Autophagy inhibition radiosensitizes *in vitro*, yet reduces radioresponses *in vivo* due to deficient immunogenic signalling. *Cell Death Differ* (2014) 21:92–9. doi: 10.1038/cdd.2013.124

61. Zou Y, Ling YH, Sironi J, Schwartz EL, Perez-Soler R, Piperdi B. The autophagy inhibitor chloroquine overcomes the innate resistance of wild-type EGFR non-small-cell lung cancer cells to erlotinib. *J Thorac Oncol* (2013) 8:693–702. doi: 10.1097/JTO.0b013e31828c7210

62. Kang M, Lee KH, Lee HS, Jeong CW, Kwak C, Kim HH, et al. Concurrent autophagy inhibition overcomes the resistance of epidermal growth factor receptor tyrosine kinase inhibitors in human bladder cancer cells. *Int J Mol Sci* (2017) 18 (2):321. doi: 10.3390/ijms18020321

63. Starobinets H, Ye J, Broz M, Barry K, Goldsmith J, Marsh T, et al. Antitumor adaptive immunity remains intact following inhibition of autophagy and antimalarial treatment. *J Clin Invest* (2016) 126:4417–29. doi: 10.1172/JCI85705

64. Yamamoto K, Venida A, Yano J, Biancur DE, Gupta S, Sohn ASW, et al. Autophagy promotes immune evasion of pancreatic cancer by degrading MHC-I. *Nature* (2020) 581:100–5. doi: 10.1038/s41586-020-2229-5

65. Michael W, Andries Zijlstra JPW and AP. Inhibiting autophagy during interleukin 2 (IL-2) immunotherapy promotes long term tumor regression. *Exp Biol Med* (2014) 239:1476–88. doi: 10.1158/0008-5472.CAN-12-0320

frontiers | Frontiers in Immunology

TYPE Original Research
PUBLISHED 15 September 2022
DOI 10.3389/fimmu.2022.991431

Check for updates

OPEN ACCESS

EDITED BY
Jian Zhang,
Southern Medical University, China

REVIEWED BY
Hidekazu Tanaka,
Yamaguchi University Graduate School of Medicine, Japan
Mattia Falchetto Osti,
Sapienza University of Rome, Italy

*CORRESPONDENCE
Haihua Yang
yhh93181@hotmail.com

SPECIALTY SECTION
This article was submitted to Cancer Immunity and Immunotherapy, a section of the journal Frontiers in Immunology

RECEIVED 11 July 2022
ACCEPTED 30 August 2022
PUBLISHED 15 September 2022

CITATION
Li S, Chen K, Yang M, Hlaing SS, Chen M, Gu P, Meng Y and Yang H (2022) Radiotherapy improves the outcomes of immunotherapy with Sintilimab in non-small-cell lung cancer: A real-world analysis. *Front. Immunol.* 13:991431. doi: 10.3389/fimmu.2022.991431

COPYRIGHT
© 2022 Li, Chen, Yang, Hlaing, Chen, Gu, Meng and Yang. This is an open-access article distributed under the terms of the Creative Commons Attribution License (CC BY). The use, distribution or reproduction in other forums is permitted, provided the original author(s) and the copyright owner(s) are credited and that the original publication in this journal is cited, in accordance with accepted academic practice. No use, distribution or reproduction is permitted which does not comply with these terms.

Radiotherapy improves the outcomes of immunotherapy with Sintilimab in non-small-cell lung cancer: A real-world analysis

Shuling Li[1,2], Kuifei Chen[1,2], Meiwen Yang[2,3], Swe Swe Hlaing[4], Meng Chen[2], Pinjun Gu[2], Yinnan Meng[2] and Haihua Yang[1,2]*

[1]Taizhou Hospital of Zhejiang Province, Shaoxing University, Taizhou, China, [2]Key Laboratory of Radiation Oncology of Taizhou, Radiation Oncology Institute of Enze Medical Health Academy, Department of Radiation Oncology, Taizhou Hospital Affiliated to Wenzhou Medical University, Taizhou, China, [3]Indiana Academy for Science Mathematics and Humanities, Munci, IN, United States, [4]Department of Internal Medicine, Crozer Chester Medical Center, Medical Center Blvd, Upland, PA, United States

Introduction: Radiotherapy may augment systemic antitumor responses to immunotherapy. We did a retrospective study to infer whether radiotherapy improves outcomes to immunotherapy in patients with stage III and IV non-small-cell lung cancer (NSCLC).

Methods: This retrospective study conducted at Enze Medical Center enrolled 259 patients with histopathology confirmed NSCLC from December 2018 to December 31, 2021. All were treated with Sintilimab, some patients received radiotherapy at an appropriate time point. Radiation type includes conventional radiotherapy and stereotactic body radiotherapy. The progression-free survival (PFS), and overall survival (OS) were the primary endpoint.

Results: A retrospective analysis was performed on 259 patients, of whom 140 had been treated with immunotherapy lonely and 119 had been remedied with immunotherapy plus radiotherapy. Baseline variables were well balanced between the two groups, including gender, age, smoking status, TNM staging, number of metastases, ECOG score, pathological type and lines of previous systemic therapy. The median PFS in the immunotherapy alone group was 5.00 months (95%CI 4.38-5.62) versus immunotherapy plus radiotherapy was 9.00 months (5.95-12.05; p<0.001). The median OS in the immunotherapy alone group was 16.00 months (12.59-19.42) versus immunotherapy plus radiotherapy was 30.00 months (20.75-39.25; p=0.027). PFS was finer in the radiotherapy plus immunotherapy group than the immunotherapy group alone in both stage III (P=0.0069) and Stage IV(P=0.006) patients. In the univariate analysis, radiotherapy, male, ECOG=0 and <2 lines of previous systemic therapy were connected with an observably better PFS (P<0.001; P=0.03; P=0.002;P=0.021). In a multivariate analysis, radiotherapy, ECOG=0 and <2 lines of previous systemic therapy were independent prognostic factors with a markedly better

PFS (P<0.001; P=0.006;P=0.009). An univariate analysis, radiotherapy, male, stage III, non-metastasis, ECOG=0 and squamous carcinoma were associated with a significantly better OS (P=0.032, P=0.036,P=0.002,P<0.001,P=0.002, P=0.025). A multivariate analysis, non-metastasis was a standalone prognostic indicator with a significantly better OS (P=0.006). However, radiotherapy was a tendency indicator with a better OS (HR0.70 95% CI 0.47-1.06). There were also no obvious increases in adverse events in the combination group.

Conclusions: Radiotherapy with addition of immunotherapy was observably linked to a better outcome in patients with III and IV staging NSCLC.

KEYWORDS

non-small-cell lung cancer, radiotherapy, immunotherapy, progression free survival, overall survival

Introduction

According to GLOBOCAN 2020 (1), lung carcinoma remains the world's major reason of cancer death, with about 1.8 million people (18%) dying per year. In most nations, the 5-year survival rate for lung cancer patients diagnosed between 2000 and 2014 is just 10 to 20% (2). And non-small cell lung cancer (NSCLC) occupies a great proportion of more than 85% of all lung cancers. Surgery or radiotherapy are the main treatment in early-stage NSCLC. Nevertheless, chemotherapy, radiotherapy (RT), and immunotherapy (IT) have an indispensable role in intermediate and advanced stage patients. It is indicated that radical concurrent radiotherapy and chemotherapy is the main therapeutic style for stage III NSCLC in the NCCN guidelines (3). what's more, RT is also used for locally late or inoperable lung carcinoma. Immune checkpoint suppression against programmed death 1(PD-1) or programmed death ligand 1(PD-L1), with or without chemotherapy, have a better prognosis in patients with metastatic NSCLC (4, 5). *The Food and Drug Administration* (FDA) authorized nivolumab as a first-line therapy for patients with NSCLC whose PD-L1 expression is greater than 1% on the basis of the CheckMate 227 results (6).

In the tumor microenvironment, antigen presentation, proper co-stimulation, optimal cytokine production, and the attenuation of immunosuppressive signaling routing are probably necessary for anti-tumor immunity (7, 8). Changes to any of these stages can result in resistance to check point inhibitors, immunotherapy. Antigen presentation through the major histocompatibility complexes of antigen presenting cells is necessary to induce a potent T lymphocyte mediated immune reaction. As a result, the effectiveness of check point inhibitors is related to tumor mutation burden (9, 10). This is because an increase in tumor mutational burden is probably indicative of an increase in the total amount of tumor antigens, which gives the immune system more antigens to target. Through immunosuppressive modifications to the cellular environment in which tumor exists, tumor intrinsic signaling path have also been linked to immunotherapy resistance (11).

Surprisingly, radiotherapy can enhance the effect of immunotherapy. Radiation initiates an anti-tumor immune response. Radiation induces the release of tumor-associated antigens (TAAs). Tumor antigen is an antigenic substance produced in tumor cell, which can trigger an immune response in the host. When radiation is combined with immunity, Immune cells recognize more TTAs and encourage immune cells to enter the tumor, thereby enhancing tumor penetration and overcoming immunosuppression. In 2019, Brooks ED et al. also put forward the multi-target irradiation, which may increase the chance of initiating an anti-tumor immune response by irradiating multiple lesions (12). Radiotherapy combined with immune checkpoint inhibitors can increase mutual sensitization and strengthen the anti-tumor effect (13).

In the PACIFIC trial (14), immunotherapy had sustained OS and PFS benefit in stage III NSCLC following chemoradiotherapy. In a second study of the PEMBRO-RT and MDACC trials (15), radiotherapy plus immunotherapy apparently increased results in 148 patients with metastatic NSCLC. But the final results didn't meet the significant benefit in any single experiment. Besides, many studies have exhibited that immunotherapy combined with radiotherapy is safe and may be effective in treating solid tumor (16, 17). Moreover, there are relatively few studies on therapeutic effect of immunotherapy with or without radiotherapy in NSCLC patients. Hence, in our retrospective study, our aim is to assess the effectivity and safety

of immunotherapy plus radiotherapy compared with immunotherapy alone in patients with stage III or IV non-small cell lung cancer.

Materials and methods

Patient eligibility and data gathering

This research was intended to evaluate the consequences of immunotherapy and radiotherapy in stage III or IV NSCLC. We review the medical records of 259 patients with NSCLC between December, 2018 to December, 31st, 2021 in Taizhou Hospital, Zhejiang Province, China. Patients were divided into two groups based on whether they received RT or not: IT alone group and IT plus RT group. Postoperative patients with positive margin or gross residual tumor were treated with CRT. Patients with isolated or localized metastasis (such as brain, adrenal, and pulmonary lesions) received SBRT or CRT. Patients with stage III received concurrent chemoradiotherapy and immune maintenance therapy. For patients in the RT and IT group, SBRT was preferred, while patients who were not suitable for SBRT were treated with CRT.

Inclusion criteria: histologically or cytologically proven NSCLC; staging was defined as III or IV; age≥18 years; There were no restrictions on the number of metastatic sites; Eastern Co-operative Group (ECOG) score of 0–1, enough organ and bone marrow function. No epidermal growth factor receptor (EGFR) and anaplastic lymphoma kinase (ALK) targetable mutations. Excluded criteria: SCLC patients; The primary tumor was outside the lung; early stage of NSCLC; a concomitant serious illness, or were pregnant or breastfeeding. Patients with other tumors, such as nasopharyngeal cancer, who have not recurred for 5 years after treatment can be included. Demographic data recorded included: age, gender, smoking status, TNM staging, number of metastases, EOOG score, histological characteristics, irradiated tumor site, number of IT, lines of previous systemic therapy(<2 vs ≥2), date of progression, death time and last follow up time. All patients were staged on the basis of the American Joint Council on Oncology TNM Staging System, Version 8 (18). The research ethics committee of Taizhou Hospital of Zhejiang Province authorized this study, and individual consent was abandoned due to retrospective analysis.

All patients had not received prior targeted therapy. Patients were included those who had received previously systemic therapy. Patients all received the treatment of Sintilimab every 21 days no matter how much the expression of PD-L1. Some patients accepted radiotherapy at a specific and appropriate time point. In radiotherapy and immunotherapy group, the modality of radiotherapy was conventional radiotherapy (CRT) or stereotactic body radiotherapy (SBRT) for cancer of any site (including pulmonary lesions, lymph node(s) in intrathoracic or extra-thoracic, brain, bone, centrum, adrenal gland and other organs). Usually 95% of the plan tumor volume at the prescribed dose is required, limiting the doses of dangerous organs (OARs). Base on the Response Evaluation Criteria in Solid Tumors (RECIST) version 1.1 (19), progression was confirmed by Professionals. The Common Terminology standard for Adverse Events (CTCAE-version 5.0) classifies adverse reaction (20).

Statistical analysis

Progression-free survival and overall survival was the primary endpoint in this study. The minor endpoint was adverse reactions to treatment. Patient characteristics at baseline were summarized using descriptive statistical methods. Patient and treatment characteristics between two groups were compared using the Mann-Whitney U tests for nonnormally distributed variables. In this analysis, progression-free survival (PFS) was counted starting from the date of first immunotherapy until tumor relapse, any cause of death, or patient censoring at the follow-up period. Overall survival (OS) was computed beginning from the time of first immunotherapy until the death or last follow-up.

Kaplan-Meier method was used to evaluate the results of PFS and OS, and log-rank test was used to compare the differences between groups. In subgroup analysis, the influences of radiotherapy plus immunotherapy on PFS and OS in preset subgroups (age, gender, smoking status, TNM stage, number of metastases, EOOG score, histological characteristics, lines of previous systemic therapy), they were evaluated using the Cox proportional risk model in the forest map in pre-determined subgroups. The forest map displays the results of all subgroup analyses. The prognostic factors of PFS and OS were assessed *via* univariate and multivariate cox proportional hazard regression analyses. Multivariate analysis is performed on variables that are significant for univariate factors. $P<0.05$ was considered to be statistically significant. Statistical analysis was conducted with IBM SPSS statistics (V.25; Armonk, New York, USA) and GraphPad Prism (V.8; San Diego, California, USA).

Results

Baseline characteristics

From December 2018 to December 31,2021,259 patients were enrolled into this study. Table 1 displayed the Patients' clinical characteristics. Demographic and clinical characteristics were well matched between two groups at baseline. 119 patients received radiotherapy plus immunotherapy (RT+IT), and 140 patients accepted the immunotherapy (IT) alone. In RT+IT group, there were 106(89.1%) male patients, while there were 124(88.6%) male patients in IT alone group. 52.9% (63/119) of

TABLE 1 Patient Clinical Characteristics.

Category	IT+RT (N=119)		IT (N=140)		P value
	N	%	N	%	
Gender					0.898
Male	106	89.10%	124	88.60%	
Female	13	10.90%	16	11.40%	
Age category					0.484
≤65	63	52.90%	68	48.60%	
>65	56	47.10%	72	51.40%	
Smoking status					0.204
Never	35	29.40%	44	31.40%	
Current	12	10.10%	26	18.60%	
Former	72	60.50%	70	50%	
TNM					0.242
III	43	36.10%	41	29.30%	
IV	76	63.90%	99	70.70%	
Number of metastases					0.495
0	45	37.80%	43	30.70%	
<3	52	43.70%	74	52.90%	
≥3	22	18.50%	23	16.40%	
ECOG score					0.682
0	60	50.40%	67	47.90%	
1	59	49.60%	73	52.10%	
Histology					0.718
adenocarcinoma	37	31.10%	48	34.30%	
squamous carcinoma	75	63.00%	73	52.10%	
Others	7	5.90%	19	13.60%	
Irradiated tumor site					
pulmonary lesions	75	63.10%			
Lymph node(s), intrathoracic	1	0.80%			
Lymph node(s), extrathoracic	3	2.50%			
bone	3	2.50%			
brain	21	17.60%			
centrum	6	5.10%			
adrenal gland	2	1.70%			
others	8	6.70%			
Number of IT, median (P25, P75)	8(3,12)		5(3,11)		0.122
The time of received RT					
before IT	88				
after IT	10				
concurrent	21				
Lines of previous systemic therapy					0.081
<2	62	52.10%	88	62.90%	
≥2	57	47.90%	52	37.10%	

RT, Radiotherapy; IT, Immunotherapy.

the patients were less than 65 years old in RT+IT group, while in IT group, 48.6% (68/140) of patients were less than 65 years old. The primary tumor was non-small cell lung cancer in all patients. In RT+IT queue, the irradiated target lesions were as following: pulmonary lesions (63.1%, n=75), lymph nodes, intrathoracic (0.8%, n=1), lymph nodes, extrathoracic (2.5%, n=3), bone (2.5%, n=3), brain (17.6%, n=21), centrum (5.1%, n=6),adrenal glands (1.7%,n=2) and others(6.7%,n=8). Some patients received radiotherapy at an appropriate time point. 88 patients have undergone RT before IT,10 patients have

undergone RT after IT, and 21 patients have received concurrent treatment of RT and IT. There was no difference in the number of immunotherapies between IT group and IT plus RT group (P=0.122). The median number of IT is 8(3,12) in IT plus RT group and 5(3.11) in the IT alone group.75 patients accepted conventional radiotherapy (CRT) whose plan was 64.8Gy in 30 fractions or 54Gy in 25 fractions.42 patients received stereotactic body radiotherapy (SBRT) whose plan was 50Gy in 5 fractions or 60Gy in 8 fractions.2 patients accepted the particle implants in Pulmonary lesions.

Progression-free survival and overall survival

The Median follow-up time for all patients in this study was 15 months (13.22-16.78). 119 patients accepted sintilimab plus radiotherapy and 140 patients accepted sintilimab alone. Median progression-free survival (PFS) was all 6.00 months (95%CI 5.03-6.97), sintilimab combined with radiotherapy (9 months [95%CI 5.95-12.05]) was observably longer than sintilimab alone (5 months [4.38-5.62]), and hazard ratio (HR) was 0.54 (95%CI 0.41-0.72; P<0.001; Figure 1A). Figure 2A exhibited a subgroup analysis of PFS, sintilimab and radiotherapy as if most beneficial in male patients(p<0.001), patients who never smoke(p=0.002) or never give up smoking (p=0.007), III stage patients(p=0.011) or IV stage patients(p=0.001), patients with less than 3 metastases(p=0.003), patients with ECOG=0(p=0.004) or ECOG=1(p=0.003), those patients whose pathologic types were adenocarcinoma(p=0.027) and squamous carcinoma(p=0.001), and patients with <2(p=0.001) or ≥2(p=0.01) lines of previous systemic therapy.

Median overall survival (OS) was all 20.00 months (95%CI 15.27-24.73), sintilimab combined with radiotherapy (30 months [95%CI 20.75-39.25]) was significantly longer than sintilimab alone (16 months [12.59-19.42]) with hazard ratio (HR) of 0.66(95%CI0.45-0.97; p=0.027; Figure 1B). The 2-year OS rate was 55.28% in the sintilimab plus radiotherapy queue and 29.08% in the sintilimab queue. The 18-months OS rate was 59.82% in the sintilimab plus radiotherapy queue and 44.98% in the sintilimab queue. The 1-year OS rate was 66.71% in the sintilimab plus radiotherapy queue and 63% in the sintilimab queue. In the subgroup analysis of overall survival (Figure 2B), sintilimab plus radiotherapy appeared to be most beneficial in male patients(p=0.03), patients aged 65 or younger(p=0.013), and patients with less than 2 lines of previous systemic therapy(p=0.029).

Figure 3 displayed the Kaplan–Meier survival curves according to with or without RT in stage III or IV patients, extrathoracic RT or intrathoracic RT, and stereotactic body radiotherapy (SBRT) or conventional radiotherapy (CRT). In our study, we can see better PFS with radiotherapy in both stage III(n=84) and stage IV(n=175) patients. The 2-year OS rate was 67.37% in the radiotherapy plus immunotherapy (RT+IT, n=43) queue and 51.42% in the immunotherapy (IT, n=41) queue in stage III patients, The 2-year OS rate was 48.58% in the RT+IT (n=76) queue and 20.73% in the IT(n=99) queue in stage IV patients. However, there are no statistical difference between extrathoracic RT and intrathoracic RT, so as SBRT and CRT.

Table 2 displayed the results of univariate and multivariate analysis. Multivariate analysis was conducted for variables which were significant for univariate factors. All variables were included in univariate analysis, such as treatment methods, gender, age, smoking status, TNM staging, the number of metastases, ECOG score, histological type and lines of previous systemic therapy. In an univariate analysis, radiotherapy, male, ECOG=0 and <2 lines of previous systemic therapy were connected with a better PFS (P<0.001; P=0.03; P=0.002;P=0.021). In the multivariate analysis, radiotherapy, ECOG=0 and <2 lines of previous systemic therapy were independent prognostic factors with a significantly improved PFS(HR0.51 95%CI 0.38-0.69,P<0.001;HR0.66 95%CI 0.50-0.89, P=0.006;HR0.68 95%CI 0.51-0.91,P=0.009).In an univariate analysis, radiotherapy, male, stage III, non-metastasis, ECOG=0 and squamous carcinoma were linked to a significantly better OS (p=0.032, P=0.036, P=0.002, P<0.001, P=0.002, P=0.025). A multivariate analysis, non-metastasis was an independent prognostic indicator with a signally better OS (HR0.41 95%CI 0.22-0.77, P=0.006). However, radiotherapy was a tendency factor with a better OS(HR0.70 95% CI 0.47-1.06, p=0.09).

Toxicity

In other words, 22.7 percent of patients in the RT+IT queue and 20.7 percent of patients in the IT queue both experienced grade 1-3 toxicity, while none of the patients had grade 4 adverse reaction (Table 3). None of the deaths ascribed to sintilimab or RT. There was no statistically significant variation in any toxicity (P = 0.813) between the two groups. Pneumonitis rates, in particular, were low and didn't significantly differ between the RT+IT (6.7%) queue and IT (6.4%) queue (p=0.947). There was no case of Grade 3-4 pneumonitis in both teams.

Discussion

In our study, in comparison to sintilimab alone, we discovered that combination treatment with sintilimab and radiotherapy may improve PFS and OS in patients with stage III and IV NSCLC. In addition, this therapeutic method did not significantly enlarge the risk of adverse events. In Figure 1, we can see that sintilimab plus radiotherapy was associated with longer 1-year OS,18-month OS and 2-year OS. A research acted by Theelen W et al (15), PFS in immunotherapy plus

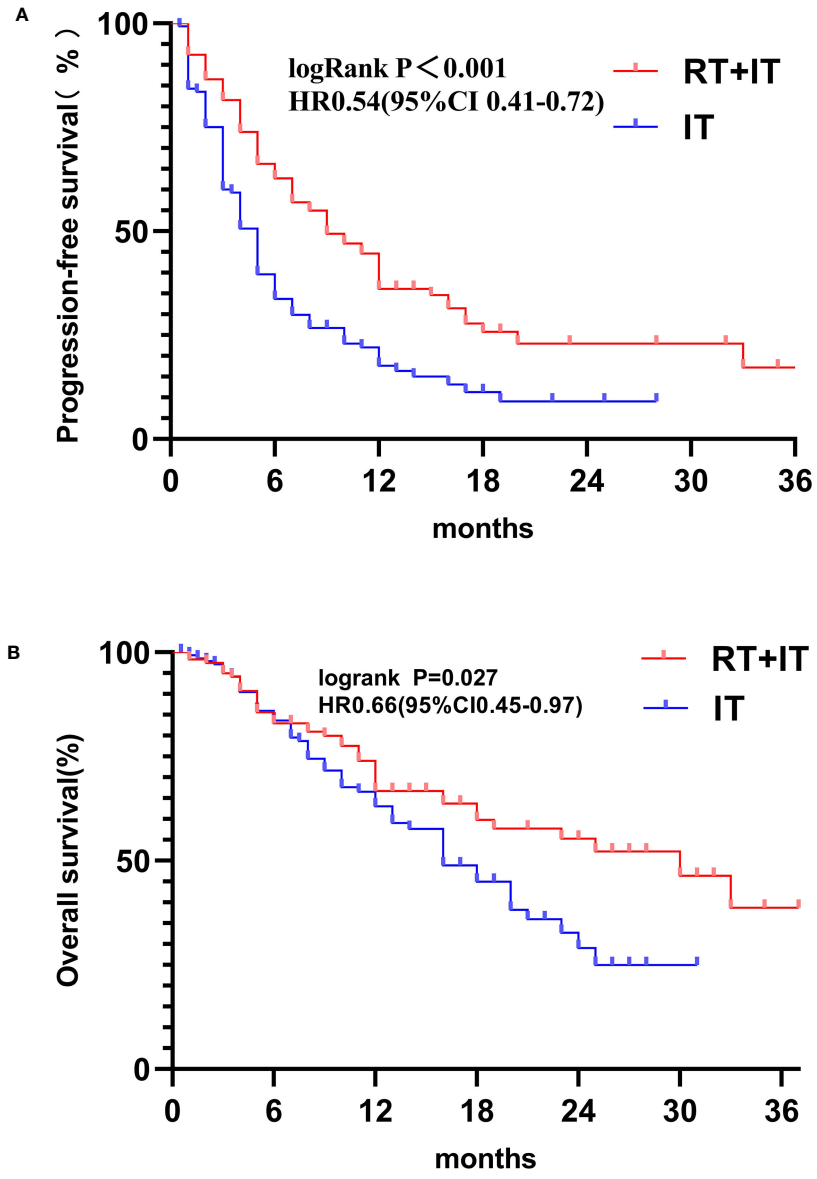

FIGURE 1
Kaplan-Meier analysis of progression-free survival **(A)** and overall survival **(B)**.

radiotherapy group was notably improved than immunotherapy alone group (p=0.045), and OS was remarkably increased in immunotherapy and radiotherapy group compared with immunotherapy alone group (p=0.0004).A study performed by Gishan et al (21), there was a significant enhancement in PFS with radiotherapy prior to or concomitant with nivolumab remedy for metastatic NSCLC than nivolumab alone, at the same time, there was no evidence of increased adverse reactions. Additionally, numerous studies show that combining immunotherapy with radiotherapy increases the effectiveness of treatment for NSCLC, with no increase in either radiation or immunological side effects (16, 22, 23).

The results of our study seemed to confirm the synergistic effect of immunotherapy combined with radiotherapy, PFS was increased from 5 months to 9 months in the immunotherapy plus radiotherapy group compared with immunotherapy group alone, and OS was enhanced from 16 months to 30 months in the immunotherapy plus radiotherapy group compared with immunotherapy group alone. It is worth noting that our control group was immunotherapy alone. We demonstrate that immunotherapy plus radiotherapy is superior to immunotherapy alone for NSCLC. Currently, there are relatively few studies on immunotherapy with or without radiotherapy in intermediate to advanced lung carcinoma. The FORCE study has shown that hypo-fractionated photon radiotherapy and

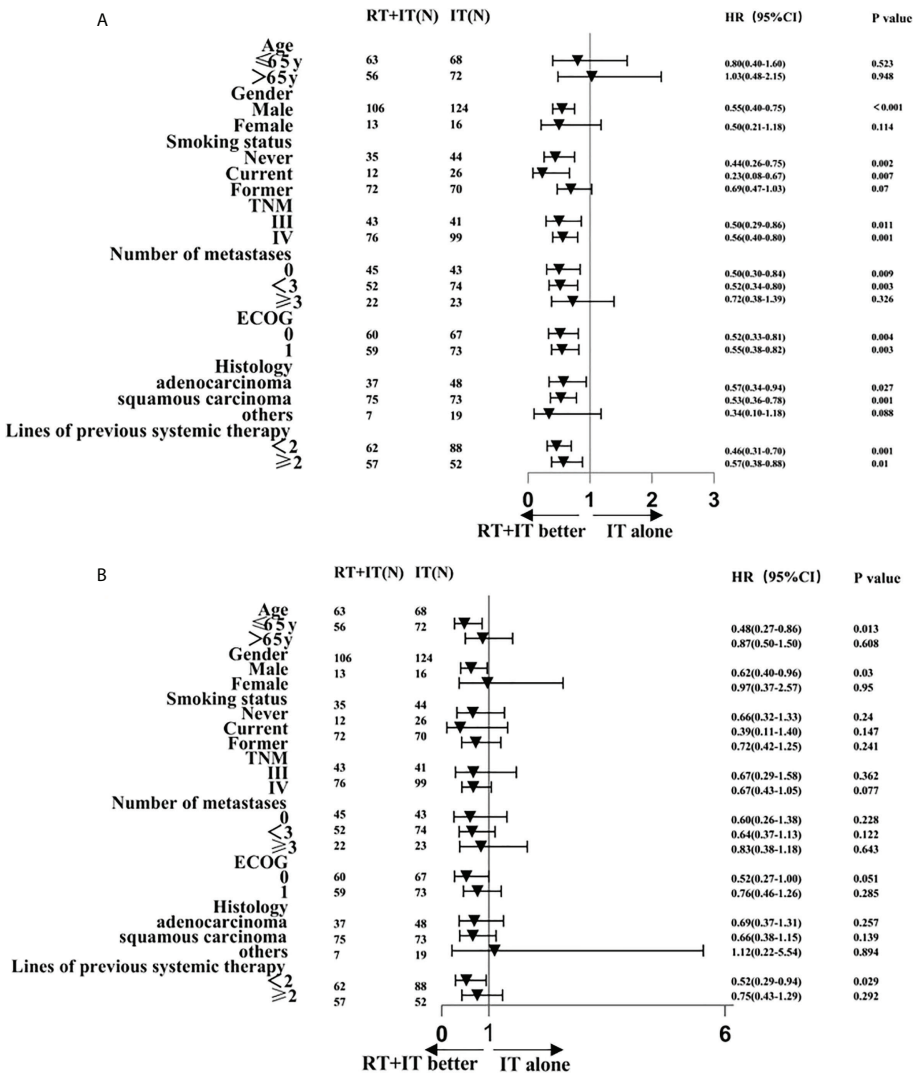

FIGURE 2
Subgroup analysis of factors associated with progression-free survival **(A)** and overall survival **(B)**.

immunotherapy are safe and promote anti-tumor immune response, but there is no final decision yet (24). A secondary analysis of PEMBRO-RT and MDACC trials exhibited groovy results with metastatic NSCLC, however, the results did not reach the meaningful endpoint in any single experiment (25, 26).

The prognostic value of a few factors has been studied in univariate (UVA) and multivariate (MUA) analysis. In UVA analysis,4 factors were statistically significant. While in MUA analysis, radiotherapy, ECOG=0 and <2 lines of previous systemic therapy were independent prognostic factors with a significantly improved PFS. And 7 factors were linked to a significantly better OS in univariate analysis. Non-metastasis was a standalone prognostic factor with a signally better OS in multivariate analysis. However, radiotherapy was a tendency factor with a better overall survival. S. Scoccianti et al. found that in non-adenocarcinoma histology, for patients receiving immunotherapy and stereotactic radiotherapy, the performance status of was a vital factor affecting prognosis (23). Another study pointed out that radiotherapy was a self-reliant factor of good prognosis in patients with NSCLC treated with immune checkpoint inhibitors (27).

Notably, progression-free survival of stage III patients in the immunotherapy plus radiotherapy (RT+IT) queue was significantly finer than the immunotherapy (IT) alone queue, and progression-free survival of stage IV patients in the RT+IT queue was also significantly higher than the IT alone queue. Nevertheless, in both stage III and IV patients, the overall survival wasn't statistically significant in the RT+IT group compared with the IT alone group, but the gap between them is growing. Since the reasons for this result may be related to the limitation of sample capacity. To more precisely determine the impact of including radiotherapy in

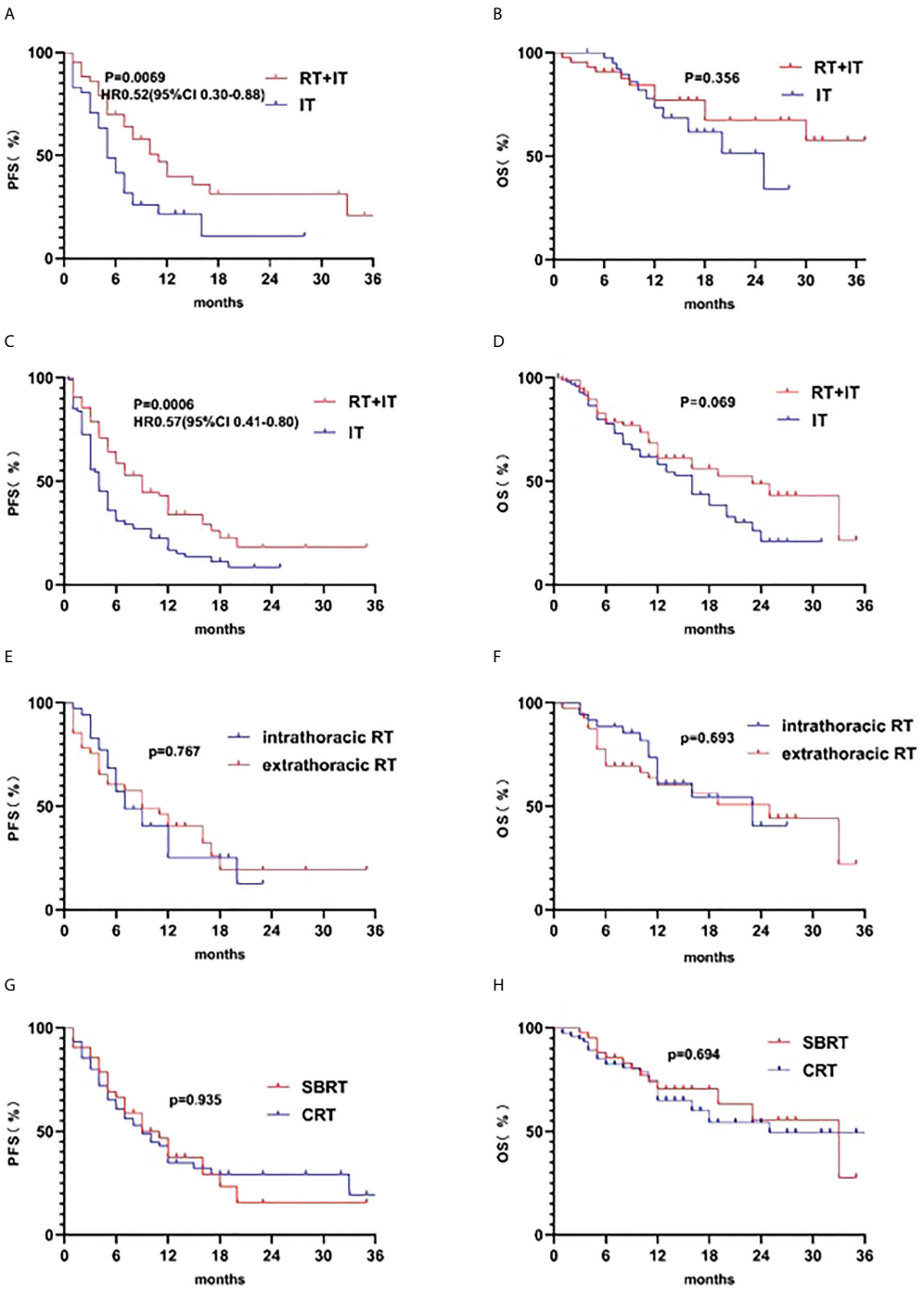

FIGURE 3
Kaplan-Meier survival curves of progression-free survival (PFS) according to **(A)** radiotherapy plus immunotherapy (RT+IT) (n=43) and immunotherapy (IT) alone (n=41) in stage III patients, **(C)** RT+IT (n=76) and IT alone (n=99) in stage IV patients, **(E)** intrathoracic RT(n=35) and extra-thoracic RT(n=41) in stage IV patients, **(G)**SBRT(n=42) and CRT(n=75) in RT+IT patients. Kaplan-Meier survival curves of overall survival (OS) according to **(B)** radiotherapy plus immunotherapy (RT+IT) (n=43) and immunotherapy (IT) alone (n=41) in stage IIIpatients, **(D)** RT+IT (n=76) and IT alone (n=99) in stage IV patients, **(F)** intrathoracic RT (n=35) and extra-thoracic RT (n=41) in stage IV patients, **(H)** SBRT (n=42) and CRT (n=75) in RT+IT patients.

TABLE 2 Univariate and Multivariable cox analysis of progression free survival and overall survival.

	Univariate PFS		Multivariable PFS		Univariate OS		Multivariable OS	
	HR (95%CI)	P value	HR (95%CI)	P value	HR (95%CI)	P value	HR (95%CI)	P value
Treatment method	0.53 (0.40-0.72)	<0.001			0.66 (0.44-0.96)	0.032		
RT+IT			0.51 (0.38-0.69)	<0.001			0.70 (0.47-1.06)	0.09
IT			1				1	
Gender	0.52 (0.40-0.96)	0.030			0.57 (0.34-0.97)	0.036		
Male			0.65(0.42-1.01)	0.054			0.76 (0.44-1.31)	0.319
Female			1				1	
Age category	0.87 (0.65-1.16)	0.351			0.89 (0.61-1.31)	0.550		
≤65								
>65	1				1			
Smoking status								
Never	1				1			
Current	0.86 (0.55-1.35)	0.522			1.06 (0.58-1.91)	0.857		
Former	0.77 (0.56-1.06)	0.114			0.86 (0.57-1.32)	0.502		
TNM	0.79 (0.58-1.08)	0.143			0.48 (0.30-0.77)	0.002		
III								
IV	1				1			
Number of metastases								
0	0.70 (0.47-1.05)	0.087			0.30 (0.17-0.53)	<0.001	0.41 (0.22-0.77)	0.006
<3	0.81 (0.55-1.18)	0.265			0.57 (0.36-0.91)	0.018	0.63 (0.39-1.01)	0.056
≥3	1				1		1	
ECOG score	0.63 (0.47-0.84)	0.002			0.54 (0.36-0.80)	0.002		
0			0.66(0.50-0.89)	0.006			0.73 (0.47-1.13)	0.162
1			1				1	
Histology								
adenocarcinoma	1				1		1	
squamous carcinoma	0.79 (0.58-1.08)	0.134			0.63 (0.42-0.94)	0.025	0.88 (0.57-1.38)	0.589
others	1.09 (0.66-1.82)	0.736			1.03 (0.53-2.02)	0.922	1.04 (0.53-2.05)	0.908
Lines of previous systemic therapy	0.72 (0.54-0.95)	0.021						
<2			0.68 (0.51-0.91)	0.009	0.72 (0.49-1.06)	0.099		
≥2			1		1			

1, reference; RT, radiotherapy; IT, immunotherapy.

immunotherapy on the prognosis of patients, a bigger sample size is therefore required.

Moreover, we surveyed a subgroup analysis, patients with combination of sintilimab and radiotherapy had better PFS than sintilimab alone in male patients, patients who never smoke or never give up smoking, patients with less than 3 metastases, those patients whose pathologic types were adenocarcinoma and squamous carcinoma, and patients with <2 or ≥2 lines of previous systemic therapy. In the subgroup analysis of OS, sintilimab plus radiotherapy appeared to be beneficial in male patients, patients under 65 years old,

TABLE 3 Adverse reaction.

	RT+IT, No. (%)				IT, No. (%)				P value
	Grade1	Grade2	Grade3	Grade4	Grade1	Grade2	Grade3	Grade4	
All toxicities	18 (15.1%)	7 (5.9%)	2 (1.7%)	0	15 (10.7%)	10 (7.1%)	4 (2.9%)	0	0.813
pneumonitis	3 (2.5%)	5 (4.2%)	0	0	2 (1.4%)	7 (5.0%)	0	0	0.947

RT, radiotherapy; IT, immunotherapy; No. number.

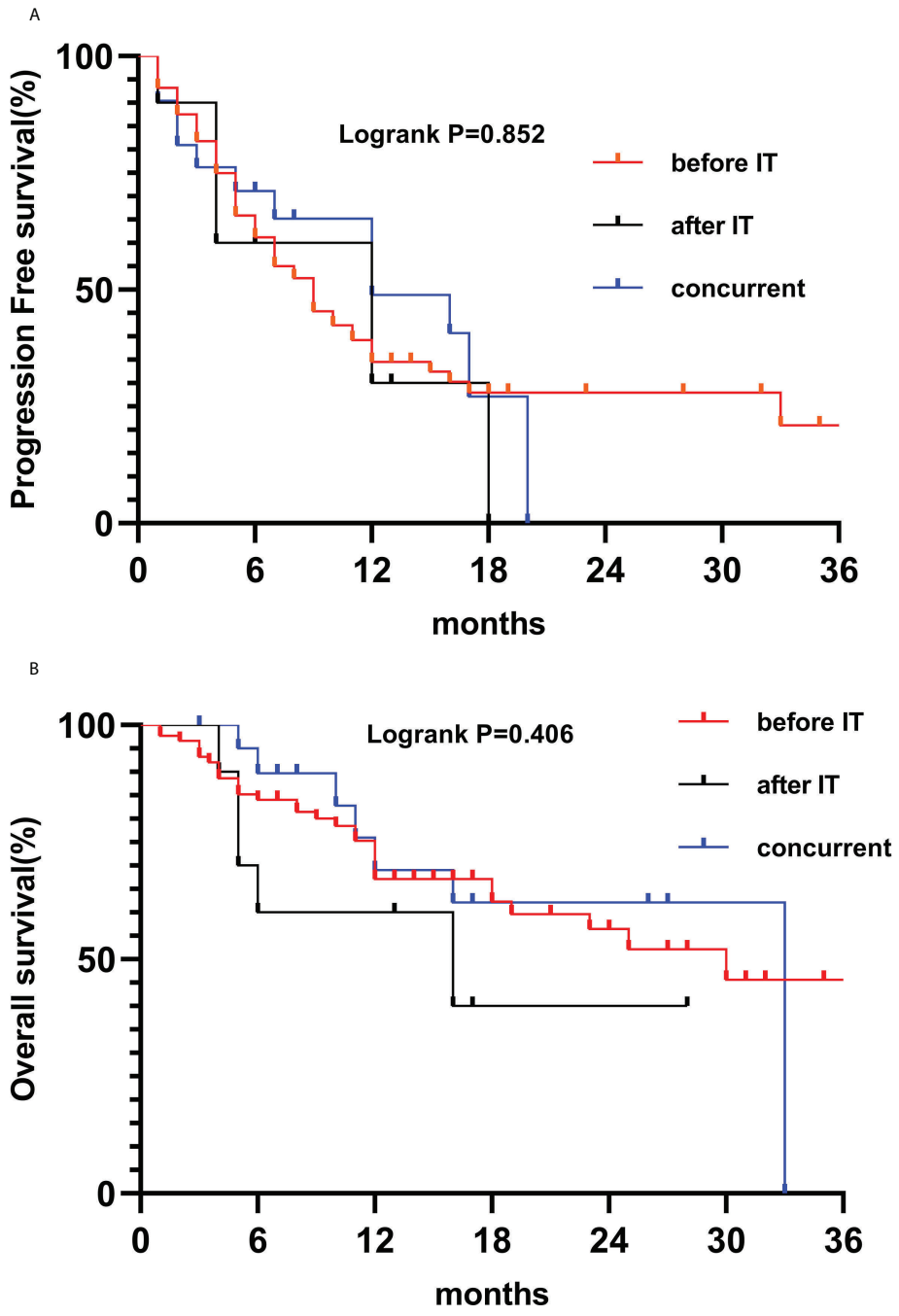

FIGURE 4
Kaplan-Meier survival curves of PFS **(A)** and OS **(B)** according to RT before IT (n=88), after IT (n=10) and concurrent (n=21).

and patients with less than 2 lines of previous systemic therapy. A study also suggested that in patients with oligometastatic NSCLC, single-site radiotherapy plus immunotherapy was more beneficial in patients with 1 to 2 metastases (28).

There are still numerous questions about the impact of various radiotherapy dosage and methods on the magnitude of immune enhancement. Our radiotherapy methods are mainly divided into stereotactic body radiotherapy (SBRT)and conventional fractionated radiotherapy (CRT). In survival analysis, we concluded that both SBRT and CRT could improve the immune efficacy. A study worked by D. Chen et al. has shown that stereotactic body radiotherapy plus immunotherapy can better protect lymphocytes and enhance

prognosis than conventional radiotherapy (29). However, our result indicated that there is no significant change in efficacy between the two sorts of radiotherapy combined with immunotherapy. There are several reasons for this phenomenon: On the one hand, it is the limitation of the number of cases. On the other hand, in our study,119 patients were enrolled in the radiotherapy plus immunization group, including 42 SBRT patients, 75 CRT patients, and 2 particle implantation patients. In the CRT group, there were 36(48%) stage III and 39(52%) stage IV patients. while in the SBRT group, there were only 6(14.3%) stage III and 36(85.7%) stage IV patients. The large proportion of stage IV patients in the SBRT group may result in insignificant difference between SBRT and CRT groups.

The combination of radiotherapy and immunotherapy may have synergistic effects. Our study indicated that intrathoracic and extrathoracic radiotherapy combined with immunity can also improve patient outcomes. Analysis of phase I/II trials in three single institutions (30), thoracic radiation therapy plus immunotherapy is safe for patients, regardless of the radiotherapy technique and grading regiments, including stereotactic body radiation therapy (50 Gy/4F or 60 Gy/10F), wide-field radiation therapy (45 Gy/15F or 45 Gy in twice-daily fractions). In addition, studies support the safety and effectiveness of multi-site radiotherapy combined with immunotherapy (31, 32). In the RT plus IT groups, there are three conditions for the time of radiotherapy: before IT, after IT, and concurrent treatment. There was no statistically significant in outcome due to the difference time of radiotherapy (Figure 4). According to a phase I trial of sequential or concurrent and SBRT in stage IV NSCLC patients (33), concurrent therapy is no more toxic than sequential therapy, patients could receive systematic therapy earlier. Hence, we should further study multimodality therapy and various metastatic sites, radiation techniques, doses on immune function of patients in the future.

Our study also has some limitations. First of all, because it is a retrospective study, some selective bias may exist. Secondly, the patients in our study accepted diverse doses, sites and regimens of radiotherapy, so we could not determine whether it affected the efficacy of immunotherapy. Third, PD-L1 expression in our patient is unknown, patients with low or no PD-L1 expression may respond poorly to immunotherapy. Notwithstanding many preclinical studies have explored the synergistic effect between radiation and immunity, there are relatively few clinical studies on radiotherapy as an immunotherapy sensitizer. Our study confirms that immunotherapy combined with radiotherapy improves PFS and OS than immunotherapy alone.

Conclusion

Patients with NSCLC seem to have better consequences when radiotherapy is combined with immunotherapy. Therefore, at least in middle and advanced stage NSCLC, adding local radiotherapy to immunotherapy is a feasible therapeutic option, and we should interpret the consequences with caution because of the retrospective nature and possible biases related to study design, timing and patients clinical features. Furthermore, radiotherapy regimens, doses, fractions, single or multiple sites, and the outcomes of combined with immunotherapy remain to be further researched in future clinical trials.

Data availability statement

The original contributions presented in the study are included in the article/supplementary material. Further inquiries can be directed to the corresponding author.

Ethics statement

The studies involving human participants were reviewed and approved by The research ethics committee of Taizhou Hospital of Zhejiang Province. Written informed consent for participation was not required for this study in accordance with the national legislation and the institutional requirements.

Author contributions

HY and SL conceived the study and participated in the study design, performance, and manuscript writing. KC, MC, PG and YM conducted the data collection and statistics analysis. MY and SH participate in language modification. All authors read and approved the final manuscript.

Funding

Zhejiang Lung Cancer center (ZLCC), Number: jbzx-201801. The Chinese National Science Foundation Projects (NSFC 81874221).

Acknowledgments

We would like to thank the researchers and study participants for their contributions.

Conflict of interest

The authors declare that the study was conducted in the absence of any commercial or financial relationships that could be construed as a potential conflict of interest.

Publisher's note

All claims expressed in this article are solely those of the authors and do not necessarily represent those of their affiliated

organizations, or those of the publisher, the editors and the reviewers. Any product that may be evaluated in this article, or claim that may be made by its manufacturer, is not guaranteed or endorsed by the publisher.

References

1. Sung H, Ferlay J, Siegel RL, Laversanne M, Soerjomataram I, Jemal A, et al. Global cancer statistics 2020: GLOBOCAN estimates of incidence and mortality worldwide for 36 cancers in 185 countries. *CA Cancer J Clin* (2021) 71(3):209–49. doi: 10.3322/caac.21660

2. Allemani C, Matsuda T, Di Carlo V, Harewood R, Matz M, Niksic M, et al. Global surveillance of trends in cancer survival 2000-14 (CONCORD-3): analysis of individual records for 37 513 025 patients diagnosed with one of 18 cancers from 322 population-based registries in 71 countries. *Lancet* (2018) 391(10125):1023–75. doi: 10.1016/S0140-6736(17)33326-3

3. Ettinger DS, Wood DE, Aisner DL, Akerley W, Bauman JR, Bharat A, et al. NCCN guidelines insights: Non-small cell lung cancer, version 2.2021. *J Natl Compr Canc Netw* (2021) 19(3):254–66. doi: 10.6004/jnccn.2021.0013

4. Frederickson AM, Arndorfer S, Zhang I, Lorenzi M, Insinga R, Arunachalam A, et al. Pembrolizumab plus chemotherapy for first-line treatment of metastatic nonsquamous non-small-cell lung cancer: a network meta-analysis. *Immunotherapy* (2019) 11(5):407–28. doi: 10.2217/imt-2018-0193

5. Socinski MA, Jotte RM, Cappuzzo F, Orlandi F, Stroyakovskiy D, Nogami N, et al. Atezolizumab for first-line treatment of metastatic nonsquamous NSCLC. *N Engl J Med* (2018) 378(24):2288–301. doi: 10.1056/NEJMoa1716948

6. Hellmann MD, Paz-Ares L, Bernabe Caro R, Zurawski B, Kim SW, Carcereny Costa E, et al. Nivolumab plus ipilimumab in advanced non-Small-Cell lung cancer. *N Engl J Med* (2019) 381(21):2020–31. doi: 10.1056/NEJMoa1910231

7. Egen JG, Ouyang W, Wu LC. Human anti-tumor immunity: Insights from immunotherapy clinical trials. *Immunity* (2020) 52(1):36–54. doi: 10.1016/j.immuni.2019.12.010

8. Gubin MM, Schreiber RD. CANCER. the odds of immunotherapy success. *Science* (2015) 350(6257):158–9. doi: 10.1126/science.aad4140

9. Valero C, Lee M, Hoen D, Wang J, Nadeem Z, Patel N, et al. The association between tumor mutational burden and prognosis is dependent on treatment context. *Nat Genet* (2021) 53(1):11–5. doi: 10.1038/s41588-020-00752-4

10. Samstein RM, Lee CH, Shoushtari AN, Hellmann MD, Shen R, Janjigian YY, et al. Tumor mutational load predicts survival after immunotherapy across multiple cancer types. *Nat Genet* (2019) 51(2):202–6. doi: 10.1038/s41588-018-0312-8

11. Spranger S, Gajewski TF. Impact of oncogenic pathways on evasion of antitumour immune responses. *Nat Rev Cancer* (2018) 18(3):139–47. doi: 10.1038/nrc.2017.117

12. Brooks ED, Chang JY. Time to abandon single-site irradiation for inducing abscopal effects. *Nat Rev Clin Oncol* (2019) 16(2):123–35. doi: 10.1038/s41571-018-0119-7

13. Bernstein MB, Krishnan S, Hodge JW, Chang JY. Immunotherapy and stereotactic ablative radiotherapy (ISABR): a curative approach? *Nat Rev Clin Oncol* (2016) 13(8):516–24. doi: 10.1038/nrclinonc.2016.30

14. Spigel DR, Faivre-Finn C, Gray JE, Vicente D, Planchard D, Paz-Ares L, et al. Five-year survival outcomes from the PACIFIC trial: Durvalumab after chemoradiotherapy in stage III non-small-cell lung cancer. *J Clin Oncol* (2022) 40 (12):1301–11. doi: 10.1200/JCO.21.01308

15. Theelen W, Chen D, Verma V, Hobbs BP, Peulen HMU, Aerts J, et al. Pembrolizumab with or without radiotherapy for metastatic non-small-cell lung cancer: a pooled analysis of two randomised trials. *Lancet Respir Med* (2021) 9 (5):467–75. doi: 10.1016/S2213-2600(20)30391-X

16. Fiorica F, Belluomini L, Stefanelli A, Santini A, Urbini B, Giorgi C, et al. Immune checkpoint inhibitor nivolumab and radiotherapy in pretreated lung cancer patients: Efficacy and safety of combination. *Am J Clin Oncol* (2018) 41 (11):1101–5. doi: 10.1097/COC.0000000000000428

17. Najafi M, Jahanbakhshi A, Gomar M, Iotti C, Giaccherini L, Rezaie O, et al. State of the art in combination Immuno/Radiotherapy for brain metastases: Systematic review and meta-analysis. *Curr Oncol* (2022) 29(5):2995–3012. doi: 10.3390/curroncol29050244

18. Kutob L, Schneider F. Lung cancer staging. *Surg Pathol Clin* (2020) 13 (1):57–71. doi: 10.1016/j.path.2019.10.003

19. Eisenhauer EA, Therasse P, Bogaerts J, Schwartz LH, Sargent D, Ford R, et al. New response evaluation criteria in solid tumours: revised RECIST guideline (version 1.1). *Eur J Cancer* (2009) 45(2):228–47. doi: 10.1016/j.ejca.2008.10.026

20. Freites-Martinez A, Santana N, Arias-Santiago S, Viera A. Using the common terminology criteria for adverse events (CTCAE - version 5.0) to evaluate the severity of adverse events of anticancer therapies. *Actas Dermosifiliogr (Engl Ed)* (2021) 112(1):90–2. doi: 10.1016/j.ad.2019.05.009

21. Ratnayake G, Shanker M, Roberts K, Mason R, Hughes BGM, Lwin Z, et al. Prior or concurrent radiotherapy and nivolumab immunotherapy in non-small cell lung cancer. *Asia Pac J Clin Oncol* (2020) 16(1):56–62. doi: 10.1111/ajco.13242

22. Enright TL, Witt JS, Burr AR, Yadav P, Leal T, Baschnagel AM. Combined immunotherapy and stereotactic radiotherapy improves neurologic outcomes in patients with non-small-cell lung cancer brain metastases. *Clin Lung Cancer* (2021) 22(2):110–9. doi: 10.1016/j.cllc.2020.10.014

23. Scoccianti S, Olmetto E, Pinzi V, Osti MF, Di Franco R, Caini S, et al. Immunotherapy in association with stereotactic radiotherapy for non-small cell lung cancer brain metastases: results from a multicentric retrospective study on behalf of AIRO. *Neuro Oncol* (2021) 23(10):1750–64. doi: 10.1093/neuonc/noab129

24. Bozorgmehr F, Hommertgen A, Krisam J, Lasitschka F, Kuon J, Maenz M, et al. Fostering efficacy of anti-PD-1-treatment: Nivolumab plus radiotherapy in advanced non-small cell lung cancer - study protocol of the FORCE trial. *BMC Cancer* (2019) 19(1):1074. doi: 10.1186/s12885-019-6205-0

25. Theelen W, Peulen HMU, Lalezari F, van der Noort V, Vries JF, Aerts J, et al. Effect of pembrolizumab after stereotactic body radiotherapy vs pembrolizumab alone on tumor response in patients with advanced non-small cell lung cancer: Results of the PEMBRO-RT phase 2 randomized clinical trial. *JAMA Oncol* (2019) 5(9):1276–82. doi: 10.1001/jamaoncol.2019.1478

26. Welsh J, Menon H, Chen D, Verma V, Tang C, Altan M, et al. Pembrolizumab with or without radiation therapy for metastatic non-small cell lung cancer: a randomized phase I/II trial. *J Immunother Cancer* (2020) 8(2): e001001. doi: 10.1136/jitc-2020-001001

27. Yamaguchi O, Kaira K, Hashimoto K, Mouri A, Miura Y, Shiono A, et al. Radiotherapy is an independent prognostic marker of favorable prognosis in non-small cell lung cancer patients after treatment with the immune checkpoint inhibitor, nivolumab. *Thorac Cancer* (2019) 10(4):992–1000. doi: 10.1111/1759-7714.13044

28. Wang P, Yin T, Zhao K, Yu J, Teng F. Efficacy of single-site radiotherapy plus PD-1 inhibitors vs PD-1 inhibitors for oligometastatic non-small cell lung cancer. *J Cancer Res Clin Oncol* (2022) 148(5):1253–61. doi: 10.1007/s00432-021-03849-3

29. Chen D, Patel RR, Verma V, Ramapriyan R, Barsoumian HB, Cortez MA, et al. Interaction between lymphopenia, radiotherapy technique, dosimetry, and survival outcomes in lung cancer patients receiving combined immunotherapy and radiotherapy. *Radiother Oncol* (2020) 150:114–20. doi: 10.1016/j.radonc.2020.05.051

30. Verma V, Cushman TR, Selek U, Tang C, Welsh JW. Safety of combined immunotherapy and thoracic radiation therapy: Analysis of 3 single-institutional phase I/II trials. *Int J Radiat Oncol Biol Phys* (2018) 101(5):1141–8. doi: 10.1016/j.ijrobp.2018.04.054

31. Doyen J, Besse B, Texier M, Bonnet N, Levy A. PD-1 iNhibitor and chemotherapy with concurrent IRradiation at VAried tumor sites in advanced non-small cell lung cAncer: the prospective randomized phase 3 NIRVANA-lung trial. *Clin Lung Cancer* (2022) 23(3):e252–6. doi: 10.1016/j.cllc.2021.10.008

32. Kroeze SGC, Schaule J, Fritz C, Kaul D, Blanck O, Kahl KH, et al. Metastasis directed stereotactic radiotherapy in NSCLC patients progressing under targeted- or immunotherapy: efficacy and safety reporting from the 'TOaSTT' database. *Radiat Oncol* (2021) 16(1):4. doi: 10.1186/s13014-020-01730-0

33. Bestvina CM, Pointer KB, Karrison T, Al-Hallaq H, Hoffman PC, Jelinek MJ, et al. A phase 1 trial of concurrent or sequential ipilimumab, nivolumab, and stereotactic body radiotherapy in patients with stage IV NSCLC study. *J Thorac Oncol* (2022) 17(1):130–40. doi: 10.1016/j.jtho.2021.08.019

frontiers | Frontiers in Immunology

TYPE Original Research
PUBLISHED 27 September 2022
DOI 10.3389/fimmu.2022.955187

Check for updates

OPEN ACCESS

EDITED BY
Jian Zhang,
Southern Medical University, China

REVIEWED BY
Kaiyun You,
Sun Yat-Sen Memorial Hospital, China
Dahai Yu,
Jiangsu Provincial Hospital of Traditional Chinese Medicine, China

*CORRESPONDENCE
He Xiao
xh1624@163.com
Dong Wang
dongwang64@hotmail.com

†These authors have contributed equally to this work and share first authorship

SPECIALTY SECTION
This article was submitted to Cancer Immunity and Immunotherapy, a section of the journal Frontiers in Immunology

RECEIVED 28 May 2022
ACCEPTED 30 August 2022
PUBLISHED 27 September 2022

CITATION
He L, Jin M, Jian D, Yang B, Dai N, Feng Y, Xiao H and Wang D (2022) Identification of four immune subtypes in locally advanced rectal cancer treated with neoadjuvant chemotherapy for predicting the efficacy of subsequent immune checkpoint blockade. *Front. Immunol.* 13:955187. doi: 10.3389/fimmu.2022.955187

COPYRIGHT
© 2022 He, Jin, Jian, Yang, Dai, Feng, Xiao and Wang. This is an open-access article distributed under the terms of the Creative Commons Attribution License (CC BY). The use, distribution or reproduction in other forums is permitted, provided the original author(s) and the copyright owner(s) are credited and that the original publication in this journal is cited, in accordance with accepted academic practice. No use, distribution or reproduction is permitted which does not comply with these terms.

Identification of four immune subtypes in locally advanced rectal cancer treated with neoadjuvant chemotherapy for predicting the efficacy of subsequent immune checkpoint blockade

Le He[1,2†], Min Jin[1†], Dan Jian[1], Bo Yang[1], Nan Dai[1], Yan Feng[1], He Xiao[1*] and Dong Wang[1*]

[1]Cancer Center, Daping Hospital and Army Medical Center of People's Liberation Army (PLA), Third Military Medical University (Army Medical University), Chongqing, China, [2]Department of Gastroenterology, Chongqing General Hospital, Chongqing, China

Introduction: Neoadjuvant chemoradiotherapy (nCRT) is the foundation treatment for locally advanced rectal cancer (LARC). The nCRT can improve the efficacy of immunotherapy because of its in situ vaccine effect.

Objective: The aim is to identify stable and reliable transcriptome signatures to predict the efficacy of immune checkpoint blockade (ICB) in patients with LARC.

Methods: Immunophenotyping was established using xCell immune cell infiltration abundance and consistent clustering in GSE39582 and verified in several data sets. The effects of immunophenotyping, follicular regulatory T cells, tumor-associated fibroblasts (CAFs), and tertiary lymphoid structure (TLS) signatures on the efficacy of ICB were analyzed using IMvigor210, GSE91061, and an independent Daping Hospital (DPH) cohort.

Results: There are four stable and repeatable immune subtypes in rectal cancer, among which C1 is a low immune infiltration type, C2 is a high interstitial infiltration type, C3 is a high immune infiltration type, and C4 is an ion channel type. C2 is mainly characterized by high infiltration of CAF. C3 is characterized by high infiltration of cytotoxic T lymphocytes, high expression of PD-L1 and TLS. In rectal cancer patients receiving nCRT, immunophenotyping was not significantly associated with pathological remission rate, but immunophenotyping was an independent prognostic factor of RFS. In IMvigor210 patients treated with atezolizumab, the pathological remission rates of C1, C2, C3, and C4 were 23.86%, 10.94%, 33.33%, and 23.08% respectively ($\chi 2$ = 8.981, P = 0.029), which were 11.76%, 50.00%, 42.86%, and 0.0% respectively in the GSE91061 patient treatment with

nivolumab (Fisher's exact probability, P = 0.018). Both follicular regulatory T cells and CAF showed a further impact on the ICB therapeutic efficacy of C2 and C3 subtypes. Additionally, both the GSE91404 and DPH cohorts showed that nCRT treatment induced a significant increase in the expression of TNFRSF9 and the abundance of macrophages in the C3 subtype.

Conclusion: Our data suggest that there are four immune types of rectal cancer, which are related to the prognosis of patients. Among them, C3 and some C2 subtypes represent the patients who may benefit from ICB after nCRT treatment.

KEYWORDS

rectal cancer (RC), immune checkpoint inhibitors, immunophenotyping, genomics, neoadjuvant (chemo)radiotherapy

Introduction

Neoadjuvant chemoradiation therapy (nCRT) and total mesorectal excision are commonly incorporated into the multimodal treatment of locally advanced rectal cancer (LARC). nCRT has been shown to reduce tumor burden, improve operative procedures and prevent local tumor recurrence (1–3). nCRT can induce an in situ vaccine effect and promote antitumor immunity. Therefore, a large number of preclinical and clinical studies have explored the feasibility of nCRT combined with immune checkpoint blockade (ICB) in LARC (4–7). There is evidence suggesting that the combination of CTLA-4 and PD-1 with chemoradiotherapy is the most effective combination therapy strategy (6). However, because of the heterogeneity of the tumor, it is speculated that this combination therapy is not effective for all patients in clinical studies. Therefore, there is an urgent clinical need to screen patients who most likely benefit from the treatment of nCRT combined with ICB based on biomarkers, especially by transcriptomic signatures, which remains a huge challenge. The main reasons are as follows: 1) there is still no universally applicable biomarkers for predicting benefit of ICB treatment across all tumor types. Although PD-L1 expression, tumor mutation burden (TMB), IFNγ-related T-cell-inflated gene expression profile (8) and tumor immune dysfunction and exclusion (TIDE) (9) have been established, these biomarkers and transcriptomic signatures have only low predictive power in independent validation (10). Second, the regulation of nCRT in the immune microenvironment is complex. In addition to the infiltration of CD8+ T lymphocytes induced by nCRT, it can also actively promote the infiltration of a large number of myeloid inhibitory cells and regulatory T cells (6). Recent studies have shown that other cell populations or tissue structures in the tumor microenvironment, such as tumor associated fibroblasts (CAF), follicular regulatory T cells, tertiary lymphoid structures (TLS) or B cells, have an important impact on the function of CD8+ T cells (11–13). These results suggest that different cell populations of the tumor microenvironment participate in the regulation of tumor immune microenvironment (TIME) heterogeneity and lead to different ICB responses. Therefore, a single immune marker cannot fully satisfy the response prediction or prognosis of patients treated with ICB under the background of different immune tumor microenvironments.

Molecular subtyping can identify tumor subsets with the same biological characteristics, which has become one of the main methods to overcome the tumor heterogeneity. In colorectal cancer, consensus molecular subtypes (CMSs) and colorectal cancer typing (CRCAssigner) based on mRNA expression profiles predict the efficacy of bevacizumab and anti-EGFR in RAS wild-type advanced colorectal cancer (14, 15). Similarly, immune subtypes (ISs) depending on immune cell abundance have revealed good capacity to discriminate patients who response to ICB from others in melanoma, sarcoma, and glioma (16–19). Therefore, we jointly used the immunophenotyping of colon cancer and transcriptomic signatures of follicular regulatory T cells, tumor associated fibroblasts (CAFs) and tertiary lymphoid structures (TLSs) to evaluate ICB response and prognosis, so as to screen the LARC patients who most likely benefit from nCRT combined with ICB.

Methods and materials

Datasets retrieving and preprocessing

Raw data of transcriptional expression (CEL files) profiled with Affymetrix were downloaded from GEO (Gene Expression Omnibus). Function "rma" or "threestep" in the limma package

was used to obtain the expression matrix at the probe level with default parameters. For raw data of transcriptional expression profiles generated with Agilent, functions "backgroundCorrect" and "normalizeBetweenArrays" were used to correct the background and normalize the data. Function "neqc" was used for preprocessing data profiles with Illumina HumanHT-12 microarrays. Features expressed in at least 30% of samples in each cohort with "Detection Pval <0.05" were retained for further analysis. For genes represented by several probes, the probe with the maximum interquartile range was finally selected as the expression of that gene. RSEM values on the log2 scale of the transcriptional profile of TCGA COADREAD (version 2017-09-08) and phenotype file (version 2019-12-06) were obtained from https://xenabrowser.net/datapages. Raw count of RNAseq and responsiveness along with other clinical characteristics of metastatic urothelial cancer treated with atezolizumab monotherapy were extracted from the R package "IMvigor210CoreBiologies." The genes were retained that had at least 10 counts for 50% of the samples and converted into FPKM by using the annotation file "Biomart.annotations.hg38" and the function "countToFPKM" from the R package "fpkm" (20). FPKM values of GSE91061 were downloaded from GEO deposition and used for statistical analysis without further modification.

The Daping Hospital cohort (DPH) was comprised of resected tissues from nine LARC patients with complete pathological response (pCR), nine without pathological response (npCR), and biopsy tissues from nine LARC patients prior to nCRT. RNAseq of DPH cohort tissues was performed with Illumina Hiseq 2500. FPKM was obtained from raw count after being adjusted for length of exons and library size. Information about datasets used in this study was summarized in Supplementary Table 1.

The studies involving human participants were reviewed and approved by ethics committee of Daping Hospital. The Helsinki Declaration was followed strictly in this study.

Development of immune subtypes and prediction

The immune cell composition of 566 colon tumor tissues deposited in the GSE39582 dataset was evaluated with "xCellAnalysis," which provides abundance scores for 64 immune cell populations (21). Consensus clustering of 64 immune cells across 566 samples was performed through the function "ExecuteCC" in the R package "CancerSubtypes" setting parameter "clusterAlg='pam', distance='pearson'" after z-value transformation of abundance scores in each sample. An average z-value in each of the 64 immune cell populations in each subtype was calculated as the centroid of each immune subtype to predict the immune subtypes of other cohorts and platforms. To predict de novo immune subtypes of additional cohorts, z-values of abundance scores of 64 immune cell populations were computed. Each sample was assigned to the closest immune subtype based on Pearson coefficients with the centroid of each immune subtype. However, samples were assigned unclassified if the maximum Pearson correlation coefficient was less than 0.15 or the difference between the maximum and the second maximum Pearson correlation coefficient was less than 0.06. These criteria were similar to those used in the CRCA classification system (22). The centroids of 64 immune cell populations derived from GSE39582 are shown in Supplementary Table 2.

GSVA analysis to infer characteristics of each immune subtype

Gene set variation analysis was used to explore the immune characteristics of each immune subtype in GES39582. The c5 gene set collection of MSigDB was used to calculate the enrichment score for a total of 10,485 pathways after infiltrating pathways with a number of component genes of less than 10 or greater than 500 genes (23, 24). The parameter mx.diff was set to TRUE in all GSVA analysis. Stepwise multiple comparisons of enrichment scores returned from GSVA among immune subtypes were performed with the R package "limma". The pathways with a P-value adjusted for multiple comparisons of less than 0.05 in all comparisons were identified. The top 10 pathways with the maximum enrichment score in each immune subtype were selected to represent the immune features of that immune subtype and are illustrated in the heatmap.

Estimation for the activity of follicular regulatory T cells in tumor tissues

Recently, Eschweiler identified an important regulatory subset of FOXP3-espressing CD4+ T cells that are highly suppressive to affect T cells and co-express BCL6 and/or CXCR5, indicated as follicular lineage (12). To establish the relevant abundance of such a subset of follicular regulatory T cells (Tfr cells) to Treg cells (TFRscore), the differentially expressed genes (DEGs) between Tfrs (CD4+CXCR5+GITR+, n = 10) and Tregs (CD4 +CD25+CXCR5−, n = 10) were first identified through the R package "edgeR" using raw count in GSE132295. The centroid of these DEGs in Tfr and Treg cells was calculated with a transformed z-value of the FPKM value. TFRscore of a given tumor tissue sample was calculated based on formula (6) proposed by Budcizies by using centroids established above and z-value of gene expression of that tumor tissue (25). The gene list of DEGs identified in GSE132295 and the centroids of Tfr and Treg cells are shown in Supplementary Table 3.

Scores for tertiary lymphoid structures and TGFβ-induced genes

The score for tertiary lymphoid structure (TLSscore) was calculated based on the average of the seven marker genes proposed by Cabrita in the original article. The marker genes for TLSscore included CCL19, CCL21, CXCL13, CCR7, CXCR5, SELL, and LAMP3 (13). A pan-fibroblast TGFβ response signature consisting of 19 genes commonly induced by TGFβ in isolated fibroblasts was used to calculate the fibroblast TGFβ response score (FTBRS). FTBRS was calculated as the average expression of the pan-fibroblast TGFβ response signature (11).

Statistical analysis

The abundance of 19 immune cell populations was evaluated with ConsensusTME (26). A Kruskal–Wallis test with multiple comparisons was used to evaluate differences in TFRscore, TLSscore, FTBRS, and abundance of infiltrated immune cells among immune subtypes. The relationship between pathological response and MSI status, MMR status, and immune subtypes was estimated with the chi-square test or Fisher's exact probability. Univariate and multivariate Cox regression were used to reveal independent prognostic factors for recurrent-free survival, progression-free survival, and overall survival. Kaplan–Meier curves along with a log-rank test were used to evaluate differences in OS among immune subtypes. All the tests were two-sided. A P-value of less than 0.05 was considered statistically significant.

Results

Four immune subtypes widely exist in colorectal cancer, which are related to RFS

Unsupervised cluster analysis found four highly consistent immune subtypes could be obtained in GSE39582 (Figures 1A, B). The accuracy was evaluated as 96.44% through the Pearson correlation coefficient method within GSE39582 (see Methods and materials). Analyzing the characteristics of the four immune subtypes, it was found that the proportions of mismatch repair defect (dMMR) in C1, C2, C3, and C4 subtypes were 0.075, 0.0569, 0.3836, and 0.2033, respectively, with significant differences ($\chi 2$ = 52.629, df = 3, P= 2.2 × 10−11). Among them, C3 is the immune subtype with the highest cytotoxic T lymphocytes, PD-L1 expression, TLS score, and TFR score value (Figure 2A). C2 also contained some expression of cytotoxic T cells and PD-L1, but fibroblast abundance and FTBRS were the highest in C2. The cytotoxic T lymphocytes, PD-L1 expression, TLS score, and TFR score value were low in C1. GSVA analysis showed that the C1 subtype is primarily based on the translation initiation regulatory pathway, C2 is the extracellular matrix or collagen-related pathway, C3 is mainly marked by the activation of IL2, which is the main marker of CD4+T and CD8+T activation, and C4 is mainly based on the activation of ion channel activity (Figure 2B). The above results showed that C1 was a low-immune infiltration type, C2 was a high-interstitial infiltration type, C3 was a high-immune infiltration type, and C4 was an ion channel type. The four immunophenotypes can be verified in GSE14333, GSE 26682, GSE 87211, and TCGA COADREAD colorectal cancer sample data (Supplementary Figure 1).

The above results are verified by GSE87211. The Chi-square test showed that there was no significant difference in the pathological remission rate among the four immune types ($\chi 2$ = 3.857, df = 3, P = 0.277), and the pathological remission rates of C1, C2, C3, and C4 subtypes were 0.55, 0.418, 0.633, and 0.467, respectively. Survival analysis revealed that immunophenotyping was an influencing factor of RFS after nCRT for rectal cancer, and the risk of recurrence of C2 relative to C1 was significantly increased by 3.2 times (c2 vs c1, HR = 3.239, 95% CI: 1.494–7.022, P = 0.003), but C3 and C4 had no significant effect relative to C1 (HR = 0.921, 95% CI: 0.289–2.937, P = 0.889; HR = 1.660, 95% CI: 0.655–4.208, P = 0.285) (Figure 3A). After adjusting for age, sex (male vs female), KRAS mutation (mutation vs wild), neoadjuvant therapy regimen (5-FU + oxaliplatin + RT ± cetuximab vs 5-FU + RT), residual lymph nodes after neoadjuvant therapy (positive vs negative), and pathological remission (remission vs non-remission), C2 was still a risk factor for recurrence (C2 vs C1, HR = 2.752, 95% CI: 1.241–6.105, P = 0.013) (Supplementary Table 4). These results suggest that rectal cancer has similar immunophenotyping characteristics as colon cancer, in which C3 is an immune infiltrative type, C2 is a mesenchymal cell infiltrative type, and C1 is an immune desert type. In rectal cancer patients receiving nCRT, there is no correlation between immunophenotyping and pathological remission rate, but it can be used as an independent prognostic factor of RFS.

Effects of immune subtypes, TFR follicular regulatory cells, and FTBRS fibroblasts on ICB therapy

We found four immune subtypes in rectal cancer, but the relationship between these immune subtypes and the efficacy of ICB therapy is unclear. Because of the lack of data on ICB therapy in rectal cancer, we attempted analyzing the relationship by analyzing the effects of immunophenotyping on the efficacy of immunotherapy for bladder cancer and melanoma.

IMvigor210 is a database for advanced bladder cancer treated with atezolizumab. A total of 298 samples were

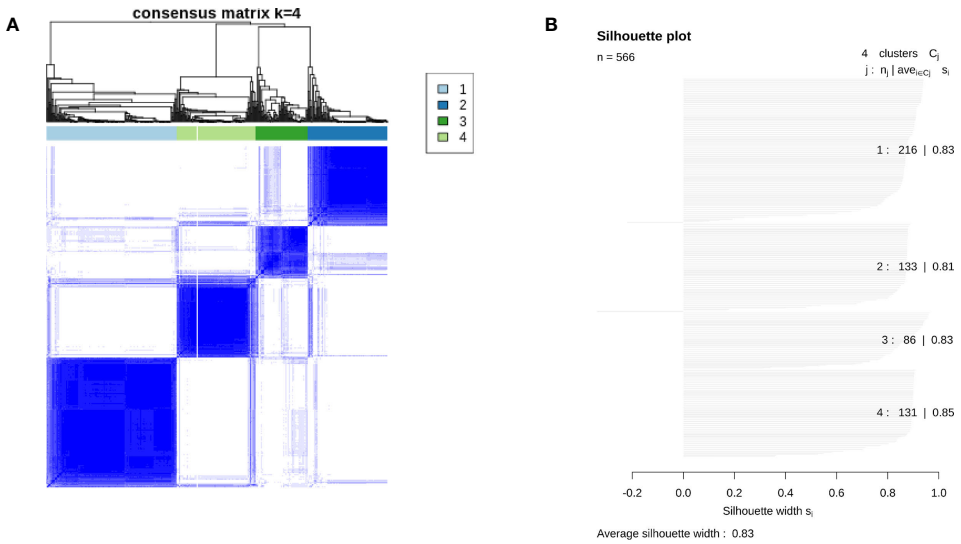

FIGURE 1
Results of consensus clustering across 566 colon tumor tissues in GSE39582. **(A)** Consensus matrix showing clustering consensus of each case in individuals of four immune subtypes. **(B)** Silhouette plot showing average silhouette score of each immune subtype and the whole population in GSE39582.

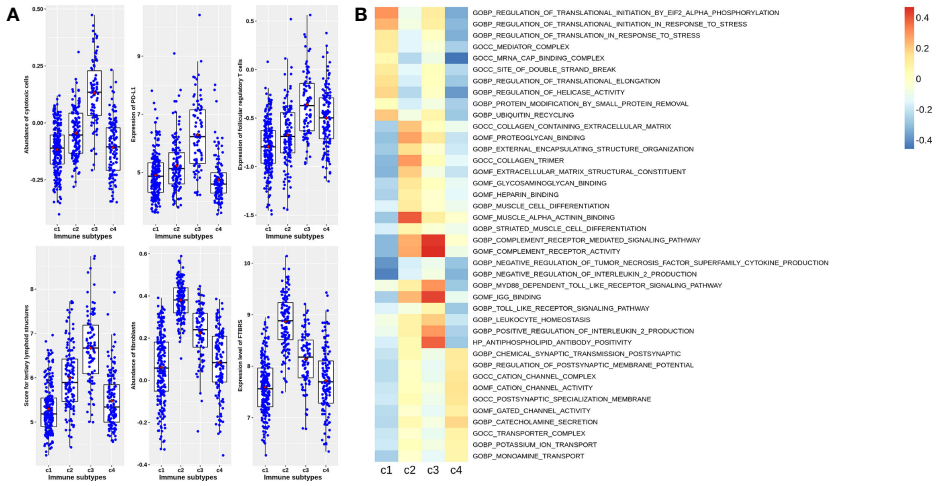

FIGURE 2
Characteristics of four immune subtypes in GSE39582. **(A)** Scatter plots overlapped with box plots illustrating differences in six major immune related scores among four immune subtypes. The red diamonds in each box indicate mean value. **(B)** Results from GSVA analysis showing ten major significantly enriched pathways in each immune subtype.

available for analysis. Among them, there were 88, 64, 60, 39, and 47 cases of C1, C2, C3, C4, and unclassified (UC), respectively, with an unclassified proportion of 15.77%. Among 251 known immunophenotyping samples, the immune grades (IC0, IC1, and IC2) obtained by PD-L1 immunohistochemistry were significantly different among the four immunophenotyping ($\chi 2$ = 56.363, df = 6, P = 2.46 × 10−10), in which the proportions of C3 in IC0, IC1 and IC2 were 4.29% (3/70), 15.05% (14/93), and 48.86% (43/88), respectively. Importantly, the objective remission rate (ORR) of ICB therapy was significantly different among different immune subtypes. The ORR of C1, C2, C3, and C4 were 23.86% (21/88),

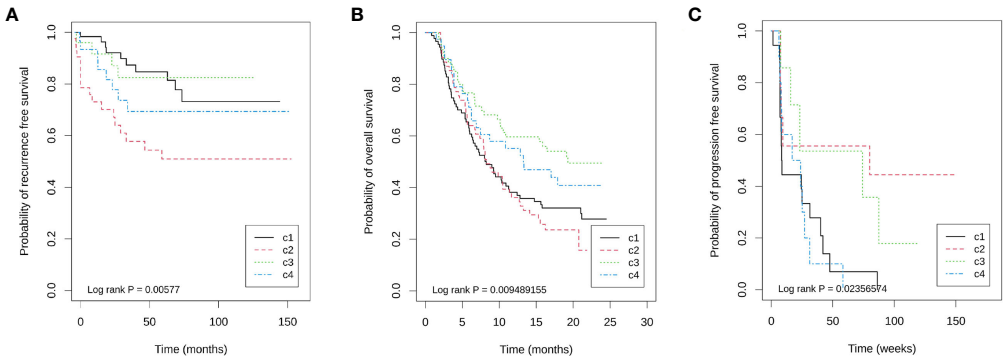

FIGURE 3
Kaplan–Meier plots showing differences in prognosis within four immune subtypes in three cohorts. **(A)** GSE87211 for recurrence free survival, **(B)** IMvigor210 for overall survival, and **(C)** GSE19106 for progression free survival.

10.94% (7/64), 33.33% (20/60), and 23.08% (9/39), respectively ($\chi 2$ = 8.981, df = 3, P = 0.029). Additionally, immunophenotyping is also a prognostic factor of OS, in which C3 has the longest overall survival time, C4 is the second, and C1 and C2 are the worst (Figure 3B).

However, there was no significant difference in TFRscore and FTBRS between the non-remission group and the good remission group (median: −1.014 vs −1.072, Kruskal–Wallis $\chi 2$ = 0.029, df = 1, P = 0.864; Median: 2.157 vs 2.001, Kruskal–Wallis $\chi 2$ = 2.765, df = 1, P = 0.096), suggesting that fibroblasts seem to have little effect on the efficacy of ICB therapy in advanced bladder cancer. Using the 66.66% quantile value of TFRsocre as the cut-off value, it was found that TFRscore was the prognostic factor of OS only in the c3 subtype, and OS was significantly longer in patients with high expression than in patients with low expression. These results suggest that the role of follicular regulatory T lymphocytes is different in different immune-infiltrating subtypes.

GSE19106 is a database of advanced melanoma treated with nivolumab, including 109 biopsy samples before and after treatment. The classifications of C1, C2, C3, C4, and UC were 34, 15, 23, 19, and 19 cases, respectively, and the unclassified proportion was 16.51%. Among 42 pre-treatment samples that could be classified, the remission rates of four immune subtypes C1, C2, C3, and C4 were 11.76% (2/17), 50.00% (4/8), 42.86% (3/7), and 0.0% (0/10), respectively (Fisher's exact probability, P = 0.018). Similarly, the PFS of C2 and C3 is longer (Figure 3C). Because the sample size of each immune subtype is small, Cox regression of OS cannot be performed in each subtype. However, to show the impact of TFR score and FTBRS on the efficacy of nivolumab in different subtypes, only the expression differences in these two indices between remission and non-remission groups in the C2 and C3 groups were analyzed. The results show that only the TFR score was significantly different between the remission and non-remission groups in C2 subtypes. The TFR score in the remission group was significantly higher than that in non-remission cases. However, in both C2 and C3 subtypes, FBRS in the non-remission group was higher than that in the remission group (Supplementary Figure 3).

The above analysis of bladder cancer and melanoma shows that C3 and C2 subtypes can benefit from ICB treatment. However, follicular regulatory T cells and fibroblasts have further regulatory effects on ICB efficacy on the basis of immunophenotyping.

nCRT treatment can activate the antitumor immunity of rectal cancer

GSE94104 is a database of 40 paired samples before and after neoadjuvant treatment with 45 Gy + 5-FU/carboplatin. A total of 20 cases in the paired samples can be classified. The composition of the four immune types before and after nCRT treatment is shown in Table 1. There were nine cases of C1 before treatment, three cases of C1 transformed into C3, and two cases of C1 transformed into C2 after treatment. After treatment, two cases of C4 changed to C2 and one case changed to C3, indicating that nCRT can increase the tumor-infiltrating lymphocytes. Additionally, the proportion of C2 after radiotherapy and chemotherapy was as high as 45% (9/20), indicating that radiotherapy and chemotherapy can also induce an increase in mesenchymal cells.

The analysis of paired samples of 20 cases before and after neoadjuvant treatment showed that the expression of cytotoxic T cells and class II antigen-presenting molecules after nCRT treatment was significantly higher than that before treatment (Figure 4). Among the four immune subtypes after nCRT, there were no significant differences in the expression of cytotoxic T lymphocytes or PD-L1 (Figure 5A). Only fibroblasts and FTBRS

TABLE 1 Immune subtypes in matched samples before and after nCRT in GSE94104.

Pre nCRT/Post nCRT	c1	c2	c3	c4	Total
c1	3	2	3	1	9
c2	1	2	0	0	3
c3	0	3	0	0	3
c4	0	2	1	2	5
Total	4	9	4	3	20

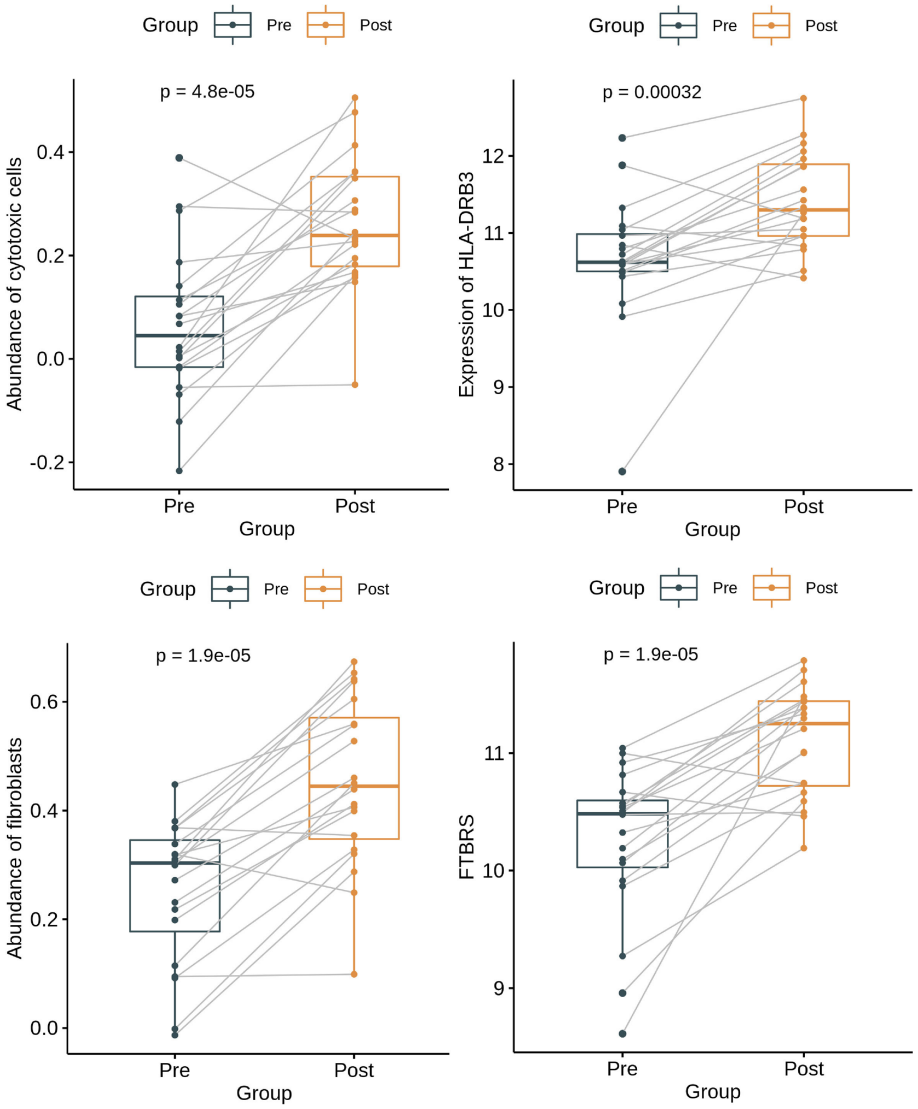

FIGURE 4
Paired box plots showing changes in abundance of cytotoxic cells, expression level of HLA-DRB3, abundance of fibroblast cells, and FTBRS between after nCRT and before nCRT.

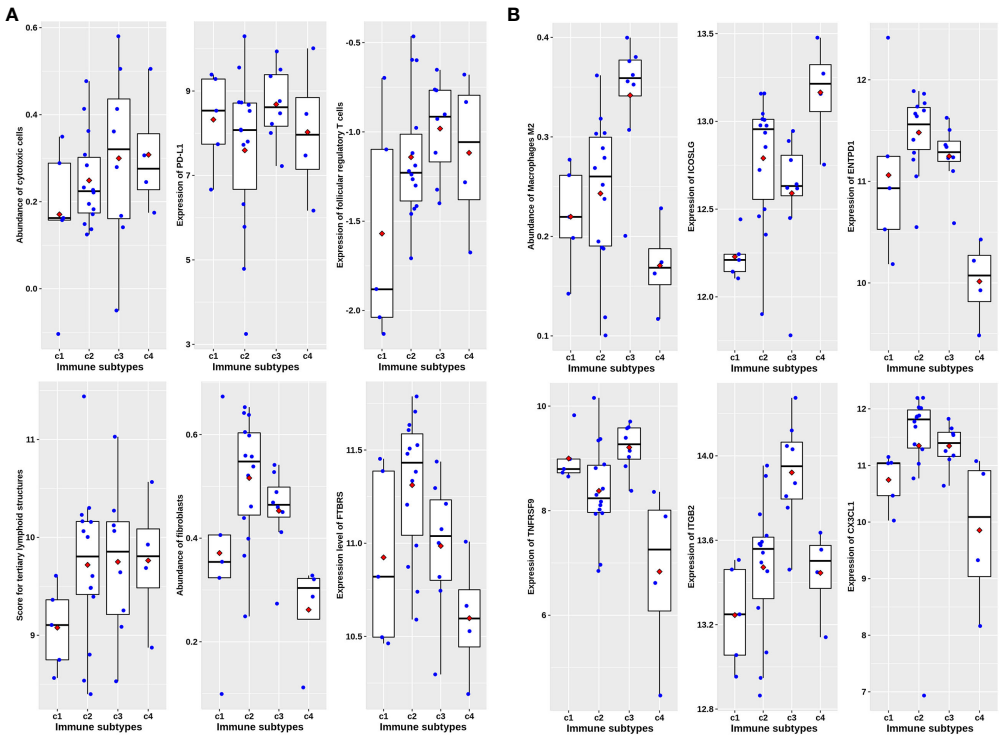

FIGURE 5
Immune characteristics among four immune subtypes in post-nCRT samples in GSE94104. **(A)** Scatter plots overlapped with box plots illustrating differences in six major immune related scores among four immune subtypes without statistical significance. **(B)** Scatter plots overlapped with box plots illustrating significant differences in six immune related scores among four immune subtypes. The red diamonds in each box indicate mean value.

scores were the highest and significantly different in C2. However, we found that the C3 expression of TNFRSF9 and ITGB2 in M2 macrophages was significantly higher than that in other subtypes (Figure 5B), in which TNFRSF9 was a marker of regulatory T-cell receptor activation. These results suggest that nCRT promotes antitumor immunity, particularly activated antigen presentation and the infiltration of effector T lymphocytes. However, due to the influence of radiotherapy and chemotherapy, the immunophenotyping characteristics after nCRT treatment are different from those before treatment.

In the 27 rectal cancer samples we collected and sequenced (DPH data set), there were no significant differences in cytotoxic T lymphocytes, PD-L1 expression, follicular regulatory T cells, and TLS indicators among non-chemoradiotherapy (uCRT), non-pathology complete remission (nPCR), and PCR groups (Figure 6), and only the FTBRS value was significantly higher in the PCR group than that in uCRT samples (adjusted P = 0.002). Among the 27 samples, only 18 had immunophenotyping. In the six cases without nCRT, there were one, two, two, and one cases of C1, C2, C3, and C4 subtypes, respectively, while in the 12 cases after nCRT, there were two, six, four, and zero cases, respectively (Fisher's exact probability, P = 0.774). Among the samples that could be classified after treatment, the PCR rates of C1, C2, and C3 subtypes were 50.0% (1/2), 83.3% (5/6), and 25.0% (1/4), respectively, which did not reach statistical significance (Fisher's exact probability, P = 0.192). Although there was no significant correlation with pathological remission before and after treatment, the expression of cytotoxic T cells, PD-L1 expression, TLS, and FTBRS increased in C1, C2, and C3 subtypes after treatment, which was consistent with the trend in the analysis of GSE39582 and GSE87211 (Figure 7A). Statistically significant were mainly macrophage and dendritic cell abundance, TNFRSF9 and ITGB2 expression, which were consistent with the results of GSE94104 (Figure 7B).

Discussion

Rectal cancer is a heterogeneous disease at the genetic and molecular levels; both aspects have major repercussions on the tumor immune context. While microsatellite status and tumor mutational load have been associated with the response to

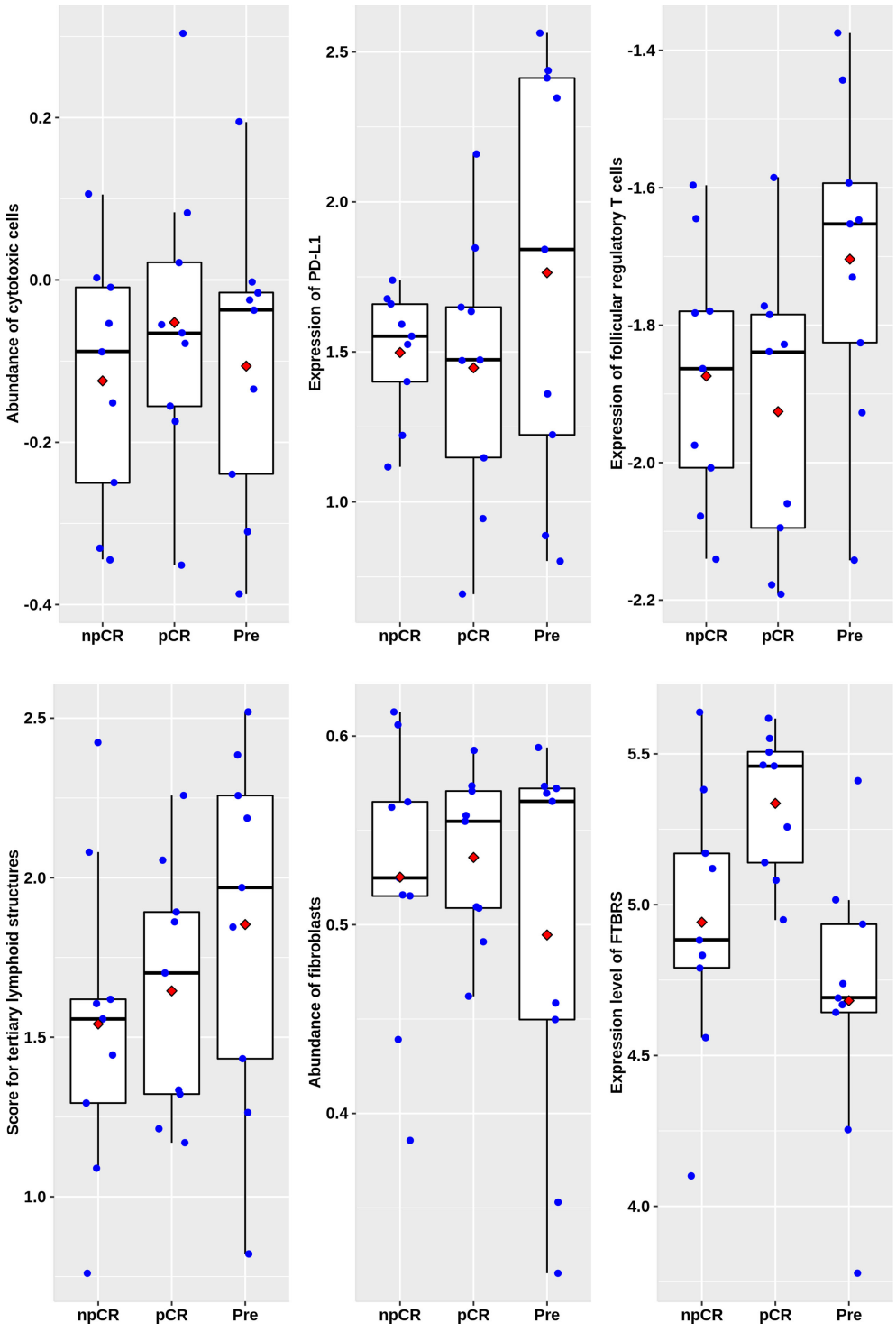

FIGURE 6
Scatter plots overlapped with box plots illustrating differences in six major immune related scores among four immune subtypes in DPH cohort. npCR indicates samples with non-pathological complete response after nCRT treatment, pCR indicates samples with pathological complete response after nCRT treatment and Pre stands for samples biopsied before nCRT.

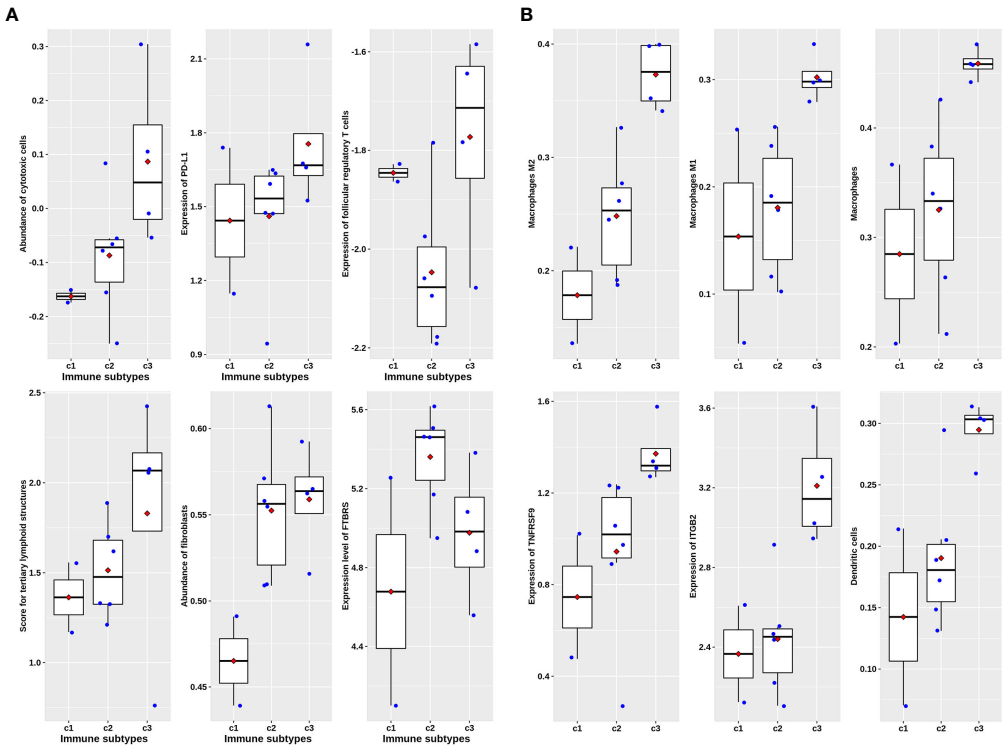

FIGURE 7
Scatter plots overlapped with box plots illustrating immune characteristics among three immune subtypes available after nCRT treatment in DPH cohort. **(A)** Six major immune related scores without statistical significance. **(B)** Six immune related scores with statistical significance revealed by Kruskal–Wallis H test.

immunotherapy, the presence of TILs is one of the most powerful prognostic and predictive biomarkers. Yet, the majority of rectal cancers are characterized by microsatellite stability, low-tumor mutational burden, and poor T-cell infiltration. These patients can also benefit from ICB treatment, suggesting that biomarkers cannot fully reflect the immune microenvironment characteristics of rectal cancer (27). Additionally, radiotherapy and chemotherapy can lead to the remodeling of the immune microenvironment (6). Therefore, this study combined different immune subtypes and TLS, follicular regulatory T cells, and fibroblasts, which have a regulatory effect on the tumor immune microenvironment, to evaluate their impact on the efficacy of ICB and identify which immune microenvironment is suitable for ICB.

Immunophenotyping based on immune cell abundance can characterize the immune heterogeneity between tumors, providing a basis for discovering specific immune characteristic populations, especially for identifying potential benefit populations of ICB treatment (17). For example, among the five sarcoma immune classes (SICs) obtained by MCP counter, the SICE subtype not only highly expresses plasma cell genes but also has the highest response rate to pembrolizumab and the longest PFS time (17). In this study, the immunophenotyping based on 64 immune cell abundance inferred from xCell also reflects the heterogeneity of colorectal cancer TIME. Among them, the C3 subtype has potentially ICB-beneficial immune characteristics (high infiltration of CTLs, high expression of PD-L1).

Preclinical investigations into the mechanisms by which various immune cell components participate in the response to anti-PD-1/PD-L1 treatment provide the foundation for our analysis. The TLS and follicular regulatory T cells in tumor tissues have a regulatory effect on the function of TILs in TIME (13). Recent studies have also suggested that TGFβ secreted by fibroblasts is the main mechanism mediating T-cell rejection (11). Fibroblasts are the main type of mesenchymal cells in the tumor microenvironment of colorectal cancer (28). Therefore, in addition to the immunophenotyping, we also included TLS, follicular regulatory T cells, and CAF to comprehensively predict the response to ICB therapy.

From the results of IMvigor210 (Figure 3 and Supplementary Figures 2, 3), the C3 subtype and follicular regulatory T cells may jointly determine the response to ICB treatment. The DHP cohort

and GSE94104 consistently revealed that the C3 subtype is featured with the highest expression of TNFRSF9 (Figures 5, 7). TNFRSF9 is the main marker of recently activated regulatory T-cell receptors and follicular regulatory T cells differentiated from such regulatory T cells (12). TIME after nCRT is quite different from untreated tumor tissues (Figures 4, 5, 7). Among them, the high activation of macrophages and other antigen presentation mechanisms is the main feature in tumor tissue after neoadjuvant therapy. In fact, research has shown that MSI-H colorectal cancer patients with a high abundance of CD68 +CD74+ macrophages can benefit significantly from the treatment of nivolumab and pembrolizumab (27). Our analysis shows that the C3 subtype has a large amount of macrophage infiltration, suggesting that the C3 subtype has a good response to ICB treatment.

Although it is generally believed that nCRT of LARC can induce hot tumors, there may be great differences in the composition of the immune microenvironment between hot tumors induced by nCRT and untreated hot tumors (6). More and more preclinical studies have shown that the response mechanism of ICB depends not only on the effector T cells themselves but also on the role of antigen-presenting cells such as macrophages and dendritic cells (27, 29). Therefore, the mechanism of macrophages and their intercellular communication with other immune cells by which ICB is effective after nCRT treatment of LARC needs to be further studied.

There are still many limitations to our study. First of all, due to the lack of expression profiles of patients with LARC treated with immunotherapy, we have only validated the predictive role of immunophenotyping for ICB through the bladder cancer and melanoma databases. Moreover, the targets of anti-PD-L1, anti-PD-1, and anti-CTLA-4 treatment are different; their response mechanisms are not exactly the same (12, 29). Secondly, the immune microenvironment of rectal cancer after nCRT depends not only on the characteristics of the tumor itself but also on the sampling time after nCRT. There are differences in the composition of immune cells sampled at different times after nCRT (6), which raises a problem relating to the window of opportunity for the benefit of specific ICB treatment. We found that the C2 subtype had the shortest RFS in GSE8721 (Figure 3A), which was consistent with previous studies on CAF involvement in radiotherapy resistance (30). C3 had the best efficacy of ICB (Figures 3B, C). These results preliminarily suggest that immunophenotyping can be used as a factor to predict the efficacy of ICB. However, from the perspective of guiding the individualized treatment of ICB, our analysis did not achieve the purpose of revealing that different immune subtypes need different ICB treatment schemes. In addition, although we used the prediction method based on immune cell infiltration abundance and quality control approach proposed by Petitprez et al. (22), 15.3%–33.3% of the samples in each cohort could not be successfully classified, mainly due to a low Pearson correlation coefficient with the four original subtypes, indicating that these samples may not belong to any of the four subtypes. It does not rule out that the immunophenotyping constructed in early colon cancer is not suitable for local advanced rectal cancer.

In conclusion, we comprehensively analyzed the predictive effect of immune types and the expression profiles of TLS, follicular regulatory T cells, and CAF on the efficacy of ICB treatment. The results suggest that these factors may be coordinated to predict the efficacy of ICB. Our present analysis indicates transcriptomic profiles can provide further biomarkers to stratify rectal cancer patients after nCRT in terms of their response to ICB treatment beyond tumor microsatellite instability status and tumor mutational burden.

Data availability statement

The date presented in the study are deposited in the GEO repository, accession number GSE213331.

Ethics statement

The studies involving human participants were reviewed and approved by the ethics committee of Daping Hospital. Written informed consent for participation was not required for this study in accordance with the national legislation and the institutional requirements.

Author contributions

Conceptualization, HX and DW. Data curation, DJ, YF, and DW. Formal analysis, MJ, BY, and DJ. Funding acquisition, DW. Investigation, LH, MJ, DJ, BY, and ND. Methodology, BY, LH, MJ, and HX. Project administration, DW. Resources, DJ, ND, and YF. Software, BY and LH. Supervision, YF and DW. Validation, LH, ND, and HX. Visualization, LH and HX. Writing—original draft, MJ and HX. Writing—review and editing, DW. All authors contributed to the article and approved the submitted version.

Funding

The study is supported by the National Key Research and Development Project (2018YFC0114402).

Conflict of interest

The authors declare that the research was conducted in the absence of any commercial or financial relationships that could be construed as a potential conflict of interest.

Publisher's note

All claims expressed in this article are solely those of the authors and do not necessarily represent those of their affiliated organizations, or those of the publisher, the editors and the reviewers. Any product that may be evaluated in this article, or claim that may be made by its manufacturer, is not guaranteed or endorsed by the publisher.

Supplementary material

The Supplementary Material for this article can be found online at: https://www.frontiersin.org/articles/10.3389/fimmu.2022.955187/full#supplementary-material

References

1. van Gijn W, Marijnen CA, Nagtegaal ID, Kranenbarg EM, Putter H, Wiggers T, et al. Preoperative radiotherapy combined with total mesorectal excision for resectable rectal cancer: 12-year follow-up of the multicentre, randomised controlled TME trial. *Lancet Oncol* (2011) 12:575–82. doi: 10.1016/S1470-2045(11)70097-3

2. Sauer R, Liersch T, Merkel S, Fietkau R, Hohenberger W, Hess C, et al. Preoperative versus postoperative chemoradiotherapy for locally advanced rectal cancer: Results of the German CAO/ARO/AIO-94 randomized phase III trial after a median follow-up of 11 years. *J Clin Oncol* (2012) 30:1926–33. doi: 10.1200/JCO.2011.40.1836

3. Yang B, Shan J, Feng Y, Dai N, Li M, Chen C, et al. Transcatheter rectal arterial chemoembolization with oxaliplatin plus s-1 concurrent chemoradiotherapy can improve the pathological remission rate in locally advanced rectal cancer: A comparative study. *Radiat Oncol* (2020) 15:94. doi: 10.1186/s13014-020-01540-4

4. Wang Y, Zenkoh J, Gerelchuluun A, Sun L, Cai S, Li X, et al. Administration of dendritic cells and anti-PD-1 antibody converts X-ray irradiated tumors into effective *in situ* vaccines. *Int J Radiat Oncol Biol Phys* (2019) 103:958–69. doi: 10.1016/j.ijrobp.2018.11.019

5. Ji D, Yi H, Zhang D, Zhan T, Li Z, Li M, et al. Somatic mutations and immune alternation in rectal cancer following neoadjuvant chemoradiotherapy. *Cancer Immunol Res* (2018) 6:1401–16. doi: 10.1158/2326-6066.CIR-17-0630

6. Lauret Marie Joseph E, Kirilovsky A, Lecoester B, El Sissy C, Boullerot L, Rangan L, et al. Chemoradiation triggers antitumor Th1 and tissue resident memory-polarized immune responses to improve immune checkpoint inhibitors therapy. *J Immunother Cancer* (2021) 9(7):e002256. doi: 10.1136/jitc-2020-002256

7. Rahma OE, Yothers G, Hong TS, Russell MM, You YN, Parker W, et al. Use of total neoadjuvant therapy for locally advanced rectal cancer: Initial results from the pembrolizumab arm of a phase 2 randomized clinical trial. *JAMA Oncol* (2021) 7:1225–30. doi: 10.1001/jamaoncol.2021.1683

8. Ayers M, Lunceford J, Nebozhyn M, Murphy E, Loboda A, Kaufman DR, et al. IFN-gamma-related mRNA profile predicts clinical response to PD-1 blockade. *J Clin Invest* (2017) 127:2930–40. doi: 10.1172/JCI91190

9. Jiang P, Gu S, Pan D, Fu J, Sahu A, Hu X, et al. Signatures of T cell dysfunction and exclusion predict cancer immunotherapy response. *Nat Med* (2018) 24:1550–8. doi: 10.1038/s41591-018-0136-1

10. Banchereau R, Leng N, Zill O, Sokol E, Liu G, Pavlick D, et al. Molecular determinants of response to PD-L1 blockade across tumor types. *Nat Commun* (2021) 12:3969. doi: 10.1038/s41467-021-24112-w

11. Mariathasan S, Turley SJ, Nickles D, Castiglioni A, Yuen K, Wang Y, et al. TGFbeta attenuates tumour response to PD-L1 blockade by contributing to exclusion of T cells. *Nature* (2018) 554:544–8. doi: 10.1038/nature25501

12. Eschweiler S, Clarke J, Ramirez-Suastegui C, Panwar B, Madrigal A, Chee SJ, et al. Intratumoral follicular regulatory T cells curtail anti-PD-1 treatment efficacy. *Nat Immunol* (2021) 22:1052–63. doi: 10.1038/s41590-021-00958-6

13. Cabrita R, Lauss M, Sanna A, Donia M, Skaarup Larsen M, Mitra S, et al. Tertiary lymphoid structures improve immunotherapy and survival in melanoma. *Nature* (2020) 577:561–5. doi: 10.1038/s41586-019-1914-8

14. Borelli B, Fontana E, Giordano M, Antoniotti C, Lonardi S, Bergamo F, et al. Prognostic and predictive impact of consensus molecular subtypes and CRCAssigner classifications in metastatic colorectal cancer: A translational analysis of the TRIBE2 study. *ESMO Open* (2021) 6:100073. doi: 10.1016/j.esmoop.2021.100073

15. Lenz HJ, Ou FS, Venook AP, Hochster HS, Niedzwiecki D, Goldberg RM, et al. Impact of consensus molecular subtype on survival in patients with metastatic colorectal cancer: Results from CALGB/SWOG 80405 (Alliance). *J Clin Oncol* (2019) 37:1876–85. doi: 10.1200/JCO.18.02258

16. Helmink BA, Reddy SM, Gao J, Zhang S, Basar R, Thakur R, et al. B cells and tertiary lymphoid structures promote immunotherapy response. *Nature* (2020) 577:549–55. doi: 10.1038/s41586-019-1922-8

17. Petitprez F, de Reynies A, Keung EZ, Chen TW, Sun CM, Calderaro J, et al. B cells are associated with survival and immunotherapy response in sarcoma. *Nature* (2020) 577:556–60. doi: 10.1038/s41586-019-1906-8

18. Wang Z, Guo X, Gao L, Wang Y, Guo Y, Xing B, et al. Classification of pediatric gliomas based on immunological profiling: implications for immunotherapy strategies. *Mol Ther Oncolytics* (2021) 20:34–47. doi: 10.1016/j.omto.2020.12.012

19. Thorsson V, Gibbs DL, Brown SD, Wolf D, Bortone DS, Ou Yang TH, et al. The immune landscape of cancer. *Immunity* (2018) 48:812–30.e14. doi: 10.1016/j.immuni.2018.03.023

20. Trapnell C, Williams BA, Pertea G, Mortazavi A, Kwan G, van Baren MJ, et al. Transcript assembly and quantification by RNA-seq reveals unannotated transcripts and isoform switching during cell differentiation. *Nat Biotechnol* (2010) 28:511–5. doi: 10.1038/nbt.1621

21. Aran D, Hu Z, Butte AJ. xCell: digitally portraying the tissue cellular heterogeneity landscape. *Genome Biol* (2017) 18:220. doi: 10.1186/s13059-017-1349-1

22. Ragulan C, Eason K, Fontana E, Nyamundanda G, Tarazona N, Patil Y, et al. Analytical validation of multiplex biomarker assay to stratify colorectal cancer into molecular subtypes. *Sci Rep* (2019) 9:7665. doi: 10.1038/s41598-019-43492-0

23. Subramanian A, Tamayo P, Mootha VK, Mukherjee S, Ebert BL, Gillette MA, et al. Gene set enrichment analysis: a knowledge-based approach for interpreting genome-wide expression profiles. *Proc Natl Acad Sci USA* (2005) 102:15545–50. doi: doi 10.1073/pnas.0506580102

24. Hanzelmann S, Castelo R, Guinney J. GSVA: gene set variation analysis for microarray and RNA-seq data. *BMC Bioinf* (2013) 14:7. doi: 10.1186/1471-2105-14-7

25. Budczies J, Kosztyla D, Trne CV, Stenzinger A, Denkert. C. Cancerclass: An r package for development and validation of diagnostic tests from high-dimensional molecular data. *J Stat Softw*, (2014) 59(1):1–19. doi: 10.18637/jss.v059.i01

26. Jimenez-Sanchez A, Cast O, Miller. ML. Comprehensive benchmarking and integration of tumor microenvironment cell estimation methods. *Cancer Res* (2019) 79:6238–46. doi: 10.1158/0008-5472.CAN-18-3560

27. Bortolomeazzi M, Keddar MR, Montorsi L, Acha-Sagredo A, Benedetti L, Temelkovski D, et al. Immunogenomics of colorectal cancer response to checkpoint blockade: Analysis of the KEYNOTE 177 trial and validation cohorts. *Gastroenterology* (2021) 161:1179–93. doi: 10.1053/j.gastro.2021.06.064

28. Li H, Courtois ET, Sengupta D, Tan Y, Chen KH, Goh JJL, et al. Reference component analysis of single-cell transcriptomes elucidates cellular heterogeneity in human colorectal tumors. *Nat Genet* (2017) 49:708–18. doi: 10.1038/ng.3818

29. Mayoux M, Roller A, Pulko V, Sammicheli S, Chen S, Sum E, et al. Dendritic cells dictate responses to PD-L1 blockade cancer immunotherapy. *Sci Transl Med* (2020) 12(534):eaav7431. doi: 10.1126/scitranslmed.aav7431

30. Isella C, Terrasi A, Bellomo SE, Petti C, Galatola G, Muratore A, et al. Corrigendum: Stromal contribution to the colorectal cancer transcriptome. *Nat Genet* (2016) 48:1296. doi: 10.1038/ng1016-1296d

frontiers | Frontiers in Immunology

TYPE Original Research
PUBLISHED 07 October 2022
DOI 10.3389/fimmu.2022.990571

Check for updates

OPEN ACCESS

EDITED BY
Linlang Guo,
Zhujiang Hospital, China

REVIEWED BY
Yongli Yang,
Zhengzhou University, China
Anqi Wang,
The First Affiliated Hospital of Soochow University, China

*CORRESPONDENCE
Jiayin Yang
doctoryjy@scu.edu.cn
Yujun Shi
shiyujun@scu.edu.cn

†These authors have contributed equally to this work

SPECIALTY SECTION
This article was submitted to Cancer Immunity and Immunotherapy, a section of the journal Frontiers in Immunology

RECEIVED 10 July 2022
ACCEPTED 20 September 2022
PUBLISHED 07 October 2022

CITATION
Yuan J, Liu Z, Wu Z, Yan L, Yang J and Shi Y (2022) A novel medication decision gene signature predicts response to individualized therapy and prognosis outcomes in hepatocellular carcinoma patients.
Front. Immunol. 13:990571.
doi: 10.3389/fimmu.2022.990571

COPYRIGHT
© 2022 Yuan, Liu, Wu, Yan, Yang and Shi. This is an open-access article distributed under the terms of the Creative Commons Attribution License (CC BY). The use, distribution or reproduction in other forums is permitted, provided the original author(s) and the copyright owner(s) are credited and that the original publication in this journal is cited, in accordance with accepted academic practice. No use, distribution or reproduction is permitted which does not comply with these terms.

A novel medication decision gene signature predicts response to individualized therapy and prognosis outcomes in hepatocellular carcinoma patients

Jingsheng Yuan[1,2†], Zijian Liu[3,4†], Zhenru Wu[5], Lvnan Yan[1,2], Jiayin Yang[1,2*] and Yujun Shi[2,5*]

[1]Department of Liver Surgery and Liver Transplantation Center, West China Hospital of Sichuan University, Chengdu, China, [2]Laboratory of Liver Transplantation, Frontiers Science Center for Disease-related Molecular Network, West China Hospital of Sichuan University, Chengdu, China, [3]Department of Head and Neck Oncology, Cancer Center and State Key Laboratory of Biotherapy, West China Hospital of Sichuan University, Chengdu, China, [4]Department of Radiation Oncology, Cancer Center and State Key Laboratory of Biotherapy, West China Hospital of Sichuan University, Chengdu, China, [5]Laboratory of Pathology, Key Laboratory of Transplant Engineering and Immunology, NHC, West China Hospital of Sichuan University, Chengdu, China

Molecular targeted therapy has shown potential in hepatocellular carcinoma (HCC) patients, and immunotherapy applications are developing rapidly. However, clinical guidance for making individualized therapy decisions for HCC patients remains lacking. MDH (Medication Decision in HCC) gene signatures comprising 70 genes were screened using transcriptomic data from multikinase inhibitor (TKI)-resistant HCC cells and HCC patient-derived xenograft model (PDX) models. Four MDH subtypes with distinct biological and clinical characteristics were defined by unsupervised cluster analysis of HCC data from The Cancer Genome Atlas (TCGA) database. To facilitate individualized and reasonable clinical guidance for each HCC patient, we constructed the MDH score. Comprehensive analysis suggested high MDH scores were associated with TKI resistance, a high proportion of stromal cell infiltration and poor survival outcomes. We recommend concomitant stromal activity intervention and immunotherapy for this type of HCC. Moreover, low MDH scores indicate TKI sensitivity, and a combination of targeted and immunotherapy is recommended. The nomogram constructed by iteration least absolute shrinkage and selection operator (LASSO) Cox regression analysis successfully predicted 3- or 5-year survival outcomes and mortality risks of HCC patients. In conclusion, TKI resistance model-based MDH gene signatures provide novel insight into potential mechanisms of drug resistance and heterogeneity in HCC. Integrative analysis plus a simplified decision model

may aid personalized treatment and prognostic assessment among HCC patients.

KEYWORDS

hepatocellular carcinoma, immunotherapy, multikinase inhibitor, individualized therapy, prognostic model

Introduction

Hepatocellular carcinoma (HCC) is one of the most common cancers worldwide and the third leading cause of cancer-related deaths (1). HCC represents ~90% of all primary liver cancers (2). Approximately half of HCC patients eventually receive systemic therapy during their disease course, especially in the advanced stages of the disease (3). The number of available systemic treatment drugs for HCC is gradually increasing (4). Sorafenib was the first multikinase inhibitor (TKI) for HCC to be approved by the FDA and increased the median patient overall survival time from 8 to 11 months (5). Several newer TKIs, including first-line levatinib and second-line regorafenib and cabozantinib, have gradually been incorporated into clinical approaches (6). Additionally, immune checkpoint inhibitors have been an option for HCC treatment since 2020, and the combination of targeted therapies and immunotherapy is emerging as the most promising clinical treatment option for this disease (7). Notably, studies have revealed that patients receiving individualized therapy have better clinical outcomes (8). However, there are no appropriate clinical recommendations for precise drug selection in HCC patients. Furthermore, despite the clinical benefits of systemic therapy, the improvement in patient prognosis is limited and has occurred gradually. Therefore, further studies are necessary to investigate the underlying mechanisms of drug resistance in HCC and facilitate accurate medication decision-making for HCC patients.

Most of the current clinical treatments for tumours address specific genes or genomes, but researchers realize that these specific genes or genomes comprise a limited number of targets. In addition to the already widely applied analysis of carcinogenic signalling pathways, previous studies have proposed tumour mutation burden (TMB) to measure gene mutation frequency (9), the mRNA-based stemness index (mRNAsi) to evaluate the stemness of tumours (10), and the ferroptosis potential index (FPI) to assess the vulnerability of tumour cells to ferroptosis (11). Moreover, tumour immune cell markers for immune infiltration analysis and the Estimation of Stromal and Immune cells in malignant tumours using Expression data (ESTIMATE) algorithm for calculating stromal and immune cell proportions have recently been proposed (12, 13). Tumour genetic alterations are complex, and these genomes comprise only a small fraction of oncogenic transformation; thus, it is necessary to identify new biomarkers or tumour-associated genomic profiles. Whole transcriptome sequencing offers new opportunities to dissect tumour heterogeneity and complexity, providing a multifaceted view of tumour characteristics for exploring and developing new therapeutic strategies, potentially driving further identification and optimization of individualized treatment options for cancer patients (14).

Although many models for tumour assessment or classification have been proposed using transcriptome sequencing or multiomics studies, most of these models are based on a known mutated gene, tumour phenotype or gene cluster (15), and few have been constructed starting from a tumour drug resistance-associated gene cluster. Multidrug resistance (MDR) refers to drug resistance to several antitumour drugs with diverse structures and various mechanisms after tumours develop resistance to certain chemotherapeutic drugs (16), which is the main reason for the failure of chemotherapy. Interestingly, our study also observed this MDR phenomenon in HCC against TKIs. Given this mechanism of MDR, we speculate that there may be a relevant set of genes mediating MDR in HCC TKI therapy. Thus, our study proposed the MDH (Medication Decision in HCC) gene signatures and characterized the MDH subtype of HCC. Moreover, we further performed MDH scoring to predict individualized therapy and prognosis outcomes in HCC patients.

Materials and methods

Clinical samples

A retrospective analysis of HCC resection samples from the West China Hospital of Sichuan University from May 2019 to December 2020 was performed. HCC samples taken at the initial surgery that met the following criteria were included: 1. a history of sorafenib; 2. prognosis information after sorafenib therapy was available; 3. a confirmed clinicopathological diagnosis of HCC through pathology reports. Formalin-fixed and paraffin-

embedded HCC tumour specimens were obtained from a tissue bank maintained at the West China Hospital. According to the Modified Response Evaluation Criteria in Solid Tumours (mRECIST) (17), we obtained 20 HCC samples from patients with progressive disease (PD) and 20 HCC samples from patients with partial response (PR). PD patient samples were considered sorafenib-resistant. The PR patient samples were considered sorafenib-sensitive. This clinical sample study was approved by the Ethics Committee on Biomedical Research, West China Hospital of Sichuan University (2016, no. 120). Informed consent was obtained from all patients or their relatives. The details of HCC patients are listed in Table S1.

Cell culture

Huh7 and HepG2 cell lines were purchased from the National Collection of Authenticated Cell Cultures (Shanghai, China) and were cultured in complete medium containing Dulbecco's modified Eagle's medium (DMEM) (HyClone, UT, USA) supplemented with 10% foetal bovine serum (FBS) (Gibco, NY, USA), 1000 U/ml penicillin and 100 μg/ml streptomycin (HyClone, UT, USA) and were grown in a humidified air atmosphere containing 5% CO_2 at 37°C. All cell lines were analysed by STR profiling for cell line authentication, and routine mycoplasma detection was performed. Sorafenib-resistant HCC cell lines generated from Huh7 and HepG2 parental cells were cultured as previously described (18).

Patient-derived xenograft model

A patient-derived xenograft model (PDX) was established as previously reported (19). Briefly, freshly procured hepatocellular carcinoma samples were cut into small tissue blocks (~50 mm^3) and kept in tissue culture media on ice until use (<5 hours). Six-week-old nude mice were anaesthetized with an isoflurane/oxygen mixture. Engrafted tissue blocks were carefully sealed under the skin of the mice using a tissue adhesive (Vetbond). Dosing was initiated when tumours reached approximately 0.2 cm^3, and sorafenib (10 mg/kg) was administered thereafter every day. Tumour that regressed significantly were considered sorafenib-sensitive HCC. Tumours did not regress significantly despite continuous dosing were considered sorafenib-induced drug-resistant HCC. Human samples were obtained patient consent and approval from the institutional review board, conforming to the ethical guidelines of the 1975 Declaration of Helsinki. Animals received humane care, and the Institutional Animal Care and Use Committee (IACUC) approved all animal experiments (2020351A). Subsequently, tumour samples were collected by GeneChem Co., Ltd. (Shanghai, China) for transcriptome sequencing and subsequent data analysis. Three PDX samples per group were used for sequencing.

Transcriptome sequencing of HCC cells

Total RNA from HCC cells was processed and extracted using a TRIzol reagent kit (Takara, Dalian, China) and collected by Novogene Co., Ltd. (Tianjin, China) for transcriptome sequencing and subsequent data analysis. Three samples of the parental and sorafenib-resistant HCC cells were used for sequencing.

Cell counting kit-8

The cell counting kit-8 (CCK-8) was performed as previously described (20).

Clonogenic cell survival assay

The indicated cells were treated with sorafenib (Selleck, S7397, TX, USA) and lenvatinib (Selleck, S1164) for 24 h, and 3000 cells were plated into 6-well plates. Two weeks later, the colonies were fixed with 4% paraformaldehyde, followed by 30 min of incubation with 0.1% crystal violet. The 6-well plates were washed and then visualized.

Immunohistochemistry

Immunohistochemistry (IHC) was performed as previously described (18). The primary antibodies used in this study are listed in Table S2.

Data sources and preprocessing

The raw data of fragment per kilobase (FPKM) values and liver hepatocellular carcinoma (LIHC) clinical information in The Cancer Genome Atlas (TCGA) and International Cancer Genome Consortium (ICGC) datasets were downloaded from the UCSC XENA database. The series matrix files of the Affymetrix and Illumina-generated microarray for GSE109211 and GSE73571 were directly downloaded from the Gene Expression Omnibus (GEO) database. The immunotherapy cohort of patients with metastatic urothelial carcinoma treated with the anti-PD-L1 antibody atezolizumab (IMvigor210) was obtained according to official guidelines. All the information about the public datasets is summarized in Table S3.

Functional and pathway enrichment analysis

The Kyoto Encyclopedia of Genes and Genomes (KEGG) pathway analysis results were obtained from The Database for

Annotation, Visualization and Integrated Discovery (DAVID) v6.8 (21). Gene set enrichment analysis (GSEA) was performed on the expression data of a specified set of transcripts according to previously published expression methods (22). To further estimate pathway and biological process activity variations in samples from expression datasets, we performed Gene Set Variation Analysis (GSVA) enrichment analysis using the "GSVA" R package, a nonparametric and unsupervised method (23). The gene set "c5.all.v6.2. symbols" was downloaded from the MSigDB database on the GSEA website, and another published pathway gene set is summarized in Table S4 (24).

Assessment of the tumour immune microenvironment

As described above, we used the GSVA method to perform gene-set enrichment analysis to quantify the relative abundance of each infiltrating cell in a single sample. The immune cell markers used in this study were extracted from two previously published authoritative studies (12, 25), as shown in Table S5, S6, referred to as immune cell signatures 1 and 2, respectively. Additionally, ESTIMATE was used to infer the fraction of stromal and immune cells in the samples (13).

Unsupervised clustering for MDH gene signatures

Based on the expression of the MDH gene signatures, unsupervised clustering analysis was performed using the TCGA-LIHC dataset to identify distinct MDH gene expression patterns and to classify HCC patients for further analysis. The number of clusters and their stability were determined by a consensus clustering algorithm. We performed the above steps using the "ConsensuClusterPlus" R package and performed 1000 repetitions to guarantee the stability of the classification.

Dimension reduction and generation of the MDH score

To quantify the MDH expression patterns of individual tumours, we constructed a scoring system based on the principal component analysis (PCA) score method to evaluate the MDA score of individual HCC patients. Gene patterns were annotated using the clusterProfiler R package. A consensus clustering algorithm was applied to define gene clusters, and PCA was performed (26). Principal components 1 and 2 were both used as gene feature scores. After obtaining the prognostic value of each gene signature score, we applied a method similar to gene expression grade index (GGI) to define the MDH score for each patient:

$$\mathrm{MDHscore} = \Sigma(\mathrm{PC1}i + \mathrm{PC2}i)$$

where i is the expression of MDH phenotype-related genes.

Calculation of the ferroptosis potential index (FPI) and mRNA-based stemness index (mRNAsi)

The index representing ferroptosis susceptibility was established from the expression data of ferroptosis core machine genes, including positive components and negative components, as shown in Table S7. The enrichment score (ES) of the gene set was calculated using the 'GSVA' R package, and the FPI was calculated as follows (11):

$$\mathrm{FPI} = \mathrm{ES}(\mathrm{positive}) - ES(negative)$$

To assess the stemness of cancer cells, a one-class logistic regression algorithm, mRNAsi, was used to calculate the stemness index for each HCC sample using the workflow available on a previously established database (10).

Predicting response to immunotherapy

The Tumor Immune Dysfunction and Exclusion (TIDE) algorithm was used to predict HCC responsiveness to immunotherapy (27). The TIDE algorithm captures two different mechanisms of the tumour immune escape score, including immunosuppressive factor rejection of tumour-infiltrating cytotoxic T lymphocytes (CTLs) score (exclusion) and CTLs dysfunction score (dysfunction). Additionally, the TIDE algorithm obtains three cell types that limit T-cell infiltration into tumours, myeloid-derived suppressor cells (MDSCs), cancer-associated fibroblasts (CAFs), and the M2 subtype of tumour-associated macrophages (TAM-M2s).

Establishment of the MDH Risk score

Univariate Cox regression analysis was used to observe the correlation between the expression level of the MDH gene set in the TCGA and patient prognosis. Genes with $p< 0.01$ in univariate Cox regression analysis were included in the construction of prognostic risk models. Next, the iteration least absolute shrinkage and selection operator (LASSO) Cox regression model was used to screen for the best gene signature involved in patient resistance to TKIs (28). Finally, multivariate Cox proportional hazards regression was performed to model the risk score and previously published algorithms were used to calculate the risk score. The median of risk scores was used as a cut-off to stratify patients into high- and low-risk groups. Differences in survival between the high- and low-risk groups

were further compared using Kaplan–Meier analysis. Univariate Cox regression analysis and multivariate Cox regression analysis were performed using the "survminer" package in R to investigate the relationship between risk score and prognosis. Using the "timeROC" package in R, the area under the curve (AUC) was used to test the performance of the classifier. We also assessed the prognostic value of these genes in the model.

Development and validation of the prognostic nomogram

Based on the risk scores of clinical risk factors and multivariate Cox regression coefficients, a prognostic nomogram was built using the "rms" R package, and the predictive accuracy of this nomogram was assessed using the calibration curve and the concordance index.

Statistical Analysis

All statistical calculations were performed using R software (version 3.6.1). Analysis of differentially expressed genes between different defined groups was performed using the empirical Bayesian approach of the "limma" R package, with significance criteria set as adjusted P-value< 0.05 and log2 |fold change (FC)| > 1. Differentially expressed mRNAs were visualized as heatmaps and volcano plots in R using the packages "pheatmap" and "ggplot2". To calculate the TMB per megabase, the total number of mutations counted was divided by the size of the coding region of the targeted territory in the TCGA-LIHC cohort (9). The mutation landscape oncoprint was generated using the R package "ComplexHeatmap. The comparison of normally distributed variables between the two groups was performed using an unpaired t test, and the statistical significance of the nonnormally distributed variables was estimated using the Mann–Whitney U test (Wilcoxon rank-sum test). Spearman's correlation analysis was performed to calculate the correlation coefficient between the two factors. Based on the correlation between gene expression and patient survival, the optimal cut-off point for each dataset was determined using the "survminer" R package, and the "surv-cutpoint" function was used to repeat all potential cut-off points to obtain the maximum rank statistic, divided into two groups: high and low. Survival curves for prognostic analysis were generated using the Kaplan–Meier method, and significant differences were determined using the log-rank test. The false discovery rate (FDR) method was used to adjust the P-value for multiple comparisons, and statistical significance was set at p<0.05; that is, the FDR was less than 0.05. The asterisks represent the statistical P-value (*P< 0.05; **P< 0.01; ***P< 0.001).

Results

Establishment of MDH gene signatures based on TKI-resistant HCC

As shown in Figure 1A, we designed this study to construct MDH gene signatures and investigate their potential value for individualized therapy and clinical application in HCC. We first cultured sorafenib-resistant HCC cell lines using our previously published method (Figures 1B, C) (18). Interestingly, CCK-8 and clonogenic cell survival assays indicated that sorafenib-resistant HCC cells were also significantly less sensitive to lenvatinib (Figures 1D, E), implying multidrug resistance. To delineate the alterations in gene expression and functional characteristics of TKI-resistant HCC cells, we conducted transcriptome sequencing of TKI-resistant HCC cells and parental HCC cells and further performed KEGG pathway enrichment analysis on the differentially expressed genes (DEGs). The results suggested that upregulated genes in TKI-resistant HCC cells were mainly enriched in the cell cycle and metabolic pathways (Figure S1A), while downregulated genes were mainly enriched in the FoxO signalling pathway, adherens junction and AMPK signalling pathway (Figure S1B). We further verified the above results using GSVA, which indicated four major variations in tumour metabolism, tumour-associated signalling, tumour phenotype and tumour immunity in TKI-resistant HCC cells (Figure 2A). Notably, tumour metabolism, such as oxidative phosphorylation, gluconeogenesis, and fatty acid metabolism, was dramatically enriched in TKI-resistant HCC cells. Among tumour-associated signalling and tumour phenotypes, TGF-β signalling, PI3K/AKT/mTOR signalling, KRAS signalling, and EMT signalling were remarkably enriched in parental HCC cells, while Wnt/β-catenin signalling, DNA repair and angiogenesis were significantly enriched in TKI-resistant HCC cells. Moreover, tumour immunity, such as the inflammatory response, IL6/JAK/STAT3 signalling and IL2/STAT5 signalling, was prominently enriched in parental HCC cells (Figure 2A). Finally, we obtained 161 genes from TKI-resistant HCC cells to establish MDH gene signatures (Figures S1C, D).

To further screen potential key genes *in vivo* for constructing MDH gene signatures, we developed and induced a TKI-resistant PDX model of HCC by *in vivo* sorafenib injection. Importantly, consistent with the *in vitro* analysis, our transcriptome sequencing and GSEA analysis demonstrated that metabolism-related signalling pathways were also markedly enriched in the TKI-resistant PDX model (Figure S1E). GSVA further emphasized that metabolism-related signalling is the main enriched pathway in TKI-resistant HCC, while EMT signalling, the inflammatory response and IL2/STAT5 signalling are the critical characteristic pathways in TKI-sensitive HCC (Figure S1F). These results revealed that among the myriad of signalling pathways, alterations in

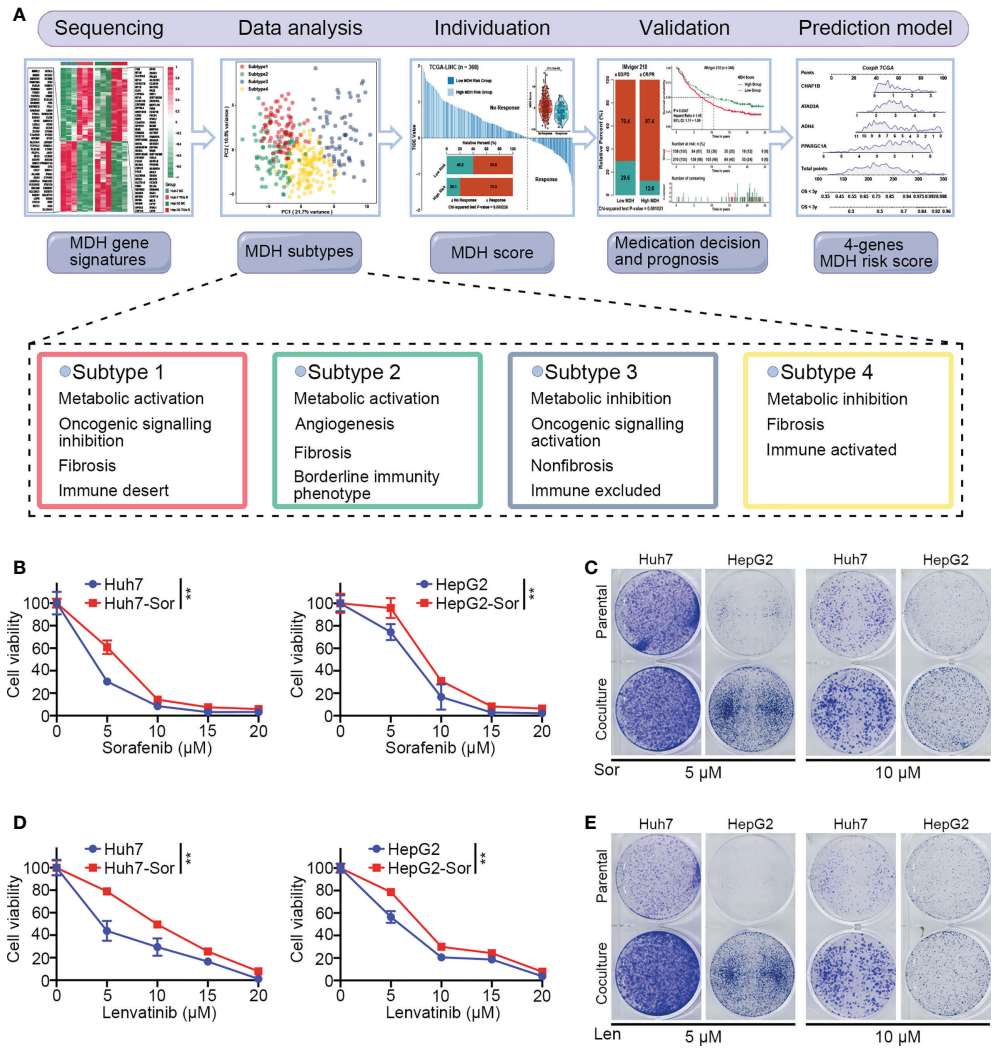

FIGURE 1
The culture of HCC sorafenib-resistant cell lines. **(A)** Schematic overview of the workflow in this study. **(B)** CCK-8 assays for parental HCC cells and corresponding sorafenib-resistant HCC cells treated with a range of concentrations of sorafenib. Cell viability was assessed 3 d after sorafenib treatment. **(C)** Clonogenic cell survival assay in specified cells treated with sorafenib for 24 h. **(D)** CCK-8 assays for parental HCC cells and corresponding sorafenib-resistant HCC cells treated with a range of concentrations of lenvatinib. Cell viability was assessed 5 d after lenvatinib treatment. **(E)** Clonogenic cell survival assay in specified cells treated with 10 μmol lenvatinib for 24 h. The asterisks in B and D represent the statistical p-value (**P< 0.01).

metabolism-related signalling, tumour phenotype and tumour immunity were potentially crucial mechanisms of TKI resistance in HCC. Combined with previous *in vitro* results, we further screened 70 genes to construct MDH gene signatures (Figure 2B and Table S8).

Unsupervised analysis of MDH gene signatures revealed four HCC subtypes

An unsupervised cluster analysis was performed using 368 HCC samples from the TCGA-LIHC dataset to recognize distinct HCC subtypes and investigate the potential value of screened MDH gene signatures in HCC. The consensus clustering algorithm determined the number and stability of clusters. This analysis revealed that the molecular profiles of HCC could be clustered into four distinct MDH subtypes (Figure S2A). PCA analysis further revealed significant distinctions in the transcriptional profiles among the four subtypes (Figure 3A). A combined heatmap was plotted to visualize MDH subtype gene expression levels and clinicopathological features to investigate the correlation between these subtypes and features in HCC (Figure 3B). Notably, we observed remarkable disparities in gene

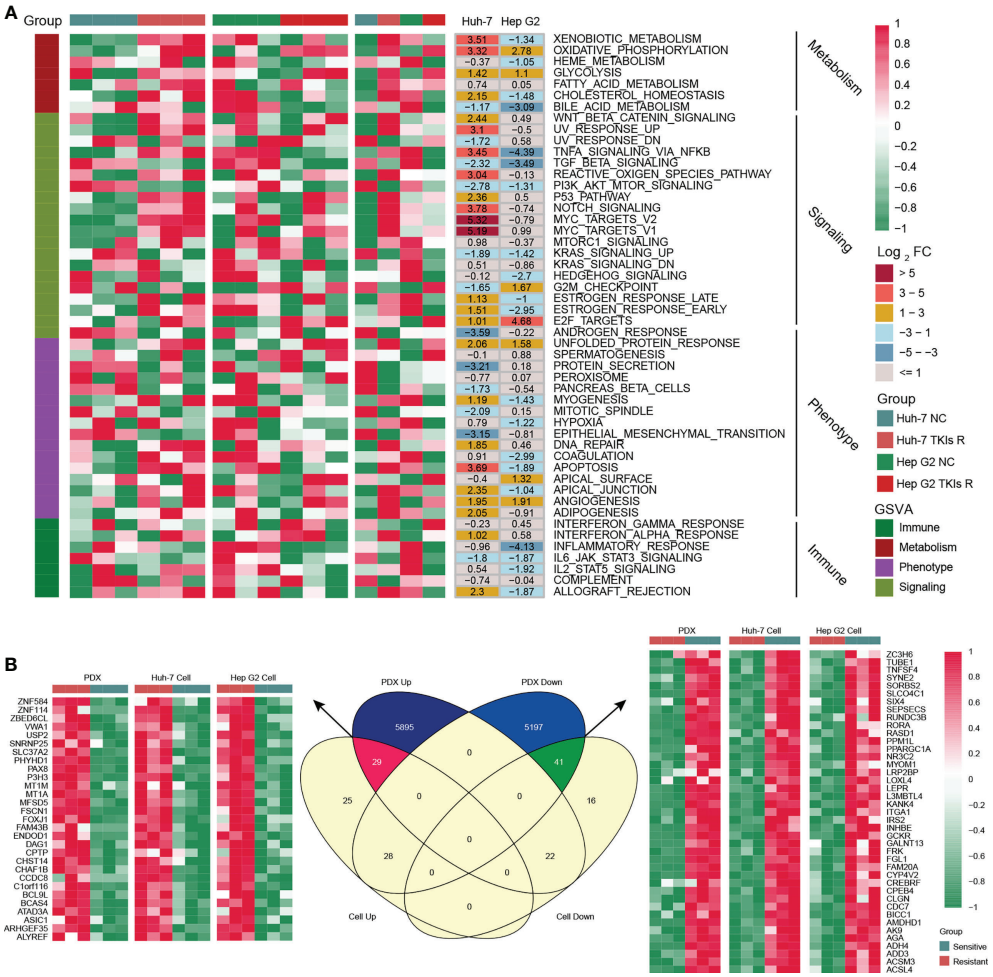

FIGURE 2
Generation of the MDH gene signatures. **(A)** GSEA enrichment analysis of differentially expressed genes (DEGs) between parental HCC cells and corresponding sorafenib-resistant HCC cells. **(B)** Venn diagram of MDH gene signatures acquired from the sorafenib-resistant PDX model and HCC cell lines.

expression abundance among different MDH subtypes. Moreover, subtypes 3/4 were markedly associated with higher histological grade and more advanced staging in HCC, and subtype 3 was strongly associated with HBV infection. Subtypes 1/2/4 were all significantly associated with HCC fibrosis relative to subtype 3 (Figure 3B). Prognostic analysis of pairwise comparisons further indicated that patients with subtype 3 HCC had significantly worse overall survival rates than those with subtypes 1/2/4, while patients with subtype 1 had a relatively better prognosis than those with subtypes 3/4 (Figure 3C).

KEGG pathway enrichment analysis was performed utilizing the gene expression profiles of each MDH subtype from the TCGA-LIHC dataset to investigate the potential mechanisms contributing to the differences in clinical features and prognosis across MDH subtypes. Interestingly, the upregulated genes in subtype 1 were dramatically associated with tumour metabolism, including metabolic pathways and drug metabolism (Figure S2B), while tumour-associated signalling pathways, such as ECM receptor interaction, focal adhesion, the NFKB signalling pathway and the TNF signalling pathway, were markedly downregulated (Figure S2C). Conversely, the upregulated genes in subtype 3 were dramatically involved in tumour-associated signalling pathways, including the cell cycle, ECM receptor interaction, P53 signalling pathways, pathways in cancer, PI3K/AKT signalling pathways, focal adhesion and DNA replication (Figure S2B), while tumour metabolism in subtype 3 was remarkably suppressed (Figure S2C). Additionally, upregulated genes in subtype 2 and downregulated genes in subtype 1 were markedly enriched in tumour metabolism-related signalling, but genes in subtype 1/2 were not distinctly connected to oncogenic-associated signalling pathways (Figures S2B, C).

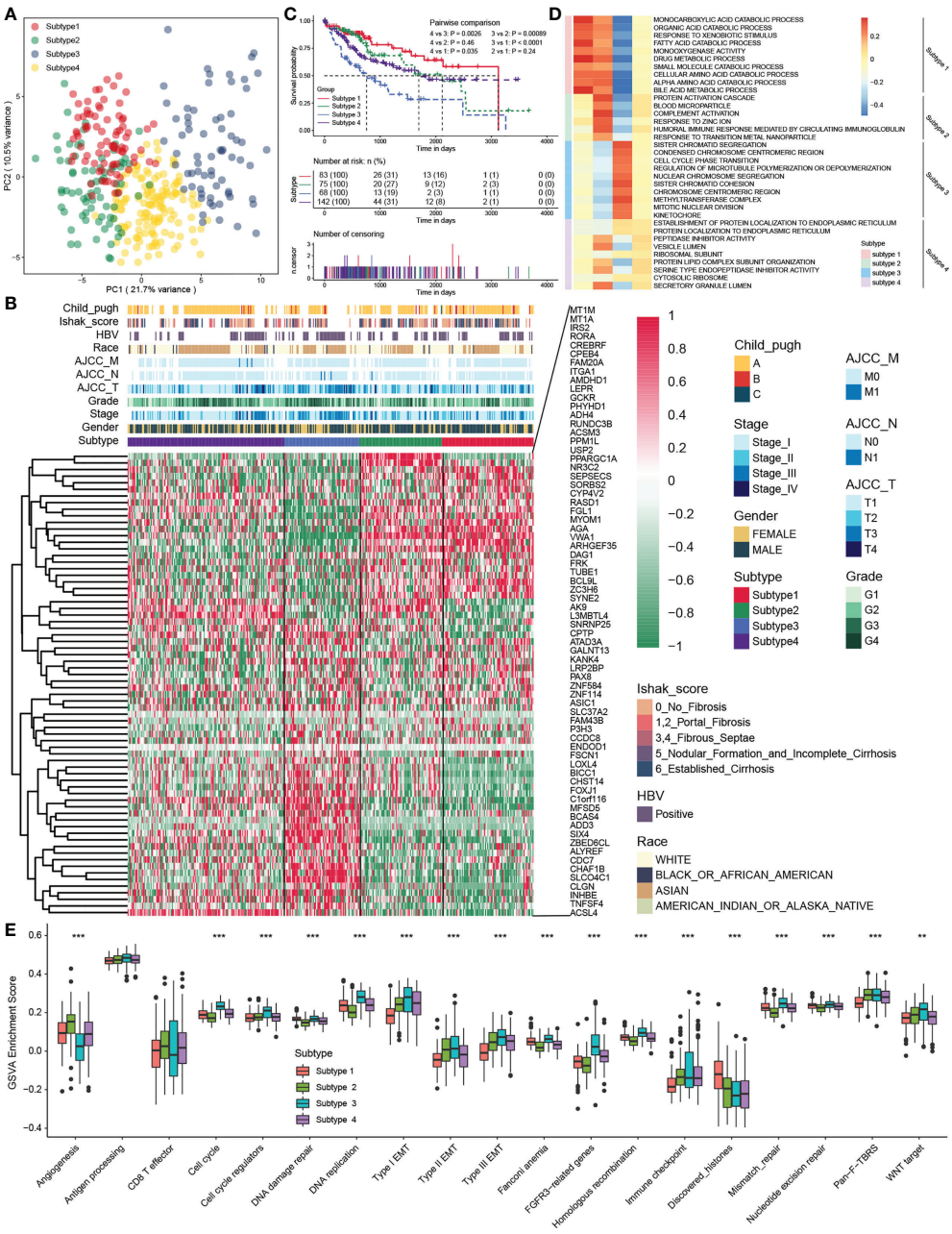

FIGURE 3
The four distinct MDH subtypes identified in HCC. **(A)** Principal component analysis for the transcriptome profiles in distinct MDH subtypes of the TCGA-LIHC cohort. **(B)** Unsupervised clustering of MDH gene signatures in the TCGA-LIHC cohort. **(C)** Survival analyses for distinct MDH subtypes of the TCGA-LIHC cohort. **(D)** GSVA enrichment analysis showing the activation states of biological pathways in distinct MDH subtypes of the TCGA-LIHC cohort. A heatmap was used to visualize these biological processes. **(E)** Differences in the expression of known signatures, including stromal activation-related signatures, tumour promotion-related signatures and immune activation-related signatures, in distinct MDH subtypes of the TCGA-LIHC cohort. The upper and lower ends of the boxes represent the interquartile range of values. The lines in the boxes represent the median value, and black dots show outliers. The asterisks represent the statistical p-value (**P< 0.01 and ***P< 0.001).

We further presented a combined heatmap using GSVA to visualize the pathway differences between subtypes and the associations with clinical features of HCC, which also validated that metabolism-related signalling pathways were enriched in subtype 1, while oncogenic signalling pathways such as cell cycle and DNA replication were enriched in subtype 3 (Figure 3D and Figure S3A). Notably, GSVA enrichment analysis of the indicated pathway sets revealed that

subtype 3 not only had the most remarkable correlation with signalling pathways such as the cell cycle, DNA replication, and EMT signalling but also had a strong association with tumour immune checkpoints, while subtype 2 was significantly correlated with angiogenesis (Figure 3E). In brief, our analysis revealed that HCC could be clustered into four distinct subtypes as shown in Figure 1A, namely, subtype 1, metabolic activation, oncogenic signalling inhibition, and fibrosis; subtype 2, metabolic activation, angiogenesis, and fibrosis; subtype 3, oncogenic signalling activation, metabolic inhibition, and nonfibrosis; and subtype 4, metabolic inhibition and fibrosis.

Immune microenvironmental characteristics of four MDH subtypes in HCC

Significant progress has been recently achieved by combining immunotherapy and TKIs to treat HCC (29), illustrating the importance of the immune microenvironment in HCC therapy. Studies have revealed that tumours with a higher TMB are more responsive to immunotherapy (30). Our results suggested that the overall TMB of subtype 1 was markedly higher than that of other subtypes with mutations mainly derived from CTNNB1 gene (Figures 4A, B), while the mutation of P53 gene in subtype 3 was remarkably more frequent than that of other subtypes (Figure 4B). Next, we analysed the association of each subtype with the tumour immune microenvironment. Based on the ESTIMATE algorithm, subtype 1 had the poorest immune cell infiltration and stromal cell proportions and had the worst ESTIMATE score relative to other subtypes. Moreover, there were no statistical differences in immune cell infiltration between subtypes 2, 3 and 4, whereas subtype 2 had comparatively higher levels of stromal cell infiltration and ESTIMATE scores (Figure S4A). According to previously published methods (12, 25), we further calculated the types of infiltrating immune cells for each subtype and performed pairwise comparisons to further elucidate the differences in immune cells between subtypes. Consistently, the analysis indicated that subtype 1 had an extremely poor innate immune cell infiltration compared to subtypes 2/3/4, including T cells, B cells, natural killer cells, macrophages, eosinophils, mast cells, monocytes, MDSCs, and plasmacytoid dendritic cells (Figure 4C). Most solid tumours exhibit three main immunological phenotypes, termed immune inflamed, immune excluded and immune desert (31). Thus, MDH subtype 1 in HCC was classified as an immune desert. Indeed, an overall decrease in the expression of MHC molecules, adhesion molecules and immune checkpoints in subtype 1 was further confirmed (Figure 4D).

In contrast, natural killer $CD56^+$ cells, Th2 cells, plasmacytoid dendritic cells (DCs) and activated CD4 T immune cells were abundant in subtype 3 (Figure 4C). Our prognostic analysis implied that natural killer $CD56^+$ cells, Th2 cells, plasmacytoid DCs and activated CD4 T immune cell infiltration were negative factors for HCC patients (Figure 4E). Notably, MHC molecules and adhesion molecules were more abundant in HCC subtype 3 than in subtypes 1/2/4 (Figure 4D). Moreover, PD1 and PD-L1 expression levels were dramatically increased in subtype 3. Cytokines with analogous expression trends include CD80 and CD86, ligands for CTLA-4 (Figure 4D). In theory, subtype 3 should be the tumour type with a better immune response in HCC; however, patients with subtype 3 did not display a matching survival advantage (Figure 3C). Previous studies have identified that tumours with an immune-excluded phenotype also exhibit infiltration of abundant immune cells, whereas these immune cells are retained in the stroma surrounding tumour cell nests rather than penetrating the parenchyma (31). Stromal activation is an essential driver of T-cell suppression (32). Our ESTIMATE analysis indicated that subtype 3 was markedly associated with stromal cell infiltration (Figure S4A). Our GSVA further implied that subtype 3 was associated with dramatically enhanced stromal activation, including increased levels of TGF-β signalling and EMT signalling (Figure S3A). Thus, MDH subtype 3 in HCC was classified as immune-excluded.

Furthermore, subtype 2 and subtype 4 contained abundant activated CD8 T cells, activated B cells, immature B cells and eosinophil cells, and HCC subtype 2 contained abundant DCs, including activated DCs (aDC), immature DCs (iDC), and plasmacytoid DCs (pDC) (Figure 4C). Our prognostic analysis implied that activated CD8 T cells, activated B cells and immature B cells, eosinophils and plasmacytoid DC infiltration were protective factors in HCC, while activated DCs and immature DCs were detrimental factors (Figure 4E). DCs are responsible for antigen presentation and the activation of naive T cells, bridging innate and adaptive immunity, and their activation depends on the expression levels of MHC molecules, costimulatory molecules, and adhesion molecules (24). Our analysis indicated that the expression of MHC molecules, costimulatory molecules and adhesion molecules was indeed somewhat higher in subtype 2 than in subtypes 1/4 (Figure 4D). However, we noticed that subtype 2 HCC had more abundant stromal cell infiltration than subtype 1/4 (Figure S4A), and angiogenesis was also enriched in subtype 2 (Figure 3E), suggesting that stromal cells in subtype 2 HCC were also partially activated. Therefore, subtype 4 was classified as immune-activated HCC, while subtype 2 was classified as at the borderline between immune-activated and immune-excluded.

The MDH score predicts the TKI response and prognosis in HCC

The ferroptosis index and mRNAsi are also scores used to measure tumour malignancy (10, 11). Notably, the mRNAsi

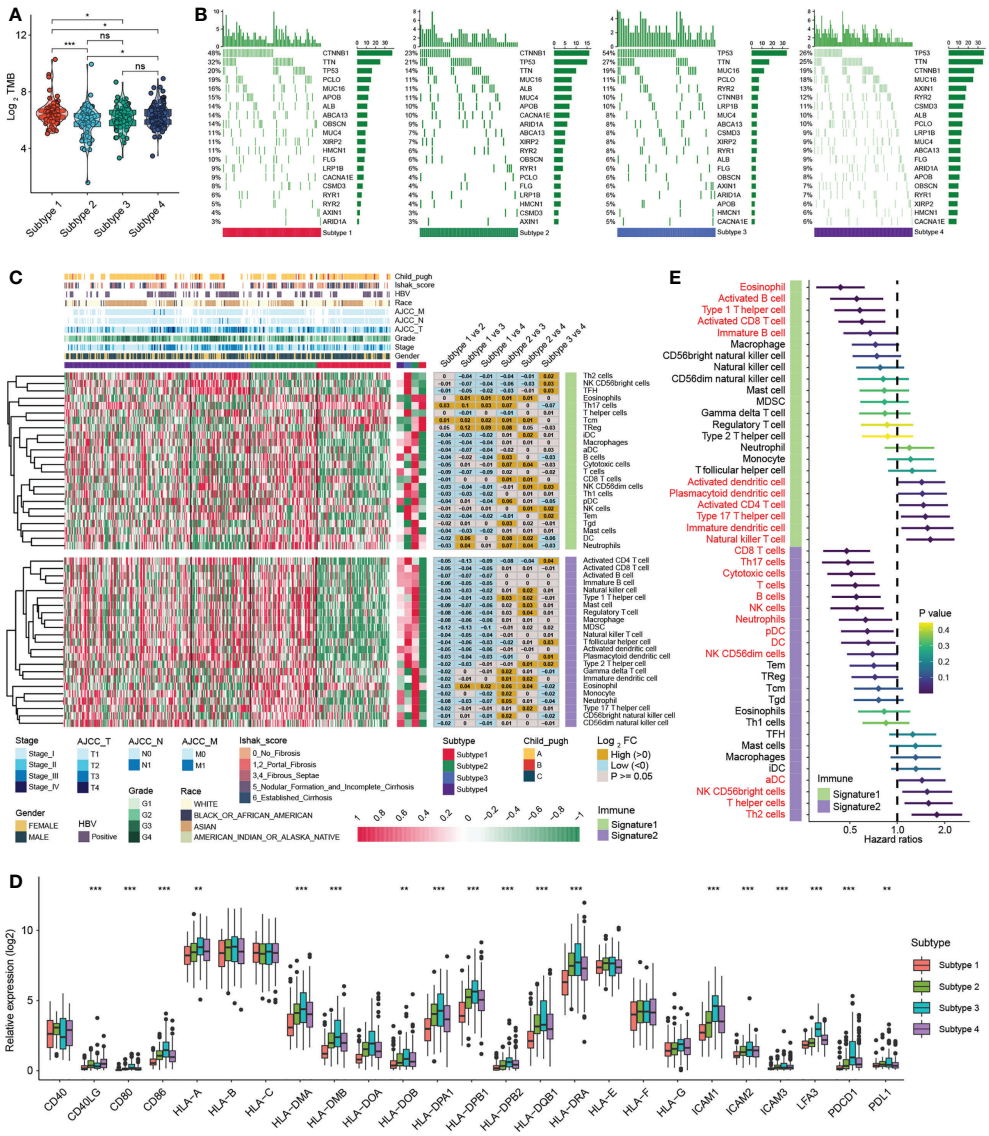

FIGURE 4
Immune infiltration analysis of distinct MDH subtypes in the TCGA-LIHC cohort. **(A)** Tumour mutation burden (TMB) in distinct MDH subtypes of the TCGA-LIHC cohort. **(B)** The gene mutation frequency in distinct MDH subtypes of the TCGA-LIHC cohort. Each column represents individual patients. The upper bar plot shows TMB. The number on the right indicates the mutation frequency in each gene. The right bar plot shows the proportion of each variant type. **(C)** Unsupervised clustering of two previously published immune cell gene signatures in distinct MDH subtypes of the TCGA-LIHC cohort. **(D)** Differences in the expression of MHC molecules, costimulatory molecules and adhesion molecules in distinct MDH subtypes of the TCGA-LIHC cohort. The upper and lower ends of the boxes represent the interquartile range of values. The lines in the boxes represent the median value, and black dots show outliers. The asterisks represent the statistical p-value (**P< 0.01 and ***P< 0.001). **(E)** Survival analyses for two previously published immune cell gene signatures based on the TCGA-LIHC cohort.

score and ferroptosis index of HCC were significantly higher than those of nontumor liver tissues, indicating that tumour stemness and ferroptosis susceptibility in HCC were markedly higher than those of nontumor tissue (Figures S5A, B). Notably, subtype 3 had a higher ferroptosis index than subtypes 1/2/4 (Figure S5A), but the mRNAsi across subtypes could not be completely distinguished (Figure S5B). Combined with previous ESTIMATE scores (Figure S4A), these results indicated that although MDH gene signatures can classify HCC into four subtypes with individual features, there are restrictions in quantifying various known features in HCC. We speculated that each gene in the MDH gene signature has different weights in predicting malignancy and individuality characteristics in HCC. Additionally, the above analysis was only based on the HCC patient population and could not precisely forecast and quantitate the gene expression patterns

of individual patients. Considering the individual heterogeneity and complexity of HCC, we constructed an MDH score based on the PCA-score algorithm to group each HCC patient and provide appropriate clinical guidance (33).

We first confirmed that there were remarkable differences in MDH scores among each subtype: subtype 3> subtype 4> subtype 2> subtype 1 (Figure 5A). We then divided the HCC patients in the TCGA-LIHC database into two groups according to the MDH score to facilitate subsequent analysis (Figure 5B). The patients with high MDH scores were mainly derived from subtype 3/4 HCC, while those with low MDH scores mostly originated from subtype 1/2 HCC (Figure S5C). We found that a high MDH score in HCC was dramatically associated with a high ferroptosis index and mRNAsi score (Figures 5C, D), and the correlation analysis revealed that the MDH score was remarkably positively correlated with the ferroptosis index and mRNAsi score (Figure 5D). We calculated the MDH scores of established TKI-resistant HCC cell lines and HCC TKI-resistant PDX models to further validate our results. The results indicated a significant distinction in the gene transcription profiles between the MDH score groups. Moreover, MDH scores were considerably higher in TKI-resistant HCC than in TKI-sensitive HCC, and MDH scores were significantly positively associated with the ferroptosis index and mRNAsi score (Figures S5D, S5E). Consistently, datasets from the GEO database were utilized to confirm the potential value of MDH scores in discriminating gene expression profiles and predicting TKI responses, the ferroptosis index and the mRNAsi score (Figures S5F, S5G). These results revealed that higher MDH scores in HCC were associated with increased TKI resistance, higher tumour stemness and reduced ferroptosis susceptibility. More importantly, clinical analysis indicated that HCC with a high MDH score was dramatically correlated with a higher histological grade and Ishak score (Figure S5C). Moreover, HCC patients with high MDH scores had markedly worse overall survival outcomes than those with low MDH scores (Figure 5E). The GSVA further implied that P53 signalling, ROS signalling, oxidative phosphorylation, glycolysis, IL2/STAT5 signalling, and DNA repair were remarkably activated in HCC with high MDH scores, while KRAS

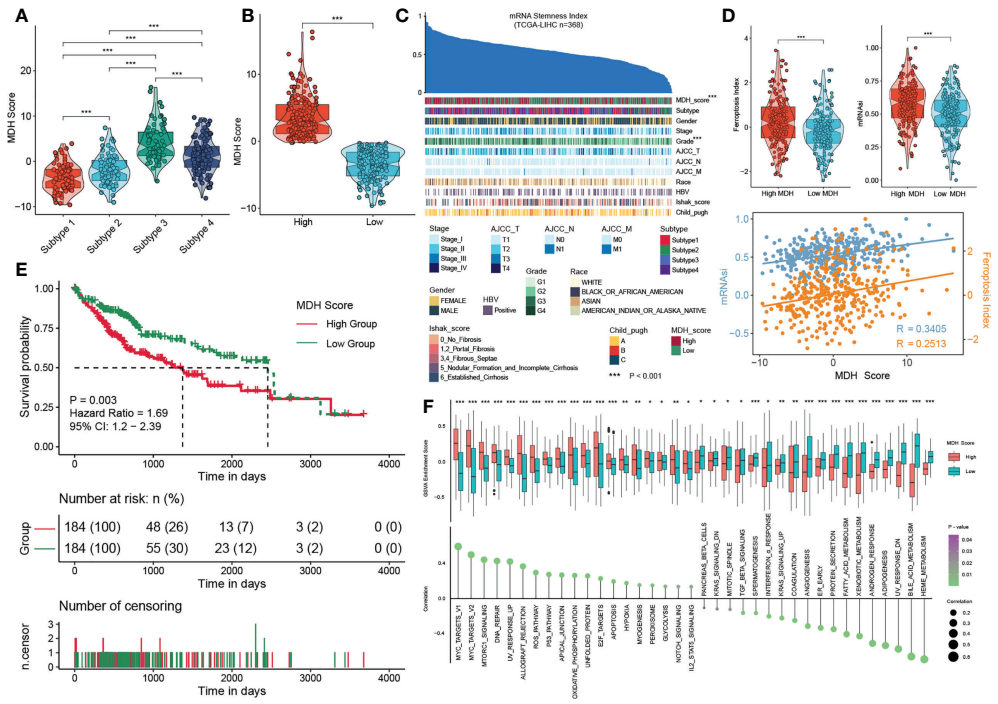

FIGURE 5
Construction of the MDH score. **(A)** MDH score of distinct MDH subtypes in the TCGA-LIHC cohort. **(B)** The TCGA-LIHC cohort was divided into two groups based on median expression values of MDH scores. **(C)** An overview of the association between known clinical features and mRNAsi in patients in the TCGA-LIHC cohort. Columns represent samples sorted by mRNAsi from low to high (top row). Rows represent known clinical and molecular features. **(D)** mRNAsi score and ferroptosis index in the MDH high- or low-score groups of the TCGA-LIHC cohort. Correlation analysis of mRNAsi scores, ferroptosis index and MDH score in patients in the TCGA-LIHC cohort. **(E)** Survival analyses for MDH high- or low-score groups of the TCGA-LIHC cohort. **(F)** GSVA enrichment analysis showing the activation states of biological pathways in the MDH high- or low-score groups. The upper and lower ends of the boxes represent the interquartile range of values. The lines in the boxes represent the median value, and black dots show outliers. The asterisks in A, B, D and F represent the statistical p-value (*P< 0.05; **P< 0.01 and ***P< 0.001).

signalling, angiogenesis, adipogenesis and fatty acid metabolism were inhibited (Figure 5F).

The MDH score predicts the response to immunotherapy in HCC

Next, we evaluated the relationship between MDH scores and immune cell infiltration using the ESTIMATE algorithm (13). No significant distinction was found in stromal cells between the two groups of HCC patients, but both immune cell infiltration and ESTIMATE scores were higher in HCC with high MDH scores than in HCC with low MDH scores (Figure S6A). Notably, MDH scores were markedly positively correlated with CD8 T cell, CD4 T cell, NK cell, B cell, DC and macrophage infiltration but significantly negatively correlated with eosinophil cell infiltration in HCC (Figures S6B, C). However, as previously stated, HCC patients with higher CD8 T cell, B cell and pDC infiltration had a better prognosis than HCC patients with lower CD8 T cell, B cell and pDC levels (Figure 4E), which appears to contradict the true overall survival time of HCC patients. This contradictory actual overall survival outcome implied that patients with high MDH scores may have an immune-excluded phenotype. Supporting insights also included that the expression levels of MHC molecules, costimulatory molecules, and adhesion molecules in high-MDH-score HCC patients were comprehensively elevated (Figures 6A, S6D), and the MDH score was positively correlated with the expression levels of PD1, CD80 and CD86 (Figure 6A).

To further evaluate whether MDH scores could predict immunotherapy response in HCC, we applied the TIDE algorithm to the TCGA-LIHC dataset. Studies have suggested that high TIDE scores are associated with poorer immune checkpoint inhibition treatment efficacy and worse overall survival outcomes in patients treated with anti-PD1 and anti-CTLA4 (27). Importantly, there is a strong positive correlation between MDH scores and TIDE scores (Figure 6B), indicating that HCC patients with high MDH scores respond poorly to immunotherapy. Moreover, our results suggested that MDH scores were positively correlated with CD8 and T cell inflamed (Merck18) levels and negatively correlated with microsatellite steady-state (MSI). We also observed that the MDH score was positively correlated with MDSC and TAM-M2 cell levels. Meanwhile, the MDH score was directly correlated with immune dysfunction and exclusion (Figure 6B), further supporting that HCC with a high MDH score is tightly associated with the immune-excluded phenotype. TIDE analysis of a testing dataset GSE109211 further demonstrated that HCC with a high MDH score, although responsive to sorafenib, was markedly less responsive to immunotherapy (Figure 6C). Correlation analysis also indicated that HCC with a high MDH score contained abundant immunosuppressive cells, including MDSCs and CAFs. Importantly, HCC with a high MDH score was indeed significantly positively correlated with immune dysfunction and exclusion (Figure 6C). These results revealed that HCC patients with a high MDH score had more immune cell infiltration than those with a low MDH score, but most of the cells were immune-escape and immunosuppressive cells; thus, HCC patients with a low MDH score responded better to immunotherapy.

Validation of the MDH score for therapy selection in HCC

To ascertain the validity of the MDH score for immunotherapy evaluation, we utilized the ICGC-LIHC dataset as a test dataset to validate our above results. We first confirmed that low MDH scores exhibited significant clinical benefits and remarkably prolonged survival compared with high MDH scores in HCC (Figure 7A). TIDE scores were then determined for ICGC-LIHC samples, and the results suggested that high MDH scores were indeed associated with high TIDE scores and poorer immune responses in HCC (Figure 7B). Consistent with the TCGA analysis, HCC with high MDH scores had higher proportion of immunosuppressive infiltrating cells, including MDSCs and CAFs (Figure 7B). High MDH scores in ICGC-LIHC samples were also positively correlated with immune exclusion (Figure 7B). Moreover, high MDH scores in ICGC-LIHC samples were markedly positively correlated with high CD8 T cell and B cell levels and negatively correlated with eosinophil cell levels in HCC (Figure S7A), and high MDH scores caused comprehensive elevated expression of MHC molecules, costimulatory molecules, and adhesion molecules in HCC (Figure S7B). Consistent results also included pathway enrichment analysis, with the analysis of ICGC-LIHC samples indicating that high MDH scores were positively correlated with the cell cycle, EMT signalling and DNA replication and adversely correlated with angiogenesis (Figure 7C).

We further investigated whether MDH scores could predict patient response to immune checkpoint blockade therapy based on a published immunotherapy cohort (IMvigor210). As expected, a survival benefit trend was observed in the anti-PD-L1 immunotherapy cohort of patients with low MDH scores (Figure 7D). Moreover, patients with low MDH scores had relatively higher TMB (Figure 7E). Importantly, the clinical response to anti-PD-L1 immunotherapy and prominent therapeutic advantages were validated in patients with low MDH scores compared with patients with high MDH scores (Figures 7F, G). Moreover, patients with high MDH scores exhibited markedly higher expression of PD1, PD-L1, CD80 and CD86, which indicated that an immune-excluded phenotype may also be present in metastatic urothelial carcinoma (Figure S7C). Inconsistent with HCC, high MDH scores in IMvigor210 cohorts were significantly positively

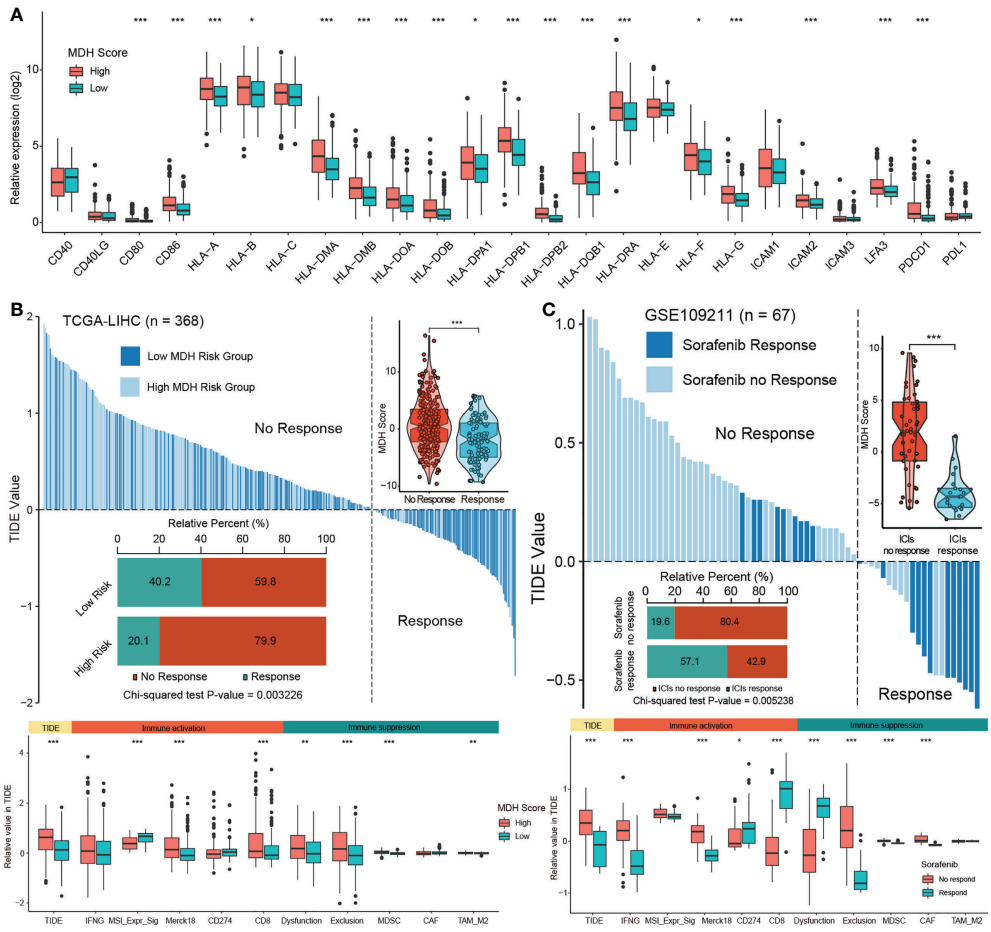

FIGURE 6
The MDH score predicts the immunotherapy response in HCC. **(A)** Differences in the expression of MHC molecules, costimulatory molecules and adhesion molecules in the MDH high- or low-score groups of the TCGA-LIHC cohort. The upper and lower ends of the boxes represent the interquartile range of values. The lines in the boxes represent the median value, and black dots show outliers. **(B)** TIDE value of MDH high- or low-score groups of TCGA-LIHC cohort. **(C)** TIDE values of sorafenib responders and nonresponders in the GSE109211 cohort. The chi-square test was used to calculate significant differences in **(B, C)** The asterisks represent the statistical p-value (*P< 0.05; **P< 0.01 and ***P< 0.001).

correlated not only with CD8 T cells and B cells but also with eosinophil cells and NK cells (Figure S7D). Moreover, GSVA suggested that high MDH scores were positively correlated with EMT signalling, immune checkpoints, angiogenesis and CD8 effectors and negatively correlated with the cell cycle and DNA replication (Figure S7E). These biological differences may be due to tumour origin and heterogeneity.

We further analysed the association between individual genes in MDH gene signatures with MDH scores and prognosis in HCC. We found that 55 genes in the MDH gene signatures were statistically significantly associated with the MDH score, 26 of which were positively correlated and 29 negatively correlated (Figure S8A). Moreover, 35 of the 70 genes could be used individually as prognostic genes for HCC patients, of which 12 genes were prognostic protective factors and 23 genes were adverse prognostic factors (Figure S8B). We further screened 8 hub genes (Figure 7H), three positive correlations and five negative correlations with MDH score and immune checkpoints (Figures 7H, S8C). Consistent correlation analysis results with immune checkpoints were also confirmed using ICGC-LIHC samples (Figure S8D). Importantly, the IHC results of our cohort validated that PD-1 expression was markedly more abundant in TKI-resistant HCC than in TKI-sensitive HCC (Figures 7I, J). We then validated the correlation of three Hub genes with sorafenib resistance using our HCC cohort. A positive correlation between sorafenib resistance and ALYREF protein expression, and a negative correlation between sorafenib resistance and NR3C2 or SORBS2 protein expression was obtained in our HCC cohort (Figures 7I, J), further supporting the relevance of the hub genes to sorafenib resistance in HCC. Furthermore, a positive correlation between PD-1 levels and ALYREF protein

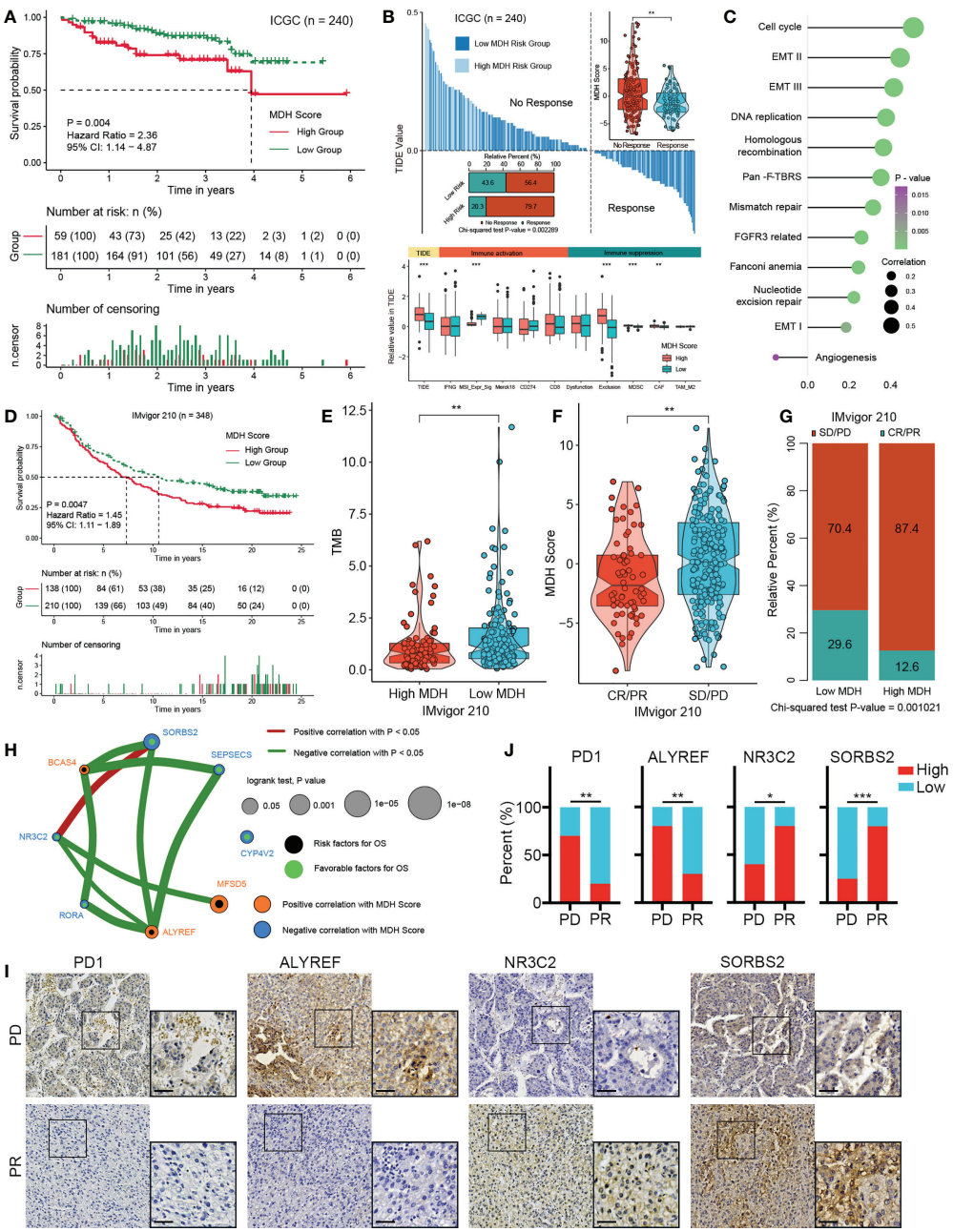

FIGURE 7
Validation of the MDH score for the immunotherapy response in HCC. **(A)** Survival analyses for MDH high- or low-score groups of the ICGC-LIHC cohort. **(B)** TIDE value of MDH high- or low-score groups in the ICGC-LIHC cohort. The chi-square test was used to calculate significant differences. **(C)** Differences expression of known signatures, including stromal activation-related signatures, tumour promotion-related signatures and immune activation-related signatures, in the MDH high- or low-score groups of the ICGC-LIHC cohort. **(D)** Survival analyses for MDH high- or low-score groups of the IMvigor210 cohort. **(E)** TMB score in the MDH high- or low-score groups of the IMvigor210 cohort. **(F)** MDH score in complete response/partial response (CR/PR) patients and stable disease/progressive disease (SD/PD) patients in the IMvigor210 cohort. **(G)** Correlation analysis of the MDH score with TKI response in the IMvigor210 cohort. The chi-square test was used to calculate significant differences. **(H)** The interaction between 8 hub genes in the MDH gene signatures of the TCGA-LIHC cohort. **(I)** Representative IHC images of PD1, ALYREF, NR3C2 and SORBS2 staining in sorafenib sensitive- and resistant- groups from our HCC cohort. Scale bar denotes 40 μm. **(J)** Correlation analysis of sorafenib sensitivity and the expression of specified proteins. The asterisks in B, E, F and J represent the statistical p-value (*P< 0.05; **P< 0.01 and ***P< 0.001).

expression and a negative correlation between PD-1 levels and NR3C2 or SORBS2 protein expression were obtained in our HCC cohort (Figure S8E).

Construction of a nomogram predicting OS in HCC based on a simplified MDH risk score

To further simplify the MDH score and facilitate the clinical application of MDH scores, we applied an iterative LASSO Cox regression model (28). A 4-gene MDH risk score (Figures 8A, S9A) then was obtained, MDH Risk score=0.19961×ATAD3A +0.19332×CHAF1B-0.07906×ADH4-0.18327×PPARGC1A. Using TCGA-LIHC data, we confirmed that the MDH risk score can be used as an alternative diagnostic predictor of the MDH score, with an AUC of 0.659 (Figure S9B), and that it could also be used as a prognostic predictor for HCC (Figure S9C). Moreover, using the Human Protein Atlas, we confirmed that HCC with a high MDH risk score had significantly higher protein levels of ATAD3A and CHAF1B and relatively lower protein levels of ADH4 (Figure 8B), but PPARGC1A was not found on the website. Importantly, the correlation between the MDH score and MDH risk score was 0.68, indicating that the MDH risk score could replace the MDH score in clinical application (Figure S9D). Univariate and multivariate analyses were performed on the four

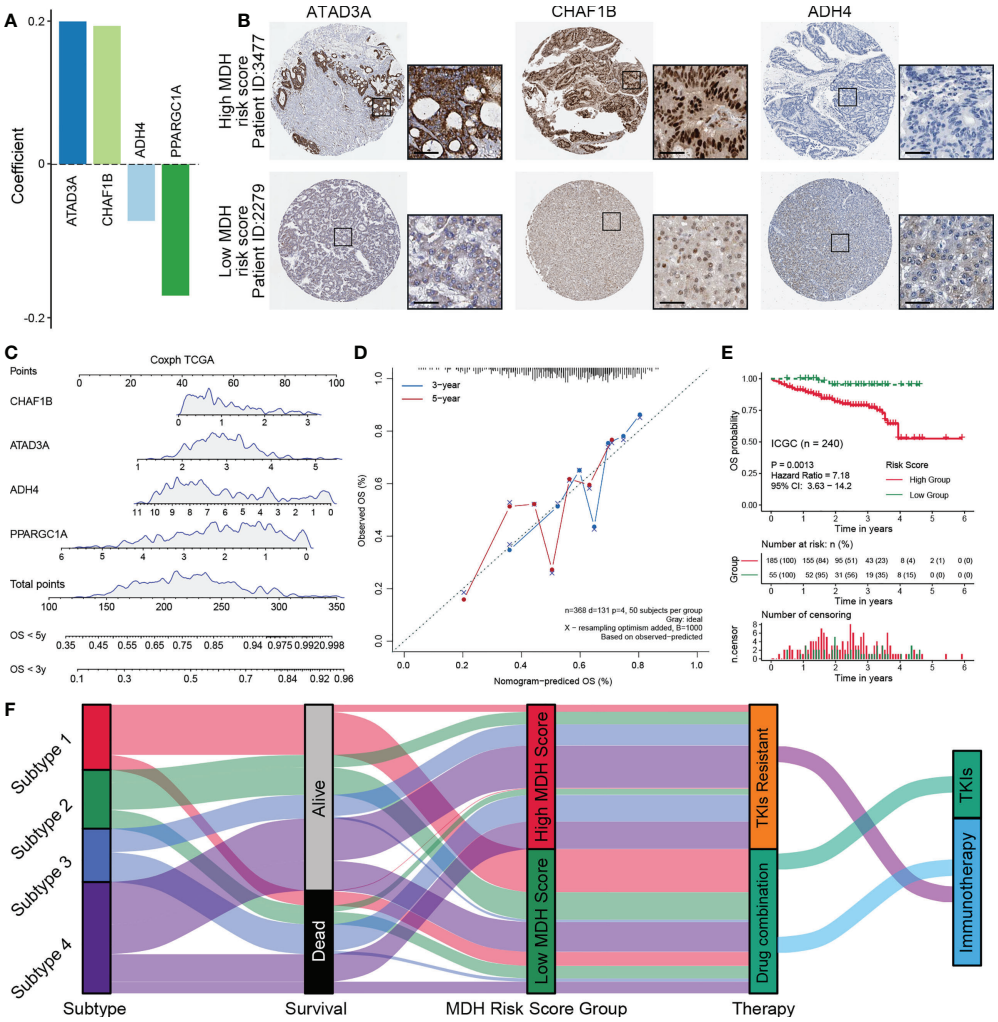

FIGURE 8
Construction of a nomogram predicting OS outcomes based on the MDH risk score in the TCGA-LIHC cohort. **(A)** Coefficients of 4 genes involved in the prognostic signatures. **(B)** Representative IHC images of ATAD3A, CHAF1B and ADH4 in MDH high- or low-score groups from the Human Protein Atlas. Scale bar denotes 50 μm. **(C)** Nomogram to predict the 3-y and 5-y overall survival of HCC patients. **(D)** Calibration curve for the comprehensive survival nomogram model in the TCGA-LIHC cohort. The dashed diagonal line represents the ideal situation, and the blue and red lines represent the 3-y and 5-y observed nomograms, respectively. **(E)** Survival analysis for the MDH risk score in the ICGC cohort. **(F)** Alluvial diagram showing the association of the MDH subtype with patient survival status, MDH score and individualized therapy.

genes, and a nomogram capable of predicting the 3- or 5-year survival probability and mortality risk of HCC patients was finally constructed (Figures 8C, S9E). The calibration curves at 3 and 5 years indicated good consistency between the prediction by the nomogram and actual overall survival outcomes (Figure 8D). We further calculated the MDH risk score for each HCC patient in the ICGC-LIHC dataset and compared the survival difference between the high MDH risk group and the low MDH risk group. Importantly, the results suggest that the MDH risk score can better predict the overall prognosis of HCC patients than the MDH score (Figures 8E, 7A), which further proves the clinical value of the MDH risk score in predicting the outcome of HCC patients.

Discussion

Immune checkpoint inhibition has revolutionized the cancer therapy paradigm, but effective durable responses are still observed in only a minority of patients, sometimes with severe side effects (34). Although the TKI resistance mechanisms in HCC have been extensively explored, comprehensive analysis based on the transcriptomic data of TKI-resistant HCC remains lacking. Comprehensive analysis of RNA transcripts greatly contributes to tissue deconstruction, provides a clear understanding of transcriptome-specific variations across various HCC subtypes and treatment responses, elucidates the mechanisms of therapeutic resistance to TKIs and immunotherapies and identifies novel therapeutic strategies.

Unlike previous reports, the MDH subtypes presented in our study were segregated into clusters defined by distinct signalling pathways and unique immune cell compositions. These MDH subtypes facilitated the interpretation of the underlying mechanisms of TKI resistance in HCC and revealed the intrinsic connections of the tumour immune microenvironment described among each subtype. Previous studies have revealed that the biological processes, stroma, and immunological activities of the immune microenvironment in various cancers are remarkably similar (35). Notably, four MDH subtypes could also be classified into four immunological subtypes with markedly distinct immune cell infiltration characteristics. Moreover, the observed MDH subtypes share multiple similarities with immune clusters identified in previous studies, reflecting or expanding those patterns. The stromal components and cytokines classified subtype 1 as an immune desert. Notably, the prognosis of subtype 1 was relatively good compared to subtype 2/3/4, which may be associated with marked suppression of oncogenic signalling pathways and effective response to TKIs in subtype 1 of HCC. In addition, subtypes 2/3/4 all had abundant immune cell infiltration and cytokine expression, which were strikingly separated by stromal activation level, immunosuppressive profile and mutational burden. Subtype 4 exhibits a consistent immune-activated phenotype accompanied by massive immune cell infiltration. However, subtype 3 clearly displayed a similar pattern to the immune-excluded phenotype, with marked stromal cell infiltration and activation and the worst prognosis in HCC patients. Subtype 2 showed similarities to the immune-enriched subtype but also had an angiogenic, fibrotic phenotype and was therefore classified as at the borderline between immune-activated and immune-excluded. The overall survival of HCC patients also reflects that the prognosis of subtype 4 is inferior to that of subtype 2. Our proposed MDH typing differs from previous ideas of cancer immunograms or cancer-immune set points, providing new insights for drug selection and mechanism exploration in HCC.

Immune checkpoint therapy is currently only recommended as the first-line treatment for HCC in clinical practice (36), but individualized advice is not explicitly proposed. Precision therapy can remarkably improve patient outcomes (37); thus, *a priori* identification of responders is urgently needed. Here, we further proposed an MDH score to predict the response to immunotherapy. Our study revealed that immune cell infiltration was more abundant in HCC with high MDH scores, and a high MDH score was significantly positively correlated with high expression of PD1, PDL1, CD80 and CD86. However, HCC with high MDH scores responded poorly to immune checkpoint blockade, which was mainly associated with the infiltration of stromal cells. Therefore, immune checkpoint blockade with concomitant inhibition of stromal cell activity or stromal signalling may be a beneficial therapeutic strategy for HCC patients with high MDH scores. Additionally, transcriptome profiling and clinical validation suggested that HCC patients with low MDH scores could benefit from TKIs and immunotherapy. Notably, patients with low MDH scores mostly had subtype 1, with an immune desert phenotype, suggesting that immune cell infiltration is not the only reference factor affecting the immune response and patient prognosis. Our results suggest that the TMB of subtype 1 was significantly higher than that of other subtypes, while stromal cell infiltration was significantly lower than that of other subtypes. Meanwhile, patients with low MDH scores also presented with higher eosinophilic infiltration and microsatellite instability. These results indicate that a comprehensive assessment of various markers, rather than individual factors or cells, would more accurately reflect the complexity and dynamics of the immune microenvironment and better describe its prognosis. Our proposed MDH score for predicting the efficacy of immunotherapy has been validated with different datasets and our HCC patient samples, which also indicates that our MDH score is superior in partial predictive performance to assessing tumor immunotherapy response based only on a single index.

Although multiomics studies have become more accessible and widespread over the past decade (38, 39), clinical tools that can be applied to medication decision-making for HCC patients

are still lacking. To address this demand, we constructed an MDH risk score and nomogram using an iterative LASSO Cox regression model, which greatly reduces clinical effort, simplifies the prediction process and is worthy of large-scale clinical application. More importantly, MDH risk scores retain the predictive abilities of the MDH score, providing a global summary of all potential targetable alterations and mechanisms for characterizing each HCC, further providing a simple and reasonable selection for personalized treatment. However, our study also has certain limitations. Since immunotherapy has only been applied to the systemic treatment of HCC in the past two years, we did not have enough HCC samples to verify the validity of the MDH score in predicting response to immunotherapy. Thus, we only applied a public dataset containing clinical outcomes of immunotherapy for validation and analyzed the correlation of huh genes using our HCC samples. Next, we will conduct prospective clinical trials to further explore the clinical significance of MDH score and MDH risk score.

Conclusions

In conclusion, as shown in Figures 1A, 8F, this study proposed a new subtyping model for HCC and deeply investigated the underlying mechanisms of TKI resistance and the cellular infiltration characteristics of the tumour microenvironment. The MDH score might help to evaluate individualized therapy and overall survival outcomes for HCC patients, providing important clinical guidance for medication decision-making for HCC patients.

Data availability statement

The data presented in the study are deposited in the GEO repository, accession number GSE213615.

Ethics statement

This clinical sample study was approved by the Ethics Committee on Biomedical Research, West China Hospital of Sichuan University. The patients/participants provided their written informed consent to participate in this study. Animals received humane care, and the Institutional Animal Care and Use Committee (IACUC) approved all animal experiments.

Author contributions

JYY, YS and LY designed the project, analyzed results and interpreted data. ZL and JSY performed the bioinformatics analysis and wrote the manuscript. ZW provided experimental assistance. JYY, YS and LY supervised the project. All authors read and approved the final manuscript.

Funding

This work was supported by grants from the National Natural Science Foundation of China (no. 82070674), the Sichuan Province Science and Technology Department Project (no. 2019YFG0036), the 1.3.5 Project for Disciplines of Excellence, West China Hospital, Sichuan University (no. ZY2017308).

Conflict of interest

The authors declare that the research was conducted in the absence of any commercial or financial relationships that could be construed as a potential conflict of interest.

Publisher's note

All claims expressed in this article are solely those of the authors and do not necessarily represent those of their affiliated organizations, or those of the publisher, the editors and the reviewers. Any product that may be evaluated in this article, or claim that may be made by its manufacturer, is not guaranteed or endorsed by the publisher.

Supplementary material

The Supplementary Material for this article can be found online at: https://www.frontiersin.org/articles/10.3389/fimmu.2022.990571/full#supplementary-material

References

1. Sung H, Ferlay J, Siegel RL, Laversanne M, Soerjomataram I, Jemal A, et al. Global cancer statistics 2020: GLOBOCAN estimates of incidence and mortality worldwide for 36 cancers in 185 countries. *CA. Cancer J Clin* (2021) 71(3):209–49. doi: 10.3322/caac.21660

2. Akce M, El-Rayes BF, Bekaii-Saab TS. Frontline therapy for advanced hepatocellular carcinoma: an update. *Therap. Adv Gastroenterol* (2022) 15:1–12. doi: 10.1177/17562848221086126

3. Reig M, Forner A, Rimola J, Ferrer-Fàbrega J, Burrel M, Garcia-Criado Á, et al. BCLC strategy for prognosis prediction and treatment recommendation: The 2022 update. *J Hepatol* (2022) 76(3):681–93. doi: 10.1016/j.jhep.2021.11.018

4. Zhang CH, Li M, Lin YP, Gao Q. Systemic therapy for hepatocellular carcinoma: Advances and hopes. *Curr Gene Ther* (2020) 20(2):84–99. doi: 10.2174/1566523220666200628014530

5. Llovet JM, Ricci S, Mazzaferro V, Hilgard P, Gane E, Blanc JF, et al. Sorafenib in advanced hepatocellular carcinoma. *N Engl J Med* (2008) 359(4):378–90. doi: 10.1056/NEJMoa0708857

6. Awosika J, Sohal D. A narrative review of systemic treatment options for hepatocellular carcinoma: state of the art review. *J Gastrointest Oncol* (2022) 13 (1):426–37. doi: 10.21037/jgo-21-274

7. Cheng AL, Hsu C, Chan SL, Choo SP, Kudo M. Challenges of combination therapy with immune checkpoint inhibitors for hepatocellular carcinoma. *J Hepatol* (2020) 72(2):307–19. doi: 10.1016/j.jhep.2019.09.025

8. Schneider BP, Jiang G, Ballinger TJ, Shen F, Chitambar C, Nanda R, et al. BRE12-158: A postneoadjuvant, randomized phase II trial of personalized therapy versus treatment of physician's choice for patients with residual triple-negative breast cancer. *J Clin Oncol* (2022) 40(4):345–55. doi: 10.1200/JCO.21.01657

9. Chalmers ZR, Connelly CF, Fabrizio D, Gay L, Ali SM, Ennis R, et al. Analysis of 100,000 human cancer genomes reveals the landscape of tumor mutational burden. *Genome Med* (2017) 9(1):34. doi: 10.1186/s13073-017-0424-2

10. Malta TM, Sokolov A, Gentles AJ, Burzykowski T, Poisson L, Weinstein JN, et al. Machine learning identifies stemness features associated with oncogenic dedifferentiation. *Cell* (2018) 173(2):338–54. doi: 10.1016/j.cell.2018.03.034

11. Liu Z, Zhao Q, Zuo ZX, Yuan SQ, Yu K, Zhang Q, et al. Systematic analysis of the aberrances and functional implications of ferroptosis in cancer. *iScience* (2020) 23(7):101302. doi: 10.1016/j.isci.2020.101302

12. Bindea G, Mlecnik B, Tosolini M, Kirilovsky A, Waldner M, Obenauf AC, et al. Spatiotemporal dynamics of intratumoral immune cells reveal the immune landscape in human cancer. *Immunity* (2013) 39(4):782–95. doi: 10.1016/j.immuni.2013.10.003

13. Yoshihara K, Shahmoradgoli M, Martínez E, Vegesna R, Kim H, Torres-Garcia W, et al. Inferring tumour purity and stromal and immune cell admixture from expression data. *Nat Commun* (2013) 4:2612. doi: 10.1038/ncomms3612

14. Pipis M, Rossor AM, Laura M, Reilly MM. Next-generation sequencing in charcot-Marie-Tooth disease: opportunities and challenges. *Nat Rev Neurol* (2019) 15(11):644–56. doi: 10.1038/s41582-019-0254-5

15. Chen L, Heikkinen L, Wang C, Yang Y, Sun H, Wong G. Trends in the development of miRNA bioinformatics tools. *Brief Bioinform* (2019) 20(5):1836–52. doi: 10.1093/bib/bby054

16. Bukowski K, Kciuk M, Kontek R. Mechanisms of multidrug resistance in cancer chemotherapy. *Int J Mol Sci* (2020) 21(9):3233. doi: 10.3390/ijms21093233

17. Llovet JM, Lencioni R. mRECIST for HCC: Performance and novel refinements. *J Hepatol* (2020) 72(2):288–306. doi: 10.1016/j.jhep.2019.09.026

18. Yuan J, Yin Z, Tan L, Zhu W, Tao K, Wang G, et al. Interferon regulatory factor-1 reverses chemoresistance by downregulating the expression of p-glycoprotein in gastric cancer. *Cancer Lett* (2019) 457:28–39. doi: 10.1016/j.canlet.2019.05.006

19. Okada S, Vaeteewoottacharn K, Kariya R. Application of highly immunocompromised mice for the establishment of patient-derived xenograft (PDX) models. *Cells* (2019) 8(8):889. doi: 10.3390/cells8080889

20. Tan L, Yuan J, Zhu W, Tao K, Wang G, Gao J. Interferon regulatory factor-1 suppresses DNA damage response and reverses chemotherapy resistance by downregulating the expression of RAD51 in gastric cancer. *Am J Cancer Res* (2020) 10(4):1255–70.

21. Sherman BT, Hao M, Qiu J, Jiao X, Baseler MW, Lane HC, et al. DAVID: a web server for functional enrichment analysis and functional annotation of gene lists (2021 update). *Nucleic Acids Res* (2022) 50(W1):W216–21. doi: 10.1093/nar/gkac194

22. Subramanian A, Tamayo P, Mootha VK, Mukherjee S, Ebert BL, Gillette MA, et al. Gene set enrichment analysis: a knowledge-based approach for interpreting genome-wide expression profiles. *Proc Natl Acad Sci USA* (2005) 102(43):15545–50. doi: 10.1073/pnas.0506580102

23. Hänzelmann S, Castelo R, Guinney J. GSVA: gene set variation analysis for microarray and RNA-seq data. *BMC Bioinf* (2013) 14:7. doi: 10.1186/1471-2105-14-7

24. Mariathasan S, Turley SJ, Nickles D, Castiglioni A, Yuen K, Wang Y, et al. TGFβ attenuates tumour response to PD-L1 blockade by contributing to exclusion of T cells. *Nature* (2018) 554(7693):544–8. doi: 10.1038/nature25501

25. Charoentong P, Finotello F, Angelova M, Mayer C, Efremova M, Rieder D, et al. Pan-cancer immunogenomic analyses reveal genotype-immunophenotype relationships and predictors of response to checkpoint blockade. *Cell Rep* (2017) 18 (1):248–62. doi: 10.1016/j.celrep.2016.12.019

26. Ben Salem K, Ben Abdelaziz A. Principal component analysis (PCA). *Tunis Med* (2021) 99(4):383–9.

27. Jiang P, Gu S, Pan D, Fu J, Sahu A, Hu X, et al. Signatures of T cell dysfunction and exclusion predict cancer immunotherapy response. *Nat Med* (2018) 24(10):1550–8. doi: 10.1038/s41591-018-0136-1

28. Zhao Z, Liu H, Zhou X, Fang D, Ou X, Ye J, et al. Necroptosis-related lncRNAs: Predicting prognosis and the distinction between the cold and hot tumors in gastric cancer. *J Oncol* (2021) 2021:6718443. doi: 10.1155/2021/6718443

29. Sangro B, Sarobe P, Hervás-Stubbs S, Melero I. Advances in immunotherapy for hepatocellular carcinoma. *Nat Rev Gastroenterol Hepatol* (2021) 18(8):525–43. doi: 10.1038/s41575-021-00438-0

30. Samstein RM, Lee CH, Shoushtari AN, Hellmann MD, Shen R, Janjigian YY, et al. Tumor mutational load predicts survival after immunotherapy across multiple cancer types. *Nat Genet* (2019) 51(2):202–6. doi: 10.1038/s41588-018-0312-8

31. Chen DS, Mellman I. Elements of cancer immunity and the cancer-immune set point. *Nature* (2017) 541:321–30. doi: 10.1038/nature21349

32. Gajewski TF, Woo SR, Zha Y, Spaapen R, Zheng Y, Corrales L, et al. Cancer immunotherapy strategies based on overcoming barriers within the tumor microenvironment. *Curr Opin Immunol* (2013) 25:268–76. doi: 10.1016/j.coi.2013.02.009

33. Yao HY, Tseng KW, Nguyen HT, Kuo CT, Wang HC. Hyperspectral ophthalmoscope images for the diagnosis of diabetic retinopathy stage. *J Clin Med* (2020) 9(6):1613. doi: 10.3390/jcm9061613

34. Khan M, Arooj S, Wang H. NK cell-based immune checkpoint inhibition. *Front Immunol* (2020) 11:167. doi: 10.3389/fimmu.2020.00167

35. Lei X, Lei Y, Li JK, Du WX, Li RG, Yang J, et al. Immune cells within the tumor microenvironment: Biological functions and roles in cancer immunotherapy. *Cancer Lett* (2020) 470:126–33. doi: 10.1016/j.canlet.2019.11.009

36. Xu F, Jin T, Zhu Y, Dai C. Immune checkpoint therapy in liver cancer. *J Exp Clin Cancer Res* (2018) 37(1):110. doi: 10.1186/s13046-018-0777-4

37. Dutta AK, Alberge JB, Sklavenitis-Pistofidis R, Lightbody ED, Getz G, Ghobrial IM. Single-cell profiling of tumour evolution in multiple myeloma - opportunities for precision medicine. *Nat Rev Clin Oncol* (2022) 19(4):223–36. doi: 10.1038/s41571-021-00593-y

38. Bagaev A, Kotlov N, Nomie K, Svekolkin V, Gafurov A, Isaeva O, et al. Conserved pan-cancer microenvironment subtypes predict response to immunotherapy. *Cancer Cell* (2021) 39(6):845–65. doi: 10.1016/j.ccell.2021.04.014

39. Liu Z, Liu Y, Qian L, Jiang S, Gai X, Ye S, et al. A proteomic and phosphoproteomic landscape of KRAS mutant cancers identifies combination therapies. *Mol Cell* (2021) 81(19):4076–90. doi: 10.1016/j.molcel.2021.07.021

frontiers | Frontiers in Immunology

TYPE Original Research
PUBLISHED 17 October 2022
DOI 10.3389/fimmu.2022.982628

Check for updates

OPEN ACCESS

EDITED BY
Linlang Guo,
Zhujiang Hospital, China

REVIEWED BY
Marxa L. Figueiredo,
Purdue University, United States
Jiaming Wen,
Zhejiang University, China
Jian Zhang,
Southern University of Science and Technology, China

*CORRESPONDENCE
Renjun Peng
prjscience@csu.edu.cn
Nan Zhang
awekevin@onethird-lab.com

†These authors have contributed equally to this work and share first authorship

SPECIALTY SECTION
This article was submitted to Cancer Immunity and Immunotherapy, a section of the journal Frontiers in Immunology

RECEIVED 30 June 2022
ACCEPTED 05 September 2022
PUBLISHED 17 October 2022

CITATION
Li H, Gu J, Tian Y, Li S, Zhang H, Dai Z, Wang Z, Zhang N and Peng R (2022) A prognostic signature consisting of metabolism-related genes and SLC17A4 serves as a potential biomarker of immunotherapeutic prediction in prostate cancer. *Front. Immunol.* 13:982628. doi: 10.3389/fimmu.2022.982628

COPYRIGHT
© 2022 Li, Gu, Tian, Li, Zhang, Dai, Wang, Zhang and Peng. This is an open-access article distributed under the terms of the Creative Commons Attribution License (CC BY). The use, distribution or reproduction in other forums is permitted, provided the original author(s) and the copyright owner(s) are credited and that the original publication in this journal is cited, in accordance with accepted academic practice. No use, distribution or reproduction is permitted which does not comply with these terms.

A prognostic signature consisting of metabolism-related genes and SLC17A4 serves as a potential biomarker of immunotherapeutic prediction in prostate cancer

He Li[1†], Jie Gu[2,3,4†], Yuqiu Tian[5], Shuyu Li[6], Hao Zhang[7], Ziyu Dai[7], Zeyu Wang[7], Nan Zhang[7,8*] and Renjun Peng[7*]

[1]The Animal Laboratory Center, Hunan Cancer Hospital and The Affiliated Cancer Hospital of Xiangya School of Medicine, Central South University, Changsha, Hunan, China, [2]Department of Geriatric Urology, Xiangya International Medical Center, Xiangya Hospital, Central South University, Changsha, Hunan, China, [3]National Clinical Research Center for Geriatric Disorders, Xiangya Hospital, Central South University, Changsha, China, [4]Martini-Klinik Prostate Cancer Center, University Hospital Hamburg-Eppendorf, Hamburg, Germany, [5]Department of Infectious Disease, Zhuzhou Central Hospital, Zhuzhou, Hunan, China, [6]Department of Thyroid and Breast Surgery, Tongji Hospital, Tongji Medical College of Huazhong University of Science and Technology, Wuhan, Hubei, China, [7]Department of Neurosurgery, Xiangya Hospital, Central South University, Changsha, Hunan, China, [8]One-Third Lab, College of Bioinformatics Science and Technology, Harbin Medical University, Harbin, Hei Longjiang, China

Background: Prostate cancer (PCa), a prevalent malignant cancer in males worldwide, screening for patients might benefit more from immuno-/chemo-therapy remained inadequate and challenging due to the heterogeneity of PCa patients. Thus, the study aimed to explore the metabolic (Meta) characteristics and develop a metabolism-based signature to predict the prognosis and immuno-/chemo-therapy response for PCa patients.

Methods: Differentially expressed genes were screened among 2577 metabolism-associated genes. Univariate Cox analysis and random forest algorithms was used for features screening. Multivariate Cox regression analysis was conducted to construct a prognostic Meta-model based on all combinations of metabolism-related features. Then the correlation between MetaScore and tumor was deeply explored from prognostic, genomic variant, functional and immunological perspectives, and chemo-/immuno-therapy response. Multiple algorithms were applied to estimate the immunotherapeutic responses of two MeteScore groups. Further *in vitro* functional experiments were performed using PCa cells to validate the association between the expression of hub gene SLC17A4 which is one of the model component genes and tumor progression. GDSC database was employed to determine the sensitivity of chemotherapy drugs.

Results: Two metabolism-related clusters presented different features in overall survival (OS). A metabolic model was developed weighted by the estimated regression coefficients in the multivariate Cox regression analysis

(0.5154*GAS2 + 0.395*SLC17A4 - 0.1211*NTM + 0.2939*GC). This MetaScoring system highlights the relationship between the metabolic profiles and genomic alterations, gene pathways, functional annotation, and tumor microenvironment including stromal, immune cells, and immune checkpoint in PCa. Low MetaScore is correlated with increased mutation burden and microsatellite instability, indicating a superior response to immunotherapy. Several medications that might improve patients` prognosis in the MetaScore group were identified. Additionally, our cellular experiments suggested knockdown of SLC17A4 contributes to inhibiting invasion, colony formation, and proliferation in PCa cells *in vitro*.

Conclusions: Our study supports the metabolism-based four-gene signature as a novel and robust model for predicting prognosis, and chemo-/immunotherapy response in PCa patients. The potential mechanisms for metabolism-associated genes in PCa oncogenesis and progression were further determined.

KEYWORDS

prostate cancer, metabolism, prognostic model, immuno-/chemotherapy response, immune infiltration

Introduction

Prostate cancer (PCa) accounts for one of the most prevalent malignancies among males worldwide and ranks the second highest cause of elderly male tumor-related deaths (1, 2). Most patients with localized PCa receive standard therapy including androgen deprivation therapy, radical prostatectomy or radiotherapy, which leads to favorable cancer control (3, 4). However, approximately 20-30% of patients will develop a castration-resistant or biochemical recurrence (BCR), and such patients are more likely to suffer metastases and cancer-specific mortality (5). Therefore, exploring the tumor biomarker model that can classify the subtypes of PCa and predictively determines efficacious risk signatures remains crucial. Over the past few decades, clinical-stage, prostate-specific antigens (PSA) and Gleason scores were mainly employed to diagnose and monitor the prognosis of PCa patients (6, 7). These clinic pathological parameters do not possess favorable specificity and sensitivity in assessing the prognosis of PCa patients (8, 9). Particularly, PSA has undergone some discredit for it might bring overdiagnosis and overtreatment in adequately treated patients through active surveillance (9). In this aspect, better informative biomarkers are desperately required to evaluate the increased risk of overall survival (OS).

PCa exhibits distinct statuses of metabolism from normal tissues thereby supplying a novel approach to distinguish tumors *via* metabolic differences. Recent research interpreted that specific metabolisms are closely associated with PCa, for instance, citrate, lipid and choline (10). A study reported urea cycle metabolites increased in PCa utilizing capillary electrophoresis and mass spectrometry (11). Studies demonstrated that PCa cells consume large amounts of glucose during the metastatic stage (12, 13) and highly glycolytic metabolism PCa patients showed a poor prognosis (14). In addition, activation of glycolysis leads to increased generation of lactic acid that facilitates several tumor-accelerating procedures, such as stemness properties, cancer invasion and metastasis, angiogenesis, inhibition of antitumor immune response, and hypoxia resistance (15, 16). However, the correlation between the metabolism gene signature and OS of PCa is yet poorly defined. An understanding of the cellular metabolism of PCa is essential in the prediction of prognosis and development of potential metabolically targeted treatments.

Here, we developed a metabolism-based four-gene model for predicting prognosis and chemo-/immuno-therapy response utilizing The Cancer Genome Atlas (TCGA-PRAD) and Gene Expression Omnibus (GEO) dataset (GSE16560). Furthermore, we performed cellular experiments to explore the correlation between the SLC17A4 expression and the *in vitro* proliferation and invasion phenotype of PCa cells.

Materials and methods

Data collection and preprocessing

We collected PCa gene expression data from several publicly available databases. A total of 777 samples from PCa patients were

enrolled in the study: 496 from TCGA-PRAD (training cohort) and 281 from GSE16560 (validation cohort). The clinical and RNA-sequencing (RNA-seq) data were obtained from The Cancer Genome Atlas (TCGA, http://cancergenome.nih.gov). The GSE16560 datasets were derived from the Gene Expression Omnibus (GEO, https://www.ncbi.nlm.nih.gov/geo/).

Identification of PCa MetaCluster

A published list of 2577 metabolism-associated genes was acquired for subsequent clustering (17). Univariate Cox was employed to filter the candidate genes ($p< 0.01$) and 46 candidate metabolic genes were screened for clustering in the TCGA-PRAD cohort. PCa patients with distinct metabolic gene profiles were stratified utilizing k-means algorithm, which confirmed metabolic-associated patterns and classified patients for further evaluation using the R "ConsensusClusterPlus" package (18). Afterward, the correlation between the MetaCluster and the collected 114 metabolic pathways was calculated (19).

Establishment of metabolic gene signature

The R "limma" package was adopted to identify differentially expressed genes $|(\log FC)| > \log2(1.5)$ & $P < 0.05$ was selected for analysis (20). Subsequently, univariate Cox regression was performed to determine prognostic MetaGenes ($P< 0.01$). We then applied random survival forest algorithm through the R "randomForestSRC" package to screen out the more valuable MetaGenes with prognostic potential (variable relative importance> 0.3) (21). The metabolic gene signature was constructed based on all different combinations of prognostic MetaGenes and weighted by their estimated regression coefficients in multivariate Cox regression analysis. The final metabolic gene signature named MetaScore was identified with the highest 5 years-area under the curve (AUC). The classification was conducted with model-based hierarchical agglomerative clustering based on the Gaussian finite mixture model (GMM) (22).

Validating the accuracy of the MetaScore

The MetaScore of the 496 PCa patients in the TCGA-PRAD dataset was estimated, and then we stratified the PCa patients into high- and low-MetaScore groups according to the best cutoff. The Kaplan-Meier curve analyzed the associations between OS and MetaScore. TimeROC was employed to verify the efficiency and accuracy of the prognosis predictions of MetaScore for 1-, 3- and 5-year. Univariate and multivariate cox regression analysis was employed on the MetaScore and individual clinical variables including age and tumor stage of patients (T and N).

Analysis of pathway enrichment and functional annotation

Gene Ontology (GO) and Kyoto Encyclopedia of Genes and Genomes (KEGG) related gene sets were obtained from the MSigDB (23). Gene set enrichment analysis (GSEA) was conducted using the R "clusterProfiler" package (24) and gene set variation analysis (GSVA) was performed through the R "GSVA" package (25).

Genomic alteration characteristics

We utilized GISTIC 2.0 (http://www.broadinstitute.org/cancer/software/genepattern) to explore the somatic copy number alternations (SCNAs) in PCa based on TCGA-PRAD. Patients were categorized into low- and high-MetaScore groups. The specific genomic enrichment, copy number alternations (CNAs), and the threshold copy number (CN) at alteration peaks related to MetaScore were detected. We used "maftools" R package for the analysis of somatic mutations. Subsequently, tumor mutation burden (TMB) (26) was calculated based on the TGCA-cohort somatic mutations to evaluate the mutation status between different MetaScore groups.

Estimation of immune infiltration and immune checkpoint

R "IOBR" package was used for immune infiltration assessment (27). CIBERSORT algorithm (28), MCPcounter algorithm (29), ssGSEA algorithm (30), and TIMER algorithm (31) were employed to evaluate the relative fraction of the immune cell in the TCGA-PRAD cohort. ESTIMATE algorithm was applied for calculating the ESTIMATE score and tumor purity (32). The correlations between MetaScore groups and immune checkpoint expression were analyzed.

Prediction of immunotherapy for PCa patients

The IMvigor dataset was downloaded from a freely available database, which included installed software and R "IMvigor210CoreBiologies" package (http://research-pub.gene.com/IMvigor210CoreBiologies). Immunotherapy predictive value of the four-gene model was verified in multi-datasets [GSE35640 (anti-recMAGE A3, metastatic melanoma and non-small-cell lung

cancer), GSE78220 (anti-PD-1, melanomas), and GSE91061 (anti-CTLA4 and ant-PD1, advanced melanoma)]. Survival probability for PCa patients with high- and low-MetaScore in the IMvigor and GSE78220 cohort was investigated. Wilcoxon test was performed in Microsatellite instability (MSI) (33) to describe the differences in immunotherapeutic response between MetaScore groups.

Prediction of chemotherapy response

The chemotherapeutic response in PCa patients was assessed using the Genomics of Drug Sensitivity in Cancer database (GDSC, https://www.cancerrxgene.org) by R "oncoPredict" package (34). PCa patients' drug sensitivity in PRISM and CTRP2.0 was measured by R "pRRophetic" package (35).

Cell culture and transfection

The prostate cancer cell lines PC3 and DU145 were employed to explore the effect of SLC17A4 on PCa. PC3 cells and DU145 cells were cultured in RPMI 1640 medium (Biological Industries) with 10% fetal bovine serum (FBS) and 1% penicillin-streptomycin (Beyotime Biotechnology, China). Cultures were done in a 37°C humidified incubator with 5% CO_2. The cells were digested and passed with a ratio of 1:6 upon attaining 80% density. Each experiment was performed in triplicate. Specific siRNAs targeting SLC17A4 were designed and synthesized from Sangon Biotech (Shanghai, China). The transfection was conducted using Lipofectamine 2000 (Invitrogen, USA) according to the manufacturer's instructions. Briefly, cells were transfected in 24-well plate in a total amount of 5 µl (20 µM) siRNA-NC or siRNA-SLC17A4 (si-RNA-626 or si-RNA-1080) with 5 µl of lipofectamine 2000. Then, the medium was changed after 6 h of transfection and samples were collected for subsequent assays after 48 h incubation.

RNA isolation and RT-qPCR

The total mRNA was extracted from transfected cells by the TRIzol solution (Thermo Fisher, USA). The mRNA reverse transcription kit was purchased from Cwbio (China) for reverse-transcription of mRNA to cDNA. The primers sequences of GAPDH were ACAGCCTCAAGATCATCAGC (Forward), GGTCATGAGTCCTTCCACGAT (Reverse). The primers of SLC17A4 were GCACTCTTCCTCCCTCAGTA (Forward), ATTCATCCACTATCCCTTTCCTG (Reverse). The cycling conditions were as follows: 95° for 10 min, followed by 40 cycles at 95° C for 15 s and 60° C for 30 s. GAPDH was employed as an internal control to normalize the relative mRNA expression levels.

Antibodies and western blot

The total protein concentration was quantified by the BCA method. Proteins were separated by 10% SDS-PAGE and then they were transferred from the gel to an NC membrane. The membrane was incubated overnight at 4 °C with primary antibody SLC17A4 (0.5µg/ml, Thermo Fisher, USA) and β-actin (1: 5000, ProteinTech, USA) after being blocked for 1.5 h. Signals were detected by ECL reagent after incubation with the corresponding secondary antibody.

CCK-8 assay

The Cell Counting Kit-8 (DOJINDO, Japan) was employed to evaluate cell proliferation. The transfected PC3 and DU145 cells with 1000 cells/well were inoculated in 96-well plates. CCK-8 solution (10 µl) was added to each well, and cell proliferation was measured at 24, 48, and 72 h.

5-ethynyl-2′-deoxyuridine assays

The transfected PC3 and DU145 cells were plated into a 20 mm round coverslip. The operations were performed following the instruction manual using the EdU Cell Proliferation Assay Kit (Ribobio, China).

Transwell assay

The upper chambers of the Transwell contain a membrane (8-µm pore; Corning, USA) that was placed into 6-well plates. Next, the upper chamber was inoculated with 100 µl cell suspensions ($2*10^6$ cells/ml) maintained in a serum-free medium, and the lower chamber was filled with a 500 µl culture medium supplemented with 10% FBS. After 48 h of culture, the invasion cells were fixed (4% Paraformaldehyde) and stained (0.1% Crystal Violet).

Colony formation assay

The transfected PC3 and DU145 cells were seeded into 6-well plates (200 cells/well) and then incubated for 2 weeks. The colonies were then fixed for 15 min with 4% Paraformaldehyde solution (1 ml/well) and stained for 30 min with crystal violet reagent (Solarbio, China). The stained colonies were photographed and computed.

Statistical analysis

The Shapiro–Wilk test was employed to detect whether the variables were normally distributed. The Wilcoxon test and Kruskal-Wallis test was utilized to compare the non-normally distributed data between the two groups and multiple groups, respectively. Unpaired Student's t-test and one-way analysis of variance (ANOVA) was used to compare normally distributed variables between the two groups and multiple groups, respectively. The Kaplan-Meier survival plots were used to estimate OS between two groups using the R package "survminer". The Cox regression for survival analysis was performed by R package "survival". Time-dependent receiver operating characteristic (ROC) curves were plotted using the R package "timeROC". All heatmaps were conducted through R "ComplexHeatmap" package. The data were mainly visualized using ggplot2 R software. All the tests were two-sided, and $P< 0.05$ was considered statistically significant.

Results

K-means algorithm identifies two metaClusters in PCa

Flowchart Figure 1A comprehensively described our study. In order to characterize metabolic heterogeneity within PCa, 46 candidate metabolic genes were confirmed for clustering using univariate cox regression. By conducting consensus clustering on the gene expression pattern of candidate genes, two resulting clusters were defined, MetaCluster 1 and MetaCluster 2. The heatmap for the expression of the 46 metabolic identified hub genes of the 496 patients is shown in Figure 1B. Notably, significant prognostic differences were observed between the two subclusters, with shorter OS for MetaCluster 2 than MetaCluster 1 ($P < 0.001$, Figure 1C). Furthermore, the correlation analyses between MetaCluster and the activity of 114 identified metabolic pathways were presented in Figure S1 and Table S1. Results revealed distinct metabolic patterns between MetaCluster 1 and MetaCluster 2.

The model constructed by multivariate cox regression analysis

The identified candidate metabolic genes (absolute (log fold change) > log2(1.5) & $P < 0.05$) were showed by Volcano plot (Figure 2A). After analyzing the selected gene with univariate cox regression, 48 prognostic genes were achieved: 32 increased in Hazard Ratio and 16 reduced in Hazard Ratio (Figure 2B). We constructed a prognostic model containing nine genes. The development of a random survival forest model and the importance of nine variables are exhibited in Figures 2C, D Subsequently, the Gaussian mixture model (GMM) combined with ROC curves was established to evaluate the predictive ability of the signatures by calculating the AUCs, the highest AUC as our model to predict the OS of PCa patients was selected from the eight clusters (Figure 2E). Hence, we finally established a prediction signature comprising four genes (NTM, GAS2, SLC17A4, GC), heatmap for the four-gene signature is shown in Figure 2F. MetaScore = 0.5154*GAS2 + 0.395*SLC17A4 + (-0.1211*NTM) + 0.2939*GC.

Patients were classified into the high- and low-MetaScore groups according to the best cutoff value of the metabolic score, termed as MetaScore, which was calculated by the four-gene signature. We then ranked the samples using MetaScore in the training cohort and internal validation cohort. The relevance between survival probability and MetaScore of patients was explored (Figure 3A). The survival analysis revealed that patients with low-MetaScore related to a better OS. What`s more, the predictive ability of MetaScore signature was validated in the GSE16560 cohort (Figure S2). The 1-, 3-, and 5-year ROC curves demonstrated a promising AUC of 0.959, 0.887 and 0.910, respectively (Figure 3B). The AUC suggested excellent clinical value in predicting the short- and long-term survival probability in PCa. Afterward, univariate and multivariate cox regression identified MetaScore as an OS-related factor (Figure 3C).

Biological behaviors of the metabolic genes

The potential functions and pathways in involved differentially expressed metabolic genes in PCa were determined using GSEA analysis. Fifteen metabolic-, immune-related signaling and tumorigenic pathways in KEGG, and 30 GO annotations were determined (Figure 3D). Enrich GO analyses revealed that the upregulation was mainly annotated to humoral immune response, cation transmembrane transporter activity, inorganic cation transmembrane transporter activity, alcohol metabolic process, fatty acid metabolic process, and monocarboxylic acid biosynthetic process (Figure 3D and Table S2). Enrich KEGG analyses demonstrated that the specific metabolic pathways were mainly gathered in arachidonic acid metabolism, drug metabolism-cytochrome P450, complement and coagulation cascades, estrogen signaling pathway, TGF-beta signaling pathway, choline metabolism in cancer, and retinol metabolism (Figure 3D and Table S3). Moreover, GSEA was also performed to determine the functional enrichments of each subtype (Tables S4, S5). We found that regulation of DNA repair and steroid hormone biosynthesis were activated, while organellar large ribosomal subunit and valine leucine and isoleucine degradation were relatively suppressed in it

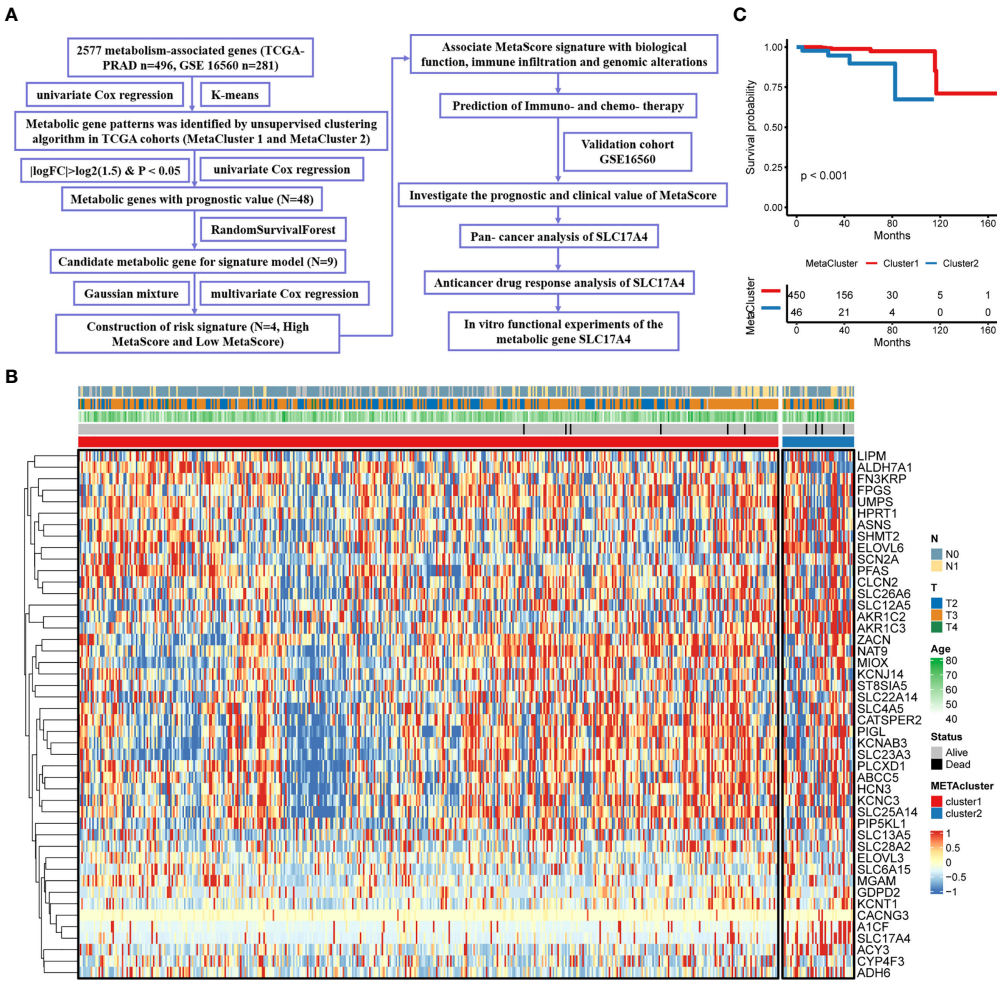

FIGURE 1
Characteristics of MetaCluster in PCa. **(A)** Flow chart of the study. **(B)** Heatmap of the candidate genes associated with MetaCluster. **(C)** Kaplan–Meier curves showing the correlation between MetaCluster and OS (log-rank test, P< 0.001).

(Figure 3E). The association between MetaScore and the activity of 114 identified metabolic pathways was explored and the most significant pathways was presented (Figure 4)

MetaScore is related to distinct profiling of genomic alterations

To explore the relationship between MetaScore and genomic patterns in PCa, CNAs and somatic mutation analyses were performed. We next assembled copy number variation regions (CNVRs) by merging overlapping CNVs of the type (loss or gain) (Figure 5A). What`s more, analysis of somatic mutation patterns demonstrated a high incidence of mutations in TP53 (20%), SPOP (15%), TTN (14%), SPTA1 (8%), SYNE1 (8%), CDK12(7%) and KMT2C (6%) in the high MetaScore group (Figure 5B), while SPOP (10%), TP53 (9%), TTN (9%), FOXA1 (7%), MUC16 (6%) and KMT2D (6%) presented higher-incidence mutations in the low MetaScore group (Figure 5C).

Immune infiltration of metabolic subtypes in PCa

The immune cell infiltration in the tumor microenvironment of the TCGA-PRAD between high- and low-MetaScore groups was presented through a heatmap (Figure S3). Monocytes, Macrophages M0, Dendritic cells activated, CD56bright.natural.killer.cell, CD56dim.natural.killer.cell, Eosinophil, Immature.dendritic.cell Plasmacytoid.dendritic.cell, and Type.17.T.helper.cell, were enriched in the low-MetaScore group. B cells naive, Monocytic lineage, Endothelial cells,

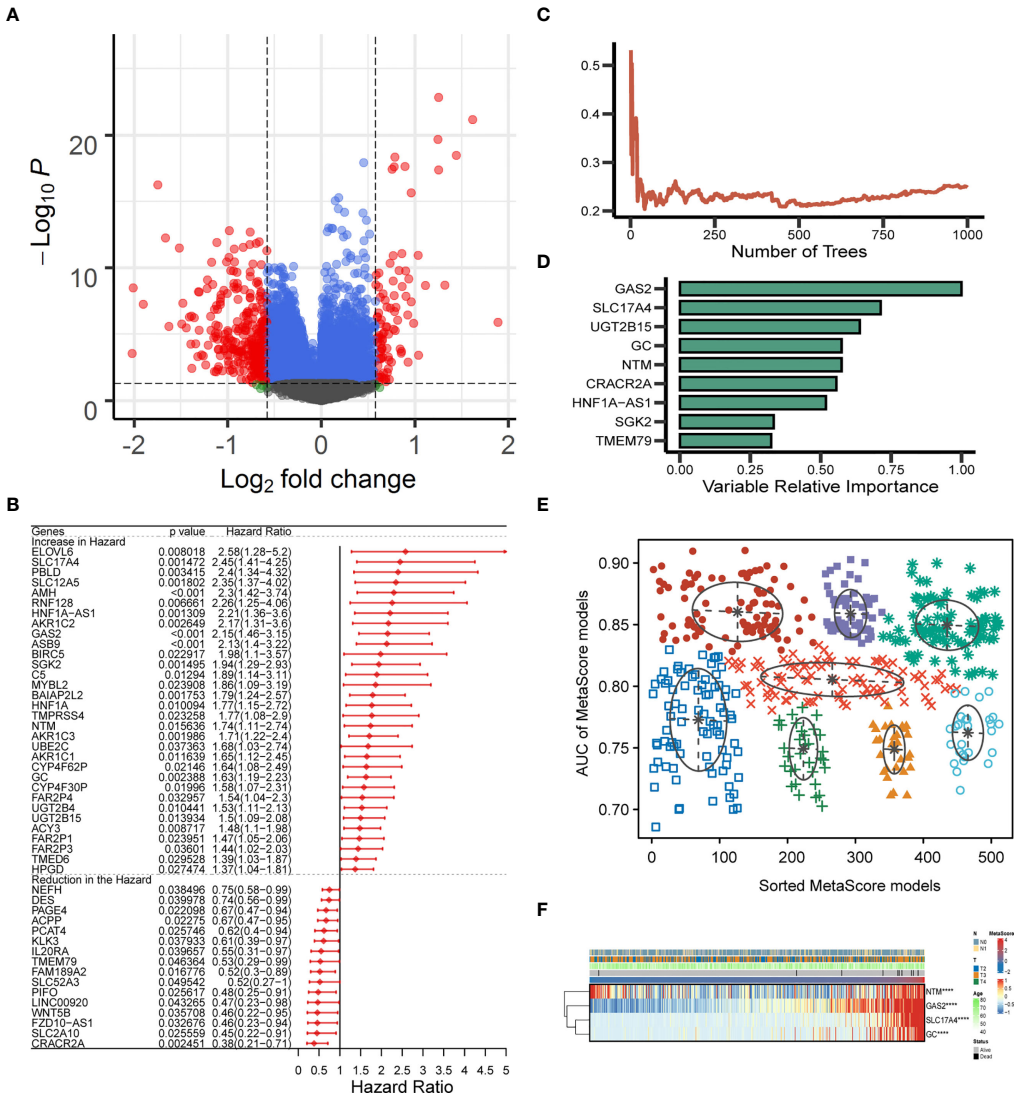

FIGURE 2
Establishment and verification of MetaScore signature. **(A)** The volcano plot of mRNA levels expression of metabolism genes. The abscissa is the log2 value of the screening condition, the ordinate is the log10 transformed p-value. The red-colored dots represent the DEGs (|logFC|> log2 (1.5) and P< 0.05). **(B)** Univariate Cox analysis of 48 selected genes. **(C, D)** The error rate of the random trees and variable relative importance for the 9 metabolism-related genes. **(E)** The pattern of the logistic regression model is related to the AUC scores and is verified by a Gaussian mixture, including 8 clusters of 511 combinations. **(F)** The heat map revealed the relationship between the four-gene signature and distribution of MetaScore ****P < 0.0001.

Activated.CD4.T.cell, Central.memory.CD8.T.cell, Type.2.T.helper.cell, and B cell were enriched in high-MetaScore group. What`s more, we also demonstrated the correlation between infiltration of immune cells and MetaScore with a heatmap (Figure S4). The expression of the immune checkpoint is the trigger of tumor-intrinsic immune escape, and the involved molecules include antigen-presenting cells, co-stimulators, co-inhibitors, receptors, ligands, cell adhesions, etc (36, 37). Therefore, we investigated the correlation between the immune checkpoint and MetaScore (Figure S5).

The role of MetaScore in the prediction of immunotherapeutic benefits

Emerging immune checkpoint blockade therapies blocking the programmed death 1 (PD-1) or its ligand PD-L1 molecules have exhibited satisfactory outcomes, with the potential to prevent the progress of advanced cancer. Therefore, we evaluated the utility of the MetaScore in estimating the therapeutic benefit in patients. For this purpose, the patients who adopted anti-PD-L1 immunotherapy in the IMvigor210

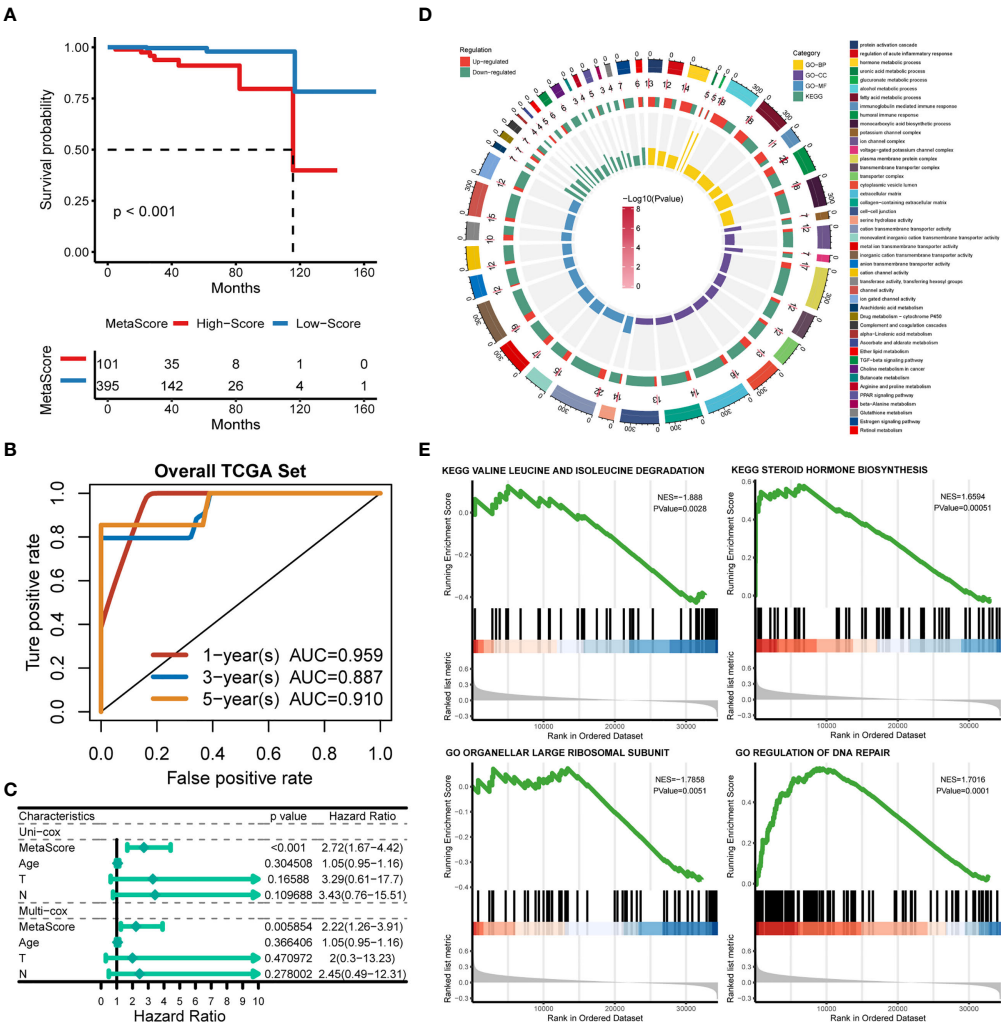

FIGURE 3
Functional annotation of low- and high-MetaSore groups. **(A)** Kaplan–Meier curves showing the correlation between MetaScore and OS (log-rank test, p < 0.001). **(B)** ROC curves exhibited the predictive capability of the MetaScore signature on the clinical value including 1-, 3- and 5-year. **(C)** Clinical variables related to OS by univariate cox and multivariate cox analysis in the TCGA-PRAD cohort. **(D)** GO and KEGG plots for enrichments based on the high- and low-MetaScore group. **(E)** GSEA plots for enrichments based on the high- and low-MetaScore group.

cohort were assigned high- and low-MetaScore groups according to our four-gene signature. Notably, MetaScore is related to objective response to anti-PD-L1 therapy in the IMvigor210 cohort (Kruskal-Wallis, p = 0.00039; Figure 6A). Patients with low MetaScore significantly outlived patients with high MetaScore in the IMvigor210 cohort (log-rank test, p = 0.001; Figure 6C). A similar outcome was observed in the GSE78220 cohort, which was also undergoing anti-PD-1 checkpoint inhibition therapy (Wilcoxon, p =0.0038, Figure 6B; log-rank test, p < 0.001, Figure 6D). Further, we verified the immunotherapeutic response in GSE35640 and GSE91061 cohorts, which received distinct immunotherapies (Wilcoxon, p =0.0016; Figure S6A; Wilcoxon, p =0.0024; Figure S6B). TMB and MSI were emerging biomarkers associated with immunotherapy response. Thus, the correlation between MetaScore and TMB/MSI in TCGA-PRAD was further investigated (Figures 6E, F). Collectively, these data demonstrated that MetaScore might serve as hazardous prognostic markers and predict immunotherapy response.

Prognostic metaScore and sensitivity to chemotherapy

To improve the therapeutic outcomes of PCa patients, we further investigated the correlation between our MetaScore and the predicting sensitivity to 16 common chemotherapy drugs (Figure 7). The analysis revealed that increased MetaScore was

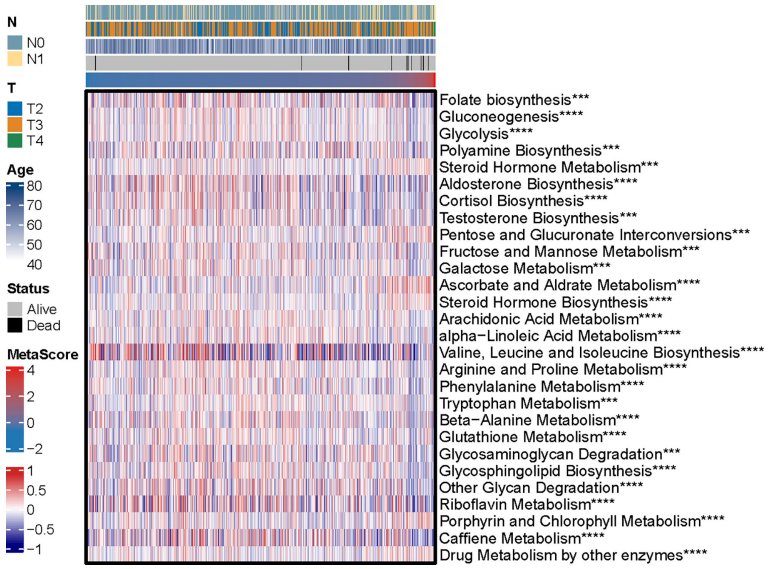

FIGURE 4
The heatmap was employed to visualize the most significant pathways among 114 identified metabolic-related pathways correlation to MetaScore. ***p < 0.001, ****P < 0.0001.

related to increased drug sensitivity of cancer cells to Cisplatin, Cyclophosphamide, Gemcitabine, Camptothecin, Irinotecan, Vorinostat, Fulvestrant, Topotecan, Cytarabine, Venetoclax, Carmustine, Entinostat, Nutlin-3a, Crizotinib, Fludarabine, Nilotinib. The correlation coefficient and corresponding estimated AUC value of another 15 chemotherapy drugs were shown in Figure 8. What`s more, in order to evaluate the broad applicability of the four-gene signature, pan-cancer analysis (33 tumors) was conducted based on TCGA and the Harzard Ratios suggested that the four-gene signature can be an increased risk predictor for 7 tumors (Figure 9A).

Bioinformatic analysis of molecular mechanisms underlying SLC17A4

Inspired by the satisfactory prognosis predicting ability of the four-gene model in the training and validation cohort, we further applied bioinformatic analyses to explore the potential underlying mechanisms of SLC17A4. To our knowledge, the role of SLC17A4 in PCa has not been explored. The correlation between the expression of SLC17A4 and prognosis was evaluated in 33 tumor types (Figure 9B). Based on the cox analysis, we suggested that SLC17A4 might be an oncogene for the 3 evaluated types of tumor. Kaplan-Meier analysis indicated that low expression of SLC17A4 is associated with better survival in PCa ($P < 0.01$, Figure 9C). Furthermore, GSVA revealed that three GO category negative regulation of interferon gamma secretion, uronic acid metabolic process, heterochromatin assembly were highly enriched in the high-SLC17A4 group, three KEGG category ascorbate and aldarate metabolism, maturity onset diabetes of the young, homologous recombination were mainly gathered in the high-SLC17A4 group (Figure 9D). The correlation analyses between SLC17A4 expression and the most significant identified metabolic pathways among 114 are shown in Figure 10. To determine the potential therapeutic drugs in high- and low-SLC17A4 PCa patients, the IC50 of 34 drugs in PCa cells was estimated utilizing the GDSC database. Remarkably, the drug sensitivity (IC50) of 34 chemotherapy compounds was significantly lower in the high-SLC17A4 group as compared to the low-SLC17A4 group, which revealed that the patients with high-SLC17A4 could be more beneficial to the application of these drugs (Figure 11).

SLC17A4 regulates the invasion, viability, and proliferation of PCa

Various *in vitro* experiments were performed to validate the pathogenic role of SLC17A4 in PCa cells. Transfection in DU145 and PC3 cells was performed using three siRNAs to prohibit the expression of SLC17A4, in which si-RNA-626 and si-RNA-1080 exhibited relatively high efficiency (Figure S7). Western blot was employed to verify the silence of SLC17A4 by siRNA (Figure 12A). The CCK8 assay interpreted that the cell proliferation ability is inhibited by silencing SLC17A4 (Figure 12B). The colony formation experiment revealed that the inhibition of SLC17A4 remarkably reduced the colony

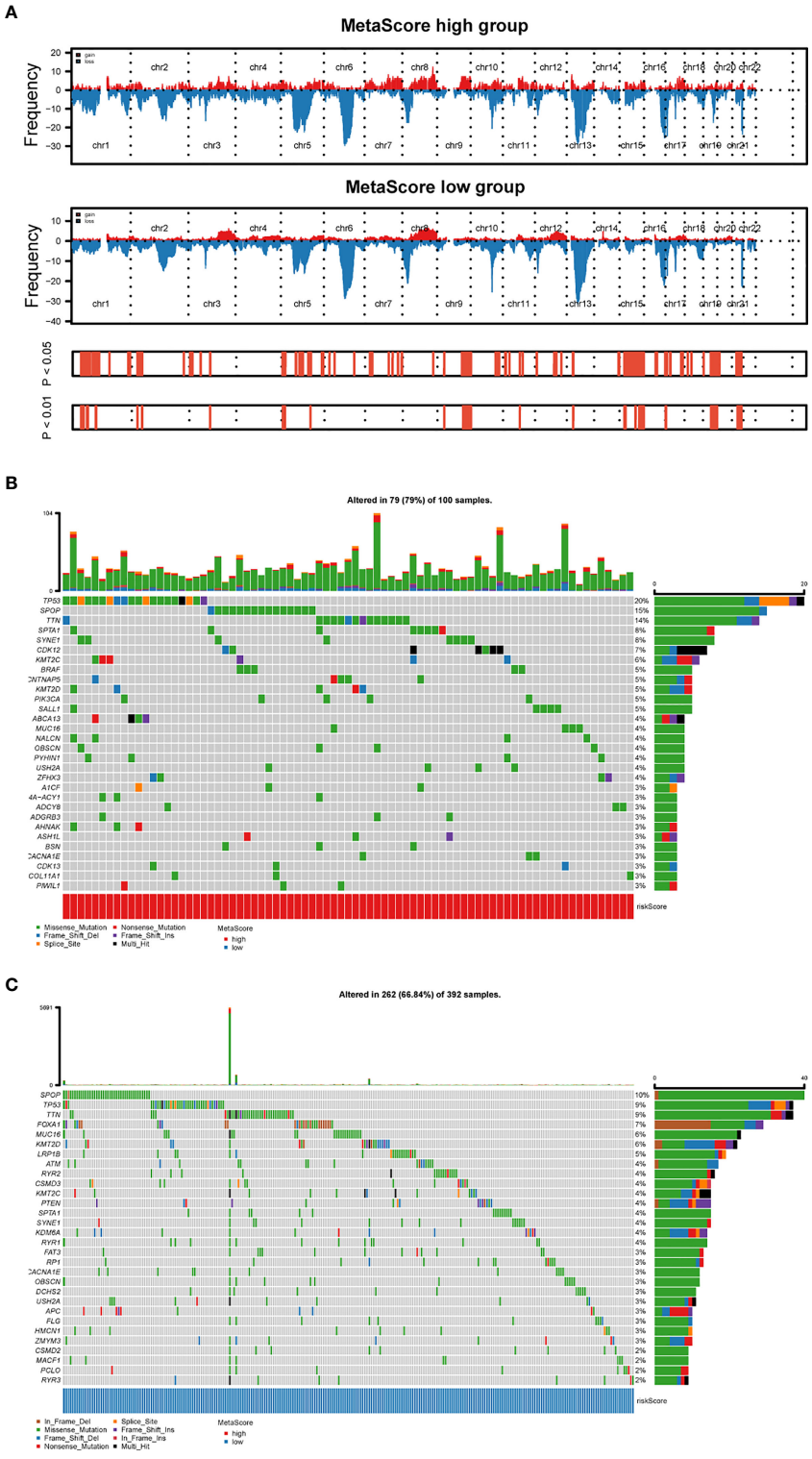

FIGURE 5
Distinct genomic pattern related to MetaScore. **(A)** Amplifications and deletions in PCa with high- and low-MetaScore. Chromosomal regions of peaks correspond to the relevant recurring focal amplification (red) and deletions (blue). **(B, C)** The overall somatic mutation profile with the highest frequency in high- and low-MetaScore groups. P< 0.05 indicates statistical significance.

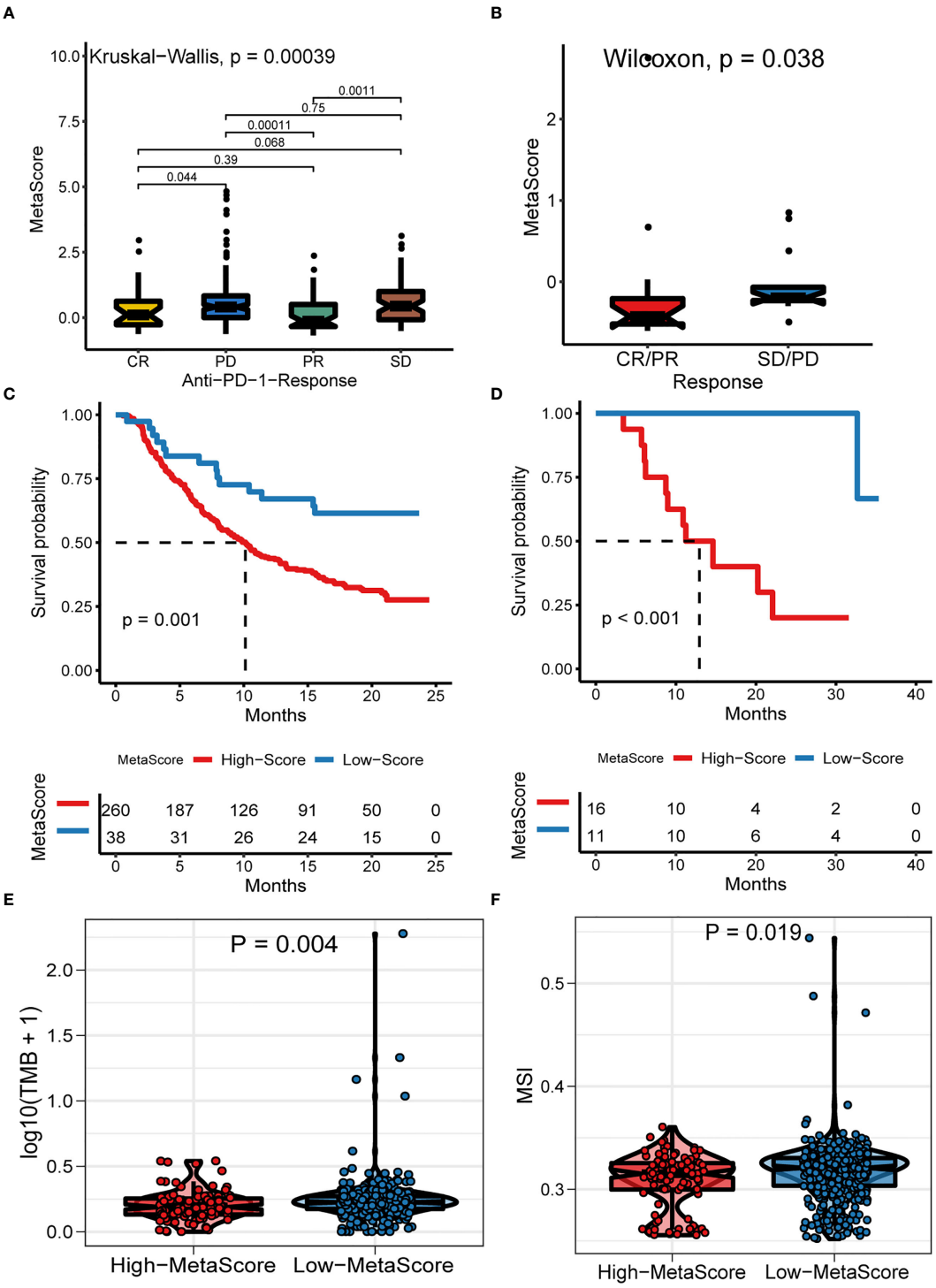

FIGURE 6
The Role of MetaScore in the prediction of immunotherapeutic benefits. MetaScore in groups with a different anti-PD-1 clinical response status (complete response [CR]/partial response [PR] and stable disease [SD]/progressive disease [PD]) in the IMvigor210 cohort **(A)** and GSE78220 cohort **(B)**. Kaplan-Meier curves for patients with high- and low-MetaScore in the IMvigor210 cohort **(C)** and GSE78220 cohort **(D)**. **(E)** The differences of TMB between MetaScore groups in the training set. **(F)** The differences of MSI between MetaScore groups in the training set. TMB, tumor mutation burden; MSI, microsatellite instability.

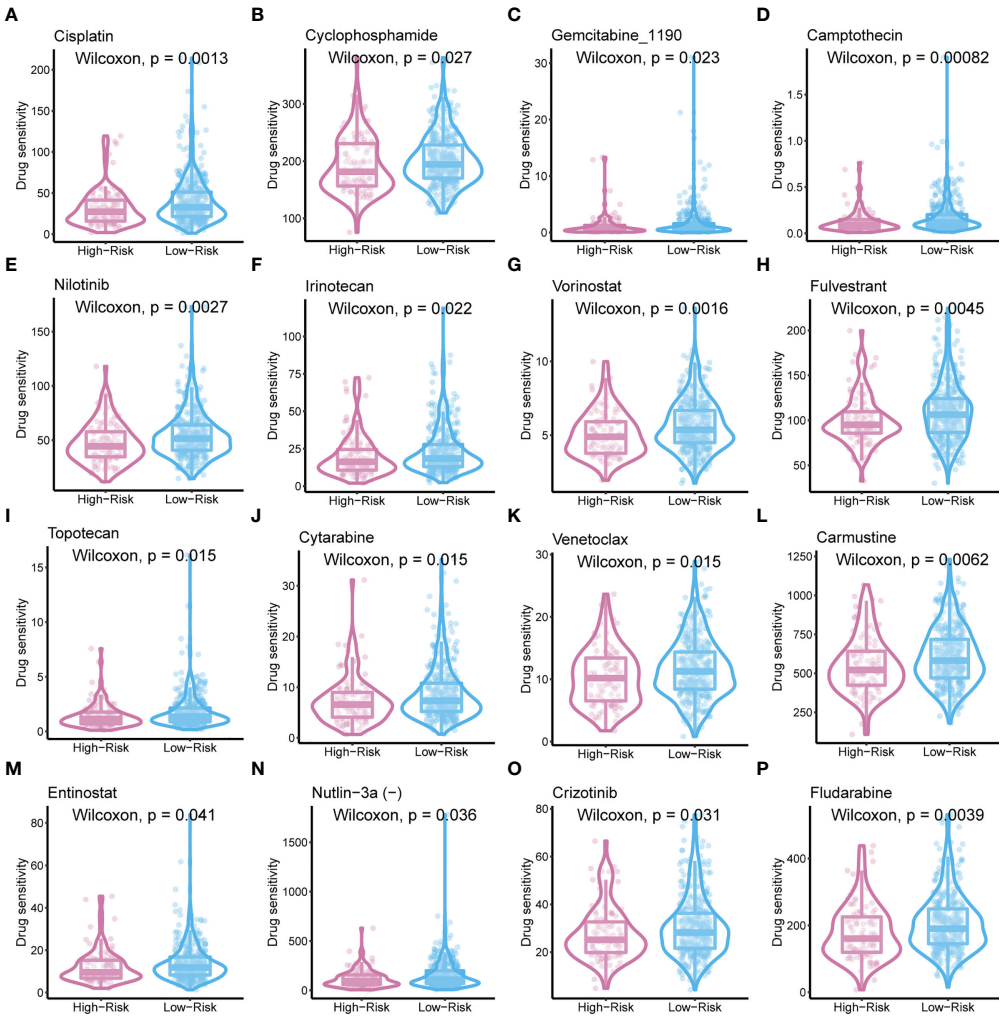

FIGURE 7
The sensitivity of 16 common chemotherapy drugs between MetaScore groups in PCa cells.

number in DU145 cell line and PC3 cell line (Figure 12C). Dramatically, the dysfunction of SLC17A4 inhibited the invasion ability of DU145 and PC3 cells (Figures 12D, S8A). What`s more, the EdU assay indicated that the proliferation ability of PCa cells was inhibited by the silence of SLC17A4 (Figures 12E, S8B). Therefore, the prognostic gene SLC17A4 was associated with the proliferation and invasion of PCa cells and may be a potential therapeutic target for PCa.

Discussion

Metabolic reprogramming has emerged as a prominent hallmark of tumors (38). Tumor cells alter their dominant oxidative phosphorylation ATP-producing procedure to aerobic glycolysis even if there is sufficient oxygen (described as the Warburg effect) (39). The metabolic characteristics of cancer cells might influence varying cells in the TME. Among them are tumor-associated fibroblasts, endothelial cells and immunocytes, which eventually facilitate the invasion, proliferation and no response to antitumor therapy of cancer cells (40). A study reported that upregulation of glycolytic metabolism might accelerate prostate cancer progression and radioresistance *via* circular RNA (41). Thereby, targeting the metabolic state of cancers with drugs would be a promising therapeutic approach for better outcomes. In this study, PCa patients were stratified into MetaCluster 1 and MetaCluster 2 according to metabolic genes to investigate the correlation between tumor metabolic profile and tumor

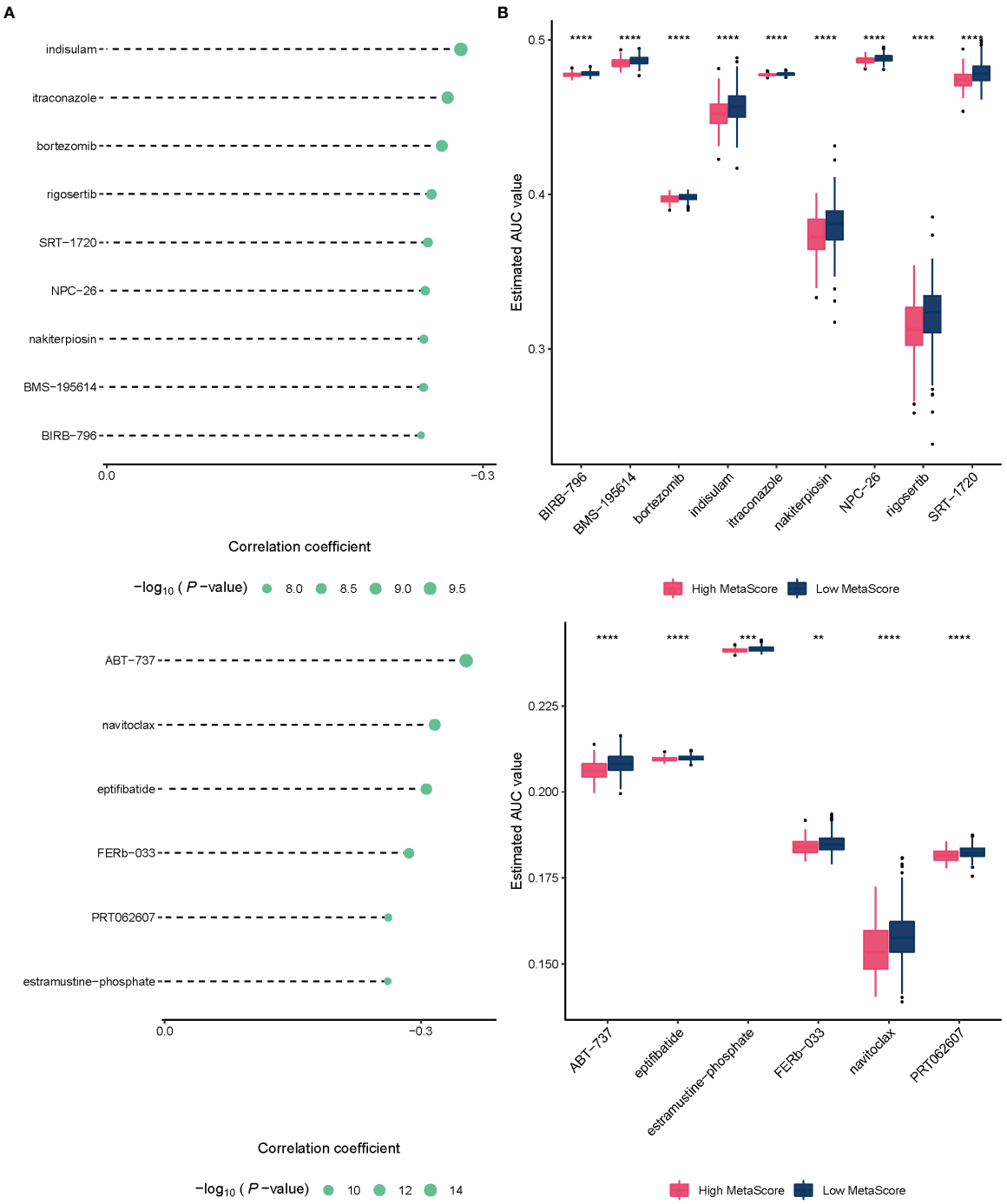

FIGURE 8
(A) The correlation coefficient of 15 chemotherapy drugs. **(B)** The estimated AUC value of 15 chemotherapy drugs between MetaScore groups. **p < 0.01, ***p < 0.001, ****P < 0.0001.

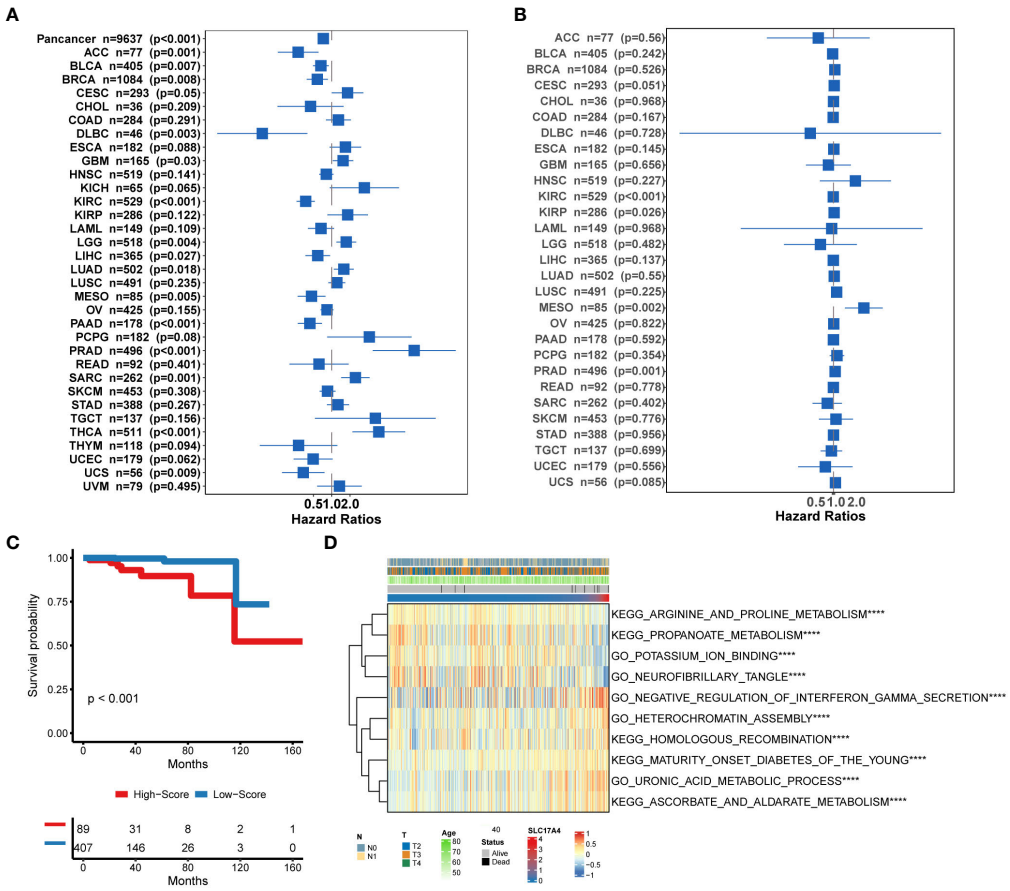

FIGURE 9
(A) Pan-cancer analysis of the 4-gene signature based on TCGA. **(B)** Correlation between the expression of SLC17A4 and overall survival in multiple tumor types based on TCGA. **(C)** Survival curves of OS between low-SLC17A4 patients and high-SLC17A4 based on TCGA-PRAD. **(D)** The differential in GO and Enrich analysis between low- and high-SLC17A4 groups. ****P < 0.0001.

phenotype. Differentially expressed metabolic-associated pathways were verified between the two MetaClusters. Subsequently, to further investigate the correlation between the cluster model and cancer progression pattern, we establish a scoring system, MetaScore, to qualify the gene model. In summary, we focus on analyzing the possible biological behavior of metabolism-associated genes in the prognosis and development of PCa by bioinformatics analysis and functional cell assays.

Integrating multiple biomarkers into one aggregate signature *via* bioinformatics might enhance the prediction compared with a single biomarker (42, 43). Here, we applied a multi-step bioinformatics analysis to establish a metabolic genes model to predict OS in PCa patients. We identified four metabolism-associated genes (GAS2, SLC17A4, NTM, and GC) related to OS in PCa. Among the four genes, the NTM gene showed negative coefficients, and the expression was upregulated in promising OS patients. What`s more, the expression of GAS2, SLC17A4, and GC was increased in patients with unfavorable outcomes, which have positive coefficients. Studies showed that some of the 4 genes are involved in tumors, including PCa. It has been reported that the 1,25(OH)2 D/25(OH)D (metabolites of GC) molar proportion was related to a reduced risk of high aggressive PCa in African-American men (44), vitamin D binding protein (the protein encoded by GC) regulates the correlation between total 25(OH)D expressions and risk of advanced and fatal PCa (45). However, the study interpreted that NTM may promote biochemical recurrence of PCa after radical prostatectomy *via* affecting regulatory T cells and M2 macrophages (46) and decreased expression of NTM in transformants is associated with hypermethylation close to the transcription start point in arsenic- or cadmium-transformed malignant prostate epithelial cells (47).

SLC17A4 is an organic anion transporter (belonging to the solute carrier 17 families) that is particularly maintained

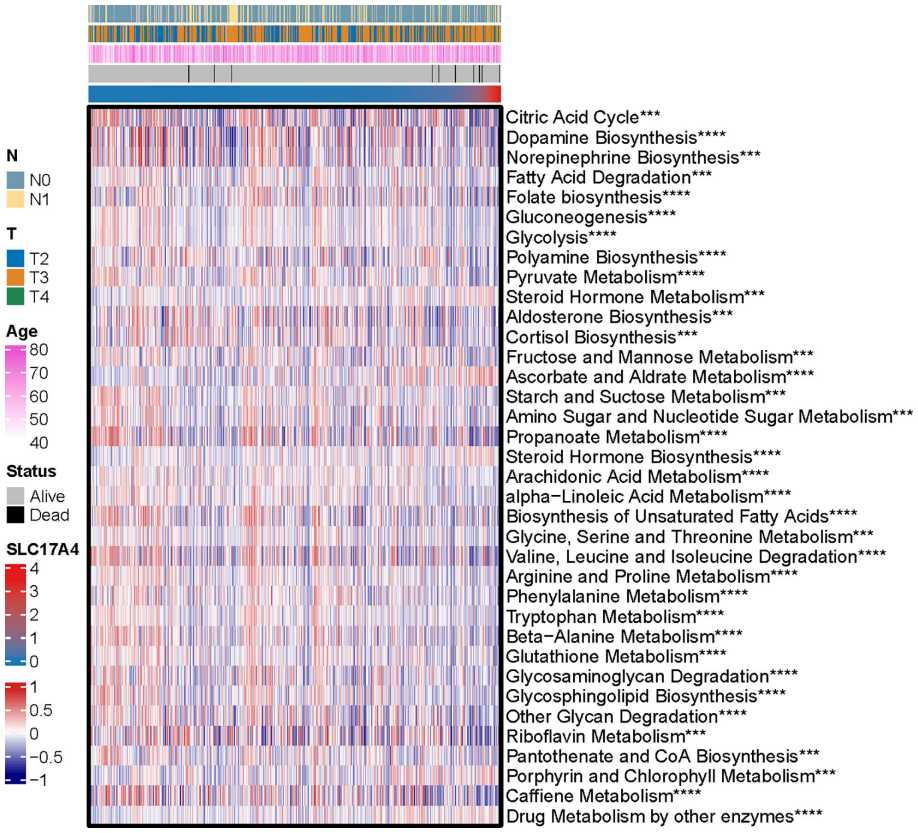

FIGURE 10
The correlation analysis between the 114 identified metabolic-related pathways and SLC17A4 (the most significant pathways was presented). ***p < 0.001, ****P < 0.0001.

phosphate homeostasis. The study reported that phosphate transporters gene SLC17A4 is linked to Ca and P metabolism and homeostasis in pig models (48). Interestingly, a metabolizing enzyme colocalized with the SLC17A4 gene is closely related to thyroid hormone pathway, insulin signaling, and glucose metabolism (49, 50). Our analysis revealed that the upregulation of SLC17A4 increases MetaScore and is associated with poor prognosis in PCa patients. Our functional experiments further reveal that human SLC17A4 is capable of promoting progression and invasion in PCa cells (Figure 12). Herein, for the first time, we recognized the roles of SLC17A4 in the development and progression of PCa. Further exploration is needed to verify the biological function and underlying mechanism of SLC174A in PCa biogenesis and progression. Further characterization of molecules from the signature will supply novel insights into the tumor etiology and may reveal potential metabolic therapeutic targets.

The tumor cell metabolism affects TME and immune infiltration patterns, thereby altering the efficiency of checkpoint-based immunotherapy. The metabolic status is different between normal tissue and PCa, so it provides a new way to identify cancers through metabolic differences. It has been interpreted that PCa cells show high consumption of glucose during the metastatic stage (12, 13), and PCa patients with highly glycolytic metabolism may promote tumor progression and aggressiveness (14). The accumulation of lactic acid, the metabolic product of glycolysis, in the extracellular matrix is conducive to the acidic TME and further influences immune cell infiltration. A study demonstrated that acidic TME might restrict T cell-mediated immunity and promote hyporesponsiveness of immune cells (51). Consistently, immunocytes including B cells naive, Monocytic lineage, Endothelial cells, Activated.CD4.T.cell, Central.memory.CD8.T.cell, Type.2.T.helper.cell, and B cell in the high-MetaScore group presented more disordered than low-MetaScore group (Figure S3).

Immune checkpoint inhibitors have presented promising outcomes in treating patients with various cancers, providing new frontiers in cancer treatment strategies (52, 53). PCa has been stratified into an immune-desert pattern and is

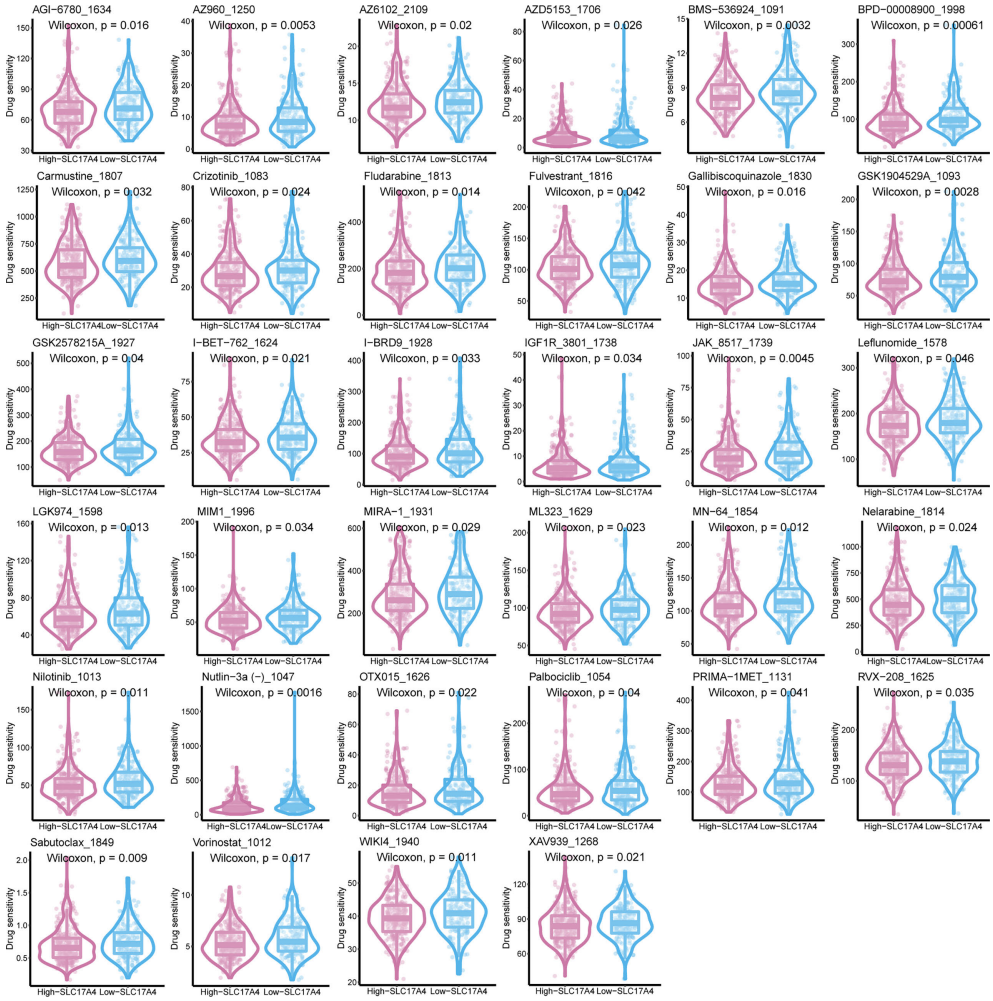

FIGURE 11
The IC50 of 38 chemotherapy drugs in PCa cells was estimated in SLC17A4 groups utilizing the GDSC database.

moderately responsive to immunotherapy (54, 55). Therefore, only partial and specific patients might benefit from the immunotherapy. Although biomarkers have been extensively explored to predict PCa prognosis, metabolic signatures for predicting the response of immuno-/chemo-therapy have not been developed. In the present study, we developed a novel system according to metabolic genes to predict the efficacy of immunotherapy. TMB and MSI were emerging biomarkers associated with immunotherapy response (56). Patients with higher TMB and MSI may benefit more from the treatment of immunotherapy (57), which is consistent with our findings (Figure 6).

Given the complexity and diversity of PCa cell lines, the selected PC3 and DU145 cell lines (less differentiated and androgen-independent) may not represent the full spectrum of the disease, a wider variety of PCa cell lines should be used in subsequent studies.

Our study is the first to comprehensively elucidate the chemo-/immuno-therapy response of PCa patients based on MetaGene-signature. A recent study reported only chemotherapy response based on MetaGene-signature but lacked immunotherapy response results (58). Interestingly, studies have shown that signature based on MetaGenes are associated with PCa recurrence undergoing radical prostatectomy (59). Two other researches also revealed that the model established by MetaGenes can predict the prognosis of PCa, which is consistent with our study (60, 61). In summary, we conducted an integrated analysis to develop a metabolism-based four-gene signature for predicting the OS and chemo-/immuno-therapy response of

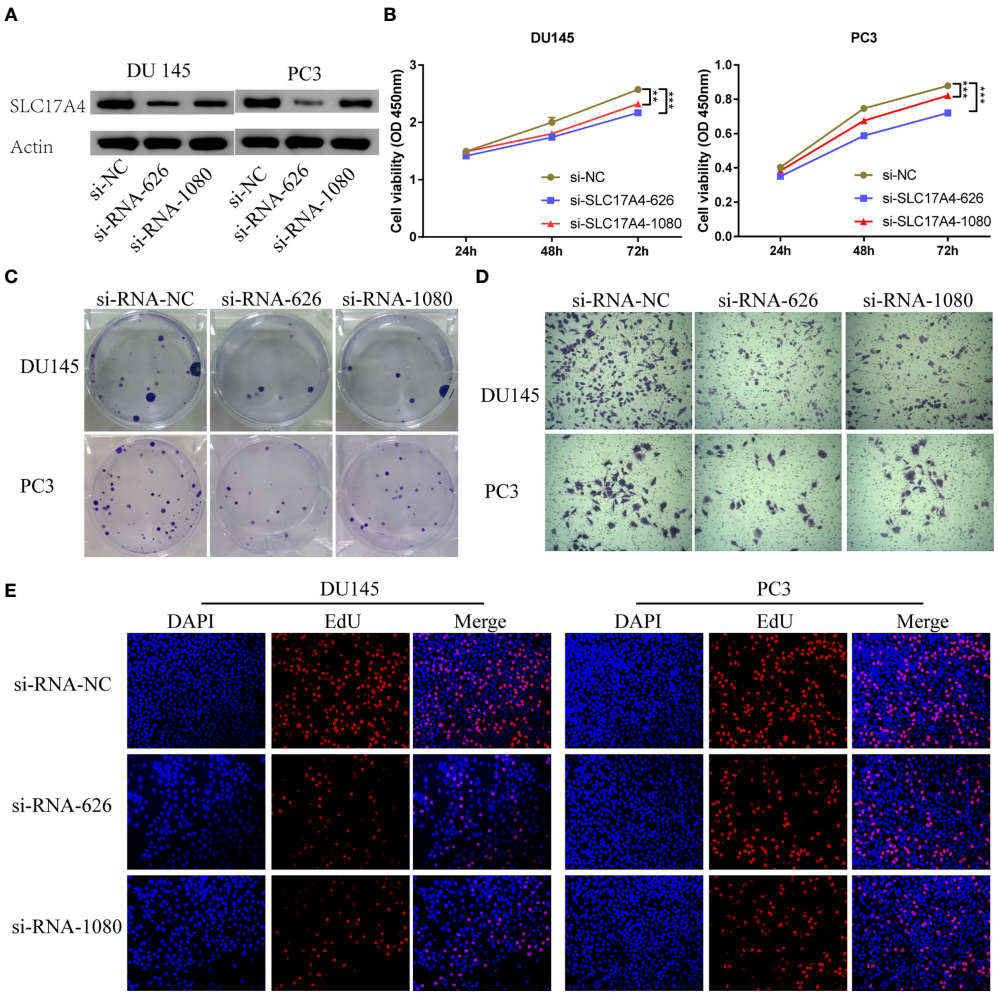

FIGURE 12
(A) Measurement of siRNA transfection efficiency in DU145 and PC3 cells at the protein level. **(B)** CCK-8 assays revealed that silence of SLC17A4 suppressed the proliferation of DU145 and PC3 cells. **(C)** Colony formation assay of DU145 and PC3 cells after the knockdown of SLC17A4. **(D)** Knock-down of SLC17A4 affected the invasion ability of DU145 cells and PC3 cells (Crystal Violet Staining). **(E)** EdU assay of PC3 and DU145 cells after the knockdown of SLC17A4 (siRNA-NC: siRNA negative control). $^{**}p < 0.01$, $^{***}p < 0.001$.

PCa patients. This study investigated the expression patterns, prognostic value, and potential mechanisms of metabolic genes in PCa. Future prospective clinical trials are required to assess the clinical utility of this signature.

Data availability statement

The datasets presented in this study can be found in online repositories. The names of the repository/repositories and accession number(s) can be found in the article/Supplementary Material.

Author contributions

JG and HL performed database analysis and drafted the manuscript. NZ and RJP contributed to all the designs and revise of the study. YQT, SYL, HZ, ZYD and ZYW, made contributions to the drafting of the manuscript. All authors reviewed and approved the final draft of the study.

Funding

This work was supported by National Natural Science Foundation of China (No. 81901268) and The Science and Technology Innovation Program of Hunan Province (2020RC2065), the Youth Natural Science Foundation of Hunan Province (2021JJ40321).

Acknowledgments

JG (CSC NO.201906370030) was supported by a scholarship from the China Scholarship Council Program.

Thanks to Shan Jiang, Tianran Zhang and Zhen Yuan for their support and help.

Conflict of interest

The authors declare that the research was conducted in the absence of any commercial or financial relationships that could be construed as a potential conflict of interest.

Publisher's note

All claims expressed in this article are solely those of the authors and do not necessarily represent those of their affiliated organizations, or those of the publisher, the editors and the reviewers. Any product that may be evaluated in this article, or claim that may be made by its manufacturer, is not guaranteed or endorsed by the publisher.

Supplementary material

The Supplementary Material for this article can be found online at: https://www.frontiersin.org/articles/10.3389/fimmu.2022.982628/full#supplementary-material

References

1. Bray F, Ferlay J, Soerjomataram I, Siegel RL, Torre LA, Jemal A. Global cancer statistics 2018: GLOBOCAN estimates of incidence and mortality worldwide for 36 cancers in 185 countries. *CA Cancer J Clin* (2018) 68(6):394–424. doi: 10.3322/caac.21492

2. Siegel RL, Miller KD, Jemal A. Cancer statistics, 2019. *CA Cancer J Clin* (2019) 69(1):7–34. doi: 10.3322/caac.21551

3. Reichard CA, Gregg JR, Achim MF, Aparicio AM, Pettaway CA, Pisters LL, et al. Radical prostatectomy in metastatic castration-resistant prostate cancer: Feasibility, safety, and quality of life outcomes. *Eur Urol* (2018) 74(2):140–3. doi: 10.1016/j.eururo.2018.03.031

4. Rebello RJ, Oing C, Knudsen KE, Loeb S, Johnson DC, Reiter RE, et al. Prostate cancer. *Nat Rev Dis Prim* (2021) 7(1):9. doi: 10.1038/s41572-020-00243-0

5. Lalonde E, Ishkanian AS, Sykes J, Fraser M, Ross-Adams H, Erho N, et al. Tumour genomic and microenvironmental heterogeneity for integrated prediction of 5-year biochemical recurrence of prostate cancer: A retrospective cohort study. *Lancet Oncol* (2014) 15(13):1521–32. doi: 10.1016/S1470-2045(14)71021-6

6. Yin Y, Zhang Q, Zhang H, He Y, Huang J. Molecular signature to risk-stratify prostate cancer of intermediate risk. *Clin Cancer Res* (2017) 23(1):6–8. doi: 10.1158/1078-0432.CCR-16-2400

7. Pernar CH, Ebot EM, Wilson KM, Mucci LA. The epidemiology of prostate cancer. *Cold Spring Harb Perspect Med* (2018) 8(12):a030361. doi: 10.1101/CSHPERSPECT.A030361

8. Peng D, Ge G, Xu Z, Ma Q, Shi Y, Zhou Y, et al. Diagnostic and prognostic biomarkers of common urological cancers based on aberrant DNA methylation. *Epigenomics* (2018) 10(9):1189–99. doi: 10.2217/epi-2018-0017

9. Mottet N, Bellmunt J, Bolla M, Briers E, Cumberbatch MG, De Santis M, et al. EAU-ESTRO-SIOG guidelines on prostate cancer. part 1: Screening, diagnosis, and local treatment with curative intent. *Eur Urol* (2017) 71(4):618–29. doi: 10.1016/j.eururo.2016.08.003

10. Nassar ZD, Mah CY, Dehairs J, Burvenich IJG, Irani S, Centenera MM, et al. Human decr1 is an androgen-repressed survival factor that regulates pufa oxidation to protect prostate tumor cells from ferroptosis. *Elife* (2020) 9:e54166. doi: 10.7554/eLife.54166

11. Shao Y, Franko A, Heni M, Hennenlotter J, Hoene M, Hu C, et al. Human prostate cancer is characterized by an increase in urea cycle metabolites. *Cancers (Basel)* (2020) 12(7):1814. doi: 10.3390/cancers12071814

12. Cutruzzolà F, Giardina G, Marani M, Macone A, Paiardini A, Rinaldo S, et al. Glucose metabolism in the progression of prostate cancer. *Front Physiol* (2017) 8:97. doi: 10.3389/fphys.2017.00097

13. Schoors S, De Bock K, Cantelmo AR, Georgiadou M, Ghesquière B, Cauwenberghs S, et al. Partial and transient reduction of glycolysis by PFKFB3 blockade reduces pathological angiogenesis. *Cell Metab* (2014) 19(1):37–48. doi: 10.1016/j.cmet.2013.11.008

14. Pertega-Gomes N, Felisbino S, Massie CE, Vizcaino JR, Coelho R, Sandi C, et al. A glycolytic phenotype is associated with prostate cancer progression and aggressiveness: A role for monocarboxylate transporters as metabolic targets for therapy. *J Pathol* (2015) 236(4):517–30. doi: 10.1002/path.4547

15. Mimeault M, Batra SK. Hypoxia-inducing factors as master regulators of stemness properties and altered metabolism of cancer- and metastasis-initiating cells. *J Cell Mol Med* (2013) 17(1):30–54. doi: 10.1111/jcmm.12004

16. Bénéteau M, Zunino B, Jacquin MA, Meynet O, Chiche J, Pradelli LA, et al. Combination of glycolysis inhibition with chemotherapy results in an antitumor immune response. *Proc Natl Acad Sci USA* (2012) 109(49):20071–6. doi: 10.1073/pnas.1206360109

17. Possemato R, Marks KM, Shaul YD, Pacold ME, Kim D, Birsoy K, et al. Functional genomics reveal that the serine synthesis pathway is essential in breast cancer. *Nature* (2011) 476(7360):346–50. doi: 10.1038/nature10350

18. Monti S, Tamayo P, Mesirov J, Golub T. Consensus clustering: A resampling-based method for class discovery and visualization of gene expression microarray data. *Mach Learn* (2003) 52 (1):91–118. doi: 10.1023/A:1023949509487

19. Rosario SR, Long MD, Affronti HC, Rowsam AM, Eng KH, Smiraglia DJ. Pan-cancer analysis of transcriptional metabolic dysregulation using the cancer genome atlas. *Nat Commun* (2018) 9(1):5330. doi: 10.1038/s41467-018-07232-8

20. Ritchie ME, Phipson B, Wu D, Hu Y, Law CW, Shi W, et al. Limma powers differential expression analyses for RNA-sequencing and microarray studies. *Nucleic Acids Res* (2015) 43(7):e47. doi: 10.1093/nar/gkv007

21. Yuan Y, Chen J, Wang J, Xu M, Zhang Y, Sun P, et al. Development and clinical validation of a novel 4-gene prognostic signature predicting survival in colorectal cancer. *Front Oncol* (2020) 10:595. doi: 10.3389/fonc.2020.00595

22. Hong HC, Chuang CH, Huang WC, Weng SL, Chen CH, Chang KH, et al. A panel of eight microRNAs is a good predictive parameter for triple-negative breast cancer relapse. *Theranostics* (2020) 10(19):8771–89. doi: 10.7150/thno.46142

23. Subramanian A, Tamayo P, Mootha VK, Mukherjee S, Ebert BL, Gillette MA, et al. Gene set enrichment analysis: A knowledge-based approach for interpreting genome-wide expression profiles. *Proc Natl Acad Sci USA* (2005) 102(43):15545–50. doi: 10.1073/pnas.0506580102

24. Ghasemi A, Zahediasl S. Normality tests for statistical analysis: A guide for non-statisticians. *Int J Endocrinol Metab* (2012) 10(2):486–9. doi: 10.5812/ijem.3505

25. Hänzelmann S, Castelo R, Guinney J. GSVA: Gene set variation analysis for microarray and RNA-seq data. *BMC Bioinf* (2013) 14:7. doi: 10.1186/1471-2105-14-7

26. Goodman AM, Kato S, Bazhenova L, Patel SP, Frampton GM, Miller V, et al. Tumor mutational burden as an independent predictor of response to immunotherapy in diverse cancers. *Mol Cancer Ther* (2017) 16(11):2598–608. doi: 10.1158/1535-7163.MCT-17-0386

27. Zeng D, Ye Z, Shen R, Yu G, Wu J, Xiong Y, et al. IOBR: Multi-omics immuno-oncology biological research to decode tumor microenvironment and signatures. *Front Immunol* (2021) 12:687975. doi: 10.3389/fimmu.2021.687975

28. Newman AM, Steen CB, Liu CL, Gentles AJ, Chaudhuri AA, Scherer F, et al. Determining cell type abundance and expression from bulk tissues with digital cytometry. *Nat Biotechnol* (2019) 37(7):773–82. doi: 10.1038/s41587-019-0114-2

29. Becht E, Giraldo NA, Lacroix L, Buttard B, Elarouci N, Petitprez F, et al. Estimating the population abundance of tissue-infiltrating immune and stromal

cell populations using gene expression. *Genome Biol* (2016) 17(1):218. doi: 10.1186/s13059-016-1070-5

30. Charoentong P, Finotello F, Angelova M, Mayer C, Efremova M, Rieder D, et al. Pan-cancer immunogenomic analyses reveal genotype-immunophenotype relationships and predictors of response to checkpoint blockade. *Cell Rep* (2017) 18 (1):248–62. doi: 10.1016/j.celrep.2016.12.019

31. Li T, Fu J, Zeng Z, Cohen D, Li J, Chen Q, et al. TIMER2.0 for analysis of tumor-infiltrating immune cells. *Nucleic Acids Res* (2020) 48(W1):W509–14. doi: 10.1093/nar/gkaa407

32. Yoshihara K, Shahmoradgoli M, Martínez E, Vegesna R, Kim H, Torres-Garcia W, et al. Inferring tumour purity and stromal and immune cell admixture from expression data. *Nat Commun* (2013) 4:2612. doi: 10.1038/ncomms3612

33. Li K, Luo H, Huang L, Luo H, Zhu X. Microsatellite instability: A review of what the oncologist should know. *Cancer Cell Int* (2020) 20:16. doi: 10.1186/s12935-019-1091-8

34. Maeser D, Gruener RF, Huang RS. oncoPredict: an r package for predicting *in vivo* or cancer patient drug response and biomarkers from cell line screening data. *Brief Bioinform* (2021) 22(6):bbab260. doi: 10.1093/bib/bbab260

35. Yang C, Huang X, Li Y, Chen J, Lv Y, Dai S. Prognosis and personalized treatment prediction in TP53-mutant hepatocellular carcinoma: An in silico strategy towards precision oncology. *Brief Bioinform* (2021) 22(3):bbaa164. doi: 10.1093/bib/bbaa164

36. Wang S, Zhang Q, Yu C, Cao Y, Zuo Y, Yang L. Immune cell infiltration-based signature for prognosis and immunogenomic analysis in breast cancer. *Brief Bioinform* (2021) 22(2):2020–31. doi: 10.1093/bib/bbaa026

37. Schreiber RD, Old LJ, Smyth MJ. Cancer immunoediting: Integrating immunity's roles in cancer suppression and promotion. *Science (80-)* (2011) 331 (6024):1565–70. doi: 10.1126/science.1203486

38. Hanahan D, Weinberg RA. Hallmarks of cancer: The next generation. *Cell* (2011) 144(5):646–74. doi: 10.1016/j.cell.2011.02.013

39. Koppenol WH, Bounds PL, Dang CV. Otto Warburg's contributions to current concepts of cancer metabolism. *Nat Rev Cancer* (2011) 11(5):325–37. doi: 10.1038/nrc3038

40. Pavlova NN, Thompson CB. The emerging hallmarks of cancer metabolism. *Cell Metab* (2016) 23(1):27–47. doi: 10.1016/j.cmet.2015.12.006

41. Du S, Zhang P, Ren W, Yang F, Du C. Circ-ZNF609 accelerates the radioresistance of prostate cancer cells by promoting the glycolytic metabolism through MiR-501-3p/hk2 axis. *Cancer Manag Res* (2020) 12:7487–99. doi: 10.2147/CMAR.S257441

42. Wu XN, Su D, De MY, MQ X, Zhang H, ZY W, et al. Identified lung adenocarcinoma metabolic phenotypes and their association with tumor immune microenvironment. *Cancer Immunol Immunother* (2021) 70(10):2835–50. doi: 10.1007/s00262-021-02896-6

43. Xu S, Tang L, Liu Z, Yang K, Cheng Q. Bioinformatic analyses identify a prognostic autophagy-related long non-coding RNA signature associated with immune microenvironment in diffuse gliomas. *Front Cell Dev Biol* (2021) 9:694633. doi: 10.3389/fcell.2021.694633

44. Ramakrishnan S, Steck SE, Arab L, Zhang H, Bensen JT, Fontham ETH, et al. Association among plasma 1,25(OH)2D, ratio of 1,25(OH)2D to 25(OH)D, and prostate cancer aggressiveness. *Prostate* (2019) 79(10):1117–24. doi: 10.1002/pros.23824

45. Yuan C, Shui IM, Wilson KM, Stampfer MJ, Mucci LA, Giovannucci EL. Circulating 25-hydroxyvitamin d, vitamin d binding protein and risk of advanced and lethal prostate cancer. *Int J Cancer* (2019) 144(10):2401–7. doi: 10.1002/ijc.31966

46. Lv D, Wu X, Chen X, Yang S, Chen W, Wang M, et al. A novel immune-related gene-based prognostic signature to predict biochemical recurrence in patients with prostate cancer after radical prostatectomy. *Cancer Immunol Immunother* (2021) 70(12):3587–602. doi: 10.1007/s00262-021-02923-6

47. Pelch KE, Tokar EJ, Merrick BA, Waalkes MP. Differential DNA methylation profile of key genes in malignant prostate epithelial cells transformed by inorganic arsenic or cadmium. *Toxicol Appl Pharmacol* (2015) 286(3):159–67. doi: 10.1016/j.taap.2015.04.011

48. Reyer H, Oster M, Wittenburg D, Murani E, Ponsuksili S, Wimmers K. Genetic contribution to variation in blood calcium, phosphorus, and alkaline phosphatase activity in pigs. *Front Genet* (2019) 10:590. doi: 10.3389/fgene.2019.00590

49. Somogyi V, Gyorffy A, Scalise TJ, Kiss DS, Goszleth G, Bartha T, et al. Endocrine factors in the hypothalamic regulation of food intake in females: A review of the physiological roles and interactions of ghrelin, leptin, thyroid hormones, oestrogen and insulin. *Nutr Res Rev* (2011) 24(1):132–54. doi: 10.1017/S0954422411000035

50. Teumer A, Chaker L, Groeneweg S, Li Y, Di Munno C, Barbieri C, et al. Genome-wide analyses identify a role for SLC17A4 and AADAT in thyroid hormone regulation. *Nat Commun* (2018) 9(1):4455. doi: 10.1038/s41467-018-06356-1

51. Chang CH, Qiu J, O'Sullivan D, Buck MD, Noguchi T, Curtis JD, et al. Metabolic competition in the tumor microenvironment is a driver of cancer progression. *Cell* (2015) 162(6):1229–41. doi: 10.1016/j.cell.2015.08.016

52. Wang Y, Wang Y, Ren Y, Zhang Q, Yi P, Cheng C. Metabolic modulation of immune checkpoints and novel therapeutic strategies in cancer. *Semin Cancer Biol* (2022) S1044-579X(22)00031-1. doi: 10.1016/j.semcancer.2022.02.010

53. Doroshow DB, Sanmamed MF, Hastings K, Politi K, Rimm DL, Chen L, et al. Immunotherapy in non-small cell lung cancer: Facts and hopes. *Clin Cancer Res* (2019). doi: 10.1158/1078-0432.CCR-18-1538

54. Thienger P, Rubin MA. Prostate cancer hijacks the microenvironment. *Nat Cell Biol* (2021). doi: 10.1038/s41556-020-00616-3

55. Pala L, De PT, Conforti F. Spotlight boosting anticancer immunotherapy through androgen receptor blockade. *Cancer Cell* (2022) 40:455–7. doi: 10.1016/j.ccell.2022.04.007

56. Cristescu R, Aurora-Garg D, Albright A, Xu L, Liu XQ, Loboda A, et al. Tumor mutational burden predicts the efficacy of pembrolizumab monotherapy: A pan-tumor retrospective analysis of participants with advanced solid tumors. *J Immunother Cancer* (2022). doi: 10.1136/jitc-2021-003091

57. Carbone DP, Reck M, Paz-Ares L, Creelan B, Horn L, Steins M, et al. First-line nivolumab in stage IV or recurrent non–Small-Cell lung cancer. *N Engl J Med* (2017). doi: 10.1056/nejmoa1613493

58. Zhou L, Fan R, Luo Y, Zhang C, Jia D, Wang R, et al. A metabolism-related gene landscape predicts prostate cancer recurrence and treatment response. *Front Immunol* (2022) 13:837991. doi: 10.3389/fimmu.2022.837991

59. Feng D, Shi X, Zhang F, Xiong Q, Wei Q, Yang L. Energy metabolism-related gene prognostic index predicts biochemical recurrence for patients with prostate cancer undergoing radical prostatectomy. *Front Immunol* (2022) 13:839362. doi: 10.3389/fimmu.2022.839362

60. Yu G, Liang B, Yin K, Zhan M, Gu X, Wang J, et al. Identification of metabolism-related gene-based subgroup in prostate cancer. *Front Oncol* (2022) 12:909066. doi: 10.3389/fonc.2022.909066

61. Zou Z, Liu R, Liang Y, Zhou R, Dai Q, Han Z, et al. Identification and validation of a PPP1R12A-related five-gene signature associated with metabolism to predict the prognosis of patients with prostate cancer. *Front Genet* (2021) 12:703210. doi: 10.3389/fgene.2021.703210

frontiers | Frontiers in Immunology

TYPE Original Research
PUBLISHED 27 October 2022
DOI 10.3389/fimmu.2022.1040256

Check for updates

OPEN ACCESS

EDITED BY
Jian Zhang,
Southern Medical University, China

REVIEWED BY
Ada Hang-Heng Wong,
Independent Researcher, Macau, Macau SAR, China
Rensheng Wan,
Hannover Medical School, Germany

*CORRESPONDENCE
Xiaodong Zheng
zhxdd@ustc.edu.cn
Rui Sun
sunr@ustc.edu.cn

SPECIALTY SECTION
This article was submitted to Cancer Immunity and Immunotherapy, a section of the journal Frontiers in Immunology

RECEIVED 09 September 2022
ACCEPTED 13 October 2022
PUBLISHED 27 October 2022

CITATION
Fang Y, Sun H, Xiao X, Tang M, Tian Z, Wei H, Sun R and Zheng X (2022) Low-dose immunogenic chemotherapeutics promotes immune checkpoint blockade in microsatellite stability colon cancer.
Front. Immunol. 13:1040256.
doi: 10.3389/fimmu.2022.1040256

COPYRIGHT
© 2022 Fang, Sun, Xiao, Tang, Tian, Wei, Sun and Zheng. This is an open-access article distributed under the terms of the Creative Commons Attribution License (CC BY). The use, distribution or reproduction in other forums is permitted, provided the original author(s) and the copyright owner(s) are credited and that the original publication in this journal is cited, in accordance with accepted academic practice. No use, distribution or reproduction is permitted which does not comply with these terms.

Low-dose immunogenic chemotherapeutics promotes immune checkpoint blockade in microsatellite stability colon cancer

Yuhang Fang[1,2], Haoyu Sun[1,2], Xinghui Xiao[1,2], Maoxing Tang[1,2], Zhigang Tian[1,2], Haiming Wei[1,2], Rui Sun[1,2]* and Xiaodong Zheng[1,2]*

[1]Hefei National Research Center for Physical Sciences at Microscale, the CAS Key Laboratory of Innate Immunity and Chronic Disease, School of Basic Medical Sciences, Division of Life Sciences and Medicine, University of Science and Technology of China, Hefei, China, [2]Institute of Immunology, University of Science and Technology of China, Hefei, China

More than 85% of colorectal cancer (CRC) patients, who are with microsatellite stability (MSS), are resistant to immune checkpoint blockade (ICB) treatment. To overcome this resistance, combination therapy with chemotherapy is the most common choice. However, many CRC patients do not benefit more from combination therapy than chemotherapy alone. We hypothesize that severe immunosuppression, caused by chemotherapy administered at the maximum tolerated dose, antagonizes the ICB treatment. In this study, we found that low-dose oxaliplatin (OX), an immunogenic cell death (ICD)-induced drug, increased the antitumor response of TIGIT blockade against CT26 tumor, which is regarded as a MSS tumor. Combined treatment with OX and TIGIT blockade fostered $CD8^+$ T-cell infiltration into tumors and delayed tumor progression. Importantly, only low-dose immunogenic chemotherapeutics successfully sensitized CT26 tumors to TIGIT blockade. In contrast, full-dose OX induces severe immunosuppression and impaired the efficacy of combination therapy. Further, we also found that lack of synergy between nonimmunogenic chemotherapeutics and TIGIT blockade. Consequently, this study suggests that the strategies of combination treatment of chemotherapy and ICB should be re-evaluated. The chemotherapeutics should be chosen for the potential to ICD and the dosage and regimen should be also optimized.

KEYWORDS

TIGIT blockade, immunogenic chemotherapeutics, immunogenic cell death, colon cancer, microsatellite stability

Abbreviations: CRC, colorectal cancer; ICB, immune checkpoint blockade; OX, oxaliplatin; CIS, cisplatin; TIL, tumor-infiltrating lymphocyte; ICD, immunogenic cell death; MTD, maximum tolerated dose; dMMR, mismatch repair deficient; MSI, microsatellite instability; pMMR, mismatch repair proficient; MSS, microsatellite stability; mAb, monoclonal antibody; WBC, white blood cell; LYMPH, lymphocyte; RBC, red blood cell; DAPI, 4′,6-diamidino-2-phenylindole; MFI, mean fluorescent intensity, CALR, calreticulin; HMGB1, high mobility group box 1.

Introduction

Colorectal cancer (CRC) is the third highest incidence tumor and the second leading cause of cancer-related deaths in the world (1). The prognosis of patients with CRC remains poor, although early detection through screening has improved the outcome of patients with CRC; approximately 20% of patients still present with metastatic cancer (2), and a further one-third present with early-stage disease but go on to develop metastatic disease with a 5-year survival of only 15% (3). Thus, the development of effective treatments for CRC patients is an urgent need.

Numerous studies have revealed that immune checkpoint blockade (ICB) therapy is one of the most successful approaches against various solid tumors, such as melanoma and non-small cell lung cancer (4). In CRC, PD-1 blockade has been approved for the treatment of heavily mutated tumors that are mismatch repair deficient (dMMR) or have microsatellite instability (MSI) (5–7). However, more than 85% of CRC patients (8), which are mismatch repair proficient (pMMR) or have microsatellite stability (MSS), are not able to benefit from PD-1 blockade therapy (9, 10). In these patients, the lack of tumor mutation and immune cell infiltration has been posited as mechanisms of ICB resistance (8, 11–13). It is important to clarify which strategies can be employed for converting tumor microenvironments lacking immune cell infiltration to those displaying antitumor immunity. Therefore, alternative immunotherapies are required for those patients with pMMR/MSS CRC.

Chemotherapy, the most common treatment for CRC (14, 15), is considered in combination with ICB therapy (16, 17). Conventional chemotherapeutic drugs have been identified based on their capacity to prevent the growth of human tumor cells cultured *in vitro* or transplanted into immunodeficient mice without considering the contribution of the immune system (18). According to this strategy, multiple cytotoxic agents are developed as antitumor drugs, which are not restricted to tumor cells but rather to most normal cells, including immune cells (19). Chemotherapies administered at the maximum tolerated dose (MTD) cause severe immunosuppression, such as lymphopenia and myelosuppression (20), which suggests a possible antagonist between chemotherapy and immunotherapy. However, a few drugs, such as oxaliplatin (OX) (21) and doxorubicin (22), are able to cause immunogenic cell death (ICD) and boost antitumor immunity (23, 24). Therefore, we hypothesize that ICD-induced drugs could enhance ICB therapy and overcome the resistance of pMMR/MSS CRC when administered at low or moderate doses.

It has been reported that TIGIT blockade can enhance the infiltration of T cells and NK cells into weakly immunogenic or metastatic tumors (25). Here, we found that low-dose OX, an ICD-induced drug, increased the antitumor response of TIGIT blockade against CT26 tumor, which is regarded as a pMMR/MSS tumor. Combined treatment with OX and TIGIT blockade fostered $CD8^+$ T-cell infiltration into tumors and delayed tumor progression. Importantly, only low-dose immunogenic chemotherapeutics successfully sensitized CT26 tumors to TIGIT blockade. In contrast, full-dose OX induces severe immunosuppression. Consequently, this study suggests that chemotherapeutic drugs, which should be rationally selected to enhance tumor immunogenicity, can be used to make resistant tumors sensitive to checkpoint blockade therapy. In addition, the dosage and regimen of combined treatment should be also optimized.

Methods

Mice

C57BL/6J and BALB/c mice were purchased from the Shanghai Experimental Animal Center (Shanghai, China). *Rag2*$^{-/-}$ mice were provided by Dr. X. Wang (Inner Mongolia University). All mice were maintained in a specific pathogen free facility and used according to the guidelines for experimental animals at the University of Science and Technology of China. Mice were used between 6 weeks and 8 weeks of age.

Cell lines

The CT26 cell line was purchased from the Cell Bank of the Chinese Academy of Sciences (Shanghai, China). The MC38 cell line was kindly provided by Professor Yangxin Fu from the University of Texas Southwestern Medical Center (Dallas, USA). All cell lines tested negative for mycoplasma contamination.

Tumor models

BALB/c or *Rag*$^{2-/-}$ mice were inoculated subcutaneously with 5×10^4 CT26 cells. C57BL/6J mice were inoculated subcutaneously with 5×10^4 MC38 cells. Eight days later, mice were randomized into different treatment groups and treated with anti-TIGIT (10 mg/kg; purified in-house from 13G6 cell supernatants), oxaliplatin (1.5 or 6 mg/kg; S1224, Selleck), cisplatin (0.25 mg/kg; S1166, Selleck) or isotype-matched control antibody (10 mg/kg; purified in-house from ratserum) by intraperitoneal injection. Tumors were measured every two days by caliper, and tumor volume was calculated as $0.5 \times \text{length} \times \text{width} \times \text{width}$.

Isolation of TILs

TILs were isolated by dissociating tumor tissue in the presence of collagenase IV (0.1% w/v, Sigma) and DNAse I

(0.005% w/v, Sigma) for 1 h before centrifugation on a discontinuous Percoll gradient (GE Healthcare, Little Chalfont, UK). Isolated cells were then used in various assays to evaluate the phenotype and function of NK cells and T cells and to calculate their absolute numbers.

Antibodies and flow cytometry

Monoclonal antibodies to mouse TIGIT were purified in-house from hybridoma cell (13G6) supernatants (25). The isotype-matched control antibodies (rat IgG) were purified in-house from rat serum. Anti-CD8β antibody (53-5.8) was purchased from Bio X Cell (Lebanon, USA). Rabbit anti-ASGM1 was purchased from Wako Pure Chemicals. The following reagents were used: PE-conjugated antibodies to mouse Granzyme B (16G6, eBioscience, San Diego, USA) and FasL (MFL3, BD Pharmingen, San Diego, USA); PerCP-CY5.5-conjugated antibody to mouse CD3ϵ (145-2C11, BioLegend, San Diego, USA), CD49b(DX5, BioLegend, San Diego, USA) and TRAIL (N2B2, BioLegend, San Diego, USA); PE-Cy7-conjugated antibodies to mouse NKp46(29A1.4, eBioscience, San Diego, USA); APC-conjugated antibodies to mouse Perforin (eBioOMAK-D, eBioscience, San Diego, USA); BV421-conjugated antibodies to mouse CD49b(DX5, BD Pharmingen, San Diego, USA) and TNF-α (MP6-XT22, BioLegend, San Diego, USA); BV510-conjugated antibody to mouse CD45(30-F11, BD Pharmingen, San Diego, USA); BV605-conjugated antibody to mouse CD3ϵ (145-2C11, BD Pharmingen, San Diego, USA); BV786-conjugated antibody to mouse IFN-γ (XMG1.2, BD Pharmingen, San Diego, USA); BUV395-conjugated antibody to mouse CD3ϵ (145-2C11, BD Pharmingen, San Diego, USA) and TCRβ(H57-597, BD Pharmingen, San Diego, USA); BUV563-conjugated antibody to mouse CD4 (GK1.5, BD Pharmingen, San Diego, USA); BUV737-conjugated antibody to mouse CD8α (53-6.7, BD Pharmingen, San Diego, USA).

Blood cell count

Fresh blood samples were collected from the posterior orbital venous plexus of the mice in a heparin-containing polypropylene tube. The whole blood count was enumerated using Automated Hematology Analyzer (XT-1800i, Sysmex).

In vivo cell depletion

For depletion of $CD8^+$ T cells, mice were given an intraperitoneal injection of 200 μg mAb against CD8β (53-5.8, Bio X Cell, Lebanon, USA) 72 h before challenge, and after challenge, the antibodies were injected once weekly. For depletion of NK cells, anti-ASGM1 was injected intravenously 72 h before challenge, and after challenge, the antibody was injected every 7 d.

CALR expression analysis

After treatment with oxaliplatin (10μM or 100 μM) or cisplatin (100 μM) for 4 h, CT26 cells were collected, washed twice with PBS and fixed in 0.25% paraformaldehyde in PBS for 5 min. After washing again twice in cold PBS, cells were incubated with the anti-calreticulin antibody (Abcam, ab2907) for 30 min at 4 °C, diluted in cold blocking buffer (2% fetal bovine serum in PBS), followed by washing and incubation with Alexa Fluor Plus 488-conjugated goat anti-rabbit antibody (A32731; Thermo Fisher Scientific) for 30 min at 4 °C. Each sample was then analyzed by flow cytometry on a FACS Celesta flow cytometer (BD Biosciences). Isotype-matched IgG antibodies were used as a control. The data were analyzed using FlowJo software (Tree Star).

Immunofluorescence

After treatment with oxaliplatin (10μM or 100 μM) or cisplatin (100 μM) for 4 h, CT26 cells were placed on ice, washed twice with PBS and fixed in 0.25% paraformaldehyde in PBS for 5 min. Then the cells were washed twice in PBS, and stained with primary antibodies against CALR (Abcam, ab2907) for 30 min at 4 °C. After three washes in cold PBS, the cells were incubated for 30 min with Alexa Fluor Plus 488-conjugated goat anti-rabbit antibody (A32731; Thermo Fisher Scientific). Subsequently, the cells were fixed with 4% paraformaldehyde for 20 min. All slides were stained with 4′,6-diamidino-2-phenylindole (DAPI, Thermo Fisher Scientific) for 4 min and mounted on coverslips in ProLong™ Gold antifade solution (Thermo Fisher Scientific). Slides were visualized using an LSM880 confocal laser scanning microscope (Zeiss, Oberkochen, Germany).

Enzyme-linked immunosorbent assay

The supernatants of CT26 cells were collected after treating with oxaliplatin (10μM or 100 μM) or cisplatin (100 μM) for 24 h. HMGB1 proteins were measured using the mouse HMGB1 ELISA KiT (NBP2-62767, Novus), according to the manufacturer's instructions.

Statistical analysis

Statistical analyses were performed in GraphPad Prism (La Jolla, USA) using appropriate tests as indicated in the legends (unpaired two-tailed t test, paired two-tailed t test, one-way ANOVA followed by Tukey's multiple comparisons test or two-way ANOVA), with significant differences marked in all figures. Significance levels were defined as ns (not significant, $p > 0.05$), * $p < 0.05$, ** $p < 0.01$, *** $p < 0.001$, and **** $p < 0.0001$.

Result

Low-dose oxaliplatin improves TIGIT blockade immunotherapy against colon tumors

In the previous reports, OX and TIGIT blockade were recommended for locally advanced or metastatic colon cancer, respectively (26, 27). Here, we investigated the synergistic antitumor response of OX and anti-TIGIT mAb in MSS CRC. BALB/c mice were subcutaneously injected with murine MSS CT26 colon tumor cells (28), followed by treatment with rat IgG, anti-TIGIT mAb (10 mg/kg), OX (1.5 mg/kg) or anti-TIGIT mAb plus OX on day 8 post-tumor challenge (Figure 1A). In our setting, OX alone did not exert any therapeutic effect; however, as expected, anti-TIGIT mAb alone showed a slight inhibition of tumor growth but failed to extend the survival of CT26-bearing mice. Although OX monotherapy was inefficient, it could synergize with anti-TIGIT immunotherapy. Combination therapy with anti-TIGIT and OX suppressed tumor growth and significantly increased survival (Figures 1B, C). Smaller volumes and weights of tumors were observed on day 21 after tumor challenge in mice treated with anti-TIGIT and OX (Figures 1D, E). These phenomena were further verified in MC38-bearing mice (Figure 1F). Combination therapy with anti-TIGIT and OX delayed tumor growth and prolonged overall survival significantly; nevertheless, anti-TIGIT or OX monotherapy was inefficacy (Figures 1G, H).

Platinum-based MTD chemotherapy has long been used as a first-line tumor therapy, including combination with ICB therapy. To assess whether MTD OX could enhance the efficacy of TIGIT blockade, intraperitoneal injection of OX at a dose of 6 mg/kg was repeated every 6 days for a total of 3 cycles with or without anti-TIGIT mAb (Figure 2A). Although MTD OX reduced tumor growth and increased overall survival in CT26-bearing mice, as expected, it failed to synergize with anti-TIGIT therapy (Figures 2B, C). We hypothesized that OX, as a chemotherapeutic drug, induced severe immunosuppression even if it could suppress the proliferation of tumor cells by itself. To verify this, the injection frequency of OX was decreased from 3 to 1 (Figure 2D). We observed that a single injection of full-dose OX (6 mg/kg) could not reduce tumor growth. Moreover, the synergistic antitumor effects of the combination therapy were not observed (Figures 2E, F). When the dose of oxaliplatin was reduced from 6 mg/kg to 1.5 mg/kg, the synergism of the combination treatment was observed; nevertheless, a single injection of low-dose OX or anti-TIGIT could not delay tumor growth or increase overall survival (Figures 2E, F). Decreased tumor size and weight were also observed on day 21 after tumor challenge in mice treated together with anti-TIGIT mAb and single-injection low-dose OX (Figures 2G, H). These results suggest that single-injection low-dose OX, but not full-dose OX, was able to synergize with anti-TIGIT immunotherapy against colon tumors.

Combination treatment with low-dose oxaliplatin and TIGIT elicits an active tumor-immune microenvironment

To explore the possible mechanisms of combination therapy, we compared the numbers and activation of tumor-infiltrating lymphocytes (TILs) in CT26-bearing mice with various treatments. Mice were sacrificed at day 21 after tumor challenge, and TILs were isolated and analyzed. The absolute number of $CD45^+$ TILs increased significantly in mice treated with anti-TIGIT mAb plus low-dose OX (Figure 3A). Furthermore, combination therapy also increased the absolute number of tumor-infiltrating $CD8^+$ T cells (Figure 3B). Tumor-bearing mice treated with combination therapy showed higher amounts of $CD8^+$ TILs that expressed IFN-γ, Granzyme B, Perforin, TNF-α, TRAIL and FasL than untreated mice, OX or TIGIT mAb alone (Figure 3C). These results suggested that combination therapy with TIGIT blockade and low-dose oxaliplatin increased the numbers and activation of $CD8^+$ TILs, induced an active tumor-immune microenvironment.

To investigate the reason why full-dose OX and TIGIT blockade had no synergism, CT26-bearing mice were treated with full-dose (6 mg/kg) or low-dose (1.5 mg/kg) OX, together with anti-TIGIT mAb. In the mice that received full-dose (6 mg/kg) OX treatment with or without anti-TIGIT mAb for 2 days, significant reductions in body weight, white blood cells (WBCs) and peripheral blood lymphocytes were observed (Figures 4A, B). The absolute numbers of $CD45^+$ TILs and $CD8^+$ TILs were also decreased significantly (Figure 4C). In contrast, the body weights were moderately increased in tumor-bearing mice treated with 1.5 mg/kg OX (Figure 4A). The numbers of white blood cells, peripheral blood lymphocytes, $CD45^+$ TILs and $CD8^+$ TILs were similar to those in untreated mice (Figures 4B, C). These findings indicated that full-dose OX, but not low-dose OX, induced severe immunosuppression and impaired the efficacy of combination therapy.

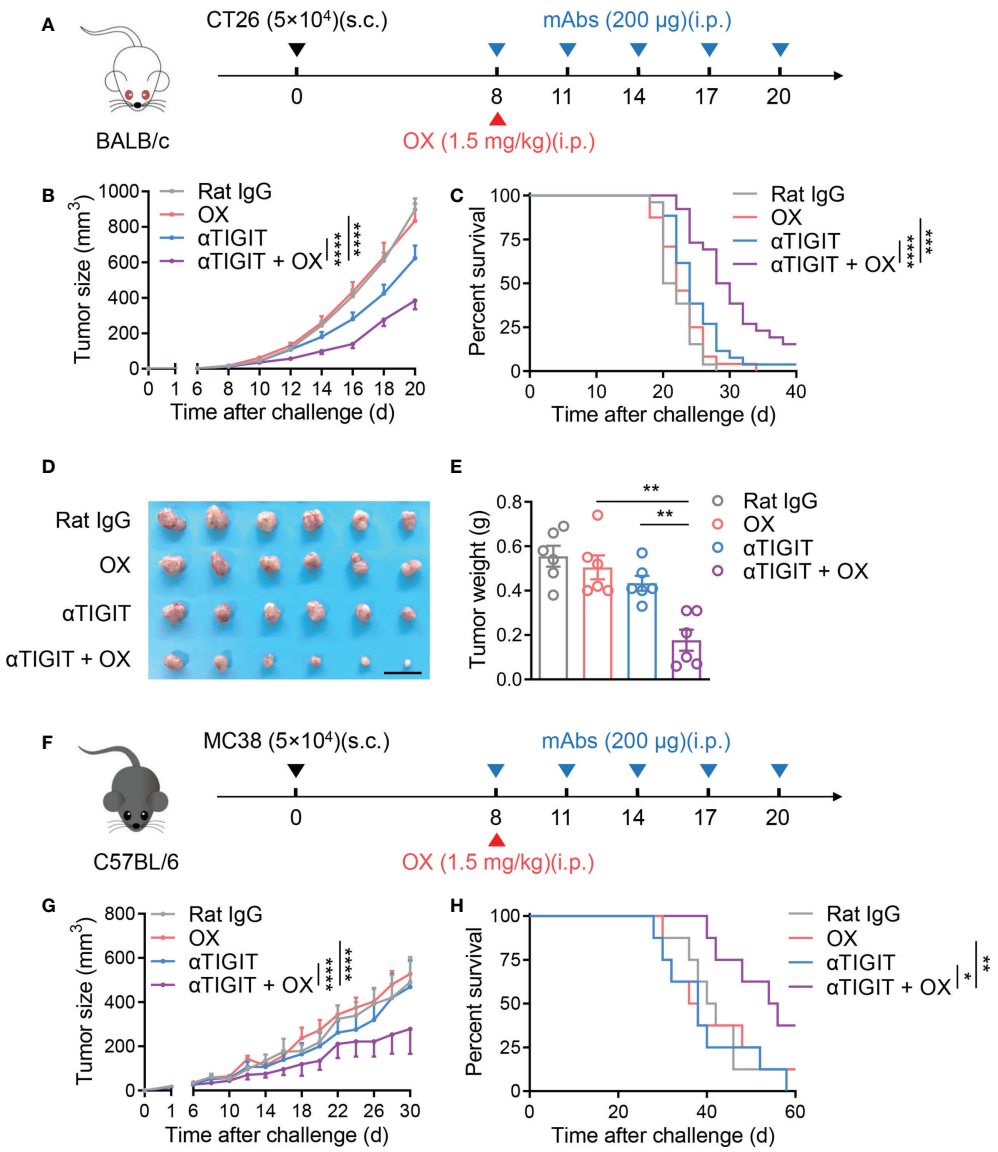

FIGURE 1
Low-dose oxaliplatin improves colon cancer immunotherapy of anti-TIGIT mAb. **(A)**, Experimental scheme for CT26 colon cancer model used in **(B–E)**. Mice were given injection of Rat IgG, anti-TIGIT mAb (10 mg/kg), oxaliplatin (OX, 1.5 mg/kg) or anti-TIGIT mAb plus OX intraperitoneally (i.p.) at various times after injection of 5×10^4 CT26 tumor cells subcutaneously (s.c.) on day 0. **(B)**, Tumor size measurement at each time point. (n=16-20 mice per group). **(C)**, Overall survival of CT26-bearing mice with various treatments. **(D)**, Representative photograph and **(E)** weight of tumor (n = 6 per group) on day 21 after challenge. Scale bar represents 2 cm. **(F)**, Experimental scheme for MC38 colon cancer model used in **(G, H)**. Mice were given injection of Rat IgG, anti-TIGIT mAb, OX or anti-TIGIT mAb plus OX intraperitoneally (i.p.) at various times after injection of 5×10^4 MC38 tumor cells subcutaneously (s.c.) on day 0. **(G)**. Tumor size measurement at each time point. (n=6-8 mice per group) **(H)**, Overall survival of MC38-bearing mice with various treatments. Data were representative of at least two independent experiments. Error bars represent means ± SEM. Statistical significance was determined using two-way ANNOVA **(B, G)**, Mantel–Cox test **(C, H)** or one-way ANOVA followed by Tukey's multiple-comparisons **(E)**. *p < 0.05; **p < 0.01; ***p < 0.001 and ****p < 0.0001.

Synergistic efficacy of low-dose oxaliplatin and TIGIT blockade depends on CD8$^+$ T

To further investigate the roles of CD8$^+$ T and NK cells in TIGIT blockade combined with low-dose OX, CD8$^+$ T cells or NK cells in tumor-bearing mice were depleted by treatment with anti-CD8β or anti-ASGM1, respectively (Figures 5A, G). As expected, the deficiency of CD8$^+$ T cells significantly led to accelerated tumor growth, including tumor size (Figure 5B), tumor volume (Figure 5C) and tumor weight (Figure 5D). TIGIT blockade combined with low-dose OX lost the

10.3389/fimmu.2022.1040256

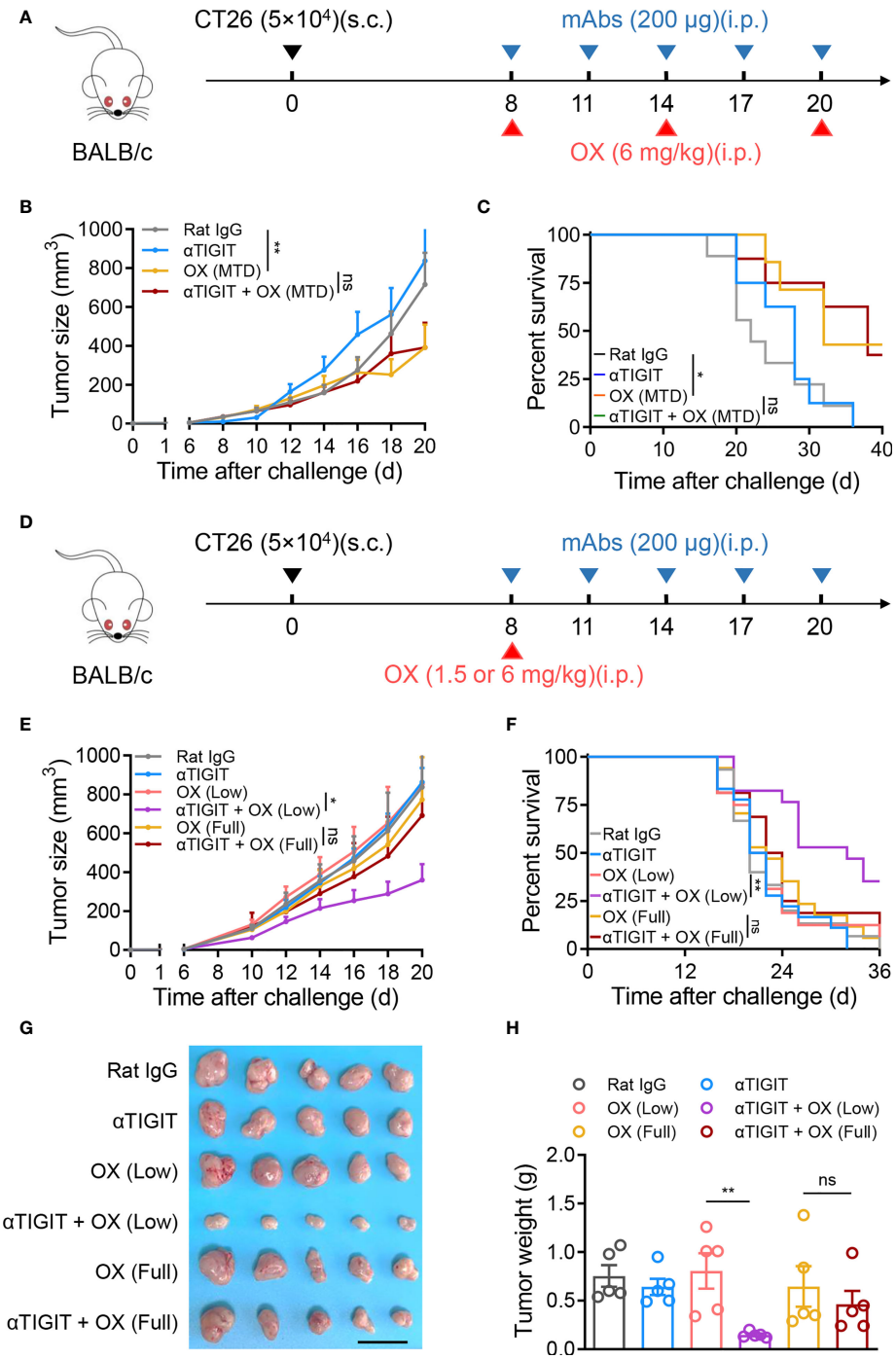

FIGURE 2
No synergistic antitumor activity of full-dose oxaliplatin and anti-TIGIT mAb. **(A)**, Experimental scheme for CT26 colon cancer model used in **(B, C)**. Mice were given injection of Rat IgG, anti-TIGIT mAb (10 mg/kg), OX (6 mg/kg), or anti-TIGIT mAb combined with OX intraperitoneally (*i.p.*) at various times after injection of 5×10^4 CT26 cells subcutaneously (*s.c.*) on day 0. **(B)**, Tumor size measurement at each time point. (n=6-8 mice per group). **(C)**, Overall survival of CT26-bearing mice with various treatments. **(D)**, Experimental scheme for CT26 colon cancer model used in **(E–H)**. Mice were given injection of Rat IgG, anti-TIGIT mAb, various-dose OX or anti-TIGIT mAb combined with various-dose OX intraperitoneally (i.p.) at various times after injection of 5×10^4 CT26 cells subcutaneously (s.c.) on day 0. **(E)**, Tumor size measurement at each time point. (n=6-8 mice per group). **(F)**, Overall survival of CT26-bearing mice with various treatments. **(G)**, Representative photograph and **(H)** weight of tumor (n = 5 per group) on day 21 after challenge. Scale bar represents 2 cm. Data were representative of at least two independent experiments. Error bars represent means ± SEM. Statistical significance was determined using two-way ANNOVA **(B, E)**, Mantel–Cox test **(C, F)** or one-way ANOVA followed by Tukey's multiple-comparisons **(H)**. ns, $p > 0.05$; *$p < 0.05$ and **$p < 0.01$.

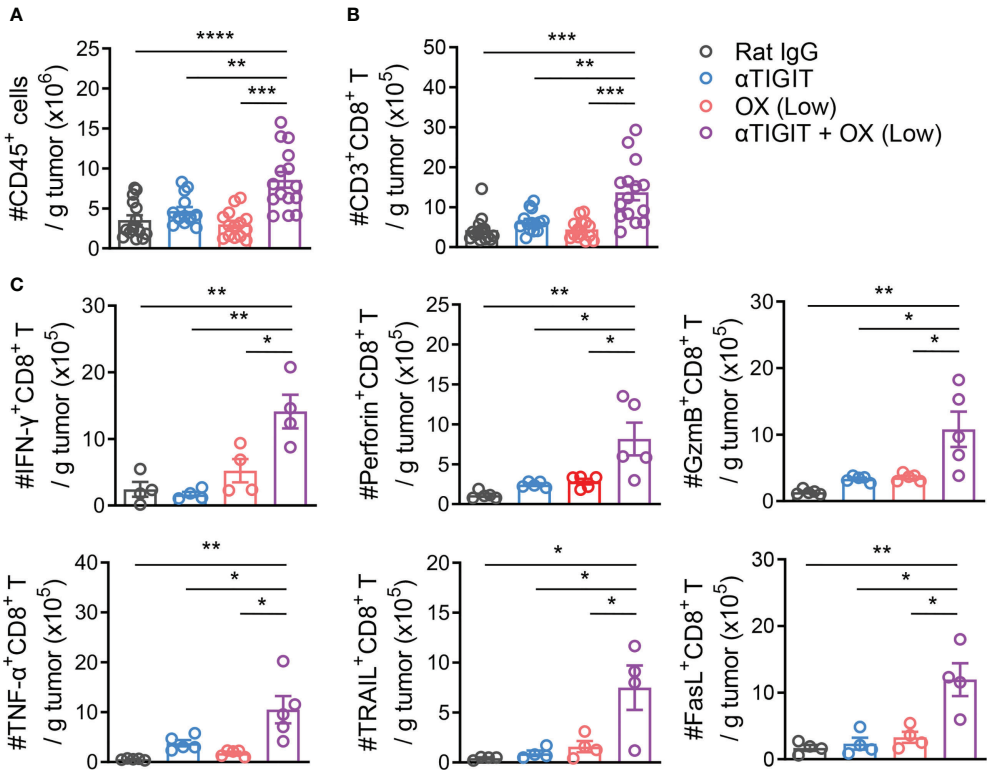

FIGURE 3
Combination treatment with Low-dose Oxaliplatin and TIGIT blockade Increases Tumor Infiltration and Activation of $CD8^+$ T Cells. **(A)**, CT26-bearing mice received various treatments or were left untreated. On day 21 after challenge, tumors were harvested and tumor-infiltrating lymphocytes were isolated. Absolute numbers of tumor-infiltrating $CD45^+$ T cells were measured by flow cytometry. **(B)**, Absolute numbers of $CD3^+CD8^+$ T cells measured by flow cytometry from mice as in **(A)**. **(C)**, Absolute numbers of tumor-infiltrating $CD8^+$ T expressing IFN-γ, Perforin, Granzyme B, TNF-α, TRAIL and FasL measured by flow cytometry from mice as in **(A)**. Each symbol represents an individual mouse. Data were representative of at least two independent experiments. Error bars represent means ± SEM. Statistical significance was determined using one-way ANOVA followed by Tukey's multiple-comparisons **(A–C)**. *p < 0.05; **p < 0.01; ***p < 0.001 and ****p < 0.0001.

inhibition of tumor growth in $CD8^+$ T deficient mice compared to that in untreated mice (Figure 5D). Additionally, in *Rag2*$^{-/-}$ mice (Figure 5E), combination treatment did not reveal synergistic efficacy on CT26 tumors (Figure 5F). The reverse results were observed in the NK-cell-depleted mice, where combination treatment could control tumor growth (Figure 5H). In other words, there were some synergies between low-dose OX and anti-TIGIT mAb, even if the absence of NK cells. These findings indicated that the therapeutic efficacy of combination treatment depends on $CD8^+$ T cells.

Lack of synergy between nonimmunogenic chemotherapeutics and TIGIT blockade

Finally, we investigated whether other low-dose chemotherapeutic drugs could also synergize with TIGIT blockade. Cisplatin (CIS), a platinum-based drug, has been used in the treatment of various types of tumors including colon cancer. In our study, CT26-bearing mice were treated with low-dose cisplatin and anti-TIGIT mAb on day 8 posttumor challenge (Figure 6A). We found that CIS treatment alone provided minimal control of CT26 tumor progression, similar to OX treatment. Furthermore, low-dose CIS treatment combined with anti-TIGIT mAb did not delay tumor progression or increase overall survival (Figures 6B, C). These results suggested that OX, but not CIS, could synergize with TIGIT blockade, even if they were both platinum-based drugs.

Considering that low-dose OX, but not CIS, showed synergistic antitumor effects with TIGIT blockade, we hypothesized that low-dose OX sensitized colon tumors to checkpoint blockade therapy. Therefore, CT26 cells were treated with various dose OX or CIS *in vitro*. High mobility group box 1 (HMGB1) release and calreticulin (CALR) exposure were used as surrogate markers for drug-induced immunogenic death (29). After 4 h of stimulation, CT26 cells treated with OX,

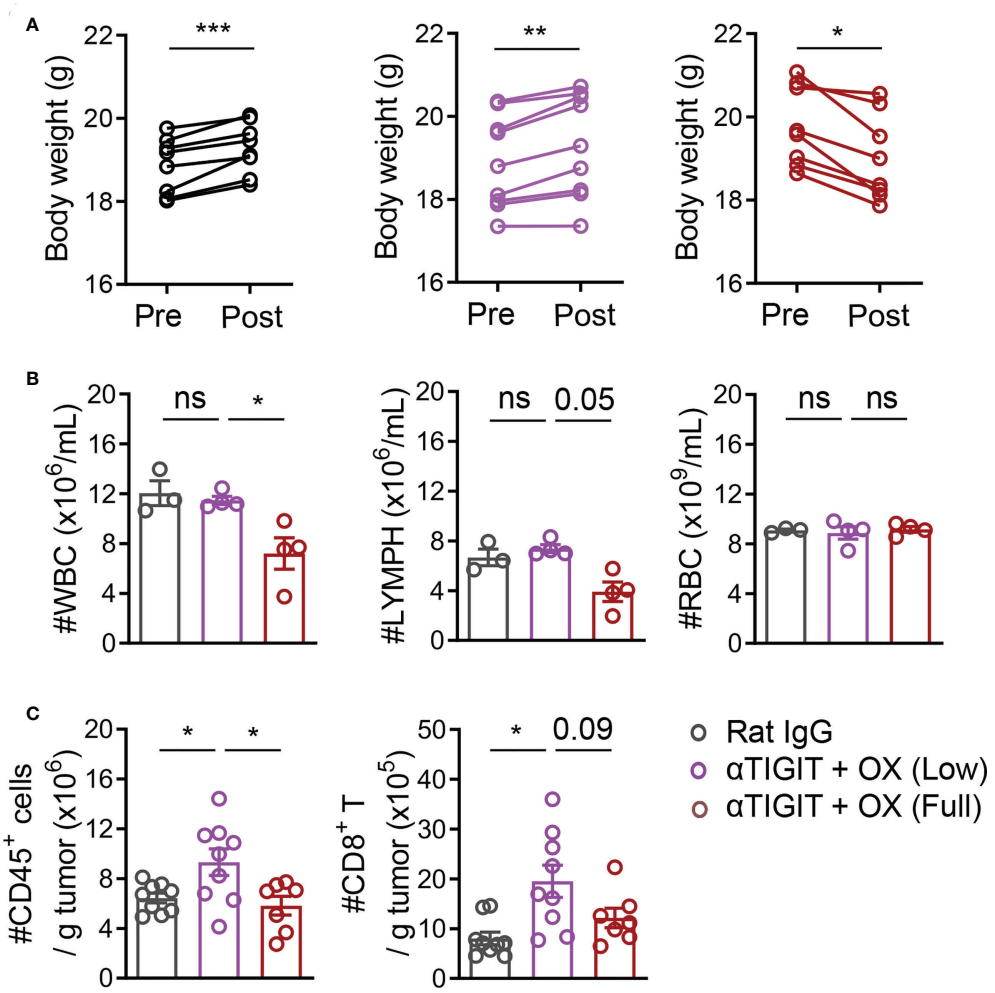

FIGURE 4
Full-dose oxaliplatin induces greater immunosuppression. **(A)**, Body weight in CT26-bearing mice before or after treatment with Rat IgG, anti-TIGIT mAbs plus various-dose OX for 2 days. **(B)**, The counts of WBC (left), Lymph (mid) and RBC (right) in peripheral blood of CT26-bearing mice. **(C)**, Absolute numbers of tumor-infiltrating $CD45^+$ cells and $CD8^+$ T cells. Each symbol represents an individual mouse. Data were representative of at least two independent experiments. Error bars represent means ± SEM. Statistical significance was determined using paired two-tailed t test **(A)** or one-way ANOVA followed by Tukey's multiple-comparisons **(B, C)**. ns, $p > 0.05$; *$p < 0.05$; **$p < 0.01$ and ***$p < 0.001$.

but not CIS, exposed CALR on the cell surface as determined by immunofluorescence staining (Figure 7A) and flow cytometric analysis (Figure 7B), and released higher levels of HMGB1 (Figure 7C). These data demonstrated that OX could induce immunogenic death of tumor cells, which might sensitize tumors to TIGIT blockade therapy.

Discussion

In recent years, combination therapies of ICB and chemotherapeutics have been clinically approved for various tumors. Nevertheless, many patients have no more benefit from combination therapies than chemotherapy alone (30–35). In this study, we found that low-dose OX, combined with TIGIT blockade, triggered a synergistic antitumor response in CT26-bearing mice. In contrast, full-dose OX induced more severe immunosuppression and impaired the efficacy of combination therapy. In addition, we reported that selected immunogenic chemotherapeutics could sensitize colon cancer to ICB therapy. The synergistic antitumor response initiated by the immunogenic chemotherapeutics depended on $CD8^+$ T cells.

Despite severe side effects, MTD chemotherapy regimen is still a standard therapy of various tumors (36). Therefore,

10.3389/fimmu.2022.1040256

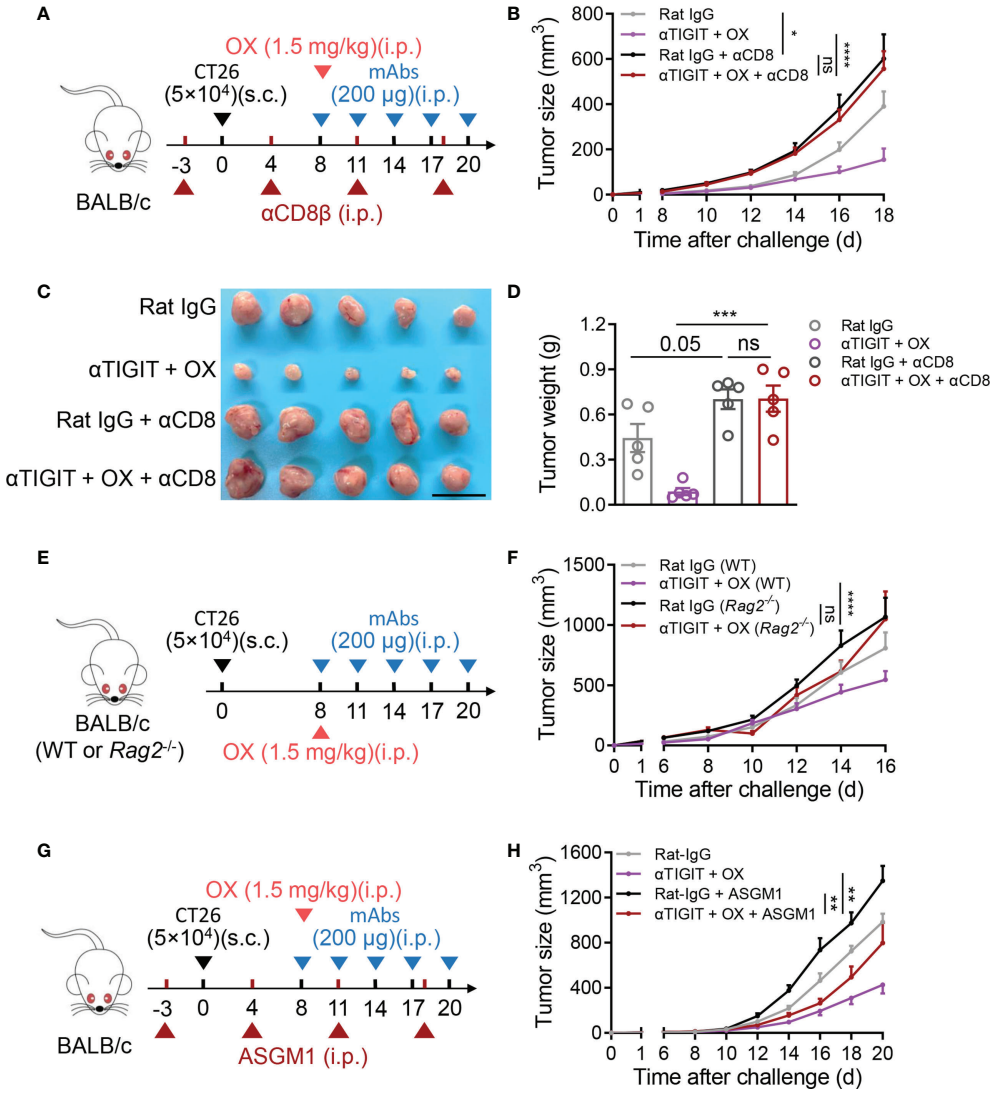

FIGURE 5
Deficiency of $CD8^+$ T cells impairs synergistic antitumor efficacy of low-dose oxaliplatin and anti-TIGIT. **(A)**, Experimental scheme for CT26 colon cancer model used in **(B–D)**. Mice were given injection of Rat IgG or anti-TIGIT (10 mg/kg) combined with OX (1.5 mg/kg) intraperitoneally (i.p.) at various times after injection of 5×10^4 CT26 cells subcutaneously (s.c.) on day 0 and weekly injection of anti-CD8β mAbs intraperitoneally (i.p.) on day -3. **(B)**, Tumor size measurement at each time point (n = 9 mice per group). **(C)**, Representative photograph and **(D)** weight of tumor on day 18 after challenge. Scale bar represents 2 cm. (n = 9 mice per group). **(E)**, Experimental scheme for CT26 colon tumor model used in **(F)** BALB/c WT or BALB/c *Rag2*$^{-/-}$ mice were given injection of Rat IgG or anti-TIGIT (10 mg/kg) combined with OX (1.5 mg/kg) intraperitoneally (i.p.) at various times after injection of 5×10^4 CT26 cells subcutaneously (s.c.) on day 0. **(F)**, Tumor size measurement at each time point (n = 9 mice per group). **(G)**, Experimental scheme for CT26 colon tumor model used in **(B)** Mice were given injection of Rat IgG or anti-TIGIT (10 mg/kg) combined with OX (1.5 mg/kg) intraperitoneally (i.p.) at various times after injection of 5×10^4 CT26 cells subcutaneously (s.c.) on day 0 and weekly injection of anti-ASGM1 intraperitoneally (i.p.) on day -3. **(H)**, Tumor size measurement at each time point (n = 8-10 mice per group). Data were representative of at least two independent experiments. Error bars represent means ± SEM. Statistical significance was determined using two-way ANNOVA **(B, F, G)**, one-way ANOVA followed by Tukey's multiple-comparisons **(D)**. ns, $p > 0.05$; *$p < 0.05$; **$p < 0.01$; ***$p < 0.001$ and ****$p < 0.0001$.

MTD chemotherapy is also the top choice of combination therapy based on ICB. For colon cancer, FOLFOX (5-fluorouracil, L-leucovorin plus oxaliplatin) and XELOX (oxaliplatin plus capecitabine) regimens were clinically approved in the 2000s (37). These chemotherapeutic drugs interfere with cell proliferation by targeting DNA/RNA synthesis and cellular metabolism. Since they have no specificity, these drugs impair not only tumor cells but also

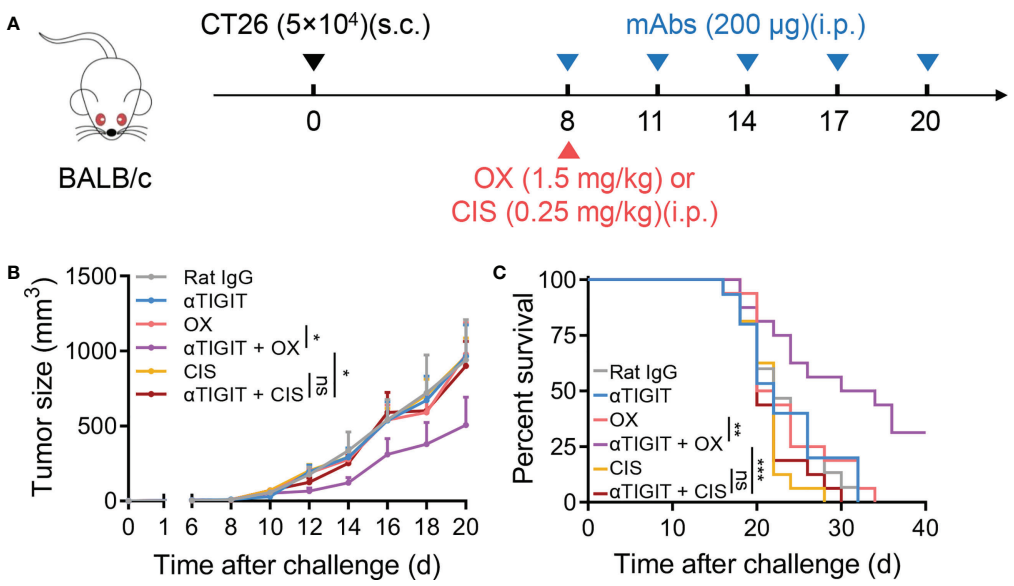

FIGURE 6
Low-dose cisplatin fails to promote anti-TIGIT mAb treatment against CT26 colon cancer. **(A)**, Experimental scheme for CT26 colon cancer model used in **(B, C)**: mice were given injection of Rat IgG, anti-TIGIT (10 mg/kg), OX (1.5 mg/kg), anti-TIGIT combined with OX, cisplatin (CIS, 0.25 mg/kg) or anti-TIGIT combined with CIS intraperitoneally (*i.p.*) after injection of 5×10^4 CT26 tumor cells subcutaneously (*s.c.*) on day 0. **(B)**, Tumor size measurement at each time point. (n=15-17 mice per group). **(C)**, Overall survival of CT26-bearing mice with various treatments. (n=7 or 8 mice per group). Data were representative of at least two independent experiments. Error bars represent means ± SEM. Statistical significance was determined using two-way ANNOVA **(B)** or Mantel–Cox test **(C)**. ns, $p > 0.05$; *$p < 0.05$; **$p < 0.01$ and ***$p < 0.001$.

lymphocytes. On the other hand, the efficacy of ICB therapy depends on the tumor infiltration of lymphocytes (38). Lymphopenia, the common side effect of MTD chemotherapy, limits the outcome of ICB. This is a possible reason why the patients did not benefit more from combination treatment of chemotherapy and ICB. In this study, we tried to improve the efficacy of combination treatment by reducing the toxicity of chemotherapy. We found that low-dose OX could not induce body weight loss or lymphocyte decrease. Importantly, it was able to sensitize tumor cells to TIGIT blockade therapy, although low-dose OX alone failed to inhibit the growth of tumor cells. These findings suggested that the dosage or regimen of chemotherapy should be optimized when it combined with ICB therapy. The balance of tumor cell sensitization and immunosuppression requires further investigation.

Due to the lack of lymphocyte infiltration, pMMR/MSS CRC patients are resistant to ICB therapy (39). Chemotherapy, as the first-line treatment for pMMR/MSS CRC patients, was chosen to overcome this resistance. Chemotherapeutic drugs reduce the growth of tumor cells by inducing cell death (40). The predominant type of drug-induced cell death is apoptosis, which is frequently nonimmunogenic or tolerogenic. Thus, most chemotherapeutic drugs fail to boost antitumor immune responses. However, several drugs, such as oxaliplatin and doxorubicin, induce immunogenic tumor cell death and increase $CD8^+$ T-cell infiltration by releasing antigens and causing inflammation in the tumor microenvironment (41). These agents might transform ‘‘cold’’ tumors into immunologic “hot” environments and reverse resistance to ICB in pMMR/MSS CRC patients. We found that OX sensitized CT26 tumors, which was regarded as a MSS CRC and resistant to ICB, to TIGIT blockade by improving $CD8^+$ T-cell infiltration. In contrast, CIS, which is a non-ICD-induced platinum-based drugs, failed to overcome this resistance. Our study indicated that the appropriate selection of drugs determined the efficacy of ICB for MSS CRC treatment. The majority of approved chemotherapeutic drugs might not synergize with ICB therapy.

In summary, our findings provided two pieces of evidence that 1) chemotherapeutic drugs should be selected for their ability to induce immunogenicity in tumors and provide synergistic benefits when combined with ICB therapy, and 2)

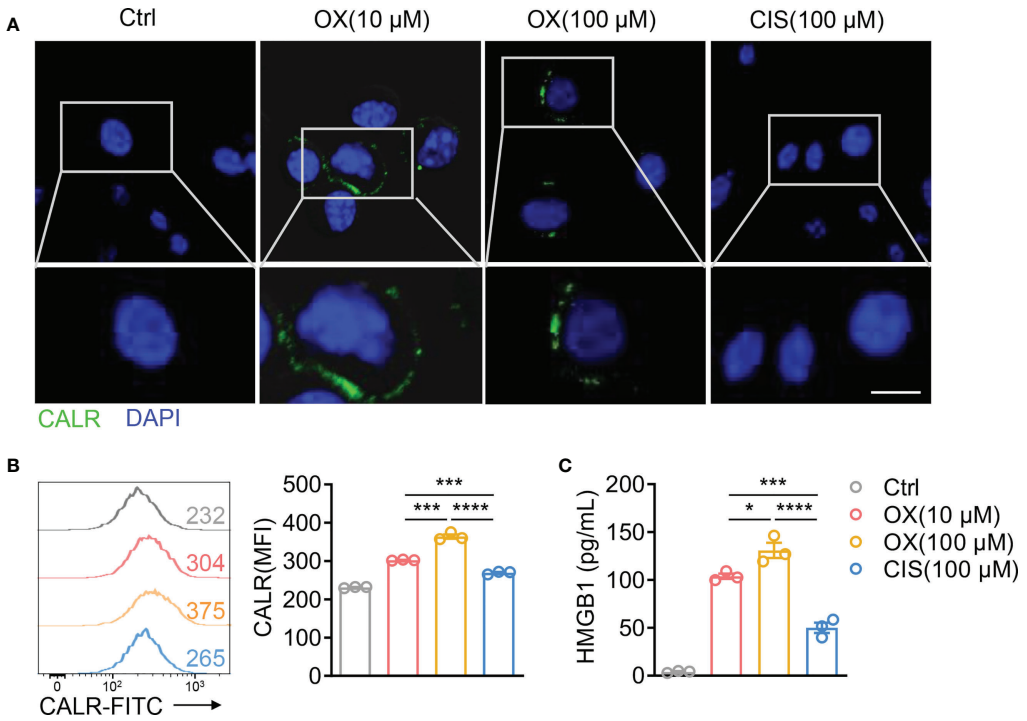

FIGURE 7
Oxaliplatin induces immunogenic cell death of CT26 colon cancer. **(A)**, Representative immunofluorescence staining of calreticulin (CALR) in CT26 cells after treatment with various dose OX or CIS for 4 h. Scale bar represents 10 μm. **(B)**, Representative histogram of CALR expression on CT26 cells after treatment with various dose OX or CIS for 4 h (left). Mean fluorescent intensity (MFI) of CALR expression on CT26 were also shown (right). **(C)**, HMGB1 concentration in the supernatants of CT26 cells treated with various dose OX or CIS for 24 h. Data were representative of at least two independent experiments. Error bars represent means ± SEM. Statistical significance was determined using unpaired two-tailed t-test **(B, C)**. *p < 0.05; ***p < 0.001 and ****p < 0.0001. .

they should be reduced to an appropriate dosage that could sensitize tumors to ICB therapy but not induce immunosuppression. These findings need to be further confirmed in various tumor models. Despite this limitation, our data suggested that the strategies of combination treatment of MSS CRC with chemotherapy and ICB should be re-evaluated. The chemotherapeutic drugs should be chosen for the potential to induce ICD and the dosage and regimen should also be optimized.

Data availability statement

The original contributions presented in the study are included in the article/supplementary material. Further inquiries can be directed to the corresponding authors.

Ethics statement

The animal study was approved by the ethics committee of the University of Science and Technology of China.

Author Contributions

YF, RS, XZ designed the study. YF, XX and MT performed the experiments and analyses. ZT, HS and HW provided advice. YF and XZ wrote and revised the manuscript. ZT, HW, RS, HS and XZ supervised the study. RS and XZ critically reviewed the manuscript. All authors contributed to the article and approved the submitted version.

Funding

This work was supported by National Key R&D Program of China (2019YFA0508502/3, 2018YFA0507403), Strategic Priority Research Program of the Chinese Academy of Science (XDB29030201) and Natural Science Foundation of China (#81788101).

Conflict of interest

The authors declare that the research was conducted in the absence of any commercial or financial relationships that could be construed as a potential conflict of interest.

Publisher's note

All claims expressed in this article are solely those of the authors and do not necessarily represent those of their affiliated organizations, or those of the publisher, the editors and the reviewers. Any product that may be evaluated in this article, or claim that may be made by its manufacturer, is not guaranteed or endorsed by the publisher.

References

1. Sung H, Ferlay J, Siegel RL, Laversanne M, Soerjomataram I, Jemal A, et al. Global cancer statistics 2020: GLOBOCAN estimates of incidence and mortality worldwide for 36 cancers in 185 countries. *CA: Cancer J Clin* (2021) 71:209–49. doi: 10.3322/caac.21660

2. Siegel RL, Miller KD, Goding Sauer A, Fedewa SA, Butterly LF, Anderson JC, et al. Colorectal cancer statistics, 2020. *CA: Cancer J Clin* (2020) 70:145–64. doi: 10.3322/caac.21601

3. Siegel RL, Miller KD, Fuchs HE, Jemal A. Cancer statistics, 2022. *CA: Cancer J Clin* (2022) 72:7–33. doi: 10.3322/caac.21708

4. Morad G, Helmink BA, Sharma P, Wargo JA. Hallmarks of response, resistance, and toxicity to immune checkpoint blockade. *Cell* (2021) 184:5309–37. doi: 10.1016/j.cell.2021.09.020

5. Le DT, Uram JN, Wang H, Bartlett BR, Kemberling H, Eyring AD, et al. PD-1 blockade in tumors with mismatch-repair deficiency. *New Engl J Med* (2015) 372:2509–20. doi: 10.1056/NEJMoa1500596

6. Le DT, Durham JN, Smith KN, Wang H, Bartlett BR, Aulakh LK, et al. Mismatch repair deficiency predicts response of solid tumors to PD-1 blockade. *Science* (2017) 357:409–13. doi: 10.1126/science.aan6733

7. Andre T, Shiu K-K, Kim TW, Jensen BV, Jensen LH, Punt CJA, et al. Pembrolizumab versus chemotherapy for microsatellite instability-high/mismatch repair deficient metastatic colorectal cancer: The phase 3 KEYNOTE-177 study. *J Clin Oncol* (2020) 38:LBA4–4. doi: 10.1200/JCO.2020.38.18_suppl.LBA4

8. Ooki A, Shinozaki E, Yamaguchi K. Immunotherapy in colorectal cancer: Current and future strategies. *J Anus Rectum Colon* (2021) 5:11–24. doi: 10.23922/jarc.2020-064

9. Ruan H, Leibowitz BJ, Zhang L, Yu J. Immunogenic cell death in colon cancer prevention and therapy. *Mol Carcinog* (2020) 59:783–93. doi: 10.1002/mc.23183

10. Du W, Frankel TL, Green M, Zou W. IFNγ signaling integrity in colorectal cancer immunity and immunotherapy. *Cell Mol Immunol* (2022) 19:23–32. doi: 10.1038/s41423-021-00735-3

11. Cancer Genome Atlas N. Comprehensive molecular characterization of human colon and rectal cancer. *Nature* (2012) 487:330–7. doi: 10.1038/nature11252

12. Llosa NJ, Cruise M, Tam A, Wicks EC, Hechenbleikner EM, Taube JM, et al. The vigorous immune microenvironment of microsatellite instable colon cancer is balanced by multiple counter-inhibitory checkpoints. *Cancer Discovery* (2015) 5:43–51. doi: 10.1158/2159-8290.CD-14-0863

13. Giannakis M, Mu XJ, Shukla SA, Qian ZR, Cohen O, Nishihara R, et al. Genomic correlates of immune-cell infiltrates in colorectal carcinoma. *Cell Rep* (2016) 15:857–65. doi: 10.1016/j.celrep.2016.03.075

14. André T, de Gramont A, Vernerey D, Chibaudel B, Bonnetain F, Tijeras-Raballand A, et al. Leucovorin, and oxaliplatin in stage II to III colon cancer: Updated 10-year survival and outcomes according to BRAF mutation and mismatch repair status of the MOSAIC study. *J Clin oncology: Off J Am Soc Clin Oncol* (2015) 33:4176–87. doi: 10.1200/JCO.2015.63.4238

15. Grothey A, Sobrero AF, Shields AF, Yoshino T, Paul J, Taieb J, et al. Duration of adjuvant chemotherapy for stage III colon cancer. *New Engl J Med* (2018) 378:1177–88. doi: 10.1056/NEJMoa1713709

16. Heinemann V, von Weikersthal LF, Decker T, Kiani A, Vehling-Kaiser U, Al-Batran SE, et al. FOLFIRI plus cetuximab versus FOLFIRI plus bevacizumab as first-line treatment for patients with metastatic colorectal cancer (FIRE-3): a randomised, open-label, phase 3 trial, the lancet. *Oncology* (2014) 15:1065–75. doi: 10.1016/S1470-2045(14)70330-4

17. Emens LA, Middleton G. The interplay of immunotherapy and chemotherapy: harnessing potential synergies. *Cancer Immunol Res* (2015) 3:436–43. doi: 10.1158/2326-6066.CIR-15-0064

18. Schirrmacher V. From chemotherapy to biological therapy: A review of novel concepts to reduce the side effects of systemic cancer treatment (Review). *Int J Oncol* (2019) 54:407–19. doi: 10.3892/ijo.2018.4661

19. Shurin MR, Naiditch H, Gutkin DW, Umansky V, Shurin GV. ChemoImmunoModulation: immune regulation by the antineoplastic chemotherapeutic agents. *Curr Med Chem* (2012) 19:1792–803. doi: 10.2174/092986712800099785

20. Harris J, Sengar D, Stewart T, Hyslop D. The effect of immunosuppressive chemotherapy on immune function in patients with malignant disease. *Cancer* (1976) 37:1058–69. doi: 10.1002/1097-0142(197602)37:2+<1058::AID-CNCR2820370813>3.0.CO;2-O

21. Tesniere A, Schlemmer F, Boige V, Kepp O, Martins I, Ghiringhelli F, et al. Immunogenic death of colon cancer cells treated with oxaliplatin. *Oncogene* (2010) 29:482–91. doi: 10.1038/onc.2009.356

22. Casares N, Pequignot MO, Tesniere A, Ghiringhelli FO, Roux SP, Chaput N, et al. Caspase-dependent immunogenicity of doxorubicin-induced tumor cell death. *J Exp Med* (2005) 202:1691–701. doi: 10.1084/jem.20050915

23. van der Most RG, Robinson BW, Lake RA. Combining immunotherapy with chemotherapy to treat cancer. *Discovery Med* (2005) 5:265–70.

24. Kroemer G, Galluzzi L, Kepp O, Zitvogel L. Immunogenic cell death in cancer therapy. *Annu Rev Immunol* (2013) 31:51–72. doi: 10.1146/annurev-immunol-032712-100008

25. Zhang Q, Bi J, Zheng X, Chen Y, Wang H, Wu W, et al. Blockade of the checkpoint receptor TIGIT prevents NK cell exhaustion and elicits potent anti-tumor immunity. *Nat Immunol* (2018) 19(7):723–32. doi: 10.1038/s41590-018-0132-0

26. André T, Boni C, Mounedji-Boudiaf L, Navarro M, Tabernero J, Hickish T, et al. (2004). Oxaliplatin, fluorouracil, and leucovorin as adjuvant treatment for colon cancer, in: *[26]*, , Vol. 350. pp. 2343–51.

27. Johnston RJ, Comps-Agrar L, Hackney J, Yu X, Huseni M, Yang Y, et al. The immunoreceptor TIGIT regulates antitumor and antiviral CD8(+) T cell effector function. *Cancer Cell* (2014) 26:923–37. doi: 10.1016/j.ccell.2014.10.018

28. Castle JC, Loewer M, Boegel S, de Graaf J, Bender C, Tadmor AD, et al. Immunomic, genomic and transcriptomic characterization of CT26 colorectal carcinoma. *BMC Genomics* (2014) 15(1):190. doi: 10.1186/1471-2164-15-190

29. Krysko DV, Garg AD, Kaczmarek A, Krysko O, Agostinis P, Vandenabeele P. Immunogenic cell death and DAMPs in cancer therapy. *Nat Rev Cancer* (2012) 12:860–75. doi: 10.1038/nrc3380

30. Salas-Benito D, Pérez-Gracia JL, Ponz-Sarvisé M, Rodriguez-Ruiz ME, Martínez-Forero I, Castañón E, et al. Paradigms on immunotherapy combinations with chemotherapy. *Cancer Discovery* (2021) 11:1353–67. doi: 10.1158/2159-8290.CD-20-1312

31. Paz-Ares L, Ciuleanu TE, Yu X, Salman P, Pluzanski A, Nagrial A, et al. LBA3 nivolumab (NIVO) + platinum-doublet chemotherapy (chemo) vs chemo as first-line (1L) treatment (tx) for advanced non-small cell lung cancer (aNSCLC): CheckMate 227 - part 2 final analysis. *Ann Oncol* (2019) 30:xi67–8. doi: 10.1093/annonc/mdz453.004

32. Jotte R, Cappuzzo F, Vynnychenko I, Stroyakovskiy D, Rodríguez-Abreu D, Hussein M, et al. Atezolizumab in combination with carboplatin and nab-paclitaxel in advanced squamous NSCLC (IMpower131): Results from a randomized phase III trial. *J Thorac Oncol* (2020) 15:1351–60. doi: 10.1016/j.jtho.2020.03.028

33. Alva A, Csőszi T, Ozguroglu M, Matsubara N, Geczi L, Cheng SYS, et al. LBA23 pembrolizumab (P) combined with chemotherapy (C) vs c alone as first-line (1L) therapy for advanced urothelial carcinoma (UC): KEYNOTE-361. *Ann Oncol* (2020) 31:S1155. doi: 10.1016/j.annonc.2020.08.2252

34. Eng C, Kim TW, Bendell J, Argilés G, Tebbutt NC, Di Bartolomeo M, et al. Atezolizumab with or without cobimetinib versus regorafenib in previously treated metastatic colorectal cancer (IMblaze370): a multicentre, open-label, phase 3, randomised, controlled trial. *Lancet Oncol* (2019) 20:849–61. doi: 10.1016/S1470-2045(19)30027-0

35. Grothey A, Tabernero J, Arnold D, De Gramont A, Ducreux MP, O'Dwyer PJ, et al. LBA19 - fluoropyrimidine (FP) + bevacizumab (BEV) + atezolizumab vs FP/BEV in BRAFwt metastatic colorectal cancer (mCRC): Findings from cohort 2 of MODUL – a multicentre, randomized trial of biomarker-driven maintenance treatment following first-line induction therapy. *Ann Oncol* (2018) 29:viii714–viii715. doi: 10.1093/annonc/mdy424.020

36. Wu J, Waxman DJ. Immunogenic chemotherapy: Dose and schedule dependence and combination with immunotherapy. *Cancer Lett* (2018) 419:210–21. doi: 10.1016/j.canlet.2018.01.050

37. Andre T, Boni C, Mounedji-Boudiaf L, Navarro M, Tabernero J, Hickish T, et al. I. multicenter international study of Oxaliplatin/5-Fluorouracil/Leucovorin in the adjuvant treatment of colon cancer, oxaliplatin, fluorouracil, and leucovorin as adjuvant treatment for colon cancer. *N Engl J Med* (2004) 350:2343–51. doi: 10.1056/NEJMoa032709

38. Paijens ST, Vledder A, de Bruyn M, Nijman HW. Tumor-infiltrating lymphocytes in the immunotherapy era. *Cell Mol Immunol* (2021) 18:842–59. doi: 10.1038/s41423-020-00565-9

39. Baraibar I, Mirallas O, Saoudi N, Ros J, Salvà F, Tabernero J, et al. Combined treatment with immunotherapy-based strategies for MSS metastatic colorectal cancer. *Cancers* (2021) 13:6311. doi: 10.3390/cancers13246311

40. Fabian KP, Wolfson B, Hodge JW. From immunogenic cell death to immunogenic modulation: Select chemotherapy regimens induce a spectrum of immune-enhancing activities in the tumor microenvironment. *Front Oncol* (2021) 11:728018. doi: 10.3389/fonc.2021.728018

41. Wang X, Waschke BC, Woolaver RA, Chen SMY, Chen Z, Wang JH. MHC class I-independent activation of virtual memory CD8 T cells induced by chemotherapeutic agent-treated cancer cells. *Cell Mol Immunol* (2021) 18:723–34. doi: 10.1038/s41423-020-0463-2

frontiers | Frontiers in Immunology

TYPE Systematic Review
PUBLISHED 10 November 2022
DOI 10.3389/fimmu.2022.1039020

Check for updates

OPEN ACCESS

EDITED BY
Jian Zhang,
Southern Medical University, China

REVIEWED BY
Haitao Wang,
National Cancer Institute, (NIH), United States
Hongyun Shi,
Affiliated Hospital of Hebei University, China

*CORRESPONDENCE
Jun Liang
liang23400@163.com

SPECIALTY SECTION
This article was submitted to Cancer Immunity and Immunotherapy, a section of the journal Frontiers in Immunology

RECEIVED 07 September 2022
ACCEPTED 24 October 2022
PUBLISHED 10 November 2022

CITATION
Xu T, Liu Y, Lu X and Liang J (2022) Toxicity profile of combined immune checkpoint inhibitors and thoracic radiotherapy in esophageal cancer: A meta-analysis and systematic review. *Front. Immunol.* 13:1039020. doi: 10.3389/fimmu.2022.1039020

COPYRIGHT
© 2022 Xu, Liu, Lu and Liang. This is an open-access article distributed under the terms of the Creative Commons Attribution License (CC BY). The use, distribution or reproduction in other forums is permitted, provided the original author(s) and the copyright owner(s) are credited and that the original publication in this journal is cited, in accordance with accepted academic practice. No use, distribution or reproduction is permitted which does not comply with these terms.

Toxicity profile of combined immune checkpoint inhibitors and thoracic radiotherapy in esophageal cancer: A meta-analysis and systematic review

Tongzhen Xu[1], Yunsong Liu[1], Xiaotong Lu[1] and Jun Liang[2]*

[1]Department of Radiotherapy Oncology, National Cancer Center/National Clinical Research Center for Cancer/Cancer Hospital, Chinese Academy of Medical Sciences and Peking Union Medical College, Beijing, China, [2]Department of Radiotherapy Oncology, National Cancer Center/National Clinical Research Center for Cancer/Cancer Hospital & Shenzhen Hospital, Chinese Academy of Medical Sciences and Peking Union Medical College, Shenzhen, China

Background: Therapies based on the combination of immune checkpoint inhibitors (ICIs) and thoracic radiotherapy (TRT) are transforming the treatment landscape of esophageal cancer. Nevertheless, the available data on adverse events (AEs) mainly stemmed from several prospective clinical trials and retrospective studies, in which, AE data are often handled and reported with less rigor than the primary beneficial outcomes of the study. Thus, we conducted a systematic review to investigate the toxicity spectrum of these novel regimens.

Method: We searched for all prospective clinical trials investigating the role of ICIs combined with TRT published between January 2010 and August 2022. Study articles and conference proceedings involving esophageal cancers and reporting the overall incidence or details of treatment-related AEs (trAEs) were synthesized to determine the toxicity profile of combination treatment. We compared trAEs between cancer type, programmed cell death 1 (PD-1) and programmed cell death ligand 1 (PD-L1) inhibitors, and between sequential and concurrent administration of ICIs and TRT to identify potentially high-risk patients.

Results: We obtained toxicity data from 14 clinical trials involving 863 patients. The pooled overall incidence was 88.97% for any-grade trAEs and 18.48% for high-grade trAEs. The three most frequent non-hematologic any-grade trAEs were reactive cutaneous capillary endothelial proliferation (RCCEP, 63.80%), esophagitis (51.54%), and fatigue (33.63%). Meanwhile, RCCEP (15.69%) was the most common non-hematologic high-grade trAE, followed by nausea (4.91%) and anorexia (3.81%). The occurrence rates of any-grade and high-grade pneumonitis were 10.82% and 0.66%, respectively. In subgroup analysis, the toxicity profiles of PD-1 and PD-L1 inhibitors were mostly similar, except for any-grade pneumonitis (15.20% vs 4.88%, p=0.03) and high-grade leukopenia (6.25% vs 59.09%, p=0.00). In addition, concurrent treatment seemed to have a

higher incidence of any-grade trAEs (95.20% vs 70.85%, p=0.03) compared with sequential treatment. ESCC seems to have higher incidence of any-grade hypothyroidism (22.55% vs 8.96%, p=0.049) compared to EAC.

Conclusion: Our study is the first systematic review to provide a toxicity profile of trAEs in esophageal cancer patients who received ICIs combined with TRT. Most AEs of this combination treatment are tolerable, although the incidence of any-grade trAEs was higher in the concurrent group. The difference in any-grade pneumonitis between PD-1 and PD-L1 inhibitor groups needs further validation in a large clinical trial.

KEYWORDS

esophageal cancer, safety, toxicity profile, immune checkpoint inhibitors, thoracic radiotherapy, systemic analysis

Introduction

Esophageal cancer is the seventh most common malignancy and the sixth leading cause of cancer-related mortality worldwide (1). Its histological subtypes mainly comprise esophageal squamous cell carcinoma (ESCC) and esophageal adenocarcinoma (EAC) and, its prognosis depends on the area involved, with estimated 5-year overall survival (OS) rates ranging from about 20% to 40% (2–4). Normally, radical resection is the first-line recommendation for early-stage tumors and while definitive chemoradiation is applied for inoperable locally advanced tumors. Nevertheless, despite ongoing development in surgical techniques and the optimization of chemoradiotherapy regimens, the OS benefits are still unable to meet clinicians' expectations.

The advent of immune checkpoint inhibitors (ICIs), which include programmed cell death 1/programmed cell death ligand 1 (PD-1/PD-L1) and cytotoxic T-lymphocyte- associated antigen 4 (CTLA-4), has broadened the horizon for the treatment of various solid tumors. Nevertheless, preliminary data from clinical trials involving single-agent pembrolizumab or nivolumab in metastatic gastroesophageal cancer found response rates of just 22% to 27% in patients with PD-L1-positive tumors, impeding their further application and popularization (5, 6). Research into multimodal treatments incorporating TRT and ICIs has long been promoted in esophageal cancer (7–9). The CheckMate 577 trial indicated that the administration of adjuvant nivolumab, compared with placebo, provided a longer disease-free survival (22.4 vs. 11.0 months, $p < 0.001$) in esophageal and gastroesophageal cancer patients who had received neoadjuvant chemoradiotherapy followed by radical surgery (10). In addition, several clinical trials conducted in recent years also demonstrated the feasibility of combined of TRT and ICIs in (neo)adjuvant and maintenance settings of esophageal and gastroesophageal cancer (11–13).

The synergistic effects of TRT and ICIs have implications for both cancer control and toxicity risks in nonmalignant tissues. The rate of autoimmune-like disorders and even fatal adverse events (AEs) may rise (14), with potentially increased risks when they are combined with other agents (15). While the potential capability of this combination modality has fallen under the spotlight, the frequency and spectrum of treatment-related AEs (trAEs) during the procedure are yet to be detailed in esophageal cancer, with most toxicity data coming from individual clinical trial reports. Given the expected increased application of this combination therapy to esophageal cancer patients in the immediate future (16), treating physicians must comprehensively understand the spectrum and severity of the toxicities associated with these therapies, in turn shedding light on their clinical application and on the design of prospective trials. Hence, we conducted a systematic review focused on prospective clinical trials evaluating the AEs of the combination of TRT with ICIs in the field of esophageal cancer.

Materials and methods

Study search and inclusion criteria

This work was performed according to the Preferred Reported Items for Systematic Reviews and Meta-analyses (PRISMA) statement (17). The study selection and data extraction were performed independently by two authors (X.T. and L.Y.). Discrepancies were adjudicated by a third reviewer (L.J.) and resolved by consensus. The inclusion criteria for the literature search were defined using the Population, Intervention, Control, Outcome, Study Design (PICOS) framework (18, 19). Medical literature, including clinical trials, clinical studies, comparative studies, and multicenter studies,

published in English up until July, 2022 was searched in PubMed, Embase, Scopus, Medline In Process, and Cochrane Library, using the following terms in combination with Boolean operators (AND, OR, NOT): esophageal cancer, radiotherapy or chemoradiotherapy, immune checkpoint inhibitors, and clinical trials. The full search strategy and results are summarized in Supplementary Table 1. Clinical trials meeting the following inclusion criteria were considered: (1) patients with histologically confirmed ESCC or EAC; (2) patients receiving combination ICI and TRT treatment; (3) clinical trials reporting the overall incidence of trAE profiles; and (4) studies published in English. Retrospective studies were excluded to minimize the risk of bias. Abstracts and presentations were also reviewed to identify relevant clinical trials from major conference proceedings between 2012 and 2022, including the American Society of Clinical Oncology, European Society of Medical Oncology, American Association for Cancer Research, and American Society for Radiation Oncology Annual Meeting. If multiple publications reporting on the same study population were identified, the article with the most up-to-date and/or comprehensive AE data was selected. We also performed a manual secondary search of all bibliographies from the final selected articles so as not to possibly miss eligible studies.

Data extraction and statistical analysis

The following data were obtained from each included study: basic information (trial identifier, first author, and publication year), study methods (trial phase, study design, and enrollment), participants (age, sex, histology, clinical stage, drug name and type as well as dose and administration cycles, line of therapy, patterns of ICI and TRT combinations, and radiation dose and segmentation), outcomes (number of patients with at least one [any-grade or grade ≥ 3] trAE, number of patients who discontinued the regimen due to trAEs, number of treatment-related deaths and their causes, and the occurrence of trAEs recorded by at least three studies). The trAEs of interest included toxicities affecting the hematological system, skin system, gastrointestinal tract, respiratory system, and endocrine system. The AE terminology was coded according to the Medical Dictionary for Regulatory Activities, and the severity was graded according to the Common Terminology Criteria for Adverse Events. AEs described as immune-related AEs (irAEs) or selected AEs suspected to be potential irAEs were also extracted as trAEs in the present study. Methodological Index for Non-randomized Studies (MINORS) and Newcastle-Ottawa -Scale (NOS) evaluations were performed to assess the quality of the included studies (20, 21).

A meta-analysis of proportions was conducted using R version 4.2.1 (R Foundation for Statistical Computing). In anticipation of marked heterogeneity, the meta-analysis of outcomes was calculated with a random-effects restricted maximum-likelihood model, *via* the meta::metaprop function (22). Because of the inconsistency of the recorded trAEs among clinical trials, the information on trAEs in each study was extracted and the incidence of each trAE documented by at least three studies was finally pooled. The pooled incidence with its 95% confidence interval (CI) was estimated using the generalized linear mixed model, which implicitly uses the logit transformation (23). This model could be used to calculate the pooled incidence of rare event without assuming an approximate normal within-study likelihood and treating the standard errors as known as the traditional approach, the summary measures.

The inconsistency index (I^2) and Cochrane chi-squared test were calculated to measure heterogeneity (24). The cut-offs 30.0%, 50.0%, and 75.0% denoted moderate, substantial, and considerable heterogeneity, respectively, as recommended by the guidance on the interpretation of heterogeneity scores in the Cochrane Handbook (25). Subgroup analyses of AE incidences and profiles were performed according to cancer type (ESCC/EAC), ICI agent types (PD-1/PD-L1) as well as the sequential and concurrent administration of ICIs and TRT. The probability of publication bias was assessed with the Egger's linear regression test (26) and with the visual inspection of funnel plots for asymmetry, *via* the meta::metabias and meta::funnel functions, respectively. The non-parametric "trim-and-fill" method was performed to minimize the influence of publication bias on the results of existing publication bias, *via* the meta::trimfill function. A p value of < 0.05 was considered statistically significant.

Results

Eligible studies and baseline characteristics

The combined systematic search strategy identified 548 records, of which, 134 duplicates were excluded; 73 records were ultimately deemed eligible for full-text screening. According to the inclusion criteria, 14 clinical trials were finally included in the analysis (10–12, 27–37). Among them, a total of 863 patients with esophageal cancer were eligible for quantitative analysis of trAE incidence, with the sample size sizes in these studies ranging from 11 to 532 participants. The main characteristics of the included studies are presented in Supplementary Table 2 (baseline information) and Supplementary Table 3 (safety information). The flow diagram of study selection is illustrated in Figure 1. Risk of bias assessments are summarized in Supplementary Tables 4 using NOS and in Supplementary Table 5 using MINORS.

The NOS of the included studies ranged from 6 to 9, while the MINORS ranged from 12 to 24. There were six phase I trials, seven phase II trials, and one phase III trial. Patients included in ten studies were all identified pathologically with esophageal

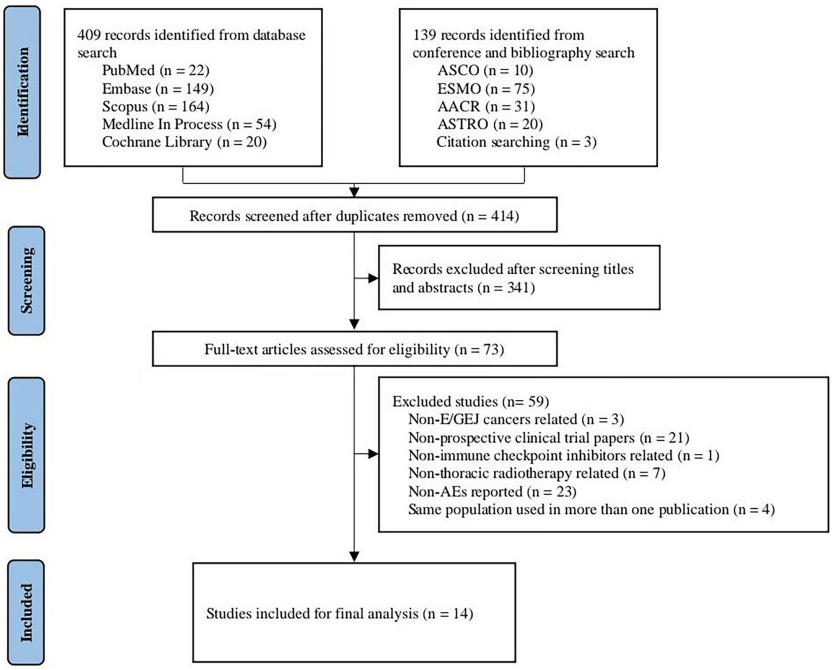

FIGURE 1
Diagram of study selection process. AEs, adverse events.

squamous cell carcinoma, while at least 70% patients included in the other four studies were identified with esophageal adenocarcinoma. Notably, PD-1 inhibitors were used in 10 trials and PD-L1 inhibitors in four. Sequential administration of ICIs and radiotherapy was performed in five trials, while concurrent therapy was conducted in nine. The duration of ICI administration ranged from 2 months to 2 years. Surgery was performed in nine trials, comprising neoadjuvant ICI and TRT in six trials and consolidation ICI therapy in three.

Among the remaining five trials involving nonsurgical patients, two involved concurrent definitive TRT with ICIs and ICI consolidation, one involved received concurrent definitive TRT with ICIs, one involved definitive TRT plus sequential ICIs, and one involved concurrent palliative TRT with ICIs. In addition, two clinical trials involved patients with chemotherapy intolerance who received only radiotherapy plus ICIs, whereas others conducted chemoradiotherapy plus ICIs. TRT combined with ICI was administered in five trials, and was concurrent in four and sequential in one.

Studies evaluating the incidence of trAEs

Of the 14 clinical trials examining the combination of TRT and ICIs, we synthesized 10 trials (76.9%) reporting the incidence of any-grade trAEs and 11 trials (84.6%) reporting the incidence of high-grade trAEs. The pooled overall incidences was were 88.97% (95%CI 71.22%-96.34%) for any-grade trAEs and 18.48% (95%CI 8.90%-34.46%) for high-grade trAEs. Moreover, the pooled incidence of the discontinuation of ICIs due to trAEs was 8.24% (95%CI 6.52%-10.36%). The forest plots of any-grade trAEs and high-grade trAEs are shown in Figure 2 and Figure 3, respectively.

Among any-grade trAEs, the most common was leukopenia (83.87%, 95%CI 34.76%-98.07%). The next most common was anemia (78.25%, 95%CI 66.03%-86.93%), after the use of "trim-and-fill" analysis to address its significant publication bias (p=0.00). Only two studies reported the incidence of any-grade lymphopenia, in which patients all developed any-grade lymphopenia (29, 35). The most common non-hematologic any-grade toxicity was reactive cutaneous capillary endothelial proliferation (RCCEP), with an incidence of 63.80% (95%CI 43.95%-79.84%), followed by esophagitis (51.54%, 95%CI 37.67%-65.18%) and fatigue (33.63%, 95%CI 13.82%-61.55%). Besides any-grade anemia, any-grade dermatitis (p=0.00) and any-grade elevated alanine transaminase (ALT, p=0.05), both of which had a positive publication bias with the Egger's test, were modified by the "trim-and-fill" method to have incidences of 15% (95%CI 7.5%-27.75%) and 20.81% (95%CI 14.17%-29.50%). The funnel plots of any-grade dermatitis and elevated ALT after "trim-and-fill" analysis are shown in Supplementary Figure 1. Besides hematologic toxicity and RCCEP, trAEs related

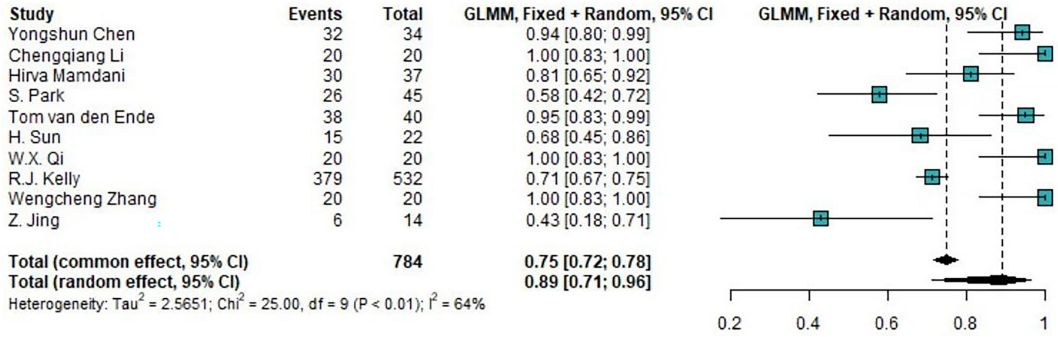

FIGURE 2
Forest plot of the incidence of any-grade treatment-related AEs. AEs, adverse events; GLMM, generalized linear mixed model.

to the gastrointestinal tract were the most frequently observed trAEs, and included anorexia (20.84%), diarrhea (15.42%), and nausea (14.34%). In addition, endocrine system trAEs were also common, including hypothyroidism (12.26%) and hyperthyroidism (6.88%). The incidences of elevated aspartate aminotransferase (AST), pneumonitis, pruritus, skin rash, and arthralgia were 12.89%, 10.82%, 10.32%, 10.03%, and 6.19%, respectively (Table 1).

Among high-grade trAEs, the Egger's test indicated publication bias for lymphopenia, leukopenia, RCCEP, nausea, anemia, and arthralgia, and the "trim-and-fill" method was applied to address the bias and calculate the pooled incidence. The funnel plots of high-grade toxicities after the "trim-and-fill" method are shown in Supplementary Figure 2. Lymphopenia was the most common high-grade trAE, with an incidence of 65.57% (95%CI 51.02%-77.69%), followed by leukopenia (21.93%, 95%CI 7.51%-49.31%). The incidence of high-grade anemia was 2.44% (95%CI 0.79%-7.29%). RCCEP (15.69%, 95% CI 8.29%-27.70%) was the most common non-hematologic high-grade trAEs, followed by nausea (4.91%, 95%CI 1.77%-12.89%) and anorexia (3.81%, 95%CI 1.44%-9.71%). High-grade esophagitis and fatigue occurrences were 2.6% (95%CI 0.98%-6.71%) and 0.41% (95%CI 0.13%-1.27%), respectively. In addition, the incidences of high-grade elevated ALT, elevated AST, hepatitis, skin rash, pneumonitis, diarrhea, and arthralgia were 1.44%, 1.16%, 0.98%, 0.90%, 0.66%, 0.43%, and 0.19%, respectively. The incidence of grade 5 AEs was 0.36% (95%CI 0.12%-1.11%) (Table 2).

trAE incidence by ICI agent type

A comparison of trAEs between PD-1 and PD-L1 inhibitors combined with TRT is shown in Table 3. A pooled subgroup analysis was not possible for RCCEP, leukopenia, lymphopenia, and anemia, because clinical trials reporting these trAEs all just used PD-1 inhibitors alone, except for high-grade leukopenia. The incidences of any-grade and high-grade trAEs were 93.14% (95%CI 64.91%-99.01%) and 16.49% (95%CI 5.87%-38.48%) in the PD-1 inhibitor group and 81.74% (95%CI 56.85%-93.83%) and 22.06% (95%CI 8.72%-45.63%) in the PD-L1 inhibitor

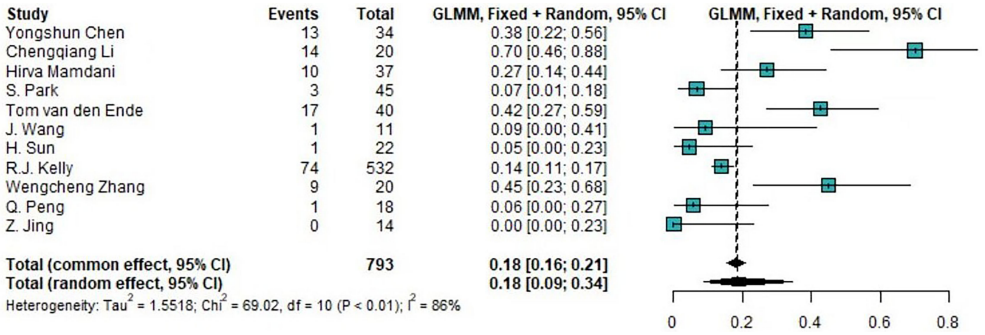

FIGURE 3
Forest plot of the incidence of high-grade treatment-related AEs. AEs, adverse events; GLMM, generalized linear mixed model.

10.3389/fimmu.2022.1039020

TABLE 1 Incidences of any-grade AEs recorded by at least three studies.

Adverse events	Pooled incidence	95%CI	Recorded studies, No.	Heterogeneity	χ^2	Egger test p
All-grade AEs	88.97%	71.22-96.34	10	64.0%	72.81	0.11
Leukopenia	83.87%	34.76-98.07	6	62.5%	59.81	0.10
Anemia	78.25%	66.03-86.93	3	0.0%	0.20	**0.00**
RCCEP	63.80%	43.95-79.84	3	56.2%	5.33	0.48
Esophagitis	51.54%	37.67-65.18	7	61.3%	18.91	0.88
Fatigue	33.63%	13.82-61.55	8	89.7%	138.53	0.16
Anorexia	20.84%	4.02-62.36	3	82.4%	28.05	0.27
Elevated ALT	20.81%	14.17-29.50	6	44.9%	14.51	**0.05**
Diarrhea	15.42%	12.92-18.30	6	0.0%	25.56	0.29
Dermatitis	15.00%	7.50-27.75	3	28.1%	5.56	**0.00**
Nausea	14.34%	6.18-29.83	8	88.0%	67.36	0.58
Elevated AST	12.89%	7.07-22.34	6	83.6%	27.08	0.21
Hypothyroidism	12.26%	5.05-26.87	5	87.9%	30.53	0.82
Pneumonitis	10.82%	6.02-18.69	8	44.3%	14.33	0.06
Pruritus	10.32%	8.11-13.04	3	0.0%	1.32	0.66
Skin rash	10.03%	7.97-12.55	5	0.0%	2.65	0.78
Hyperthyroidism	6.88%	5.14-9.15	4	0.0%	0.50	0.08
Arthralgia	6.19%	4.54-8.39	3	67.9%	5.10	0.72

The bold values mean that these AEs have significant publication bias in the Egger test, and the pooled incidence of there AEs was calculated by using the "trim-and-fill" method to addressing this publication bias.

group. There were no significant differences in any-grade and high-grade toxicities between the PD-1 and PD-L1 inhibitor groups, except for any-grade pneumonitis (15.20% vs 4.88%, p=0.03) and high-grade leukopenia (6.25% vs 59.09%, p=0.00). There was no significant difference in high-grade pneumonitis (0.62% vs 2.44%, p=0.11). The incidence of high-grade fatigue was nonsignificantly higher in the PD-L1 inhibitor group than in the PD-1 inhibitor group (1.64% vs 0.17%, p=0.06).

trAE incidence by the concurrent and sequential administration of ICIs and TRT

A comparison of trAEs between the concurrent and sequential administration of ICIs and TRT is shown in Table 4. A pooled subgroup analysis was not possible for esophagitis, arthralgia, hyperthyroidism, dermatitis, leukopenia, and anemia, because clinical trials reporting these trAEs could not be divided as they

TABLE 2 Incidences of high-grade AEs recorded by at least three studies.

Adverse events	Pooled incidence	95%CI	Recorded studies, No.	Heterogeneity	χ^2	Egger test p
High-grade AEs	18.48%	8.90-34.46	11	85.5%	79.75	0.57
Lymphopenia	65.57%	51.02-77.69	3	66.9%	6.05	**0.00**
Leukopenia	21.93%	7.51-49.31	6	77.8%	31.52	**0.01**
RCCEP	15.69%	8.29-27.70	4	43.0%	8.77	**0.01**
Nausea	4.91%	1.77-12.89	8	53.1%	23.47	**0.05**
Anorexia	3.81%	1.44-9.71	3	0.0%	7.98	0.15
Esophagitis	2.60%	0.98-6.71	7	0.0%	17.08	0.88
Anemia	2.44%	0.79-7.29	4	0.0%	0.00	**0.00**
Elevated ALT	1.44%	0.36-5.57	5	0.0%	3.61	0.18
Elevated AST	1.16%	0.24-5.44	5	66.3%	12.9	0.79
Hepatitis	0.98%	0.14-6.63	3	0.0%	2.05	0.53
Skin rash	0.90%	0.40-1.98	5	17.2%	5.52	0.57
Pneumonitis	0.66%	0.20-1.38	9	0.0%	4.88	0.21
Diarrhea	0.43%	0.14-1.33	6	0.0%	3.13	0.10
Fatigue	0.41%	0.13-1.27	8	0.0%	12.05	0.29
Grade 5 AEs	0.36%	0.12-1.11	13	0.0%	14.53	0.12
Arthralgia	0.19%	0.05-0.67	3	41.7%	6.86	**0.04**

The bold values mean that these AEs have significant publication bias in the Egger test, and the pooled incidence of there AEs was calculated by using the "trim-and-fill" method to addressing this publication bias.

10.3389/fimmu.2022.1039020

TABLE 3 Differences in the incidence of AEs with PD-1 vs PD-L1 inhibitors combined with TRT.

	PD-1 Incidence (%) (95%CI)	PD-L1 Incidence (%) (95%CI)	p value
All-grade AEs	93.14 (64.91-99.01)	81.74 (56.85-93.83)	0.35
Esophagitis	49.68 (33.46-65.97)	60.00 (44.35-73.85)	0.38
Anorexia	45.00 (25.32-66.38)	12.09 (1.01-64.91)	0.20
Fatigue	29.93 (17.08-46.98)	40.24 (3.38-92.83)	0.77
Diarrhea	15.73 (12.97-18.95)	13.93 (8.84-21.28)	0.62
Elevated ALT	15.56 (9.43-24.57)	14.29 (8.09-23.99)	0.99
Pneumonitis	15.20 (9.25-23.95)	4.88 (1.84-12.29)	**0.03**
Nausea	14.90 (7.78-26.65)	9.50 (0.55-66.74)	0.74
Pruritus	9.93 (7.70-12.71)	16.22 (7.47-31.69)	0.23
Skin rash	9.89 (7.65-12.69)	10.66 (6.29-17.49)	0.80
Hypothyroidism	9.59 (7.42-12.31)	12.97 (1.38-61.30)	0.78
Elevated AST	7.31 (5.48-9.68)	14.29 (8.09-23.99)	0.82
Hyperthyroidism	6.63 (4.82-9.06)	8.54 (4.12-16.84)	0.53
Arthralgia	5.64 (3.97-7.95)	9.37 (3.76-21.49)	0.30
High-grade AEs	16.49 (5.87-38.48)	22.06 (8.72-45.63)	0.66
Leukopenia	6.25 (2.83-13.22)	59.09 (38.17-77.16)	**0.00**
Elevated ALT	1.61 (0.23-10.57)	1.30 (0.18-8.64)	0.88
Skin rash	0.73 (0.28-1.94)	1.64 (0.41-6.32	0.35
Pneumonitis	0.62 (0.23-1.65)	2.44 (0.61-9.23)	0.11
Elevated AST	0.52 (0.17-1.61)	2.83 (0.27-23.65)	0.20
Diarrhea	0.35 (0.09-1.39)	0.82 (0.12-5.58)	0.49
Grade 5 AEs	0.23 (0.01-4.05)	0.69 (0.10-4.76)	0.53
Arthralgia	0.19 (0.00-0.74)	0.00 (0.00-1.17)	0.46
Fatigue	0.17 (0.02-1.16)	1.64 (0.41-6.32)	0.06

The bold values mean that there are significant statistical differences in subgroup analysis of these AEs.

TABLE 4 Differences in the incidence of AEs with concurrent vs sequential ICIs combined with TRT.

	Sequential Incidence (%) (95%CI)	Concurrent Incidence (%) (95%CI)	p value
All-grade AEs	70.85 (67.13-74.31)	95.20 (73.75-99.29)	**0.04**
RCCEP	54.55 (26.81-79.72)	67.70 (40.32-86.67)	0.51
Fatigue	14.91 (7.46-27.56)	52.04 (21.11-81.49)	**0.03**
Anorexia	2.22 (0.31-14.16)	43.33 (31.46-56.03)	**0.00**
Nausea	7.52 (3.05-17.40)	29.51 (14.78-50.28)	**0.01**
Hypothyroidism	11.50 (7.27-17.74)	15.00 (4.92-37.58)	0.65
Elevated AST	5.80 (4.15-8.05)	19.92 (13.08-29.15)	**0.00**
Elevated ALT	10.81 (4.12-25.49)	15.81 (9.66-24.79)	0.47
Pruritus	10.37 (8.12-13.15)	9.09 (2.28-29.96)	0.85
Skin rash	9.93 (7.81-12.56)	11.11 (5.08-22.60)	0.78
Diarrhea	15.47 (12.82-18.55)	15.00 (8.72-24.58)	0.91
Pneumonitis	9.11 (2.31-29.79)	13.00 (7.70-21.11)	0.61
High-grade AEs	14.08 (11.57-17.03)	21.59 (7.00-50.18)	0.44
Leukopenia	59.09 (38.17-77.16)	6.25 (2.83-13.22)	**0.00**
Elevated AST	1.54 (0.17-12.70)	1.22 (0.17-8.15)	0.88
Pneumonitis	0.89 (0.30-1.78)	0.00 (0.00-0.96)	0.08
Elevated ALT	2.70 (0.38-16.85)	0.98 (0.14-6.63)	0.47
Skin rash	0.65 (0.24-1.72)	3.70 (0.93-13.64)	**0.04**
Fatigue	0.16 (0.02-1.15)	1.75 (0.44-6.74)	**0.051**

The bold values mean that there are significant statistical differences in subgroup analysis of these AEs.

were all separate concurrent or sequential studies. The incidences of any-grade and high-grade trAEs were 95.20% (95%CI 73.75%-99.29%) and 21.59% (95%CI 7.00%-50.18%) in the concurrent group, and 70.85% (95%CI 67.13%-74.31%) and 14.08% (95%CI 11.57%-17.03%) in the sequential group. There was a significant difference between the concurrent and sequential groups in any-grade trAEs (p=0.03). In addition, the concurrent group seemed to show significantly increased incidences of any-grade fatigue (52.04% vs 14.91%, p=0.02), anorexia (43.33% vs 2.22%, p=0.00), nausea (29.51% vs 7.52%, p=0.01), and elevated AST (17.07% vs 5.80%, p=0.00).

In terms of high-grade trAEs, the incidences of leukopenia (6.25% vs 59.09%, p=0.00) and skin rash (0.65% vs 3.70%, p=0.04) were higher in the sequential group than in the concurrent group. The incidence of high-grade fatigue was nonsignificantly higher in the concurrent group (1.75% vs 0.16%, p=0.051).

trAE incidence by cancer type

A comparison of trAEs between ESCC and EAC is shown in Table 5. We compared the toxicity profile between studies which only included ESCC patients and studies which mainly included EAC patients (at least 70%). A pooled subgroup analysis was not possible for RCCEP, dermatitis, leukopenia, anemia and lymphopenia because clinical trials reporting these trAEs could not be divided into different cancer type groups. The incidences of any-grade and high-grade trAEs were 92.96% (95%CI 61.56%-99.09%) and 14.41% (95%CI 4.62%-36.91%) in the ESCC group, and 60.00% (95%CI 44.35%-73.85%) and 24.75% (95%CI 13.43%-41.09%) in the EAC group. There were no significant differences in any-grade and high-grade toxicities between the ESCC and EAC groups, except for any-grade hypothyroidism (22.55% vs 8.96%, p=0.049) and high-grade leukopenia (6.25% vs 59.09%, p=0.00).

Discussion

Ours study is the first systematic review to provide a relatively comprehensive toxicity profile of trAEs in esophageal cancer patients who received ICIs combined with TRT. We reached the following conclusions: (1) a high proportion of patients experienced at least one any-grade trAE, with a marked variation between the sequential and concurrent administration of TRT and ICIs; (2) the prevalence of grade ≥ 3 treatment-related toxicity was substantial, with approximately one-tenth of patients discontinuing ICI administration due to trAEs, and treatment-related mortality was only 0.36%; and (3) by pooling the incidence of trAEs in esophageal cancer in an approaching era marked by the inevitable growth in the combination of ICIs with TRT in the treatment practice for esophageal cancer, we are the first to find that dermatological and gastrointestinal reactions are the most common non-hematological toxicities.

TABLE 5 Differences in the incidence of AEs with ESCC vs EAC groups.

	ESCC Incidence (%) (95%CI)	EAC (at least 70%) Incidence (%) (95%CI)	p value
All-grade AEs	92.96 (61.56-99.09)	83.31 (66.21-92.71)	0.41
Esophagitis	49.68 (33.46-65.97)	60.00 (44.35-73.85)	0.38
Fatigue	25.16 (10.22-49.83)	51.80 (9.65-91.54)	0.37
Hypothyroidism	22.55 (9.34-45.15)	8.96 (6.88-11.60)	**0.049**
Elevated AST	20.26 (10.22-36.19)	8.84 (4.53-16.53)	0.08
Skin rash	15.25 (8.13-26.79)	9.52 (7.43-12.12)	0.17
Elevated ALT	14.19 (6.89-26.98)	14.29 (8.09-23.99)	0.99
Pneumonitis	12.89 (7.70-20.80)	2.70 (0.38-16.85)	0.11
Anorexia	12.23 (0.95-66.87)	42.50 (28.31-58.04)	0.23
Nausea	10.05 (2.70-31.04)	20.94 (7.39-46.76)	0.36
Pruritus	9.09 (2.28-29.96)	10.37 (8.12-13.15)	0.85
Hyperthyroidism	8.93 (3.77-19.72)	6.68 (4.90-9.05)	0.53
Arthralgia	4.44 (1.11-16.11)	8.01 (3.57-16.96)	0.46
Diarrhea	1.12 (0.02-34.05)	17.24 (14.44-20.45)	0.14
High-grade AEs	14.41 (4.62-36.91)	24.75 (13.43-41.09)	0.37
Leukopenia	6.25 (2.83-13.22)	59.09 (38.17-77.16)	**0.00**
Elevated AST	2.38 (0.33-15.06)	0.99 (0.12-7.64)	0.55
Fatigue	1.68 (0.42-6.47)	0.12 (0.00-7.80)	0.24
Elevated ALT	1.61 (0.23-10.57)	1.30 (0.18-8.64)	0.88
Grade 5 AEs	0.98 (0.25-3.83)	0.10 (0.00-6.72)	0.33
Pneumonitis	0.64 (0.09-4.41)	0.88 (0.37-2.09)	0.77

The bold values mean that there are significant statistical differences in subgroup analysis of these AEs.

Overall, our pooled analysis identified rates of 88.97% and 18.48% for any-grade trAEs and high-grade trAEs, respectively. The most frequent high-grade trAE was lymphopenia (65.57%), followed by leukopenia (21.93%), RCCEP (15.69%), nausea (4.91%), and anorexia (3.81%). This toxicity profile of combined TRT and ICIs was remarkably different from that of previous studies without the addition of ICIs. As is well known, definitive chemoradiotherapy was established decades ago as a curative alternative for inoperable patients with esophageal squamous cell carcinoma that confers a substantial improvement (38, 39). Treatment-related toxicity was not uniformly reported, with roughly 30%-60% of patients experiencing at least one high-grade AE. Of high-grade AEs, the most common hematotoxicity was leukopenia (10%-50%), followed by gastrointestinal toxicity (10%-25%) (40–43). Skin reaction, mostly radiation dermatitis, was uncommon at 8.9% (41). In the perioperative setting, neoadjuvant chemoradiotherapy followed by surgery has been proved to have greater local tumor control but similar OS when compared to definitive chemoradiation without surgery (44, 45) and to have a longer OS as well as and disease-free survival when compared to surgery alone (46). The incidences of grade ≥ 3 hematological and gastrointestinal toxicities were 10%-50% and 5%-10% in the neoadjuvant group. The frequencies of the other AEs were, in descending order, as follows: leukopenia (6%-48.8%), anorexia (2.2%-5%), vomiting (1%-4%), and esophagitis (1%-2.7%) (47, 48).

The incidences of blood and gastrointestinal toxicities in chemoradiation alone groups are similar to those of our data, indicating that the addition of ICIs to chemoradiation likely does not markedly increase the toxicity of these two treatments. In our results, the most common high-grade toxicity was lymphopenia. Korese et al. (49) determined that severe lymphopenia may lead to a worser prognosis in esophageal cancer patients treated with chemoradiation followed by surgery. Our results show that the concurrent group might develop an exacerbation of any-grade trAEs, mainly comprising fatigue (52.04% vs 14.91%, p=0.02), gastrointestinal tract disorders (anorexia, 43.33% vs 2.22%, [p=0.00]; nausea, 29.51% vs 7.52%, [p=0.01]), and hepatic dysfunction (elevated AST, 17.07% vs 5.80%, [p=0.00]). Thus, gastrointestinal toxicity should be monitored more carefully during concurrent TRT and ICIs.

RCCEP occurs on the skin surface, mainly on the surface of the head, face, and trunk. It is more likely to be considered immune-related, with incidences ranging from 8.9%-97.3% for grade 1 and 2 and 0% for grade ≥ 3 in ICI-related trials for various carcinomas (50–52). The evidence even suggests that the development of RCCEP may be positively associated with a longer OS and PFS (52). Our results show that the risk of high-grade RCCEP increases with combined TRT with ICIs. The addition of ICIs to chemoradiation may increase the presence of RCCEP, complicating the spectrum of dermatological toxicity, which is dominated by dermatitis induced by prior radiation (41, 53). Previous studies have suggested that radiotherapy-induced changes in proinflammatory cytokines and growth factors may contribute to surrounding normal tissue toxicities (54) and that immunotherapy may also promote vascular proliferation by releasing specific cytokines from immune cells (52). The synergistic effect may increase the probability of skin toxicity *via* the combination of TRT with ICIs.

The overall incidence of pneumonitis in chemoradiotherapy for esophageal cancer ranges from 10% to 15% (42, 43), with Chen et al. (42) reporting no presence of grade 3 or higher pneumonitis and Ji. et al. (43) identifying an incidence of 1.4% for high-grade pneumonitis. Previous studies illustrated that lung injury may be augmented by the combination of TRT with ICIs through the compound effect of tumor necrosis factor- (TNF), transforming growth factor-β (TGF-β), and other immune cytokines (55–59). This phenomenon conformed to the practice in the non-small cell lung cancer (NSCLC) setting, where grade 3 and 4 pneumonitis is observed at 4.4% and lethal pneumonitis is 0.8% with combined TRT and ICIs (60). In our study, 10% of patients experienced any-grade treatment-related pneumonitis and a markedly lower proportion (0.6%) encountered high-grade pneumonitis; there was no pneumonitis-related death. The incidence of any-grade pneumonitis was higher in the PD-1 inhibitor group than in the PD-L1 inhibitor group (15.20% vs 4.88%, p=0.03). However, there was no significant difference in high-grade pneumonitis between the two groups. These results differed from that of a previous study stating that PD-L1 inhibitors potentially carry a lower risk of pneumonitis (61, 62). The reasons underpinning this observation remain to be determined. We consider that this may have resulted from the inadequate inclusion of available full texts in our analysis. However, it is important to understand and investigate this situation in the esophageal cancer setting because such AEs may still deteriorate and require high-dose corticosteroids treatment, delaying patients' definitive surgical treatment or other local treatment.

Hepatitis, thyroiditis, and colitis are the common autoimmune diseases of ICI monotherapy, with the incidences of 8.6%, 5.2%, and 3.8%, respectively (63). Only three clinical trials reported data on irAEs but they were inconsistent in their definitions (10, 32, 34), leading to an inadequate for pooled analysis of irAEs in our study. Therefore, we presented the pooled trAE data for hepatitis, thyroiditis, and colitis. First, the pooled incidences of treatment-related elevated ALT and AST were 20.81% and 12.89% for any-grade and 1.16% and 1.44% for high-grade, respectively (10–12, 29, 30, 33, 34, 37). This seems slightly higher than that of ICI monotherapy, but the role of concurrent chemotherapy during radiotherapy may have contributed to this increase in our systematic review. Kelly et al. (10) reported the presence of two patients, recorded specifically as serious hepatitis and requiring hospitalization, but the authors did not explain whether these events were treatment-related. Second, only one clinical trial (n=22) reported immune-related thyroiditis—two cases—and both were limited to grade 2 (32), although several clinical trials identified a treatment-related thyroid functional abnormality, leading to pooled incidences of any-grade hypothyroidism and hyperthyroidism of

12.26% and 6.88%, respectively (10, 12, 31, 33, 34). All treatment-related thyroid dysfunctions were mild without ≥ grade 3 events. It is noted that ESCC seems to have higher incidence of any-grade hypothyroidism in the combination treatment compared to EAC, which may be linked to the esophageal tumor's locations. Esophageal cancer in the cervical and upper esophageal areas are mainly ESCC, while EAC occurs usually in the lower esophagus or the gastroesophageal junction. A lack of details on the irradiated site of the primary tumor prevents further investigation, because the thyroid dysfunction may be related to its irradiation when the tumor is located in cervical and upper esophageal areas. Thirdly, unlike the clear description of just two patients (out of 37) who developed possibly immune-related colitis by Mamdani et al. (34) and of three serious any-cause colitis (out of 532) requiring for hospitalization by Kelly et al. (10), most trials reported data on treatment-related diarrhea, one of the manifestations of colitis and other gastrointestinal tract AEs, with pooled incidence of 15.42% for any-grade and 0.43% for high-grade (10–12, 33–35). It should be noted that this apparent high frequency is likely due to a mixed diagnosis of different gastrointestinal toxicities, which often cause ill-defined and nonspecific symptoms. In addition, the studies included in our analysis did not provide detailed reasons for the discontinuation of ICI administration, preventing any further meaningful clinical conclusion and comparison with our data. This difference implies the need for the accurate monitoring of the corresponding organ function in clinical practice, with laboratory tests, ultrasonic examination, and imaging, to facilitate the identification of early AEs and promote timely intervention in these events.

This study has several limitations. First, this clinical trial-based meta-analysis limits the generalizability of our results to ordinary people in the real-world setting. Second, the relatively small number of eligible studies included in our analysis and the diagnosis and inconsistent recording of AEs performed by investigators without strict standardization somewhat hinder our further overview of trAEs and irAEs. Third, potential considerable heterogeneity and unobserved cofounders might prevent the interpretation of the overall incidence of various trAEs. Nevertheless, our systematic review of trAEs for combined TRT and ICIs can provide a relatively comprehensive insight into esophageal cancer for clinicians, promoting clinical vigilance and patient counseling. Further larger-scale, multicenter, randomized controlled trials and real-world studies are warranted to evaluate the safety of the combination of ICIs and TRT in patients with esophageal cancer.

Conclusions

Our study is the first systematic review to provide a relatively comprehensive toxicity profile of trAEs in esophageal cancer patients who received ICIs combined with TRT. Most AEs of this combination treatment are tolerable, with the concurrent modality possibly having a higher incidence of any-grade trAEs than the sequential approach. Compared with PD-L1 inhibitors, PD-1 inhibitors might increase the incidence of any-grade pneumonitis. ESCC seems to have higher incidence of any-grade hypothyroidism compared to EAC. This finding needs further validation in larger clinical trials. These results indicate the importance of the early recognition of AE onset to facilitate efficient interventions that mitigate their severity and optimize outcomes in these patients.

Data availability statement

The original contributions presented in the study are included in the article/Supplementary Material. Further inquiries can be directed to the corresponding author.

Author contributions

Methodology, TX, YL, and JL. Software, TX, YL, XL. Validation, TX, YL, and JL. Formal analysis, TX and YL. Data curation, TX, YL, XL. Writing-original draft preparation, TX, YL and XL. Writing–review and editing, JL. Visualization, TX and YL. Project administration, TX and JL. Funding acquisition, JL. All authors contributed to the article and approved the submitted version.

Funding

This work was supported by National Cancer Center/National Clinical Research Center for Cancer/Cancer Hospital & Shenzhen Hospital, Chinese Academy of Medical Sciences and Peking Union Medical College (SZ2020MS004).

Conflict of interest

The authors declare that the research was conducted in the absence of any commercial or financial relationships that could be construed as a potential conflict of interest.

Publisher's note

All claims expressed in this article are solely those of the authors and do not necessarily represent those of their affiliated organizations, or those of the publisher, the editors and the reviewers. Any product that may be evaluated in this article, or claim that may be made by its manufacturer, is not guaranteed or endorsed by the publisher.

Supplementary material

The Supplementary Material for this article can be found online at: https://www.frontiersin.org/articles/10.3389/fimmu.2022.1039020/full#supplementary-material

References

1. Zheng R, Zhang S, Zeng H, Wang S, Sun K, Chen R, et al. Cancer incidence and mortality in China, 2016. *J Natl Cancer Center* (2022) 2(1):1–9. doi: 10.1016/j.jncc.2022.02.002

2. He Y, Liang D, Du L, Guo T, Liu Y, Sun X, et al. Clinical characteristics and survival of 5283 esophageal cancer patients: A multicenter study from eighteen hospitals across six regions in China. *Cancer Commun (Lond)* (2020) 40(10):531–44. doi: 10.1002/cac2.12087

3. Njei B, McCarty TR, Birk JW. Trends in esophageal cancer survival in united states adults from 1973 to 2009: A SEER database analysis. *J Gastroenterol Hepatol* (2016) 31(6):1141–6. doi: 10.1111/jgh.13289

4. Kjaer DW, Larsson H, Svendsen LB, Jensen LS. Changes in treatment and outcome of oesophageal cancer in Denmark between 2004 and 2013. *Br J Surg* (2017) 104(10):1338–45. doi: 10.1002/bjs.10586

5. Muro K, Chung HC, Shankaran V, Geva R, Catenacci D, Gupta S, et al. Pembrolizumab for patients with PD-L1-positive advanced gastric cancer (KEYNOTE-012): a multicentre, open-label, phase 1b trial. *Lancet Oncol* (2016) 17(6):717–26. doi: 10.1016/S1470-2045(16)00175-3

6. Janjigian YY, Bendell JC, Calvo E, Kim JW, Ascierto PA, Sharma P, et al. CheckMate-032: Phase I/II, open-label study of safety and activity of nivolumab (nivo) alone or with ipilimumab (ipi) in advanced and metastatic (A/M) gastric cancer (GC). *J Clin Oncol* (2016) 34(15_suppl):4010–0. doi: 10.1200/JCO.2016.34.15_suppl.4010

7. Yu R, Wang W, Li T, Li J, Zhao K, Wang W, et al. RATIONALE 311: Tislelizumab plus concurrent chemoradiotherapy for localized esophageal squamous cell carcinoma. *Future Oncol* (2021) 17(31):4081–9. doi: 10.2217/fon-2021-0632

8. Yang Y, Zhu L, Cheng Y, Liu Z, Cai X, Shao J, et al. Three-arm phase II trial comparing camrelizumab plus chemotherapy versus camrelizumab plus chemoradiation versus chemoradiation as preoperative treatment for locally advanced esophageal squamous cell carcinoma (NICE-2 study). *BMC Cancer* (2022) 22(1):506. doi: 10.1186/s12885-022-09573-6

9. Wang L, Chen M, Kato K, Wyrwicz L, Smyth EC, Jiang A, et al. A phase 3 randomized, doubleblind, placebo-controlled, multicenter, global study of durvalumab with and after chemoradiotherapy in patients with locally advanced, unresectable esophageal squamous cell carcinoma: KUNLUN. *J Clin Oncol* (2022) 40(Suppl 4):TPS373. doi: 10.1200/JCO.2022.40.4_suppl.TPS373

10. Kelly RJ, Ajani JA, Kuzdzal J, Zander T, Cutsem Van E, Piessen G, et al. Adjuvant nivolumab in resected esophageal or gastroesophageal junction cancer. *New Engl J Med* (2021) 384(13):1191–203. doi: 10.1056/NEJMoa2032125

11. Ende Tvd, Clercq NCD, Henegouwen MLVB, Gisbertz SS, Meijer SL, Schokker S, et al. A phase II feasibility trial of neoadjuvant chemoradiotherapy combined with atezolizumab for resectable esophageal adenocarcinoma: the PERFECT trial. *J Clin Oncol* (2019) 37(Suppl 15):4045. doi: 10.1200/JCO.2019.37.15_suppl.4045

12. Zhang W, Yan C, Zhang T, Chen X, Dong J, Zhao J, et al. Addition of camrelizumab to docetaxel, cisplatin, and radiation therapy in patients with locally advanced esophageal squamous cell carcinoma: a phase 1b study. *Oncoimmunology* (2021) 10(1):1971418. doi: 10.1080/2162402X.2021.1971418

13. Chao J, He TF, D'Apuzzo M, Chen YJ, Frankel P, Tajon M, et al. A phase 2 trial combining pembrolizumab and palliative radiation therapy in gastroesophageal cancer to augment abscopal immune responses. *Adv Radiat Oncol* (2022) 7(1):100807. doi: 10.1016/j.adro.2021.100807

14. Hwang WL, Pike LRG, Royce TJ, Mahal BA, Loeffler JS. Safety of combining radiotherapy with immune-checkpoint inhibition. *Nat Rev Clin Oncol* (2018) 15(8):477–94. doi: 10.1038/s41571-018-0046-7

15. Zhou X, Yao Z, Bai H, Duan J, Wang Z, Wang X, et al. Treatment-related adverse events of PD-1 and PD-L1 inhibitor-based combination therapies in clinical trials: a systematic review and meta-analysis. *Lancet Oncol* (2021) 22(9):1265–74. doi: 10.1016/S1470-2045(21)00333-8

16. Patel MA, Kratz JD, Lubner SJ, Loconte NK, Uboha NV. Esophagogastric cancers: Integrating immunotherapy therapy into current practice. *J Clin Oncol* (2022) 40(24):2751–62. doi: 10.1200/JCO.21.02500

17. Page MJ, Amir-Behghadami M, Janati A. The PRISMA 2020 statement: An updated guideline for reporting systematic reviews. *Bmj* (2021) 372:n71. doi: 10.1136/emermed-2020-209567

18. Amir-Behghadami M, Janati A. Population, intervention, comparison, outcomes and study (PICOS) design as a framework to formulate eligibility criteria in systematic reviews. *Emerg Med J* (2020) 37(6):387. doi: 10.1136/emermed-2020-209567

19. Huang X, Lin J, Demner-Fushman D. Evaluation of PICO as a knowledge representation for clinical questions. *AMIA Annu Symp Proc* (2006) 2006:359–63.

20. Slim K, Nini E, Forestier D, Kwiatkowski F, Panis Y, Chipponi J. Methodological index for non-randomized studies (minors): development and validation of a new instrument. *ANZ J Surg* (2003) 73(9):712–6. doi: 10.1046/j.1445-2197.2003.02748.x

21. Wells G. *The Newcastle-Ottawa scale (NOS) for assessing the quality of nonrandomised studies in meta-analyses* (2022). Available at: https://www.ohri.ca//programs/clinical_epidemiology/oxford.asp.

22. Balduzzi S, Rücker G, Schwarzer G. How to perform a meta-analysis with r: a practical tutorial. *Evidence Based Ment Health* (2019) 22(4):153–60. doi: 10.1136/ebmental-2019-300117

23. Stijnen T, Hamza TH, Ozdemir P. Random effects meta-analysis of event outcome in the framework of the generalized linear mixed model with applications in sparse data. *Stat Med* (2010) 29(29):3046–67. doi: 10.1002/sim.4040

24. Higgins JP, Thompson SG, Deeks JJ, Altman DG. Measuring inconsistency in meta-analyses. *Bmj* (2003) 327(7414):557–60. doi: 10.1136/bmj.327.7414.557

25. Higgins JP, Thomas J, Chandler J, Cumpston M, Li T, Page MJ, et al. *Cochrane handbook for systematic reviews of interventions*. Chichester (UK): John Wiley & Sons (2019).

26. Egger M, Smith Davey G, Schneider M, Minder C. Bias in meta-analysis detected by a simple, graphical test. *Bmj* (1997) 315(7109):629–34. doi: 10.1136/bmj.315.7109.629

27. Jing Z, Du D, Zhang N, Dai H, Wang X, Hua Y, et al. Combination of radiation therapy and anti-PD-1 antibody SHR-1210 in treating patients with esophageal squamous cell cancer. *Int J Radiat Oncology Biology Phys* (2018) 102:e31. doi: 10.1016/j.ijrobp.2018.07.520

28. Pang Q, Li X, Zhang W, Qian D, Zhang B, Chen X, et al. Safety and effect of radiation therapy combined with anti-PD-1 antibody SHR-1210 as first-line treatment on patients with intolerable concurrent chemoradiotherapy esophageal cancer: A phase 1B clinical trial. *Int J Radiat Oncology Biology Phys* (2018) 102(3):e39. doi: 10.1016/j.ijrobp.2018.07.538

29. Qi WX, Zhao S, Li H, Chen J. Safety and tolerability of neoadjuvant chemoradiotherapy combined with pembrolizumab for local advanced, resectable esophageal cancer: Preliminary results of a prospective phase IB trial. *Int J Radiat Oncology Biology Phys* (2020) 108(3):e576–7. doi: 10.1016/j.ijrobp.2020.07.1773

30. Sun H, Yang W, Luo J, Lin H, Zhou T, Gong H, et al. Safety and tolerability of neoadjuvant radiotherapy combined with anti-PD-1 antibody toripalimab for locally advanced, resectable esophageal squamous cell cancer: A prospective phase IB trial. *Int J Radiat Oncology Biology Phys* (2021) 111(3):S102–3. doi: 10.1016/j.ijrobp.2021.07.238

31. Wang J, Cheng Y, Wu Y, Cao F, Liu Q, Gao G. 978P a prospective study of camrelizumab monotherapy following definitive concurrent chemoradiotherapy in patients with unresectable locally advanced esophageal squamous cell cancer. *Ann Oncol* (2021) 32:S838. doi: 10.1016/j.annonc.2021.08.1362

32. Uboha NV, Eickhoff JC, Maloney JD, McCarthy D, DeCamp M, Deming DA, et al. Phase I/II trial of perioperative avelumab in combination with chemoradiation (CRT) in the treatment of stage II/III resectable esophageal and gastroesophageal junction (E/GEJ) cancer. *J Clin Oncol* (2022) 40(16_suppl):4034–4. doi: 10.1200/JCO.2022.40.16_suppl.4034

33. Park S, Sun JM, Choi YL, Oh D, Kim HK, Lee T, et al. Adjuvant durvalumab for esophageal squamous cell carcinoma after neoadjuvant chemoradiotherapy: A placebo-controlled, randomized, double-blind, phase II study. *Esmo Open* (2022) 7(1):100385. doi: 10.1016/j.esmoop.2022.100385

34. Mamdani H, Schneider B, Perkins SM, Burney HN, Kasi PM, Abushahin LI, et al. A phase II trial of adjuvant durvalumab following trimodality therapy for locally advanced esophageal and gastroesophageal junction adenocarcinoma: A big ten cancer research consortium study. *Front Oncol* (2021) 11:736620. doi: 10.3389/fonc.2021.736620

35. Li C, Zhao S, Zheng Y, Han Y, Chen X, Cheng Z, et al. Preoperative pembrolizumab combined with chemoradiotherapy for oesophageal squamous cell carcinoma (PALACE-1). *Eur J Cancer* (2021) 144:232–41. doi: 10.1016/j.ejca.2020.11.039

36. Chen Y, Zhao W, Zuo Z, Ke S, Shi W, Li B, et al. A prospective clinical trial of camrelizumab in combination with chemoradiotherapy in patients with metastatic esophageal squamous cell carcinoma. *J Clin Oncol* (2022) 40(Suppl 4):326. doi: 10.1200/JCO.2022.40.4_suppl.326

37. Lee S, Ahn BC, Park SY, Kim DJ, Lee CG, Cho J, et al. A phase II trial of preoperative chemoradiotherapy and pembrolizumab for locally advanced esophageal squamous cell carcinoma (ESCC). *Ann Oncol* (2019) 30:v754. doi: 10.1093/annonc/mdz065.004

38. Cooper JS, Guo MD, Herskovic A, Macdonald JS, Martenson JA Jr, Al-Sarraf M, et al. Chemoradiotherapy of locally advanced esophageal cancer: long-

term follow-up of a prospective randomized trial (RTOG 85-01). radiation therapy oncology group. *JAMA* (1999) 281(17):1623–7. doi: 10.1001/jama.281.17.1623

39. Smith TJ, Ryan LM, Douglass HO Jr, Haller DG, Dayal Y, Kirkwood J, et al. Combined chemoradiotherapy vs. radiotherapy alone for early stage squamous cell carcinoma of the esophagus: a study of the Eastern cooperative oncology group. *Int J Radiat Oncol Biol Phys* (1998) 42(2):269–76. doi: 10.1016/s0360-3016(98)00232-6

40. Nishimura Y, Mitsumori M, Hiraoka M, Koike R, Nakamatsu K, Kawamura M, et al. A randomized phase II study of cisplatin/5-FU concurrent chemoradiotherapy for esophageal cancer: Short-term infusion versus protracted infusion chemotherapy (KROSG0101/JROSG021). *Radiother Oncol* (2009) 92 (2):260–5. doi: 10.1016/j.radonc.2008.12.012

41. Noronha V, Prabhash K, Joshi A, Patil VM, Talole S, Nakti D, et al. Clinical outcome in definitive concurrent chemoradiation with weekly paclitaxel and carboplatin for locally advanced esophageal and junctional cancer. *Oncol Res* (2016) 23(4):183–95. doi: 10.3727/096504016X14537290676865

42. Chen B, Li Q, Li Q, Qiu B, Xi M, Liu M, et al. Weekly chemotherapy of 5-fluorouracil plus cisplatin concurrent with radiotherapy for esophageal squamous cell carcinoma patients with postoperative locoregional recurrence: Results from a phase II study. *Oncologist* (2020) 25(4):308–e625. doi: 10.1634/theoncologist.2019-0931

43. Ji Y, Du X, Zhu W, Yang Y, Ma J, Zhang L, et al. Efficacy of concurrent chemoradiotherapy with s-1 vs radiotherapy alone for older patients with esophageal cancer: A multicenter randomized phase 3 clinical trial. *JAMA Oncol* (2021) 7(10):1459–66. doi: 10.1001/jamaoncol.2021.2705

44. Stahl M, Stuschke M, Lehmann N, Meyer H-J, Walz MK, Seeber S, et al. Chemoradiation with and without surgery in patients with locally advanced squamous cell carcinoma of the esophagus. *J Clin Oncol* (2005) 23(10):2310–7. doi: 10.1200/JCO.2005.00.034

45. Bedenne L, Michel P, Bouché O, Milan C, Mariette C, Conroy T, et al. Chemoradiation followed by surgery compared with chemoradiation alone in squamous cancer of the esophagus: FFCD 9102. *J Clin Oncol* (2007) 25(10):1160–8. doi: 10.1200/JCO.2005.04.7118

46. Yang H, Liu H, Chen Y, Zhu C, Fang W, Yu Z, et al. Long-term efficacy of neoadjuvant chemoradiotherapy plus surgery for the treatment of locally advanced esophageal squamous cell carcinoma: The NEOCRTEC5010 randomized clinical trial. *JAMA Surg* (2021) 156(8):721–9. doi: 10.1001/jamasurg.2021.2373

47. van Hagen P, Hulshof MC, Lanschot van JJ, Steyerberg EW, Henegouwen Berge van MI, Wijnhoven BP, et al. Preoperative chemoradiotherapy for esophageal or junctional cancer. *N Engl J Med* (2012) 366(22):2074–84. doi: 10.1056/NEJMoa1112088

48. Yang H, Liu H, Chen Y, Zhu C, Fang W, Yu Z, et al. Neoadjuvant chemoradiotherapy followed by surgery versus surgery alone for locally advanced squamous cell carcinoma of the esophagus (NEOCRTEC5010): A phase III multicenter, randomized, open-label clinical trial. *J Clin Oncol* (2018) 36(27):2796–803. doi: 10.1200/JCO.2018.79.1483

49. Kroese TE, Jairam J, Ruurda JP, Lin SH, Mohan R, Mook S, et al. Severe lymphopenia acquired during chemoradiotherapy for esophageal cancer: Incidence and external validation of a prediction model. *Radiother Oncol* (2021) 163:192–8. doi: 10.1016/j.radonc.2021.08.009

50. Lan C, Shen J, Wang Y, Li J, Liu Z, He M, et al. Camrelizumab plus apatinib in patients with advanced cervical cancer (CLAP): A multicenter, open-label, single-arm, phase II trial. *J Clin Oncol* (2020) 38(34):4095–106. doi: 10.1200/JCO.20.01920

51. Song Y, Wu J, Chen X, Lin T, Cao J, Liu Y, et al. A single-arm, multicenter, phase II study of camrelizumab in relapsed or refractory classical Hodgkin lymphoma. *Clin Cancer Res* (2019) 25(24):7363–9. doi: 10.1158/1078-0432.CCR-19-1680

52. Wang F, Qin S, Sun X, Ren Z, Meng Z, Chen Z, et al. Reactive cutaneous capillary endothelial proliferation in advanced hepatocellular carcinoma patients treated with camrelizumab: data derived from a multicenter phase 2 trial. *J Hematol Oncol* (2020) 13(1):47. doi: 10.1186/s13045-020-00886-2

53. Dreyfuss AD, Barsky AR, Wileyto EP, Eads JR, Kucharczuk JC, Williams NN, et al. The efficacy and safety of definitive concurrent chemoradiotherapy for non-operable esophageal cancer. *Cancer Med* (2021) 10(4):1275–88. doi: 10.1002/cam4.3724

54. Citrin DE, Hitchcock YJ, Chung EJ, Frandsen J, Urick ME, Shield W, et al. Determination of cytokine protein levels in oral secretions in patients undergoing radiotherapy for head and neck malignancies. *Radiat Oncol* (2012) 7:64. doi: 10.1186/1748-717X-7-64

55. Piguet PF. Cytokines involved in pulmonary fibrosis. *Int Rev Exp Pathol* (1993) 34 Pt B:173–81. doi: 10.1016/B978-0-12-364935-5.50017-1

56. Hashimoto S, Gon Y, Takeshita I, Matsumoto K, Maruoka S, Horie T. Transforming growth factor-beta1 induces phenotypic modulation of human lung fibroblasts to myofibroblast through a c-Jun-NH2-terminal kinase-dependent pathway. *Am J Respir Crit Care Med* (2001) 163(1):152–7. doi: 10.1164/ajrccm.163.1.2005069

57. Oikonomou N, Harokopos V, Zalevsky J, Valavanis C, Kotanidou A, Szymkowski DE, et al. Soluble TNF mediates the transition from pulmonary inflammation to fibrosis. *PLoS One* (2006) 1(1):e108. doi: 10.1371/journal.pone.0000108

58. Sprung CN, Forrester HB, Siva S, Martin OA. Immunological markers that predict radiation toxicity. *Cancer Lett* (2015) 368(2):191–7. doi: 10.1016/j.canlet.2015.01.045

59. Mehrotra P, Collett JA, Gunst SJ, Basile DP. Th17 cells contribute to pulmonary fibrosis and inflammation during chronic kidney disease progression after acute ischemia. *Am J Physiol Regul Integr Comp Physiol* (2018) 314(2):R265–r273. doi: 10.1152/ajpregu.00147.2017

60. Antonia SJ, Villegas A, Daniel D, Vicente D, Murakami S, Hui R, et al. Durvalumab after chemoradiotherapy in stage III non-Small-Cell lung cancer. *N Engl J Med* (2017) 377(20):1919–29. doi: 10.1056/NEJMoa1709937

61. Fukuda M, Yamaguchi H, Mukae H, Ashizawa K. Programmed death ligand-1 inhibitors potentially carry a lower risk of pneumonitis compared with programmed death-1 inhibitors in patients with non-small cell lung cancer. *J Thorac Dis* (2018) 10(Suppl 33):S4082–s4084. doi: 10.21037/jtd.2018.09.103

62. Pillai RN, Behera M, Owonikoko TK, Kamphorst AO, Pakkala S, Belani CP, et al. Comparison of the toxicity profile of PD-1 versus PD-L1 inhibitors in non-small cell lung cancer: A systematic analysis of the literature. *Cancer* (2018) 124 (2):271–7. doi: 10.1002/cncr.31043

63. De Velasco G, Je Y, Bossé D, Awad MM, Ott PA, Moreira RB, et al. Comprehensive meta-analysis of key immune-related adverse events from CTLA-4 and PD-1/PD-L1 inhibitors in cancer patients. *Cancer Immunol Res* (2017) 5 (4):312–8. doi: 10.1158/2326-6066.CIR-16-0237

frontiers | Frontiers in Immunology

TYPE Original Research
PUBLISHED 17 November 2022
DOI 10.3389/fimmu.2022.1050421

Check for updates

OPEN ACCESS

EDITED BY
Jian Zhang,
Southern Medical University, China

REVIEWED BY
Yongfeng He,
Cornell University, United States
Gurcan Gunaydin,
Hacettepe University, Turkey

*CORRESPONDENCE
Hao Chen
ery_chenh@lzu.edu.cn

†These authors have contributed equally to this work and share first authorship

SPECIALTY SECTION
This article was submitted to Cancer Immunity and Immunotherapy, a section of the journal Frontiers in Immunology

RECEIVED 21 September 2022
ACCEPTED 02 November 2022
PUBLISHED 17 November 2022

CITATION
Gu B, Wang B, Li X, Feng Z, Ma C, Gao L, Yu Y, Zhang J, Zheng P, Wang Y, Li H, Zhang T and Chen H (2022) Photodynamic therapy improves the clinical efficacy of advanced colorectal cancer and recruits immune cells into the tumor immune microenvironment. *Front. Immunol.* 13:1050421. doi: 10.3389/fimmu.2022.1050421

COPYRIGHT
© 2022 Gu, Wang, Li, Feng, Ma, Gao, Yu, Zhang, Zheng, Wang, Li, Zhang and Chen. This is an open-access article distributed under the terms of the Creative Commons Attribution License (CC BY). The use, distribution or reproduction in other forums is permitted, provided the original author(s) and the copyright owner(s) are credited and that the original publication in this journal is cited, in accordance with accepted academic practice. No use, distribution or reproduction is permitted which does not comply with these terms.

Photodynamic therapy improves the clinical efficacy of advanced colorectal cancer and recruits immune cells into the tumor immune microenvironment

Baohong Gu[1†], Bofang Wang[1†], Xuemei Li[1†], Zedong Feng[1†], Chenhui Ma[1], Lei Gao[1], Yang Yu[1], Jing Zhang[1], Peng Zheng[1], Yunpeng Wang[1], Haiyuan Li[1], Tao Zhang[1,2] and Hao Chen[1,3,4*]

[1]Second Clinical Medical College, Lanzhou University, Lanzhou, Gansu, China, [2]Department of Oncology, The First Hospital of Lanzhou University, Lanzhou, Gansu, China, [3]Key Laboratory of the Digestive System Tumors of Gansu Province, Lanzhou, Gansu, China, [4]Department of Oncology, Lanzhou University Second Hospital, Lanzhou, Gansu, China

Objective: Although photodynamic therapy (PDT) has been proven effective in various tumors, it has not been widely used as a routine treatment for colorectal cancer (CRC), and the characteristics of changes in the tumor microenvironment (TME) after PDT have not been fully elucidated. This study evaluated the efficacy of PDT in patients with advanced CRC and the changes in systemic and local immune function after PDT.

Methods: Patients with stage III-IV CRC diagnosed in our hospital from November 2020 to July 2021 were retrospectively analyzed to compare the survival outcomes among each group. Subsequently, short-term efficacy, systemic and local immune function changes, and adverse reactions were assessed in CRC patients treated with PDT.

Results: A total of 52 CRC patients were enrolled in this retrospective study from November 2020 to July 2021, and the follow-up period ended in March 2022. The overall survival (OS) of the PDT group was significantly longer than that of the non-PDT group (p=0.006). The objective response rate (ORR) and disease control rate two months after PDT were 44.4% and 88.9%, respectively. Differentiation degree (p=0.020) and necrosis (p=0.039) are two crucial factors affecting the short-term efficacy of PDT. The systemic immune function of stage III patients after PDT decreased, whereas that of stage IV patients increased. Local infiltration of various immune cells such as $CD3^+$ T cells, $CD4^+$ T cells, $CD8^+$ T cells, $CD20^+$ B cells and macrophages in the tumor tissue were significantly increased. No severe adverse reactions associated with PDT were observed.

10.3389/fimmu.2022.1050421

Conclusion: PDT is effective for CRC without significant side effects according to the available data. It alters the TME by recruiting immune cells into tumor tissues.

KEYWORDS

photodynamic therapy (PDT), colorectal cancer, clinical efficacy, tumor microenvironment, immunity

1 Introduction

Colorectal cancer (CRC) is one of the most common gastrointestinal malignancies. According to the global cancer statistics 2020, the overall incidence of CRC has jumped to third place, ranking second among all cancer deaths (1). In China, CRC is the second most common cancer and the fifth leading cause of cancer death, with about 560,000 new cases and 290,000 deaths. China has become the country with the most significant number of new cases and deaths of CRC every year (1, 2).

CRC has an insidious onset, and many patients are already at an advanced stage when the tumor is detected (3), losing the opportunity for radical surgical treatment. The 5-year relative survival rate for the localized lesion is higher than 90%, whereas that for the lesion with concomitant distant metastasis is less than 10% (4). However, even if they are eligible for surgery, patients with low rectal cancer usually prefer to remain anal to avoid quality-of-life changes associated with a colostomy or low anterior resection syndrome (5). Traditional CRC therapies such as chemotherapy and radiotherapy often accompany myelosuppression, non-targeting tumor-damaging normal cells, and multidrug resistance (6). Some patients may not be treated on time or give up halfway due to severe side effects and adverse events that cannot be tolerated. Additionally, cell therapy, immunotherapy, and targeted therapy have shown great potential in treating CRC, but the low benefit rate and high cost limit the number of people who benefit (6). These current situations pose severe challenges to the current treatment of CRC.

Photodynamic therapy (PDT) can effectively complement the abovementioned CRC treatment methods. Due to a series of advantages such as high safety, robust targeting, low invasiveness, and fewer side effects, PDT may even become one of the conventional anti-tumor treatments in the future (7). The principle of PDT is utilizing a specific wavelength of red light to irradiate and excite photosensitizers taken up by tumor tissue to generate cytotoxic factors such as reactive oxygen species, which induce tumor cell death (8). In addition to the direct killing effect, the anti-tumor effect of PDT is primarily based on its impact on the body's immune and inflammatory responses. PDT frequently provokes a solid acute inflammatory reaction, which increases the immunogenicity of tumor cells and stimulates the body's anti-tumor immune response (9).

Although numerous studies and clinical data suggest that PDT can affect immune responses, the effect of PDT on the immune system of patients with CRC has not been reported so far, and many questions remain unanswered regarding CRC. For example, what effect does PDT have on systemic and local immune function in CRC patients of different clinical stages? Is there a connection between the two? It is necessary and interesting to clarify these questions. Based on the evaluation of the safety and efficacy of PDT in the treatment of CRC, this study further explored the changes and relationship between the peripheral blood and tumor tissue local immune microenvironment of patients after PDT.

2 Materials and methods

2.1 Patient information

We retrospectively reviewed the data of all patients diagnosed with CRC from November 2020 to July 2021 in the Lanzhou University Second Hospital, Lanzhou, China. Selected patients were divided into the PDT group (n=8), PDT+systemic therapy (ST) group (n=10), ST group (n=19), and untreated group (n=15) according to what treatment the patient has received. The primary inclusion criteria were patients with a first diagnosis of CRC and not receiving any conventional anti-tumor therapy, clinical stage III to IV, refusal to undergo palliative surgery, or the presence of a physical adverse event that would make the surgery intolerable. All patient information was collected from medical records, including colonoscopy images, immunoassay data, and pathology reports. This study was approved by the Research Institutions Review Board and

carried out under the ethical principles of the Declaration of Helsinki.

2.2 Photosensitizer and laser device

The photosensitizer was Hematoporphyrin (Milelonge Biopharmaceutical Co., LTD, China), molecular formula: C34H38N4O6, molecular weight: 598.70, which can be excited by a visible red light with a wavelength of 630 nm. The laser (Xingda Photoelectric Medical Instrument Co., LTD, China) emitted by the treatment light source is 630 nm with pulse output. The optical fiber is a columnar optical fiber, and the luminous band (Xingda Photoelectric Medical Instrument Co., LTD, China) at the end can be selected from 1 to 6 cm.

2.3 Therapeutic schedule

Patients were divided into the PDT group and the non-PDT group. Patients in the PDT group were given Hematoporphyrin 48 hours before treatment. Before infusion, the original solution was taken for a skin scratch test on the patient's forearm. If there was no swelling or induration within 15 minutes, Hematoporphyrin was added to 250ml normal saline (NS) at 5mg/kg, and intravenous infusion was completed within one hour. The patient was subsequently protected from exposure to sunlight. PDT therapy was initiated 48h after infusion. An expandable uncovered metal intestinal stent (WallFlex, Boston Scientific) was placed before irradiation for patients with an obstruction or tumor that protruded significantly into the lumen to gain maximum treatment area. The appropriate columnar fiber was chosen according to the lesion size. If it is a circumferential growing tumor, the optical fiber is placed in the center of the lumen, and if an eccentric growing tumor, the optical fiber is placed on the tumor surface as much as possible, far away from the normal bowel wall. Segmented irradiation is adopted when the lesion exceeds the optical fiber's length. Generally, the irradiation parameters are as follows: wavelength is 630 nm, power is 800nW, energy density is 200J/cm^2, and continuous irradiation for 3 or 4 days. Necrotic tissue was removed by colonoscopy 48 hours after PDT. The patient will decide whether to combine with other tumor treatments one week later. Patients should avoid direct exposure to sunlight or any other strong light source for one month after the photosensitizer injection.

The non-PDT group did not receive PDT intervention, and the other treatments were the same as the PDT group.

2.4 Response evaluation of PDT

2.4.1 Short-term response evaluation

The surface necrosis of the irradiation site was observed by colonoscopy 48h after PDT. The evaluation of the necrosis degree according to the following criteria: Mild: the necrosis area of the lesion is less than 30%; Moderate: 30%-70% necrosis area of lesion area; Severe: necrosis occurs over 70% of the lesion area.

After two months, patients who received PDT need to undergo computed tomography (CT) or magnetic resonance imaging (MRI) examinations to compared with the results before treatment. Patients should undergo colonoscopy again to determine the degree of intestinal tract patency and tumor necrosis. Afterward, experienced researchers record target lesion measurements, development of new lesions, and tumor response in patients treated with PDT according to the response assessment criteria in Response to Solid Tumors (RECIST) 1.1 (10). Changes in quality-of-life before and after treatment were assessed using the KPS score.

2.4.2 Assessment of adverse reactions

Patients were recorded for fever, abdominal pain, intestinal perforation, bleeding at the end of PDT treatment, and photoallergic reactions under strict photoprotective conditions.

2.5 Evaluation of immune function

Peripheral blood was collected before and 48 hours after PDT. The systemic immune function status of CRC patients was assessed by flow cytometry. The antibodies used for flow cytometry, including CD3 (#Z6410026), CD19 (#Z6410014), CD127 (Z6410046) were purchased from QuantoBio Biotechnology (Beijing, China), antibodies against CD4 (#347413), CD8 (#348793), CD25 (#555434), CD45RO (#340438), CD45RA (#564359) and CD56 (#335791) were bought from BD Biosciences (San Jose, CA,USA). Immunohistochemistry (IHC) was used to detect local immune cell infiltration of the tumor before and 48h after PDT. The tissue materials were obtained from the paraffin-embedded tissue samples used for preoperative diagnosis and postoperative efficacy evaluation. IHC-relevant antibodies against CD3 (#Kit-0003), CD4 (#RMA-0620), CD8 (#RMA-0514), CD20 (Kit-0001), CD56 (MAB-0743), and CD68 (Kit-0026) were obtained from Maixin Biotechnology (Fuzhou, China).

2.6 Follow-up

Clinical follow-up for all patients ended on March 10, 2022. The medical history data were obtained from regular inspection records, and the survival information was obtained through telephone follow-up.

2.7 Statistical analysis

Numerical data were presented as mean ± SD. Categorical data were presented as absolute frequency with relative frequency in parenthesis. The nonparametric Wilcoxon test and *t* test was used to compare paired data, $\chi 2$ test or Fisher's exact test was used to analyze categorical data. Survival was compared by log-rank test and plotted as Kaplan-Meier diagrams. All *p* values were reported as two-tailed, with a significance level of 0.05. SPSS Statistics 22.0 and GraphPad Prism 9.3 were used for statistical analysis and mapping.

3 Results

3.1 Tumor and patient characteristics

A complete flow chart for all patients is presented in Figure 1. A total of 52 CRC patients were enrolled in this retrospective study from November 2020 to July 2021. Table 1 lists the essential characteristics of the patients, including age, sex, location, degree of differentiation, clinical stage, KPS score, tumor length, and treatment plan. Eighteen patients received PDT and 34 did not. Rectal cancer was predominant in both groups, with 11 (61.1%) and 22 (64.7%) patients respectively. Regarding pathological type and degree of differentiation, moderately differentiated adenocarcinoma accounts for the highest proportion, followed by well-differentiated adenocarcinoma, and poorly differentiated adenocarcinoma is the lowest. Many patients had distant metastases at diagnosis, and the proportion was more than 50% in both groups (55.6% vs. 70.6%). Patients were differentiated by a KPS score of 70, divided into one group greater than 70 and another group less than 70, and the composition ratio of the KPS score was similar between the PDT group and the non-PDT group. Most patients had lesions longer than 4cm, meaning that patients in the PDT group often required segmental irradiation. Ten patients (55.6%) in the PDT group received systemic therapy, while 15 patients in the non-PDT group received no treatment after diagnosis. There were no significant differences between the two groups concerning all baseline parameters.

3.2 Survival analysis

Kaplan-Meier analysis of overall survivals (OS) in the PDT and non-PDT groups are shown in Figures 2A–C. Compared with non-PDT (median OS: 202 days), the PDT group (median OS: not reached) showed a longer OS (log-rank p=0.006) (Figure 2A). Subgroup analysis showed that PDT alone (median OS: not reached) had significantly longer OS compared to untreated patients (median OS: 99 days, log-rank p=0.037) (Figure 2B). Patients in the PDT+ST group (median OS: not reached) also

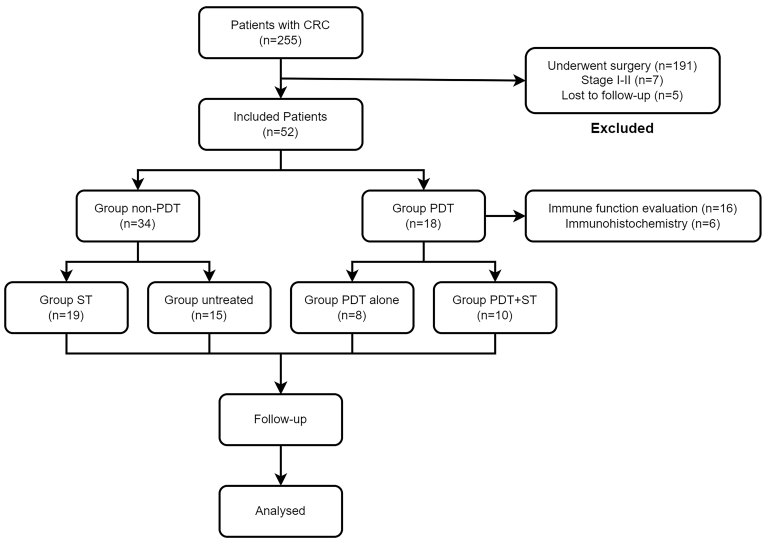

FIGURE 1
Flowchart of all patients in this study. CRC, colorectal cancer; PDT, photodynamic therapy; ST, systemic therapy.

TABLE 1 Clinical characteristics of 52 CRC patients.

Clinical data	PDT group	Non-PDT group	*p*-value*
Number of patients (n)	18	34	
Age, years (mean ± SD)	58.0 ± 15.0	61.1 ± 11.5	0.425
Sex, n (%)			0.250
Male	12 (66.7)	17 (50.0)	
Female	6 (33.3)	17 (50.0)	
Location, n (%)			0.798
Colon	7 (38.9)	12 (35.3)	
Rectum	11 (61.1)	22 (64.7)	
Histologic differentiation, n (%)			0.843
W/D	6 (33.3)	10 (29.4)	
M/D	9 (50.0)	16 (47.1)	
P/D	3 (16.7)	8 (23.5)	
Clinical stage, n (%)			0.278
III	8 (44.4)	10 (29.4)	
IV	10 (55.6)	24 (70.6)	
KPS score, n (%)			0.488
≥70	7 (38.9)	10 (29.4)	
<70	11 (61.1)	24 (70.6)	
Length (cm), n (%)			0.369
≤4	4 (22.2)	6 (17.6)	
4<, ≤8	11 (61.1)	16 (47.1)	
>8	3 (16.7)	12 (35.3)	
Treatment regimen, n (%)			0.432
PDT alone	8 (44.4)	0	
PDT+ST	10 (55.6)	0	
ST	0	19 (55.9)	
Untreated	0	15 (44.1)	

*CRC, colorectal cancer; PDT, photodynamic therapy; W/D, well-differentiated; M/D, moderately differentiated; P/D, poorly differentiated; ST, systemic therapy.

had superior OS to those in the ST group (median OS: 352 days, log-rank p=0.047) (Figure 2C).

3.3 Short-term response

The short-term efficacy and possible influencing factors of PDT are shown in Tables 2, 3. Of the 18 patients treated with PDT, 1 patient achieved complete response (CR), 7 patients achieved partial response (PR), 8 patients achieved stable disease (SD), and 2 patients died due to infection and other tumor-related adverse events. The objective response rate was 44.4%, and the disease control rate was 88.9% (Table 3). We further explored the possible causes affecting the short-term efficacy of PDT, and the degree of differentiation (p=0.020) and the degree of endoscopic necrosis (p=0.039) were two crucial factors (Table 3). Moderately differentiated had the best therapeutic effect, followed by well and poorly differentiated. The degree of necrosis under colonoscopy was positively correlated with short-term efficacy and positively correlated with short-term efficacy. More severe tumor necrosis means better short-term outcomes for patients. Figure 3 shows a typical case of a patient who achieved complete remission of the local lesion shortly after diagnosing CRC with PDT.

3.4 Immune evaluation

To explore the effect of PDT on the immune microenvironment of CRC patients, we examined the changes of immune cells in peripheral blood and tumor tissues of patients receiving PDT. Detailed data from peripheral blood tests are shown in Supplementary Tables S1, 2. The results before and after PDT are shown in Figures 4, 5. Before and after PDT, the systemic immune cell numbers of stage III patients and stage IV patients showed an opposite trend. The former showed a majority decrease after PDT, while the latter showed an overall increase. Specifically, in 8 patients with stage III CRC, Total T cells, $CD4^+$ T cells, $CD8^+$ T cells, $CD4^+CD45RA^+$ T cells, $CD4^+CD45RO^+$ T cells, $CD8^+CD45RA^+$ T cells Cells, and

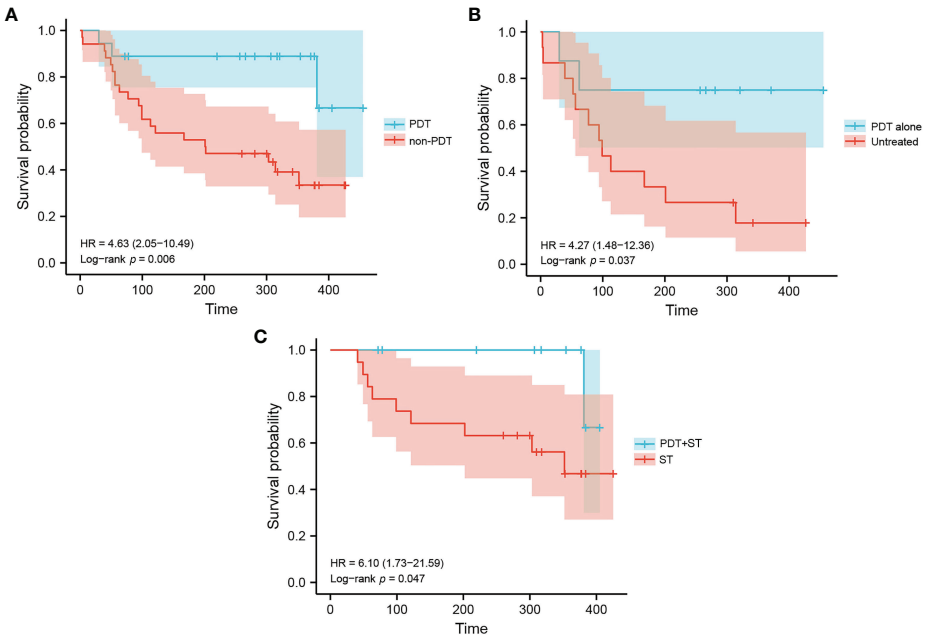

FIGURE 2
Kaplan-Meier estimation of patient survival in each group. **(A)** Overall survival of patients in the PDT group and non-PDT group. **(B)** Overall survival of patients in the PDT alone group and untreated group. **(C)** Overall survival of patients in the PDT+ST group and ST group.

$CD4^+CD45RO^+$ T cells were significantly decreased compared with those before PDT. B cells and NK cells were also decreased in most cases, although there was no statistical difference (Figure 4). In patients with stage IV, however, most of the immune cells increased after PDT. Among them are T cells, B cells, $CD8^+$T cells, $CD8^+CD45RA^+$T cells, and $CD4^+CD45RO^+$T cells (Figure 5).

H-E staining showed that many inflammatory cells and immune cells infiltrated the tumor tissue 48h after PDT (Figure 6). Immunohistochemical results showed that T cells (p=0.0053), B cells (p=0.0216), $CD4^+$ T cells (p=0.0341), $CD8^+$ T cells (p=0.0132), and macrophages (p=0.0172) increased significantly after PDT, while the number of NK cells (p=0.3276) did not change significantly (Figure 7; Supplementary Figure S1).

3.5 Adverse reactions

The distribution of adverse reactions after PDT is shown in Table 4. Transient leukocytosis occurred in 2 patients, and fever occurred in 3 patients on the night of treatment and returned to normal after physical cooling. One patient developed abdominal pain shortly after treatment and improved after rest. After discharge, 2 patients did not comply with the strict requirements of avoiding light and developed pigmentation of the skin on the face, forearm, and back of the hand. None of the patients had severe complications such as hematochezia and perforation.

4 Discussion

Despite the increasing availability of an arsenal of anti-tumor weapons, non-specificity, drug resistance, low response rates, and toxic severe side effects are still the main challenges faced by current tumor treatment strategies (11). As an alternative intervention to destroy cancer cells, PDT can compensate for some deficiencies associated with conventional tumor therapy (12). In addition to the precise clinical efficacy, PDT also has the advantages of less pain, high acceptance, and repeatable operation. For some early or occult tumors, PDT may achieve the effect of a radical cure. For patients with advanced cancers or patients who cannot undergo surgery due to physical limitations, PDT is a palliative treatment that can effectively relieve pain, improve quality of life and prolong life (8). Clinical studies on PDT therapy in CRC are rarely seen compared with other gastrointestinal tumors. In this study, 52 CRC patients with advanced stages (III-A to IV-C) were included, all unable or unwilling to undergo surgical resection, including 18 patients receiving PDT and 34 patients not receiving PDT. More than 50% of patients have distant metastasis, indicating a poor

10.3389/fimmu.2022.1050421

TABLE 2 Clinical data for the eighteen CRC patients undergoing PDT.

Case	Stent	Clinical stage	Treatment regimen	KPS (Before)	KPS (After 2 mo)	Degree of necrosis (After 48h)	Short-term efficacy (After 2 mo)	Survival (Days)	Outcome
1	Yes	IIIC	PDT	70	80	Severe	SD	455	Alive
2	Yes	IVB	PDT+ST	70	90	Severe	PR	381	Death
3	No	IIIB	PDT+ST	80	90	Severe	CR	384	Alive
4	Yes	IIIC	PDT+ST	20	70	Moderate	SD	405	Alive
5	Yes	IVA	PDT	50	0	Moderate	PD	30	Death
6	Yes	IIIC	PDT+ST	60	80	Severe	SD	377	Alive
7	No	IIIC	PDT	60	70	Severe	PR	371	Alive
8	No	IVB	PDT+ST	60	80	Severe	PR	354	Alive
9	No	IVA	PDT	70	80	Severe	PR	321	Alive
10	Yes	IVC	PDT+ST	70	80	Moderate	PR	317	Alive
11	Yes	IIIC	PDT	30	0	Mild	PD	62	Death
12	No	IIIC	PDT+ST	60	70	Severe	SD	307	Alive
13	No	IVB	PDT	70	80	Moderate	SD	281	Alive
14	Yes	IVA	PDT	30	50	Moderate	SD	266	Alive
15	Yes	IVB	PDT	50	70	Severe	SD	257	Alive
16	Yes	IVC	PDT+ST	50	70	Moderate	PR	220	Alive
17	Yes	IVA	PDT+ST	70	80	Severe	SD	72	Alive
18	Yes	IIIC	PDT+ST	60	80	Severe	PR	78	Alive

ST, systemic therapy; CR, complete response; PR, partial response; SD, stable disease; PD, progressive disease.

prognosis (4), especially without any treatment.

We made a detailed comparison between the PDT group and the non-PDT group. The current short-term follow-up results show that the overall prognosis of the PDT group is better than that of the non-PDT group (p=0.006). Among them, the median survival time of the non-PDT group was only 6.7 months, while the median survival time of patients receiving PDT at the same time had not yet reached, which was encouraging. Comparing CRC patients who received PDT alone with those who did not receive any treatment, the results were also gratifying in this case (p=0.037). Cause PDT can directly kill tumor cells and eliminate tumors by destroying the microcirculation of tumor tissues and enhancing the body's anti-tumor immunity, thus prolonging the survival time of patients (13–15). Some patients with CRC received PDT combined with other therapies, such as chemotherapy, immunotherapy, or targeted therapy. Compared with patients who only received other treatments, the survival rate of the PDT combined with other therapies was significantly better (p=0.047), which may be due to the synergistic reaction between PDT and other therapies (16, 17). Unfortunately, one patient died of severe infection and multiple organ failures due to multiple liver and lung metastases. The above results showed that PDT alone or combined with other therapies showed significant advantages. However, the number of patients receiving PDT in each subgroup was small, and the survival data were only exploratory. However, the pilot series contains a minimal number of patients, and the survival data are only preliminary experimental.

To assess the direct efficacy of PDT, we evaluated the short-term efficacy of patients with CRC who had completed PDT by endoscopic and radiographic examinations after two months, Taking RECIST version 1.1 as the judge. Not surprisingly, the therapeutic effect of PDT was rapid and pronounced, especially in the remission of local lesions. In fact, PDT continues to play a therapeutic role. Many patients could still see pieces of necrotic tissue falling off the original tumor site when they were reviewed by colonoscopy one month later. Objective response was achieved in nearly half of the 18 CRC patients (8/18), and the disease control rate was 88.9% (16/18). By analyzing the factors that might affect the short-term efficacy of PDT, we found two valuable indicators: endoscopic necrosis degree and tumor differentiation degree. Obviously, the more severe the necrosis, the better the treatment effect of PDT. This process includes apoptosis, regulated necrosis (such as necroptosis and lysosome-dependent cell death), and other cell death mechanisms (18, 19). Due to the limited penetration depth of the laser in tissues (5-7mm), large and deeply infiltrated tumors could not be eliminated at a time. Therefore, the complete remission rate of this group of cases was only 5.6% (1/18). The short-term efficacy of PDT was also correlated with differentiation degree. Moderately differentiated colorectal tumors performed best, mainly because the tumor tissues were enriched in

10.3389/fimmu.2022.1050421

TABLE 3 Short-term efficacy and the efficacy comparison of different types.

Types	n	Short-term efficacy				Objective response rate (%)	Disease control rate (%)	Invalid rate (%)			
		CR	PR	SD	PD	(CR+PR)/n	(CR+PR+SD)/n	PD/n	CR+PR +SD	PD	*p*-value*
All patients	18	1	7	8	2	44.4	88.9	11.1	16	2	
Location											0.641
Colon	7	0	3	3	1	42.9	85.7	14.3	6	1	
Rectum	11	1	4	5	1	45.5	90.9	9.1	10	1	
Differentiation											0.020
W/D	6	0	1	5	0	16.7	100	0	6	0	
M/D	9	1	5	3	0	66.7	100	0	9	0	
P/D	3	0	1	0	2	33.3	33.3	66.7	1	2	
Clinical stage											1.000
III	8	1	2	4	1	37.5	87.5	12.5	7	1	
IV	10	0	5	4	1	50	90	10	9	1	
KPS score											0.491
≥70	7	1	3	3	0	57.1	100	0	7	0	
<70	11	0	4	5	2	36.4	81.8	18.2	9	2	
Length (cm)											1.000
≤4	4	1	2	1	0	75	100	0	4	0	
<4 ≤ 8	11	0	3	6	2	27.3	81.8	18.2	9	2	
>8	3	0	2	1	0	66.7	100	0	3	0	
Stent											0.529
Yes	12	0	4	6	2	33.3	83.3	16.7	10	2	
No	6	1	3	2	0	66.7	100	0	6	0	
Treatment line											0.183
PDT	8	0	2	4	2	25	75	25	6	2	
PDT+ST	10	1	5	4	0	60	100	0	10	0	
Necrosis							0				
Mild	1	0	0	0	1	0	0	100	0	1	0.039
Moderate	6	0	2	3	1	33.3	83.3	16.7	5	1	
Severe	11	1	5	5	0	54.5	100	0	11	0	

*W/D, well-differentiated; M/D, moderately differentiated; P/D, poorly differentiated; ST, systemic therapy; CR, complete response; PR, partial response; SD, stable disease; PD, progressive disease.

photosensitizers and had sufficient blood supply, and the objective response rate reached 66.7% (6/9); the reason may be that the characteristics of well-differentiation tumors are close to normal tissues, and the enrichment of photosensitizer in tumor tissues is almost the same as that in normal tissues, so the efficacy of PDT is not ideal (20, 21). Patients with poorly differentiation have a higher degree of malignancy and faster disease progression, resulting in a relative lack of blood supply as well as insufficient free radical production, thus the effect is not good.

The changes in the immune function of patients before and after PDT are a focus of our attention. Interestingly, the systemic immune function of almost all patients with stage III CRC decreased compared to before PDT. In contrast, the immune indicators of stage IVpatients generally showed an upward trend. Further observation illustrated that the number of immune cells in patients with stage III remained normal or slightly low before PDT, while the initial immune function of patients with stage IV was decreased. We speculate that this change is that a mass of immune cells quickly gathered at the tumor site, decreasing blood content. However, since the total amount of various types of immune cells was not low before the intervention, the overall level still fluctuated around the lower limit of the normal range, which may be a time difference problem. CRC patients with stage III are generally in good condition, basically normal organ function, well nutritional status with near-normal peripheral blood immune cells. The peripheral immune cells rapidly reach the local tumor lesions after antigen is released from necrotic tumor cells, decreasing peripheral immune cell numbers after PDT. However, due to distant metastasis, organ dysfunction,

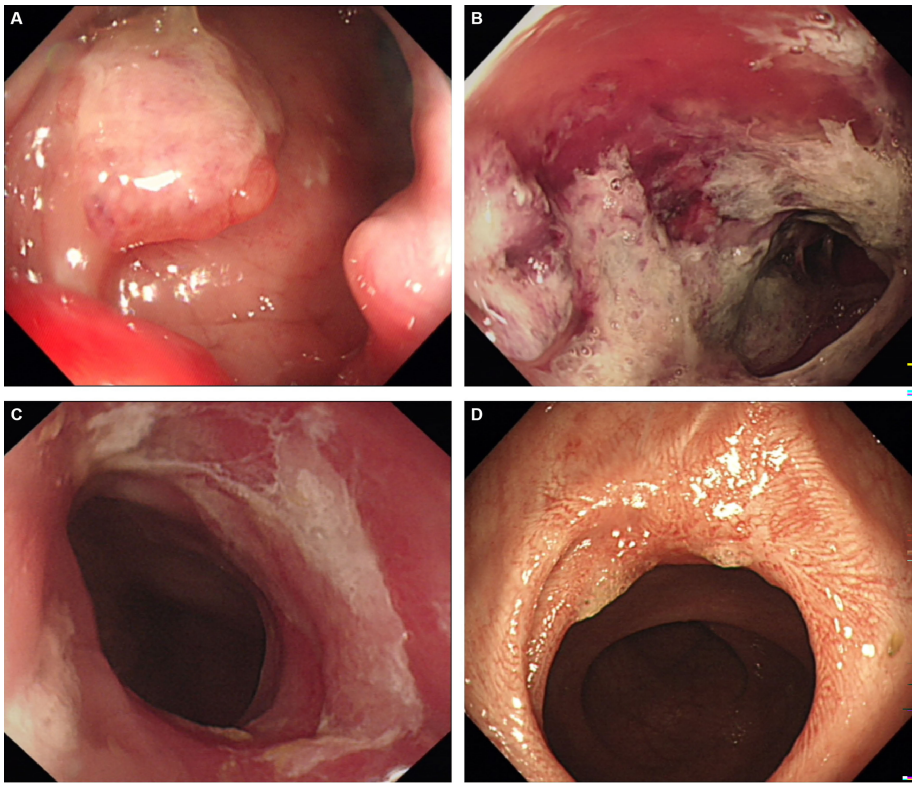

FIGURE 3
A representative case of achieving complete response after PDT. **(A)** The cauliflower-like protrusion was seen on the lateral wall of the rectum, and the clinical stage is stage IIIB; **(B)** 48h after PDT, a large amount of gray necrotic tissue was formed at the lesion site, with hyperemia and edema at the edge; **(C)** One month after PDT, the lesion's surface was covered with a small amount of residual necrotic tissue, and the tumor almost disappeared; **(D)** Three months after PDT, the tumor tissue disappeared and a scar formed. Biopsy confirmed that the tumor cells were negative, so complete remission was achieved.

malnutrition, and cachexia, the immune cells of stage IV patients have been partially depleted, and the initial immune function in the body is relatively deficient. PDT intervention, on the one hand, can stimulate immune organs to generate more immune cells and improve the body's overall immune level, causing an increase in peripheral immune cell numbers after PDT; on the other hand, it can promote the local recruitment of systemic immune cells to tumor tissues and play an anti-tumor immune role. To test this idea, we detected the changes of immune cells in tumor tissues before and after PDT by IHC. The results showed that a large number of inflammatory cells and immune cells were infiltrated in the tumor tissues of almost all CRC patients. In addition, NK cells, T cells, B cells, $CD4^+$ T cells, $CD8^+$ T cells, and macrophages were markedly increased, which provided an answer for the decline of immune cells in the peripheral blood of stage III patients.

These processes indicate that PDT is likely to trigger immunogenic cell death (ICD) through chemical damage, recruit DCs and antigen-specific cytotoxic T lymphocytes (CTLs) to the tumor microenvironment (TME), reverse the "cold tumor" to "hot tumor", and activate the anti-tumor immune response. In addition to killing *in situ* tumors, it can effectively inhibit distal and metastatic tumors by improving the survival rate of patients with malignant tumors (22, 23). Once the signal of photo-oxidative damage caused by PDT is sensed, neutrophils are the first to reach the tumor site and subsequently direct a large number of monocytes/macrophages to rapidly invade the PDT-irradiated tumor margin to remove injured and dead cells (24, 25). In contrast, studies have shown that the therapeutic effect of PDT is significantly reduced if the above inflammatory cells are absent or their activity is inhibited (26). Acute inflammatory response increases the presentation of tumor antigens, paving the way for subsequent adaptive immunity (8). Studies have shown that PDT intervention enhances the activation of tumor-specific $CD8^+$ T cells (26, 27). In the absence of $CD8^+$ T cell activation and/or tumor

10.3389/fimmu.2022.1050421

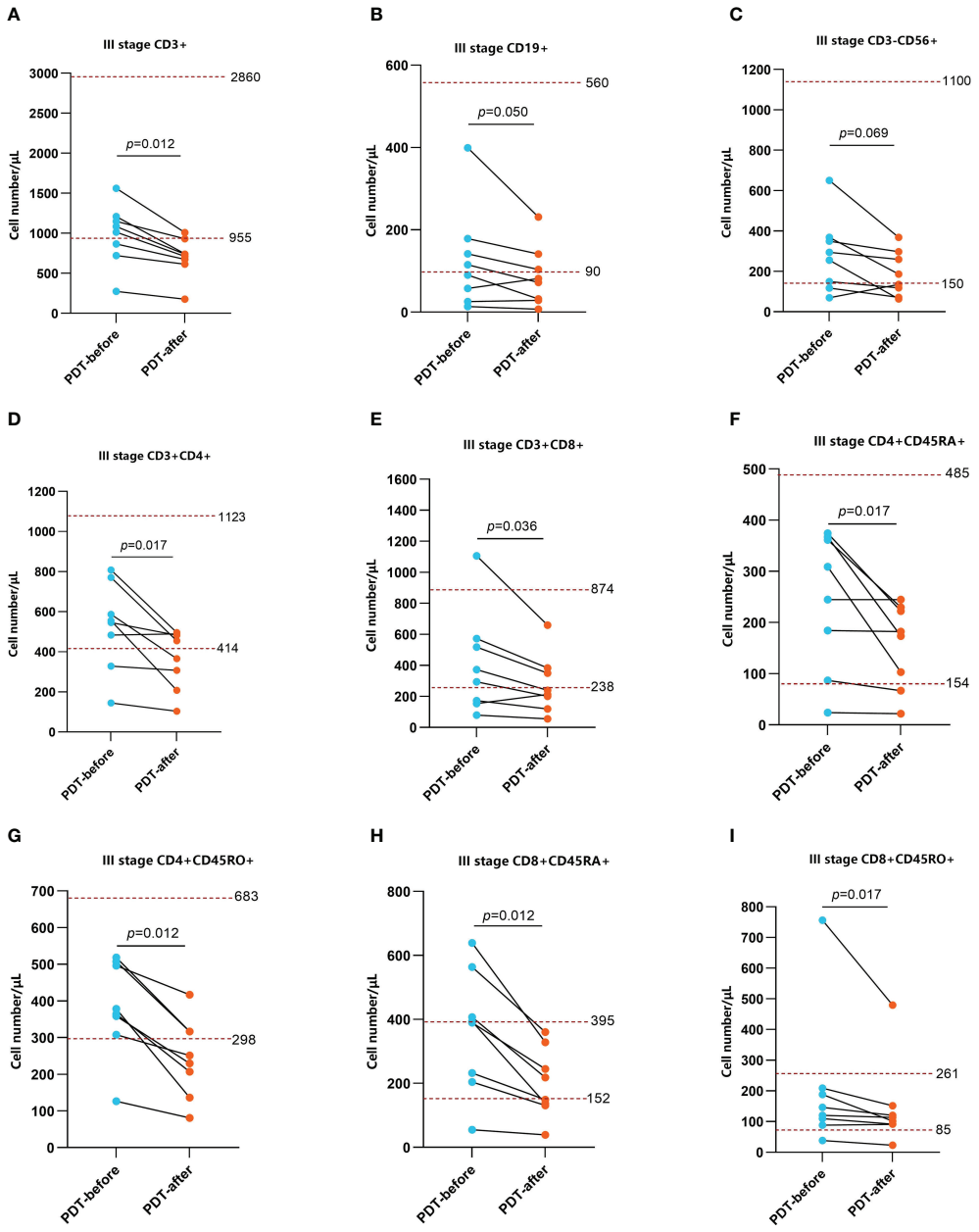

FIGURE 4
Changes in peripheral blood immune function before and after 48h of PDT in stage III CRC patients (n=8). The number of $CD3^+$ T cells, $CD3^+CD4^+$ T cells, $CD3^+CD8^+$ T cells, $CD4^+CD45RA^+$ T cells, $CD4^+CD45RO^+$ T cells, $CD8^+CD45RA^+$ T cells, $CD8^+CD45RO^+$ T cells were basically at a normal level before PDT but significantly decreased at 48h after PDT **(A, D, E–I)**. $CD19^+$ B cells and $CD3^-CD56^+$ NK cells were at lower than normal levels. Although there was no statistical difference in CD cells, the overall trend was still downward **(B, C)**.

invasion, the efficacy of PDT is significantly reduced (28), suggesting that $CD8^+$ T cells play a central role in PDT-induced anti-tumor immunity. In most cases, the $CD8^+$ effect and memory T cell generation depend on the presence and activation of $CD4^+$ T cells. Earlier studies have shown that immune deficiency of helper T cells leads to a significant reduction in PDT-mediated tumor healing (29). However, some studies reveal that $CD4^+$ T cells play a limited role in PDT therapy (28). In this study, $CD4^+$ T cells increased significantly after treatment, which may help $CD8^+$ T cells function.

In addition to immune cells, PDT may also affect stromal components of the TME. Fibroblasts constitute one of the most important cells in the stroma. They play an active role in the

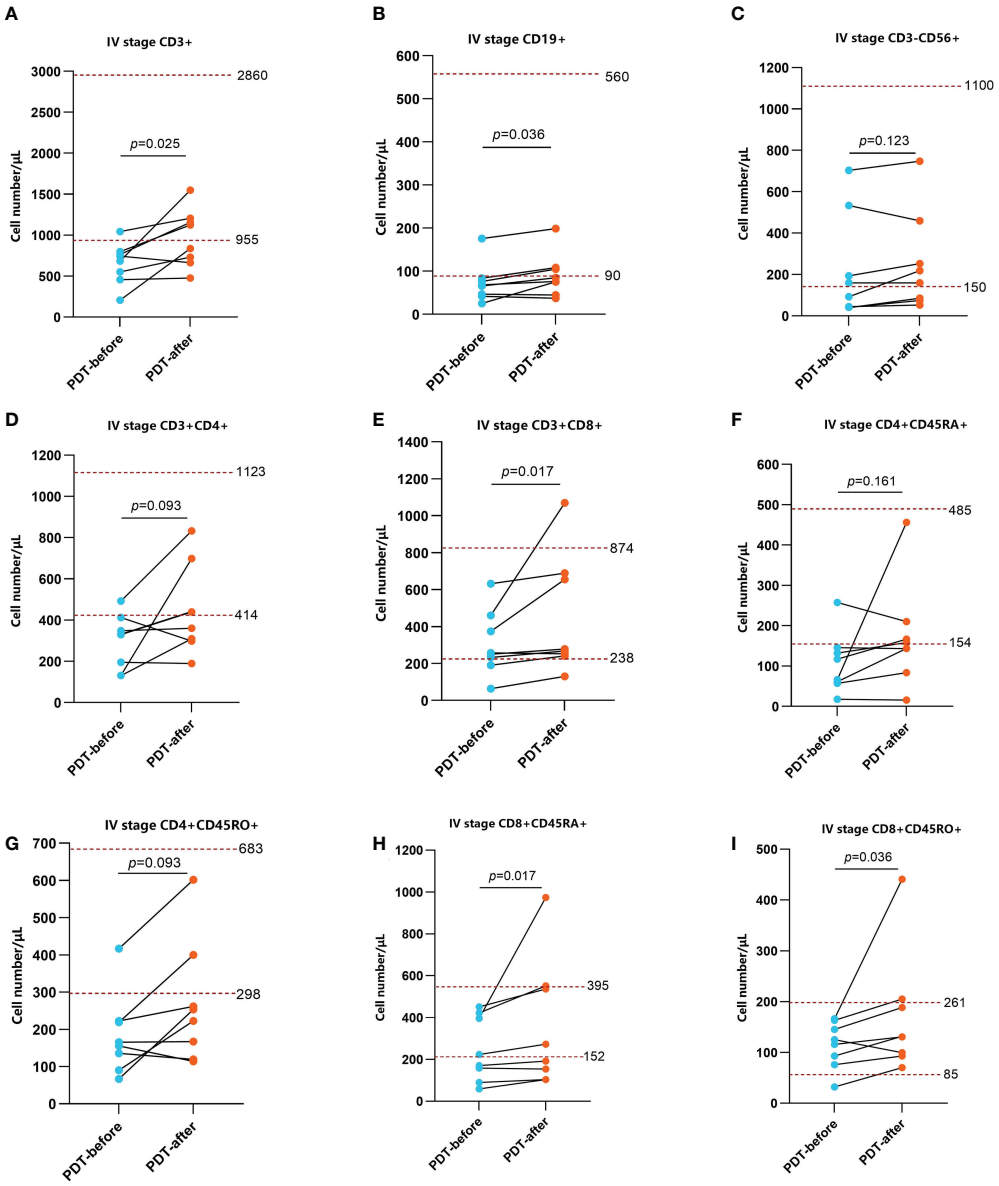

FIGURE 5
Changes in peripheral blood immune function in stage IV patients before and after PDT 48h (n=8). The number of $CD3^+$ T cells, $CD19^+$ B cells, $CD3^+CD8^+$ T cells, $CD8^+CD45RA^+$ T cells, $CD8^+CD45RO^+$ T cells were relatively lower before PDT and increased significantly 48h after PDT **(A, B, E, H, I)**. The changes of $CD3^-CD56^+$ NK cells, $CD3^+CD4^+$ T cells, $CD4^+CD45RA^+$ T cells $CD4^+CD45RO^+$ T cells were not obvious **(C, D, F, G)**.

initiation and progression of various tumors, and shape the TME by directly inhibiting anti-tumor immune response or recruiting immunosuppressive cells (30). On the one hand, some studies have shown that PDT may reverse the fibroblast-myofibroblast differentiation and reshape the extracellular matrix (ECM) (31). However, others believe that PDT has no apparent cytotoxicity to fibroblasts (32), further research must be revealed. On the other hand, the effect of PDT is less affected by the therapeutic resistance induced by carcinoma-associated fibroblasts (CAFs) (33).

Of course, it is difficult to eliminate all tumor cells by PDT alone, especially in the case of distant metastasis. The combination of PDT with other therapies has considerable appeal in terms of enhancing efficacy against tumors because it

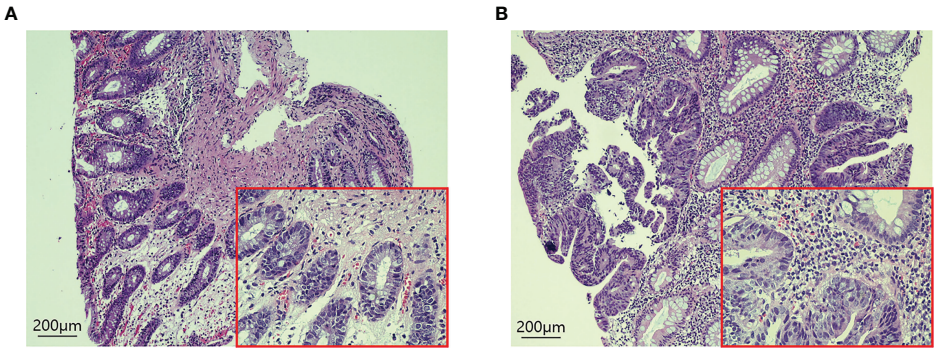

FIGURE 6
H-E staining of tumor tissues in CRC patients before and 48 hours after PDT. **(A)** Before PDT, a small number of immune cells were infiltrated around the tumor tissue. **(B)** 48h after PDT, the number of immune cells in tumor tissue increased significantly.

exploits the advantages and offsets the disadvantages of each treatment method to produce additional or even synergistic therapeutic effects (34, 35). Moreover, using lower doses in combination therapy may cause fewer side effects and better results than single therapy (35). Chemotherapy relieves the restriction of light penetration in PDT and enhances the sensitivity of cancer cells to reactive oxygen species. The broad-spectrum activity and non-drug resistance of PDT can also combat the troublesome problem of drug resistance in chemotherapy (36, 37). Chemotherapy and PDT are combined

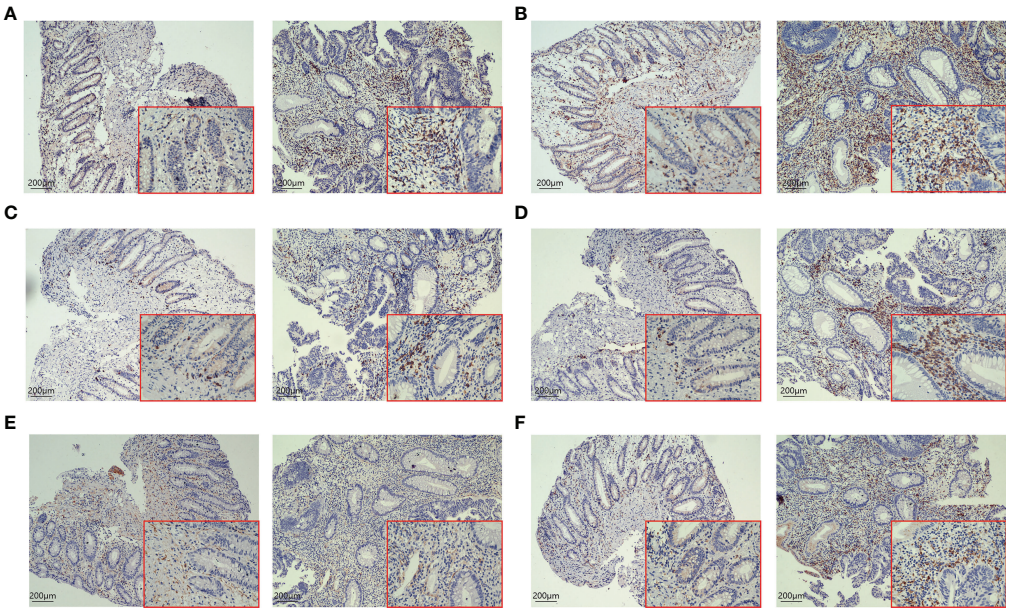

FIGURE 7
IHC staining of tumor tissues in CRC patients before and after 48h of PDT (n=6). Images are shown at 20× magnification; bars indicate 200 μm; the left is before PDT, and the right is 48h after PDT. **(A)** $CD3^+$ T cells in tumor tissue were increased significantly after PDT. **(B)** The number of $CD4^+$ T cells in tumor tissue was increased after PDT. **(C)** Changes in the number of $CD8^+$ T cells in tumor tissues. $CD8^+$ T cells were increased after PDT. **(D)** The number of $CD20^+$ B cells goes up after PDT. **(E)** There was no significant change in $CD56^+$ T cells. **(F)** The number of macrophages increased significantly after PDT.

TABLE 4 Toxicities related to PDT.

Events	Number	Rate (%)
WBC increase	2	11.1
Fever	3	16.7
Abdominal pain	1	5.6
Skin phototoxicity	2	11.1
Hematochezia	0	0
Perforation	0	0

WBC, white blood cells.

in mutual assistance has significantly improved the clinical efficacy compared with single PDT or chemotherapy (38). The combination of PDT and immunotherapy can effectively eradicate target tumors and possible residual cancer cells and metastases and trigger immune memory to prevent tumor recurrence and provide a possible cure (34). Some targeted drugs, such as anti-angiogenesis or anti-vascular drugs (39) and anti-epidermal growth factor receptor drugs (40), have also been proven to improve the efficacy of PDT further and significantly improve tumor growth control after PDT. In our study, one patient with low rectal cancer received chemotherapy combined with targeted and immunotherapy after one week of PDT. After three months of follow-up, a complete pathological complete response (pCR) was achieved.

The adverse reactions of the enrolled patients during PDT were similar to those reported in the literature (41), mainly transient leukocyte elevation and mild fever, which may be related to inflammatory reactions caused by treatment. Occasionally, patients may have mild abdominal pain, which can be relieved after rest. Other common adverse reactions include photoallergic reactions such as redness and pigmentation at the exposure site, associated with irregular light avoidance after PDT. Once it occurs, it can be improved by giving antiallergic drugs and topical corticosteroid scrubs.

Some limitations of this study need to be mentioned. First, this study is a single-center retrospective study, selection bias is inevitable, and other investigators' findings are subject to external validation. Second, the short follow-up time and the absence of some outcome indicators may lead to the overestimation of the therapeutic effect of PDT. Third and most important, the relatively small number of patients limits our ability to perform statistical analyses, especially when comparing different subgroups. Further multicenter prospective randomized trials are needed to compare the effects of PDT on the CRC immune microenvironment and in combination with other measures.

5 Conclusions

In this study, PDT effectively relieved the obstructive symptoms of CRC patients, inhibited tumor growth, and prolonged the survival time of patients with reasonable safety. Subsequently, we further evaluated CRC patients' systemic and tumor local immune microenvironment changes before and after PDT. PDT recruits various immune cells to surround tumors, transforms "cold tumors" into "hot tumors", activates the body's anti-tumor immune effect, and then exerts tumor-killing effects at local and distant sites. PDT has synergistic effects when combined with chemotherapy, immunotherapy, or targeted therapy. With the development of more clinical studies and more efficient photosensitizers, PDT will occupy a space to treat more tumors.

Data availability statement

The original contributions presented in the study are included in the article/Supplementary Material. Further inquiries can be directed to the corresponding author.

Ethics statement

The studies involving human participants were reviewed and approved by the Committee of Medical Ethics Experts of the Second Hospital of Lanzhou University. Written informed consent for participation was not required for this study in accordance with the national legislation and the institutional requirements.

Author contributions

Study conception and design: BG, BW, and HC. Acquisition of data: BG, CM, LG, JZ, PZ, YW. Analysis and interpretation of data: BG, BW, XL, ZF. Statistical analysis: BG, BW, YY. Drafting the article: BG, BW, XL, ZF. Critical revision of the article: HL, TZ, HC. All authors contributed to the article and approved the submitted version.

Funding

This research was supported by Key Project of Science and Technology in Gansu Province (19ZD2WA001), Key Talents Program of Gansu Province (2019RCXM020), Cuiying Scientific and Technological Innovation Program of Lanzhou University Second Hospital (CY2017-ZD01), Science and

Technology Project of Chengguan District of Lanzhou City (2020SHFZ0039), Outstanding Doctoral Program of Natural Science Foundation of Gansu Province (22JR5RA945), "Innovation Star" Project for Outstanding Graduate Students in Gansu Province (2022CXZX-162).

Conflict of interest

The authors declare that the research was conducted in the absence of any commercial or financial relationships that could be construed as a potential conflict of interest.

Publisher's note

All claims expressed in this article are solely those of the authors and do not necessarily represent those of their affiliated organizations, or those of the publisher, the editors and the reviewers. Any product that may be evaluated in this article, or claim that may be made by its manufacturer, is not guaranteed or endorsed by the publisher.

Supplementary material

The Supplementary Material for this article can be found online at: https://www.frontiersin.org/articles/10.3389/fimmu.2022.1050421/full#supplementary-material

SUPPLEMENTARY FIGURE 1
Immune cell infiltration in tumor tissues of CRC patients before and after 48h PDT (n=6). The results showed that T cells (p=0.0053), B cells (p=0.0216), $CD4^+$ T cells (p=0.0341), $CD8^+$ T cells (p=0.0132), and macrophages (p=0.0172) increased significantly after PDT, and NK cells did not change much.

References

1. Sung H, Ferlay J, Siegel RL, Laversanne M, Soerjomataram I, Jemal A, et al. Global cancer statistics 2020: Globocan estimates of incidence and mortality worldwide for 36 cancers in 185 countries. *CA Cancer J Clin* (2021) 71(3):209–49. doi: 10.3322/caac.21660

2. Zhou J, Zheng R, Zhang S, Zeng H, Wang S, Chen R, et al. Colorectal cancer burden and trends: Comparison between China and major burden countries in the world. *Chin J Cancer Res* (2021) 33(1):1–10. doi: 10.21147/j.issn.1000-9604.2021.01.01

3. Dekker E, Tanis PJ, Vleugels JLA, Kasi PM, Wallace MB. Colorectal cancer. *Lancet* (2019) 394(10207):1467–80. doi: 10.1016/s0140-6736(19)32319-0

4. Siegel RL, Miller KD, Goding Sauer A, Fedewa SA, Butterly LF, Anderson JC, et al. Colorectal cancer statistics, 2020. *CA Cancer J Clin* (2020) 70(3):145–64. doi: 10.3322/caac.21601

5. Battersby NJ, Bouliotis G, Emmertsen KJ, Juul T, Glynne-Jones R, Branagan G, et al. Development and external validation of a nomogram and online tool to predict bowel dysfunction following restorative rectal cancer resection: The polars score. *Gut* (2018) 67(4):688–96. doi: 10.1136/gutjnl-2016-312695

6. Mishra J, Drummond J, Quazi SH, Karanki SS, Shaw JJ, Chen B, et al. Prospective of colon cancer treatments and scope for combinatorial approach to enhanced cancer cell apoptosis. *Crit Rev Oncol Hematol* (2013) 86(3):232–50. doi: 10.1016/j.critrevonc.2012.09.014

7. Kaleta-Richter M, Kawczyk-Krupka A, Aebisher D, Bartusik-Aebisher D, Czuba Z, Cieślar G. The capability and potential of new forms of personalized colon cancer treatment: Immunotherapy and photodynamic therapy. *Photodiagnosis Photodyn Ther* (2019) 25:253–8. doi: 10.1016/j.pdpdt.2019.01.004

8. Agostinis P, Berg K, Cengel KA, Foster TH, Girotti AW, Gollnick SO, et al. Photodynamic therapy of cancer: An update. *CA Cancer J Clin* (2011) 61(4):250–81. doi: 10.3322/caac.20114

9. Gollnick SO, Vaughan L, Henderson BW. Generation of effective antitumor vaccines using photodynamic therapy. *Cancer Res* (2002) 62(6):1604–8.

10. Kimura M, Miyajima K, Kojika M, Kono T, Kato H. Photodynamic therapy (Pdt) with chemotherapy for advanced lung cancer with airway stenosis. *Int J Mol Sci* (2015) 16(10):25466–75. doi: 10.3390/ijms161025466

11. Simelane NWN, Kruger CA, Abrahamse H. Targeted nanoparticle photodynamic diagnosis and therapy of colorectal cancer. *Int J Mol Sci* (2021) 22(18):9779. doi: 10.3390/ijms22189779

12. Winifred Nompumelelo Simelane N, Abrahamse H. Nanoparticle-mediated delivery systems in photodynamic therapy of colorectal cancer. *Int J Mol Sci* (2021) 22(22):12405. doi: 10.3390/ijms222212405

13. Kwiatkowski S, Knap B, Przystupski D, Saczko J, Kędzierska E, Knap-Czop K, et al. Photodynamic therapy - mechanisms, photosensitizers and combinations. *BioMed Pharmacother* (2018) 106:1098–107. doi: 10.1016/j.biopha.2018.07.049

14. Spring BQ, Rizvi I, Xu N, Hasan T. The role of photodynamic therapy in overcoming cancer drug resistance. *Photochem Photobiol Sci* (2015) 14(8):1476–91. doi: 10.1039/c4pp00495g

15. van Straten D, Mashayekhi V, de Bruijn HS, Oliveira S, Robinson DJ. Oncologic photodynamic therapy: Basic principles, current clinical status and future directions. *Cancers (Basel)* (2017) 9(2):19. doi: 10.3390/cancers9020019

16. Hong MJ, Cheon YK, Lee EJ, Lee TY, Shim CS. Long-term outcome of photodynamic therapy with systemic chemotherapy compared to photodynamic therapy alone in patients with advanced hilar cholangiocarcinoma. *Gut Liver* (2014) 8(3):318–23. doi: 10.5009/gnl.2014.8.3.318

17. Nkune NW, Kruger CA, Abrahamse H. Possible enhancement of photodynamic therapy (Pdt) colorectal cancer treatment when combined with cannabidiol. *Anticancer Agents Med Chem* (2021) 21(2):137–48. doi: 10.2174/1871520620666200415102321

18. Bacellar IO, Tsubone TM, Pavani C, Baptista MS. Photodynamic efficiency: From molecular photochemistry to cell death. *Int J Mol Sci* (2015) 16(9):20523–59. doi: 10.3390/ijms160920523

19. Kessel D. Death pathways associated with photodynamic therapy. *Med Laser Appl* (2006) 21(4):219–24. doi: 10.1016/j.mla.2006.05.006

20. Allison RR, Sibata CH. Oncologic photodynamic therapy photosensitizers: A clinical review. *Photodiagnosis Photodyn Ther* (2010) 7(2):61–75. doi: 10.1016/j.pdpdt.2010.02.001

21. Juzeniene A, Peng Q, Moan J. Milestones in the development of photodynamic therapy and fluorescence diagnosis. *Photochem Photobiol Sci* (2007) 6(12):1234–45. doi: 10.1039/b705461k

22. Fan Z, Liu H, Xue Y, Lin J, Fu Y, Xia Z, et al. Reversing cold tumors to hot: An immunoadjuvant-functionalized metal-organic framework for multimodal imaging-guided synergistic photo-immunotherapy. *Bioact Mater* (2021) 6(2):312–25. doi: 10.1016/j.bioactmat.2020.08.005

23. Li Z, Zhu L, Sun H, Shen Y, Hu D, Wu W, et al. Fluorine assembly nanocluster breaks the shackles of immunosuppression to turn the cold tumor hot. *Proc Natl Acad Sci USA* (2020) 117(52):32962–9. doi: 10.1073/pnas.2011297117

24. Dougherty TJ, Gomer CJ, Henderson BW, Jori G, Kessel D, Korbelik M, et al. Photodynamic therapy. *J Natl Cancer Inst* (1998) 90(12):889–905. doi: 10.1093/jnci/90.12.889

25. Krosl G, Korbelik M, Dougherty GJ. Induction of immune cell infiltration into murine sccvii tumour by photofrin-based photodynamic therapy. *Br J Cancer* (1995) 71(3):549–55. doi: 10.1038/bjc.1995.108

26. Kousis PC, Henderson BW, Maier PG, Gollnick SO. Photodynamic therapy enhancement of antitumor immunity is regulated by neutrophils. *Cancer Res* (2007) 67(21):10501–10. doi: 10.1158/0008-5472.Can-07-1778

27. Mroz P, Vatansever F, Muchowicz A, Hamblin MR. Photodynamic therapy of murine mastocytoma induces specific immune responses against the Cancer/Testis antigen P1a. *Cancer Res* (2013) 73(21):6462–70. doi: 10.1158/0008-5472.Can-11-2572

28. Kabingu E, Vaughan L, Owczarczak B, Ramsey KD, Gollnick SO. Cd8+ T cell-mediated control of distant tumours following local photodynamic therapy is independent of Cd4+ T cells and dependent on natural killer cells. *Br J Cancer* (2007) 96(12):1839–48. doi: 10.1038/sj.bjc.6603792

29. Korbelik M, Cecic I. Contribution of myeloid and lymphoid host cells to the curative outcome of mouse sarcoma treatment by photodynamic therapy. *Cancer Lett* (1999) 137(1):91–8. doi: 10.1016/s0304-3835(98)00349-8

30. Gok Yavuz B, Gunaydin G, Kosemehmetoglu K, Karakoc D, Ozgur F, Guc D. The effects of cancer-associated fibroblasts obtained from atypical ductal hyperplasia on anti-tumor immune responses. *Breast J* (2018) 24(6):1099–101. doi: 10.1111/tbj.13139

31. Zhang C, Wang J, Chou A, Gong T, Devine EE, Jiang JJ. Photodynamic therapy induces antifibrotic alterations in primary human vocal fold fibroblasts. *Laryngoscope* (2018) 128(9):E323–e31. doi: 10.1002/lary.27219

32. Gomes-Filho JE, Sivieri-Araujo G, Sipert CR, da Silva Santos LM, de Azevedo Queiroz ÍO, Men Martins C, et al. Evaluation of photodynamic therapy on fibroblast viability and cytokine production. *Photodiagnosis Photodyn Ther* (2016) 13:97–100. doi: 10.1016/j.pdpdt.2016.01.007

33. Chen YC, Lou X, Zhang Z, Ingram P, Yoon E. High-throughput cancer cell sphere formation for characterizing the efficacy of photo dynamic therapy in 3d cell cultures. *Sci Rep* (2015) 5:12175. doi: 10.1038/srep12175

34. Li X, Lovell JF, Yoon J, Chen X. Clinical development and potential of photothermal and photodynamic therapies for cancer. *Nat Rev Clin Oncol* (2020) 17(11):657–74. doi: 10.1038/s41571-020-0410-2

35. Gunaydin G, Gedik ME, Ayan S. Photodynamic therapy for the treatment and diagnosis of cancer-a review of the current clinical status. *Front Chem* (2021) 9:686303. doi: 10.3389/fchem.2021.686303

36. He C, Liu D, Lin W. Self-assembled core-shell nanoparticles for combined chemotherapy and photodynamic therapy of resistant head and neck cancers. *ACS Nano* (2015) 9(1):991–1003. doi: 10.1021/nn506963h

37. Wang Z, Ma R, Yan L, Chen X, Zhu G. Combined chemotherapy and photodynamic therapy using a nanohybrid based on layered double hydroxides to conquer cisplatin resistance. *Chem Commun (Camb)* (2015) 51(58):11587–90. doi: 10.1039/c5cc04376j

38. Chen Y, Zhang L, Li F, Sheng J, Xu C, Li D, et al. Combination of chemotherapy and photodynamic therapy with oxygen self-supply in the form of mutual assistance for cancer therapy. *Int J Nanomedicine* (2021) 16:3679–94. doi: 10.2147/ijn.S298146

39. Ferrario A, von Tiehl KF, Rucker N, Schwarz MA, Gill PS, Gomer CJ. Antiangiogenic treatment enhances photodynamic therapy responsiveness in a mouse mammary carcinoma. *Cancer Res* (2000) 60 (15):4066–9.

40. Cengel KA, Hahn SM, Glatstein E. C225 and pdt combination therapy for ovarian cancer: The play's the thing. *J Natl Cancer Inst* (2005) 97(20):1488–9. doi: 10.1093/jnci/dji360

41. Zeng R, Liu C, Li L, Cai X, Chen R, Li Z. Clinical efficacy of hiporfin photodynamic therapy for advanced obstructive esophageal cancer. *Technol Cancer Res Treat* (2020) 19:1533033820930335. doi: 10.1177/1533033820930335

frontiers | Frontiers in Immunology

TYPE Original Research
PUBLISHED 18 November 2022
DOI 10.3389/fimmu.2022.967277

Check for updates

OPEN ACCESS

EDITED BY
Linlang Guo,
Zhujiang Hospital, China

REVIEWED BY
Jamshid Hadjati,
Tehran University of Medical Sciences, Iran
Ying Hong Li,
Chongqing University of Posts and Telecommunications, China

*CORRESPONDENCE
Yan Han
13720086335@163.com
Qixu Zhang
qzhang5@mdanderson.org

†These authors have contributed equally to this work

SPECIALTY SECTION
This article was submitted to Cancer Immunity and Immunotherapy, a section of the journal Frontiers in Immunology

RECEIVED 12 June 2022
ACCEPTED 04 November 2022
PUBLISHED 18 November 2022

CITATION
Xu Y, Chen Y, Jiang W, Yin X, Chen D, Chi Y, Wang Y, Zhang J, Zhang Q and Han Y (2022) Identification of fatty acid metabolism–related molecular subtype biomarkers and their correlation with immune checkpoints in cutaneous melanoma.
Front. Immunol. 13:967277.
doi: 10.3389/fimmu.2022.967277

COPYRIGHT
© 2022 Xu, Chen, Jiang, Yin, Chen, Chi, Wang, Zhang, Zhang and Han. This is an open-access article distributed under the terms of the Creative Commons Attribution License (CC BY). The use, distribution or reproduction in other forums is permitted, provided the original author(s) and the copyright owner(s) are credited and that the original publication in this journal is cited, in accordance with accepted academic practice. No use, distribution or reproduction is permitted which does not comply with these terms.

Identification of fatty acid metabolism–related molecular subtype biomarkers and their correlation with immune checkpoints in cutaneous melanoma

Yujian Xu[1†], Youbai Chen[1,2†], Weiqian Jiang[1], Xiangye Yin[1], Dongsheng Chen[1], Yuan Chi[1], Yuting Wang[1], Julei Zhang[1], Qixu Zhang[2*] and Yan Han[1*]

[1]Department of Plastic and Reconstructive Surgery, The First Medical Center of Chinese PLA General Hospital, Beijing, China, [2]Department of Plastic Surgery, The University of Texas MD Anderson Cancer Center, Houston, TX, United States

Purpose: Fatty acid metabolism (FAM) affects the immune phenotype in a metabolically dynamic tumor microenvironment (TME), but the use of FAM-related genes (FAMGs) to predict the prognosis and immunotherapy response of cutaneous melanoma (CM) patients has not been investigated. In this study, we aimed to construct FAM molecular subtypes and identify key prognostic biomarkers in CM.

Methods: We used a CM dataset in The Cancer Genome Atlas (TCGA) to construct FAM molecular subtypes. We performed Kaplan–Meier (K-M) analysis, gene set enrichment analysis (GSEA), and TME analysis to assess differences in the prognosis and immune phenotype between subtypes. We used weighted gene co-expression network analysis (WGCNA) to identify key biomarkers that regulate tumor metabolism and immunity between the subtypes. We compared overall survival (OS), progression-free survival (PFS), and disease-specific survival (DSS) between CM patients with high or low biomarker expression. We applied univariable and multivariable Cox analyses to verify the independent prognostic value of the FAM biomarkers. We used GSEA and TME analysis to investigate the immune-related regulation mechanism of the FAM subtype biomarker. We evaluated the immune checkpoint inhibition (ICI) response and chemotherapy sensitivity between CM patients with high or low biomarker expression. We performed real-time fluorescent quantitative PCR (qRT-PCR) and semi-quantitative analysis of the immunohistochemical (IHC) data from the Human Protein Atlas to evaluate the mRNA and protein expression levels of the FAM biomarkers in CM.

Results: We identified 2 FAM molecular subtypes (cluster 1 and cluster 2). K-M analysis showed that cluster 2 had better OS and PFS than cluster 1 did. GSEA

showed that, compared with cluster 1, cluster 2 had significantly upregulated immune response pathways. The TME analysis indicated that immune cell subpopulations and immune functions were highly enriched in cluster 2 as compared with cluster 1. WGCNA identified 6 hub genes (*ACSL5, ALOX5AP, CD1D, CD74, IL4I1, and TBXAS1*) as FAM biomarkers. CM patients with high expression levels of the six biomarkers had better OS, PFS, and DSS than those with low expression levels of the biomarkers. The Cox regression analyses verified that the 6 FAM biomarkers can be independent prognostic factors for CM patients. The single-gene GSEA showed that the high expression levels of the 6 genes were mainly enriched in T-cell antigen presentation, the PD-1 signaling pathway, and tumor escape. The TME analysis confirmed that the FAM subtype biomarkers were not only related to immune infiltration but also highly correlated with immune checkpoints such as PD-1, PD-L1, and CTLA-4. TIDE scores confirmed that patients with high expression levels of the 6 biomarkers had worse immunotherapy responses. The 6 genes conveyed significant sensitivity to some chemotherapy drugs. qRT-PCR and IHC analyses verified the expression levels of the 6 biomarkers in CM cells.

Conclusion: Our FAM subtypes verify that different FAM reprogramming affects the function and phenotype of infiltrating immune cells in the CM TME. The FAM molecular subtype biomarkers can be independent predictors of prognosis and immunotherapy response in CM patients.

KEYWORDS

cutaneous melanoma, tumor metabolism, fatty acid metabolism, immune infiltration, immune checkpoint, prognosis, tumor microenvironment

Introduction

Cutaneous melanoma (CM), the most fatal skin cancer, accounts for less than 5% of skin cancers but greater than 80% of skin cancer-caused deaths (1). Immunotherapy such as immune checkpoint inhibition (ICI) can significantly improve the prognosis of CM patients. However, up to 70% of CM patients have either innate or acquired ICI resistance, leading to high rates of recurrence, metastasis, and mortality (2–4). To provide these patients with evidence-based treatment and improve their clinical outcomes, we must be able to reliably predict immunotherapy responses.

The current Tumor Node Metastasis (TNM) classification of CM reflects primary tumor size and thickness, lymph node invasion, and distant metastasis based on the American Joint Committee on Cancer (AJCC)/Union for International Cancer Control(UICC) (5, 6), but it cannot predict prognosis and immunotherapy response in CM patients (7). Recent studies have demonstrated that, compared with the AJCC/UICC TNM classification system, classification systems that account for the immune component of the tumor microenvironment (TME) have superior prognostic value for predicting immunotherapy response (8, 9). For example, "hot" CM may respond well to immunotherapy, whereas "cold" CM with programmed cell death protein 1 (PD-1) inhibitor resistance, interferon γ inactivation, and $CD8^+$ T-cell exhaustion may respond poorly to immunotherapy (10). Therefore, it is urgent to develop a CM classification system with promising biomarkers that predict the prognosis and immunotherapy response.

Abnormal metabolism promotes tumorigenesis and disease progression by disturbing the energy supply and regulating the TME (11, 12). Some metabolites, such as lactic acid, can inhibit the cytolytic ability of $CD8^+$ effector T cells and downregulate immunity components in the TME (13). Tumor metabolic reprogramming plays a critical role in TME regulation and immunotherapy resistance (14–16). Metabolomic analyses have uncovered many novel biomarkers related to the diagnosis, prognosis, and treatment of many cancers, leading to the development of several antitumor strategies (17). As one of the most important intermediate products of lipid metabolism, fatty acid metabolism (FAM) is essential for many biological activities and maybe a promising immunotherapy target (18, 19). For

example, Shang et al. (20) found that certain molecules can promote cervical cancer metastasis by reprogramming FAM. Ding et al. constructed a FAM signature that identified molecular subtypes of colorectal cancer and predicted prognosis and immunotherapy response (21). Zhang et al. reported that $CD8^+$ tumor-infiltrating lymphocytes enhance the catabolism of fatty acids to preserve their effector functions and slow lung cancer progression (22). However, the prognostic and therapeutic value of FAM-related biomarkers in CM has not been reported. How CM cells sustain FAM in a metabolically dynamic TME and how FAM affects the phenotype and function of immune cells remain unclear.

The four aims of the present study were to 1) identify a FAM-related molecular subtype that represents the clinicopathological and immune features of CM; 2) identify and validate FAM-related genes (FAMGs); 3) unveil the association between FAM biomarkers and the immune phenotype and function of CM, and 4) determine the extent to which FAM molecular subtypes and biomarkers predict immunotherapy response.

Materials and methods

Collection of publicly available data

The analysis process of this study is shown in Figure 1. The RNA sequencing data and corresponding clinical data of CM samples were downloaded from The Cancer Genome Atlas (TCGA) (http://cancergenome.nih.gov/) (23). The RNA sequencing data of normal skin samples were downloaded from the Genotype-Tissue Expression (GTEx) database (https://gtexportal.org/home/) (24). The expression values of all genes were publicly available and in level 3 HTseq fragments per kilobase of exon per million mapped fragments format. The merged RNA expression profile of the TCGA CM cohort (471 samples) and GTEx normal skin cohort (234 samples) was normalized, and batch effects between the TCGA and GTEX data were removed using the limma package in R (25). GSE65904 (26) and GSE72056 (27) were downloaded from the Gene Expression Omnibus (GEO) database (https://www.ncbi.nlm.nih.gov/) and used for molecular subtyping and single-cell validation. A total of 531 FAMGs were derived from 6 FAMG sets in the Molecular Signatures Database (http://www.gsea-msigdb.org/gsea/msigdb/) (28) and were listed in Supplementary Table 1. And the clinical detail of TCGA samples were listed in Supplementary Table 2

Identification of differentially expressed FAMGs

To identify differentially expressed FAMGs (DEFAMGs), we analyzed the gene transcription data of the TCGA and GTEx cohorts using the limma package in R with a false discovery rate (FDR) < 0.05 and log2 fold change > 1. We used the pheatmap package in R to construct heatmaps of DEFAMGs. We used Gene Ontology (GO) (29) and Kyoto Encyclopedia of Genes and Genomes (KEGG) pathway (30) analyses to identify pathways in the Database for Annotation Visualization and Integrated Discovery associated with DEFAMGs (31). We used Metascape (https://metascape.org) (32) to verify and visualize the functional enrichment of the DEFAMGs.

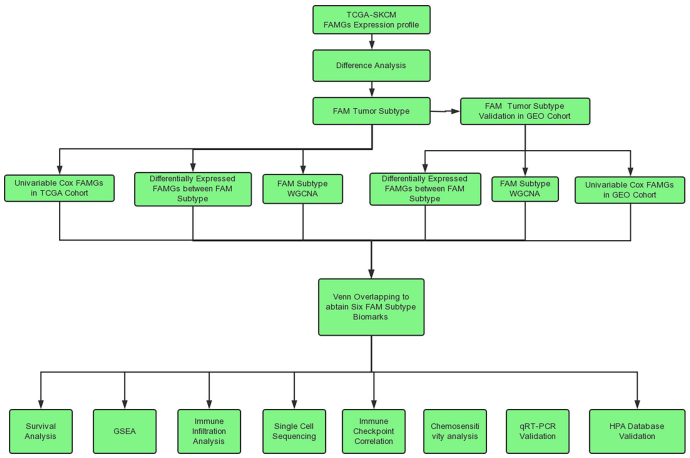

FIGURE 1
Flow chart.

Identification and differential analysis of FAM molecular subtypes

We adopted non–negative matrix factorization (NMF) consensus clustering (33) to divide all TCGA CM patients into 2 molecular subtypes using the R "NMF" package based on FAMGs expression pattern. Principal component analysis (34) was used to visualize FAM molecular subtypes by dimensionality reduction. Overall survival (OS) and progression-free survival (PFS) were compared between the FAM molecular subtype groups. Gene set enrichment analysis (GSEA) (35) was performed to assess differences in immune-related pathways between the molecular subtypes. In addition, we used ESTIMATE (36) and ssGSEA (37) algorithms to compare the immune cell infiltration and function between the molecular subtypes. To validate the reliability of the FAM subtypes, we also performed the abovementioned analyses using a GEO dataset (GSE65904) as an external verification dataset.

We identified the DEFAMGs between FAM molecular subtypes in the TCGA and GEO datasets and performed GO and KEGG analyses. The protein-protein interaction (PPI) network was built on the intersection of the TCGA and GEO cohorts using STRING (https://cn.string-db.org/) (38) and reconstructed in Cytoscape v3.6 (39) to select hub biomarkers.

Weighted gene co-expression network analysis

The expression profiles of the FAMGs were analyzed using a weighted gene co-expression network analysis (WGCNA) network (40) to select gene modules that were highly associated with FAM molecular subtypes. Among the soft threshold values, the β with the highest mean connectivity (β = 3) was chosen. The module eigengene was associated with molecular subtypes. Modules with the highest correlation were selected, and the genes in these modules were identified as genes related to FAM molecular subtypes. The minimum module size was 25. The module with the threshold of membership>0.4 and P value <0.05 was identified.

Identification of hub biomarkers of FAM molecular subtypes

To identify hub biomarkers of FAM molecular subtypes, we used a Venn plot to identify overlapping PPI genes, WGCNA module genes, and DEFAMGs with statistical significance in univariable Cox regressions in both the TCGA and GEO datasets. We used correlation-based network analysis to identify interactions among core biomarkers. We analyzed the prognostic value of the hub biomarkers in predicting OS, PFS, and disease-specific survival (DSS) in the TCGA and GEO cohorts.

GSEA of FAM biomarkers

To assess the immune-related and immune checkpoint–related pathways of the FAM biomarkers, we divided the patients in the TCGA CM cohort into groups with either high or low expression of each biomarker. The median expression level was used as the cut-off value. GSEA (41) was performed to identify significantly regulated pathways between the 2 groups. GSEA software was downloaded from the Broad Institute (http://www.broadinstitute.org/gsea/index.jsp). The gene sets of "c2.cp.kegg. v6.2. symbols","BIOCARTA_TCR_PATHWAY","REACTOME_PD_1_SIGNALING","LIN_TUMOR_ESCAPE_FROM_IMMUNE_ATTACK","WP_CANCER_IMMUNOTHERAPY_BY_PD1_BLOCKADE" and "WP_FERROPTOSIS" were downloaded from the Molecular Signatures Database (MSigDB). The normalized enrichment score (NES) was calculated for each gene set. Statistical significance was set at $|NES| > 1$, nominal P value < 0.05, and FDR q-value < 0.25.

TME analysis

We used the ESTIMATE algorithm to calculate the immune score, tumor purity, ESTIMATE score, and stromal score for each CM sample. For each core biomarker, the differences between the high- and low-expression groups were analyzed using violin plots. Furthermore, the association between the expression of FAM biomarkers and immune cell infiltration was assessed by Pearson correlation analysis. The Tumor Immune Estimation Resource (TIMER) database (https://cistrome.shinyapps.io/timer/) (42) was used to identify correlations between immune cells and FAM biomarkers.

Single-cell sequencing analysis

The GSE72056 single-cell dataset (4,645 single-cell sequencing samples of *Homo sapiens*; platform: GPL18573 Illumina NextSeq 500) was used to verify the expression of the FAMGs in the TME and assess the relationship between immune cells and FAMGs. We used the Seurat package in R for batch calibration and data normalization (43). We used the t-SNE package (44) to perform cell cluster analysis and used the SingleR package (45) to identify cell subpopulation annotations. We verified the connections between immune cells and molecular subtype biomarkers by evaluating the biomarker expression level of each cell.

Correlation with immune checkpoints

We assessed differences in the expression of 30 genes that previous studies suggested to be immune checkpoint–related genes (46–48) between groups with high or low expression of each FAM biomarker. In addition, we used Pearson correlation analysis based on the TIMER database to assess associations between the expression of FAM biomarkers and that of key immune checkpoints, including PD-1, programmed death-ligand 1 (PD-L1), and cytotoxic T-lymphocyte antigen 4 (CTLA-4). We used TIDE scores to assess differences in immunotherapy response between groups with high or low expression levels of each FAM biomarker.

Chemotherapy sensitivity analysis

We used the CellMiner database (https://discover.nci.nih.gov/cellminer) to construct an interaction network between chemotherapy sensitivity and FAM molecular subtype biomarkers. We performed Pearson correlation analysis to assess drug-gene associations.

Human protein atlas database

The protein expression of the FAM biomarkers in normal and CM tissues was verified by analyzing immunohistochemical and immunofluorescent data extracted from The Human Protein Atlas (HPA; https://www.proteinatlas.org/).

Cell culture and qRT-PCR

Human melanoma A375 cell line was purchased from American Type Culture Collection (Manassas, VA); the M14, human immortalized keratinocyte (HaCaT), and normal human skin melanocyte (PIG1) cell lines with STR certification were purchased from Shanghai Guandao Biological Engineering Company (Shanghai, China); and the SK-MEL-28 cell line was purchased from the Chinese National Infrastructure of Cell Line Resource. All cells were cultured in Roswell Park Memorial Institute (RPMI) 1640 medium supplemented with 10% fetal bovine serum at 37°C in a 5% CO_2 atmosphere. Real-time quantitative polymerase chain reaction (qRT-PCR) was performed to determine relative gene expression levels. Total RNA was extracted with TRIzol reagent 24 hours. The concentration of RNA was determined by ultraviolet spectrophotometry. RNAs were reverse-transcribed into complementary DNAs (50 ng/μl) using a commercial complementary DNA reverse transcription kit. PCR with SYBR Green Master Mix (TaKaRa Bio, Kusatsu, Japan) was used to evaluate mRNA expression levels. Glyceraldehyde-3-phosphate dehydrogenase was used as the internal reference. All primers were synthesized by Servicebio Technology Co. (Wuhan, China). The primer sequences are shown in Supplementary Table 3. The PCR program consisted of an initial denaturation at 95°C for 10 minutes followed by 45 cycles of 95°C for 10 seconds, 60°C for 30 seconds, and 72°C for 20 seconds. Target gene expression was calculated using the $2^{-\Delta\Delta CT}$ method.

Statistical analysis

The survival, ggplot2, corrplot, pheatmap, singleR, and limma packages were executed using R software version 4.1.1 (https://www.r-project.org). A P value <0.05 was defined as statistically significant. The unpaired Student t-test was used to analyzing normally distributed continuous variables. Univariable Cox regressions and WGCNA were performed to identify FAMGs with significant prognostic values. Kaplan–Meier survival analyses and log-rank tests were used to assess OS, PFS, and DSS.

Results

DEFAMGs and functional enrichment

A total of 219 FAMGs were differentially expressed between CM tissues (n = 471) and normal skin tissues (n = 234), including 124 downregulated and 95 upregulated genes in the tumor samples (Figures 2A, B). GO analysis showed that the DEFAMGs were mainly enriched in lipid and FAM-related biological processes, cellular components, and molecular functions (Figure 2C). KEGG analysis showed that the DEFAMGs were mainly enriched in metabolic pathways and FAM pathways (arachidonic acid, linolenic acid, glycerophospholipid, etc.) (Figure 2D). Metascape functional annotation confirmed that DEFAMGs were mainly enriched in FAM processes (Figure 2E).

FAM molecular subtypes

Univariable Cox regression revealed that 49 of the 219 DEFAMGs were significantly correlated with OS (Figure 3A). The NMF algorithm divided the TCGA CM samples into 2 clusters (cluster 1 and 2) (Figure 3B). The relationship between cophenetic, dispersion, and silhouette coefficients showed that the 2 clusters were significantly different (Figure 3C), which was further verified by principal component analysis (Figure 3D). Survival analysis showed that cluster 2 patients had better OS and DFS than cluster 1 patients did (Figures 3E, F). The GSEA results indicated that the immune response and immune system

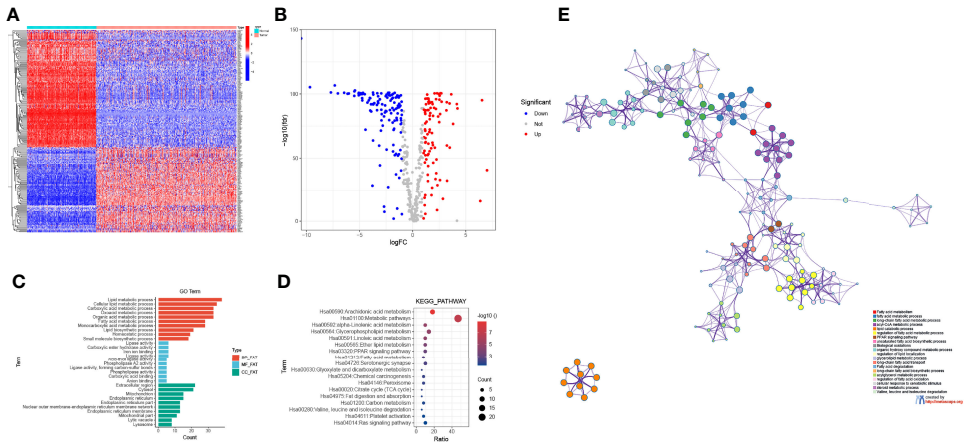

FIGURE 2
Identification of DEFAMGs in the TCGA cohort. **(A)** Heatmap of DEFAMGs. **(B)** Volcano plot of DEFAMGs. **(C)** GO enrichment analysis of DEFAMGs, showing only the first 10 terms respectively in the BP, MF and CC. **(D)** KEGG enrichment analysis of DEFAMGs, showing top 18 Fatty acid metabolism-related pathways. **(E)** Metascape displayed the functional enrichment network of fatty acid metabolism.

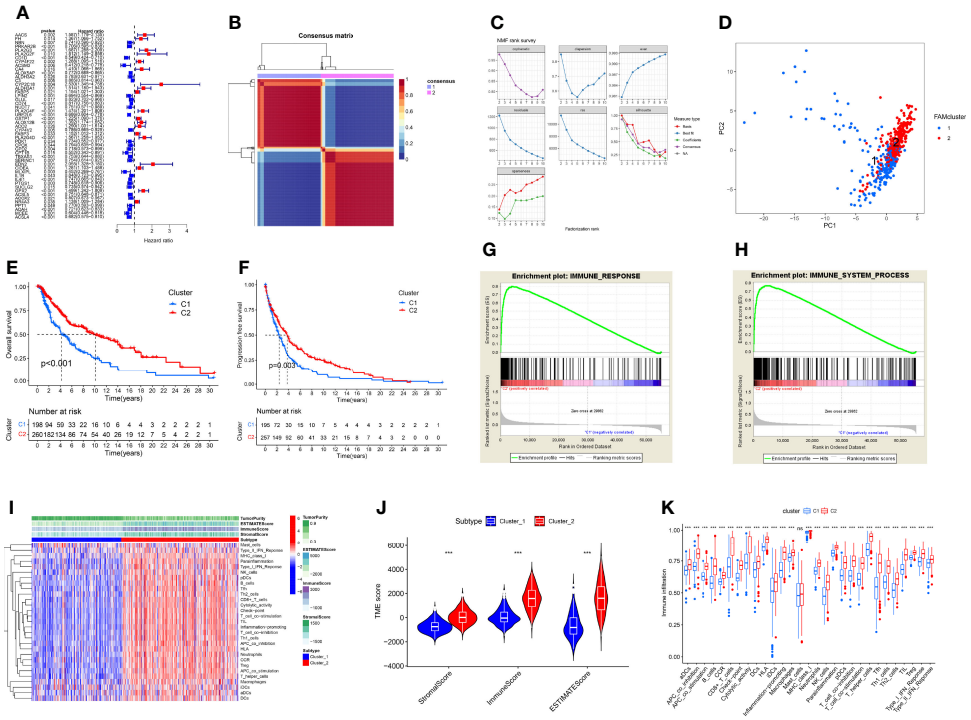

FIGURE 3
Construction of FAM molecular subtypes using TCGA CM samples. **(A)** A forest map of 49 prognostic FAMGs identified by univariable Cox regression. **(B)** The 2 FAM subtypes identified by the NMF algorithm. **(C)** The cophenetic, dispersion, and silhouette coefficients for the 2 FAM molecular subtypes. **(D)** Principal component analysis visualization of the 2 FAM molecular subtypes (cluster 1 and cluster 2). **(E, F)** The OS and DFS of patients with samples in cluster 2 were better than those of patients with samples in cluster 1. **(G, H)** GSEA results suggest that the immune system process and response pathways are upregulated in cluster 2. **(I)** Heatmap of TME components in the 2 FAM clusters, showing that cluster 2 had higher level of immune infiltrations than cluster 1. **(J)** Violin plot of TME ESTIMATE scores for the 2 FAM clusters. **(K)** Differences in immune infiltration and function between the 2 FAM clusters, showing immune functions were more activated in cluster 2 than cluster 1. ns, no significant, P>0.05; ***P≤0.001.

process were upregulated in cluster 2 (Figures 3G, H). Given the higher immune level and better prognosis in cluster 2, we compared the TME between the two clusters and found that immunocyte subpopulations were highly enriched in cluster 2 (Figure 3I). Compared with cluster 1, cluster 2 had significantly higher stromal, immune, and ESTIMATE scores (Figure 3J). The ssGSEA showed that cluster 2 also had higher levels of immune infiltration and more activated immune functions (Figure 3K). These findings were consistent with those of identical analyses performed using a GEO dataset (GSE65904) as an external validation dataset (Supplementary Figures 1A–J).

DEFAMGs between FAM molecular subtypes

We identified 55 DEFAMGs between the 2 clusters of the TCGA CM samples (Figure 4A), including 22 upregulated and 33 downregulated genes in cluster 2 (Figure 4B). GO and KEGG analyses revealed that the DEFAMGs were enriched in the oxidation-reduction process, arachidonic acid metabolism, and metabolic pathways (Figure 4C). Using GEO samples, we identified 76 DEFAMGs between the 2 clusters (Figure 4D), including 48 upregulated and 28 downregulated genes in cluster 2 (Figure 4E). GO and KEGG analyses showed that these DEFAMGs were enriched in the oxidation-reduction process, the lipid metabolic process, and metabolic pathways (Figure 4F). The PPI network included 28 downregulated and 36 upregulated DEFAMGs (Figure 4G).

WGCNA-selected FAM molecular subtypes modules and genes

We extracted the expressions of 531 FAMGs in TCGA samples and GSE65904 samples for WGCNA. Seven modules

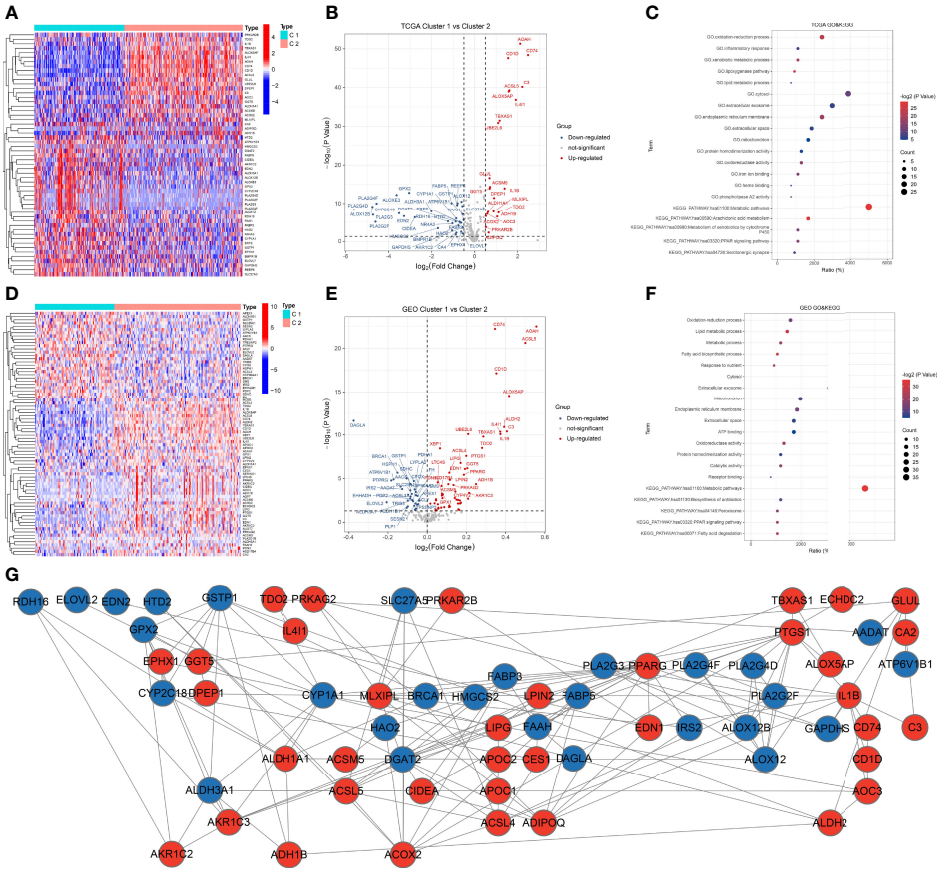

FIGURE 4
DEFAMGs between FAM molecular subtypes. **(A, B)** Heatmap and volcano plot of DEFAMGs between cluster 1 and cluster 2 in the TCGA cohort. **(C)** GO and KEGG enrichment analyses of DEFAMGs in the TCGA cohort. **(D, E)** Heatmap and volcano plot of DEFAMGs between cluster 1 and cluster 2 in the GEO cohort. **(F)** GO and KEGG enrichment analyses of DEFAMGs in GEO cohort. **(G)** The PPI network that includes an intersection of TCGA and GEO cohorts.

were identified by the average linkage hierarchical clustering based on the soft-thresholding power in TCGA samples, and the WGCNA traits heat map showed that the Module Eigengenes (ME) turquoise was selected (Figure 5A). The Module Eigengenes (ME) turquoise had the highest correlation with the FAM clusters (|cor| =0.59, P-value =5e-44) and contained 110 FAMGs. The dendrogram of genes clustered according to a dissimilarity measure (1-Topological Overlap Matrix, TOM) was shown in Figure 5B. The Sample dendrogram and soft threshold of WGCNA according to FAM Molecular subtypes were shown in Figures 5C, D. The co-expression network was constructed, and 3 modules were determined in GEO samples. Correlation analysis between the module eigengenes and FAM cluster showed that the ME turquoise (Figures 5E–H, Module–trait relationships = 0.39, P = 0.000) had the highest association with the FAM clusters. 92 genes in the module were considered to be hub FAM-related Modules genes. The overlapping part of the Venn plots identified 6 genes (i.e. ACSL5, ALOX5AP, CD1D, CD74, IL4I1 and TBXAS1) as core FAM biomarkers of CM (Figure 5I).

Prognostic value of the 6 hub FAM biomarkers

Kaplan-Meier analyses showed that higher expression of *ACSL5, ALOX5AP, CD1D, CD74, IL4I1, or TBXAS1* was associated with better OS, PFS, and DSS in the TCGA cohort, and with better OS in GEO cohorts (Figures 6A–D). In addition, univariable and multivariable Cox regressions showed that the 6 genes were independent prognostic factors for OS (Supplementary Table 4).

GSEA findings

GSEA revealed that antigen processing and presentation, T-cell receptor, the PD-1 signaling pathway, cancer immunotherapy by PD-1 blockade, tumor escape, and ferroptosis were all positively correlated with the expression levels of the 6 FAMGs (Figures 7A–F). These results indicate that the 6 genes may be involved in tumor immune regulation, immune evasion, and tumor cell response to PD-1 blockade.

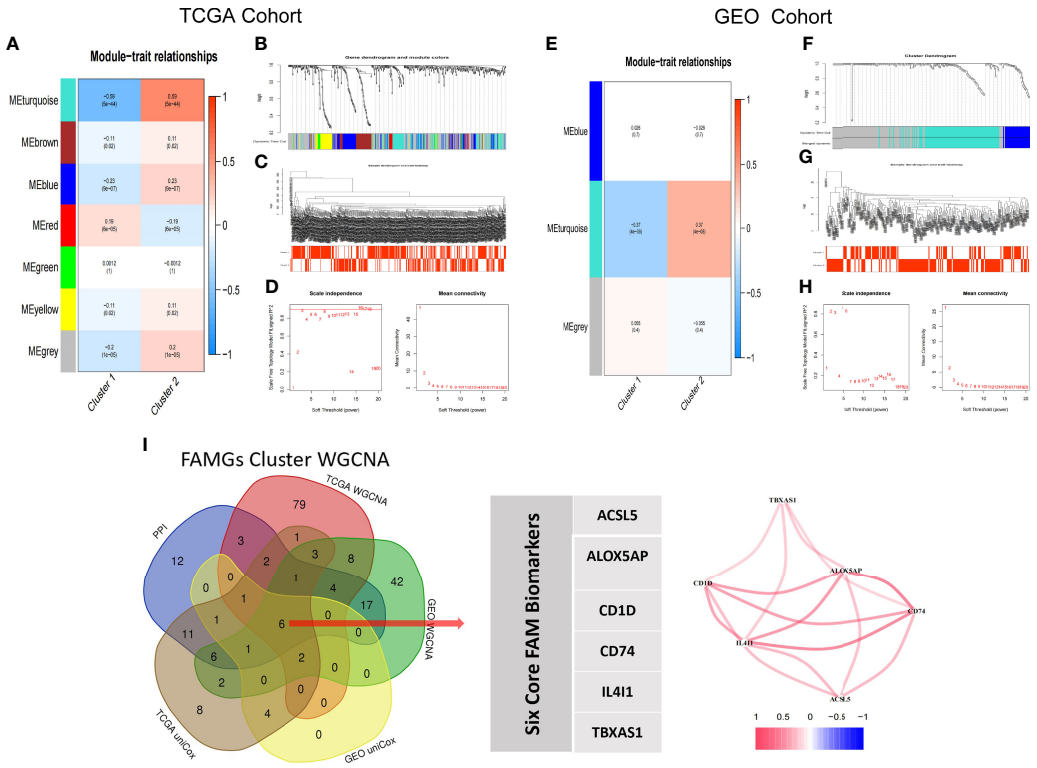

FIGURE 5
WGCNA-selected FAM molecular subtypes modules and genes. **(A–D)** TCGA Cohort WGCNA, **(A)** Seven modules are identified by WGCNA in TCGA samples; the turquoise module is highly correlation with FAM molecular subtypes (Cor= ± 0.59, p<0.001). **(B)** Dynamic Tree plot. **(C)** Sample heatmap of cluster 1 and cluster 2. **(D)** scale independence and mean connectivity. **(E–H)** Three modules are identified by WGCNA in GEO samples; the turquoise module is highly correlation with FAM molecular subtypes (Cor= ± 0.39, p<0.001). **(I)** Venn Diagram. ACSL5, ALOX5AP, CD1D, CD74, IL4I1 and TBXAS1 are identified as core biomarkers of FAM molecular subtype in CM patients.

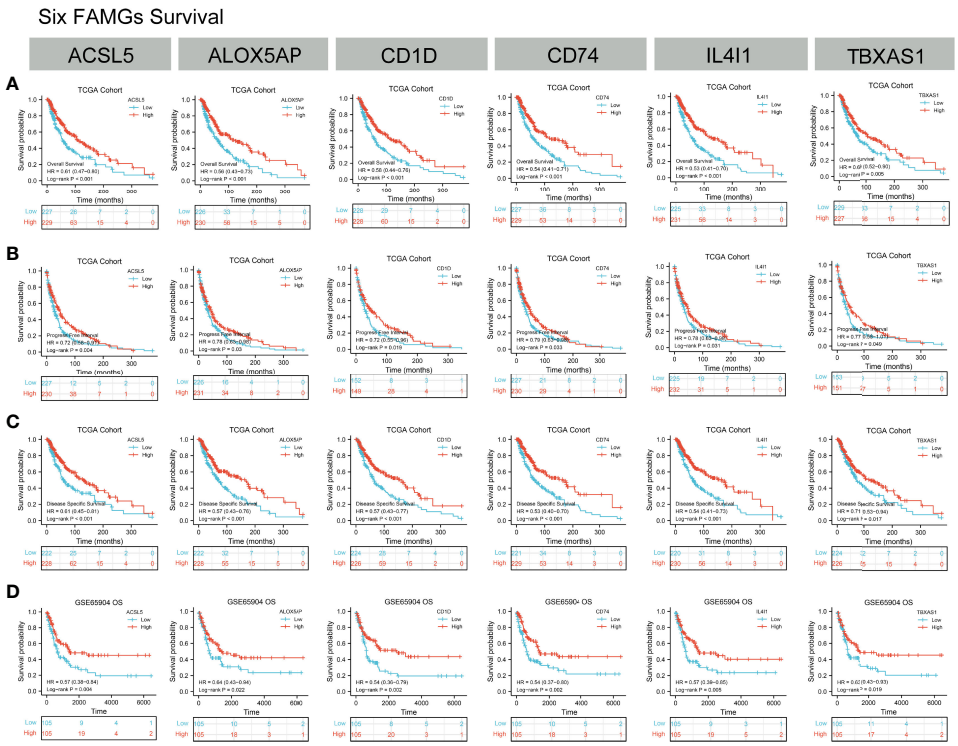

FIGURE 6
Kaplan-Meier analyses. **(A–C)** OS, PFS and DSS according to *ACSL5, ALOX5AP, CD1D, CD74, IL4I1*, and *TBXAS1* expression status in TCGA samples. **(D)** OS, PFS, and DSS according to *ACSL5, ALOX5AP, CD1D, CD74, IL4I1*, and *TBXAS1* expression status in GEO samples. K-M results showed the high-expression of *ACSL5, ALOX5AP, CD1D, CD74, IL4I1*, and *TBXAS1* had a better prognosis in CM patients.

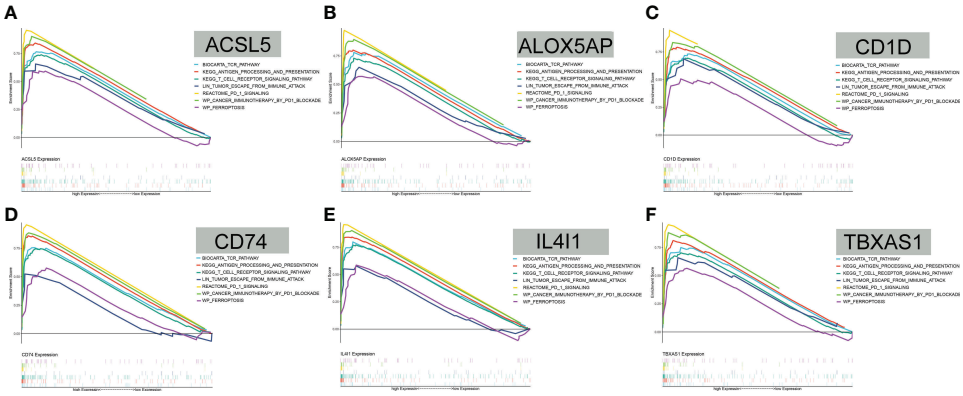

FIGURE 7
GSEA. **(A–F)** GSEA showed that antigen processing and presentation, T-cell receptor, the PD-1 signaling pathway, cancer immunotherapy by PD-1 blockade, tumor escape, and ferroptosis were all positively correlated with *ACSL5, ALOX5AP, CD1D, CD74, IL4I1*, and *TBXAS1* expression levels.

TME analysis findings

Compared with the groups with low expression of the 6 FAMGs, those with high expression of the 6 FAMGs had significantly higher ESTIMATE, immune, and stromal scores but lower tumor purity (Supplementary Figure 2). The expression levels of the 6 FAMGs were significantly positively correlated with the ESTIMATE, immune, and stromal scores but negatively correlated with tumor purity (Supplementary Figure 3). The expression levels of the 6 FAMGs were also positively correlated with the infiltration of B cells, $CD8^+$ T cells, $CD4^+$ T cells, macrophages, neutrophils, and dendritic cells (Figure 8).

Single-cell analysis findings

The single-cell analysis confirmed that the expression levels of the 6 FAMGs were relatively high in the $CD8^+$ T cell, B cell, and natural killer (NK) cell subsets (Figures 9A, B). The average and percent expressions of the 6 FAMGs are illustrated in a bubble chart of single-cell data (Figure 9C). The expression levels of the 6 FAMGs are illustrated in a violin chart of single-cell data (Figure 9D).

Relationship between immune checkpoints and FAM molecular subtype biomarkers

A total of 30 immune checkpoints, including PD-L1, PD-1, and CTLA-4, were found to be differentially expressed between groups with low or high expression of the 6 FAMGs (Supplementary Figure 4). The expression levels of the 6 FAMGs were significantly correlated with those of PD-L1, PD-1, and CTLA-4 (Figures 10A–C). A comparison of the groups' TIDE scores demonstrated that the group with high expression of the 6 FAMGs had better immunotherapy responses (Figure 10D).

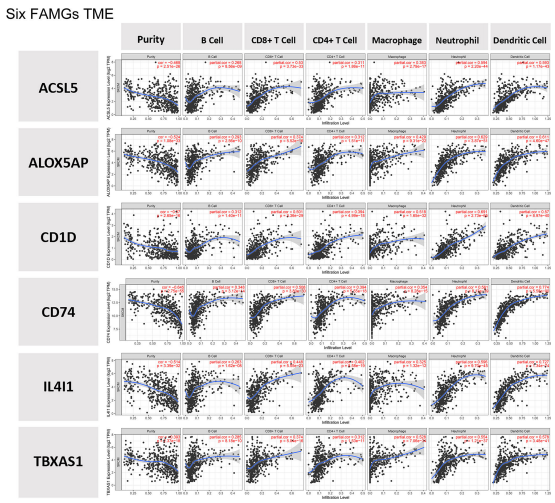

FIGURE 8
TME. The expression levels of the 6 FAMGs expression were positively correlated with the infiltration of B cells, $CD8^+$ T cells, $CD4^+$ T cells, macrophages, neutrophils, and dendritic cells.

Chemotherapy sensitivity

Chemotherapy sensitivity analysis showed that positive expression of the 6 FAMGs was associated with high sensitivity to certain chemotherapy drugs (Figure 11A). Pearson correlation analysis confirmed that higher expression levels of the 6 FAMGs were associated with higher sensitivity to some chemotherapy and targeted drugs, such as trametinib, selumetinib, cobimetinib, carboplatin, oxaliplatin, cisplatin, and dacarbazine (Figure 11B).

Validation of the 6 FAM molecular subtype biomarkers

Semiquantitative analyses of immunohistochemical images confirmed the expression levels of the 6 FAMGs were significantly higher in CM tissues than in normal skin (Figure 12A). Immunofluorescence analysis revealed that *ACSL5, CD1D, CD74, IL4I1, and TBXAS1* were mainly located in the cytosol and nucleoplasm (Figure 12B). qRT-PCR analysis revealed that the 6 FAMGs had significantly upregulated expression in A375, m14, and SK-MEL-28 cell lines compared with HaCaT and PIG1 cell lines (Figure 12).

Discussion

Major findings

This study comprehensively analyzed the role of FAMGs in the subtypes, prognosis, immune infiltration and immunotherapy response in CM. We first systematically investigated the correlation between DEFAMGs and the prognosis of patients with CM. Then we applied the NMF method to deconvolute the FAMGs expression profiles and identified 2 FAM clusters, cluster 1 and cluster 2, based on the TCGA CM cohort and further validated using the GEO cohort. According to the FAM subtypes, we identified 6 hub genes (*ACSL5, ALOX5AP, CD1D, CD74, IL4I1, TBXAS1*) as FAM subtype biomarkers. Finally, we verified the expression levels of the 6 genes in the HPA database and the qRT-PCR. Overall, our findings show that ACSL5, ALOX5AP, CD1D, CD74, IL4I1, and TBXAS1 are key FAM biomarkers that affect the function

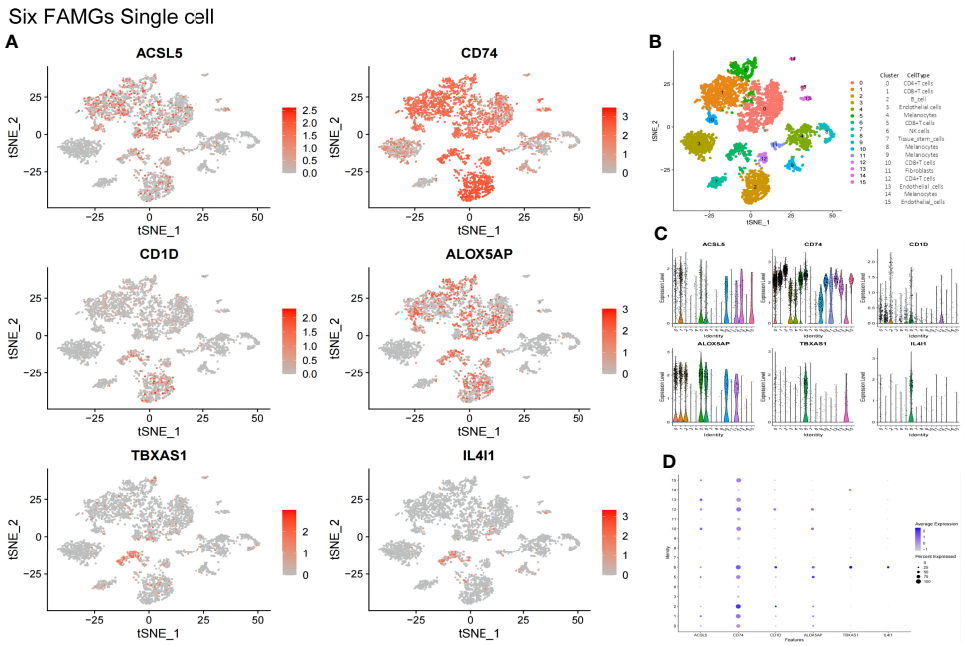

FIGURE 9
The expression of the 6 FAMGs was validated in a GEO single-cell cohort. **(A)** The expression levels of ACSL5, ALOX5AP, CD1D, CD74, IL4I1, and TBXAS1 were relatively high in the $CD8^+$ T-cell, $CD4^+$ T-cell, B-cell, and NK cell subsets. **(B)** Immunocyte annotation, Cluster 0, CD4+T cells; 1, CD8+T cells; 2, B cell; 3, Endothelial cells; 4, Melanocytes; 5, CD8+T cells; 6NK cells; 7, Tissue stem cells; 8, Melanocytes; 9, Melanocytes; 10, CD8+T cells; 11, Fibroblasts; 12, CD4+T cells; 13, Endothelial cells 14, Melanocytes;15, Endothelial cells. **(B)** A bubble chart of single-cell data shows the average and percent expression of *ACSL5, ALOX5AP, CD1D, CD74, IL4I1,* and *TBXAS1*. **(C)** A violin chart of single-cell data shows the expression levels of the 6 FAMGs. **(D)** A bubble chart of single-cell data shows the average and percent expression of *ACSL5, ALOX5AP, CD1D, CD74, IL4I1,* and *TBXAS1*.

and phenotype of infiltrating immune cells and are associated with immunosuppression in the TME.

FAM molecular subtype in CM

Tumor molecular subtypes that are based on predicted prognosis and TME composition have become a hotspot in cancer research, but few studies have provided comprehensive insight into the integral role of FAM in tumor molecular subtypes, especially in CM. For example, Ying et al. used a method of consensus clustering to build specific FAM-related molecular subtypes that were associated with malignancy and prognosis in glioma (49), but they did not explore the differences in immunocyte infiltration into the TME between the FAM-related molecular subtypes. Samson et al. constructed a mutational subtype of melanoma based on the BRAF mutation patterns of 2 FAM-related genes, *ALDH1A1* and *ALDH1A3*; however, this CM subtype accounts for ALDH1A3 expression as only a prognostic marker for BRAF/MEK inhibitor treatment response in BRAF-mutant metastatic melanoma patients (50). In the present study, we identified 2 FAM subtypes (cluster 1 and cluster 2) with different immune infiltration patterns based on the FAMG phenotype of CM. GSEA showed that immune response and immune system process were significantly regulated in FAM cluster 2. Immunocyte subsets, such as $CD8^+$ T cells, B cells, tumor-infiltrating lymphocytes, T follicular helper cells, regulatory T cells, and T helper cells, were highly enriched in FAM cluster 2, indicating that cluster 2 had higher levels of T-cell subset infiltration than cluster 1 did.

T cells degrade fatty acids through fatty acid oxidation to acquire lipids for energy. In addition, the development and function of different T-cell subsets are closely linked to the balance between fatty acid synthesis and fatty acid oxidation in the TME. For example, the preferential usage of fatty acid oxidation has been linked to the development of $CD8^+$ memory T cells and the induction of $CD4^+$ regulatory T cells over other T-cell lineages. Especially in $CD4^+$ T-cell subsets, the FAM profile changes during an immune response and is influenced by different tissues and different types of inflammation. Our FAM subtypes provide further evidence that different FAM patterns affect the abundance of T-cell subsets in the CM TME. Recent studies confirmed that T-cell

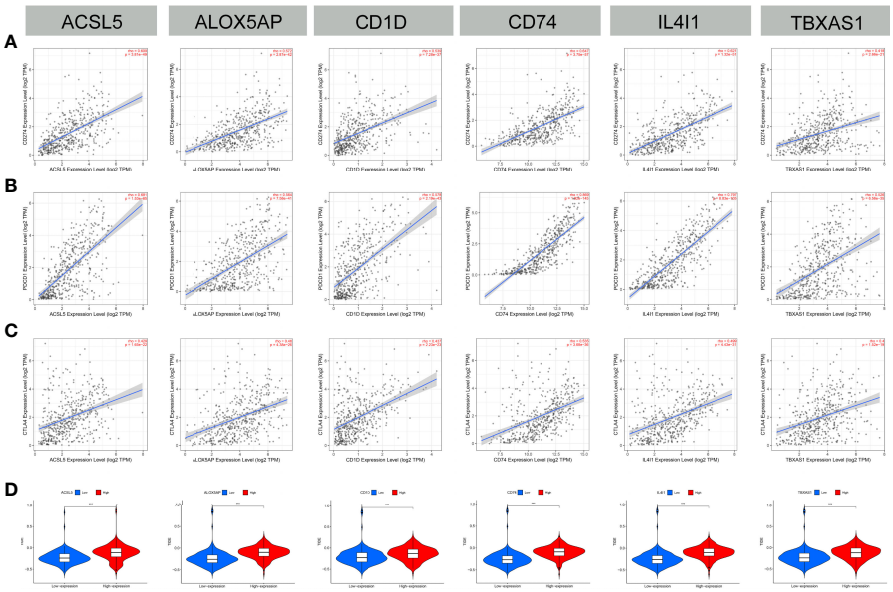

FIGURE 10
Immune checkpoint correlation and TIDE score. **(A–C)** The expression of the 6 FAMGs (ACSL5, ALOX5AP, CD1D, CD74, IL4I1 and TBXAS1) and that of immune checkpoints (PD-L1, PD-1, and CTLA-4) were significantly positively correlated. **(D)** The TIDE scores of the groups with high or low expression levels of the FAMGs showed that the high-expression group had worse immunotherapy responses. ***P≤0.001.

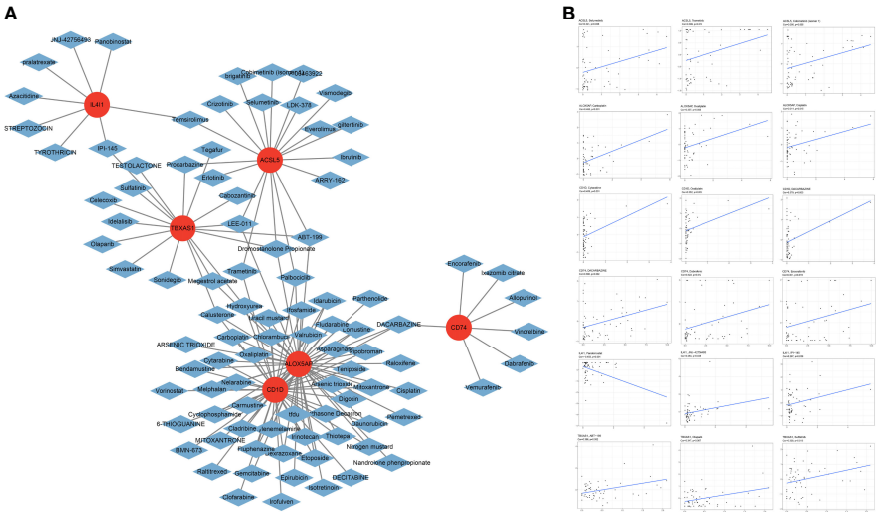

FIGURE 11
Chemotherapy sensitivity. **(A)** Chemotherapy sensitivity network shows that CM expressing the 6 genes has significant sensitivity to some chemotherapy drugs. **(B)** The scatter plot of the relationship shows that increased expression of *ACSL5, ALOX5AP, CD1D, CD74, IL4I1*, and TBXAS1 is associated with sensitivity to trametinib, selumetinib, cobimetinib, carboplatin, oxaliplatin, cisplatin, and dacarbazine.

10.3389/fimmu.2022.967277

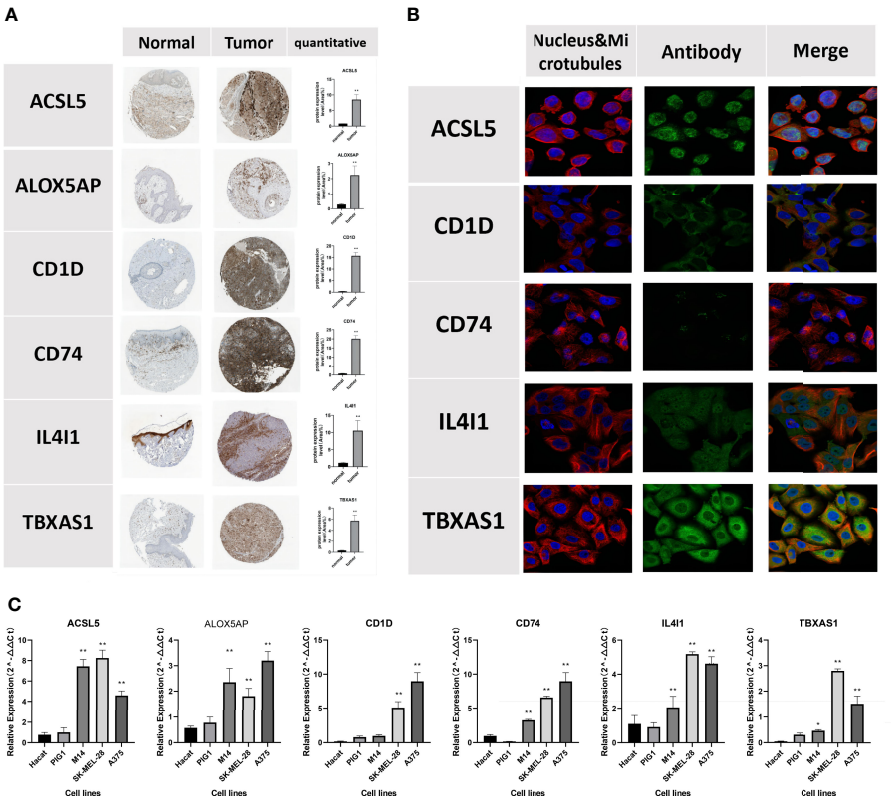

FIGURE 12
Verification of the protein expression of the 6 FAMGs using the HPA database. **(A)** Immunohistochemical images show the protein expression of ACSL5, ALOX5AP, CD1D, CD74, IL4I1, and TBXAS1 in CM and skin tissue. **(B)** Immunofluorescence show that *ACSL5, CD1D, CD74, IL4I1*, and *TBXAS1* are mainly located in the cytosol and nucleoplasm. **(C)** qRT-PCR, showing the relative expression of ACSL5, CD1D, CD74, IL4I1 and TBXAS1 were significant differences between 2 normal human cell lines and 3 melanoma cell lines. *P≥0.05; **P≥0.01.

subpopulations are the targets of ICI and chimeric antigen receptor T-cell therapy and that the status of T cells can strongly influence patients' prognosis (51, 52). Our results also showed that FAM cluster 2, with its high levels of T-cell infiltration, was associated with favorable outcomes, which suggests that cluster 2 may be more responsive to immunotherapy than cluster 1. In addition, our GO and KEGG analyses showed that the DEFAMGs between cluster 2 and cluster 1 were mainly enriched in the oxidation-reduction process, peroxisome proliferator-activated receptor (PPAR) signaling pathway, and lipid metabolic pathways. Accumulating evidence shows that the PPAR signaling pathway, which is involved in lipid metabolism, energy homeostasis maintenance, inflammation, and immune tolerance, has a role in carcinogenesis. Lee et al. found that AMP-activated kinase induces the upregulation of CPT1 and PGC-1 to activate the PPAR signaling pathway, which may more indirectly favor fatty acid oxidation (53). Therefore, the PPAR signaling pathway may be a key determinant of FAM patterns between FAM subtypes, and it may be used in the context of novel therapeutic strategies against CM.

FAM molecular subtype biomarkers

Based on the FAM molecular subtypes, we identified the 6 FAMGs (*ACSL5, ALOX5AP, CD1D, CD74, IL4I1, TBXAS1*) that play vital regulatory roles in the melanoma TME. Among the 6 hub FAMGs, IL4I1 (interleukin-4-induced gene 1) has a vital role in immunosuppressive functions and tumor immune escape. In 2009, Carbonnelle et al. were the first to propose that the novel immunosuppressive enzyme IL4I1, which is produced by the neoplastic cells of several B-cell lymphomas and by tumor-associated macrophages, is a prognostic biomarker and therapeutic target in cancer (54). Later, Fanette et al. found that tumor-associated macrophages with high IL4I1 expression can inhibit T-cell proliferation *in vitro* through H_2O_2 production. They also confirmed that in human melanoma and mesothelioma, minimal IL4I1 activity-induced tumor escape was preceded by a rapid diminution of interferon γ–producing cytotoxic antitumor $CD8^+$ T cells (55). Cousin et al. further showed that IL4I1 stimulates the generation of $Foxp3^+$ regulatory T cells and limits T helper 1 and T helper 2 polarization *in vitro*, and their findings

reinforced the concept that IL4I1 facilitates tumor escape from the immune response (56). Sadik et al. recently identified IL4I1 as a major aryl hydrocarbon receptor (AHR)-activating enzyme that promotes AHR-driven cancer cell motility and suppresses adaptive immunity. Compared with IDO1 or TDO2, IL4I1 had a stronger effect on AHR activity, which suggests that IL4I1 is an alternative metabolic immune checkpoint that could be therapeutically targeted in patients in whom combined ICI and IDO1 inhibition therapy has failed (57).. In the present study, we consistently observed that the PD-1, T-cell receptor, and tumor escape from immune attack signaling pathways were significantly enriched in CM samples with high IL4I1 expression. The differential expression of IL4I1 was significantly correlated with the infiltration of immune cells such as B cells, $CD8^+$ T cells, macrophages, and neutrophils in the TME. These findings suggest that IL4I1 can be an indicator of response to anti–PD-1 treatments and is a novel metabolic immune checkpoint in CM.

Previous studies showed that *ACSL5* (acyl-CoA synthetase 5), a nuclear-coded FAMG expressed in the mitochondria, can convert carbons from citrate to bioactive fatty acids to stimulate the inflammatory response in the TME (58, 59). For example, Klaus et al. found that the high activity of *ACSL5* enhances caspase-3 and caspase-7 activity to promote apoptosis regulated by TP53 status *via* WNT2B palmitoylation in enterocytes and colorectal adenocarcinomas (60). In addition, *ACSL5* can be used to predict survival and immunotherapy response. Gassler et al. showed that lower *ACSL5* expression is a prognostic marker for early recurrence in patients with colorectal adenocarcinoma (61). Chen et al. showed that breast, colorectal, lung, or ovarian cancer patients who have higher *ACSL5* expression have good survival outcomes (62). Our results showed that *ACSL5* is an important indicator of the OS, PFS, and DSS of CM patients. We also found that *ACSL5* is correlated with the ferroptosis signaling pathway in CM, which suggests that *ACSL5* can inhibit the proliferation of tumor cells by inducing ferroptosis.

ALOX5AP is a key enzyme that facilitates the activity of 5-lipoxygenase (5-LOX), which metabolizes arachidonic acid to leukotrienes. Moore et al. found that the 5-LOX/ALOX5AP pathway can affect cancer-related immune evasion in the TME (63). Ye et al. confirmed that *ALOX5AP* is involved in M2 macrophage recruitment, infiltration, and polarization, which can indirectly block tumor-specific T-cell activity to promote immune evasion in the ovarian cancer TME (64).

CD1D, a major histocompatibility complex class I–like molecule, presents lipoidal antigen to NK T cells, which are involved in the innate anticancer immune response. Bernal et al. confirmed that the CD1D molecule plays a crucial role in the induction of melanoma immune evasion by forming a complex with β2 microglobulin in the CD1D/NK T-cell axis (65). $CD1D^+$ tumors can evade recognition by NK T cells in the CD1D/NK T-cell axis by shedding glycolipids, which presumably replace the endogenous lipids that are bound to *CD1D* and cannot be recognized by NK T cells (66).

CD74 has been implicated to play a tumor-progression role in the immune microenvironment of CM patients. Figueiredo et al. confirmed that *CD74*, as a macrophage migration inhibitory factor (MIF), regulates the activity of macrophages and other immune cells *via* the CD74-MIF signaling pathway. Interfering with MIF-CD74 immunosuppressive signaling can restore the antitumor immune response in metastatic melanoma (67). According to other studies, the polarization of macrophages to M2 macrophages induces immunosuppression by suppressing cytotoxic T cells in the TME (68). In the present study, we also showed that *CD74* is positively associated with the infiltration of macrophages, dendritic cells, and neutrophils in CM. Our single-cell analysis of the TME further showed that high *CD74* expression was enriched in $CD8^+$ T cells, $CD4^+$ T cells, macrophages, neutrophils, and dendritic cells in the CM TME.

In the arachidonic acid cascade, *TBXAS1* encodes for thromboxane synthase, which converts prostaglandin H2 into thromboxane A2, a process that involves the modulation of cell cytotoxicity and tumor growth and metastasis (69, 70). Abraham et al. showed that *TBXAS1* genes are associated with breast cancer risk (71). We found that TBXAS1 is significantly correlated with neutrophils in the TME, indicating that high TBXAS1 expression upregulates the inflammation response in the TME.

Limitations

Although it presents encouraging results, our study had several limitations. First, the FAM tumor subtype was constructed and validated using open data sources (TCGA and GEO). Testing the subtype in an independent patient cohort would validate the reliability of our subtypes in identifying CM patients. Second, our study lacked *in vivo* experiments to verify the molecular function of the 6 hub genes. Future studies are needed to investigate the mechanisms underlying the 6 FAM biomarkers' mediation of CM progression and the immune microenvironment.

Conclusion

Our FAM subtypes verify that different FAM reprogramming affects the function and phenotype of infiltrating immune cells in the CM TME. Our findings suggest that the FAM molecular subtype biomarkers *ACSL5, ALOX5AP, CD1D, CD74, IL4I1*, and *TBXAS1* can be independent predictors of prognosis and immunotherapy response in CM patients. These findings may provide potential therapeutic targets in CM.

Data availability statement

The datasets presented in this study can be found in online repositories. The names of the repository/repositories and accession number(s) can be found in the article/Supplementary Material.

Author contributions

YX and YBC performed the data procedures and the writing. WJ, XY, and DC were involved in the review of the manuscript. YC and JZ contributed to data management, QZ and YH provided the idea for this study. All authors contributed to the study conception and design and approved the final manuscript.

Acknowledgments

We are grateful to those who provide and maintain the public databases and datasets we used in this study. We thank Joseph Munch in MD Anderson's Research Medical Library for editing the manuscript.

Conflict of interest

The authors declare that the research was conducted in the absence of any commercial or financial relationships that could be construed as a potential conflict of interest.

Publisher's note

All claims expressed in this article are solely those of the authors and do not necessarily represent those of their affiliated organizations, or those of the publisher, the editors and the reviewers. Any product that may be evaluated in this article, or claim that may be made by its manufacturer, is not guaranteed or endorsed by the publisher.

Supplementary material

The Supplementary Material for this article can be found online at: https://www.frontiersin.org/articles/10.3389/fimmu.2022.967277/full#supplementary-material

References

1. Fischer GM, Vashisht Gopal YN, McQuade JL, Peng W, DeBerardinis RJ, Davies MA. Metabolic strategies of melanoma cells: Mechanisms, interactions with the tumor microenvironment, and therapeutic implications. *Pigment Cell Melanoma Res* (2018) 31(1):11–30. doi: 10.1111/pcmr.12661

2. Jerby-Arnon L, Shah P, Cuoco MS, Rodman C, Su MJ, Melms JC, et al. A cancer cell program promotes T cell exclusion and resistance to checkpoint blockade. *Cell* (2018) 175(4):984–997.e24. doi: 10.1016/j.cell.2018.09.006

3. Braun DA, Burke KP, Van Allen EM. Genomic approaches to understanding response and resistance to immunotherapy. *Clin Cancer Res* (2016) 22(23):5642–50. doi: 10.1158/1078-0432.CCR-16-0066

4. Trojaniello C, Vitale MG, Scarpato L, Esposito A, Ascierto PA. Melanoma immunotherapy: strategies to overcome pharmacological resistance. *Expert Rev Anticancer Ther* (2020) 20(4):289–304. doi: 10.1080/14737140.2020.1745634

5. Keung EZ, Gershenwald JE. Clinicopathological features, staging, and current approaches to treatment in high-risk resectable melanoma. *J Natl Cancer Inst* (2020) 112(9):875–85. doi: 10.1093/jnci/djaa012

6. Crocetti E, Stanganelli I, Mancini S, Vattiato R, Giuliani O, Ravaioli A, et al. Evaluation of the agreement between TNM 7th and 8th in a population-based series of cutaneous melanoma. *J Eur Acad Dermatol Venereol* (2019) 33(3):521–4. doi: 10.1111/jdv.15285

7. Tang B, Chi Z, Chen Y, Liu X, Wu D, Chen J, et al. Safety, efficacy, and biomarker analysis of toripalimab in previously treated advanced melanoma: Results of the POLARIS-01 multicenter phase II trial. *Clin Cancer Res* (2020) 26 (16):4250–9. doi: 10.1158/1078-0432.CCR-19-3922

8. Galon J, Lugli A, Bifulco C, Pages F, Masucci G, Marincola FM, et al. World-wide immunoscore task force: meeting report from the "Melanoma bridge", napoli, November 30th-December 3rd, 2016. *J Transl Med* (2017) 15(1):212. doi: 10.1186/s12967-017-1310-9

9. Ros-Martínez S, Navas-Carrillo D, Alonso-Romero JL, Orenes-Piñero E. Immunoscore: a novel prognostic tool. association with clinical outcome, response to treatment and survival in several malignancies. *Crit Rev Clin Lab Sci* (2020) 57 (7):432–43. doi: 10.1080/10408363.2020.1729692

10. Wang Z, Wu X. Study and analysis of antitumor resistance mechanism of PD1/PD-L1 immune checkpoint blocker. *Cancer Med* (2020) 9(21):8086–121. doi: 10.1002/cam4.3410

11. Hanahan D, Weinberg RA. Hallmarks of cancer: the next generation. *Cell* (2011) 144(5):646–74. doi: 10.1016/j.cell.2011.02.013

12. Hainaut P, Plymoth A. Targeting the hallmarks of cancer: towards a rational approach to next-generation cancer therapy. *Curr Opin Oncol* (2013) 25(1):50–1. doi: 10.1097/CCO.0b013e32835b651e

13. Watson MJ, Vignali P, Mullett SJ, Overacre-Delgoffe AE, Peralta RM, Grebinoski S, et al. Metabolic support of tumour-infiltrating regulatory T cells by lactic acid. *Nature* (2021) 591(7851):645–51. doi: 10.1038/s41586-020-03045-2

14. DeBerardinis RJ, Chandel NS. Fundamentals of cancer metabolism. *Sci Adv* (2016) 2(5):e1600200. doi: 10.1126/sciadv.1600200

15. Rangel Rivera GO, Knochelmann HM, Dwyer CJ, Smith AS, Wyatt MM, Rivera-Reyes AM, et al. Fundamentals of T cell metabolism and strategies to enhance cancer immunotherapy. *Front Immunol* (2021) 12:645242. doi: 10.3389/fimmu.2021.645242

16. Wu S, Kuang H, Ke J, Pi M, Yang DH. Metabolic reprogramming induces immune cell dysfunction in the tumor microenvironment of multiple myeloma. *Front Oncol* (2020) 10:591342. doi: 10.3389/fonc.2020.591342

17. Martínez-Reyes I, Chandel NS. Cancer metabolism: looking forward. *Nat Rev Cancer* (2021) 21(10):669–80. doi: 10.1038/s41568-021-00378-6

18. Currie E, Schulze A, Zechner R, Walther TC, Farese RVJr. Cellular fatty acid metabolism and cancer. *Cell Metab* (2013) 18(2):153–61. doi: 10.1016/j.cmet.2013.05.017

19. Carracedo A, Cantley LC, Pandolfi PP. Cancer metabolism: fatty acid oxidation in the limelight. *Nat Rev Cancer* (2013) 13(4):227–32. doi: 10.1038/nrc3483

20. Shang C, Wang W, Liao Y, Chen Y, Liu T, Du Q, et al. LNMICC promotes nodal metastasis of cervical cancer by reprogramming fatty acid metabolism. *Cancer Res* (2018) 78(4):877–90. doi: 10.1158/0008-5472.CAN-17-2356

21. Ding C, Shan Z, Li M, Chen H, Li X, Jin Z. Characterization of the fatty acid metabolism in colorectal cancer to guide clinical therapy. *Mol Ther Oncolytics* (2021) 20:532–44. doi: 10.1016/j.omto.2021.02.010

22. Zhang L, Chen Y, Wang H, Xu Z, Wang Y, Li S, et al. Massive PD-L1 and CD8 double positive TILs characterize an immunosuppressive microenvironment with high mutational burden in lung cancer. *J Immunother Cancer* (2021) 9(6):1–11. doi: 10.1136/jitc-2021-002356

23. Blum A, Wang P, Zenklusen JC. SnapShot: TCGA-analyzed tumors. *Cell* (2018) 173(2):530. doi: 10.1016/j.cell.2018.03.059

24. Carithers LJ, Ardlie K, Barcus M, Branton PA, Britton A, Buia SA, et al. A novel approach to high-quality postmortem tissue procurement: The GTEx project. *Biopreserv Biobank* (2015) 13(5):311–9. doi: 10.1089/bio.2015.0032

25. Ritchie ME, Phipson B, Wu D, Hu Y, Law CW, Shi W, et al. Limma powers differential expression analyses for RNA-sequencing and microarray studies. *Nucleic Acids Res* (2015) 43(7):e47. doi: 10.1093/nar/gkv007

26. Cabrita R, Lauss M, Sanna A, Donia M, Skaarup Larsen M, Mitra S, et al. Tertiary lymphoid structures improve immunotherapy and survival in melanoma. *Nature* (2020) 577(7791):561–5. doi: 10.1038/s41586-019-1914-8

27. Tirosh I, Izar B, Prakadan SM, Wadsworth MH2nd, Treacy D, Trombetta JJ, et al. Dissecting the multicellular ecosystem of metastatic melanoma by single-cell RNA-seq. *Science* (2016) 352(6282):189–96. doi: 10.1126/science.aad0501

28. Liberzon A, Birger C, Thorvaldsdóttir H, Ghandi M, Mesirov JP, Tamayo P. The molecular signatures database (MSigDB) hallmark gene set collection. *Cell Syst* (2015) 1(6):417–25. doi: 10.1016/j.cels.2015.12.004

29. The Gene Ontology Consortium. 20 years and still GOing strong. *Nucleic Acids Res* (2019) 47(D1):D330–8. doi: 10.1093/nar/gky1055

30. Kanehisa M, Goto S. KEGG: kyoto encyclopedia of genes and genomes. *Nucleic Acids Res* (2000) 28(1):27–30. doi: 10.1093/nar/28.1.27

31. Dennis GJr, Sherman BT, Hosack DA, Yang J, Gao W, Lane HC, et al. DAVID: Database for annotation, visualization, and integrated discovery. *Genome Biol* (2003) 4(5):P3.

32. Zhou Y, Zhou B, Pache L, Chang M, Khodabakhshi AH, Tanaseichuk O, et al. Metascape provides a biologist-oriented resource for the analysis of systems-level datasets. *Nat Commun* (2019) 10(1):1523. doi: 10.1038/s41467-019-09234-6

33. Wilkerson MD, Hayes DN. ConsensusClusterPlus: a class discovery tool with confidence assessments and item tracking. *Bioinformatics* (2010) 26 (12):1572–3. doi: 10.1093/bioinformatics/btq170

34. Hess AS, Hess JR. Principal component analysis. *Transfusion* (2018) 58 (7):1580–2. doi: 10.1111/trf.14639

35. Subramanian A, Tamayo P, Mootha VK, Mukherjee S, Ebert BL, Gillette MA, et al. Gene set enrichment analysis: a knowledge-based approach for interpreting genome-wide expression profiles. *Proc Natl Acad Sci U.S.A.* (2005) 102(43):15545–50. doi: 10.1073/pnas.0506580102

36. Yoshihara K, Shahmoradgoli M, Martínez E, Vegesna R, Kim H, Torres-Garcia W, et al. Inferring tumour purity and stromal and immune cell admixture from expression data. *Nat Commun* (2013) 4:2612. doi: 10.1038/ncomms3612

37. Foroutan M, Bhuva DD, Lyu R, Horan K, Cursons J, Davis MJ. Single sample scoring of molecular phenotypes. *BMC Bioinf* (2018) 19(1):404. doi: 10.1186/s12859-018-2435-4

38. von Mering C, Jensen LJ, Snel B, Hooper SD, Krupp M, Foglierini M, et al. STRING: known and predicted protein-protein associations, integrated and transferred across organisms. *Nucleic Acids Res* (2005) 33(Database issue):D433–7. doi: 10.1093/nar/gki005

39. Shannon P, Markiel A, Ozier O, Baliga NS, Wang JT, Ramage D, et al. Cytoscape: a software environment for integrated models of biomolecular interaction networks. *Genome Res* (2003) 13(11):2498–504. doi: 10.1101/gr.1239303

40. Zhang B, Horvath S. A general framework for weighted gene co-expression network analysis. *Stat Appl Genet Mol Biol* (2005) 4:Article17. doi: 10.2202/1544-6115.1128

41. Subramanian A, Kuehn H, Gould J, Tamayo P, Mesirov JP. GSEA-p: a desktop application for gene set enrichment analysis. *Bioinf (Oxford England)* (2007) 23(23):3251–3. doi: 10.1093/bioinformatics/btm369

42. Li T, Fan J, Wang B, Traugh N, Chen Q, Liu JS, et al. TIMER: A web server for comprehensive analysis of tumor-infiltrating immune cells. *Cancer Res* (2017) 77(21):e108–10. doi: 10.1158/0008-5472.CAN-17-0307

43. Pereira WJ, Almeida FM, Conde D, Balmant KM, Triozzi PM, Schmidt HW, et al. Asc-seurat: analytical single-cell seurat-based web application. *BMC Bioinf* (2021) 22(1):556. doi: 10.1186/s12859-021-04472-2

44. Melit Devassy B, George S. Dimensionality reduction and visualisation of hyperspectral ink data using t-SNE. *Forensic Sci Int* (2020) 311:110194. doi: 10.1016/j.forsciint.2020.110194

45. Senabouth A, Lukowski SW, Hernandez JA, Andersen SB, Mei X, Nguyen QH, et al. Ascend: R package for analysis of single-cell RNA-seq data. *Gigascience* (2019) 8(8):1–6. doi: 10.1093/gigascience/giz087

46. Li B, Chan HL, Chen P. Immune checkpoint inhibitors: Basics and challenges. *Curr Med Chem* (2019) 26(17):3009–25. doi: 10.2174/0929867324666170804143706

47. Darvin P, Toor SM, Sasidharan Nair V, Elkord E. Immune checkpoint inhibitors: recent progress and potential biomarkers. *Exp Mol Med* (2018) 50 (12):1–11. doi: 10.1038/s12276-018-0191-1

48. Harjunpää H, Guillerey C. TIGIT as an emerging immune checkpoint. *Clin Exp Immunol* (2020) 200(2):108–19. doi: 10.1111/cei.13407

49. Qi Y, Chen D, Lu Q, Yao Y, Ji C. Bioinformatic profiling identifies a fatty acid metabolism-related gene risk signature for malignancy, prognosis, and immune phenotype of glioma. *Dis Markers* (2019) 2019:3917040. doi: 10.1155/2019/3917040

50. Samson JM, Ravindran Menon D, Smith DE, Baird E, Kitano T, Gao D, et al. Clinical implications of ALDH1A1 and ALDH1A3 mRNA expression in melanoma subtypes. *Chem Biol Interact* (2019) 314:108822. doi: 10.1016/j.cbi.2019.108822

51. Li J, Byrne KT, Yan F, Yamazoe T, Chen Z, Baslan T, et al. Tumor cell-intrinsic factors underlie heterogeneity of immune cell infiltration and response to immunotherapy. *Immunity* (2018) 49(1):178–193.e7. doi: 10.1016/j.immuni.2018.06.006

52. June CH, O' Connor RS, Kawalekar OU, Ghassemi S, Milone MC. CAR T cell immunotherapy for human cancer. *Science* (2018) 359(6382):1361–5. doi: 10.1126/science.aar6711

53. Lee WJ, Kim M, Park HS, Kim HS, Jeon MJ, Oh KS, et al. AMPK activation increases fatty acid oxidation in skeletal muscle by activating PPARalpha and PGC-1. *Biochem Biophys Res Commun* (2006) 340(1):291–5. doi: 10.1016/j.bbrc.2005.12.011

54. Carbonnelle-Puscian A, Copie-Bergman C, Baia M, Martin-Garcia N, Allory Y, Haioun C, et al. The novel immunosuppressive enzyme IL4I1 is expressed by neoplastic cells of several b-cell lymphomas and by tumor-associated macrophages. *Leukemia* (2009) 23(5):952–60. doi: 10.1038/leu.2008.380

55. Lasoudris F, Cousin C, Prevost-Blondel A, Martin-Garcia N, Abd-Alsamad I, Ortonne N, et al. IL4I1: an inhibitor of the CD8+ antitumor T-cell response. *vivo. Eur J Immunol* (2011) 41(6):1629–38. doi: 10.1002/eji.201041119

56. Cousin C, Aubatin A, Le Gouvello S, Apetoh L, Castellano F, Molinier-Frenkel V. The immunosuppressive enzyme IL4I1 promotes FoxP3(+) regulatory T lymphocyte differentiation. *Eur J Immunol* (2015) 45(6):1772–82. doi: 10.1002/eji.201445000

57. Sadik A, Somarribas Patterson LF, Öztürk S, Mohapatra SR, Panitz V, Secker PF, et al. IL4I1 is a metabolic immune checkpoint that activates the AHR and promotes tumor progression. *Cell* (2020) 182(5):1252–1270.e34. doi: 10.1016/j.cell.2020.07.038

58. Rajkumar A, Liaghati A, Chan J, Lamothe G, Dent R, Doucet É, et al. ACSL5 genotype influence on fatty acid metabolism: a cellular, tissue, and whole-body study. *Metabolism* (2018) 83:271–9. doi: 10.1016/j.metabol.2018.03.019

59. Zhang L, Lv J, Chen C, Wang X. Roles of acyl-CoA synthetase long-chain family member 5 and colony stimulating factor 2 in inhibition of palmitic or stearic acids in lung cancer cell proliferation and metabolism. *Cell Biol Toxicol* (2021) 37 (1):15–34. doi: 10.1007/s10565-020-09520-w

60. Klaus C, Schneider U, Hedberg C, Schütz AK, Bernhagen J, Waldmann H, et al. Modulating effects of acyl-CoA synthetase 5-derived mitochondrial Wnt2B palmitoylation on intestinal wnt activity. *World J Gastroenterol* (2014) 20 (40):14855–64. doi: 10.3748/wjg.v20.i40.14855

61. Gassler N, Roth W, Funke B, Schneider A, Herzog F, Tischendorf JJ, et al. Regulation of enterocyte apoptosis by acyl-CoA synthetase 5 splicing. *Gastroenterology* (2007) 133(2):587–98. doi: 10.1053/j.gastro.2007.06.005

62. Chen WC, Wang CY, Hung YH, Weng TY, Yen MC, Lai MD. Systematic analysis of gene expression alterations and clinical outcomes for long-chain acyl-coenzyme a synthetase family in cancer. *PLos One* (2016) 11(5):e0155660. doi: 10.1371/journal.pone.0155660

63. Moore GY, Pidgeon GP. Cross-talk between cancer cells and the tumour microenvironment: The role of the 5-lipoxygenase pathway. *Int J Mol Sci* (2017) 18 (2):1–27. doi: 10.3390/ijms18020236

64. Ye X, An L, Wang X, Zhang C, Huang W, Sun C, et al. ALOX5AP predicts poor prognosis by enhancing M2 macrophages polarization and immunosuppression in serous ovarian cancer microenvironment. *Front Oncol* (2021) 11:675104. doi: 10.3389/fonc.2021.675104

65. Bernal M, Ruiz-Cabello F, Concha A, Paschen A, Garrido F. Implication of the β2-microglobulin gene in the generation of tumor escape phenotypes. *Cancer Immunol Immunother* (2012) 61(9):1359–71. doi: 10.1007/s00262-012-1321-6

66. Brutkiewicz RR, Yunes-Medina L, Liu J. Immune evasion of the CD1d/NKT cell axis. *Curr Opin Immunol* (2018) 52:87–92. doi: 10.1016/j.coi.2018.04.021

67. Figueiredo CR, Azevedo RA, Mousdell S, Resende-Lara PT, Ireland L, Santos A, et al. Blockade of MIF-CD74 signalling on macrophages and dendritic cells restores the antitumour immune response against metastatic melanoma. *Front Immunol* (2018) 9:1132. doi: 10.3389/fimmu.2018.01132

68. Najafi M, Hashemi Goradel N, Farhood B, Salehi E, Nashtaei MS, Khanlarkhani N, et al. Macrophage polarity in cancer: A review. *J Cell Biochem* (2019) 120(3):2756–65. doi: 10.1002/jcb.27646

69. Minami D, Takigawa N, Kato Y, Kudo K, Isozaki H, Hashida S, et al. Downregulation of TBXAS1 in an iron-induced malignant mesothelioma model. *Cancer Sci* (2015) 106(10):1296–302. doi: 10.1111/cas.12752

70. Ulrich CM, Carlson CS, Sibert J, Poole EM, Yu JH, Wang LH, et al. Thromboxane synthase (TBXAS1) polymorphisms in African-American and Caucasian populations: evidence for selective pressure. *Hum Mutat* (2005) 26 (4):394–5. doi: 10.1002/humu.9371

71. Abraham JE, Harrington P, Driver KE, Tyrer J, Easton DF, Dunning AM, et al. Common polymorphisms in the prostaglandin pathway genes and their association with breast cancer susceptibility and survival. *Clin Cancer Res* (2009) 15 (6):2181–91. doi: 10.1158/1078-0432.CCR-08-0716

frontiers | Frontiers in Immunology

TYPE Original Research
PUBLISHED 24 November 2022
DOI 10.3389/fimmu.2022.1049485

Check for updates

OPEN ACCESS

EDITED BY
Jian Zhang,
Southern Medical University, China

REVIEWED BY
Elisabetta Dondi,
Université Sorbonne Paris Nord, France
Yuanyong Wang,
People 's Liberation Army General Hospital, China
Yimin Li,
Fudan University China

*CORRESPONDENCE
Fei Wei
weifei@njucm.edu.cn
Zhiguang Sun
zhiguangsun@njucm.edu.cn

†These authors have contributed equally to this work

SPECIALTY SECTION
This article was submitted to Cancer Immunity and Immunotherapy, a section of the journal Frontiers in Immunology

RECEIVED 20 September 2022
ACCEPTED 07 November 2022
PUBLISHED 24 November 2022

CITATION
Cui G, Liu J, Wang M, Shon K, Wang C, Wei F and Sun Z (2022) Crosstalk of angiogenesis-related subtypes, establishment of a prognostic signature and immune infiltration characteristics in colorectal adenocarcinoma. *Front. Immunol.* 13:1049485. doi: 10.3389/fimmu.2022.1049485

COPYRIGHT
© 2022 Cui, Liu, Wang, Shon, Wang, Wei and Sun. This is an open-access article distributed under the terms of the Creative Commons Attribution License (CC BY). The use, distribution or reproduction in other forums is permitted, provided the original author(s) and the copyright owner(s) are credited and that the original publication in this journal is cited, in accordance with accepted academic practice. No use, distribution or reproduction is permitted which does not comply with these terms.

Crosstalk of angiogenesis-related subtypes, establishment of a prognostic signature and immune infiltration characteristics in colorectal adenocarcinoma

Guoliang Cui[1†], Jinhui Liu[2†], Manli Wang[3†], Kinyu Shon[1†], Can Wang[4], Fei Wei[5*] and Zhiguang Sun[1,3*]

[1]Department of Gastroenterology, The Second Affiliated Hospital of Nanjing University of Chinese Medicine, Nanjing, Jiangsu, China, [2]Department of Gynecology, The First Affiliated Hospital of Nanjing Medical University, Nanjing, Jiangsu, China, [3]The First Clinical Medical College, Nanjing University of Chinese Medicine, Nanjing, Jiangsu, China, [4]Department of Colorectal Surgery, Affiliated Hospital of Nanjing University of Chinese Medicine, Jiangsu Province Hospital of Chinese Medicine, Nanjing, Jiangsu, China, [5]Department of Physiology, School of Medicine & Holistic Integrative Medicine, Nanjing University of Chinese Medicine, Nanjing, Jiangsu, China

Background: Colorectal adenocarcinoma (COAD) is one of the most common malignancies and angiogenesis is vital to the development of cancer. Here, we explored the roles of angiogenesis-related genes (ARGs) that affect the prognosis of COAD and constructed risk models to assess patient prognosis, immune characteristics, and treatment outcomes.

Methods: We comprehensively characterized the transcriptional and genetic modifications of 48 ARGs in COAD and evaluated the expression patterns. We identified two ARG subgroups using the consensus clustering algorithm. Based on the differentially expressed genes (DEGs) of two ARG subtypes, we calculated risk score, namely ARG_scores, and calssified COAD patients into different risk groups. To investigate the expression of ARG_score-related genes, qRT-PCR was performed. Subsequently, we mapped the nomogram to visually and accurately describe the value of the application of ARG_score. Finally, the correlation between ARG_score and clinical features, immune infiltration along with drug sensitivity were explored.

Results: We identified two ARG related subgroups and there were great differences in overall survival (OS) and tumor microenvironment. Then, we created an ARG_score for predicting overall survival based on eight DEGs and confirmed its reliable predictive power in COAD patients, with higher ARG_score associated with worse prognosis. Furthermore, eight ARG_score-related genes expression was investigated by qRT-PCR. To make the ARG_score clinically feasible, we created a highly reliable nomogram. We also found a higher proportion of microsatellite instability-high (MSI-H) and higher tumor mutational burden (TMB) in the high-risk group. In addition,

ARG_score was notably correlated with cancer stem cell indices and drug sensitivity.

Conclusion: This scoring model has potential clinical application value in the prognosis, immune microenvironment and therapeutic drug sensitivity of COAD, which provides new insights for personalized treatment.

KEYWORDS

colorectal cancer, angiogenesis, prognosis, tumor microenviroment, risk score signature

Introduction

Colorectal cancer (CRC) is one of the most common malignant tumors. According to the latest global cancer statistics, CRC has the third highest incidence (10.0%) and the second highest mortality rate (9.4%) in the world (1). Moreover, the incidence of CRC is trending younger, with an annual increase of 2% in incidence and 1.3% in mortality among people under 50 years of age (2). It seriously endangers people's lives and health, thus imposing a great socioeconomic burden worldwide.

With the continuous in-depth research on the pathogenesis and molecular mechanism of CRC, the treatment of this disease has made great progress. Surgical/polypectomy, chemotherapy and radiotherapy have benefited some CRC patients (3), but the tumor still has a high probability of local recurrence and metastasis. With the opening of the era of immunotherapy with PD-1 monoclonal antibody for metastasis colorectal cancer (mCRC), neoadjuvant therapy for CRC has seen a new dawn, but significant benefit has been observed only in selected patients (4). Therefore, there is a need to find accurate and reliable biomarkers to predict treatment response in the clinic for patients with different immune profiles.

The complex interactions between tumor cells and their microenvironment regulate the development and progression of cancer. The tumor microenvironment (TME) is composed of tumor cells, resident and recruited host cells (cancer-associated stromal cells and immune cells), as well as secreted substances of the corresponding cells (e.g. cytokines and chemokines) and non-cellular components of the extracellular matrix (ECM) (5), of which angiogenesis plays an important role. Angiogenesis is the physiological process of forming new blood vessels from pre-existing ones. This process provides oxygen and nutrients to the tumor, and excretes metabolic waste and carbon dioxide. During tumor progression, angiogenesis is always activated and contributes to tumor growth. In 2005, Prof. Jain first introduced the concept of "Normalization of tumor vasculature" (6). To date, some studies have also confirmed that the rational use of anti-angiogenic drugs, combining them with immune checkpoint inhibitors, can induce normalization of tumor blood vessels, improve the tumor microenvironment, and generate effective anti-tumor immunity (7). Several bioinformatics-based analyses have identified angiogenesis-related genes (ARGs) as potential prognostic biomarkers for several cancers (8–10).However, it is unclear whether ARGs can be used as potential prognostic markers for CRC.

CRC can be divided into colon and rectal cancer according to the primary tumor site. Colon adenocarcinoma (COAD) is the most common types of colon cancer among many pathologies. In this study, we collated samples from TCGA-COAD and GSE39582 cohort, identified different ARG subgroups, and developed a COAD prognostic scoring model, which can well differentiate the prognosis, immune characteristics, and treatment outcomes of patients with different risk scores. We further analyzed the sensitivity of chemotherapeutic agents of different risk scores. We hope that this study will contribute to the discovery of new diagnostic and prognostic biomarkers and new therapeutic targets for patients with COAD.

Methods and materials

Data collection

RNA expression, somatic mutation, copy number variation (CNV) datasets, and matching clinicopathological information for COAD were downloaded from the TCGA-COAD database (11), including 473 tumor datasets and 41 normal datasets. Clinical parameters and normalized gene expression data were acquired from GSE39582 in GEO database. Tumor samples from GSE39582 cohort and TCGA-COAD cohort were retained for further analysis. The batch effects between the TCGA and GEO datasets were removed using "ComBat" algorithm from the "sva" package (12). Based on a previous study, 48 ARGs were obtained from the MSigDB database (Hallmark Gene Set) (13).

Consensus clustering analysis

To identify different angiogenesis patterns, clustering analysis was performed by k-means algorithm (14). The number and consistency of clusters were established by the consensus clustering algorithm in the "consuclusterplus" package (15). The process was repeated 1000 times to ensure the stability of these categories.

Gene set variation analysis

To determine the biological functional differences of ARGs, we performed a gene set variation analysis (GSVA) based on "c2.cp.kegg.v6.2.symbols.gmts" in the MsigDB database (16).

Assessment of tumor microenvironment

We used the ESTIMATE algorithm to estimate stromal scores and immune scores in COAD patients with the aim of assessing tumor purity (17). Next, the CIBERSORT algorithm was used to calculate the levels of 22 immune cell subtypes for each patient (18). The relative infiltration abundance of immune cells was calculated by single sample gene set enrichment analysis (ssGSEA) (19). Then, we evaluated the expression of two immune checkpoints, PD-L1 and CTLA-4, in two clusters.

DEGs identification and functional enrichment analysis

We used "limma" package to identify differentially expressed genes (DEGs) in different angiogenesis subgroups, and its standard is | log2-fold change (FC) | ≥ 2, P value < 0.05. Then used the "clusterprofiler" package for GO and KEGG analysis (20).

Construction of the angiogenesis-related prognostic ARG_score

In order to quantitatively evaluate angiogenesis in each COAD patient, we constructed a scoring model called ARG_score (risk score). All COAD patients were randomly separated into training cohort (n=594), testing cohort (n=396) and entire cohort (n=990). There were no significant differences in clinicopathological factors among the three cohorts (Supplementary Table 1). The expression data of DEGs from different angiogenesis clusters were normalized, and the intersecting genes were selected. Differential assessment revealed 1587 DEGs between the two angiogenesis clusters. Next, we performed univariate Cox regression (unicox) analysis on the DEGs in the training cohort. 466 prognosis related genes were reserved for further analysis, and then the 466 survival related genes were analyzed by lasso and multivariate Cox (multicox), and finally 8 candidate genes were included in this angiogenesis-related signature. ARG_scores (risk socre) were calculated using the following method: ARG_ Score = gene expression (1) × Corresponding coefficient (1) + gene expression (2) × Corresponding coefficient (2) + gene expression [n] × Corresponding coefficient [n]. The patients were categorized into high-risk and low-risk groups based on the median score. Survival analysis were performed using "survminer" package and the receiver operating characteristic (ROC) curve was used to reveal the predictive effect of this model. Moreover, we also performed same analysis on testing and entire cohort.

Cell culture and qRT-PCR

Caco-2, HT-29, HCT-116, the human colorectal cancer cell lines, were obtained from the China Center for Type Culture Collection (CCTCC, Wuhan, China) and cultured in McCoy's 5A, RPMI-1640, high-glucose DMEM medium (Gibco, Shanghai, China) respectively. FHC, the normal colon epithelial cell line, was purchased from the Cell Bank of Type Culture Collection of the Chinese Academy of Sciences (Shanghai, China) and cultured in RPMI-1640 (Gibco, Shanghai, China). The medium were supplemented with 10% fetal bovine serum (FBS, Gibco, Shanghai, China) and 1% antibiotics. All cells were incubated at 37°C with 5% CO_2. Total RNA was isolated by TRIZOL reagent and cDNA was synthesized (Vazyme, China). β-actin was selected as an internal reference. The $2^{-\Delta\Delta CT}$ method was used to estimate the relative expression of target genes. Primer sequences are listed in Supplementary Table 2.

Clinical significance and classification analysis of ARG_score

We performed uniCox and multiCox analyses on all cohorts to determine whether ARG_score could be used as an independent prognostic factor. Afterwards, to explore whether the predictive function of ARG_score was reliable in different subgroups of clinical variables, a classification analysis was performed. Moreover, the levels of immune cells and immune checkpoints (ICPs) in different risk score subgroups were compared. In addition, we investigated the correlation between

ARG_score and tumor mutational burden (TMB) score, microsatellite instability (MSI) score and cancer stem cell (CSC) score. One-class logistic regression (OCLR) machine-learning algorithm was used to quantify the stemness of tumor samples by calculating cancer stem cell indices (21).

Creation and validation of nomogram

To predict the 1-year, 3-year and 5-year OS of each COAD patient, we integrated ARG _score and other clinicopathological features to create a nomogram with the "rms" package (22). And then, calibration curve analysis was used to assess the predictive power of the model (23).

Mutation and drug sensitivity analysis

We used the "maftools" package to create a mutation annotation format (MAF) in the TCGA database to understand the genetic variants in COAD patients in different risk groups (24). In addition, to investigate the sensitivity of chemotherapeutic drugs in different risk groups, we calculated the semi-inhibitory concentration (IC50) values of common drugs using the "pRophetic" package (25). We also analyzed the correlation of eight ARGs with the sensitivity of commonly used chemotherapeutic agents.

Statistical analysis

Data processing, analysis and presentation were carried out with R software (version 4.1.2). The prognosis survival curve was drawn by Kaplan Meier plotter. Spearman analysis was used for correlation analysis. P <0.05 means the results are statistically significant.

Results

Expression and mutation of angiogenesis-related genes in COAD

To find out whether genetic variants in ARGs are associated with COAD, we determined the mutation landscape of ARGs. From MSigDB database, 48 angiogenesis-related genes (ARGs) were included in this study according to the previous study (13), of which a total of 40 differentially expressed genes (DEGs) were identified between normal and tumor tissues (Figure 1A). The protein-protein interaction (PPI) network established by the STRING website showed the interactions of these DEGs (Figure 1B). We then recognized the incidence of somatic mutations in these ARGs, and the result revealed that among the 399 samples, 138 samples carried mutant ARGs, with a mutation rate of 34.59%. Meanwhile, MYH9 and STAB1 had the highest mutation rate (Figure 1C). In addition, we confirmed the

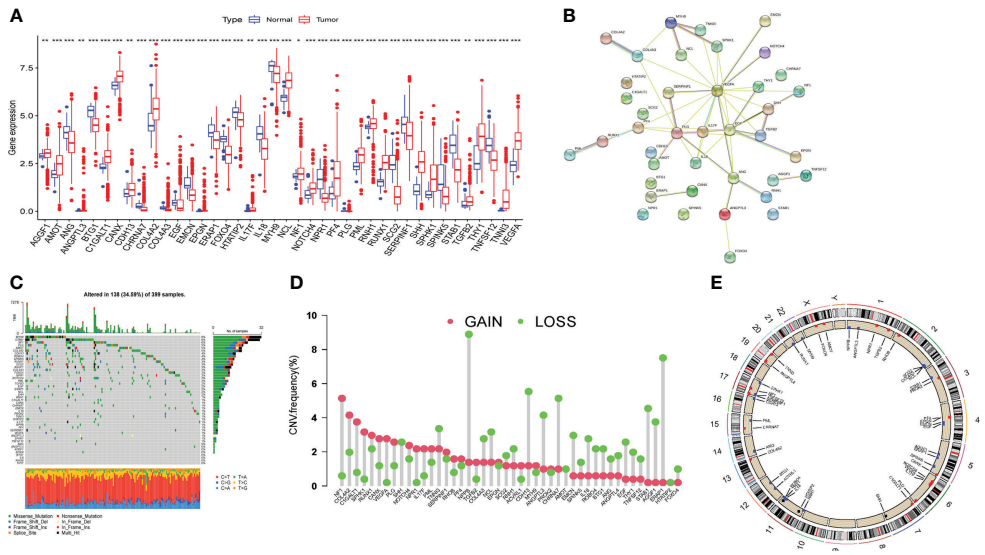

FIGURE 1
Expression and mutation of angiogenesis related genes in TCGA-COAD cohort. **(A)** Differential expression of angiogenesis related genes (ARGs) between tumor tissue and normal tissue. **(B)** The protein-protein interaction (PPI) network of the differentially expressed genes. **(C)** The incidence of somatic mutations of ARGs in COAD patients. **(D)** The CNV frequency of ARGs in TCGA cohort. **(E)** The locus of CNV alterations of 48 ARGs on 23 chromosomes. Adjusted p-values were shown as *P<0.05, **P<0.01, ***P<0.001.

prevalence of CNV alterations in ARGs in COAD patients (Figure 1D), and CNVs seem associated with higher expression of ARGs in tumor tissues, such as NF1, COL4A2, C1GALT1, SPHK1, RUNX1, implying a potential regulatory role of CNVs on the expression of ARGs (Figure 1D). Figure 1E showed the CNVs locus of 48 ARGs on 23 chromosomes. The above study indicated that the expression and mutation of ARGs differed greatly between normal and COAD samples, suggesting that ARGs may played an important role in the COAD.

Formation of angiogenesis-related genes clusters

To explore the survival significance of ARGs, we integrated samples from TCGA-COAD and GSE39582 cohort, and investigated the expression levels of ARGs in relation to overall survival (OS) by using Kaplan-Meier analysis, the results showed that 31 ARGs were related with OS and higher expression of most genes (22/31) implied a worse prognosis in COAD patients (Supplementary Figure 1). The interactions and risk/favorable factors of ARGs in COAD were exhibited Figure 2A, showing the complex crosstalk of these prognosis-related ARGs. To determine the subtypes of COAD, we used the consensus clustering algorithm to classify the samples according to the expression of ARGs and divided the integrated cohort into two clusters, namely ARGcluster (ARGcluster A and ARGcluster B) (Figure 2B), the survival analysis revealed that ARGcluster A had a better survival expectation (Figure 2C). Principal component analysis (PCA) confirmed a significant difference in the distribution of the two ARGclusters (Figure 2D). Furthermore, we compared the gene expression and clinical information of the two ARGclusters, found that the expression of ARGs differed significantly, with most ARGs being more highly expressed in ARGcluster B (Figure 2E). The above results showed that the two ARGclusters had significant differences in OS and ARGs expression, with clusterB having higher ARGs expression and poorer survival expectations.

Difference of biological features and tumor immune infiltration between two ARG clusters

In order to understand the differences in the biological functions of the two ARGclusters, KEGG-related GSVA analysis was performed. The results indicated that cell proliferation and differentiation-related (MAPK signaling pathways) and metastasis-related (focal adhesion, ECM receptor interaction) were more abundant in ARGcluster B (Figure 3A). The abundance of immune cells affects the tumor microenvironment and regulates tumors development, therefore we compared the abundance of immune cell subpopulations in two ARGclusters with ssGSEA. The abundance of 18 immune cell subpopulations were statistically different in the two ARGclusters, and all are more highly expressed in ARGcluster B (Figure 3B). Furthermore, we performed the ESTIMATE algorithm to infer differences in stromal score and immune score between the two clusters, and it turned out that ARGcluster B was significantly abundant in immune cells and stromal cells (Figure 3C), which means cluster B has relatively lower tumor purity. Besides, the expression of immune checkpoint genes PD-L1 and CTLA4 in ARGcluster B were also notably higher than that in ARGcluster A (Figure 3D).These results further comfirmed the differences between two ARGcluster, such as biological characteristics and tumor microenvironment, higher infiltration of immune cells and higher ESTIMATE score were found in clusterB.

Construction gene clusters based on angiogenesis-related DEGs

To further investigate the potential biological behavior of each angiogenesis subgroup, we identified 1587 DEGs between two ARGclusters using the "limma" package (Supplementary Figure 2), and performed functional enrichment analysis on these DEGs. GO and KEGG enrichment analysis indicated that these DEGs were mainly enriched in tumor metastasis-related pathways (Figures 4A, B). To determine the prognostic value of these DEGs, uniCox analysis was performed on 1587 DEGs and 466 DEGs associated with prognosis were screened out with a criterion of $p < 0.05$. Based on prognosis-related DEGs, patients from TCGA-COAD cohort and GSE39582 cohort were divided into three clusters (namely, gene cluster A, B, and C) using the consensus clustering algorithm (Figure 4C). Survival analysis showed that gene cluster B had the best prognosis, while cluster C had the opposite (Figure 4D). Heatmap reflected the expression level of prognosis-related DEGs and the difference of clinicopathological factors in two ARGclusters and three gene clusters (Figure 4E). We also used the estimate algorithm to determine the differences in stromal score, immune score and ESTIMATE socre between three gene clusters. The immune cells and stromal cells in cluster C were significantly more than those in the other two gene clusters, while the stromal cells in group B were the least (Figure 4F). In addition, the expressions of prognosis-related AGRs in the three gene clusters were investigated, 26 of the 31 prognosis-related AGRs were differentially expressed. (Figure 4G). The above results reflect the differences in survival expectancy, clinical characteristics, and ESTIMATE scores among the three gene clusters, which also proved that DEG between two ARGclusters well distinguished the prognosis and immune microenvironment of COAD patients.

10.3389/fimmu.2022.1049485

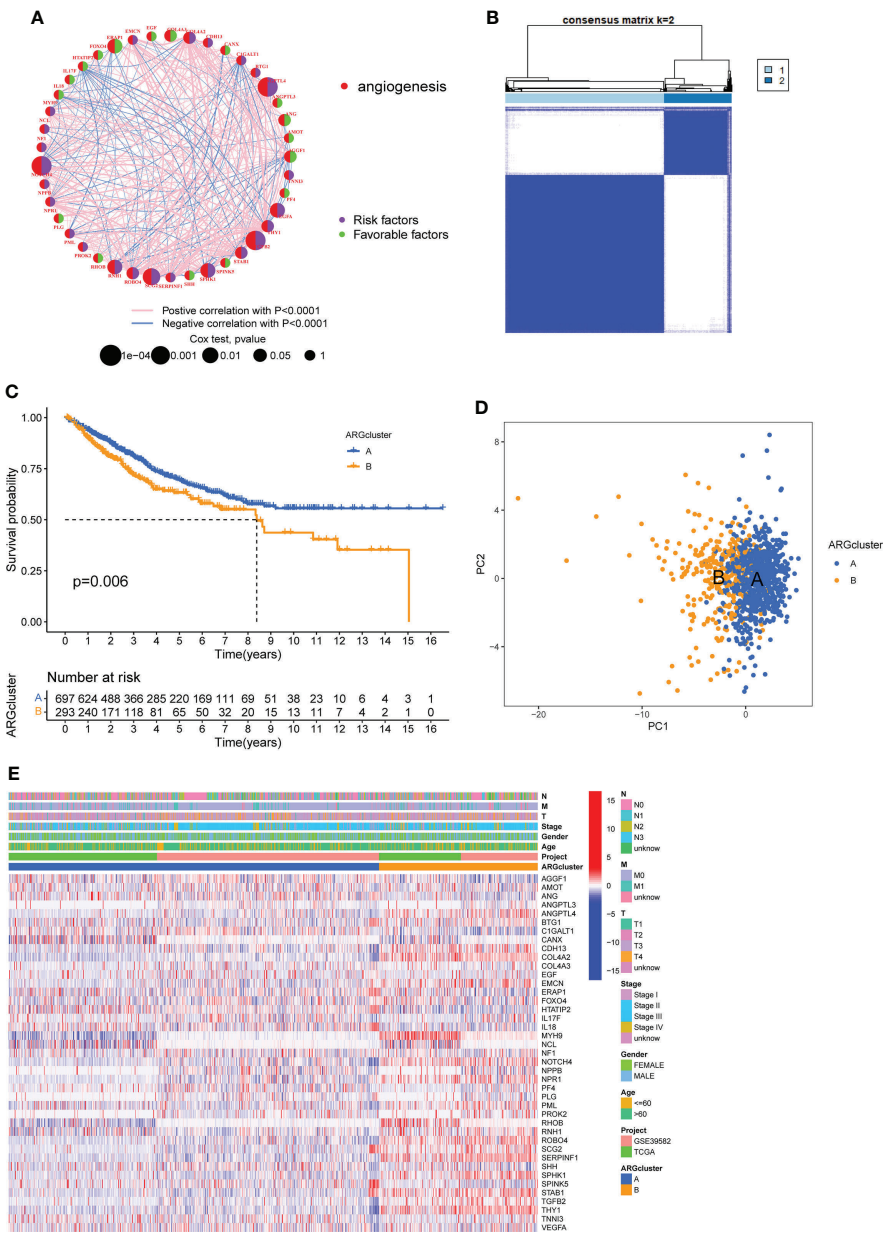

FIGURE 2
Formation of angiogenesis-related genes clusters (ARGclusters). **(A)** The network showing the correlation of ARGs in COAD. **(B)** All samples from TCGA-COAD cohort and GSE39582 cohort were divided into 2 clusters using consensus clustering algorithm (k = 2). **(C)** Kaplan-Meier curves show the different overall survival (OS) between two ARGclusters. **(D)** Principal component analysis (PCA) showed significant differences between the two ARGclusters. **(E)** Heatmap showed the differences between two clusters in clinical information and ARGs expression.

Construction and validation of the prognostic ARG_score model

To predict the outcome of each patient with COAD, we created a scoring model based on prognosis-related DEGs between two ARGclusters, called ARG score (risk score). We randomly divided all the COAD patients into training cohort and testing cohort, and performed LASSO and multiCox analysis on 466 prognosis-related DEGs in the training cohort to build the prognostic model (Supplementary Figure 3). The LASSO Cox regression model was used to narrow the most robust ARGs for prognosis and ten-fold cross-validation was applied to overcome the over-fitting. To generate a prognostic signature model (risk score), multivariate Cox regression analysis was applied to evaluate the connection between ARGs and OS in the training set. At last, we constructed a risk signature in the light of 8 ARGs. Eight ARGs were finally

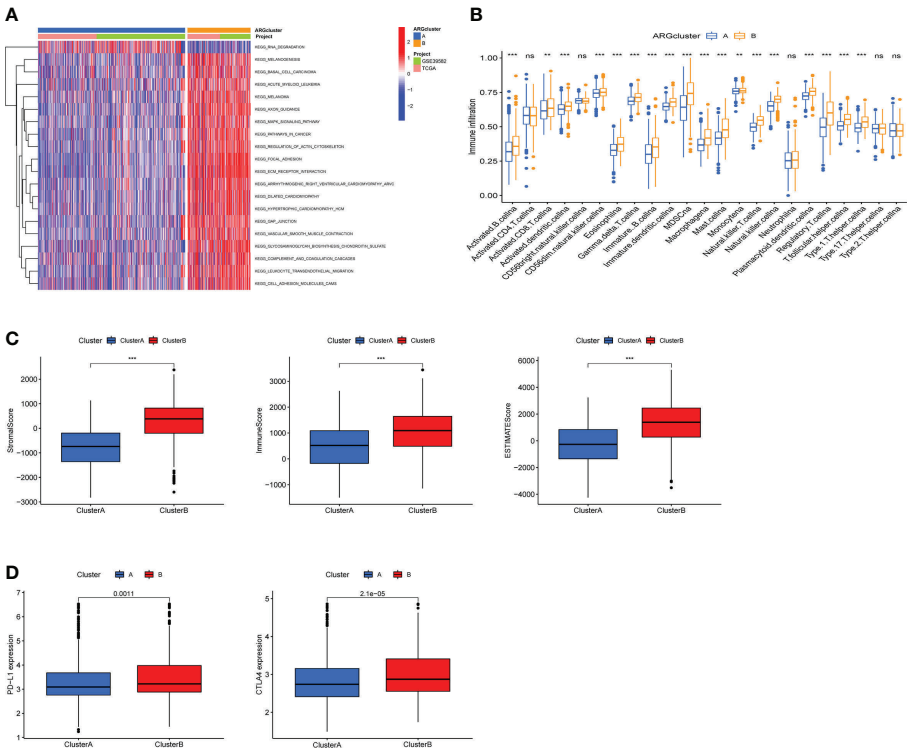

FIGURE 3
Analysis of biological features and tumor immune infiltration in two ARGclusters. **(A)** KEGG-related GSVA analysis showing the biological pathways of two ARGclusters. **(B)** Infiltration of 23 types of immune cells in two ARGclusters. **(C)** Differences of stromal score, immune score and ESTIMATE score between the two ARGclusters. **(D)** Expression levels of immune checkpoints PD-L1 and CTLA-4 in the two ARGclusters. Adjusted p-values were shown as ns, nosignificant, **P<0.01, ***P<0.001.

included, namely SEMA4C, PIM1, TIMP1, JAGN1, TRIB2, ASNS, RPS24, NOX1. The formula for calculating the ARG score was: ARG score/Risk score = [expression of SEMA4C*0.0765] + [expression of PIM1*0.0304] + [expression of TIMP1 * 0.0035] + [expression of JAGN1 * (-0.03625)] + [expression of TRIB2 * 0.0332] + [expression of ASNS * 0.0546] + [expression of RPS24 * 0.0049] + [expression of NOX1 * (-0.0076)]. According to the median value of ARG_score, COAD patients were divided into high-risk and low-risk groups. Figure 5A showed the distribution, survival status of patients and the expression of eight genes in different risk groups in training cohort. With the increase of risk score, the survival time of patients decreased and the mortality increased. In the high-risk group, the expression of SEMA4C, PIM1, TIMP1, TRIB2, ASNS, RPS24 was higher, while the expression of JAGN1 and NOX1 was lower (Figure 5A). Furthermore, we performed survival analysis on the training cohort, which indicates that patients with higher risk scores had lower OS (Figure 5D). ROC curve shows that the prediction model had good sensitivity and specificity, the AUC values of 1-, 3-,5-years were 0.726, 0.693 and 0.659 respectively (Figure 5G). We conducted the same analysis on testing cohort and entire cohort, and similar results confirmed the accuracy of the risk score model (Figures 5B, C, E, F, H, I). To visually reflect the distribution of patients in two ARGclusters, three gene clusters, two risk score groups and their survival status, we constructed an alluvial plot (Figure 5J). Moreover, we compared the differences in risk scores of different subgroups. For ARGclusters, ARGcluster B had a higher risk score, and as for gene clusters, gene cluster C had the highest risk score (Figures 5K, L).

In addition, we verified the expression of 8 ARG score-related genes in CRC cell lines including Caco-2, HT-29, and HCT-116 by qRT-PCR (Supplementary Figure 4). Compared with normal colon epithelial cells, SEMA4C and ASNS expression were significantly increased in three CRC cell lines. PIM1, JAGN1 and RPS24 expression were significantly increased in Caco-2 and HT-29, but not in HCT-116. TRIB2 expression was significantly increased in HT-29 and HCT-116, but not in Caco-2. In this section, we developed the ARG-related score model, confirmed its good predictive value and verified the expression level of eight candidate ARGs in CRC cell lines

Correlation between clinical pathological factors and risk score

We discussed the relationship between several clinicopathological factors (survival status, age, gender, stage)

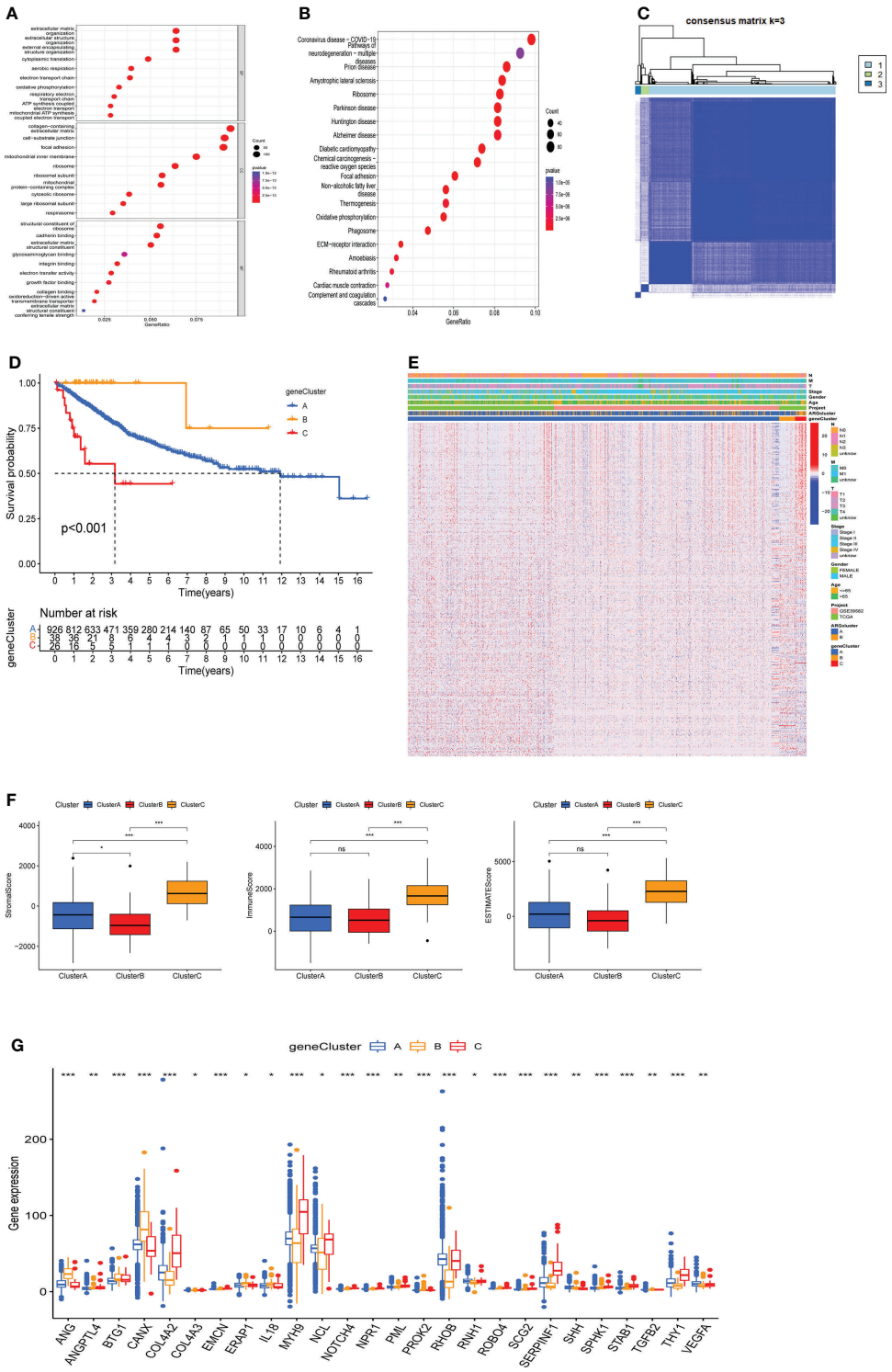

FIGURE 4
Construction of gene clusters based on the differentially expressed genes (DEGs) and analysis of prognosis, pathological features and tumor immune microenvironment (TME) in gene clusters. **(A)** Gene Ontology (GO) enrichment analysis of DEGs between two ARGclusters. **(B)** Kyoto Encyclopedia of Genes and Genomes (KEGG) enrichment analysis of DEGs between two ARGclusters. **(C)** The consensus matrixes for TCGA-COAD cohorts based on the DEGs among the 2 ARG clusters(k=3). **(D)** Kaplan-Meier analysis showing the different OS of the three gene clusters. **(E)** Heatmap shows the different clinicopathological features of the three gene clusters. **(F)** Differences of stromal score, immune score and ESTIMATE score between the 3 gene clusters. **(G)** Expressions level of ARGs in three gene clusters. Adjusted p-values were shown as ns, no significant, * $P < 0.05$, ** $P < 0.01$, *** $P < 0.001$.

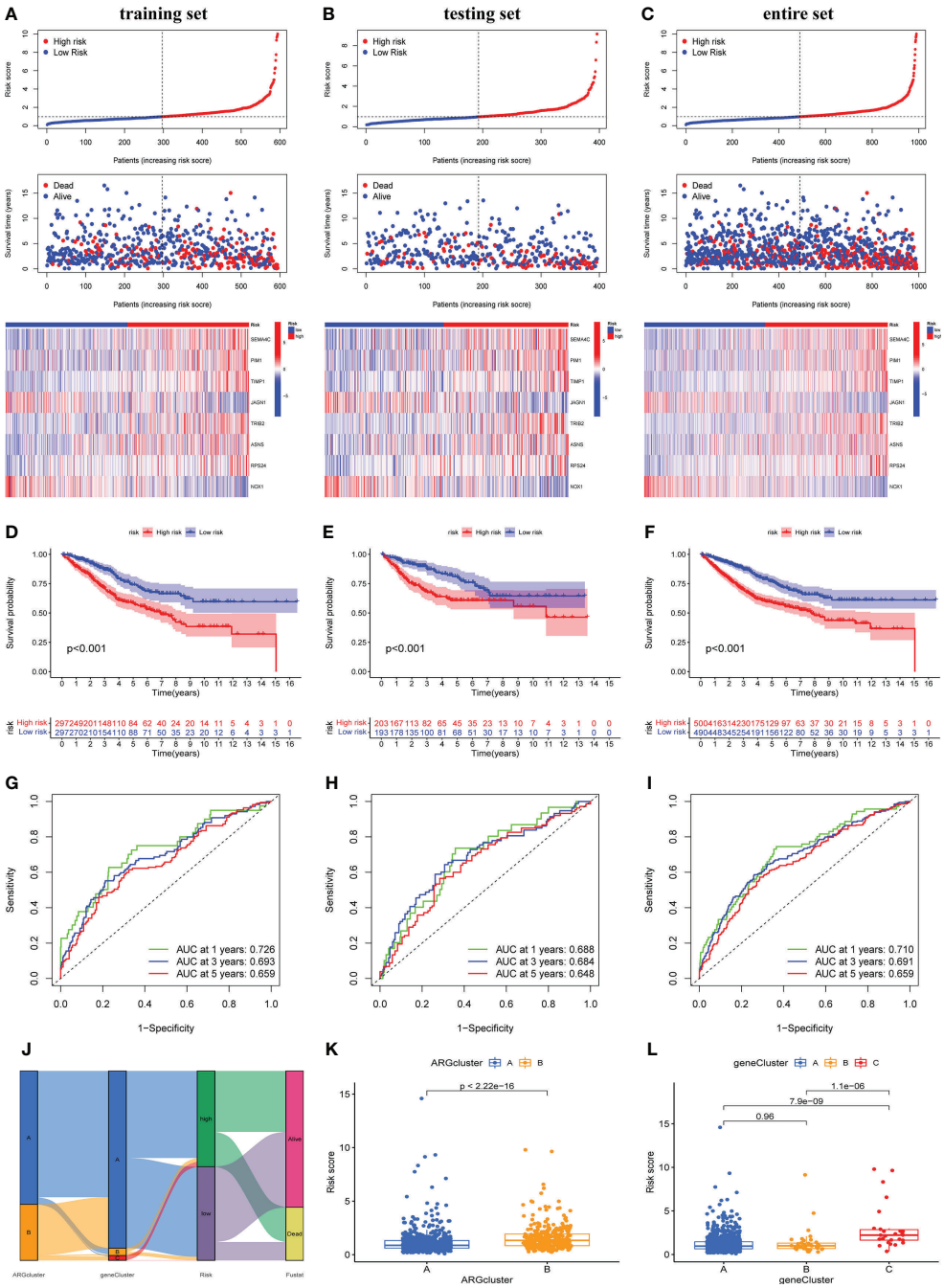

FIGURE 5
Construction and validation of the prognostic ARG score model. Significant differences in survival time and expression of 8 prognosis-related genes between high-risk and low-risk groups in training cohort **(A)**, testing cohort **(B)** and entire cohort **(C)**. Survival analysis of the overall survival (OS) for high-risk and low-risk patients in training cohort **(D)**, testing cohort **(E)** and entire cohort **(F)**. The ROC curves for 1-,3-,5-years survival of COAD patients in training cohort **(G)**, testing cohort **(H)** and entire cohort **(I)**. **(J)** Alluvial plot shows the distribution of patients in two ARGclusters, three gene clusters, two risk groups and their survival status. The differences in risk score of two ARGclusters **(K)** and three gene clusters **(L)**.

and risk score. It turned out that the mortality of high-risk group was significantly higher, and the proportion of advanced stage in high-risk group was higher (Supplementary Figures 5A–D). In addition, survival analysis was used to analyze the prognosis of patients in high-risk or low-risk groups with different pathological feature. The results show that the OS of COAD patients in the high-risk group was markedly lower than that in the low-risk group, regardless of age, gender or tumor stage.

(Supplementary Figures 5E–G). The tumor primary sites in the cecum, ascending colon, and hepatic flexure are right-sided CRC (RCRC), while the tumor primary sites in splenic flexure, descending colon, sigmoid colon, and rectosigmoid junction are left-sided CRC (LCRC) (26). Compared with low-risk group, the proportion of RCRC patients in the high-risk group was higher, and the risk score of patients with RCRC was significantly higher than that of LCRC patients (Supplementary Figure 6).

Construction and validation of a nomogram

We further explored whether individual pathological factors had independent prognostic value, and both uniCOX and multiCOX analysis show that age, stage, and risk score have independent prognostic value in the entire cohort (Figures 6A, B). Based on the correlation between the above clinicopathological features and ARG_scores, we created a nomogram for predicting 1-, 3-, and 5-year survival in COAD patients (Figure 6C). Calibration curve show that the nomogram was able to make accurate predictions (Figure 6D).

ARG_score was correlated with tumor microenvironment and immune infiltration

A large number of immune cells tend to accumulate in and around tumors, and these immune cells have complex interactions and regulation with tumor cells (27). Using the CIBERSORT algorithm to assess the relationship between the degree of infiltration of immune cell subtypes and the risk score, we found that the immune cell subtypes were positively associated with the ARG_score, including neutrophils, resting NK cells, Macrophages M0, T follicular helper cells, and Macrophages M1, while naive B cells, activated dendritic cells, resting dendritic cells, eosinophils, monocytes, plasma cells,

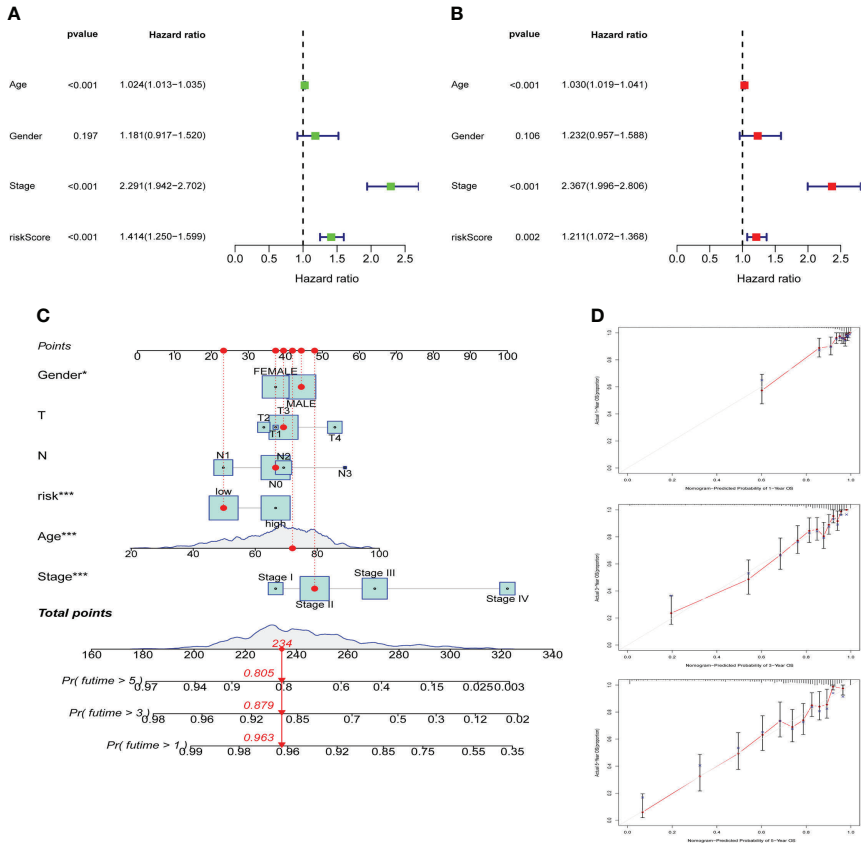

FIGURE 6
Construction and validation of a nomogram. Univariate cox regression **(A)** and multivariate cox regression **(B)** analysis of risk scores and clinicopathological factors. **(C)** Nomogram construction for predicting the 1-,3-,5-years OS of COAD patients. **(D)** Calibration curve analysis for predicting patients' survival at 1-,3-,5-year, the grey line represents the ideal performance, and the actual performance of the signature is represented by the red lines.

resting memory CD4+ T cells are inversely correlated (Figure 7A). The correlation heatmap between the 8 candidate DEGs and immune cell abundance showed that most immune cells had an outstanding correlation with these 8 genes (Figure 7B). Moreover, the results based on ssGSEA confirmed that there were significant differences in some immune cells and immune function between high-risk and low-risk groups (Supplementary Figure 7). We further evaluated the expression of 30 ICPs in different risk groups and most ICPs were more expressed in the high-risk group (Figure 7C). In addition, we also evaluated the TME scores in both two risk groups, not surprisingly, stromal score, immune score, and ESTIMATE score were higher in the high-risk group than in the low-risk group (Figure 7D). Tumor stemness index is an index to assess the similarity between tumor cells and stem cells, which is related to active biological processes in tumor cells, such as cancer recurrence, tumor proliferation and drug resistance (28). Therefore, we evaluated the correlation between DNA stemness score (DNAss) along with RNA stemness score (RNAss) and risk score. The results showed that the risk score was significantly negatively correlated with DNAss and RNAss, implying that COAD cells suggestive of lower ARG scores had more prominent stem cell characteristics and lower levels of cell differentiation (Figure 7E).

Association between ARG_score and Tumor mutation burden along with microsatellite instability

We explored the differences in somatic mutations between two risk groups based on TCGA-COAD dataset. Top 20 genes in terms of mutation rate were exhibited in the waterfall plot (Figures 8A, B). The waterfall plot displayed that genes of top 3 mutation rate were APC, TP53 and TTN in two risk groups. Moreover, the mutation frequency of APC, TP53 and TTN was higher in the low-risk group. TMB could help predict patient response to immunotherapy, so we next analyzed the difference of TMB between the two risk groups, and found that the TMB level was higher in the high-risk group than in the low-risk group (Figure 8C). Furthermore, there was a positive correlation between ARG_score and TMB (Figure 8D). A prognosis analysis was implemented on TMB of two risk groups and turned out that patients with lower TMB have a better OS (Figure 8E). In addition, we analyzed the OS taking together TMB with ARG_score, indicating that high-TMB along with high-ARG_score presents the worst OS among the four groups (Figure 8F). The microsatellite instability (MSI) accompanied by defective DNA mismatch repair was an important prognostic marker for tumors in clinical practice, so we did a series of analyses related to MSI for different risk groups. As is shown in Figure 8G, the proportion of MSI-high (MSI-H) was higher in the high-risk group than in the low-risk group, while the proportion of MSS (microsatellite stability) was lower than in the low-risk group. The risk score in the MSI-H subtype was significantly higher than that in MSS and MSI-low (MSI-L) subtypes (Figure 8H). The expression of the four mismatch repair (MMR) related genes, except MSH6, the other three (MLH1, MSH2, and EPCAM) were significantly higher in the low-risk group than in the high-risk group (Figures 8I–L). MMR or MSI status is still the most important molecular marker to predict the efficacy of immunotherapy for colorectal cancer (29). Our analysis results were helpful to predict the effect of immunotherapy, and COAD patients with higher risk scores may have better effect on immunotherapy.

Drug sensitivity analysis

To explore the differences in sensitivity to chemotherapeutic drugs in two risk groups, we evaluated the IC50 values of drugs, and the results showed that patients with higher ARG_score were more sensitive to Cisplatin, Docetaxel, Gemcitabine, Paclitaxel, Obatoclax.mecylate, and Vinblastine (Figure 9A). Moreover, we analyzed the correlation between the expression of eight candidate genes included in the risk score model and the sensitivity of chemotherapeutic drugs. For instance, our results revealed a positive correlation between the expression of TRIB2 and the sensitivity of Vemurafenib, Encorafenib, and Dabrafenib, while a negative correlation with the sensitivity of Nitrogen mustard (Figure 9B). The results suggested that ARGs were correlated with drug sensitivity and lower ARG_score in this model suggests better treatment outcomes for patients with COAD.

Discussion

In recent years, more and more immunotherapeutic methods have been applied to the treatment of tumors as the research on immunotherapy has intensified. However, satisfactory efficacy have been observed only in CRC patients with defective mismatch repair (dMMR) or high microsatellite instability (MSI-H), while pMMR-MSI-L CRC patients are insensitive to immunotherapy (4, 30).Therefore, it is of great importance to find new biomarkers at the molecular level to predict the prognosis of CRC patients, so as to guide clinical treatment, improve patient prognosis and prolong their survival time.

In this study, we developed and validated a risk score model capable of predicting survival in COAD patients based on the angiogenesis-related genes (ARGs). The model can robustly predict the clinical prognosis of patients, which is related to tumor microenvironment (TME) and immune characteristics. In addition, we also found that the ARG_score model can distinguish the sensitivity of patients with different risks to

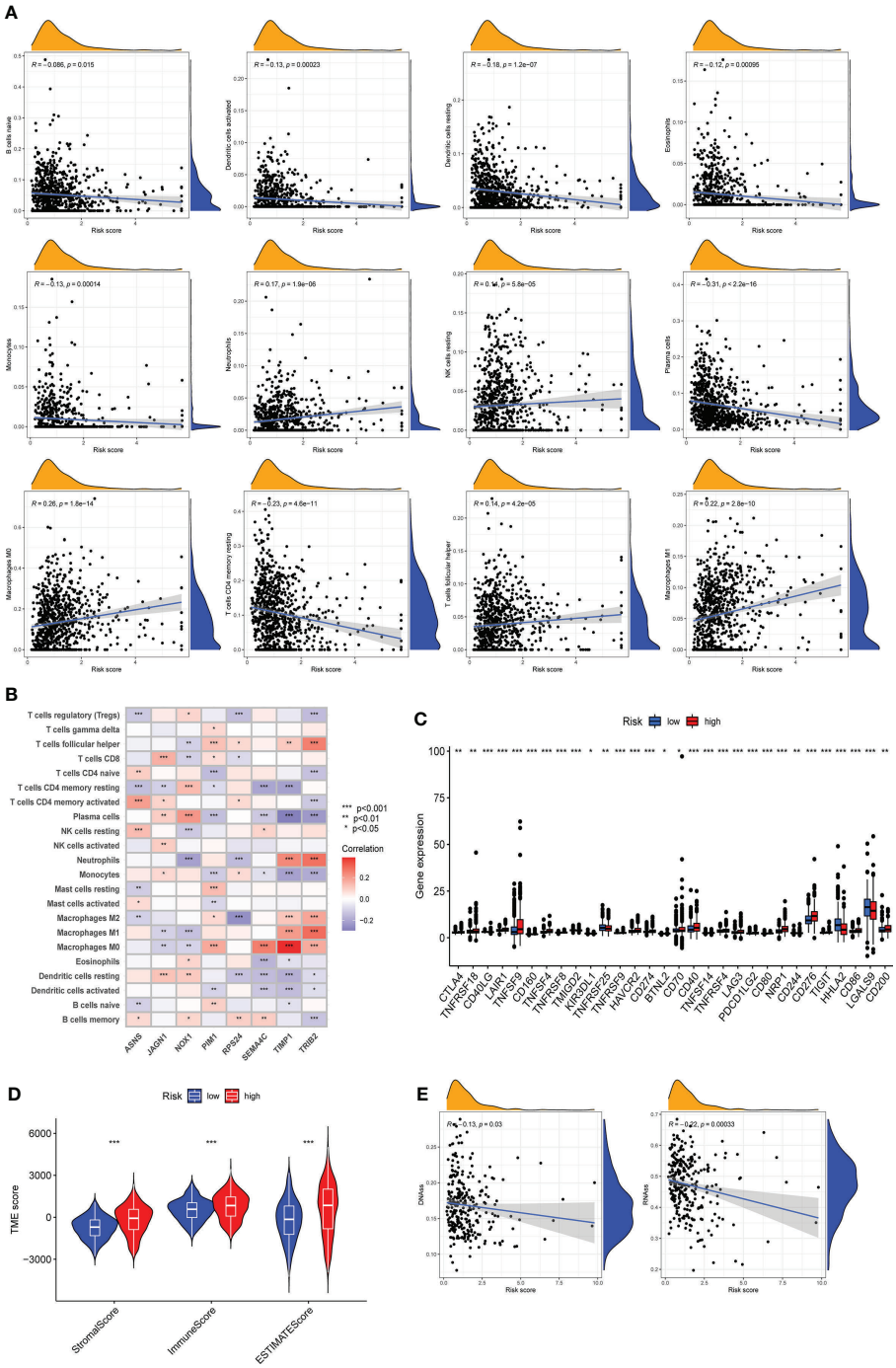

FIGURE 7
Assessment of tumor microenvironment (TME) and immune infiltration between different risk groups. **(A)** CIBERSORT algorithm reveals the correlation of risk score and immune cell subtypes. **(B)** Correlation between 8 candidate genes and immune cell abundance. **(C)** Expression levels of immune checkpoints in high-risk and low-risk groups. **(D)** Differences of Stromal score, Immune score and ESTIMATE score between the two risk groups. **(E)** Correlation of two cancer stemness cell indices (RNAss and DNAss) with risk score. Adjusted p-values were shown as * $P < 0.05$, ** $P < 0.01$, *** $P < 0.001$.

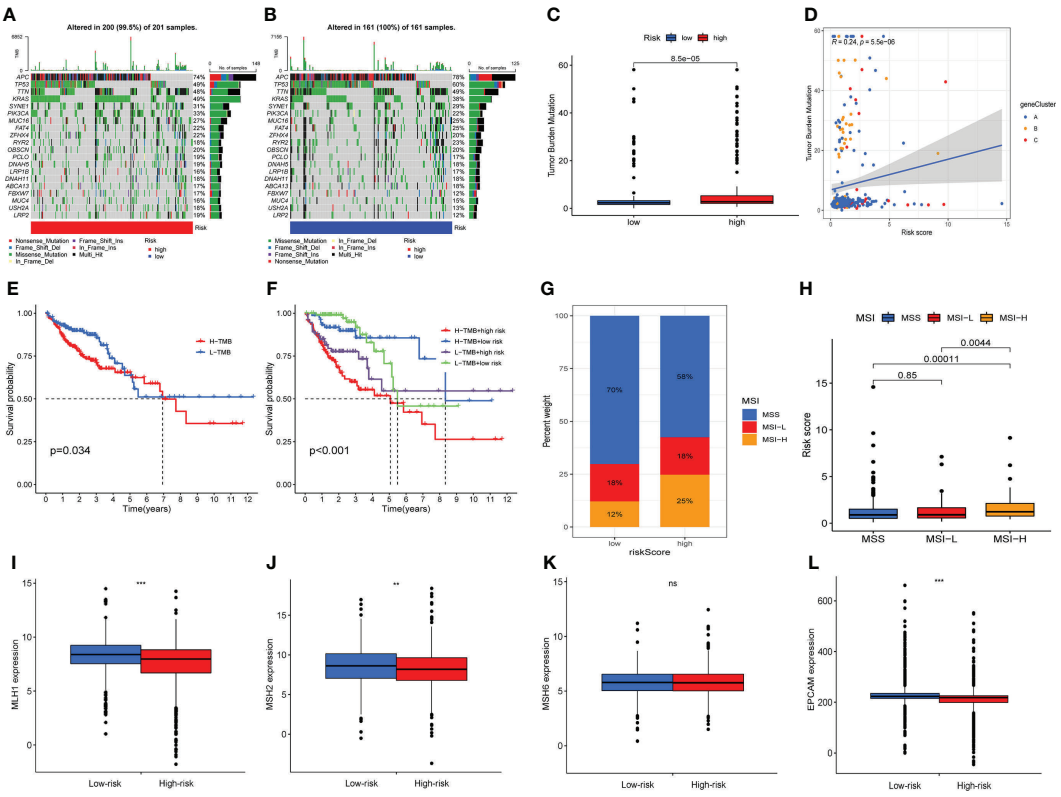

FIGURE 8
Association between ARG score and tumor mutation burden (TMB) along with microsatellite instability (MSI). The waterfall plot of 20 genes with the highest mutation rates in high-risk **(A)** and low-risk groups **(B)**. **(C)** Differences in tumor mutational burden between high-risk and low-risk groups. **(D)** Correlation between tumor mutational burden and risk score. **(E)** Survival analysis shows the OS differences between two TMB subgroups. **(E)** Survival analysis shows OS differences stratified by TMB and risk score. **(F)** The proportion of MSS, MSI-L and MSI-H in different risk groups. **(F)** Differences in risk score between MSS, MSI-L and MSI-H subgroups. **(I–L)** Expression levels of four mismatch repair related genes in different risk groups. Adjusted p-values were shown as ns, no significant, ** $P < 0.01$, *** $P < 0.001$.

treatment, which indicates that the model has application value in clinical efficacy.

First, we identified ARGs mutations and expression in the TCGA-COAD cohort. Most of them are upregulated in COAD patients and associated with worse prognosis, suggesting a potential role of ARGs in COAD. Then, we divided COAD patients from TCGA-COAD cohort and GSE39582 cohort into two angiogenesis-related cluster (ARGcluster A and B) using the consensus clustering algorithm. There are significant differences in ARGs expression, OS and TME between the two ARGclusters. In addition to malignant tumor cells, tumor tissue includes various types of cells (immune cells, fibroblasts, endothelial cells, etc.), intercellular stroma, and extracellular factors (cytokines, chemokines, and growth factors) (31). These components and their complex interactions form the tumor-associated microenvironment. It is well known that the immune system has both pro-cancer and anti-cancer effects. There is a complex biological process between immune cells and malignant tumor cells in the tumor stroma with significant prognostic relevance (32). In colorectal cancer, the distribution, tissue localization, and cell type of different types of immune cells are significantly associated with tumor progression. In this study, the immune infiltration level of 23 human immune cell subpopulations in 2 clusters was assessed using ssGSEA, of which 18 immune cells were all more infiltrated in cluster B.

To quantify the angiogenesis subgroups, a scoring model, namely ARG_score, was constructed using LASSO and multivariate cox regression analysis. Among the two ARG_clusters and three gene clusters, ARG_cluster B and gene cluster A with the highest risk score have the worst prognosis, while ARG_cluster A and gene cluster B with the lowest risk score have the best prognosis. This indicates that the higher the ARG_score, the worse the prognosis. Our results show remarkable differences in genomic alterations between the low-risk and high-risk groups, with the expression of SEMA4C, PIM1, TIMP1, TRIB2, ASNS, and RPS24 being higher in the high-risk group, while the expression of JAGN1 and NOX1 was higher in the low-risk group. Previous studies have had similar findings.

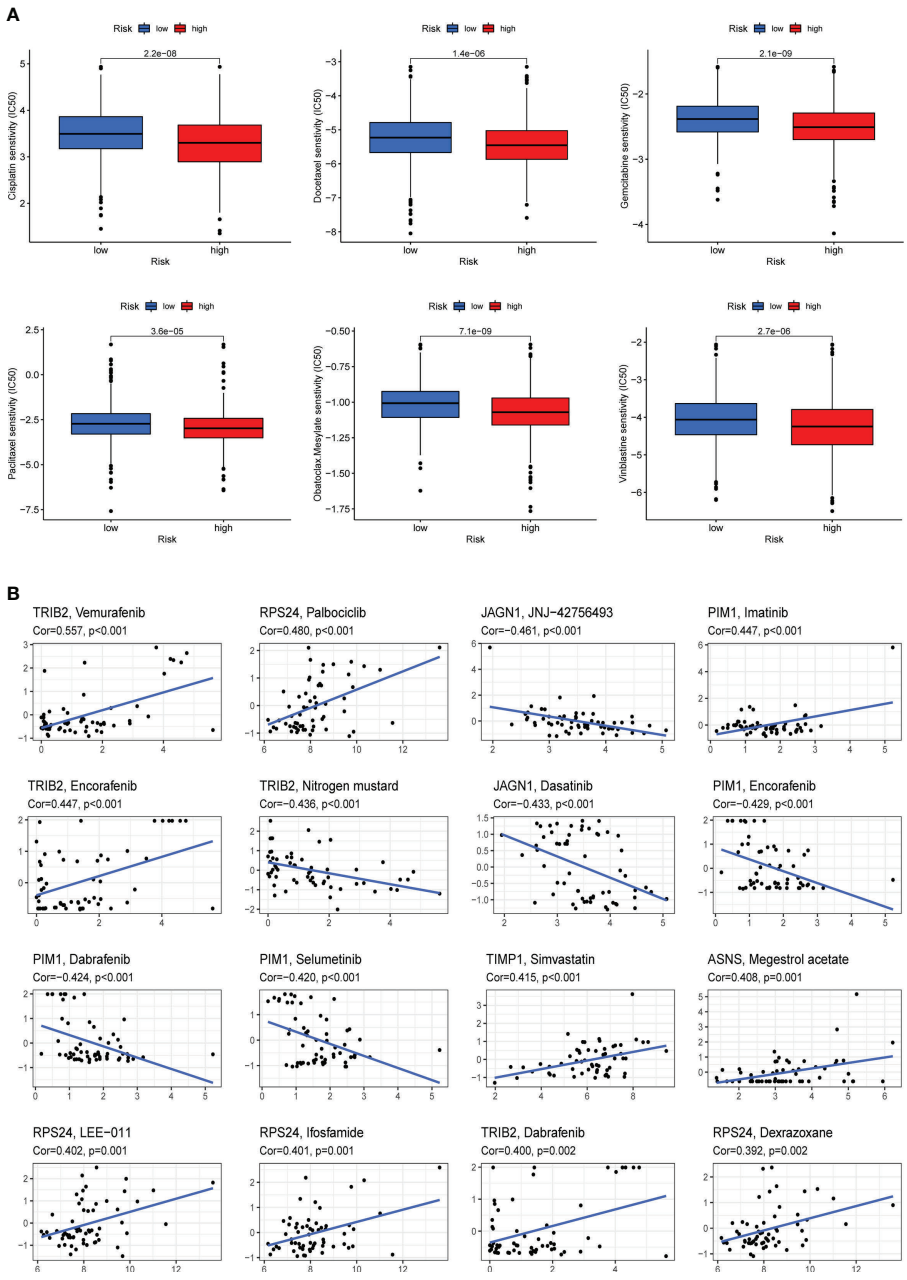

FIGURE 9
Drug sensitivity analysis. **(A)** Cisplatin, Docetaxel, Gemcitabine, Paclitaxel, Obatoclax.mecylate, and Vinblastine were observed to have lower IC50 values in the high-risk group, that is, the high-risk group was more sensitive to these drugs. **(B)** Analysis of the correlation between the expression of eight candidate genes included in the risk score model and chemotherapy drug sensitivity.

Semaphorins (SEMAs) are membrane-bound or soluble proteins involved in organ development and cancer progression, and among the SEMAs differentially expressed in colon cancer tissues, patients with tumors with higher SEMA4C (Semaphorins-4C) expression have lower survival rates (33). PIM1 expression is positively associated with CRC progression, and it was found to promote CRC growth and metastasis (34). Overexpression of TRIB2 accelerates cancer cell growth, cell cycle progression, and is associated with poor prognosis of CRC patients (35). High expression of asparagine synthetase (ASNS) is associated with poorer survival in women with right-sided colon cancer (RCC) (36). RPS24 is a gene that significantly promotes CRC cell proliferation (37), and knockdown of RPS24 can inhibit colorectal cancer cell migration and proliferation *in vitro* (38).

Both univariate and multivariate cox regression analysis showed that ARG_score was an independent predictor of survival outcome in COAD patients. The ROC validated its predictive robustness for 1-, 3- and 5-year OS. Thus, ARG_score may have reliable predictive power for COAD patient prognosis. We also analyzed the correlation between ARG score as well as ARG-related prognostic genes and immune cell infiltration. The results suggested that both ARG_score and candidate genes were strongly correlated with immune cells. Infiltration of some immune cells, such as dendritic cells (DCs) and CD4+ memory T cells, decreased as the risk score increased, while others, such as macrophages M0 and M1, did the opposite. These cells play complex roles in tumor immunity. For example, DCs are able to mediate cross-priming of tumor-specific T cells, which is essential for initiating and maintaining anti-tumor immunity. In tumors, the presence of DCs often induces T-cell response and mitigates cancer progression (39). In TME, macrophages, also known as tumor associated macrophages (TAMs), are one of the most abundant immune cells, which play an indispensable role in promoting tumor immune escape and inhibiting the immune function (40). Antitumor M1 TAMs and tumor-promoting M2 TAMs coexist in the TME (41). The interaction between M1/M2 TAMs directly affects the progress of CRC tumors and clinical treatment strategies (42, 43). One of the mechanisms of tumor immune escape is the metabolic reprogramming of TAMs, which prevents the increased inflammatory response mediated by M1 TAMs from killing tumor cells (44). Regulating the transformation of M2 TAMs into M1 TAMs has become a new direction for targeted treatment of tumor diseases (41, 45). In this study, the proportion of TAMs was significantly higher in ARGcluster B and high-risk group. Moreover, positive association was comfirmed between ARG_score and M1 TAMs, while significant correlation was identified between candidate ARGs and M2 TAMs. These results revealed that the prognostic signature and ARGclusters constructed by ARGs can distinguish the difference of tumor immune cells in COAD. Compared with the hot tumor, the cold tumor means that there are fewer immune cells infiltrating in the tumor, which means that the response to immunotherapy is weaker (46). Our results indicated that patients in ARGclusterA and low-risk group belonged to the cold tumor subtype. The proportion of immune cells and ESTIMATE score in the ARGclusterA and low-risk group were significantly lower, which consistent with the difintion of "immune-desert" phenotype (47). The above results revealed that immune monitoring function of patients in ARGclusterA and low-risk group was weakened, which was conducive to immune escape, and the effect of immunotherapy was poor.

Compared with left-sided CRC (LCRC), right-sided CRC (RCRC) is usually associated with poor prognosis, and also presents more advanced N stage, larger tumor size, poorly differentiated tumors, as well as higher probability of lymphatic vascular invasion (48). In addition, RCRC also presented higher hypermethylation and higher microsatellite instability (MSI) frequency than LRCR (26, 49). Higher risk score was associated with worse survival rate and higher MSI-high proportion, which was consistent with phenotypic characteristics of RCRC. Moreover, our results revealed that angiogenesis-related signature had a strong ability to discriminate LCRC and RCRC.

Previous studies on microsatellite stable CRC noted that patients with high TMB have longer median survival time (50). In most cancers, the higher the TMB level, the longer the OS of patients after immunotherapy (51, 52). About 12% to 15% of all CRC patients are MSI-H/dMMR (53).It was concluded that in early stages of CRC, MSI-H/dMMR CRC patients have a good prognosis, but in patients with mCRC, this status is associated with a poor prognosis (54). Immunotherapy in advanced CRC patients with MSI-H/dMMR has a high efficiency and can improve the OS of patients (55). We found a higher percentage of MSI-H in the high-risk group, while they had a higher TMB, which suggest that they are more sensitive to immunotherapy.

The development of resistance to chemotherapy in colorectal cancer is often a problem for physicians and patients (56). COAD patients with higher ARG_score were more sensitive to Cisplatin, Docetaxel, Gemcitabine, Paclitaxel, Obatoclax.mecylate, and Vinblastine, which means that the effect of chemotherapeutic drugs was better in the high-risk groups. Our findings may provide more evidence for the follow-up study of ARGs and tumor resistance, which may help to reduce drug resistance and improve clinical outcomes.

This study has shortcomings. All conclusions of the article were derived from the processing of data from public databases and retrospective analysis, and prospective clinical studies are lacking to validate the results. In addition, our analysis lacks *in vivo* and *in vitro* experiments to corroborate accuracy of this model in depth.

Conclusion

In summary, we constructed a risk score model for assessing the prognosis, immune infiltration, and drug sensitivity of COAD patients. The results of this study facilitate individualized assessment of patient prognosis and drug therapy in clinical.

Data availability statement

The datasets presented in this study can be found in online repositories. The names of the repository/repositories and accession number(s) can be found in the article/Supplementary Material.

Author contributions

ZGS and FW conceived the study and participated in the study design and manuscript writing. GLC, JHL and MLW

conducted the bioinformatics analysis. KYS and CW revised the manuscript. All authors read and approved the final manuscript.

Acknowledgments

We would like to extend our gratitude to the researchers and study patients for their contributions.

Conflict of interest

The authors declare that the research was conducted in the absence of any commercial or financial relationships that could be construed as a potential conflict of interest.

Publisher's note

All claims expressed in this article are solely those of the authors and do not necessarily represent those of their affiliated organizations, or those of the publisher, the editors and the reviewers. Any product that may be evaluated in this article, or claim that may be made by its manufacturer, is not guaranteed or endorsed by the publisher.

Supplementary material

The Supplementary Material for this article can be found online at: https://www.frontiersin.org/articles/10.3389/fimmu.2022.1049485/full#supplementary-material

SUPPLEMENTARY FIGURE 1
Kaplan-Meier survival analysis of different angiogenesis-related genes in COAD. The red and blue line represent patients with higher expression and lower expression of ARGs respectively.

SUPPLEMENTARY FIGURE 2
1587 differentially expressed gene (DEGs) between two ARGclusters were showed in Venn diagram.

SUPPLEMENTARY FIGURE 3
Prognostic value of ARGs in training set. **(A, B)** Multivariate Cox regression *via* LASSO is presented, and eight candidate ARGs were selected in training cohort.

SUPPLEMENTARY FIGURE 4
The expression level of 8 angiogenesis-related genes. **(A–F)** Compared with normal colon epithelial cells, SEMA4C, and ASNS expression were significantly increased in three CRC cell lines. PIM1, JAGN1 and RPS24 expression were significantly increased in Caco-2 and HT29 cells, but not in HCT-116 cells. TRIB2 expression was significantly increased in HT-29 and HCT-116 cells, but not in Caco- 2 cells.

SUPPLEMENTARY FIGURE 5
Stratification analysis of the ARG_score in COAD. **(A–D)** In terms of survival status and tumor stage, the proportion of deaths and stage III-IV tumors was significantly higher in the high-risk group than that in the low-risk group; in terms of age and gender, there were no significant differences between the two risk groups. **(E–G)** Kaplan-Meier curves depicted the survival difference between lower and higher ARG_score in the stratified analysis of COAD patients. Survival expectations were lower in the high-risk group than in the low-risk group, regardless of age, gender, or tumor stage.

SUPPLEMENTARY FIGURE 6
The correlation of risk score and different sided colorectal cancer (CRC). **(A)** The proportion of right-sided CRC (RCRC) and left-sided CRC (LCRC) patients in the different risk group. **(B)** The risk score of patients with RCRC and LRCR, higher risk score was found in RCRC.

SUPPLEMENTARY FIGURE 7
The difference of immune cells and immune functions between two risk groups.

References

1. Deo S, Sharma J, Kumar S. GLOBOCAN 2020 report on global cancer burden: Challenges and opportunities for surgical oncologists. *Ann Surg Oncol* (2022) 29(11):6497–500. doi: 10.1245/s10434-022-12151-6

2. Siegel RL, Miller KD, Goding Sauer A, Fedewa SA, Butterly LF, Anderson JC, et al. Colorectal cancer statistics, 2020. *CA Cancer J Clin* (2020) 70(3):145–64. doi: 10.3322/caac.21601

3. Biller L, Schrag D. Diagnosis and treatment of metastatic colorectal cancer: A review. *JAMA* (2021) 325(7):669–85. doi: 10.1001/jama.2021.0106

4. Le D, Uram J, Wang H, Bartlett B, Kemberling H, Eyring A, et al. PD-1 blockade in tumors with mismatch-repair deficiency. *New Engl J Med* (2015) 372 (26):2509–20. doi: 10.1056/NEJMoa1500596

5. Whiteside T. The tumor microenvironment and its role in promoting tumor growth. *Oncogene* (2008) 27(45):5904–12. doi: 10.1038/onc.2008.271

6. Jain R. Normalization of tumor vasculature: an emerging concept in antiangiogenic therapy. *Sci (New York NY)* (2005) 307(5706):58–62. doi: 10.1126/science.1104819

7. Kikuchi H, Matsui A, Morita S, Amoozgar Z, Inoue K, Ruan Z, et al. Increased CD8+ T-cell infiltration and efficacy for multikinase inhibitors after PD-1 blockade in hepatocellular carcinoma. *J Natl Cancer Inst* (2022) 114(9):1301–5. doi: 10.1093/jnci/djac051

8. Zhen Z, Shen Z, Hu Y, Sun P. Screening and identification of angiogenesis-related genes as potential novel prognostic biomarkers of hepatocellular carcinoma through bioinformatics analysis. *Aging* (2021) 13(13):17707–33. doi: 10.18632/aging.203260

9. Qing X, Xu W, Liu S, Chen Z, Ye C, Zhang Y. Molecular characteristics, clinical significance, and cancer immune interactions of angiogenesis-associated genes in gastric cancer. *Front Immunol* (2022) 13:843077. doi: 10.3389/fimmu.2022.843077

10. Wang J, Guo M, Zhou X, Ding Z, Chen X, Jiao Y, et al. Angiogenesis related gene expression significantly associated with the prognostic role of an urothelial bladder carcinoma. *Trans androl Urol* (2020) 9(5):2200–10. doi: 10.21037/tau-20-1291

11. Conesa A, Madrigal P, Tarazona S, Gomez-Cabrero D, Cervera A, McPherson A, et al. A survey of best practices for RNA-seq data analysis. *Genome Biol* (2016) 17:13. doi: 10.1186/s13059-016-0881-8

12. Leek JT, Johnson WE, Parker HS, Jaffe AE, Storey JD. The sva package for removing batch effects and other unwanted variation in high-throughput experiments. *Bioinf (Oxford England)* (2012) 28(6):882–3. doi: 10.1093/bioinformatics/bts034

13. Wang G, Hu JQ, Liu JY, Zhang XM. Angiogenesis-related gene signature-derived risk score for glioblastoma: Prospects for predicting prognosis and immune

heterogeneity in glioblastoma. *Front Cell Dev Biol* (2022) 10:778286. doi: 10.3389/fcell.2022.778286

14. Sabah A, Tiun S, Sani N, Ayob M, Taha A. Enhancing web search result clustering model based on multiview multirepresentation consensus cluster ensemble (mmcc) approach. *PloS One* (2021) 16(1):e0245264. doi: 10.1371/journal.pone.0245264

15. Seiler M, Huang C, Szalma S, Bhanot G. ConsensusCluster: A software tool for unsupervised cluster discovery in numerical data. *Omics* (2010) 14(1):109–13. doi: 10.1089/omi.2009.0083

16. Hänzelmann S, Castelo R, Guinney J. GSVA: gene set variation analysis for microarray and RNA-seq data. *BMC Bioinf* (2013) 14:7. doi: 10.1186/1471-2105-14-7

17. Meng Z, Ren D, Zhang K, Zhao J, Jin X, Wu H. Using ESTIMATE algorithm to establish an 8-mRNA signature prognosis prediction system and identify immunocyte infiltration-related genes in pancreatic adenocarcinoma. *Aging* (2020) 12(6):5048–70. doi: 10.18632/aging.102931

18. Chen B, Khodadoust MS, Liu CL, Newman AM, Alizadeh AA. Profiling tumor infiltrating immune cells with CIBERSORT. *Methods Mol Biol* (2018) 1711:243–59. doi: 10.1007/978-1-4939-7493-1_12

19. Huang L, Wu C, Xu D, Cui Y, Tang J. Screening of important factors in the early sepsis stage based on the evaluation of ssGSEA algorithm and ceRNA regulatory network. *Evolutionary Bioinf Online* (2021) 17:11769343211058463. doi: 10.1177/11769343211058463

20. Yu G, Wang LG, Han Y, He QY. clusterProfiler: an r package for comparing biological themes among gene clusters. *Omics* (2012) 16(5):284–7. doi: 10.1089/omi.2011.0118

21. Liu Z, Xu H, Weng S, Ren Y, Han X. Stemness refines the classification of colorectal cancer with stratified prognosis, multi-omics landscape, potential mechanisms, and treatment options. *Front Immunol* (2022) 13:828330. doi: 10.3389/fimmu.2022.828330

22. Iasonos A, Schrag D, Raj GV, Panageas KS. How to build and interpret a nomogram for cancer prognosis. *J Clin Oncol* (2008) 26(8):1364–70. doi: 10.1200/JCO.2007.12.9791

23. Liu Z, Xu H, Ge X, Weng S, Dang Q, Han X. Gene expression profile reveals a prognostic signature of non-MSI-H/pMMR colorectal cancer. *Front Cell Dev Biol* (2022) 10:790214. doi: 10.3389/fcell.2022.790214

24. Mayakonda A, Lin DC, Assenov Y, Plass C, Koeffler HP. Maftools: efficient and comprehensive analysis of somatic variants in cancer. *Genome Res* (2018) 28 (11):1747–56. doi: 10.1101/gr.239244.118

25. Geeleher P, Cox N, Huang RS. pRRophetic: an r package for prediction of clinical chemotherapeutic response from tumor gene expression levels. *PloS One* (2014) 9(9):e107468. doi: 10.1371/journal.pone.0107468

26. Lee DW, Han SW, Cha Y, Bae JM, Kim HP, Lyu J, et al. Association between mutations of critical pathway genes and survival outcomes according to the tumor location in colorectal cancer. *Cancer* (2017) 123(18):3513–23. doi: 10.1002/cncr.30760

27. Liu Z, Guo Y, Yang X, Chen C, Fan D, Wu X, et al. Immune landscape refines the classification of colorectal cancer with heterogeneous prognosis, tumor microenvironment and distinct sensitivity to frontline therapies. *Front Cell Dev Biol* (2021) 9:784199. doi: 10.3389/fcell.2021.784199

28. Sher G, Masoodi T, Patil K, Akhtar S, Kuttikrishnan S, Ahmad A, et al. Dysregulated FOXM1 signaling in the regulation of cancer stem cells. *Semin Cancer Biol* (2022). doi: 10.1016/j.semcancer.2022.07.009

29. Ganesh K, Stadler ZK, Cercek A, Mendelsohn RB, Shia J, Segal NH, et al. Immunotherapy in colorectal cancer: rationale, challenges and potential. *Nat Rev Gastroenterol Hepatol* (2019) 16(6):361–75. doi: 10.1038/s41575-019-0126-x

30. Overman M, Lonardi S, Wong K, Lenz H, Gelsomino F, Aglietta M, et al. Durable clinical benefit with nivolumab plus ipilimumab in DNA mismatch repair-Deficient/Microsatellite instability-high metastatic colorectal cancer. *J Clin Oncol* (2018) 36(8):773–9. doi: 10.1200/JCO.2017.76.9901

31. Quail D, Joyce J. Microenvironmental regulation of tumor progression and metastasis. *Nat Med* (2013) 19(11):1423–37. doi: 10.1038/nm.3394

32. Karpinski P, Rossowska J, Sasiadek M. Immunological landscape of consensus clusters in colorectal cancer. *Oncotarget* (2017) 8(62):105299–311. doi: 10.18632/oncotarget.22169

33. Hung Y, Lai M, Hung W, Chen L. Semaphorin 4C promotes motility and immunosuppressive activity of cancer cells *via* CRMP3 and PD-L1. *Am J Cancer Res* (2022) 12(2):713–28.

34. Zhang M, Liu T, Sun H, Weng W, Zhang Q, Liu C, et al. Pim1 supports human colorectal cancer growth during glucose deprivation by enhancing the warburg effect. *Cancer Sci* (2018) 109(5):1468–79. doi: 10.1111/cas.13562

35. Hou Z, Guo K, Sun X, Hu F, Chen Q, Luo X, et al. TRIB2 functions as novel oncogene in colorectal cancer by blocking cellular senescence through AP4/p21 signaling. *Mol Cancer* (2018) 17(1):172. doi: 10.1186/s12943-018-0922-x

36. Cai Y, Rattray N, Zhang Q, Mironova V, Santos-Neto A, Hsu K, et al. Sex differences in colon cancer metabolism reveal a novel subphenotype. *Sci Rep* (2020) 10(1):4905. doi: 10.1038/s41598-020-61851-0

37. Zou D, Zhang H, Ke J, Li J, Zhu Y, Gong Y, et al. Three functional variants were identified to affect RPS24 expression and significantly associated with risk of colorectal cancer. *Arch Toxicol* (2020) 94(1):295–303. doi: 10.1007/s00204-019-02600-9

38. Wang Y, Sui J, Li X, Cao F, He J, Yang B, et al. RPS24 knockdown inhibits colorectal cancer cell migration and proliferation *in vitro*. *Gene* (2015) 571(2):286–91. doi: 10.1016/j.gene.2015.06.084

39. Kambayashi T, Laufer TM. Atypical MHC class II-expressing antigen-presenting cells: Can anything replace a dendritic cell? *Nat Rev Immunol* (2014) 14(11):719–30. doi: 10.1038/nri3754

40. Lopez-Yrigoyen M, Cassetta L, Pollard JW. Macrophage targeting in cancer. *Ann New York Acad Sci* (2021) 1499(1):18–41. doi: 10.1111/nyas.14377

41. Mantovani A, Marchesi F, Malesci A, Laghi L, Allavena P. Tumour-associated macrophages as treatment targets in oncology. *Nat Rev Clin Oncol* (2017) 14(7):399–416. doi: 10.1038/nrclinonc.2016.217

42. Cassetta L, Pollard JW. Targeting macrophages: therapeutic approaches in cancer. *Nat Rev Drug Discovery* (2018) 17(12):887–904. doi: 10.1038/nrd.2018.169

43. Wu K, Lin K, Li X, Yuan X, Xu P, Ni P, et al. Redefining tumor-associated macrophage subpopulations and functions in the tumor microenvironment. *Front Immunol* (2020) 11:1731. doi: 10.3389/fimmu.2020.01731

44. Liu Y, Xu R, Gu H, Zhang E, Qu J, Cao W, et al. Metabolic reprogramming in macrophage responses. *biomark Res* (2021) 9(1):1. doi: 10.1186/s40364-020-00251-y.45

45. Boutilier AJ, Elsawa SF. Macrophage polarization states in the tumor microenvironment. *Int J Mol Sci* (2021) 22(13):6695. doi: 10.3390/ijms22136995

46. Hugo W, Zaretsky JM, Sun L, Song C, Moreno BH, Hu-Lieskovan S, et al. Genomic and transcriptomic features of response to anti-PD-1 therapy in metastatic melanoma. *Cell* (2017) 168(3):542. doi: 10.1016/j.cell.2017.01.010

47. Zhang B, Wu Q, Li B, Wang D, Wang L, Zhou YL. m(6)A regulator-mediated methylation modification patterns and tumor microenvironment infiltration characterization in gastric cancer. *Mol Cancer* (2020) 19(1):53. doi: 10.1186/s12943-020-01170-0

48. Mirón Fernández I, Mera Velasco S, Turiño Luque JD, González Poveda I, Ruiz López M, Santoyo Santoyo J. Right and left colorectal cancer: Differences in post-Surgical-Care outcomes and survival in elderly patients. *Cancers* (2021) 13(11):2647. doi: 10.3390/cancers13112647

49. Ahmad Zawawi SS, Musa M. Dynamic Co-evolution of cancer cells and cancer-associated fibroblasts: Role in right- and left-sided colon cancer progression and its clinical relevance. *Biology* (2022) 11(7):1014. doi: 10.3390/biology11071014

50. Romero D. TMB is linked with prognosis. *Nat Rev Clin Oncol* (2019) 16 (6):336. doi: 10.1038/s41571-019-0206-4

51. Samstein RM, Lee CH, Shoushtari AN, Hellmann MD, Shen R, Janjigian YY, et al. Tumor mutational load predicts survival after immunotherapy across multiple cancer types. *Nat Genet* (2019) 51(2):202–6. doi: 10.1038/s41588-018-0312-8

52. Goodman AM, Kato S, Bazhenova L, Patel SP, Frampton GM, Miller V, et al. Tumor mutational burden as an independent predictor of response to immunotherapy in diverse cancers. *Mol Cancer Ther* (2017) 16(11):2598–608. doi: 10.1158/1535-7163.MCT-17-0386

53. Overman MJ, McDermott R, Leach JL, Lonardi S, Lenz HJ, Morse MA, et al. Nivolumab in patients with metastatic DNA mismatch repair-deficient or microsatellite instability-high colorectal cancer (CheckMate 142): an open-label, multicentre, phase 2 study. *Lancet Oncol* (2017) 18(9):1182–91. doi: 10.1016/S1470-2045(17)30422-9

54. Gelsomino F, Barbolini M, Spallanzani A, Pugliese G, Cascinu S. The evolving role of microsatellite instability in colorectal cancer: A review. *Cancer Treat Rev* (2016) 51:19–26. doi: 10.1016/j.ctrv.2016.10.005

55. Benson AB, Venook AP, Al-Hawary MM, Arain MA, Chen YJ, Ciombor KK, et al. Colon cancer, version 2.2021, NCCN clinical practice guidelines in oncology. *J Natl Compr Cancer Network* (2021) 19(3):329–59. doi: 10.6004/jnccn.2021.0012

56. Kishore C, Bhadra P. Current advancements and future perspectives of immunotherapy in colorectal cancer research. *Eur J Pharmacol* (2021) 893:173819. doi: 10.1016/j.ejphar.2020.173819

frontiers | Frontiers in Immunology

TYPE Original Research
PUBLISHED 13 December 2022
DOI 10.3389/fimmu.2022.1048503

Check for updates

OPEN ACCESS

EDITED BY
Linlang Guo,
Zhujiang Hospital, China

REVIEWED BY
Ziyun Li,
Nanjing University of Chinese Medicine, China
Lifei Hou,
Boston Children's Hospital and Harvard Medical School, United States

*CORRESPONDENCE
Ruifa Feng
c71339@qq.com
Weiyi Pang
p.weiyi@live.cn
Wenjie Shi
wenjie.shi-oldenburg@outlook.com

†These authors have contributed equally to this work and share first authorship

SPECIALTY SECTION
This article was submitted to Cancer Immunity and Immunotherapy, a section of the journal Frontiers in Immunology

RECEIVED 19 September 2022
ACCEPTED 28 November 2022
PUBLISHED 13 December 2022

CITATION
Wang G, Miao C, Mo L, Kahlert UD, Wu J, Ou M, Huang R, Feng R, Pang W and Shi W (2022) MYCBP2 expression correlated with inflammatory cell infiltration and prognosis immunotherapy in thyroid cancer patients. *Front. Immunol.* 13:1048503. doi: 10.3389/fimmu.2022.1048503

COPYRIGHT
© 2022 Wang, Miao, Mo, Kahlert, Wu, Ou, Huang, Feng, Pang and Shi. This is an open-access article distributed under the terms of the Creative Commons Attribution License (CC BY). The use, distribution or reproduction in other forums is permitted, provided the original author(s) and the copyright owner(s) are credited and that the original publication in this journal is cited, in accordance with accepted academic practice. No use, distribution or reproduction is permitted which does not comply with these terms.

MYCBP2 expression correlated with inflammatory cell infiltration and prognosis immunotherapy in thyroid cancer patients

Guilin Wang[1†], Chen Miao[2†], Lijun Mo[1†], Ulf D. Kahlert[3], Jinfeng Wu[1], Minglin Ou[1], Renxiang Huang[1], Ruifa Feng[1*], Weiyi Pang[4*] and Wenjie Shi[3,5*]

[1]Breast Center, The Second Affiliated Hospital of Guilin Medical University, Guilin, Guangxi, China, [2]Department of Pathology, The First Affiliated Hospital of Nanjing Medical University, Nanjing, China, [3]Molecular and Experimental Surgery,University Clinic for General, Visceral, Vascular and Transplantation Surgery, Faculty of Medicine, Otto-von-Guericke-University, Magdeburg, Germany, [4]Guangxi Key Laboratory of Environmental Exposomics and Entire Lifecycle Heath, Guilin Medical University, Guilin, Guangxi, China, [5]University Hospital for Gynecology, Pius-Hospital, University Medicine Oldenburg, Oldenburg, Germany

Introduction: Immune checkpoint inhibitors (ICIs) have shown promising results for the treatment of multiple cancers. ICIs and related therapies may also be useful for the treatment of thyroid cancer (TC). In TC, Myc binding protein 2 (MYCBP2) is correlated with inflammatory cell infiltration and cancer prognosis. However, the relationship between MYCBP2 expression and ICI efficacy in TC patients is unclear.

Methods: We downloaded data from two TC cohorts, including transcriptomic data and clinical prognosis data. The Tumor Immune Dysfunction and Exclusion (TIDE) algorithm was used to predict the efficacy of ICIs in TC patients. MCPcounter, xCell, and quanTIseq were used to calculate immune cell infiltration scores. Gene set enrichment analysis (GSEA) and single sample GSEA (ssGSEA) were used to evaluate signaling pathway scores. Immunohistochemical (IHC) analysis and clinical follow up was used to identify the MYCBP2 protein expression status in patients and associated with clinical outcome.

Results: A higher proportion of MYCBP2-high TC patients were predicted ICI responders than MYCBP2-low patients. MYCBP2-high patients also had significantly increased infiltration of CD8+ T cells, cytotoxic lymphocytes (CTLs), B cells, natural killer (NK) cells and dendritic cells (DC)s. Compared with MYCBP2-low patients, MYCBP2-high patients had higher expression of genes associated with B cells, CD8+ T cells, macrophages, plasmacytoid dendritic cells (pDCs), antigen processing and presentation, inflammatory stimulation, and interferon (IFN) responses. GSEA and ssGSEA also showed that MYCBP2-high patients had significantly increased activity of inflammatory

factors and signaling pathways associated with immune responses.In addiation, Patients in our local cohort with high MYCBP2 expression always had a better prognosis and greater sensitivity to therapy while compared to patients with low MYCBP2 expression after six months clinic follow up.

Conclusions: In this study, we found that MYCBP2 may be a predictive biomarker for ICI efficacy in TC patients. High MYCBP2 expression was associated with significantly enriched immune cell infiltration. MYCBP2 may also be involved in the regulation of signaling pathways associated with anti-tumor immune responses or the production of inflammatory factors.

KEYWORDS

immune checkpoint inhibitors, MYCBP2, myc binding protein 2, prognosis, thyroid cancer

Introduction

Thyroid cancer (TC) originates from follicular epithelial cells or parafollicular epithelial cells of the thyroid. It is the most common malignant tumor in endocrine system and comprises about 90% of endocrine cancers (1, 2). Although most TCs are relatively inert and can be effectively treated by surgery, radiation,131 and thyroid stimulating hormone (TSH) inhibition therapy, some cases are refractory and eventually lead to disease progression, recurrence, and even death (3). Although targeted therapies such as kinase inhibitors can prolong patient prognosis, the effectiveness of kinase inhibitors is severely limited due to the rapid development of drug resistance and the occurrence of adverse reactions (4–8). In recent years, with increasing use of immune checkpoint inhibitors (ICIs) for anti-cancer therapy, research on the use of ICIs for TC is also rapidly advancing, with the hope of improving the prognosis of TC patients.

Previous research has shown that biomarkers predicting the efficacy of ICIs can help to screen patients and further improve prognoses (9, 10). At present, Programmed Cell Death-Ligand 1 (PD-L1) expression and tumor mutation burden (TMB) are the main markers of ICI effectiveness (9–12). However, these biomarkers also have some disadvantages: thresholds of TMB are different across studies, and PD-L1 detection platforms vary (13–16). Therefore, there is need to identify biomarkers that more comprehensively predict the efficacy of ICIs, allowing for the development of tumor precision medicine.

Myc binding protein 2 (MYCBP2) is a E3 ubiquitin ligase (17). Previous studies have shown that MYCBP is associated with the occurrence and prognosis of lung cancer, gastric cancer, breast cancer, and glioma (18–20). Pierre et al. found that MYCBP2 expression was associated with an M2-like macrophage phenotype in a mouse model (21). Schaid et al. found that MYCBP2 expression was associated with an elevated risk of invasive prostate cancer (22). However, the relationship between MYCBP2 expression and ICI efficacy in TC remains unclear.

In the present study, we downloaded data on a TC cohort from the Gene Expression Omnibus (GEO) database and a thyroid carcinoma (THCA) cohort from the Cancer Genome Atlas (TCGA) database. We used the Tumor Immune Dysfunction and Exclusion (TIDE) algorithm to predict the therapeutic effect of ICIs in TC patients. Next, we evaluated the relationship between MYCBP2 expression and ICI efficacy in TC patients and explored its potential molecular mechanism.

Methods

THCA cohort and ICIs datasets

We downloaded a THCA cohort (GSE138042-THCA) with transcriptomic data from the GEO database (https://www.ncbi.nlm.nih.gov/geo/) (23). We also downloaded another THCA cohort (TCGA-THCA) with gene expression profile data from TCGA database (https://portal.gdc.cancer.gov/) (24). Because the public databases did not publish data on the efficacy of ICIs by THCA, we used the TIDE algorithm (http://tide.dfci.harvard.edu) (25). The transcriptomic data from GSE138042-THCA and TCGA-THCA were used to predict the response of each patient to ICIs, and each patient was categorized as a responder or non-responder. We also downloaded data from an ICI-treated melanoma cohort (26) and an ICI-treated urothelial

cancer (UC) (27) cohort, including transcriptomic data and prognostic data from the cbioportal webtools (https://www.cbioportal.org/) (28). Also, we downloaded two datasets related to the mice model treated with the ICIs [GSE146027 (29) and GSE151829 (30)]. We downloaded the expression data and survival data of different cancer types [GSE26304 (31), GSE1456 (32), GSE5327 (33), GSE30929 (34), GSE26939 (35), GSE30219 (36), GSE41271 (37), GSE30219 (36), GSE37745 (38), GSE50081 (39), GSE62452 (40), and GSE16560 (41)] to further validate the relationship between the expression of MYCBP2 and the survival time.

Analysis of tumor immune microenvironment

We downloaded the gene set of immune checkpoint (IC) related molecules and immune related molecules from CAMOIP (http://camoip.net/) (42). We used three immune cell evaluation algorithms (1.MCPcounter, 2.xCell, and 3.quanTIseq) to calculate the immune cell infiltration score of each THCA patient from the expression data (43–45).

Pathway enrichment analysis

We used gene set enrichment analysis (GSEA) to analyze the transcriptomic data of THCA patients and obtained pathway enrichment scores and P values of pathways from the Kyoto Encyclopedia of Genes and Genomes (KEGG) (https://www.kegg.jp/), Reactome (https://reactome.org/), Gene Ontology-Biological Process (GO-BP), Gene Ontology- Cellular Component (GO-CC), and Gene Ontology- Molecular Function (GO-MF) databases (46). We also applied the single sample GSEA (ssGSEA) algorithm to analyze the transcriptomic data of each THCA patient and then obtained the enrichment scores of each patient in the Molecular Signatures Database (MsigDB) database (http://www.gsea-msigdb.org/gsea/downloads.jsp) (47).

Immunohistochemical analysis and clinical follow up

To identify the MYCBP2 protein expression status in patients and associated with clinical outcome. We collect tissues samples from thyroid cancer patients,who accepted surgery operation in Breast Center of The Second Affiliated Hospital of Guilin Medical University, to conduct immunohistochemical analysis and follow up six months to evaluate the prognosis difference between high and low expression groups. Thirty-six tissues from twelve patients, each patient has three tissues obtained from different surgery sections, and these tissues were washed with Phosphate-Buffered Saline (PBS) and then incubated with 3% H2O2 for 10 minutes. Samples were incubated with antibody against MYCBP2 (1 mg/mL diluted 1:200, 27951, Proteintech, CA) at room temperature for two hours. After incubation with polymer enhancer for 20 minutes, the tissue was incubated with polymer enhancer and enzyme-labeled rabbit polymers. Slides were washed with PBS and fresh diaminobenzidine and counterstained with hematoxylin; antigen retrieval was performed using 0.1% HCl, and slides were then dehydrated with ethanol, cleaned with xylene, and fixed with neutral balata. The images were observed and photographed using a fluorescence microscope and visualized under a light microscope at 100× magnification by a blinded observer. Light to dark brown staining indicated a positive result from low to high. The stained areas were analyzed using Image J. Patients who donated samples for IHC also accepted clinical follow up to evaluate the association between MYCBP2 expression and patient outcomes following surgery. All patient and tissue studies were approved by the Ethics Committee of Breast Center of The Second Affiliated Hospital of Guilin Medical University.

Statistical analysis

The Mann-Whitney U test was used to compare differences between the MYCBP2-high and MYCBP2-low groups in continuous variables. Fisher's exact test was used to compare differences between the two groups in categorical variables. Kaplan-Meier curves were used to visualize differences in overall survival (OS) time between the two groups, and a log rank test was used to calculate the difference in OS time. We used the ggplot2 R package to generate boxplots. Visualization and data analysis for the present study were conducted in Rstudio software (Version 4.1.2). P values were bilateral and P values < 0. 05 were considered statistically significant.

Results

Relationship between MYCBP2 expression and ICI efficacy in THCA

In the present study, we explored the relationship between MYCBP2 expression and ICI efficacy in THCA patients and analyzed potential molecular mechanisms for this relationship (Figure 1A). In the GSE138042-THCA cohort, MYCBP2-high patients receiving ICIs had a higher proportion of predicted responders than MYCBP2-low patients receiving ICIs (evaluated by the TIDE algorithm) (Figure 1B, P < 0. 05). MYCBP2-high patients in TCGA-THCA cohort also had a higher predicted response rate to ICIs (Figure 1C, P < 0. 05). Next, we used the ICI-treated melanoma and urothelial cohorts to further verify the relationship between MYCBP2 expression and prognosis in ICI-

treated patients (Figures 1D, E). Figure 1D shows that MYCBP2-high melanoma patients had significantly longer OS time than MYCBP2-low patients (log rank P = 0. 019, HR = 0. 3). Figure 1E shows that MYCBP2-high urothelial cancer patients had a significantly longer OS time than MYCBP2-low patients (log rank P = 0. 041; HR = 0. 59, 95% CI: 0. 35-1). In the mice model, we found that the expression of Mycbp2 was significantly increased in the ICIs-responders compared with ICIs-non-responders (Supplementary Figures 1A, B). Also, in the multiple cancer types, we found that MYCBP2-high patients had significantly prolonged survival time compared with MYCBP2-low patients (Supplementary Table 1, Supplementary Figure 2).

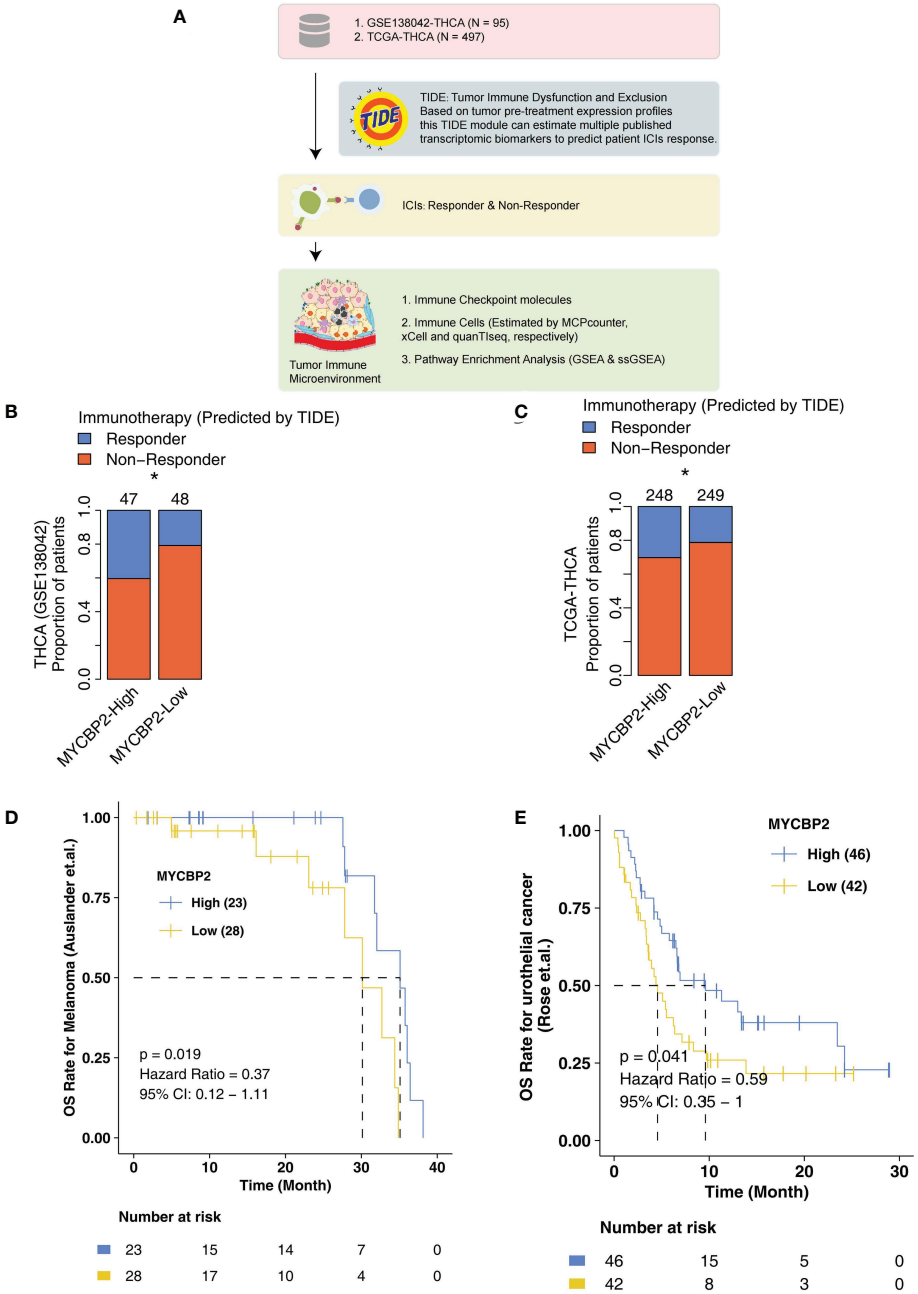

FIGURE 1
The association between the MYCBP2 expression and ICI efficacy. **(A)** The overall design of the study. The differences in predicted ICI efficacy between the MYCBP2-High and MYCBP2-Low TC patients in the GSE138042-TC **(B)** and TCGA-THCA **(C)** cohorts. KM curve showing the differences in the prognoses of ICI-treated patients between the MYCBP2-High and MYCBP2-Low groups in the melanoma **(D)** and urothelial cancer **(E)** cohorts. (*: P < 0.05).

10.3389/fimmu.2022.1048503

Relationship between MYCBP2 expression, IC-related molecules, and immune related genes

In TCGA-THCA cohort, MYCBP2-high patients had significantly higher expression of IC-related molecules, such as LAG3, IDO1, CTLA4, TIGIT, PD-1 and PDCD1LG2, than MYCBP2-low patients (Figure 2A, P < 0. 05). In the GSE138042-THCA cohort, the heatmap also revealed differences between MYCBP2-high and MYCBP2-low patients in the expression of genes associated with antigen presentation, B cells, CD8+ T cells, macrophages, pDCs, inflammatory stimulation, and IFN responses (Figure 2B). In the TCGA-THCA cohort, these genes were expressed at significantly higher levels in MYCBP2-high patients than in MYCBP2-low patients (Supplementary Figure 3).

Relationship between MYCBP2 expression and immune cell infiltration

We used the MCPcounter algorithm to evaluate immune cell infiltration in the TIME of THCA patients (Figures 3A, B). In both the GSE138042-THCA (Figure 3A) and TCGA-THCA

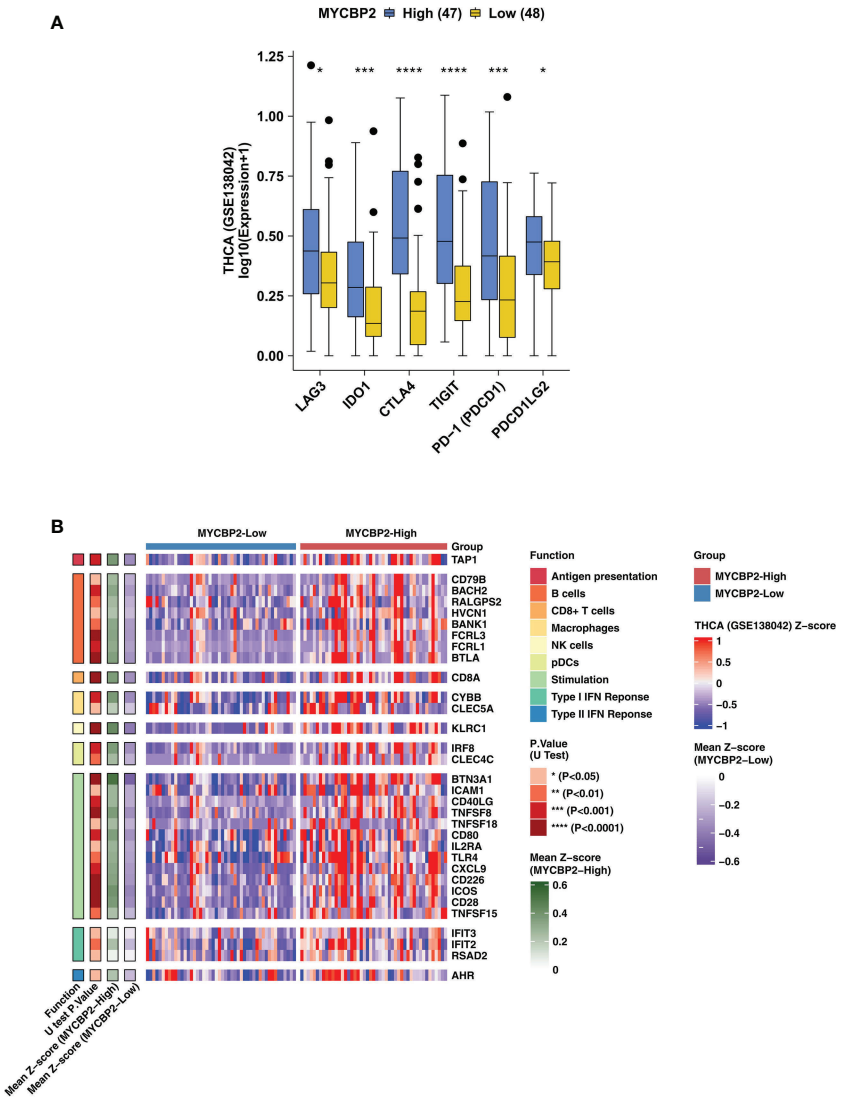

FIGURE 2
The association between the MYCBP2 expression and immune-related gene expression. **(A)** Differences in the expression of immune checkpoint molecules between MYCBP2-High and MYCBP2-Low patients in the GSE138042-TC cohort. **(B)** Heatmap depicting differences the expression of immune-related genes (antigen presentation, B cells, CD8+ T cells, macrophages, NK cells, pDCs, stimulation, and IFN responses) between MYCBP2-High and MYCBP2-Low patients in the GSE138042-TC cohort. (*: P < 0.05; ***: P < 0.001; ****: P < 0.0001).

(Figure 3B) cohorts, MYCBP2-high patients had significantly higher infiltration of CD8+ T cells, cytotoxic lymphocytes (CTLs), B cells, and NK cells than MYCBP2-low patients. The quanTIseq algorithm was also used to verify immune cell infiltration fractions (Figures 3C, D). Using the quanTIseq algorithm, we found that MYCBP2-high patients had significantly enriched B cells, NK cells, and DCs (Figure 3C: GSE138042-THCA; Figure 3D: TCGA-THCA, all $P < 0.05$). We also used the xCell algorithm to evaluate the proportions of tumor infiltrating immune cells (Figures 3E, F). Compared with MYCBP2-low patients, MYCBP2-high patients had significantly increased B cells, memory CD4+ T cells, CD8+ T cells, central memory CD8 + T cells (TCMs), and class-switched memory B-cells (Figure 3E: GSE138042-THCA; Figure 3F: TCGA-THCA).

Relationship between MYCBP2 expression and immune signaling pathways

We found that MYCBP2-high patients had higher activation of immune signaling pathways than MYCBP2-low patients (Figure 4A: GSE138042-THCA; Figure 4B: TCGA-THCA, ES > 0, P < 0. 05), including pathways regulating cell surface receptor signaling and phagocytosis, Fc receptor signaling, signal transduction, chemokine production, molecular mediators of immune responses, interleukin-12 (IL-12) production, MHC protein complex binding, interleukin-15 (IL-15) signaling, and interleukin-2 (IL-2) family signaling. Signaling pathways related to immune responses and immune cell activation were also significantly upregulated in MYCBP2-high patients, including B cell activation, lymphocyte mediated immunity, leukocyte migration, B cell proliferation, and NK cell mediated cytotoxicity (Figure 4C: GSE138042-THCA; Figure 4D: TCGA-THCA, ES > 0, P < 0. 05). The results of ssGSEA showed that MYCBP2-high patients had higher immune response pathway scores than MYCBP2-low patients, including pathways for MHC class I protein complex binding, DC cytokine production, MHC class IB receptor activity, IL-12 production, lymphocyte mediated immunity, NK cell mediated cytotoxicity, T cell mediated immunity, interleukin-18 (IL-18) production, NK cell mediated immunity, NK cell activation, DC antigen processing and presentation, and IL-15 signaling (Figure 4E: GSE138042-THCA; Figure 4F: TCGA-THCA, P < 0. 05). On the contrary, lipid metabolism related pathways (such as short chain fatty acid metabolism, fatty acid beta oxidation using acyl COA oxidase, and positive regulation of vascular permeability) were significantly downregulated in MYCBP2-high patients compared to MYCBP2-low patients (Figure 4E: GSE138042-THCA; Figure 4F: TCGA-THCA, P < 0. 05).

Validation of the local cohort based on MYCBP2 status

IHC revealed MYCBP2 expression levels in TC tissues. Patients in our local cohort with high MYCBP2 expression always had a better prognosis and greater sensitivity to therapy compared to patients with low MYCBP2 expression after six months clinic follow up (Figure 5).

Discussion

Compared to conventional chemotherapy, ICIs has higher safety and fewer adverse reactions, making it a useful treatment regimen for various advanced cancers (48). ICIs is now a potential treatment for patients with advanced and refractory TC (49–51). In this study, we found that higher MYCBP2 expression was associated with better outcomes in TC patients receiving ICIs. Immune cell infiltration analysis showed that higher MYCBP2 expression was associated with significantly enriched inflammatory immune cell infiltration and higher expression of inflammatory molecules. Pathway enrichment analysis showed that MYCBP2 may be involved in anti-tumor immune responses. Therefore, MYCBP2 may be a novel biomarker for ICI efficacy in TC patients.

The significantly enriched inflammatory immune cell infiltration in MYCBP2-high patients is a potential molecular mechanism for the greater efficacy of ICIs in these patients. Bastman et al. found that some TC patients with greater programmed death 1 [PD-1(+)] CD4+ T cell and PD-1(+) CD8+ T cell infiltration could benefit from anti-PD-1/PD-L1 treatment (52). CD8 + T cells can kill target cells in an antigen-specific manner, and improve the disease-free survival (DFS) rate of patients (53). NK cells also play a key role in anti-tumor immune monitoring. NK cells can not only kill tumor or infected cells directly, but they can also indirectly enhance antibody and T-cell-mediated anti-tumor immune responses (54). NK cells also release lysosomes containing perforin and granzyme to kill target cells (55). Many studies have also shown that DCs are a key regulatory factor for the efficacy of ICIs and other tumor immunotherapies (56). Accordingly, researchers are now attempting to engineer DCs to activate and drive T cells into the TIME, particularly for tumors with weak immunogenicity (non-inflammatory of "cold" tumors), to improve the efficacy of ICIs (51, 57). In our study, we found that MYCBP2-high patients had significantly increased CD8+ T cells, B cells, NK cells, and DCs in the TIME compared to MYCBP2-low patients.

The high expression of inflammatory molecules and activation of immune response pathways in MYCBP2-high patients is another potential molecular mechanism for the greater ICI efficacy in MYCBP2-high patients. IL-15 can maintain NK cell populations and tumor killing ability in the

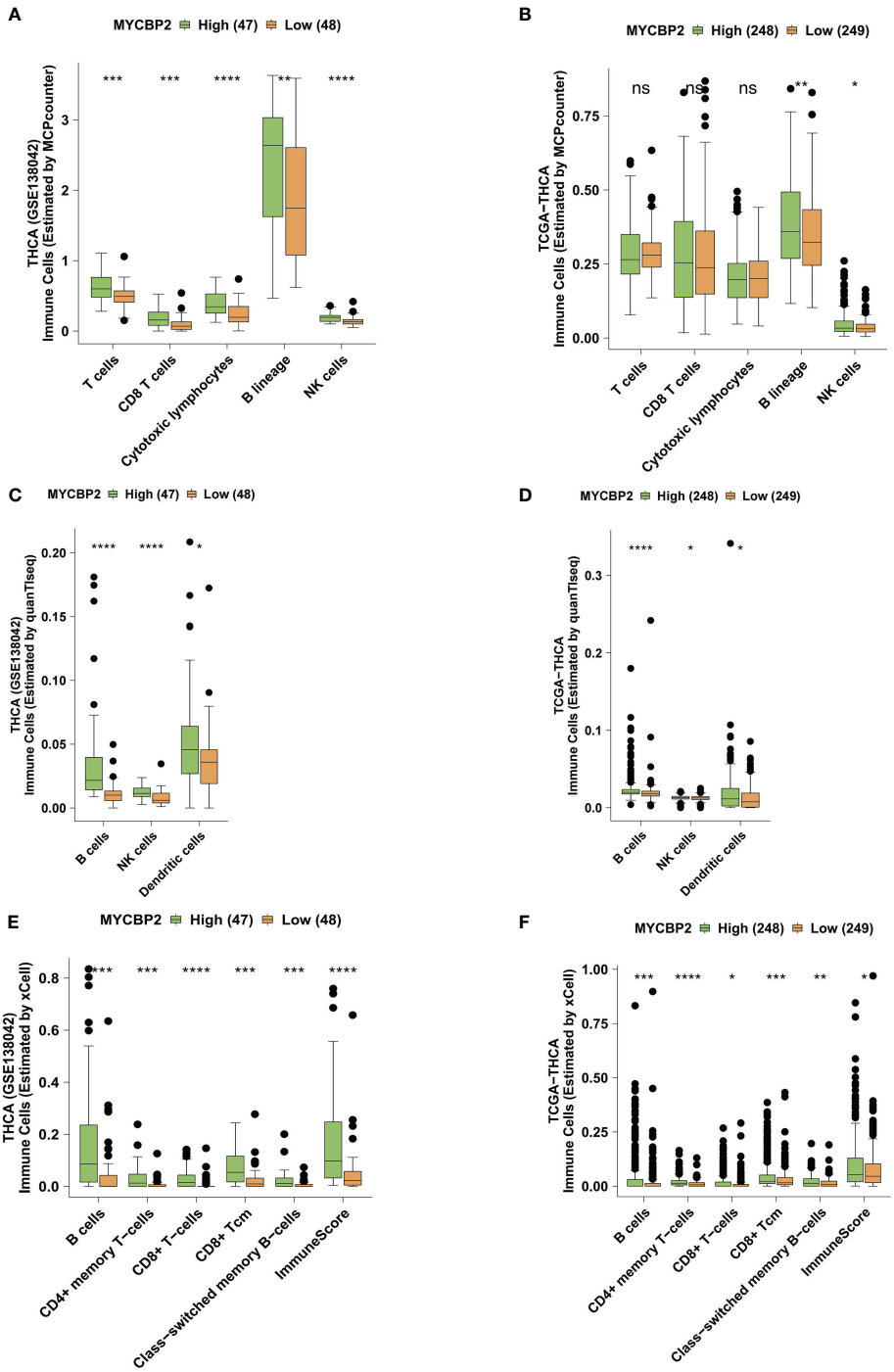

FIGURE 3
The association between the MYCBP2 expression and immune cell infiltration. Differences in tumor infiltrating immune cells estimated by MCPcounter, between the MYCBP2-High and MYCBP2-Low TC patients in the GSE138042-TC **(A)** and TCGA-THCA **(B)** cohorts. Differences in tumor infiltrating immune cells estimated by quanTIseq, between the MYCBP2-High and MYCBP2-Low TC patients in the GSE138042-TC **(C)** and TCGA-THCA **(D)** cohorts. Differences in tumor infiltrating immune cells estimated by xCell, between the MYCBP2-High and MYCBP2-Low TC patients in the GSE138042-TC **(E)** and TCGA-THCA **(F)** cohorts. (ns: not significant; *: $P < 0.05$; **: $P < 0.01$; ***: $P < 0.001$; ****: $P < 0.0001$).

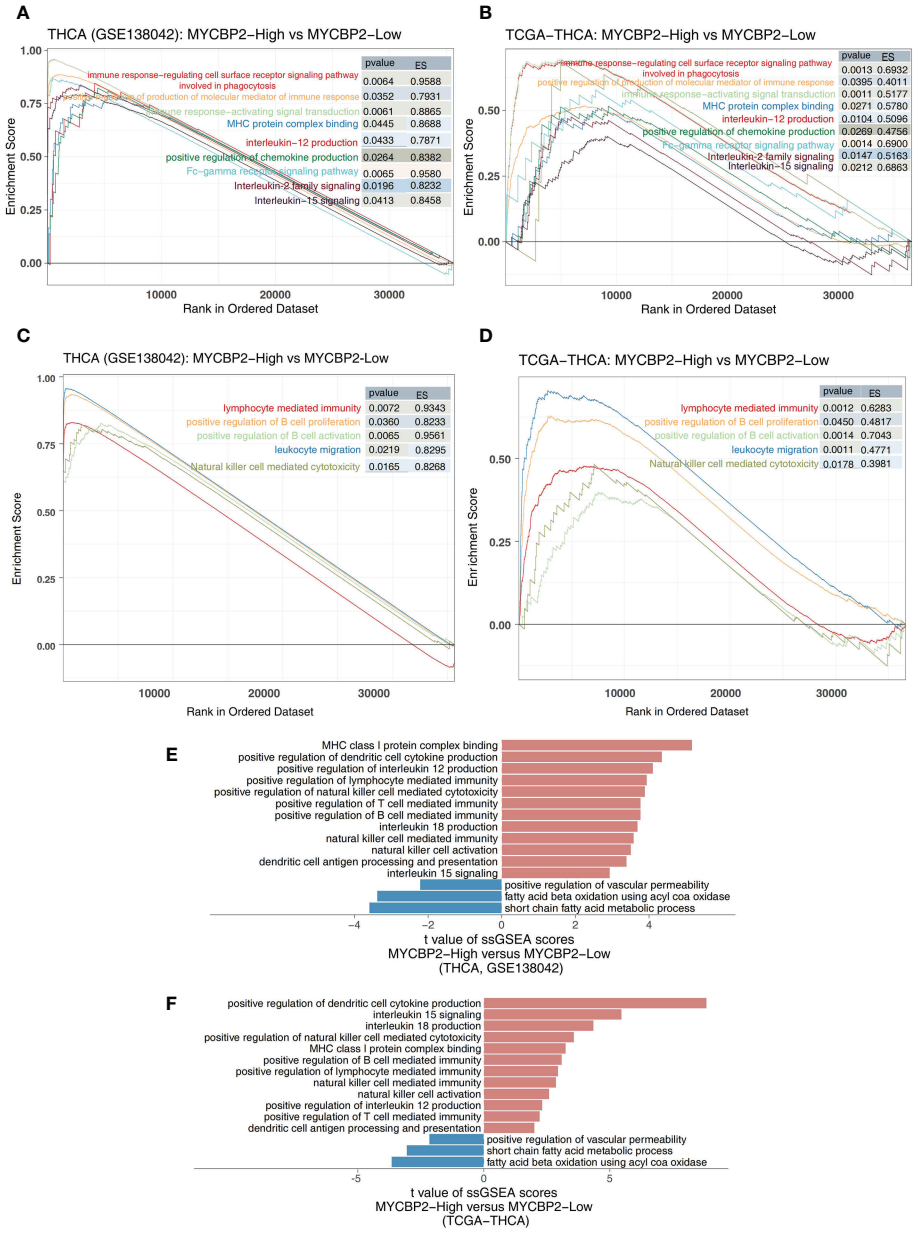

FIGURE 4
The association between the MYCBP2 and immune-related signaling pathways. Differences in inflammatory molecule related signaling pathways between MYCBP2-High and MYCBP2-Low TC patients in the GSE138042-TC **(A)** and TCGA-THCA **(B)** cohorts. Differences in immune response related signaling pathways between the MYCBP2-High and MYCBP2-Low TC patients in the GSE138042-TC **(C)** and TCGA-THCA **(D)** cohorts. Barplot showing the differences in ssGSEA scores between the MYCBP2-High and MYCBP2-Low TC patients in the GSE138042-TC **(E)** and TCGA-THCA **(F)** cohorts.

TIME (58). Recently, a clinical trial showed that IL-15 can increase CD8+ T cell and NK cell numbers up to 5.8 and 38 times that of the control group, respectively, and 17 of the 27 patients treated with IL-15 showed no tumor progression (59). Several other studies have attempted to activate NK cells for immunotherapy using cytokines. For example, IL-21 has been shown to improve the exhaustion status of the NK cells (60), and the combination of IL-12, IL-15, and IL-18 can increase memory NK cells and stimulate IFN-γ secretion (61, 62). In our study, we found that MYCBP2-high patients had significantly upregulated IL-12 production, IL-15 signaling, IL-2 family signaling, and IL-18 signaling compared to MYCBP2-low patients.

The pattern of fatty acid metabolism in TME is also crucial in the immunomodulatory function of tumor tissues and

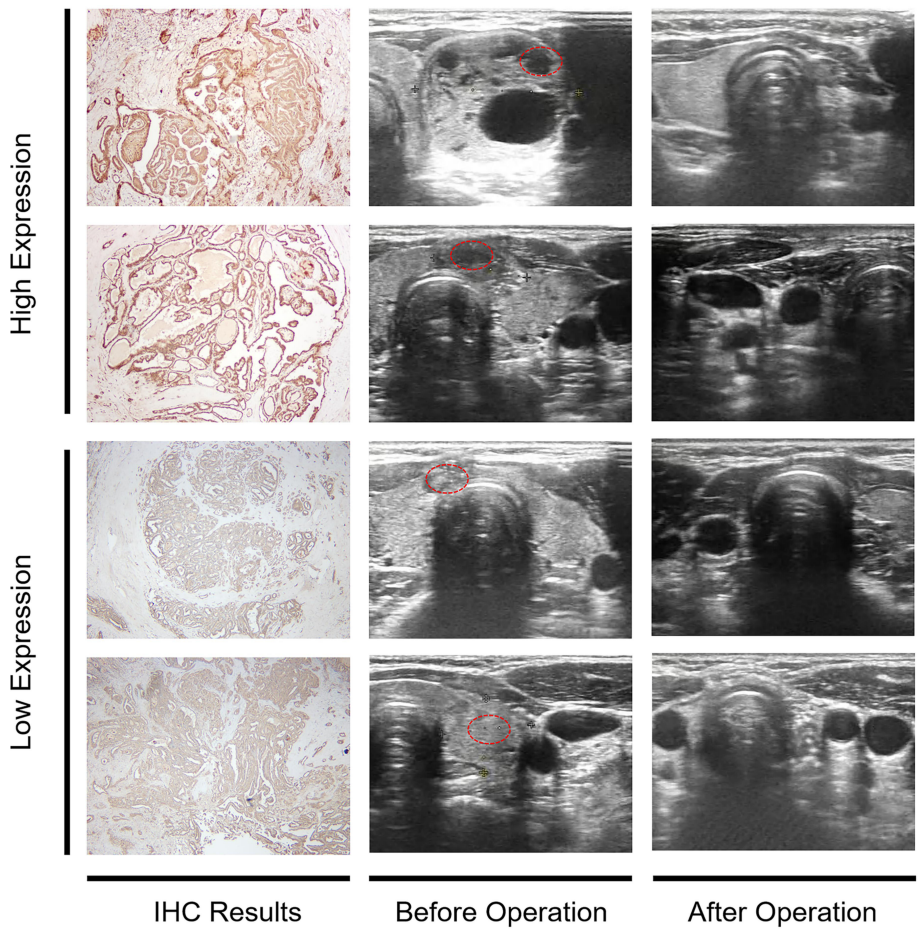

FIGURE 5
IHC analysis of MYCBP2 expression and clinical follow up of TC patients based on their MYCBP2 expression status.Here, we show four representive IHC results of patients and corresponding ultrasound follow-up image.

immunotherapy tolerance. It has been shown that the expression of genes for fatty acid oxidation is upregulated in Treg and that the level of fatty acid oxidation is increased, thus promoting Treg production (63). The rate of *de novo* synthesis of the fatty acid in tumor cells is usually increased, thus shifting energy production to anabolic pathways for the production of plasma membrane phospholipids and signaling molecules (64). Lipid accumulation in tumor-infiltrating myeloid cells has been shown to predispose these immune cells to an immunosuppressive and anti-inflammatory phenotype through metabolic reprogramming (65, 66). In our study, we found that lipid metabolism related pathways (such as short chain fatty acid metabolism, fatty acid beta oxidation using acyl COA oxidase, and positive regulation of vascular permeability) were significantly downregulated in MYCBP2-high patients compared to MYCBP2-low patients.

Some limitations are not ignored in our study, first, clinical long-time follow-up was not conducted, and in the future, a more clinical trial should be considered to demonstrate this gene's clinical value, and in addition, Due to experimental constraints, organoid-related experiments have not been considered, which is a regret, and we hope we will complete this procedure in future cooperation with another excellent laboratory.

Conclusions

In summary, we found that MYCBP2-high TC patients had better responses to ICIs than MYCBP2-low patients, with a higher proportion of predicted ICI responders in the MYCBP2-high group. Higher MYCBP2 expression was

associated with significantly enriched inflammatory immune cell infiltration and higher immune response pathway activity.

Data availability statement

The datasets presented in this study can be found in online repositories. The names of the repository/repositories and accession number(s) can be found in the article/Supplementary Material.

Ethics statement

The studies involving human participants were reviewed and approved by The Ethics Committee of Breast Center of The Second Affiliated Hospital of Guilin Medical University. The patients/participants provided their written informed consent to participate in this study.

Author contributions

Conceptualization, RF, WP, WS. Formal analysis, GW, CM, LM, UK. Software, GW, CM, LM, UK. Supervision, GW, CM, LM. Resources, GW, CM, LM, UK. Visualization, GW, CM, LM, UK. Writing–original draft, JW, MO, RH. Writing–review & editing, GW, CM, LM, JW, MO, RH, RF, WP, WS. All authors contributed to the article and approved the submitted version.

Funding

This study was supported by Guangxi Medical and Health Key Cultivation Discipline Construction Project.

Conflict of interest

The authors declare that the research was conducted in the absence of any commercial or financial relationships that could be construed as a potential conflict of interest.

Publisher's note

All claims expressed in this article are solely those of the authors and do not necessarily represent those of their affiliated organizations, or those of the publisher, the editors and the reviewers. Any product that may be evaluated in this article, or claim that may be made by its manufacturer, is not guaranteed or endorsed by the publisher.

Supplementary material

The Supplementary Material for this article can be found online at: https://www.frontiersin.org/articles/10.3389/fimmu.2022.1048503/full#supplementary-material

SUPPLEMENTARY FIGURE 1
The differences of the expression of the Mycbp2 between the ICIs-responders and ICIs-non-responders in the GSE146027 **(A)** and GSE151829 **(B)**.

SUPPLEMENTARY FIGURE 2
The Kaplan-Meier curves depicting differences in the prognoses of cancer patients between the MYCBP2-High and MYCBP2-Low groups (GSE26304, GSE1456, GSE5327, GSE30929, GSE26939, GSE30219, GSE41271, GSE30219, GSE37745, GSE50081, GSE62452, and GSE16560).

SUPPLEMENTARY FIGURE 3
Heatmap depicting differences in the expression of immune-related genes (antigen presentation, B cells, CD8+ T cells, macrophages, NK cells, pDCs, stimulation, and IFN responses) between MYCBP2-High and MYCBP2-Low patients in TCGA-THCA.

SUPPLEMENTARY TABLE 1
The Kaplan-Meier result of the relationship between the expression of MYCBP2 and survival times of the different cancer patients (GSE26304, GSE1456, GSE5327, GSE30929, GSE26939, GSE30219, GSE41271, GSE30219, GSE37745, GSE50081, GSE62452, and GSE16560).

References

1. Lim H, Devesa SS, Sosa JA, Check D, Kitahara CM. Trends in thyroid cancer incidence and mortality in the united states, 1974-2013. *JAMA* (2017) 317:1338–48. doi: 10.1001/jama.2017.2719

2. Sung H, Ferlay J, Siegel RL, Laversanne M, Soerjomataram I, Jemal A, et al. Global cancer statistics 2020: GLOBOCAN estimates of incidence and mortality worldwide for 36 cancers in 185 countries. *CA Cancer J Clin* (2021) 71:209–49. doi: 10.3322/caac.21660

3. Berdelou A, Lamartina L, Klain M, Leboulleux S, Schlumberger M. Treatment of refractory thyroid cancer. *Endocr Relat Cancer* (2018) 25:R209–23. doi: 10.1530/ERC-17-0542

4. Brose MS, Nutting CM, Jarzab B, Elisei R, Siena S, Bastholt L, et al. Sorafenib in radioactive iodine-refractory, locally advanced or metastatic differentiated thyroid cancer: A randomised, double-blind, phase 3 trial. *Lancet (London England)* (2014) 384:319–28. doi: 10.1016/S0140-6736(14)60421-9

5. Elisei R, Schlumberger MJ, Müller SP, Schöffski P, Brose MS, Shah MH, et al. Cabozantinib in progressive medullary thyroid cancer. *J Clin Oncol Off J Am Soc Clin Oncol* (2013) 31:3639–46. doi: 10.1200/JCO.2012.48.4659

6. Schlumberger M, Tahara M, Wirth LJ, Robinson B, Brose MS, Elisei R, et al. Lenvatinib versus placebo in radioiodine-refractory thyroid cancer. *N Engl J Med* (2015) 372:621–30. doi: 10.1056/NEJMoa1406470

7. Wells SAJ, Robinson BG, Gagel RF, Dralle H, Fagin JA, Santoro M, et al. Vandetanib in patients with locally advanced or metastatic medullary thyroid cancer: A randomized, double-blind phase III trial. *J Clin Oncol Off J Am Soc Clin Oncol* (2012) 30:134–41. doi: 10.1200/JCO.2011.35.5040

8. Subbiah V, Kreitman RJ, Wainberg ZA, Cho JY, Schellens JHM, Soria JC, et al. Dabrafenib and trametinib treatment in patients with locally advanced or metastatic BRAF V600-mutant anaplastic thyroid cancer. *J Clin Oncol Off J Am Soc Clin Oncol* (2018) 36:7–13. doi: 10.1200/JCO.2017.73.6785

9. Chan TA, Yarchoan M, Jaffee E, Swanton C, Quezada SA, Stenzinger A, et al. Development of tumor mutation burden as an immunotherapy biomarker: Utility for the oncology clinic. *Ann Oncol Off J Eur Soc Med Oncol* (2019) 30:44–56. doi: 10.1093/annonc/mdy495

10. Reck M, Rodríguez-Abreu D, Robinson AG, Hui R, Csőszi T, Fülöp A, et al. Pembrolizumab versus chemotherapy for PD-L1-Positive non-Small-Cell lung cancer. *N Engl J Med* (2016) 375:1823–33. doi: 10.1056/NEJMoa1606774

11. Zhong X, Zhang H, Zhu Y, Liang Y, Yuan Z, Li J, et al. Circulating tumor cells in cancer patients: Developments and clinical applications for immunotherapy. *Mol Cancer* (2020) 19:15. doi: 10.1186/s12943-020-1141-9

12. Maibach F, Sadozai H, Seyed Jafari SM, Hunger RE, Schenk M. Tumor-infiltrating lymphocytes and their prognostic value in cutaneous melanoma. *Front Immunol* (2020) 11:2105. doi: 10.3389/fimmu.2020.02105

13. Rittmeyer A, Barlesi F, Waterkamp D, Park K, Ciardiello F, von Pawel J, et al. Atezolizumab versus docetaxel in patients with previously treated non-small-cell lung cancer (OAK): A phase 3, open-label, multicentre randomised controlled trial. *Lancet (London England)* (2017) 389:255–65. doi: 10.1016/S0140-6736(16)32517-X

14. Brahmer J, Reckamp KL, Baas P, Crinò L, Eberhardt WEE, Poddubskaya E, et al. Nivolumab versus docetaxel in advanced squamous-cell non-Small-Cell lung cancer. *N Engl J Med* (2015) 373:123–35. doi: 10.1056/NEJMoa1504627

15. Lin A, Qiu Z, Zhang J, Luo P. Effect of NCOR1 mutations on immune microenvironment and efficacy of immune checkpoint inhibitors in patient with bladder cancer. *Front Immunol* (2021) 12:630773. doi: 10.3389/fimmu.2021.630773

16. Lyu Q, Lin A, Cao M, Xu A, Luo P, Zhang J. Alterations in TP53 are a potential biomarker of bladder cancer patients who benefit from immune checkpoint inhibition. *Cancer Control* (2020) 27:1073274820976665. doi: 10.1177/1073274820976665

17. Ge Z, Guo X, Li J, Hartman M, Kawasawa YI, Dovat S, et al. Clinical significance of high c-MYC and low MYCBP2 expression and their association with ikaros dysfunction in adult acute lymphoblastic leukemia. *Oncotarget* (2015) 6:42300–11. doi: 10.18632/oncotarget.5982

18. Gong L, Xia Y, Qian Z, Shi J, Luo J, Song G, et al. Overexpression of MYC binding protein promotes invasion and migration in gastric cancer. *Oncol Lett* (2018) 15:5243–9. doi: 10.3892/ol.2018.7944

19. Lehrer S, Rheinstein PH, Rosenzweig KE. Loss of MycBP may be associated with the improved survival in 1P co-deletion of lower grade glioma patients. *Clin Neurol Neurosurg* (2018) 172:112–5. doi: 10.1016/j.clineuro.2018.07.003

20. Li M, Li A, Zhou S, Lv H, Yang W. SPAG5 upregulation contributes to enhanced c-MYC transcriptional activity *via* interaction with c-MYC binding protein in triple-negative breast cancer. *J Hematol Oncol* (2019) 12:14. doi: 10.1186/s13045-019-0700-2

21. Pierre S, Zhang DD, Suo J, Kern K, Tarighi N, Scholich K. Myc binding protein 2 suppresses M2-like phenotypes in macrophages during zymosan-induced inflammation in mice. *Eur J Immunol* (2018) 48:239–49. doi: 10.1002/eji.201747129

22. Schaid DJ, McDonnell SK, FitzGerald LM, DeRycke L, Fogarty Z, Giles GG, et al. Two-stage study of familial prostate cancer by whole-exome sequencing and custom capture identifies 10 novel genes associated with the risk of prostate cancer. *Eur Urol* (2021) 79:353–61. doi: 10.1016/j.eururo.2020.07.038

23. Nan B-Y, Xiong G-F, Zhao Z-R, Gu X, Huang X-S. Comprehensive identification of potential crucial genes and miRNA-mRNA regulatory networks in papillary thyroid cancer. *BioMed Res Int* (2021) 2021:6752141. doi: 10.1155/2021/6752141

24. Tomczak K, Czerwińska P, Wiznerowicz M. The cancer genome atlas (TCGA): An immeasurable source of knowledge. *Contemp Oncol (Poznan Poland)* (2015) 19:A68–77. doi: 10.5114/wo.2014.47136

25. Jiang P, Gu S, Pan D, Fu J, Sahu A, Hu X, et al. Signatures of T cell dysfunction and exclusion predict cancer immunotherapy response. *Nat Med* (2018) 24:1550–8. doi: 10.1038/s41591-018-0136-1

26. Auslander N, Zhang G, Lee JS, Frederick DT, Miao B, Moll T, et al. Robust prediction of response to immune checkpoint blockade therapy in metastatic melanoma. *Nat Med* (2018) 24:1545–9. doi: 10.1038/s41591-018-0157-9

27. Rose TL, Weir WH, Mayhew GM, Shibata Y, Eulitt P, Uronis JM, et al. Fibroblast growth factor receptor 3 alterations and response to immune checkpoint inhibition in metastatic urothelial cancer: A real world experience. *Br J Cancer* (2021) 125:1251–60. doi: 10.1038/s41416-021-01488-6

28. Gao J, Aksoy BA, Dogrusoz U, Dresdner G, Gross B, Sumer SO, et al. Integrative analysis of complex cancer genomics and clinical profiles using the cBioPortal. *Sci Signal* (2013) 6:pl1. doi: 10.1126/scisignal.2004088

29. Nagaoka K, Shirai M, Taniguchi K, Hosoi A, Sun C, Kobayashi Y, et al. Deep immunophenotyping at the single-cell level identifies a combination of anti-IL-17 and checkpoint blockade as an effective treatment in a preclinical model of dataguided personalized immunotherapy. *J Immunother Cancer* (2020) 8:e001358. doi: 10.1136/jitc-2020-001358

30. Benitez AA, Khalil-Agüero S, Nandakumar A, Gupta NT, Zhang W, Atwal GS, et al. Absence of central tolerance in aire-deficient mice synergizes with immune-checkpoint inhibition to enhance antitumor responses. *Commun Biol* (2020) 3:355. doi: 10.1038/s42003-020-1083-1

31. Muggerud AA, Hallett M, Johnsen H, Kleivi K, Zhou W, Tahmasebpoor S, et al. Molecular diversity in ductal carcinoma *in situ* (DCIS) and early invasive breast cancer. *Mol Oncol* (2010) 4:357–68. doi: 10.1016/j.molonc.2010.06.007

32. Hall P, Ploner A, Bjöhle J, Huang F, Lin C-Y, Liu ET, et al. Hormone-replacement therapy influences gene expression profiles and is associated with breast-cancer prognosis: a cohort study. *BMC Med* (2006) 4:16. doi: 10.1186/1741-7015-4-16

33. Minn AJ, Gupta GP, Padua D, Bos P, Nguyen DX, Nuyten D, et al. Lung metastasis genes couple breast tumor size and metastatic spread. *Proc Natl Acad Sci U.S.A.* (2007) 104:6740–5. doi: 10.1073/pnas.0701138104

34. Gobble RM, Qin L-X, Brill ER, Angeles CV, Ugras S, O'Connor RB, et al. Expression profiling of liposarcoma yields a multigene predictor of patient outcome and identifies genes that contribute to liposarcomagenesis. *Cancer Res* (2011) 71:2697–705. doi: 10.1158/0008-5472.CAN-10-3588

35. Wilkerson MD, Yin X, Walter V, Zhao N, Cabanski CR, Hayward MC, et al. Differential pathogenesis of lung adenocarcinoma subtypes involving sequence mutations, copy number, chromosomal instability, and methylation. *PloS One* (2012) 7:e36530. doi: 10.1371/journal.pone.0036530

36. Rousseaux S, Debernardi A, Jacquiau B, Vitte A-L, Vesin A, Nagy-Mignotte H, et al. Ectopic activation of germline and placental genes identifies aggressive metastasis-prone lung cancers. *Sci Transl Med* (2013) 5:186ra66. doi: 10.1126/scitranslmed.3005723

37. Parra ER, Behrens C, Rodriguez-Canales J, Lin H, Mino B, Blando J, et al. Image analysis-based assessment of PD-L1 and tumor-associated immune cells density supports distinct intratumoral microenvironment groups in non-small cell lung carcinoma patients. *Clin Cancer Res an Off J Am Assoc Cancer Res* (2016) 22:6278–89. doi: 10.1158/1078-0432.CCR-15-2443

38. Goldmann T, Marwitz S, Nitschkowski D, Krupar R, Backman M, Elfving H, et al. PD-L1 amplification is associated with an immune cell rich phenotype in squamous cell cancer of the lung. *Cancer Immunol Immunother* (2021) 70:2577–87. doi: 10.1007/s00262-020-02825-z

39. Der SD, Sykes J, Pintilie M, Zhu C-Q, Strumpf D, Liu N, et al. Validation of a histology-independent prognostic gene signature for early-stage, non-small-cell lung cancer including stage IA patients. *J Thorac Oncol Off Publ Int Assoc Study Lung Cancer* (2014) 9:59–64. doi: 10.1097/JTO.0000000000000042

40. Yang S, He P, Wang J, Schetter A, Tang W, Funamizu N, et al. A novel MIF signaling pathway drives the malignant character of pancreatic cancer by targeting NR3C2. *Cancer Res* (2016) 76:3838–50. doi: 10.1158/0008-5472.CAN-15-2841

41. Sboner A, Demichelis F, Calza S, Pawitan Y, Setlur SR, Hoshida Y, et al. Molecular sampling of prostate cancer: A dilemma for predicting disease progression. *BMC Med Genomics* (2010) 3:8. doi: 10.1186/1755-8794-3-8

42. Lin A, Qi C, Wei T, Li M, Cheng Q, Liu Z, et al. CAMOIP: A web server for comprehensive analysis on multi-omics of immunotherapy in pan-cancer. *Brief Bioinform* (2022) 23:bbac129. doi: 10.1093/bib/bbac129

43. Becht E, Giraldo NA, Lacroix L, Buttard B, Elarouci N, Petitprez F, et al. Estimating the population abundance of tissue-infiltrating immune and stromal cell populations using gene expression. *Genome Biol* (2016) 17:218. doi: 10.1186/s13059-016-1070-5

44. Aran D, Hu Z, Butte AJ. xCell: Digitally portraying the tissue cellular heterogeneity landscape. *Genome Biol* (2017) 18:220. doi: 10.1186/s13059-017-1349-1

45. Plattner C, Finotello F, Rieder D. Deconvoluting tumor-infiltrating immune cells from RNA-seq data using quanTIseq. *Methods Enzymol* (2020) 636:261–85. doi: 10.1016/bs.mie.2019.05.056

46. Subramanian A, Kuehn H, Gould J, Tamayo P, Mesirov JP. GSEA-p: A desktop application for gene set enrichment analysis. *Bioinformatics* (2007) 23:3251–3. doi: 10.1093/bioinformatics/btm369

47. Hänzelmann S, Castelo R, Guinney J. GSVA: Gene set variation analysis for microarray and RNA-seq data. *BMC Bioinf* (2013) 14:7. doi: 10.1186/1471-2105-14-7

48. Lin A, Zhang H, Hu X, Chen X, Wu G, Luo P, et al. Age, sex, and specific gene mutations affect the effects of immune checkpoint inhibitors in colorectal cancer. *Pharmacol Res* (2020) 159:105028. doi: 10.1016/j.phrs.2020.105028

49. Kollipara R, Schneider B, Radovich M, Babu S, Kiel PJ. Exceptional response with immunotherapy in a patient with anaplastic thyroid cancer. *Oncologist* (2017) 22:1149–51. doi: 10.1634/theoncologist.2017-0096

50. Spalart V, Legius B, Segers K, Coolen J, Maes B, Decoster L. Dramatic response to first line single agent pembrolizumab in anaplastic thyroid carcinoma. *Case Rep Endocrinol* (2019) 2019:9095753. doi: 10.1155/2019/9095753

51. Peng Q, Qiu X, Zhang Z, Zhang S, Zhang Y, Liang Y, et al. PD-L1 on dendritic cells attenuates T cell activation and regulates response to immune checkpoint blockade. *Nat Commun* (2020) 11:4835. doi: 10.1038/s41467-020-18570-x

52. Bastman JJ, Serracino HS, Zhu Y, Koenig MR, Mateescu V, Sams SB, et al. Tumor-infiltrating T cells and the PD-1 checkpoint pathway in advanced differentiated and anaplastic thyroid cancer. *J Clin Endocrinol Metab* (2016) 101:2863–73. doi: 10.1210/jc.2015-4227

53. Cunha LL, Morari EC, Guihen ACT, Razolli D, Gerhard R, Nonogaki S, et al. Infiltration of a mixture of immune cells may be related to good prognosis in patients with differentiated thyroid carcinoma. *Clin Endocrinol (Oxf)* (2012) 77:918–25. doi: 10.1111/j.1365-2265.2012.04482.x

54. Sivori S, Pende D, Quatrini L, Pietra G, Della Chiesa M, Vacca P, et al. NK cells and ILCs in tumor immunotherapy. *Mol Aspects Med* (2021) 80:100870. doi: 10.1016/j.mam.2020.100870

55. Colonna M. Innate lymphoid cells: Diversity, plasticity, and unique functions in immunity. *Immunity* (2018) 48:1104–17. doi: 10.1016/j.immuni.2018.05.013

56. Nouri-Shirazi M, Banchereau J, Bell D, Burkeholder S, Kraus ET, Davoust J, et al. Dendritic cells capture killed tumor cells and present their antigens to elicit tumor-specific immune responses. *J Immunol* (2000) 165:3797–803. doi: 10.4049/jimmunol.165.7.3797

57. de Mingo Pulido Á, Gardner A, Hiebler S, Soliman H, Rugo HS, Krummel MF, et al. TIM-3 regulates CD103(+) dendritic cell function and response to chemotherapy in breast cancer. *Cancer Cell* (2018) 33:60–74.e6. doi: 10.1016/j.ccell.2017.11.019

58. Ali AK, Nandagopal N, Lee S-H. IL-15-PI3K-AKT-mTOR: A critical pathway in the life journey of natural killer cells. *Front Immunol* (2015) 6:355. doi: 10.3389/fimmu.2015.00355

59. Conlon KC, Potter EL, Pittaluga S, Lee C-CR, Miljkovic MD, Fleisher TA, et al. IL15 by continuous intravenous infusion to adult patients with solid tumors in a phase I trial induced dramatic NK-cell subset expansion. *Clin Cancer Res an Off J Am Assoc Cancer Res* (2019) 25:4945–54. doi: 10.1158/1078-0432.CCR-18-3468

60. Seo H, Jeon I, Kim B-S, Park M, Bae E-A, Song B, et al. IL-21-mediated reversal of NK cell exhaustion facilitates anti-tumour immunity in MHC class I-deficient tumours. *Nat Commun* (2017) 8:15776. doi: 10.1038/ncomms15776

61. Lusty E, Poznanski SM, Kwofie K, Mandur TS, Lee DA, Richards CD, et al. IL-18/IL-15/IL-12 synergy induces elevated and prolonged IFN-γ production by ex vivo expanded NK cells which is not due to enhanced STAT4 activation. *Mol Immunol* (2017) 88:138–47. doi: 10.1016/j.molimm.2017.06.025

62. Romee R, Schneider SE, Leong JW, Chase JM, Keppel CR, Sullivan RP, et al. Cytokine activation induces human memory-like NK cells. *Blood* (2012) 120:4751–60. doi: 10.1182/blood-2012-04-419283

63. Zhang C, Yue C, Herrmann A, Song J, Egelston C, Wang T, et al. STAT3 activation-induced fatty acid oxidation in CD8(+) T effector cells is critical for obesity-promoted breast tumor growth. *Cell Metab* (2020) 31:148–161.e5. doi: 10.1016/j.cmet.2019.10.013

64. Currie E, Schulze A, Zechner R, Walther TC, Farese RVJ. Cellular fatty acid metabolism and cancer. *Cell Metab* (2013) 18:153–61. doi: 10.1016/j.cmet.2013.05.017

65. Cubillos-Ruiz JR, Silberman PC, Rutkowski MR, Chopra S, Perales-Puchalt A, Song M, et al. ER stress sensor XBP1 controls anti-tumor immunity by disrupting dendritic cell homeostasis. *Cell* (2015) 161:1527–38. doi: 10.1016/j.cell.2015.05.025

66. Herber DL, Cao W, Nefedova Y, Novitskiy SV, Nagaraj S, Tyurin VA, et al. Lipid accumulation and dendritic cell dysfunction in cancer. *Nat Med* (2010) 16:880–6. doi: 10.1038/nm.2172

frontiers | Frontiers in Immunology

TYPE Original Research
PUBLISHED 09 January 2023
DOI 10.3389/fimmu.2022.1085491

Check for updates

OPEN ACCESS

EDITED BY
Linlang Guo,
Zhujiang Hospital, China

REVIEWED BY
Hao Zhang,
Chongqing Medical University, China
Yingkun Xu,
Chongqing Medical University, China
Kai Zhang,
Zhengzhou University, China

*CORRESPONDENCE
Hongjun Li
lihongjun@pumch.cn

†These authors have contributed equally to this work

SPECIALTY SECTION
This article was submitted to Cancer Immunity and Immunotherapy, a section of the journal Frontiers in Immunology

RECEIVED 31 October 2022
ACCEPTED 13 December 2022
PUBLISHED 09 January 2023

CITATION
Wang Y, Yan K, Guo Y, Lu Y, Su H and Li H (2023) IP-score correlated to endogenous tumour antigen peptide processing: A candidate clinical response score algorithm of immune checkpoint inhibitors therapy in multiple cohorts.
Front. Immunol. 13:1085491.
doi: 10.3389/fimmu.2022.1085491

COPYRIGHT
© 2023 Wang, Yan, Guo, Lu, Su and Li. This is an open-access article distributed under the terms of the Creative Commons Attribution License (CC BY). The use, distribution or reproduction in other forums is permitted, provided the original author(s) and the copyright owner(s) are credited and that the original publication in this journal is cited, in accordance with accepted academic practice. No use, distribution or reproduction is permitted which does not comply with these terms.

IP-score correlated to endogenous tumour antigen peptide processing: A candidate clinical response score algorithm of immune checkpoint inhibitors therapy in multiple cohorts

Yutao Wang[1†], Kexin Yan[2†], Ye Guo[3†], Yi Lu[1], Hao Su[1] and Hongjun Li[1*]

[1]Department of Urology, Chinese Academy of Medical Sciences, Peking Union Medical College, Peking Union Medical College Hospital, Beijing, China, [2]Institute of Dermatology, Chinese Academy of Medical Sciences and Peking Union Medical College, Nanjing, China, [3]Department of Clinical Laboratory, Peking Union Medical College Hospital, Chinese Academy of Medical Science and Peking Union Medical College, Beijing, China

The processing of endogenous tumour antigen peptides was essential for anti-tumour immunity in the tumour microenvironment. A high degree of Endogenous tumour antigen peptide processing has been demonstrated to improve the prognosis of carcinoma patients. However, there is insufficient evidence to prove its effect on the clinical response to immune checkpoint inhibitor therapy. To undertake a more in-depth analysis of the effects of the aforementioned genes on immunotherapy, we constructed a gene set evaluation score system relevant to tumour endogenous antigen peptide therapy using the GSVA approach. This rating mechanism is known as IP score (IPs). Immediately afterwards, we used the TCGA pan-cancer cohorts to conduct a comprehensive analysis of 6 genes in the IPs, and the analysis results showed that these six genes were related to the proportion of $CD8^+$ T lymphocytes in a variety of solid tumours. As a prognostic protective factor for solid tumours, patients had better prognosis outcomes in the group with high expression levels of the above genes. We analysed the differential expression of six genes between immune checkpoint inhibitor treatment response and disease progression groups using several treatment cohorts. The results revealed that after treatment with PD-1 or CTLA4 inhibitors, the expression levels of the above six genes were comparatively high in the effective group, but the expression of the signature genes was dramatically downregulated in the ICI-insensitive groups. This indicates that the 6 genes are related to the clinical response to ICI treatment. Finally, we used the GSVA method to evaluate the above signatures, and the results showed that PDCD1, CTAL4, CD274 and LAG3 were significantly higher expressed in the IPs high-expression group; therefore, based on the processing of endogenous antigenic peptides in

tumours, a predictive score of clinical response to immune checkpoint inhibitor therapy composed of 6 genes(PSMB8/PSMB9/PSMB10/PSME1/PSME2/IRF1) was constructed, and the role of each independent variable in the signature in the solid tumour microenvironment and the impact on ICI treatment were comprehensively analysed. This study provides a candidate evaluation score for predicting clinical response to immune checkpoint inhibitor therapy.

KEYWORDS

IP score, ICI therapy clinical response, gene signature, single-cell analysis, endogenous tumour antigen peptide processing

Introduction

Malignant tumours claim the lives of millions of people every year, and cancer has come to symbolise a danger to people's lives and health. The incidence of cancer and mortality will continue to rise significantly in the future due to population growth and increased awareness of life and health among people (1). Malignant tumours have a substantial impact on the safety of public life around the globe, and it has been estimated that by 2060, cancer may become the leading cause of death; thus, it is important to understand the mechanism of tumour genesis and coping measures (2).

Surgical treatment, adjuvant cytotoxic chemotherapy, radiotherapy, oncogene-targeted therapy, immunotherapy, and other methods are primarily used to treat tumours. Although these methods have proven successful for patients with advanced tumours, the techniques mentioned above and strategies cannot achieve satisfactory efficacy. Immunotherapy is employed primarily in patients with enormous tumour burdens and advanced malignancies. Immunotherapy is a significant invention that offers hope to cancer patients and has produced promising outcomes in a range of cancers (3, 4).

Allison and Honjo have contributed to the pathways of cytotoxic T lymphocyte-associated protein 4 and programmed death 1 (PD-1) (5). PD-1 and CTAL4 have become the novel immune checkpoint inhibitor approaches (6). Today, chimeric antigen T cells, adoptive cell therapy, and oncolytic viruses are revolutionising cancer treatment (7, 8). Despite the exciting efficacy of immune checkpoint inhibitor therapy, it still faces low clinical response rates and large side effects (9–11). The lack of T cells, various mechanisms preventing T cell migration and invasion, low tumour mutation burden, low PD-1/PDL1 expression, hyper angiogenesis, and high expression of vascular endothelial growth factor (VEGF) are some of the main factors of clinical treatment's poor effectiveness (12–15). According to a study, the modulation of local chemokines or suppression of VEGF expression boosted T cell migration and infiltration in malignancies (16). Tumour cell antigen peptides are phagocytosed and integrated into human leukocyte antigen (HLA) class I molecules, processed by proteasomes (17). APCs ingest tumour antigens and migrate to lymphatic organs to elicit a subsequent immune response (18, 19). Subsequently, studies have shown a significant positive correlation between PSMB8 and $CD8^+$ T lymphocytes (20, 21).

Our previous research examined the co-expression network linked with $CD8^+$ T cells in urothelial cancer. The results revealed co-expressed genes included PSMB8, PSMB9, PSMB10, PSME1, PSME2, IRF1, TAP1, etc. The majority of these genes are concentrated in the presentation and processing of endogenous tumour antigen peptides (22), PSMB8, PSMB9, and PSMB10 are the core subunits of the immune proteasome, and PSME1 and PSME2 are the regulatory subunits. Since the level of T-lymphocyte infiltration is closely related to the clinical response to immune checkpoint inhibitor therapy, we hypothesise that the level of the above genes may affect the outcome of the clinical response to ICI therapy.

In this study, we first demonstrated the relationship among PSMB8, PSMB9, PSMB10, PSME1, PSME2, and IRF1 in the immune micro-environment and immune score through TCGA whole cancer cohorts, and further, we proved the correlation between PSMB8, PSMB9, PSMB10, PSME1, PSME2, IRF1, and immune cells. The mechanism of these genes and its impact on clinical characteristics in several immune checkpoint inhibitor cohorts were further analysed. Finally, we enriched the aforementioned gene sets using the GSVA scoring method and generated a new scoring method, the IP-score, that can predict the outcome of ICI treatment.

Material and methodology

Data collection

The Cancer Genome Atlas (TCGA) database yielded 33 different cancer database categories. The clinical data was also downloaded, including age, gender, and survival event.

Meanwhile, the dataset for single-cell RNA sequencing (scRNA-seq) was downloaded from the Gene Expression Omnibus (GEO) database (https://www.ncbi.nlm.nih.gov/geo/). The bladder cancer (BLCA) scRNA-seq datasets were downloaded from BLCA-GSE145137 and PRAD-GSE137829. The GSE145140 (23) data set contained three samples: the single-cell RNA sequencing of chemotherapy-resistant muscle-invasive urothelial bladder cancer. GSE137829 (24) is the prostate single single-cell research which report luminal-neuroendocrine transdifferentiation prostate cancer samples.

Immune therapy cohorts

Immunotherapy cohorts were acquired from the Immune Checkpoint Blockade Therapy Atlas (ICBatlas) (25). ICBatlas is a database that provides complete expression resources and functional analyses for ICB therapy patients. It also analyses the expression between the ICB groups of Response and Non-Response (R versus NR) and the Pre-treatment and On-treatment groups (Pre vs On). It is the first database of ICB treatment expression resources, and we intend to provide useful information and hints for ICB therapy-related clinical research.

ICBatlas encompasses 1515 samples dealt with by using PD-1/PD-L1, CTLA-4 inhibitors (1388 RNA-seq samples and 127 RNA-microarray samples) throughout 9 exclusive most cancers consisting of pores and skin cutaneous melanoma (SKCM), renal carcinoma (RCC), urothelial most cancers (UC), hepatocellular carcinoma (HCC), non-small lung most cancers (NSCLC), gastric most cancers (GC), head and neck squamous carcinoma (HNSCC), malignant pleural mesothelioma (MPM), and glioblastoma (GBM) from 25 datasets. The detailed cohort information was uploaded in Supplementary Table 1. Genomic, transcriptomic, and matched scientific statistics from sufferers with metastatic urothelial cancers dealt with an anti-PD-L1 agent (atezolizumab) are reachable beneath the Creative Commons three license and can be downloaded from http://research-pub.gene.com/IMvigor210CoreBiologies.

The GSE78220 immunotherapy cohort was acquired from the GEO website (26). The annotation platform was GPL11154. The cohort consists of 28 patients with melanoma. Complete response, partial response, stable disease, and progressing disease were immunotherapy responses.

Immune micro-environment database

Using various techniques, we investigated the impact of PSMB8, PSMB9, PSMB10, PSME1, and PSME2 on immune cells and immunological microenvironments in distinct solid tumours. There is a multitude of available databases for evaluating TCGA tumours. TIMER is a valuable tool for the systematic examination of immune infiltrates in the majority of cancer types. This webserver model affords immune infiltrates' abundances estimated through more than one immune deconvolution method and permits customers to generate top-notch figures dynamically to discover tumour immunological, medical and genomic points comprehensively. EPIC (27) is a tool to estimate the proportions of different cell types from bulk gene expression data. CIBERSORTx (28) is an analytical device from the Alizadeh Lab and Newman Lab to impute gene expression profiles and supply an estimation of the abundances of member telephone kinds in a combined phone population, the use of gene expression data.

GSVA analysis

Gene set enrichment analysis (GSEA) is a computational method to determine the significance and consistency differences between two biological states of a predefined data set (29). The IP-score was conducted by GSVA analysis, the geneset contained PSMB8, PSMB9, PSMB10, PSME1, PSME2 and IRF1.

Single cell sequencing analysis

The Anchors function of the "Seurat" R package was utilised to integrate BLCA-GSE145137 and PRAD-GSE137829. The scRNA-seq analysis was performed as part of the study (30). After scaling the data, PCA analysis was employed to decrease the dimension and then used the UMAP feature for the visualisation. The R package "InferCNV" (31) and "CopyKAT" (32) were applied for the identification of malignant cells. And the annotation of stromal cells and immune cells was based on the specific markers. The Dimplot, FeaturePlot, and VlnPlot were used to visualise the expression of PSMB8 further.

TMB analysis

Tumour RNAseq data (level3) and corresponding clinical information were obtained from the Cancer Genome Atlas (TCGA) dataset (https://portal.gdc.com). Spearman's correlation analysis describes the correlation between quantitative variables without normal distribution. And the genes with significant mutation differences in the high and low IP groups were calculated. A P-value of less than 0.05 was considered statistically significant.

Prognostic analysis

To analyse the association between genes and overall survival in cancer patients, a Kaplan - Meier analysis was

conducted to determine the overall survival (OS) of TCGA cohort patients. We aimed to demonstrate that these genes, as predictive protective genes, had an impact on overall survival.

Results

Flow chat

Based on previous research, we discovered the $CD8^+$ T lymphocyte-related co-expression network, in which PSMB8, PSMB9, PSMB10, PSME1 and other genes are primarily enriched in the functional subunits of immunoproteasome; therefore, we first presented the core subunits and regulatory subunits of immunoproteasome in Part 1 as well as images of the immunoproteasome-related mechanism in our previous article. In Part 2, we demonstrate the connection between PSMB8 and immune cells and the immunological microenvironment in additional solid tumours. In Part 3, we demonstrate that PSMB8 and IP-score can be utilised as biomarkers for ICI therapy and examine the relationship between IPS and immune checkpoint inhibitor medication (Figure 1).

PSMB8 up-regulation correlates with immune response

The infiltration of immune cells into the tumour microenvironment has been shown to have a significant effect on the progression of cancer, but there is currently no effect of the genes mentioned above on the tumour microenvironment, so we carried out a thorough analysis of PSMB8 using the TCGA database. In our investigation, PSMB8 demonstrated a close association among different immune cells, including B cells and T cells, in KIRP, LGG, and LIHC (Supplementary Figure 1A).

LGG, TGCT, and THCA were the pan-cancer cohorts whose PSMB8 expression was most strongly correlated with the stromal score, and BLCA, BRCA, and CESC were the top three tumours whose PSMB8 expression was most strongly associated with the immune score. BLCA, BRCA, and LGG were the top three correlations between PSMB8 and ESTIMATE scores (Supplementary Figure 1B).

In addition, we mapped the connection between immune cell concentration and PSMB8 in TCGA other using the EPIC algorithm. The results demonstrate that PSMB8 was favourably and strongly linked with T cells and macrophages in various malignancies (Supplementary Figure 1C).

The influence of the PSMB8 with immune checkpoint genes

Recent studies have found that immune checkpoint expression levels can be used as effective immunotherapy response biomarkers. Therefore, we summarised 47 immune checkpoint-related genes, and we discovered that PSMB8 is associated with immune checkpoints in a variety of solid tumours (33). We found that PSMB8 is related to immune checkpoints in a variety of solid tumours (Supplementary Figure 1D). In contrast, there was no significant relationship between PSMB8 and immune checkpoint in Lymphoid Neoplasm Large B-cell carcinoma. Similar results of PSMB9 and PSMB10 were uploaded as Supplementary Figure 2 and Supplementary Figure 3.

PSMB8 correlation with immune phenotype and clinical phenotype

Using the CIBERSORT method, we further evaluated the correlation between various T cell subtypes and PSMB8, and the results revealed a significant positive correlation between PSMB8 expression levels and $CD8^+$ T cells in BRCA, CESC, UCEC, COAD, HNSC, KIRC, KIRP, LGG, LUAD, LUSC, OSCC, and THCA tumours (Figure 2). Moreover, The expression level of PSMB8 in KIRP, LIHC, LUAD, LUSC, OV, SKCM, SARC, PAAD, and PCPG tumours has significant positive correlation with macrophages (Supplementary Figure 4). Meanwhile, the overall survival of patients with the PSMB8 low expression group was worse in multiple cancers, including BLCA, BRCA, MESO, OV, READ, SKCM, STAD, THCA, and UCEC. These results suggest that PSMB8 may increase the anti-tumour response and further improve the prognosis of cancer patients (Figure 3).

PSMB8 and T cell correlation based on single cell analysis

We have analysed the distribution of PSMB8 and immune cells using two single-cell sequencing cohorts, BLCA - GSE145137 and PRAD - GSE137829. PSMB8 was shown to be substantially expressed on T cells in different malignancies. We determined the expression level and immune infiltration involvement of PSMB8 in BLCA and PRAD using scRNA-seq. In each tumour sample, distinct clusters of immune cell types were marked by immune cell-specific molecular markers. We discovered a significant association between T cells and PSMB8 (Figure 4).

The PSMB8 acts as a biomarker for immune checkpoint therapy

Immunotherapy has been successful, although most people are not immunosensitive. In the tumour microenvironment, these insensitive patients had decreased levels of PD-1 expression and

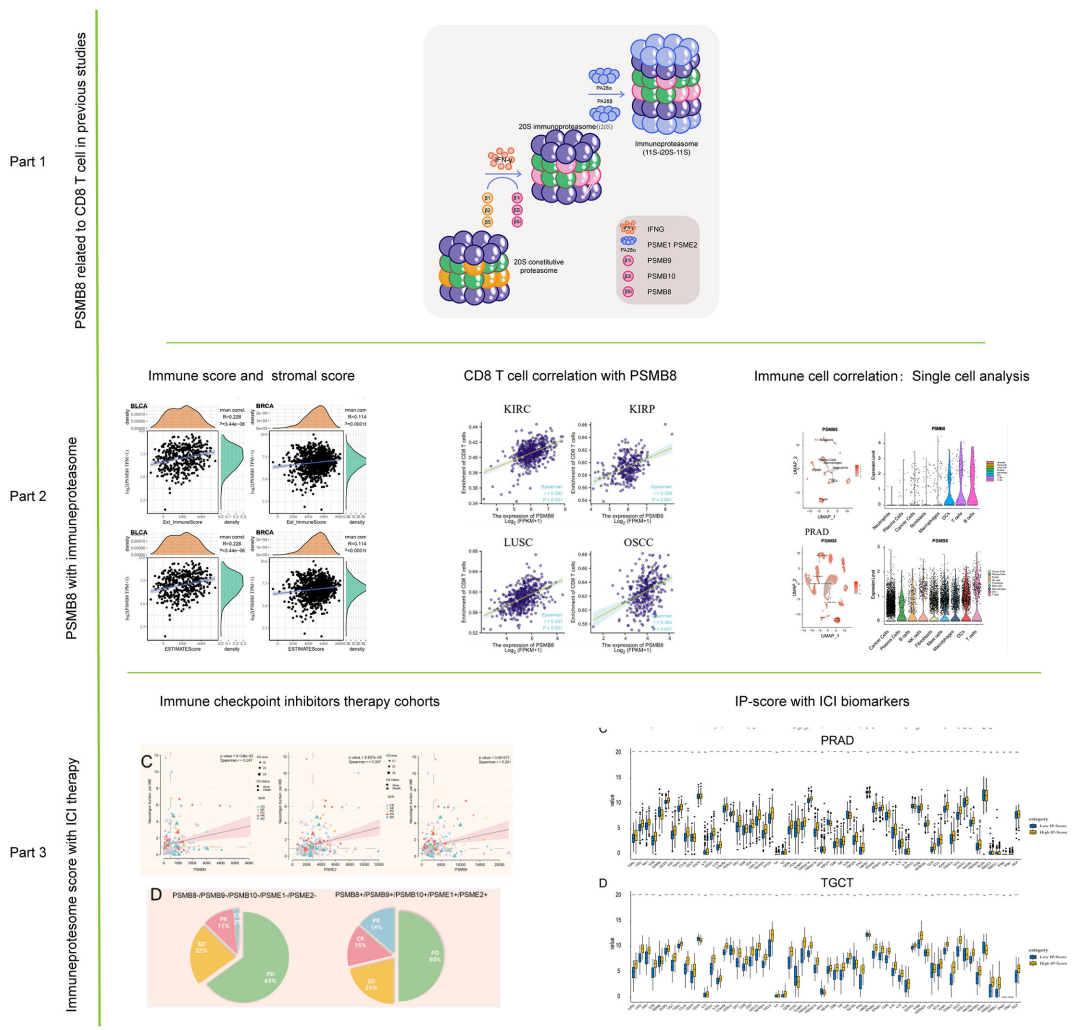

FIGURE 1
Flow chart of this study. The role of PSMB8 in cancer was obtained from previous studies. The correlation analysis of PSMB8 as an important gene of immune proteasome was studied by immune infiltration study and single cell analysis. Finally, the role of PSMB8 score in immunotherapy was studied.

cytotoxic T cells. We believe that the PSMB8 concentration influences the $CD8^+$ T lymphocyte concentration in the microenvironment. This effect may mitigate the immune checkpoint treatment's insensitivity induced by the low cytotoxic T cell concentration. The immunotherapy cohort from IMvigor210 CoreBiologies was utilised. The cohort included 348 immune checkpoint treatment participants. The rates of disease progression in patients with high expression levels of the core subunits after using immune checkpoint inhibitors were lower than the patients with low expression levels. The PD-1 expression scores of tumour cells and immune cells in patients with high expression levels of PSMB8, PSMB9, and PSMB10 were greater than low expression samples (Figure 5A). Based on the greatest sensitivity and specificity of PSMB10, PSMB9, PSMB8, PSME1, PSME2, and IRF1, we then separated samples into two groups. We discovered that the overall survival rates of patients with low PSMB8 and IRF1 expression were higher. Other factors' results were not statistically significant, although their trends were comparable to those of prognosis protective factors (Figure 5B). Figure 5C illustrates the connection between PSMB8 subunits and tumour mutation burden over a spectrum of immunotherapy response phases. Patients with complete responses had a greater positive connection between PSMB8 and tumour mutation burden. In conclusion, we discovered that PSMB8 improves outcomes and boosts immunotherapy's complete response. For $PSMB8^+/PSMB9^+/PSMB10^+/PSME1^+/PSME2^+$ (these genes are

10.3389/fimmu.2022.1085491

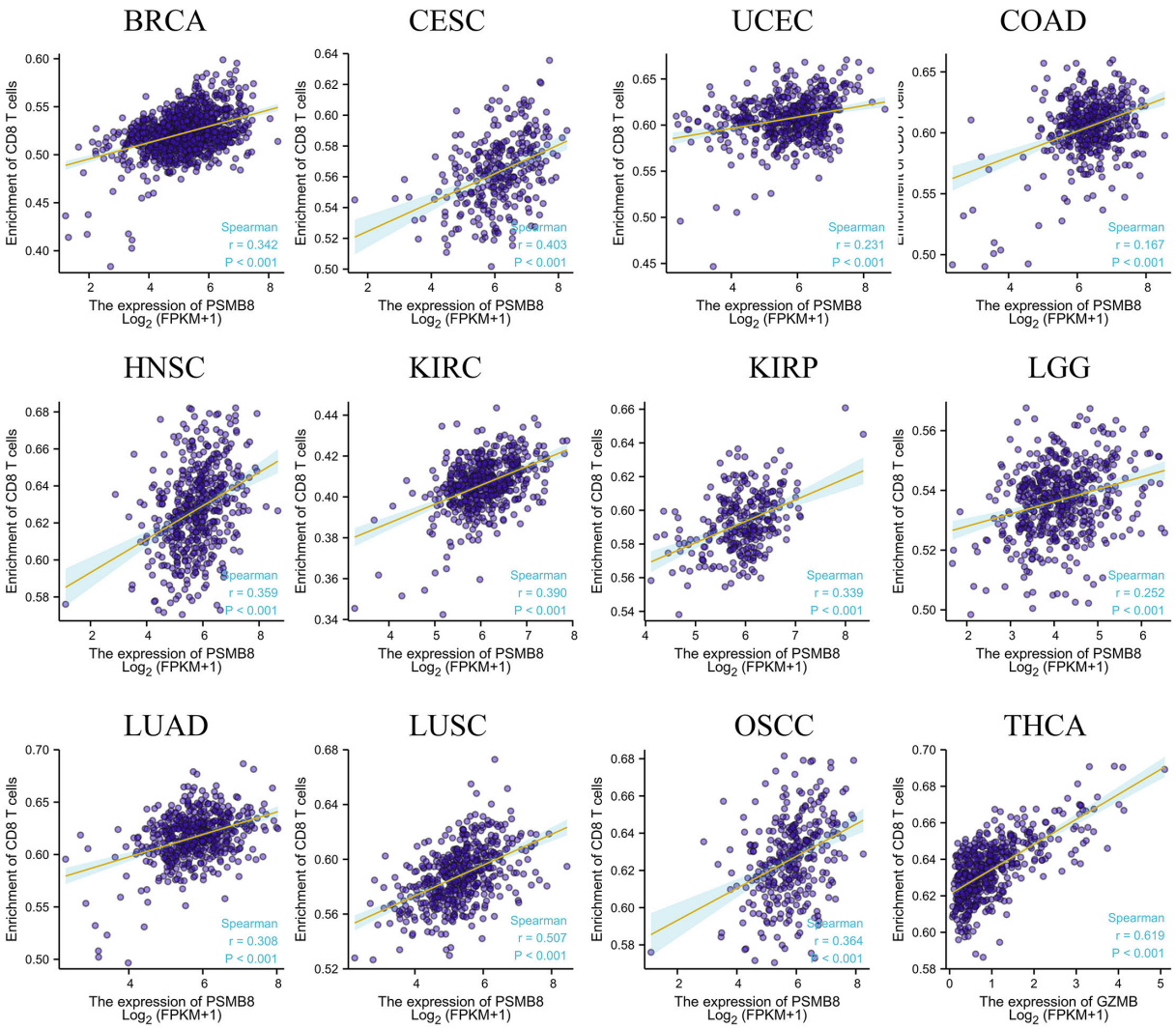

FIGURE 2
Correlation between PSMB8 expression and CD8$^+$T cells in different cancers.

highly expressed) samples, the complete response rate of immune checkpoint treatment was 15%, and the partial response rate was 14%. For PSMB8-/PSMB9-/PSMB10-/PSME1-/PSME2- (these genes are lowly expressed) samples, the complete response rate of checkpoint treatment was 2%, and the partial response rate was 11% (Figure 5D). When the PD-1 expression level was used as the criterion for the efficacy of immunotherapy, 13% of patients in the PD-1 overexpression group had a complete response, and 12% had a partial response. In the PD-1 low-expression group, 4% of patients had a complete response, and 17% had a partial response. Using the tumour mutation burden level as the criterion for the efficacy of immunotherapy, 14% of patients had a complete response, and 15% had a partial response in the mutation burden overexpression group. In the mutation load low-expression group, 3% of patients had a complete response, and 10% had a partial response (Figure 5E). Finally, univariate Cox regression analysis was performed for all variables in the urothelial epithelial carcinoma immune checkpoint cohort, taking the time corresponding to the complete response as termination time. The same result was found in the GSE78220 melanoma cohort (Figure 6).

IP - score correlation with immune inflammation response

We selected several classic immune - related subgene sets, including major histocompatibility complex class II (MHC-II),

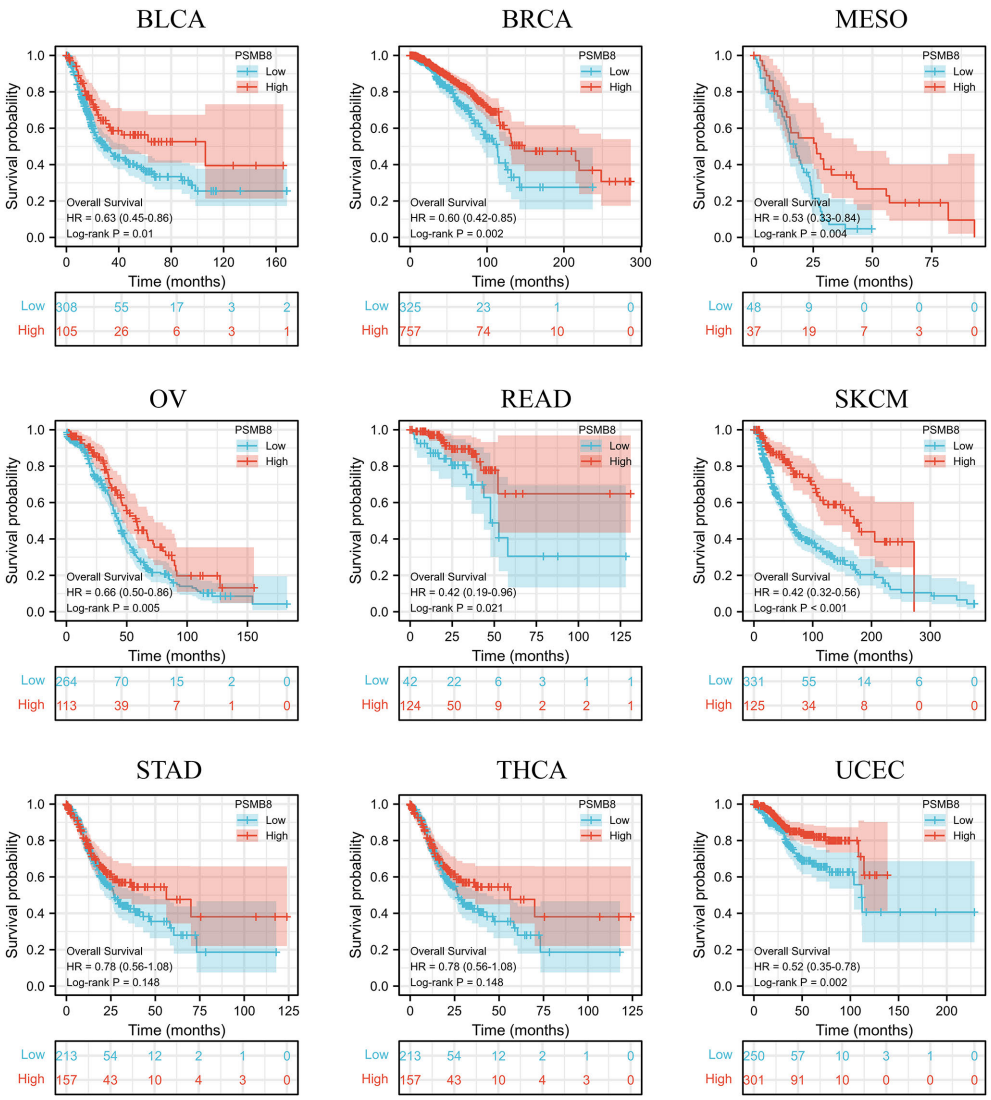

FIGURE 3
In different cancers, survival and prognosis analysis of PSMB8 showed that PSMB8 high expression group had a better prognosis.

lymphocyte-specific kinase (LCK), hematopoietic cell kinase (HCK), immunoglobulin G (IgG), signal transduction and activation transcription 1 (STAT1), co-stimulatory molecules (B7-CD28), interferon and TNF gene sets. We analysed the relationship between IP scores and immune inflammatory responses. We found that as the IP score increased, the igG immunoglobulin secreted by B cells increased, and the expression of biomarkers in macrophages and monocytes/myeloid cells also increased significantly. The content of histocompatibility class II complex, histocompatibility class I complex increased, and the expression level of surface markers of T cells and macrophages also increased significantly in KIRC, BLCA, PRAD and THCA (Figure 7).

IP - score establishment and its role in TMB and immune check point genes

Establishment of IP score and its function in TMB and immune checkpoint genes. We use the immune checkpoint database for PSMB8/PSMB9/PSMB10/PSME1/PSME2/IRF1 in light of the study above. Based on the above research, we use the immune checkpoint database for PSMB8/PSMB9/PSMB10/PSME1/PSME2/IRF1. The role of these genes in the immunotherapy queue was analysed, and the results show that PSMB8/PSMB9/PSMB10/PSME1/PSME2/IRF1 in multiple clinical response immune checkpoint inhibitor treatment group had expressed, in the stable group of disease, the low expression of queue these solid tumours

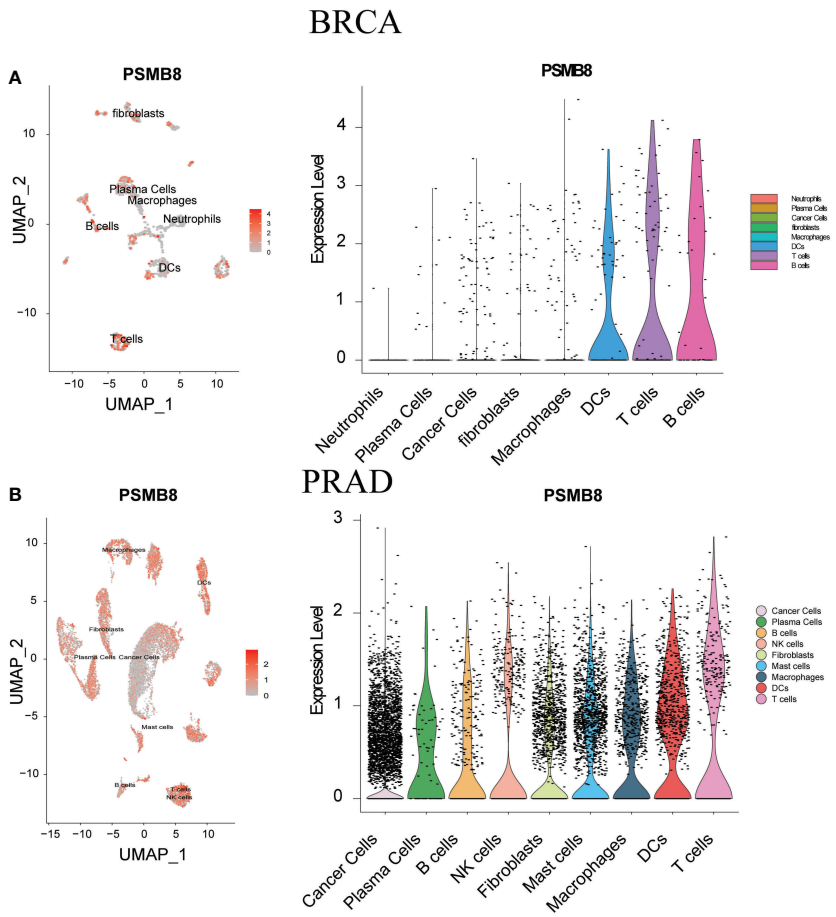

FIGURE 4
ScRNA-seq was used to show tumour cell localisation, cell classification and PSMB8 expression distribution. **(A)** The scRNA-seq results of PSMB8 expression in BLCA. **(B)** The scRNA-seq results of PSMB8 expression in PRAD.

including lung cancer, kidney cancer, bladder cancer, detailed gap analysis statistical data as shown in Tables 1–5. These results suggested that all six genes could be prospective biomarkers for predicting clinical response to ICI therapy. Then, using the GSVA approach, we assigned an IP-score to the gene set comprised of the above six genes. To verify the influence of IP-score on tumour mutation and immune response in greater detail, we initially examined the association between IP-score and mutation in solid urological tumours. The results demonstrated that the mutation frequencies of the PIK3CA, BRCA2, RNF213, and SACS genes in the urothelial cancer cohort were significantly different between low and high IP-score groups (Figure 8A).

In the clear cell renal cell carcinoma cohort, the DST, MED13 and ABCC6 gene mutation frequencies significantly differed among different low and high IP-score groups (Figure 8B). In the prostate cancer cohort, the mutation frequencies of ARID2, CNTN6, CHD1 and other genes were significantly different in different IP-score groups (Figure 8C). In urinary solid tumours, the immune checkpoint genes such as LAG3/CTLA4/PD-1/PD-L1 were over-expressed in the group with high IP-score, while the immune checkpoint genes such as LAG3/CTLA4/PD-1/PD-L1 were low-expressed in the group with low IP-score. This indicates that the IP score is an essential predictor of immune checkpoint inhibitor therapy (Figures 9A–D).

Discussion

Immune checkpoints can regulate the body's immune system, among which stimulatory checkpoint molecules can promote the activation of T cells and activate the body's immune response; As the immune system's natural "brake," inhibitory checkpoint molecules are utilised to restrict the body's immunological response and avoid autoimmunity (34).

To avoid being eliminated by the body's immune system, tumour cells suppress the body's immunological response by producing inhibitory immune checkpoint molecules that interact with T cells (35–37).

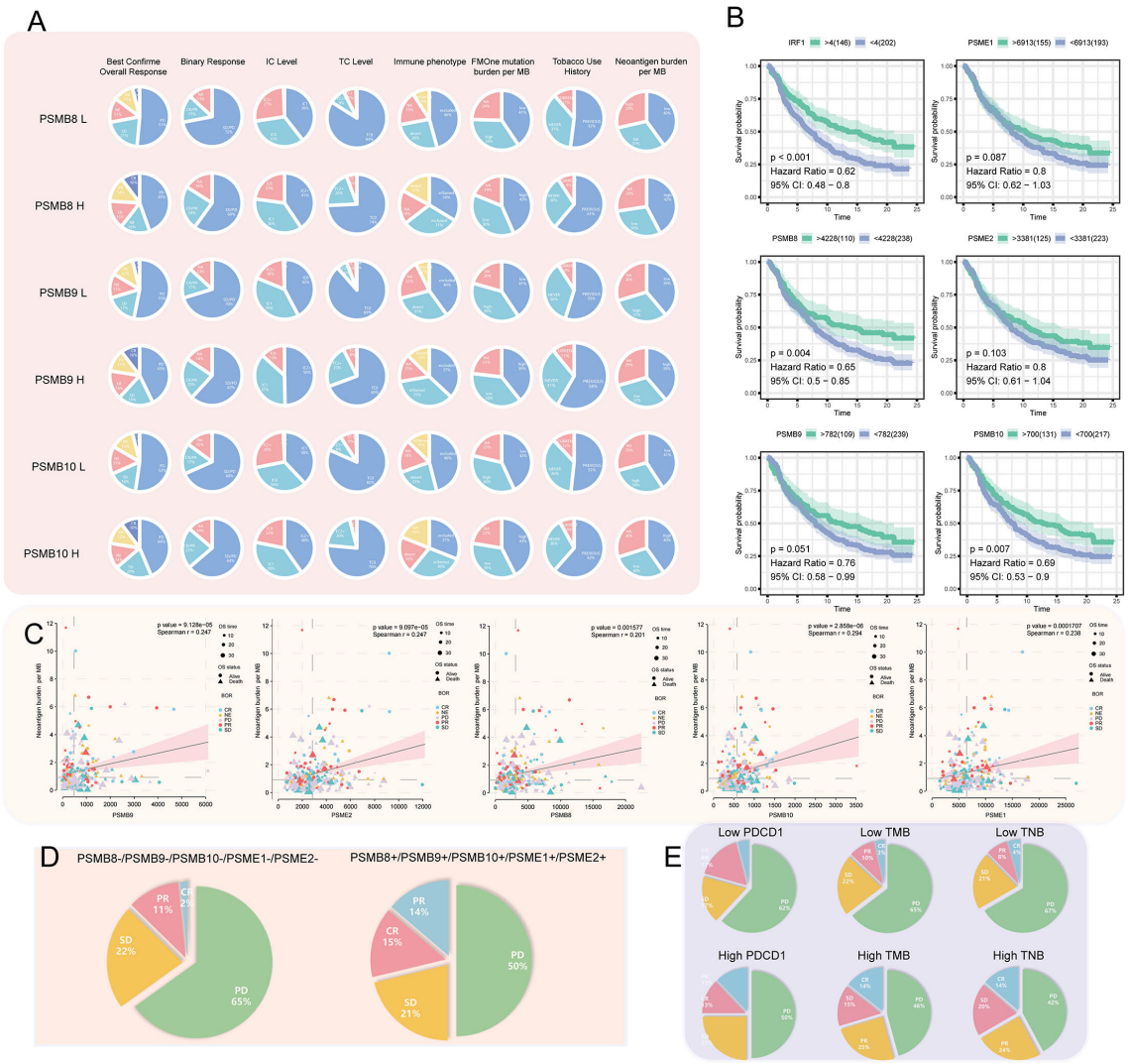

FIGURE 5
(A) Among the high- and low-expression groups of PSMB8, PSMB9, and PSMB10, difference analysis for the proportion of best confirmation of overall response, binary response, IC level, TC level, immune phenotype, FMOne mutation burden per MB, tobacco use history, and neoantigen burden per MB was carried out. In review CR, complete response; PR, partial response; NE, No effect; SD, Stable disease; PD, Progressive disease. **(B)** Survival analysis of IFNG (P < 0.001; HR = 0.62), PSME1 (P = 0.087; HR = 0.8), PSMB8 (P = 0.004; HR = 0.65), PSME2 (P = 0.103; HR = 0.8), PSMB9 (P = 0.051; HR = 0.76), and PSMB10 (P = 0.007; HR = 0.69) that are factors associated PSMB8. **(C)** In factors associated with the PSMB8, the correlation between CR, PR, NE, SD, and PD with neoantigen burden per MB. **(D)** In pan-cancer, the proportion of CR, PR, SD, and PD in the low- and high-expression groups of factors associated with the PSMB8. **(E)** The proportion of CR, PR, SD, and PD in the low- and high-expression groups of PDCD1 and TMB that have been reported as indicators of the efficacy of cancer treatment. Compared with Figure D, factors associated with PSMB8 had the strongest predictive ability.

Consequently, appropriate antibody medicines can be designed for common suppressive immune checkpoints, the body's immune system can be boosted by blocking suppressive immune checkpoints, and the tumour is subsequently eliminated. More than a dozen immunological checkpoints have been identified, with CTLA-4 and PD-1/PDL1 being the most extensively investigated. CTLA-4 is a T cell surface receptor that transmits immunosuppressive signals and functions as an immunosuppressive molecule (34).

Research indicated that CTLA-4 deletion in mice models can result in enormous lymphocyte proliferation, organ damage, and even mouse death. Further research discovered that inhibiting CTLA-4 could significantly suppress tumour growth in tumour model mice (38). Following multiple clinical trials, the FDA authorised ipilimumab, the first antibody medication against the immunological checkpoint CTLA-4, in 2011 (39).

The antibody drug is mainly used for the treatment of melanoma, which can improve the survival of patients for 1~2 year. In addition to

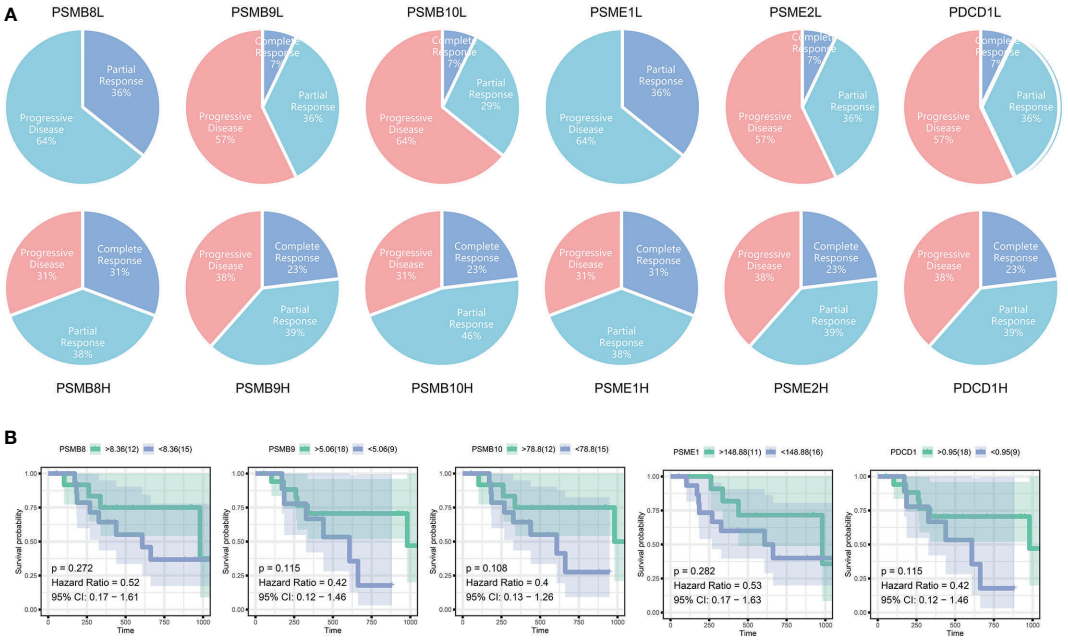

FIGURE 6
(A) The immunotherapy outcomes in GSE78220. **(B)** Survival analysis of different subunit genes of immune proteasome in cutaneous malignant melanoma.

CTLA-4, PD-1 is a prominent immunosuppressive protein on the surface of T cells, and its ligand. PD-L1 is expressed in a variety of tumour cells. P. By binding to PD-1 on the surface of T cells, T cell activation is suppressed, resulting in tumour immune evasion. Inhibitors of PD-1/PD-L1 suppress these immunological checkpoints, increasing T cells' activity and destroying tumour cells. In 2014, the FDA approved the first PD-1 inhibitor, pembrolizumab, for treating melanoma and lung cancer. In 2016, the FDA approved the first PD-L1 inhibitor, atezolizumab, to treat bladder cancer (40, 41).

Immune checkpoint blocking therapy for CTLA4 or PD-1 (PD-L1) has made great breakthroughs in the treatment of different types of tumours. However, only a subset of patients benefit. Therefore, analytical immunotherapy drivers of resistance and finding predictors are critical. The efficacy of immune checkpoint inhibitors is influenced by a variety of factors, including tumour genomics, host genetics, PD-L1 levels, tumour micro-environment and intestinal microbiome, etc (42). In addition, the use of new technology to analyse the heterogeneity of immune cells in the tumour micro-environment has important guiding significance for developing targeted therapies for immune cells and predicting the effect of immune checkpoint blockade therapy. The development of new technologies represented by single-cell sequencing has extensively promoted research in this field. Zhang Zemin's research group (43) of Peking University used Smart sequencing technology (Smart-seq) to map the immune map of T cells at the single-cell level in lung cancer and colon cancer and comprehensively analysed tumour leaching. The subpopulation characteristics, cell heterogeneity, tissue distribution, and T cells' drug target gene expression demonstrated the T cells' dynamic alterations in the tumour microenvironment.

Our previous studies found a co-expression network associated with $CD8^+$ T lymphocyte invasion in urothelial carcinoma, which contains PSMB8, PSMB9, PSMB10, PSME2, IRF1 and other genes. These co-expressed genes are mainly enriched in the processing and presentation of endogenous tumour antigen peptides. Further review of the literature found that these genes are mainly involved in the composition of the core subunits of PSMB8. PSMB8 have been extensively studied in tumours. However, their roles in the solid tumour microenvironment and its relationship to immune checkpoint inhibitor therapy have not been fully studied. Therefore, the TCGA database was initially utilised to investigate the impact of PSMB8 core subunit and regulatory subunit constituent genes on the tumour microenvironment of solid tumours and whether they may be utilised as predictors of clinical survival. Then, using several cohorts receiving PD-1/PDL1 and CTLA-4 treatment, we analysed the variations in the expression levels of the genes mentioned above between the responsive and insensitive groups of drug treatment to identify potential biological biomarkers for ICI treatment. The results demonstrated that PSMB8/PSMB9/PSMB10/PSME1/PSME2 could be a biotarget for clinical response in multiple cohorts receiving PD-1/PDL1 and CTLA-4 therapy, and these cohorts from various centres provide us with an exciting foundation. After that, we calculated the expression levels of PSMB8/PSMB9/PSMB10/PSME1/PSME2/IRF1 as a unified score using the GSVA method. This score was dubbed IP-score, and the

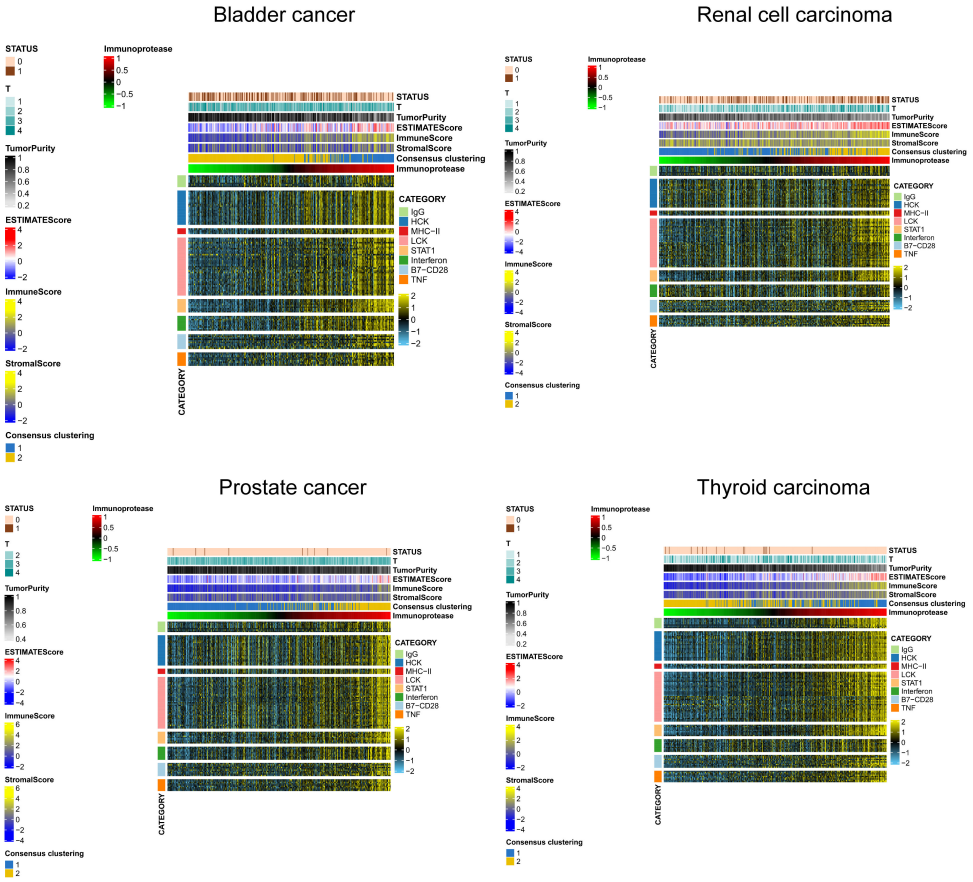

FIGURE 7
IP - Score correlation with immune inflammation response.

TABLE 1 PSMB8 expression distribution for response and non-response based on pre-treatment samples in all datasets.

PSMB8	Study	Cancers	Anti Target	Response Mean	Non-Response Mean	Log2FC	FDR	P Value
1	ERP105482,SRP150548,SRP128156	Melanoma, RCC	anti-PD1 + anti-CTLA4	3,743.00	1,698.00	1.42	0.002	0.001
2	ERP105482	Melanoma	anti-PD1 + anti-CTLA4	4,685.00	1,698.00	1.519	0.003	0.001
3	ERP107734	Gastric Cancer	anti-PD1	6,223.50	3,111.00	0.862	0.01	0.001
4	ERP105482,SRP011540,SRP070710, SRP094781,SRP150548,SRP230414, SRP250849,SRP302761	Melanoma	anti-PD1/anti-CTLA4/anti-PD1 + anti-CTLA4	2,819.00	2,495.00	0.258	0.103	0.016
5	anti-PD1	Melanoma, NSCLC,GBM, RCC,GC	anti-PD1	2,466.50	2,410.00	0.215	0.121	0.024
6	ERP105482	Melanoma	anti-PD1	2,625.00	1,734.50	0.648	0.143	0.009
7	IMvigor210	Urothelial Cancer	anti-PDL1	4,453.91	3,642.02	0.253	0.262	0.089
8	SRP183455,SRP217040	NSCLC	anti-PD1/PDL1	2,434.00	1,652.00	0.577	0.299	0.064

10.3389/fimmu.2022.1085491

TABLE 2 PSMB9 expression distribution for response and non-response based on pre-treatment samples in all datasets.

PSMB9	Study	Cancers	Anti Target	Response Mean	Non-Response Mean	Log2FC	FDR	P Value
1	ERP107734	Gastric Cancer	anti-PD1	5,739.00	1,407.00	1.303	0.002	0.001
2	anti-PD1	Melanoma, NSCLC,GBM, RCC,GC	anti-PD1	895	946	0.416	0.011	0.001
3	ERP105482,SRP150548,SRP128156	Melanoma, RCC	anti-PD1 + anti-CTLA4	1,253.00	305	1.466	0.028	0.001
4	ERP105482	Melanoma	anti-PD1 + anti-CTLA4	1,026.00	305	1.559	0.035	0.001
5	IMvigor210	Urothelial Cancer	anti-PDL1	918.88	674.66	0.418	0.075	0.012
6	SRP183455,SRP217040	NSCLC	anti-PD1/PDL1	1,368.00	711	1.035	0.078	0.006
7	ERP105482,SRP011540,SRP070710, SRP094781,SRP150548,SRP230414, SRP250849,SRP302761	Melanoma	anti-PD1/anti-CTLA4/anti-PD1 + anti-CTLA4	875	859.5	0.347	0.087	0.013
8	ERP105482	Melanoma	anti-PD1	711	262.5	0.865	0.134	0.008
9	GSE136961	Non-small Cell Lung Cancer	anti-PD1	13.1	11.63	1.462	0.169	0.012
10	SRP217040	Non-small Cell Lung Cancer	anti-PDL1	1,982.50	1,099.00	1.106	0.243	0.031

TABLE 3 PSMB10 expression distribution for response and non-response based on pre-treatment samples in all datasets.

PSMB10	Study	Cancers	Anti Target	Response Mean	Non-Response Mean	Log2FC	FDR	P Value
1	anti-PD1	Melanoma, NSCLC,GBM, RCC,GC	anti-PD1	384.5	379.5	0.486	0	0.001
2	ERP105482,SRP011540,SRP070710, SRP094781,SRP150548,SRP230414, SRP250849,SRP302761	Melanoma	anti-PD1/anti-CTLA4/anti-PD1 + anti-CTLA4	315.5	334.5	0.438	0.003	0.001
3	ERP107734	Gastric Cancer	anti-PD1	1,588.00	780	0.976	0.02	0.001
4	IMvigor210	Urothelial Cancer	anti-PDL1	807.81	639.4	0.281	0.031	0.003
5	ERP105482	Melanoma	anti-PD1	236	131	0.748	0.04	0.001
6	ERP105482,SRP150548,SRP128156	Melanoma, RCC	anti-PD1 + anti-CTLA4	374	178	0.964	0.073	0.001
7	ERP105482	Melanoma	anti-PD1 + anti-CTLA4	342	178	1.037	0.093	0.002
8	SRP183455,SRP217040	NSCLC	anti-PD1/PDL1	463	223	0.783	0.123	0.013
9	SRP011540	Melanoma	anti-PD1	268	267	0.411	0.211	0.033
10	SRP183455	Non-small Cell Lung Cancer	anti-PD1	198	142.5	0.767	0.235	0.029

10.3389/fimmu.2022.1085491

TABLE 4 PSME1 expression distribution for response and non-response based on pre-treatment samples in all datasets.

PSME1	Study	Cancers	Anti Target	Response Mean	Non-Response Mean	Log2FC	FDR	P Value
1	ERP105482,SRP011540,SRP070710, SRP094781,SRP150548,SRP230414, SRP250849,SRP302761	Melanoma	anti-PD1/anti-CTLA4/anti-PD1 + anti-CTLA4	5,179.00	4,281.50	0.31	0.004	0.001
2	anti-PD1	Melanoma, NSCLC,GBM, RCC,GC	anti-PD1	4,481.50	4,047.00	0.25	0.008	0.001
3	ERP105482,SRP150548,SRP128156	Melanoma, RCC	anti-PD1 + anti-CTLA4	6,757.00	3,799.00	0.99	0.033	0.001
4	ERP105482	Melanoma	anti-PD1 + anti-CTLA4	6,825.00	3,799.00	1.105	0.04	0.001
5	ERP107734	Gastric Cancer	anti-PD1	6,480.50	4,259.00	0.437	0.115	0.013
6	ERP105482	Melanoma	anti-PD1	5,751.00	3,690.00	0.495	0.222	0.021
7	IMvigor210	Urothelial Cancer	anti-PDL1	7,837.81	7,005.39	0.12	0.228	0.071
8	SRP183455,SRP217040	NSCLC	anti-PD1/PDL1	4,281.50	3,004.00	0.472	0.352	0.09

expression levels of immune checkpoints in different IP-score groups in urinary solid tumours were analysed. It was discovered that IP-score was closely associated with PDCD1, CD274, CTLA-4, and LAG3 expression levels in urinary solid tumours, indicating that IP-score was closely associated with tumour escape and immune depletion.

Using high-throughput sequencing technology and computational biological research, this paper creates biomarkers and scoring methodologies related to the clinical response to ICI treatment based on current public sequencing datasets. In this work, sequencing technology was employed to examine and analyse vast amounts of data, and the biological targets of clinical immunotherapy response were enhanced. To locate relevant antigens, enhance the reference database, and validate the conclusions of this work in animal models and clinical follow-ups, however, we will need to continue to innovate sequencing technology in the future.

TABLE 5 PSME2 expression distribution for response and non-response based on pre-treatment samples in all datasets.

PSME2	Study	Cancers	Anti Target	Response Mean	Non-Response Mean	Log2FC	FDR	P Value
1	ERP107734	Gastric Cancer	anti-PD1	7,174.50	3,535.00	0.773	0.015	0.001
2	anti-PD1	Melanoma, NSCLC,GBM, RCC,GC	anti-PD1	3,336.50	3,237.50	0.246	0.016	0.001
3	ERP105482,SRP011540,SRP070710, SRP094781,SRP150548,SRP230414, SRP250849,SRP302761	Melanoma	anti-PD1/anti-CTLA4/anti-PD1 + anti-CTLA4	3,918.00	3,710.00	0.244	0.033	0.003
4	ERP105482,SRP150548,SRP128156	Melanoma, RCC	anti-PD1 + anti-CTLA4	5,418.00	3,897.00	0.962	0.038	0.001
5	ERP105482	Melanoma	anti-PD1 + anti-CTLA4	5,905.00	4,668.00	0.937	0.108	0.002
6	IMvigor210	Urothelial Cancer	anti-PDL1	3,586.49	3,105.91	0.169	0.143	0.034
7	ERP105482	Melanoma	anti-PD1	4,174.00	2,862.00	0.546	0.156	0.011
8	SRP183455,SRP217040	NSCLC	anti-PD1/PDL1	3,612.50	1,957.00	0.477	0.325	0.075

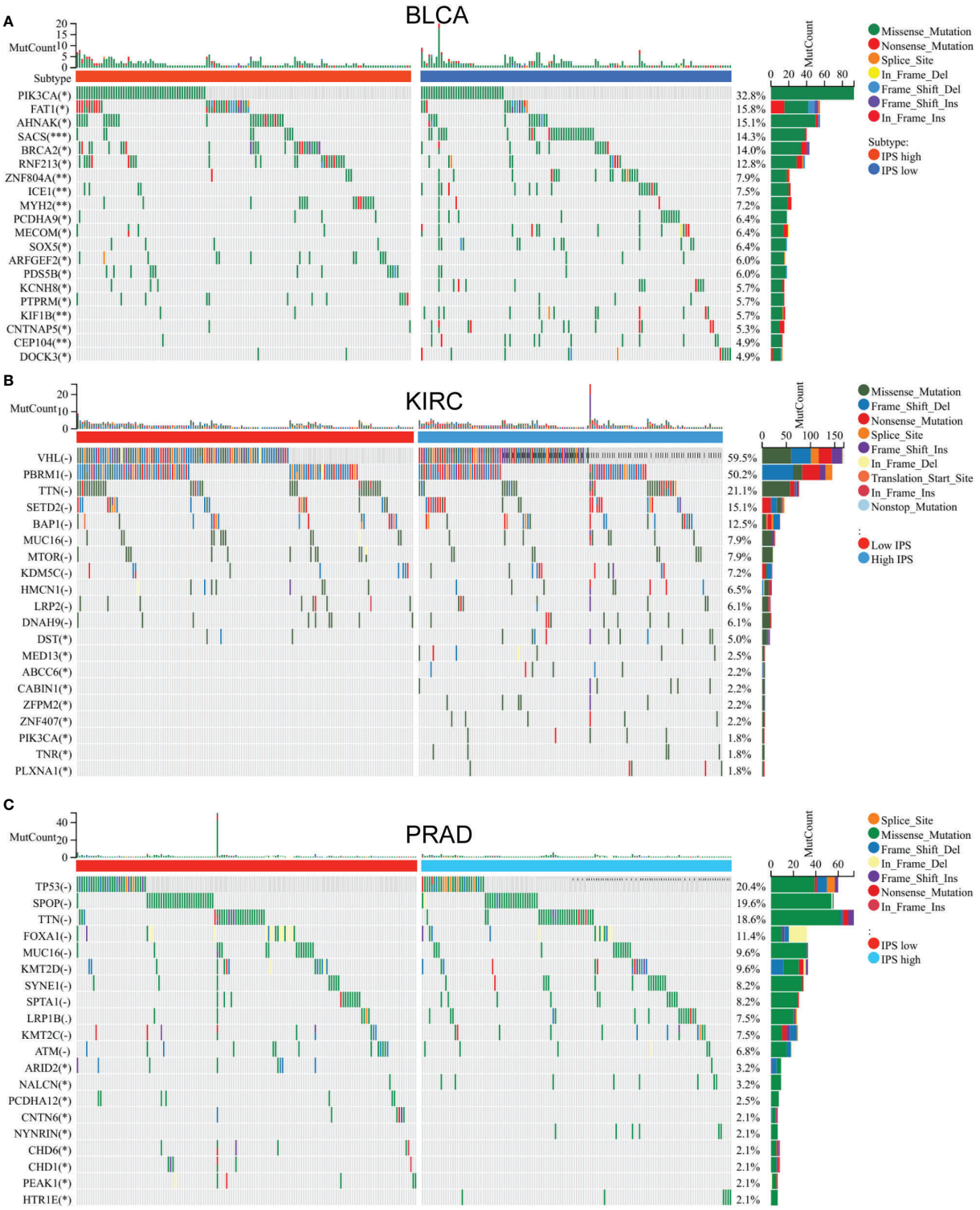

FIGURE 8
Mutation gene difference between low IP - score and high IP - score. Mutation gene difference between low IP - score and high IP - score in **(A)** Bladder carcinoma. **(B)** Kidney renal clear cell carcinoma. **(C)** Testicular Germ Cell Tumors.

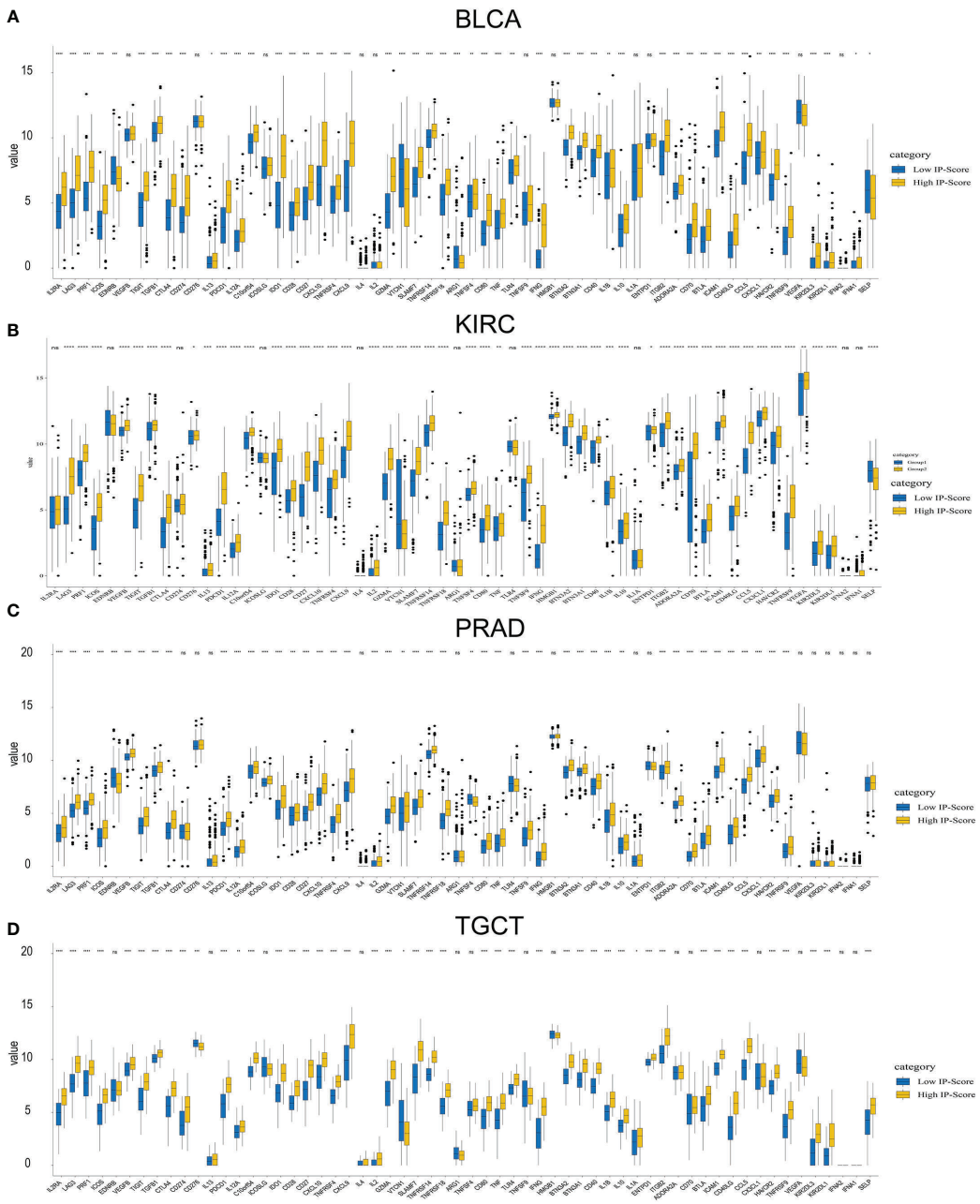

FIGURE 9
Immune check point expression difference between low ip-score and high ip-score. Immune check point expression difference between low ip-score and high ip-score. **(A)** Bladder carcinoma **(B)** Kidney renal clear cell carcinoma **(C)** Prostate carcinoma **(D)** Testicular Germ Cell Tumors. * represent p<0.05; ** represent p<0.01; *** represent p<0.001; **** represent p<0.0001; ns, represent non significant.

Conclusion

It is concluded that the transcriptome level and single-cell level PSMB8, PSMB9, PSMB10, PSME1, PSME2 and IRF1 are closely associated with $CD8^+$ T lymphocyte levels in solid tumours. PSMB8, PSMB9, PSMB10, PSME1, PSME2, and IRF1 can be used as prognostic protective factors for various solid tumours and improve the overall survival of patients. In addition, PSMB8, PSMB9, PSMB10, PSME1, PSME2, and IRF1 can be used as biological markers for ICI treatment and to predict clinical response rates after receiving treatment. Finally, we scored the above six biomarkers with GSVA and constructed a scoring method for predicting immune checkpoint inhibitor therapy named IP-score.

Data availability statement

The original data of the samples in this study can be obtained from the open source databases TCGA and GEO. The original immune therapy data could be downloaded from Immune Checkpoint Blockade therapy Atlas (ICBatlas).

Ethics statement

This study has been conducted in accordance with ethical standards and the national and international guidelines. This study was approved by the Research Ethics Committee and all patients signed the written informed consent in china medical university.

Author contributions

YW, KY, YG, YL, HS, and HL analysed the data and wrote the article. YW, KY, and HL designed and modified the article. YW, KY, and HL designed and modified the article. All authors contributed to the article and approved the submitted version.

Funding

The research was funded by National High Level Hospital Clinical Research Funding: 2022-PUMCH-A-057.

Acknowledgments

The authors would like to thank GEO (https://www.ncbi.nlm.nih.gov/geo/), HPA database (https://www.proteinatlas.org/about/licence), TCGA (http://cancergenome.nih.gov) and Immune Checkpoint Blockade therapy Atlas (ICBatlas) for data collection.

Conflict of interest

The authors declare that the research was conducted in the absence of any commercial or financial relationships that could be construed as a potential conflict of interest.

Publisher's note

All claims expressed in this article are solely those of the authors and do not necessarily represent those of their affiliated organizations, or those of the publisher, the editors and the reviewers. Any product that may be evaluated in this article, or claim that may be made by its manufacturer, is not guaranteed or endorsed by the publisher.

Supplementary material

The Supplementary Material for this article can be found online at: https://www.frontiersin.org/articles/10.3389/fimmu.2022.1085491/full#supplementary-material

References

1. Torre LA, Siegel RL, Ward EM, Jemal A. Global cancer incidence and mortality rates and trends–an update. *Cancer Epidemiol Biomarkers Prev* (2016) 25(1):16–27. doi: 10.1158/1055-9965.EPI-15-0578

2. Mattiuzzi C, Lippi G. Current cancer epidemiology. *J Epidemiol Glob Health* (2019) 9(4):217–22. doi: 10.2991/jegh.k.191008.001

3. Pennock GK, Chow LQ. The evolving role of immune checkpoint inhibitors in cancer treatment. *Oncologist* (2015) 20(7):812–22. doi: 10.1634/theoncologist.2014-0422

4. Park J, Kwon M, Shin EC. Immune checkpoint inhibitors for cancer treatment. *Arch Pharm Res* (2016) 39(11):1577–87. doi: 10.1007/s12272-016-0850-5

5. Altmann DM. A Nobel prize-worthy pursuit: cancer immunology and harnessing immunity to tumour neoantigens. *Immunology* (2018) 155(3):283–4. doi: 10.1111/imm.13008

6. Wolchok J. Putting the immunologic brakes on cancer. *Cell* (2018) 175 (6):1452–4. doi: 10.1016/j.cell.2018.11.006

7. Batlevi CL, Matsuki E, Brentjens RJ, Younes A. Novel immunotherapies in lymphoid malignancies. *Nat Rev Clin Oncol* (2016) 13(1):25–40. doi: 10.1038/nrclinonc.2015.187

8. Marin-Acevedo JA, Soyano AE, Dholaria B, Knutson KL, Lou Y. Cancer immunotherapy beyond immune checkpoint inhibitors. *J Hematol Oncol* (2018) 11 (1):8. doi: 10.1186/s13045-017-0552-6

9. Borghaei H, Paz-Ares L, Horn L, Spigel DR, Steins M, Ready NE, et al. Nivolumab versus docetaxel in advanced nonsquamous non-Small-Cell lung cancer. *N Engl J Med* (2015) 373(17):1627–39. doi: 10.1056/NEJMoa1507643

10. Kanjanapan Y, Day D, Wang L, Al-Sawaihey H, Abbas E, Namini A, et al. Hyperprogressive disease in early-phase immunotherapy trials: Clinical predictors and association with immune-related toxicities. *Cancer* (2019) 125(8):1341–9. doi: 10.1002/cncr.31999

11. Gobbini E, Charles J, Toffart AC, Leccia MT, Moro-Sibilot D, Giaj Levra M. Current opinions in immune checkpoint inhibitors rechallenge in solid cancers. *Crit Rev Oncol Hematol* (2019) 144:102816. doi: 10.1016/j.critrevonc.2019.102816

12. Wang Z, Wu X. Study and analysis of antitumor resistance mechanism of PD1/PD-L1 immune checkpoint blocker. *Cancer Med* (2020) 9(21):8086–121. doi: 10.1002/cam4.3410

13. Perrier A, Didelot A, Laurent-Puig P, Blons H, Garinet S. Epigenetic mechanisms of resistance to immune checkpoint inhibitors. *Biomolecules* (2020) 10(7). doi: 10.3390/biom10071061

14. Spranger S, Bao R, Gajewski TF. Melanoma-intrinsic β-catenin signalling prevents anti-tumour immunity. *Nature* (2015) 523(7559):231–5. doi: 10.1038/nature14404

15. Hugo W, Zaretsky JM, Sun L, Song C, Moreno BH, Hu-Lieskovan S, et al. Genomic and transcriptomic features of response to anti-PD-1 therapy in metastatic melanoma. *Cell* (2016) 165(1):35–44. doi: 10.1016/j.cell.2016.02.065

16. Zhang J, Endres S, Kobold S. Enhancing tumor T cell infiltration to enable cancer immunotherapy. *Immunotherapy* (2019) 11(3):201–13. doi: 10.2217/imt-2018-0111

17. Yewdell JW, Reits E, Neefjes J. Making sense of mass destruction: quantitating MHC class I antigen presentation. *Nat Rev Immunol* (2003) 3 (12):952–61. doi: 10.1038/nri1250

18. Sanmamed MF, Chen L. A paradigm shift in cancer immunotherapy: From enhancement to normalisation. *Cell* (2018) 175(2):313–26. doi: 10.1016/j.cell.2018.09.035

19. Kurts C, Robinson BW, Knolle PA. Cross-priming in health and disease. *Nat Rev Immunol* (2010) 10(6):403–14. doi: 10.1038/nri2780

20. Mishto M, Liepe J, Textoris-Taube K, Keller C, Henklein P, Weberruß M, et al. Proteasome isoforms exhibit only quantitative differences in cleavage and epitope generation. *Eur J Immunol* (2014) 44(12):3508–21. doi: 10.1002/eji.201444902

21. Apavaloaei A, Brochu S, Dong M, Rouette A, Hardy M-P, Villafano G, et al. PSMB11 orchestrates the development of CD4 and CD8 thymocytes *via* regulation of gene expression in cortical thymic epithelial cells. *J Immunol* (2019) 202(3):966–78. doi: 10.4049/jimmunol.1801288

22. Wang Y, Yan K, Lin J, Liu Y, Wang J, Li X, et al. CD8+ T cell Co-expressed genes correlate with clinical phenotype and microenvironments of urothelial cancer. *Front Oncol* (2020) 10:553399. doi: 10.3389/fonc.2020.553399

23. Lee HW, Chung W, Lee HO, Jeong DE, Jo A, Lim JE, et al. Single-cell RNA sequencing reveals the tumor microenvironment and facilitates strategic choices to circumvent treatment failure in a chemorefractory bladder cancer patient. *Genome Med* (2020) 12(1):47. doi: 10.1186/s13073-020-00741-6

24. Dong B, Miao J, Wang Y, Luo W, Ji Z, Lai H, et al. Single-cell analysis supports a luminal-neuroendocrine transdifferentiation in human prostate cancer. *Commun Biol* (2020) 3(1):778. doi: 10.1038/s42003-020-01476-1

25. Yang M, Miao YR, Xie GY, Luo M, Hu H, Kwok HF, et al. ICBatlas: A comprehensive resource for depicting immune checkpoint blockade therapy characteristics from transcriptome profiles. *Cancer Immunol Res* (2022). doi: 10.1158/2326-6066.CIR-22-0249

26. Mariathasan S, Turley SJ, Nickles D, Castiglioni A, Yuen K, Wang Y, et al. TGFβ attenuates tumour response to PD-L1 blockade by contributing to exclusion of T cells. *Nature* (2018) 554(7693):544–8. doi: 10.1038/nature25501

27. Racle J, Gfeller D. EPIC: A tool to estimate the proportions of different cell types from bulk gene expression data. *Methods Mol Biol* (2020) 2120:233–48. doi: 10.1007/978-1-0716-0327-7_17

28. Newman AM, Liu CL, Green MR, Feng W, Xu Y, Hoang CD, et al. Robust enumeration of cell subsets from tissue expression profiles. *Nat Methods* (2015) 12 (5):453–7. doi: 10.1038/nmeth.3337

29. Subramanian A, Tamayo P, Mootha VK, Mukherjee S, Ebert BL, Gillette MA, et al. Gene set enrichment analysis: A knowledge-based approach for interpreting genome-wide expression profiles. *Proc Natl Acad Sci U S A* (2005) 102(43):15545–50. doi: 10.1073/pnas.0506580102

30. Zhang H, He J, Dai Z, Wang Z, Liang X, He F, et al. PDIA5 is correlated with immune infiltration and predicts poor prognosis in gliomas. *Front Immunol* (2021) 12:628966. doi: 10.3389/fimmu.2021.628966

31. Patel AP, Tirosh I, Trombetta JJ, Shalek AK, Gillespie SM, Wakimoto H, et al. Single-cell RNA-seq highlights intratumoral heterogeneity in primary glioblastoma. *Science* (2014) 344(6190):1396–401. doi: 10.1126/science.1254257

32. Gao R, Bai S, Henderson YC, Lin Y, Schalck A, Yan Y, et al. Delineating copy number and clonal substructure in human tumors from single-cell transcriptomes. *Nat Biotechnol* (2021) 39(5):599–608. doi: 10.1038/s41587-020-00795-2

33. Topalian SL, Drake CG, Pardoll DM. Immune checkpoint blockade: A common denominator approach to cancer therapy. *Cancer Cell* (2015) 27(4):450–61. doi: 10.1016/j.ccell.2015.03.001

34. Buchbinder EI, Desai A. CTLA-4 and PD-1 pathways: Similarities, differences, and implications of their inhibition. *Am J Clin Oncol* (2016) 39 (1):98–106. doi: 10.1097/COC.0000000000000239

35. Gondhowiardjo SAHandoko, , Jayalie VF, Apriantoni R, Barata AR, Senoaji F, et al. Tackling resistance to cancer immunotherapy: What do we know. *Molecules* (2020) 25(18). doi: 10.3390/molecules25184096

36. Abdin SM, Zaher DM, Arafa EA, Omar HA. Tackling cancer resistance by immunotherapy: Updated clinical impact and safety of PD-1/PD-L1 inhibitors. *Cancers (Basel)* (2018) 10(2). doi: 10.3390/cancers10020032

37. Omar HA, Tolba MF. Tackling molecular targets beyond PD-1/PD-L1: Novel approaches to boost patients response to cancer immunotherapy. *Crit Rev Oncol Hematol* (2019) 135:21–9. doi: 10.1016/j.critrevonc.2019.01.009

38. Rowshanravan B, Halliday N, Sansom DM. CTLA-4: A moving target in immunotherapy. *Blood* (2018) 131(1):58–67. doi: 10.1182/blood-2017-06-741033

39. Syn NL, Teng M, Mok T, Soo RA. De-novo and acquired resistance to immune checkpoint targeting. *Lancet Oncol* (2017) 18(12):e731–41. doi: 10.1016/S1470-2045(17)30607-1

40. Sul J, Blumenthal GM, Jiang X, He K, Keegan P, Pazdur R. FDA Approval summary: Pembrolizumab for the treatment of patients with metastatic non-small cell lung cancer whose tumors express programmed death-ligand 1. *Oncologist* (2016) 21(5):643–50. doi: 10.1634/theoncologist.2015-0498

41. Pai-Scherf L, Blumenthal GM, Li H, Subramaniam S, Mishra-Kalyani PS, He K, et al. FDA Approval summary: Pembrolizumab for treatment of metastatic non-small cell lung cancer: First-line therapy and beyond. *Oncologist* (2017) 22 (11):1392–9. doi: 10.1634/theoncologist.2017-0078

42. Havel JJ, Chowell D, Chan TA. The evolving landscape of biomarkers for checkpoint inhibitor immunotherapy. *Nat Rev Cancer* (2019) 19(3):133–50. doi: 10.1038/s41568-019-0116-x

43. Zhang L, Yu X, Zheng L, Zhang Y, Li Y, Fang Q, et al. Lineage tracking reveals dynamic relationships of T cells in colorectal cancer. *Nature* (2018) 564 (7735):268–72. doi: 10.1038/s41586-018-0694-x

frontiers | Frontiers in Immunology

TYPE Mini Review
PUBLISHED 10 January 2023
DOI 10.3389/fimmu.2022.1088886

Check for updates

OPEN ACCESS

EDITED BY
Jian Zhang,
Southern Medical University, China

REVIEWED BY
Jake ODonnell,
The University of Queensland, Australia
Dalil Hannani,
Grenoble (TIMC-IMAG), France
Jian Qiao,
University of Texas Southwestern Medical Center, United States

*CORRESPONDENCE
Ke Wang
wangke@fmmu.edu.cn
Zhi-Nan Chen
znchen@fmmu.edu.cn

†These authors have contributed equally to this work

SPECIALTY SECTION
This article was submitted to Cancer Immunity and Immunotherapy, a section of the journal Frontiers in Immunology

RECEIVED 03 November 2022
ACCEPTED 20 December 2022
PUBLISHED 10 January 2023

CITATION
Shi M-Y, Liu H-G, Chen X-H, Tian Y, Chen Z-N and Wang K (2023) The application basis of immuno-checkpoint inhibitors combined with chemotherapy in cancer treatment. *Front. Immunol.* 13:1088886. doi: 10.3389/fimmu.2022.1088886

COPYRIGHT
© 2023 Shi, Liu, Chen, Tian, Chen and Wang. This is an open-access article distributed under the terms of the Creative Commons Attribution License (CC BY). The use, distribution or reproduction in other forums is permitted, provided the original author(s) and the copyright owner(s) are credited and that the original publication in this journal is cited, in accordance with accepted academic practice. No use, distribution or reproduction is permitted which does not comply with these terms.

The application basis of immuno-checkpoint inhibitors combined with chemotherapy in cancer treatment

Ming-Yan Shi†, Han-Ge Liu†, Xiao-Hong Chen, Ye Tian, Zhi-Nan Chen* and Ke Wang*

National Translational Science Center for Molecular Medicine & Department of Cell Biology, Fourth Military Medical University, Xi'an, China

Immuno-checkpoint inhibitors (ICIs) bring a promising prospect for patients with cancers, which restrains the growth of tumor cells by enhancing anti-tumor activity. Nevertheless, not all patients benefit from the administration of ICIs monotherapy. The partial response or resistance to ICIs is mainly due to the complex and heterogenous tumor microenvironment (TME). The combined therapy is necessary for improving the efficacy of tumor treatment. Chemotherapy is reported not only to kill tumor cells directly, but also to stimulate effective anti-tumor immune responses. Several combined therapies of ICIs and chemotherapeutic agents have been approved for the first-line treatment of cancers, including PD-1/PD-L1 inhibitors. This review summarizes the potential mechanisms of the combined therapy of ICIs and chemotherapeutic agents in inducing immunogenic cell death (ICD) and reprogramming TME, and elucidates the possible anti-tumor effects of combined therapy from the perspective of metabolic reprogramming and microbiome reprogramming.

KEYWORDS

immuno-checkpoint inhibitors, chemotherapy, tumor microenvironment, immunogenic cell death, anti-tumor activity

Introduction

Malignant tumors, as a type of incurable diseases, have threatened human health seriously owing to the immunosuppressive tumor microenvironment. The tumor immunotherapies dramatically make a monumental breakthrough for cancer treatment and bring significant improvement for patient survival by boosting effective immune response to eliminate malignant cells (1, 2). Oncolytic virus therapies, cancer vaccines, cytokine therapies, adoptive cell transfer therapies, and ICIs are included, and ICIs, which include inhibitors of the programmed cell death protein 1 (PD-1),

programmed cell death-ligand 1 (PD-L1), and the cytotoxic T lymphocyte-associated protein 4 (CTLA-4), have been broadly used in clinical applications and contribute to prolonged survival for lung cancer patients (2–5).

However, not all patients benefit from immune checkpoint blockade therapy (6, 7). Based on response to ICIs, three broad population of patients are identified, which include responders, those that acquire resistance, and those that never respond (8–10). Unfortunately, only 20% of NSCLC patients response to ICIs, which shows a relatively lower clinical effect compared to other cancers (7). The complex and heterogenous TME is reported to be involved in the response to ICIs (11, 12). Based on the status of T cell infiltration, TME is classified as the immune-inflamed phenotype, the immune-excluded phenotype, and the immune-desert phenotype (13, 14). The reactivation and clonal-proliferation of antigen-experienced T cells in the TME are necessary for an effective anti-tumor response after ICI administration. Nevertheless, the tumor-associated macrophages (TAMs), cancer-associated fibroblasts (CAFs), myeloid-derived suppressor cells (MDSCs), and regulated T cells (Tregs) in TME have an inhibitory impact on the infiltration and activation of effector T cells (15). As a result, ICIs combined with other therapies that activate the immune effects of TME seems to be a better choice for tumor treatment. As of December 2021, 4,897 clinical trials are conducted to test the efficacy of PD-1/PD-L1 inhibitors. Among them, 83% are ICIs combined with other therapies, such as chemotherapy, radiotherapy, and other immuno-oncology therapies (16). Several clinical trials show that ICIs combined with chemotherapy have a better clinical effect compared to ICIs monotherapy (17–19). For example, pembrolizumab, a humanized monoclonal antibody against PD-1, plus platinum-based chemotherapy significantly improved overall survival rates of NSCLC patients with a PD-L1 ≥ 50% and negative for genomic alterations in the EGFR and ALK genes, compared with pembrolizumab monotherapy (19). Meanwhile, ICIs combined with chemotherapy also prolong the NSCLC patient survival, compared with chemotherapy (20–23), which have been approved for the first-line treatment in advanced NSCLC patients (24).

In this review, we summarize the synergetic effects of chemotherapy with ICI therapy in tumor treatment from the perspective of inducing ICD, remodeling TME, metabolic reprogramming, and microbiome reprogramming (Figure 1). In addition, further researches need to be conducted to explore the novel mechanisms of above-mentioned therapy in cancers, which may provide a solid foundation for future clinical applications.

Inducing immunogenic cell death

Several studies have shown that chemotherapeutic agents have the ability of inducing ICD in animal experiments, including anthracyclines, cyclophosphamide, oxaliplatin, pemetrexed, and paclitaxel (25–30). For example, anthracyclines, including doxorubicin, idarubicin and mitoxantrone, are identified as ICD inducers in the mouse models of colorectal cancer (27), and cyclophosphamide can also induce ICD as shown in glioma mouse models (30). In addition, single-agent pemetrexed or docetaxel can induce ICD in 16 NSCLC patients, with increasing plasma concentration of soluble calreticulin (31). ICD is a form of regulated cell death, which activates an adaptive immune response in immunocompetent hosts (32, 33). The hallmarks of ICD include the exposure and release of numerous damage-associated molecular patterns (DAMPs), the phosphorylation of eukaryotic translation initiation factor 2 subunit-α (eIF2α), and the activation of type I IFN signaling and autophagy. Among them, DAMPs play a vital role in stimulating adaptive immune response, which contain increasing extracellular ATP, surface-exposed calreticulin, and released high mobility group box protein 1 (HMGB1) (34, 35). Increasing extracellular ATP, which provides a 'find me' signal, attracts antigen-presenting cells through binding with the purinergic receptors (36, 37) and stimulates dendritic cell (DC) maturation (38–41). Moreover, ATP triggers the formation of the NOD-like receptor family, pyrin domain containing-3 protein (NLRP3)-dependent caspase-1 activation complex (42), which promotes the secretion of IL-1β and IL-18 (43), to stimulate adaptive

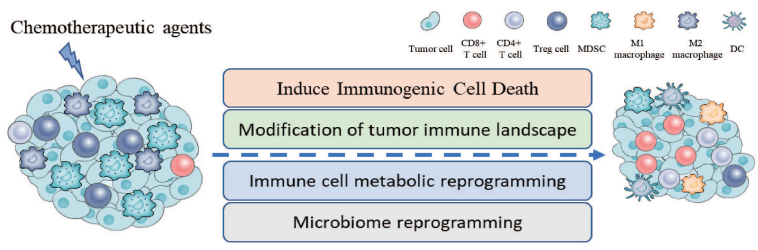

FIGURE 1
Chemotherapeutic agents enhance the anti-tumor activity of ICIs through several mechanisms, including inducing immunogenic cell death, changing the proportion and activity of immune cells in TME, immune cell metabolic reprogramming, and microbiome reprogramming.

immune response (44). In addition, the P2X7 receptor (P2X7R), is expressed on various immune cells, and its expression sensitizes cells to enhanced ambient ATP concentrations, which modulates energy metabolism and T cell growth and differentiation (45). The exposure of calreticulin from endoplasmic reticulum to cell surface depends on the rapid phosphorylation of eIF2α and ERp57 (46), and provides an 'eat me' signal to promote phagocytosis by DCs, provoking the adaptive immune response (27, 47). However, mutant calreticulin with loss of the KDEL sequence is secreted to extracellular space, and may inhibit the phagocytosis of dying cancer cells by DCs through saturating binding sites on DCs (48). Moreover, the interaction between calreticulin and toll-like receptor 4 (TLR4) expressed on tumor cell surface promotes the secretion of TNFα and CCL19, which facilitates the migration and maturation of DCs, to limit the tumor progression *in vivo* (49). HMGB1, released from dying cancer cells, binds with TLR4 expressed on DCs to strengthen the antigen-presenting activity of DCs through activating the PI3K/AKT/mTOR signaling pathway, and promotes anti-tumor immune response of T cells (50, 51). Different HMGB1 isoforms exert different effects on immune response, and the reduced form is responsible for the activation of DCs (52). In addition, the administration of carboplatin, cisplatin, and gemcitabine increases the PD-L1 expression on tumor cells, and shows a better efficacy when combining with ICIs in NSCLC mouse models (53–55), in which the role of cisplatin has been validated in human NSCLC tumor samples (56). Moreover, cisplatin increases the expression level of MHC class I antigen on tumor cells, and subsequently augment CTL-mediated attack to tumor cells (57, 58). In summary, chemotherapy-induced ICD promotes the cross-presentation of tumor antigen to CD8+ cytotoxic T lymphocytes (CTLs), which limits tumor progression effectively.

Changing the proportion and activity of immune cells in TME

Chemotherapeutic agents have been validated that they can interact directly with immune cells to stimulate anticancer immunity through several mechanisms, which changes the infiltration and activity of immune cells in TME, including the depletion of immunosuppressive cells, the activation of immune effector cells, and promoting the proliferation of immune cells. Tumor-infiltrating Tregs promote tumor progression by inhibiting endogenous cytotoxic T cell responses (59), and it has been reported that some chemotherapy drugs can decrease the amount of Tregs (60–63). For example, the frequencies of intra-tumoral Tregs decreases significantly after the pretreatment of paclitaxel and cisplatin in a murine lung carcinoma model (64). Paclitaxel selectively decreases the size of Treg population in peripheral blood of patients with NSCLC, which may promote the upregulation of CD95 on Tregs, leading to cell apoptosis (65). Moreover, cyclophosphamide also decreases the amount of intra-tumoral Tregs in NSCLC mouse model (66), which is also identified in patients with recurrent prostate cancer (67). In addition, the amount of MDSCs, another immunosuppressive cell that helps tumor cells evade immune destruction (68, 69), is decreased after the administration of docetaxel, gemcitabine and 5-fluorouracil in mouse experiments (70–73). As shown in mouse models of melanoma (B16F10), gemcitabine significantly reduces the immunosuppressive state by decreasing the size of MDSCs and Tregs (70). Moreover, the number of circulating MDSCs in patients with pancreatic cancer decreases after the administration of gemcitabine, which provides precise clinical evidence (74), which is also validated in glioblastoma patients (75). The combination of gemcitabine and cisplatin reduce the amount of Tregs and regulatory B cells in in nasopharyngeal carcinoma patients (76). In addition, cyclophosphamide plus gemcitabine combination chemotherapy reduces the immunosuppressive state through decreasing the number of Tregs and MDSCs, enhancing anti-tumor immune response in colon carcinoma-bearing mice (63). In summary, the use of chemotherapeutic agents impairs the immunosuppressive role of TME by reducing the number of immunosuppressive cells, which enhances the anti-tumor activity.

In addition, several animal studies have validated that some chemotherapeutic agents, including platinum drugs and docetaxel, have the ability to promote the infiltration of CD8+ T cells, enhancing their anti-tumor effects (53, 60, 77–79). It has been reported that the administration of cisplatin and docetaxel increases intra-tumoral CD8+ T cell infiltration in a phase I/II study of neoadjuvant chemotherapy for resectable NSCLC (80). The increasing CD8+ T cell infiltration contributes to enhancing the anti-tumor activity and limits the tumor progression (81). Meanwhile, further studies explaining the mechanisms that platinum drugs increase the infiltration of CD8+ T cells have been conducted. For example, oxaliplatin enhances the secretion of CXCL9, CXCL10, and CXCL11 from tumor cells, which attracts CD8+ effector T cells through interacting with CXCR3 (82, 83), and subsequently promotes T cell infiltration in tumor tissues. In addition, neoadjuvant chemotherapy increases the infiltration of tissue resident memory T cells (TRMs) in resectable NSCLC patients, which will provide long-term anti-tumor immune response (84). TRMs express high levels of inhibitory receptors, such as PD-1 and Tim-3, and it has been validated that TRMs show a significant expansion and enhancing cytotoxic capacity after the administration of PD-1 inhibitors (85–88). Moreover, cisplatin can increase the infiltration of CD8+ T cells *via* activating cGAS-STING signaling in K-ras-driven tumor cells (77), and enhance the killing effects of CD8+ T cells through Fas/Fas ligand interactions in NSCLC mouse model (89), which may provide an inflammatory environment to enhance the anti-tumor activity of ICIs.

Chemotherapeutic agents also increase the infiltration of APCs in tumor tissues, such as DCs and macrophages, and enhances the anti-tumor immune response. Anthracycline-based chemotherapy increases the intra-tumoral infiltration of DCs in fibrosarcoma and breast cancer mouse models (90, 91). A prospective study suggests that the responsiveness of DCs recovers after anthracycline-based neoadjuvant chemotherapy in breast cancer patients (92). Except for above mentioned ATP signaling, CCL2/CCR2 axis may also be required for the intratumoral recruitment of DCs (90). In addition, platinum (IV) complexes increase the infiltration of M1 macrophages by decreasing the expression of CD47 in lung cancer mouse model, which is overexpressed on tumor cells and limits the antigen-presenting activity of APCs (93, 94). DCs play a vital role in maintaining CD8+ T cell function within tumors, and promote ICIs mediated anti-tumor immunity (95, 96). Furthermore, DCs may license PD-1 blockade *via* CD28 costimulation (97), and conventional DCs express genes correlated with CXCL9, which is related to PD-1 inhibitor response (98–100). In summary, chemotherapy-induced APCs increase in tumor tissues may contribute to ICI-enhanced anti-tumor activity.

Immune cell metabolic reprogramming

As a crucial hallmark of cancer, metabolism reprogramming provides a favorable immunosuppressive microenvironment for the tumor progression (101–103). Chemotherapy usually influences patients' nutritional status, and the serum of patients with lung cancer is accompanied by metabolic alterations, including glycolysis and lipid metabolism, phosphatidylcholine biosynthesis as well as amino acid metabolism (104). What's more, metabolic reprogramming is closely involved in the activation and of T cells. For example, the activation of T cells needs higher levels of glycolysis and mitochondrial respiration (105). Thus, chemotherapy may influence the immune effects of T cells through metabolic processes. Pemetrexed has been validated to increase mitochondrial function of T cells in colon cancer mouse model, which is necessary for the activation of T cells (26, 106). Nevertheless, there is little researches about the influence of other chemotherapeutic agents on metabolic reprogramming of immune cells, and further metabolomics study is necessary to explore this influence in preclinical and clinical studies.

Microbiome reprogramming

Gut microbiome is a complex ecosystem that regulates the interaction of the human and their environment, which has a potential impact on anti-tumor immune responses through various mechanisms (107), and is closely correlated with the efficacy of ICIs in cancer treatment (108–110). Chemotherapy has been validated to change the proportion of gut microbiome. The abundance of the Firmicutes phylum and Enterobacteriaceae increase after the administration of pemetrexed in the patient-lung-derived tumor xenograft mouse models (111). The selected species of Gram-positive bacteria are induced into the secondary lymphoid organs by cyclophosphamide, and stimulates the memory Th1 immune responses, which promotes the anti-tumor immune response (112). Therefore, the microbiome reprogramming induced by chemotherapy may provoke the anti-tumor effects of ICIs. However, the influence of chemotherapy on local microbiome needs to be investigated further, and the impacts of chemotherapy on ICI administration are required to be validated in clinical researches from the perspective of microbiome reprogramming.

ICIs combined with chemotherapy in various cancers

Considering the limitations of ICIs monotherapy in controlling tumor progression, a large amount of studies are devoted to the safety and effectiveness of ICIs combined with standard-of-care chemotherapies. ICIs combined with chemotherapy has been approved for the treatment of certain cancer types by FDA, and more than 600 ongoing clinical trials are devoted to exploring or optimizing for various oncological indications. In patients with NSCLC, pembrolizumab plus a platinum and pemetrexed provides a better prognosis compared to pembrolizumab monotherapy (113), owing to the immune activation of these chemotherapy drugs. Similar effects are also observed in patients with untreated locally incurable recurrent or metastatic head and neck squamous cell carcinoma treated with pembrolizumab plus a platinum and 5-fluorouracil (114, 115). In addition, atezolizumab plus carboplatin and nab-paclitaxel prolongs the overall survival and progression-free survival in patients with advanced non-squamous NSCLC (116). Neoadjuvant carboplatin and paclitaxel chemotherapy increases the amount of central memory CD8+ T cell in peripheral blood of patients with advanced serous ovarian cancer, enhancing antigen processing and presentation (117). However, the further studies are needed to investigate the corresponding mechanisms of neoadjuvant carboplatin and paclitaxel chemotherapy in inhibiting NSCLC progression. Although ICIs combined with chemotherapy significantly prolongs the survival of patients with tumors, it is necessary for us to evaluate the toxicity of the combination therapies. ICIs combined with chemotherapy may cause hematological, gastrointestinal, and renal toxicity, and contribute to hypothyroidism, hyperthyroidism, pneumonitis, hepatitis,

severe skin reactions, colitis, and infusion reactions (118–121). However, the current understanding of adverse reactions of combined therapies is incomplete, and it is necessary to describe the preferable adverse reactions of different combinations, which is beneficial for balancing the safety and efficiency of the corresponding treatment.

Discussion

ICIs have made great contributions to the survival of patients with cancers. However, the low response rate of patients to ICIs prompts us to explore the possibility of ICIs combination with other therapies. As a routine therapy, chemotherapy attracts much attention because of its immune stimulation activity, and ICIs combination with chemotherapy achieves great effects in clinical trials. FDA has approved several combination therapies for the treatment of advanced NSCLC in the first-line setting (122). To clarify the mechanism how chemotherapy promotes curative effect of ICIs is beneficial for the application of the combination therapies. As mentioned above, chemotherapeutic agents-induced ICD and their immune stimulation activity are considered as the main mechanism of combination therapy. However, the impacts of chemotherapy are so complex that chemotherapy may influence ICI-mediated anti-tumor responses through various routes.

With the development of sequencing technology, the landscape of immune cells within tumor tissues has been gradually revealed, and more and more cellular components have been recognized. For example, B cells represent a vital component of infiltrating immune cells in a variety of solid tumors, and play a dual role in modulating anti-tumor immune response (123). Chemotherapy reduces the amount of adenosine-producing B cells, which may reduce potential immunosuppression in TME (124). However, there is little research about the influence of chemotherapy on B cell subpopulations and their activity.

Moreover, cancer-associated fibroblasts (CAFs) account for more than 50% of stroma cells in TME, and various CAF populations have been identified based on the results of single-cell sequencing analyses, including the cancer-associated myofibroblasts (myCAFs), inflammatory-like CAFs (iCAFs), and the antigen-presenting CAFs (apCAFs) (125). CAFs are involved in regulating tumor immune response and the efficacy of immunotherapy through several routes (126). For example, CAFs increase the ratio of FoxP3+ (Tregs) and CD8+ tumor-infiltrating lymphocytes *via* IL-6 in TME, and IL-6 blockade enhances the immunotherapy efficacy in esophageal cancer models (127). Several studies have reported that CAFs protect tumor cells from apoptosis induced by chemotherapy, while insulin-like growth factors secreted by CAFs enhanced the anti-tumor effects of osimertinib in mice model (125, 128). Moreover, CAFs can activate the NLRP3 inflammasome through sensing DAMPs in breast cancer, which leads to a pro-inflammatory signaling (129). The influence of chemotherapy on diverse CAFs and their association with the immunotherapy efficacy has not been explored comprehensively, and further researches are needed.

Except for the influence of chemotherapeutic agents on novel cellular components in TME, chemotherapy-induced microbiome reprogramming also contributes to the combination of ICIs and chemotherapy. Although the impacts of chemotherapy on gut microbiome have been explained partly in animal experiments, the overall landscape of gut microbiome reprogramming after treating with different chemotherapeutic agents needs to be described in more preclinical and clinical researches. Beyond that, the influence of chemotherapy on local microbiome also needs to be investigated further, and the impacts of chemotherapy on ICI administration are required to be validated in clinical researches from the perspective of microbiome reprogramming.

In addition, the administration approaches of ICIs combination with chemotherapy are necessary to be improved. Firstly, a proper combination therapy can maximize the clinical benefit and minimize the adverse drug reactions. As mentioned above, different chemotherapy drugs stimulate effective anti-tumor immune responses through different mechanisms, and cancer patients may reap more benefits with appropriate combination therapies after evaluating the tumor conditions, including PD-L1 expression level, immune cell infiltration, and tumor mutation burden. However, there is little clinical trials about comparing the effectiveness of combination therapies of different chemotherapeutic drugs and ICIs. Secondly, chemotherapeutic regimens and ICIs are administrated simultaneously in most clinical trials. Nevertheless, it has reported that the sequence of administrating chemotherapeutic agents and ICIs has an impact on the efficiency of the combined therapies in several animal experiments. The administration of anti-CTLA-4 antibody after injecting cyclophosphamide significantly inhibits the tumor progression in the CT26 colon carcinoma model, while the reverse administration sequence leads to the apoptosis of anti-tumor CD8+ T cells (130). Apart from this, the time interval from chemotherapy to immunotherapy may also influence the response to ICIs. In the long rest period group, the frequency of the Th1 subset and PD-1 + CD8+ T cells are significantly higher than that in the short rest period group, which provides a novel perspective for the application of combination therapies (131). However, there is no more research about appropriate sequence and proper time interval, and it needs more researches to study the influence of time interval on anti-tumor effects. Lastly, proper dose may be the most important respect to effectively stimulate the maximum anti-tumor immune response and minimize adverse reactions. For example, low dose cisplatin and oxaliplatin increase the number of circulating CD4+ and CD8+ T cells, while high dose regimens decrease the size of lymphocyte in a mouse model of

colon cancer (132). Metronomic low dose cyclophosphamide enhance anti-tumor immune response by selectively reducing the amount of Treg cells in tumor patients (133), while high dose cyclophosphamide completely eradicates the hemopoietic cell (134). In addition, a novel administration mode called medium-dose intermittent chemotherapy provokes a striking response depending on the activation of a sustaining anti-tumor immune response (66, 135). Therefore, appropriate dosage for combined therapies is necessary to be investigated in further studies.

In summary, ICIs combination with chemotherapy has shown a better anti-tumor response and provides a more beneficial survival, compared to ICIs monotherapy. This benefit is supported by a strong cancer biology rationale, which induce a better immune response. Hence, the evaluation of the panoramic dynamic immune landscape of TME will be helpful to understand tumor pathogenesis and provide novel approaches for cancer treatment.

Author contributions

All authors have made a direct contribution to the work, and approved it for publication.

Funding

This work was supported by Science and Technology Project of Shaanxi Province (2021PT-047), National Natural Science Foundation of China (82002425, 82273226), and the Young Elite Scientist Sponsorship Program by Cast of China Association for Science and Technology (2020QNRC001).

Conflict of interest

The authors declare that the research was conducted in the absence of any commercial or financial relationships that could be construed as a potential conflict of interest.

Publisher's note

All claims expressed in this article are solely those of the authors and do not necessarily represent those of their affiliated organizations, or those of the publisher, the editors and the reviewers. Any product that may be evaluated in this article, or claim that may be made by its manufacturer, is not guaranteed or endorsed by the publisher.

References

1. Esfahani K, Roudaia L, Buhlaiga N, Del Rincon SV, Papneja N, Miller W HJr. A review of cancer immunotherapy: From the past, to the present, to the future *Curr Oncol* (2020) 27:S87–97 doi: 10.3747/co.27.5223

2. Zhang Y, Zhang Z. The history and advances in cancer immunotherapy: Understanding the characteristics of tumor-infiltrating immune cells and their therapeutic implications. *Cell Mol Immunol* (2020) 17:807–21. doi: 10.1038/s41423-020-0488-6

3. Gettinger S, Horn L, Jackman D, Spigel D, Antonia S, Hellmann M, et al. Five-year follow-up of nivolumab in previously treated advanced non-Small-Cell lung cancer: Results from the CA209-003 study. *J Clin Oncol* (2018) 36:1675–84. doi: 10.1200/JCO.2017.77.0412

4. Garon EB, Hellmann MD, Rizvi NA, Carcereny E, Leighl NB, Ahn MJ, et al. Five-year overall survival for patients with advanced NonSmall-cell lung cancer treated with pembrolizumab: Results from the phase I KEYNOTE-001 study. *J Clin Oncol* (2019) 37:2518–27. doi: 10.1200/JCO.19.00934

5. Horn L, Mansfield AS, Szczesna A, Havel L, Krzakowski M, Hochmair MJ, et al. First-line atezolizumab plus chemotherapy in extensive-stage small-cell lung cancer. *N Engl J Med* (2018) 379:2220–9. doi: 10.1056/NEJMoa1809064

6. Haslam A, Prasad V. Estimation of the percentage of US patients with cancer who are eligible for and respond to checkpoint inhibitor immunotherapy drugs. *JAMA Netw Open* (2019) 2:e192535. doi: 10.1001/jamanetworkopen.2019.2535

7. Ribas A, Wolchok JD. Cancer immunotherapy using checkpoint blockade. *Science* (2018) 359:1350–5. doi: 10.1126/science.aar4060

8. Jenkins RW, Barbie DA, Flaherty KT. Mechanisms of resistance to immune checkpoint inhibitors. *Br J Cancer* (2018) 118:9–16. doi: 10.1038/bjc.2017.434

9. Gide TN, Wilmott JS, Scolyer RA, Long GV. Primary and acquired resistance to immune checkpoint inhibitors in metastatic melanoma. *Clin Cancer Res* (2018) 24:1260–70. doi: 10.1158/1078-0432.CCR-17-2267

10. Sharma P, Hu-Lieskovan S, Wargo JA, Ribas A. Primary, adaptive, and acquired resistance to cancer immunotherapy. *Cell* (2017) 168:707–23. doi: 10.1016/j.cell.2017.01.017

11. Petitprez F, Meylan M, de Reynies A, Sautes-Fridman C, Fridman WH. The tumor microenvironment in the response to immune checkpoint blockade therapies. *Front Immunol* (2020) 11:784. doi: 10.3389/fimmu.2020.00784

12. Wu T, Dai Y. Tumor microenvironment and therapeutic response. *Cancer Lett* (2017) 387:61–8. doi: 10.1016/j.canlet.2016.01.043

13. Chen DS, Mellman I. Elements of cancer immunity and the cancer-immune set point. *Nature* (2017) 541:321–30. doi: 10.1038/nature21349

14. Herbst RS, Soria JC, Kowanetz M, Fine GD, Hamid O, Gordon MS, et al. Predictive correlates of response to the anti-PD-L1 antibody MPDL3280A in cancer patients. *Nature* (2014) 515:563–7. doi: 10.1038/nature14011

15. Horvath L, Thienpont B, Zhao L, Wolf D, Pircher A. Overcoming immunotherapy resistance in non-small cell lung cancer (NSCLC) - novel approaches and future outlook. *Mol Cancer* (2020) 19:141. doi: 10.1186/s12943-020-01260-z

16. Upadhaya S, Neftelinov ST, Hodge J, Campbell J. Challenges and opportunities in the PD1/PDL1 inhibitor clinical trial landscape. *Nat Rev Drug Discovery* (2022) 21:482–3. doi: 10.1038/d41573-022-00030-4

17. Chen Y, Yang Z, Wang Y, Hu M, Zhang B, Zhang Y, et al. Pembrolizumab plus chemotherapy or anlotinib vs. pembrolizumab alone in patients with previously treated EGFR-mutant NSCLC. *Front Oncol* (2021) 11:671228. doi: 10.1016/S0140-6736(20)32531-9

18. Kim R, Keam B, Hahn S, Ock CY, Kim M, Kim TM, et al. First-line pembrolizumab versus pembrolizumab plus chemotherapy versus chemotherapy alone in non-small-cell lung cancer: A systematic review and network meta-analysis. *Clin Lung Cancer* (2019) 20:331–338 e4. doi: 10.1016/j.cllc.2019.05.009

19. Chen Y, Wang Y, Yang Z, Hu M, Zhang Y, Qian F, et al. Pembrolizumab alone or combined with chemotherapy in advanced NSCLC with PD-L1 >/=50%: Results of a retrospective study. *Front Oncol* (2021) 11:691519. doi: 10.1016/S0140-6736(19)32591-7

20. Rodriguez-Abreu D, Powell SF, Hochmair MJ, Gadgeel S, Esteban E, Felip E, et al. Pemetrexed plus platinum with or without pembrolizumab in patients with previously untreated metastatic nonsquamous NSCLC: Protocol-specified final analysis from KEYNOTE-189. *Ann Oncol* (2021) 32:881–95. doi: 10.1016/j.annonc.2021.04.008

21. Reck M, Mok TSK, Nishio M, Jotte RM, Cappuzzo F, Orlandi F, et al. Atezolizumab plus bevacizumab and chemotherapy in non-small-cell lung cancer

(IMpower150): key subgroup analyses of patients with EGFR mutations or baseline liver metastases in a randomised, open-label phase 3 trial. *Lancet Respir Med* (2019) 7:387–401. doi: 10.1016/S2213-2600(19)30084-0

22. Paz-Ares L, Vicente D, Tafreshi A, Robinson A, Soto Parra H, Mazieres J, et al. Placebo-controlled trial of pembrolizumab plus chemotherapy in patients with metastatic squamous NSCLC: Protocol-specified final analysis of KEYNOTE-407. *J Thorac Oncol* (2020) 15:1657–69. doi: 10.1016/j.jtho.2020.06.015

23. West H, McCleod M, Hussein M, Morabito A, Rittmeyer A, Conter HJ, et al. Atezolizumab in combination with carboplatin plus nab-paclitaxel chemotherapy compared with chemotherapy alone as first-line treatment for metastatic non-squamous non-small-cell lung cancer (IMpower130): a multicentre, randomised, open-label, phase 3 trial. *Lancet Oncol* (2019) 20:924–37. doi: 10.1016/S1470-2045(19)30167-6

24. Kim SY, Halmos B. Choosing the best first-line therapy: NSCLC with no actionable oncogenic driver. *Lung Cancer Manag* (2020) 9:LMT36. doi: 10.2217/lmt-2020-0003

25. Tesniere A, Schlemmer F, Boige V, Kepp O, Martins I, Ghiringhelli F, et al. Immunogenic death of colon cancer cells treated with oxaliplatin. *Oncogene* (2009) 29:482–91. doi: 10.1038/onc.2009.356

26. Schaer DA, Geeganage S, Amaladas N, Lu ZH, Rasmussen ER, Sonyi A, et al. The folate pathway inhibitor pemetrexed pleiotropically enhances effects of cancer immunotherapy. *Clin Cancer Res* (2019) 25:7175–88. doi: 10.1158/1078-0432.CCR-19-0433

27. Obeid M, Tesniere A, Ghiringhelli F, Fimia GM, Apetoh L, Perfettini JL, et al. Calreticulin exposure dictates the immunogenicity of cancer cell death. *Nat Med* (2007) 13:54–61. doi: 10.1038/nm1523

28. Lau TS, Chan LKY, Man GCW, Wong CH, Lee JHS, Yim SF, et al. Paclitaxel induces immunogenic cell death in ovarian cancer *via* TLR4/IKK2/SNARE-dependent exocytosis. *Cancer Immunol Res* (2020) 8:1099–111. doi: 10.1158/2326-6066.CIR-19-0616

29. Galluzzi L, Humeau J, Buque A, Zitvogel L, Kroemer G. Immunostimulation with chemotherapy in the era of immune checkpoint inhibitors. *Nat Rev Clin Oncol* (2020) 17:725–41. doi: 10.1038/s41571-020-0413-z

30. Du B, Waxman DJ. Medium dose intermittent cyclophosphamide induces immunogenic cell death and cancer cell autonomous type I interferon production in glioma models. *Cancer Lett* (2020) 470:170–80. doi: 10.1016/j.canlet.2019.11.025

31. Furukawa R, Inoue H, Yoneshima Y, Tsutsumi H, Iwama E, Ikematsu Y, et al. Cytotoxic chemotherapeutic agents and the EGFR-TKI osimertinib induce calreticulin exposure in non-small cell lung cancer. *Lung Cancer* (2021) 155:144–50. doi: 10.1016/j.lungcan.2021.03.018

32. Galluzzi L, Vitale I, Aaronson SA, Abrams JM, Adam D, Agostinis P, et al. Molecular mechanisms of cell death: Recommendations of the nomenclature committee on cell death 2018. *Cell Death Differ* (2018) 25:486–541. doi: 10.1038/s41418-017-0012-4

33. Galluzzi L, Vitale I, Warren S, Adjemian S, Agostinis P, Martinez AB, et al. Consensus guidelines for the definition, detection and interpretation of immunogenic cell death. *J Immunother Cancer* (2020) 8(1):e000337. doi: 10.1136/jitc-2019-000337corr1

34. Galluzzi L, Buque A, Kepp O, Zitvogel L, Kroemer G. Immunogenic cell death in cancer and infectious disease. *Nat Rev Immunol* (2017) 17:97–111. doi: 10.1038/nri.2016.107

35. Kroemer G, Galassi C, Zitvogel L, Galluzzi L. Immunogenic cell stress and death. *Nat Immunol* (2022) 23:487–500. doi: 10.1038/s41590-022-01132-2

36. Elliott MR, Chekeni FB, Trampont PC, Lazarowski ER, Kadl A, Walk SF, et al. Nucleotides released by apoptotic cells act as a find-me signal to promote phagocytic clearance. *Nature* (2009) 461:282–6. doi: 10.1038/nature08296

37. Saez PJ, Vargas P, Shoji KF, Harcha PA, Lennon-Dumenil AM, Saez JC. ATP promotes the fast migration of dendritic cells through the activity of pannexin 1 channels and P2X7 receptors. *Sci Signal 10* (2017) 10:eaah7107. doi: 10.1126/scisignal.aah7107

38. Idzko M, Hammad H, van Nimwegen M, Kool M, Willart MA, Muskens F, et al. Extracellular ATP triggers and maintains asthmatic airway inflammation by activating dendritic cells. *Nat Med* (2007) 13:913–9. doi: 10.1038/nm1617

39. Kroemer G, Galluzzi L, Kepp O, Zitvogel L. Immunogenic cell death in cancer therapy. *Annu Rev Immunol* (2013) 31:51–72. doi: 10.1146/annurev-immunol-032712-100008

40. Yu Y, Feng S, Wei S, Zhong Y, Yi G, Chen H, et al. Extracellular ATP activates P2X7R-NF-kappaB (p65) pathway to promote the maturation of bone marrow-derived dendritic cells of mice. *Cytokine* (2019) 119:175–81. doi: 10.1016/j.cyto.2019.03.019

41. Wilkin F, Duhant X, Bruyns C, Suarez-Huerta N, Boeynaems JM, Robaye B. The P2Y11 receptor mediates the ATP-induced maturation of human monocyte-derived dendritic cells. *J Immunol* (2001) 166:7172–7. doi: 10.4049/jimmunol.166.12.7172

42. Ghiringhelli F, Apetoh L, Tesniere A, Aymeric L, Ma Y, Ortiz C, et al. Activation of the NLRP3 inflammasome in dendritic cells induces IL-1beta-dependent adaptive immunity against tumors. *Nat Med* (2009) 15:1170–8. doi: 10.1038/nm.2028

43. Zhang Y, Yang W, Li W, Zhao Y. NLRP3 inflammasome: Checkpoint connecting innate and adaptive immunity in autoimmune diseases. *Front Immunol* (2021) 12:732933. doi: 10.3389/fimmu.2021.732933

44. Garlanda C, Dinarello CA, Mantovani A. The interleukin-1 family: Back to the future. *Immunity* (2013) 39:1003–18. doi: 10.1016/j.immuni.2013.11.010

45. Di Virgilio F, Dal Ben D, Sarti AC, Giuliani AL, Falzoni S. The P2X7 receptor in infection and inflammation. *Immunity* (2017) 47:15–31. doi: 10.1016/j.immuni.2017.06.020

46. Panaretakis T, Joza N, Modjtahedi N, Tesniere A, Vitale I, Durchschlag M, et al. The co-translocation of ERp57 and calreticulin determines the immunogenicity of cell death. *Cell Death Different* (2008) 15:1499–509. doi: 10.1038/cdd.2008.67

47. Obeid M, Panaretakis T, Tesniere A, Joza N, Tufi R, Apetoh L, et al. Leveraging the immune system during chemotherapy: Moving calreticulin to the cell surface converts apoptotic death from "silent" to immunogenic. *Cancer Res* (2007) 67:7941–4. doi: 10.1158/0008-5472.CAN-07-1622

48. Liu P, Zhao L, Loos F, Marty C, Xie W, Martins I, et al. Immunosuppression by mutated calreticulin released from malignant cells. *Mol Cell* (2020) 77:748–760.e9. doi: 10.1016/j.molcel.2019.11.004

49. Chen R, Huang M, Yang X, Chen XH, Shi MY, Li ZF, et al. CALR-TLR4 complex inhibits non-small cell lung cancer progression by regulating the migration and maturation of dendritic cells. *Front Oncol* (2021) 11:743050. doi: 10.3389/fonc.2021.743050

50. Li R, Zou X, Huang H, Yu Y, Zhang H, Liu P, et al. HMGB1/PI3K/Akt/mTOR signaling participates in the pathological process of acute lung injury by regulating the maturation and function of dendritic cells. *Front Immunol* (2020) 11. doi: 10.3389/fimmu.2020.01104

51. Apetoh L, Ghiringhelli F, Tesniere A, Obeid M, Ortiz C, Criollo A, et al. Toll-like receptor 4-dependent contribution of the immune system to anticancer chemotherapy and radiotherapy. *Nat Med* (2007) 13:1050–9. doi: 10.1038/nm1622

52. Hubert P, Roncarati P, Demoulin S, Pilard C, Ancion M, Reynders C, et al. Extracellular HMGB1 blockade inhibits tumor growth through profoundly remodeling immune microenvironment and enhances checkpoint inhibitorbased immunotherapy. *J Immunother Cancer* (2021) 9(3):e001966. doi: 10.1136/jitc-2020-001966

53. Zhou L, Xu Q, Huang L, Jin J, Zuo X, Zhang Q, et al. Low-dose carboplatin reprograms tumor immune microenvironment through STING signaling pathway and synergizes with PD-1 inhibitors in lung cancer. *Cancer Lett* (2021) 500:163–71. doi: 10.1016/j.canlet.2020.11.049

54. Du B, Wen X, Wang Y, Lin M, Lai J. Gemcitabine and checkpoint blockade exhibit synergistic anti-tumor effects in a model of murine lung carcinoma. *Int Immunophar* (2020) 86:106694. doi: 10.1016/j.intimp.2020.106694

55. Lu CS, Lin CW, Chang YH, Chen HY, Chung WC, Lai WY, et al. Antimetabolite pemetrexed primes a favorable tumor microenvironment for immune checkpoint blockade therapy. *J Immunother Cancer* (2020) 8(2):e001392. doi: 10.1136/jitc-2020-001392

56. Fournel L, Wu Z, Stadler N, Damotte D, Lococo F, Boulle G, et al. Cisplatin increases PD-L1 expression and optimizes immune check-point blockade in non-small cell lung cancer. *Cancer Lett* (2019) 464:5–14. doi: 10.1016/j.canlet.2019.08.005

57. Zhou Y, Bastian IN, Long MD, Dow M, Li W, Liu T, et al. Activation of NF-kappaB and p300/CBP potentiates cancer chemoimmunotherapy through induction of MHC-I antigen presentation. *Proc Natl Acad Sci U.S.A.* (2021) 118(8):e2025840118. doi: 10.1073/pnas.2025840118

58. Okita R, Yukawa T, Nojima Y, Maeda A, Saisho S, Shimizu K, et al. MHC class I chain-related molecule a and b expression is upregulated by cisplatin and associated with good prognosis in patients with non-small cell lung cancer. *Cancer Immunol Immunother* (2016) 65:499–509. doi: 10.1007/s00262-016-1814-9

59. Ganesan AP, Johansson M, Ruffell B, Yagui-Beltran A, Lau J, Jablons DM, et al. Tumor-infiltrating regulatory T cells inhibit endogenous cytotoxic T cell responses to lung adenocarcinoma. *J Immunol* (2013) 191:2009–17. doi: 10.4049/jimmunol.1301317

60. Ye J, Zou MM, Li P, Lin XJ, Jiang QW, Yang Y, et al. Oxymatrine and cisplatin synergistically enhance anti-tumor immunity of CD8(+) T cells in non-small cell lung cancer. *Front Oncol* (2018) 8:631. doi: 10.3389/fonc.2018.00631

61. Leonetti A, Wever B, Mazzaschi G, Assaraf YG, Rolfo C, Quaini F, et al. Molecular basis and rationale for combining immune checkpoint inhibitors with chemotherapy in non-small cell lung cancer. *Drug Resist Update* (2019) 46:100644. doi: 10.1016/j.drup.2019.100644

62. Ghiringhelli F, Larmonier N, Schmitt E, Parcellier A, Cathelin D, Garrido C, et al. CD4+CD25+ regulatory T cells suppress tumor immunity but are sensitive to

cyclophosphamide which allows immunotherapy of established tumors to be curative. *Eur J Immunol* (2004) 34:336–44. doi: 10.1002/eji.200324181

63. Tongu M, Harashima N, Monma H, Inao T, Yamada T, Kawauchi H, et al. Metronomic chemotherapy with low-dose cyclophosphamide plus gemcitabine can induce anti-tumor T cell immunity in vivo. *Cancer Immunol Immunother* (2013) 62:383–91. doi: 10.1007/s00262-012-1343-0

64. Huang X, Huang G, Song H, Chen L. Preconditioning chemotherapy with paclitaxel and cisplatin enhances the antitumor activity of cytokine induced-killer cells in a murine lung carcinoma model. *Int J Cancer* (2011) 129:648–58. doi: 10.1002/ijc.25702

65. Zhang L, Dermawan K, Jin M, Liu R, Zheng H, Xu L, et al. Differential impairment of regulatory T cells rather than effector T cells by paclitaxel-based chemotherapy. *Clin Immunol* (2008) 129:219–29. doi: 10.1016/j.clim.2008.07.013

66. Zhong H, Lai Y, Zhang R, Daoud A, Feng Q, Zhou J, et al. Low dose cyclophosphamide modulates tumor microenvironment by TGF-beta signaling pathway. *Int J Mol Sci* (2020) 21(3):957. doi: 10.3390/ijms21030957

67. Laheurte C, Thiery-Vuillemin A, Calcagno F, Legros A, Simonin H, Boullerot L, et al. Metronomic cyclophosphamide induces regulatory T cells depletion and PSA-specific T cells reactivation in patients with biochemical recurrent prostate cancer. *Int J Cancer* (2020) 147:1199–205. doi: 10.1002/ijc.32803

68. Gabrilovich DI. Myeloid-derived suppressor cells. *Cancer Immunol Res* (2017) 5:3–8. doi: 10.1158/2326-6066.CIR-16-0297

69. Kumar V, Patel S, Tcyganov E, Gabrilovich DI. The nature of myeloid-derived suppressor cells in the tumor microenvironment. *Trends Immunol* (2016) 37:208–20. doi: 10.1016/j.it.2016.01.004

70. Zhang Y, Bush X, Yan B, Chen JA. Gemcitabine nanoparticles promote antitumor immunity against melanoma. *Biomaterials* (2019) 189:48–59. doi: 10.1016/j.biomaterials.2018.10.022

71. Kodumudi KN, Woan K, Gilvary DL, Sahakian E, Wei S, Djeu JY. A novel chemoimmunomodulating property of docetaxel: Suppression of myeloid-derived suppressor cells in tumor bearers. *Clin Cancer Res* (2010) 16:4583–94. doi: 10.1158/1078-0432.CCR-10-0733

72. Suzuki E, Kapoor V, Jassar AS, Kaiser LR, Albelda SM. Gemcitabine selectively eliminates splenic gr-1+/CD11b+ myeloid suppressor cells in tumor-bearing animals and enhances antitumor immune activity. *Clin Cancer Res* (2005) 11:6713–21. doi: 10.1158/1078-0432.CCR-05-0883

73. Vincent J, Mignot G, Chalmin F, Ladoire S, Bruchard M, Chevriaux A, et al. 5-fluorouracil selectively kills tumor-associated myeloid-derived suppressor cells resulting in enhanced T cell-dependent antitumor immunity. *Cancer Res* (2010) 70:3052–61. doi: 10.1158/0008-5472.CAN-09-3690

74. Eriksson E, Wenthe J, Irenaeus S, Loskog A, Ullenhag G. Gemcitabine reduces MDSCs, tregs and TGFbeta-1 while restoring the teff/treg ratio in patients with pancreatic cancer. *J Transl Med* (2016) 14:282. doi: 10.1186/s12967-016-1037-z

75. Peereboom DM, Alban TJ, Grabowski MM, Alvarado AG, Otvos B, Bayik D, et al. Metronomic capecitabine as an immune modulator in glioblastoma patients reduces myeloid-derived suppressor cells. *JCI Insight* (2019) 4(22):e130748. doi: 10.1172/jci.insight.130748

76. Li XM, Zhang XM, Li JY, Jiang N, Chen L, Tang LL, et al. The immune modulation effects of gemcitabine plus cisplatin induction chemotherapy in nasopharyngeal carcinoma. *Cancer Med* (2022) 11:3437–44. doi: 10.1002/cam4.4705

77. Glorieux C, Xia X, You X, Wang Z, Han Y, Yang J, et al. Cisplatin and gemcitabine exert opposite effects on immunotherapy with PD-1 antibody in K-ras-driven cancer. *J Adv Res* (2022) 40:109–24. doi: 10.1016/j.jare.2021.12.005

78. Gao Q, Wang S, Chen X, Cheng S, Zhang Z, Li F, et al. Cancer-cell-secreted CXCL11 promoted CD8(+) T cells infiltration through docetaxel-induced-release of HMGB1 in NSCLC. *J Immunother Cancer* (2019) 7:42. doi: 10.1186/s40425-019-0511-6

79. Fang Y, Sun H, Xiao X, Tang M, Tian Z, Wei H, et al. Low-dose immunogenic chemotherapeutics promotes immune checkpoint blockade in microsatellite stability colon cancer. *Front Immunol* (2022) 13:1040256. doi: 10.3389/fimmu.2022.1040256

80. Cascone T, Sepesi B, Lin HY, Kalhor N, Parra ER, Jiang M, et al. A phase I/II study of neoadjuvant cisplatin, docetaxel, and nintedanib for resectable non-small cell lung cancer. *Clin Cancer Res* (2020) 26:3525–36. doi: 10.1158/1078-0432.CCR-19-4180

81. Xin M, Lin D, Yan N, Li H, Li J, Huang Z. Oxaliplatin facilitates tumor-infiltration of T cells and natural-killer cells for enhanced tumor immunotherapy in lung cancer model. *Anticancer Drugs* (2022) 33:117–23. doi: 10.1097/CAD.0000000000001248

82. Karin N. CXCR3 ligands in cancer and autoimmunity, chemoattraction of effector T cells, and beyond. *Front Immunol* (2020) 11:976. doi: 10.3389/fimmu.2020.00976

83. Agostini C, Calabrese F, Rea F, Facco M, Tosoni A, Loy M, et al. CXCR3 and its ligand CXCL10 are expressed by inflammatory cells infiltrating lung allografts and mediate chemotaxis of T cells at sites of rejection. *Am J Pathol* (2001) 158:1703–11. doi: 10.1016/S0002-9440(10)64126-0

84. Gaudreau PO, Negrao MV, Mitchell KG, Reuben A, Corsini EM, Li J, et al. Neoadjuvant chemotherapy increases cytotoxic T cell, tissue resident memory T cell, and b cell infiltration in resectable NSCLC. *J Thorac Oncol* (2021) 16:127–39. doi: 10.1016/j.jtho.2020.09.027

85. Edwards J, Wilmott JS, Madore J, Gide TN, Quek C, Tasker A, et al. CD103 (+) tumor-resident CD8(+) T cells are associated with improved survival in immunotherapy-naive melanoma patients and expand significantly during anti-PD-1 treatment. *Clin Cancer Res* (2018) 24:3036–45. doi: 10.1158/1078-0432.CCR-17-2257

86. Djenidi F, Adam J, Goubar A, Durgeau A, Meurice G, de Montpreville V, et al. CD8+CD103+ tumor-infiltrating lymphocytes are tumor-specific tissue-resident memory T cells and a prognostic factor for survival in lung cancer patients. *J Immunol* (2015) 194:3475–86. doi: 10.4049/jimmunol.1402711

87. Ganesan AP, Clarke J, Wood O, Garrido-Martin EM, Chee SJ, Mellows T, et al. Tissue-resident memory features are linked to the magnitude of cytotoxic T cell responses in human lung cancer. *Nat Immunol* (2017) 18:940–50. doi: 10.1038/ni.3775

88. Mami-Chouaib F, Tartour E. Editorial: Tissue resident memory T cells. *Front Immunol* (2019) 10:1018. doi: 10.3389/fimmu.2019.01018

89. Merritt RE, Mahtabifard A, Yamada RE, Crystal RG, Korst RJ. Cisplatin augments cytotoxic t-lymphocyte–mediated antitumor immunity in poorly immunogenic murine lung cancer. *J Thorac Cardiovasc Surg* (2003) 126:1609–17. doi: 10.1016/S0022-5223(03)00707-4

90. Ma Y, Mattarollo SR, Adjemian S, Yang H, Aymeric L, Hannani D, et al. CCL2/CCR2-dependent recruitment of functional antigen-presenting cells into tumors upon chemotherapy. *Cancer Res* (2014) 74:436–45. doi: 10.1158/0008-5472.CAN-13-1265

91. Ma Y, Adjemian S, Mattarollo SR, Yamazaki T, Aymeric L, Yang H, et al. Anticancer chemotherapy-induced intratumoral recruitment and differentiation of antigen-presenting cells. *Immunity* (2013) 38:729–41. doi: 10.1016/j.immuni.2013.03.003

92. Bernal-Estevez DA, Garcia O, Sanchez R, Parra-Lopez CA. Monitoring the responsiveness of T and antigen presenting cell compartments in breast cancer patients is useful to predict clinical tumor response to neoadjuvant chemotherapy. *BMC Cancer* (2018) 18:77. doi: 10.1186/s12885-017-3982-1

93. Tan Y, Chen H, Zhang J, Cai L, Jin S, Song D, et al. Platinum(IV) complexes as inhibitors of CD47-SIRPalpha axis for chemoimmunotherapy of cancer. *Eur J Med Chem* (2022) 229:114047. doi: 10.1016/j.ejmech.2021.114047

94. Lian S, Xie R, Ye Y, Xie X, Li S, Lu Y, et al. Simultaneous blocking of CD47 and PD-L1 increases innate and adaptive cancer immune responses and cytokine release. *EBioMedicine* (2019) 42:281–95. doi: 10.1016/j.ebiom.2019.03.018

95. Salmon H, Idoyaga J, Rahman A, Leboeuf M, Remark R, Jordan S, et al. Expansion and activation of CD103(+) dendritic cell progenitors at the tumor site enhances tumor responses to therapeutic PD-L1 and BRAF inhibition. *Immunity* (2016) 44:924–38. doi: 10.1016/j.immuni.2016.03.012

96. Spranger S, Bao R, Gajewski TF. Melanoma-intrinsic beta-catenin signalling prevents anti-tumour immunity. *Nature* (2015) 523:231–5. doi: 10.1038/nature14404

97. Duraiswamy J, Turrini R, Minasyan A, Barras D, Crespo I, Grimm AJ, et al. Myeloid antigen-presenting cell niches sustain antitumor T cells and license PD-1 blockade *via* CD28 costimulation. *Cancer Cell* (2021) 39:1623–1642.e20. doi: 10.1016/j.ccell.2021.10.008

98. Gardner A, de Mingo Pulido A, Ruffell B. Dendritic cells and their role in immunotherapy. *Front Immunol* (2020) 11:924. doi: 10.3389/fimmu.2020.00924

99. de Mingo Pulido A, Gardner A, Hiebler S, Soliman H, Rugo HS, Krummel MF, et al. TIM-3 regulates CD103(+) dendritic cell function and response to chemotherapy in breast cancer. *Cancer Cell* (2018) 33:60–74.e6. doi: 10.1016/j.ccell.2017.11.019

100. Chow MT, Ozga AJ, Servis RL, Frederick DT, Lo JA, Fisher DE, et al. Intratumoral activity of the CXCR3 chemokine system is required for the efficacy of anti-PD-1 therapy. *Immunity* (2019) 50:1498–1512.e5. doi: 10.1016/j.immuni.2019.04.010

101. Hanahan D, Weinberg RA. Hallmarks of cancer: the next generation. *Cell* (2011) 144:646–74. doi: 10.1016/j.cell.2011.02.013

102. Cascone T, McKenzie JA, Mbofung RM, Punt S, Wang Z, Xu C, et al. Increased tumor glycolysis characterizes immune resistance to adoptive T cell therapy. *Cell Metab* (2018) 27:977–987 e4. doi: 10.1016/j.cmet.2018.02.024

103. Renner K, Singer K, Koehl GE, Geissler EK, Peter K, Siska PJ, et al. Metabolic hallmarks of tumor and immune cells in the tumor microenvironment. *Front Immunol* (2017) 8. doi: 10.3389/fimmu.2017.00248

104. Ma Y, Yang H, Pitt JM, Kroemer G, Zitvogel L. Therapy-induced microenvironmental changes in cancer. *J Mol Med (Berl)* (2016) 94:497–508. doi: 10.1007/s00109-016-1401-8

105. Buck MD, O'Sullivan D, Pearce EL. T Cell metabolism drives immunity. *J Exp Med* (2015) 212:1345–60. doi: 10.1084/jem.20151159

106. Tan H, Yang K, Li Y, Shaw TI, Wang Y, Blanco DB, et al. Integrative proteomics and phosphoproteomics profiling reveals dynamic signaling networks and bioenergetics pathways underlying T cell activation. *Immunity* (2017) 46:488–503. doi: 10.1016/j.immuni.2017.02.010

107. McCoy KD, Mager LF. Impact of the microbiome on tumor immunity. *Curr Opin Immunol* (2021) 69:39–46. doi: 10.1016/j.coi.2021.01.002

108. Jin Y, Dong H, Xia L, Yang Y, Zhu Y, Shen Y, et al. The diversity of gut microbiome is associated with favorable responses to anti-programmed death 1 immunotherapy in Chinese patients with NSCLC. *J Thorac Oncol* (2019) 14:1378–89. doi: 10.1016/j.jtho.2019.04.007

109. Gopalakrishnan V, Spencer CN, Nezi L, Reuben A, Andrews MC, Karpinets TV, et al. Gut microbiome modulates response to anti-PD-1 immunotherapy in melanoma patients. *Science* (2018) 359:97–103. doi: 10.1126/science.aan4236

110. Peng Z, Cheng S, Kou Y, Wang Z, Jin R, Hu H, et al. The gut microbiome is associated with clinical response to anti-PD-1/PD-L1 immunotherapy in gastrointestinal cancer. *Cancer Immunol Res* (2020) 8:1251–61. doi: 10.1158/2326-6066.CIR-19-1014

111. Pensec C, Gillaizeau F, Guenot D, Bessard A, Carton T, Leuillet S, et al. Impact of pemetrexed chemotherapy on the gut microbiota and intestinal inflammation of patient-lung-derived tumor xenograft (PDX) mouse models. *Sci Rep* (2020) 10:9094. doi: 10.1038/s41598-020-65792-6

112. Viaud S, Saccheri F, Mignot G, Yamazaki T, Daillere R, Hannani D, et al. The intestinal microbiota modulates the anticancer immune effects of cyclophosphamide. *Science* (2013) 342:971–6. doi: 10.1126/science.1240537

113. Gandhi L, Rodriguez-Abreu D, Gadgeel S, Esteban E, Felip E, De Angelis F, et al. Pembrolizumab plus chemotherapy in metastatic non-Small-Cell lung cancer. *N Engl J Med* (2018) 378:2078–92. doi: 10.1056/NEJMoa1801005

114. Burtness B, Harrington KJ, Greil R, Soulières D, Tahara M, de Castro G, et al. Pembrolizumab alone or with chemotherapy versus cetuximab with chemotherapy for recurrent or metastatic squamous cell carcinoma of the head and neck (KEYNOTE-048): a randomised, open-label, phase 3 study. *Lancet* (2019) 394:1915–28. doi: 10.1016/S0140-6736(19)32591-7

115. Leduc C, Adam J, Louvet E, Sourisseau T, Dorvault N, Bernard M, et al. TPF induction chemotherapy increases PD-L1 expression in tumour cells and immune cells in head and neck squamous cell carcinoma. *ESMO Open* (2018) 3:e000257. doi: 10.1136/esmoopen-2017-000257

116. Jotte R, Cappuzzo F, Vynnychenko I, Stroyakovskiy D, Rodriguez-Abreu D, Hussein M, et al. Atezolizumab in combination with carboplatin and nab-paclitaxel in advanced squamous NSCLC (IMpower131): Results from a randomized phase III trial. *J Thorac Oncol* (2020) 15:1351–60. doi: 10.1016/j.jtho.2020.03.028

117. Liu M, Tayob N, Penter L, Sellars M, Tarren A, Chea V, et al. Improved T-cell immunity following neoadjuvant chemotherapy in ovarian cancer. *Clin Cancer Res* (2022) 28:3356–66. doi: 10.1158/1078-0432.CCR-21-2834

118. Hoffner B, Leighl NB, Davies M. Toxicity management with combination chemotherapy and programmed death 1/programmed death ligand 1 inhibitor therapy in advanced lung cancer. *Cancer Treat Rev* (2020) 85:101979. doi: 10.1016/j.ctrv.2020.101979

119. Schmid P, Salgado R, Park YH, Munoz-Couselo E, Kim SB, Sohn J, et al. Pembrolizumab plus chemotherapy as neoadjuvant treatment of high-risk, early-stage triple-negative breast cancer: Results from the phase 1b open-label, multicohort KEYNOTE-173 study. *Ann Oncol* (2020) 31:569–81. doi: 10.1016/j.annonc.2020.01.072

120. Hu F, Zhai Y, Yuan L, Liang J, Xu J, Guo X, et al. Renal toxicities in immune checkpoint inhibitors with or without chemotherapy: An observational, retrospective, pharmacovigilance study leveraging US FARES database. *Cancer Med* (2021) 10:8754–62. doi: 10.1002/cam4.4343

121. Cui W, Luo Q, Sun SL, Xu JL, Gu H. Efficacy and safety of PD-1/PD-L1 inhibitors plus chemotherapy for triple-negative breast cancer: A systematic review and meta-analysis. *Recenti Prog Med* (2022) 113:722–32. doi: 10.1701/3914.38974

122. Segal EM. Immunotherapy in the frontline management of advanced and metastatic NSCLC. *Am J Manag Care* (2021) 27:S323–32. doi: 10.37765/ajmc.2021.88769

123. Leong TL, Bryant VL. B cells in lung cancer-not just a bystander cell: A literature review. *Transl Lung Cancer Res* (2021) 10:2830–41. doi: 10.21037/tlcr-20-788

124. Ziebart A, Huber U, Jeske S, Laban S, Doescher J, Hoffmann TK, et al. The influence of chemotherapy on adenosine-producing b cells in patients with head and neck squamous cell carcinoma. *Oncotarget* (2018) 9:5834–47. doi: 10.18632/oncotarget.23533

125. Barrett RL, Pure E. Cancer-associated fibroblasts and their influence on tumor immunity and immunotherapy. *Elife* (2020) 9:e57243. doi: 10.7554/eLife.57243

126. Barrett R, Pure E. Cancer-associated fibroblasts: Key determinants of tumor immunity and immunotherapy. *Curr Opin Immunol* (2020) 64:80–7. doi: 10.1016/j.coi.2020.03.004

127. Kato T, Noma K, Ohara T, Kashima H, Katsura Y, Sato H, et al. Cancer-associated fibroblasts affect intratumoral CD8(+) and FoxP3(+) T cells *Via* IL6 in the tumor microenvironment. *Clin Cancer Res* (2018) 24:4820–33. doi: 10.1158/1078-0432.CCR-18-0205

128. Remsing Rix LL, Sumi NJ, Hu Q, Desai B, Bryant AT, Li X, et al. IGF-binding proteins secreted by cancer-associated fibroblasts induce context-dependent drug sensitization of lung cancer cells. *Sci Signal* (2022) 15:eabj5879. doi: 10.1126/scisignal.abj5879

129. Ershaid N, Sharon Y, Doron H, Raz Y, Shani O, Cohen N, et al. NLRP3 inflammasome in fibroblasts links tissue damage with inflammation in breast cancer progression and metastasis. *Nat Commun* (2019) 10:4375. doi: 10.1038/s41467-019-12370-8

130. Iida Y, Harashima N, Motoshima T, Komohara Y, Eto M, Harada M. Contrasting effects of cyclophosphamide on anti-CTL-associated protein 4 blockade therapy in two mouse tumor models. *Cancer Sci* (2017) 108:1974–84. doi: 10.1111/cas.13337

131. Kang DH, Choi SW, Sun P, Chung C, Park D, Lee SI, et al. The rest period between chemotherapy and immunotherapy influences the efficacy of immune checkpoint inhibitors in lung cancer. *Thorac Cancer* (2022) 13:2346–54. doi: 10.1111/1759-7714.14568

132. Fu D, Wu J, Lai J, Liu Y, Zhou L, Chen L, et al. T Cell recruitment triggered by optimal dose platinum compounds contributes to the therapeutic efficacy of sequential PD-1 blockade in a mouse model of colon cancer. *Am J Cancer Res* (2020) 10:473–90.

133. Ghiringhelli F, Menard C, Puig PE, Ladoire S, Roux S, Martin F, et al. Metronomic cyclophosphamide regimen selectively depletes CD4+CD25+ regulatory T cells and restores T and NK effector functions in end stage cancer patients. *Cancer Immunol Immunother* (2007) 56:641–8. doi: 10.1007/s00262-006-0225-8

134. Ahlmann M, Hempel G. The effect of cyclophosphamide on the immune system: implications for clinical cancer therapy. *Cancer Chemother Pharmacol* (2016) 78:661–71. doi: 10.1007/s00280-016-3152-1

135. Wu J, Waxman DJ. Immunogenic chemotherapy: Dose and schedule dependence and combination with immunotherapy. *Cancer Lett* (2018) 419:210–21. doi: 10.1016/j.canlet.2018.01.050

frontiers | Frontiers in Immunology

TYPE Mini Review
PUBLISHED 02 February 2023
DOI 10.3389/fimmu.2023.1084926

Check for updates

OPEN ACCESS

EDITED BY
Jian Zhang,
Southern Medical University, China

REVIEWED BY
Zhengrui Li,
Shanghai Jiao Tong University, China
Valerio Iebba,
University of Trieste, Italy
Maryam Tidjani Alou,
Aix Marseille Université, France

*CORRESPONDENCE
Jinzhong Cai
c2000jz@tom.com
Yuqi Liu
825580357@qq.com

SPECIALTY SECTION
This article was submitted to Cancer Immunity and Immunotherapy, a section of the journal Frontiers in Immunology

RECEIVED 31 October 2022
ACCEPTED 24 January 2023
PUBLISHED 02 February 2023

CITATION
Zheng H, Chen X, Li Q, Liu Y and Cai J (2023) Effects of chemotherapy and immunotherapy on microbial diversity in TME and engineered bacterial-mediated tumor therapy.
Front. Immunol. 14:1084926.
doi: 10.3389/fimmu.2023.1084926

COPYRIGHT
© 2023 Zheng, Chen, Li, Liu and Cai. This is an open-access article distributed under the terms of the Creative Commons Attribution License (CC BY). The use, distribution or reproduction in other forums is permitted, provided the original author(s) and the copyright owner(s) are credited and that the original publication in this journal is cited, in accordance with accepted academic practice. No use, distribution or reproduction is permitted which does not comply with these terms.

Effects of chemotherapy and immunotherapy on microbial diversity in TME and engineered bacterial-mediated tumor therapy

Heng Zheng[1,2], Xianxian Chen[3], Qiyang Li[3], Yuqi Liu[3]* and Jinzhong Cai[1,3]*

[1]School of Chemistry, Chemical Engineering and Life Sciences, Wuhan University of Technology, Wuhan, China, [2]School of Resources and Environmental Engineering, Wuhan University of Technology, Wuhan, China, [3]Department of Interventional Radiology, Shenzhen People's Hospital (The First Affiliated Hospital, Southern University of Science and Technology), Shenzhen, China

Tumor microbiota is a group of microorganisms located in tumor tissues with rich diversity that can promote tumorigenesis and development, and different types of tumors have different tumor microbiotas, which has important implications for tumor research, detection, and clinical treatment. In this review, we examine the diversity of the tumor microbiota, discuss the impact of chemotherapy and immunotherapy on tumor microbiota diversity, and summarize recent advances in the use of genetically engineered bacteria for the treatment of tumors. In addition, we propose key questions that need to be further addressed by the tumor microbiota.

KEYWORDS

tumor, microbiome, chemotherapy, immunotherapy, engineered bacteria

1 Introduction

The cancer is a major global health issue. In the past, tumorigenesis and microbial infection were considered as independent diseases from each other, since the discovery of bacteria in tumor tissues, it has revolutionized the perception of the relationship between microorganisms and tumors. Microorganisms exist in the tumor microenvironment (TME), which are located inside tumor tissues or in tumor cells, and they differ between healthy populations and cancer patients. The relationship between the microorganisms and the tumor cells (or other parts of the TME) is most likely a symbiotic relationship, rather than a simple positional one. Tumors can create more suitable conditions for microorganisms to survive and reshape the microbial spectrum, and at the same time, microorganisms can also promote tumorigenesis and progression by establishing an inflammatory environment and influencing host immunity(1). Fu et al. showed that bacteria within breast tumor cells contribute to cancer cell metastasis, in part by enhancing tumor cell survival in response to mechanical fluid shear stress(2). Prostate cancer is a malignant tumor and its occurrence and progression are influenced by a variety of factors, including ethnicity, and a growing number

of studies have confirmed that the prostate microbiota(it may come from urinary tract flora and intestinal flora) may play an important role in the occurrence, progression, and prognosis of prostate cancer, and that microorganisms and their metabolites influence the occurrence and metastasis of cancer cells (3). In addition, there is a close correlation between some systemic diseases and microbiota. For example, patients with oral cancer had a more enriched oral microbiota composition in precancerous lesions, and at the genus level, the main differentially enriched taxa were *Prevotella*, and *Carnobacterium*, *Peptostreptococcus*($P<0.05$)(4). Gut microbiota plays an important role in colorectal carcinogenesis, and *Bacteroides fragilis*, *Helicobacter pylori*, *Peptostreptococcus anaerobius*, Sulfate-reducing bacteria, and *Fusobacterium nucleatum* can mediate cancer development (5).

The microorganisms present in the TME (e.g. viruses, bacteria, fungi and protozoa), regulate the TME in a species-dependent manner due to the specific physiological and pathological characteristics of each microorganism, thereby inhibiting or promoting tumor growth (6). Recent studies of cancer-associated microbial communities have enriched the body of knowledge on the interactions between microorganisms, the immune system, and tumor cells.

Microbial communities that have an impact on tumor progression and are associated with tumors are defined as the tumor microbiota, but this article focuses on microbes between tumor tissues. For example, studies of bacteria in the induction of lung cancer have been largely neglected, and although there is a correlation between lung cancer and the lung microbiota, and the effect of microbes on lung cancer progression has been much confirmed, little is known about the underlying mechanisms. Microorganisms can promote tumorigenesis and progression through the production of toxins(such as Cytolethal distending toxin, cytotoxic necrotizing factor 1, and *Bacteroides fragilis* toxin) and other pro-inflammatory factors(7). The human microbiome is composed of different microorganisms that play important roles in processes such as metabolism and host defense, and high-throughput sequencing technologies can contribute to a broader understanding of microbial composition and diversity. Through high-throughput sequencing, microorganisms in TME can be comprehensively identified, and in the future, these microorganisms can be used as effective probes, monitors, drugs. Therefore, understanding the tumor microbiota is important for clinical care and research of tumors.

Emerging evidence suggests many roles for the microbiota in tumors, including immune responses to tumors, Effects to the TME, and alterations of the microbiota by chemotherapy. The balance of the microbiota in normal tissues helps to defend against tissue lesions, microbiota in TME will influence tumor development and treatment, and a comprehensive understanding of the tumor microbiota will improve the way cancer patients use anticancer drugs. Although the relationship between the microbiota and cancer has made significant progress in the past, however, the relationship between bacteria within tumors and cancer is unclear. A growing body of evidence suggests that intratumoral bacteria are an important component of the cancer microenvironment and that they may directly influence tumorigenesis, progression, and treatment, as well as modulate innate and adaptive immunity to potentially influence tumor immunotherapy(8). Furthermore, the interaction of the tumor microbiota with TME has recently been mimicked, making related microbes potentially powerful cancer therapeutic agents. Bacteria have been used as anticancer agents since the 19th century, when William B. Coley used *Streptococcus pyogenes* to successfully heal patients with inoperable sarcomas(9). With the development of synthetic biology, several bacteria have been genetically engineered and their applicability for cancer treatment has increased significantly. Compared to other therapeutic approaches, genetically engineered bacteria for cancer treatment have unique properties in that they can specifically accumulate within tumors and inhibit cancer growth(10). In addition, genetically engineered bacteria can be combined with materials, used as carriers for delivering antitumor drugs, or used in combination with radiotherapy to improve the effectiveness of cancer treatment.

2 Microbial diversity in TME

Cancer is a series of genetic changes that transform normal cells into tumor cells, caused by biological, chemical or physical factors, including the microbiota. The link between microbial species and cancer is mainly stimulated by immune responses in tumor cells, such as inflammation induction. The association between bacteria and cancer has recently been found to be through two mechanisms, the first stimulating chronic inflammation and the second producing oncogenic metabolites (11). Conventional cancer treatments include chemotherapy, radiotherapy, surgery, and immunotherapy, which increase the chances of survival of patients, but these therapies are associated with many side effects, including high toxicity to tissues and normal cells.

Poore et al. (12) analyzed nucleic acid sequences from human cancers, adjacent tissue samples and blood samples to reveal the microorganisms present in various tumors. They used The Cancer Genome Atlas (TCGA) to analyze data from 33 cancer types, with a total of more than 17,000 samples from about 10,000 patients, and they used multiple computational methods, including independently trained artificial intelligence models, to filter, normalize, and classify microbial sequences in these samples, resulting in findings that approximately one-third mapped to known bacterial, archaeal, or viral sequences. By training machine learning models, the above microbial sequences can be used to differentiate cancer types, and cancerous versus normal tissue. In addition, *Clostridium perfringens* was found in gastrointestinal tumors, and viruses such as Metapneumovirus and Hepatovirus were found in cervical, head and neck, and liver cancers. Poore et al. also analyzed the characteristics of microorganisms in the blood of cancer patients, and showed that blood-borne microbial DNA can be used to distinguish between cancer types. The tumor microbiota can be classified according to the habitat of microorganisms in TME, which can be divided into commensal microbial enrichment (esophagus, oral cavity, colon, etc.) and acquired microbial enrichment (lung, liver, breast, etc.). The microbial diversity in different tumors is shown in Table 1.

TABLE 1 Statistical table of microbial diversity of different tumor types.

Cancer Type	Microbial diversity	Reference
Breast tumors	*Pseudomonas* sp., *Brevundimonas*, *Staphylococcus*, *Pseudomonas aeruginosa*	13
Pancreatic ductal adenocarcinoma	Enterobacteriaceae	14
Esophageal squamous cell carcinoma	Proteobacteria, Firmicutes, Bacteroidetes, *Deinococcus-Thermus*, *Actinobacteria*, *Streptococcus*, *Labrys*; *Rhodotorula mucilaginosa*, *Porphyromonas endodontalis*, *Neisseria subflava*, *H.pylori*, *Acinetobacter parahaemolyticus*, *Acinetobacter rhizosphaerae*	15, 16
Colorectal cancer	*Actinomyces*, *Schaalia cardiffensis*, Bacteroidia, Gammaproteobacteria, *Pseudomonas*, *Actinomycetes*; Firmicutes, Bacteroidetes, Proteobacteria	17, 18
Pancreatic cancer	*Pseudoxanthomonas*, *Streptomyces*, *Saccharopolyspora*, *Bacillus clausii*	19
Lung cancer	*Veillonella*, *Megasphaera* sp.; *Modestobacter*, *Propionibacterium*, *Enterobacteriaceae*	20, 21
Hepatocellular carcinoma	Bacteroidetes, Firmicutes, Proteobacteria, *Bacteroides*, *Romboutsia* and uncultured bacterium of *Lachnospiraceae*	22
Carcinoma of the anus	*Clostridia*, *Clostridiales*, *Actinobacteria*	23

2.1 Congenital microbial enrichment

Esophageal squamous cell carcinoma(ESCC) is a disease of high malignancy. Shen et al. (15) analyzed the microbial community structure and differences in tumor tissues and adjacent non-tumor tissues of 51 patients with esophageal squamous cell carcinoma by 16S rDNA sequencing and showed that Proteobacteria, Firmicutes, Bacteroidetes, *Deinococcus-Thermus* and *Actinobacteria* were the predominant bacteria in tumor tissues and adjacent non-tumor tissues. At the genus level, *Streptococcus*(median relative abundance of 6.39%) and *Labrys*(median relative abundance of 11.1%) were the bacteria with the highest relative proportions in tumor and adjacent non-tumor tissues. *Labrys* mostly exists in the natural environment, and its high abundance might be a contamination or an artifact. In addition, the complexity of microbial interactions in tumor tissues was weaker than in adjacent non-tumor tissues, with 24 taxa of microorganisms statistically different between tumor and adjacent non-tumor tissues, and lipopolysaccharides were more significant in the synthesis and metabolism of the tumor tissue microbiota. Using the same method, Yang et al. investigated the esophageal microbiota of 18 ESCC patients and 11 physiologically normal (PN) esophageal patients and found that the composition of the microbiota in the tumor tissues of ESCC patients was significantly different from that of PN patients. The ESCC microbiota was characterized by reduced microbial diversity and decreased abundance of Bacteroidetes, Fusobacteria and Spirochetes. In addition, the inclusion of these taxa in the microbial dysbiosis index distinguished well between the ESCC and PN groups. Functional analysis showed that the nitrate reductase and nitrite reductase functions were altered in the ESCC microbiota compared to the PN group, for reasons that need to be further investigated (24). In addition, esophageal microbiota may influence the pathophysiology of ESCC. 16S rRNA sequencing of samples from esophageal tumor tissues and tumor-adjacent tissues of 120 ESCC patients resulted in the detection of 56 taxa with different abundances, such as *Rhodotorula mucilaginosa*, *Porphyromonas endodontalis*, *Neisseria subflava*, *H.pylori*, *Acinetobacter parahaemolyticus*, and *Acinetobacter rhizosphaerae*. Microbial diversity and composition of ESCC tumor tissues were significantly different from tumor-adjacent tissues, and this inter-subjective beta-diversity variation was mainly caused by region and sampling season. Quantitative PCR showed a higher species abundance of *P.endodontalis* and a lower abundance of *H.pylori* in tumor-adjacent tissues. In addition, denser and more complex association networks were formed in tumor-adjacent tissues than in tumor-adjacent tissues. In addition, alterations in microbial symbiotic networks and functional pathways in ESCC tissues may be involved in the oncogenic process of the local microenvironment of ESCC (16).

In addition to lung cancer, the third most common form of cancer is colorectal cancer (CRC), and the incidence of sporadic young adult colorectal cancer (yCRC) has been increasing. Xu et al. (18) found microbiota differences between yCRC patients and patients with old-onset colorectal cancer(oCRC). 16S rRNA sequencing analysis revealed decreased tumor microbial α diversity in yCRC, suggesting the presence of microbial community dysbiosis in yCRC. At the genus level, two microbiota were enriched in yCRC patients compared to the oCRC group: *Enterococci* and *Castellaniella*. *Castellaniella* mostly exists in the intestinal environment, and its high concentration might be a contamination or an artifact. Among all yCRC samples, Proteobacteria being the most abundant phylum, while *Actinomyces* and *Schaalia cardiffensis* were the key microbiota in the yCRC group. Correlation analysis revealed that *Actinomyces* coexisted with various tumor-promoting microbial taxa, including *Bacteroidia*, *Gammaproteobacteria* and *Pseudomonas*. This is because *Actinomycetes* in yCRC co-localized with cancer-associated fibroblasts and activated the TLR2/NF-kappa B pathway, reducing CD8+T lymphocyte infiltration in the yCRC microenvironment. The tumor microbiota plays an important role in promoting tumorigenesis and thus has the potential to be a non-invasive tool and target of intervention for antitumor therapy. Although the relevance of the gut microbiota to checkpoint immunotherapy has been thoroughly explored, there are few data on the local tumor microbiota. Boesch et al. used 16S rRNA gene amplicon sequencing to characterize the molecular profile of patients treated with PD-1/PD-L1-targeted checkpoint inhibitors. The results showed a significant

diversity of tumor microbiota, with high proportions of Firmicutes, Bacteroidetes and Proteobacteria. Combined with clinical data, high microbial diversity was associated with improved patient survival. Furthermore, the presence of γ-proteobacteria was associated with low PD-L1 expression and poor response to checkpoint-based immunotherapy, which translated into poor survival. Thus, new microbiota-specific/derived biomarkers could be used for the prediction and prognosis of immune checkpoint therapies (17).

Which microorganisms are functionally active in the endometrium of patients with endometrial cancer (EC) and how the human host responds to functionally active microorganisms? More than 5,000 functionally active microorganisms were described by metatranscriptomic analysis in 9 endometrial cancer patients and 8 normal individuals, and differences in microorganisms between the EC and normal groups were analyzed. The results revealed that these microorganisms are involved in some of the metabolic processes of endometrial cancer, such as 6-sulfosalicylic acid Lewis x epitope, and N-acetyl-β-glucosaminyl. In addition, the host-microbiota crosstalk in endometrial cancer includes many biological processes, mainly functions related to tumor migration and Apelin signaling pathway. *Pannonibacter phragmitetus* with high abundance in EC endometrium was significantly and positively correlated with Wnt signaling pathway, IL-17 signaling pathway and MAPK signaling pathway. In conclusion, functionally active microorganisms in EC endometrium play a crucial role in tumorigenesis and migration, and their role in the treatment of endometrial cancer cannot be ignored (25).

2.2 Acquired microbial enrichment

One-fifth of cancers are attributed to infectious agents, usually viruses, followed by parasites and bacteria (26). There is a growing number of evidence that changes in microbial communities influence cancer development as well as treatment. By analyzing microbial sequences from head and neck squamous cell carcinoma (HNSC), hepatocellular carcinoma of the liver (LIHC), and gastric adenocarcinoma (STAD), bacterial diversity within cancer samples was found to be related with the survival rate of associated cancers, and varies by tissue type and is dependent on interactions with gender and race (27). Patients with pancreatic cancer (PDAC) resection survive for less than 5 years, but a small percentage survive longer, by dissecting the role of PDAC tumor microbiota and immune system in influencing long-term survival. Using 16S rRNA sequencing, the tumor microbiota of PDAC patients with short-term survival and long-term survival were analyzed, and the results showed that long-term patients have a higher alpha diversity in their tumor microbiota, and that *Pseudoxanthomonas-Streptomyces-Saccharopolyspora-Bacillus clausii* can be used as a tumor microbiota signature that is highly predictive of long-term survival. Immediately following the human-mouse fecal microbiota transplantation experiment, it was found that cross-linking of the PDAC microbiota with the gut microbiota influences the host immune response and disease (19).

Lung cancer is one of the most common cancers and the impact of the bacterial flora in the lung microenvironment on lung cancer development and progression is not yet clear. The pathogenesis and progression of lung cancer are associated with increased respiratory bacterial loads and changes in bacterial communities, due to the fact that the microbiota affects tumors in multiple ways, including carcinogenesis, metastasis, angiogenesis, and therapy. The microbiota may enhance tumor susceptibility by altering metabolic, promoting inflammation, and facilitating immune responses. The microbiota(such as *Haemophilus influenzae*, *Morganella morganii*, and *Escherichia fergusonii*) may also modulate tumor metastasis by altering multiple cellular signaling pathways and participate in tumor angiogenesis through vascular endothelial growth factor (VEGF), endothelial cells (EC), inflammatory factors and inflammatory cells (28). Tumor angiogenesis not only maintains tumor growth at the primary site, but also promotes tumor metastasis. Therefore, angiogenesis is an important mediator of microbiota-tumor interactions. Antibiotic-induced microbiota alterations can regulate tumor growth and metastasis. In addition, the microbiota influences the efficacy and toxicity of tumor immunotherapy and chemotherapy. Mao et al.(29) investigated microbial composition and diversity in tumor tissues and adjacent tissues of 55 lung cancer patients and showed that tumor samples had significantly lower alpha diversity, higher taxon interactions, and fewer potentially pro-inflammatory microbial genera compared to non-malignant adjacent tissues, but no significant differences in overall microbiota heterogeneity. It should be noted that sometimes lung cancer may not be driven by the infection itself, but by a major transformation of its microbial community. Lung microbiota diversity is an important indicator of malignant transformation in lung cancer, with alpha diversity tending to be lower in lung cancer patients and conversely beta diversity not significantly different in the lungs of healthy and cancer patients (30). Therefore, the microbiota should be considered an important diagnostic and preventive indicator of lung cancer. Lee and colleagues analyzed the differences in the microbiotas of patients with benign and malignant lung tumors by 16S rRNA high-throughput sequencing and suggested that *Veillonella* and *Megasphaera* spp. could be used as biomarkers for lung cancer (20). In addition, compared to adjacent normal tissues, lung cancer tissues contained higher levels of *Modestobacter* but lower levels of *Propionibacterium* and *Enterobacteriaceae* (21). In terms of diversity, there was no significant difference in beta diversity between non-malignant lung cancer tissues and lung tumor tissues, but alpha diversity of the microbiota was significantly reduced in lung tumor tissues (30). During carcinogenesis, microecological deviations from homeostasis gradually create a microenvironment that promotes cancer induction and ultimately causes carcinogenesis. Thus, microecological imbalances in the lung may affect lung carcinogenesis through inflammation, immunity, metabolism and genotoxicity.

Hepatocellular carcinoma is the fourth leading cause of cancer-related death, and hepatocellular carcinoma is a primary liver cancer resulting from chronic hepatitis caused by multiple susceptibility factors such as viruses, alcohol consumption, and nonalcoholic fatty liver disease. Komiyama et al. characterized the tumor-associated microbiota in patients with hepatocellular carcinoma. It was found that the number of amplicon sequence variants in the tumor-associated microbiota was significantly increased compared with non-tumor areas of the liver, and the tumor-associated microbiota consisted mainly of Bacteroidetes, Firmicutes, and Proteobacteria. In addition, *Bacteroides*, *Romboutsia* and uncultured bacterium of

Lachnospiraceae could be used as signature taxa for primary liver cancer (22).

In addition to clinical samples, Zhang et al. (31) used high-throughput sequencing to identify and compare microbial diversity in human and murine tumors, and principal component analysis and β-diversity showed low microbial similarity between mouse artificial tumors, mouse spontaneous tumors, and human tumors, with *Serratia*, Pseudomonas spp. and *Ochrobactrum* as the dominant bacteria at the genus level. The intracellular microbiota of tumors is an emerging class of tumor components whose biological functions are still unclear. Fu et al. (32) used a mouse model of spontaneous mammary tumors to explore the function of these intratumoral bacteria. It was found that depletion of intratumoral bacteria significantly reduced metastasis of tumor cells without affecting the growth of the primary tumor. Furthermore, during metastatic colonization, intratumoral bacteria enhanced resistance to fluid shear stress by reorganizing the actin cytoskeleton, thereby promoting host cell survival. In addition, bacterial strains isolated from tumor cells can promote tumor metastasis. Although small in number, microorganisms in tumor cells play an important role in promoting cancer metastasis, and there is a need to intervene to advance tumor control.

3 Effect of chemotherapy on microbial diversity in TME

The microbiota in TME may also alter the efficacy and toxicity of chemotherapy through the effects of chemotherapeutic drug metabolism, enzymatic degradation, etc., thus reducing diversity and variability (33). *In vitro* cell line experiments, the efficacy of chemotherapeutic drugs(gemcitabine) on cancer cell killing seems to be influenced by different species of bacteria, some improving cell killing and some reducing efficacy (34). The specific bacterial species and the mechanism of influence need to be further explored. To address this issue of microbial metabolism of anticancer drugs in the TME leading to chemotherapy failure, Qiu et al. (35) developed antibiotic and anticancer drug co-delivery micelles, called colistin cross-linked gemcitabine micelles (CCGM), capable of on-demand release without compromising their antimicrobial and anticancer effects. Once the CCGM is delivered to the TME, intracellular glutathione triggers the release of colistin and gemcitabine to inhibit the growth of microorganisms in the tumor, thereby eliminating microbial-induced tumor drug resistance. The combinations and ratios of different antibiotics and anticancer drugs should be further explored. In addition, antibiotics inhibit the toxicity of oxaliplatin to cells in tumors by reducing microbiota-dependent ROS production in TME (36).

Breast tumors have their specific microbiota, which is different from normal breast tissue. By aseptically collecting breast tumor tissues from patients receiving neoadjuvant chemotherapy and patients who had not received treatment at the time of surgery and using 16S rRNA high-throughput sequencing, it was found that the number of *Pseudomonas* spp. in breast tumors increased significantly after chemotherapy administration (doxorubicin), and primary breast tumors from patients with distant metastases showed increased abundance of *Brevundimonas* and *Staphylococcus* spp. and the presence of *Pseudomonas aeruginosa* in breast tumor tissue was confirmed by IHC staining (13). In conclusion, chemotherapy alters the tumor microbiota of breast tissue and specific microorganisms are associated with tumor recurrence. Future studies could increase the size of the patient populations to gain insight into the role of microbiota in chemotherapy and develop novel bacterial biomarkers that can predict distant tumor metastasis.

The development, treatment and post-treatment survival of pancreatic ductal adenocarcinoma (PDAC) are associated with the tumor microbiota. Tumor tissue and normal pancreatic tissue samples were obtained from 27 patients who had undergone surgical resection of PDAC, and 16S rRNA high-throughput sequencing showed detectable bacterial communities in 26 of the 54 samples. The relative abundance($P = 0.04$) of microbiota from Enterobacteriaceae was significantly higher in samples from patients who underwent biliary stenting or neoadjuvant therapy with a combination of gemcitabine and paclitaxel. The above findings suggest that biliary stenting and neoadjuvant chemotherapy are associated with alterations in tumor microbiota diversity that promote infiltration and growth of intra-tumor bacteria in PDAC (14). Further exploration of whether specific bacterial communities contribute to increased chemoresistance can follow, which is critical for optimizing future therapies.

Pancreatic cancer is a malignant tumor of the digestive system with a very high mortality rate. Gemcitabine-based chemotherapy is the main treatment for end-stage pancreatic cancer, but its therapeutic effect is often poor. Microorganisms(*Escherichia-Shigella*, *Malassezia* spp., *Adenoviruses*, *Herpes simplex* virus type 1, *Vaccinia* viruses) in TME not only play an indirect role in the development and progression of pancreatic cancer, but also influence the effectiveness of chemotherapy to some extent. In addition, microorganisms may be important biomarkers for predicting pancreatic carcinogenesis and detecting pancreatic cancer prognosis. However, the available data are insufficient, for example, what are the mechanisms by which lysoviruses and bacteria affect pancreatic cancer chemotherapy? The next step could be focus on specific microbial species in TME to improve the efficacy of chemotherapy in the treatment of pancreatic cancer (37).

Patients with localized squamous cell carcinoma of the anus (SCCA) have few treatment options after experiencing treatment toxicity or recurrence, and the impact of the microbiota in TME on treatment toxicity and its potential use as a predictive biomarker could improve the prognosis of these patients. Lin et al. (23) used 16S rRNA high-throughput sequencing of the tumor site of 22 patients with SCCA to the microbiota and showed that alpha diversity remained relatively stable throughout the chemoradiotherapy period and the tumor microbiota changed during and after chemotherapy. In addition, different levels of bacterial enrichment ($P = 0.03$ for all), such as *Clostridia*, *Clostridiales*, and *Actinobacteria*, occurred at specific time points (during CRT) during treatment, which would play an important role in predicting the tumor microbiota for SCCA patients.

4 Effect of immunotherapy on microbial diversity in TME

As a very promising strategy for oncology treatment, immunotherapy is highly relevant to microorganisms in TME. Immunotherapy has shown great promise in the treatment of patients with metastatic malignancies, dramatically changing the cancer treatment, especially after the discovery of immune checkpoint inhibitors. However, the response to immunotherapy is heterogeneous and often transient. More importantly, a large proportion of cancer patients are resistant to this treatment. Much effort has been expended to identify reliable biomarkers to accurately predict clinical response to immunotherapy (38–40). Unfortunately, such biomarkers are still lacking and the mechanisms underlying their efficacy and safety are poorly understood. Emerging evidence suggests that microbes in TME can alter the efficacy and toxicity of immunotherapies by modulating the local and systemic immune response of the host. Therefore, it is critical to use the microbiota to develop biomarkers that can be used for cancer immunotherapy (41). A growing number of findings demonstrate that microorganisms in TME have a significant impact on tumorigenesis, progression and metastasis. In particular, the effect of bacteria on tumor immunity. Bacteria can suppress the function of the immune system through a variety of mechanisms, and some bacteria(such as *E. coli*, *Salmonella*, *Clostridium butyricum*, *Listeria*) can enhance immunity and inhibit tumor progression (42).

Intratumoral and tumor local microbes remain a promising direction for oncology research. Boesch et al. (17) found that lung tissue from patients with non-small cell lung cancer had a higher abundance of Gammaproteobacteria compared to healthy lung tissue, which was associated with lower expression of programmed death ligand 1 and worse overall survival under immune checkpoint inhibitor(ICI) therapy. Furthermore, an interesting study showed that bacteria(*Akkermansia muciniphila*) within mouse PDAC tissue can drive IL-33 secretion, which further recruites and activates Th2 cells and type 2 innate lymphoid cells in tumor tissue, ultimately leading to suppression of antitumor immune responses and promoting tumor progression (43). Bone marrow cells are a major component of the TME and can induce antitumor immune responses, mainly promoting immune evasion, tumor progression and metastasis. Myeloid cells respond to environmental factors, including signals from commensal microbes. The commensal microbiota is a major player in influencing carcinogenesis, tumor progression, cancer comorbidity, and treatment outcomes by setting inflammatory/immune tone and modulating host responses to oncogenic pathogens, cancer-associated inflammation, and tumor-induced tissue damage (44). In general, oncogenic microbial infections and microbiota in TME dysbiosis are strongly associated with tumorigenesis, and intratumoral and local tumor microbes contribute significantly to tumor progression. However, the causal relationship between them still needs further investigation.

5 Bacteria-mediated cancer therapy

Conventional cancer treatments, including radiotherapy, chemotherapy, surgery and immunotherapy, have limitations that negatively affect the health of patients. Bacterial-mediated tumor therapy is emerging as a promising approach in cancer treatment because specialized anaerobic microorganisms (e.g., *Clostridium* spp., *Bifidobacterium* spp.) or pathogenic anaerobic microorganisms (e.g., *Lactobacillus* spp. and *Lactobacillus* sp.) can penetrate and proliferate in tumor hypoxic regions. Anaerobic bacteria are known to cause tumor regression and inhibit metastasis through multiple mechanisms (toxin production, anaerobic lifestyle, and synergy with anticancer drugs) (45). The above-mentioned bacterial functions have the potential to be used as a complementary tool to conventional cancer therapy. In the last decade or so, the use of bacteria as a treatment for cancer has attracted a lot of attention. There are various approaches to the use of bacteria for cancer treatment, including the use of live, attenuated or genetically engineered microorganisms, bacterial-based cancer immunotherapy, bacterial vectors for genetically targeted enzyme precursors, and probiotics. Ma et al. (46) analyzed the composition of prostate cancer intratumoral bacteria to determine the impact of the microbiota on metastatic tumor growth. Specific microorganisms (*Listeria monocytogenes* and *Metacoccus radiodurans* JCM 2831) were identified that could significantly halt prostate cancer progression. Bacterial therapies, either alone or in combination with other therapies, can have a positive impact on cancer treatment. Moreover, bacteria can be used as carriers of drugs, genes or therapies, which is a breakthrough in the treatment of cancer (11). Bacteria-directed multimodal synergistic cancer therapies (e.g., photothermal therapy, targeted synergistic approaches, and bacterial metabolite therapy) offer a range of advantages. Representative studies of bacterial-directed multimodal synergistic cancer therapies are described next.

5.1 Photothermal therapy

For the medical application of engineered bacteria, strict regulation of the function of engineered bacteria has been the goal pursued. However, existing regulation methods do not meet the needs of *in vivo* applications of engineered bacteria. Li et al. (47) constructed thermosensitive engineered bacteria that could respond to thermal stimulation within 30 min and could colonize the TME in mice, and thermal stimulation could control the production of protein tumor necrosis factor α by engineered bacteria in tumors, and the growth of tumors was significantly inhibited, indicating that heat can be used as a strategy to precisely control *in vivo* engineered bacteria. Furthermore, intra-tumor hypoxia significantly limits the susceptibility of solid tumors to oxygen-dependent photodynamic therapy(PDT). Ding et al. (48)developed a novel engineered bacterium capable of targeting hypoxic tumor tissues and effectively mediating photodynamic therapy for these tumors. *E.coli* were genetically engineered to express peroxidase, and black phosphorus quantum dots(BPQDs) were attached to the surface of these bacteria by electrostatic adsorption to produce an engineered *Escherichia coli*/BPQDs(EB) system. After intravenous injection, EBs can target hypoxic tumor tissue, and when laser-driven EBs produce reactive oxygen species(ROS) and disrupt the bacteria's membrane, it is able to release catalase and subsequently degrade hydrogen peroxide to produce oxygen. The increased oxygen alleviates intra-tumor

hypoxia, thereby enhancing BPQDs-mediated photodynamic therapy. The system can kill tumor cells effectively *in vivo*, showing good therapeutic efficacy.

5.2 Targeted synergistic approach

A biologically targeted synergistic system consisting of genetically engineered bacteria and multifunctional nanoparticles, Wang et al. (49) genetically modified *E.coli* to carry an acoustic reporter gene encoding the formation of gas vesicles (GVs), then targeted the tumor hypoxic environment in mice, followed by ultrasound imaging and collaborative FUAS, and enriched multifunctional nanoparticles in the tumor target area by electrostatic adsorption. Multifunctional cationic lipid nanoparticles containing IR780, perfluorohexane, and banoanthraquinone hydrochloride (AQ4N) were then co-loaded into the tumors for targeted multimodal imaging and enhanced FUAS efficacy. AQ4N was stimulated by the tumor hypoxic environment to kill tumor cells in synergy with focused ultrasound ablation procedures. Natural bacteria are potential targets for cancer therapy due to their unique autonomously driven and hypoxic targeting properties. Genetically engineered bacteria can effectively cross complex physiological barriers to deliver antitumor drugs to deep tumor tissues with a favorable biosafety profile. In addition, bacteria can secrete cytokines and activate antitumor immune responses in the TME, leading to tumor suppression. By combining bacterial-based drugs with other therapeutic approaches, synergistic antitumor strategies can be developed (50). Bacteria-driven drug delivery systems are of high interest for their therapeutic specificity and efficacy in cancer treatment. YB1 is a particularly attractive transgenic safe strain of *Salmonella typhimurium* that can penetrate hypoxic tumor tissue, with self-driven properties, while avoiding damage to normal tissue. Chen et al. (51) have attached nanophotosensitizers (indocyanine (ICG)-loaded nanoparticles INPs) attached to YB1 surface with amide bonds to develop bio/non-biological cross-linked systems (YB1-INPs) for tumor precision therapy. The YB1-INPs therapeutic strategy demonstrated specific hypoxic targeting to solid tumors, thanks to the combined contribution of tumor tissue destruction and nutrient uptake production by bacteria after photothermal treatment, with bioaccumulation of YB1-INPs compared to no photothermal intervention was significantly increased by 14-fold. Furthermore, YB1-INPs were spread throughout large solid tumors and exhibited reliable and efficient photothermal killing ability under near-infrared (NIR) laser irradiation to eradicate large solid tumors without recurrence. This bacterially driven hypoxia-targeted delivery strategy is valuable for large solid tumor treatment with great applications.

5.3 Bacterial metabolite therapy

Bacterial-targeted enzyme precursor drug therapy (BDEPT) is an emerging alternative targeted and tumor-specific approach. Microbial-based oncology treatments include lysoviral therapy and bacteriotherapy, both of which use tumor-specific infectious microorganisms to treat cancer. The approach is based on the conversion of non-toxic precursor drugs into toxic drugs in the TME by bacterial enzymes. BDEPT therapy is based on the ability of *E.coli* DH5 to activate glycyrrhizic acid(GL), a naturally occurring non-toxic compound derived from licorice, to glycyrrhetinic acid (GA) only in the TME, and the bacteria can effectively activate GL to GA to inhibit the growth of tumor cells. The anticancer effect of the bacteria used in combination with GL was studied in a mouse model of colon cancer and it was found that the combination treatment greatly inhibited tumor growth and histopathological analysis also showed an increase in apoptosis of tumor cells after the combination treatment with no significant damage to the spleen and liver of the mice (52). Therefore, the BDEPT approach can be considered an effective tumor-specific therapy. l-arginine availability in tumors is a key determinant of effective antitumor T-cell responses, and increased intra-tumor l-arginine concentrations may greatly enhance the antitumor response to immune checkpoint inhibitors. However, there is currently no way to locally increase intra-tumor l-arginine levels, and Canale et al. used a synthetic biology approach to develop an engineered *E. coli strain Nissle 1917*. Colonization of tumors with these bacteria increased intra-tumor L-arginine concentrations, and increased the number of tumor-infiltrating T cells, and had a significant synergistic effect with PD-L1 blocking antibodies in tumor clearance (53). In addition, a novel strategy combining bacterial therapy with high-intensity focused ultrasound (HIFU) therapy may lead to more effective breast cancer treatment. Acoustic reporter genes (ARG) were successfully expressed in *E.coli* by genetic engineering to produce protein nanoparticle-air sacs (GVs). After intravenous injection, GVs-containing *E.coli* can specifically target tumor sites, colonize continuously in the TME, and significantly inhibit tumor growth. Meanwhile, GVs-containing *E.coli* could effectively synergize HIFU treatment both *in vitro* and *in vivo*. The tumor inhibition rate of the combination treatment group could be as high as 87% compared to the control group (54).Therefore, bacterial metabolite therapy has some prospects for application.

6 Conclusion

In recent years, oncology treatment has made great progress, which has significantly improved the quality of life and survival rate of cancer patients. However, conventional cancer treatment still has many limitations. For the past few years, with the rise of tumor microbiota and bacterium-based therapies, it is expected to remedy these limitations. For example, bacterial species such as *Salmonella*, *Clostridium* and *Listeria* have been shown to control tumor growth and improve prognosis in experimental animal models and clinical settings (55). The current research and clinical status of the tumor microbiota should be of interest to relevant scientists and clinicians, and future work could be carried out in the following areas.The accuracy of gene sequencing should be enhanced to provide a more comprehensive and accurate understanding of the microbiotas of different types of tumors and their core microorganisms. Although viral infections are known to cause tumors, studies on related viral diversity are scarce, and with the development of high-throughput sequencing technology, viral variety in tumor tissues should also be taken into account.

It is necessary to consider the tumor microbiota during tumor-related clinical treatment or scientific research. In addition, it is necessary to redefine the tumor microbiota. At this stage, research on the relationship between tumor therapies and tumor microbiota is still in its initial stage, and a lot of *in vivo* and *in vitro* studies are still needed. In this regard, an in-depth understanding of the distribution and function of the tumor microbiota is important to facilitate the understanding of oncogenic effects and to provide new therapeutic strategies for cancer(56). The tumor heterogeneity is a major issue especially in retrieving in a reliable and reproducible manner specific TME microbial markers. In addition, tumor tissue sampling methods are more or less limited, and microbial contamination can occur at any time between sampling and sequencing. Therefore, exogenous contamination must be eliminated through a strict sampling process.

Given the current paucity of clinical studies, studies at this stage have not been able to fully determine the relationship between tumor microbiota and tumor, and so many of the results are speculative. Therefore, further studies are needed to investigate how microorganisms enter tumor tissues, their relationship with tumor cells, and how to use them for cancer prevention, diagnosis, and prognosis.

Author contributions

HZ, JC, and YL conceived and wrote the first draft of the manuscript. JC, HZ, YL, XC, and QL revised each part of the manuscript in detail. All authors contributed to the article and approved the submitted version.

Acknowledgments

We would like to thank all the authors for their critical discussion of this manuscript and apologize to those publications not mentioned due to space limitations.

Conflict of interest

The authors declare that the research was conducted in the absence of any commercial or financial relationships that could be construed as a potential conflict of interest.

Publisher's note

All claims expressed in this article are solely those of the authors and do not necessarily represent those of their affiliated organizations, or those of the publisher, the editors and the reviewers. Any product that may be evaluated in this article, or claim that may be made by its manufacturer, is not guaranteed or endorsed by the publisher.

References

1. Zong Y, Zhou Y, Liao B, Liao M, Shi Y, Wei Y, et al. The interaction between the microbiome and tumors. *Front Cell Infection Microbiol* (2021) 11. doi: 10.3389/fcimb.2021.673724

2. Longmore GD. Bacteria in tumors "hit the road" together. *Cell* (2022) 185 (8):1292–+. doi: 10.1016/j.cell.2022.03.013

3. Che B, Zhang W, Xu S, Yin J, He J, Huang T, et al. Prostate microbiota and prostate cancer: A new trend in treatment. *Front Oncol* (2021) 11. doi: 10.3389/fonc.2021.805459

4. Li Z, Chen G, Wang P, Sun M, Zhao J, Li A, et al. Alterations of the oral microbiota profiles in Chinese patient with oral cancer. *Front Cell Infection Microbiol* (2021) 11. doi: 10.3389/fcimb.2021.780067

5. Karpinski TM, Ozarowski M, Stasiewicz M. Carcinogenic microbiota and its role in colorectal cancer development. *Semin Cancer Biol* (2022) 86(Pt 3):420–30. doi: 10.1016/j.semcancer.2022.01.004

6. Jiang T, Yang T, Chen Y, Miao Y, Xu Y, Jiang H, et al. Emulating interactions between microorganisms and tumor microenvironment to develop cancer theranostics. *Theranostics* (2022) 12(6):2833–59. doi: 10.7150/thno.70719

7. Kovaleva OV, Romashin D, Zborovskaya IB, Davydov MM, Shogenov MS, Gratchev A. Human lung microbiome on the way to cancer. *J Immunol Res* (2019) (10):1–6. doi: 10.1155/2019/1394191

8. Zhang Z, Liao Y, Tang D. Intratumoral microbiota: new frontiers in tumor immunity. *Carcinogenesis* (2022) 8):8. doi: 10.1093/carcin/bgac063

9. Kucerova P, Cervinkova M. Spontaneous regression of tumour and the role of microbial infection – possibilities for cancer treatment. *Anti-Cancer Drugs* (2016) 27 (4):269–77. doi: 10.1097/CAD.0000000000000337

10. Mai Thi-Quynh D, Qin Y, You S-H, Min J-J. Bacteria-cancer interactions: bacteria-based cancer therapy. *Exp Mol Med* (2019) 51:1–15. doi: 10.1038/s12276-019-0297-01

11. Al-Hilu SA, Al-Shujairi WH. Dual role of bacteria in carcinoma: Stimulation and inhibition. *Int J Microbiol* (2020) 2020:4639761–4639761. doi: 10.1155/2020/4639761

12. Ajami NJ, Wargo JA. Microbial signatures in tumours and blood. *Nature* (2020) 579(7800):502–3. doi: 10.1038/d41586-020-00637-w

13. Chiba A, Bawaneh A, Velazquez C, Clear KYJ, Wilson AS, Howard-McNatt M, et al. Neoadjuvant chemotherapy shifts breast tumor microbiota populations to regulate drug responsiveness and the development of metastasis. *Mol Cancer Res* (2020) 18 (1):130–9. doi: 10.1158/1541-7786.MCR-19-0451

14. Nalluri H, Jensen E, Staley C. Role of biliary stent and neoadjuvant chemotherapy in the pancreatic tumor microbiome. *BMC Microbiol* (2021) 21(1). doi: 10.1186/s12866-021-02339-3

15. Shen W, Tang D, Wan P, Peng Z, Sun M, Guo X, et al. Identification of tissue-specific microbial profile of esophageal squamous cell carcinoma by full-length 16S rDNA sequencing. *Appl Microbiol Biotechnol* (2022) 106(8):3215–29. doi: 10.1007/s00253-022-11921-2

16. Lin Z, Rao W, Xiang Z, Zeng Q, Liu S, Yu K, et al. Characteristics and interplay of esophageal microbiota in esophageal squamous cell carcinoma. *BMC Cancer* (2022) 22(1). doi: 10.1186/s12885-022-09771-2

17. Boesch M, Baty F, Albrich WC, Flatz L, Rodriguez R, Rothschild SI, et al. Local tumor microbial signatures and response to checkpoint blockade in non-small cell lung cancer. *Oncoimmunology* (2021) 10(1):2162–402X. doi: 10.1080/2162402X.2021.1988403

18. Xu Z, Lv Z, Chen F, Zhang Y, Xu Z, Huo J, et al. Dysbiosis of human tumor microbiome and aberrant residence of actinomyces in tumor-associated fibroblasts in young-onset colorectal cancer. *Front Immunol* (2022) 13. doi: 10.3389/fimmu.2022.1008975

19. Riquelme E, Zhang Y, Zhang LL, Montiel M, Zoltan M, Dong WL, et al. Tumor microbiome diversity and composition influence pancreatic cancer outcomes. *Cell* (2019) 178(4):795–+. doi: 10.1016/j.cell.2019.07.008

20. Lee SH, Sung JY, Yong D, Chun J, Kim SY, Song JH, et al. Characterization of microbiome in bronchoalveolar lavage fluid of patients with lung cancer comparing with benign mass like lesions. *Lung Cancer* (2016) 102:89–95. doi: 10.1016/j.lungcan.2016.10.016

21. Mao Q, Hu J. Differential microbiota features in lung tumor and adjacent normal tissues in lung cancer patients. *J Thorac Oncol* (2018) 13(10):S911–2. doi: 10.1016/j.jtho.2018.08.1680

22. Komiyama S, Yamada T, Takemura N, Kokudo N, Hase K, Kawamura YI. Profiling of tumour-associated microbiota in human hepatocellular carcinoma. *Sci Rep* (2021) 11 (1):10589. doi: 10.1038/s41598-021-89963-1

23. Lin D, El Alam MB, Jaoude JA, Kouzy R, Phan JL, Elnaggar JH, et al. Microbiome dynamics during chemoradiation therapy for anal cancer. *Int J Radiat Oncol Biol Phys* (2022) 113(5):974–84. doi: 10.1016/j.ijrobp.2022.04.037

24. Yang W, Chen C-H, Jia M, Xing X, Gao L, Tsai H-T, et al. Tumor-associated microbiota in esophageal squamous cell carcinoma. *Front Cell Dev Biol* (2021) 9. doi: 10.3389/fcell.2021.641270

25. Chen P, Guo Y, Jia L, Wan J, He T, Fang C, et al. Interaction between functionally activate endometrial microbiota and host gene regulation in endometrial cancer. *Front Cell Dev Biol* (2021) 9. doi: 10.3389/fcell.2021.727286

26. Parkin DM. The global health burden of infection -associated cancers in the year 2002. *Int J Cancer* (2006) 118(12):3030–44. doi: 10.1002/ijc.21731

27. Rodriguez RM, Menor M, Hernandez BY, Deng Y, Khadka VS. Bacterial diversity correlates with overall survival in cancers of the head and neck, liver, and stomach. *Molecules (Basel Switzerland)* (2021) 26(18):5659. doi: 10.3390/molecules26185659

28. Wang D, Cheng J, Zhang J, Zhou F, He X, Shi Y, et al. The role of respiratory microbiota in lung cancer. *Int J Biol Sci* (2021) 17(13):3646–58. doi: 10.7150/ijbs.51376

29. Mao Q, Ma W, Wang Z, Liang Y, Zhang T, Yang Y, et al. Differential flora in the microenvironment of lung tumor and paired adjacent normal tissues. *Carcinogenesis* (2020) 41(8):1094–103. doi: 10.1093/carcin/bgaa044

30. Morgan XC, Huttenhower C. Chapter 12: Human microbiome analysis. In: *PLos computational biology* (Department of Biostatistics, Harvard School of Public Health, Boston, Massachusetts, United States of America: PLos computational biology), vol. 8. (2012).

31. Zhang F, Zhang M, Wang Y, Li C, Chen T. Comparison of the common bacteria in human and mouse tumours using high-throughput sequencing. *Mol Med Rep* (2018) 17 (5):6717–22. doi: 10.3892/mmr.2018.8689

32. Fu A, Yao B, Dong T, Chen Y, Yao J, Liu Y, et al. Tumor-resident intracellular microbiota promotes metastatic colonization in breast cancer. *Cell* (2022) 185(8):1356–+. doi: 10.1016/j.cell.2022.02.027

33. Tsilimigras MCB, Fodor AA. Compositional data analysis of the microbiome: fundamentals, tools, and challenges. *Ann Epidemiol* (2016) 26(5):330–5. doi: 10.1016/j.annepidem.2016.03.002

34. Lehouritis P, Cummins J, Stanton M, Murphy CT, McCarthy FO, Reid G, et al. Local bacteria affect the efficacy of chemotherapeutic drugs. *Sci Rep* (2015) 5:14554. doi: 10.1038/srep14554

35. Qiu Q, Lu D, Liu G, Yang X, Li J, Ren H, et al. Colistin crosslinked gemcitabine micelles to eliminate tumor drug resistance caused by intratumoral microorganisms. *Bioconjugate Chem* (2022) (33):1944–52. doi: 10.1021/acs.bioconjchem.2c00407

36. Pabst O. New concepts in the generation and functions of IgA. *Nat Rev Immunol* (2012) 12(12):821–32. doi: 10.1038/nri3322

37. Lu S-Y, Hua J, Xu J, Wei M-Y, Liang C, Meng Q-C, et al. Microorganisms in chemotherapy for pancreatic cancer: An overview of current research and future directions. *Int J Biol Sci* (2021) 17(10):2666–82. doi: 10.7150/ijbs.59117

38. Derosa L, Routy B, Thomas AM. Intestinal Akkermansia muciniphila predicts clinical response to PD-1 blockade in patients with advanced non-small-cell lung cancer. *Nat Med* (2022) 28:315–324.

39. Andrews MC, Duong CPM, Gopalakrishnan V. Gut microbiota signatures are associated with toxicity to combined CTLA-4 and PD-1 blockade. *Nature Medicine* (2021) 27:1432–1441.

40. McCulloch JA, Davar D, Rodrigues RR, Badger JH, Fang JR, Cole AM, et al. Intestinal microbiota signatures of clinical response and immune-related adverse events in melanoma patients treated with anti-PD-1. *Nat Med* (2022) 28:545–56. doi: 10.1038/s41591-022-01698-2

41. Inamura K. Roles of microbiota in response to cancer immunotherapy. *Semin Cancer Biol* (2020) 65:164–75. doi: 10.1016/j.semcancer.2019.12.026

42. Zhao M, Chen X, Yang Z, Yang X, Peng Q. Bacteria and tumor: Understanding the roles of bacteria in tumor genesis and immunology. *Microbiological Res* (2022) 261127082. doi: 10.1016/j.micres.2022.127082

43. Shi LL, Sheng JY, Chen GZ, Zhu P, Shi CP, Li B, et al. Combining IL-2-based immunotherapy with commensal probiotics produces enhanced antitumor immune response and tumor clearance. *J Immunotherapy Cancer* (2020) 8(2):e000973. doi: 10.1136/jitc-2020-000973

44. Goldszmid RS, Dzutsev A, Viaud S, Zitvogel L, Restifo NP, Trinchieri G. Microbiota modulation of myeloid cells in cancer therapy. *Cancer Immunol Res* (2015) 3(2):103–9. doi: 10.1158/2326-6066.CIR-14-0225

45. Drozdz M, Makuch S, Cieniuch G, Wozniak M, Ziolkowski P. Obligate and facultative anaerobic bacteria in targeted cancer therapy: Current strategies and clinical applications. *Life Sci* (2020) 261:118296. doi: 10.1016/j.lfs.2020.118296

46. Schwabe RF, Greten TF. Gut microbiome in HCC - mechanisms, diagnosis and therapy. *J Hepatol* (2020) 72(2):230–8. doi: 10.1016/j.jhep.2019.08.016

47. Li L, Pan H, Pang G, Lang H, Shen Y, Sun T, et al. Precise thermal regulation of engineered bacteria secretion for breast cancer treatment *In vivo*. *ACS Synthetic Biol* (2022) 11(3):1167–77. doi: 10.1021/acssynbio.1c00452

48. Ding S, Liu Z, Huang C, Zeng N, Jiang W, Li Q. Novel engineered Bacterium/Black phosphorus quantum dot hybrid system for hypoxic tumor targeting and efficient photodynamic therapy. *ACS Appl Materials Interfaces* (2021) 13(8):10564–73. doi: 10.1021/acsami.0c20254

49. Wang Y, Tang Y, Du Y, Lin L, Zhang Z, Ou X, et al. Genetically engineered bacteria-mediated multi-functional nanoparticles for synergistic tumor-targeting therapy. *Acta Biomaterialia* (2022) 150:337–52. doi: 10.1016/j.actbio.2022.07.056

50. Yin T, Diao Z, Blum NT, Qiu L, Ma A, Huang P. Engineering bacteria and bionic bacterial derivatives with nanoparticles for cancer therapy. *Small* (2022) 18(12):2104643. doi: 10.1002/smll.202104643

51. Chen F, Zang Z, Chen Z, Cui L, Chang Z, Ma A, et al. Nanophotosensitizer-engineered salmonella bacteria with hypoxia targeting and photothermal-assisted mutual bioaccumulation for solid tumor therapy. *Biomaterials* (2019) 214:119226. doi: 10.1016/j.biomaterials.2019.119226

52. Afkhami-Poostchi A, Mashreghi M, Iranshahi M, Matin MM. Use of a genetically engineered e. coli overexpressing beta-glucuronidase accompanied by glycyrrhizic acid, a natural and anti-inflammatory agent, for directed treatment of colon carcinoma in a mouse model. *Int J Pharmaceutics* (2020) 579:119159. doi: 10.1016/j.ijpharm.2020.119159

53. Canale FP, Basso C, Antonini G, Perotti M, Li N, Sokolovska A, et al. Metabolic modulation of tumours with engineered bacteria for immunotherapy. *Nature* (2021) 598 (7882):662–+. doi: 10.1038/s41586-021-04003-2

54. Yang H, Jiang F, Ji X, Wang L, Wang Y, Zhang L, et al. Genetically engineered bacterial protein nanoparticles for targeted cancer therapy. *Int J Nanomedicine* (2021) 16:105–17. doi: 10.2147/IJN.S292432

55. Mayakrishnan V, Kannappan P, Tharmalingam N, Bose RJC, Madheswaran T, Ramasamy M. Bacterial cancer therapy: A turning point for new paradigms. *Drug Discovery Today* (2022) 27(8):2043–50. doi: 10.1016/j.drudis.2022.03.007

56. Nino JLG, Wu H, LaCourse KD, Kempchinsky AG, Baryiames A, Barber B, et al. Effect of the intratumoral microbiota on spatial and cellular heterogeneity in cancer. *Nature* (2022). doi: 10.1038/s41586-022-05435-0

frontiers | Frontiers in Immunology

TYPE Original Research
PUBLISHED 13 February 2023
DOI 10.3389/fimmu.2023.1034416

Check for updates

OPEN ACCESS

EDITED BY
Clare Y. Slaney,
Peter MacCallum Cancer Centre, Australia

REVIEWED BY
Haitao Wang,
Center for Cancer Research, (NIH), United States
Zhiming Yao,
Beijing Hospital, China
Chiara Colarusso,
University of Salerno, Italy
Eric Chi-ching Ko,
University of Massachusetts Medical School, United States

*CORRESPONDENCE
Sheng Lin
lslinsheng@163.com

†These authors have contributed equally to this work

SPECIALTY SECTION
This article was submitted to Cancer Immunity and Immunotherapy, a section of the journal Frontiers in Immunology

RECEIVED 01 September 2022
ACCEPTED 25 January 2023
PUBLISHED 13 February 2023

CITATION
Tang S, Zhang Y, Li Y, Zhang Y, Xu Y, Ding H, Chen Y, Ren P, Ye H, Fu S and Lin S (2023) Predictive value of ^{18}F-FDG PET/CT for evaluating the response to hypofractionated radiotherapy combined with PD-1 blockade in non-small cell lung cancer.
Front. Immunol. 14:1034416.
doi: 10.3389/fimmu.2023.1034416

COPYRIGHT
© 2023 Tang, Zhang, Li, Zhang, Xu, Ding, Chen, Ren, Ye, Fu and Lin. This is an open-access article distributed under the terms of the Creative Commons Attribution License (CC BY). The use, distribution or reproduction in other forums is permitted, provided the original author(s) and the copyright owner(s) are credited and that the original publication in this journal is cited, in accordance with accepted academic practice. No use, distribution or reproduction is permitted which does not comply with these terms.

Predictive value of ^{18}F-FDG PET/CT for evaluating the response to hypofractionated radiotherapy combined with PD-1 blockade in non-small cell lung cancer

Shan Tang[1,2†], Yan Zhang[3†], Yunfei Li[1†], Yan Zhang[4], Yuke Xu[5], Haoyuan Ding[4], Yue Chen[4], Peirong Ren[1], Hua Ye[1], Shaozhi Fu[1] and Sheng Lin[1*]

[1]Department of Oncology, The Affiliated Hospital of Southwest Medical University, Luzhou, China, [2]Department of Oncology, The First People's Hospital of Guangyuan, Guangyuan, China, [3]Department of Oncology, The People's Hospital of Luzhou, Luzhou, China, [4]Department of Nuclear Medicine, The Affiliated Hospital of Southwest Medical University, Luzhou, China, [5]Department of Radiology, The Affiliated Hospital of Southwest Medical University, Luzhou, China

Purpose: This retrospective study aimed to investigate ^{18}F-fluorodeoxyglucose (^{18}F-FDG)-positron emission tomography/computed tomography (PET/CT) as a predictor of response to hypofractionated radiotherapy (HFRT) combined with programmed cell death-1 (PD-1) blockade for lung cancer.

Methods: We included 41 patients with advanced non-small cell lung cancer (NSCLC) in this study. PET/CT was performed before (SCAN-0) and one month (SCAN-1), three months (SCAN-2), and six months (SCAN-3) after treatment. Using the European Organization for Research and Treatment of Cancer 1999 criteria and PET response criteria in solid tumors, treatment responses were classified as complete metabolic response (CMR), partial metabolic response (PMR), stable metabolic disease (SMD), or progressive metabolic disease (PMD). Patients were further categorized as those with metabolic benefits (MB; SMD, PMR, and CMR) and those without MBs (NO-MB; PMD). We analyzed the prognosis and overall survival (OS) of patients with new visceral/bone lesions during treatment. Based on the findings, we generated a nomogram to predict survival. Receiver operating characteristics and calibration curves were used to evaluate the accuracy of the prediction model.

Results: The mean OS based on SCANs 1, 2, and 3 was significantly higher in patients with MB and those without new visceral/bone lesions. The prediction nomogram for survival had a high area under the curve and a high predictive value based on the receiver operating characteristics and calibration curves.

Conclusion: ^{18}FDG-PET/CT has the potential to predict the outcomes of HFRT combined with PD-1 blockade in NSCLC. Therefore, we recommend using a nomogram to predict patient survival.

KEYWORDS

^{18}F-FDG PET/CT, NSCLC, PD-1 blockade, hypofractionated radiotherapy, predictive value

1 Introduction

The treatment of lung cancer is constantly updated, but about 50% of patients have distant metastases at the time of diagnosis. Only 20–30% of patients have the opportunity to undergo surgery, and the overall survival (OS) rate remains low (1, 2). Immune checkpoint inhibitors (ICIs; immunotherapy) targeting programmed cell death-1 (PD-1) have been recently approved for locally advanced and metastatic non-small cell lung cancer (NSCLC) (3), irrespective of the histologic subtype. They have gradually attracted attention and are given in combination with chemotherapy because of their excellent systemic control effect. However, the low patient response to the use of a single drug is a drawback. Some pioneering clinical trials have shown that PD-1 blockade can reactivate the immune system, and encouraging data have been obtained regarding its ability to treat NSCLC (4–8). Many methods have been explored to enhance the systemic efficacy of ICIs [8–10], and a large area of active research is investigating the combination of ICIs with radiation therapy (RT), termed immunoradiotherapy (iRT) (9–11). However, its side effects and increased cost make careful monitoring during therapy necessary. The early recognition of response to therapy or progressive disease could potentially guide treatment alterations, which could benefit the patients.

As a surrogate for intracellular glucose metabolism, ^{18}F-fluorodeoxyglucose (^{18}F-FDG) positron emission tomography (PET) is used to detect metabolic changes before anatomical changes occur. Previous studies have used PET/CT as an important method for radiotherapy effect evaluation and prognosis judgment of lung cancer (12). The European Organization for Research and Treatment of Cancer (EORTC) 1999 criteria based on standardized uptake value (SUV) (13), as well as the first criterion used to monitor immunotherapy (14), are commonly used to assess the efficacy of treatments based on PET/computed tomography (CT). The PET response criteria in solid tumors (PERCIST V1.0) (15), published in 2009, overcomes the shortcomings of EORTC and uses the liver ^{18}F-FDG uptake rate for reference calculation, including the peak standard uptake value-lean (SULpeak) and total lesion glycolysis (TLG).

In recent years, many studies have demonstrated the efficacy of PET/CT in evaluating chemotherapy, RT, immunotherapy, and targeted therapy for NSCLC (16–19). However, the response to iRT is still being explored, and there are few studies on the application of ^{18}F-FDG PET/CT in hypofractionated radiotherapy (HFRT) combined with PD-1 blockade in patients with lung cancer. Hence, this study aimed to evaluate the potential of PET/CT for monitoring response to HFRT combined with ICIs in patients with NSCLC and to seek an accurate method for assessing and predicting response.

2 Materials and methods

The subjects were patients with pathologically confirmed NSCLC. The inclusion criteria were (1) Eastern Cooperative Oncology Group performance status score ≤ 2; (2) age 18–70 years; (3) previous treatment with at least one line of therapy; (4) at least three measurable lesions on imaging; and (5) serum creatinine level ≤ 2 of the upper normal limit (UNL), aspartate transaminase and alanine transaminase ≤ 3 of the UNL, and hemoglobin level at the lower normal limit. Patients with severe cardiopulmonary dysfunction, active pulmonary tuberculosis, and noninfectious pneumonitis requiring long-term glucocorticoid use and active autoimmune disease were excluded. Forty-one NSCLC patients (31 men and 10 women) admitted to our department between September 2017 and December 2020 who met the inclusion criteria were included in this retrospective study. The decision to administer PD-1 blockade therapy was based on the patient's financial status. The medication included Nivolumab, Camrelizumab, Sintilimab, Tislelizumab,and Pembrolizuma. The dosage was determined as per the instructions, and the dosage and medication frequency remained unchanged throughout the treatment. The first dose was administered 3–7 days after RT, and the second was given two weeks after the first dose. The PD-1 blockade maintenance dose was administered for one month in the first year, two months in years 2–3, and three months in years 4–5. The RT regimen in this study included stereotactic body radiation therapy (SBRT) (40–50 Gy/5F) and hypofractionated brachytherapy (30 Gy/1F).

2.1 ^{18}F-FDG PET/CT data acquisition

All 41 patients underwent ^{18}F-FDG PET/CT before the start of RT (SCAN-0) and one month after RT (SCAN-1). Of the 41 patients, 26 underwent a third PET/CT scan three months after RT (SCAN-2), and 21 underwent a fourth PET/CT scan six months after RT (SCAN-3).

PET/CT was performed according to the European Association of Nuclear Medicine guidelines version 1.0 (20). Whole-body PET/CT (Philips Gemini TF/16; Philips, Cleveland, OH, USA) was performed after the intravenous administration of ^{18}F-FDG (5.55 MBq/kg). The patients fasted for at least six hours before ^{18}F-FDG administration, and their blood glucose level was ≤ 11 mmol/L. Low-dose helical CT transmission scanning (pitch, 0.813; current, 100 mA; peak voltage, 120 kV; slice thickness, 5.0 mm) was performed with attenuation correction and lesion localization. PET was performed at 1.5 min per bed position using 19–21 bed positions. ^{18}F-FDG PET/CT was performed from the vertex of the head to the feet. Patients held their breath during the chest scans to reduce the impact of respiratory motion on image acquisition and ensure the accuracy of the results.

2.2 ^{18}F-FDG PET/CT data analysis

PET/CT images were analyzed by two nuclear medicine physicians using a workstation. Target lesions were selected according to the PERCIST criteria. A maximum of two lesions were selected in each organ when multiple measurable lesions were available, and no more than five target lesions with highest SUV were selected. PET-based target lesion delineation was carried out with an SUV of 2.5 as the initial threshold. The maximum SUV (SUVmax), metabolic tumor volume (MTV), SULpeak, and TLG were calculated for the target lesions.

2.3 Response evaluation

The patient responses to RT were evaluated by ^{18}F-FDG PET/CT as per the EORTC (13) and PERCIST criteria. Both criteria classify

tumor responses as progressive metabolic disease (PMD), stable metabolic disease (SMD), partial metabolic response (PMR), or complete metabolic response (CMR). Stable disease represents a satisfactory outcome following immunotherapy since, in contrast to conventional chemotherapy, it can be durable, and survival rates related to stable disease are comparable to those associated with response. Based on the responses, patients were further divided into two groups: those demonstrating metabolic benefit (MB; including SMD, PMR, and CMR) and those demonstrating NO-MB (NO-MB; including patients with PMD).

In addition, we focused on new visceral/bone lesions in three scans after treatment and analyzed the prognosis of these patients separately.

2.4 Consistency evaluation of short-term response

The Kappa test was used to assess the consistency of PET scan evaluation results in each period, and the total Kappa value ranged from 0 to 1. When the Kappa value was less than 0.4, it indicated that the consistency was poor, and when the Kappa value was between 0.4 and 0.75, it indicated that the consistency was moderate. When the Kappa value is greater than or equal to 0.75, the consistency between the two is high. A separate analysis was conducted for those cases with a difference in evaluation results.

2.5 Depth of response

Depth of response (DpR) was defined as the percentage change in SUVmax of the target lesion from baseline. Following SCAN-1, patients were divided into three groups based on the percentage change in SUVmax in the tumor target lesions: group 1 (G1; < 30% decrease), group 2 (G2; 30–50% decrease), and group 3 (G3; > 50% decrease). G1 included patients with no change in SUVmax.

2.6 Construction of prediction model

Imaging parameters were collected one month before and one month after treatment. From SCAN-0, we collected the sum of PET parameters of target lesions, named SUVmax0, SULpeak0, TLG0 and MTV0. The imaging parameters of the same lesion were recorded again in SCAN-1 as SUVmax1, SULpeak1, TLG1, and MTV1. The changes in the imaging parameters were calculated as $\triangle$SUVmax = SUVmax0 - SUVmax1, $\triangle$SULpeak = SULpeak0 - SULpeak1, $\triangle$TLG0 = TLG0 - TLG1, and $\triangle$MTV = MTV0 - MTV1. The average baseline PET parameters were also calculated and recorded as the baseline SUVmax, baseline SULpeak, baseline TLG, and baseline MTV. Patient age, sex, pathological type, Eastern Cooperative Oncology Group (ECOG) status, and response evaluation (MB/NO-MB) were all included in the preliminary screening characteristics. In the preliminary preparation work, we confirmed that the immunotherapy and RT regimens of the patients had no significant correlation with OS, so they were not included in the preliminary features for screening.

2.7 Statistical analysis

OS was recorded and defined as the time from RT to death from any cause. Survival curves according to each variable were estimated using Kaplan-Meier and log-rank tests. The Cox proportional hazards regression model was used for the univariate and multivariate analyses of preliminary characteristics. The multivariate model used the AIC criterion to screen the variables, and the results were visualized using a nomogram. The receiver operating characteristic curve was used to analyze the value of the lipopograph model to determine the prognosis. Internal consistency was verified using bootstrap and demonstrated using the calibration curve. Statistical analyses were performed using R, version 3.5.0. software. Statistical significance was set at $p < 0.05$.

3 Results

3.1 Patient characteristics

Table 1 summarizes the characteristics of patients included in this analysis. The mean age of the 41 patients was 57.7 ± 9.3 years (range 37–75 years). All patients had stage III–IV NSCLC; 34.1% (14/41) had squamous cell carcinoma and 65.9% (27/41) had adenocarcinoma. While 65.85% (27/41) of the patients were treated with nivolumab, 19.51% (8/41) received camrelizumab, 7.32% (3/41) received sintilimab, 4.88% (2/41) received tislelizumab, and 2.44% (1/41) received pembrolizumab. While 29.27% (12/41) of patients were treated with hypofractionated brachytherapy, 70.73% (29/41) of them were treated with SBRT.

TABLE 1 Patient's clinical characteristics at baseline.

	N	Percent(%)
Total patients	41	100.00
Age in years, mean ± SD	57.7 ± 9.3	
Sex		
Male	31	75.61
Female	10	24.39
Histology		
Squamous cell carcinoma	14	34.15
Adenocarcinoma	27	65.85
PD-1 blockades		
Nivolumab	27	65.85
Camrelizumab	8	19.51
Sintilimab	3	7.32
Tislelizumab	2	4.88
Pembrolizumab.	1	2.44
Radiotherapy		
HFBT	12	29.27
SBRT	29	70.73

HFRT, hypofractionated brachytherapy; SBRT, stereotactic body radiation therapy.

3.2 Response evaluation

3.2.1 SCAN-1

SCAN-1 findings were evaluated for all 41 patients. According to the EORTC criteria, 24 patients showed MB (0 CMR, 18 PMR, and 6 SMD), whereas 17 patients had NO-MB (PMD). Using the PERCIST criteria, 24 patients had MB (3 CMR, 13 PMR, and 8 SMD), whereas 17 had NO-MB (PMD). Based on the clinical follow-up data on SCAN-1, the median OS of patients with PMD was 9.4 months (mean 13.3 months), with 13 (76.47%) deaths by the end date. In patients with MB, the median OS was 29.5 months (mean 36.0 months), with 10 (41.67%) deaths. The difference between the group MB and group NO-MB was statistically significant (log-rank p = 0.0014). The Kaplan-Meier plots for OS are shown in Figure 1A.

3.2.2 SCAN-2

For the 26 patients who underwent three PET/CT examinations, the SCAN-2 results showed that while 18 patients had MB (3 CMR, 11 PMR, and 4 SMD) according to the EORTC criteria, 8 had NO-MB (PMD). According to the PERCIST criteria, 18 patients had MB (6 CMR, 7 PMR, and 5 SMD) and 8 had NO-MB (PMD). Based on the clinical follow-up data on SCAN-2, the mean OS of patients with PMD was 15.4 months with 6 (75%) deaths, while in those with MB, it was 41.8 months with 6 (33.33%) deaths. The difference between the group MB and group NO-MB was statistically significant (log-rank p = 0.00046). The Kaplan-Meier plots for OS are shown in Figure 1B. The median OS was unavailable because the mortality rate of patients with MB did not exceed 50%. These data are summarized in Table 2.

3.2.3 SCAN-3

SCAN-3 revealed that 13 patients had MB (3 CMR, 7 PMR, and 3 SMD) and 8 patients had NO-MB (PMD) based on the EORTC criteria. According to the PERCIST criteria, 13 patients had MB (6 CMR, 3 PMR, and 4 SMD) and 8 had NO-MB (PMD). Based on the clinical follow-up data on SCAN-3, the mean OS of patients with PMD was 18.0 months with 8 (100%) deaths, and in those with MB, it was 49.4 months with 2 (15.38%) deaths. The difference between the group MB and group NO-MB was statistically significant (log-rank p < 0.0001). The Kaplan-Meier plots of OS are shown in Figure 1C. The median OS could not be obtained because the mortality rate of the patients with MB did not exceed 50%.

3.2.4 New visceral/Bone lesion(s)

The median OS in 9 patients with new visceral/bone lesions on SCAN-1 was 7.1 months (mean 9.5 months), with 7 (77.78%) deaths by the end date of follow-up. The median OS in the other 32 patients without new lesions was 24.4 months (mean 32.2 months), with 16 (50%) deaths. The difference between the two groups was statistically significant (log-rank p = 0.002). The Kaplan-Meier plots for OS are shown in Figure 2A. The mean OS in 4 patients

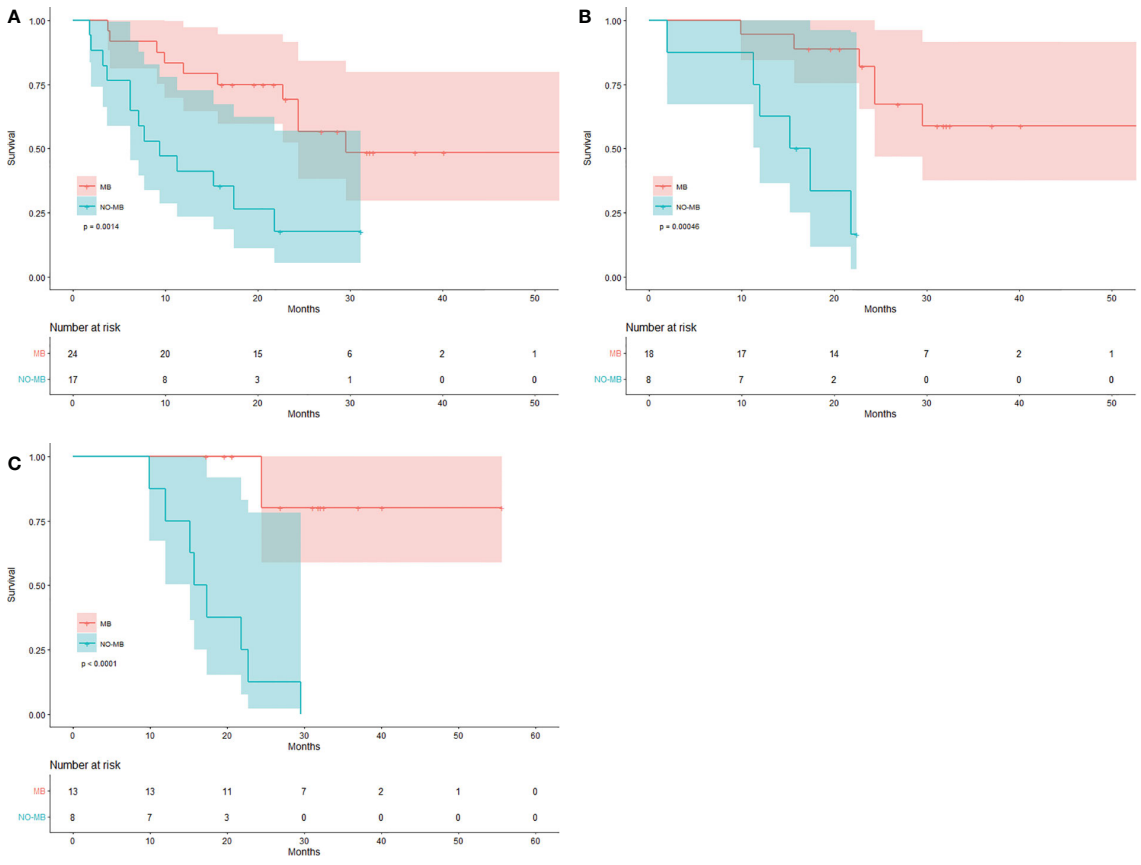

FIGURE 1
Kaplan-Meier curves for response evaluation. Patients with MB and NO-MB on **(A)** SCAN-1, **(B)** SCAN-2, and **(C)** SCAN-3.

10.3389/fimmu.2023.1034416

TABLE 2 Treatment response of the patients investigated in the study.

Patient no.	Treatment response evaluation			MB/NO-MB			Whether there are new visceral/ bone lesion(s)(Yes/No)			OS(months)	Status
	SCAN-1	SCAN-2	SCAN-3	SCAN-1	SCAN-2	SCAN-3	SCAN-1	SCAN-2	SCAN-3		
1	PMR	PMR	PMD	MB	MB	NO-MB	NO	NO	YES	9.9	dead
2	PMR	PMR	PMR	MB	MB	MB	NO	NO	NO	31.8	alive
3	SMD	SMD	SMD	MB	MB	MB	NO	NO	NO	24.4	dead
4	SMD	PMD	PMD	MB	NO-MB	NO-MB	NO	NO	YES	12.0	dead
5	PMD	PMD	PMD	NO-MB	NO-MB	NO-MB	NO	NO	NO	17.4	dead
6	PMR	PMR	PMR	MB	MB	MB	NO	NO	NO	32.1	alive
7	PMD	PMD	PMD	NO-MB	NO-MB	NO-MB	NO	YES	YES	21.8	dead
8	PMR	CMR	CMR	MB	MB	MB	NO	NO	NO	55.6	alive
9	PMR	CMR	CMR	MB	MB	MB	NO	NO	NO	37.0	alive
10	PMR	PMR	PMR	MB	MB	MB	NO	NO	NO	40.1	alive
11	PMD	PMD	PMD	NO-MB	NO-MB	NO-MB	NO	YES	YES	15.2	dead
12	PMR	SMD	PMR	MB	MB	MB	NO	NO	NO	20.6	alive
13	SMD	SMD	SMD	MB	MB	MB	NO	NO	NO	19.6	alive
14	PMR	PMR	PMD	MB	MB	NO-MB	NO	NO	YES	15.7	dead
15	PMD	PMR	PMR	NO-MB	MB	MB	NO	NO	NO	31.1	alive
16	PMR	PMR	PMD	MB	MB	NO-MB	NO	NO	NO	22.7	dead
17	SMD	PMR	PMR	MB	MB	MB	NO	NO	NO	24.4	dead
18	SMD	CMR	CMR	MB	MB	MB	NO	NO	NO	32.5	alive
19	PMR	PMR	PMD	MB	MB	NO-MB	NO	NO	NO	29.5	dead
20	SMD	SMD	SMD	MB	MB	MB	NO	NO	NO	17.3	alive
21	PMR	PMR	PMR	MB	MB	MB	NO	NO	NO	26.9	alive
22	PMD	PMD		NO-MB	NO-MB		YES	YES		11.3	dead
23	PMD	PMD		NO-MB	NO-MB		YES	YES		22.4	alive
24	PMD	PMD		NO-MB	NO-MB		NO	NO		3.0	dead
25	PMD	PMD		NO-MB	NO-MB		NO	NO		15.9	alive
26	PMR	PMR		MB	MB		NO	NO		23.0	alive
27	PMD			NO-MB			YES			6.2	dead
28	PMD			NO-MB			YES			3.3	dead
29	PMR			MB			NO			4.0	dead
30	PMD			NO-MB			YES			3.7	dead
31	PMR			MB			NO			3.8	dead
32	PMD			NO-MB			YES			1.8	dead
33	PMR			MB			NO			9.1	dead
34	PMD			NO-MB			YES			7.1	dead
35	PMR			MB			NO			21.7	alive
36	PMD			NO-MB			NO			9.4	dead
37	PMD			NO-MB			NO			6.2	dead
38	PMD			NO-MB			YES			7.7	dead

(Continued)

TABLE 2 Continued

Patient no.	Treatment response evaluation			MB/NO-MB			Whether there are new visceral/bone lesion(s)(Yes/No)			OS(months)	Status
	SCAN-1	SCAN-2	SCAN-3	SCAN-1	SCAN-2	SCAN-3	SCAN-1	SCAN-2	SCAN-3		
39	PMD			NO-MB			YES			15.9	alive
40	PMR			MB			NO			28.6	alive
41	PMR			MB			NO			16.1	alive

PMD, progressive metabolic disease; SMD, stable metabolic disease; PMR, partial metabolic response. MB, metabolic benefit, including SMD, PMR, and CMR. NO-MB; no metabolic benefit, including patients with PMD.

with new visceral/bone lesions on SCAN-2 was 17.7 months, with 3 (75%) deaths. The mean OS in the other 22 patients without new lesions was 37.5 months, with 9 (40.91%) deaths. The difference between the two groups was statistically significant (log-rank p = 0.048). The Kaplan-Meier plots of OS are shown in Figure 2B. The mean OS in 5 patients with new visceral/bone lesions on SCAN-3 was 14.9 months with 5 (100%) deaths, while in the other 16 patients without new lesions, it was 43.4 months with 5 (31.25%) deaths. The difference between the two groups was statistically significant (log-rank p < 0.0001). The Kaplan-Meier plots for OS are shown in Figure 2C. For SCAN-2 and SCAN-3, the median OS could not be obtained because the mortality rates in patients with MB did not exceed 50%.

3.3 Consistent evaluation of short-term response

3.3.1 Consistency comparison of SCAN-1 and SCAN-2

Table 3 presents Consistency of short-term response of PET/CT. A total of 26 patients were included in the evaluation, including 18 patients with MB and 8 with NO-MB as assessed by SCAN-1, as well as 18 patients with MB and 8 with NO-MB as assessed by SCAN-2. However, 1 patient was evaluated as having PMD (NO-MB) in SCAN-1 due to several new lesions in the lung. In SCAN-2, all the new lesions disappeared, and the tumor burden of the primary lesion was reduced. The patient's OS was 31.1 months, and he was still alive

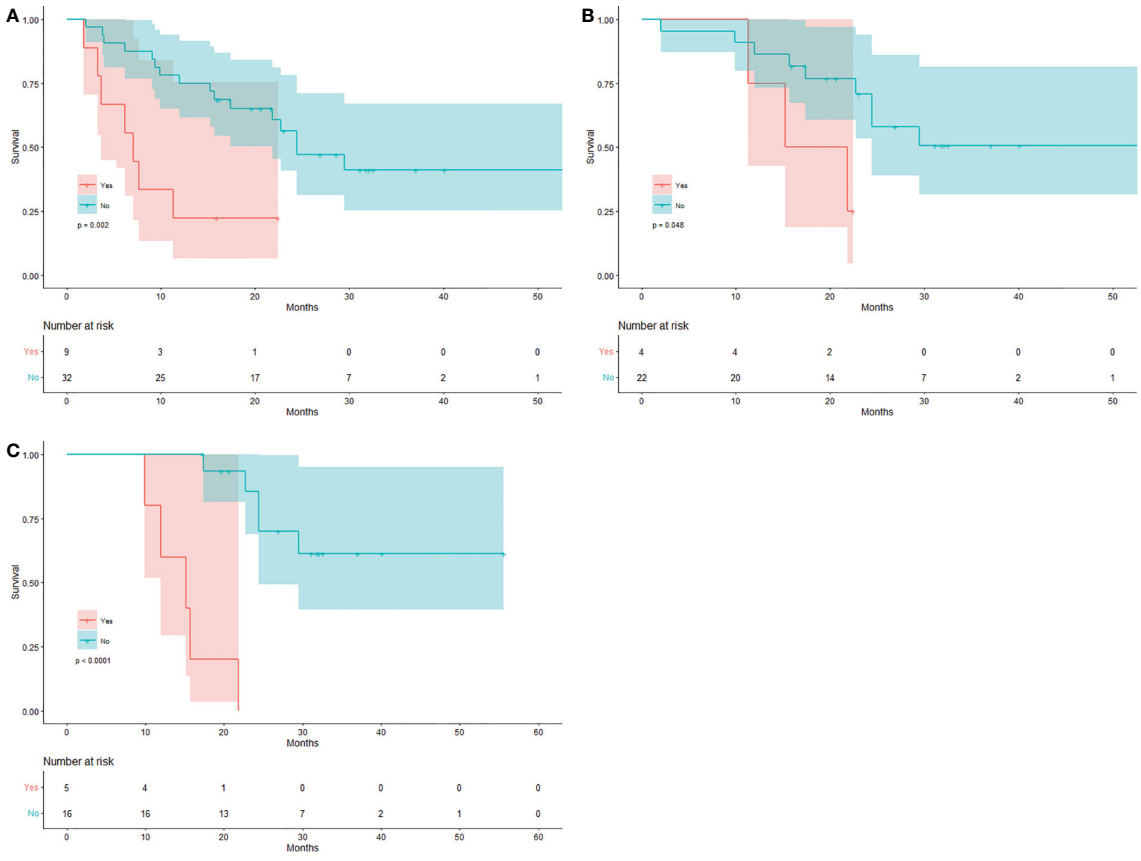

FIGURE 2
Kaplan-Meier curves for the new visceral/bone lesion(s). Patients with/without new visceral/bone lesion(s) on **(A)** SCAN-1, **(B)** SCAN-2, and **(C)** SCAN-3.

TABLE 3 Consistency of short-term response of PET/CT.

	KAPPA value	P
SCAN-1 and SCAN-2	0.819	0.000029
SCAN-1 and SCAN-3	0.33	0.091
SCAN-2 and SCAN-3	0.553	0.005

The consistency of the response evaluation results of SCAN-1 and SCAN-2 were generally consistent. The consistency of the response evaluation results of SCAN-1 and SCAN-3 was low. The consistency of the response evaluation results of SCAN-2 and SCAN-3 was moderate.

by the end follow-up date, with good clinical benefit. Therefore, his disease status was considered as pseudoprogression and evaluated as PMR (MB) in SCAN-2. One patient diagnosed with SMD (MB) in SCAN-1 was diagnosed with PMD (NO-MB) in SCAN-2. This patient exhibited lymph node metastasis on a PET scan 3 months after treatment, and the SUVmax value of the original lesion increased. The response evaluation results of two PET/CT treatments were consistent (p = 0.000029, Kappa value was 0.819). Therefore, PET evaluation at 1 month after treatment can roughly predict efficacy at 3 months after treatment.

3.3.2 Consistency comparison of SCAN-1 and SCAN-3

A total of 21 patients were included in the evaluation, including 17 patients with MB and 4 patients with NO-MB on SCAN-1, as well as 13 patients with MB and 8 patients with NO-MB on SCAN-3. Five patients with MB (4 PMR, 1 SMD) at SCAN-1 had progression at SCAN-3, including 3 new visceral/bone metastases. All 3 patients died, with an average OS of 12.5 months. The other 2 patients with only new lymph node metastases had an average OS of 26.1 months. One patient who was evaluated as having PMD (NO-MB) in SCAN-1 was evaluated as having PMR (MB) in SCAN-2 and SCAN-3, which was the same patient with the above pseudoprogression. The consistency of the response evaluation results of two PET/CT treatments was low (p = 0.091, Kappa value was 0.33).

3.3.3 Consistency comparison of SCAN-2 and SCAN-3

A total of 21 patients were included in the evaluation, including 17 with MB and 4 with NO-MB on SCAN-2 and 13 with MB and 8 with NO-MB on SCAN-3. Four patients with MB (4 PMR) on SCAN-2 had new metastases on SCAN-3. The mean OS times of 2 patients with new bone metastases and 2 patients with new lymph node metastases were 12.8 months and 26.1 months, respectively. The consistency of the response evaluation results of two PET/CT treatments was moderate (p = 0.005, Kappa value was 0.553).

3.3.4 Depth of response

On SCAN-1, 26 (63.41%), 5 (12.20%), and 10 (24.39%) patients were classified into G1, G2, and G3, respectively. The mean OS values for patients in the G1, G2, and G3 groups were 15.98, 28.97, and 37.85 months, respectively. There were 18 (69.23%), 1 (20.00%), and 4 (40.00%) deaths in the G1, G2, and G3 groups, respectively. The difference in OS between the three groups was statistically significant (log-rank p = 0.021). The Kaplan-Meier plots for OS are shown in Figure 3.

3.3.5 Prediction model

The Cox proportional hazards regression model results showed that ΔTLG, baseline MTV, ECOG performance status, and response evaluation were independent factors for death after correction for other factors (p < 0.05) (Table 4). The risk of death was 0.997 (0.996–0.999) times higher for each unit increase in ΔTLG, 1.042 (1.009–1.075) times higher for each unit increase in baseline MTV, and 2.762 (1.028–7.421) times higher for patients with an ECOG of 2 than those with an ECOG of 1. The risk of death was 3.703 (1.441–9.516) times greater in patients with PMD than in those with MB. These four features were used to establish a nomogram model (Figure 4). The C index of the model was 0.801 (95% confidence interval [CI]: 0.731–0.884). Figures 5, 6 show the internal validation of the model. Based on the receiver operating characteristics curve analysis, the model had a high area under the curve (1 year: 0.88, 95% CI: 0.75–1.00, 2 years: 0.84, 95% CI: 0.71–0.98) (Figure 5). The calibration curves for the 1-year and 2-year OS prediction models were closer to the 45° diagonal, indicating that the model predicted survival rates closer to the actual rates (Figure 6).

4 Discussion

In recent years, some clinical trials have shown that iRT could potentially be utilized for any stage of NSCLC. For metastatic cases, there is randomized evidence to support the addition of RT to immunotherapy (21–23). For locally advanced non-metastatic cases, the randomized PACIFIC trial demonstrated the efficacy of combining definitive RT with subsequent immunotherapy (24). Lastly, for early-stage NSCLC, there are several randomized trials aiming to evaluate stereotactic RT with or without adjuvant immunotherapy (e.g.NCT03110978, NCT03446547, NCT03833154, NCT03924869, NCT04214262). Some investigators suggest that SBRT is more effective in activating the body's anti-tumor

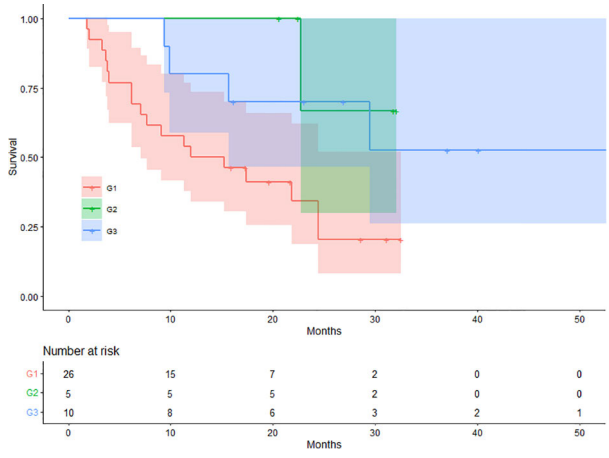

FIGURE 3
Kaplan-Meier curves for the depth of response.

TABLE 4 The results of COX proportional hazards regression model.

Characteristic	Univariate analysis		Multivariate analysis	
	P	*HR(95%CI)*	*P*	*HR(95%CI)*
Baseline SUVmax	0.809	0.986(0.876-1.109)		
△SUVmax	0.004	0.948(0.914-0.983)		
Baseline SULpeak	0.770	0.974(0.817-1.161)		
△SULpeak	0.010	0.942(0.901-0.986)		
Baseline TLG	0.029	1.005(1-1.009)		
△TLG	0.046	0.999(0.997-1)	0.001	0.997(0.996-0.999)
Baseline MTV	0.044	1.025(1.001-1.051)	0.011	1.042(1.009-1.075)
△MTV	0.248	0.993(0.981-1.005)		
Gender male v.s female	0.820	0.898(0.353-2.282)		
Age	0.765	0.993(0.946-1.042)		
Pathological pattern squamous carcina v.s adenocarcinoma	0.375	0.668(0.274-1.629)		
ECOG 2 v.s 1	0.008	3.478(1.386-8.73)	0.044	2.762(1.028-7.421)
Response evaluation PMD v.s MB	0.003	3.773(1.589-8.958)	0.007	3.703(1.441-9.516)

Baseline SUVmax, mean SUVmax of target lesion in SCAN-0; △SUVmax, SUVmax1 - SUVmax1; Baseline SULpeak, mean SULpeak of target lesion in SCAN-0; △SULpeak, SULpeak0 - SULpeak1; Baseline TLG, mean TLG of target lesion in SCAN-0; △TLG0, TLG0 - TLG1; Baseline MTV, mean MTV of target lesion in SCAN-0; △MTV, MTV0 - MTV1.

immunity than conventional fractionated RT and is the best "companion" for combined ICIs (25). A phase I study evaluated multisite SBRT followed by pembrolizumab for metastatic solid tumors, including NSCLC, and the results showed that the combination therapy had a high control rate in both post-RT and non-RT metastatic tumors. The RECIST-based overall response rate was 13.2%. Moreover, the median OS and progression-free survival were 9.6 months (95% CI: 6.5 months–undetermined) and 3.1 months (95% CI: 2.9–3.4 months), respectively (26). In our preliminary clinical trial study, we enrolled 31 patients with advanced lung cancer pathologically confirmed to have progressive disease, and 23 patients who completed the treatment were evaluated. At the 1-year follow-up, no patients had developed grade ≥ 3 pneumonitis. The overall objective response and complete remission rates were 39.13% and 13.04%, respectively. The 1-year OS and median progression-free survival were 60.9% and 6 months, respectively (27).

To our knowledge, the published data, though limited, indicate that the combination treatment has considerable promise in future NSCLC treatment. There is therefore an urgent need for reliable monitoring programs and predictors. Although PD-L1 positivity is enriched in populations with clinical benefits, PD-L1 testing alone appears to be insufficient for patient selection (28). Since there are no

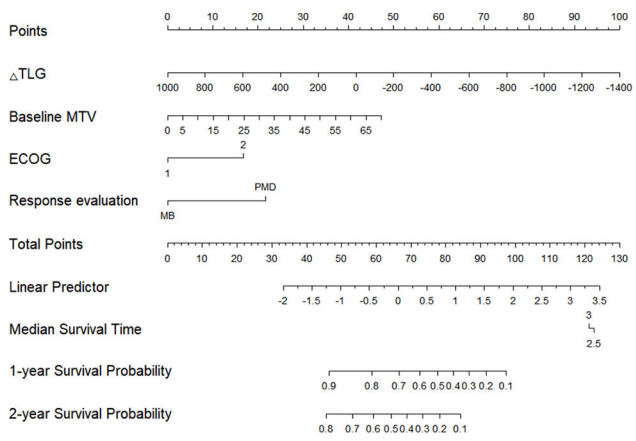

FIGURE 4
The nomogram based on the combination of clinical and PET/CT features.

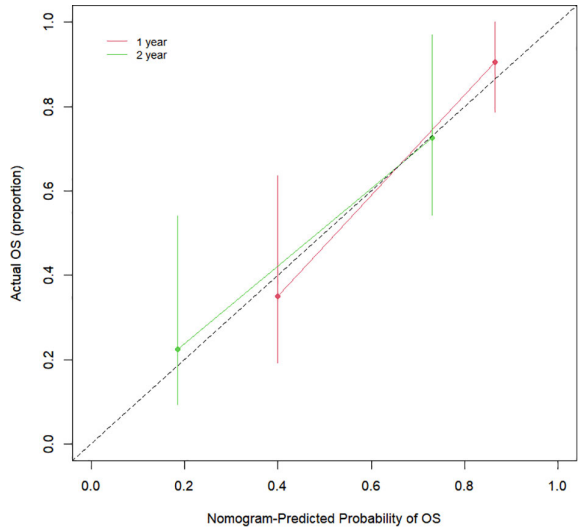

FIGURE 5
Calibration curves for the clinical parameters combined with the PET/CT features model.

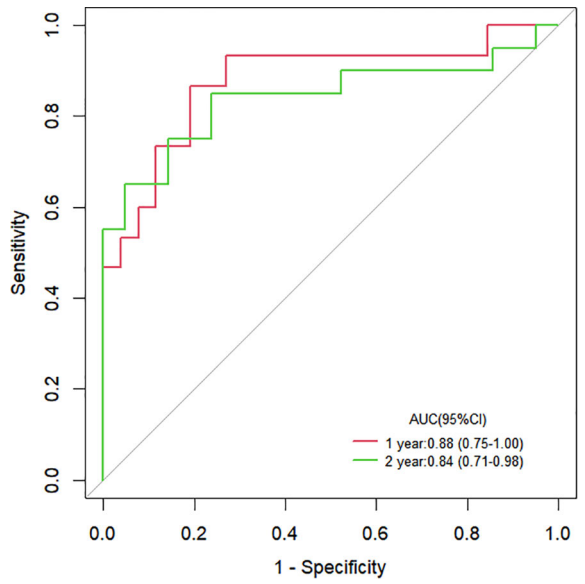

FIGURE 6
ROC curves for the clinical parameters combined with the PET/CT features model.

validated biomarkers that help identify NSCLC patients who are more likely to benefit from the combination of ICIs and RT, therapeutic decisions currently rely on imaging combined with a clinical evaluation. In 1999, for the first time, the EORTC defined PET criteria for standard response assessment using ^{18}F-FDG PET for solid tumors (13). Ten years later, the refined PERCIST system was developed based on additional literature (15). In addition, due to a limited cohort of patients, new immune-related PET criteria have been proposed, mainly focusing on melanoma or lymphoma (29–32). However, the response pattern for RT combined with immunotherapy by imaging is still poorly understood. The immune-related PET criteria for immunotherapy were established based on small-sized clinical studies, and the accuracy of evaluation still needs to be confirmed. Therefore, based on the clinical trials conducted by our group, the EORTC and PERCIST criteria were used for response evaluation. We established a preliminary training set to determine the response prediction value of PET/CT for HFRT combined with PD-1 blockade.

Christos et al. (14) used the EORTC criteria for the first time to evaluate the response to immunotherapy and found that the response to early PET (after two cycles of treatment) could effectively predict the outcomes of the intermediate PET (four cycles). They could determine a predictive value for the prognosis of PMD and SMD by studying 22 patients with melanoma treated with epirimizumab who underwent PET/CT before and two and four cycles after treatment. In this study, it was also found that the evaluation results of SCAN-1 and SCAN-2 were generally consistent and the response of PET at 1 month after treatment could roughly predict the response at 3 months after treatment. Therefore, we suggest that patients undergo only one PET scan within 3 months after treatment, this therapeutic strategy should reduce both economic burden and radiation side effects for patients. Meanwhile, both criteria were highly predictive of OS in studies of NSCLC patients treated with RT plus chemotherapy, with a high agreement in efficacy evaluation between the two (Kappa value = 0.95) (33). A previous study on small cell lung cancer treated with RT and chemotherapy reached similar conclusions, with both criteria in complete agreement, and a significant difference was seen in OS between the CMR and No CMR groups ($p = 0.0431$) (34). However, in this study, due to the addition of PD-1 blockade, both SMD and PMR patients received good clinical benefits; therefore, we grouped the patients into PMD and No PMD groups. When patients were classified into the CMR, PMR, SMD, and PMD groups, we found slight differences in the evaluation based on the two criteria. When patients were further dichotomized into the MB (No PMD) and NO-MB (PMD) groups, the findings were identical with both criteria. PET was able to classify most patients in all periods, although some were still misclassified.

In addition, we explored other indicators associated with OS to identify prognostic factors. In this study, the number of new visceral/bone lesions was low and was seen in 9/41(21.95%), 4/26(15.38%), and 5/21(23.81%) patients in the SCAN-1, SCAN-2, and SCAN-3 groups, respectively. Although the lesions could not be counted effectively, a preliminary trend could be seen in the Kaplan-Meier survival curve. Compared to patients with no metastases, those with metastases had significantly longer OS times. Previous studies have suggested that the presence of new visceral/bone lesions was the strongest surrogate indicator of poor prognosis following treatment with ICIs in patients with NSCLC; only 5/20 patients achieved durable clinical benefits. Sensitivity, specificity, positive predictive value, negative predictive value, and Youden's indices for predicting no benefit were 71.4%, 82.8%, 75%, 80%, and 0.54, respectively. However, there was still a high number of responding patients who were misclassified (positive predictive value = 75%) (18). Therefore, we hypothesized that new visceral/bone lesions might indicate a poor prognosis in NSCLC patients receiving RT combined with ICIs. These patients should be removed from the group and either switched to regimens that combine other treatments or enrolled in other clinical trials.

We aimed to identify patients with a poor prognosis as early as possible, and therefore, we focused on the correlation between PET parameters in SCAN-1 and prognosis. This study classified patients using SUVmax decline rates of 30% and 50% as the cutoff points. An SUVmax decline rate of > 50% was associated with significantly longer OS, suggesting that the DpR is correlated with prognosis in early PET after treatment to some extent. However, the potential of △SUV (before and after treatment) as a prognostic indicator remains unclear. In a study on nasopharyngeal carcinoma patients (35), Qi et al. used percent SUV decline during RT to assess radiosensitivity. They reported that a 70% SUVmax decline after two cycles of treatment was a good cutoff point for PET to predict tumor regression after RT and chemotherapy in these patients. In a study of 46 patients with advanced lung adenocarcinoma who received gefitinib-targeted therapy, they found that compared to patients with △SUV% ≥ 25% (PMD), the survival time was significantly prolonged in those with △SUV

% < -25% (including CMR and PMR) (10.6/18.4, p = 0.000) but not in patients with -25% ≤ △SUV% < 25% (SMD) (10.6/10.7, p = 0.088) (36).

In summary, although the indicators explored in this study were correlated with prognosis to a certain extent, some patients were still misclassified. Establishing a personalized prediction model is necessary to ensure precise treatment and accurate prediction of which patients would benefit from the treatment. Based on the data from this clinical trial, we established a training set to help develop subsequent clinical trials. PET/CT provides information on metabolic parameters, such as SUV, SUL, MTV, and TLG. Lin et al. (37) demonstrated that > 50% decreases in lymph node SUVmean, MTV, and TLG during RT are prognostic predictors of locally advanced head and neck squamous carcinoma. Changes in MTV and TLG before and after treatment are accurate and independent prognostic indicators in various tumors, including nasopharyngeal, esophageal, pancreatic, and ovarian cancers (38–41). In a retrospective study of NSCLC patients receiving chemotherapy, Moon et al. found that patients with a ΔTLG of > 50% had a longer progression-free survival after one cycle of chemotherapy (42). In another prospective study of 37 patients with NSCLC treated with RT and chemotherapy, Huang et al. (43) found that patients with more significant changes in SUVmax and MTV before and after treatment had better treatment sensitivity. In this study, ΔTLG, baseline MTV, ECOG performance status, and response evaluation were screened using the Cox proportional hazards regression model to generate a nomogram graph and a model to predict survival with an ideal predictive value for patients treated with HFRT combined with PD-1 blockade.

5 Limitations and conclusion

This study has some limitations. First, like the previous studies, it was a small-sized, single-center clinical study. Currently, available response evaluation criteria are based on single treatment modalities. Studies with larger sample sizes are urgently needed to evaluate RT combined with immunotherapy as a prospective treatment option and to establish precise and complete evaluation criteria. Second, the prediction model in this study used only the metabolic parameters of PET and not PET radiomics to analyze the texture-structure parameters of the images. PET-based radiomics is also a critical prognostic tool for patients with NSCLC after RT or immunotherapy.

In conclusion, our preliminary data show that PET/CT can correctly classify most patients using the EORTC and PERCIST criteria, and it is recommended that only one PET scan be performed 3 months after treatment. Additionally, new visceral/bone lesions and DpR may be prognostic indicators, and a predictive model of survival probability with an optimal predictive value has been established. To the best of our knowledge, this is the first trial to investigate the potential of PET/CT for monitoring and predicting the outcomes of HFRT plus PD-1 blockade therapy in patients with NSCLC. A PET/CT scan after treatment could be a reliable indicator of patient outcomes and should be investigated further.

We are conducting a multicenter prospective study of HFRT combined with PD-1 blockade for NSCLC, including more patients, to explore further the value of PET/CT for evaluating the response to RT combined with ICIs. In the future, we plan to improve the validation set of the prediction model and develop a complete and accurate patient monitoring system.

Data availability statement

The original contributions presented in the study are included in the article/Supplementary Material. Further inquiries can be directed to the corresponding author.

Ethics statement

The studies involving human participants were reviewed and approved by the Affiliated Hospital of Southwest Medical University Clinical Trial Ethics Committee. The patients/participants provided their written informed consent to participate in this study. Written informed consent was obtained from the individual(s) for the publication of any potentially identifiable images or data included in this article.

Author contributions

Conception and design: SL, and ST. Administrative support: SL. Provision of study materials or patients: YZ (2nd author), YL and YZ (4th author). Collection and assembly of data: YX, HD, and YC. Data analysis and interpretation: ST, PR, HY, and SF. Manuscript writing: ST. Final approval of manuscript: SL. All authors contributed to the article and approved the submitted version.

Funding

This work was supported by grants from the National Natural Science Foundation of China (no. 81201682), Scientific Research Foundation of the Luzhou Science and Technology Bureau (no. 2016LZXNYD-J05), and Southwest Medical University Foundation (No. 201617).

Acknowledgments

We thank the patients who voluntarily participated in this study. We would like to thank Editage (www.editage.cn) for the English language editing. We thank ZG-Z for his contribution to this study.

Conflict of interest

The authors declare that the research was conducted in the absence of any commercial or financial relationships that could be construed as a potential conflict of interest.

Publisher's note

All claims expressed in this article are solely those of the authors and do not necessarily represent those of their affiliated organizations, or those of the publisher, the editors and the reviewers. Any product that may be evaluated in this article, or claim that may be made by its manufacturer, is not guaranteed or endorsed by the publisher.

Supplementary material

The Supplementary Material for this article can be found online at: https://www.frontiersin.org/articles/10.3389/fimmu.2023.1034416/full#supplementary-material

References

1. Chen VW, Ruiz BA, Hsieh MC, Wu XC, Ries LA, Lewis DR. Analysis of stage and clinical/prognostic factors for lung cancer from SEER registries: AJCC staging and collaborative stage data collection system. *Cancer* (2014) 120 Suppl;23:3781–92. doi: 10.1002/cncr.29045

2. Goldstraw P, Chansky K, Crowley J, Rami-Porta R, Asamura H, Eberhardt WE, et al. The IASLC lung cancer staging project: Proposals for revision of the TNM stage groupings in the forth coming (Eighth) edition of the TNM classification for lung cancer. *J Thorac Oncol* (2016) 11(1):39–51. doi: 10.1016/j.jtho.2015.09.009

3. Brahmer J, Reckamp KL, Baas P, Crinò L, Eberhardt WE, Poddubskaya E, et al. Nivolumab versus docetaxel in advanced squamous-cell non-Small-Cell lung cancer. *N Engl J Med* (2015) 373(2):123–35. doi: 10.1056/NEJMoa1504627

4. Gandhi L, Rodríguez-Abreu D, Gadgeel S, Esteban E, Felip E, De Angelis F, et al. Pembrolizumab plus chemotherapy in metastatic non-Small-Cell lung cancer. *N Engl J Med* (2018) 378(22):2078–92. doi: 10.1056/NEJMoa1801005

5. Mok TSK, Wu YL, Kudaba I, Kowalski DM, Cho BC, Turna HZ, et al. Pembrolizumab versus chemotherapy for previously untreated, PD-L1-expressing, locally advanced or metastatic non-small-cell lung cancer (KEYNOTE-042): a randomised, open-label, controlled, phase 3 trial. *Lancet* (2019) 393(10183):1819–30. doi: 10.1016/S0140-6736(18)32409-7

6. Borghaei H, Paz-Ares L, Horn L, Spigel DR, Steins M, Ready NE, et al. Nivolumab versus docetaxel in advanced nonsquamous non-Small-Cell lung cancer. *N Engl J Med* (2015) 373(17):1627–39. doi: 10.1056/NEJMoa1507643

7. Horn L, Spigel DR, Vokes EE, Holgado E, Ready N, Steins M, et al. Nivolumab versus docetaxel in previously treated patients with advanced non-Small-Cell lung cancer: Two-year outcomes from two randomized, open-label, phase III trials (CheckMate 017 and CheckMate 057). *J Clin Oncol* (2017) 35(35):3924–33. doi: 10.1200/JCO.2017.74.3062

8. Gettinger S, Horn L, Jackman D, Spigel D, Antonia S, Hellmann M, et al. Five-year follow-up of nivolumab in previously treated advanced non-Small-Cell lung cancer: Results from the CA209-003 study. *J Clin Oncol* (2018) 36(17):1675–84. doi: 10.1200/JCO.2017.77.0412

9. Hui R, Özgüroğlu M, Villegas A, Daniel D, Vicente D, Murakami S, et al. Patient-reported outcomes with durvalumab after chemoradiotherapy in stage III, unresectable non-small-cell lung cancer (PACIFIC): a randomised, controlled, phase 3 study. *Lancet Oncol* (2019) 20(12):1670–80. doi: 10.1016/S1470-2045(19)30519-4

10. Faivre-Finn C, Vicente D, Kurata T, Planchard D, Paz-Ares L, Vansteenkiste JF, et al. Four-year survival with durvalumab after chemoradiotherapy in stage III NSCLC-an update from the PACIFIC trial. *J Thorac Oncol* (2021) 16(5):860–7. doi: 10.1016/j.jtho.2020.12.015

11. Jabbour SK, Lee KH, Frost N, Breder V, Kowalski DM, Pollock T, et al. Pembrolizumab plus concurrent chemoradiation therapy in patients with unresectable, locally advanced, stage III non-small cell lung cancer: The phase 2 KEYNOTE-799 nonrandomized trial. *JAMA Oncol* (2021) 7(9):1–9. doi: 10.1001/jamaoncol.2021.2301

12. Sheikhbahaei S, Mena E, Yanamadala A, Reddy S, Solnes LB, Wachsmann J, et al. The value of FDG PET/CT in treatment response assessment, follow-up, and surveillance of lung cancer. *AJR Am J Roentgenol* (2017) 208(2):420–33. doi: 10.2214/AJR.16.16532

13. Young H, Baum R, Cremerius U, Herholz K, Hoekstra O, Lammertsma AA, et al. Measurement of clinical and subclinical tumour response using [^{18}F]-fluorodeoxyglucose and positron e mission tomography: review and 1999 EORTC recommendations. *Eur Organ Res Treat Cancer (EORTC) PET Study Group Eur J Cancer* (1999) 35(13):1773–82. doi: 10.1016/s0959-8049(99)00229-4

14. Sachpekidis C, Larribere L, Pan L, Haberkorn U, Dimitrakopoulou-Strauss A, Hassel JC. Predictive value of early ^{18}F-FDG PET/CT studies for treatment response evaluation to ipilimumab in m etastatic melanoma: preliminary results of an ongoing study. *Eur J Nucl Med Mol Imaging* (2015) 42(3):386–96. doi: 10.1007/s00259-014-2944-y

15. Wahl RL, Jacene H, Kasamon Y, Lodge MA. From RECIST to PERCIST: Evolving considerations for PET response criteria in solid tumors. *J Nucl Med* (2009) 50 Suppl 1:122s–50s. doi: 10.2967/jnumed.108.057307

16. Mattoli MV, Massaccesi M, Castelluccia A, Scolozzi V, Mantini G, Calcagni ML. The predictive value of ^{18}F-FDG PET-CT for assessing the clinical outcomes in locally advanced NSCLC patients after a new induction treatment: low-dose fractionated radiotherapy with concurrent chemotherapy. *Radiat Oncol* (2017) 12(1):4. doi: 10.1186/s13014-016-0737-0

17. Lee HY, Choi WH, Yoo IR, Park JK, Sung SW, Kim YS, et al. Prognostic value of ^{18}F-FDG PET parameters in patients with locally advanced non-small cell lung canc er treated with induction chemotherapy. *Asia Pac J Clin Oncol* (2020) 16(1):70–4. doi: 10.1111/ajco.13288

18. Humbert O, Cadour N, Paquet M, Schiappa R, Poudenx M, Chardin D, et al. ^{18}FDG PET/CT in the early assessment of non-small cell lung cancer response to immunotherapy: frequen cy and clinical significance of atypical evolutive patterns. *Eur J Nucl Med Mol Imaging* (2020) 47(5):1158–67. doi: 10.1007/s00259-019-04573-4

19. Stefano A, Russo G, Ippolito M, Cosentino S, Murè G, Baldari S, et al. Evaluation of erlotinib treatment response in non-small cell lung cancer using metabolic and anatomic criteria. *Q J Nucl Med Mol Imaging* (2016) 60(3):264–73.

20. Boellaard R, O'Doherty MJ, Weber WA, Mottaghy FM, Lonsdale MN, Stroobants SG, et al. FDG PET and PET/CT: EANM procedure guidelines for tumour PET imaging: version 1.0. *Eur J Nucl Med Mol Imaging* (2010) 37(1):181–200. doi: 10.1007/s00259-009-1297-4

21. Theelen W, Peulen HMU, Lalezari F, van der Noort V, de Vries JF, Aerts J, et al. Effect of pembrolizumab after stereotactic body radiotherapy vs pembrolizumab alone on tumor response in patients with advanced non-small cell lung cancer: Results of the PEMBRO-RT phase 2 randomized clinical trial. *JAMA Oncol* (2019) 5(9):1276–82. doi: 10.1001/jamaoncol.2019.1478

22. Theelen W, Chen D, Verma V, Hobbs BP, Peulen HMU, Aerts J, et al. Pembrolizumab with or without radiotherapy for metastatic non-small-cell lung cancer: A pooled analysis of two randomised trials. *Lancet Respir Med* (2021) 9(5):467–75. doi: 10.1016/S2213-2600(20)30391-X

23. Welsh J, Menon H, Chen D, Verma V, Tang C, Altan M, et al. Pembrolizumab with or without radiation therapy for metastatic non-small cell lung cancer: A randomized phase I/II trial. *J Immunother Cancer* (2020) 8(2):e001001. doi: 10.1136/jitc-2020-001001

24. Antonia SJ, Villegas A, Daniel D, Vicente D, Murakami S, Hui R, et al. Durvalumab after chemoradiotherapy in stage III non-Small-Cell lung cancer. *N Engl J Med* (2017) 377 (20):1919–29. doi: 10.1056/NEJMoa1709937

25. Chen Y, Gao M, Huang Z, Yu J, Meng X. SBRT combined with PD-1/PD-L1 inhibitors in NSCLC treatment: a focus on the mechanisms, advances, and future challenges. *J Hematol Oncol* (2020) 13(1):105. doi: 10.1186/s13045-020-00940-z

26. Luke JJ, Lemons JM, Karrison TG, Pitroda SP, Melotek JM, Zha Y, et al. Safety and clinical activity of pembrolizumab and multisite stereotactic body radiotherapy in patients with advanced solid tumors. *J Clin Oncol* (2018) 36(16):1611–8. doi: 10.1200/JCO.2017.76.2229

27. Ye H, Pang H, Shi X, Ren P, Huang S, Yu H, et al. Nivolumab and hypofractionated radiotherapy in patients with advanced lung cancer: ABSCOPAL-1 clinical trial. *Front Oncol* (2021) 11:657024. doi: 10.3389/fonc.2021.657024

28. Gibney GT, Weiner LM, Atkins MB. Predictive biomarkers for checkpoint inhibitor-based immunotherapy. *Lancet Oncol* (2016) 17(12):e542–e51. doi: 10.1016/S1470-2045(16)30406-5

29. Sachpekidis C, Anwar H, Winkler J, Kopp-Schneider A, Larribere L, Haberkorn U, et al. The role of interim ^{18}F-FDG PET/CT in prediction of response to ipilimumab treatment in metastatic melanoma. *Eur J Nucl Med Mol Imaging* (2018) 45(8):1289–96. doi: 10.1007/s00259-018-3972-9

30. Goldfarb L, Duchemann B, Chouahnia K, Zelek L, Soussan M. Monitoring anti-PD-1-based immunotherapy in non-small cell lung cancer with FDG PET: introduction of iPERCIST. *EJNMMI Res* (2019) 9(1):8. doi: 10.1186/s13550-019-0473-1

31. Cho SY, Lipson EJ, Im HJ, Rowe SP, Gonzalez EM, Blackford A, et al. Prediction of response to immune checkpoint inhibitor therapy using early-Time-Point ^{18}F-FDG PET/CT I maging in patients with advanced melanoma. *J Nucl Med* (2017) 58(9):1421–8. doi: 10.2967/jnumed.116.188839

32. Cheson BD, Ansell S, Schwartz L, Gordon LI, Advani R, Jacene HA, et al. Refinement of the lugano classification lymphoma response criteria in the era of immunomodulatory therapy. *Blood* (2016) 128(21):2489–96. doi: 10.1182/blood-2016-05-718528

33. Turgeon GA, Iravani A, Akhurst T, Beaulieu A, Callahan JW, Bressel M, et al. What ^{18}F-FDG PET response-assessment method best predicts survival after curative-intent chemoradiati on in non-small cell lung cancer: EORTC, PERCIST, Peter mac criteria, or deauville criteria? *J Nucl Med* (2019) 60(3):328–34. doi: 10.2967/jnumed.118.214148

34. Ziai D, Wagner T, El Badaoui A, Hitzel A, Woillard JB, Melloni B, et al. Therapy response evaluation with FDG-PET/CT in small cell lung cancer: A prognostic and comparison st udy of the PERCIST and EORTC criteria. *Cancer Imaging* (2013) 13:73–80. doi: 10.1102/1470-7330.2013.0008

35. Qi S, Zhongyi Y, Yingjian Z, Chaosu H. (^{18})F-FLT and (18)F-FDG PET/CT in predicting response to chemoradiotherapy in nasopharyngeal carcinoma: Preliminary results. *Sci Rep* (2017) 7:40552. doi: 10.1038/srep40552

36. Rong X, Cai X, Li R, Chen J, Wang Q, You C, et al. Positron emission tomography-computed tomography on predicting the efficacy of targeted therapy for lung adenocarcinoma. *Thorac Cancer* (2014) 5(4):297–303. doi: 10.1111/1759-7714.12092

37. Lin P, Min M, Lee M, Holloway L, Forstner D, Bray V, et al. Nodal parameters of FDG PET/CT performed during radiotherapy for locally advanced mucosal primary hea d and neck squamous cell carcinoma can predict treatment outcomes: SUVmean and response rate are use ful imaging biomarkers. *Eur J Nucl Med Mol Imaging* (2017) 44 (5):801–11. doi: 10.1007/s00259-016-3584-1

38. Huang Y, Feng M, He Q, Yin J, Xu P, Jiang Q, et al. Prognostic value of pretreatment ^{18}F-FDG PET-CT for nasopharyngeal carcinoma patients. *Med (Baltimore)* (2017) 96(17):e6721. doi: 10.1097/MD.0000000000006721

39. Tamandl D, Ta J, Schmid R, Preusser M, Paireder M, Schoppmann SF, et al. Prognostic value of volumetric PET parameters in unresectable and metastatic esophageal cancer. *Eur J Radiol* (2016) 85(3):540–5. doi: 10.1016/j.ejrad.2016.01.002

40. Zhu D, Wang L, Zhang H, Chen J, Wang Y, Byanju S, et al. Prognostic value of ^{18}F-FDG-PET/CT parameters in patients with pancreatic carcinoma: A systematic rev iew and meta-analysis. *Med (Baltimore)* (2017) 96(33):e7813. doi: 10.1097/MD.0000000000007813

41. Chung HH, Kwon HW, Kang KW, Park NH, Song YS, Chung JK, et al. Prognostic value of preoperative metabolic tumor volume and total lesion glycolysis in patients with epithelial ovarian cancer. *Ann Surg Oncol* (2012) 19(6):1966–72. doi: 10.1245/s10434-011-2153-x

42. Moon SH, Cho SH, Park LC, Ji JH, Sun JM, Ahn JS, et al. Metabolic response evaluated by ^{18}F-FDG PET/CT as a potential screening tool in identifying a subgrou p of patients with advanced non-small cell lung cancer for immediate maintenance therapy after first -line chemotherapy. *Eur J Nucl Med Mol Imaging* (2013) 40(7):1005–13. doi: 10.1007/s00259-013-2400-4

43. Huang W, Zhou T, Ma L, Sun H, Gong H, Wang J, et al. Standard uptake value and metabolic tumor volume of ^{18}F-FDG PET/CT predict short-term outcome early i n the course of chemoradiotherapy in advanced non-small cell lung cancer. *Eur J Nucl Med Mol Imaging* (2011) 38(9):1628–35. doi: 10.1007/s00259-011-1838-5

frontiers | Frontiers in Immunology

TYPE Original Research
PUBLISHED 20 February 2023
DOI 10.3389/fimmu.2023.960339

Check for updates

OPEN ACCESS

EDITED BY
Feng-Ming (Spring) Kong,
The University of Hong Kong, Hong Kong SAR, China

REVIEWED BY
Yan-Yang Wang,
General Hospital of Ningxia Medical University, China
Yingming Sun,
Fujian Medical University, China
Mohamed Rahouma,
NewYork-Presbyterian, United States

*CORRESPONDENCE
Hui Zhu
drzhuh@126.com

SPECIALTY SECTION
This article was submitted to Cancer Immunity and Immunotherapy, a section of the journal Frontiers in Immunology

RECEIVED 02 June 2022
ACCEPTED 07 February 2023
PUBLISHED 20 February 2023

CITATION
Xu S, Xu X and Zhu H (2023) Pre-immunotherapy radiotherapy enhanced the efficacy of multi-line sintilimab in unresectable advanced esophageal squamous cell carcinoma.
Front. Immunol. 14:960339.
doi: 10.3389/fimmu.2023.960339

COPYRIGHT
© 2023 Xu, Xu and Zhu. This is an open-access article distributed under the terms of the Creative Commons Attribution License (CC BY). The use, distribution or reproduction in other forums is permitted, provided the original author(s) and the copyright owner(s) are credited and that the original publication in this journal is cited, in accordance with accepted academic practice. No use, distribution or reproduction is permitted which does not comply with these terms.

Pre-immunotherapy radiotherapy enhanced the efficacy of multi-line sintilimab in unresectable advanced esophageal squamous cell carcinoma

Shuhui Xu[1], Xianxing Xu[2] and Hui Zhu[1]*

[1]Department of Radiation Oncology, Shandong Cancer Hospital and Institute, Shandong First Medical University and Shandong Academy of Medical Sciences, Jinan, Shandong, China, [2]Department of Joint Surgery, Shandong Provincial Hospital Affiliated to Shandong First Medical University, Jinan, Shandong, China

Background: The use of immunotherapy for the treatment of esophageal squamous cell carcinoma (ESCC) is gradually increasing. In this retrospective study, we evaluated the efficacy and explored potential factors of prognosis in multi-line sintilimab for unresectable advanced ESCC.

Methods: All pathological specimens were available from our Department of Pathology. We performed PD-L1 immunohistochemical staining of surgical or puncture specimens from 133 patients. We evaluated the efficacy of multi-line sintilimab and found potential factors according to multivariate analysis. We assessed the relationship between radiotherapy and immunotherapy, and according to whether patients had received radiotherapy within 3 months prior to immunotherapy, we attempted to analyze differences in progression-free survival (PFS) and overall survival (OS).

Results: A total of 133 patients were enrolled in this retrospective study between January 2019 and December 2021. The median follow-up was 16.1 months. All patients were treated with at least two cycles of sintilimab. Of all patients, a total of 74 experienced disease progression, with a median progression-free survival of 9.0 months (95% CI 7.701–10.299). We found that pre-immunotherapy radiotherapy was a possible predictor that affected the prognosis of multi-line sintilimab and that 3 months was a significant cutoff. A total of 128 patients (96.2%) had received radiotherapy prior to immunotherapy. Of those patients, 89 (66.9%) had received radiation therapy within 3 months prior to immunotherapy. PFS was considerably longer in patients who were treated within 3 months of radiotherapy than in patients who did not receive radiation therapy within 3 months of radiation therapy prior to immunotherapy (median progression-free survival 10.0 months [95% CI 8.030–11.970] *vs.* 5.0 months [95% CI 2.755–7.245]). Among all patients, the median overall survival was 14.9 months (95% CI 12.558–17.242). Overall survival was significantly longer in patients who had previously received radiotherapy within 3 months prior to immunotherapy than

in those who had not (median overall survival 15.3 months [95% CI 13.724–16.876] *vs.* 12.2 months [10.001–14.399].

Conclusion: Based on this retrospective study, sintilimab is a significant option for patients with unresectable advanced ESCC who have been previously treated, and pre-immunotherapy radiotherapy within 3 months enhanced the efficacy.

KEYWORDS

pre-immunotherapy, immunotherapy, sintilimab, esophageal squamous cell carcinoma, efficacy

1 Introduction

Esophageal cancer (EC) is the primary cancer-related cause of death worldwide (1). Esophageal squamous cell carcinoma (ESCC) is one of the main typical epidemiological subtypes of EC, 95% of EC cases in China are ESCC, and 60% to 70% of patients have already reached a locally advanced or late stage at their first consultation (2, 3). For patients in an inoperable stage, it is hoped that the combination of chemotherapy and radiotherapy will improve the positive outcome of either treatment alone. These schemes aim to stabilize the patient's disease progression and improve the prognosis but, unfortunately, do not cure or control the disease progression in the long term. Therefore, there is an unmet need for the development of more treatment options to treat refractory or relapsed advanced ESCC.

In recent years, significant efforts have been made to improve the prognosis of advanced ESCC patients. Among the studies of immune checkpoint inhibitors (ICIs), most focus on anti-programmed cell death protein 1(PD-1)/programmed cell-death protein 1 ligand 1 (PD-L1) antibodies (4–7). In the ATTRACTION-3 study, nivolumab demonstrated significant efficacy in unresectable advanced or recurrent ESCC (6). The KEYNOTE-028 and KEYNOTE-180 studies also proved the efficacy and safety of pembrolizumab in the treatment of advanced EC (8, 9). The results of the clinical trial showed that anti-PD-1 antibodies demonstrated promising anti-tumor effects in patients with advanced ESCC (10). These studies have revolutionized the therapeutic strategy for advanced ESCC. Sintilimab is a humanized IgG4 monoclonal antibody that binds to PD-1, targeting the interaction between PD-1 receptors and their ligands to block them, and effectively improves the function of T cells, enhancing immune surveillance and eliminating the ability of T cells in the tumor to produce the tumor immune response. Although the evidence of sintilimab in first-line treatment is strong in resectable advanced ESCC (11, 12), there have been limited reports of unresectable advanced ESCC patients who received multi-line sintilimab to date.

The combination of radiotherapy and PD-L1 blockade has shown promising responses in many tumors with multi-line treatments. Previous studies have shown that radiotherapy induces an organismal immune response that allows patients to escape from immunosuppression after receiving radiotherapy, which can promote systemic anti-tumor immune activation and upregulation of PD-L1 expression on tumor cells (13–16). Radiotherapy is also a double-edged sword, capable of producing both immune stimulation and immunosuppression. There is growing evidence that radiotherapy enhances the intrinsic and adaptive immune responses against tumors, thereby reducing immunosuppression. Therefore, in this retrospective study, we evaluated the efficacy of sintilimab in unresectable advanced esophageal squamous cell carcinoma and investigated whether radiotherapy within 3 months before immunotherapy could improve the effectiveness of multi-line sintilimab in unresectable advanced ESCC.

2 Materials and methods

2.1 Data collection

We retrospectively included the medical records of 133 unresectable advanced ESCC patients from Shandong Cancer Hospital between January 2019 and December 2021. The inclusion criteria were as follows: 1) confirmed unresectable advanced ESCC, 2) complete imaging reports before and after immunotherapy, 3) at least one measurable lesion, 4) available histological samples were taken in our hospital, 5) patients received sintilimab as third-line or multi-line treatment, 6) patients did not receive any immunotherapy treatment before sintilimab, 7) all patients were treated with at least two cycles of sintilimab, and 8) the Eastern Cooperative Oncology Group (ECOG) score was ≥1. Data regarding clinical features, disease characteristics, previous treatments, disease response, and outcomes were collected. All patients underwent a complete physical examination and complete history collection. All pathological diagnoses were confirmed by pathologists in our department. TNM stage was determined according to the eighth American Joint Committee on Cancer guidelines. The study was conducted in accordance with the Declaration of Helsinki and International Good Clinical Practice Guidelines (17).

2.2 PD-L1 expression and radiotherapy

Tumor tissue samples from 133 participants were obtained for PD-L1 expression by immunohistochemistry. In this study, the measure of PD-L1 expression analysis was the combined positive score (CPS), defined as the sum of the number of PD-L1 stained cells, including tumor cells, lymphocytes, and macrophages, divided by the total number of tumor cells multiplied by 100. Expression of at least 1% was considered positive. PD-L1 was expressed both on the cell membrane and in the cytoplasm. In this retrospective study, PD-L1 expression showed heterogeneity in 133 patients (Figure 1).

The number of patients treated with radiotherapy within 1 month before immunotherapy was small and had no statistical significance. After a retrospective analysis of all patients, we found that 3 months could be used as the cutoff value of the interval between radiotherapy and immunotherapy. Based on that and to reduce the impact of other treatments on immunotherapy, patients were recorded as having received radiotherapy if they had received radiotherapy within 3 months prior to their first dose of sintilimab. We considered radiation therapy (RT) and sintilimab interval times beyond 3 months or no radiation as the same status, and these patients were classified in the group that did not receive radiotherapy. Based on the extensive data that were collected, local radiotherapy stimulated a systemic immune response.

2.3 Clinical response assessment

All patients were regularly followed up until the deadline (December 2021) or death by using clinical records. Follow-up visits were scheduled every 3 months. Progressive disease was verified by imaging review. Based on the Response Evaluation Criteria in Solid Tumors version 1.1, our study assessed objective tumor response by computed tomography (CT) scan (18). The CT before immunotherapy was used as a baseline, after which efficacy was assessed every 8 weeks, with the categories of responses being: complete response (CR), partial response (PR), stable disease (SD), or disease progression (PD). All patients were monitored regularly for possible adverse events (AEs). AEs were evaluated during the entire course of immunotherapy and up to 30 days after immunotherapy and were graded 0–4 in accordance with the National Cancer Institute Common Terminology Criteria for Adverse Events (version 4.0). The primary endpoints of this study were progression-free survival (PFS) and overall survival (OS). PFS was calculated from the date of initial treatment with sintilimab to the date of progression or death. OS was defined as the time from the first dose of sintilimab to the date of death from any cause. The secondary endpoints were objective response rate (ORR) (the percentage of patients with a confirmed complete or partial response) and disease control rate (DCR) (the proportion of patients with CR, PR, or SD in all cohorts receiving sintilimab).

2.4 Statistical analysis

Patients who lacked any of the indicators we needed were excluded from the study. We performed a multifactorial analysis with a Cox proportional hazards model, which was used to find possible predictors that affect prognosis. We used the χ^2 test and Fisher's exact test to compare the differences in baseline characteristics of patients between subgroups. We estimated progression-free survival, overall survival, median survival, and 95% CIs using the Kaplan–Meier analysis and compared subgroups (those who had received radiotherapy and those who had not received radiotherapy within 3 months before immunization) using the log-rank test. We used log-rank tests to detect the significant differences. The results with a p-value <0.05 were considered statistically significant.

3 Results

3.1 Patient characteristics

Between January 2019 and December 2021, 133 patients were assessed in this retrospective study. The clinical characteristics of both cohorts are presented in Table 1. Of the 133 patients tested, the median patient age was 65 years (range 48–78). Out of these, 24 patients (15.7%) had stage III disease, and 129 (84.3%) had stage IV disease. A total of 133 patients had samples that were evaluated for PD-L1 expression, and the median CPS was 15. A total of 33 (24.8%) had a CPS of 1% or greater, including 24 (18.0%) who had a CPS of 10% or greater. All patients received previous therapy before immunotherapy. A total of 133 patients were treated with systematic chemotherapy schemes before immunotherapy. Only five patients did not receive radiotherapy before immunotherapy. A total of 89 patients were treated with radiotherapy within 3 months prior to immunotherapy.

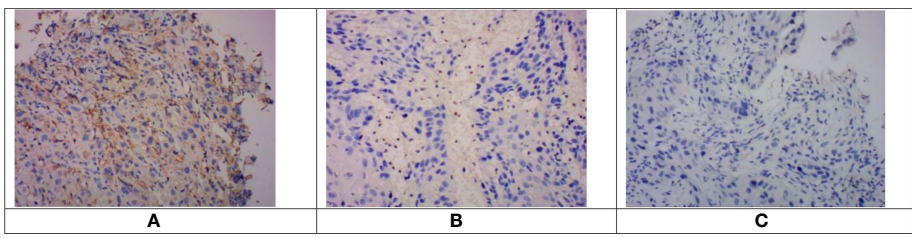

FIGURE 1
Immunohistochemical staining of PD-L1 in esophageal squamous cell carcinoma tissues. Images were obtained from three different patients. **(A)**. CPS > 10. **(B)** 1 < CPS 5 < 10. **(C)** CPS < 1 (negative of PD-L1 expression). PD-L1, programmed cell death protein ligand 1; CPS, combined positive score.

10.3389/fimmu.2023.960339

TABLE 1 Patient characteristics at baseline (N = 133).

Characteristics	N%	%
Sex		
Male	100	75.2
Female	33	24.8
Age (years) (median 65)		
<65	73	54.9
≥65	60	45.1
ECOG performance status score		
0	69	51.9
1	64	48.1
Tumor location		
Upper thoracic	41	30.8
Middle thoracic	55	41.4
Lower thoracic	37	27.8
T stage		
≤3	97	72.9
4	36	27.1
N stage		
≤2	78	58.6
3	55	41.4
M stage		
0	65	48.9
1	68	51.1
PD-L1 status		
Negative	100	75.2
Positive	33	24.8
PD-L1 expression (CPS)		
<1	100	75.2
1–10	9	6.8
>10	24	18.0
Previous chemotherapy schemes before immunotherapy	133	100
Only chemotherapy	5	3.8
Before radiotherapy	82	61.7
Concurrent radiotherapy	55	41.4
Sequential chemotherapy	44	33.1
Previous radiotherapy before immunotherapy	128	96.2
No radiotherapy	5	3.8
In 3 months	89	66.9
Beyond 3 months	39	29.3
Immunotherapy scheme		
Sintilimab alone	34	25.6
Sintilimab and chemotherapy	99	74.4
Immunotherapy-related toxicities		
White blood cell count decreased	49	36.8
Anemia	26	19.5
Rash	12	9.0
Aminotransferase increased	7	5.3
Diarrhea	4	3.0
Asthenia	1	0.8
Death	66	49.6

ECOG, Eastern Cooperative Oncology Group; CPS, combined positive score; PD-L1, programmed cell death protein ligand 1.

3.2 Potential factors in efficacy enhancement

On multivariate analysis, the gender, age, TNM stage, tumor location PD-L1 expression, and the number of lines of previous systemic therapies were not indicative of progression-free survival and overall survival, and previous radiotherapy within 3 months was significantly related to longer PFS and OS ($p < 0.05$) (Table 2). Patients who had received radiotherapy within 3 months prior to immunotherapy had significantly longer progression-free survival with sintilimab than those who did not receive radiotherapy (median progression-free survival 10.0 months [95% CI 8.030–11.970] *vs.* 5.0 months [95% CI 2.755–7.245]) (Figure 2C). In contrast, overall survival was significantly longer in patients who had received radiotherapy within 3 months prior to sintilimab than in those who had not (median overall survival 15.3 months [95% CI 13.724–16.876] *vs.* 12.2 months [10.001–14.399]) (Figure 2D). Progression events occurred in 44 (49%) of the 89 patients who had received radiotherapy for ESCC within 3 months prior to immunotherapy, compared to 30 (68.2%) of the 44 patients who had not previously received radiotherapy. Therefore, ORR and DCR were higher in the subgroup that had received radiotherapy for ESCC within 3 months prior to immunotherapy (Table 3). Our results showed that radiotherapy within 3 months before sintilimab can enhance the efficiency of immunotherapy and benefit the prognosis in unresectable advanced ESCC patients who received multi-line sintilimab.

3.3 Efficacy and safety of multi-line sintilimab

Of 133 patients, 15 patients experienced a partial response, and 14 patients had stable disease. The ORR was 11.3% and the DCR was 45.9% (Table 3). A total of 72 patients experienced disease progression, and the median PFS with sintilimab treatment was 9.0 months (95% CI 7.701–10.299) (Figure 2A). In 66 patients who

TABLE 2 Cox regression analyses of factors affecting the PFS and OS of ESCC patients (n = 133).

Variable	PFS		OS	
	p	HR (95% CI)	p	HR (95% CI)
Sex (male/female)	0.823	0.944 (0.568–1.567)	0.342	0.773 (0.454–1.315)
Age (years) (<65/≥65)	0.755	0.927 (0.576–1.492)	0.913	0.972 (0.588–1.609)
T stage	0.906	0.982 (0.721–1.336)	0.196	0.803 (0.575–1.120)
N stage	0.737	0.923 (0.576–1.477)	0.991	0.997 (0.606–1.640)
M stage	0.443	1.216 (0.737–2.006)	0.288	0.758 (0.455–1.264)
Tumor location (upper/middle/lower thoracic)	0.637	1.084 (0.775–1.516)	0.738	1.061 (0.748–1.506)
Number of previous systemic therapies	0.705	0.851 (0.369–1.961)	0.116	3.183 (0.751–13.499)
PD-L1 expression before immunotherapy (negative/positive)	0.826	0.944 (0.562–1.585)	0.075	0.582 (0.321–1.056)
Radiation before immunotherapy within 3 months (yes/no)	**0.006**	0.479 (0.285–0.806)	**0.030**	0.510 (0.278–0.936)

Statistically significant values appear in bold ($p < 0.05$).
ESCC, esophageal squamous cell carcinoma; PD-L1, programmed cell death protein ligand 1; PFS, progression-free survival; OS, overall survival; HR, hazard ratio.

died, the median overall survival was 14.9 months (95% CI 12.558–17.242) (Figure 2B).

All patients were treated with at least two cycles of sintilimab, and no patient was withdrawn from the course of immunotherapy due to toxic effects. AEs of sintilimab in patients were also recorded, such as a white blood cell count decrease (36.8%), anemia (19.5%), rash (9.0%), aminotransferase increase (5.3%), diarrhea (3.0%), and asthenia (0.8%), all common AEs of sintilimab. According to the

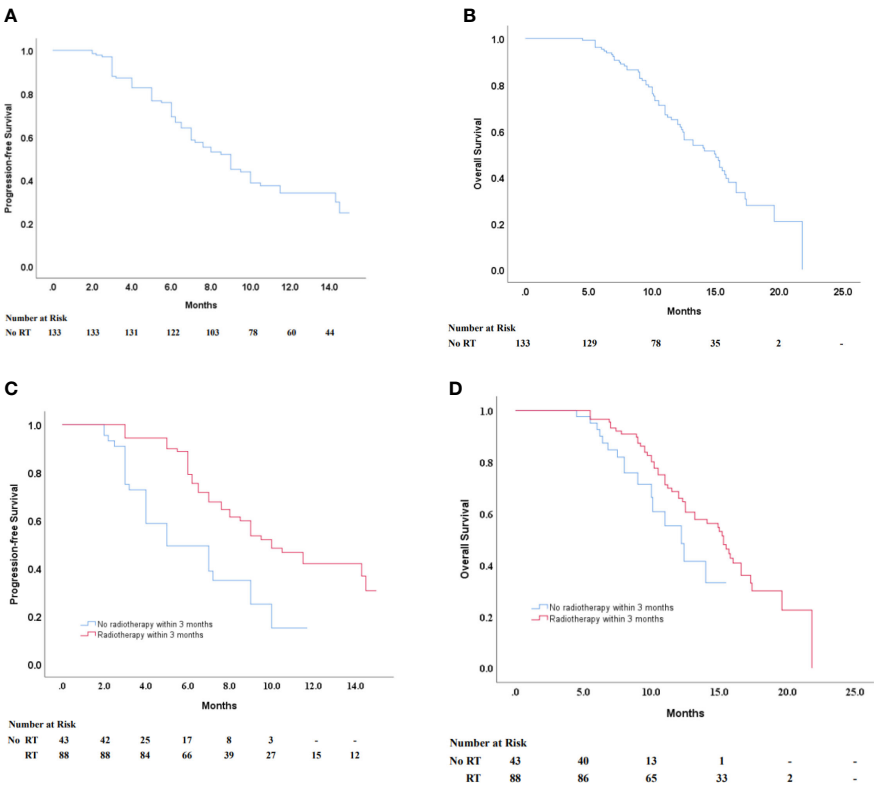

FIGURE 2
(A, B) Kaplan–Maier survival curves of PFS and OS of ESCC patients in all patients. Progression-free survival according to their history of radiotherapy within 3 months before immunotherapy **(C)** in all patients regardless of PD-L1 expression status **(D)** in a negative PD-L1 expression status. PFS, progression-free survival; OS, overall survival; ESCC, esophageal squamous cell carcinoma.

radiotherapy and immunotherapy interval, 133 patients were divided into two subgroups, and there was no statistical difference in adverse reactions between the two groups (Table 4). No immune-related deaths occurred. All adverse reactions were handled appropriately. A total of 66 patients died in this study, and the immediate causes of death were tumor progression. All deaths were determined to be related to immunotherapy.

4 Discussion

In this retrospective study, sintilimab exhibited significant efficacy in unresectable advanced ESCC that had been previously treated, and pre-immunotherapy radiotherapy within 3 months could enhance the efficacy of multi-line sintilimab.

Radiation therapy (RT) has an important place in the treatment of advanced ESCC, providing effective relief of dysphagia and leading to improved long-term survival through enhanced local disease control (13, 14). To avoid overactive immune responses leading to excessive inflammatory responses and autoimmune diseases, the body has evolved immune checkpoint mechanisms to control the intensity and duration of immune responses and minimize the damage of immune responses to healthy tissues, mainly the CTLA4-B7 pathway and PD-1/PD-L1 pathway. However, after tumor cell invasion, tumor cells will use this suppressive pathway to suppress T-cell activation and thus escape the immune system's siege, a process known as an immune escape (15). The anti-tumor effects of radiotherapy are achieved by directly inducing DNA damage in the target cells. Radiotherapy controls local lesions through direct action and also controls distant metastases by inducing the abscopal effect. A commonly hypothesized theory is that local radiotherapy leads to immunogenic cell death, resulting in an inflammatory microenvironment. This is characterized by the release of tumor antigens and damage-associated pattern molecules (DAMPs) from the dead cells. Radiotherapy also induces the expression of chemokines, leading T cells to the tumor microenvironment (13–15), thus improving efficiency and reducing adverse effects (16–18). However, immune escape often occurs with the recurrence of the tumor, limiting the ability of radiotherapy to produce an anti-tumor immune response (19, 20). Therefore, radiotherapy plays a crucial role in tumor suppression as a bridge between innate and acquired immune responses.

Previous studies have shown the additional efficacy of immunotherapy in combination with RT in solid tumors (19, 20). Postow et al. reported on the first-time tumor regression in a melanoma patient after receiving ipilimumab combined with RT, even outside the radiation area (21). A growing body of clinical evidence suggests that two to three courses of combination therapy (checkpoint inhibitors in combination with RT) have good potential and are well tolerated in patients with a variety of locally advanced or metastatic malignancies, including non-small cell lung cancer (NSCLC), melanoma, and renal cancer. To the best of our knowledge, the present study, which combined short-term radiotherapy and PD-L1 expression status, is the first to evaluate retrospective data on patients with advanced ESCC cancer who received sintilimab and prior radiotherapy and were divided into two subgroups for comparison based on the time interval between radiotherapy and immunotherapy. Most studies have reported that higher PD-L1 expression in EC was related to a poor prognosis; however, high PD-L1 expression patients responded well to anti-PD1/PD-L1 monoclonal antibodies and had significantly higher OS rates (22, 23). These results indicate that PD-L1 expression can be a meaningful biomarker to identify the most optimal population for anti-PD-1/PD-L1 therapy. In our study, although fewer patients with high PD-L1 expression were in the subgroup, these patients who received radiotherapy within 3 months prior to immunotherapy had significantly longer progression-free survival than those who did not receive radiotherapy, suggesting that radiotherapy may have upregulated PD-L1 expression in patients, thereby converting traditional non-responders into responders and contributing to the efficacy of immunotherapy.

After successful clearance of the infecting pathogen or malignant cells, the presence of a population of suppressor immune cells allows the body to restore immune homeostasis to avoid immune damage caused by an excessive immune response. A variety of suppressive immune cells are distributed in the tumor microenvironment, including CD+8T cells, macrophages and myeloid-derived suppressor cells (MDSCs), and other stromal cells. When tumorigenesis occurs, large numbers of immature MDSCs promote tumor invasion and metastasis through accumulation and suppression of T-cell immune function by

TABLE 3 Tumor response in advanced ESCC.

Tumor response	All (n = 133)	Received radiotherapy before sintilimab	
		Beyond 3 months or no radiotherapy (n = 44)	Within 3 months (n = 89)
PR	15	2	13
SD	46	12	34
PD	72	30	42
ORR	11.3%	4.5%	14.6%
DCR	45.9%	31.8%	52.8%

ESCC, esophageal squamous cell carcinoma; CR, complete response; PR, partial response; SD, stable disease; PD, disease progression; ORR, objective response rate; DCR, disease control rate.

TABLE 4 Adverse events of subgroup patients (n = 133).

	Received radiotherapy before sintilimab	
	Beyond 3 months or no radiotherapy (n = 44)	Within 3 months (n = 89)
Any event	34 (77.3%)	65 (73.0%)
White blood cell count decreased	13 (29.5%)	36 (40.4%)
Rash	14 (31.8%)	12 (13.5%)
Anemia	5 (11.4%)	7 (7.9%)
Aminotransferase increased	1 (2.3%)	6 (6.7%)
Diarrhea	1 (2.3%)	3 (3.4%)
Asthenia	0 (0%)	1 (1.1%)

direct cell-to-cell interactions or secretion of cytokines. Tumor-associated macrophages (TAMs) can as well be initiated by different isoforms and in an environment-dependent manner. An increasing body of research has shown that the quantity of T cells in immune organs increases significantly when patients are exposed to local or systemic radiation (24). A recent study by Dovedi et al. showed that PD-L1 expression was upregulated in tumor cells through interferon-γ production by CD8+ T cells after radiotherapy (25). In addition, radiation therapy can trigger a local inflammatory response while stimulating the induction of PD-L1 expression in the tumor microenvironment and decreasing the sensitivity of the anti-tumor immune response (13). Thus, if the PD-1/PD-L1-induced immune escape mechanism can be overcome, radiotherapy has the potential to have a more sustained effect on tumor cells.

Our study is the first retrospective study to assess the association between a previous history of radiotherapy and the clinical value of sintilimab in patients with advanced ESCC, which may provide evidence for future randomized clinical studies. At the same time, the study has limitations. This was a retrospective study, which may result in selection bias. We observed that pre-immunotherapy radiotherapy resulted in significant differences in PFS and OS, and there was no correlation between PD-L1 expression status from this study. First, relatively few patients were enrolled in our study, and they were all from a single institution. Although our pooled analysis alleviated the sample size issue for each trial, subgroup analysis was still limited by the low sample size, and therefore, a larger sample size is needed to more accurately detect the impact of the combination of radiotherapy and immunotherapy on patient outcomes. There were no uniform criteria for positive PD-L1 expression, which may also have resulted in different outcomes than previous studies. Since this study did not differentiate the efficacy of different treatment modalities, the exact effect of specific treatment regimens could not be determined in this study. We are expanding the sample size to reduce the impact of different treatment options on outcomes.

In conclusion, sintilimab is an option for multi-line treatment in unresectable advanced esophageal squamous cell carcinoma patients, and radiotherapy within 3 months prior to immunotherapy enhances the immune efficacy of sintilimab, resulting in longer PFS and OS.

Data availability statement

The raw data supporting the conclusions of this article will be made available by the authors, without undue reservation.

Ethics statement

The study was approved by all participating institutions. The study was conducted in accordance with the Declaration of Helsinki and International Good Clinical Practice Guidelines. All patients provided written informed consent before study participation.

Author contributions

SX: conceptualization, data curation, formal analysis, and writing—original draft. XX: data curation, formal analysis, and writing—original draft. HZ: conceptualization, funding acquisition, project administration, and writing—review and editing. All authors contributed to the article and approved the submitted version.

Funding

This work was supported by the National Natural Science Foundation of China (grant number: 81972862).

Conflict of interest

The authors declare that the research was conducted in the absence of any commercial or financial relationships that could be construed as a potential conflict of interest.

Publisher's note

All claims expressed in this article are solely those of the authors and do not necessarily represent those of their affiliated organizations, or those of the publisher, the editors and the reviewers. Any product that may be evaluated in this article, or claim that may be made by its manufacturer, is not guaranteed or endorsed by the publisher.

References

1. Bray F, Ferlay J, Soerjomataram I, Siegel RL, Torre LA, Jemal A. Global cancer statistics 2018: GLOBOCAN estimates of incidence and mortality worldwide for 36 cancers in 185 countries. *CA Cancer J Clin* (2018) 68(6):394–424. doi: 10.3322/caac.21492

2. Di Pardo BJ, Bronson NW, Diggs BS, Thomas CR Jr., Hunter JG, Dolan JP. The global burden of esophageal cancer: A disability-adjusted life-year approach. *World J Surg* (2016) 40(2):395–401. doi: 10.1007/s00268-015-3356-2

3. Li H, Fang W, Yu Z, Mao Y, Chen L, He J, et al. Chinese Expert consensus on mediastinal lymph node dissection in esophagectomy for esophageal cancer (2017 edition). *J Thorac Dis* (2018) 10(4):2481–9. doi: 10.21037/jtd.2018.03.175

4. Fuchs CS, Doi T, Jang RW, Muro K, Satoh T, Machado M, et al. Safety and efficacy of pembrolizumab monotherapy in patients with previously treated advanced gastric and gastroesophageal junction cancer: Phase 2 clinical KEYNOTE-059 trial. *JAMA Oncol* (2018) 4(5):e180013. doi: 10.1001/jamaoncol.2018.0013

5. Sharpe AH, Pauken KE. The diverse functions of the PD1 inhibitory pathway. *Nat Rev Immunol* (2018) 18(3):153–67. doi: 10.1038/nri.2017.108

6. Kato K, Cho BC, Takahashi M, Okada M, Lin CY, Chin K, et al. Nivolumab versus chemotherapy in patients with advanced oesophageal squamous cell carcinoma refractory or intolerant to previous chemotherapy (ATTRACTION-3): a multicentre, randomised, open-label, phase 3 trial. *Lancet Oncol* (2019) 20(11):1506–17. doi: 10.1016/S1470-2045(19)30626-6

7. Kudo T, Hamamoto Y, Kato K, Ura T, Kojima T, Tsushima T, et al. Nivolumab treatment for oesophageal squamous-cell carcinoma: an open-label, multicentre, phase 2 trial. *Lancet Oncol* (2017) 18(5):631–9. doi: 10.1016/S1470-2045(17)30181-X

8. Tamura S, Imano M, Takiuchi H, Kobayashi K, Imamoto H, Miki H, et al. Phase II study of docetaxel, cisplatin and 5-fluorouracil (DCF) for metastatic esophageal cancer (OGSG 0403). *Anticancer Res* (2012) 32(4):1403–8.

9. Yamasaki M, Miyata H, Tanaka K, Shiraishi O, Motoori M, Peng YF, et al. Multicenter phase I/II study of docetaxel, cisplatin and fluorouracil combination chemotherapy in patients with advanced or recurrent squamous cell carcinoma of the esophagus. *Oncology* (2011) 80(5-6):307–13. doi: 10.1159/000329806

10. Van Cutsem E, Kato K, Ajani J, Shen L, Xia T, Ding N, et al. Tislelizumab versus chemotherapy as second-line treatment of advanced or metastatic esophageal squamous cell carcinoma (RATIONALE 302): impact on health-related quality of life. *ESMO Open* (2022) 7(4):100517. doi: 10.1016/j.esmoop.2022.100517

11. Lv H, Tian Y, Li J, Huang C, Sun B, Gai C, et al. Neoadjuvant sintilimab plus chemotherapy in resectable locally advanced esophageal squamous cell carcinoma. *Front Oncol* (2022) 12:864533. doi: 10.3389/fonc.2022.864533

12. Zhang Z, Hong ZN, Xie S, Lin W, Lin Y, Zhu J, et al. Neoadjuvant sintilimab plus chemotherapy for locally advanced esophageal squamous cell carcinoma: a single-arm, single-center, phase 2 trial (ESONICT-1). *Ann Transl Med* (2021) 9(21):1623. doi: 10.21037/atm-21-5381

13. Deng L, Liang H, Burnette B, Beckett M, Darga T, Weichselbaum RR, et al. Irradiation and anti-PD-L1 treatment synergistically promote antitumor immunity in mice. *J Clin Invest* (2014) 124(2):687–95. doi: 10.1172/JCI67313

14. Twyman-Saint Victor C, Rech AJ, Maity A, Rengan R, Pauken KE, Stelekati E, et al. Radiation and dual checkpoint blockade activate non-redundant immune mechanisms in cancer. *Nature* (2015) 520(7547):373–7. doi: 10.1038/nature14292

15. Jesinghaus M, Steiger K, Slotta-Huspenina J, Drecoll E, Pfarr N, Meyer P, et al. Increased intraepithelial CD3+ T-lymphocytes and high PD-L1 expression on tumor cells are associated with a favorable prognosis in esophageal squamous cell carcinoma and allow prognostic immunogenic subgrouping. *Oncotarget* (2017) 8(29):46756–68. doi: 10.18632/oncotarget.18606

16. Zhang W, Yan C, Gao X, Li X, Cao F, Zhao G, et al. Safety and feasibility of radiotherapy plus camrelizumab for locally advanced esophageal squamous cell carcinoma. *Oncologist* (2021) 26(7):e1110–24. doi: 10.1002/onco.13797

17. World Medical Association. World medical association declaration of Helsinki: ethical principles for medical research involving human subjects. *JAMA* (2013) 310 (20):2191–4. doi: 10.1001/jama.2013.281053

18. Therasse P, Arbuck SG, Eisenhauer EA, Wanders J, Kaplan RS, Rubinstein L, et al. New guidelines to evaluate the response to treatment in solid tumors. European organization for research and treatment of cancer, national cancer institute of the united states, national cancer institute of Canada. *J Natl Cancer Inst* (2000) 92(3):205–16. doi: 10.1093/jnci/92.3.205

19. Van Limbergen EJ, De Ruysscher DK, Olivo Pimentel V, Marcus D, Berbee M, Hoeben A, et al. Combining radiotherapy with immunotherapy: the past, the present and the future. *Br J Radiol* (2017) 90(1076):20170157. doi: 10.1259/bjr.20170157

20. Reynders K, Illidge T, Siva S, Chang JY, De Ruysscher D. The abscopal effect of local radiotherapy: using immunotherapy to make a rare event clinically relevant. *Cancer Treat Rev* (2015) 41(6):503–10. doi: 10.1016/j.ctrv.2015.03.011

21. Postow MA, Callahan MK, Barker CA, Yamada Y, Yuan J, Kitano S, et al. Immunologic correlates of the abscopal effect in a patient with melanoma. *N Engl J Med* (2012) 366(10):925–31. doi: 10.1056/NEJMoa1112824

22. Wu P, Wu D, Li L, Chai Y, Huang J. PD-L1 and survival in solid tumors: A meta-analysis. *PloS One* (2015) 10(6):e0131403. doi: 10.1371/journal.pone.0131403

23. Alsaab HO, Sau S, Alzhrani R, Tatiparti K, Bhise K, Kashaw SK, et al. PD-1 and PD-L1 checkpoint signaling inhibition for cancer immunotherapy: Mechanism, combinations, and clinical outcome. *Front Pharmacol* (2017) 8:561. doi: 10.3389/fphar.2017.00561

24. Kachikwu EL, Iwamoto KS, Liao YP, DeMarco JJ, Agazaryan N, Economou JS, et al. Radiation enhances regulatory T cell representation. *Int J Radiat Oncol Biol Phys* (2011) 81(4):1128–35. doi: 10.1016/j.ijrobp.2010.09.034

25. Dovedi SJ, Adlard AL, Lipowska-Bhalla G, McKenna C, Jones S, Cheadle EJ, et al. Acquired resistance to fractionated radiotherapy can be overcome by concurrent PD-L1 blockade. *Cancer Res* (2014) 74(19):5458–68. doi: 10.1158/0008-5472.CAN-14-1258

frontiers | Frontiers in Immunology

TYPE Mini Review
PUBLISHED 06 March 2023
DOI 10.3389/fimmu.2023.1140541

Check for updates

OPEN ACCESS

EDITED BY
Jian Zhang,
Southern Medical University, China

REVIEWED BY
Marta Barisa,
University College London,
United Kingdom

*CORRESPONDENCE
Joe Jiang Zhu
joe.zhu@petermac.org

†These authors share first authorship

‡These authors share senior authorship

SPECIALTY SECTION
This article was submitted to Cancer Immunity and Immunotherapy, a section of the journal Frontiers in Immunology

RECEIVED 09 January 2023
ACCEPTED 22 February 2023
PUBLISHED 06 March 2023

CITATION
Wang AX, Ong XJ, D'Souza C, Neeson PJ and Zhu JJ (2023) Combining chemotherapy with CAR-T cell therapy in treating solid tumors. *Front. Immunol.* 14:1140541. doi: 10.3389/fimmu.2023.1140541

COPYRIGHT
© 2023 Wang, Ong, D'Souza, Neeson and Zhu. This is an open-access article distributed under the terms of the Creative Commons Attribution License (CC BY). The use, distribution or reproduction in other forums is permitted, provided the original author(s) and the copyright owner(s) are credited and that the original publication in this journal is cited, in accordance with accepted academic practice. No use, distribution or reproduction is permitted which does not comply with these terms.

Combining chemotherapy with CAR-T cell therapy in treating solid tumors

Arthur Xuan Wang[1†], Xiao Jing Ong[1†], Criselle D'Souza[1,2‡], Paul J. Neeson[1,2‡] and Joe Jiang Zhu[1,2*‡]

[1]Cancer Immunology Program, Peter MacCallum Cancer Centre, Melbourne, VIC, Australia, [2]Sir Peter MacCallum Department of Oncology, Faculty of Medicine, Dentistry and Health Science, University of Melbourne, Melbourne, VIC, Australia

Chemotherapy has long been a standard treatment for a wide range of malignancies, where patients typically undergo multiple rounds of chemotherapy regimens to control tumor growth. In the clinic, the chemotherapy drugs cyclophosphamide and fludarabine are commonly used prior to Chimeric Antigen Receptor T (CAR-T) cell therapy to lymphodeplete and improve CAR-T cell engraftment. In this review, we discuss the use of chemotherapy in combination with CAR-T cell therapy. We also show that chemotherapy can deplete immunosuppressive cells, promote a pro-inflammatory tumor microenvironment, disrupt tumor stroma, and improve CAR-T cell recruitment to the tumor. Although the combination of chemotherapy plus CAR-T cell therapy is promising, certain aspects of chemotherapy also pose a challenge. In addition, the combined therapeutic effect may be heavily dependent on the dose and the treatment schedule. Thus, we also discussed the obstacles to effective clinical outcomes of the combination therapy.

KEYWORDS

chemotherapy, Chimeric Antigen Receptor T cell (CAR-T), solid tumor, tumor microenvironment (TME), personalized combination

Abbreviations: ALL, acute lymphoblastic leukaemia; BCMA, B-cell maturation antigen; CAFs, cancer associated fibroblast; CAIX, carbonic anhydrase IX; CCL, C-C motif ligand; CLL, chronic lymphocytic leukaemia; CR, complete response; CXCL, C-X-C motif chemokine ligand; ECM, extracellular matrix; EGFR, epidermal growth factor receptor; IDO, indolamine-2,3-dioxygenase 1; MDSCs, myeloid-derived suppressor cells; MM, multiple myeloma; NHL, non-Hodgkin lymphoma; NK cells, natural killer cells; NSCLC, non-small cell lung cancer; PD-1, programmed cell death protein 1; PD-L1, programmed cell death ligand 1; PD-L2, programmed cell death ligand 2; PR, partial response; PSCA, prostate stem cell antigen; ROR1, tyrosine kinase-like orphan receptor 1; SD, stable disease; TAMs, tumor-associated macrophages; TGFβ, transforming growth factor beta; TILs, tumor-infiltrating lymphocytes; TME, tumor microenvironment; Tregs, regulatory T cells; T_{EM} T effector memory; CAR, Chimeric Antigen Receptor; CRS, Cytokine Release Syndrome; ICANS, Immune effector cell-associated neurotoxicity syndrome.

1 Introduction

Recently, a large number of cancer therapies have been developed to facilitate a patient's immune system against cancers. One such therapy is called the Chimeric Antigen Receptor (CAR) T cell therapy, which involves the adoptive transfer of autologous T cells that have been genetically engineered with a CAR to target tumor cells (1). CAR-T cell therapy has induced remission in patients with relapsed/refractory B-cell malignancies (2–4). However, this success has not occurred in patients with solid tumors. The reasons for this poor outcome include tumor heterogeneity, an immunosuppressive tumor microenvironment (TME), insufficient T-cell trafficking to the tumor site, and poor T-cell persistence (5).

Chemotherapy has long been a standard-of-care treatment for many cancers, especially advanced solid tumors. The successful treatment of cancers requires a combination of different approaches. However, because chemotherapy can exert negative effects on the immune system, it is not clear whether chemotherapy can be combined with immunotherapy more broadly. Indeed, different classes of chemotherapeutic drugs such as alkylating agents (e.g., cyclophosphamide), platinum compounds (e.g., cisplatin, carboplatin, oxaliplatin), antimetabolites (e.g., methotrexate), anthracyclines, DNA methyltransferase inhibitors and spindle poisons (e.g., taxanes) have mixed effects on the immune system (6). Certain drugs can induce profound immunosuppression, while some drugs can enhance anti-tumor immunity. Some synergistic effects include relieving tumor-induced immunosuppression, augmenting the anti-tumor activity of cytotoxic immune cells, and improving immune cell trafficking to tumor sites. As a result, these positive effects of chemotherapy could overcome some of the roadblocks for CAR-T cell therapy in treating solid cancers. Hence, this review will summarise the main effects of chemotherapy when combined with CAR-T cells, including the promises and challenges of combination therapy for solid cancers.

2 How can chemotherapy be used in conjunction with CAR-T cell therapy?

CAR-T cell therapy have produced impressive clinical responses in relapsed/refractory B cell malignancies. However, there are numerous factors to be considered during the treatment, including the need for a bridging therapy or conditioning regimen prior to the infusion of CAR-T cell product. These regimens significantly impact the clinical outcomes.

2.1 Chemotherapy as a bridging therapy

The infusion of CAR-T cells must be performed in a timely manner to control disease progression (7). However, the period between apheresis and CAR-T cell infusion can be weeks to months, e.g. a maximum of 105 days (median time of 45 days) in the ELIANA trial (NCT02435849) (3). This time interval may lead to a treatment gap where some patients may experience disease progression and/or death. As a result, 7% of patients did not survive while awaiting the production of CAR-T cells (8, 9). Therefore, bridging therapy is critical in controlling disease burden prior to CAR-T cell treatment.

The choice of bridging therapy is highly variable, depending on the patient's cancer type, disease stage, prior treatments, and disease burden. Chemotherapy is one of the most widely used bridging therapies, including kinase modulators, topoisomerase inhibitors, platinum-based agents, and drugs that interfere with DNA replication, synthesis and repair (10). These drugs can inhibit tumor growth to achieve disease control in the bridging period. As a bridging therapy, chemotherapy can also debulk the tumor before CAR-T cell infusion in some cases. This is an important consideration as high disease burdens have been associated with toxicities following CAR-T cell infusions, such as cytokine release syndrome (CRS) and immune effector cell-associated neurotoxicity syndrome (ICANS) (11).

2.2 Chemotherapy as a conditioning regimen

Studies showed that lymphodepletion prior to adoptive T-cell transfer significantly enhanced their expansion, engraftment, and anti-tumor efficacy (12). This enhancement is likely due to reduced immunosuppressive cells (e.g., myeloid-derived suppressor cells and regulatory T cells) (12, 13), increased homeostatic cytokine production (14, 15), and the downregulation of indoleamine 2,3-dioxygenase (IDO) expression in the tumor (16). Together, these mechanisms may create an optimal environment for the anti-tumor function of infused CAR-T cells. Along with improved CAR-T cell engraftment and homeostatic expansion, these findings led to the introduction of lymphodepletion conditioning regimens with CAR-T cell therapy.

Chemotherapeutic drugs such as cyclophosphamide (Cy) and fludarabine (Flu) are the most commonly used lymphodepleting regimen in CAR-T cell therapy (250-500 mg/m^2 cyclophosphamide, 25-30 mg/m^2 fludarabine, 3-5 days before infusion) (17, 18). Compared to Cy alone, the combination of Cy/Flu significantly enhanced CAR-T cell expansion and was associated with better clinical responses (Cy/Flu = 50% CR, 72% ORR versus Cy alone = 8% CR, 50% ORR) (19). In the JULIET trial, patients with the Cy-resistant disease also received bendamustine (90 mg/m^2, 2-11 days before infusion) in lieu of Cy/Flu, with similar clinical outcomes (20). However, there are risks associated with intense lymphodepletion, including prolonged neutropenia and toxicities. Therefore, further studies are needed to investigate the favourable dose and schedule of lymphodepletion with minimal side effects and enhanced clinical response to CAR-T therapy.

2.3 Chemotherapy as a neoadjuvant/adjuvant treatment

Although chemotherapy has not been conventionally utilized as a neoadjuvant or adjuvant treatment for CAR-T cell therapy,

emerging evidence suggests that specific chemotherapy drugs may work in concert with CAR-T cells (6, 21) (Table 1). This novel combination strategy shows great potential to overcome some barriers in CAR-T cell therapy and provide synergistic effects in treating solid tumors.

The immunosuppressive tumor microenvironment (TME) in solid tumors is a significant obstacle to achieving clinical response to CAR-T cell therapy (62). Numerous immune suppressive cells infiltrate the TME, including myeloid-derived suppressor cells (MDSCs), tumor-associated macrophages (TAMs), and regulatory T cells (Tregs). These cells promote immunosuppression and negatively regulate CAR-T cell effector function (63). In addition, cancer-associated fibroblasts (CAFs) produce extracellular matrix components in the TME (64), forming a physical barrier restricting CAR-T cell penetration. Together, these cells play a pro-tumorigenic role that interferes with CAR-T cell efficacy (65–67). This anti-inflammatory milieu would lead to poor CAR-T cell penetration, expansion, and persistence, rendering the therapy ineffective.

In this regard, chemotherapy is a promising approach for remodelling the TME, and could lead to the enhanced therapeutic efficacy of CAR-T cells in solid tumors. Chemotherapy drugs can modify the TME in four main ways: reducing immune suppressor cells, repolarising the anti-inflammatory immune microenvironment, disrupting the tumor stroma, and altering the chemokine profile for T cell trafficking. These mechanisms are discussed in the following sections of this review.

2.3.1 Chemotherapy reduces immune suppressor cells in the TME

Chemotherapy has been shown to reduce the various immune suppressor cells in the TME. Cy/Flu conditioning regimen have enhanced CAR-T cell expansion and clinical responses in cancer

TABLE 1 Chemotherapeutic drugs that can be used as neoadjuvant or adjuvant regimen with CAR-T cell therapy - preclinical and clinical evidence.

Immunomodulatory effects of chemotherapeutic agents				
Drug class	Agent	Cancer type/Animal model	Effect	Reference
Alkylating agents	Cyclophosphamide	Pleural mesothelioma	Treg depletion and expansion of $CD8^+$ T_{EM} cells.	(22)
		Metastatic solid tumors	Treg depletion and restoration of T-cell function.	(23)
		Metastatic breast cancer	Treg depletion and expansion of tumor-specific T cells.	(24)
		Metastatic colorectal cancer	Reduced proportions of Tregs, B cells and NK cells. Expansion of tumor-specific T cells.	(25)
	Dacarbazine	Melanoma	Increased T-cell recruiting chemokine production.	(26)
		Stage III/IV melanoma	Increased chemokine production and ECM remodelling.	(27)
	Temozolomide	Murine glioma model	Treg depletion and inhibition of Treg function.	(28)
		Advanced melanoma	Depletion of Tregs.	(29)
		Human/murine melanoma model	Increased T-cell recruiting chemokine production and T-cell infiltration.	(26)
Anti-metabolites	Gemcitabine	Pancreatic ductal adenocarcinoma	Depletion of granulocytic MDSCs and Tregs in the peripheral blood and reduction of plasma TGFβ-1 levels.	(30)
		Pancreatic ductal adenocarcinoma	Polarisation of TAMs into M1-like phenotype and induced secretion of immunostimulatory cytokines.	(31)
		Various murine cancers	Depletion of MDSCs and inhibition of MDSC function.	(32)
	Gemcitabine and 5-fluorouracil	Pancreatic and oesophageal cancer	Depletion of MDSCs in peripheral blood.	(33)
		Murine thymoma model	Depletion of MDSCs in spleen and at tumor site.	(34)

(Continued)

TABLE 1 Continued

Immunomodulatory effects of chemotherapeutic agents				
Drug class	Agent	Cancer type/Animal model	Effect	Reference
Anthracyclines	Doxorubicin	Murine mammary cancer	Depletion of MDSCs and inhibition of MDSC function.	(35)
Taxanes	Docetaxel	NSCLC patients	Depletion of Tregs in the peripheral blood.	(36)
		Murine mammary tumor model	Inhibition of MDSC function and restoration of T cell function. Polarisation of MDSCs into M1-like phenotype.	(37)
	Paclitaxel	Advanced non-small cell lung cancer	Depletion of Tregs and inhibition of Treg function.	(38)
		Murine orthotopic renal cell carcinoma model	Depletion of Tregs and inhibition of Treg function.	(39)
		Murine spontaneous melanoma model	Depletion of MDSCs and inhibition of MDSC function.	(40)
		Murine breast cancer and melanoma models	Polarisation of TAMs into M1-like phenotype.	(41)
		Human pancreatic cancer xenograft models	Depletion of tumor stroma.	(42)
		Advanced pancreatic cancer	Depletion of CAFs and disruption of tumor ECM.	(43)
Platinum compounds	Carboplatin, cisplatin and oxaliplatin	Melanoma and colorectal cancer	Downregulation of PD-L1/L2 on tumor and dendritic cells.	(44)
	Carboplatin + anthracyclines and taxanes	Human breast cancer	Increased T-cell recruiting chemokine production.	(45)
	Carboplatin	Human NSCLC cell lines and murine Lewis lung carcinoma mouse model	Increased T-cell recruiting chemokine production and infiltration of $CD8^+$ T cells.	(46)
	Oxaliplatin + cyclophosphamide	Murine lung adenocarcinoma models	Increased T-cell infiltration through immunogenic tumor cell death. Increased $CD8^+$ T cells:Treg ratio at tumor.	(47)

Combination with CAR-T cells			
Drug combination	Cancer type/Animal model	Outcome	Reference
Cyclophosphamide pre-conditioning + BCMA-CAR T cells	Phase I trial for multiple myeloma (MM) patients	7 out of 11 patients achieved partial response (PR) or better.	NCT02546167 (48)
Cyclophosphamide pre-conditioning + CD19-CAR T cells	Phase I trial for chemotherapy-refractory chronic lymphocytic leukaemia (CLL) & Relapsed B-cell acute lymphoblastic leukaemia (B-ALL)	2 out of 5 patients with this combination achieved stable disease (SD).	NCT00466531, NCT01044069 (49)
Cyclophosphamide pre-conditioning + PSCA-CAR T cells	Human PSCA knock-in mice bearing subcutaneous human PSCA tumors	Induced complete responses (CR) in 3/7 mice. Increased CAR-T cell infiltration into TME. Polarisation of TME into pro-inflammatory state. Reduced M2-like myeloid cells.	(50)
Cyclophosphamide/ Fludarabine pre-conditioning + CD19-CAR T cells	Phase I/II for relapsed/refractory CLL, NHL and ALL	16 out of 17 patients achieved complete response (CR).	NCT01865617 (51)

(Continued)

TABLE 1 Continued

Combination with CAR-T cells			
Drug combination	Cancer type/Animal model	Outcome	Reference
Cyclophosphamide/Fludarabine pre-conditioning + CD19-CAR T cells	Murine subcutaneous lymphoma xenograft model	Downregulation of IDO expression in lymphoma cell lines and increased efficacy of CAR T-cells against tumors.	(16)
Cyclophosphamide/Fludarabine pre-conditioning + GD2-CAR T cells	Phase I relapsed/refractory neuroblastoma	Increased CAR T cell expansion and serum IL-15 levels. Greater patient survival (6 out of 7).	NCT01822652 (52)
Cyclophosphamide/Fludarabine pre-conditioning + CD19-CAR T cells	Phase I/II trial for advanced-stage B cell lymphoma	Increased serum IL-15 levels. 12 out of 22 patients achieved complete response (CR) and 4 achieved partial remission (PR).	NCT00924326 (15)
Docetaxel + PSMA-CAR T cells	Human prostate cancer subcutaneous xenograft model	Remodelling of TME by inducing tumor damage and altering tumor stroma. Increased infiltration of CAR-T cells Reduction of tumor growth.	(53)
Docetaxel adjuvant + PSMA-CAR T cells	Human prostate cancer liver metastasis mouse model & human prostate cancer xenograft mouse model	Reduction of exhaustion markers (PD-1, TIM3, CTLA3) on CAR T cells. Depletion of MDSCs in peripheral blood.	(54)
Doxorubicin + systemic IL-2 + CD19-CAR T cells	Various murine and human xenograft solid tumors	Increased infiltration of CAR T-cells into tumor. Reduction in tumor infiltrating Tregs. Suppression of co-inhibitory receptor (PD-1 & LAG3) expression on T cells. Promotes expression of T-cell recruiting chemokines in tumor cells (CXCL9, CXCL10) and CXCR3 receptors on CAR T cells.	(55)
Doxorubicin pre-treatment + GD2-CAR T cells	Osteosarcoma cell lines	Decreased PD-L1 expression on tumor cells.	(56)
Gemcitabine pre-treatment + CD19-CAR T cells	Phase I/IIa trial for CD19-positive B-cell lymphoma or leukaemia	3 out of 5 patients achieved complete response (CR) and 1 achieved SD.	NCT02132624 (57)
Low dose cyclophosphamide pre-conditioning + Ig kappa (κ)-CAR-T cells	Phase I trial for non-Hodgkin lymphoma/chronic lymphocytic leukaemia (NHL/CLL) & Multiple Myeloma (MM)	4 out of 9 NHL/CLL and 4 out of 7 MM patients achieved clinical response.	NCT00881920 (58)
Nab-paclitaxel/Cyclophosphamide/Fludarabine pre-conditioning + Claudin18.1-CAR T cells	Phase I trial for gastric cancers	Achieved responses in 21/28 patients who had previously failed taxane treatment.	NCT03874897 (59)
Oxaliplatin + Cyclophosphamide + ROR1-CAR T cells	Murine metastatic transplantable lung adenocarcinoma model	Polarisation of TME into pro-inflammatory state. Promoting the expression of T-cell recruiting chemokines in tumor-infiltrating macrophages. Increased CAR-T cell infiltration into TME.	(60)
Temozolomide pre-conditioning + EGFRvIII-CAR T cells	Murine glioblastoma models	Increased CAR-T:Treg ratio in the tumors. Increased CAR-T cell expansion and persistence.	(61)

patients (48, 49, 51, 52). Several preclinical and clinical studies have shown that metronomic, low-dose Cy regimen (12.5mg/kg, single dose) reduced the number and function of Tregs, thereby restoring tumor-specific T cell responses (22–25, 58, 68) (Figure 1A). Importantly, low-dose Cy does not affect tumor-responding T cells (24), suggesting that low-dose Cy could be used as an adjuvant treatment post-CAR-T cell infusion.

Temozolomide is another potential neoadjuvant treatment for patients with glioblastoma receiving CAR-T cells. Temozolomide reduced Tregs in both mouse models and in patients (28, 29). In murine glioblastoma models, temozolomide treatment also increased CAR-T cell expansion resulting in a greater CAR-T cell to Treg ratio (61).

Two taxane drugs (paclitaxel and docetaxel) reduced immune suppressor cells in the TME. Tregs in non-small cell lung cancer patients were reduced after four cycles of docetaxel (30 mg/m^2) and cisplatin (75 mg/m^2) (36). A similar reduction in Tregs and impairment of their inhibitory function were also observed with paclitaxel treatment (38, 39). In addition, when given as neoadjuvant treatment prior to CAR-T cell infusion, docetaxel was found to enhance the PSMA-CAR-T cell efficacy in prostate cancer mouse models, by reducing MDSCs in the tumor (54). Similarly, paclitaxel has also been found to reduce the tumor-infiltrating MDSCs and restore effector functions of CD8$^+$ T cells (40). However, this impact was not consistently observed across other studies (34, 69). This discrepancy could be due to differences in drug dosage and treatment schedule.

Gemcitabine can also deplete MDSCs in cancer patients. In a Phase I/IIa trial of CAR-T cell therapy, three out of five patients who received gemcitabine as neoadjuvant treatment achieved complete response (CR) following CAR-T infusion (57). Preclinical and clinical studies demonstrated that gemcitabine treatment reduced the amount of MDSCs (30, 33) and increased the cytotoxicity of anti-tumor CD8$^+$ T cells and NK cells (32), this may contribute to enhanced responses to CAR-T cells.

Doxorubicin is another chemotherapeutic drug shown to reduce Tregs and MDSCs in the TME. When combined with CAR-T cells (55) or adoptively transferred T-helper cells (35), doxorubicin synergistically increased anti-tumor activity by diminishing the Tregs and MDSCs, leading to tumor suppression in both murine and human xenograft models.

2.3.2 Chemotherapy polarizes the TME

In solid tumors, tumor cells can express high levels of immune checkpoint molecules, including PD-L1 and PD-L2, to inhibit the effector functions of tumor-infiltrating T cells and CAR-T cells (70). In this regard, doxorubicin has been shown to affect CAR-T cell activity by lowering the expression of the immune checkpoint PD-L1 on tumor cells in osteosarcomas (56). Platinum-based chemotherapeutic drugs such as carboplatin, cisplatin, and oxaliplatin have also been shown to reduce PD-L2 expression on tumor cells, resulting in increased tumor cell recognition, proliferation and cytokine secretion of tumor-specific T cells (44) (Figure 1B).

Studies also revealed that oxaliplatin ameliorates the anti-inflammatory TME and enhances the recruitment of ROR1-CAR-T cells through modulating the TME chemokine profile (60). This polarisation of anti-inflammatory TME into a favourable pro-inflammatory state was also observed in CAR-T cell therapy with prior Cy treatment (50). The change in TME polarisation into a more inflammatory milieu is most likely accomplished through the activation and differentiation of myeloid cells into a pro-inflammatory phenotype. This TME change produces chemokines that recruit CAR-T cells, transforming the “cold” tumor into a “hot” tumor. In addition, paclitaxel, docetaxel, and gemcitabine were also shown to polarise macrophages into an M1-like phenotype to facilitate anti-tumor immunity (31, 37, 41, 71). This further provides a rationale for the combination therapy of CAR-T cells with chemotherapeutic drugs to overcome the immunosuppression in solid tumors.

2.3.3 Chemotherapy disrupts the tumor stroma

Besides the suppressor cells, the immunosuppressive tumor microenvironment is also enriched with stroma that could exclude CAR-T cell infiltration. The anti-microtubule agent, nab-paclitaxel, damaged the tumor stroma in primary tumors of advanced-stage prostate cancer patients (42, 43). Patients treated with nab-paclitaxel demonstrated less abundant fibrillar collagen matrices and lower CAF numbers, which were also confirmed using mice patient-derived xenograft (PDX) models (43). In a Phase I clinical trial of combination treatment of Claudin18.2-CAR-T cells with paclitaxel plus Cy, 21 out of 28 patients who failed prior taxane treatment achieved a significant clinical response to the combination treatment. The author suggested that this effect may be due to the accumulated nab-paclitaxel in the tumor stroma, which disrupted cancer-stromal interactions and helped with the CAR-T cell infiltration (59) (Figure 1C). Similarly, in a human xenograft mouse model, it was found that PSMA-CAR-T cells, in combination with low-dose, non-ablative docetaxel as a neoadjuvant regimen, eradicated large established tumors (53). Further analysis revealed that docetaxel could remodel the TME by altering the tumor stroma, which allowed the infiltration of CAR-T cells into the tumor site. These findings raise the possibility of using chemotherapy to overcome the physical barrier of TME, allowing CAR-T cell penetration.

2.3.4 Chemotherapy enhances T cell trafficking to tumors

T-cell trafficking to tumors remains a significant challenge for CAR-T cell efficacy. Successful T-cell trafficking depends on various chemokines including CCL5, CXCL9 and CXCL10 (72), and is critical for the response to CAR-T cell therapy. In cutaneous melanoma mouse models, temozolomide increased the expression of CCL5, CXCL9, and CXCL10, resulting in increased T-cell trafficking to the tumor (26). Furthermore, in patients treated with dacarbazine, CCL5, CXCL9, and CXCL10 expression was increased in chemotherapy-sensitive tumors, which was associated with increased T-cell infiltrate and enhanced patient

10.3389/fimmu.2023.1140541

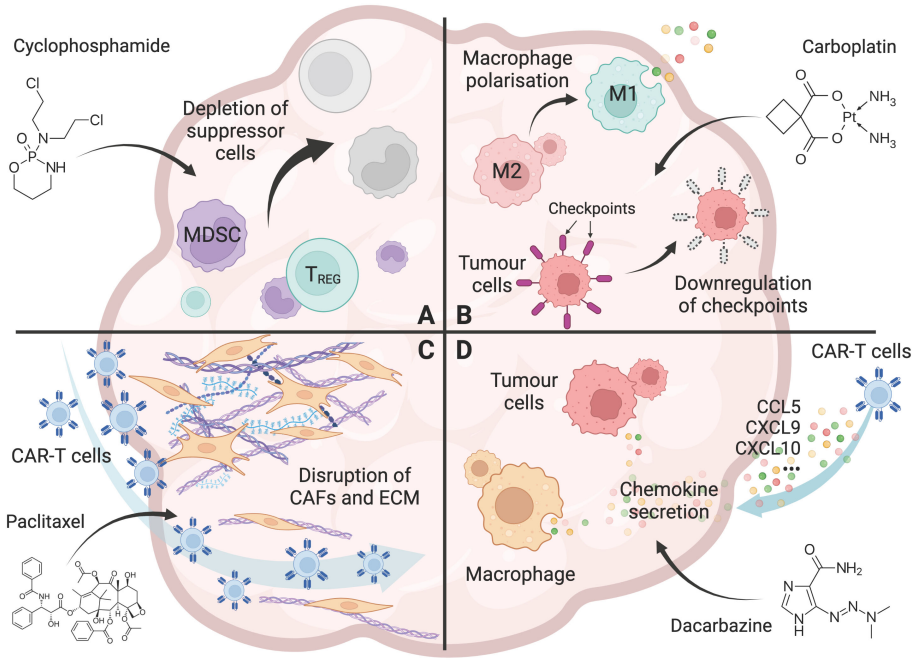

FIGURE 1
Chemotherapy overcomes the hurdles for CAR-T cells in solid tumors. **(A)** The effect of chemotherapy (Cyclophosphamide as an example) on the depletion of immunosuppressive cells, including Tregs, tumor associated macrophages (TAMs), and myeloid-derived suppressor cells (MDSCs) in the tumor microenvironment. **(B)** The effect of chemotherapy (Carboplatin as an example) on promoting a pro-inflammatory tumor microenvironment, including polarisation of macrophages from an M2 to an M1 phenotype, and downregulation of immune checkpoint molecules including PD-L1 and PD-L2 on tumor cells. **(C)** The effect of chemotherapy (Paclitaxel as an example) on the disruption of the tumor stroma, including removal of cancer-associated fibroblasts (CAFs) and their associated extracellular matrix (ECM) from the tumor barrier, allowing increased T-cell infiltration into the tumor. **(D)** The effect of chemotherapy (Dacarbazine as an example) on enhanced T-cell trafficking to the tumor, including the increased chemokine CCL5, CXCL9, and CXCL10 secretion by tumor cells and macrophages. Created with BioRender.com.

survival (26). Other chemotherapeutic agents, such as dacarbazine, carboplatin, anthracycline and taxane, were also seen to increase the secretion of these chemokines and enhanced T cell trafficking to tumors (27, 45) (Figure 1D).

In preclinical mouse models, poor T-cell trafficking was associated with low levels of chemokine expression, such as ligands for CXCR3 and CXCR4 (73). Pre-treatment with oxaliplatin and cyclophosphamide induced a pro-inflammatory tumor microenvironment and enhanced secretion of CCL5, CXCL9, CXCL10, and CXCL16 by tumor-infiltrating macrophages, leading to enhanced ROR1-CAR-T cell infiltration (60). The combination was also able to increase $CD8^+$ T cell infiltration and improved tumor control (47). This immunomodulatory effect was not restricted to oxaliplatin, other platinum-based drugs, such as carboplatin, have also increased tumor $CD8^+$ T cell populations and enhanced CCL5 and CXCL10 mRNA levels in lung cancer cells (46).

Taken together, certain chemotherapeutic drugs can alter the immunosuppressive tumor microenvironment to facilitate CAR-T cell trafficking, infiltration, expansion, and anti-tumor efficacy in solid tumors. However, the evidence listed above also indicated the choice of chemotherapeutic drugs, the dosage and the treatment schedule must be taken into serious consideration when designed in combination with CAR-T cell therapy.

3 Challenges for the combination of chemotherapy with CAR-T cell therapy

Chemotherapy is well known for its cytotoxic effects, which may also have a deleterious effect on CAR-T cell viability and function, inducing apoptosis of immune cells, and often leading to lymphopenia (6). The cytotoxic effect of chemotherapy is often mediated *via* mechanisms such as DNA damage and cell cycle arrest, and preferentially targets rapidly dividing cells such as tumour cells and bone marrow stem cells. The effect is drug and dosage dependent. Some drugs, such as cyclophosphamide and fludarabine, are considered as non-myeloablative but lymphodepleting. They may affect the transferred CAR-T cells both in circulation and at tumor site. Thus, the systemic delivery of chemotherapy may not only affect the endogenous T cell population generated at bone marrow, but also induces cytotoxicity on transferred CAR-T cells directly. Because CAR-T cells are usually given in one dose or several doses in a short period of time, the long persistence of the CAR-T cells and sustained anti-tumor function are the keys to therapeutic success. Thus, any adjuvant treatment post-CAR-T infusion may have an impact on long-term CAR-T cell efficacy.

After chemotherapy regimens, T cell numbers decrease, which gradually recovers over time (74). Notably, chemotherapy may preferentially deplete certain T-cell populations over others. In glioblastoma patients treated with combined radiotherapy and temozolomide, an increased effector memory T-cell (T_{EM}) population and a decreased CD45RA-expressing effector memory T-cell population (T_{EMRA}) population was observed (75). Additionally, cyclophosphamide treatment was found to decrease the mitochondrial function of naïve T-cells significantly more than central memory (T_{CM}) and effector memory (T_{EM}) T cells (76). The evidence indicated that certain chemotherapeutic drugs might significantly impair the CAR-T cell function when used in combination.

Chemotherapy may also negatively regulate the $CD4^+$ T-cell population. Compared with $CD8^+$ T cells, naïve $CD4^+$ T cells did not recover to pre-treatment numbers in breast cancer patients following chemotherapy (77). Another study found that naïve $CD4^+$ T cells were preferentially depleted after chemotherapy, with memory $CD4^+$ T cells forming the majority of the $CD4^+$ T cell population instead (78). This preferential depletion of naïve $CD4^+$ T cells may negatively affect CAR-T cell efficacy, given the importance of $CD4^+$ T cells in achieving long-term remission (79).

In CAR-T cell therapy, less differentiated T-cell subsets, including naïve T-cells and T_{CM} cells, have shown greater efficacy compared to more differentiated effector T-cell and T_{EM} cells (80). Thus, the susceptibility of naïve T-cells towards chemotherapy may decrease CAR-T cell efficacy when the chemotherapy is used as an adjuvant treatment.

Besides the effect on T-cell subsets, chemotherapy, such as carboplatin and taxane, may also induce the expression of immune checkpoint molecules on T cells, including PD-1 and CTLA4 in breast cancer patients, as a feedback immunosuppressive pathway following immune activation (45). This effect was also seen in other drugs, such as the oxaliplatin plus cyclophosphamide combination (47). Although combining with checkpoint blockades such as anti-PD1 or anti-CTLA4 may overcome this issue, the potential chemotherapy-induced early T-cell exhaustion should be considered for combination treatments.

Despite these challenges, the heterogenous response between studies highlights the multitude of factors affecting chemotherapy efficacy in combination with CAR-T therapy, including the type of drugs, treatment dose, regimen schedule, and cancer types. Thus, a successful combination of chemotherapy and CAR-T cell therapy relies greatly on the design of the treatment. To achieve this, the treatment plan must be optimised to allow long-term CAR-T cell persistence and anti-tumor function to provide the best clinical outcomes. In addition, CAR-T cells can also be engineered to resist these drugs, making it easier to optimise this combination. Such engineering may take inspirations from the chemo-resistance mechanisms observed in cancers, such as the upregulation of detoxifying molecules in response to platinum-based chemotherapies (81). The engineered expression chemo-resistance proteins such as platinum transporters and chelators may confer CAR-T cell resistance against platinum-based drugs. The CRISPR drug screening technology can also be used to select potential targets for drug resistance in CAR-T cells. Such candidates can then be conditionally expressed in CAR-T cells to gain chemo-resistance. In addition, chemotherapeutic drugs targeting DNA damage and the cell cycle also induce apoptosis in CAR-T cells. Thus, engineering mutated apoptotic machinery, such as the BCL-2 family proteins, may facilitate resistance to this drug-induced apoptosis in CAR-T cells. However, engineering CAR-T cells to make them resistant to apoptosis should be viewed with caution to avoid unexpected uncontrolled CAR-T cell proliferation.

Moreover, clinical strategies for combining chemotherapy with CAR-T cell therapy need to be evaluated. This combination therapy could be performed *via* two approaches. Chemotherapy's anti-tumor effect and immunomodulatory properties are traditionally studied in the context of specific tumor types. Thus, chemotherapeutic drugs could be selected based on the patient's tumor type. However, given the significant heterogeneity between tumor subtypes, such as in breast cancer, different drugs may be needed for different patients with the same cancer (82). Alternatively, a more personalised approach where drug choices are tailored to the patient's TME may be used. By testing patient samples, the TME components can be revealed. This information can be used to select the best chemotherapeutic drugs to facilitate the CAR-T cell attack. For instance, if poor T cell trafficking is due to immunosuppressive cells such as MDSCs and Tregs, cyclophosphamide may be used. If the immune exclusion is caused by CAFs, paclitaxel could be used instead. In addition, it should be noted that many chemotherapeutic drugs, including paclitaxel, have a wide range of effects on the TME, e.g., depleting MDSCs, Tregs and CAFs at the same time, as outlined in Table 1. These personalised strategies focus more on the challenges for CAR-T cells in each individual patient's tumor microenvironment and will be more likely to achieve better clinical outcomes for the 'chemo plus CAR-T' combination therapy.

4 Conclusion

Although a limited number of clinical trials have been performed, the combination treatment of chemotherapy and CAR-T cell therapy has significant capacity to improve the current clinical outcomes. It is a promising option for patients with advanced solid tumors, and further studies on the dose, treatment schedule, immune context, tumor types, and CAR-T cell engineering should be investigated to achieve best clinical outcomes. In addition, more mechanistic studies are still needed to understand how these therapies will best work together. Our increased understanding of the immunomodulatory effects of chemotherapy, together with the engineering of novel CAR-T cells, will further facilitate this combination strategy in the clinic and benefit more cancer patients.

Author contributions

Writing-original draft preparation, AW, XO. Writing-review and editing, CD'S, PN, JZ. Supervision, PN. AW and XO share first

authorship. JZ, PN and CD'S share senior authorship. All authors contributed to the article and approved the submitted version.

Conflict of interest

The authors declare that the research was conducted in the absence of any commercial or financial relationships that could be construed as a potential conflict of interest.

Publisher's note

All claims expressed in this article are solely those of the authors and do not necessarily represent those of their affiliated organizations, or those of the publisher, the editors and the reviewers. Any product that may be evaluated in this article, or claim that may be made by its manufacturer, is not guaranteed or endorsed by the publisher.

References

1. June CH, Sadelain M. Chimeric antigen receptor therapy. *N Engl J Med* (2018) 379(1):64–73. doi: 10.1056/NEJMra1706169

2. Berdeja JG, Madduri D, Usmani SZ, Jakubowiak A, Agha M, Cohen AD, et al. Ciltacabtagene autoleucel, a b-cell maturation antigen-directed chimeric antigen receptor T-cell therapy in patients with relapsed or refractory multiple myeloma (CARTITUDE-1): a phase 1b/2 open-label study. *Lancet* (2021) 398(10297):314–24. doi: 10.1016/S0140-6736(21)00933-8

3. Maude SL, Laetsch TW, Buechner J, Rives S, Boyer M, Bittencourt H, et al. Tisagenlecleucel in children and young adults with b-cell lymphoblastic leukemia. *N Engl J Med* (2018) 378(5):439–48. doi: 10.1056/NEJMoa1709866

4. Neelapu SS, Locke FL, Bartlett NL, Lekakis LJ, Miklos DB, Jacobson CA, et al. Axicabtagene ciloleucel CAR T-cell therapy in refractory large b-cell lymphoma. *N Engl J Med* (2017) 377(26):2531–44. doi: 10.1056/NEJMoa1707447

5. Marofi F, Motavalli R, Safonov VA, Thangavelu L, Yumashev AV, Alexander M, et al. CAR T cells in solid tumors: challenges and opportunities. *Stem Cell Res Ther* (2021) 12(1):81. doi: 10.1186/s13287-020-02128-1

6. Zitvogel L, Apetoh L, Ghiringhelli F, Kroemer G. Immunological aspects of cancer chemotherapy. *Nat Rev Immunol* (2008) 8(1):59–73. doi: 10.1038/nri2216

7. Johnson PC, Abramson JS. Patient selection for chimeric antigen receptor (CAR) T-cell therapy for aggressive b-cell non-Hodgkin lymphomas. *Leuk Lymphoma* (2020) 61(11):2561–7. doi: 10.1080/10428194.2020.1786563

8. Jain MD, Jacobs MT, Nastoupil LJ, Spiegel JY, Feng G, Lin Y, et al. Characteristics and outcomes of patients receiving bridging therapy while awaiting manufacture of standard of care axicabtagene ciloleucel CD19 chimeric antigen receptor (CAR) T-cell therapy for Relapsed/Refractory Large b-cell lymphoma: Results from the US lymphoma CAR-T consortium. *Blood* (2019) 134(Supplement_1):245–5. doi: 10.1182/blood-2019-129624

9. Nastoupil LJ, Jain MD, Spiegel JY, Ghobadi A, Lin Y, Dahiya S, et al. Axicabtagene ciloleucel (Axi-cel) CD19 chimeric antigen receptor (CAR) T-cell therapy for Relapsed/Refractory Large b-cell lymphoma: Real world experience. *Blood* (2018) 132(Supplement 1):91–1. doi: 10.1182/blood-2018-99-114152

10. Amini L, Silbert SK, Maude SL, Nastoupil LJ, Ramos CA, Brentjens RJ, et al. Preparing for CAR T cell therapy: patient selection, bridging therapies and lymphodepletion. *Nat Rev Clin Oncol* (2022) 19(5):342–55. doi: 10.1038/s41571-022-00607-3

11. Santomasso BD, Park JH, Salloum D, Riviere I, Flynn J, Mead E, et al. Clinical and biological correlates of neurotoxicity associated with CAR T-cell therapy in patients with b-cell acute lymphoblastic leukemia. *Cancer Discovery* (2018) 8(8):958–71. doi: 10.1158/2159-8290.CD-17-1319

12. Muranski P, Boni A, Wrzesinski C, Citrin DE, Rosenberg SA, Childs R, et al. Increased intensity lymphodepletion and adoptive immunotherapy–how far can we go? *Nat Clin Pract Oncol* (2006) 3(12):668–81. doi: 10.1038/ncponc0666

13. Wrzesinski C, Paulos CM, Kaiser A, Muranski P, Palmer DC, Gattinoni L, et al. Increased intensity lymphodepletion enhances tumor treatment efficacy of adoptively transferred tumor-specific T cells. *J Immunother* (2010) 33(1):1–7. doi: 10.1097/CJI.0b013e3181b88ffc

14. Gattinoni L, Finkelstein SE, Klebanoff CA, Antony PA, Palmer DC, Spiess PJ, et al. Removal of homeostatic cytokine sinks by lymphodepletion enhances the efficacy of adoptively transferred tumor-specific CD8+ T cells. *J Exp Med* (2005) 202(7):907–12. doi: 10.1084/jem.20050732

15. Kochenderfer JN, Somerville RPT, Lu T, Shi V, Bot A, Rossi J, et al. Lymphoma remissions caused by anti-CD19 chimeric antigen receptor T cells are associated with high serum interleukin-15 levels. *J Clin Oncol* (2017) 35(16):1803–13. doi: 10.1200/JCO.2016.71.3024

16. Ninomiya S, Narala N, Huye L, Yagyu S, Savoldo B, Dotti G, et al. Tumor indoleamine 2,3-dioxygenase (IDO) inhibits CD19-CAR T cells and is downregulated by lymphodepleting drugs. *Blood* (2015) 125(25):3905–16. doi: 10.1182/blood-2015-01-621474

17. Sesques P, Ferrant E, Safar V, Wallet F, Tordo J, Dhomps A, et al. Commercial anti-CD19 CAR T cell therapy for patients with relapsed/refractory aggressive b cell lymphoma in a European center. *Am J Hematol* (2020) 95(11):1324–33. doi: 10.1002/ajh.25951

18. Grigor EJM, Fergusson D, Kekre N, Montroy J, Atkins H, Seftel MD, et al. Risks and benefits of chimeric antigen receptor T-cell (CAR-T) therapy in cancer: A systematic review and meta-analysis. *Transfus Med Rev* (2019) 33(2):98–110. doi: 10.1016/j.tmrv.2019.01.005

19. Turtle CJ, Hanafi L-A, Berger C, Hudecek M, Pender B, Robinson E, et al. Immunotherapy of non-hodgkin's lymphoma with a defined ratio of CD8+ and CD4+ CD19-specific chimeric antigen receptor-modified T cells. *Sci Transl Med* (2016) 8 (355):355ra116. doi: 10.1126/scitranslmed.aaf8621

20. Andreadis C, Tam CS, Borchmann P, Jaeger U, McGuirk JP, Holte H, et al. Correlation of bridging and lymphodepleting chemotherapy with clinical outcomes in patients with relapsed/refractory diffuse large b-cell lymphoma treated with tisagenlecleucel. *Blood* (2019) 134(Supplement_1):2883–3. doi: 10.1182/blood-2019-124492

21. Bracci L, Schiavoni G, Sistigu A, Belardelli F. Immune-based mechanisms of cytotoxic chemotherapy: implications for the design of novel and rationale-based combined treatments against cancer. *Cell Death Differ* (2014) 21(1):15–25. doi: 10.1038/cdd.2013.67

22. Noordam L, Kaijen MEH, Bezemer K, Cornelissen R, Maat LAPWM, Hoogsteden HC, et al. Low-dose cyclophosphamide depletes circulating naïve and activated regulatory T cells in malignant pleural mesothelioma patients synergistically treated with dendritic cell-based immunotherapy. *Oncoimmunology* (2018) 7(12): e1474318. doi: 10.1080/2162402X.2018.1474318

23. Ghiringhelli F, Menard C, Puig PE, Ladoire S, Roux S, Martin F, et al. Metronomic cyclophosphamide regimen selectively depletes CD4+CD25+ regulatory T cells and restores T and NK effector functions in end stage cancer patients. *Cancer Immunol Immunother* (2007) 56(5):641–8. doi: 10.1007/s00262-006-0225-8

24. Ge Y, Domschke C, Stoiber N, Schott S, Heil J, Rom J, et al. Metronomic cyclophosphamide treatment in metastasized breast cancer patients: immunological effects and clinical outcome. *Cancer Immunol Immunother* (2012) 61(3):353–62. doi: 10.1007/s00262-011-1106-3

25. Scurr M, Pembroke T, Bloom A, Roberts D, Thomson A, Smart K, et al. Low-dose cyclophosphamide induces antitumor T-cell responses, which associate with survival in metastatic colorectal cancer. *Clin Cancer Res* (2017) 23(22):6771–80. doi: 10.1158/1078-0432.CCR-17-0895

26. Hong M, Puaux A-L, Huang C, Loumagne L, Tow C, Mackay C, et al. Chemotherapy induces intratumoral expression of chemokines in cutaneous melanoma, favoring T-cell infiltration and tumor control. *Cancer Res* (2011) 71 (22):6997–7009. doi: 10.1158/0008-5472.CAN-11-1466

27. Nardin A, Wong W-C, Tow C, Molina TJ, Tissier F, Audebourg A, et al. Dacarbazine promotes stromal remodeling and lymphocyte infiltration in cutaneous melanoma lesions. *J Invest Dermatol* (2011) 131(9):1896–905. doi: 10.1038/jid.2011.128

28. Banissi C, Ghiringhelli F, Chen L, Carpentier AF. Treg depletion with a low-dose metronomic temozolomide regimen in a rat glioma model. *Cancer Immunol Immunother* (2009) 58(10):1627–34. doi: 10.1007/s00262-009-0671-1

29. Ridolfi L, Petrini M, Granato AM, Gentilcore G, Simeone E, Ascierto PA, et al. Low-dose temozolomide before dendritic-cell vaccination reduces (specifically) CD4 +CD25++Foxp3+ regulatory T-cells in advanced melanoma patients. *J Transl Med* (2013) 11(1):135. doi: 10.1186/1479-5876-11-135

30. Eriksson E, Wenthe J, Irenaeus S, Loskog A, Ullenhag G. Gemcitabine reduces MDSCs, tregs and TGFβ-1 while restoring the teff/treg ratio in patients with pancreatic cancer. *J Transl Med* (2016) 14(1):282. doi: 10.1186/s12967-016-1037-z

31. Di Caro G, Cortese N, Castino GF, Grizzi F, Gavazzi F, Ridolfi C, et al. Dual prognostic significance of tumour-associated macrophages in human pancreatic adenocarcinoma treated or untreated with chemotherapy. *Gut* (2016) 65(10):1710–20. doi: 10.1136/gutjnl-2015-309193

32. Suzuki E, Kapoor V, Jassar AS, Kaiser LR, Albelda SM. Gemcitabine selectively eliminates splenic gr-1+/CD11b+ myeloid suppressor cells in tumor-bearing animals

and enhances antitumor immune activity. *Clin Cancer Res* (2005) 11(18):6713–21. doi: 10.1158/1078-0432.CCR-05-0883

33. Gabitass RF, Annels NE, Crawshaw J, Pandha HS, Middleton GW. Use of gemcitabine- (Gem) and fluropyrimidine (FP)-based chemotherapy to reduce myeloid-derived suppressor cells (MDSCs) in pancreatic (PC) and esophagogastric cancer (EGC). *J Clin Orthod* (2011) 29(15_suppl):2588–8. doi: 10.1200/jco.2011.29.15_suppl.2588

34. Vincent J, Mignot G, Chalmin F, Ladoire S, Bruchard M, Chevriaux A, et al. 5-fluorouracil selectively kills tumor-associated myeloid-derived suppressor cells resulting in enhanced T cell-dependent antitumor immunity. *Cancer Res* (2010) 70 (8):3052–61. doi: 10.1158/0008-5472.CAN-09-3690

35. Alizadeh D, Trad M, Hanke NT, Larmonier CB, Janikashvili N, Bonnotte B, et al. Doxorubicin eliminates myeloid-derived suppressor cells and enhances the efficacy of adoptive T-cell transfer in breast cancer. *Cancer Res* (2014) 74(1):104–18. doi: 10.1158/0008-5472.CAN-13-1545

36. Li J-Y, Duan X-F, Wang L-P, Xu Y-J, Huang L, Zhang T-F, et al. Selective depletion of regulatory T cell subsets by docetaxel treatment in patients with nonsmall cell lung cancer. *J Immunol Res* (2014) 2014:286170. doi: 10.1155/2014/286170

37. Kodumudi KN, Woan K, Gilvary DL, Sahakian E, Wei S, Djeu JY. A novel chemoimmunomodulating property of docetaxel: suppression of myeloid-derived suppressor cells in tumor bearers. *Clin Cancer Res* (2010) 16(18):4583–94. doi: 10.1158/1078-0432.CCR-10-0733

38. Zhang L, Dermawan K, Jin M, Liu R, Zheng H, Xu L, et al. Differential impairment of regulatory T cells rather than effector T cells by paclitaxel-based chemotherapy. *Clin Immunol* (2008) 129(2):219–29. doi: 10.1016/j.clim.2008.07.013

39. Vicari AP, Luu R, Zhang N, Patel S, Makinen SR, Hanson DC, et al. Paclitaxel reduces regulatory T cell numbers and inhibitory function and enhances the anti-tumor effects of the TLR9 agonist PF-3512676 in the mouse. *Cancer Immunol Immunother* (2009) 58(4):615–28. doi: 10.1007/s00262-008-0586-2

40. Sevko A, Michels T, Vrohlings M, Umansky L, Beckhove P, Kato M, et al. Antitumor effect of paclitaxel is mediated by inhibition of myeloid-derived suppressor cells and chronic inflammation in the spontaneous melanoma model. *J Immunol* (2013) 190(5):2464–71. doi: 10.4049/jimmunol.1202781

41. Wanderley CW, Colón DF, Luiz JPM, Oliveira FF, Viacava PR, Leite CA, et al. Paclitaxel reduces tumor growth by reprogramming tumor-associated macrophages to an M1 profile in a TLR4-dependent manner. *Cancer Res* (2018) 78(20):5891–900. doi: 10.1158/0008-5472.CAN-17-3480

42. Von Hoff DD, Ramanathan RK, Borad MJ, Laheru DA, Smith LS, Wood TE, et al. Gemcitabine plus nab-paclitaxel is an active regimen in patients with advanced pancreatic cancer: a phase I/II trial. *J Clin Oncol* (2011) 29(34):4548–54. doi: 10.1200/JCO.2011.36.5742

43. Alvarez R, Musteanu M, Garcia-Garcia E, Lopez-Casas PP, Megias D, Guerra C, et al. Stromal disrupting effects of nab-paclitaxel in pancreatic cancer. *Br J Cancer* (2013) 109(4):926–33. doi: 10.1038/bjc.2013.415

44. Lesterhuis WJ, Punt CJA, Hato SV, Eleveld-Trancikova D, Jansen BJH, Nierkens S, et al. Platinum-based drugs disrupt STAT6-mediated suppression of immune responses against cancer in humans and mice. *J Clin Invest* (2011) 121(8):3100–8. doi: 10.1172/JCI43656

45. Denkert C, von Minckwitz G, Brase JC, Sinn BV, Gade S, Kronenwett R, et al. Tumor-infiltrating lymphocytes and response to neoadjuvant chemotherapy with or without carboplatin in human epidermal growth factor receptor 2-positive and triple-negative primary breast cancers. *J Clin Oncol* (2015) 33(9):983–91. doi: 10.1200/JCO.2014.58.1967

46. Zhou L, Xu Q, Huang L, Jin J, Zuo X, Zhang Q, et al. Low-dose carboplatin reprograms tumor immune microenvironment through STING signaling pathway and synergizes with PD-1 inhibitors in lung cancer. *Cancer Lett* (2021) 500:163–71. doi: 10.1016/j.canlet.2020.11.049

47. Pfirschke C, Engblom C, Rickelt S, Cortez-Retamozo V, Garris C, Pucci F, et al. Immunogenic chemotherapy sensitizes tumors to checkpoint blockade therapy. *Immunity* (2016) 44(2):343–54. doi: 10.1016/j.immuni.2015.11.024

48. Cohen AD, Garfall AL, Stadtmauer EA, Melenhorst JJ, Lacey SF, Lancaster E, et al. B cell maturation antigen-specific CAR T cells are clinically active in multiple myeloma. *J Clin Invest* (2019) 129(6):2210–21. doi: 10.1172/JCI126397

49. Brentjens RJ, Rivière I, Park JH, Davila ML, Wang X, Stefanski J, et al. Safety and persistence of adoptively transferred autologous CD19-targeted T cells in patients with relapsed or chemotherapy refractory b-cell leukemias. *Blood* (2011) 118(18):4817–28. doi: 10.1182/blood-2011-04-348540

50. Murad JP, Tilakawardane D, Park AK, Lopez LS, Young CA, Gibson J, et al. Pre-conditioning modifies the TME to enhance solid tumor CAR T cell efficacy and endogenous protective immunity. *Mol Ther* (2021) 29(7):2335–49. doi: 10.1016/j.ymthe.2021.02.024

51. Turtle CJ, Hanafi L-A, Berger C, Gooley TA, Cherian S, Hudecek M, et al. CD19 CAR-T cells of defined CD4+:CD8+ composition in adult b cell ALL patients. *J Clin Invest* (2016) 126(6):2123–38. doi: 10.1172/JCI85309

52. Heczey A, Louis CU, Savoldo B, Dakhova O, Durett A, Grilley B, et al. CAR T cells administered in combination with lymphodepletion and PD-1 inhibition to patients with neuroblastoma. *Mol Ther* (2017) 25(9):2214–24. doi: 10.1016/j.ymthe.2017.05.012

53. Alzubi J, Dettmer-Monaco V, Kuehle J, Thorausch N, Seidl M, Taromi S, et al. PSMA-directed CAR T cells combined with low-dose docetaxel treatment induce tumor regression in a prostate cancer xenograft model. *Mol Ther Oncolytics* (2020) 18:226–35. doi: 10.1016/j.omto.2020.06.014

54. Zhang X, Sun S, Miao Y, Yuan Y, Zhao W, Li H, et al. Docetaxel enhances the therapeutic efficacy of PSMA-specific CAR-T cells against prostate cancer models by suppressing MDSCs. *J Cancer Res Clin Oncol* (2022) 148(12):3511–20. doi: 10.1007/s00432-022-04248-y

55. Hu J, Sun C, Bernatchez C, Xia X, Hwu P, Dotti G, et al. T-Cell homing therapy for reducing regulatory T cells and preserving effector T-cell function in large solid tumors. *Clin Cancer Res* (2018) 24(12):2920–34. doi: 10.1158/1078-0432.CCR-17-1365

56. Chulanetra M, Morchang A, Sayour E, Eldjerou L, Milner R, Lagmay J, et al. GD2 chimeric antigen receptor modified T cells in synergy with sub-toxic level of doxorubicin targeting osteosarcomas. *Am J Cancer Res* (2020) 10(2):674–87.

57. Enblad G, Karlsson H, Gammelgård G, Wenthe J, Lövgren T, Amini RM, et al. A phase I/IIa trial using CD19-targeted third-generation CAR T cells for lymphoma and leukemia. *Clin Cancer Res* (2018) 24(24):6185–94. doi: 10.1158/1078-0432.CCR-18-0426

58. Ramos CA, Savoldo B, Torrano V, Ballard B, Zhang H, Dakhova O, et al. Clinical responses with T lymphocytes targeting malignancy-associated κ light chains. *J Clin Invest* (2016) 126(7):2588–96. doi: 10.1172/JCI86000

59. Qi C, Gong J, Li J, Liu D, Qin Y, Ge S, et al. Claudin18.2-specific CAR T cells in gastrointestinal cancers: Phase 1 trial interim results. *Nat Med* (2022) 28(6):1189–98. doi: 10.1038/s41591-022-01800-8

60. Srivastava S, Furlan SN, Jaeger-Ruckstuhl CA, Sarvothama M, Berger C, Smythe KS, et al. Immunogenic chemotherapy enhances recruitment of CAR-T cells to lung tumors and improves antitumor efficacy when combined with checkpoint blockade. *Cancer Cell* (2021) 39(2):193–208.e10. doi: 10.1016/j.ccell.2020.11.005

61. Suryadevara CM, Desai R, Abel ML, Riccione KA, Batich KA, Shen SH, et al. Temozolomide lymphodepletion enhances CAR abundance and correlates with antitumor efficacy against established glioblastoma. *Oncoimmunology* (2018) 7(6): e1434464. doi: 10.1080/2162402X.2018.1434464

62. Zhao Z, Xiao X, Saw PE, Wu W, Huang H, Chen J, et al. Chimeric antigen receptor T cells in solid tumors: a war against the tumor microenvironment. *Sci China Life Sci* (2020) 63(2):180–205. doi: 10.1007/s11427-019-9665-8

63. Quail DF, Joyce JA. Microenvironmental regulation of tumor progression and metastasis. *Nat Med* (2013) 19(11):1423–37. doi: 10.1038/nm.3394

64. Santi A, Kugeratski FG, Zanivan S. Cancer associated fibroblasts: The architects of stroma remodeling. *Proteomics* (2018) 18(5–6):e1700167. doi: 10.1002/pmic.201700167

65. Binnewies M, Roberts EW, Kersten K, Chan V, Fearon DF, Merad M, et al. Understanding the tumor immune microenvironment (TIME) for effective therapy. *Nat Med* (2018) 24(5):541–50. doi: 10.1038/s41591-018-0014-x

66. Guo F, Cui J. CAR-T in solid tumors: Blazing a new trail through the brambles. *Life Sci* (2020) 260(118300):118300. doi: 10.1016/j.lfs.2020.118300

67. Yin Y, Boesteanu AC, Binder ZA, Xu C, Reid RA, Rodriguez JL, et al. Checkpoint blockade reverses anergy in IL-13Rα2 humanized scFv-based CAR T cells to treat murine and canine gliomas. *Mol Ther Oncolytics* (2018) 11:20–38. doi: 10.1016/j.omto.2018.08.002

68. Lutsiak MEC, Semnani RT, De Pascalis R, Kashmiri SVS, Schlom J, Sabzevari H. Inhibition of CD4(+)25+ T regulatory cell function implicated in enhanced immune response by low-dose cyclophosphamide. *Blood* (2005) 105(7):2862–8. doi: 10.1182/blood-2004-06-2410

69. Cattin S, Fellay B, Pradervand S, Trojan A, Ruhstaller T, Rüegg C, et al. Bevacizumab specifically decreases elevated levels of circulating KIT+CD11b+ cells and IL-10 in metastatic breast cancer patients. *Oncotarget* (2016) 7(10):11137–50. doi: 10.18632/oncotarget.7097

70. Seliger B, Quandt D. The expression, function, and clinical relevance of B7 family members in cancer. *Cancer Immunol Immunother* (2012) 61(8):1327–41. doi: 10.1007/s00262-012-1293-6

71. Michels T, Shurin GV, Naiditch H, Sevko A, Umansky V, Shurin MR. Paclitaxel promotes differentiation of myeloid-derived suppressor cells into dendritic cells *in vitro* in a TLR4-independent manner. *J Immunotoxicol* (2012) 9(3):292–300. doi: 10.3109/1547691X.2011.642418

72. Harlin H, Meng Y, Peterson AC, Zha Y, Tretiakova M, Slingluff C, et al. Chemokine expression in melanoma metastases associated with CD8+ T-cell recruitment. *Cancer Res* (2009) 69(7):3077–85. doi: 10.1158/0008-5472.CAN-08-2281

73. Kohli K, Pillarisetty VG, Kim TS. Key chemokines direct migration of immune cells in solid tumors. *Cancer Gene Ther* (2022) 29(1):10–21. doi: 10.1038/s41417-021-00303-x

74. Truong NTH, Gargett T, Brown MP, Ebert LM. Effects of chemotherapy agents on circulating leukocyte populations: Potential implications for the success of CAR-T cell therapies. *Cancers (Basel)* (2021) 13(9):2225. doi: 10.3390/cancers13092225

75. Fadul CE, Fisher JL, Gui J, Hampton TH, Côté AL, Ernstoff MS. Immune modulation effects of concomitant temozolomide and radiation therapy on peripheral blood mononuclear cells in patients with glioblastoma multiforme. *Neuro-Oncology* (2011) 13(4):393–400. doi: 10.1093/neuonc/noq204

76. Das RK, O'Connor RS, Grupp SA, Barrett DM. Lingering effects of chemotherapy on mature T cells impair proliferation. *Blood Advances* (2020) 4 (19):4653–64. doi: 10.1182/bloodadvances.2020001797

77. Fagnoni FF, Lozza L, Zibera C, Zambelli A, Ponchio L, Gibelli N, et al. T-Cell dynamics after high-dose chemotherapy in adults: Elucidation of the elusive CD8+ subset reveals multiple homeostatic T-cell compartments with distinct implications for immune competence. *Immunology* (2002) 106(1):27–37. doi: 10.1046/j.1365-2567.2002.01400.x

78. Verma R, Foster RE, Horgan K, Mounsey K, Nixon H, Smalle N, et al. Lymphocyte depletion and repopulation after chemotherapy for primary breast cancer. *Breast Cancer Res* (2016) 18(1):10. doi: 10.1186/s13058-015-0669-x

79. Melenhorst JJ, Chen GM, Wang M, Porter DL, Chen C, Collins MA, et al. Decade-long leukaemia remissions with persistence of CD4+ CAR T cells. *Nature* (2022) 602(7897):503–9. doi: 10.1038/s41586-021-04390-6

80. McLellan AD, Ali Hosseini Rad SM. Chimeric antigen receptor T cell persistence and memory cell formation. *Immunol Cell Biol* (2019) 97(7):664–74. doi: 10.1111/imcb.12254

81. Zhou J, Kang Y, Chen L, Wang H, Liu J, Zeng S, et al. The drug-resistance mechanisms of five platinum-based antitumor agents. *Front Pharmacol* (2020) 11:343. doi: 10.3389/fphar.2020.00343

82. Yersal O, Barutca S. Biological subtypes of breast cancer: Prognostic and therapeutic implications. *World J Clin Oncol* (2014) 5(3):412–24. doi: 10.5306/wjco.v5.i3.412

frontiers | Frontiers in Immunology

TYPE Original Research
PUBLISHED 13 March 2023
DOI 10.3389/fimmu.2023.1022942

Check for updates

OPEN ACCESS

EDITED BY
Feng-Ming (Spring) Kong,
The University of Hong Kong, Hong Kong SAR, China

REVIEWED BY
Sushil Kumar,
Oregon Health and Science University, United States
Eswari Dodagatta-Marri,
University of California, San Francisco, United States

*CORRESPONDENCE
Shuzhen Wang
darrywang2003@163.com
Lei Zhu
zhulei@coga.org.cn

†These authors have contributed equally to this work and share first authorship

SPECIALTY SECTION
This article was submitted to Cancer Immunity and Immunotherapy, a section of the journal Frontiers in Immunology

RECEIVED 19 August 2022
ACCEPTED 27 February 2023
PUBLISHED 13 March 2023

CITATION
Cao G, Hua D, Li J, Zhang X, Zhang Z, Zhang B, Bei T, Cui L, Chen S, Wang S and Zhu L (2023) Tumor immune microenvironment changes are associated with response to neoadjuvant chemotherapy and long-term survival benefits in advanced epithelial ovarian cancer: A pilot study.
Front. Immunol. 14:1022942.
doi: 10.3389/fimmu.2023.1022942

COPYRIGHT
© 2023 Cao, Hua, Li, Zhang, Zhang, Zhang, Bei, Cui, Chen, Wang and Zhu. This is an open-access article distributed under the terms of the Creative Commons Attribution License (CC BY). The use, distribution or reproduction in other forums is permitted, provided the original author(s) and the copyright owner(s) are credited and that the original publication in this journal is cited, in accordance with accepted academic practice. No use, distribution or reproduction is permitted which does not comply with these terms.

Tumor immune microenvironment changes are associated with response to neoadjuvant chemotherapy and long-term survival benefits in advanced epithelial ovarian cancer: A pilot study

Guangming Cao[1†], Dingchao Hua[2†], Jinfeng Li[1], Xuefang Zhang[1], Zhiqiang Zhang[1], Bei Zhang[2], Ting Bei[2], Lina Cui[2], Shiqing Chen[2], Shuzhen Wang[1*] and Lei Zhu[1*]

[1]Department of Obstetrics and Gynecology, Beijing Chao-Yang Hospital, Capital Medical University, Beijing, China, [2]Department of Medical Affairs, 3D Medicines Inc., Shanghai, China

Little is known about the association between efficacy of neoadjuvant chemotherapy (NACT)/survival and the dynamic change of tumor immune environment (TIME) during treatment in epithelial ovarian cancer (EOC). This study investigated the TIME landscape of treatment-naive EOC tumors using multiplex immunofluorescence and associated the TIME before and after platinum-based NACT with treatment efficacy and prognosis in 33 patients with advanced EOC. NACT significantly increased the density of $CD8^+$ T cells ($P = 0.033$), $CD20^+$ B cells ($P = 0.023$), CD56 NK cells ($P = 0.041$), PD-1^+ cells ($P = 0.042$), and PD-$L1^+CD68^+$ macrophages ($P = 0.005$) in the tissue specimens. Response to NACT was evaluated using CA125 response and chemotherapy response score (CRS). Compared with the non-responders, the responders displayed a larger proportion of tumors showing increase in the infiltration of $CD20^+$ cells ($P = 0.046$) and in the M1/M2 ratio ($P = 0.038$) as well as fewer tumors showing increase in the infiltration of $CD56^{bright}$ cells ($P = 0.041$). No association was found between pre-NACT TIME and response to NACT. Density of pre-NACT $CD8^+$ cells was positively associated with longer progression-free survival (PFS) ($P = 0.011$) and overall survival (OS) ($P = 0.048$). Post-NACT $CD20^+$ and $CD163^+$ macrophages (M2) infiltrates were associated with prolonged ($P = 0.005$) and shortened PFS ($P = 0.021$), respectively. Increase in the density of $CD4^+$ T cells was predictive for longer PFS ($P = 0.022$) and OS ($P = 0.023$). In the multivariate analysis, high density of $CD8^+$ cells pre-NACT ($P = 0.042$) were independently associated with improved OS.

KEYWORDS

epithelial ovarian cancer, neoadjuvant chemotherapy, tumor immune microenvironment, treatment efficacy, prognosis

Introduction

Ovarian cancer is the most lethal gynecologic malignancy (1). Epithelial ovarian cancer (EOC) accounts for about 90% of ovarian malignancies (2), and the majority of EOC patients present with advanced tumor stage at diagnosis. The prognosis of patients with a late-stage disease is dismal, with a 5-year survival rate of less than 30% (3). Complete resection combined with platinum-based chemotherapy has been the primary choice for patients with EOC. In advanced and metastatic EOC where complete resection is not feasible, neoadjuvant chemotherapy (NACT) followed by interval debulking surgery (IDS) and adjuvant chemotherapy is an alternative (4, 5). However, NACT is associated with a moderate survival benefit, and with NACT, a considerable proportion of patients with advanced disease still succumb to recurrence (4, 6–8).

Increasing clinical evidence has suggested that analyses of tumor immune environment (TIME) of treatment-naïve tumor has allowed for identifying components of immune contexture that are beneficial [including tumor-infiltrating lymphocytes (TILs): $CD8^+$ cytotoxic cells, and $CD3^+$ T cells] or deleterious (including $Foxp3^+$ T cells, and $CD163^+$ macrophages) to ovarian cancer patients (9–12). Other studies have attempted to unveil the effect of conventional cytotoxics on TIME (13–15). Little, however, is known about the association of TIME changes upon NACT with NACT efficacy and survival benefit. Findings from that analyses may identify predictive signatures for treatment efficacy and survival as well as uncover potential pathways, mechanisms, and biomolecules that could be co-targeted in new treatment combinations to prolong disease control in advanced EOC.

This study aimed to investigate the association of TIME orientation with NACT efficacy and survival outcomes in a cohort of annotated EOC tissue biopsies obtained at diagnosis and at IDS following chemotherapy.

Method

Study design

We retrospectively reviewed EOC patients who received at least one cycle of platinum-based NACT between February 22, 2011, and November 15, 2018, at Beijing Chao-Yang Hospital. Patients who had III/IV EOC as defined by the International Federation of Gynecology and Obstetrics (FIGO) and pre-NACT and post-NACT tumor tissue specimens were eligible. Pre-NACT samples were biopsy specimens obtained with diagnostic laparoscopy, and post-NACT samples were taken from the tumor tissues obtained at IDS. All the samples were subjected to mIF to evaluate TIME. Depending on data availability and sample quality, the association of TIME with NACT efficacy and survival outcomes was explored. The flow diagram of the study design was shown in Supplementary Figure S1. This study was approved by the ethics committee of Beijing Chao-Yang Hospital (2021-Science-639).

Treatment

All patients received NACT of taxane/platinum combinations for a median of three cycles (range, 2–4 cycles) before IDS. No other treatment such as radiation or endocrine therapy was performed before IDS. For IDS, all patients underwent surgery with the intent to achieve complete cytoreduction with no gross residual tumor. Subsequently, at the discretion of the physician, patients underwent 4–8 cycles of adjuvant chemotherapy.

Evaluation of response to NACT

As radiological evaluation of response using response evaluation criteria in solid tumors (RECIST) is not suitable for EOC characterized of cancer dissemination, we used CA125 response and CRS, which are extensively utilized in clinical practice, to evaluate the response to platinum-based NACT. CA125 response using gynecological cancer intergroup (GCIG) CA125 criteria (16) and chemotherapy response score (CRS) recommended by the European Society for Medical Oncology and European Society for Gynecological Oncology (ESMO-ESGO) (17). CA125 response is defined as at least a 50% reduction in CA125 levels from a pretreatment sample. The response must be confirmed and maintained for at least 28 days. Patients can be evaluated according to CA125 only if they have a pretreatment sample that was at least twice the upper limit of the reference range within two weeks before starting the treatment. CRS is a three-tier system based on pathological reaction of surgical specimens in which CRS1 shows no or minimal tumor response, CRS2 shows moderate/appreciable tumor response, and CRS3 usually shows complete or near-complete response. In this study, patients with samples scored as CRS3 or CRS2 were defined as CRS responders and patients with biopsies scored as CRS1 were non-responders.

Tumor microenvironment by multiplex immunofluorescence

Surgical tissue specimens were subjected to the examination of the TIME, which was performed as previously described by 3D Medicines, Inc., a College of American Pathologists (CAP)-accredited and Clinical Laboratory Improvement Amendments (CLIA)-certified laboratory (18). Primary antibodies targeting CD163, CD68, PD-1, PD-L1, CD3, CD4, CD8, CD56, CD20, Foxp3 and pan-CK or S100 were sequentially applied to FFPE tissue slides (Supplementary Table S1). After the incubation with secondary antibodies, corresponding reactive Opal fluorophores, and nuclei acids staining reagent DAPI, multiplex stained slides were scanned using a Vectra Polaris Quantitative Pathology Imaging System (Akoya Biosciences), which was configured to capture fluorescent spectra at 20 nm wavelength intervals from 440 nm to 780 nm with a fixed exposure time. All scans for each

slide were then superimposed to obtain a single image. Unstained and monoplex stained slide images were applied to extract Tissue autofluorescence was extracted with unstained and monoplex stained slide images. Fluorescence images were analyzed using the APTIME software developed by 3D Medicines. Tumor parenchyma and stroma were differentiated according to CK staining. The CK-positive area with DAPI staining was defined as tumor region, and the CK negative area with DAPI staining was considered stroma region. The quantities of various cell subsets were expressed as the count number of positively stained cells per square millimeter (cells per mm^2). The density of immune cell subsets in tumor and stroma regions were figured out by detecting signal channel or multiple-channel, namely $CD3^+$, $CD3^+CD4^+$, $CD8^+$, $Foxp3^+$, $PD\text{-}1^+CD8^+$, $CD4^+Foxp3^+$ (Treg), $CD68^+CD163^-$ (M1 macrophage), $CD68^+CD163^+$ (M2 macrophage), $PD\text{-}L1^+$ $CD68^+$, CD56 bright (NK cell), CD56 dim (NK cell), etc. The co-occurrence of $CD3^+$ T cells and $CD20^+$ B cells indicates the formation of tertiary lymphoid structures (TLS).

Statistical analysis

For paired comparisons we used wilcoxon matched-paired signed-ranked test, and for non-paired comparisons, wilcoxon rank-sum test was considered. Survival curve and median survival time were depicted using Kaplan-Meier survival curve. Nonparametric log-rank testing was employeed to determine the differences among different immune cell infiltration groups, with a median cutoff used to distinguish low vs high levels. The hazard ratio (HR) and 95% confidence interval (CI) were estimated using the Cox proportional hazard model. Univariate survival analyses were performed using the Cox proportional-hazards model, and multivariate Cox regression analysis was performed to select independent prognostic factors. A two-side $P \leq 0.05$ was considered to represent a statistically significant difference. Statistical analysis was performed using R software (version 3.6.1).

Results

Clinicopathological characteristics of patients

A total of 33 EOC patients received NACT + IDS and had paired pre-NACT and post-NACT tumor specimens. The median age of the cohort was 60 years [interquartile range (IQR), 53–65]. Serous carcinoma was the predominant histologic subtype (26/33, 78.8%), and most of the patients had FIGO stage III disease (30/33, 90.9%). Almost all the tumors were grade 3 (32/33, 97.0%). Approximately half of the patients had lymph node metastasis. The median CA125 level was 1632.0 U/mL at baseline. Seventy-six percent of patients received two cycles of NACT (2 cycles, n = 25; 3 cycles, n = 5; 4 cycles, n = 3). CA125 response to 1^{st} cycle NACT was assessed in 31 cases (CA-125 1^{st} cycle responder, n = 22; CA-125 1^{st} cycle non-responder, n = 9), and chemotherapy response score was evaluated in 25 cases (CRS1, n = 8; CRS2, n = 16; CRS3, n = 1). Twenty-six (26/33, 78.8%) patients were platinum-sensitive, and the rest seven cases were platinum-resistant. The median follow-up of the cohort was 40.9 months. Complete cytoreduction was achieved at interval surgery in 19 of the 33 patients (57.6%) (Table 1).

TIME changes upon NACT

Using mIF, the tissue biopsies were stained for multiple markers of immune cells. The baseline cell density in the malignant cell areas and adjacent stromal areas of 30 patients was shown in Supplementary Figure S2. Depending on sample quality, we analyzed the infiltration of tumor immune cell subsets in paired tumor tissue specimens from 21 patients to examine the TIME changes of EOC with NACT. Upon NACT, in the tumor center the density of $CD8^+$ T cells, significantly increased (pre-NACT vs. post-NACT: $CD8^+$ T cell, $P = 0.033$) (Figures 1A, B). The density of $CD68^+CD163^+$ M2 macrophages significantly decreased (pre-NACT vs. post-NACT: $CD68^+CD163^+$ T cell, $P = 0.039$) (Supplementary Figure S3). In the tumor stroma, significantly increased infiltration of $CD20^+$ B cells, CD56 NK cells, $PD\text{-}1^+$ cells and $PD\text{-}L1^+CD68^+$ macrophages was observed (pre-NACT vs. post-NACT: $CD20^+$ B cell, $P = 0.023$; $CD56^{bright}$ cells, $P = 0.041$; $CD56^{dim}$ cells, $P = 0.024$; $PD\text{-}1^+$ cells, $P = 0.042$; $PD\text{-}L1^+CD68^+$ macrophages, $P = 0.005$) (Figures 1A–G). The expression of PD-L1 in the post-NACT tumor specimens was significantly elevated than in the pre-NACT tumor tissues ($P < 0.001$, Data not shown). No significant difference was found in the density of other immune cell subsets, including $CD3^+$, $CD4^+Foxp3^+$, $CD4^+$, $CD68^+CD163^-$ and $PD\text{-}1^+CD8^+$ (Supplementary Table S2; Supplementary Figure S3) between pre-NACT and post-NACT tissue biopsies.

Association of NACT efficacy with TIME

Response to platinum-based chemotherapy was evaluated using CA125 response and CRS. We examined the association of NACT response with the change of TIME during NACT and TIME pre- and post-NACT. The 1^{st} cycle CA-125 changes were determined in 19 of 21 patients with TIME information of both pre- and post-NACT tissue specimens. Compared with pre-NACT specimens, there was a significant increase in the density of $CD8^+$ T cells in the tumor areas of post-NACT tissue biopsies in the 1^{st} cycle CA125 responders ($P = 0.039$). We also observed a significant increase in the infiltrates of $PD\text{-}1^+$ cells ($P = 0.048$), $PD\text{-}L1^+CD68^+$ macrophages ($P = 0.017$), $CD20^+$ B cells ($P = 0.033$), and $CD56^{dim}$ ($P = 0.022$) (Figures 2A–E) in the stroma of the 1^{st} cycle CA125 responders. In the 1^{st} cycle CA125 non-responders, the density of $CD56^{bright}$ NK cells tended to increase after NACT ($P = 0.059$, Supplementary Tables S3–S6).

CRS was assessed in 18 patients, of whom 7 were CRS1 and 11 were CRS2. In CRS2 biopsies, NACT significantly increased the infiltration $CD20^+$ B cells ($P = 0.050$), $PD\text{-}1^+$ cells ($P = 0.011$), $PD\text{-}L1^+CD68^+$ macrophages ($P = 0.023$) and $PD\text{-}1^+CD8^+$ cells ($P = 0.035$) in the stoma of CRS2 responders (Figures 2F–I). NACT significantly increased infiltrates of $CD4^+Foxp3^+$ Treg cells ($P =$

10.3389/fimmu.2023.1022942

TABLE 1 Clinicopathological characteristics of patients (n=33).

Variable	n (%) N = 33
Age at diagnosis, Median (IQR)	60 (53, 65)
Histologic type	
Serous	26 (78.8%)
Clear cell	3 (9.1%)
Mucinous	1 (3.0%)
Mixed	3 (9.1%)
2014 FIGO stage	
III	30 (90.9%)
IV	3 (9.1%)
Histologic tumor grade	
Grade 1	1 (3.0%)
Grade 3	32 (97%)
ECOG	
1	7 (21.2%)
2	20 (60.6%)
3	6 (18.2%)
Baseline CA125 (U/mL),Median (IQR)	1632 (91-17980)
Lymph node metastasis	
No	18 (56.3%)
Yes	14 (43.7%)
Unknown	1
NACT cycles, Median (Min, Max)	2 (2, 4)
Adjuvant chemotherapy cycles, Median (Min, Max)	6 (4, 8)
CA125 1st cycle response	
No	9 (29.0%)
Yes	22 (71.0%)
Unknown	2
Chemotherapy response score	
1	8 (32.0%)
2	16 (64.0%)
3	1 (4.0%)
R0	
Yes	19 (57.6%)
No	14 (42.4%)
Platinum sensitivity	
Platinum sensitive	26 (78.8%)
Platinum resistant	7 (21.2%)

FIGO, International Federation of Gynecology and Obstetrics; ECOG, Eastern Cooperative Oncology Group score; NACT, neoadjuvant chemotherapy; IQR, interquartile range.

0.036) and PD-L1$^+$CD68$^+$ macrophages (P = 0.022) in the stroma and decreased M1/M2 ratio (P = 0.016) in the tumor of CRS1 non-responders (Figures 2H, J, K). Moreover, compared with the non-responders, the responders displayed a larger proportion of tumors showing increase in the infiltration of CD20$^+$ cells (P = 0.046) and in the M1/M2 ratio (P = 0.038) as well as fewer tumors showing increase in the infiltration of CD56^{bright} cells (P = 0.041) (Figures 2L–O). We also tried to examine the association between pre-NACT TIME and response to NACT and failed to find TIME markers predictive for response to NACT. With regard to the correlation between TIME post-NACT and response to NACT, CA125 responders displayed a lower density of PD-L1$^+$CD68$^+$ macrophages in the stroma than CA125 non-responders. Compared with CRS1 non-responders, CRS2 responders displayed a significant lower degree of infiltration of M1 macrophages (tumor, P = 0.006) and M2 macrophages (tumor, P = 0.0497) in the tumor (Supplementary Tables S3–S6).

Association of TIME with prognosis

We also attempted to explore the predictive factors for survival. Univariate cox regression analysis of clinical characteristics revealed R0 resection and platinum sensitivity favorable for predicting better OS and PFS (Table 2). Subsequently, we examined the predictive value of pre-NACT TIME for survival. Using median value as a cut-off, high infiltration of CD8$^+$ cells in the pre-NACT tumor was positively associated with prolonged OS (CD8^{high} vs. CD8^{low}, NR vs. 28.7 months, HR, 0.23, 95% CI, 0.05-1.1, log-rank P = 0.048) and PFS (CD8^{high} vs. CD8^{low}, 40.9 vs. 14.0 months, HR, 0.31, 95% CI, 0.12-0.79, log-rank P = 0.011) (Figures 3A, B; Supplementary Table S7).

When considering the predictive value of post-NAT TIME for survival, high density of CD20$^+$ B cells (CD20^{high} vs. CD20^{low}, mPFS, 28.65 vs. 12.30 months; HR, 0.17; 95% CI, 0.04-0.67; log-rank P = 0.005) (Figure 3C), more abundant TLS (TLS-negative vs. TLS-positive, mPFS, NR vs. 14.7 months; HR, 0.15; 95% CI, 0.02-1.1; log-rank P = 0.034) (Data not shown), and lower density of CD68$^+$CD163$^+$ M2 macrophages (M2 macrophages^{high} vs. M2 macrophages^{low}, mPFS, 12.30 vs. 25.40 months; HR, 3.2; 95% CI, 1.14-9.01; log-rank P = 0.021) in the post-NACT tumor were found to predict better PFS (Figure 3D; Supplementary Table S8).

Considering the potential association between TIME change and PFS or OS, we stratified patients into infiltration ^{increase} and infiltration $^{no\ increase}$ subgroups according to infiltration changes of specific immune cell subsets during NACT. Compared with patients with no increase in the density of CD4$^+$ cells in the stromal, patients with increase in this cell subset had significantly prolonged PFS (log-rank P = 0.022) and OS (log-rank P = 0.023) (Figures 3E, F; Supplementary Table S9). In the multivariate analysis, among R0 resection, platinum-sensitivity, tumoral CD8$^+$ pre-NACT, tumoral CD20$^+$ post-NACT, tumoral M2 macrophages post-NACT, and the increase of stromal CD4$^+$ upon NACT, only platinum-sensitivity was independently associated with PFS (HR, 9.83; 95% CI, 1.98–48.83; P < 0.001), and OS (HR, 52.74; 95% CI, 1.45–1916.12; P = 0.031) and tumoral CD8$^+$ pre-NACT (HR, 0.06;

10.3389/fimmu.2023.1022942

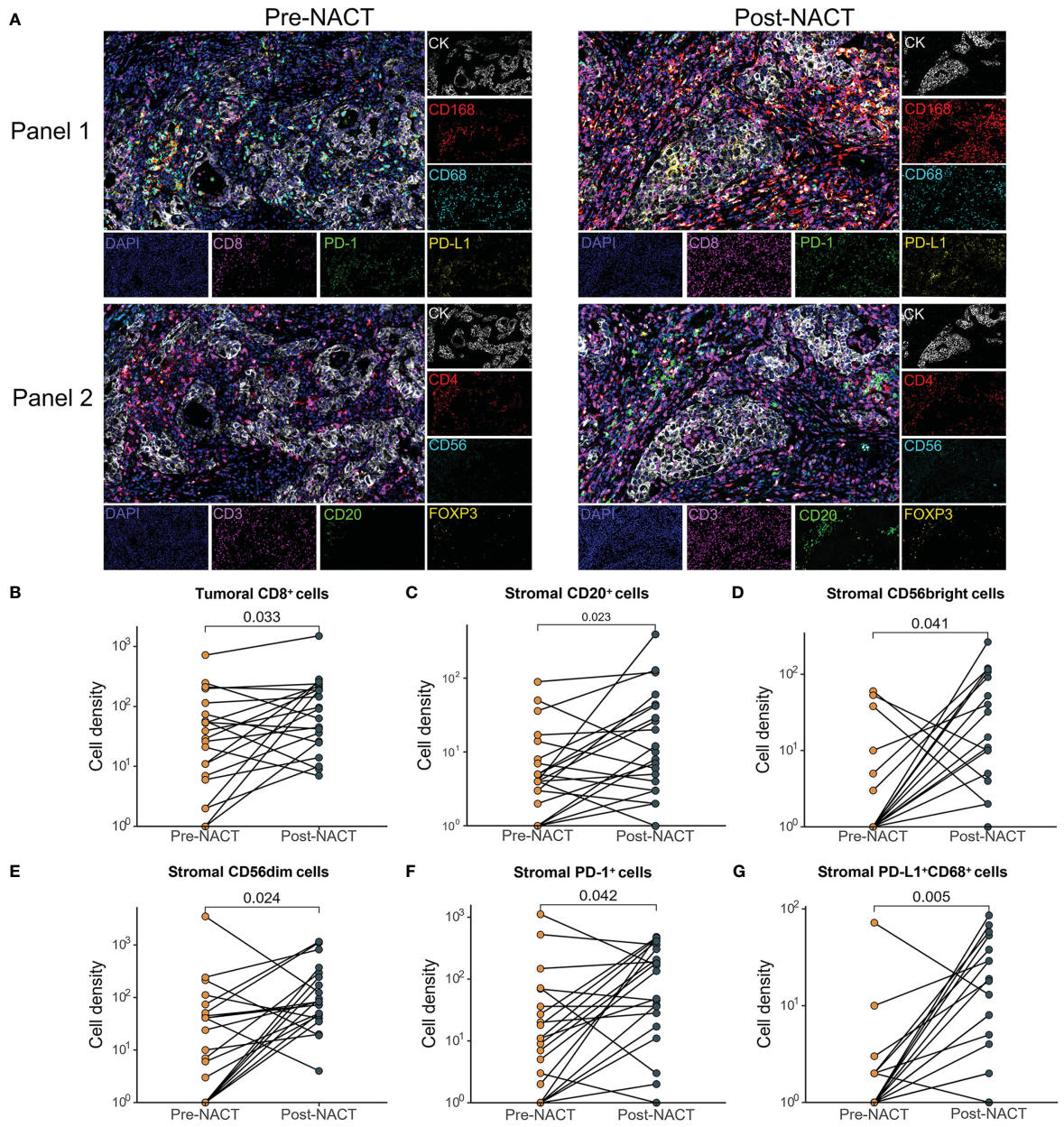

FIGURE 1
Comparison of changes in the tumor immune microenvironment between pre- and post-NACT matched tumor samples (n=21). **(A)** Images of representative mIF results. Pre-NACT mIF image on left, post-NACT mIF image on right. **(B–G)** Comparison of density of **(B)** tumoral $CD8^+$ cell; **(C)** stromal $CD20^+$ cell; **(D)** stromal CD56bright cell; **(E)** stromal CD56dim cell; **(F)** stromal PD-1^+ cell; **(G)** stromal PD-$L1^+$ $CD68^+$ cells between pre- and post-NACT tumor samples. P value, Wilcoxon matched-paired signed-ranked test for paired samples.

95% CI, 0–0.91; P = 0.042) were independently associated with improved OS. The difference in PFS between pre-NACT $CD8^{high}$ and pre-NACT $CD8^{low}$ patients was marginally significant (P = 0.054) (Table 3).

Discussion

In the current study, we reported that the infiltration of immune cells in the tumor lesions pre-NACT and post-NACT was associated with response to NACT and long-term survival benefits. With mIF, we analyzed multiple immune cell subsets closely associated with cancer dissemination in a cohort of patients with paired pre-NACT and post-NACT specimens. We show that NACT altered the balance of immune cell subsets of T cells, B cells, and macrophages, showing significantly elevated density of $CD8^+$ T cell, $CD20^+$ B cells, and PD-$L1^+CD68^+$ macrophages. The biopsies pre-NACT from patients with good response to NACT had significantly increased infiltration of $CD8^+$ T cells and $CD20^+$ B cells compared with tumor specimens post-

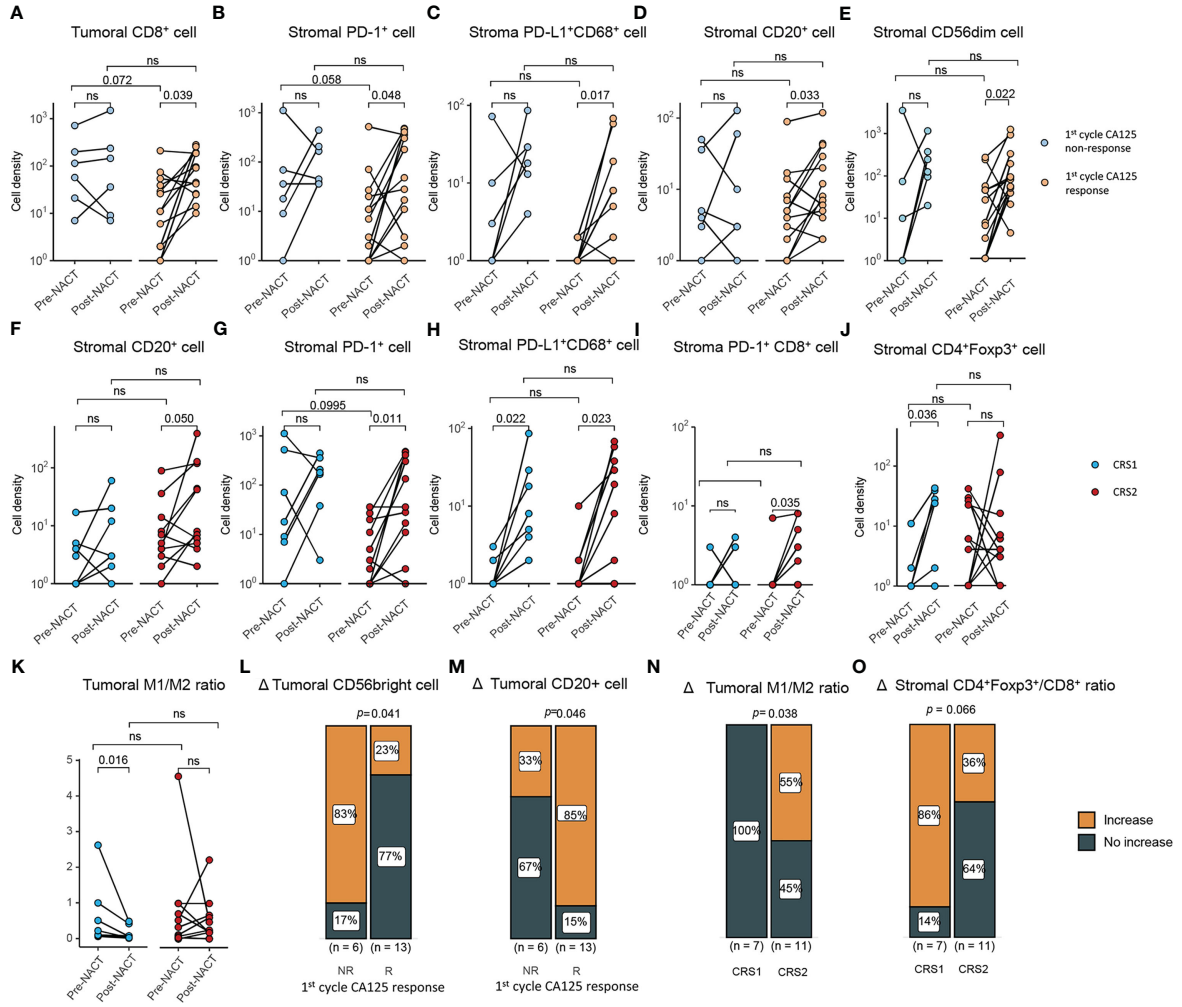

FIGURE 2
Correlations between the change of tumor immune microenvironment and response to NACT. **(A–D)** Comparison of density of **(A)** tumoral CD8$^+$ cells, **(B)** stromal PD-1$^+$ cells, **(C)** stromal PD-L1$^+$ CD68$^+$ cell, **(D)** stromal CD20$^+$ cell, **(E)** CD56dim cells between pre- and post-NACT tumor samples in CA125 responders and CA125 non-responders (CA125 responders, n=13; CA125 non-responders, n=6). **(F–J)** Comparison of density of **(F)** stromal CD20$^+$ cell **(G)** stromal PD-1$^+$ cells, **(H)** stromal PD-L1$^+$ CD68$^+$ cell, **(I)** stromal PD-1$^+$CD8$^+$ cell, **(J)** stromal CD4$^+$Foxp3$^+$ cells between pre- and post-NACT tumor samples in CRS1 and CRS2 group (CRS1, n=7; CRS2, n=11). **(K)** Tumoral M1/M2 macrophage density ratio of pre- and post-NACT tumor samples. **(L, M)** Density change in CD56 bright cells **(L)** and CD20+ cells **(M)** between the CA125 responders and non-responders after the first cycle of NACT treatment. **(N, O)** Density change in CD56 bright cells **(N)** and CD20+ cells **(O)** between the CRS1 and CRS2 groups. P value, Wilcoxon matched-paired signed-ranked test for paired samples. ns, no significance.

TABLE 2 Univariate cox regression analysis of clinical characteristics in all available samples.

	PFS			OS		
Characteristic	HR	95%CI	p-value	HR	95%CI	p-value
Age						
≤50	Ref			Ref		
>50	2.82	0.83, 9.59	0.096	3.15	0.41, 24.5	0.272
ECOG						
I-II	Ref			Ref		
III	0.59	0.23, 1.50	0.266	0.49	0.15, 1.65	0.249

(Continued)

TABLE 2 Continued

	PFS			OS		
Characteristic	HR	95%CI	p-value	HR	95%CI	p-value
Lymph node metastasis						
No	Ref			Ref		
Yes	1.06	0.46, 2.44	0.889	1.52	0.48, 4.81	0.475
CA-125 1st cycle response						
No	Ref			Ref		
Yes	0.53	0.22, 1.27	0.153	0.36	0.11, 1.20	0.097
CRS						
1	Ref			Ref		
2-3	0.91	0.33, 2.52	0.862	1.22	0.22, 6.69	0.815
R0						
No	Ref			Ref		
Yes	0.42	0.18, 0.97	0.042	0.27	0.08, 0.94	0.039
Platinum sensitivity						
Platinum resistant	Ref			Ref		
Platinum sensitive	0.09	0.03, 0.30	<0.001	0.21	0.06, 0.75	0.016

HR, hazard ratio; CI, confidence interval, Ref, reference.

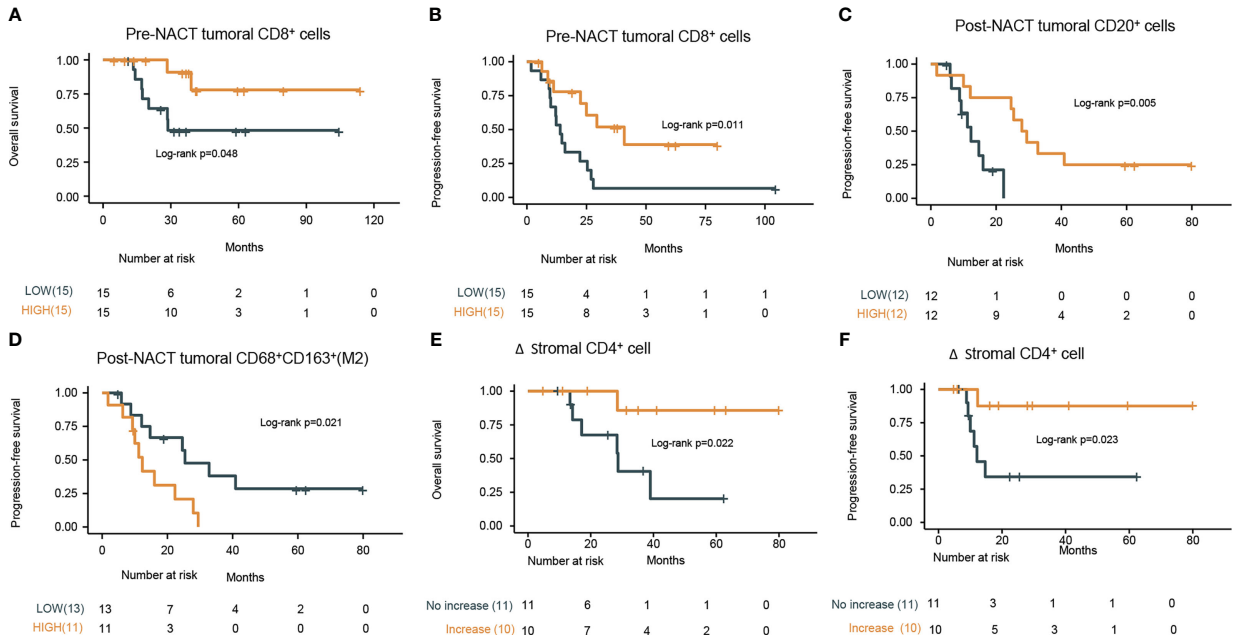

FIGURE 3
Prognostic values of pre-NACT and post-NACT immune cell density. Kaplan–Meier curves of the **(A)** overall survival (OS) and **(B)** progression-free survival (PFS) stratified by infiltration degree of pre-NACT tumoral $CD8^+$ cells (low or high based on the median value) in the tumor specimens. **(C)** Kaplan–Meier curves of PFS stratified by the infiltration degree of tumoral $CD20^+$ cells post-NACT (low or high based on the median value) in the tumor specimens. **(D)** Kaplan–Meier curves of PFS stratified by the infiltration degree of tumoral $CD68^+CD163^+$ (M2 macrophages) cells post-NACT (low or high based on the median value) in the tumor specimens. **(E)** Kaplan–Meier curves of the OS stratified by the increase in the density of stromal $CD4^+$ cells (increase or no increase) in the tumor specimens. **(F)** Kaplan–Meier curves of the progression-free survival (PFS) stratified by the increase in the density of stromal $CD4^+$ cells (increase or no increase) in the tumor specimens. P values refers to log rank tests between the indicated groups.

10.3389/fimmu.2023.1022942

TABLE 3 Multivariate cox regression analysis of potential risk factors in pre- and post-NACT paired samples.

	PFS			OS		
Characteristic	N	Event N	p-value	N	Event N	p-value
R0						
No	10	7		10	4	
Yes	11	8	0.460	11	3	0.622
Platinum sensitivity						
Platinum sensitive	4	4		4	2	
Platinum resistant	17	11	<0.001	17	5	0.031
Pre-NACT tumoral CD8+						
Low	10	10		10	5	
High	11	5	0.054	11	2	0.042
Δ Stromal CD4+						
No increase	11	9		11	6	
Increase	10	6	0.217	10	1	0.293
Post-NACT Tumoral CD20+						
Low	12	9				
High	9	6	0.081			
Post-NACT tumoral $CD68^+CD163^+$(M2)						
Low	11	6				
High	10	9	0.130			

NACT. Infiltrates of $CD8^+$ T cells pre-NACT, $CD20^+$ B cells and $CD163^+$ macrophages post-NACT, and marked change in $CD4^+$ T cells during NACT are associated with prolonged survival.

Previous studies have shown the effect of chemotherapeutic regimens on tumor immune microenvironment, including an increase in infiltration of $CD8^+$ T cells, $CD3^+$ T cells, $CD20^+$ B cells, and PD-1^+ cells (13–15, 19, 20). Regulation of tumor-promoting immune suppressors and immune effectors of the immune system might result in the enhanced antitumor activity of immunotherapies. It is, therefore, encouraging that NACT had significantly increased the infiltration of TILs in our and previous studies. Albeit no difference in the density of immune cell subsets positive for markers in the pretreatment specimens between responders and non-responders, responders displayed significantly increased infiltration of $CD8^+$ T cells in the tumor, $CD20^+$ T cells, PD-1^+ cells, PD-$L1^+$ cells, and PD-$L1^+CD68^+$ macrophages in the stroma; $CD4^+Foxp3^+$ Treg cell and PD-$L1^+CD68^+$ macrophage density in the stroma significantly increased in non-responders. Consistently, Bohm S et al. reported that density of $Foxp3^+$ cells in biopsies from good responders significantly declined after NACT (14). Interestingly, the fact that infiltrates of PD-$L1^+CD68^+$ macrophage density increased in both responders and non-responders suggested a rationale for immunotherapy of immune checkpoint blockade after NACT for both patients responding and not-responding to NACT. Taken with the finding of a marked increase in infiltration of immune effectors in the biopsies from responders, it is rationale to speculate that TIME changes are associated with response to NACT. Of note, although PD-$L1^+$ macrophages significantly elevated after NACT in both responders and non-responders, the observation that the infiltration of PD-$L1^+$ macrophages in the post-NACT biopsies of responders was significantly lower than in non-responders further implies that patients resistant to NACT might be more responsive to PD-1 blockade.

We attempted to examine immune cell signatures predicting long-term survival under the following conditions. Pretreatment, first, the density of $CD8^+$ T cells was positively associated with longer PFS and OS, consistent with previous reports (10, 12). Other immune cell subset markers in pretreatment biopsies were not predictive for PFS and OS in our observation. Second, post-NACT $CD20^+$ and $CD163^+$ macrophages (M2) were associated with prolonged and shortened PFS, respectively. There is evidence that a high M1:M2 ratio post-NACT is predictive of improved PFS and OS (13, 21), which supports our findings. The correlation of post-NACT $CD20^+$ B cell with survival is a novel finding discovered herein. Third, with regard to the association between TIME change and survival, we revealed for the first time that the increase in the density of $CD4^+$ T cells was predictive for longer PFS and OS. In the multivariate analysis, among R0 resection, platinum sensitivity, and the above immune cell subset markers predicting survival in the univariate analysis, only platinum-sensitive and tumoral $CD8^{+high}$ pre-NACT were independently associated with improved OS.

This study was limited by its retrospective design and small sample size. Nevertheless, the mIF workflow employed in this study allowed the characterization of multiple biomarkers closely correlating to immune activators and suppressors, rendering it feasible to monitor TIME upon NACT in a one-set test. As we focused on the TIME change at the protein level assessed by mIF, further studies should integrate analysis from diverse confirmatory experimental methods, including mRNA sequencing, whole-exome sequencing, and immunoproteomics.

Conclusions

This study examined the dynamics of tumor-infiltrating immune cells using the matched pre-NACT and post-NACT tissue biopsies and compared these to the response to NACT and long-term survival. Evaluation of dynamics in the TIME could help reflect NACT efficacy, predict survival benefit, and perhaps most importantly, guide rational immunotherapy after NACT rather than in relapsed disease.

Data availability statement

The original contributions presented in the study are included in the article/Supplementary Material. Further inquiries can be directed to the corresponding authors.

Ethics statement

The studies involving human participants were reviewed and approved by The ethics committee of Beijing Chao-Yang Hospital. The patients/participants provided their written informed consent to participate in this study. Written informed consent was obtained from the individual(s) for the publication of any potentially identifiable images or data included in this article.

Author contributions

GC: Acquisition of data, writing-review and editing. DH: Methodology, writing-review and editing. JL: Data curation, formal analysis, writing-review and editing. XZ: Data curation, formal analysis, writing-review and editing. ZZ: Data curation, formal analysis, writing-review and editing. BZ: Data curation, formal analysis, writing-review and editing. TB: Writing–original draft, writing–review and editing. LC: Conceptualization, resources, supervision, writing–review and editing. SC: Conceptualization, resources, supervision, writing–review and editing. SW: Resources, data curation, writing-review and editing. LZ: Conceptualization, resources, supervision, methodology, project administration, writing–review and editing. All authors contributed to the article and approved the submitted version.

Funding

This study was supported by the National Natural Science Foundation of China (No. 82003245 and 82001559), the Key Projects of Sailing Plan of Beijing Medical Administration (No. ZYLX201713) and Guangdong Basic and Applied Basic Research Foundation (No. 2019A1515110884).

Acknowledgments

We would like to thank all coordinators at the Beijing Chao-Yang Hospital, China and 3D Medicines Inc., Shanghai, China for supporting this study.

Conflict of interest

DH, BZ, TB, LC, and SC are employees of 3D Medicines Inc.

The remaining authors declare that the research was conducted in the absence of any commercial or financial relationships that could be construed as a potential conflict of interest.

Publisher's note

All claims expressed in this article are solely those of the authors and do not necessarily represent those of their affiliated organizations, or those of the publisher, the editors and the reviewers. Any product that may be evaluated in this article, or claim that may be made by its manufacturer, is not guaranteed or endorsed by the publisher.

Supplementary material

The Supplementary Material for this article can be found online at: https://www.frontiersin.org/articles/10.3389/fimmu.2023.1022942/full#supplementary-material

References

1. Siegel RL, Miller KD, Fuchs HE, Jemal A. Cancer statistics, 2022. *CA: A Cancer J Clin* (2022) 72(1):7–33. doi: 10.3322/caac.21708

2. Torre LA, Trabert B, DeSantis CE, Miller KD, Samimi G, Runowicz CD, et al. Ovarian cancer statistics, 2018. *CA: Cancer J Clin* (2018) 68(4):284–96. doi: 10.3322/caac.21456

3. Lheureux S, Braunstein M, Oza AM. Epithelial ovarian cancer: Evolution of management in the era of precision medicine. *CA: A Cancer J Clin* (2019) 69(4):280–304. doi: 10.3322/caac.21559

4. Vergote I, Tropé CG, Amant F, Kristensen GB, Ehlen T, Johnson N, et al. Neoadjuvant chemotherapy or primary surgery in stage IIIC or IV ovarian cancer. *New Engl J Med* (2010) 363(10):943–53. doi: 10.1056/NEJMoa0908806

5. NCCN. *NCCN clinical practice guidelines in oncology. epithelial ovarian Cancer/ Fallopian tube Cancer/Primary peritoneal cancer. version 1. 2022*. National Comprehensive Cancer Network (NCCN (2022). 3025 Chemical Road, Suite 100, Plymouth Meeting, PA 19462, USA

6. Vergote I, Coens C, Nankivell M, Kristensen GB, Parmar MKB, Ehlen T, et al. Neoadjuvant chemotherapy versus debulking surgery in advanced tubo-ovarian cancers: Pooled analysis of individual patient data from the EORTC 55971 and CHORUS trials. *Lancet Oncol* (2018) 19(12):1680–7. doi: 10.1016/S1470-2045(18)30566-7

7. Kehoe S, Hook J, Nankivell M, Jayson GC, Kitchener H, Lopes T, et al. Primary chemotherapy versus primary surgery for newly diagnosed advanced ovarian cancer (CHORUS): An open-label, randomised, controlled, non-inferiority trial. *Lancet* (2015) 386(9990):249–57. doi: 10.1016/S0140-6736(14)62223-6

8. Coleridge SL, Bryant A, Kehoe S, Morrison J. Chemotherapy versus surgery for initial treatment in advanced ovarian epithelial cancer. *Cochrane Database Syst Rev* 2021(2). doi: 10.1002/14651858.CD005343.pub5

9. Fridman WH, Pagès F, Sautès-Fridman C, Galon J. The immune contexture in human tumours: impact on clinical outcome. *Nat Rev Cancer* (2012) 12(4):298–306. doi: 10.1038/nrc3245

10. Sato E, Olson SH, Ahn J, Bundy B, Nishikawa H, Qian F, et al. Intraepithelial CD8+ tumor-infiltrating lymphocytes and a high CD8+/regulatory T cell ratio are associated with favorable prognosis in ovarian cancer. *Proc Natl Acad Sci USA* (2005) 102(51):18538–43. doi: 10.1073/pnas.0509182102

11. Barnett JC, Bean SM, Whitaker RS, Kondoh E, Baba T, Fujii S, et al. Ovarian cancer tumor infiltrating T-regulatory (Treg) cells are associated with a metastatic phenotype. *Gynecol Oncol* (2010) 116(3):556–62. doi: 10.1016/j.ygyno.2009.11.020

12. Hamanishi J, Mandai M, Abiko K, Matsumura N, Baba T, Yoshioka Y, et al. The comprehensive assessment of local immune status of ovarian cancer by the clustering of multiple immune factors. *Clin Immunol* (2011) 141(3):338–47. doi: 10.1016/j.clim.2011.08.013

13. Leary A, Genestie C, Blanc-Durand F, Gouy S, Dunant A, Maulard A, et al. Neoadjuvant chemotherapy alters the balance of effector to suppressor immune cells in advanced ovarian cancer. *Cancer Immunol Immunother* (2021) 70(2):519–31. doi: 10.1007/s00262-020-02670-0

14. Böhm S, Montfort A, Pearce OMT, Topping J, Chakravarty P, Everitt GLA, et al. Neoadjuvant chemotherapy modulates the immune microenvironment in metastases of tubo-ovarian high-grade serous carcinoma. *Clin Cancer Res* (2016) 22(12):3025–36. doi: 10.1158/1078-0432.CCR-15-2657

15. Lo CS, Sanii S, Kroeger DR, Milne K, Talhouk A, Chiu DS, et al. Neoadjuvant chemotherapy of ovarian cancer results in three patterns of tumor-infiltrating lymphocyte response with distinct implications for immunotherapy. *Clin Cancer Res* (2017) 23(4):925–34. doi: 10.1158/1078-0432.CCR-16-1433

16. Rustin GJS, Vergote I, Eisenhauer E, Pujade-Lauraine E, Quinn M, Thigpen T, et al. Definitions for response and progression in ovarian cancer clinical trials incorporating RECIST 1.1 and CA 125 agreed by the gynecological cancer intergroup (GCIG). *Int J Gynecol Cancer* (2011) 21(2):419. doi: 10.1097/IGC.0b013e3182070f17

17. Böhm S, Faruqi A, Said I, Lockley M, Brockbank E, Jeyarajah A, et al. Chemotherapy response score: Development and validation of a system to quantify histopathologic response to neoadjuvant chemotherapy in tubo-ovarian high-grade serous carcinoma. *J Clin Oncol* (2015) 33(22):2457–63. doi: 10.1200/JCO.2014.60.5212

18. Zhang W, Gong C, Peng X, Bi X, Sun Y, Zhou J, et al. Serum concentration of CD137 and tumor infiltration by M1 macrophages predict the response to sintilimab plus bevacizumab biosimilar in advanced hepatocellular carcinoma patients. *Clin Cancer Res* (2022), 28(16):3499-3508. doi: 10.1158/1078-0432.CCR-21-3972

19. Lee YA-O, Woo HA-O, Kim YN, Park JA-O, Nam EJ, Kim SA-O, et al. Dynamics of the tumor immune microenvironment during neoadjuvant chemotherapy of high-grade serous ovarian cancer. *Cancers* (2022) 14(9):2308 doi: 10.3390/cancers14092308

20. Pölcher M, Braun M, Friedrichs N, Rudlowski C, Bercht E, Fimmers R, et al. Foxp3+ cell infiltration and granzyme B+/Foxp3+ cell ratio are associated with outcome in neoadjuvant chemotherapy-treated ovarian carcinoma. *Cancer Immunol Immunother* (2010) 59(6):909–19. doi: 10.1007/s00262-010-0817-1

21. Yuan X, Zhang J, Li D, Mao Y, Mo F, Du W, et al. Prognostic significance of tumor-associated macrophages in ovarian cancer: A meta-analysis. *Gynecol Oncol* (2017) 147(1):181–7. doi: 10.1016/j.ygyno.2017.07.007

frontiers | Frontiers in Immunology

TYPE Review
PUBLISHED 24 March 2023
DOI 10.3389/fimmu.2023.1149122

Check for updates

OPEN ACCESS

EDITED BY
Clare Y. Slaney,
Peter MacCallum Cancer Centre, Australia

REVIEWED BY
Xiaoxiang Rong,
Southern Medical University, China
Sanjima Pal,
McGill University, Canada

*CORRESPONDENCE
Gong Chen
chengong@sysucc.org.cn
Weiwei Xiao
xiaoww@sysucc.org.cn

†These authors share first authorship

SPECIALTY SECTION
This article was submitted to Cancer Immunity and Immunotherapy, a section of the journal Frontiers in Immunology

RECEIVED 21 January 2023
ACCEPTED 15 March 2023
PUBLISHED 24 March 2023

CITATION
Xiao W, Luo H, Yao Y, Wang Y, Liu S, Sun R and Chen G (2023) Total neoadjuvant treatment and PD-1/PD-L1 checkpoint inhibitor in locally advanced rectal cancer. *Front. Immunol.* 14:1149122. doi: 10.3389/fimmu.2023.1149122

COPYRIGHT
© 2023 Xiao, Luo, Yao, Wang, Liu, Sun and Chen. This is an open-access article distributed under the terms of the Creative Commons Attribution License (CC BY). The use, distribution or reproduction in other forums is permitted, provided the original author(s) and the copyright owner(s) are credited and that the original publication in this journal is cited, in accordance with accepted academic practice. No use, distribution or reproduction is permitted which does not comply with these terms.

Total neoadjuvant treatment and PD-1/PD-L1 checkpoint inhibitor in locally advanced rectal cancer

Weiwei Xiao[1†*], Huilong Luo[1†], Ye Yao[1], Yaqin Wang[1], Shuang Liu[1], Rui Sun[1] and Gong Chen[2*]

[1]Department of Radiation Oncology, State Key Laboratory of Oncology in South China, Collaborative Innovation Center for Cancer Medicine, Sun Yat-Sen University Cancer Center, Guangzhou, China, [2]Department of Colorectal Surgery, State Key Laboratory of Oncology in South China, Collaborative Innovation Center for Cancer Medicine, Sun Yat-Sen University Cancer Center, Guangzhou, China

For local advanced rectal cancer (LARC), total neoadjuvant treatment (TNT) has shown more complete response (CR), reduced risk of distant metastasis (DM) and increase of the sphincter preservation rate. Now it is the one and only recommendation for high-risk group of LARC according to National Comprehensive Cancer Network (NCCN) rectal cancer guideline, while it is also preferentially recommended for low-risk group of LARC. TNT is also beneficial for distant rectal cancer patients who have need for organ preservation. Even though the prognostic value of programmed cell death-ligand 1 (PD-L1) in the neoadjuvant chemoradiotherapy (NACRT) of LARC patients is undetermined yet, the combination of NACRT and programmed cell death-1 (PD-1)/PD-L1 antibodies seem bring new hope for mismatch repair proficient (pMMR)/microsatellite stable (MSS) LARC patients. Accumulating small sample sized studies have shown that combining NACRT with PD-1/PD-L1 antibody yield better short-term outcomes for pMMR/MSS LARC patients than historic data. However, ideal total dose and fractionation of radiotherapy remains one of unresolved issues in this combination setting. Thorough understanding the impact of radiotherapy on the tumor microenvironment and their interaction is needed for in-depth understanding and exquisite design of treatments combination model.

KEYWORDS

locally advanced rectal cancer, total neoadjuvant treatment, long-course radiotherapy, PD-1/PD-L1, short-course radiotherapy

1 Introduction

Neoadjuvant chemoradiotherapy (NACRT) or short-course radiotherapy (SCRT) followed by total mesorectal excision plus adjuvant chemotherapy (ACT) was the standard treatment modality for locally advanced rectal cancer (LARC). Despite the improvement in local control with the standard treatment regimen, the rate of distant

metastasis (DM) is still as high as 35% (1). Additionally, chemoradiotherapy (CRT) plus total mesorectal excision surgery may result in the impairment of defecation, urinary and sexual function. Thus, perioperative treatment strategies are needed to be further developed to decrease surgical morbidity and improve quality of life in LARC patients.

Total neoadjuvant treatment (TNT), a new treatment strategy, shifts all or part of adjuvant chemotherapy to the preoperative phase in the setting of CRT, increases neoadjuvant chemotherapy cycles and prolongs surgical waiting time. The LARC patients who received TNT had better tumor regression and some of them underwent sphincter-preservation operation instead of abdominal pelvic resection (APR). More importantly, there is greater chance that the surgery can be avoided when LARC patients achieve clinical complete remission (cCR) after TNT (2) (Figure 1). Moreover, TNT also can contribute to solving the problem of insufficient adjuvant chemotherapy due to surgical complications and consequent poor compliance. It intensifies chemotherapy before total mesorectal excision in order to reduce the risk of DM. In recent years, the administration of immunotherapy combined with TNT or TNT-like treatment has become a hot research topic. As reported by Jing Jin et al, treatment guidelines in the China also recommend TNT as an option for LARC patients (3). Our team also performed a comprehensive meta-analysis to determine the roles of TNT in improving the pathologic complete response (pCR) and survival value compared with standard CRT among LARC patients (4). Major information of clinical trials with published data comparing TNT with standard CRT is summarized in Table 1 (5–12). In this review, we will discuss the evolution and progress of treatment regimens for LARC patients.

2 When should we select TNT strategy?

According to recent National Comprehensive Cancer Network (NCCN) rectal cancer guideline, risk classification was crucial in neoadjuvant treatment decisions for LARC patients. LARC patients were stratified into the low risk (T3Nany with clear circumferential resection margin (CRM) or T1-2N1-2) and high risk (T3Nany with involved or threatened CRM, T4Nany or locally unresectable or medically inoperable) groups based on 2021 NCCN guidelines (version 1) (13). For the high-risk group, patients are suggested strongly to perform TNT rather than NACRT, and the recommendation continues to date (14). Several TNT treatment regimens, including LCRT or SCRT followed by sequential chemotherapy and induction chemotherapy plus LCRT or SCRT, are available to high-risk LARC patients. RAPIDO trial, a phase 3 randomized controlled trial (RCT), with 3-year disease-related treatment failure as primary endpoint, enrolled high-risk LARC patients, such as cT4, cN2, extramural vascular invasion, involved mesorectal fascia, and enlarged lateral lymph nodes (12). The results showed that rate of disease-related treatment failure decreased significantly in TNT group compared with standard NACRT (Hazard Ratio (HR) = 0.75, 95% Confidence interval (CI): 0.60–0.95, p= .019). And there was also significant difference in distant metastasis-free survival (DMFS) (HR = 0.69, 95% CI: 0.54 to 0.90, p = .005) between TNT group and CRT group. However, no significant difference in overall survival (OS) was observed between the two groups (HR = 0.92, 95% CI: 0.67–1.25, p= .59). Exceptionally patients with lateral lymph node (LLN) metastasis may benefit from NACRT strategy although the difference was not statistically significant shown in the forest map. This suggested that, for patient with positive LLN, TNT treatment led to the protracted surgical waiting time or SCRT may also bring severe fibrosis than long course radiotherapy (LCRT), which ultimately had a negative impact on survival outcomes. Nevertheless, clinical practice guidelines from both Chinese Society of Clinical Oncology (CSCO) and European Society for Medical Oncology (ESMO) also recommend TNT as preferred treatment approach for high-risk LARC patients (15, 16).

For low-risk LARC patients, both standard NACRT and TNT were suggested by the 2021 NCCN guideline (version 1) (13). But in the 2022 NCCN guideline (version 3), TNT was preferred for low-risk LARC patients although standard NACRT is still a choice (14). The updates of treatment paradigm in recent NCCN guidelines for low-risk LARC patients were based on the results of several RCTs (7, 11). For example, PRODIGE23 trial, enrolled all LARC patients regardless of risk classification, showed higher 3-year disease-free survival (DFS) rate (HR = 0.69, 95% CI: 0.49–0.97, p= .034) and 3-year DMFS rate (HR = 0.64, 95% CI: 0.44–0.93, p= .017) in TNT arm compared with standard NACRT arm (7). The difference of 3-year OS between TNT and standard NACRT arms was not statistically significant (HR = 0.65, 95% CI: 0.40–1.05, p= .0773), most likely because the sample size was relatively small. Unfortunately, subgroup analysis of the PRODIGE23 study based on the tumor stage and risk classification hasn't been reported yet. Hence, it remained unclear whether low-risk LARC patients stood to benefit the most from TNT. Similarly, in another prospective and phase III STELLAR trial, patients with distal or middle-third, cT3-4 Nany rectal cancer were randomly assigned to SCRT plus four cycles of CAPOX (TNT-like arm) or standard NACRT arm (11). The results showed that TNT-like arm achieved a higher three-year OS rate compared to CRT arm (86.5% vs. 75.1%, p = .033). At 3 years, the cumulative probability of DFS was 64.5% in the TNT-like

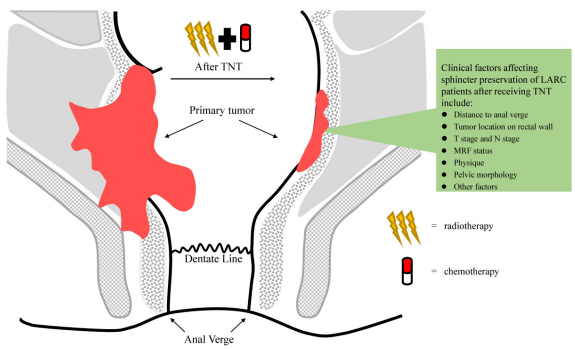

FIGURE 1
Tumor regression in patients with local advanced rectal cancer (LARC) receiving total neoadjuvant treatment (TNT).

TABLE 1 Randomized clinical trials comparing total neoadjuvant treatment (TNT) with standard chemotherapy treatment (CRT) in LARC.

Study	Author/ PI	Publication year	Study ID numbers	Phase	Sample size		Study design	Results
					TNT treatment	Standard treatment		
Maréchal/ 2011 (5)	Raphaël Maréchal et al.	2011	EudraCT: 2006-006646-34	Phase 2 RCT	28	29	mFOLFOX6 × 2 - CRT [5FU + 50.4 Gy] - TME	ypT0-1N0 rate: 32.1% vs. 34.5% (p= .85)
							vs.	pCR rate: 25% vs. 28% (p= .92)
							CRT [5FU + 50.4 Gy] - TME	
GCR-3 (6)	Carlos Fernandez-Martos et al.	2015	NA	Phase 2 RCT	56	52	Capeox × 4 - CRT [Capeox + 50.4 Gy] - TME	5-year DFS: 62% vs. 64% (p= .85)
							vs.	5-year OS:75% vs. 78% (p= .64)
							CRT [Capeox + 50.4 Gy] - TME - Capeox × 4	5-year cumulative LR: 5% vs. 2% (p= .61)
								5-year cumulative DM: 23% vs. 21% (p= .79)
PRODIGE 23 (7)	Thierry Conroy et al.	2021	NCT01804790	Phase 3 RCT	231	230	mFOLFIRINOX × 6 - CRT [50.4Gy/25F + Cape] - TME - mFOLFOX6 × 6/ Cape × 4	pCR: 28% vs. 12% (p<.0001)
			PRODIGE 23 - UCGI 23				vs.	3-year DFS: 76% vs. 69% (HR=0.69, 95% CI: 0.49-0.97; p= .034)
							CRT [50.4Gy/25F + Cape] – TME - mFOLFOX6 × 12/ Cape × 8	3-year OS: 91% vs. 88% (HR=0.65, 95% CI: 0.40-1.05; p= .0773)
								3-year MFS: 79% vs. 72% (HR=0.64, 95% CI: 0.44-0.93; p= .017)
POLISH II (8)	Krzysztof Bujko et al.	2016	NCT00833131	Phase 3 RCT	261	254	5 × 5Gy - FOLFOX4 × 3 -TME	pCR: 16% vs. 12% (p= .17)
			PGBRJG0109				vs.	Median OS: 89 months vs. 81 months
							CRT [5FU + LV + OXA + 50.4 Gy] - TME	8-year DFS: 43% vs. 41%
WAIT (9)	James Moore et al.	2017	ACTRN12611000339954	Phase 2 RCT	25	24	CRT [5FU + 50.4 Gy] -5FU + LV × 3 -TME	pCR rate: 16% vs. 25% (p= .49)
							vs.	cCR rate: 12% vs. 8.3% (p= 1.0)
							CRT [5FU + 50.4 Gy] - TME	

(Continued)

10.3389/fimmu.2023.1149122

TABLE 1 Continued

Study	Author/ PI	Publication year	Study ID numbers	Phase	Sample size		Study design	Results
					TNT treatment	Standard treatment		
KCSG CO 14-03 (10)	Ji Yeon Baek et al.	2018	NCT01952951	Phase 2 RCT	53	55	CRT [Cape/5FU + 50.4 Gy] -Capeox × 2 -TME	pCR: 13.6% vs.5.8% (p= .167)
			KCSG CO14-03				vs.	Downstage rate: 36.4% vs. 21.2% (p= .077)
							CRT [Cape/5FU + 50.4 Gy] - TME	MPR rate: 29.5% vs. 19.2% (p= .167) Mean NAR: 15.66 vs. 20.59 (mean difference= 4.93, 95% CI: 0.20-10.06; p= .06)
STELLAR (11)	Jing Jin et al.	2019	NCT02533271	Phase 3 RCT	302	297	5 × 5Gy - Capeox × 4 - TME ± Capeox × 2 vs CRT [Cape + 25 × 2Gy] - TME ± Capeox × 6	pCR+cCR: 21.8% vs. 12.3% (p= .002)
			XT2015-03				vs.	3-year DFS: 64.5% vs. 62.3% (HR=0.88, 95% CI: not applicable to 1.11; Noninferiority test p<.001)
			CH-GI-090				5 × 5Gy - Capeox × 4 - TME ± Capeox × 2 vs CRT [Cape + 25 × 2Gy] - TME ± Capeox × 6	3-year OS: 86.5% vs. 75.1% (HR=0.67, 95% CI: 0.46-0.97; p= .033)
								3-year MFS: 77.1% vs. 75.3% (HR=0.88, 95% CI: 0.63-1.24; p= .475)
RAPIDO (12)	Geke A P Hospers et al.	2020	NCT01558921	Phase 3 RCT	462	450	5 × 5Gy - Capeox × 6/FOLFOX4 × 9- TME	pCR: 28% vs. 14% (p<.0001)
			NL36315.042.11				vs.	3-year disease-related treatment failure: 23·7% vs. 30·4% (HR=0.75, 95%CI: 0.60-0.95; p= .019)
			2010-023957-12 (EudraCT Number)				CRT [Cape + 28×1.8Gy/25 × 2Gy] - TME - Capeox × 8/FOLFOX4 × 12	3-year OS: 89.1% vs. 88.8% (HR=0.82, 95% CI: 0.67-1.25; p= .59)
								3-year DM: 20.0% vs. 26.8% (HR=0.69, 95% CI: 0.54-0.90; p= .0048)

RCT, randomed clinical trial; CRT, chemoradiotherapy; TME, total mesorectal excision; mFOLFOX, modify oxaliplatin + leucovorin + 5-fluorouracil; Capeox, capecitabine + oxaliplatin; mFOLFIRINOX, modify oxaliplatin + irinotecan + calcium folinate + 5-fluorouracil; Cape, capecitabin; 5FU, 5-fluorouracil; AF, ; LV, leucovorin; OXA, oxaliplatin; FOLFOX, oxaliplatin + calcium folinate + 5-fluorouracil; cCR, clinical complete response; pCR, pathologic complete response; DFS, disease free survival; OS, overall survival; LR, local relapse; DM, distant metastases; MFS, distant metastasis-free survival; MPR, major pathological response; NAR, neoadjuvant rectal score; HR, Hazard Ratio.

arm compared with 62.3% in CRT arm (HR = 0.883), even though its design was a non-inferior study.

In a retrospective study presented at ASCO GI 2019, William Chapman et al. compared the clinical outcomes of SCRT in the setting of TNT (SC-TNT) to standard CRT for LARC patients (17). The results suggested that PROSPECT-eligible patients had better DFS in SC-TNT strategy compared with standard NACRT strategy although the difference was not statistically significant potentially due to the small sample size (17, 18). The randomized PSSR study, which enrolled low-risk LARC patients with negative magnetic resonance imaging (MRI)-predicted CRM, also compared direct surgery plus selective CRT with standard NACRT followed by surgery and adjuvant chemotherapy (19). Significant difference in the 3-year cumulative incidence of DFS between the upfront surgery group (81.1%, 95%CI: 77.3%-84.9%) and NACRT group (86.6%, 95%CI: 82.7%-90.5%) was reported at 2022 ASCO meeting (HR = 2.02, 95%CI: 1.01-4.06, p= .048). And the difference of rates for 3-year DFS was 5.4% (95%CI: 5.3%-5.6%), which failed to meet its predetermined criterial of noninferiority. It suggested that NACRT was essential even for low-risk LARC patients with negative MRI-predicted CRM. For LARC with uninvolved mesorectal fascia (MRF), neoadjuvant chemotherapy with CAPOX may be another effective treatment strategy as it yielded similar pCR (11.0% vs. 13.8%, p= .33) and downstaging rates (40.8% vs. 45.6%, p= .27) compared to NACRT in CONVERT trial (20). Another prospective, phase II/III randomized PROSPECT study, including any cT2 cN1 or cT3 cN1-2 rectal cancer patients, now is in progress to determine whether neoadjuvant chemotherapy (FOLFOX or CAPOX) could be used as an alternative to NACRT (18). It is urgent to identify the optimal treatment strategy for low-risk LARC patients.

Owing to special anatomical location and functions of rectum, the distance of the tumor from the anal verge is one of the key factors which should be considered when radiation oncologists choose neoadjuvant treatment options for patients. For the rectal cancer patients who desire a sphincter-preserving procedure, TNT strategy downstages tumor and increases cCR probability so that patients are more likely to have sphincter-preserving operation or even avoid surgery to receive watch and wait strategy. This treatment perspective was recommended by 2017 ESMO, 2020 American Society for Radiotherapy and Oncology (ASTRO) and CSCO rectal cancer guidelines (15, 21, 22). Therefore, TNT should be suggested for distal LARC patients, even those with early-stage tumors. PKUCH-R01 trial enrolled patients with mid-low cT2 or early cT3 rectal cancer to receive LCRT followed by 4 cycles of induction CAPOX (23). Of the 64 patients, cCR was achieved in 31 patients (48.4%) and 41 patients (64.1%) received sphincter-preserving surgery. We now are conducting a clinical trial (TESS study, NCT03840239) to determine the minimum number of cycles of chemotherapy in the setting of TNT that can increase the cCR rates of low rectal cancer (24). In the TESS study, patients with low LARC received 2 cycles of CAPOX performed before, during and after LCRT, followed by total mesorectal excision and 2 cycles of adjuvant chemotherapy. This trial has completed enrollment, and the results will be reported soon.

3 When should we choose SCRT or LCRT?

The option of neoadjuvant SCRT versus LCRT remains controversial for LARC patients. The differences between two radiation fractionation schemes can be compared under three main aspects as follows: local control rates, toxicity, and the impacts on tumor microenvironment (TME) when combined with immunotherapy.

There were three clinical trials (Polish I, TROG01.04 and Stockholm III) comparing the local recurrence of SCRT followed by immediate surgery with LCRT followed by surgery (25–27). And other three RCTs (Polish II, RAPIDO and STELLAR trials) focused mainly on the comparison of SCRT followed by chemotherapy and subsequent surgery with LCRT followed by surgery (8, 11, 12). In the six RCTs, the local recurrence rates were not significantly different between SCRT and LCRT groups although biologically effective dose (BED) value calculated according to a linear quadratic (LQ) model of SCRT is lower than LCRT. It is unclear whether the similar short-term outcomes between the two groups were related to the underestimated BED values of SCRT calculated by simple LQ model, or diversity of radiosensitivity of rectal tumor.

In terms of therapeutic toxicity, RAPIDO trial showed a higher incidence of acute gastrointestinal toxicity in the SCRT-TNT group compared to the NACRT group (28). Diarrhea was the most common adverse event in both groups. It may be mainly associated with severe intestinal edema caused by hypofractionated radiotherapy. In addition, both 6-months waiting times from the end of radiotherapy to surgery and hypofractionated radiotherapy can lead to intestinal fibrosis, which has an adverse impact on surgical procedures. Intraoperative blood loss was more in the short-course arm compared to the long-course arm (300ml vs 250ml, p= .007). The intact of mesorectal plain as assessed by surgeon were also worse in SCRT-TNT arm compared to NACRT arm (78% vs 85%, p= .032).

4 Prognostic value of PD-L1 in LARC after NACRT

Programmed cell death-ligand 1 (PD-L1) pathway mediates immune exhaustion and is a potent target for anticancer immunotherapy.

Lianzhou Yang et al. performed a meta-analysis and found PD-L1 overexpression was relevant to inferior tumor stage (OR= 0.57), vascular invasion-negativity (Odds Ratio (OR)= 0.75), shorter OS (HR= 1.47) and shorter recurrence-free survival (RFS)/DFS (HR= 1.47). But the expression of PD-L1 is not related to age, sex, tumor location, tumor differentiation, pathological T (pT) stage, pathological N (pN) stage, or microsatellite instability (MSI)/mismatch repair (MMR) status (29).

Peter G Alexander et al. focused on the prognostic value of PD-L1 in colorectal cancer receiving anti-PD-1 therapy and published a meta-analysis. They found that programmed cell death-1 (PD-1)

on immune cells (iPD-L1) was associated with favorable prognosis, but PD-L1 expression on tumour cells (tPD-L1) has inconsistent outcomes and failed to perform as a useful biomarker (30).

About LARC patients receiving NACRT, accumulating studies reported that PD-L1 expression and T-cell infiltration would increase after NACRT (31–33), however, the association of PD-L1 expression level with tumor response and survival outcomes of LARC after NACRT is not determined yet.

Hecht et al. studied 103 pre-RCT biopsies and 159 post-RCT surgical specimens, and found that low PD-L1 expression in cancer and immune cells (32). Still, both PD-L1 expression in pre-CRT samples and in the invasive front of post-CRT samples were independent positive prognostic markers for OS. Ogura A et al. studied immunostainings of PD-L1 and CD8 in 287 LARC patients (33). tPD-L1 and stromal iPD-L1 expression were evaluated before and after CRT in 287 patients. High iPD-L1 expression significantly increased from 31.7% before CRT to 49.2% after CRT and the increase of iPD-L1 expression was only observed in patients with tumor regression grades 1 and 2. High tCD8+ cell density before CRT was associated with better DFS, but its improved effect on DFS could be only observed in patients with high iPD-L1 expression. Hyungwoo Cho et al. evaluated dynamic changes of TME in patients enrolled in ADORE study and found that high delta values of CD3+ T cells and PD-L1+ lymphocytes after CRT were associated with good DFS, while that of CD4+FoxP3+ regulatory T cells was associated with poor DFS (34).

The above four studies include patients treated with NACRT, while translation study of Voltage clinical trial, which prospectively treated LARC patients with NACRT followed by 5 cycles of Nivolumab, showed that high PD-L1 expression is correlated with higher ratio of pCR (35).

On the contrary, Saigusa et al. reported immunohistochemistry analysis results in 90 LARC patients underwent NACRT (36). Patients with higher PD-L1 expression was significantly associated with more vascular invasion, poor RFS and poor OS. Infiltrating CD8+ T cells in patients with high PD-L1 expression were significantly less than in patients with low PD-L1 expression. Shao L et al. studied the 68 rectal cancer patients treated with neoadjuvant SCRT or standard NACRT and found that tPD-L1 expression is significantly correlated with poor local relapse-free survival (LRFS) (37). Lim YJ et al. performed a paired analysis using pre-CRT and post- CRT tumor tissues of 123 rectal cancer patients undergoing NACRT. Sustained higher expression of PD-L1 at pre- and post-CRT (high-to-high) was associated with less increase in the density of CD8+ tumor infiltrating lymphocytes (TILs) (38). Two subgroups with high baseline PD-L1 expression level, the high-to-low and high-to-high alterations, showed worse OS (HR=8.34 and 11.03, respectively), with the highest mortality risk observed in the high-to-high group. Hiroyuki Takahashi et al. reported study results of 109 NACRT-treated LARC cases (39). They revealed that membranous tPD-L1 was only associated with mismatch repair deficient (dMMR), but not other clinical characteristics. In contrast, iPD-L1 expression were significantly correlated with tumor vessel invasion, nuclear β-catenin-positive tumor budding cancer stem cell (CSC)-like features, and poorer OS.

What's more, Jomrich G et al. and Richter I et al. reported no PD-L1 expression was noticed rectal cancer tissue before and after NACRT, let alone its prognostic value (40).

In summary, whether PD-L1 expression has also a predictive value for LARC after NACRT is yet unclear. At least, we need to use standardized method to score its expression and use common thresholds enabling comparison between studies and further analysis.

Moying Li et al. summarized biomarkers and tumor models predicting response to NACRT in rectal cancer, which also include TME factors, cytokines and chemokines (41). Consistently, high intratumoral CD8+ and CD4+ lymphocyte infiltration exhibits better survival and better response to NACRT (31, 42–46). And the level of FOXP3+ Treg negatively correlates with responsiveness to NACRT (47, 48). In contrast, there are relatively few reports on the association of the proportion of tumour-associated macrophages (TAM), dentritic cells (DCs) or B cells in TME with tumor response to NACRT.

Liwen Qian et al. established a model based on 15 immune-related genes, which was associated with response to neoadjuvant CRT (49). The 15 immune-related genes were found to be enriched in inflammation pathways through the Gene Set Enrichment Analysis (GSEA). They also showed that CD4 naive T cells, T exhaustion (Tex) cells and T helper 1 (Th1) cells are significantly more while T follicular helper (Tfh) cells are significantly less in responder group than non-responder group.

In another research, patients with MSS tumors were separated into three groups: IG1, IG2 and IG3 (50). Interestingly, IG3 displays features of immunologically hot tumors (immune cell infiltration and elevated immune checkpoint expression) compared with IG1 and IG2. In addition, the study has demonstrated good response to NACRT and prolonged DFS in IG3. But due to the small sample size of IG3, the reproducibility of results remains to be further investigated.

5 Adding PD-1/PD-L1 checkpoint inhibitor

The interaction of immune and radiotherapy has been a major focus of research lately. Data on NACRT combined with PD-1 or PD-L1 inhibitors in mismatch repair proficient (pMMR)/microsatellite stable (MSS) rectal cancer patients has been gradually disclosed. A team from Cancer Hospital, Medical Center of Fudan University, led by Fan Xia, has already summarized the available data in detail (51). Detailed information of each trial combining NACRT with PD-1/PD-L1 antibodies for LARC is provided in Table 2 (35, 52–62).

Up to date, the NRG-GI002 trial is the only phase II RCT in which patients with LARC were randomized (1:1) to neoadjuvant FOLFOX for 4 months and then underwent chemoradiotherapy (capecitabine with 50.4 Gy) with or without intravenous pembrolizumab (60). Median neoadjuvant rectal scores (NAR) were 11.53 (95%CI: 8.5-14.6) and 14.08 (95% CI: 10.7-17.4) in the TNT arm and TNT combined with pembrolizumab arm,

TABLE 2 Clinical trials of neoadjuvant chemoradiotherapy combined with PD-1/PD-L1 antibodies for LARC.

Study	Author/PI	Initiation Year	Country	Study ID Numbers	Phase	Sample Size	Characteristics	Study Design	Duration of Neoadjuvant therapy (Weeks)	Results
Voltage-A (35)	Takayuki Yoshino et al.	2016	Japan	NCT02948348	Phase 2	39	cT3-4N0-2M0; 23% Stage III; MSS	CRT [50.4Gy + Cape] - Nivolumab × 5 - TME	17	pCR rate: 30% (11/37)
NSABP FR-2 (52)	Thomas J. George et al.	2018	American	NCT03102047	Phase 2	45	Stage II/III; MSS	CRT [n.i.] - Durvalumab × 4 - TME	14	mNAR: 12.03 (p= .06 one-sided) pCR rate: 22.2% cCR rate: 31.1% sphincter preservation rate: 71.4%
PANDORA (53)	Stefano Tamberi et al.	2020	Italy	NCT04083365	Phase 2	55	cT3-4cN+M0	CRT [Cape + 50.4Gy] - Durvalumab × 3 – TME	17	pCR rate: 32.7% (18/55)
Averectal (54)	Ali Shamseddine et al.	2018	Belgium	NCT03503630	Phase 2	44	stage II/III	5 × 5Gy - mFOLFOX × 6 + Ave × 6 - TME	13	pCR rate: 37.5% (15/40) MPR: 67.5% (27/40)
Wuhan (55)	Tao Zhang et al.	2019	China	NCT04231552	Phase 2	30	T3-4N0M0 or T1-4N+M0 (86.7% stage III)	5 × 5Gy - Capeox × 2 + Camrelizumab × 2 - TME	8	pCR rate (pMMR): 46.2% (12/26) pCR rate(dMMR): 100% (1/1)
AVANA (56)	Lisa Salvatore et al.	2019	Italy	NCT03854799	Phase 2	101	cT4/high risk cT3/cN+(93% stage III)	CRT [Cape + 50.4Gy] + Avelumab × 6 - TME	12	pCR rate: 23% (22/96) MPR: 61.5% (59/96)
R-IMMUNE (57)	Javier Carrasco et al.	2017	Belgium	NCT03127007	Phase 2	25	stage II/III (92% stage III)	CRT [5-FU + 50Gy] + Atezolizumab × 4 - TME	15	pCR rate: 24% (6/25)
Changhai hospital (58)	Wei Zhang et al.	2022	China	NCT05215379	Phase 2	23	T1-3aN0-1M0; pMMR/MSS; ultra-low	CRT [50Gy] + Sintilimab × 2 - Cape/Capeox × 6 + Sintilimab × 2 - TME	23	cCR rate: 43.5% (10/23) ncCR rate: 26.1% (6/23)

(Continued)

10.3389/fimmu.2023.1149122

TABLE 2 Continued

Study	Author/PI	Initiation Year	Country	Study ID Numbers	Phase	Sample Size	Characteristics	Study Design	Duration of Neoadjuvant therapy (Weeks)	Results
										sphincter preservation rate: 95.5% (21/22)
										CR (pCR + cCR) rate: 52.2% (pCR: 2/10; cCR: 10/23)
Beijing Friendship (59)	Zhongtao Zhang et al.	2022	China	NCT04911517	Phase 2	20	cT3N0M0; cT1-3N1-2M0; <= 10 cm from anal verge; pMMR/non-MSI-H	CRT [Cape + 50Gy] + Tislelizumab × 2 - Cape × 1 + Tislelizumab × 1 – TME	9	pCR rate: 58.7% (7/12)
										NAR: 7.18
NRG-GI002 (60, 61)	Thomas J. George et al.	2016	American	NCT02921256	Phase 2 RCT	Experimental arm: 90	distal location (<= 5 cm from anal verge, any N)/bulky (any cT4 or tumor within 3 mm of mesorectal fascia)/high risk for metastatic disease (cN2)/not a SSS candiate	Experimental arm: FOLFOX × 8 - CRT [Cape + 50.4Gy] + Pembrolizumab × 6 - TME vs FOLFOX × 8 - CRT [Cape + 50.4Gy] - TME	34	mNAR: 11.53 vs. 14.08 (p =.26)
										pCR rate: 31.9% (22/69) vs. 29.4% (20/68) (p= .75)
										cCR rate: 13.9% (11/79) vs. 13.6% (11/81) (p= .95)
						Control arm: 95		Control arm:FOLFOX × 8 - CRT [Cape + 50.4Gy] - TME vs FOLFOX × 8 - CRT [Cape + 50.4Gy] - TME		3-year DFS: 64% vs. 64% (HR=0.95, 95%CI= 0.58-1.55; p= .82)
										3-year OS: 95% vs. 87% (HR=0.35, 95%CI= 0.12-1.00; p= .04)
PKUCH-04 (62)	Zhongwu Li et al.	2020	China	NCT04340401	Phase 2	25	LARC (76% N2, 56% MRF+, 80% EMVI+); pMMR/MSS	Capeox × 3 + Camrelizumab × 3 - CRT [Cape + 50.4Gy] - Capeox × 2 - TME	20	pCR rate: 33.3% (7/21)
										cCR or ncCR rate: 16% (4/25)

RCT, randomed clinical trial; MRF, mesorectal fascia; EMVI, MRI-extramural vascular invasion; pMMR, mismatch repair-proficient; MSS, microsatellite stable; LARC, local advanced rectal cancer; MSI-H, microsatellite instability; SSS, sphincter-sparing surgery; CRT, chemoradiotherapy; TME, total mesorectal excision; mFOLFOX, modify oxaliplatin + leucovorin + 5-fluorouracil; Capeox, capecitabine + oxaliplatin; mFOLFIRINOX, modify oxaliplatin + irinotecan + calcium folinate + 5-fluorouracil; Cape, capecitabin; 5FU, 5-fluorouracil; LV, leucovorin; OXA, oxaliplatin; FOLFOX, oxaliplatin + calcium folinate + 5-fluorouracil; cCR, clinical complete response; pCR, pathologic complete response; DFS, disease free survival; OS, overall survival; MPR, major pathological response; NAR, neoadjuvant rectal score; HR, Hazard Ratio; n.i., no information.

10.3389/fimmu.2023.1149122

respectively (p= .26). But the results of other single-arm studies look very encouraging. Although most of patients with high-risk rectal cancer were enrolled in two phase II trials (Wuhan study and Averectal study) in the setting of SCRT with immunotherapy, the pCR rates still approximated 50% (54, 55). For another two LCRT-based studies (Changhai Hospital study and Beijing Friendship Hospital study) enrolled early-stage patients, the pCR rates were above 50% (58, 59).

In LARC, despite it is unclear whether PD-L1 promotes resistance to neoadjuvant chemoradiation, the progress resulting from clinical studies is still quite active, expecting for more data coming.

It seems better antitumor effects could be achieved in both SCRT and LCRT when in combination with immunotherapy. However, Basic questions have not been answered: what dose-fractionation pattern is best? It is necessary to understand the interactions of different radiation fractionation schemes with TME.

TME is composed of stromal cells, immune cells, and molecular components (extracellular matrix, cytokines, and chemokines). The cells in TME vary in radiosensitivity (63). Therefore, different fractionation schemes result in distinct immunological changes within the tumor microenvironment.

A previous review discussed the radiosensitivity of various cells in TME and the change of TME after different dose of irradiation in exquisite detail (64). Proliferating tumor cells is most radiosensitive than stromal cells. Low dose radiation (LDR) promotes apoptosis of tumor cells while high dose radiation (HDR) trigger necrosis, which is characterized by the loss of membrane integrity and the release of damage associated molecular patterns (DAMPs) that contribute to initiate immune responses (64, 65). Additionally, endothelial cell (EC) is resistant to doses up to 10 Gy. Therefore, EC can survival after LDR (<2 Gy). And daily irradiation with a 2 Gy dose can stimulate the process of angiogenesis and vascular permeability to improve tumor hypoxia. Intermediate dose radiation (IDR) can promote the delivery of chemotherapeutics to tumor cells by increasing vascular normalization in tumors, thereby improving the potent of the anti-tumor drug. On the contrary, HDR (>10 Gy) damages vascular EC to increases intratumoural hypoxia, and ultimately, renders cancer cells more resistant to radiotherapy. Within immune cells, DCs are the most radioresistant immune cells. HDR and IDR can trigger anti-tumor response by promoting antigen presentation and activation of DCs while LDR is unable to change the phenotype of DCs. LDR increase the amount of immune-suppressive cells and the production of cytokines, such as M2 macrophages, Myeloid-derived suppressor cells (MDSCs) and transforming growth factor-β (TGF-β) and a high dose of irradiation decreases these immunosuppressive cells and molecules. But high doses per fraction > 10 Gy promotes a hypoxic tumor microenvironment which in turn further aggravates immunosuppression.

Immune system plays a diverse role in different fractionation schemes. In the absent of immune system, 3×8 Gy yielded best tumor control among three different fractionation protocols with similar BED including a single dose of 16.4 Gy, 24 Gy in 3 fraction and 36 Gy in 2 fraction in animal experiments (66). When in immunocompetent murine tumor model, Radiotherapy, whatever the regimen used, improved the tumor-inhibitory effects. Among them, both 18×2 Gy and 3×8 Gy significantly delayed tumor growth. And the study also performed dynamic monitoring of various immune cell subclasses after different fractionation schemes. Conventional fractional radiotherapy (18×2 Gy) increased the number of immunosuppressive cells (such as Myeloid cells, MDSCs and TAM2), while the hypofractionated radiotherapy (1×16.4 Gy or 3×8 Gy) increase the number of immunostimulatory cells (CD8+ and CD4+ T cells). Low-dose radiation also activate anti-tumor immune response by triggering cGAS-STING pathway and type-I interferon pathway. And high-dose radiation promotes the activation and differentiation of T cells and the production of interferon gamma. The selection of immune checkpoint inhibitors is another critical factor to consider when given with different fractionation schemes. The combination of RT (3×8 Gy) and anti-TIGIT and anti-PD-L1 achieve the better CR rate (9/10) compared with all other treatment groups, and the 18×2 Gy is also effective in combination with anti-PD-L1 (CR rate: 8/12).

Tumors with an abundance of infiltrating T-cells appear to be most likely to respond to immune checkpoint inhibitors (ICIs), whereas tumors with an abundance of immunosuppressive myeloid cells and few infiltrating T-cells fail to exhibit a durable response (67). It is necessary to choose optimal fractionation schemes to remodel the TME and enhance efficacy of ICIs. Jessica et al. proposed that different immunotherapeutic strategies should be adopted against different consensus molecular subtypes (CMS) (68). Among all phase III trials for cancer, 78 (3%) investigate a combination of radiotherapy with immunotherapy in one study conducted in 2020. Immunotherapy drugs includes checkpoint inhibitors, cytokines, cell therapy, vaccines, and other targeted immune drugs. These results suggested that with the increasing number of cancer treatment approaches, we need to select the optimal combination of radiation fractionation schemes and immunotherapeutic agent based on the characteristics of tumor. Additional studies are needed to investigate which patients are suitable for SCRT or LCRT.

6 Summary

In summary, TNT has become the standard of care for neoadjuvant treatment of rectal cancer, replacing conventional CRT. It can achieve more cCR and reduce the risk of distant metastasis of high-risk patients. The standing role of TNT in high-risk LARC patients has already been established and gained popular usage in clinic. While the value of TNT in low-risk LARC patients is also been praised even though evidence is still accumulating, future studies are still important to gain more evidence on the possible benefits of TNT in low-risk patients. With the discovery of immune activating responses after radiotherapy, there is growing interest in combining NACRT with immune checkpoints to enhance treatment response. Total dose, fractionation, dose distribution and timing of radiotherapy are key variables in determining the effects of radiotherapy on the immune system. In the era of immunotherapy, radiotherapy plays a greater role in clinical treatment of rectal cancer. we are confident that RT combined with immunotherapy will shift the paradigm of treatment strategy of some pMMR/MSS LARC patients.

Author contributions

GC and WX selected the topic. WX and HL reviewed all published articles and posters, and wrote the manuscript. YY and YW provided some revising suggestions on the Discussion section. YY, SL, and RS revised the manuscript. All authors contributed to the article and approved the submitted version.

Funding

The study was supported by the CSCO Cancer Research Foundation (CSCO-Y-XD202001-0144).

Conflict of interest

The authors declare that the research was conducted in the absence of any commercial or financial relationships that could be construed as a potential conflict of interest.

Publisher's note

All claims expressed in this article are solely those of the authors and do not necessarily represent those of their affiliated organizations, or those of the publisher, the editors and the reviewers. Any product that may be evaluated in this article, or claim that may be made by its manufacturer, is not guaranteed or endorsed by the publisher.

References

1. Breugom AJ, Swets M, Bosset J-F, Collette L, Sainato A, Cionini L, et al. Adjuvant chemotherapy after preoperative (chemo)radiotherapy and surgery for patients with rectal cancer: a systematic review and meta-analysis of individual patient data. *Lancet Oncol* (2015) 16:200–7. doi: 10.1016/S1470-2045(14)71199-4

2. Benson AB, Venook AP, Al-Hawary MM, Cederquist L, Chen Y-J, Ciombor KK, et al. Rectal cancer, version 2.2018, NCCN clinical practice guidelines in oncology. *J Natl Compr Canc Netw* (2018) 16:874–901. doi: 10.6004/jnccn.2018.0061

3. Liu S, Jin J. Radiotherapy guidelines for rectal cancer in China (2020 edition). *Prec Radiat Oncol* (2022) 6:4–31. doi: 10.1002/pro6.1141

4. Liu S, Jiang T, Xiao L, Yang S, Liu Q, Gao Y, et al. Total neoadjuvant therapy (TNT) versus standard neoadjuvant chemoradiotherapy for locally advanced rectal cancer: A systematic review and meta-analysis. *Oncologist* (2021) 26:e1555–66. doi: 10.1002/onco.13824

5. Maréchal R, Vos B, Polus M, Delaunoit T, Peeters M, Demetter P, et al. Short course chemotherapy followed by concomitant chemoradiotherapy and surgery in locally advanced rectal cancer: a randomized multicentric phase II study. *Ann Oncol* (2012) 23:1525–30. doi: 10.1093/annonc/mdr473

6. Fernandez-Martos C, Garcia-Albeniz X, Pericay C, Maurel J, Aparicio J, Montagut C, et al. Chemoradiation, surgery and adjuvant chemotherapy versus induction chemotherapy followed by chemoradiation and surgery: long-term results of the Spanish GCR-3 phase II randomized trial†. *Ann Oncol* (2015) 26:1722–8. doi: 10.1093/annonc/mdv223

7. Conroy T, Bosset J-F, Etienne P-L, Rio E, François É, Mesgouez-Nebout N, et al. Neoadjuvant chemotherapy with FOLFIRINOX and preoperative chemoradiotherapy for patients with locally advanced rectal cancer (UNICANCER-PRODIGE 23): a multicentre, randomised, open-label, phase 3 trial. *Lancet Oncol* (2021) 22:702–15. doi: 10.1016/S1470-2045(21)00079-6

8. Ciseł B, Pietrzak L, Michalski W, Wyrwicz L, Rutkowski A, Kosakowska E, et al. Long-course preoperative chemoradiation versus 5 × 5 gy and consolidation chemotherapy for clinical T4 and fixed clinical T3 rectal cancer: long-term results of the randomized polish II study. *Ann Oncol* (2019) 30:1298–303. doi: 10.1093/annonc/mdz186

9. Moore J, Price T, Carruthers S, Selva-Nayagam S, Luck A, Thomas M, et al. Prospective randomized trial of neoadjuvant chemotherapy during the "wait period" following preoperative chemoradiotherapy for rectal cancer: results of the WAIT trial. *Colorectal Dis* (2017) 19:973–9. doi: 10.1111/codi.13724

10. Kim SY, Joo J, Kim TW, Hong YS, Kim JE, Hwang IG, et al. A randomized phase 2 trial of consolidation chemotherapy after preoperative chemoradiation therapy versus chemoradiation therapy alone for locally advanced rectal cancer: KCSG CO 14-03. *Int J Radiat Oncol Biol Phys* (2018) 101:889–99. doi: 10.1016/j.ijrobp.2018.04.013

11. Jin J, Tang Y, Hu C, Jiang L-M, Jiang J, Li N, et al. Multicenter, randomized, phase III trial of short-term radiotherapy plus chemotherapy versus long-term chemoradiotherapy in locally advanced rectal cancer (STELLAR). *J Clin Oncol* (2022) 40:1681–92. doi: 10.1200/JCO.21.01667

12. Bahadoer RR, Dijkstra EA, van Etten B, Marijnen CAM, Putter H, Kranenbarg EM-K, et al. Short-course radiotherapy followed by chemotherapy before total mesorectal excision (TME) versus preoperative chemoradiotherapy, TME, and optional adjuvant chemotherapy in locally advanced rectal cancer (RAPIDO): a randomised, open-label, phase 3 trial. *Lancet Oncol* (2021) 22:29–42. doi: 10.1016/S1470-2045(20)30555-6

13. Benson AB, Venook AP, Al-Hawary MM, Arain MA, Chen Y-J, Ciombor KK, et al. *Rectal cancer, version 1.2021, NCCN clinical practice guidelines in oncology* (2020). Available at: https://www.NCCN.org.

14. Benson AB, Venook AP, Al-Hawary MM, Azad N, Chen Y-J, Ciombor KK, et al. *Rectal cancer, version 3.2022, NCCN clinical practice guidelines in oncology* (2022). Available at: https://www.NCCN.org.

15. Yuan Z, Weng S, Ye C, Hu H, Zhang S, Yuan Y. CSCO guidelines for colorectal cancer version 2022: Updates and discussions. *Chin J Cancer Res* (2022) 34:67–70. doi: 10.21147/j.issn.1000-9604.2022.02.01

16. Glynne-Jones R, Wyrwicz L, Tiret E, Brown G, Rödel C, Cervantes A, et al. Rectal cancer: ESMO clinical practice guidelines for diagnosis, treatment and follow-up. *Ann Oncol* (2018) 29:iv263. doi: 10.1093/annonc/mdy161

17. Chapman W, Kim H, Bauer P, Makhdoom B, Trikalinos N, Pedersen K, et al. Total neoadjuvant therapy with short course radiation compared to concurrent chemoradiation in rectal cancer. *JCO* (2019) 37:486–6. doi: 10.1200/JCO.2019.37.4_suppl.486

18. Schrag D, Weiser M, Saltz L, Mamon H, Gollub M, Basch E, et al. Challenges and solutions in the design and execution of the PROSPECT phase II/III neoadjuvant rectal cancer trial (NCCTG N1048/Alliance). *Clin Trials* (2019) 16:165–75. doi: 10.1177/1740774518824539

19. Ding K-F, Li J, Hu Y, Liu C, Wang Z, Wang L-H, et al. Primary surgery followed by selective radiochemotherapy versus conventional preoperative radiochemotherapy for patients with locally advanced rectal cancer with MRI-negative circumferential margin (PSSR): A multicenter, randomized, open-label, noninferiority, phase 3 trial. *JCO* (2022) 40:3515–5. doi: 10.1200/JCO.2022.40.16_suppl.3515

20. Mei W-J, Wang X-Z, Li Y-F, Sun Y-M, Yang C-K, Lin J-Z, et al. Neoadjuvant chemotherapy with CAPOX versus chemoradiation for locally advanced rectal cancer with uninvolved mesorectal fascia (CONVERT): Initial results of a phase III trial. *Ann Surg* (2022) 227:557–64. doi: 10.1097/SLA.0000000000005780

21. Glynne-Jones R, Wyrwicz L, Tiret E, Brown G, Rödel C, Cervantes A, et al. Rectal cancer: ESMO clinical practice guidelines for diagnosis, treatment and follow-up. *Ann Oncol* (2017) 28:iv22–40. doi: 10.1093/annonc/mdx224

22. Wo JY, Anker CJ, Ashman JB, Bhadkamkar NA, Bradfield L, Chang DT, et al. Radiation therapy for rectal cancer: Executive summary of an ASTRO clinical practice guideline. *Pract Radiat Oncol* (2021) 11:13–25. doi: 10.1016/j.prro.2020.08.004

23. Wang L, Zhang X-Y, Zhao Y-M, Li S-J, Li Z-W, Sun Y-S, et al. Intentional watch & wait or organ preservation surgery following neoadjuvant chemoradiotherapy plus consolidation CAPEOX for MRI-defined low-risk rectal cancer: Findings from a prospective phase 2 trial (PKUCH-R01 trial, NCT02860234). *Ann Surg* (2022) 277:647–54. doi: 10.1097/SLA.0000000000005507

24. Xiao W, Wu X, Cai P, Zhuang Y, Wang X, Bai S, et al. Total neoadjuvant treatment versus standard chemoradiation to increase the sphincter preservation rate for distal locally advanced rectal cancer (TESS). *JCO* (2021) 39:TPS3615–TPS3615. doi: 10.1200/JCO.2021.39.15_suppl.TPS3615

25. Bujko K, Nowacki MP, Nasierowska-Guttmejer A, Michalski W, Bebenek M, Kryj M. Long-term results of a randomized trial comparing preoperative short-course radiotherapy with preoperative conventionally fractionated chemoradiation for rectal cancer. *Br J Surg* (2006) 93:1215–23. doi: 10.1002/bjs.5506

26. Ngan SY, Burmeister B, Fisher RJ, Solomon M, Goldstein D, Joseph D, et al. Randomized trial of short-course radiotherapy versus long-course chemoradiation comparing rates of local recurrence in patients with T3 rectal cancer: Trans-Tasman radiation oncology group trial 01.04. *J Clin Oncol* (2012) 30:3827–33. doi: 10.1200/JCO.2012.42.9597

27. Erlandsson J, Holm T, Pettersson D, Berglund Å, Cedermark B, Radu C, et al. Optimal fractionation of preoperative radiotherapy and timing to surgery for rectal

cancer (Stockholm III): a multicentre, randomised, non-blinded, phase 3, non-inferiority trial. *Lancet Oncol* (2017) 18:336–46. doi: 10.1016/S1470-2045(17)30086-4

28. van der Valk MJM, Marijnen CAM, van Etten B, Dijkstra EA, Hilling DE, Kranenbarg EM-K, et al. Compliance and tolerability of short-course radiotherapy followed by preoperative chemotherapy and surgery for high-risk rectal cancer - results of the international randomized RAPIDO-trial. *Radiother Oncol* (2020) 147:75–83. doi: 10.1016/j.radonc.2020.03.011

29. Yang L, Xue R, Pan C. Prognostic and clinicopathological value of PD-L1 in colorectal cancer: a systematic review and meta-analysis. *Onco Targets Ther* (2019) 12:3671–82. doi: 10.2147/OTT.S190168

30. Alexander PG, McMillan DC, Park JH. A meta-analysis of CD274 (PD-L1) assessment and prognosis in colorectal cancer and its role in predicting response to anti-PD-1 therapy. *Crit Rev Oncol Hematol* (2021) 157:103147. doi: 10.1016/j.critrevonc.2020.103147

31. Teng F, Meng X, Kong L, Mu D, Zhu H, Liu S, et al. Tumor-infiltrating lymphocytes, forkhead box P3, programmed death ligand-1, and cytotoxic T lymphocyte-associated antigen-4 expressions before and after neoadjuvant chemoradiation in rectal cancer. *Transl Res* (2015) 166:721–732.e1. doi: 10.1016/j.trsl.2015.06.019

32. Hecht M, Büttner-Herold M, Erlenbach-Wünsch K, Haderlein M, Croner R, Grützmann R, et al. PD-L1 is upregulated by radiochemotherapy in rectal adenocarcinoma patients and associated with a favourable prognosis. *Eur J Cancer* (2016) 65:52–60. doi: 10.1016/j.ejca.2016.06.015

33. Ogura A, Akiyoshi T, Yamamoto N, Kawachi H, Ishikawa Y, Mori S, et al. Pattern of programmed cell death-ligand 1 expression and CD8-positive T-cell infiltration before and after chemoradiotherapy in rectal cancer. *Eur J Cancer* (2018) 91:11–20. doi: 10.1016/j.ejca.2017.12.005

34. Cho H, Kim JE, Hong YS, Kim SY, Kim J, Ryu Y-M, et al. Comprehensive evaluation of the tumor immune microenvironment and its dynamic changes in patients with locally advanced rectal cancer treated with preoperative chemoradiotherapy: From the phase II ADORE study. *Oncoimmunology* (2022) 11:2148374. doi: 10.1080/2162402X.2022.2148374

35. Bando H, Tsukada Y, Inamori K, Togashi Y, Koyama S, Kotani D, et al. Preoperative chemoradiotherapy plus nivolumab before surgery in patients with microsatellite stable and microsatellite instability-high locally advanced rectal cancer. *Clin Cancer Res* (2022) 28:1136–46. doi: 10.1158/1078-0432.CCR-21-3213

36. Saigusa S, Toiyama Y, Tanaka K, Inoue Y, Mori K, Ide S, et al. Implication of programmed cell death ligand 1 expression in tumor recurrence and prognosis in rectal cancer with neoadjuvant chemoradiotherapy. *Int J Clin Oncol* (2016) 21:946–52. doi: 10.1007/s10147-016-0962-4

37. Shao L, Peng Q, Du K, He J, Dong Y, Lin X, et al. Tumor cell PD-L1 predicts poor local control for rectal cancer patients following neoadjuvant radiotherapy. *Cancer Manag Res* (2017) 9:249–58. doi: 10.2147/CMAR.S139889

38. Lim YJ, Koh J, Kim S, Jeon S-R, Chie EK, Kim K, et al. Chemoradiation-induced alteration of programmed death-ligand 1 and CD8(+) tumor-infiltrating lymphocytes identified patients with poor prognosis in rectal cancer: A matched comparison analysis. *Int J Radiat Oncol Biol Phys* (2017) 99:1216–24. doi: 10.1016/j.ijrobp.2017.07.004

39. Takahashi H, Watanabe H, Hashimura M, Matsumoto T, Yokoi A, Nakagawa M, et al. A combination of stromal PD-L1 and tumoral nuclear β-catenin expression as an indicator of colorectal carcinoma progression and resistance to chemoradiotherapy in locally advanced rectal carcinoma. *J Pathol Clin Res* (2022) 8:458–69. doi: 10.1002/cjp2.285

40. Jomrich G, Silberhumer GR, Marian B, Beer A, Müllauer L. Programmed death-ligand 1 expression in rectal cancer. *Eur Surg* (2016) 48:352–6. doi: 10.1007/s10353-016-0447-8

41. Li M, Xiao Q, Venkatachalam N, Hofheinz R-D, Veldwijk MR, Herskind C, et al. Predicting response to neoadjuvant chemoradiotherapy in rectal cancer: from biomarkers to tumor models. *Ther Adv Med Oncol* (2022) 14:17588359221077972. doi: 10.1177/17588359221077972

42. Kamran SC, Lennerz JK, Margolis CA, Liu D, Reardon B, Wankowicz SA, et al. Integrative molecular characterization of resistance to neoadjuvant chemoradiation in rectal cancer. *Clin Cancer Res* (2019) 25:5561–71. doi: 10.1158/1078-0432.CCR-19-0908

43. Matsutani S, Shibutani M, Maeda K, Nagahara H, Fukuoka T, Nakao S, et al. Significance of tumor-infiltrating lymphocytes before and after neoadjuvant therapy for rectal cancer. *Cancer Sci* (2018) 109:966–79. doi: 10.1111/cas.13542

44. Yasuda K, Nirei T, Sunami E, Nagawa H, Kitayama J. Density of CD4(+) and CD8(+) T lymphocytes in biopsy samples can be a predictor of pathological response to chemoradiotherapy (CRT) for rectal cancer. *Radiat Oncol* (2011) 6:49. doi: 10.1186/1748-717X-6-49

45. Akiyoshi T, Gotoh O, Tanaka N, Kiyotani K, Yamamoto N, Ueno M, et al. T-Cell complexity and density are associated with sensitivity to neoadjuvant chemoradiotherapy in patients with rectal cancer. *Cancer Immunol Immunother* (2021) 70:509–18. doi: 10.1007/s00262-020-02705-6

46. Shinto E, Hase K, Hashiguchi Y, Sekizawa A, Ueno H, Shikina A, et al. CD8+ and FOXP3+ tumor-infiltrating T cells before and after chemoradiotherapy for rectal cancer. *Ann Surg Oncol* (2014) 21(Suppl 3):S414–421. doi: 10.1245/s10434-014-3584-y

47. McCoy MJ, Hemmings C, Miller TJ, Austin SJ, Bulsara MK, Zeps N, et al. Low stromal Foxp3+ regulatory T-cell density is associated with complete response to neoadjuvant chemoradiotherapy in rectal cancer. *Br J Cancer* (2015) 113:1677–86. doi: 10.1038/bjc.2015.427

48. Zhang S, Bai W, Tong X, Bu P, Xu J, Xi Y. Correlation between tumor microenvironment-associated factors and the efficacy and prognosis of neoadjuvant therapy for rectal cancer. *Oncol Lett* (2019) 17:1062–70. doi: 10.3892/ol.2018.9682

49. Qian L, Lai X, Gu B, Sun X. An immune-related gene signature for predicting neoadjuvant chemoradiotherapy efficacy in rectal carcinoma. *Front Immunol* (2022) 13:784479. doi: 10.3389/fimmu.2022.784479

50. Chatila WK, Kim JK, Walch H, Marco MR, Chen C-T, Wu F, et al. Genomic and transcriptomic determinants of response to neoadjuvant therapy in rectal cancer. *Nat Med* (2022) 28:1646–55. doi: 10.1038/s41591-022-01930-z

51. Wang Y, Shen L, Wan J, Zhang H, Wu R, Wang J, et al. Neoadjuvant chemoradiotherapy combined with immunotherapy for locally advanced rectal cancer: A new era for anal preservation. *Front Immunol* (2022) 13:1067036. doi: 10.3389/fimmu.2022.1067036

52. George TJ, Yothers G, Lee JJ, Jacobs SA, Deutsch M, Allegra CJ, et al. NSABP FR-2: Phase II study of durvalumab following neoadjuvant chemoRT in stage II-IV rectal cancer. *JCO* (2019) 37:TPS727–7. doi: 10.1200/JCO.2019.37.4_suppl.TPS727

53. Tamberi S, Grassi E, Corbelli J, Papiani G, Barbera Ma, Zingaretti C, et al. A phase II study of capecitabine plus concomitant radiation therapy followed by durvalumab (MEDI4736) as preoperative treatment in rectal cancer: PANDORA study first-stage. *JCO* (2021) 39:3607–7. doi: 10.1200/JCO.2021.39.15_suppl.3607

54. Shamseddine A, Zeidan YH, El Husseini Z, Kreidieh M, Al Darazi M, Turfa R, et al. Efficacy and safety-in analysis of short-course radiation followed by mFOLFOX-6 plus avelumab for locally advanced rectal adenocarcinoma. *Radiat Oncol* (2020) 15:233. doi: 10.1186/s13014-020-01673-6

55. Lin Z, Cai M, Zhang P, Li G, Liu T, Li X, et al. Single-arm trial of preoperative short-course radiotherapy followed by chemotherapy and camrelizumab in locally advanced rectal cancer. *J Immunother Cancer* (2021) 9:e003554. doi: 10.1136/jitc-2021-003554

56. Salvatore L, Bensi M, Corallo S, Bergamo F, Pellegrini I, Rasola C, et al. Phase II study of preoperative (PREOP) chemoradiotherapy (CTRT) plus avelumab (AVE) in patients (PTS) with locally advanced rectal cancer (LARC): The AVANA study. *JCO* (2021) 39:3511–1. doi: 10.1200/JCO.2021.39.15_suppl.3511

57. Carrasco J, Schröder D, Sinapi I, Cuyper A, Beniuga G, Delmarcelle S. A phase II study of capecitabine plus concomitant radiation therapy followed by durvalumab (MEDI4736) as preoperative treatment in rectal cancer: PANDORA study final results. (2021) 32:S530–85. doi: 10.1016/annonc/annonc698

58. Zhou L, Yu G, Shen Y, Ding H, Zheng K, Wen R, et al. The clinical efficacy and safety of neoadjuvant chemoradiation therapy with immunotherapy for the organ preservation of ultra low rectal cancer: A single arm and open label exploratory study. *JCO* (2022) 40:e15603–3. doi: 10.1200/JCO.2022.40.16_suppl.e15603

59. Yao H, Yang Z, Gao J, Zhang X, Wu G, Wei D, et al. Safety and efficacy evaluation of long course neoadjuvant chemoradiotherapy plus tislelizumab followed by total mesorectal excision for locally advanced rectal cancer: Short-term results of a multicenter, phase II study. *JCO* (2022) 40:e15599–9. doi: 10.1200/JCO.2022.40.16_suppl.e15599

60. George TJ, Yothers G, Hong TS, Russell MM, You YN, Parker W, et al. NRG-GI002: A phase II clinical trial platform using total neoadjuvant therapy (TNT) in locally advanced rectal cancer (LARC)–first experimental arm (EA) initial results. *Chicago* (2019) 37:3505. doi: 10.1200/JCO.2019.37.15_suppl.3505

61. George TJ, Yothers G, Rahma OE, Hong TS, Russell MM, You YN, et al. Long-term results from NRG-GI002: A phase II clinical trial platform using total neoadjuvant therapy (TNT) in locally advanced rectal cancer (LARC). *San Francisco* (2023) 41:7. doi: 10.1200/JCO.2023.41.4_suppl.7

62. Wu A, Li Y, Ji D, Zhang L, Zhang X, Cai Y, et al. PKUCH 04 trial: Total neoadjuvant chemoradiation combined with neoadjuvant PD-1 blockade for pMMR/MSS locally advanced middle to low rectal cancer. *JCO* (2022) 40:3609–9. doi: 10.1200/JCO.2022.40.16_suppl.3609

63. Jarosz-Biej M, Smolarczyk R, Cichoń T, Kułach N. Tumor microenvironment as a "Game changer" in cancer radiotherapy. *Int J Mol Sci* (2019) 20:3212. doi: 10.3390/ijms20133212

64. Hellevik T, Martinez-Zubiaurre I. Radiotherapy and the tumor stroma: the importance of dose and fractionation. *Front Oncol* (2014) 4:1. doi: 10.3389/fonc.2014.00001

65. Rückert M, Deloch L, Fietkau R, Frey B, Hecht M, Gaipl US. Immune modulatory effects of radiotherapy as basis for well-reasoned radioimmunotherapies. *Strahlenther Onkol* (2018) 194:509–19. doi: 10.1007/s00066-018-1287-1

66. Grapin M, Richard C, Limagne E, Boidot R, Morgand V, Bertaut A, et al. Optimized fractionated radiotherapy with anti-PD-L1 and anti-TIGIT: a promising new combination. *J Immunother Cancer* (2019) 7:160. doi: 10.1186/s40425-019-0634-9

67. Colton M, Cheadle EJ, Honeychurch J, Illidge TM. Reprogramming the tumour microenvironment by radiotherapy: implications for radiotherapy and immunotherapy combinations. *Radiat Oncol* (2020) 15:254. doi: 10.1186/s13014-020-01678-1

68. Roelands J, Kuppen PJK, Vermeulen L, Maccalli C, Decock J, Wang E, et al. Immunogenomic classification of colorectal cancer and therapeutic implications. *Int J Mol Sci* (2017) 18:2229. doi: 10.3390/ijms18102229

frontiers | Frontiers in Oncology

TYPE Original Research
PUBLISHED 14 April 2023
DOI 10.3389/fonc.2023.1068592

Check for updates

OPEN ACCESS

EDITED BY
Jian Zhang,
Southern Medical University, China

REVIEWED BY
Mattia Falchetto Osti,
Sapienza University of Rome, Italy
Yang-Gun Suh,
National Cancer Center, Republic of Korea

*CORRESPONDENCE
Meng Xu
641704010@qq.com
Linbo Cai
13503030491@163.com

†These authors have contributed equally to this work and share last authorship

SPECIALTY SECTION
This article was submitted to Cancer Immunity and Immunotherapy, a section of the journal Frontiers in Oncology

RECEIVED 13 October 2022
ACCEPTED 29 March 2023
PUBLISHED 14 April 2023

CITATION
Bashir S, Wen L, Zhang P, Ye M, Li Y, Hong W, Zhen J, Lai M, Wang H, Yang Y, Chen X, Luo R, Jia G, Guo Y, Cai L and Xu M (2023) Efficacy and safety of combined immunotherapy and stereotactic radiosurgery in NSCLCBM patients and a novel prognostic nomogram: A real-world study.
Front. Oncol. 13:1068592.
doi: 10.3389/fonc.2023.1068592

COPYRIGHT
© 2023 Bashir, Wen, Zhang, Ye, Li, Hong, Zhen, Lai, Wang, Yang, Chen, Luo, Jia, Guo, Cai and Xu. This is an open-access article distributed under the terms of the Creative Commons Attribution License (CC BY). The use, distribution or reproduction in other forums is permitted, provided the original author(s) and the copyright owner(s) are credited and that the original publication in this journal is cited, in accordance with accepted academic practice. No use, distribution or reproduction is permitted which does not comply with these terms.

Efficacy and safety of combined immunotherapy and stereotactic radiosurgery in NSCLCBM patients and a novel prognostic nomogram: A real-world study

Shoaib Bashir[1], Lei Wen[2], Ping Zhang[2], Minting Ye[2], Yin Li[1], Weiping Hong[2], Junjie Zhen[2], Mingyao Lai[2], Hui Wang[2], Yanying Yang[2], Xingrui Chen[2], Rishun Luo[2], Guoxia Jia[1], Yao Guo[1], Linbo Cai[2*†] and Meng Xu[1*†]

[1]Oncology Department, First Affiliated Hospital of Jinan University, Guangzhou, China, [2]Oncology Department, Guangdong Sanjiu Brain Hospital, Guangzhou, China

Objective: To explore the effectiveness of combined immunotherapy (IT) and stereotactic radiosurgery (SRS) and address the gap between evidence-based clinical practice and academic knowledge of optimal timing of IT relative to SRS. In addition, to meet the unmet need for an up-to-date prognostic assessment model in the era of IT.

Methods: The data of 86 non-small cell lung cancer brain metastasis (NSCLCBM) patients treated with SRS to 268 brain metastases (BMs) were retrospectively extracted from our hospital database. The Kaplan–Meier analysis was employed for overall survival (OS) and a log-rank test for comparison between groups. Cox proportional hazards regression models were used to identify the significant prognostic factors. The prognostic nomogram was established utilizing the rms package of R software.

Results: IT was found to be associated with improved OS (from BM diagnosis: HR 0.363, 95% CI 0.199 - 0.661, $P < 0.001$; from SRS: HR 0.472, 95% CI 0.260 - 0.857, $P = 0.014$). Individuals who received IT in combination with SRS had better OS than those who didn't (from the day of BM diagnosis: 16.8 vs. 8.4 months, $P = 0.006$; from the day of SRS: 12 vs. 7 months, $P = 0.037$). Peri-SRS timing of IT administration was a significant prognostic factor for OS (from BM diagnosis: HR 0.132, 95% CI 0.034 - 0.517, $P = 0.004$; from SRS: HR 0.14, 95% CI 0.044 - 0.450, $P = 0.001$). Initiating IT after SRS led to superior OS than concurrent or before (from BM diagnosis: 26.5 vs. 14.1 vs. 7.1 months; from SRS: 21.4 vs. 9.9 vs. 4.1 months, respectively). Additionally, we build a nomogram incorporating IT, cumulative intracranial tumor volume (CITV), and recursive partitioning analysis (RPA), demonstrating a remarkable prognosis prediction performance for SRS-treated NSCLCBM patients.

Conclusion: Peri-SRS IT is a promising approach in treating NSCLCBM, as improved OS was observed without significantly increasing adverse events. Receipt of IT post-SRS was associated with superior OS than those who received IT concurrently or before. Incorporating IT and CITV into the RPA index could augment its prognosis assessment value for SRS-treated NSCLCBM patients, predominantly in the wild-type.

KEYWORDS

non-small cell lung cancer, brain metastases, stereotactic radiosurgery, immunotherapy, prognostic nomogram

Introduction

Lung cancer is one of the most devastating illnesses, responsible for most cancer-related deaths. It is divided into small cell lung cancer (SCLC) and non-small cell lung cancer (NSCLC) based on histology; the latter accounts for 85% of all lung cancer cases (1). Lung cancer patients often develop brain metastases (BMs). BMs are roughly ten times more prevalent than their primary counterpart (2), and lung cancer accounts for the majority of cases of BMs (3). The incidence of BMs at the time of initial lung cancer diagnosis is over 25% and 20% within a year of primary tumor diagnosis (4, 5). BMs are associated with poor prognosis and are considered challenging to treat because of their unique blood-brain barrier (BBB) (6), making local therapy such as radiation therapy and surgery upfront choices for treating BMs. Per the current guidelines, surgery should be offered to the population with large tumors with mass effect, and stereotactic radiosurgery (SRS) alone is recommended in patients with limited brain metastases (7). However, SRS alone is the standard therapy for patients with 1-4 BMs but also can be considered for patients with more than 4 lesions (8–10). SRS, whole brain radiation therapy, or their combination are reasonable options for other patients. Nonetheless, SRS is preferred because it is well known to preserve neurocognitive function, as neurocognitive impairment is the biggest concern of patients and clinicians.

Further, immunotherapy (IT) has revolutionized the treatment approach in patients with advanced cancers. A study reported that 44% of the metastatic cancer population was eligible for IT (11). IT has become the first-line therapy in metastatic NSCLC, predominantly in wild-type or non-targetable mutation cases (12). IT has been reported to have a considerable response in advanced-stage NSCLC patients (13–15). The growing use of IT in metastatic cancer has led to more and more patients receiving the combined IT and SRS for BMs. However, the right sequence and right timing of IT relative to SRS are still unclear. Therefore, it has become more crucial to explore the determinants of IT responsiveness and its interaction with the SRS to determine the right timing and sequence for IT.

With growing insight into the IT response determinants, traditionally used prognostic indices may not be equally efficient in predicting OS for every BM patient. At present, there are several established prognostic grading indexes for BM, including the recursive partitioning analysis (RPA), disease-specific graded prognostic assessment (DS-GPA), score index for radiosurgery (SIR), and a basic score for brain metastases (BS-BM) which comprised of some or all of the following parameters: Karnofsky Performance Status (KPS), age, extra-cranial disease status, primary diagnosis, number of BMs, mutation status, and PD-L1 expression status (16–18). Cumulative tumor volume is an important prognostic factor; its prognostic importance has previously been reported in different cancers (19–21). Despite that, it is not included in any traditionally used prognostic indexes. On the other hand, PD-L1 expression in cancer is found to be transient and shows topographic heterogeneity, creating uncertainty about it as a biomarker for predicting IT effectiveness (22). Moreover, the dynamics of the PD-1 and PD-L1 axis might change subject to the type of therapy and sequence of administration (23, 24). However, it has been given immense importance when predicting prognosis. Hence, there is an imperative need for an up-to-date prognostic assessment model.

In line with evolving insights into determinants of IT responsiveness and SRS role in reshaping tumor immune microenvironment, we hypothesize that the use of combined IT and SRS in treating NSCLCBM can be more beneficial than SRS alone, and there is an optimal window for initiating IT in relation to SRS. Peri-SRS IT and CITV might serve as prognosis predictors.

Materials and methods

Study population and data acquisition

This study was approved by the Guangdong Sanjiu brain hospital ethical committee. Due to the retrospective nature of the cohort, the requirement to obtain informed consent was waived. In total, 86 NSCLCBM patients who received SRS between January 2018 and September 2021 were included. First, the data of 43 patients with NSCLCBM who received SRS and IT for BM were extracted from our hospital's electronic medical records. Then, a propensity-score matching (PSM) analysis (selecting covariates = age, gender, KPS, and mutation status; method = nearest; caliper = 0.05) was performed to find the closest matched 43 patients from a pool of over 200 NSCLCBM patients in whom IT was not used but SRS. To be included in the present cohort, patients had to be histologically proven NSCLC, BM diagnosed with contrast-enhanced MRI, and had undergone SRS for BM. The endpoint of

the current cohort was the death or last follow-up, whichever occurred first; to overcome time bias, two zero times were selected, one from the day of the first SRS and the second from the day of the initial BM diagnosis. The OS was calculated from the initial BM diagnosis and first SRS to the death or last follow-up. Follow-up data were collected retrospectively from the electronic medical database, treating physicians or patients to diminish missing data.

Patients' characteristics

Detailed data of each patient, including demographic, clinical, and laboratory parameters, were collected from the electronic medical record upon admission for undergoing SRS for BMs. If some laboratory tests were done more than once, a test reading closest to the date of the initial SRS was recorded. Continuous predictors such as age, CITV, number of tumors, lactate dehydrogenase (LDH), neutrophil-lymphocyte ratio (NLR), neuron-specific enolase (NSE), carcinoembryonic antigen (CEA), and squamous cell carcinoma (SCC) antigen were classified into 2 groups. The cutoffs for age, LDH, NLR, NSE, CEA, SCC, CITV, and the number of BMs were 60 years, 250 U/L, 3.0, 16.3 ng/ml, 5 ng/ml, 1.5 ng/ml, 4 cm^3, and 3 BMs, respectively. They were analyzed as categorical variables. The CITV was defined as the sum of the tumor volume of all treated BM lesions. Contrast-enhanced MRI was used to evaluate BMs.

Stereotactic radiosurgery parameters

Patients were treated either by single-SRS or fractionated-SRS by the Novalis Tx® system (BrainLAB AG, Feldkirchen, Germany; Varian Medical System, Palo Alto, CA, USA). Dosage and fraction details are presented in Table 1. In the case of fractionated-SRS, fractions were delivered with a gap of 1–3 days. Supportive measures included regular administration of mannitol after SRS, contraindicated otherwise.

TABLE 1 Patients' baseline clinicodemographic characteristics.

Characteristics	SRS with IT (N = 43) n (%)	SRS without IT (N = 43) n (%)	P-value
Gender			
Female	3 (7)	3 (7)	1
Male	40 (93)	40 (93)	
Age (years)			
≤60	24 (45.8)	21 (48.8)	0.666
>60	19 (44.2)	22 (51.2)	
Median (IQR)	59 (49-65)	61 (56-66.5)	
Smoking			
Smoker	24 (45.8)	20 (46.5)	0.518
Non-smoker	19 (44.2)	23 (53.5)	
KPS			
90	9 (20.9)	6 (14)	0.813
80	12 (27.9)	13 (30.2)	
70	11 (25.6)	13 (30.2)	
60	7 (16.3)	9 (20.9)	
50	3 (7)	2 (4.7)	
40	1 (2.3)	0 (0)	
Median (IQR)	70 (65-80)	70 (65-80)	
Comorbidities			
Present	11 (25.6)	17 (39.5)	0.250
Absent	32 (74.4)	26 (60.5)	

(Continued)

10.3389/fonc.2023.1068592

TABLE 1 Continued

Characteristics	SRS with IT (N = 43) n (%)	SRS without IT (N = 43) n (%)	P-value
Histology			
Adenocarcinoma	31 (72.1)	39 (90.7)	0.075
Squamous cell carcinoma	11 (25.6)	4 (9.3)	
Sarcomatoid carcinoma	1 (2.3)	0 (0)	
Mutation status			
EGFR/ROS1/ALK mutation	6 (14)	6 (14)	0.854
Wild type	37 (86)	27 (62.8)	
Unknown	0 (0)	10 (23.2)	
Extra-cranial metastases			
Present	24 (45.8)	21 (48.8)	0.666
Absent	19 (44.2)	22 (51.2)	
Extra-cranial metastasis control			
Controlled	12 (27.9)	11 (25.6)	0.286
Uncontrolled	11 (25.6)	6 (14)	
Non-applicable	16 (37.2)	24 (55.8)	
Unknown	4 (9.3)	2 (4.6)	
Leptomeningeal metastases			
Present	7 (16.3)	2 (4.7)	0.159
Absent	36 (83.7)	41 (95.3)	
TNM classification 8th			
T stage			
T1	1 (2.3)	5 (11.6)	0.181
T2	9 (20.9)	14 (32.6)	
T3	8 (18.6)	7 (16.3)	
T4	13 (30.2)	8 (18.6)	
Unknown	12 (28)	9 (20.9)	
N stage			
N1	5 (11.6)	1 (2.3)	0.076
N2	13 (30.2)	20 (46.5)	
N3	19 (44.2)	13 (30.2)	
Unknown	6 (14)	9 (21)	
M stage			
M1b	10 (23.3)	8 (18.6)	0.791
M1c	33 (76.7)	35 (81.4)	
RPA score			
1	3 (7)	6 (14)	0.538
2	30 (69.7)	29 (67.4)	
3	10 (23.3)	8 (18.6))	

(Continued)

10.3389/fonc.2023.1068592

TABLE 1 Continued

Characteristics	SRS with IT (N = 43) n (%)	SRS without IT (N = 43) n (%)	P-value
Lung-molGPA index			
0.5	1 (2.3)	4 (9.3)	0.514
1	7 (16.3)	8 (18.6)	
1.5	8 (18.6)	4 (9.3)	
2	10 (23.3)	12 (27.9)	
2.5	7 (16.3)	9 (20.9)	
3	9 (20.9)	6 (14)	
3.5	1 (2.3)	0 (0)	
Number of BMs			
≤3	32 (74.4)	30 (69.7)	0.81
>3	11 (25.6)	13 (30.3)	
Total number of BMs	135	133	
Median (IQR)	2 (1-3.5)	2 (1-4.5)	
Cumulative intracranial tumor volume (cm^3)			
≤4	15 (34.9)	10 (23.3)	0.273
>4	26 (60.5)	33 (76.7)	
Unknown	2 (4.6)	0 (0)	
Median (IQR)	5.7 (2-14.8)	11.2 (4.55-22.7)	
Distribution of BMs			
Supra-tentorium	24 (55.8)	22 (51.1)	0.665
Infra-tentorium	5 (11.6)	8 (18.6)	
Both	14 (32.6)	13 (30.3)	
LDH (U/L)			
≤250	18 (41.8)	26 (60.4)	0.118
>250	12 (27.9)	6 (14)	
Unknown	13 (30.3)	11 (25.6)	
Median (IQR)	239.6 (206.3-271.7)	198.1 (161-221)	
NLR			
≤3.0	10 (23.3)	11 (25.6)	1
>3.0	33 (76.7)	32 (74.4)	
Median (IQR)	4.1 (3.1-6.45)	4.2 (3.1-5.85)	
NSE (ng/ml)			
≤16.3	21 (48.8)	25 (58.1)	0.177
>16.3	21 (48.8)	12 (27.9)	
Unknown	1 (2.4)	6 (14)	
Median (IQR)	15.2 (11.1-21.3)	14.9 (11.8-19.7)	
CEA (ng/ml)			
≤5	24 (55.8)	24 (55.8)	0.975

(Continued)

TABLE 1 Continued

Characteristics	SRS with IT (N = 43) n (%)	SRS without IT (N = 43) n (%)	P-value
>5	19 (44.2)	17 (39.5)	
Unknown	0 (0)	2 (4.7)	
Median (IQR)	4.1 (2.4-21)	4.3 (2.7-13.1)	
SCC antigen (ng/ml)			
≤1.5	29 (67.4)	30 (69.7)	1
>1.5	7 (16.3)	6 (14)	
Unknown	7 (16.3)	7 (16.3)	
Median (IQR)	0.8 (0.4-1.3)	0.9 (0.6-1.3)	
Radiation type			
Single-fraction SRS dose (Gy)			
15	1 (2.4)	0 (0)	
16	15 (34.8)	12 (27.9)	
18	13 (30.2)	9 (20.9)	
Multi-fraction SRS dose(Gy)/fraction, total fractions			
8/F, 3F	9 (20.9)	9 (20.9)	
10/F, 2F	4 (9.3)	12 (27.9)	
11/F, 2F	1 (2.4)	1 (2.4)	

SRS, stereotactic radiosurgery; IT, immunotherapy; IQR, interquartile range; KPS, Karnofsky performance status; T, tumor; N, node; M, metastasis; RPA, recursive partitioning analysis; Lung-molGPA, molecular graded prognostic assessment for lung cancer; BMs, brain metastases; LDH, lactate dehydrogenase; NLR, neutrophil-lymphocyte ratio; NSE, neuron-specific enolase; CEA, carcinoembryonic antigen; SCC, squamous cell carcinoma; FSRS, fractionated stereotactic radiosurgery; Gy, gray; F, fraction.

Construction of prognosis prediction model

Cox proportional hazards regression analysis was used to construct a prognosis assessment model. A P-value of a variable had to be ≤ 0.15 in univariable analysis to fit in the multivariable analysis. The nomogram was established utilizing the rms package in R. The concordance index (C-index), calibration curves, and receiver operating characteristic (ROC) curves were implemented to determine the predictive model accuracy.

Statistical analysis

Descriptive statistics for quantitative variables were demonstrated as medians (interquartile range, IQR) and categorical variables as numbers (percentages, %). Wilcoxon rank sum test or Kruskal Wallis rank sum test was conducted for continuous variables, and categorical variables were analyzed *via* Chi-square or Fisher's exact tests, as appropriate. OS was estimated using Kaplan–Meier analysis, and a log-rank test evaluated the differences between groups. Cox regression was utilized to identify significant prognostic factors. Hazard ratios (HRs) are presented with 95% confidence intervals (CIs). All analyses were done using R version 4.1.2 (http://www.R-project.org). P-value was considered statistically significant if it was <0.05.

Results

Patient cohort

The data of 86 NSCLCBM patients treated with SRS to 268 BMs were retrospectively obtained from the Guangdong Sanjiu Brain Hospital database of the patients treated for BMs between January 2018 and September 2021. The median follow-up time was 11.3 months (IQR, 6.8 - 21.4) and 8.5 (IQR, 4.2 - 15.8) following BM diagnosis and SRS, respectively. Of 86, 51 (59.3%) were diagnosed with BM at the time of primary tumor diagnosis (≤ 2 weeks); 11 patients were alive at the time of analysis. The patients' median age was 60 years (age range 28–80 years), of whom 80 (80/86, 93%) were males. Most patients (70/86, 81.4%) had adenocarcinoma histology, followed by squamous cell carcinoma (15/86, 17.4%) and sarcomatoid carcinoma (1/86, 1.2%). Most patients (64/86, 74.4%) were wild-type, 12 (14%) harbored an EGFR/ALK/ROS1 mutation, and 10 (11.6%) had unknown mutation status. Based on treatment, patients were stratified into two groups, "SRS with IT" (n=43, 50%) and "SRS without IT" (n=43, 50%). No significant discrepancies were found in patients' clinicodemographic characteristics between the two groups (Table 1).

Overall survival

The median OS for the entire population was 420 days (14 months) and 266 days (8.7 months) from the date of BM diagnosis and SRS, respectively (Figures 1A, B). The log-rank test identified a significant difference in OS between SRS with IT and SRS without IT groups (Figures 1C, D). Patients treated with IT had better OS than those in whom IT wasn't used. The median OS for the IT group from the day of BM diagnosis was 505 days (16.8 months) and 252 days (8.4 months) for no IT group. OS for the IT group from the day of SRS was 360 days (12 months) and 211 days (7 months) for no IT group. Univariate analysis revealed several clinical factors were potentially associated with OS (Table 2). IT and RPA were the independent prognostic factors in multivariate analysis, whereas CITV was marginally significant. However, SCC antigen tumor marker was significant, and NLR was marginally significant only when the OS was calculated from BM diagnosis.

Optimal sequencing and timing of IT in relation to SRS

In total, 43 patients who received IT for BMs at any point during the disease course were divided into three groups by IT timing to SRS. If the IT was initiated more than a month before the date of SRS, they were allocated to the IT before SRS group; if IT was administrated within a month before or after the day of SRS or started more than a month before but continued at the time of SRS were assigned to the concurrent group; if IT was started more than a month after the day of SRS were allotted to the IT after SRS group. If patients have undergone FSRS, the start date was considered the zero time. The number of patients who received IT before, concurrent, and after were 9, 17, and 17, respectively. The patients' median age was 59 years (range 29-79 years). Of 43, 40 (93%) were males. Patients' relevant characteristics are presented in Table 3. None of the characteristics were significantly different between the three groups.

As per our analysis, the recipient of IT after SRS had an excellent OS, and those who received IT before SRS had the worst OS (Figures 2A, B). The median OS for those in whom IT was initiated after SRS was 796 days (26.5 months) from the day of BM diagnosis and 643 days (21.4 months) from SRS, which was the highest among the three groups. Recipient of IT before SRS had a median OS of 212 days (7.1 months) following BM diagnosis and 122 days (4.1 months) from SRS, which was the worst among the three groups. Individuals who received IT and SRS concurrently showed a median OS of 423 days (14.1 months) and 298 days (9.9 months) from the date of BM diagnosis and SRS, respectively. In univariate analysis, we found several clinical factors were potentially associated with OS. Multivariate analysis identified that the peri-SRS timing of IT administration was the significant independent prognostic factor for OS, as shown in Table 4. Smoking was a significant survival predictor when OS was calculated from the date of BM diagnosis.

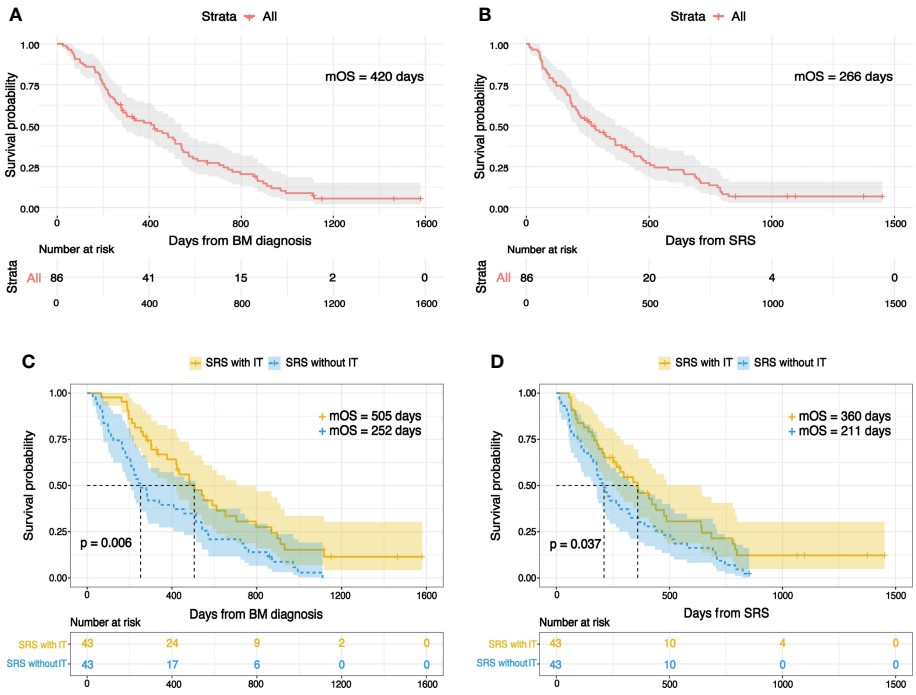

FIGURE 1
Kaplan-Meier overall survival plots for the entire study population following **(A)** BM diagnosis **(B)** SRS. Overall survival for individuals treated by SRS with IT or SRS without IT from **(C)** BM diagnosis **(D)** SRS.

10.3389/fonc.2023.1068592

TABLE 2 Univariate and multivariate analysis for overall survival.

Variables	From BM diagnosis		From SRS	
	HR (95% CI)	P-value	HR (95% CI)	P-value
Univariate analysis				
Sex	1.1 (0.474 - 2.552)	0.824	0.827 (0.357 - 1.918)	0.658
Age	1.097 (0.697 - 1.727)	0.689	1.004 (0.635 - 1.59)	0.985
Smoking	1.273 (0.803 - 2.019)	0.305	1.347 (0.851 - 2.133)	0.203
Histology	0.974 (0.733 - 1.293)	0.854	0.948 (0.716 - 1.257)	0.712
Mutation	0.656 (0.343 - 1.254)	0.202	0.688 (0.362 - 1.308)	0.254
Extra-cranial Metastasis	1.823 (1.141 - 2.912)	0.012	1.618 (1.02 - 2.565)	0.041
Leptomeningeal Metastasis	0.837 (0.400 - 1.751)	0.637	0.918 (0.439 - 1.922)	0.821
T stage	1.029 (0.771 - 1.374)	0.845	1.084 (0.820 - 1.433)	0.571
N stage	1.116 (0.749 - 1.663)	0.59	1.109 (0.754 - 1.633)	0.599
M stage	0.954 (0.523 - 1.741)	0.879	0.961 (0.526 - 1.753)	0.896
RPA	1.88 (1.216 - 2.907)	0.004	1.945 (1.282 - 2.952)	0.001
molGPA	0.683 (0.496 - 0.943)	0.020	0.724 (0.530 - 0.99)	0.043
KPS	0.981 (0.961 - 1.001)	0.057	0.983 (0.963 - 1.003)	0.09
CITV (cm^3)	0.56 (0.335 - 0.936)	0.027	0.679 (0.409 - 1.129)	0.136
Distribution of BMs	1.1 (0.851 - 1.422)	0.466	1.052 (0.815 - 1.358)	0.698
Number of BMs	0.618 (0.377 - 1.013)	0.056	0.678 (0.414 - 1.109)	0.122
Immunotherapy	0.527 (0.332 - 0.838)	0.006	0.617 (0.39 - 0.975)	0.038
NLR	1.528 (0.896 - 2.606)	0.12	1.379 (0.810 - 2.347)	0.236
LDH	1.352 (0.723 - 2.527)	0.345	1.299 (0.708 - 2.384)	0.398
NSE	1.635 (0.997 - 2.682)	0.051	1.803 (0.098 - 2.961)	0.020
CEA	0.864 (0.541 - 1.379)	0.54	0.866 (0.543 - 1.382)	0.547
SCC antigen	2.193 (1.103 - 4.358)	0.025	2.746 (1.353 - 5.574)	0.005
Multivariate analysis				
Immunotherapy	0.363 (0.199 - 0.661)	<0.001	0.472 (0.260 - 0.857)	0.014
Extra-cranial Metastasis	1.374 (0.617 - 3.06)	0.436	0.918 (0.419 - 2.008)	0.830
RPA	2.219 (1.163 - 4.235)	0.016	2.562 (1.340- 4.900)	0.004
molGPA	1.047 (0.571 - 1.919)	0.882	1.051 (0.553- 1.998)	0.878
KPS	1.012 (0.976 - 1.049)	0.517	1.028 (0.991 - 1.066)	0.138
CITV (cm^3)	1.716 (0.922 - 3.196)	0.089	1.783 (0.941 - 3.376)	0.076
Number of BMs	0.673 (0.326 - 1.390)	0.285	0.579 (0.269 - 1.245)	0.162
NSE	1.171 (0.557 - 2.458)	0.677	1.504 (0.742 - 3.045)	0.257
SCC antigen	2.542 (1.112 – 5.810)	0.027	1.917 (0.847 - 4.337)	0.118
NLR	1.856 (0.976 - 3.530)	0.060		

T, tumor; N, node; M, metastasis; RPA, recursive partitioning analysis; Lung-molGPA, molecular graded prognostic assessment for lung cancer; KPS, Karnofsky performance status; CITV, cumulative intracranial tumor volume; BMs, brain metastases; NLR, neutrophil-lymphocyte ratio; LDH, lactate dehydrogenase; NSE, neuron-specific enolase; CEA, carcinoembryonic antigen; SCC, squamous cell carcinoma; SRS, stereotactic radiosurgery.

10.3389/fonc.2023.1068592

TABLE 3 Relevant characteristics of NSCLCBM patients treated with SRS plus IT.

Characteristics	IT before SRS (n = 9) n (%)	Concurrent (n = 17) n (%)	IT after SRS (n = 17) n (%)	P value
Histology				
Adenocarcinoma	5 (55.6)	11 (64.7)	15 (88.3)	0.202
Squamous cell carcinoma	4 (44.4)	5 (29.4)	2 (11.7)	
Sarcomatoid carcinoma	0 (0)	1 (5.9)	0 (0)	
Mutation status				
Wild type	8 (88.9)	14 (82.4)	15 (88.3)	1
EGFR/ROS1/ALK mutation	1 (11.1)	3 (17.6)	2 (11.7)	
PD-L1 expression				
>50%	1 (11.1)	2 (11.8)	0 (0)	0.423
1-50%	1 (11.1)	3 (17.6)	3 (17.6)	
<1%	0 (0)	4 (23.5)	4 (23.5)	
unknown	7 (77.8)	8 (47.1)	10 (58.8)	
KPS				
90	1 (11.1)	4 (23.5)	4 (23.5)	0.527
80	1 (11.1)	5 (29.5)	6 (35.3)	
70	3 (33.4)	4 (23.5)	4 (23.5)	
60	2 (22.2)	4 (23.5)	1 (5.9)	
50	1 (11.1)	0 (0)	2 (11.8)	
40	1 (11.1)	0 (0)	0 (0)	
Median (IQR)	70 (60-70)	80 (70-80)	80 (70-80)	
Extra-cranial metastases				
Present	7 (77.8)	7 (41.2)	10 (58.8)	0.202
Absent	2 (22.2)	10 (58.8)	7 (41.2)	
Number of BMs				
≤3	5 (55.6)	15 (88.2)	12 (70.6)	0.191
>3	4 (44.4)	2 (11.8)	5 (29.4)	
Total number of BMs (median)	37	39	57	
Median (IQR)	3 (1-4)	1 (1-3)	2 (1-4)	
CITV (cm^3)				
≤4	3 (33.3)	6 (35.3)	6 (35.3)	1
>4	5 (55.6)	11 (64.7)	10 (58.8)	
Unknown	1 (11.1)	0 (0)	1 (5.9)	
Median (IQR)	7.3 (2.6-13.3)	7.5 (1.8-14.8)	5.7 (3.1-11.4)	
Immunotherapeutic agents				
Nivolumab (PD-1); Pembrolizumab (PD-1); Sintilimab (PD-1); Toripalimab (PD-1); Tislelizumab (PD-1); Camrelizumab (PD-1); KN046 (PD-L1 and CTLA-4)				
IT cycles				
Median (range)	6.5 (2-14)	4 (1-19)	7 (1-28)	
Timing of IT (months)				

(Continued)

TABLE 3 Continued

Characteristics	IT before SRS (n = 9) n (%)	Concurrent (n = 17) n (%)	IT after SRS (n = 17) n (%)	P value
Median (range)	4.4 (1.2-15.5)	–	6.3 (1.8-16.4)	
Radiation type				
Single-fraction SRS dose (Gy)				
15	1 (11.1)	0 (0)	0 (0)	
16	3 (33.4)	7 (41.2)	5 (29.4)	
18	2 (22.2)	4 (23.5)	7 (41.1)	
Multi-fraction SRS dose(Gy)/fraction, total fractions				
8/F, 3F	2 (22.2)	5 (29.4)	2 (11.8)	
10/F, 2F	1 (11.1)	1 (5.9)	2 (11.8)	
11/F, 2F	0 (0)	0 (0)	1 (5.9)	
irAE (CTCAE)				
Skin	1 (11.1)	1 (5.9)	–	
Lung	1 (11.1)	–	–	
Gastro-intestinal tract	–	1 (5.9)	–	
RTOG Radiation Toxicity Grading (grade 3 onward)				
RTOG acute radiation morbidity	–	–	–	
RTOG late radiation morbidity	–	–	–	

IT, immunotherapy; SRS, stereotactic radiosurgery; BM, brain metastases; IQR, interquartile range; KPS, Karnofsky performance status; CITV, cumulative intracranial tumor volume; FSRS, fractionated stereotactic radiosurgery; Gy, gray; F, fraction; irAE, immune-related adverse events; RTOG, Radiation Therapy Oncology Group; CTCAE, common terminology criteria for adverse events.

Toxicity

The adverse events related to combined IT and SRS were manageable and consistent with previous publications (25, 26). In our analysis, 4 patients (4/43, 9.3%) appeared to have grade 3 immune-related adverse events, 2 (2/43, 4.65%) had skin complications, 1 (1/43, 2.3%) lung, and 1 (1/43, 2.3%) gastrointestinal tract complication. All patients recovered utterly within a few days of treatment. No patient exhibited grade 4 or 5 toxicity. Moreover, no grade 3 onward radiation toxicity was reported based on the data obtained from our hospital's electronic medical database, treating physicians, and patients (Table 3).

Prognostic nomogram

The entire study population was stratified into the training set and validation set by random number generator using R software (total population = 86, training cohort = 43, validation cohort = 43).

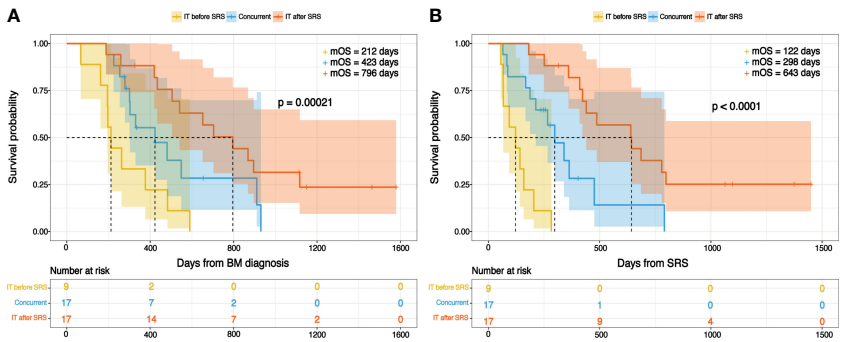

FIGURE 2
Overall survival with reference to immunotherapy timing from the day of **(A)** BM diagnosis **(B)** SRS.

TABLE 4 Univariate and multivariate analysis for overall survival in NSCLCBM patients treated with SRS plus IT.

Variables	From BM diagnosis		From SRS	
	HR (95% CI)	P-value	HR (95% CI)	P-value
Univariate analysis				
Sex	1.91 (0.574 - 6.353)	0.292	1.242 (0.374 - 4.129)	0.723
Age	1.269 (0.635 - 2.537)	0.501	1.051 (0.517 - 2.133)	0.891
Smoking	1.697 (0.835 - 3.449)	0.144	1.6 (0.791 - 3.236)	0.191
Histology	0.986 (0.717 - 1.356)	0.931	0.971 (0.71 - 1.33)	0.856
Mutation	0.718 (0.273 - 1.889)	0.502	0.701 (0.269 - 1.826)	0.467
Extra-cranial Metastasis	2.027 (0.963 – 4.264)	0.063	1.719 (0.843 - 3.506)	0.136
Leptomeningeal Metastasis	0.766 (0.313 - 1.871)	0.558	0.931 (0.382 - 2.271)	0.876
T stage	1.745 (1.004 - 3.033)	0.048	1.858 (1.078 – 3.201)	0.026
N stage	1.206 (0.692 - 2.102)	0.509	1.246 (0.728 - 2.134)	0.422
M stage	1.457 (0.560 - 3.791)	0.44	1.343 (0.516 - 3.493)	0.546
RPA	1.786 (0.848 - 3.762)	0.127	1.482 (0.744 - 2.954)	0.264
molGPA	0.747 (0.468 – 1.192)	0.221	0.817 (0.521 - 1.281)	0.378
KPS	0.987 (0. 958 - 1.014)	0.313	0.993 (0.966 - 1.02)	0.6
CITV (cm^3)	0.683 (0.326 - 1.429)	0.311	1.294 (0.614 - 2.726)	0.498
Distribution of BMs	1.016 (0.691 - 1.495)	0.935	0.860 (0.579 - 1.277)	0.454
Number of BMs	0.589 (0.278 - 1.248)	0.167	0.782 (0.369 - 1.656)	0.521
Immunotherapy timing	0.397 (0.243 - 0.648)	0.0002	0.206 (0.112 - 0.381)	<0.001
NLR	1.664 (0.719 - 3.848)	0.234	1.59 (0.689 - 3.674)	0.277
LDH	1.974 (0.794 - 4.905)	0.143	1.832 (0.773 - 4.345)	0.169
NSE	1.644 (0.815 - 3.314)	0.165	1.854 (0.915 - 3.756)	0.087
CEA	0.965 (0.484 - 1.923)	0.919	0.894 (0.447 - 1.788)	0.752
SCC antigen	1.922 (0.699 - 5.287)	0.206	2.542 (0.867 - 7.451)	0.089
Multivariate analysis				
Immunotherapy timing	0.132 (0.034 - 0.517)	0.004	0.14 (0.044 - 0.450)	0.001
Extra-cranial Metastasis	4.704 (0.737 - 30.026)	0.102	0.587 (0.166 - 2.074)	0.408
Smoking	8.169 (1.417 - 47.082)	0.019		
RPA	0.492 (0.138 - 1.754)	0.274		
T stage	0.887 (0.385 - 2.047)	0.779	1.77 (0.862 - 3.634)	0.120
NSE			1.989 (0.617 - 6.416)	0.25
SCC antigen			0.442 (0.080 - 2.428)	0.347
LDH	1.787 (0.493 - 6.473)	0.377		

BMs, brain metastases; SRS, stereotactic radiosurgery; T, tumor; N, node; M, metastasis; RPA, recursive prognostic assessment; Lung-molGPA, molecular graded prognostic assessment for lung cancer; KPS, Karnofsky performance status; CITV, cumulative intracranial tumor volume; NLR, neutrophil-lymphocyte ratio; LDH, lactate dehydrogenase; NSE, neuron-specific enolase; CEA, carcinoembryonic antigen; SCC, squamous cell carcinoma.

In the training cohort, the number of patients received IT was 22, and 21 didn't receive IT. Kaplan-Meier analysis revealed OS was significantly different between SRS with IT and SRS without IT groups in the training cohorts. The patient who received IT had improved OS than those who didn't, as shown in Figures 3A, B. The median OS for the IT group from the day of BM diagnosis was 483 days (16.1 months) and 221 days (7.4 months) for the no IT group. OS for the IT group from the day of SRS was 360 days (12 months) and 185 days (6.2 months) for no IT group.

The clinicodemographic and laboratory variables of the patients in the training set were evaluated to develop the prognosis prediction model. A univariate cox regression analysis was

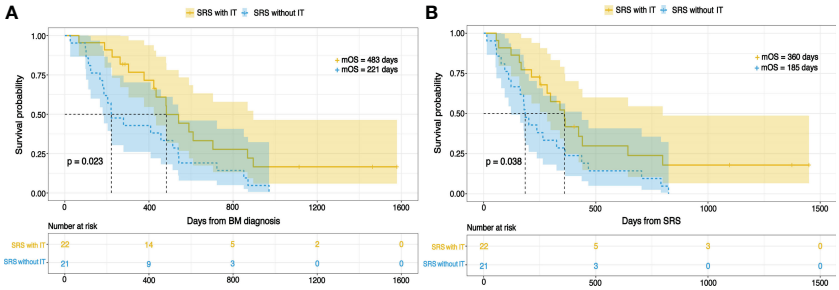

FIGURE 3
The Kaplan-Meier curves for OS in NSCLCBM patients treated by SRS with IT or SRS without IT from **(A)** BM diagnosis **(B)** SRS.

TABLE 5 Univariate and multivariate analysis for overall survival.

Variables	Training cohort (n = 43)		Validation cohort (n = 43)	
	HR (95% CI)	P-value	HR (95% CI)	P-value
Univariate analysis				
Sex	0.820 (0.248 - 2.705)	0.744	0.677 (0.205 - 2.236)	0.522
Age	0.919 (0.479 - 1.764)	0.8	1.920 (0.480 - 1.765)	0.801
Smoking	0.957 (0.499 - 1.834)	0.894	1.014 (0.531 - 1.937)	0.966
Histology	1.911 (0.771 - 4.733)	0.162	1.981 (0.787 - 4.986)	0.147
Mutation	0.724 (0.652 - 2.469)	0.505	0.850 (0.329 - 2.197)	0.737
Extra-cranial Metastasis	1.269 (1.141 - 2.912)	0.483	1.364 (0.698 - 2.667)	0.364
Leptomeningeal Metastasis	0.876 (0.307 - 2.498)	0.804	1.012 (0.356 - 2.878)	0.982
T stage	0.858 (0.575 - 1.28)	0.452	0.942 (0.644 - 1.379)	0.76
N stage	1.027 (0.642 - 1.643)	0.991	1.026 (0.657 - 1.603)	0.91
M stage	0.45 (0.170 - 1.188)	0.107	0.716 (0.285 - 1.8)	0.477
RPA	1.636 (0.843 - 3.174)	0.145	1.859 (0.978 - 3.537)	0.059
molGPA	0.832 (0.521 - 1.329)	0.442	0.810 (0.521 - 1.262)	0.352
KPS	0.998 (0.970 - 1.026)	0.864	0.994 (0.967 - 1.022)	0.671
CITV (cm^3)	1.947 (0.880 - 4.306)	0.1	1.942 (0.877 - 4.301)	0.102
Distribution of BMs	0.896 (0.617 - 1.302)	0.565	0.882 (0.611 - 1.272)	0.501
Number of BMs	0.690 (0.340 - 1.4)	0. 303	0.753 (0.371 - 1.528)	0.432
Immunotherapy	0.475 (0.246 - 0.915)	0.026	0.505 (0.262 - 0.974)	0.042
NLR	1.637 (0.832 - 3.222)	0.154	1.238 (0.631 - 2.428)	0.534
LDH	0.999 (0.997 - 1.002)	0.673	0.999 (0.996 - 1.002)	0.461
NSE	1.135 (0.559 - 2.303)	0.726	1.135 (0.560 - 2.299)	0.725
CEA	0.999 (0.996 - 1.001)	0.217	0.999 (0.996 - 1.001)	0.216
SCC antigen	1.529 (0.519 - 4.501)	0.441	1.432 (0.480 - 4.273)	0.52
Multivariate analysis				
Immunotherapy	0.412 (0.208 - 0.818)	0.011	0.267 (0.117 - 0.610)	0.002
RPA	2.064 (1.064 - 4.001)	0.032	3.069 (1.471- 6.402)	0.003

(Continued)

TABLE 5 Continued

Variables	Training cohort (n = 43)		Validation cohort (n = 43)	
	HR (95% CI)	P-value	HR (95% CI)	P-value
Univariate analysis				
CITV (cm^3)	2.486 (1.108 - 5.576)	0.027	2.334 (1.018 - 5.353)	0.045
M stage	0.409 (0.151 - 1.109)	0.079		
Histology			2.462 (0.862 - 7.034)	0.092

T, tumor; N, node; M, metastasis; RPA, recursive prognostic assessment; Lung-molGPA, molecular graded prognostic assessment for lung cancer; KPS, Karnofsky performance status; CITV, cumulative intracranial tumor volume; BMs, brain metastases; NLR, neutrophil-lymphocyte ratio; LDH, lactate dehydrogenase; NSE, neuron-specific enolase; CEA, carcinoembryonic antigen; SCC, squamous cell carcinoma.

conducted to explore possible variables related to the survival in the training cohort population. Unifactorial analysis indicated several potential prognosis predictors (Table 5). Multivariate cox regression analysis with stepwise forward selection was run, integrating significant variables in the univariate analyses, revealing that IT, RPA, and CITV were the significant independent prognostic factors. By integrating these significant independent prognostic variables, we developed a nomogram for predicting OS in NSCLCBM patients treated with SRS (Figure 4).

Discussion

Theoretically, PD-L1 expression level, neoantigen, microsatellite, tumor mutation burden, tumor heterogeneity, tumor-infiltrating lymphocytes, regulatory T cells, and damage-associated molecular patterns (DAMPs) are well-known determinants of IT responsiveness (27). These determinants can be modulated by radiotherapy, immunogenic chemotherapeutic agents, and combination therapies. Radiotherapy is widely known as an inducer of immunogenic cell death. In addition, radiotherapy can increase PD-L1 expression level (23), inhibit T regulatory cells, release antigens and damage-associated molecular patterns from cancer cells (27), increase BBB permeability (28–30), and convert immunologically cold tumors to hot ones (31). Furthermore, radiotherapy can also affect non-treatment lesions when combined with IT, known as an abscopal effect (32). Immunogenic chemotherapeutic agents not only sensitize previously resistant but also enhance the response of IT by increasing tumor-infiltrating lymphocytes (33). Taken together, the right combination, right sequence, and right timing can improve IT response even in tumors known to be intrinsically resistant.

In line with theoretical knowledge, our analysis revealed that combined use of IT and SRS was associated with OS in NSCLCBM patients (from BM diagnosis: HR 0.363, 95% CI 0.199 - 0.661, $P < 0.001$; from SRS: HR 0.472, 95% CI 0.260 - 0.857, $P = 0.014$). Individuals receipt IT in combination with SRS had better OS than those who didn't receive IT (from the day of BM diagnosis: 16.8 vs. 8.4 months, P = 0.006; from the day of SRS: 12 vs. 7 months, P = 0.037), which is consistent with the studies conducted by Abdulhaleem et al. (40 vs. 8 months), Lanier and colleagues (15.9 vs. 6.1 months), and Chen and partners (19.4 vs. 12.9 months) (34–36). Similarly, Enright and colleagues insisted that SRT plus immune checkpoint inhibitors (ICIs) improved long-term survival in NSCLCBM patients compared to SRT alone (37). Meanwhile, there was no increase in adverse events, which is consistent with present cohort findings. Moreover, Stokes et al. (10.8 vs. 6.1 months), Diao et al. (15.1 vs. 7.8 months), Knisely et al. (21.3 vs. 4.9 months), Gabani et al. (11.1 vs. 6.2 months), and Kaidar-Person et al. (15 vs. 6 months) also reported similar results in melanoma patients (38–42). Taken together, we can conclude that IT can be a powerful tool when combined with radiotherapy.

Despite the growing evidence of the positive synergy of radiotherapy and IT, the optimal window for initiating IT relative to SRS remains unclear. Intuitively, delay of specific time duration

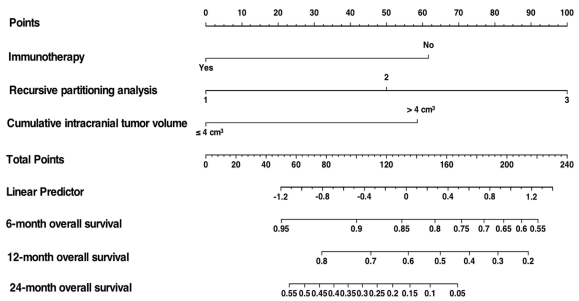

FIGURE 4
Nomogram to predict OS in NSCLCBM patients treated with SRS based on 3 independent prognostic factors identified in the training cohort.

in IT administration post-SRS can be beneficial for allowing some time to get the immune system in action (release antigen from dying cancer cells, their recognition and processing by antigen-presenting cells, and delivery to T cells) and early and delayed effects of radiotherapy on vascular permeability to take place. Interestingly, our analysis revealed that peri-SRS timing of IT is an independent prognostic factor for OS (from BM diagnosis: HR 0.132, 95% CI 0.034 - 0.517, $P = 0.004$; from SRS: HR 0.14, 95% CI 0.044 - 0.450, $P = 0.001$). Use of IT after SRS led to better OS than concurrent or before (from BM diagnosis: 26.5 vs. 14.1 vs. 7.1 months; from SRS: 21.4 vs. 9.9 vs. 4.1 months, respectively). Several studies have echoed partially similar results regarding IT timing in relation to SRS. Wegner and partners found improved OS in those in whom IT was started at least 21 days after radiotherapy in stage IV NSCLC patients than in those receiving IT within 21 days after radiotherapy (19 vs. 14 months) (43). Schapira and colleagues recorded a longer OS in the recipient of IT post-SRS compared to those who received IT concurrently or before SRS (OS at 1 year, 87.3% vs. 70.0% vs. 0%) (25). A phase 1 KEYNOTE-001 trial revealed that exposure to radiation therapy prior to IT led to better OS than no prior radiation therapy (10.7 vs. 5.3 months) (44). However, some studies claim better OS for both concurrent or IT after SRS. A recent study in the USA reported that adding IT after/concurrent relative to SRS had improved OS than before (13 vs. 3.3 months) (45). Kamran et al. and Cohen-Inbar et al. revealed trends for better OS in the group who received SRS before or during IT administration (26, 46). Contrarily, some insisted that IT and SRS concurrent use is associated with a good OS than before or after (36, 47).

Of note, there seems to be a reasonable agreement that the use of IT prior to SRS is associated with the worst OS compared with concurrent or post-SRS. However, results are inconclusive regarding the concurrent or post-SRS use of IT, which might be due to an inconsistent approach of allocating patients to treatment groups, i.e., some studies considered receipt of IT within 3 months before or after SRS as concurrent, some within 1 month, and some within 2 weeks. In addition, most studies compared concurrent vs. nonconcurrent, prior/during vs. post, and before vs. during/after but rarely before, concurrent, or after, which led to inconclusive results. Although, per current and previous studies trends, there appears to be an optimal time window for IT administration just before SRS or after SRS. Therefore, a larger multi-institutional randomized prospective clinical trial with a more practical approach towards IT timing (with 4 study arms: IT onset immediate before SRS [within 3 weeks prior to SRS], post-SRS early onset of IT, delayed onset, and late-onset) is warranted to identify the optimal time window.

Given the growing use of combined SRS and IT in treating NSCLCBM, traditionally used prognostic tools may not be equally efficient in predicting survival in every BM patient, predominantly in wild-type, since our analysis showed that the median OS has doubled for those who received IT peri-SRS regardless of PD-L1 expression. At present, RPA and DS-GPA are the most widely used prognostic indexes. The RPA index was established based on three consecutive Radiation Therapy Oncology Group (RTOG) trials analysis conducted between 1979 and 1993 (16). RPA introduced three prognostic classes using four clinical variables: age, primary tumor control, KPS, and extra-cranial metastases. Likewise, the GPA index was established in 2008 based on five randomized trials (48). Nevertheless, the classical GPA and RPA indices were all established before the era of IT.

We comprehensively assessed the prognostic significance of clinicodemographic variables and brain metastatic lesions' physical characteristics in the present analysis. The latter included the number of BMs, BMs' distribution, BMs' location, and CITV (Table 5). Multifactor analysis disclosed that IT, RPA, and CITV were the only significant prognostic factors for OS in patients with NSCLCBM. Previously, numerous studies have reported the favorable prognostic role of IT in NSCLCBM patients, which is consistent with our findings (35–37). Likewise, several studies previously reported cumulative tumor volume as an important prognostic factor (19–21). Although the number of BMs is widely considered to impact the patient's long-term survival, it was not the case in our analysis. Based on multivariate analysis, we developed a nomogram incorporating IT, CITV, and RPA, demonstrating excellent performance. It was found to have a high AUC for the prediction of OS (Figure 5).

The internal validation cohort was used to validate the training cohort-based nomogram. Each patient's risk scores based on the training set's results were regarded as a variable to conduct Cox proportional hazard regression. The concordance index (C-index) was calculated with the Hmisc package in R to assess the model's discrimination for prognosis. A C-index of 0.5 designates the absence of discrimination; contrarily, 1.0 indicates a perfect separation of patients with different outcomes. The C-index of a nomogram to predict OS in the training, validation, and overall cohorts were 0.732, 0.665, and 0.690, respectively. The sensitivity and specificity of the nomogram were evaluated by the area under the curve (AUC) of the receiver operating characteristic (ROC) curve using the timeROC package in R. The AUC for the prediction of 6-month OS was 0.926 for the training cohort (Figure 5A), 0.845 for the validation cohort (Figure 5B), and 0.891 for the overall cohort (Figure 7A).

Furthermore, the calibration curves plotted through the bootstrap method with 1000 resampling were utilized to reflect the constancy between the actual and nomogram-predicted probability. The calibration plots presented a considerable agreement for the 6-, 12- and 24-month OS in the training and validation sets between the nomogram-predicted and actual OS rates (Figures 6A-F). The prediction value of this nomogram was compared with traditionally practiced prognostic indexes, including the lung-molGPA and RPA, as well as the CITV alone and the number of BMs alone. The nomogram established in the present study demonstrated superior discrimination efficacy in training, validation, and overall cohort (Figures 7A-C).

According to nomogram predicted risk scores, patients from the training and validation cohort were classified into high-risk and low-risk groups. The Kaplan–Meier survival curve demonstrated a significant difference in OS between low-and high-risk patients in both training and validation cohorts (Figures 8A, B). Although the RPA index alone has shown considerable prognosis predictability, its performance was significantly enhanced with the combination of peri-SRS IT, RPA, and CITV. To our knowledge, we are among the

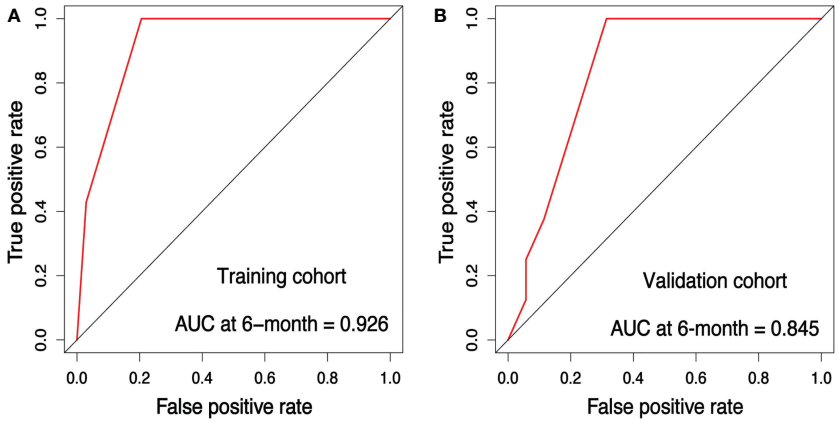

FIGURE 5
Receiver operating characteristic (ROC) analysis for the training and validation cohort. ROC curve for the prediction model **(A)** in the training cohort **(B)** in the validation cohort.

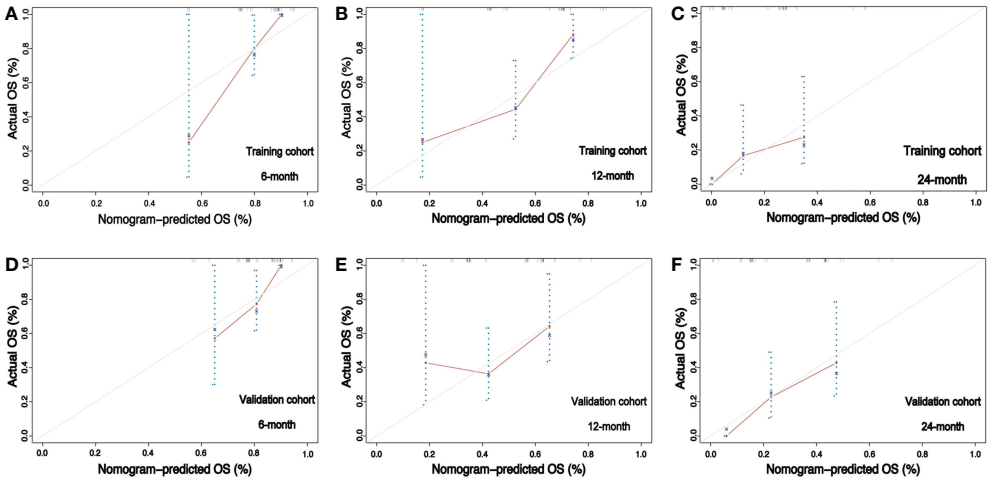

FIGURE 6
Calibration curves for the training and validation cohorts. (A–C) Calibration plots comparing nomogram-predicted and observed overall survival in the training cohort at 6, 12, and 24 months, respectively. (D–F) Calibration plots comparing nomogram-predicted and observed overall survival in the validation cohort at 6, 12, and 24 months, respectively.

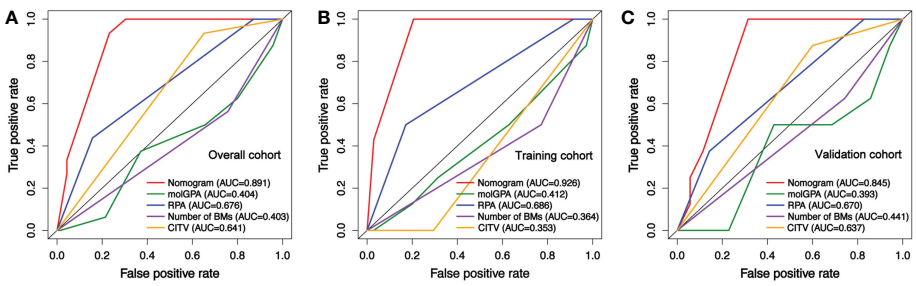

FIGURE 7
Receiver operating characteristic curves (ROC) comparing the predictive value of the nomogram with lung-molGPA, RPA models, cumulative intracranial tumor volume (CITV), and number of BMs for the prognosis of NSCLCBM patients. **(A)** In the overall cohort, **(B)** in training, and **(C)** in validation cohorts.

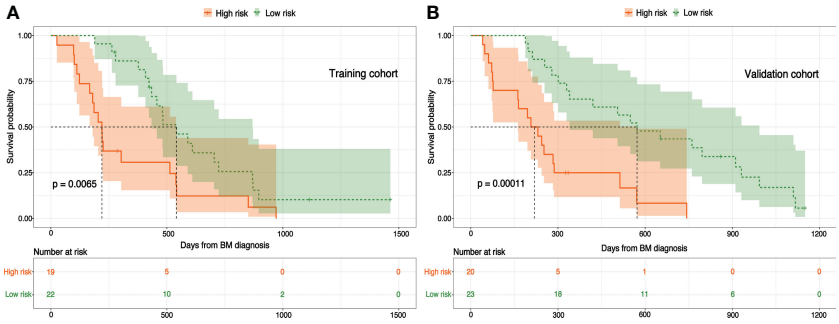

FIGURE 8
Nomogram-based risk stratifications for NSCLCBM patients and Kaplan–Meier OS curves for patients with low- and high-risk scores in the **(A)** training cohort and **(B)** validation cohort.

first to propose integrating IT and CITV into the RPA index for predicting survival in NSCLCBM patients treated with SRS, especially in those with negative for actionable molecular biomarkers.

Our study had some limitations. The present study is a single-center retrospective cohort with a relatively small sample size. Due to follow-up data limitations, we didn't estimate the overall response rate (ORR), local control (LC), or progression-free survival (PFS). However, we believe it shouldn't affect our study outcome as OS is the gold standard endpoint to estimate treatment efficacy. Moreover, several studies previously reported pseudoprogression and abscopal effect in patients who received combined IT and SRS, which makes ORR, LC, and PFS less significant. Over and above, in the real-world setting, patients may undergo multiple rounds of SRS and IT, which can be problematic in dividing patients into groups and may introduce selection bias. Our results might be confounded by other treatment modalities introduced at any time during cancer care. Furthermore, our nomogram was developed based on the training cohort, which was validated with an internal validation cohort but not with an external validation cohort. Further multi-center-based external validation cohort is needed.

Despite these shortcomings inherent to a retrospective study, prolonged OS was evident in patients treated with combined SRS and IT. Receipt of IT post-SRS was associated with better median OS than those who received IT concurrently or before SRS. The adverse events of combined IT and SRS were manageable. Incorporating IT and CITV into the RPA index could augment its survival prediction value in NSCLCBM patients treated with SRS, predominantly in wild-type.

Data availability statement

The raw data supporting the conclusions of this article will be made available by the authors, without undue reservation.

Ethics statement

The studies involving human participants were reviewed and approved by Guangdong Sanjiu Brain Hospital ethical committee. Written informed consent for participation was not required for this study in accordance with the national legislation and the institutional requirements.

Author contributions

Conceptualization: SB, MX, and LC. Methodology: SB, LW, MX, LC, WH, JZ, and ML. Formal analysis and investigation: SB, LW, PZ, MY, YL, HW, YY, XC, RL, GJ, and YG. Writing-original draft preparation: SB. Writing-review and editing: SB, LW, MX, and LC. Supervision: MX and LC. All authors contributed to the article and approved the submitted version.

Funding

This study was supported by the National Natural Science Foundation of China (No. 81774376).

Acknowledgments

We thank all the investigators who contributed to our study.

Conflict of interest

The authors declare that the research was conducted in the absence of any commercial or financial relationships that could be construed as a potential conflict of interest.

Publisher's note

All claims expressed in this article are solely those of the authors and do not necessarily represent those of their affiliated organizations, or those of the publisher, the editors and the reviewers. Any product that may be evaluated in this article, or claim that may be made by its manufacturer, is not guaranteed or endorsed by the publisher.

References

1. Basumallik N, Agarwal M. *Small cell lung cancer*. Treasure Island (FL: StatPearls (2022).

2. Lin X, DeAngelis LM. Treatment of brain metastases. *J Clin Oncol* (2015) 33 (30):3475–84. doi: 10.1200/JCO.2015.60.9503

3. Achrol AS, Rennert RC, Anders C, Soffietti R, Ahluwalia MS, Nayak L, et al. Brain metastases. *Nat Rev Dis Primers* (2019) 5(1):5. doi: 10.1038/s41572-018-0055-y

4. Cagney DN, Martin AM, Catalano PJ, Redig AJ, Lin NU, Lee EQ, et al. Incidence and prognosis of patients with brain metastases at diagnosis of systemic malignancy: a population-based study. *Neuro Oncol* (2017) 19(11):1511–21. doi: 10.1093/neuonc/nox077

5. Davis FG, Dolecek TA, McCarthy BJ, Villano JL. Toward determining the lifetime occurrence of metastatic brain tumors estimated from 2007 united states cancer incidence data. *Neuro Oncol* (2012) 14(9):1171–7. doi: 10.1093/neuonc/nos152

6. Rathi S, Griffith JI, Zhang W, Zhang W, Oh JH, Talele S, et al. The influence of the blood-brain barrier in the treatment of brain tumours. *J Intern Med* (2022) 292(1):3–30. doi: 10.1111/joim.13440

7. Vogelbaum MA, Brown PD, Messersmith H, Brastianos PK, Burri S, Cahill D, et al. Treatment for brain metastases: ASCO-SNO-ASTRO guideline. *J Clin Oncol* (2022) 40(5):492–516. doi: 10.1200/JCO.21.02314

8. Yamamoto M, Serizawa T, Shuto T, Akabane A, Higuchi Y, Kawagishi J, et al. Stereotactic radiosurgery for patients with multiple brain metastases (JLGK0901): a multi-institutional prospective observational study. *Lancet Oncol* (2014) 15(4):387–95. doi: 10.1016/S1470-2045(14)70061-0

9. Yamamoto M, Kawabe T, Sato Y, Higuchi Y, Nariai T, Watanabe S, et al. Stereotactic radiosurgery for patients with multiple brain metastases: a case-matched study comparing treatment results for patients with 2-9 versus 10 or more tumors. *J Neurosurg* (2014) 121 Suppl:16–25. doi: 10.3171/2014.8.GKS141421

10. Shuto T, Akabane A, Yamamoto M, Serizawa T, Higuchi Y, Sato Y, et al. Multiinstitutional prospective observational study of stereotactic radiosurgery for patients with multiple brain metastases from non-small cell lung cancer (JLGK0901 study-NSCLC). *J Neurosurg* (2018) 129(Suppl1):86–94. doi: 10.3171/2018.7.GKS181378

11. Haslam A, Gill J, Prasad V. Estimation of the percentage of US patients with cancer who are eligible for immune checkpoint inhibitor drugs. *JAMA Netw Open* (2020) 3(3):e200423. doi: 10.1001/jamanetworkopen.2020.0423

12. Gandhi L, Rodriguez-Abreu D, Gadgeel S, Esteban E, Felip E, De Angelis F, et al. Pembrolizumab plus chemotherapy in metastatic non-Small-Cell lung cancer. *N Engl J Med* (2018) 378(22):2078–92. doi: 10.1056/NEJMoa1801005

13. Brahmer J, Reckamp KL, Baas P, Crino L, Eberhardt WE, Poddubskaya E, et al. Nivolumab versus docetaxel in advanced squamous-cell non-Small-Cell lung cancer. *N Engl J Med* (2015) 373(2):123–35. doi: 10.1056/NEJMoa1504627

14. Borghaei H, Paz-Ares L, Horn L, Spigel DR, Steins M, Ready NE, et al. Nivolumab versus docetaxel in advanced nonsquamous non-Small-Cell lung cancer. *N Engl J Med* (2015) 373(17):1627–39. doi: 10.1056/NEJMoa1507643

15. Herbst RS, Baas P, Kim DW, Felip E, Perez-Gracia JL, Han JY, et al. Pembrolizumab versus docetaxel for previously treated, PD-L1-positive, advanced non-small-cell lung cancer (KEYNOTE-010): a randomised controlled trial. *Lancet* (2016) 387(10027):1540–50. doi: 10.1016/S0140-6736(15)01281-7

16. Gaspar L, Scott C, Rotman M, Asbell S, Phillips T, Wasserman T, et al. Recursive partitioning analysis (RPA) of prognostic factors in three radiation therapy oncology group (RTOG) brain metastases trials. *Int J Radiat Oncol Biol Phys* (1997) 37(4):745–51. doi: 10.1016/S0360-3016(96)00619-0

17. Yamamoto M, Serizawa T, Sato Y, Kawabe T, Higuchi Y, Nagano O, et al. Validity of two recently-proposed prognostic grading indices for lung, gastro-intestinal, breast and renal cell cancer patients with radiosurgically-treated brain metastases. *J Neurooncol* (2013) 111(3):327–35. doi: 10.1007/s11060-012-1019-9

18. Lorenzoni J, Devriendt D, Massager N, David P, Ruiz S, Vanderlinden B, et al. Radiosurgery for treatment of brain metastases: estimation of patient eligibility using three stratification systems. *Int J Radiat Oncol Biol Phys* (2004) 60(1):218–24. doi: 10.1016/j.ijrobp.2004.02.017

19. Joshi RS, Hirshman BR, Ali MA, Alattar A, Carroll K, Nagano O, et al. Prognostic importance of cumulative intracranial tumor volume in patients with gastrointestinal brain metastasis treated with stereotactic radiosurgery. *World Neurosurg* (2019) 121:e747–e54. doi: 10.1016/j.wneu.2018.09.209

20. Hirshman BR, Wilson BR, Ali MA, Schupper AJ, Proudfoot JA, Goetsch SJ, et al. Cumulative intracranial tumor volume augments the prognostic value of diagnosis-specific graded prognostic assessment model for survival in patients with melanoma cerebral metastases. *Neurosurgery* (2018) 83(2):237–44. doi: 10.1093/neuros/nyx380

21. Ali MA, Hirshman BR, Wilson B, Schupper AJ, Joshi R, Proudfoot JA, et al. Improving the prognostic value of disease-specific graded prognostic assessment model for renal cell carcinoma by incorporation of cumulative intracranial tumor volume. *World Neurosurg* (2017) 108:151–6. doi: 10.1016/j.wneu.2017.07.109

22. Gibney GT, Weiner LM, Atkins MB. Predictive biomarkers for checkpoint inhibitor-based immunotherapy. *Lancet Oncol* (2016) 17(12):e542–e51. doi: 10.1016/S1470-2045(16)30406-5

23. Patel KR, Martinez A, Stahl JM, Logan SJ, Perricone AJ, Ferris MJ, et al. Increase in PD-L1 expression after pre-operative radiotherapy for soft tissue sarcoma. *Oncoimmunology* (2018) 7(7):e1442168. doi: 10.1080/2162402X.2018.1442168

24. Sakai H, Takeda M, Sakai K, Nakamura Y, Ito A, Hayashi H, et al. Impact of cytotoxic chemotherapy on PD-L1 expression in patients with non-small cell lung cancer negative for EGFR mutation and ALK fusion. *Lung Cancer* (2019) 127:59–65. doi: 10.1016/j.lungcan.2018.11.025

25. Schapira E, Hubbeling H, Yeap BY, Mehan WAJr., Shaw AT, Oh K, et al. Improved overall survival and locoregional disease control with concurrent PD-1 pathway inhibitors and stereotactic radiosurgery for lung cancer patients with brain metastases. *Int J Radiat Oncol Biol Phys* (2018) 101(3):624–9. doi: 10.1016/j.ijrobp.2018.02.175

26. Ahmed KA, Kim S, Arrington J, Naghavi AO, Dilling TJ, Creelan BC, et al. Outcomes targeting the PD-1/PD-L1 axis in conjunction with stereotactic radiation for patients with non-small cell lung cancer brain metastases. *J Neurooncol* (2017) 133 (2):331–8. doi: 10.1007/s11060-017-2437-5

27. Kwon M, Jung H, Nam GH, Kim IS. The right timing, right combination, right sequence, and right delivery for cancer immunotherapy. *J Control Release* (2021) 331:321–34. doi: 10.1016/j.jconrel.2021.01.009

28. Yuan H, Gaber MW, Boyd K, Wilson CM, Kiani MF, Merchant TE. Effects of fractionated radiation on the brain vasculature in a murine model: blood-brain barrier permeability, astrocyte proliferation, and ultrastructural changes. *Int J Radiat Oncol Biol Phys* (2006) 66(3):860–6. doi: 10.1016/j.ijrobp.2006.06.043

29. Teng F, Tsien CI, Lawrence TS, Cao Y. Blood-tumor barrier opening changes in brain metastases from pre to one-month post radiation therapy. *Radiother Oncol* (2017) 125(1):89–93. doi: 10.1016/j.radonc.2017.08.006

30. Lim WH, Choi SH, Yoo RE, Kang KM, Yun TJ, Kim JH, et al. Does radiation therapy increase gadolinium accumulation in the brain?: quantitative analysis of T1 shortening using R1 relaxometry in glioblastoma multiforme patients. *PLoS One* (2018) 13(2):e0192838. doi: 10.1371/journal.pone.0192838

31. McLaughlin M, Patin EC, Pedersen M, Wilkins A, Dillon MT, Melcher AA, et al. Inflammatory microenvironment remodelling by tumour cells after radiotherapy. *Nat Rev Cancer* (2020) 20(4):203–17. doi: 10.1038/s41568-020-0246-1

32. Aliru ML, Schoenhals JE, Venkatesulu BP, Anderson CC, Barsoumian HB, Younes AI, et al. Radiation therapy and immunotherapy: what is the optimal timing or sequencing? *Immunotherapy* (2018) 10(4):299–316. doi: 10.2217/imt-2017-0082

33. Pfirschke C, Engblom C, Rickelt S, Cortez-Retamozo V, Garris C, Pucci F, et al. Immunogenic chemotherapy sensitizes tumors to checkpoint blockade therapy. *Immunity* (2016) 44(2):343–54. doi: 10.1016/j.immuni.2015.11.024

34. Abdulhaleem M, Johnston H, D'Agostino RJr., Lanier C, LeCompte M, Cramer CK, et al. Local control outcomes for combination of stereotactic radiosurgery and immunotherapy for non-small cell lung cancer brain metastases. *J Neurooncol* (2022) 157(1):101–7. doi: 10.1007/s11060-022-03951-7

35. Lanier CM, Hughes R, Ahmed T, LeCompte M, Masters AH, Petty WJ, et al. Immunotherapy is associated with improved survival and decreased neurologic death after SRS for brain metastases from lung and melanoma primaries. *Neurooncol Pract* (2019) 6(5):402–9. doi: 10.1093/nop/npz004

36. Chen L, Douglass J, Kleinberg L, Ye X, Marciscano AE, Forde PM, et al. Concurrent immune checkpoint inhibitors and stereotactic radiosurgery for brain metastases in non-small cell lung cancer, melanoma, and renal cell carcinoma. *Int J Radiat Oncol Biol Phys* (2018) 100(4):916–25. doi: 10.1016/j.ijrobp.2017.11.041

37. Enright TL, Witt JS, Burr AR, Yadav P, Leal T, Baschnagel AM. Combined immunotherapy and stereotactic radiotherapy improves neurologic outcomes in patients with non-small-cell lung cancer brain metastases. *Clin Lung Cancer* (2021) 22(2):110–9. doi: 10.1016/j.cllc.2020.10.014

38. Stokes WA, Binder DC, Jones BL, Oweida AJ, Liu AK, Rusthoven CG, et al. Impact of immunotherapy among patients with melanoma brain metastases managed with radiotherapy. *J Neuroimmunol* (2017) 313:118–22. doi: 10.1016/j.jneuroim.2017.10.006

39. Diao K, Bian SX, Routman DM, Yu C, Ye JC, Wagle NA, et al. Stereotactic radiosurgery and ipilimumab for patients with melanoma brain metastases: clinical outcomes and toxicity. *J Neurooncol* (2018) 139(2):421–9. doi: 10.1007/s11060-018-2880-y

40. Knisely JP, Yu JB, Flanigan J, Sznol M, Kluger HM, Chiang VL. Radiosurgery for melanoma brain metastases in the ipilimumab era and the possibility of longer survival. *J Neurosurg* (2012) 117(2):227–33. doi: 10.3171/2012.5.JNS111929

41. Gabani P, Fischer-Valuck BW, Johanns TM, Hernandez-Aya LF, Keller JW, Rich KM, et al. Stereotactic radiosurgery and immunotherapy in melanoma brain metastases: Patterns of care and treatment outcomes. *Radiother Oncol* (2018) 128 (2):266–73. doi: 10.1016/j.radonc.2018.06.017

42. Kaidar-Person O, Zagar TM, Deal A, Moschos SJ, Ewend MG, Sasaki-Adams D, et al. The incidence of radiation necrosis following stereotactic radiotherapy for melanoma brain metastases: the potential impact of immunotherapy. *Anticancer Drugs* (2017) 28(6):669–75. doi: 10.1097/CAD.0000000000000497

43. Wegner RE AS, Hasan S, White RJ, Finley G, Monga D, Colonias A, et al. Time from stereotactic radiotherapy to immunotherapy is a predictor for outcome in stage IV non-small cell lung cancer. *J Immunol Sci* (2019) 3(2):6–13. doi: 10.29245/2578-3009/2019/2.1171

44. Shaverdian N, Lisberg AE, Bornazyan K, Veruttipong D, Goldman JW, Formenti SC, et al. Previous radiotherapy and the clinical activity and toxicity of pembrolizumab in the treatment of non-small-cell lung cancer: a secondary analysis of the KEYNOTE-001 phase 1 trial. *Lancet Oncol* (2017) 18(7):895–903. doi: 10.1016/S1470-2045(17)30380-7

45. Woody S, Hegde A, Arastu H, Peach MS, Sharma N, Walker P, et al. Survival is worse in patients completing immunotherapy prior to SBRT/SRS compared to those receiving it concurrently or after. *Front Oncol* (2022) 12:785350. doi: 10.3389/fonc.2022.785350

46. Cohen-Inbar O, Shih HH, Xu Z, Schlesinger D, Sheehan JP. The effect of timing of stereotactic radiosurgery treatment of melanoma brain metastases treated with ipilimumab. *J Neurosurg* (2017) 127(5):1007–14. doi: 10.3171/2016.9.JNS161585

47. Koenig JL, Shi S, Sborov K, Gensheimer MF, Li G, Nagpal S, et al. Adverse radiation effect and disease control in patients undergoing stereotactic radiosurgery and immune checkpoint inhibitor therapy for brain metastases. *World Neurosurg* (2019) 126:e1399–e411. doi: 10.1016/j.wneu.2019.03.110

48. Sperduto PW, Berkey B, Gaspar LE, Mehta M, Curran W. A new prognostic index and comparison to three other indices for patients with brain metastases: an analysis of 1,960 patients in the RTOG database. *Int J Radiat Oncol Biol Phys* (2008) 70 (2):510–4. doi: 10.1016/j.ijrobp.2007.06.074

frontiers | Frontiers in Immunology

TYPE Original Research
PUBLISHED 27 April 2023
DOI 10.3389/fimmu.2023.1145441

Check for updates

OPEN ACCESS

EDITED BY
Feng-Ming (Spring) Kong,
The University of Hong Kong, Hong Kong SAR, China

REVIEWED BY
Gerardo Ferrer,
Josep Carreras Leukaemia Research Institute (IJC), Spain
Maysaloun Merhi,
Hamad Medical Corporation, Qatar

*CORRESPONDENCE
Fankai Meng
doctormeng@163.com
Jue Wang
jeff_wangjue@hotmail.com
Yong You
youyong@hust.edu.cn

†These authors have contributed equally to this work and share first authorship

‡These authors have contributed equally to this work and share last authorship

RECEIVED 16 January 2023
ACCEPTED 17 April 2023
PUBLISHED 27 April 2023

CITATION
Tang L, Kong Y, Wang H, Zou P, Sun T, Liu Y, Zhang J, Jin N, Mao H, Zhu X, Wang J, Meng F and You Y (2023) Demethylating therapy increases cytotoxicity of CD44v6 CAR-T cells against acute myeloid leukemia.
Front. Immunol. 14:1145441.
doi: 10.3389/fimmu.2023.1145441

COPYRIGHT
© 2023 Tang, Kong, Wang, Zou, Sun, Liu, Zhang, Jin, Mao, Zhu, Wang, Meng and You. This is an open-access article distributed under the terms of the Creative Commons Attribution License (CC BY). The use, distribution or reproduction in other forums is permitted, provided the original author(s) and the copyright owner(s) are credited and that the original publication in this journal is cited, in accordance with accepted academic practice. No use, distribution or reproduction is permitted which does not comply with these terms.

Demethylating therapy increases cytotoxicity of CD44v6 CAR-T cells against acute myeloid leukemia

Ling Tang[1†], Yingjie Kong[1†], Haobing Wang[1], Ping Zou[1], Ting Sun[2], Ying Liu[3], Juan Zhang[3], Na Jin[4], Hanwen Mao[5], Xiaojian Zhu[2], Jue Wang[2*‡], Fankai Meng[2*‡] and Yong You[1*‡]

[1]Institute of Hematology, Union Hospital, Tongji Medical College, Huazhong University of Science and Technology, Wuhan, China, [2]Department of Hematology, Tongji Hospital, Tongji Medical College, Huazhong University of Science and Technology, Wuhan, China, [3]Department of R&D, Wuhan Biological Sample Bank Co., Ltd., Wuhan, China, [4]Department of Oncology, The First People's Hospital of Jiangxia District, Wuhan City and Union Jiangnan Hospital, Huazhong University of Science and Technology, Wuhan, China, [5]Oncology Department, Wuhan Dongxihu District People's Hospital, Wuhan, China

Background: CD44v6 chimeric antigen receptor T (CD44v6 CAR-T) cells demonstrate strong anti-tumor ability and safety in acute myeloid leukemia (AML). However, the expression of CD44v6 on T cells leads to transient fratricide and exhaustion of CD44v6 CAR-T cells, which affect the application of CD44v6 CAR-T. The exhaustion and function of T cells and CD44v6 expression of AML cells are associated with DNA methylation. Hypomethylating agents (HAMs) decitabine (Dec) and azacitidine (Aza) have been widely used to treat AML. Therefore, there may be synergy between CD44v6 CAR-T cells and HAMs in the treatment of AML.

Methods: CD44v6 CAR-T cells pretreated with Dec or Aza were co-cultured with CD44v6+ AML cells. Dec or aza pretreated AML cells were co-cultured with CD44v6 CAR-T cells. The cytotoxicity, exhaustion, differentiation and transduction efficiency of CAR-T cells, and CD44v6 expression and apoptosis in AML cells were detected by flow cytometry. The subcutaneous tumor models were used to evaluate the anti-tumor effect of CD44v6 CAR-T cells combined with Dec *in vivo*. The effects of Dec or Aza on gene expression profile of CD44v6 CAR-T cells were analyzed by RNA-seq.

Results: Our results revealed that Dec and Aza improved the function of CD44v6 CAR-T cells through increasing the absolute output of CAR+ cells and persistence, promoting activation and memory phenotype of CD44v6 CAR-T cells, and Dec had a more pronounced effect. Dec and Aza promoted the apoptosis of AML cells, particularly with DNA methyltransferase 3A (DNMT3A) mutation. Dec and Aza also enhanced the CD44v6 CAR-T response to AML by

upregulating CD44v6 expression of AML cells regardless of FMS-like tyrosine kinase 3 (FLT3) or DNMT3A mutations. The combination of Dec or Aza pretreated CD44v6 CAR-T with pretreated AML cells demonstrated the most potent anti-tumor ability against AML.

Conclusion: Dec or Aza in combination with CD44v6 CAR-T cells is a promising combination therapy for AML patients.

KEYWORDS

decitabine, azacitidine, CD44v6 chimeric antigen receptor-T cells, acute myeloid leukemia, demethylating therapy

Highlights

1. Decitabine and azacitidine pretreatment of CD44v6 CAR-T enhanced the anti-tumor ability of CD44v6 CAR-T against AML.
2. Decitabine and azacitidine enhanced the CD44v6 CAR-T response to AML by upregulating CD44v6 expression of AML cells.
3. Decitabine promoted stronger cytotoxicity of CD44v6 CAR-T cells towards AML compared to azacitidine.

Introduction

Although patients with acute myeloid leukemia (AML) can achieve complete remission after standardized induction chemotherapy or allogeneic hematopoieticstem cell transplantation, most patients eventually relapse and have poor outcomes (1, 2).

Monoclonal antibodies, such as those targeting FMS-like tyrosine kinase 3 (FLT3), have increased remission rates in AML patients, while relapse and acquired drug resistance remain a major challenge (3, 4). In the past few years, several chimeric antigen receptor T (CAR-T) cells therapies have been explored to treat AML, including CD33, CD123, FLT3, and CLL-1 CAR-Ts (5–8). However, these antigens are also found in hematopoietic stem cells and progenitor cells, restricting their development.

CD44 isoform variant 6 (CD44v6) was highly expressed in AML blasts in contrast to hematopoietic stem cells and progenitor cells, making CD44v6 an optimal target for AML (9–11). Our previous study revealed that FLT3 or DNA methyltransferase 3A (DNMT3A) mutant AML cells overexpressed CD44v6 and CD44v6 CAR-T cells are significantly effective against them (9). CAR-T cells may become dysfunctional, expand and persist poorly due to inherent T-cell deficiencies (12, 13). T cells expressing CD44v6 resulted in transient fratricide and exhaustion of CD44v6 CAR-T (9). Therefore, it is necessary to explore effective strategies for improving CD44v6 CAR-T applications.

Our previous study revealed that FLT3 or DNMT3A mutations decreased CD44 promoter methylation, leading to CD44v6 overexpression (9), suggesting that CD44v6 expression was related to DNA methylation levels. Other studies have also shown that hypomethylating agents (HMAs) decitabine (Dec) or azacitidine (Aza) enhance immunotherapy by upregulating the expression of tumor-associated antigen in cancer cells (14–18). In recent years, Dec and Aza have been widely used to treat refractory AML patients and significantly improve the survival of patients (19–21). Therefore, we hypothesized that the up-regulation of CD44v6 expression by Dec or Aza may enhance the cytotoxicity of CD44v6 CAR-T against tumor cells. Furthermore, DNMT3a-mediated DNA methylation induces T cell exhaustion (22), as well as affecting T cell differentiation and activity (23–25). In T-cell studies with Dec or Aza, DNA methylation-induced exhaustion was reversed and the anti-tumor response was enhanced (26). These data suggest a potential synergy between CD44v6 CAR-T therapy and HMAs, both of which have shown significant efficacy in AML.

Hence, we proposed that CD44v6 CAR-T in combination with HMAs is a more prospective therapy for AML. Here, we evaluated the influence of Dec and Aza on CD44v6 CAR-T, AML cells, and responses of CD44v6 CAR-T cells to AML. We additionally compared the difference in the effects of Dec and Aza in this combined treatment.

Abbreviations: CD44v6, CD44 isoform variant 6; CAR-T, chimeric antigen receptor T; AML, acute myeloid leukemia; HAMs, hypomethylating agents; Dec, decitabine; Aza, azacitidine; DNMT3A, DNA methyltransferase 3A; FLT3, FMS-like tyrosine kinase 3; FBS, fetal bovine serum; NT, non-transduced T; E: T, effector cells: target cells; CBA, cytometric bead array; PBS, phosphate buffered saline; IVC, individually ventilated cage; SPF, specific pathogen-free; Luc^+ MV4-11, luciferase-expressing MV4-11; dCAR-T, Dec pretreated CD44v6 CAR-T; aCAR-T, Aza pretreated CD44v6 CAR-T; BLI, bioluminescence imaging; DEGs, differentially expressed genes; KEGG, Kyoto Encyclopedia of Genes and Genomes; GO, Gene Ontology; BP, biological process; Teff, effector T cells; Tem, effector memory T cells.

Materials and methods

Cell culture

The China Center for Type Culture Collection provided human AML cell lines MV4-11 and SKM-1. The DNMT3A R882H (CGC>CAC) mutant clones of SKM-1 cells were constructed using lentiviral transduction, named SKM-1-DNMT3A-SC2 and SKM-1-DNMT3A-SC3, respectively. We used RPMI 1640 (Gibco) with 10% fetal bovine serum (FBS, Gibco) to culture AML cells and X-VIVO 15 (Lonza, USA) with 5% FBS and 200 U/mL recombinant human IL-2 (PeproTech, USA) to culture T cells.

Construction of CD44v6 CAR-T

CD3/CD28 beads (Miltenyi Biotech, Cat# 130-091-441) were used to activate CD3+ T cells isolated from peripheral blood of healthy donors, from whom the informed consent was obtained. After two days, CAR lentivirus carrying anti-CD44v6-scFv-CD8-4-1BB-CD3ζ was added to activated T cells cultured in a density of 2×10^6/mL. The multiplicity of infection was 3. Thirty min were spent centrifuging the mixture at 800 × *g*. After 24 h, transduction was terminated by replacing the medium with fresh medium.

Flow cytometry analysis

The CAR-expressing T cells were identified by incubating with Biotinylated Protein L (GeneScript, Cat# M00097) at 4°C for 45 min and then washing them off before incubating with streptavidin-FITC (BD Biosciences, Cat# 554060) for 15 min in the dark. To analyze apoptosis, Annexin V-FITC/PI kit (BD Biosciences, Cat# 556547) was used to detect Dec (Selleck, NSC 127716) or Aza (Sigma, A2385) treated CAR-T cells or tumor cells. Assays involving cells surface antigens were performed in the dark at 4°C for 30 min with the corresponding antibodies. Antibodies (BD Biosciences) TIM3-PE (Cat# 563422) and CD69-BV421 (Cat# 562884) were applied to test the exhaustion and activation of CD44v6 CAR-T. CD4-BB700 (Cat# 566392), CD8-PE-cy7 (Cat# 557746), CCR7-Alexa 647 (Cat#557734), CD45RA-PE (Cat#555489) or CD45RA-BV421 (Cat# 562885) were utilized for detecting the phenotype of non-transduced T (NT) or CAR-T cells. CD44v6-PE (Cat# 566803) was applied to test the CD44v6 expression in AML cells. The samples were all detected by BD LSRFortessa X-20 flow cytometry, and these data were analyzed with FlowJo_V10.4 software.

Number of CAR+ cells

On day 6 after transfection, CD44v6 CAR-T (1×10^5) cells were treated with Dec (0.05, 0.1 μM) or Aza (0.5, 1 μM) for 6 days, the number of CD44v6 CAR-T cells in the untreated and drug-treated groups was counted under the microscope. We calculated the absolute number of CAR+ based on the counts of CD44v6 CAR-T cells and the percentage of CAR+ detected by flow cytometry.

Cytotoxicity analysis

A 10:1 ratio of effector cells: target cells (E: T) was used in co-culturing NT or CAR-T cells pretreated with Dec (0.05, 0.1 μM) and Aza (0.5, 1 μM) for 6 days with CFSE-labeled (BD Biosciences, Cat#565082) CD44v6$^+$ MV4-11 cells for 24 h. The same E: T ratio and co-culture time were used in incubating Dec 1 μM or Aza 1 μM pretreated AML cells with CD44v6 CAR-T cells. Dead cells were detected *via* flow cytometry using Fixable Viability Kit (Biolegend, Cat#423102) staining. The percentage of dead CFSE-positive cells was used to evaluate the cytotoxicity.

Degranulation assay

A 1: 1 ratio was used in co-culturing NT or CAR-T cells pretreated with Dec (0.05, 0.1μM) or Aza (0.5, 1μM) with MV4-11 cells for 16 h. Meanwhile CD107a-BV421 (BD Biosciences, Cat#562623) and protein transport inhibitor (BD Biosciences, Cat#554724) were added to the culture medium. After cells collection, Antibodies CD3-APC/Cy7 (Biolegend, Cat#300318), CD4-BB700 (BD Biosciences, Cat# 566392), and CD8-BB515 (BD Biosciences, Cat# 564526) were applied to stain the cells.

Cytokine release analysis

CD44v6 CAR-T cells (2×10^5) pretreated with Dec (0.05, 0.1 μM) and Aza (0.5, 1 μM) for 6 days were co-cultured with 2×10^5 MV4-11 cells in 100ul RPMI-1640 complete medium for 24 h. BD cytometric bead array (CBA) (BD Biosciences, Cat# 551809) was used to measure cytokines in supernatants.

Repetitive stimulus analysis

MV4-11 cells treated with 10 μg/ml Mitomycin-C (Selleck, S8146) for 2 h were used to stimulate CD44v6 CAR-T cells pretreated with Dec 0.1 μM or Aza 1 μM. The E: T ratio and stimulation time were the same in each round. A round of stimulation was followed by staining CAR-T cells with trypan-blue and counting them under the microscope. CAR-T cells were isolated from MV4-11 cells that had been lysed. All CAR-T cells obtained in the last round were used as the initial cells for the next round of stimulation. The proliferation fold change is the ratio of cell counts after different rounds of stimulation compared to cell counts before stimulation.

Animal experiments

Vital River Laboratory Animal Technology (Beijing, China) provided us with male five-week-old BALB/c-nu mice. Nanjing Biomedical Research Institute of Nanjing University (Nanjing, China) provided us with male five-week-old NOD-Prkdc^{em26Cd52}il2rg^{em26Cd22}/Nju (NCG) mice. These mice were housed in the individually ventilated cage (IVC) of the specific pathogen-free (SPF) environment at the Experimental Animal Center of Huazhong University of Science and Technology. All animal experiments were approved by the Institutional Animal Care and Use Committee of Huazhong University of Science and Technology.

Subcutaneous xenografted of 5×10^6 luciferase-expressing MV4-11 (Luc$^+$ MV4-11) cells were constructed in BALB/c-nu mice. These mice were randomly divided into 6 groups. Mice in the NT, CAR-T and Dec-pretreated-CD44v6 CAR-T (dCAR-T) groups were all intraperitoneally injected with 100 µl phosphate-buffered saline (PBS) on days 7, 8, 9, 14, 15, and 16, then intratumorally treated with NT, CAR-T or dCAR-T cells (5×10^6) on days 10 and 17, respectively. Mice in the Dec, Dec+CAR-T and Dec+dCAR-T groups were all intraperitoneally injected with Dec 1 mg/kg on days 7, 8, 9, 14, 15, and 16, then intratumorally injected with 200 µl PBS, 5×10^6 CAR-T or dCAR-T cells on days 10 and 17, respectively. An assessment of tumor burdens in mice was performed on days 7, 14, 21, and 28 by bioluminescence imaging (BLI). After the fourth BLI evaluation, the mice were humanely euthanized.

In NCG mice, MV4-11 cells (1×10^7) and CD44v6 CAR-T cells (1×10^7) pretreated with or without Dec or Aza were injected intravenically into NCG mice on day 0. After 3 weeks, peripheral blood of NCG mice was collected, and the percentage of CD44v6 CAR-T cells in peripheral blood was detected by flow cytometry.

RNA-seq analysis

CD44v6 CAR-T cells from three healthy donors were treated with Dec or Aza for 6 days for RNA-seq analysis. Total RNA was isolated using the standard Trizol protocol. The RNA quality was determined with the Nano Drop and Agilent 2100 Bioanalyzer (Thermo Fisher Scientific, USA).The libraries for RNA-seq were sequenced on the DNBSEQ platform (BGI Genomics, Shenzhen, China). After RNA-seq, raw reads containing sequencing adapters with more than 5% unknown base or more than 20% low-quality base were removed using SOAPnuke software to obtain clean reads. Clean reads were aligned to the Homo-sapines reference genome (GRCh38.p13) sequence, taking the comparison ratio and the distribution of the reference sequence as conditions for further analysis. Quantitative analysis of gene expression levels in different samples was performed using RSEM software. Briefly, clean reads obtained from RNA-seq were mapped onto reference full-length transcripts using the Bowtie2 software. Subsequently, the expression level of each sample was calculated using RSEM software, and the read counts were normalized using fragment per kilobase of transcript per million fragments mapped (FPKM). In order to improve the accuracy of differentially expression genes (DEGs), we define genes with fold change >2 and Q-value ≤ 0.001, which are screened as significant DEGs. The R package pheatmap was used to perform hierarchical clustering analysis on the union set differential genes. DEGs were mapped to GO and KEGG databases to obtain annotated information by Phyper based on a hypergeometric test for further enrichment and classification analyses. The P values were corrected to Q values with a threshold Q value of ≤ 0.05 using a Bonferroni correction. And the RNA-seq data have been made publicly available in SRA under the accession number SRP417784.

Statistical analysis

Results were expressed as mean ± SD and analyzed using GraphPad Prism 7. Student's t test was used to compare two groups, and one-way or two-way ANOVA with Tukey's multiple comparison test was used for comparing multiple groups. The p values <0.05 were considered statistically significant, and "ns" indicated no significance ($p > 0.05$).

Results

Decitabine and azacitidine increase the transduction efficiency and persistence of CD44v6 CAR-T

Six days after transduction, Dec (0.05-1 µM) or Aza (0.1-10 µM) was added to CD44v6 CAR-T cells for 3 or 6 days. Dec and Aza were freshly added once a day at different final concentrations. Untreated CD44v6 CAR-T cells served as controls. Subsequently, we examined the proliferation, cytotoxicity, persistence, transduction efficiency, and apoptosis of CD44v6 CAR-T cells (Figure 1A). CAR-T cells proliferation was inhibited dose- and time- dependently by Dec or Aza (Figure 1B). To assess cytotoxicity, CD44v6 CAR-T cells received Dec (0.05, 0.1 µM) or Aza (0.5, 1 µM) treatment for 3 or 6 days before being co-cultured with MV4-11 cells. Cytotoxicity assay results showed that Dec 0.1 µM or Aza 1 µM treatment for 6 days significantly increased the cytotoxicity of CD44v6 CAR-T, which were not observed at treatment for 3 days (Figure 1C). Although we found that Dec and Aza slightly promoted CD44v6 CAR-T cell apoptosis (Figure S1A), Dec 0.1 µM and Aza 1 µM improved the transfection efficiency of CD44v6 CAR-T (Figure 1D) and increased the absolute number of CAR+ cells (Figure 1E). Therefore, we chose the drug concentration of Dec (0.05, 0.1 µM) and Aza (0.5, 1 µM), and the treatment time of 6 days for the subsequent experiments. In addition, repeated antigen stimulation experiments showed that CD44v6 CAR-T cells pretreated with Dec 0.1 µM or Aza 1 µM for 6 days showed accelerated expansion and enhanced persistence after three rounds of tumor cells stimulation (Figure 1F). The result that Dec or Aza enhanced the persistence of CD44v6 CAR-T cells was also confirmed *in vivo*. On day 0, MV4-11 cells (1×10^7) and CD44v6 CAR-T cells (1×10^7) pretreated with or without Dec or Aza were injected intravenically into NCG mice. After 3 weeks,

10.3389/fimmu.2023.1145441

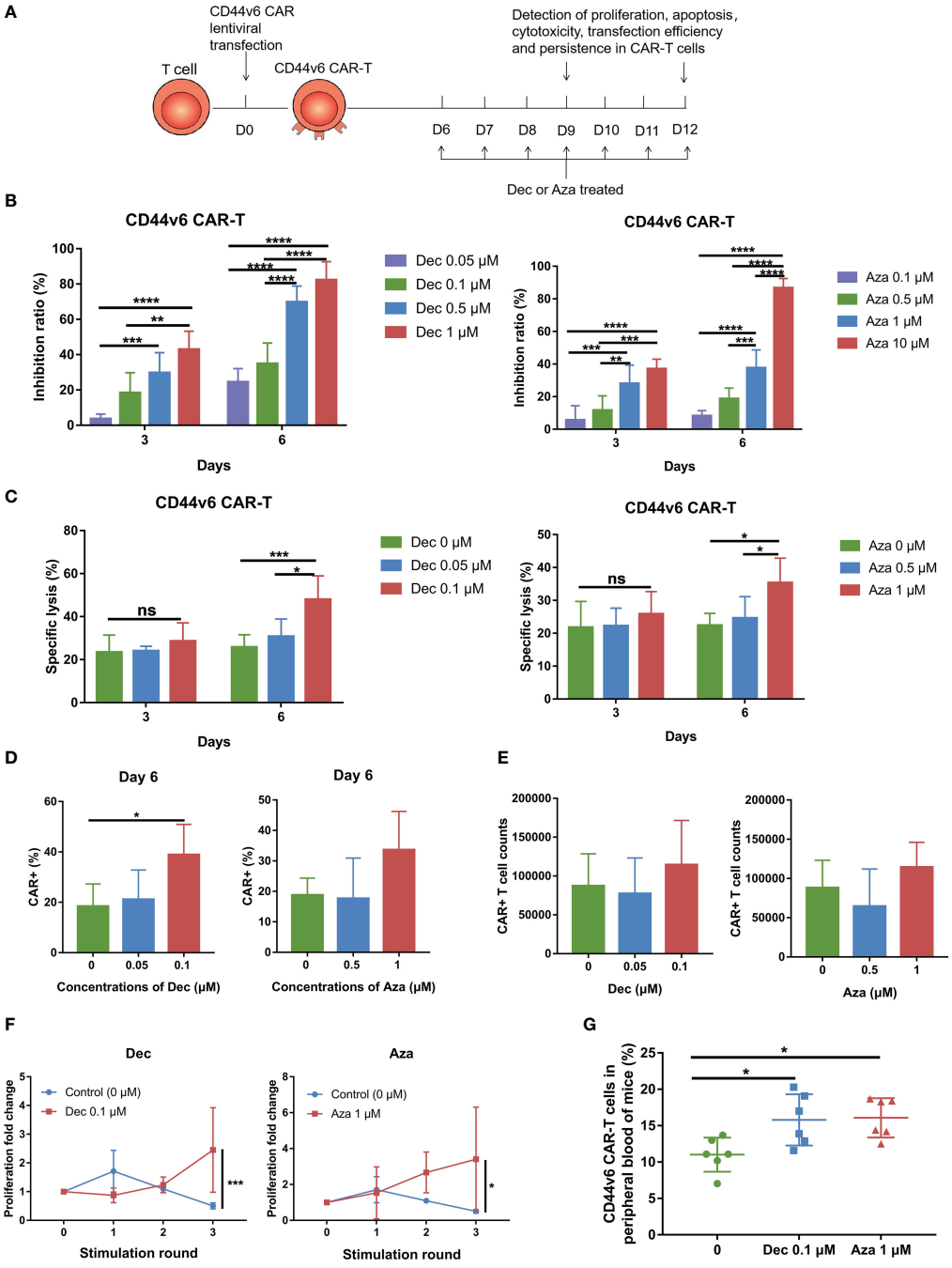

FIGURE 1
Dec and Aza treated CD44v6 CAR-T cells exhibit increased CAR+ cells and persistence. **(A)** Experimental design of CD44v6 CAR-T cells treated with Dec and Aza. **(B)** Inhibition ratio of CD44v6 CAR-T cells treated with various concentrations of Dec (left, n=6) and Aza (right, n=8) for 3 or 6 days. **(C)** Cytotoxicity of CD44v6 CAR-T cells treated with Dec (0.05, 0.1 μM) (left, n=6) and Aza (0.5, 1 μM) (right, n=5) for 3 or 6 days against MV4-11 cells in an E:T ratio of 10:1 for 24 h. **(D, E)** Percentage **(D)** and absolute number **(E)** of CAR+ cells in CD44v6 CAR-T cells treated with Dec (0.05, 0.1 μM) (n=4) and Aza (0.5, 1 μM) (n=5) for 6 days. **(F)** Proliferation fold of CD44v6 CAR-T cells treated with Dec 0.1uM and Aza 1uM for 6 days in response to repeated stimulation of MV4-11 cells (n=4). **(G)** CD44v6 CAR-T cells treated with or without Dec or Aza were injected intravenously into NCG mice simultaneously with MV4-11, and the percentage of CD44v6 CAR-T cells in peripheral blood was detected by flow cytometry 3 weeks later (n=6). CD44v6, CD44 isoform variant 6; CAR-T, chimeric antigen receptor T; Dec, decitabine; Aza, azacitidine. Data are depicted as the mean± SD. *p<.05; **p<.01; ***p<.001; ****p<.0001; ns, not significant.

peripheral blood of mice was collected to detect the percentage of CD44v6 CAR-T cells in peripheral blood. We found a higher percentage of Dec or Aza pretreated CD44v6 CAR-T than untreated CD44v6 CAR-T cells in mice (Figure 1G). These results suggested that Dec and Aza enhanced the function of CD44v6 CAR-T by increasing their transduction efficiency, absolute number of CAR+ cells and persistence. And CD44v6 CAR-T cells were more sensitive to Dec.

Decitabine and azacitidine promote activation and memory phenotype of CD44v6 CAR-T

It has been demonstrated that DNMT3A-mediated *de novo* DNA methylation program induces T cell exhaustion and negatively influences T cell differentiation and function (22–24). Our results showed that low-dose Dec and Aza inhibited DNMT3A mRNA expression in CD44v6 CAR-T cells (Figure S1B). Dec and Aza also inhibited the proliferation of NT cells which served as controls (Figure S1C). Flow cytometry results showed that Dec and Aza inhibited TIM3 expression and promoted LAG3 expression, but had no effect on PD-1 expression in CD44v6 CAR-T cells (Figures 2A, B).Although Dec or Aza had inconsistent effects on the exhaustion markers of CD44v6 CAR-T cells, Dec and Aza promoted the expression of CD69, an activation marker of CD44v6 CAR-T cells (Figure 2C). Dec- or Aza-treated NT or CD44v6 CAR-T cells had fewer effector T cells (Teff) and more effector memory T cells (Tem) compared to untreated NT and CD44v6 CAR-T cells (Figures 2D, E, S1D). These data indicated that Dec and Aza promoted activation and Tem differentiation of CD44v6 CAR-T.

Decitabine and azacitidine enhance the cytotoxicity of CD44v6 CAR-T

To assess cytotoxicity *in vitro*, CD44v6 CAR-T or NT cells received Dec (0.05, 0.1μM) or Aza (0.5, 1μM) treatment for 6 days before being co-cultured with MV4-11 cells. After 24 h, we found that Dec 0.1 μM and Aza 1 μM improved the cytotoxicity of CD44v6 CAR-T, but not in NT cells (Figures 3A, S2A). Compared to untreated CD44v6 CAR-T, Dec or Aza pretreated CD44v6 CAR-T cells expressed more CD107a (Figure 3B) and released more cytokines (Figures 3C, D, S2B, C). RNA-seq data also demonstrated that Dec and Aza upregulated the expression of multiple tumor necrosis factor and interleukin genes in CD44v6 CAR-T cells (Figure 3E). We then evaluated the anti-tumor capacity of Dec-pretreated-CD44v6 CAR-T (dCAR-T) within the body, based on the promotion of anti-tumor activity by Dec *in vitro*. Subcutaneous xenografted of 5×10^6 Luc^+ MV4-11 cells were constructed in BALB/c-nu mice, that were subsequently treated with 5×10^6 NT, CD44v6 CAR-T and dCAR-T cells on days 10 and 17. The tumor burden was assessed weekly using BLI (Figure 3F). BLI results showed that dCAR-T cells had the strongest effect in preventing tumor progression in all three groups (Figures 3G, H). According to these data, Dec and Aza promoted the anti-tumor activity of CD44v6 CAR-T cells both *in vitro* and *in vivo*.

Decitabine and azacitidine affect the transcriptome of CD44vv6 CAR-T cells

We performed RNA-seq to explore the transcriptome differences between Dec 0.1μM or Aza 1 μM treated CD44v6 CAR-T and untreated CD44v6 CAR-T. We found 825 and 450 differentially expressed genes (DEGs) in these two comparisons (Dec_CART vs. CART, and Aza_CART vs. CART), respectively (Figure 4A). The DEGs were significantly enriched in the Natural killer cell mediated cytotoxicity, Antigen processing and presentation, Cytokine-cytokine receptor interaction, and Chemokine signaling pathway, etc (Figure 4B). Further, GO BP enrichment results also showed that these DEGs involved immune response, cell adhesion, cell-cell signaling, and cell migration, etc (Figure 4C). Cytotoxicity-related genes such as *GZMB*, *NKG7*, *PRF1*, *CST7*, *CTSW*, *GNLY*, *GZMH*, *KIR3DL2*, *KIR2DL3*, and *KIR2DS4* were significantly upregulated in Dec- or Aza-treated CD44v6 CAR-T cells (Figure 4D). These RNA-seq results again demonstrated that Dec and Aza strengthened the function of CD44v6 CAR-T cells.

Decitabine and azacitidine promote CD44v6 expression in AML cells

Studies have shown that Dec and Aza can enhance immunotherapy by upregulating the expression of tumor-associated antigens on AML and other cancer cells [14-18]. We then investigated the effect of Dec and Aza on AML tumor cells. Dec and Aza were freshly added once a day at different final concentrations for 3 days. In our previous study, SKM-1-DNMT3A-SC2 and SKM-1-DNMT3A-SC3 are clones of DNMT3A-R882H mutant cells generated by lentiviral transduction of SKM-1 cells (9). Dec and Aza inhibited proliferation and promoted apoptosis of AML cell lines MV4-11, SKM-1, and DNMT3A mutant SKM-1 cells dose-dependently (Figures 5A, B, S3A, B). Dec specifically promoted the apoptosis of DNMT3A mutant SKM-1 cells. Our previous study revealed that SKM-1 cells expressed low levels of CD44v6, DNMT3A mutation promoted CD44v6 expression in DNMT3A mutant SKM-1 cells, and FLT3 mutant MV4-11 cells expressed high levels of CD44v6 (9). No matter whether FLT3 or DNMT3A mutations were present, Dec and Aza promoted CD44v6 expression in these AML cells (Figures 5C, D, S3C).

Decitabine and azacitidine pretreated AML cells improve the anti-tumor ability of CD44v6 CAR-T

To investigate whether Dec or Aza pretreatment of AML cells could enhance the anti-tumor ability of CD44v6 CAR-T, AML cells were treated with Dec 1 μM or Aza 1 μM for 3 days and then

10.3389/fimmu.2023.1145441

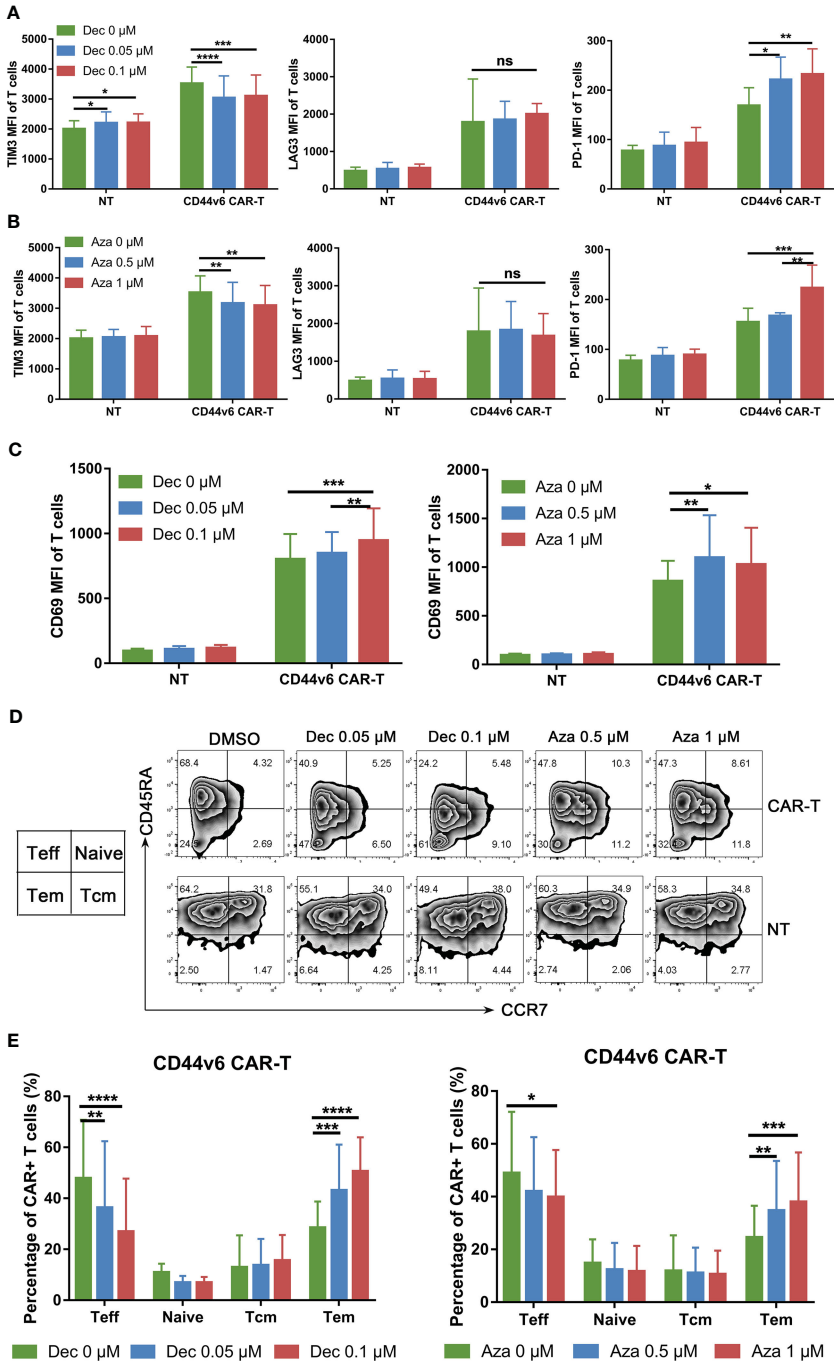

FIGURE 2
Effects of Dec and Aza on the exhaustion and phenotypic differentiation of CD44v6 CAR-T. **(A, B)** TIM3, LAG3 and PD-1 expression levels of non-transduced T (NT) and CD44v6 CAR-T cells treated with Dec (0.05, 0.1 μM) **(A)** and Aza (0.5, 1 μM) **(B)** for 6 days (n=4). **(C)** CD69 expression level of NT and CD44v6 CAR-T cells treated with Dec (0.05, 0.1 μM) (left) and Aza (0.5, 1 μM) (right) for 6 days (n=4) **(D, E)** CCR7 and CD45RA surface staining was performed on NT and CD44v6 CAR-T cells (n=5) treated with Dec (0.05, 0.1 μM) and Aza (0.5, 1 μM) for 6 days, representative flow cytometry is shown in D, the changes of phenotype of CD44v6 CAR-T cells are indicated in **(E)** MFI, mean fluorescence intensity; Teff, effector T cells; Tcm, central memory T cells; Tem, effector memory T cells. Data are depicted as the mean ± SD. *p<.05; **p<.01; ***p<.001; ****p<.0001; ns, not significant.

incubated with CD44v6 CAR-T cells at an E: T ratio of 10:1 for 24 h. Cytotoxicity assays showed that Dec or Aza pretreated AML combined with CD44v6 CAR-T had the highest cytotoxicity compared to Dec or Aza alone or CD44v6 CAR-T alone (Figures 6A, B). This finding was also observed *in vivo*. Subcutaneous inoculation of Luc$^+$ MV4-11 cells was performed on BALB/c-nu mice and the tumor burden was assayed by BLI. The protocols using these agents were shown in Figure 6C. BLI results showed that Dec followed by CD44v6 CAR-T therapy had the strongest ability to prevent tumor progression than Dec or CAR-T therapy alone (Figures 6D, E). These data proved that Dec or Aza pretreated AML enhanced the anti-tumor ability of CD44v6 CAR-T.

10.3389/fimmu.2023.1145441

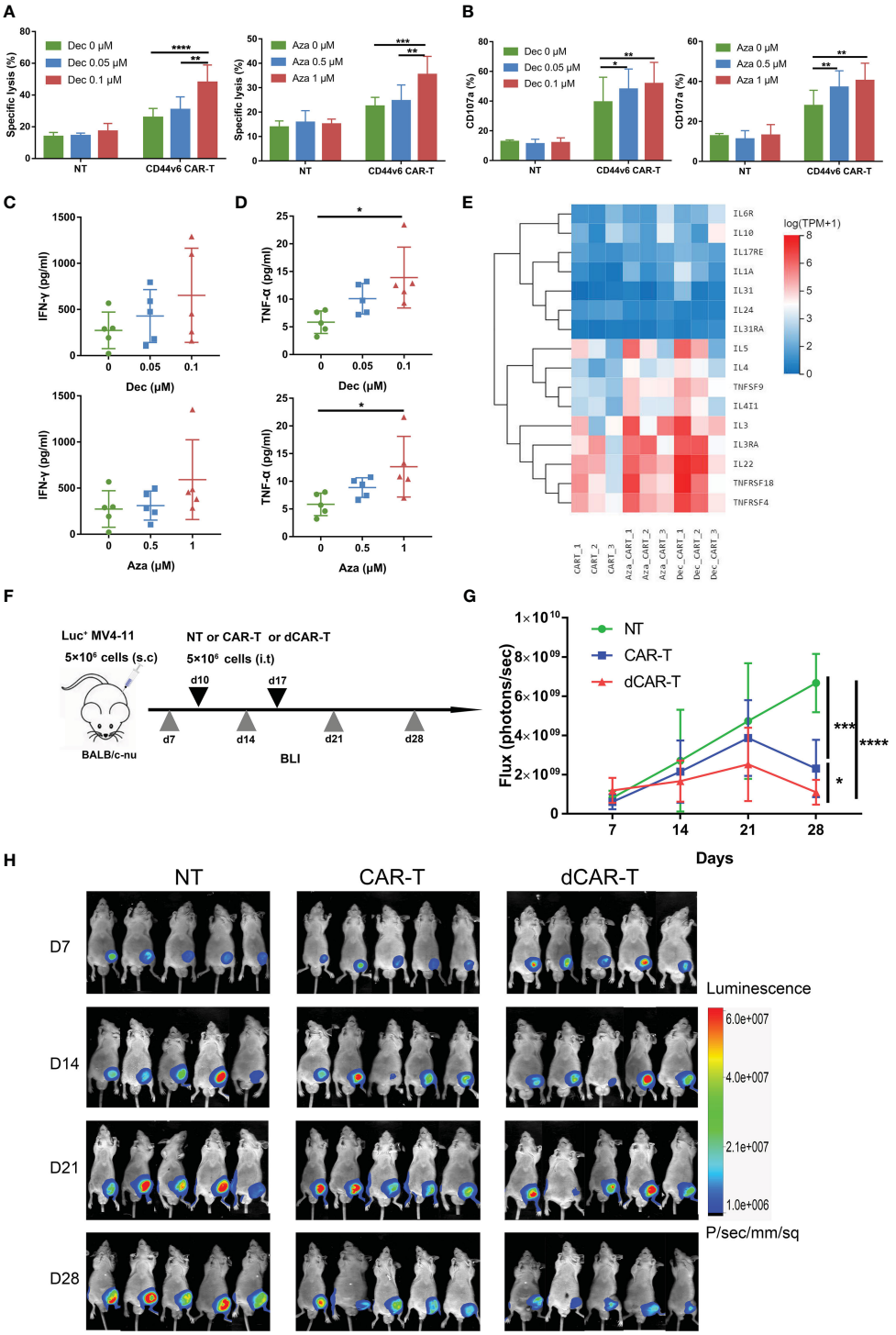

FIGURE 3
Dec and Aza pretreated CD44v6 CAR-T cells exhibit enhanced anti-tumor ability *in vitro* and *in vivo*. **(A)** Cytotoxicity of NT and CD44v6 CAR-T cells treated with Dec (0.05, 0.1 μM) (left, n=6) and Aza (0.5, 1 μM) (right, n=5) for 6 days against MV4-11 cells in an E:T ratio of 10:1 for 24 h. **(B)** Percentage of CD107a$^+$ NT and CD44v6 CAR-T cells treated with Dec (0.05, 0.1 μM) (left, n=3) and Aza (0.5, 1 μM) (right, n=4) for 6 days against MV4-11 cells in an E:T ratio of 1:1 for 16 h. **(C, D)** Cytokine IFN-γ **(C)** and TNF-α **(D)** release of CD44v6 CAR-T cells (n=5) treated with Dec (0.05, 0.1 μM) and Aza (0.5, 1 μM) for 6 days against MV4-11 cells in an E:T ratio of 1:1 for 24 h. **(E)** Heatmap shows expression of elevated tumor necrosis factor and interleukin genes of CD44v6 CAR-T cells treated with Dec 0.1 μM and Aza 1 μM for 6 days in RNA-seq. **(F)** Schematic of Dec pretreated CD44v6 CAR-T treatment of MV4-11 cells xenografts mice. BALB/c-nu mice were subcutaneously injected with 5x10^6 MV4-11-firefly luciferase (Luc$^+$ MV4-11) cells on day 0. NT (n=5), CD44v6 CAR-T (n=5) and Dec pretreated CD44v6 CAR-T (dCAR-T, n=5) (5x10^6) were intratumorally injected on day 10 and day 17. Tumor burden was analyzed by BLI on days 7, 14, 21 and 28. **(G, H)** Graph **(G)** and BLI images **(H)** showing the progress of tumor burden at the indicated time point. Luc$^+$ MV4-11, luciferase-expressing MV4-11 cells; dCAR-T, Dec pretreated CD44v6 CAR-T; BLI, bioluminescence imaging. Data are depicted as the mean ± SD. *p<.05; **p<.01; ***p<.001; ****p<.0001; ns, not significant.

10.3389/fimmu.2023.1145441

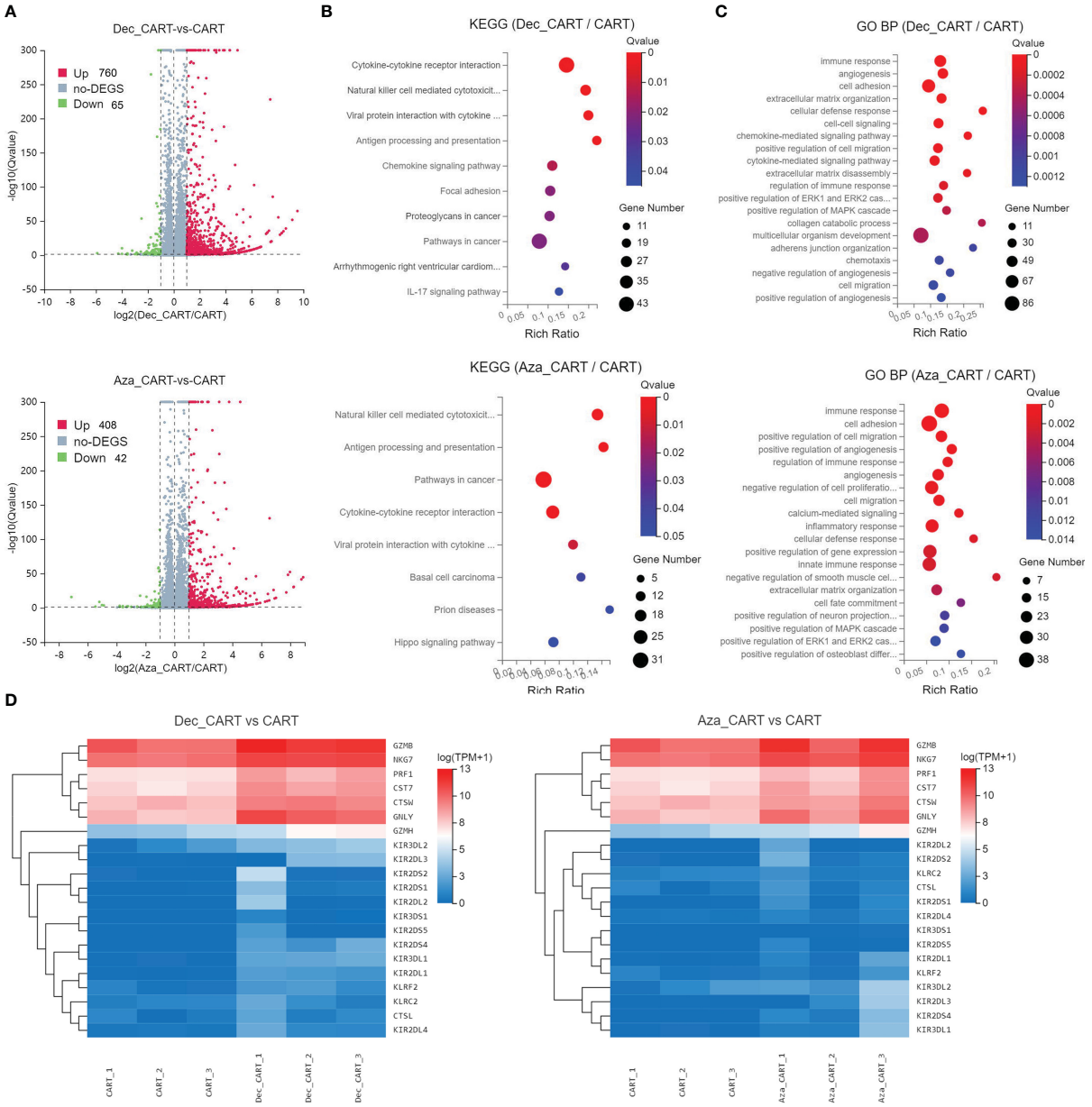

FIGURE 4
Analysis of differentially expressed genes and functions of CD44v6 CAR-T cells treated with Dec and Aza. CD44v6 CAR-T cells (n=3) treated with Dec 0.1 μM (Dec_CAR-T) and Aza 1 μM (Aza_CAR-T) for 6 days were measured by RNA-seq. Untreated CD44v6 CAR-T cells were used as controls (CAR-T). **(A)** Volcano plot of differentially expressed genes (DEGs) in Dec_CAR-T (above) or Aza_CAR-T (below) compared with CAR-T. Red dots represent genes upregulated in Dec_CAR-T or Aza_CAR-T (Qvalue < 0.05 and log2(fold change) ≥1), while blue dots represent genes downregulated in Dec_CAR-T or Aza_CAR-T (Qvalue < 0.05 and log2(fold change) ≤ −1). **(B, C)** Significantly enriched (Qvalue < 0.05) KEGG pathways **(B)** and GO BP **(C)** of all DEGs from Dec_CAR-T (above) or Aza_CAR-T (below) compared to CAR-T. Dot color indicates the statistical significance of enrichment (Qvalue), and dot size represents gene count enriched in each term. **(D)** Heatmap of differentially expressed cytotoxicity-related genes (Qvalue < 0.001 and log2(fold change) ≥1) from Dec_CAR-T (left) or Aza_CAR-T (right) compared to CAR-T. KEGG, Kyoto Encyclopedia of Genes and Genomes; GO, Gene Ontology; BP, biological process.

Combination of decitabine and azacitidine pretreated AML cells and pretreated CD44v6 CAR-T enhanced the anti-tumor capacity

The combination of Dec or Aza pretreated AML and pretreated CD44v6 CAR-T (dCAR-T, aCAR-T) significantly enhanced the anti-tumor capacity compared to dCAR-T or aCAR-T alone *in vitro* (Figure 7A), which was also verified *in vivo*. Subcutaneous BALB/c-nu mouse models inoculated with Luc$^+$ MV4-11 cells were intraperitoneally injected with 1 mg/kg Dec or 100 ul PBS on days 7, 8, 9, 14, 15, and 16, followed by intratumoral injection of dCAR-T on days 10 and 17 (Figure 7B). We found that Dec+dCAR-T therapy significantly eliminated tumor burden in mice compared to dCAR-T therapy (Figures 7C, D). These results demonstrated that the combination of Dec or Aza pretreated AML and pretreated

10.3389/fimmu.2023.1145441

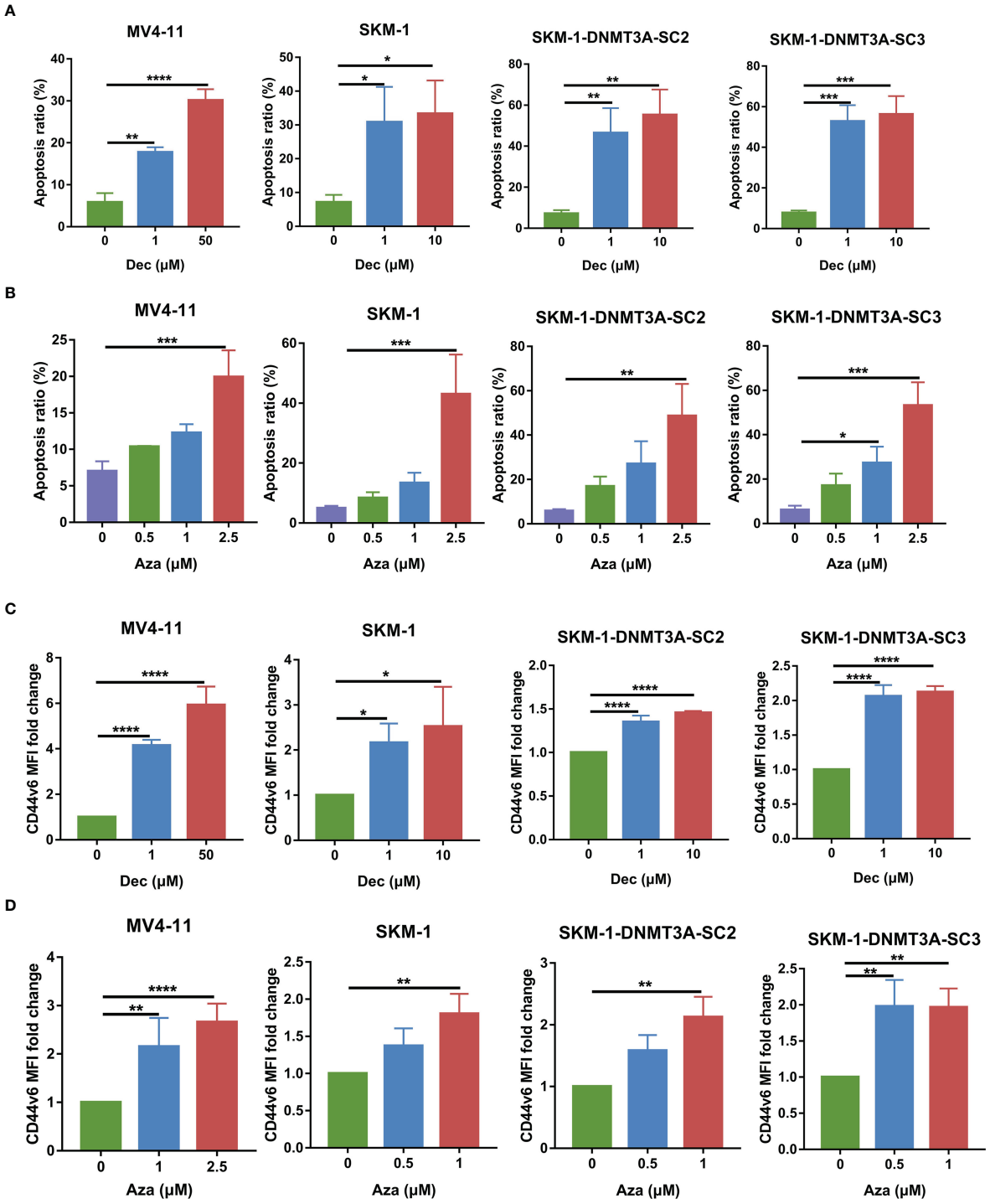

FIGURE 5
Dec and Aza treatment promotes the apoptosis and CD44v6 expression on AML cells. **(A, B)** Apoptosis of MV4-11, SKM-1, SKM-1-DNMT3A-SC2 and SKM-1-DNMT3A-SC3 cells (n=3) after treatment with different concentrations of Dec **(A)** and Aza **(B)** for 3 days. **(C, D)** CD44v6 MFI fold change of MV4-11, SKM-1, SKM-1-DNMT3A-SC2 and SKM-1-DNMT3A-SC3 cells (n=4) after treatment with different concentrations of Dec **(C)** and Aza **(D)** for 3 days. CD44v6 MFI fold change is the ratio of CD44v6 MFI of Dec and Aza treated CD44v6 CAR-T divided by the CD44v6 MFI of untreated CD44v6 CAR-T. SKM-1-DNMT3A-SC2 and SKM-1-DNMT3A-SC3: two clones of DNMT3A-R882H mutant of SKM-1 cells. MFI, mean fluorescence intensity. Data are depicted as the mean ± SD. *p<.05; **p<.01; ***p<.001; ****p<.0001; ns, not significant.

10.3389/fimmu.2023.1145441

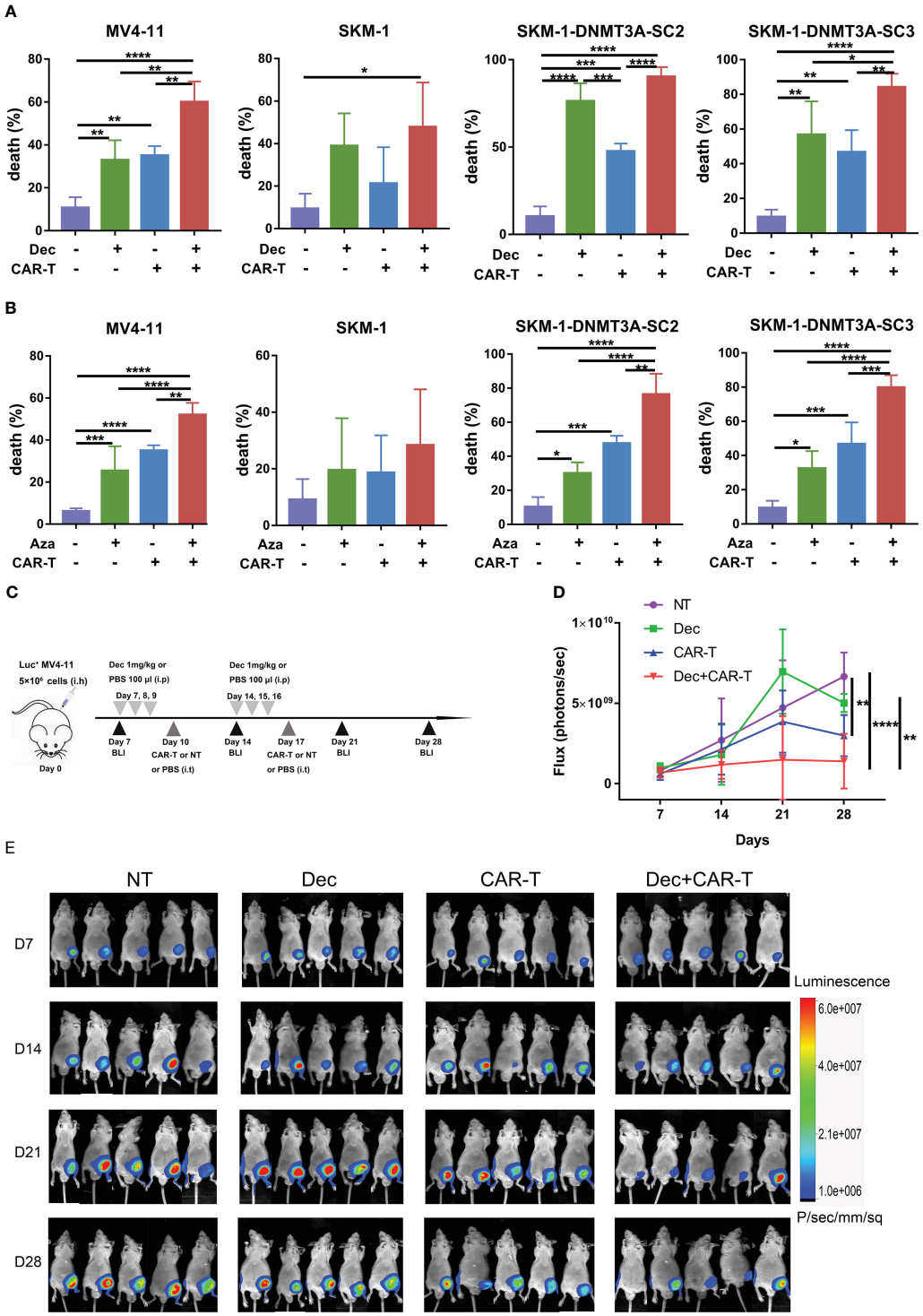

FIGURE 6
Effect of Dec and Aza pretreated AML cells on the anti-tumor capacity of CD44v6 CAR-T *in vitro* and *in vivo*. **(A, B)** Dec **(A)** and Aza **(B)** pretreated AML cells for 3 days were then co-cultured with CD44v6 CAR-T at an E:T of 10:1 for 24 **(h)** Flow cytometric detected the percentage of dead cells in MV4-11, SKM-1, SKM-1-DNMT3A-SC2 and SKM-1-DNMT3A-SC3 cells (n≥4) pretreated with Dec or Aza alone, CD44v6 CAR-T alone, and Dec or Aza in combination with CD44v6 CAR-T. **(C)** Dec pretreated MV4-11 cell xenograft model. BALB/c-nu mice were subcutaneously injected with $5x10^6$ MV4-11-firefly luciferase (Luc^+ MV4-11) cells on day 0. Dec 1 mg/kg or 100 µl PBS were injected intraperitoneally on days 7, 8, 9, 14, 15 and 16. CD44v6 CAR-T cells (5×10^6), NT cells (5×10^6), or 200 µl PBS were intratumorally injected on day 10 and day 17. Tumor burden was analyzed by BLI on days7, 14, 21 and 28. **(D, E)** Graph **(D)** and BLI images **(E)** showing the progress of tumor burden at the indicated time point. Data are depicted as the mean ± SD. *p<.05; **p<.01; ***p<.001; ****p<.0001; ns, not significant.

10.3389/fimmu.2023.1145441

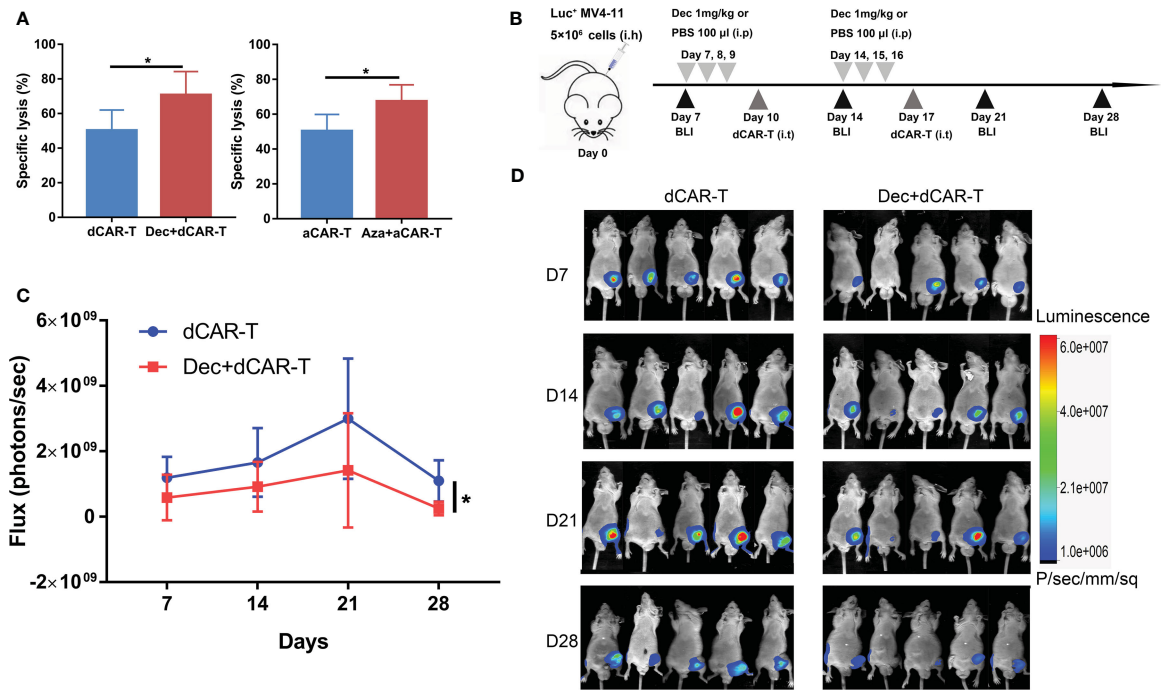

FIGURE 7
The anti-tumor ability of Dec or Aza pretreated CD44v6 CAR-T against Dec and Aza pretreated AML *in vitro* and *in vivo*. **(A)** Cytotoxicity of Dec (left) and Aza (right) pretreated CD44v6 CAR-T (dCAR-T, aCAR-T, n=6) to MV4-11 cells pretreated with or without Dec and Aza in an E:T ratio of 10:1 for 24 h. **(B)** Schematic of Dec pretreated CD44v6 CAR-T treatment of Dec pretreated MV4-11 cells xenografts mice. BALB/c-nu mice were subcutaneously injected with 5×10^6 MV4-11-firefly luciferase (Luc^+ MV4-11) cells on day 0. Dec 1 mg/kg or 100 μl PBS were intraperitoneally injected on day 7, 8, 9, 14, 15 and 16. Then dCAR-T cells (5×10^6) were intratumorally injected on day 10 and day 17. Tumor burden was analyzed by BLI on days 7, 14, 21 and 28. **(C, D)** Graph **(C)** and BLI images **(D)** showing the progress of tumor burden at the indicated time point. dCAR-T: Dec pretreated CD44v6 CAR-T; aCAR-T: Aza pretreated CD44v6 CAR-T. Data are depicted as the mean± SD. *$p<.05$; ns, not significant.

CAR-T had a higher anti-tumor capacity compared to pretreated CAR-T alone.

Security of Dec and Aza pretreatment

Our previous study showed that activated T cells express low levels of CD44v6, so there is transient fratricide of CD44v6 CAR-T cells. Does Dec or Aza pretreatment of NT or CD44v6 CAR-T cells increase fratricide? We found that Dec or Aza treatment of NT or CD44v6 CAR-T cells for 6 days slightly increased the expression of CD44v6 in NT and CD44v6 CAR-T cells (Figure 8A). Next, NT cells pretreated with or without Dec, Aza were co-cultured with CD44v6 CAR-T cells at E: T ratios of 0:1 and 10:1 for 24 h. We found that Dec and Aza pretreatment of NT cells did not significantly increase the cytotoxicity of CD44v6 CAR-T cells against NT cells (Figure 8B). K562 cells are chronic myeloid leukemia cells that do not express CD44v6. Treatment of K562 cells with Dec and Aza for 3 days inhibited their proliferation (Figure S3D) and slightly increased their CD44v6 expression (Figure 8C), but did not significantly increase the cytotoxicity of CD44v6 CAR-T cells against K562 cells (Figure 8D). These data suggested that Dec and Aza pretreatment of T cells or other cells that do not express CD44v6 did not increase fratricide and off-target toxicity of CD44v6 CAR-T cells.

Discussion

Our previous study demonstrated that CD44v6 was an optimal target for AML, and CD44v6 CAR-T showed specific and effective anti-leukemic ability against AML (9). However, the early expansion of CD44v6 CAR-T cells was limited by the transient fratricide. Expansion of CD44v6 CAR-T by extending culture time resulted in differentiation of effector T cells. Study shows effector T cells are detrimental to the anti-tumor capacity and persistence of CAR-T (27). Therefore, new strategies are needed to improve the functions of CD44v6 CAR-T. Here, we found Dec and Aza strengthened the cytotoxicity of CD44v6 CAR-T by increasing their persistence and the number of CAR+ cells, promoting their activation, and facilitating their memory phenotype. Dec and Aza also enhanced the sensitivity of AML cells to CD44v6 CART-mediated cytotoxicity by upregulating the expression of CD44v6 in AML cells. And Dec and Aza pretreatment did not increase fratricide and off-target toxicity of CD44v6 CAR-T cells.

Dec or Aza are demonstrated to promote the anti-tumor ability of CD19 CAR-T and CD123 CAR-T (28, 29). Does Dec or Aza promote the anti-tumor ability of CD44v6 CAR-T? Low doses of Dec and Aza inhibit DNA methylation, while high doses induce apoptosis (20, 24). To avoid inhibiting CAR-T cell activity, we used low doses of Dec (0.05-1 μM) and Aza (0.1-10 μM) to investigate their effects on CD44v6 CAR-T proliferation. We found that Dec

10.3389/fimmu.2023.1145441

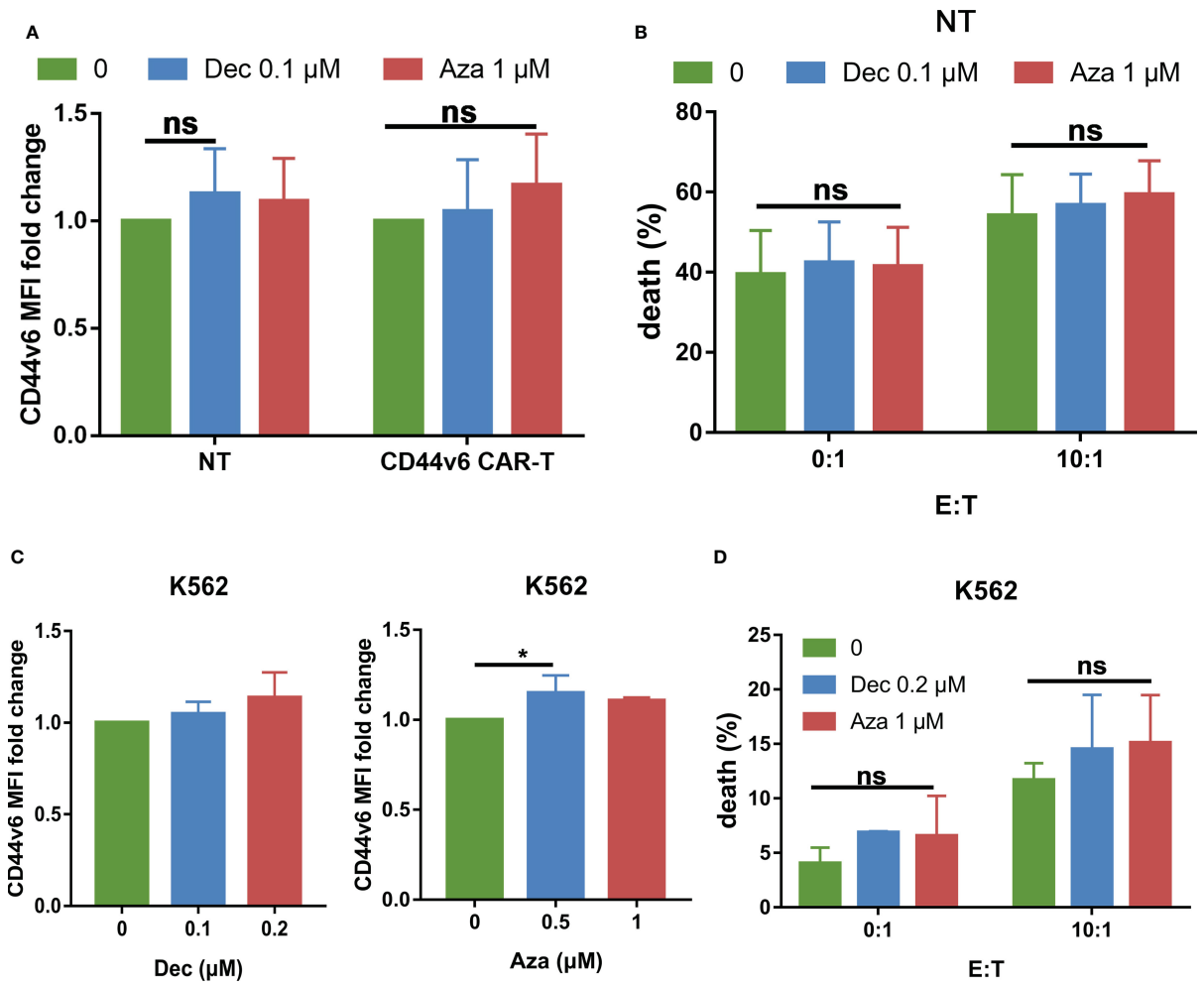

FIGURE 8
Effects of Dec and Aza on CD44v6 expression and safety in T cells and K562 cells. **(A)** CD44v6 MFI fold change of NT and CD44v6 CAR-T cells (n=4) after treatment with Dec and Aza for 6 days. **(B)** Cytotoxicity of CD44v6 CAR-T cells (n=8) against NT cells pretreated with Dec 0.1 μM or Aza 1 μM for 6 days in E:T ratios of 0: 1 and 10:1 for 24 h. **(C)** CD44v6 MFI fold change of K562 cells (n=4) after treatment with Dec and Aza for 3 days. **(D)** Cytotoxicity of CD44v6 CAR-T cells against K562 cells pretreated with Dec 0.2 μM or Aza 1 μM for 3 days in E:T ratios of 0: 1 and 10:1 for 24 h (n=3). Data are depicted as the mean± SD. *p<.05; ns, not significant.

and Aza inhibited CD44v6 CAR-T proliferation in a dose-dependent and time-dependent manner. CD44v6 CAR-T cells were more sensitive to Dec. Stübig et al. also revealed that Aza inhibited T cell proliferation dose-dependently (30). Although Dec and Aza inhibited CD44v6 CAR-T proliferation and slightly promoted apoptosis, Dec 0.1 μM and Aza 1 μM treatment of CD44v6 CAR-T for 6 days significantly improved their transduction efficiency, absolute number of CAR+ cells, and anti-tumor capacity *in vitro* and *in vivo*. Moreover, CD44v6 CAR-T cells pretreated with Dec or Aza showed enhanced persistence *in vitro* and *in vivo*. These data suggested that Dec or Aza pretreatment of CD44v6 CAR-T significantly enhanced its anti-tumor ability against AML.

Several factors determine whether CAR-T cells are effective. HMAs can reverse the exhaustion associated with the *de novo* DNA methylation (22). However, in our study, Dec and Aza inhibited TIM3 expression and promoted LAG3 expression in CD44v6 CAR-T cells. The effects of Dec and Aza on the exhaustion markers of CD44v6 CAR-T cells were not consistent. Since the expression level of TIM3 was significantly higher than that of LAG3, we speculated that the effect of Dec and Aza on the exhaustion of CD44v6 CAR-T cells was dominated by a decrease in TIM3, which needs to be verified by follow-up experiments in the future. Moreover, Dec and Aza promoted CD44v6 CAR-T cells activation, which helped to improve the function of CD44v6 CAR-T cells. Tumors are eliminated more effectively by naive or memory T cells than effector T cells (27). According to clinical research, CD19 CAR-T cells from patients who responded well to CAR-T for CLL had more memory T cells, while CD19 CAR-T cells from non-responders had more effector T cells (31). Knockout of the *DNMT3A* gene in T cells drives T cells to a higher proportion of memory phenotypes (32), and the DNMT3A inhibitors Dec and Aza have similar effects on T cells (28, 29). Our study also found that CD44v6 CAR-T cells treated with Dec or Aza had more memory T cells and fewer effector T cells than untreated CAR-T cells. Therefore, we speculated that Dec and Aza promoted the anti-tumor capacity of CD44v6 CAR-T

cells by promoting activation and memory phenotype differentiation of CD44v6 CAR-T cells.

Dec and Aza have achieved significant efficacy in the induction of differentiation therapy in AML (19–21, 33–35). Low doses of Dec or Aza produced the best clinical response in hematologic malignancies, while high doses inhibited clinical response. Low doses of Dec and Aza induce differentiation, reduce proliferation and increase apoptosis by altering the gene expression profile of tumor cells (20, 34). In MV4-11, SKM-1 and DNMT3A mutant SKM-1 cells, low doses of Dec and Aza inhibited proliferation and induced apoptosis. Furthermore, Dec especially promoted apoptosis in DNMT3A mutant SKM-1 cells, which may be related to their high expression of DNMT3A mRNA (9, 36). Several studies have demonstrated that Dec and Aza promote the efficacy of immunotherapy by upregulating the expression of tumor-associated antigens in AML or other tumors. Our results are consistent with this, Dec and Aza enhanced the cytotoxicity of CD44v6 CAR-T against AML cells *in vitro* and *in vivo*, by promoting CD44v6 expression in AML cells regardless of FLT3 or DNMT3A mutations. Therefore, we concluded that Dec and Aza improved the anti-tumor ability of CD44v6 CAR-T cells by upregulating CD44v6 expression of AML cells.

Based on the two pretreatment protocols mentioned above, Dec or Aza pretreatment of CD44v6 CAR-T cells or AML cells both promoted the anti-tumor capacity of CD44v6 CAR-T cells. The combination of Dec or Aza pretreated CD44v6 CAR-T cells and pretreated AML was then investigated and found to have the strongest anti-tumor capacity.

In summary, this study presents the first evidence that the combination of Dec or Aza with CD44v6 CAR-T cells is potent for treating AML. Dec and Aza strengthened the anti-tumor capacity of CD44v6 CAR-T cells towards AML by increasing the counts of CAR+ cells and persistence, promoting activation and memory phenotype of CD44v6 CAR-T cells, and upregulating CD44v6 expression in AML cells. Thus, we proved that Dec or Aza combined with CD44v6 CAR-T is a promising therapy for AML.

Data availability statement

The datasets presented in this study can be found in online repositories. The names of the repository/repositories and accession number(s) can be found below: NCBI *via* accession ID: PRJNA924523.

Ethics statement

After obtaining written informed consent in accordance with the Declaration of Helsinki and approval by the Institutional Review Board of Tongji Medical College and the Hubei committee, peripheral blood of healthy donor was obtained from Union Hospital, Tongji Medical College, Huazhong University of Science and Technology. All animal experiments were approved by the Institutional Animal Care and Use Committee of Huazhong University of Science and Technology, and strictly followed the animal regulations of Hubei Province.

Author contributions

FM, JW, and YY: Conceptualization, Funding acquisition, Writing - review and editing. LT and YK: Experimental implementation, Data curation, Formal analysis, Writing - original draft. HW and TS: Investigation, Methodology. JZ: Supervision. XZ and PZ: Project administration. NJ: Validation. HM and YL: Software. All authors contributed to the article and approved the submitted version.

Funding

This work was supported by National Key R&D Program of China (2021YFF0703704), National Natural Science Foundation of China (82270183, 81570110), the Excellent Young Science Foundation Project of Tongji Hospital (No.2020YQ0012) and the Wuhan Joint Fund Project 2019 (WJ2019H383), Natural Sciences Foundation of Hubei Province of China (2021CFB561).

Acknowledgments

We thank doctors Wei Li, Juan Ren, Si Cheng, and Kai Shen for collecting peripheral blood from healthy donors.

Conflict of interest

Authors YL and JZ are employed by Wuhan Biological Sample Bank Co., Ltd.

The remaining authors declare that the research was conducted in the absence of any commercial or financial relationships that could be construed as a potential conflict of interest.

Publisher's note

All claims expressed in this article are solely those of the authors and do not necessarily represent those of their affiliated organizations, or those of the publisher, the editors and the reviewers. Any product that may be evaluated in this article, or claim that may be made by its manufacturer, is not guaranteed or endorsed by the publisher.

Supplementary material

The Supplementary Material for this article can be found online at: https://www.frontiersin.org/articles/10.3389/fimmu.2023.1145441/full#supplementary-material

References

1. Yang X, Wang J. Precision therapy for acute myeloid leukemia. *J Hematol Oncol* (2018) 11(1):3. doi: 10.1186/s13045-017-0543-7

2. Thol F, Ganser A. Treatment of relapsed acute myeloid leukemia. *Curr Treat Option On* (2020) 21(8):66. doi: 10.1007/s11864-020-00765-5

3. Daver N, Schlenk RF, Russell NH, Levis MJ. Targeting FLT3 mutations in AML: review of current knowledge and evidence. *Leukemia* (2019) 33(2):299–312. doi: 10.1038/s41375-018-0357-9

4. DiNardo CD, Tiong IS, Quaglieri A, MacRaild S, Loghavi S, Brown FC, et al. Molecular patterns of response and treatment failure after frontline venetoclax combinations in older patients with AML. *Blood* (2020) 135(11):791–803. doi: 10.1182/blood.2019003988

5. Borot F, Wang H, Ma Y, Jafarov T, Raza A, Ali AM, et al. Gene-edited stem cells enable CD33-directed immune therapy for myeloid malignancies. *Proc Natl Acad Sci* (2019) 116(24):11978–87. doi: 10.1073/pnas.1819992116

6. Arcangeli S, Rotiroti MC, Bardelli M, Simonelli L, Magnani CF, Biondi A, et al. Balance of anti-CD123 chimeric antigen receptor binding affinity and density for the targeting of acute myeloid leukemia. *Mol Ther* (2017) 25(8):1933–45. doi: 10.1016/j.ymthe.2017.04.017

7. Wang J, Chen S, Xiao W, Li W, Wang L, Yang S, et al. CAR-T cells targeting CLL-1 as an approach to treat acute myeloid leukemia. *J Hematol Oncol* (2018) 11(1):7. doi: 10.1186/s13045-017-0553-5

8. Wang Y, Xu Y, Li S, Liu J, Xing Y, Xing H, et al. Targeting FLT3 in acute myeloid leukemia using ligand-based chimeric antigen receptor-engineered T cells. *J Hematol Oncol* (2018) 11(1):60. doi: 10.1186/s13045-018-0603-7

9. Tang L, Huang H, Tang Y, Li Q, Wang J, Li D, et al. CD44v6 chimeric antigen receptor T cell specificity towards AML with FLT3 or DNMT3A mutations. *Clin Trans Med* (2022) 12(9):e1043. doi: 10.1002/ctm2.1043

10. Monica Casucci BNDR, Pietro Genovese BGFG, Aurore Saudemont CBBS, Chiara Bonini AAB. CD44v6-targeted T cells mediate potent antitumor effects against acute myeloid leukemia and multiple myeloma. *Blood* (2013) 122(20):3461–72. doi: 10.1182/blood-2013-04

11. Heider K, Kuthan H, Stehle G, Munzert G. CD44v6: a target for antibody-based cancer therapy. *Cancer Immunology Immunotherapy* (2004) 53(7):567–79. doi: 10.1007/s00262-003-0494-4

12. Shah NN, Fry TJ. Mechanisms of resistance to CAR T cell therapy. *Nat Rev Clin Oncol* (2019) 16(6):372–85. doi: 10.1038/s41571-019-0184-6

13. Majzner RG, Mackall CL. Clinical lessons learned from the first leg of the CAR T cell journey. *Nat Med* (2019) 25(9):1341–55. doi: 10.1038/s41591-019-0564-6

14. Maus MBLH. Non-cleavable hinge enhances avidity and expansion of CAR-T cells for acute myeloid leukemia. *Cancer Cell* (2022) 40:494–508. doi: 10.1016/j.ccell.2022.04.001

15. Cao X, Dai H, Cui Q, Li Z, Shen W, Pan J, et al. CD7-directed CAR T-cell therapy: a potential immunotherapy strategy for relapsed/refractory acute myeloid leukemia. *Exp Hematol Oncol* (2022) 11(1):67. doi: 10.1186/s40164-022-00318-6

16. Grunewald CM, Haist C, König C, Petzsch P, Bister A, Nößner E, et al. Epigenetic priming of bladder cancer cells with decitabine increases cytotoxicity of human EGFR and CD44v6 CAR engineered T-cells. *Front Immunol* (2021) 12:782448. doi: 10.3389/fimmu.2021.782448

17. Wong KK, Hassan R, Yaacob NS. Hypomethylating agents and immunotherapy: therapeutic synergism in acute myeloid leukemia and myelodysplastic syndromes. *Front Oncol* (2021) 11:624742. doi: 10.3389/fonc.2021.624742

18. Klar AS, Gopinadh J, Kleber S, Wadle A, Renner C. Treatment with 5-Aza-2'-Deoxycytidine induces expression of NY-ESO-1 and facilitates cytotoxic T lymphocyte-mediated tumor cell killing. *PloS One* (2015) 10(10):e139221. doi: 10.1371/journal.pone.0139221

19. Stahl M, Menghrajani K, Derkach A, Chan A, Xiao W, Glass J, et al. Clinical and molecular predictors of response and survival following venetoclax therapy in relapsed/refractory AML. *Blood Adv* (2021) 5(5):1552–64. doi: 10.1182/bloodadvances.2020003734

20. Issa JJ, Garcia-Manero G, Giles FJ, Mannari R, Thomas D, Faderl S, et al. Phase 1 study of low-dose prolonged exposure schedules of the hypomethylating agent 5-aza-2′-deoxycytidine (decitabine) in hematopoietic malignancies. *Blood* (2004) 103 (5):1635–40. doi: 10.1182/blood-2003-03-0687

21. DiNardo CD, Pratz K, Pullarkat V, Jonas BA, Arellano M, Becker PS, et al. Venetoclax combined with decitabine or azacitidine in treatment-naive, elderly patients with acute myeloid leukemia. *Blood* (2019) 133(1):7–17. doi: 10.1182/blood-2018-08-868752

22. Ghoneim HE, Fan Y, Moustaki A, Abdelsamed HA, Dash P, Dogra P, et al. *De Novo* Epigenetic programs inhibit PD-1 blockade-mediated T cell rejuvenation. *Cell* (2017) 170(1):142–57. doi: 10.1016/j.cell.2017.06.007

23. Lee PP, Fitzpatrick DR, Beard C, Jessup HK, Lehar S, Makar KW, et al. A critical role for Dnmt1 and DNA methylation in T cell development, function, and survival. *Immun (Cambridge Mass.)* (2001) 15(5):763–74. doi: 10.1016/S1074-7613(01)00227-8

24. Craig Chappell CBJA. DNA Methylation by DNA methyltransferase 1 is critical for e ector CD8 T cell expansion 1. *J Immunol* (2006) 176(8):4562–72. doi: 10.4049/jimmunol.176.8.4562

25. Cherkassky L, Morello A, Villena-Vargas J, Feng Y, Dimitrov DS, Jones DR, et al. Human CAR T cells with cell-intrinsic PD-1 checkpoint blockade resist tumor-mediated inhibition. *J Clin Invest* (2016) 126(8):3130–44. doi: 10.1172/JCI83092

26. Youngblood B, Hale JS, Kissick HT, Ahn E, Xu X, Wieland A, et al. Effector CD8 T cells dedifferentiate into long-lived memory cells. *Nature* (2017) 552(7685):404–9. doi: 10.1038/nature25144

27. McLellan AD, Ali HRS. Chimeric antigen receptor T cell persistence and memory cell formation. *Immunol Cell Biol* (2019) 97(7):664–74. doi: 10.1111/imcb.12254

28. You L, Han Q, Zhu L, Zhu Y, Bao C, Yang C, et al. Decitabine-mediated epigenetic reprograming enhances anti-leukemia efficacy of CD123-targeted chimeric antigen receptor T-cells. *Front Immunol* (2020) 11:1787. doi: 10.3389/fimmu.2020.01787

29. Wang Y, Tong C, Dai H, Wu Z, Han X, Guo Y, et al. Low-dose decitabine priming endows CAR T cells with enhanced and persistent antitumour potential *via* epigenetic reprogramming. *Nat Commun* (2021) 12(1):409. doi: 10.1038/s41467-020-20696-x

30. Stübig T, Badbaran A, Luetkens T, Hildebrandt Y, Atanackovic D, Binder TMC, et al. 5-azacytidine promotes an inhibitory T-cell phenotype and impairs immune mediated antileukemic activity. *Med Inflamm* (2014) 2014:1–12. doi: 10.1155/2014/418292

31. Joseph A, Fraietta SFLE, Mercy Gohil SLAC, Wilcox FBCD, Minnal Gupta RMYF, Sadik H. Kassim MMDB, et al. Determinants of response and resistance to CD19 chimeric antigen receptor (CAR) T cell therapy of chronic lymphocytic leukemia. *Nat Med* (2018) 24(5):563–71. doi: 10.1038/s41591

32. Ladle BH, Li K, Phillips MJ, Pucsek AB, Haile A, Powell JD, et al. *De novo* DNA Methylation by DNA methyltransferase 3a controls early effector CD8+ T-cell fate decisions following activation. *Proc Natl Acad Sci* (2016) 113(38):10631–6. doi: 10.1073/pnas.1524490113

33. DiNardo CD, Maiti A, Rausch CR, Pemmaraju N, Naqvi K, Daver NG, et al. 10-day decitabine with venetoclax for newly diagnosed intensive chemotherapy ineligible, and relapsed or refractory acute myeloid leukaemia: a single-centre, phase 2 trial. *Lancet Haematology* (2020) 7(10):e724–36. doi: 10.1016/S2352-3026(20)30210-6

34. Schmelz K, Wagner M, Dörken B, Tamm I. 5-Aza-2′-deoxycytidine induces p21WAF expression by demethylation of p73 leading to p53-independent apoptosis in myeloid leukemia. *Int J Cancer* (2005) 114(5):683–95. doi: 10.1002/ijc.20797

35. Greve G, Schüler J, Grüning BA, Berberich B, Stomper J, Zimmer D, et al. Decitabine induces gene derepression on monosomic chromosomes : *In Vitro* and *In Vivo* effects in adverse-risk cytogenetics AML. *Cancer Res* (2021) 81(4):834–46. doi: 10.1158/0008-5472.CAN-20-1430

36. Que Y, Li H, Lin L, Zhu X, Xiao M, Wang Y, et al. Study on the immune escape mechanism of acute myeloid leukemia with DNMT3A mutation. *Front Immunol* (2021) 12. doi: 10.3389/fimmu.2021.653030

frontiers | Frontiers in Immunology

TYPE Original Research
PUBLISHED 19 May 2023
DOI 10.3389/fimmu.2023.1138054

Check for updates

OPEN ACCESS

EDITED BY
Clare Y. Slaney,
Peter MacCallum Cancer Centre, Australia

REVIEWED BY
Ada Hang-Heng Wong,
Independent researcher, Macau, Macao SAR, China
Haitao Wang,
National Cancer Institute (NIH), United States

*CORRESPONDENCE
Wencheng Zhang
wczhang@tmu.edu.cn
Qingsong Pang
pangqingsong@tjmuch.com
Ping Wang
wangping@tjmuch.com

†These authors share first authorship

RECEIVED 05 January 2023
ACCEPTED 04 May 2023
PUBLISHED 19 May 2023

CITATION
Yan C, Huang H, Zheng Z, Ma X, Zhao G, Zhang T, Chen X, Cao F, Wei H, Dong J, Tang P, Jiang H, Wang M, Wang P, Pang Q and Zhang W (2023) Spatial distribution of tumor-infiltrating T cells indicated immune response status under chemoradiotherapy plus PD-1 blockade in esophageal cancer. *Front. Immunol.* 14:1138054. doi: 10.3389/fimmu.2023.1138054

COPYRIGHT
© 2023 Yan, Huang, Zheng, Ma, Zhao, Zhang, Chen, Cao, Wei, Dong, Tang, Jiang, Wang, Wang, Pang and Zhang. This is an open-access article distributed under the terms of the Creative Commons Attribution License (CC BY). The use, distribution or reproduction in other forums is permitted, provided the original author(s) and the copyright owner(s) are credited and that the original publication in this journal is cited, in accordance with accepted academic practice. No use, distribution or reproduction is permitted which does not comply with these terms.

Spatial distribution of tumor-infiltrating T cells indicated immune response status under chemoradiotherapy plus PD-1 blockade in esophageal cancer

Cihui Yan[1†], Hui Huang[2†], Zhunhao Zheng[2], Xiaoxue Ma[2], Gang Zhao[3], Tian Zhang[2], Xi Chen[2], Fuliang Cao[4], Hui Wei[2], Jie Dong[5], Peng Tang[6], Hongjing Jiang[6], Meng Wang[7], Ping Wang[2*], Qingsong Pang[2*] and Wencheng Zhang[2*]

[1]Department of Immunology, Tianjin Medical University Cancer Institute and Hospital, National Clinical Research Center for Cancer, Key Laboratory of Cancer Immunology and Biotherapy, Tianjin's Clinical Research Center for Cancer, Tianjin, China, [2]Department of Radiation Oncology, Tianjin Medical University Cancer Institute and Hospital, National Clinical Research Center for Cancer, Key Laboratory of Cancer Prevention and Therapy, Tianjin's Clinical Research Center for Cancer, Tianjin, China, [3]Department of Pathology, Tianjin Medical University Cancer Institute and Hospital, National Clinical Research Center for Cancer, Key Laboratory of Cancer Prevention and Therapy, Tianjin's Clinical Research Center for Cancer, Tianjin, China, [4]Department of Endoscopy Diagnosis and Therapy, Tianjin Medical University Cancer Institute and Hospital, National Clinical Research Center for Cancer, Key Laboratory of Cancer Prevention and Therapy, Tianjin's Clinical Research Center for Cancer, Tianjin, China, [5]Department of Nutrition Therapy, Tianjin Medical University Cancer Institute and Hospital, National Clinical Research Center for Cancer, Key Laboratory of Cancer Prevention and Therapy, Tianjin's Clinical Research Center for Cancer, Tianjin, China, [6]Department of Esophageal Cancer, Tianjin Medical University Cancer Institute and Hospital, National Clinical Research Center for Cancer, Key Laboratory of Cancer Prevention and Therapy, Tianjin's Clinical Research Center for Cancer, Tianjin, China, [7]Department of Lung Cancer, Tianjin Medical University Cancer Institute and Hospital, National Clinical Research Center for Cancer, Key Laboratory of Cancer Prevention and Therapy, Tianjin's Clinical Research Center for Cancer, Tianjin, China

Background: The spatial distribution of tumor-infiltrating T cells and its dynamics during chemoradiotherapy combined with PD-1 blockade is little known in esophageal squamous cell carcinoma (ESCC).

Methods: We applied the multiplex immunofluorescence method to identify T cells ($CD4^+$, $CD8^+$ T cells, and their $PD\text{-}1^-$ or $PD\text{-}1^+$ subsets) and myeloid-derived cells ($CD11c^+$ dendritic cells, $CD68^+$ macrophages, and their $PD\text{-}L1^+$ subpopulations) in paired tumor biopsies (n = 36) collected at baseline and during combination (40 Gy of radiation) from a phase Ib trial (NCT03671265) of ESCC patients treated with first-line chemoradiotherapy plus anti-PD-1 antibody camrelizumab. We used the FoundationOne CDx assay to evaluate tumor mutational burden (TMB) in baseline tumor biopsies (n = 14). We dynamically assessed the nearest distance and proximity of T-cell subsets to tumor cells under combination and estimated the association between T-cell spatial distribution and combination outcome, myeloid-derived subsets, TMB, and patient baseline characteristics.

Findings: We found that the tumor compartment had lower T-cell subsets than the stromal compartment but maintained a comparable level under

combination. Both before and under combination, PD-1$^-$ T cells were located closer than PD-1$^+$ T cells to tumor cells; T cells, dendritic cells, and macrophages showed the highest accumulation in the 5–10-μm distance. Higher CD4$^+$ T cells in the tumor compartment and a shorter nearest distance of T-cell subsets at baseline predicted poor OS. Higher baseline CD4$^+$ T cells, dendritic cells, and macrophages were associated with worse OS in less than 10-μm distance to tumor cells, but related with better OS in the farther distance. Higher on-treatment PD-1-positive-expressed CD4$^+$ and CD8$^+$ T cells within the 100-μm distance to tumor cells predicted longer OS. T cells, dendritic cells, and macrophages showed a positive spatial correlation. Both high TMB and smoking history were associated with a closer location of T cells to tumor cells at baseline.

Conclusions: We firstly illustrated the T-cell spatial distribution in ESCC. Combining chemoradiotherapy with PD-1 blockade could improve the antitumor immune microenvironment, which benefits the treatment outcome. Further understanding the precision spatiality of tumor-infiltrating T cells would provide new evidence for the tumor immune microenvironment and for the combination treatment with immunotherapy.

KEYWORDS

esophageal squamous cell carcinoma, spatial analysis, immunotherapy, chemoradiotherapy, PD-1, tumor-infiltrating T cell

Introduction

Chemoradiotherapy (CRT) is the standard treatment strategy for patients with inoperable locally advanced esophageal squamous cell carcinoma (ESCC) (1, 2). However, survival remains poor for these patients. During the past 5 years, we carried out the first phase Ib clinical study of radiotherapy (RT) combined with the anti-PD-1 antibody camrelizumab in inoperable locally advanced ESCC (NCT03222440) (3) and then the first phase Ib clinical study of CRT plus camrelizumab as first-line treatment in these patients (NCT03671265) (4). Our ESCORT-CRT (NCT04426955) study and other studies, such as KEYNOTE-975 (NCT04210115) and RATIONALE 311 (NCT03957590), are phase III multicenter randomized clinical trials which are still ongoing combining CRT and anti-PD-1 antibody. The preliminary results showed that the 2-year overall survival (OS) rate was 69.6% in CRT plus PD-1 blockade (4). A fraction of the patients did not benefit from the combination treatment. Potential biomarkers are urgently needed in locally advanced ESCC patients treated with this combination treatment.

T cells, the major component of the adaptive immune response, play a vital role in immune surveillance and tumor control. T cells are important targets of checkpoint inhibitors and critical for the treatment outcome of immunotherapy in tumor therapy (5, 6). Recent studies revealed that T cells in treatment-naïve ESCC were always in a dysfunctional and exhausted status (7–9) which supported the deterioration of antitumor immune condition in locally advanced ESCC. We previously found that more tumor-infiltrating immune cells and less resident tumor cells during CRT predicted improved OS in locally advanced ESCC (10). In the phase Ib study of RT plus PD-1 blockade in locally advanced ESCC, we found that high PD-L1$^+$CD4$^+$ and PD-1$^+$CD8$^+$ T cells at baseline predicted poor OS (3). Meanwhile, we did not find an association between the total tumor-infiltrating T cells and survival in ESCC patients receiving CRT combined with PD-1 blockade (4). Multiregional sequencing illustrated the intratumor heterogeneity of the T-cell receptor (TCR) repertoire and its tight correlation with genomic mutation in ESCC (11). Single-cell sequencing also demonstrated the diverse signaling from heterogeneous stromal cells devoted to the divergent traits of immune cells in ESCC (7). Spatial analyses of immune cells in the tumor microenvironment would provide new evidence in immune-oncology research (12–14). However, precision spatial analysis of tumor-infiltrating T cells under CRT combined with immunotherapy is less studied so far.

Multiplex immunofluorescence uncovers the complicated interaction between multiple subpopulations in the tumor microenvironment (15–17). By using multiplex immunofluorescence, we previously identified the nearest distance of myeloid-derived cells, dendritic cells, and macrophages to tumor cells in the samples collected from the phase Ib clinical trial of CRT combined with camrelizumab (NCT03671265) (18). As a serial study, we here prospectively evaluated the nearest distance and proximity of T-cell subsets to tumor cells at baseline and on-treatment tumor tissues collected from these patients

and its association with myeloid-derived cells, which provided precision biomarker candidates for predicting the outcome of CRT plus PD-1 blockade in ESCC.

Materials and methods

Study design

The phase Ib study evaluated the safety and feasibility of definitive CRT concurrently combined with anti-PD-1 antibody, camrelizumab, as the first-line treatment in inoperable locally advanced ESCC (NCT03671265) (4). Specifically, camrelizumab was given on day 1 of every 2-week period from the beginning of RT up to 32 weeks, concurrently with RT for 6 weeks, and with chemotherapy for 4 weeks (4). The exploratory endpoints of this phase Ib study were local and systematic immune characteristics and potential predictive biomarkers for treatment outcome.

Sample collection

Tumor biopsies were collected before (baseline, within 3 days before treatment, $n = 20$) and under combination (on-treatment, after 40 Gy of radiation and two rounds of camrelizumab treatment, $n = 18$) (Additional File: Table S1). Deep biopsy samples of tumor tissues were collected under endoscopic ultrasonographic guidance (19, 20) and made into formalin-fixed paraffin-embedded (FFPE) tissue blocks.

Ethics statement

This study conformed to the ethical principles outlined in the Declaration of Helsinki, and the protocol was approved by the Institutional Review Board and Ethics Committee of Tianjin Medical University Cancer Institute & Hospital (E2018142). All patients provided written informed consent to participate. This study was registered on ClinicalTrials.gov (NCT03671265).

Multiplex immunofluorescence staining

To comprehensively describe the tumor immune microenvironment, we used the serial FFPE slides of the biopsy specimens collected at baseline or during the combination in multiplex immunofluorescence staining. The FFPE slides were 4 μm thick so monolayer cells could be identified in the following imaging analysis. The multiplex immunofluorescence staining was automatically performed in a Bond III automated stainer (Leica, USA). The TSA 5-color kit (#D110051-50T) and TSA 670 (#D110016-100T) were bought from Yuanxibio, Shanghai, China. Two staining panels were applied. The staining order was as follows: panel 1—anti-CD4 (#YX32005, Yuanxibio, 1:300)/TSA 620, anti-CD8 (#YX63005, Yuanxibio, 1:300)/TSA 670, anti-panCK (#GM351507, GeneTech, Shanghai, China, 1:6)/TSA 520, and anti-PD-1 (#10377-MM23, Sino Biological, Beijing, China, 1:200)/TSA 570; panel 2—anti-PD-L1 (#13684, CST, Danvers, USA, 1:800)/TSA 570, anti-panCK (#GM351507, GeneTech, 1:6)/TSA 520, anti-CD11c (#45581, CST, 1:300)/TSA 620, and anti-CD68 (#GM087602, GeneTech, ready-to-use)/TSA 670. To visualize the cell nuclei, the tissue was stained with 4′,6-diamidino-2-phenylindole (D1306; Thermo Fisher, Waltham, USA).

Imaging and analysis

We performed a whole slide scan for each fluorescence-stained slide by using the digital microscopy scanner Pannoramic MIDI tissue imaging system (3DHISTECH Ltd., Hungary). Because the surface marker CK was expressed on both tumor and normal epithelial cells, it is hard to distinguish these two types of cells in immunofluorescence staining. We applied hematoxylin and eosin (H&E) staining in the tissue sections after finishing the panel 2 fluorescence scan in order to exclude the normal epithelial cells in the analysis. At the same time, we could clearly identify the tumor and normal epithelial cells on the serial tissue section for panel 1 staining according to the tumor cells judged by H&E staining in the serial slide. Images were analyzed by the HALO software (Version 3.5.3577, Indica Labs, Albuquerque, NM, USA). An experienced pathology specialist supervised to segment the tumor and stromal compartment using the HALO software. HALO Highplex FL (version 4.1) was used for nuclear segmentation and tumor-infiltrating lymphocyte quantification. In brief, all nuclei in the whole slide image were automatically segmented based on DAPI staining. Positivity thresholds for each marker were set based on cytoplasmic or nuclear staining intensity and were reviewed across all samples. Data for each cell's expression of all the markers and the x and y locations within the tissue were stored in HALO for spatial analysis. Finally, cells were phenotyped as follows: panel 1—$CD4^+$ T cell, $CD8^+$ T cell, $CD4^+PD\text{-}1^+$ T cell, $CD4^+PD\text{-}1^-$ T cell, $CD8^+PD\text{-}1^+$ T cell, $CD8^+PD\text{-}1^-$ T cell, and tumor cell ($panCK^+$); panel 2—dendritic cell ($CD11c^+$), macrophage ($CD68^+$), tumor cell ($panCK^+$), and $PD\text{-}L1^+$ subpopulations of these cells.

Immune cell infiltration was evaluated as the number of cells per whole slide, in the tumor compartment, stromal compartment, or individual regions of the slides, respectively. Spatial analysis was performed using the HALO Spatial Analysis module. To better evaluate the position relationship between immune cells and tumor cells, two algorithms, namely, the HALO nearest neighbor analysis and proximity analysis, were used. In analyzing the nearest distance, the distance between each tumor cell (as the core cell) and its nearest neighbor immune cells ($CD4^+$, $CD8^+$, $CD4^+PD\text{-}1^+$, $CD4^+PD\text{-}1^-$, $CD8^+PD\text{-}1^+$, and $CD8^+PD\text{-}1^-$ T cells) was measured. In the proximity analysis, total immune cells detected in each 5-μm interval within the 100-μm distance to each tumor cell (as the core cell) were counted.

Tumor mutational burden test

To investigate the tumor mutation at baseline, the biopsy specimens from 14 patients before the combination treatment were sequenced by using FoundationOne CDx (F1CDx) and the FDA-approved 324-gene panel assay conducted by DIAN

(Hangzhou Lab, Hangzhou, China) with licensed technologies, to assess the tumor mutational burden (TMB) (Additional File: Table S1) (21).

Statistical analyses

Non-parametric two-sided Mann–Whitney *U* test or the Wilcoxon signed-rank test was used to evaluate the statistical significance between two independent or paired groups, respectively. The Kruskal–Wallis test was used to estimate the statistical significance for comparing more than two groups. Non-Gaussian distribution (Spearman correlation) was applied to assess the correlations unless otherwise indicated. OS was defined as the time from inclusion until death from any cause or the last date of follow-up time. Progression-free survival (PFS) was defined as the time from inclusion until the date of objective disease progression or death from any cause in the absence of progression. The Kaplan–Meier analysis was used to estimate OS and PFS. Differences in survival were compared with the log-rank tests. The best cutoff of the Kaplan–Meier survival analysis was calculated by the Youden index of the ROC curve.

Analyses were performed using SPSS v.25.0 (STATA, College Station, TX, USA). All statistical tests were two-sided, and the significance level was set at 0.05. Survival curves and summary graphs were presented using GraphPad Prism v.8.0. The relevance between T cells, dendritic cells, and macrophages was developed using R version 4.2.2. The data cutoff date for all analyses was 30 August 2022.

Results

Different T-cell infiltration between the tumor and stromal compartment

Twenty treatment-naive patients were finally included in the phase Ib study (NCT03671265, Additional File: Table S2). To explore the spatial characteristics of T cells, dendritic cells, and macrophages and their dynamic alteration in ESCC patients under the combination treatment of CRT plus PD-1 blockade, we applied multiplex immunofluorescence staining in 38 tumor biopsies collected at baseline or during the combination treatment (Figures 1A, B; Additional File: Table S1). We firstly excluded two baseline slides without tumor tissues and finally included 36 scanned slides in the following analysis, consisting of 18 baseline and 18 on-treatment specimens, with 16 matched pairs at these two time points (Additional File: Table S1).

With the updated data cutoff date of 30 August 2022, the median follow-up duration was 44.3 months (95% CI 41.8–46.7). Seven patients were alive and free of progressive disease. The median OS and PFS were 36.8 months (95% CI 22.2 to 42.3) and 31.9 months (95% CI 15.9–42.3), respectively (Additional File: Figure S1).

We previously reported the comparable levels of $CD4^+$ and $CD8^+$ T cells before and during CRT combined with PD-1 blockade in ESCC patients (4). Since T cells located in the tumor and stromal area had various features and capabilities in immune response (22, 23), we here segmented the tumor tissues into tumor and stromal compartments to identify T-cell levels in these two compartments (defined as tumor T cells and stromal T cells, respectively) (Figure 1C). The level of tumor $CD4^+$ T cells was lower than that of stromal $CD4^+$ T cells at baseline, while it was not different during combination (Figure 2A). The levels of tumor $CD8^+$ T cells, tumor PD-1^+CD4^+, and tumor PD-1^+CD8^+ T cells remained lower than those in stromal cells both at baseline and during combination treatment (Figures 2B–D). Next, we dynamically monitored the T-cell levels in these two compartments. CRT plus PD-1 blockade did not affect the levels of tumor $CD4^+$ and tumor $CD8^+$ T cells. However, the stromal $CD8^+$ T cells and stromal PD-1^+ T cells decreased significantly after combination treatment (Figures 2E, F). Finally, we assessed the association between each T-cell subset and patient survival. The patients having higher tumor $CD4^+$ T cells at baseline had worse OS and worse PFS compared with those having lower baseline tumor $CD4^+$ T cells (Figure 2G; Additional File: Figure S2). These results indicated the inhibitory immune microenvironment in ESCC tumors before treatment, and CRT combined with PD-1 blockade alleviated the repressive immune status which might benefit the treatment outcome.

Nearest distance of T cells to tumor cells

Since tumor-infiltrating T cells exhibited different compartmental distribution (tumor *vs.* stromal compartment) (Figure 2), we then focused on the spatial distribution of tumor-infiltrating T cells as it more precisely reflected the regional tumor immune microenvironment and the probability of interaction between the effective T cells and target tumor cells (Figure 3). We applied two types of spatial parameters. The nearest distance demonstrated possible interaction between the nearest neighbors of the T cells and tumor cells by integrating the spatial distribution and count number traits of T cells in the tumor microenvironment (Figure 3A). The proximity between T cells and tumor cells illustrated not only the heterogeneous spatial location of T cells but also the heterogeneous tumor immune microenvironment (Figure 3B).

T-cell subsets had diverse nearest distances to tumor cells among each patient (Figure 4A, Additional File: Figure S3). The PD-1-negative-expressed $CD4^+$ and $CD8^+$ T cells were located significantly nearer to the tumor cells than PD-1-positive-expressed T cells (Figure 4B). Moreover, $CD4^+$PD-1^- T cells migrated closer to the tumor cells, while $CD4^+$PD-1^+ T cells moved even farther away from the tumor cells under the combination treatment (Figures 4B, C). A higher density of tumor-infiltrating $CD8^+$ T cells was reported in heavy smokers with advanced non-small cell lung cancer (24). We also found that ESCC patients with a smoking history had a shorter distance of $CD4^+$PD-1^- T cells to tumor cells before treatment than those without (Figure 4D). However, the other baseline characteristics of the patients, such as aging, gender, and alcohol, were not associated with the nearest distance of T-cell subsets to tumor cells. Interestingly, we found a close association between higher TMB and smaller nearest distance of $CD4^+$ and $CD8^+$ T

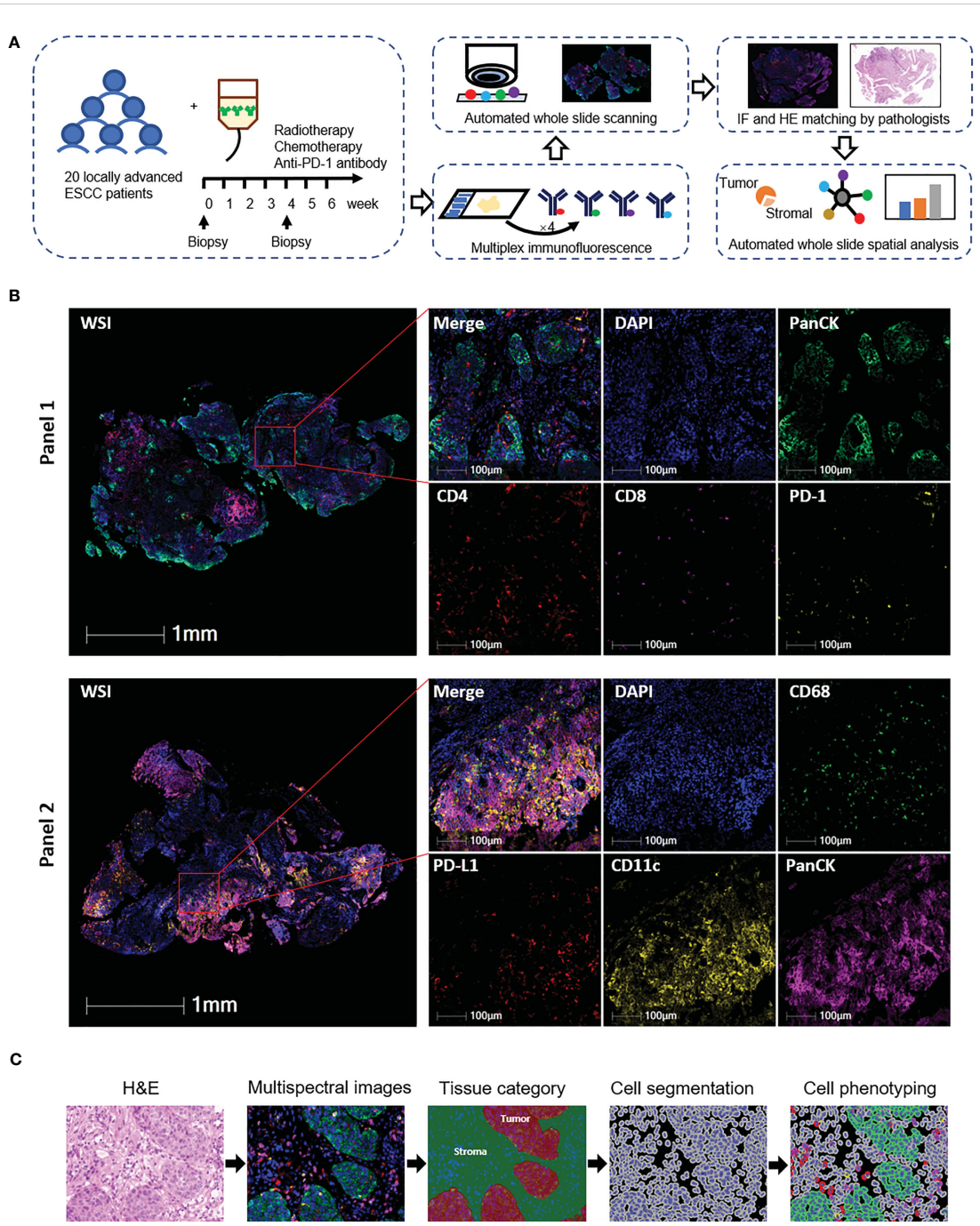

FIGURE 1
Identification of tumor-infiltrating T cells, dendritic cells, and macrophages in esophageal squamous cell carcinoma (ESCC) tissues. **(A)** Schematic diagram of the study design and analysis process. Top middle, representative panel 1 staining of baseline tumor tissue from patient 18. Top right, representative panel 2 staining of baseline tumor tissue from patient 8. **(B)** Representative images of multiplex immunofluorescence panels. WSI, whole slide imaging. From patients 6 (panel 1) and 19 (panel 2). **(C)** Automated image analysis pipeline. From patient 18 baseline tumor tissue.

cells to tumor cells in baseline tumor tissues (Figure 4E). This association was in accordance with the PD-1-negative- or PD-1-positive-expressed $CD8^+$ T cells (Figure 4E), and this turned marginal in $CD4^+PD\text{-}1^+$ T cells before combination treatment (p = 0.060, Additional File: Figure S4). In the survival analysis, we found that patients who had $CD4^+$ and $CD8^+$ T cells or their $PD\text{-}1^-$ subsets located nearer to tumor cells at baseline experienced worse OS and PFS (Figure 4F, Additional File: Figure S5). These findings again suggested that these tumor-infiltrating T cells were inhibited in ESCC before CRT combined with PD-1 blockade, and spatialized T cells with distinctive PD-1 expression were linked with the heterogenicity of the tumor microenvironment.

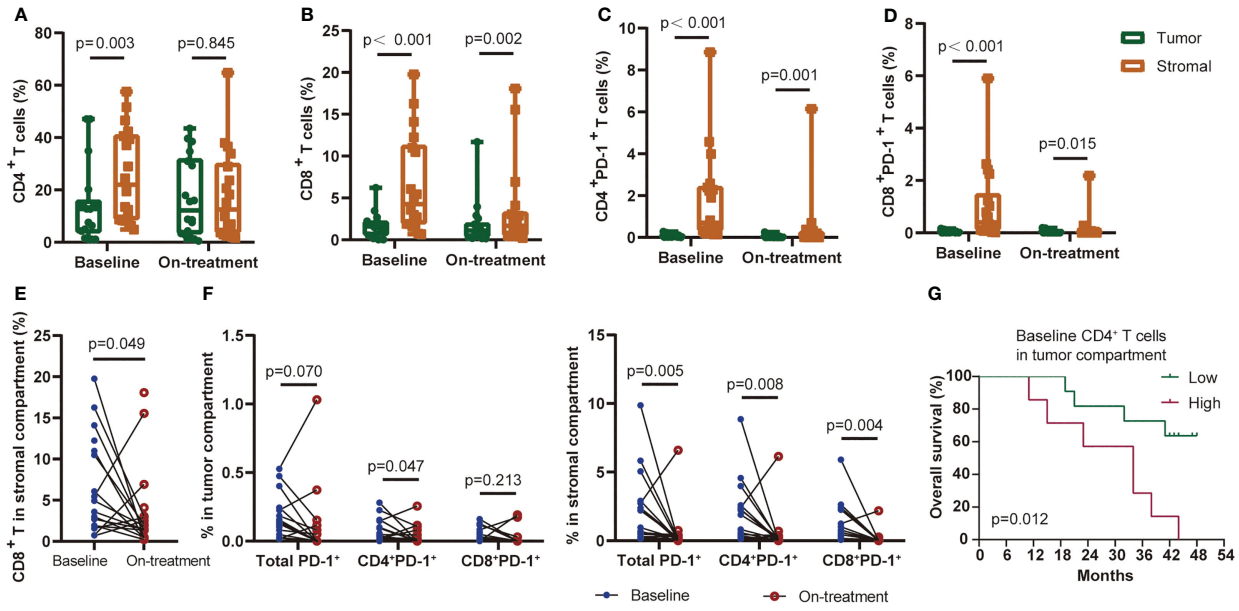

FIGURE 2
T-cell subsets distributed in the tumor or stromal compartment. $CD4^+$ T cells **(A)**, $CD8^+$ T cells **(B)**, $CD4^+PD\text{-}1^+$ T cells **(C)**, and $CD8^+PD\text{-}1^+$ T cells **(D)** distributed in the tumor or stromal compartment at baseline and during treatment. **(E)** Baseline and on-treatment $CD8^+$ T cells in the stromal compartment. **(F)** PD-1-positive-expressed T cells in the tumor (left) or stromal (right) compartment at baseline and during the combination treatment. **(G)** Kaplan–Meier curve showing overall survival based on $CD4^+$ T cells in the tumor compartment at baseline. Cutoff value: 13.97%. On-treatment, after 40 Gy of radiotherapy. Wilcoxon signed-rank tests in **(A-F)**. $p < 0.05$, statistically significant.

Proximity of T cells in ESCC

To further evaluate the position of T cells in each tumor cell, we narrowed the observation area within the 100-μm radius of the tumor cells and assessed T cells in a continuous 5-μm distance away from the tumor cells (Figure 3B). The baseline $CD4^+$, $CD8^+$ T cells, and their PD-1-positive-expressed subsets were mostly located within the 100-μm distance to tumor cells (Figure 5A). Under the combination treatment, part of these cells dispersed out of the 100-μm distance (Figure 5A). Higher PD-1-positive-expressed $CD4^+$ and $CD8^+$ T cells within the 100-μm distance during treatment predicted better OS (Figure 5B, Additional File: Figure S6). The average distance within the 100-μm distance of T-cell subsets to tumor cells also indicated an underlying interaction between T cells and tumor cells. In our study, a smaller average distance of the on-treatment $CD8^+PD\text{-}1^+$ T cells within the 100-μm distance to the tumor cells was associated with longer OS and PFS (Figure 5B, Additional File: Figure S6). These findings exhibited an improved antitumor immune microenvironment under CRT plus PD-1 blockade.

In analyzing the distribution pattern of T-cell subsets in each 5-μm range across the 100-μm distance to tumor cells, we defined the relative density of T-cell subset A as the number of T-cell subset A in one range divided by the total T-cell subset A detected in tumor tissue. We found few $CD4^+$ and $CD8^+$ T cells infiltrated in the 0–5-μm distance both at baseline and during combination treatment (Figure 5C, Additional File: Figure S7). Meanwhile, these T cells increased sharply in the 5–10-μm range, then decreased gradually in the 10–30-μm range, and finally maintained at a low level beyond the 30-μm distance (Figure 5C, Additional File: Figure S7A). A similar distribution pattern in PD-1-positive-expressed $CD4^+$ and $CD8^+$ T cells was also observed at baseline and during treatment (Figure 5C, Additional File: Figure S7B). Because the imbalanced expression of PD-1 on T cells might influence the distribution pattern of $PD\text{-}1^+$ T cells, we assessed the ratio of $PD\text{-}1^+$ T cells to T cells in each 5-μm range across the 100-μm distance. However, both $CD4^+$ and $CD8^+$ T cells remained at a stable level of PD-1 expression among each range at baseline although heterogeneity was also found among individual patient (Additional File: Figure S8A). The on-treatment PD-1 expression on T cells remained at a low level across each range in the 100-μm distance except for one patient who had a large fluctuation of PD-1 expression (Additional File: Figure S8B). We did not find any association between the distribution traits of these T-cell subsets in the 100-μm distance and the patient baseline characteristics (aging, gender, alcohol, and smoking). However, patients with higher TMB had higher baseline $CD4^+PD\text{-}1^+$ T cells, baseline $CD8^+PD\text{-}1^+$ T cells, and on-treatment $CD4^+$ T cells in the 10–35-μm distance (Figure 5D). In the survival analysis, we found that baseline $CD4^+$ T cells in the 0–5- and 5–10-μm distance were correlated with poor OS and PFS, but this association was reversed in the 35–40-μm range (Figure 5E, Additional File: Figure S9). These findings illustrated a precise spatial distribution of tumor-infiltrating T cells in ESCC, which presented a heterogeneous interaction between regional T cells and tumor cells.

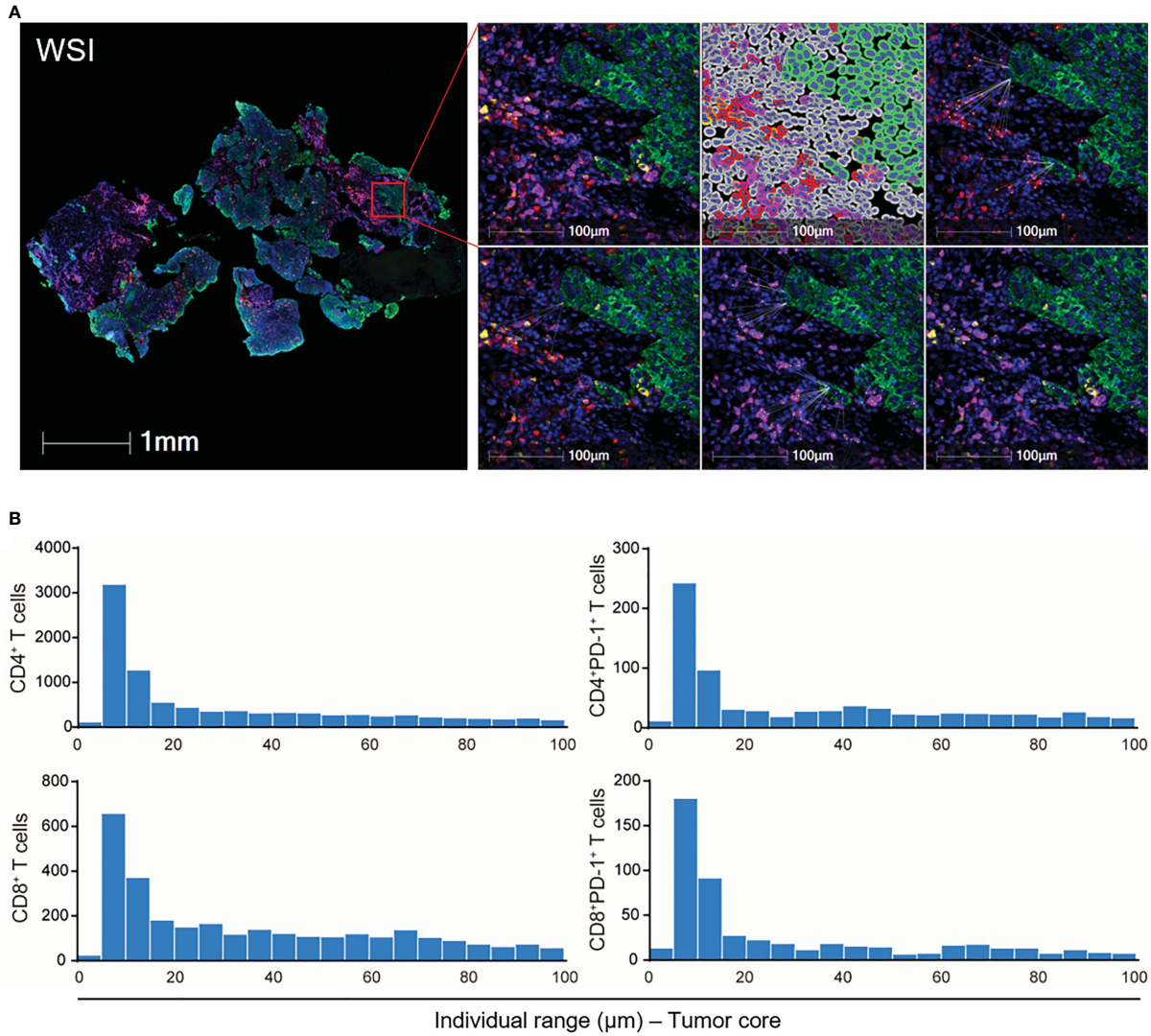

FIGURE 3
Spatial analysis of tumor-infiltrating T cells in ESCC. **(A)** Schematic graph of the nearest distance analysis. Green: tumor cells. Red: $CD4^+$ T cells. Purple: $CD8^+$ T cells. Yellow: $PD\text{-}1^+$ cells. Upper right panel: from left to right, merged fluorescence, cell phenotyping, nearest neighbors of $CD4^+$ T cells to tumor cells. Lower right panel: from left to right, nearest neighbors of $CD4^+PD\text{-}1^+$, $CD8^+$, and $CD8^+PD\text{-}1^+$ T cells to tumor cells. **(B)** Proximity analysis in WSI in **(A)**. WSI, whole slide imaging. From patient 18 baseline tumor tissue.

Proximity of DCs and macrophages in ESCC

We previously reported the nearest distance of myeloid-derived immune cells, $CD11c^+$ DCs, and $CD68^+$ macrophages and its close association with outcome under CRT plus PD-1 blockade (18). We here evaluated the precision distribution of these cells in ESCC. Similar to the findings in T cells (Figure 5), the majority of DCs, macrophages, and their PD-L1+ subsets distributed at the 100-mm distance to the tumor cells (Figure 6A). A high proportion of these subsets was located between the 5- and 30-μm distance, with the highest in the 5–10-μm range at baseline and during combination (Figure 6B, Additional File: Figure S10). Both higher DCs and higher macrophages in the 5–10-μm distance at baseline were associated with higher TMB, and the correlation tended to have significance during combination (Figure 6C). DCs and macrophages exhibited an evenness level of PD-L1 expression across the 0–100-μm distance in each patient (Additional File: Figure S11). The myeloid-derived cells distributed at different distances to tumor cells had divergent associations with patient survival. Patients with lower subsets of DCs and macrophages at a nearer distance (0–5 and 5–10 μm) at baseline had shorter OS and PFS (Figure 6D, Additional File: Figure S12). On the contrary, patients with higher subsets of these cells in relatively farther distances (20–25, 25–30, and 30–35 μm) at baseline had longer OS and PFS (Figure 6D, Additional File: Figure S13). We found one exception between T and myeloid-derived cells. The myeloid-derived cells had declined distribution in the 5–10-, 10–15-, and 15–20-μm range during combination compared with those at baseline (Figure 6E), but there was no alteration in T cells in any range across the 100-μm distance during combination. The similar distribution patterns of T cells, DCs, and macrophages to tumor

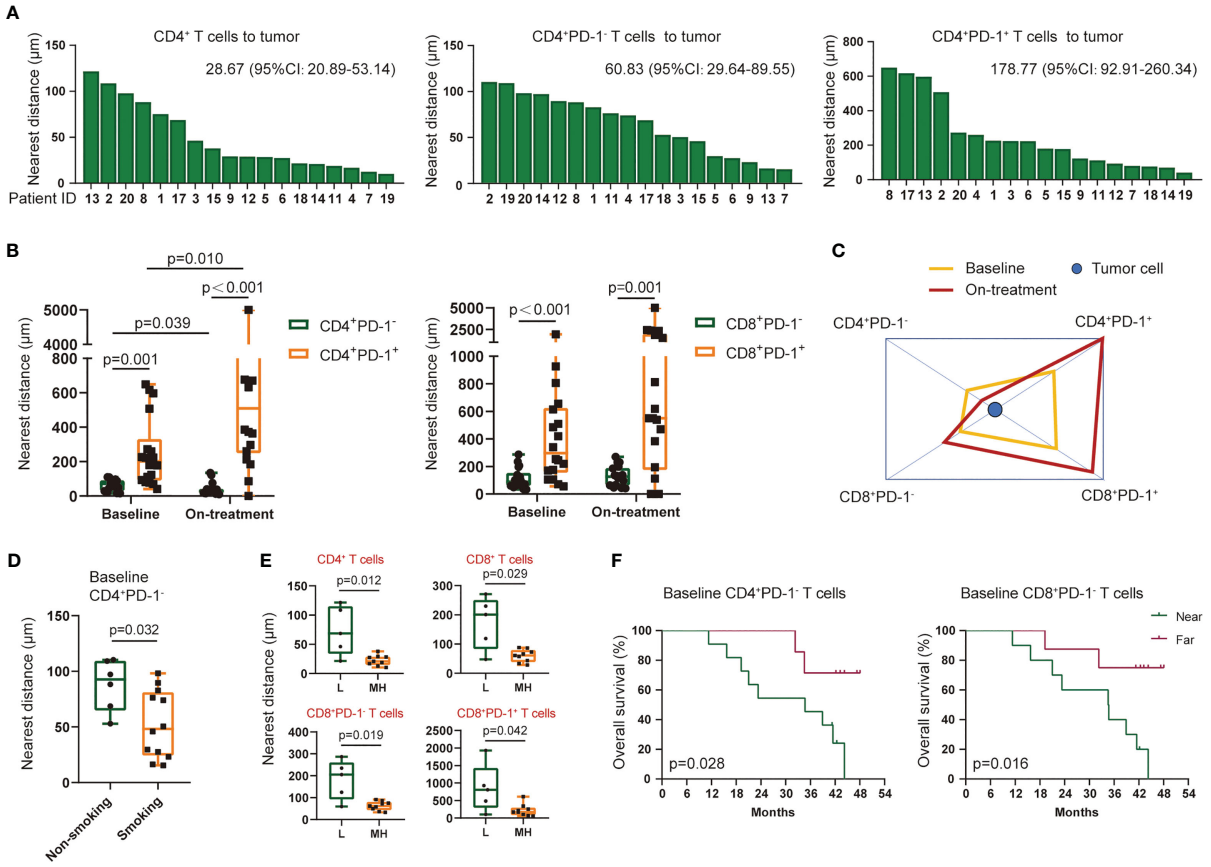

FIGURE 4
Nearest distance of T-cell subsets to tumor cells. **(A)** Nearest distance of $CD4^+$ T cells (left), $CD4^+PD\text{-}1^-$ T cells (middle), and $CD4^+PD\text{-}1^+$ T cells (right) to tumor cells for each patient. Statistics: median (95% confidence interval). Arranged by distance from high to low. **(B)** Comparation of the nearest distance to tumor cells between $CD4^+PD\text{-}1^-$ and $CD4^+PD\text{-}1^+$ T cells and between $CD8^+PD\text{-}1^-$ and $CD8^+PD\text{-}1^+$ T cells at baseline and under the combination treatment. **(C)** Schematic diagram of the nearest distance of T-cell subsets to tumor cells. $CD4^+PD\text{-}1^+$ and $CD8^+PD\text{-}1^+$ T cells had the farthest distance from tumors both at the two time points. **(D)** Nearest distance of baseline $CD4^+PD\text{-}1^-$ T cells to tumor cells between patients with and without a smoking history. **(E)** Nearest distance of T-cell subsets to tumor cells between patients with low and middle/high TMB at baseline. **(F)** Kaplan–Meier curve showing the overall survival based on the nearest distance of baseline $CD4^+PD\text{-}1^-$ T cells and baseline $CD8^+PD\text{-}1^-$ T cells to tumor cells. Cutoff value: 79.58 μm for $CD4^+PD\text{-}1^-$ T cells and 95.88 μm for $CD8^+PD\text{-}1^-$ T cells. Wilcoxon signed-rank tests in **(B)**. Kruskal–Wallis tests used among subsets at baseline and under the combination treatment in **(C)**, respectively. Mann–Whitney *U* tests in **(D, E)**. L, TMB low (≤5 Muts/Mb); MH, TMB middle or high (>5 Muts/Mb); on-treatment, after 40 Gy of radiotherapy. $p < 0.05$, statistically significant.

cells strongly indicated the potential association between these cells in ESCC.

Association between T cells, DCs, and macrophages in ESCC

We firstly determined the relationship between the subsets of T cells, DCs, and macrophages in the 0–15-μm distance to the tumor cells, as a large part of these cells were located in this area and had the most possibility to interact with tumor cells directly. Before the combination treatment, the strongest correlation was observed between DCs and macrophages and their PD-L1-positive subsets, moderate correlation between T-cell subsets, and low correlation between the T and DC/macrophage subsets (Figure 7A). After the combination treatment, the correlation between the DC/macrophage subsets was even higher than that at baseline, and the correlation between the $CD8^+$ T and DC/macrophage subsets also improved (Figure 7B). Meanwhile, we evaluated the relevance of the nearest distance between the T-cell and DC/macrophage subsets. High relevance was found between T-cell subsets and moderate between DC/macrophage subsets at baseline (Figure 7C). Macrophages were more relevant than DCs with the T-cell subsets at baseline (Figure 7C). After the combination treatment, the T-cell subsets became weakly correlated, while DCs and macrophages still had a strong correlation (Figure 7D). Finally, we used TIMER2.0 (http://timer.cistrome.org/) (25) to evaluate the correlation between T cells, DCs, and macrophages in esophageal cancer and found a consistent correlation between these cells (Figure 7E).

Discussion

In the present study, we precisely depicted the inhibitory status of T cells in locally advanced ESCC by using spatial analysis. We

10.3389/fimmu.2023.1138054

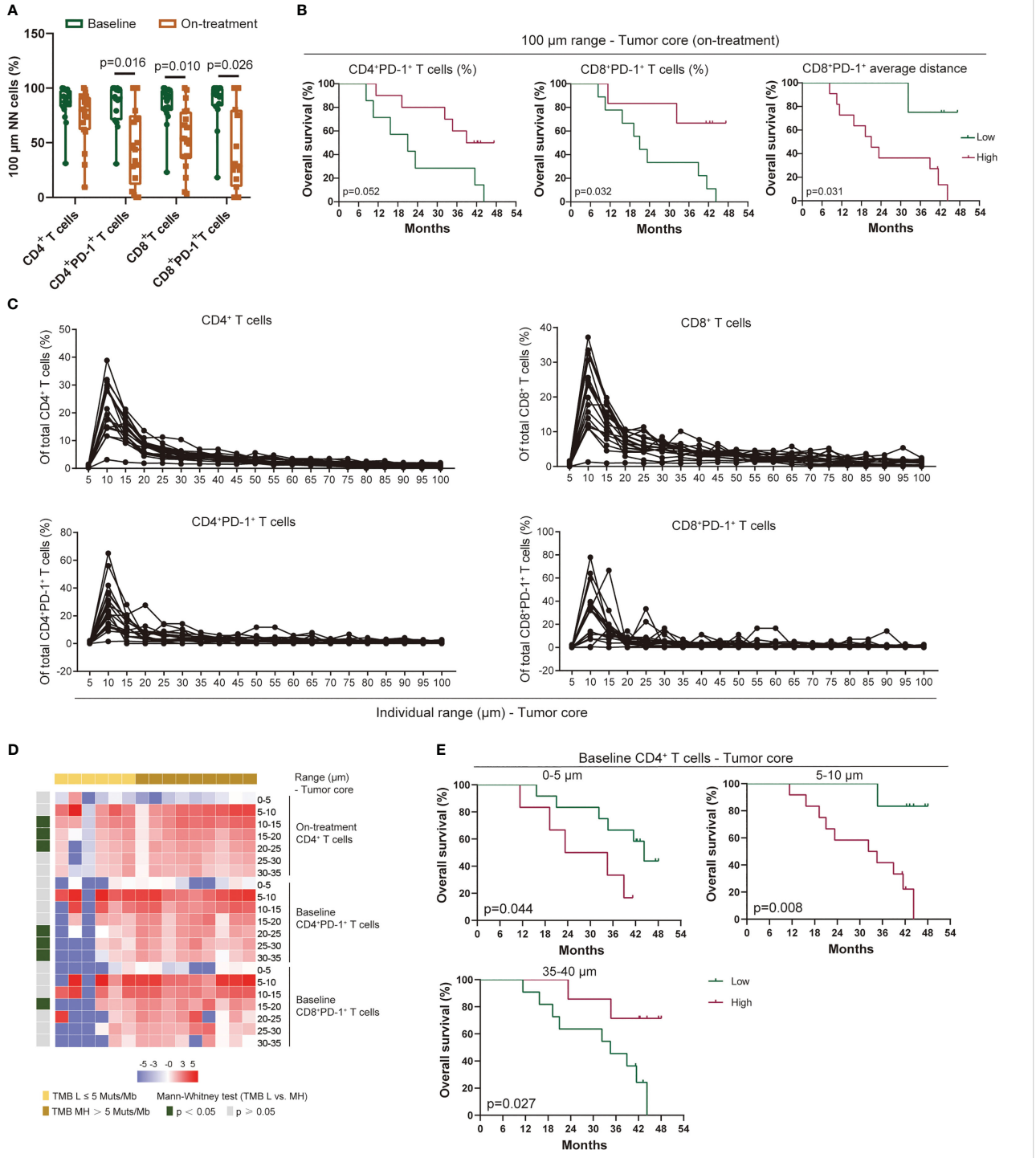

FIGURE 5
Proximity of T-cell subsets in ESCC. **(A)** T-cell subsets within the 100-μm distance to tumor cells. **(B)** Kaplan–Meier curve showing the overall survival based on the proportion of $CD4^+PD\text{-}1^+$ and $CD8^+PD\text{-}1^+$ T cells and the average distance of $CD8^+PD\text{-}1^+$ T cells within the 100-μm distance to tumor cells during treatment. Cutoff value: 31.51% for $CD4^+PD\text{-}1^+$ T cells and 38.72% for $CD8^+PD\text{-}1^+$ T cells; 47.75 μm for the average distance of $CD8^+PD\text{-}1^+$ T cells. **(C)** Proportion of T-cell subsets in each 5-μm range across the 100-μm distance to tumor cells at baseline. **(D)** Heatmap illustrating the association between TMB and the proportion of T-cell subsets in individual distance to tumor cells. **(E)** Kaplan–Meier curve showing the overall survival based on the proportion of $CD4^+$ T cells in the 0–5-, 5–10-, and 35–40-μm distance to tumor cells at baseline. Cutoff values: 0.97%, 14.95%, and 3.81%. On-treatment, after 40 Gy of radiotherapy. Wilcoxon signed-rank tests in **(A)**. Mann–Whitney *U* test in **(D)**. $p < 0.05$, statistically significant.

10.3389/fimmu.2023.1138054

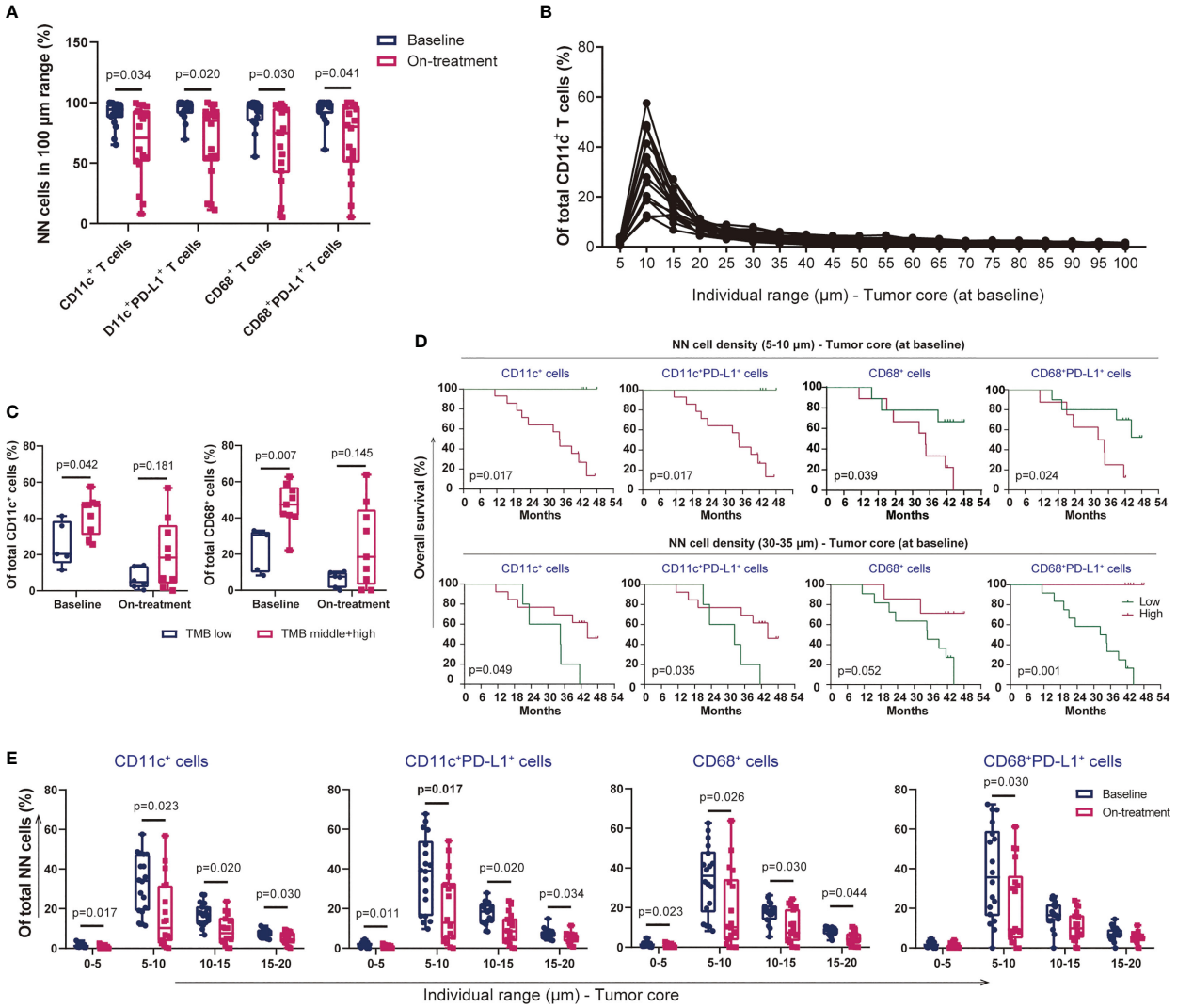

FIGURE 6
Proximity of dendritic cells and macrophages in ESCC. **(A)** $CD11c^+$ dendritic cells, $CD68^+$ macrophages, and their PD-$L1^+$ subsets within the 100-μm distance to tumor cells. **(B)** Proportion of $CD11c^+$ dendritic cells in each 5-μm range across the 100-μm distance to tumor cells at baseline. **(C)** Dendritic cells and $CD68^+$ macrophages within the 100-μm distance to tumor cells in patients with low or middle/high TMB. **(D)** Kaplan–Meier curve showing the overall survival based on the proportion of myeloid-derived cells in the 5–10- and 30–35-μm distance to tumor cells at baseline. Cutoff values: 18.79%, 16.14%, 20.91%, and 40.89% in the 5–10-μm distance; 2.75%, 2.11%, 3.55%, and 3.40% in the 30–35-μm distance. Similar groups divided according to the cutoff values of 18.79% and 16.14% in $CD11c^+$ and $CD11c^+$PD-$L1^+$ cells in the 5–10-μm distance. Consequently, the survival curves and significant differences were the same (two graphs in the top left corner). **(E)** Decreased proportion of myeloid-derived cells within the 20-μm distance to tumor cells under the combination treatment. On-treatment, after 40 Gy of radiotherapy. Wilcoxon signed-rank tests in **(A)** and **(E)**. Mann–Whitney *U* test in **(C)**. $p < 0.05$, statistically significant.

found an improved antitumor immune microenvironment under CRT plus PD-1 blockade, which predicted better treatment outcome. Our results also revealed the significant spatial connection between T cells and myeloid-derived cells, which was consistently maintained throughout the combination treatment. TMB and smoking exposure promoted T cells to accumulate near tumor cells in ESCC.

We found that tumor $CD4^+$ T cells and the nearest distance of $CD4^+$PD-1^- and $CD8^+$PD-1^- to tumor cells at baseline predicted poor survival in ESCC patients. Recent evidence revealed an inhibitory and exhausted status of T-cell subsets in the immune microenvironment of ESCC (7–9). The heterotypic interaction between cancer cells and non-cancer cells of the tumor microenvironment remolded a tumor-supportive and immune-repressive environment. Direct intercellular contact and paracrine signaling both contributed to the dysfunctional status of immune cells. The inhibitory induction factors might be derived from tumor cells (26, 27), abnormally regulated immune and stromal cells in the tumor microenvironment (28, 29), and distant endocrine cytokines (30), as well as metabolic changes in tumor cells and non-cancer cells. We found that the tumor compartment had lower T cells than the stromal compartment, and PD-1^+ T cells were located farther away from the tumor cells compared with the PD-1^- T cells at baseline. The PD-1^+ T cells might be composed of more tumor-specific T cells in the tumor microenvironment (31, 32). These

10.3389/fimmu.2023.1138054

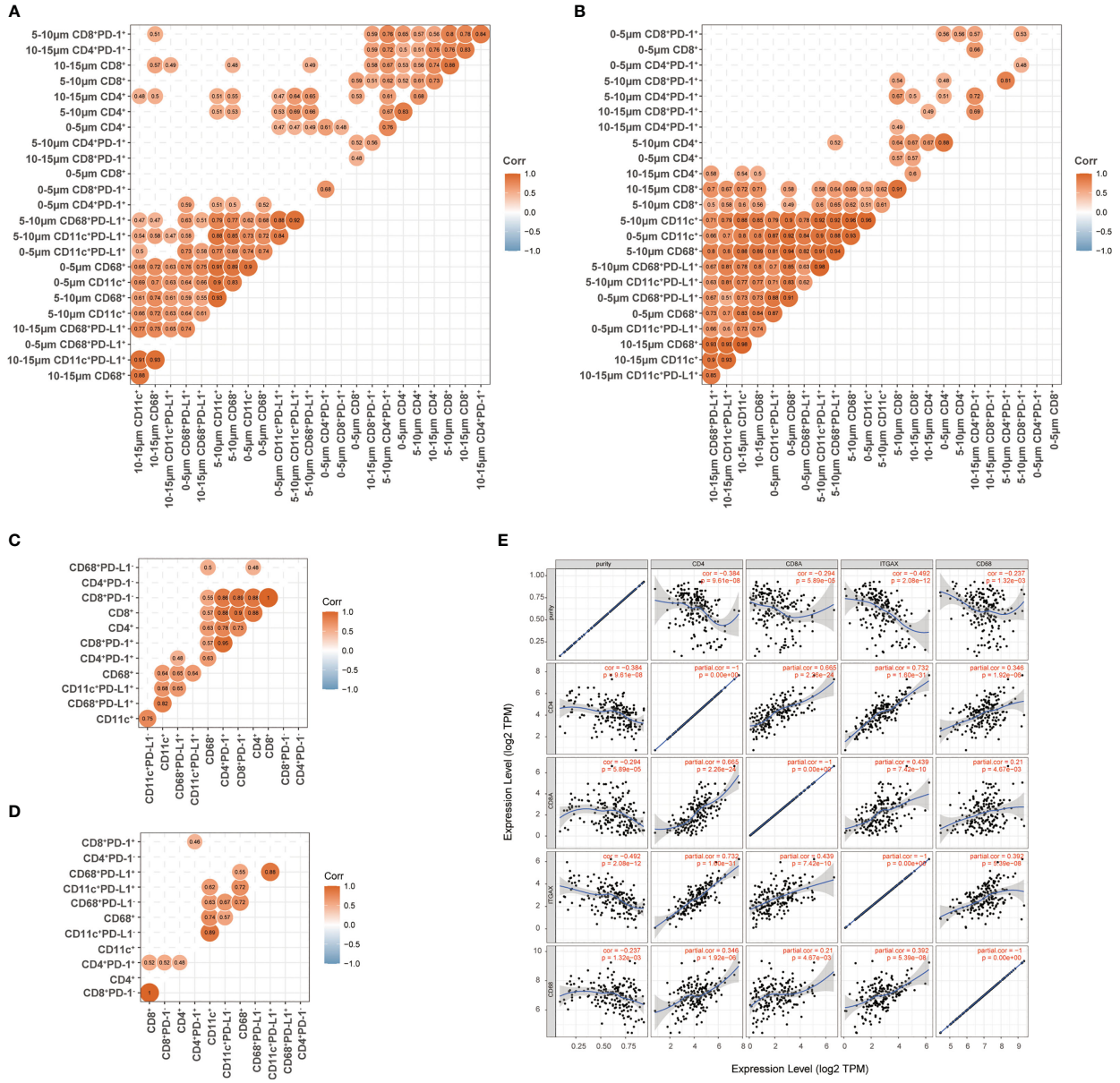

FIGURE 7
Association between T cells, dendritic cells, and macrophages in ESCC. **(A, B)** Association between the proportion of T cells and the proportion of dendritic cells and macrophages in the 0–15-μm distance to tumor cells at baseline **(A)** and during treatment **(B)**. **(C, D)** Association between the nearest distance of T cells and the nearest distance of dendritic cells and macrophages to tumor cells at baseline **(C)** and during treatment **(D)**. **(E)** TIMER2.0 evaluated the correlation between T cells and myeloid-derived cells in esophageal cancer. Spearman correlation in **(A-D)**. Correlation coefficient was shown when p <0.05 with statistical significance.

results indicated that the potential tumor-specific T cells were probably secluded from the tumor cells at a distance in locally advanced ESCC without any therapeutic intervention. This spatial distribution pattern of T-cell subsets in ESCC accelerated the loss of immune surveillance and promoted immune escape. We found that high levels of $CD4^+$ T cells distributed in the 0–10-μm distance to tumor cells at baseline predicted poor survival. ESCC has been shown to harbor tumor-infiltrating $Foxp3^+CD4^+$ regulatory T cells (Tregs) (33, 34). However, the infiltrating Tregs could not predict survival in ESCC patients (35). Various bystander T cells that recognized a wide range of epitopes unrelated to cancer accumulated in tumor tissues but had no antitumor efficiency (36). Identifying subgroups and tumor specificity of infiltrating T cells could provide new evidence for the underlying mechanisms of immune response. All these findings supported a deteriorated antitumor immune microenvironment in locally advanced ESCC, which was partially characterized by the dysfunction and distance barrier for the tumor-infiltrating T cells with potential antitumor capability.

We found comparable levels of T-cell subsets in the tumor compartment before and after the combination treatment. T cells were more sensitive to CRT compared with myeloid-derived cells (37). Hematological toxicity was always one of the most serious side

effects of CRT or CRT plus PD-1 blockade (1, 4). However, we indeed found clonal expansion of tumor-infiltrating T cells that had already existed in local ESCC tumors before the combination treatment of CRT plus PD-1 blockade (38). Meanwhile, more than 90% of T-cell clones in on-treatment tumors were newly acquired after the combination treatment (38). The peripheral blood provided an abundant T-cell pool to support the local antitumor immune response (39, 40). A recent study also revealed that tumor-specific memory $CD8^+$ T cells in draining lymph nodes respond to PD-1/PD-L1 blockade (5). CRT disturbed the suppressive tumor immune microenvironment and improved the antitumor immune response, which was further strengthened with the addition of PD-1 blockade. Taking these results together with our findings into consideration, it can be inferred that combining PD-1 blockade rejuvenated and recruited T cells to the tumor microenvironment, which enriched the tumor-infiltrating T cells and contributed to improved treatment outcome.

We found that high PD-1-positive-expressed $CD4^+$ and $CD8^+$ T cells within the 100-μm distance to the tumor cells during the combination treatment were significantly associated with better OS. The tumor-infiltrating $PD\text{-}1^+$ T cells during treatment indicated activated status and antitumor potential, although the specificity of these cells was unavailable in the present study. In our findings, most of the T cells, DCs, and macrophages were distributed within the distance of 5–30 μm, especially in the 5–10-μm distance. However, our results did not show that the high density of T/DCs/macrophages within the 10-μm distance had an effect on tumor control. In contrast, those distributed in the 20-μm or farther distance were probably the antitumor candidates. Interleukin-33 induced CCL2 and IL-7 induced CXCL9, CXCL10, CCL2, and CCL20 expression in ESCC tissues (41, 42). $CD4^+$, $CD8^+$ T cells, macrophages, and DCs expressing the receptors of these chemokines were recruited into ESCC (41–44), where these cells were regulated by complex signaling from the regional tumor microenvironment and presented diverse capabilities participating in pro- or antitumor immune response. These results enlightened the spatial and functional heterogenicity of tumor-infiltrating immune cells critically and were diversely devoted to the treatment outcome of CRT plus PD-1 blockade. We are now working on the precise mechanisms that inhibit or activate immune cells in these heterogeneous tumor regions before and under the combination treatment.

CRT promoted the release of danger signals and chemokines that recruited DCs and macrophages into tumor sites and provoked tumor cell killing by activating cytotoxic T-cell function (18, 45, 46). However, the interaction between T cells and antigen-presenting cells (APCs) under CRT plus immunotherapy is little known. We here illustrated the spatial connection of these two types of immune cells when adding PD-1 blockade to CRT in ESCC patients. An accordant distribution pattern between T cells and DCs/macrophages in the 100-μm distance to tumor cells throughout the combination treatment as well as their association with patient survival in our findings was observed. Close spatial positions facilitated the signal transmission between these two types of cells. The T-cell and APC crosstalk was a double-edged sword in immune response, resulting in immune activation as well as anergy or tolerance (47, 48). These lines of evidence as well as our findings supported the vital role of the mutual regulation and influence among T and APC subsets in the tumor immune microenvironment both during tumor progression and during therapeutic interventions. Additionally, we found that the relevance between DCs and macrophages became even higher after the combination treatment. These two myeloid-derived subsets either acted as suppressors or activators in tumor immune responses (49, 50). High inflexible plasticity, one of the most intriguing features in myeloid-derived cells, led to diverse subgroups in these cells and their sensitive and rapid response to the internal and external signaling from the tumor microenvironment (51, 52). More precisely, identifying the subgroups of these myeloid-derived cells and their association with other immune cells, stromal cells, and tumor cells would provide important clues that will help interpret the mechanisms and treatment outcome of CRT plus immunotherapy.

The present study and our previous study (18) showed a significant association between higher TMB and more T cells, DCs, and macrophages that accumulated near the tumor cells at baseline. Tumors with high TMB probably had high tumor neoantigens that induced the antitumor immune response (53). On neoantigens presented by APCs, tumor-specific T cells underwent clonal expansion with significant correlation between high TMB, high TCR Simpson, and low Shannon index in ESCC patients (38). High levels of TMB not only facilitated the tumor infiltration and activation of T cells but also optimized the spatial distribution of these cells in the tumor microenvironment. However, we (3, 4) and others (54) failed to connect the TMB and survival in RT or even adding immunotherapy in ESCC. Other factors that regulated the tumor immune microenvironment under CRT combined with PD-1 blockade contributed to the treatment outcome aside from the TMB effect.

Lastly, we firstly reported that smoking history was associated with a shorter distance of $PD\text{-}1^-CD4^+$ T cells to tumor cells in ESCC. Smoking is a major risk factor resulting in ESCC. The serum metabolites of cigarette (55), lncRNA H19 (56), and p53 mutation or overexpression (57, 58) induced by smoking exposure were closely correlated with ESCC incidence. Mechanically, smoking facilitated ESCC by the Y-linked LINC00278/Yin Yang 1 (YY1)-binding micropeptide/YY1/androgen receptor signaling pathway (59). However, whether smoking exposure attracted T-cell accumulation in tumor tissues is still unknown. The activation of the NF-κB pathway and alteration in metabolites, tumor, and stromal cells induced by exposure to smoking might affect the tumor immune microenvironment (60).

Several limitations existed in our study. As expected in phase Ib clinical studies, the sample size of this study was also small. Control groups, such as samples from standard CRT or PD-1 blockade alone, were not available. Functional evaluation was not applied in the study because of the limitation of ESCC tissues collected under endoscopic ultrasonography. In addition, we did not identify the subgroups of tumor-infiltrating immune cells in the present exploration study. Our ongoing phase III study (NCT04426955) of CRT combined with camrelizumab is under follow-up, which

would help provide more evidence to strengthen the findings of this study.

In conclusion, we firstly illustrated the precise spatial distribution of tumor-infiltrating T cells in ESCC patients who received CRT combined with PD-1 blockade. Combining CRT and PD-1 blockade could improve the inhibitory status of tumor-infiltrating T cells, which could benefit the combination outcome. The characteristic distribution patterns of T cells, DCs, and macrophages could be promising predictive candidates for this combination treatment. Further studies on precision tumor fields would provide new mechanisms in immunotherapy in solid tumors.

Data availability statement

The original contributions presented in the study are included in the article/Supplementary Material, further inquiries can be directed to the corresponding authors.

Ethics statement

The studies involving human participants were reviewed and approved by The institutional review board and ethics committee at Tianjin Medical University Cancer Institute and Hospital (E2018142). The patients/participants provided their written informed consent to participate in this study.

Author contributions

WZ conceived and designed the study. CY, HH, ZZ, XM, and HW performed the exploration experiments. FC, TZ, XC, and JD collected the samples and clinical information. GZ, PT, HJ, MW, PW, and QP interpreted the data. WZ and CY drafted the manuscript. All authors contributed to the article and approved the submitted version.

Funding

This work was supported by the National Natural Science Foundation of China (under grant numbers 81872462, 82272733, 81972772, and 82273083) and Tianjin Key Medical Discipline (Specialty) Construction Project (TJYXZDXK-009A).

Acknowledgments

We are grateful to all the patients and their families and all the members of the collaborative group in this trial. We thank Jiangsu Hengrui Pharmaceuticals Co., Ltd., China, for providing camrelizumab and apatinib freely.

Conflict of interest

The authors declare that the research was conducted in the absence of any commercial or financial relationships that could be construed as a potential conflict of interest.

Publisher's note

All claims expressed in this article are solely those of the authors and do not necessarily represent those of their affiliated organizations, or those of the publisher, the editors and the reviewers. Any product that may be evaluated in this article, or claim that may be made by its manufacturer, is not guaranteed or endorsed by the publisher.

Supplementary material

The Supplementary Material for this article can be found online at: https://www.frontiersin.org/articles/10.3389/fimmu.2023.1138054/full#supplementary-material

References

1. Chen Y, Ye J, Zhu Z, Zhao W, Zhou J, Wu C, et al. Comparing paclitaxel plus fluorouracil versus cisplatin plus fluorouracil in chemoradiotherapy for locally advanced esophageal squamous cell cancer: a randomized, multicenter, phase III clinical trial. *J Clin Oncol* (2019) 37(20):1695–703. doi: 10.1200/JCO.18.02122

2. Xu Y, Dong B, Zhu W, Li J, Huang R, Sun Z, et al. A phase III multicenter randomized clinical trial of 60 gy vs 50 gy radiation dose in concurrent chemoradiotherapy for inoperable esophageal squamous cell carcinoma. *Clin Cancer Res* (2022) 28(9):1792–9. doi: 10.1158/1078-0432.CCR-21-3843

3. Zhang W, Yan C, Gao X, Li X, Cao F, Zhao G, et al. Safety and feasibility of radiotherapy plus camrelizumab for locally advanced esophageal squamous cell carcinoma. *Oncologist* (2021) 26(7):e1110–24. doi: 10.1002/onco.13797

4. Zhang W, Yan C, Zhang T, Chen X, Dong J, Zhao J, et al. Addition of camrelizumab to docetaxel, cisplatin, and radiation therapy in patients with locally advanced esophageal squamous cell carcinoma: a phase 1b study. *Oncoimmunology* (2021) 10(1):1971418. doi: 10.1080/2162402X.2021.1971418

5. Huang Q, Wu X, Wang Z, Chen X, Wang L, Lu Y, et al. The primordial differentiation of tumor-specific memory CD8(+) T cells as bona fide responders to PD-1/PD-L1 blockade in draining lymph nodes. *Cell* (2022) 185(22):4049–4066.e25. doi: 10.1016/j.cell.2022.09.020

6. Banta KL, Xu X, Chitre AS, Au-Yeung A, Takahashi C, O'Gorman WE, et al. Mechanistic convergence of the TIGIT and PD-1 inhibitory pathways necessitates co-blockade to optimize anti-tumor CD8(+) T cell responses. *Immunity* (2022) 55(3):512–526.e9. doi: 10.1016/j.immuni.2022.02.005

7. Dinh HQ, Pan F, Wang G, Huang QF, Olingy CE, Wu ZY, et al. Integrated single-cell transcriptome analysis reveals heterogeneity of esophageal squamous cell carcinoma microenvironment. *Nat Commun* (2021) 12(1):7335. doi: 10.1038/s41467-021-27599-5

8. Zhang X, Peng L, Luo Y, Zhang S, Pu Y, Chen Y, et al. Dissecting esophageal squamous-cell carcinoma ecosystem by single-cell transcriptomic analysis. *Nat Commun* (2021) 12(1):5291. doi: 10.1038/s41467-021-25539-x

9. Zheng Y, Chen Z, Han Y, Han L, Zou X, Zhou B, et al. Immune suppressive landscape in the human esophageal squamous cell carcinoma microenvironment. *Nat Commun* (2020) 11(1):6268. doi: 10.1038/s41467-020-20019-0

10. Qian D, Wang Y, Zhao G, Cao F, Er P, Chen X, et al. Tumor remission and tumor-infiltrating lymphocytes during chemoradiation therapy: predictive and prognostic markers in locally advanced esophageal squamous cell carcinoma. *Int J Radiat Oncol Biol Phys* (2019) 105(2):319–28. doi: 10.1016/j.ijrobp.2019.06.079

11. Yan T, Cui H, Zhou Y, Yang B, Kong P, Zhang Y, et al. Multi-region sequencing unveils novel actionable targets and spatial heterogeneity in esophageal squamous cell carcinoma. *Nat Commun* (2019) 10(1):1670. doi: 10.1038/s41467-019-09255-1

12. Roelands J, van der Ploeg M, Ijsselsteijn ME, Dang H, Boonstra JJ, Hardwick JCH, et al. Transcriptomic and immunophenotypic profiling reveals molecular and immunological hallmarks of colorectal cancer tumourigenesis. *Gut* (2022) 0:1–14. doi: 10.1136/gutjnl-2022-327608

13. Ferguson AL, Sharman AR, Allen RO, Ye T, Lee JH, Low TH, et al. High-dimensional and spatial analysis reveals immune landscape-dependent progression in cutaneous squamous cell carcinoma. *Clin Cancer Res* (2022) 28(21):4677–88. doi: 10.1158/1078-0432.CCR-22-1332

14. Wu R, Guo W, Qiu X, Wang S, Sui C, Lian Q, et al. Comprehensive analysis of spatial architecture in primary liver cancer. *Sci Adv* (2021) 7(51):eabg3750. doi: 10.1126/sciadv.abg3750

15. Gazinska P, Milton C, Iacovacci J, Ward J, Buus R, Alaguthurai T, et al. Dynamic changes in the NK-, neutrophil-, and b-cell immunophenotypes relevant in high metastatic risk post neoadjuvant chemotherapy-resistant early breast cancers. *Clin Cancer Res* (2022) 28(20):4494–508. doi: 10.1158/1078-0432.CCR-22-0543

16. Dias Costa A, Vayrynen SA, Chawla A, Zhang J, Vayrynen JP, Lau MC, et al. Neoadjuvant chemotherapy is associated with altered immune cell infiltration and an anti-tumorigenic microenvironment in resected pancreatic cancer. *Clin Cancer Res* (2022) 28(23):5167–79. doi: 10.1158/1078-0432.CCR-22-1125

17. Lin Y, Peng L, Dong L, Liu D, Ma J, Lin J, et al. Geospatial immune heterogeneity reflects the diverse tumor-immune interactions in intrahepatic cholangiocarcinoma. *Cancer Discovery* (2022) 12(10):2350–71. doi: 10.1158/2159-8290.CD-21-1640

18. Ma X, Guo Z, Wei X, Zhao G, Han D, Zhang T, et al. Spatial distribution and predictive significance of dendritic cells and macrophages in esophageal cancer treated with combined chemoradiotherapy and PD-1 blockade. *Front Immunol* (2021) 12:786429. doi: 10.3389/fimmu.2021.786429

19. Noordman BJ, Spaander MCW, Valkema R, Wijnhoven BPL, van Berge Henegouwen MI, Shapiro J, et al. Detection of residual disease after neoadjuvant chemoradiotherapy for oesophageal cancer (preSANO): a prospective multicentre, diagnostic cohort study. *Lancet Oncol* (2018) 19(7):965–74. doi: 10.1016/S1470-2045(18)30201-8

20. Shapiro J, ten Kate FJ, van Hagen P, Biermann K, Wijnhoven BP, van Lanschot JJ. Residual esophageal cancer after neoadjuvant chemoradiotherapy frequently involves the mucosa and submucosa. *Ann Surg* (2013) 258(5):678–88; discussion 688-9. doi: 10.1097/SLA.0b013e3182a6191d

21. Frampton GM, Fichtenholtz A, Otto GA, Wang K, Downing SR, He J, et al. Development and validation of a clinical cancer genomic profiling test based on massively parallel DNA sequencing. *Nat Biotechnol* (2013) 31(11):1023–31. doi: 10.1038/nbt.2696

22. Nirmal AJ, Maliga Z, Vallius T, Quattrochi B, Chen AA, Jacobson CA, et al. The spatial landscape of progression and immunoediting in primary melanoma at single-cell resolution. *Cancer Discovery* (2022) 12(6):1518–41. doi: 10.1158/2159-8290.CD-21-1357

23. Salmon H, Franciszkiewicz K, Damotte D, Dieu-Nosjean MC, Validire P, Trautmann A, et al. Matrix architecture defines the preferential localization and migration of T cells into the stroma of human lung tumors. *J Clin Invest* (2012) 122(3):899–910. doi: 10.1172/JCI45817

24. Shimoda Y, Yoshida T, Shirasawa M, Mizuno T, Jo H, Matsumoto Y, et al. Smoking history predicts high presence of TILs and efficacy of PD-1 blockade in PD-L1 expression-negative non-small cell lung cancer patients. *Anticancer Res* (2021) 41(11):5739–47. doi: 10.21873/anticanres.15390

25. Li T, Fu J, Zeng Z, Cohen D, Li J, Chen Q, et al. TIMER2.0 for analysis of tumor-infiltrating immune cells. *Nucleic Acids Res* (2020) 48(W1):W509–14. doi: 10.1093/nar/gkaa407

26. Niu N, Shen X, Zhang L, Chen Y, Lu P, Yang W, et al. Tumor cell-intrinsic SETD2 deficiency reprograms neutrophils to foster immune escape in pancreatic tumorigenesis. *Adv Sci (Weinh)* (2022) 10(2):e2202937. doi: 10.1002/advs.202202937

27. Meraviglia-Crivelli D, Villanueva H, Zheleva A, Villalba-Esparza M, Moreno B, Menon AP, et al. IL-6/STAT3 signaling in tumor cells restricts the expression of frameshift-derived neoantigens by SMG1 induction. *Mol Cancer* (2022) 21(1):211. doi: 10.1186/s12943-022-01679-6

28. Gong Z, Li Q, Shi J, Wei J, Li P, Chang CH, et al. Lung fibroblasts facilitate pre-metastatic niche formation by remodeling the local immune microenvironment. *Immunity* (2022) 55(8):1483–1500 e9. doi: 10.1016/j.immuni.2022.07.001

29. Derynck R, Turley SJ, Akhurst RJ. TGFbeta biology in cancer progression and immunotherapy. *Nat Rev Clin Oncol* (2021) 18(1):9–34. doi: 10.1038/s41571-020-0403-1

30. Huang Q, Wu M, Wu X, Zhang Y, Xia Y. Muscle-to-tumor crosstalk: the effect of exercise-induced myokine on cancer progression. *Biochim Biophys Acta Rev Cancer* (2022) 1877(5):188761. doi: 10.1016/j.bbcan.2022.188761

31. Duhen R, Fesneau O, Samson KA, Frye AK, Beymer M, Rajamanickam V, et al. PD-1 and ICOS coexpression identifies tumor-reactive CD4+ T cells in human solid tumors. *J Clin Invest* (2022) 132(12):e156821. doi: 10.1172/JCI156821

32. Thommen DS, Koelzer VH, Herzig P, Roller A, Trefny M, Dimeloe S, et al. A transcriptionally and functionally distinct PD-1(+) CD8(+) T cell pool with predictive potential in non-small-cell lung cancer treated with PD-1 blockade. *Nat Med* (2018) 24(7):994–1004. doi: 10.1038/s41591-018-0057-z

33. Nan H, Zhou L, Liang W, Meng J, Lin K, Li M, et al. Epigenetically associated CCL20 upregulation correlates with esophageal cancer progression and immune disorder. *Pathol Res Pract* (2021) 228:153683. doi: 10.1016/j.prp.2021.153683

34. Han L, Chen S, Chen Z, Zhou B, Zheng Y, Shen L. Interleukin 32 promotes Foxp3(+) treg cell development and CD8(+) T cell function in human esophageal squamous cell carcinoma microenvironment. *Front Cell Dev Biol* (2021) 9:704853. doi: 10.3389/fcell.2021.704853

35. Yoshioka T, Miyamoto M, Cho Y, Ishikawa K, Tsuchikawa T, Kadoya M, et al. Infiltrating regulatory T cell numbers is not a factor to predict patient's survival in oesophageal squamous cell carcinoma. *Br J Cancer* (2008) 98(7):1258–63. doi: 10.1038/sj.bjc.6604294

36. Simoni Y, Becht E, Fehlings M, Loh CY, Koo SL, Teng KWW, et al. Bystander CD8(+) T cells are abundant and phenotypically distinct in human tumour infiltrates. *Nature* (2018) 557(7706):575–9. doi: 10.1038/s41586-018-0130-2

37. Heylmann D, Ponath V, Kindler T, Kaina B. Comparison of DNA repair and radiosensitivity of different blood cell populations. *Sci Rep* (2021) 11(1):2478. doi: 10.1038/s41598-021-81058-1

38. Yan C, Ma X, Guo Z, Wei X, Han D, Zhang T, et al. Time-spatial analysis of T cell receptor repertoire in esophageal squamous cell carcinoma patients treated with combined radiotherapy and PD-1 blockade. *Oncoimmunology* (2022) 11(1):2025668. doi: 10.1080/2162402X.2022.2025668

39. Han J, Yu R, Duan J, Li J, Zhao W, Feng G, et al. Weighting tumor-specific TCR repertoires as a classifier to stratify the immunotherapy delivery in non-small cell lung cancers. *Sci Adv* (2021) 7(21):eabd6971. doi: 10.1126/sciadv.abd6971

40. Han J, Duan J, Bai H, Wang Y, Wan R, Wang X, et al. TCR repertoire diversity of peripheral PD-1(+)CD8(+) T cells predicts clinical outcomes after immunotherapy in patients with non-small cell lung cancer. *Cancer Immunol Res* (2020) 8(1):146–54. doi: 10.1158/2326-6066.CIR-19-0398

41. Yue Y, Lian J, Wang T, Luo C, Yuan Y, Qin G, et al. Interleukin-33-nuclear factor-kappaB-CCL2 signaling pathway promotes progression of esophageal squamous cell carcinoma by directing regulatory T cells. *Cancer Sci* (2020) 111(3):795–806. doi: 10.1111/cas.14293

42. Lu L, Weng C, Mao H, Fang X, Liu X, Wu Y, et al. IL-17A promotes migration and tumor killing capability of b cells in esophageal squamous cell carcinoma. *Oncotarget* (2016) 7(16):21853–64. doi: 10.18632/oncotarget.7869

43. Yang H, Zhang Q, Xu M, Wang L, Chen X, Feng Y, et al. CCL2-CCR2 axis recruits tumor associated macrophages to induce immune evasion through PD-1 signaling in esophageal carcinogenesis. *Mol Cancer* (2020) 19(1):41. doi: 10.1186/s12943-020-01165-x

44. Kretschmer I, Freudenberger T, Twarock S, Yamaguchi Y, Grandoch M, Fischer JW. Esophageal squamous cell carcinoma cells modulate chemokine expression and hyaluronan synthesis in fibroblasts. *J Biol Chem* (2016) 291(8):4091–106. doi: 10.1074/jbc.M115.708909

45. Lauret Marie Joseph E, Kirilovsky A, Lecoester B, El Sissy C, Boullerot L, Rangan L, et al. Chemoradiation triggers antitumor Th1 and tissue resident memory-polarized immune responses to improve immune checkpoint inhibitors therapy. *J Immunother Cancer* (2021) 9(7):e002256. doi: 10.1136/jitc-2020-002256

46. Hanoteau A, Newton JM, Krupar R, Huang C, Liu HC, Gaspero A, et al. Tumor microenvironment modulation enhances immunologic benefit of chemoradiotherapy. *J Immunother Cancer* (2019) 7(1):10. doi: 10.1186/s40425-018-0485-9

47. Lurje I, Hammerich L, Tacke F. Dendritic cell and T cell crosstalk in liver fibrogenesis and hepatocarcinogenesis: implications for prevention and therapy of liver cancer. *Int J Mol Sci* (2020) 21(19):7378. doi: 10.3390/ijms21197378

48. Zhang L, Li Z, Skrzypczynska KM, Fang Q, Zhang W, O'Brien SA, et al. Single-cell analyses inform mechanisms of myeloid-targeted therapies in colon cancer. *Cell* (2020) 181(2):442–45.e29. doi: 10.1016/j.cell.2020.03.048

49. Cui K, Hu S, Mei X, Cheng M. Innate immune cells in the esophageal tumor microenvironment. *Front Immunol* (2021) 12:654731. doi: 10.3389/fimmu.2021.654731

50. Tcyganov E, Mastio J, Chen E, Gabrilovich DI. Plasticity of myeloid-derived suppressor cells in cancer. *Curr Opin Immunol* (2018) 51:76–82. doi: 10.1016/j.coi.2018.03.009

51. De Sanctis F, Adamo A, Cane S, Ugel S. Targeting tumour-reprogrammed myeloid cells: the new battleground in cancer immunotherapy. *Semin Immunopathol* (2022) 45(2):1–24. doi: 10.1007/s00281-022-00965-1

52. Christofides A, Strauss L, Yeo A, Cao C, Charest A, Boussiotis VA. The complex role of tumor-infiltrating macrophages. *Nat Immunol* (2022) 23(8):1148–56. doi: 10.1038/s41590-022-01267-2

53. Sholl LM, Hirsch FR, Hwang D, Botling J, Lopez-Rios F, Bubendorf L, et al. The promises and challenges of tumor mutation burden as an immunotherapy biomarker: a

perspective from the international association for the study of lung cancer pathology committee. *J Thorac Oncol* (2020) 15(9):1409–24. doi: 10.1016/j.jtho.2020.05.019

54. Xu X, Wang Y, Bai Y, Lu J, Guo Y, Wang X, et al. Identifying key mutations of radioresponsive genes in esophageal squamous cell carcinoma. *Front Immunol* (2022) 13:1001173. doi: 10.3389/fimmu.2022.1001173

55. Wei M, Zhao L, Lv J, Li X, Zhou G, Fan B, et al. The mediation effect of serum metabolites on the relationship between long-term smoking exposure and esophageal squamous cell carcinoma. *BMC Cancer* (2021) 21(1):415. doi: 10.1186/s12885-021-08151-6

56. Wang G, Ye M, Zheng S, Wu K, Geng H, Liu C. Cigarette smoke extract induces H19 in esophageal squamous cell carcinoma in smoking patients: based on a chronic exposed cell model. *Toxicol Lett* (2020) 333:62–70. doi: 10.1016/j.toxlet.2020.07.030

57. Wu XC, Zheng YF, Tang M, Li XF, Zeng R, Zhang JR. Association between smoking and p53 mutation in oesophageal squamous cell carcinoma: a meta-analysis. *Clin Oncol (R Coll Radiol)* (2015) 27(6):337–44. doi: 10.1016/j.clon.2015.02.007

58. Yao W, Qin X, Qi B, Lu J, Guo L, Liu F, et al. Association of p53 expression with prognosis in patients with esophageal squamous cell carcinoma. *Int J Clin Exp Pathol* (2014) 7(10):7158–63.

59. Wu S, Zhang L, Deng J, Guo B, Li F, Wang Y, et al. A novel micropeptide encoded by y-linked LINC00278 links cigarette smoking and AR signaling in Male esophageal squamous cell carcinoma. *Cancer Res* (2020) 80(13):2790–803. doi: 10.1158/0008-5472.CAN-19-3440

60. Liu J, Chen SJ, Hsu SW, Zhang J, Li JM, Yang DC, et al. MARCKS cooperates with NKAP to activate NF-kB signaling in smoke-related lung cancer. *Theranostics* (2021) 11(9):4122–36. doi: 10.7150/thno.53558

Frontiers in Immunology

Explores novel approaches and diagnoses to treat immune disorders.

The official journal of the International Union of Immunological Societies (IUIS) and the most cited in its field, leading the way for research across basic, translational and clinical immunology.

Discover the latest Research Topics

See more →

Frontiers

Avenue du Tribunal-Fédéral 34
1005 Lausanne, Switzerland
frontiersin.org

Contact us

+41 (0)21 510 17 00
frontiersin.org/about/contact

Community series in combining chemo/radio therapy and immunotherapy for cancers—perfect mix of old and new - volume II

Topic editors

Jian Zhang — Southern Medical University, China

Linlang Guo — Zhujiang hospital, China

Feng-Ming (Spring) Kong — The University of Hong Kong, Hong Kong, SAR China

Clare Y. Slaney — Peter MacCallum Cancer Centre, Australia

Citation

Zhang, J., Guo, L., Kong, F.-M., Slaney, C. Y., eds. (2023). *Community series in combining chemo/radio therapy and immunotherapy for cancers—perfect mix of old and new - volume II*. Lausanne: Frontiers Media SA.

doi: 10.3389/978-2-8325-3227-0

Table of contents

07 Crosstalk of RNA Adenosine Modification-Related Subtypes, Establishment of a Prognostic Model, and Immune Infiltration Characteristics in Ovarian Cancer
Xiaoge Ni, Can Chen, Guoliang Cui, Wei Ding and Jinhui Liu

26 CD8+ T cell trajectory subtypes decode tumor heterogeneity and provide treatment recommendations for hepatocellular carcinoma
Long Liu, Zaoqu Liu, Jie Gao, Xudong Liu, Siyuan Weng, Chunguang Guo, Bowen Hu, Zhihui Wang, Jiakai Zhang, Jihua Shi, Wenzhi Guo and Shuijun Zhang

43 Identification of a novel cuproptosis-related gene signature and integrative analyses in patients with lower-grade gliomas
Jia-hao Bao, Wei-cheng Lu, Hao Duan, Ya-qi Ye, Jiang-bo Li, Wen-ting Liao, Yong-chun Li and Yang-peng Sun

69 Integrated driver mutations profile of chinese gastrointestinal-natural killer/T-cell lymphoma
Shanshan Li, Tingzhi Liu, Hailing Liu, Xiaohui Zhai, Taiyuan Cao, Hongen Yu, Wanjia Hong, Xiaoru Lin, Ming Li, Yan Huang and Jian Xiao

81 An open, observational, three-arm clinical study of 2–3 cycles of treatment as neoadjuvant therapy in operable locally advanced non-small cell lung cancer: An interim analysis
Linping Gu, Xue Wang, Yile Sun, Yunhua Xu, Xiaomin Niu, Ruiying Zhao, Yaxian Yao, Hong Jian, Yuchen Han, Jinwang Wei, Zhiwei Chen and Shun Lu

92 Robust pyroptosis risk score guides the treatment options and predicts the prognosis of bladder carcinoma
Dingshan Deng, Fenglian Liu, Zhi Liu, Zuowei Wu, Yunbo He, ChunYu Zhang, Xiongbin Zu, Zhenyu Ou and Yongjie Wang

111 Definition of a new blood cell count score for early survival prediction for non-small cell lung cancer patients treated with atezolizumab: Integrated analysis of four multicenter clinical trials
Jian-Guo Zhou, Ada Hang-Heng Wong, Haitao Wang, Su-Han Jin, Fangya Tan, Yu-Zhong Chen, Si-Si He, Gang Shen, Benjamin Frey, Rainer Fietkau, Markus Hecht, Shamus R. Carr, Ruihong Wang, Bo Shen, David S. Schrump, Hu Ma and Udo S. Gaipl

122 Integrated genomic, transcriptomic, and epigenetic analyses identify a leukotriene synthesis-related M2 macrophage gene signature that predicts prognosis and treatment vulnerability in gliomas
Hang Ji, Zhihui Liu, Nan Wang, Jiaqi Jin, Jiheng Zhang, Jiawei Dong, Fang Wang, Xiuwei Yan, Qin Gong, Hongtao Zhao, Haogeng Sun, Yongzhe Li, Shaoshan Hu and Chao You

139 Novel macrophage-related gene prognostic index for glioblastoma associated with M2 macrophages and T cell dysfunction
Hang Ji, Zhihui Liu, Fang Wang, Haogeng Sun, Nan Wang, Yi Liu, Shaoshan Hu and Chao You

155 Combining autophagy and immune characterizations to predict prognosis and therapeutic response in lung adenocarcinoma
Qiaxuan Li, Daipeng Xie, Lintong Yao, Hongrui Qiu, Peimeng You, Jialong Deng, Congsen Li, Weijie Zhan, Maotao Weng, Shaowei Wu, Fasheng Li, Yubo Zhou, Fanjun Zeng, Yong Zheng and Haiyu Zhou

174 Radiotherapy improves the outcomes of immunotherapy with Sintilimab in non-small-cell lung cancer: A real-world analysis
Shuling Li, Kuifei Chen, Meiwen Yang, Swe Swe Hlaing, Meng Chen, Pinjun Gu, Yinnan Meng and Haihua Yang

186 Identification of four immune subtypes in locally advanced rectal cancer treated with neoadjuvant chemotherapy for predicting the efficacy of subsequent immune checkpoint blockade
Le He, Min Jin, Dan Jian, Bo Yang, Nan Dai, Yan Feng, He Xiao and Dong Wang

198 A novel medication decision gene signature predicts response to individualized therapy and prognosis outcomes in hepatocellular carcinoma patients
Jingsheng Yuan, Zijian Liu, Zhenru Wu, Lvnan Yan, Jiayin Yang and Yujun Shi

216 A prognostic signature consisting of metabolism-related genes and SLC17A4 serves as a potential biomarker of immunotherapeutic prediction in prostate cancer
He Li, Jie Gu, Yuqiu Tian, Shuyu Li, Hao Zhang, Ziyu Dai, Zeyu Wang, Nan Zhang and Renjun Peng

235 Low-dose immunogenic chemotherapeutics promotes immune checkpoint blockade in microsatellite stability colon cancer
Yuhang Fang, Haoyu Sun, Xinghui Xiao, Maoxing Tang, Zhigang Tian, Haiming Wei, Rui Sun and Xiaodong Zheng

248 Toxicity profile of combined immune checkpoint inhibitors and thoracic radiotherapy in esophageal cancer: A meta-analysis and systematic review
Tongzhen Xu, Yunsong Liu, Xiaotong Lu and Jun Liang

260 Photodynamic therapy improves the clinical efficacy of advanced colorectal cancer and recruits immune cells into the tumor immune microenvironment
Baohong Gu, Bofang Wang, Xuemei Li, Zedong Feng, Chenhui Ma, Lei Gao, Yang Yu, Jing Zhang, Peng Zheng, Yunpeng Wang, Haiyuan Li, Tao Zhang and Hao Chen

275 Identification of fatty acid metabolism–related molecular subtype biomarkers and their correlation with immune checkpoints in cutaneous melanoma
Yujian Xu, Youbai Chen, Weiqian Jiang, Xiangye Yin, Dongsheng Chen, Yuan Chi, Yuting Wang, Julei Zhang, Qixu Zhang and Yan Han

292 Crosstalk of angiogenesis-related subtypes, establishment of a prognostic signature and immune infiltration characteristics in colorectal adenocarcinoma
Guoliang Cui, Jinhui Liu, Manli Wang, Kinyu Shon, Can Wang, Fei Wei and Zhiguang Sun

309 MYCBP2 expression correlated with inflammatory cell infiltration and prognosis immunotherapy in thyroid cancer patients
Guilin Wang, Chen Miao, Lijun Mo, Ulf D. Kahlert, Jinfeng Wu, Minglin Ou, Renxiang Huang, Ruifa Feng, Weiyi Pang and Wenjie Shi

321 IP-score correlated to endogenous tumour antigen peptide processing: A candidate clinical response score algorithm of immune checkpoint inhibitors therapy in multiple cohorts
Yutao Wang, Kexin Yan, Ye Guo, Yi Lu, Hao Su and Hongjun Li

338 The application basis of immuno-checkpoint inhibitors combined with chemotherapy in cancer treatment
Ming-Yan Shi, Han-Ge Liu, Xiao-Hong Chen, Ye Tian, Zhi-Nan Chen and Ke Wang

347 Effects of chemotherapy and immunotherapy on microbial diversity in TME and engineered bacterial-mediated tumor therapy
Heng Zheng, Xianxian Chen, Qiyang Li, Yuqi Liu and Jinzhong Cai

356 Predictive value of ^{18}F-FDG PET/CT for evaluating the response to hypofractionated radiotherapy combined with PD-1 blockade in non-small cell lung cancer
Shan Tang, Yan Zhang, Yunfei Li, Yan Zhang, Yuke Xu, Haoyuan Ding, Yue Chen, Peirong Ren, Hua Ye, Shaozhi Fu and Sheng Lin

368 Pre-immunotherapy radiotherapy enhanced the efficacy of multi-line sintilimab in unresectable advanced esophageal squamous cell carcinoma
Shuhui Xu, Xianxing Xu and Hui Zhu

376 Combining chemotherapy with CAR-T cell therapy in treating solid tumors
Arthur Xuan Wang, Xiao Jing Ong, Criselle D'Souza, Paul J. Neeson and Joe Jiang Zhu

387 Tumor immune microenvironment changes are associated with response to neoadjuvant chemotherapy and long-term survival benefits in advanced epithelial ovarian cancer: A pilot study
Guangming Cao, Dingchao Hua, Jinfeng Li, Xuefang Zhang, Zhiqiang Zhang, Bei Zhang, Ting Bei, Lina Cui, Shiqing Chen, Shuzhen Wang and Lei Zhu

397 Total neoadjuvant treatment and PD-1/PD-L1 checkpoint inhibitor in locally advanced rectal cancer
Weiwei Xiao, Huilong Luo, Ye Yao, Yaqin Wang, Shuang Liu, Rui Sun and Gong Chen

408 Efficacy and safety of combined immunotherapy and stereotactic radiosurgery in NSCLCBM patients and a novel prognostic nomogram: A real-world study
Shoaib Bashir, Lei Wen, Ping Zhang, Minting Ye, Yin Li, Weiping Hong, Junjie Zhen, Mingyao Lai, Hui Wang, Yanying Yang, Xingrui Chen, Rishun Luo, Guoxia Jia, Yao Guo, Linbo Cai and Meng Xu

426 Demethylating therapy increases cytotoxicity of CD44v6 CAR-T cells against acute myeloid leukemia
Ling Tang, Yingjie Kong, Haobing Wang, Ping Zou, Ting Sun, Ying Liu, Juan Zhang, Na Jin, Hanwen Mao, Xiaojian Zhu, Jue Wang, Fankai Meng and Yong You

441 Spatial distribution of tumor-infiltrating T cells indicated immune response status under chemoradiotherapy plus PD-1 blockade in esophageal cancer
Cihui Yan, Hui Huang, Zhunhao Zheng, Xiaoxue Ma, Gang Zhao, Tian Zhang, Xi Chen, Fuliang Cao, Hui Wei, Jie Dong, Peng Tang, Hongjing Jiang, Meng Wang, Ping Wang, Qingsong Pang and Wencheng Zhang

Frontiers in Immunology

Explores novel approaches and diagnoses to treat immune disorders.

The official journal of the International Union of Immunological Societies (IUIS) and the most cited in its field, leading the way for research across basic, translational and clinical immunology.

Discover the latest Research Topics

See more →

Frontiers

Avenue du Tribunal-Fédéral 34
1005 Lausanne, Switzerland
frontiersin.org

Contact us

+41 (0)21 510 17 00
frontiersin.org/about/contact

frontiers | Research Topics

Community series in combining chemo/radio therapy and immunotherapy for cancers—perfect mix of old and new, volume II

Edited by
Jian Zhang, Linlang Guo, Feng-Ming (Spring) Kong and Clare Y. Slaney

Published in
Frontiers in Immunology
Frontiers in Oncology

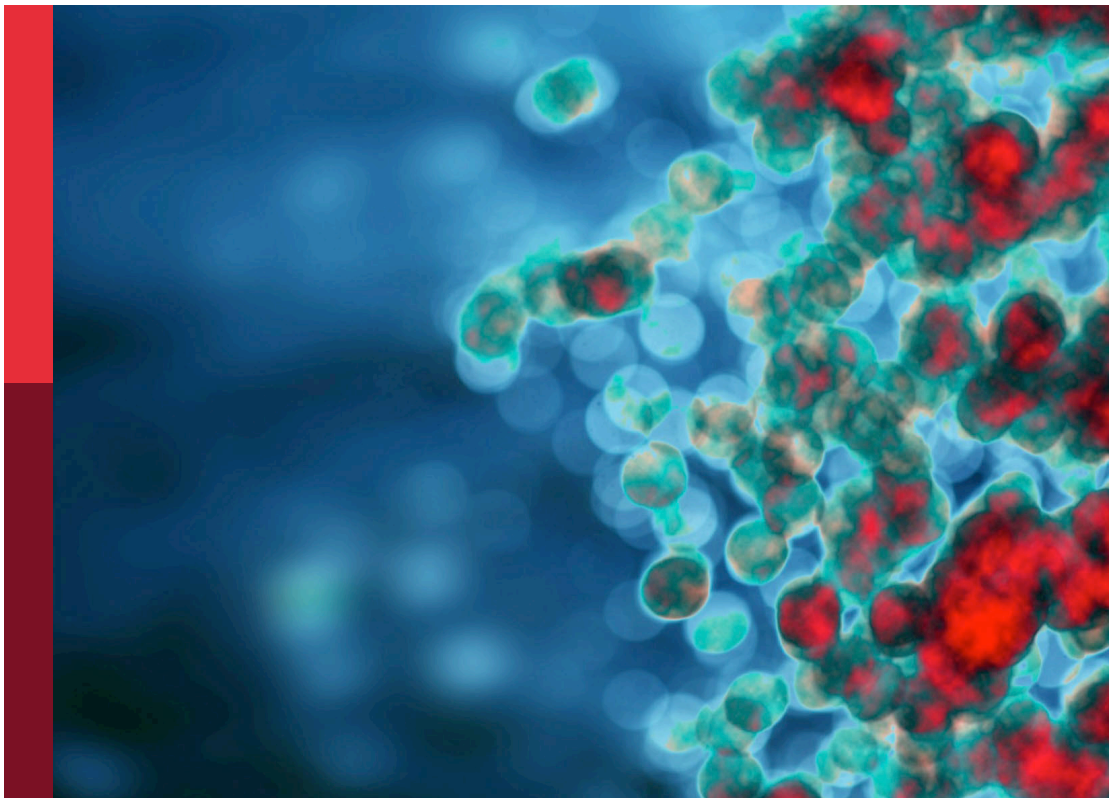

Community series in combining chemo/radio therapy and immunotherapy for cancers—perfect mix of old and new - volume II

Topic editors

Jian Zhang — Southern Medical University, China

Linlang Guo — Zhujiang hospital, China

Feng-Ming (Spring) Kong — The University of Hong Kong, Hong Kong, SAR China

Clare Y. Slaney — Peter MacCallum Cancer Centre, Australia

Citation

Zhang, J., Guo, L., Kong, F.-M., Slaney, C. Y., eds. (2023). *Community series in combining chemo/radio therapy and immunotherapy for cancers—perfect mix of old and new - volume II*. Lausanne: Frontiers Media SA.

doi: 10.3389/978-2-8325-3227-0

Table of contents

07 Crosstalk of RNA Adenosine Modification-Related Subtypes, Establishment of a Prognostic Model, and Immune Infiltration Characteristics in Ovarian Cancer
Xiaoge Ni, Can Chen, Guoliang Cui, Wei Ding and Jinhui Liu

26 CD8+ T cell trajectory subtypes decode tumor heterogeneity and provide treatment recommendations for hepatocellular carcinoma
Long Liu, Zaoqu Liu, Jie Gao, Xudong Liu, Siyuan Weng, Chunguang Guo, Bowen Hu, Zhihui Wang, Jiakai Zhang, Jihua Shi, Wenzhi Guo and Shuijun Zhang

43 Identification of a novel cuproptosis-related gene signature and integrative analyses in patients with lower-grade gliomas
Jia-hao Bao, Wei-cheng Lu, Hao Duan, Ya-qi Ye, Jiang-bo Li, Wen-ting Liao, Yong-chun Li and Yang-peng Sun

69 Integrated driver mutations profile of chinese gastrointestinal-natural killer/T-cell lymphoma
Shanshan Li, Tingzhi Liu, Hailing Liu, Xiaohui Zhai, Taiyuan Cao, Hongen Yu, Wanjia Hong, Xiaoru Lin, Ming Li, Yan Huang and Jian Xiao

81 An open, observational, three-arm clinical study of 2–3 cycles of treatment as neoadjuvant therapy in operable locally advanced non-small cell lung cancer: An interim analysis
Linping Gu, Xue Wang, Yile Sun, Yunhua Xu, Xiaomin Niu, Ruiying Zhao, Yaxian Yao, Hong Jian, Yuchen Han, Jinwang Wei, Zhiwei Chen and Shun Lu

92 Robust pyroptosis risk score guides the treatment options and predicts the prognosis of bladder carcinoma
Dingshan Deng, Fenglian Liu, Zhi Liu, Zuowei Wu, Yunbo He, ChunYu Zhang, Xiongbin Zu, Zhenyu Ou and Yongjie Wang

111 Definition of a new blood cell count score for early survival prediction for non-small cell lung cancer patients treated with atezolizumab: Integrated analysis of four multicenter clinical trials
Jian-Guo Zhou, Ada Hang-Heng Wong, Haitao Wang, Su-Han Jin, Fangya Tan, Yu-Zhong Chen, Si-Si He, Gang Shen, Benjamin Frey, Rainer Fietkau, Markus Hecht, Shamus R. Carr, Ruihong Wang, Bo Shen, David S. Schrump, Hu Ma and Udo S. Gaipl

122 Integrated genomic, transcriptomic, and epigenetic analyses identify a leukotriene synthesis-related M2 macrophage gene signature that predicts prognosis and treatment vulnerability in gliomas
Hang Ji, Zhihui Liu, Nan Wang, Jiaqi Jin, Jiheng Zhang, Jiawei Dong, Fang Wang, Xiuwei Yan, Qin Gong, Hongtao Zhao, Haogeng Sun, Yongzhe Li, Shaoshan Hu and Chao You

139 Novel macrophage-related gene prognostic index for glioblastoma associated with M2 macrophages and T cell dysfunction
Hang Ji, Zhihui Liu, Fang Wang, Haogeng Sun, Nan Wang, Yi Liu, Shaoshan Hu and Chao You

155 Combining autophagy and immune characterizations to predict prognosis and therapeutic response in lung adenocarcinoma
Qiaxuan Li, Daipeng Xie, Lintong Yao, Hongrui Qiu, Peimeng You, Jialong Deng, Congsen Li, Weijie Zhan, Maotao Weng, Shaowei Wu, Fasheng Li, Yubo Zhou, Fanjun Zeng, Yong Zheng and Haiyu Zhou

174 Radiotherapy improves the outcomes of immunotherapy with Sintilimab in non-small-cell lung cancer: A real-world analysis
Shuling Li, Kuifei Chen, Meiwen Yang, Swe Swe Hlaing, Meng Chen, Pinjun Gu, Yinnan Meng and Haihua Yang

186 Identification of four immune subtypes in locally advanced rectal cancer treated with neoadjuvant chemotherapy for predicting the efficacy of subsequent immune checkpoint blockade
Le He, Min Jin, Dan Jian, Bo Yang, Nan Dai, Yan Feng, He Xiao and Dong Wang

198 A novel medication decision gene signature predicts response to individualized therapy and prognosis outcomes in hepatocellular carcinoma patients
Jingsheng Yuan, Zijian Liu, Zhenru Wu, Lvnan Yan, Jiayin Yang and Yujun Shi

216 A prognostic signature consisting of metabolism-related genes and SLC17A4 serves as a potential biomarker of immunotherapeutic prediction in prostate cancer
He Li, Jie Gu, Yuqiu Tian, Shuyu Li, Hao Zhang, Ziyu Dai, Zeyu Wang, Nan Zhang and Renjun Peng

235 Low-dose immunogenic chemotherapeutics promotes immune checkpoint blockade in microsatellite stability colon cancer
Yuhang Fang, Haoyu Sun, Xinghui Xiao, Maoxing Tang, Zhigang Tian, Haiming Wei, Rui Sun and Xiaodong Zheng

248 Toxicity profile of combined immune checkpoint inhibitors and thoracic radiotherapy in esophageal cancer: A meta-analysis and systematic review
Tongzhen Xu, Yunsong Liu, Xiaotong Lu and Jun Liang

260 Photodynamic therapy improves the clinical efficacy of advanced colorectal cancer and recruits immune cells into the tumor immune microenvironment
Baohong Gu, Bofang Wang, Xuemei Li, Zedong Feng, Chenhui Ma, Lei Gao, Yang Yu, Jing Zhang, Peng Zheng, Yunpeng Wang, Haiyuan Li, Tao Zhang and Hao Chen

275 Identification of fatty acid metabolism–related molecular subtype biomarkers and their correlation with immune checkpoints in cutaneous melanoma
Yujian Xu, Youbai Chen, Weiqian Jiang, Xiangye Yin, Dongsheng Chen, Yuan Chi, Yuting Wang, Julei Zhang, Qixu Zhang and Yan Han

292 Crosstalk of angiogenesis-related subtypes, establishment of a prognostic signature and immune infiltration characteristics in colorectal adenocarcinoma
Guoliang Cui, Jinhui Liu, Manli Wang, Kinyu Shon, Can Wang, Fei Wei and Zhiguang Sun

309 MYCBP2 expression correlated with inflammatory cell infiltration and prognosis immunotherapy in thyroid cancer patients
Guilin Wang, Chen Miao, Lijun Mo, Ulf D. Kahlert, Jinfeng Wu, Minglin Ou, Renxiang Huang, Ruifa Feng, Weiyi Pang and Wenjie Shi

321 IP-score correlated to endogenous tumour antigen peptide processing: A candidate clinical response score algorithm of immune checkpoint inhibitors therapy in multiple cohorts
Yutao Wang, Kexin Yan, Ye Guo, Yi Lu, Hao Su and Hongjun Li

338 The application basis of immuno-checkpoint inhibitors combined with chemotherapy in cancer treatment
Ming-Yan Shi, Han-Ge Liu, Xiao-Hong Chen, Ye Tian, Zhi-Nan Chen and Ke Wang

347 Effects of chemotherapy and immunotherapy on microbial diversity in TME and engineered bacterial-mediated tumor therapy
Heng Zheng, Xianxian Chen, Qiyang Li, Yuqi Liu and Jinzhong Cai

356 Predictive value of ^{18}F-FDG PET/CT for evaluating the response to hypofractionated radiotherapy combined with PD-1 blockade in non-small cell lung cancer
Shan Tang, Yan Zhang, Yunfei Li, Yan Zhang, Yuke Xu, Haoyuan Ding, Yue Chen, Peirong Ren, Hua Ye, Shaozhi Fu and Sheng Lin

368 Pre-immunotherapy radiotherapy enhanced the efficacy of multi-line sintilimab in unresectable advanced esophageal squamous cell carcinoma
Shuhui Xu, Xianxing Xu and Hui Zhu

376 Combining chemotherapy with CAR-T cell therapy in treating solid tumors
Arthur Xuan Wang, Xiao Jing Ong, Criselle D'Souza, Paul J. Neeson and Joe Jiang Zhu

387 Tumor immune microenvironment changes are associated with response to neoadjuvant chemotherapy and long-term survival benefits in advanced epithelial ovarian cancer: A pilot study
Guangming Cao, Dingchao Hua, Jinfeng Li, Xuefang Zhang, Zhiqiang Zhang, Bei Zhang, Ting Bei, Lina Cui, Shiqing Chen, Shuzhen Wang and Lei Zhu

397 Total neoadjuvant treatment and PD-1/PD-L1 checkpoint inhibitor in locally advanced rectal cancer
Weiwei Xiao, Huilong Luo, Ye Yao, Yaqin Wang, Shuang Liu, Rui Sun and Gong Chen

408 Efficacy and safety of combined immunotherapy and stereotactic radiosurgery in NSCLCBM patients and a novel prognostic nomogram: A real-world study
Shoaib Bashir, Lei Wen, Ping Zhang, Minting Ye, Yin Li, Weiping Hong, Junjie Zhen, Mingyao Lai, Hui Wang, Yanying Yang, Xingrui Chen, Rishun Luo, Guoxia Jia, Yao Guo, Linbo Cai and Meng Xu

426 Demethylating therapy increases cytotoxicity of CD44v6 CAR-T cells against acute myeloid leukemia
Ling Tang, Yingjie Kong, Haobing Wang, Ping Zou, Ting Sun, Ying Liu, Juan Zhang, Na Jin, Hanwen Mao, Xiaojian Zhu, Jue Wang, Fankai Meng and Yong You

441 Spatial distribution of tumor-infiltrating T cells indicated immune response status under chemoradiotherapy plus PD-1 blockade in esophageal cancer
Cihui Yan, Hui Huang, Zhunhao Zheng, Xiaoxue Ma, Gang Zhao, Tian Zhang, Xi Chen, Fuliang Cao, Hui Wei, Jie Dong, Peng Tang, Hongjing Jiang, Meng Wang, Ping Wang, Qingsong Pang and Wencheng Zhang

Frontiers in Immunology

Explores novel approaches and diagnoses to treat immune disorders.

The official journal of the International Union of Immunological Societies (IUIS) and the most cited in its field, leading the way for research across basic, translational and clinical immunology.

Discover the latest Research Topics

See more →

Frontiers

Avenue du Tribunal-Fédéral 34
1005 Lausanne, Switzerland
frontiersin.org

Contact us

+41 (0)21 510 17 00
frontiersin.org/about/contact

Community series in combining chemo/radio therapy and immunotherapy for cancers—perfect mix of old and new - volume II

Topic editors

Jian Zhang — Southern Medical University, China

Linlang Guo — Zhujiang hospital, China

Feng-Ming (Spring) Kong — The University of Hong Kong, Hong Kong, SAR China

Clare Y. Slaney — Peter MacCallum Cancer Centre, Australia

Citation

Zhang, J., Guo, L., Kong, F.-M., Slaney, C. Y., eds. (2023). *Community series in combining chemo/radio therapy and immunotherapy for cancers—perfect mix of old and new - volume II*. Lausanne: Frontiers Media SA.

doi: 10.3389/978-2-8325-3227-0

Table of contents

07 Crosstalk of RNA Adenosine Modification-Related Subtypes, Establishment of a Prognostic Model, and Immune Infiltration Characteristics in Ovarian Cancer
Xiaoge Ni, Can Chen, Guoliang Cui, Wei Ding and Jinhui Liu

26 CD8+ T cell trajectory subtypes decode tumor heterogeneity and provide treatment recommendations for hepatocellular carcinoma
Long Liu, Zaoqu Liu, Jie Gao, Xudong Liu, Siyuan Weng, Chunguang Guo, Bowen Hu, Zhihui Wang, Jiakai Zhang, Jihua Shi, Wenzhi Guo and Shuijun Zhang

43 Identification of a novel cuproptosis-related gene signature and integrative analyses in patients with lower-grade gliomas
Jia-hao Bao, Wei-cheng Lu, Hao Duan, Ya-qi Ye, Jiang-bo Li, Wen-ting Liao, Yong-chun Li and Yang-peng Sun

69 Integrated driver mutations profile of chinese gastrointestinal-natural killer/T-cell lymphoma
Shanshan Li, Tingzhi Liu, Hailing Liu, Xiaohui Zhai, Taiyuan Cao, Hongen Yu, Wanjia Hong, Xiaoru Lin, Ming Li, Yan Huang and Jian Xiao

81 An open, observational, three-arm clinical study of 2–3 cycles of treatment as neoadjuvant therapy in operable locally advanced non-small cell lung cancer: An interim analysis
Linping Gu, Xue Wang, Yile Sun, Yunhua Xu, Xiaomin Niu, Ruiying Zhao, Yaxian Yao, Hong Jian, Yuchen Han, Jinwang Wei, Zhiwei Chen and Shun Lu

92 Robust pyroptosis risk score guides the treatment options and predicts the prognosis of bladder carcinoma
Dingshan Deng, Fenglian Liu, Zhi Liu, Zuowei Wu, Yunbo He, ChunYu Zhang, Xiongbin Zu, Zhenyu Ou and Yongjie Wang

111 Definition of a new blood cell count score for early survival prediction for non-small cell lung cancer patients treated with atezolizumab: Integrated analysis of four multicenter clinical trials
Jian-Guo Zhou, Ada Hang-Heng Wong, Haitao Wang, Su-Han Jin, Fangya Tan, Yu-Zhong Chen, Si-Si He, Gang Shen, Benjamin Frey, Rainer Fietkau, Markus Hecht, Shamus R. Carr, Ruihong Wang, Bo Shen, David S. Schrump, Hu Ma and Udo S. Gaipl

122 Integrated genomic, transcriptomic, and epigenetic analyses identify a leukotriene synthesis-related M2 macrophage gene signature that predicts prognosis and treatment vulnerability in gliomas
Hang Ji, Zhihui Liu, Nan Wang, Jiaqi Jin, Jiheng Zhang, Jiawei Dong, Fang Wang, Xiuwei Yan, Qin Gong, Hongtao Zhao, Haogeng Sun, Yongzhe Li, Shaoshan Hu and Chao You

139 Novel macrophage-related gene prognostic index for glioblastoma associated with M2 macrophages and T cell dysfunction
Hang Ji, Zhihui Liu, Fang Wang, Haogeng Sun, Nan Wang, Yi Liu, Shaoshan Hu and Chao You

155 Combining autophagy and immune characterizations to predict prognosis and therapeutic response in lung adenocarcinoma
Qiaxuan Li, Daipeng Xie, Lintong Yao, Hongrui Qiu, Peimeng You, Jialong Deng, Congsen Li, Weijie Zhan, Maotao Weng, Shaowei Wu, Fasheng Li, Yubo Zhou, Fanjun Zeng, Yong Zheng and Haiyu Zhou

174 Radiotherapy improves the outcomes of immunotherapy with Sintilimab in non-small-cell lung cancer: A real-world analysis
Shuling Li, Kuifei Chen, Meiwen Yang, Swe Swe Hlaing, Meng Chen, Pinjun Gu, Yinnan Meng and Haihua Yang

186 Identification of four immune subtypes in locally advanced rectal cancer treated with neoadjuvant chemotherapy for predicting the efficacy of subsequent immune checkpoint blockade
Le He, Min Jin, Dan Jian, Bo Yang, Nan Dai, Yan Feng, He Xiao and Dong Wang

198 A novel medication decision gene signature predicts response to individualized therapy and prognosis outcomes in hepatocellular carcinoma patients
Jingsheng Yuan, Zijian Liu, Zhenru Wu, Lvnan Yan, Jiayin Yang and Yujun Shi

216 A prognostic signature consisting of metabolism-related genes and SLC17A4 serves as a potential biomarker of immunotherapeutic prediction in prostate cancer
He Li, Jie Gu, Yuqiu Tian, Shuyu Li, Hao Zhang, Ziyu Dai, Zeyu Wang, Nan Zhang and Renjun Peng

235 Low-dose immunogenic chemotherapeutics promotes immune checkpoint blockade in microsatellite stability colon cancer
Yuhang Fang, Haoyu Sun, Xinghui Xiao, Maoxing Tang, Zhigang Tian, Haiming Wei, Rui Sun and Xiaodong Zheng

248 Toxicity profile of combined immune checkpoint inhibitors and thoracic radiotherapy in esophageal cancer: A meta-analysis and systematic review
Tongzhen Xu, Yunsong Liu, Xiaotong Lu and Jun Liang

260 Photodynamic therapy improves the clinical efficacy of advanced colorectal cancer and recruits immune cells into the tumor immune microenvironment
Baohong Gu, Bofang Wang, Xuemei Li, Zedong Feng, Chenhui Ma, Lei Gao, Yang Yu, Jing Zhang, Peng Zheng, Yunpeng Wang, Haiyuan Li, Tao Zhang and Hao Chen

275 Identification of fatty acid metabolism–related molecular subtype biomarkers and their correlation with immune checkpoints in cutaneous melanoma
Yujian Xu, Youbai Chen, Weiqian Jiang, Xiangye Yin, Dongsheng Chen, Yuan Chi, Yuting Wang, Julei Zhang, Qixu Zhang and Yan Han

292 Crosstalk of angiogenesis-related subtypes, establishment of a prognostic signature and immune infiltration characteristics in colorectal adenocarcinoma
Guoliang Cui, Jinhui Liu, Manli Wang, Kinyu Shon, Can Wang, Fei Wei and Zhiguang Sun

309 MYCBP2 expression correlated with inflammatory cell infiltration and prognosis immunotherapy in thyroid cancer patients
Guilin Wang, Chen Miao, Lijun Mo, Ulf D. Kahlert, Jinfeng Wu, Minglin Ou, Renxiang Huang, Ruifa Feng, Weiyi Pang and Wenjie Shi

321 IP-score correlated to endogenous tumour antigen peptide processing: A candidate clinical response score algorithm of immune checkpoint inhibitors therapy in multiple cohorts
Yutao Wang, Kexin Yan, Ye Guo, Yi Lu, Hao Su and Hongjun Li

338 The application basis of immuno-checkpoint inhibitors combined with chemotherapy in cancer treatment
Ming-Yan Shi, Han-Ge Liu, Xiao-Hong Chen, Ye Tian, Zhi-Nan Chen and Ke Wang

347 Effects of chemotherapy and immunotherapy on microbial diversity in TME and engineered bacterial-mediated tumor therapy
Heng Zheng, Xianxian Chen, Qiyang Li, Yuqi Liu and Jinzhong Cai

356 Predictive value of ^{18}F-FDG PET/CT for evaluating the response to hypofractionated radiotherapy combined with PD-1 blockade in non-small cell lung cancer
Shan Tang, Yan Zhang, Yunfei Li, Yan Zhang, Yuke Xu, Haoyuan Ding, Yue Chen, Peirong Ren, Hua Ye, Shaozhi Fu and Sheng Lin

368 Pre-immunotherapy radiotherapy enhanced the efficacy of multi-line sintilimab in unresectable advanced esophageal squamous cell carcinoma
Shuhui Xu, Xianxing Xu and Hui Zhu

376 Combining chemotherapy with CAR-T cell therapy in treating solid tumors
Arthur Xuan Wang, Xiao Jing Ong, Criselle D'Souza, Paul J. Neeson and Joe Jiang Zhu

387 Tumor immune microenvironment changes are associated with response to neoadjuvant chemotherapy and long-term survival benefits in advanced epithelial ovarian cancer: A pilot study
Guangming Cao, Dingchao Hua, Jinfeng Li, Xuefang Zhang, Zhiqiang Zhang, Bei Zhang, Ting Bei, Lina Cui, Shiqing Chen, Shuzhen Wang and Lei Zhu

397 Total neoadjuvant treatment and PD-1/PD-L1 checkpoint inhibitor in locally advanced rectal cancer
Weiwei Xiao, Huilong Luo, Ye Yao, Yaqin Wang, Shuang Liu, Rui Sun and Gong Chen

408 Efficacy and safety of combined immunotherapy and stereotactic radiosurgery in NSCLCBM patients and a novel prognostic nomogram: A real-world study
Shoaib Bashir, Lei Wen, Ping Zhang, Minting Ye, Yin Li, Weiping Hong, Junjie Zhen, Mingyao Lai, Hui Wang, Yanying Yang, Xingrui Chen, Rishun Luo, Guoxia Jia, Yao Guo, Linbo Cai and Meng Xu

426 Demethylating therapy increases cytotoxicity of CD44v6 CAR-T cells against acute myeloid leukemia
Ling Tang, Yingjie Kong, Haobing Wang, Ping Zou, Ting Sun, Ying Liu, Juan Zhang, Na Jin, Hanwen Mao, Xiaojian Zhu, Jue Wang, Fankai Meng and Yong You

441 Spatial distribution of tumor-infiltrating T cells indicated immune response status under chemoradiotherapy plus PD-1 blockade in esophageal cancer
Cihui Yan, Hui Huang, Zhunhao Zheng, Xiaoxue Ma, Gang Zhao, Tian Zhang, Xi Chen, Fuliang Cao, Hui Wei, Jie Dong, Peng Tang, Hongjing Jiang, Meng Wang, Ping Wang, Qingsong Pang and Wencheng Zhang